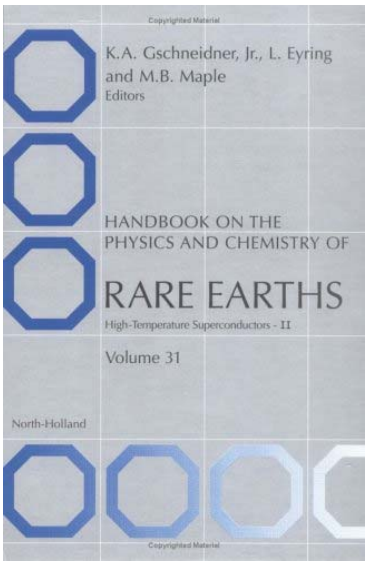

Handbook on the Physics and Chemistry of Rare Earths, volume 31

High-Temperature Superconductors - II

Elsevier, 2001

Edited by: Karl A. Gschneidner, Jr., LeRoy Eyring and M. Brian Maple
ISBN: 978-0-444-50719-8

Handbook on the Physics and Chemistry of Rare Earths
Vol. 31
edited by K.A. Gschneidner, Jr., L. Eyring and M.B. Maple

PREFACE

Karl A. GSCHNEIDNER, Jr., LeRoy EYRING, and M. Brian MAPLE

These elements perplex us in our rearches [sic], *baffle us in our speculations, and haunt us in our very dreams. They stretch like an unknown sea before us – mocking, mystifying, and murmuring strange revelations and possibilities.*

Sir William Crookes (February 16, 1887)

This volume of the Handbook is the second of a two-volume set of reviews devoted to the rare-earth-based high-temperature oxide superconductors (commonly known as hiT_c superconductors). The history of hiT_c superconductors is nearly 15 years old. The initial breakthrough came late in 1986 when Bednorz and Müller published their results which showed that $(La,Ba)_2CuO_{4-y}$ had a superconducting transition of ~30 K, which was about 7 K higher than any other known superconducting material. Within a year the upper temperature limit was raised to nearly 100 K with the discovery of an ~90 K superconducting transition in $YBa_2Cu_3O_{7-x}$. The announcement of a superconductor with a transition temperature higher than the boiling point of liquid nitrogen set-off a frenzy of research on trying to find other oxide hiT_c superconductors. Within a few months the maximum superconducting transition reached 110 K ($Ba_2Sr_2Ca_2Cu_3O_{10}$), and then 122 K ($TlBa_2Ca_3Cu_4O_{11}$). It took several years to push T_c another 11 K to 133 K with the discovery of superconductivity in $HgBa_2Ca_2Cu_3O_8$, which is still the record holder today.

Because of the rapid development of our knowledge of these materials, a review on this topic several years ago would have been hopelessly out of date even before the paper would be sent to the publisher. About five years ago the field began to mature, and we felt it would be a good time to look into the possibility of publishing a series of review papers on rare-earth-containing hiT_c superconductors.

Because of the size of this project and the limited knowledge of the senior editors on this topic, we recruited Professor Brian Maple to assist us in undertaking this task. The result of our efforts have paid off as volumes 30 and 31 of the Handbook series.

In this volume we have ten chapters to complement the eight which appeared in print as volume 30 at the end of 2000.

The first chapter (195), by Emanuel Kaldis, is an extensive review of oxygen nonstoichiometry and lattice effects in $YBa_2Cu_3O_x$ (often referred to as YBCO). As noted

by the author, the oxygen content of YBCO which is significant for structural changes is also important for changes in other properties, i.e. more often than not there is a one-to-one correlation of the superconducting properties with lattice defects. Kaldis points out that many of the difficulties in the preparation and characterization of the high-temperature superconductors is due to the extremely small coherence length in these materials which induces a large sensitivity to nano- and mesoscopic inhomogeneities. On the other hand, this property presents a great advantage for materials research since it can be used as a probe to investigate phase relationships at a very small length scale.

The next chapter (196), by Harald W. Weber, concentrates on flux pinning effects which result in high critical current densities even at high temperatures and in high magnetic fields, i.e. applications of YBCO-based materials near the boiling point of liquid N_2. The influence of chemical substitutions is also reviewed, especially that of Nd. Although the main emphasis is on the characteristics of strong flux pinning, weak flux pinning is also reviewed. The nature of the defects which are responsible for flux pinning is reviewed, including those intentionally introduced by melt-texturing, or developed during the growth process, or artificially induced by suitable types of radiation.

The magnetoresistance and Hall effect in both normal and superconducting states of the cuprate superconductors are reviewed in chapter 197 by Carmen C. Almasan and M. Brian Maple. These measurements address several issues: (1) in the normal state, the temperature dependence of the Hall coefficient and the cotangent of the Hall angle; and (2) in the superconducting state, the temperature dependence of the upper critical field and the irreversibility line, as well as the anomalous sign change of the Hall effect near the superconducting transition temperature. This information is valuable in understanding the electronic structure and various excitations in both states, and vortex pinning and dynamics in the superconducting phase.

Chapters 198 and 199 are devoted to neutron scattering studies. In chapter 198 Thomas E. Mason describes neutron scattering investigations of spin fluctuations in the CuO_2 planes. As noted by Mason, since many of the theories of high-temperature superconductivity include spin fluctuations as central feature of the mechanism for superconductivity it is important to obtain a detailed picture of the energy, momentum, temperature and doping dependence of the magnetic dynamics of the cuprates. But because of the small spin quantum number ($\frac{1}{2}$) and the large energy scale over which spin fluctuations exist (hundreds of meV), large single crystals are required (>1 cm^3). As a result, only two systems, $La_{2-x}(Sr,Ba)_xCuO_4$ and $YBa_2Cu_3O_{7-x}$, have been studied in any detail by inelastic neutron scattering techniques.

The second neutron scattering chapter (199), by Jeffrey W. Lynn and S. Skanthakumar, deals with the ordering of the lanthanide ions in various cuprates. In these cuprate materials, the lanthanide (R) ions are electronically isolated from the Cu–O layers where the Cooper pairs form and have low ordering temperatures (~1 K) which make them prototypical "magnetic superconductors". Furthermore, because of the layered crystal structure they are some of the best two-dimensional magnets known. However, in several of these magnetic superconductors, the magnetic ordering temperature is too high to be explained by dipolar interactions, and R–R exchange interactions must play a dominant role in the magnetism. The authors have also reviewed the behavior of the praseodymium ion in the cuprates, which differs from the other lanthanides. In the

praseodymium cuprate, the 4f electrons are strongly hybridized with the conduction electrons which accounts for the high magnetic ordering temperature and the absence of superconductivity.

Chapter 200, by Peter M. Allenspach and M. Brian Maple, reviews some aspects of the low-temperature heat capacity of the ceramic oxide superconductors. These measurements yield valuable information about the electronic, lattice, magnetic, crystalline electric field and hyperfine nature of the various rare-earth cuprate materials, and in that respect compliment other physical property studies, such as neutron diffraction, inelastic neutron scattering, and various spectroscopic measurements. The authors review the heat-capacity properties of the stoichiometric $RBaCu_3O_7$ compounds and oxygen-deficient materials, and show that there are significant differences. The heat capacities of other lanthanide cuprates, such as $RBa_2Cu_4O_8$ and $R_2B_4Cu_7O_{14+x}$, are also discussed.

The next three chapters in this volume are concerned with various spectroscopies – photoemission (chapter 201), infrared (chapter 202) and Raman (chapter 203). In chapter 201, Matthias Schabel and Zhi-xun Shen discuss the angle-resolved photoemission studies of untwinned $YBa_2Cu_3O_{9-x}$. This technique is able to directly probe both the energy and momentum scales of these highly correlated materials, and because of the two-dimensional nature of the cuprates, has unambiguously detailed their planar band structure.

The infrared properties of the high-temperature oxide superconductors and knowledge obtained from such measurements are reviewed in chapter 202 by Dimitri N. Basov and Thomas Timusk. Infrared spectroscopic studies have yielded important information about the influence of doping the antiferromagnetic cuprate insulating phases with charge carriers; some novel features in both the charge dynamics in the normal state and the electrodynamics in the superconducting state; and the structure of vortices by magneto-optical measurement of thin films of YBCO. The authors also note that magneto-optical studies at high magnetic field may be useful in resolving the controversy about relaxation mechanisms in the cuprate superconductors.

S. Lance Cooper's review (chapter 203) on the electronic and magnetic Raman scattering studies describes the contributions made by this technique to our understanding of the nature of the four distinct regimes of these copper-oxide-based materials as a function of oxygen doping. These are: the antiferromagnetic insulator at zero doping, the underdoped superconductor; the optimally doped superconductor; and the overdoped superconductor. Raman scattering is a powerful tool since it is sensitive to spin, electronic and phonon degrees of freedom, and thus it can provide information on energy, symmetry and lifetimes of various excitations which occur in these complex cuprate phase diagrams. It can also increase our knowledge of the nature of the superconducting pairing mechanism, how antiferromagnetic correlations evolve into the metallic phase, and the relationship between the pseudogap and the superconducting phases in the underdoped copper oxides.

The tunneling spectra of the cuprate superconductors and the characterization of these materials by scanning tunneling microscopy are discussed in chapter 204 by Hiroharu Sugawara, Tetsuya Hasegawa and Koichi Kitazawa. Tunneling spectroscopy is a powerful tool for exploring the density of states near the Fermi level, and because its energy resolution ($\leqslant 1$ meV) is higher than any other technique, it is crucial for determining

the gap structures of superconductors. The authors note that the tunneling spectra have revealed some strange features: a finite differential conductance (and sometimes a peak) in the gap; and various energy dependences (including linear and parabolic) in the background spectra outside of the gap region. Cryogenic vacuum scanning tunneling microscopy (STM) allows one to demonstrate atomic resolution on the surface of materials in a chemical-free environment on the interface between the specimen and insulating layer. STM studies of the high-temperature superconducting cuprates have revealed many unique and unexpected features in these materials.

CONTENTS

CONTENTS OF VOLUMES 1–30

VOLUME 4: Non-metallic compounds – II
1979, 1st repr. 1984; ISBN 0-444-85216-6

VOLUME 5
1982, 1st repr. 1984; ISBN 0-444-86375-3

VOLUME 6
1984; ISBN 0-444-86592-6

VOLUME 7
1984; ISBN 0-444-86851-8

VOLUME 8
1986; ISBN 0-444-86971-9

VOLUME 9
1987; ISBN 0-444-87045-8

VOLUME 10: High energy spectroscopy
1988; ISBN 0-444-87063-6

VOLUME 11: Two-hundred-year impact of rare earths on science
1988; ISBN 0-444-87080-6

VOLUME 12

1989; ISBN 0-444-87105-5

VOLUME 13

1990; ISBN 0-444-88547-1

VOLUME 14

1991; ISBN 0-444-88743-1

VOLUME 15

1991; ISBN 0-444-88966-3

MASTER INDEX, Vols. 1–15
1993; ISBN 0-444-89965-0

VOLUME 16
1993; ISBN 0-444-89782-8

VOLUME 17: Lanthanides/Actinides: Physics – I
1993; ISBN 0-444-81502-3

VOLUME 18: Lanthanides/Actinides: Chemistry
1994; ISBN 0-444-81724-7

VOLUME 19: Lanthanides/Actinides: Physics – II
1994; ISBN 0-444-82015-9

VOLUME 20
1995; ISBN 0-444-82014-0

VOLUME 21
1995; ISBN 0-444-82178-3

VOLUME 22
1996; ISBN 0-444-82288-7

VOLUME 23

1996; ISBN 0-444-82507-X

VOLUME 24

1997; ISBN 0-444-82607-6

VOLUME 25

1998; ISBN 0-444-82871-0

VOLUME 26

1999; ISBN 0-444-50815-1

VOLUME 27

1999; ISBN 0-444-50342-0

VOLUME 28

2000; ISBN 0-444-50346-3

VOLUME 29: The role of rare earths in catalysis

2000; ISBN 0-444-50472-9

VOLUME 30: High-Temperature Superconductors – I

2000; ISBN 0-444-50528 8

Handbook on the Physics and Chemistry of Rare Earths
Vol. 31
edited by K.A. Gschneidner, Jr., L. Eyring and M.B. Maple

Chapter 195

OXYGEN NONSTOICHIOMETRY AND LATTICE EFFECTS IN $YBa_2Cu_3O_x$

Phase Transitions, Structural Distortions and Phase Separation

Emanuel KALDIS
i.R. Laboratorium für Festkörperphysik ETH, 8093 Zurich, Switzerland;
kaldis@solid.phys.ethz.ch, kaldis@swissonline.ch

Contents

List of abbreviations

2D	Two-dimensional
3D	Three-dimensional
AF	Antiferromagnetic
ASYNNNI	Asymmetric Next-Nearest Neighbor Ising model
BAO	Synthesis of 123-O_x using BaO as Ba source, by previously expelling the carbonate of $BaCO_3$ with high temperature annealing
BVS	Bond Valence Sum method
CAR	Synthesis of 123-O_x using $BaCO_3$ as Ba source
CVM	Clusters Variation Method
DO	Synthesis of 123-O_x using Ba metal as Ba source (directly oxidized)
DPDF	Difference Pair Density Function
ED	Electron diffraction
EELS	Electron energy loss spectroscopy
EM	Electron microscopy
EXAFS	Extended X-ray absorption fine structure
FWHM	Full width at half maximum

HREM	High-resolution electron microscopy
HT_c	High critical temperature
HT_cS	High critical temperature superconductivity
I–M	Insulator–metal transition
LT	Low temperature
LO	Longitudinal optical phonon
MS	Multiple backscattering
ND	Neutron diffraction
NEXAFS	Near edge X-ray absorption fine structure
n_h	positive superconducting carriers (holes)
NN	Nearest neighbors
NPD	Neutron powder diffraction
O	Orthorhombic phase
O_p	Oxygen of the planes (O2, O3)
Ortho-I	Orthorhombic phase of 123-O_x
Ortho-II	Superstructure of the orthorhombic phase of 123-O_x, with only every second chain occupied
PDF	Pair distribution function
PICTM	Pressure-induced charge transfer model
Raman	Raman spectroscopy
RT	Room temperature
SQUID	Superconducting quantum interference device
SS	Single backscattering
T–O	Tetragonal–Orthorhombic transition
T_c	Critical temperature of superconductivity
$T_{c,max}$	Maximal temperature of diamagnetic transition as a function of doping
$T_{c,onset}$	Onset temperature of diamagnetic transition
XPS	X-ray photoelectron spectroscopy
XRD	X-ray diffraction

1. Introduction

A very fruitful approach to investigate the properties of a solid is the variation of the carrier concentration. This can be achieved either by doping with a foreign atom or, for "bertholidic" compounds, by manipulating the nonstoichiometry. In nonstoichiometric solids variation of the stoichiometric ratio leads to an intrinsic change of doping and allows the synthesis of *a series of samples* with different carrier and/or defect concentrations. The investigation of the structural, chemical and physical properties of such series allows the construction of the various pseudo-binary phase diagrams (thermodynamic, structural, magnetic etc.) as a function of intrinsic (and extrinsic) doping. In view of the almost-always existing interaction between the structural and physical properties, this integrated approach leads to the most balanced picture of the properties of a solid, showing clearly their evolution and their interactions with the change of the carriers.

On the contrary, the investigation of only a few "representative" compositions, very popular in the literature because it saves time, may lead, in the case of complex materials, to misinterpretations. In such cases, overseeing the existence of superstructures, other homologous phases, miscibility gaps, phase transitions, etc., can lead to substantial errors. In particular, the homogeneity of large nonstoichiometric regions should be questioned in that respect. An example from solid-state chemistry is the phase diagram of the praseodymium–oxygen system whose homogeneity ranges were found with HREM to consist of a very large number of hitherto unknown phases (Eyring 1979). An example

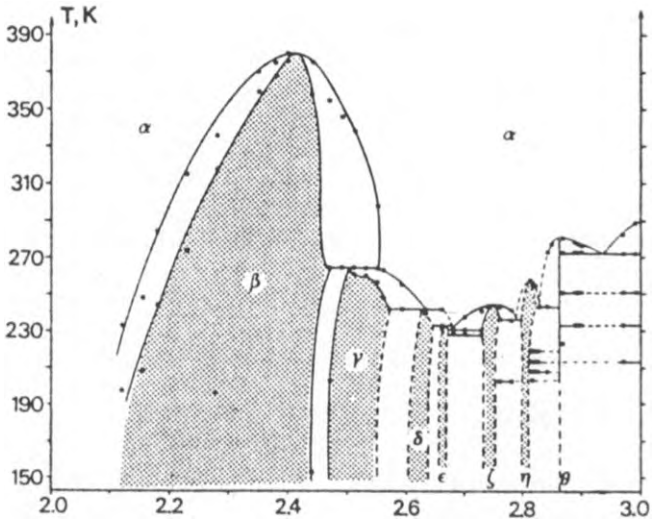

Fig. 1. Subsolidus T–x phase diagram of the LaH_2 (metallic)–LaH_3 (semiconducting) system based on differential scanning calorimetry and X-ray diffraction measurements. Instead of the originally assumed continuous solid solution with cubic Fm3m structure, the metal to semiconductor transition proceeds via at least 9 phases separated by miscibility gaps. After Conder et al. (1991).

from solid-state physics of the materials with valence instabilities is the $TmSe_x$ phase (NaCl structure) of the Tm–Se system whose large homogeneity range was found to consist of several phases with different Tm valence (Kaldis and Fritzler 1982). Another intimidating example from the physics of the hydrides is the compositionally driven metal–semiconductor transition in the hydrides of lanthanum LaH_2–LaH_3 and cerium CeH_2–CeH_3 (fig. 1) which have been shown to consist of up to 9 subsolidus phases separated by miscibility gaps (Conder et al. 1991)! Up to now the physical properties of these new hydride phases have not been completely investigated due to their extreme sensitivity to contamination.

$YBa_2Cu_3O_x$ (123-O_x), ingeniously discovered by Wu et al. (1987) shortly after the historical opening of the HT_c era by Bednorz and Müller (1986), is a nonstoichiometric solid par excellence: its oxygen content x varies between 6.0 and 6.990, and dramatically affects its properties. As we will discuss later, the oxygen nonstoichiometry of 123 results from the less stable square planar coordination of the Cu1 in the chains. With increasing O content the tetragonal antiferromagnetic insulator $YBa_2Cu_3O_6$ (123-O_6) undergoes at $x \approx 6.30$ a structural transformation to orthorhombic structure and at $x \approx 6.38$ to a superconductor with low T_c. Further increase of the carrier concentration by O-doping leads to an increase of T_c, through the *underdoped* ($x \leqslant 6.90$), up to the *optimally doped* phase with 92.5 K ($6.90 \leqslant x \leqslant 6.95$). In the narrow *overdoped* phase ($6.95 \leqslant x \leqslant 7.00$) T_c decreases to ~88 K. The nonlinear change of T_c with oxygen content (fig. 2) indicates the possibility of the existence of complex phase relationships in 123-O_x associated with changing superconducting interactions. In fact this fascinating compound and the rest of

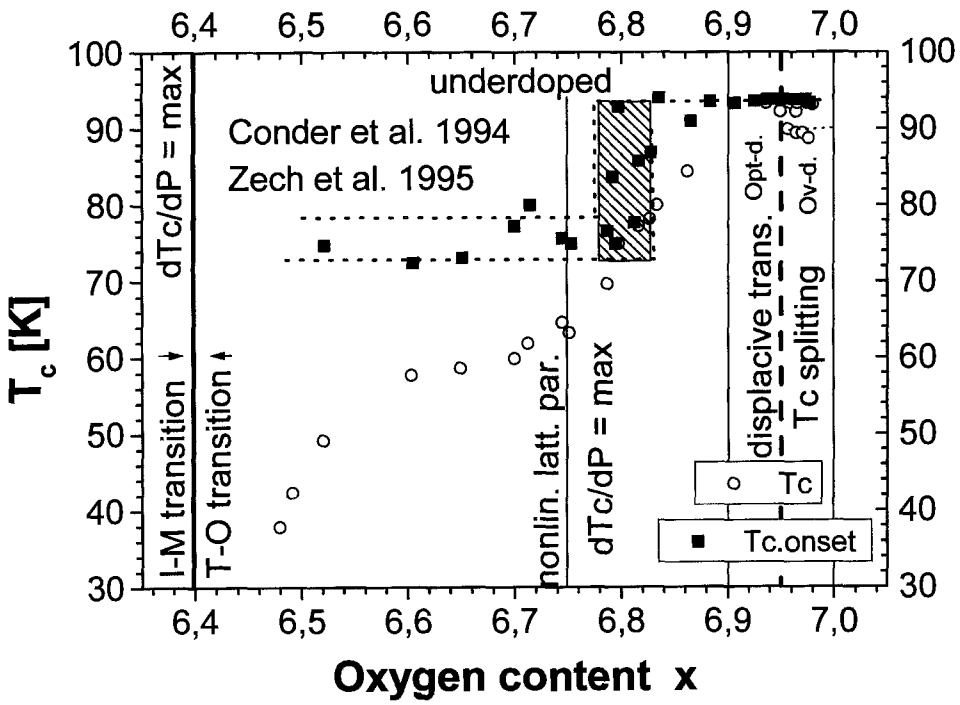

Fig. 2. T_c and $T_{c,onset}$ as a function of the oxygen nonstoichiometry. The nonlinear dependence of T_c due to changing superconducting interactions indicates the existence of complex phase relationships. The T_c and $T_{c,onset}$ vs. x curves have clear differences. Note the abrupt step in $T_{c,onset}$ at $x = 6.75$–6.80, indicating a miscibility gap (hatched) consistent with fig. 28. After data of Conder et al. (1994a) and Zech et al. (1995a,b).

the HT_c cuprate superconductors are among the most complex solids investigated up to now. As some of this complexity is revealed only with sophisticated methods of synthesis and characterization, it is no wonder that 14 years after the great discovery of Bednorz and Müller (1986) there is an appreciable gap between theoretical models and experimental results.

Some of the reasons for the existence of this gap lie in the materials. With the exception of discovering new structures and their homologues, research in the controlled synthesis of the known materials in order to understand their chemical and thermodynamic properties, their numerous deviations from the average structure, their instabilities and metastabilities, the mechanism of defect formation and the structure–properties relationships have been scarcely funded, being considered as not of primary importance to superconductivity. The lack of such profound knowledge about the materials combined with low accuracy of the oxygen determination or in most cases only "estimations" of it, and the investigation each time of a small number of "representative" compositions obscured many important but subtle trends. HT_c superconductors have a stability range squeezed between the insulator and metal regimes and are very near to the border of thermodynamic instability, as is

already visible from the properties of the chains in 123-O_x. Subtle changes of their structural properties result from changes in the superconducting properties, which are easy to overlook, if painstaking work is avoided. Other difficulties concerning some single-crystalline samples are the time-consuming diffusion of oxygen in macroscopic crystals, the difficulty to anneal and control defects in larger single crystals, the difficulty to use high-resolution oxygen analysis, and their impurity content from flux and crucible. Based on the above, we may, therefore, estimate that more than 70% of the work in HT_c superconductivity up to now has been performed with samples having several of the above drawbacks.

The situation becomes much more complex if we take into consideration that some of the extraordinary difficulties concerning the preparation and characterization of HT_c materials are due to their *intrinsic inhomogeneities* (see, e.g., Bordet et al. 1993). This is a completely new characteristic for solid-state materials, opposing all precedents. For five decades, materials research, inspired from the properties of semiconductors, had as ultimate goal the ideally homogeneous and structurally perfect material. On the other hand, with progressing time the importance of intrinsic inhomogeneities for superconductivity is increasingly recognized. The ordered charge and spin separation leading to stripes (Tranquada et al. 1995) is an intrinsic inhomogeneity par excellence. Most structural instabilities and thermodynamic metastabilities are not due to "bad samples" but are closely related to the anomalous properties of these strange metals. Thus, we have to differentiate much more carefully than in other materials between intrinsic and extrinsic ("bad samples") inhomogeneities. Figure 3 illustrates this aspect. The width of the diamagnetic transition is generally considered to be a very sensitive criterion of high-quality crystals with very good homogeneity. The figure shows a crystal with $\Delta T_c = 300$ mK! Nevertheless it still has several domains with oxygen inhomogeneities (different lengths of c-axis). Probably this is an extrinsic effect, but how many crystals have been investigated with that method?

Additional complexity is due to the *very small correlation length* of the HT_c superconductors. This induces a great sensitivity to nanoscale inhomogeneities, but also lessens sensitivity to grain size reductions, segregations and precipitations down to mesoscopic scale. This extraordinary physical property has, however, also an advantage for materials research in general as it can be used as a probe to investigate for the first time phase relationships in a very small length scale. This is another important – but much less known – advantage of the discovery of Bednorz and Müller (1986), which may widen our understanding of complex materials in the future.

As most properties of 123-O_x change – some of them, like T_c, dramatically – with the oxygen content, a complete review of the changes of properties as a function of the nonstoichiometry would occupy the space of a large monograph. In this review we will focus mainly on the complexity of the structural phenomena and of the phase relationships of 123-O_x, as well as on some of their consequences for the physical properties. Particular attention will be given to lattice-parameter anomalies, the local structure, and some hitherto unknown phase transitions triggered by doping. Using slowly cooled samples and high-resolution oxygen determination some of these anomalies are becoming visible

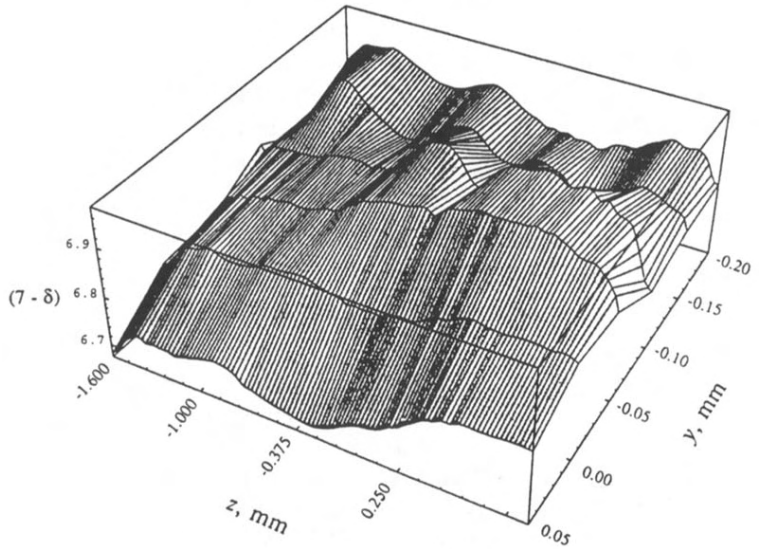

Fig. 3. Oxygen content $7-\delta$ in the (z,y) plane of a "high-quality" single crystal of 123-O_x ($T_c \approx 93$ K, $\Delta T_c < 300$ mK!). Investigations with very high energy synchrotron radiation allow the measurement of minute changes of the c-axis throughout the bulk of the crystal, and the detection of the corresponding changes due to inhomogeneous oxygen distribution. The plot shows that this crystal contains bands of different c-axis lengths along the z-direction. After Qadri et al. (1997).

even by diffraction methods. Investigations by mesoscopic length scale methods (EXAFS, micro-Raman) show *phase separation* phenomena, which are supported by the splitting of the diamagnetic transition, and complex structural changes in the as yet less investigated overdoped region. This is the reason why an appreciable part of this review will focus on the overdoped region (oxygen and Ca doping). It is hoped that these new results may contribute towards moving the focus of many theoretical models away from the ideal lattice and homogeneous phases.

The simple strategy followed here is to discuss structural anomalies appearing at certain oxygen contents and scout the field of physical measurements for changes of properties at the same oxygen content. The opposite is useful as well: looking for structural anomalies where changes in the properties appear. Both approaches can also be used for proposing the existence of new phases to be confirmed (or not) by later investigations. Based on structural, magnetic and Raman investigations discussed in this review, we will propose a tentative T–x phase diagram in sect. 9.

As the literature of 123-O_x is extremely large, it is outside the scope of this review to give complete references. Thus, many but not all papers related to the aspects discussed in this review are given in the list of references (as of late November 2000). Some facets of the problem which have been discussed in detail in past reviews will be discussed only briefly here, or references will be given. This includes, e.g., a large part of the diffraction crystallography of single crystals, inelastic neutron scattering, and NMR investigations.

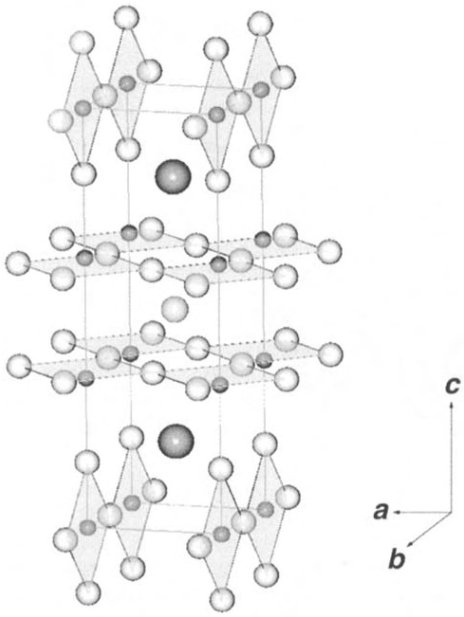

Fig. 4. Schematic drawing illustrating the two different coordinations of Cu (chains and planes) due to the existence of two vacant oxygen sites, and the tripling of the perovskite cell of $YBa_2Cu_3O_7$. After Beyers and Shaw (1989).

2. Average crystallographic structure

The atomic positions of the "real crystal" are to some degree different from the atomic positions of the "ideal crystal" given by the space group (see, e.g., Kaldis 1994). The structure used to describe the real crystal is the "average structure" and is only an approximation of the real atomic structure (local structure). We will discuss the local structure in sect. 4 and some subsequent sections. Here we give the highlights of the average structure, as detailed descriptions have been given in previous reviews. Detailed references of the discovery of Wu et al. (1987) and the early studies of the 123-O_x structure are given, e.g., in the first review on this subject (Beyers and Shaw 1989). The reviews in the series edited by Ginsberg (1990–95) and Narlikar (since 1990), as well as the most recent review of Radaelli (1998) are recommended reading.

$YBa_2Cu_3O_x$ has a structure derived from the cubic perovskite structure ABO_3. In this structure the larger cations A occupy the center of the cage formed by corner-sharing oxygen octahedra and the smaller B cations occupy the centers of the oxygen octahedra, see e.g., Goodenough and Longo (1970). The smaller cation is Cu here, but there are two larger cations Y and Ba occupying the A sites. Due to ordering of the two Ba and the one Y cations the unit cell is tripled with the sequence Ba–Y–Ba of the subcells (fig. 4).

Ideally such a perovskite structure contains $3 \times 3 = 9$ oxygen atom sites. It was found, however, that the 123 unit cell contains only 7 oxygen atoms. The vacant oxygen sites are in the plane of Y (oxygen coordination 8, slightly distorted square prism) and in the basal copper plane (Ba oxygen coordination 10). In this way two different Cu sites result, forming the chains and planes of the 123 structure:

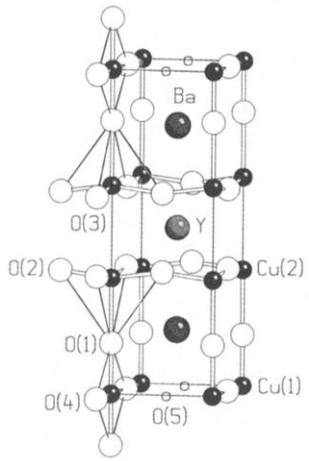

Fig. 5. Unit cell of the average structure of the orthorhombic $YBa_2Cu_3O_7$ (Pmmm space group) with labels of the various atom sites. The O5 sites are shown empty. The (almost) completely oxygen-depleted Cu1–(O5)–Cu1 chains form the *a*-axis and the full Cu1–O4–Cu1 chains form the *b*-axis. The *c*-axis is along the Cu1–O1–Cu2–Cu2–O1–Cu1 strings. The five-fold oxygen coordination of the Cu2 and the four-fold coordination of Cu1 are clearly seen. Note that the superconducting Cu2–O2,O3 planes are not flat. (cf. fig. 7).

- The Cu1 occupy the corners of the basal plane and have a *square planar coordination* of oxygen, forming CuO_2 chains parallel to the *b*-axis (fig. 4). The oxygen vacancies are along the *a*-axis between the Cu1 of neighboring chains (O5 or antichain site), and as we will see they may also be, under certain conditions, partly occupied (fig. 34). The occupied oxygen sites near Cu1 (fig. 5) are the chain oxygen O4 (along the *b*-axis) and the apex oxygen O1[1] along the *c*-axis. Due to this asymmetric occupancy of the *a*- and *b*-axis the latter is longer (1.8%) than the *a*-axis, leading to an orthorhombic structure near $x \approx 6.4$, crystallizing in the centrosymmetric Pmmm space group. At lower oxygen contents the structure is tetragonal (P4/mmm) (fig. 6). This leads to a tetragonal–orthorhombic (T–O) phase transition with increasing oxygen content, near the onset of superconductivity (sect. 3.3).
- The Cu2 sites have a *fivefold pyramidal* oxygen coordination, forming CuO_5 pyramids with apex the bridging O1 and basis the O2 and O3 oxygens. Cu2 and O2, O3 form the superconducting $Cu2O_2$ planes. These are not flat planes, because a deformation (Capponi et al. 1987), *dimpling,* exists along the *c*-axis, the O2 and O3 lying above Cu2 at different heights (O3 higher than O2) (fig. 7).

The O2–Cu2–O2 zig-zag chains lie along the *a*-axis and the O3–Cu2–O3 along the *b*-axis. Usually the $Cu2O_2$ plane is considered as one block layer. However, as neutron diffraction (Conder et al. 1994a; see also sect. 6.1, fig. 66) and EXAFS (Röhler et al. 1997a,b, Kaldis et al. 1997b) have shown that the separation between Cu2 and O2, O3 changes sensitively with the carrier concentration, one may consider the $Cu2O_2$ planes as consisting of three stacked layers: Cu2 and the double O2/O3. We note that, as shown in

[1] Throughout this review we use the O1 label for the apical oxygen site and O4 for for the chain oxygen. As the reverse notation for the chain and apex oxygen sites often occurs in the literature, some authors call the apical oxygen "bridging oxygen" to avoid misunderstandings. In fact, an important function of this oxygen is that it provides a bridge between the Cu1 system of the chains and the Cu2 system of the planes.

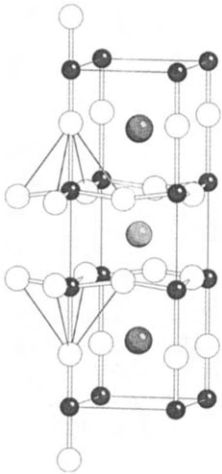

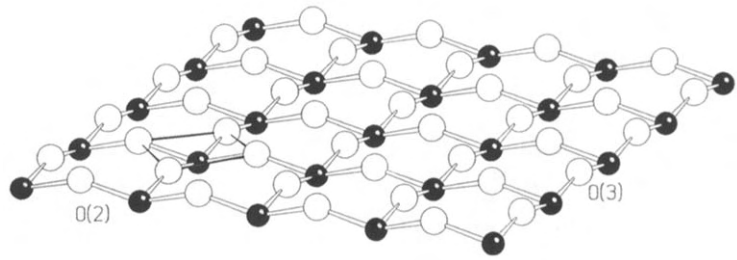

Fig. 7. View of the Cu2O2 superconducting plane to illustrate dimpling. At the front the Cu2–O2–Cu2 zig-zag chains can be seen ($\|$ *a*-axis). The Cu2–O3–Cu2 zig-zag chains are $\|$ *b*-axis. As a result of the different lengths of the Cu2–O3 and Cu2–O2 bonds a corrugation exists along the Cu2–Cu2 (110) chains – lying lower (cf. figs. 15 and 70). Also the O2–O3–O2 (100) strings have a modulation with O2 lying higher than O3. Black spheres, Cu, white spheres, O. On the left-hand side the basis of one Cu2–O_5 pyramid is shown (single solid bond lines).

Fig. 6. Unit cell of the average structure of the tetragonal $YBa_2Cu_3O_6$ (P4/m mm space group) with oxygen-depleted Cu1–Cu1 chains along the *b*-axis.

Table 1
Structural parameters (Å units) in highly overdoped $YBa_2Cu_3O_x$ with $x = 6.994$, measured with neutron diffraction refinement, at $T = 1.5$ K (ILL-Grenoble, DIA diffractometer)[a]

Cu2–O1 = 2.268(2)	Cu2–O2 = 1.9265(4)	Cu2–O3 = 1.9589(4)	Cu2–Cu2 = 3.396(2)
Cu1–O1 = 1.857(2)	Cu1–O4 = 1.9407(0)		
Y–O2 = 2.403(1)	Y–O3 = 2.384(1)		
Ba–O2 = 2.988(2)	Ba–O3 = 2.954(2)	Ba–O1 = 2.7342(3)	Ba–O4 = 2.862(2)
a [Å] = 3.811548(5),	*b* [Å] = 3.88137(7),	*c* [Å] = 11.6477(2),	*V* [Å^3] = 172.32(1).

[a] This is the highest oxygen content measured with the high-resolution method described in sect. 3.1.3. The sample was prepared similar to the CAR samples (sect. 3.1.2). The synthesis conditions are described in sect. 8. As usual in neutron diffraction the standard deviations of the cell parameters do not include the uncertainty in the effective neutron wavelength $\lambda = 1.90797$ Å. After Böttger et al. (1996).

fig. 5, two neighboring $Cu2O_2$ planes are separated by the Y-layer. The $Cu2O_2$–Y–$Cu2O_2$ triple layers are separated by the chains.

Table 1 gives selected bond lengths for the 123-O_x structure. Appreciable differences exist among the various Cu–O bond lengths:

- The Cu1–O4 bond length along the chain (*b*-axis) is 1.9407(0) Å.
- The bond of Cu1 to the apical oxygen, Cu1–O1, at 1.857(2) Å is the shortest Cu–O bond in the structure and is the one which changes strongly with increasing oxygen nonstoichiometry (sect. 3.2.1.2).

- In contrast, the Cu2 bond to apex oxygen is, with 2.268(2) Å, the largest of the structure. Its length also varies with stoichiometry, and influences the degree of coupling between the chains and the planes.
- The Cu2 bonds to the O2, O3 oxygens of the planes (at the basis of the CuO_5 pyramid) are not equal, Cu2–O2 = 1.9265(4)–Å, Cu2–O3 = 1.9589(4) Å, leading to O–Cu2–O angles smaller than 180°. This destroys the planar character of the Cu2 planes and introduces the above-mentioned *dimpling*. As we will see, dimpling is dependent on the oxygen nonstoichiometry and scales with T_c (sect. 6). Although hitherto rather neglected, as we will see later it is an important parameter of HT_c superconductivity.

In addition to the deviation from planarity of the $Cu2O_2$ planes, a zig-zag modulation of the chains has been found due to large anisotropic thermal vibrations perpendicular to the *b*-axis (Capponi et al. 1987, Francois et al. 1988). This is in agreement with the thermal instability of the chains which start losing oxygen at $T > 350$°C, as will be discussed in sect. 4.1. The diffusion coefficient of the various oxygen sites was investigated (isotope exchange) in detail by Conder et al. (1994b) and Conder (2000), cf. sect. 7.2.1.

3. Structural evolution of 123-O_x with nonstoichiometry

The nonstoichiometry of 123-O_x became apparent very early from the differences in structural and superconducting properties of samples synthesized under various conditions. The large thermal ellipsoids of the structure refinements (Capponi et al. 1987) indicated also the relative instability of the oxygens of the chains (O4), resulting from the less stable bonding of the square planar coordination of Cu1.

At the same time it was found that T_c changes with nonstoichiometry. The charge-transfer model gave a first insight to this dependence: The superconductivity in the $Cu2O_2$ planes depends on the charge transfer between the chains and the planes (Miceli et al. 1988, Cava et al. 1988a,b) and this increases with the occupation of the O4 sites of the chains as the apical bond decreases (sect. 3.2.1.2). Thus, nonstoichiometry became an instrument to vary the properties of 123-O_x from the tetragonal antiferromagnetic insulator 123-$O_{6.4}$ to the superconductor 123-$O_{6.9}$ with $T_c \approx 92$ K! Since then, structural and thermodynamic investigations as a function of the oxygen nonstoichiometry have become very important in understanding some aspects of HT_c superconductivity.

The lability of the Cu1–O4 bond, responsible for the oxygen nonstoichiometry, also allows ordering processes in the chains. Indeed, it was found very soon that T_c depends not only on the occupancy of the chains but also on the ordering imposed by the thermal history (sect. 3.2.1.5), pressure (sect. 5.4), chemical history (sect. 3.2.2.5) and the general conditions of synthesis of the samples. Thus, *the appreciable dependence of structure on oxygen content varies considerably with synthesis conditions.* With a lot of fantasy and mostly no adherence to equilibrium thermodynamics many variations of the synthesis conditions have been tried.

3.1. *Synthesis, oxygen and carbonate control*

Independently of the advantages and disadvantages of the synthesis method used, a great disadvantage of many publications in the literature concerned with changes of various

properties as a function of nonstoichiometry is the relatively small number of investigated compositions. The complex perovskite structure of the HT_c cuprates is a sensitive probe of the changes of various physical parameters. As some of these changes are abrupt and rather small, one needs a large number of investigated compositions and a highly accurate determination of the oxygen content in order to see the trends and be able to detect these effects. Both have been missing in the mainstream literature so that, e.g., some structural aspects of the overdoped regime could not be systematically investigated. Thus, the discussion of the structural properties of nonequilibrium samples (sect. 3.2.1) deals with the underdoped phase. Several properties of the overdoped phase have been studied with equilibrium samples and will be discussed in sections 3.2.2, 6, 7 and 8.0.

3.1.1. *Nonequilibrium synthesis, quenching*

To reach low oxygen contents (tetragonal samples) at rather low temperatures, low oxygen partial pressures p_{O_2} are necessary. As it is rather difficult to reach a good control of low p_{O_2}, most researchers have used a "practical" alternative: reduction of oxygen by annealing at high temperatures followed by quenching. This leaves the open question of how the extremely sensitive defects react, e.g., to the strains resulting from this rather brutal procedure. In view of the practical impossibility to reach complete quenching, which soon enough became clear (e.g., Jorgensen et al. 1990a), it is rather astonishing that a large majority of researchers followed this technique.

Thus, a large number of laboratories prepared nonstoichiometric samples by quenching them rapidly from high temperatures, 600–1000°C (Jorgensen et al. 1987a, Takayama-Muromachi et al. 1987, Farneth et al. 1988, among others) to liquid nitrogen or room temperatures. According to an in-situ neutron diffraction investigation (Jorgensen et al. 1987b) quenching from high temperatures crosses the phase-transition line tetragonal $\rightarrow$ orthorhombic ($T \rightarrow O$) and, therefore, increases the degree of disorder of the samples. Thus, e.g., these samples show a rather smooth variation of the dependence of T_c on oxygen content and lose superconductivity at $x \approx 6.5$. Variation of the oxygen stoichiometry at lower temperatures (<500°C) produced more pronounced plateaus of the T_c vs. oxygen curve, with $T_c \approx 91$ K in the range $x > 6.9$, $T_c \approx 60$ K for $6.5 > x > 6.4$ and loss of superconductivity at $x \approx 6.45$.

Another reason for using quenching has been to avoid the appearance, during cooling, of a mixture of phases with various defects and oxygen ordering reactions. These were shown to exist by electron microscopy (EM) studies (e.g., Van Tendeloo et al. 1987, Van Tendeloo and Amelinckx 1990, Cava et al. 1990) and proposed by various theoretical models (e.g., de Fontaine et al. 1990a,b, Semenovskaya and Khachaturyan 1993). As the mobility of oxygen was considered to freeze at lower temperatures, quenching was used to produce "pure" phases. As we will see, the mobility of oxygen is appreciable even at low temperatures, so there is no need for quenching. Slow cooling leads as near as possible to the thermodynamic equilibrium state (sect. 3.2.2). A different method, although still using quenching, is Zr-gettering, developed at Bell Labs by the late J. Remeika (Chaillout and Remeika 1985). This method has been used extensively by Cava and colleagues, and combined with moderate quenching it gave – as we will discuss later – good results.

3.1.2. *Synthesis near thermodynamic equilibrium*

A small group of researchers preferred synthesis near thermodynamic equilibrium. Jacobson et al. (1989) applied very early the equilibration of mixtures of 123-O_6 and 123-O_7 in a closed system. A similar method was used by Radaelli et al. (1992). Conder et al. (1994a,b), Krüger et al. (1994, 1997), Kaldis (1997) and Kaldis et al. (1997b) used equilibration via the vapor phase of locally separated 123-O_x and Y metal for their near-equilibrium samples (table 2).

Annealing in a reducing atmosphere was also used (e.g., Farneth et al. 1988, Monod et al. 1987); near equilibration in an open system (O_2–Ar mixtures) was applied, e.g., by Rusiecki et al. (1990) for $x \geqslant 6.45$. Electrochemical titration in a solid-state ionic cell was applied by Beyers et al. (1987) and Ahn et al. (1990). Its reversibility is an appreciable advantage.

Table 2
Synthesis conditions for equilibrium samples

Expelling carbonate (BAO method)	**Ba-metal oxidation (DO Method)**	**Carbonate as Ba source. Minimum carbonate content (CAR Method)**	**Carbonate as Ba source**
Rusiecki et al.(1990), Kaldis et al. (1997a)	Conder et al. (1994a), Kaldis et al. (1997a,b)	Krüger et al. (1994, 1997), Kaldis et al. (1997a,b)	Jacobson et al. (1989), Radaelli et al. (1992)
Master batch			
$Ba_2CO_3 \rightarrow BaO$ 950°C, 40 h; Solid-state reaction with CuO and Y_2O_3 in flowing oxygen; 3 X 950°C, 20 h; interm. grindings	Oxidation of Ba at low oxygen partial pressure; Solid-state reaction with CuO and Y_2O_3 in flowing oxygen; Further like CAR method	Solid-state reaction of Ba_2CO_3 (4N) in oxygen with CuO and Y_2O_3; 6 annealings with T increasing 860 → 935°C, each time cooling at RT and grinding; Annealing at 935°C for 75 h, 50 h cooling at RT 30°C/h, grinding; Annealing at 935°C for 80 h in oxygen, then **cooling 10°C/h; $x = 6.990$; Diamagnetic transition $\Delta T(10\%–50\%) = 3$ K** (cf. fig. 8, for 6.912)	Solid-state reaction of Ba_2CO_3 (4N) in oxygen with CuO (5N) and Er_2O_3 (5N); 900°C 12 h, in flowing oxygen, slow cooling, several times grinding and reheating up to 970°C; Final grinding; Annealing at 500°C; **slowly cooled** oxygen-rich material $x \approx 6.9$; **Diamagnetic transition $\Delta T(10\%–90\%) = 15$ K** Oxygen-poor 123-O_x $x \approx 6.1$ with vacuum annealing
Reduction			
With gas mixtures ($Ar + O_2$)	With Y-turnings (or Cu, or 123-$O_{6.5}$) like the CAR samples	With Y-turnings (or Cu, or 123-$O_{6.5}$) in separate Al_2O_3 crucibles placed in evacuated ampoules; 600°C for 15 h; **cooling 10°C/h**	Mixtures $x = 6.9$ and $x = 6.1$ in different proportions, sealed in evacuated ampoules; Annealing 14 days, slowly cooled in steps of 50°C, down to 50°C, in two months

Measurements of the diffusion coefficient of oxygen by isotope exchange showed that at least down to 250°C thermodynamic equilibrium exists (Conder et al. 1994a,b, Conder and Krüger 1996, Krüger et al. 1994). Quenching in liquid nitrogen and annealing at temperatures as low as 0°C have shown changes of T_c due to the mobility of the oxygen atoms (Veal et al. 1990a, Claus et al. 1990, Jorgensen et al. 1990b). Recently, it was also found that the mobility of oxygen in another important cuprate, La_2CuO_{4+y}, remains down to 200 K (Wells et al. 1997).

Slow cooling down to room temperature was applied under a controlled atmosphere in order to produce samples as "near as possible" to the thermodynamic equilibrium. This cautious expression is necessary in view of the complex structure of the HT_c cuprates which may hinder complete relaxation even in polycrystalline samples. These equilibrium samples show hitherto unknown properties which shed new light on the problem of the intrinsic inhomogeneities of the HT_c cuprates (Rusiecki et al. 1990, Conder et al. 1994a,b, Kaldis 1997, Kaldis et al. 1997b) (sects. 5.3, 6, 7).

In addition to the thermal history, the chemical synthesis reaction also contributes to the formation of defects. In particular, the carbonate content of the starting materials and the precursor reactions for its elimination are important (sect. 3.1.4). Thus, several methods of preparation can be derived for equilibrium samples. The general strategy is to synthesize samples as oxygen-rich and as impurity-poor as possible (sect. 3.1.2.1), and then decrease their oxygen content by equilibration with a reducing agent having an affinity to oxygen *comparable* to that of 123-O_x. To avoid any contaminating components, yttrium, copper metal or oxygen-poor 123-O_x have been used as reducing agents (sect. 3.1.2.2).

3.1.2.1. *Overdoped samples, $x > 6.95$.* Three different methods may be used to keep very low the carbonate content of equilibrium samples. High-purity oxides, Y_2O_3, CuO and $BaCO_3$, and high-purity Y and Cu metals, all 4N (99.99%), have been used as precursors. Only Ba metal was 3N, the main impurity being Sr.

(A) *Expelling carbonate (BAO samples).* $BaCO_3$ is decomposed in an oxygen atmosphere to BaO, by firing for a long time (40 h) at high temperature (950°C) to expel the carbonates. To avoid recapture of carbonate the oxide is taken from the furnace when still hot, and then introduced in a glove box with an argon atmosphere (gettered with hot cerium turnings to react with traces of oxygen, carbonate, hydrocarbons and humidity). There, it is mixed by grinding with the other oxides and then reacted in a furnace with a flowing oxygen atmosphere at 950°C for 20 h. Three grindings and annealings are performed under similar conditions, the last annealing in ceramic pellet form. These oxygen-rich samples are then reduced to lower oxygen contents by controlled reduction with O_2–Ar mixtures. Due to the very low oxygen partial pressure necessary, sometimes, at this early period the equilibration could not be completely reached in one step. That is why the scattering of lattice parameter data is higher than that of the CAR samples (sect. 3.2.2). Nevertheless, work with these samples showed for the first time anomalies of the lattice parameters, the existence of a maximum in the T_c vs. x curve (Rusiecki et al. 1990) and the dimpling transition

with elastic neutron scattering (Conder et al. 1994a) (sect. 6). Judged from these results, it seems that this method is sensitive for metastable phases (sect. 3.2.2.4).

(B) *Ba source without carbonate, directly oxidized Ba metal (DO samples).* Oxidation in a closed, evacuated system with controlled partial pressure of oxygen to avoid burning of barium, followed by a reaction with the other binary oxides. The experimental setup did not allow simultaneous processing of the whole batch, and therefore, some scattering of the data from these samples appears. Some of this scattering was found to be of an intrinsic nature, indicating pinning of the structure by phase transitions or latent structural changes in the "homogeneity" range of 123 (sect. 3.2.2.4).

(C) *Carbonate as Ba source, minimum carbonate content (CAR samples).* Almost all the investigations in the literature have been performed with samples synthesized with $BaCO_3$. With the exception of the work mentioned above – in BAO and DO samples – the non-linearity of the lattice parameters as a function of the oxygen doping (Rusiecki et al. 1990, Conder et al. 1994a, Kaldis et al. 1997b, Krüger et al. 1997) (sect. 3.2.2, 5.4.2) was not discussed elsewhere in the literature. It was imperative, therefore, to investigate samples synthesized with a $BaCO_3$ precursor under near-equilibrium conditions and compare them with those of samples from the above non-carbonate methods and the literature.

Ba carbonate (99.99%) was reacted in an oxygen atmosphere with the other high-purity oxides in 6 annealing steps (each 35 h) interrupted by grinding in the glove box. The temperature of the first step was 860°C in order to avoid melting due to the formation of eutectics. This would form compact material and hinder the reaction kinetics. The subsequent steps were performed with increasing temperature, up to 935°C. This last annealing was repeated twice for 75 and 50 h and was followed by cooling to room temperature with a rate of 30°C/h. The final step was annealing for 80 h in oxygen and then slow cooling down to room temperature with 1–10°C/h. As shown with mass spectrometry combined with thermogravimetry (Macejewski et al. 1994) (sect. 3.1.4) the above procedure (Krüger et al. 1997) leads to a minimum of carbonate content, due to the extended high temperature annealing.

The phase purity was determined with microprobe and calibrated X-ray powder diffraction. Only traces of $BaCuO_2$ were detected. The detection limit was estimated using powder mixtures of $YBa_2Cu_3O_{6.8}$ with exactly known amounts of $BaCuO_2$ in the range of 1–10 wt.%. Thus, it was possible to deduce by extrapolation a detection limit of 0.5 wt.%. The actual $BaCuO_2$ content of the CAR samples was below this limit. The oxygen content was $x \cong 6.990$.

A similar method, discussed in sect. 8, has been used for the synthesis of 11 Ca-doped and one O-overdoped 123 samples.

3.1.2.2. *Optimally doped, and underdoped samples, $x < 6.95$.* Reduction of these high-oxygen-content DO and CAR samples to achieve various oxygen nonstoichiometries is performed by equilibrating with an exactly known weight of Y-metal turnings in sealed ampoules. Alternatively, Cu-metal turnings or 123-O_x with lower x value can be used. Sample and reducing agent are placed in *separate* small alumina crucibles in evacuated,

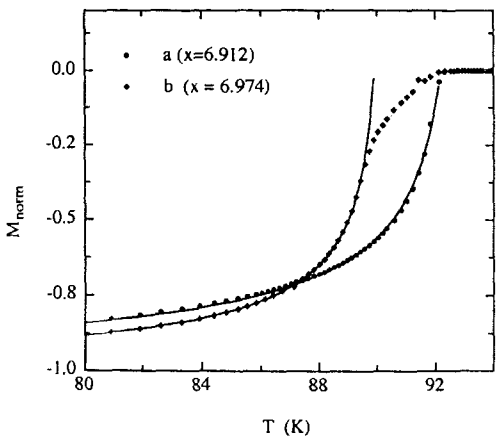

Fig. 8. DC normalized magnetization curve (SQUID, $H = 10$ Oe, field cooling) of $x = 6.974$ and $x = 6.912$ compositions. The high temperature resolution (0.1 K) allows a very high density of measurements. The solid lines represent a two-parameter fit of the Shoenberg model which perfectly describes the optimally doped sample $x = 6.912$. For discussion see sect. 7.3. After Conder et al. (1994b).

horizontal ampoules. The reduction is performed at 600°C for 15 h, and the furnace is cooled with 10°C/h. Alumina does not react with the cuprates at these low temperatures. 100 samples covering the complete nonstoichiometric range $6.00 \leqslant x \leqslant 6.990$ of tetragonal and orthorhombic 123-O_x were synthesized with this method.

An advantage of the CAR samples seems to be their increased apparent homogeneity. Measurements of their structural and physical properties show much less scattering. This is particularly evident in lattice parameters and micro-Raman measurements investigating with a microscope individual microcrystallites. This increased homogeneity is possibly due to traces of carbonate functioning as flux (homogenizing agent). However, *this homogeneity is not necessarily intrinsic* (sect. 3.2.2). It tends to mask transitions and metastable phases.

It is interesting to make a comparison of the methods of synthesis described here (sect. 3.1.2.1 and 3.1.2.2) with some well-equilibrated samples using a $BaCO_3$ precursor in the literature (Jacobson et al. 1989, Radaelli et al. 1992). Two points are probably detrimental in their experiments: The expulsion of the carbonate at higher temperature (970°C) which introduces traces of decomposition products, and the equilibration of a *mixture* of 123-$O_{6.1}$ and 123-$O_{6.9}$ powders in sealed ampoules. As the authors observe themselves (Radaelli et al. 1992), this method leads to a slightly inhomogeneous product in the range of the T → O transition. Thus, the first-order phase-transition line is crossed for different crystallites from opposite directions, causing *c*-axis discontinuities at different compositions. The same problem arises if, due to kinetic reasons, equilibrium is not attained at the same rate from both sides. Thus, the above-mentioned local separation of the reducing agent (Conder et al. 1994a, Krüger et al. 1997, Kaldis 1997) has clear advantages.

Polycrystalline, stoichiometric samples ($x = 6.912$) prepared with the above methods have d.c. susceptibilities with sharp diamagnetic transitions, as shown in fig. 8 (Conder et al. 1994a) for the optimally doped material with $\Delta T_c(10\text{–}50\%) = 2.8$ K (cf. sect. 7.3, figs. 86, 87).

3.1.3. *High-accuracy determination of the oxygen content*

Stoichiometry control cannot be better than the accuracy of the determination of nonstoichiometry. In the literature the nonstoichiometry of 123-O_x has been determined with various methods:

Iodometry. Standard iodometry has been used (Hume and Kolthoff 1944, Harris et al. 1987) with an error limit, but more sensitive is the use of bromide (Appelman et al. 1987). Often the achieved error limit is larger ($\Delta x = \pm 0.02$). Details of the methods are given by Harris (1990).

Thermogravimetry. More popular, because less time consuming, is thermogravimetry with error margin $\Delta x \geqslant \pm 0.02$ (see, e.g., ± 0.04, Jorgensen et al. 1990a). Conder (2000) calculated the shifts of T_c ($\Delta T_c/\Delta x$) corresponding to an error of $\Delta x = 0.01$. Figure 9a reminds that, as expected, the error in T_c is not linear with x but oscillates between −2 K (for $x = 6.980$) and +4 K (for $x = 6.450$)!

Thermogravimetric reduction. One should be very cautious with thermogravimetric reduction in reducing atmosphere, usually hydrogen (Gallagher et al. 1987, Swaminathan et al. 1988). A certain advantage is the universality of the method, as it can be used for all cuprates, independently of the copper valence in the sample, as the final state is metallic copper. Also, it contributes to its popularity that no wet chemistry is involved.

A plateau appears in the thermogravimetric curve near 650°C. Karppinen et al. (1996) proposed that this marks the stability range of Cu_2O. Conder (2000) found, however, from the weight loss that only a mixture of $2BaO + 3CuO + YOOH$ seems to fit to this plateau. Unfortunately, the existence of YOOH has not yet been proved experimentally. In the cooling curve there is a plateau in the 750–550°C range which can be used for the determination of the endpoint (Graf 1991). At lower temperatures, the increase of weight is probably due to a reaction of BaO with H_2O and/or CO_2. An additional source of error could appear if the temperature difference of the weight measurement at the beginning

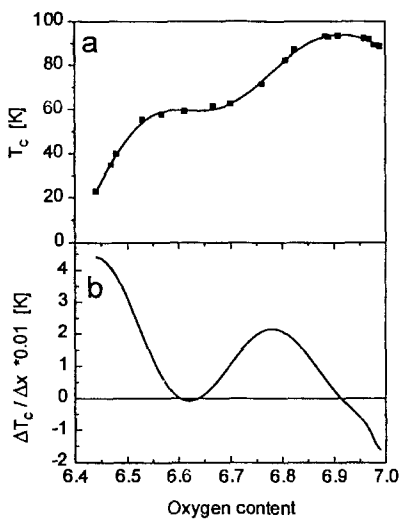

Fig. 9a. Lower part: shifts of T_c caused by an error of $\Delta x = 0.01$ in the determination of the oxygen content. As the slope of the $T_c(x)$ curve is not constant the errors in T_c vary between −2 and +4 K!. Upper part: $T_c(x)$. After Conder (2000).

(room temperature) and the end of the reaction (high temperature) is neglected. Also the existence of volatile impurities in the samples (CO_2, H_2O) may add to the errors.

Volumetric method. *One order of magnitude more accurate is a volumetric method* (Conder et al. 1989). This method is based on an old principle of analytical chemistry and has been used in the past for the determination of the hydrogen in RE hydrides (Bischof et al. 1983, Conder and Kaldis 1989). The accuracy of the hydrogen determination is lower, because hydrogen is lost easily by diffusion through the seals (O-rings etc.) and the walls of the analytical apparatus. As this is not the case for oxygen, the extreme accuracy of $\Delta x = \pm 0.001$ is achieved, for single-phase 123-O_x. Rusiecki et al. (1990) have calculated errors for the common second phase $BaCuO_2$. For 5 mol%, which is clearly above the limit of detection by X-rays, the analytical error for an oxygen-poor sample near $x = 6.53$ would be $\Delta x = +0.0006$; and for an oxygen-rich sample near 6.94 $\Delta x = +0.0081$, i.e. still under the limit of detection of iodometry. As mentioned above, equilibrium samples may sometimes have up to 0.5 wt% $BaCuO_2$!

The application of this method to HT_c superconductors is based on the oxidizing power of the $(Cu–O)^{+p}$ complex, shown by its reaction with acid, water and other oxidizable species. Thus, when superconductors containing holes, i.e. $(Cu–O)^{+p}$, come in contact with water or acid, oxygen is evolved. The important point is that this oxygen is not the result of the oxidation of the solution but *its origin is the solid superconductor,* as shown first by Shafer et al. (1988). Assuming an intermediate hexahydrate this process is schematically written for 123-O_x as

$$123\text{-}O_x \rightarrow [Cu(H_2O)_6]^{2+p} \rightarrow [Cu(H_2O)_6]^{2+} + 0.25\,O_2.$$

The quantity of oxygen evolved from the decomposition of water is a measure of the hole concentration of the 123-O_x sample (Shafer and Penney 1990).

In the case of the dissolution of the sample in dilute nitric acid the hole concentration is quantitatively calculated after the formal (quite simplified) reaction (Conder et al. 1989)

$$n\,Cu^{3+}_{sol.} + \tfrac{1}{2}n\,H_2O \rightarrow \tfrac{1}{4}n\,O_2 \uparrow + n\,H^+ + n\,Cu^{2+}.$$

It is necessary to recall, however, that according to early XPS (Nücker et al. 1987), EELS (Nücker et al. 1988), and XAS (Bianconi et al. 1987) investigations, the positive charge is generally considered not to be on the Cu but on the $(Cu–O)^+$ bond, and 80% on the oxygen p-orbitals (see e.g., Müller 1994).

The great absolute accuracy of this analytical method lies in the very accurate calibration. This is done by producing the necessary oxygen in the apparatus not by the decomposition of a sample but by electrolysis of H_2O. Coulometry is one of the most accurate physical measurements and therefore permits both high sensitivity and absolute accuracy. The method needs ~100 mg for each determination, which is no problem for polycrystalline samples, but is unfortunately too large for most of the currently available single crystals. 2–3 determinations are made from each sample. Samples of the composition $x \leqslant 6.45$ cannot be analyzed with this method because no excess holes exist when the superconductivity disappears. The method is applicable also to La cuprates (Conder 1999).

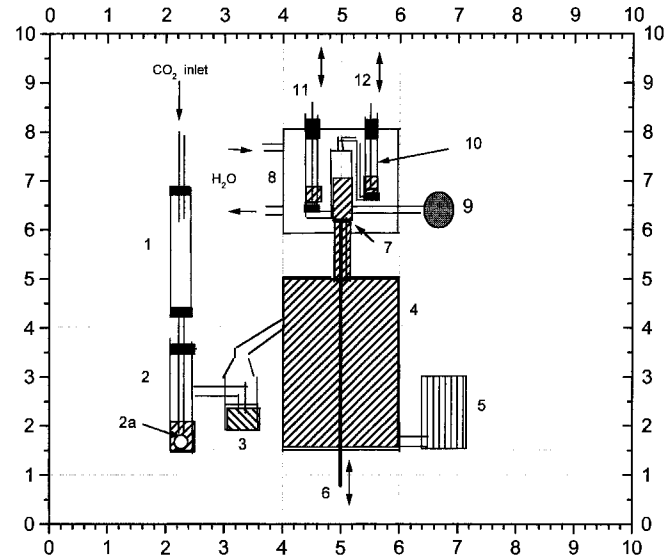

Fig. 9b. Apparatus for the volumetric oxygen determination of 123, after Conder et al. (1989) (schematically): (1) Flowmeter for the pure CO_2 stream. (2) Reaction vessel containing some diluted nitric acid, a piece of a stirring magnet, and the fragile glass capsule (2a) containing the 123 sample, which is broken with an external magnet. (3) Trap for KOH, filled with mercury, to avoid neutralization of the acid in the reaction vessel. (4) Absorption chamber filled with KOH to absorb the CO_2. (5) Niveau vessel joined with a long flexible tube to the absorption vessel, to change the niveau of KOH in (4). (6) Plexiglass rod with conical tip, operated vertically, to open and close the conical ground glass join of valve (7). (8) Water thermostat ($T = 22.50 \pm 0.01$°C) to keep the gas burette (10) and the oxygen volume at constant temperature. (9) Micrometer-driven syringe for the measurement of the volume of the evolved oxygen. (11,12) Valves (like 6) enabling the circulation of KOH and oxygen in the various chambers of the apparatus.

The high accuracy of this method permitted for the first time the study of oxygen doping of 123-O_x in very small intervals. This is conditio sine qua non for the discovery of latent phase transitions and lattice changes (Rusiecki et al. 1990, Conder et al. 1994a, Kaldis 1997, Kaldis et al. 1997b) (sect. 6).

Figure 9b schematically shows the apparatus for oxygen determination. The 4N8(!) pure CO_2 gas (constant flow rate 40 cm^3/min) carries the oxygen evolved by the reaction of diluted HNO_3 acid ($1HNO_3 : 9H_2O$) with Y-123-O_x (in reaction vessel 2) into the absorption chamber (4). There the CO_2 is absorbed by the KOH solution and the oxygen to be measured gathers at the entrance of valve 7, and is then measured in 9 (or 10).

At the beginning of the experiment, after purging the system for 20 min. the rest-oxygen value of the apparatus is determined, at least two times. If the gas flow system is clean and tight, the blank test value is in the range 0.006–0.015 cm^3 for the gas purity used. This value has to be subtracted from the oxygen volume measured after breaking the sample capsule. At the end of the experiment another blank test is measured. If the flushing of oxygen is complete the initial and the final blank test values have to be equal.

After the blank rest-oxygen value is found constant in at least two determinations giving equal values, the evacuated glass capsule containing the sample is broken in the reaction vessel 2 and the carrier gas transfers the oxygen into the absorption chamber 4. When all the gas is transferred, valve 7 is opened and the gas is measured either with the thermostatized (±0.01°C) gas burette with measuring accuracy ±0.1 mbar, or, preferably, in a micrometer-driven syringe with measuring accuracy ±0.001 ml. Depending on the sample weight and composition an oxygen volume of 1.5–3.0 cm^3 is measured.

As mentioned above, the high accuracy of the method is due to the calibration with electrolysis of water. This is done by changing the reaction vessel 2 with the oxygen electrode of the electrolysis of water (Conder et al. 1989). The current is coulometrically controlled with very high accuracy and, therefore, the amount of oxygen introduced into the apparatus also. For further information the author can be contacted.

Coulometric titration. This method was used by Ahn et al. (1988, 1990) for the determination of phase equilibria, and by Tetenbaum et al. (1989) for the determination of a possible miscibility gap. A drawback is that the absolute accuracy depends on the oxygen content of the starting material. This was determined by iodometry and therefore the accuracy was only $\Delta x = \pm 0.02$. The near equilibrium conditions of the synthesis of their samples allowed the determination by EM of the various superstructures (sect. 5.1.1).

3.1.4. *Mass-spectrometric determination of the carbonate content*

The incorporation of carbonate in the cuprates was investigated from the early stage of the HT_c era and was found to decrease the superconducting properties and particularly T_c (e.g., Gallagher et al. 1988, Lindemer et al. 1990, Greaves and Slater 1991, Wang et al. 1996). These investigations later triggered the synthesis of a series of copper oxycarbonates, some of them with appreciable T_c's (e.g., Domanges et al. 1993, Raveau et al. 1993). The CO_2 was measured with various methods e.g., by heating up to 1100°C and measuring with a Leco carbon analyzer (Lindemer et al. 1990), absorbing in $Ba(OH)_2$ (Karen and Kjekshus 1991) or using DTA and thermogravimetric methods (Gallagher et al. 1988). Structurally, the number of carbons involved was estimated in 123 from the number of C–O short bonds (Greaves and Slater 1991). Thermal desorption combined with mass spectrometry were performed up to 900°C (Keller et al. 1987) and the desorbed gas composition was found to be 0.59 wt.% CO_2 and 0.28 wt.% CO. In a later investigation up to 820°C (Wada et al. 1992) no quantitative determination of the carbon-containing species was made.

Using a combination of a thermobalance and a mass spectrometer DO and CAR samples (sect. 3.1.2.1) were investigated (Macejewski et al. 1994). A highlight of these investigations is that they led to low carbonate contents of the order of 2000 wt. ppm or less. Part of this carbonate is due to contamination from the atmosphere. As an example, a sample synthesized with $BaCO_3$ precursor and annealed for 12 h at 900°C in oxygen atmosphere is shown in fig. 10 (curve a). As a result of this rapid synthesis, it contained ~5–10% $BaCuO_2$ and Y_2BaCuO_5 as shown by XRD. The thermogravimetric determination gave a total of 5800 wt. ppm CO_2 (0.58 wt%). Following a procedure

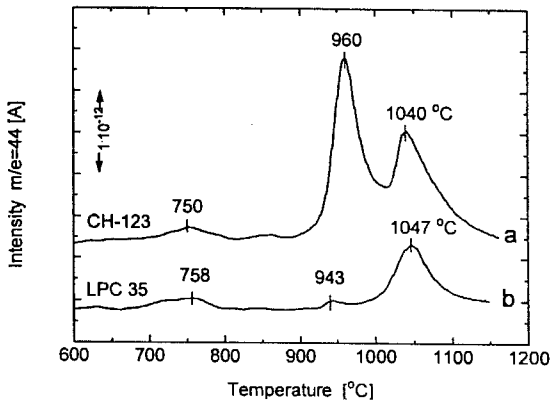

Fig. 10. Simultaneous thermal and mass-spectrometric analysis of a CAR sample (Ba source: carbonate, sect. 3.1.2.1) heated in oxygen stream: (a) evolution of CO_2 from a rapidly synthesized sample (CH-123, 5800 wt.ppm) and the same sample after CAR procedure annealings (LPC 35, 1050 wt.ppm); (b) DTA and TG curves. The desorption of CO_2 takes place at three temperatures, indicating incorporation at three different sites of the lattice. After Macejewski et al. (1994).

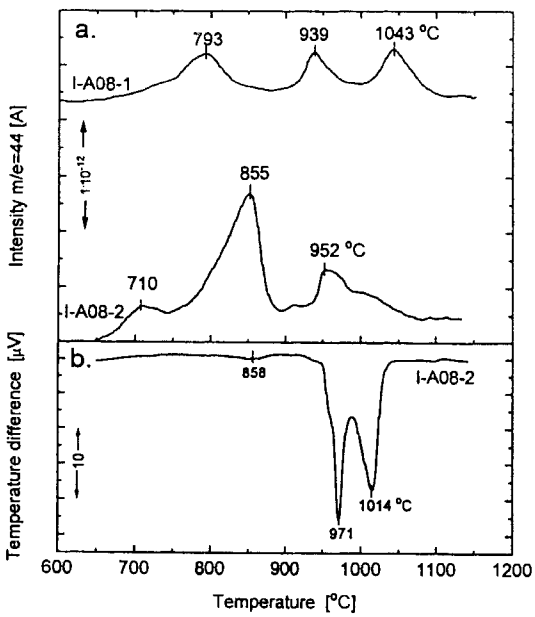

Fig. 11. As fig. 10, but for a DO sample (sect. 3.1.2.1), Ba source: metal not carbonate: (a) I-A08-1 sample stored 250 h in CO_2 atmosphere at room temperature, and I-A08-2 at 120°C. Note the shift of desorption temperatures and intensities (concentrations) indicating changes of the CO_2 bonding depending on adsorption temperatures. Sample I-A08-2 contained nearly twice as much CO_2. Experiment in oxygen atmosphere. (b) DTA signal of I-A08-2. After Macejewski et al. (1994).

similar to that of the CAR samples, the same sample was then annealed exhaustively 2×24 h (in air), 2×48 h (air) and 5 h (air), each time with intermediate grindings (total of six). As a result, only a small peak remained at 1047°C, with a total CO_2 content of 1050 wt. ppm (fig. 10, curve b). This is a temperature at which the compound decomposes (>970°C) and, therefore, this residual CO_2 content can be removed only if the CAR sample is destroyed. The T_c's for figs. 10a and 10b were the same, but the transition width of the a sample was four times that of b. Figure 11 shows the behavior of a DO sample. The same three peaks of CO_2 evolution were found (cf. fig. 10a), indicating the existence of three different sites of incorporation in the 123 lattice. However, whereas

the total residual amount at 1043°C was 2350 ppm (similar to the above), more than 50% evolved at lower temperatures. The reason for the existence of a similar residual CO_2 in the DO and CAR samples (sect. 3.1.2.1) must be attributed to the closed system in which the oxidation of the metals and all annealings of DO took place. The desorbed gas was absorbed again during cooling. Annealing in an open system with flowing oxygen would decrease the carbonate. The origin of CO_2 in the DO samples is very probably in the starting materials and the exposure to air.

Experiments in argon atmosphere showed that the evolution from the CAR samples is coupled with evolution of O and therefore decomposition. This supports the strong bonding of CO_2 in CAR and the conclusion that it would be possible to expel most of the carbonate from the DO samples without decomposition, but not from CAR samples. As we will discuss later (sect. 3.2.2.5), some characteristic structural anomalies of the lattice constants do not appear or are different for CAR samples. We note that almost all samples used in the literature have been synthesized with a $BaCO_3$ precursor.

3.2. *Changes of the lattice parameters and bond lengths with the oxygen nonstoichiometry: the structural T → O transformation*

3.2.1. *Nonequilibrium samples, mainly underdoped regime*

3.2.1.1. *Lattice parameters of non-equilibrium samples.* Figures 12a–c show the dependence of the lattice parameters, on the oxygen nonstoichiometry from the data of Cava et al. (1990) and Jorgensen et al. (1990a). We note in the data of Cava et al. (1990) the appreciable stepwise contraction of the *c*-axis by ~0.6% in the $x \approx 6.35$–6.45 range where the T → O structural transformation takes place. Similar steps appear also in the *a*- and *b*-axis. This effect appears both at RT X-ray investigations (Cava et al. 1988a,b) and LT neutron diffraction refinements (Cava et al. 1990). Electrical transport and magnetic measurements showed that the onset of superconductivity (insulator–metal transition) for these samples takes place at $x = 6.45$. In sect. 3.2.2 we will see that *equilibrium samples do show also abrupt steps of the lattice parameters.*

The abrupt change of the lattice parameters has been contested by many other investigators, the reason being, like in so many HT_cS issues, the different thermal and chemical histories of the samples. Jorgensen et al. (1990a) found in their RT neutron diffraction investigation a change of the slope of the *c*-axis but not an abrupt step, for samples quenched from higher temperatures than those of Cava et al. (1990), and without gettering (fig. 12c). This has been confirmed also by later investigations with samples equilibrated at lower temperatures (e.g., Radaelli et al. 1992).

The step appears also in the apical bond (Cu2–O1) (fig. 14). Cava et al. (1990) concluded from this abrupt structural change that the superconductivity is triggered by the T → O transition and, therefore, it appears at the onset of the orthorhombic phase. Their paper presents the first systematic interdisciplinary investigation of the structural parameters and magnetic properties as a function of the nonstoichiometry, supporting the charge-transfer model from the chains to the planes which is now generally accepted.

From the measurements of fig. 12 and many others at the time, the general impression remained that in all other ranges of *x* the lattice parameters change linearly. Investigations

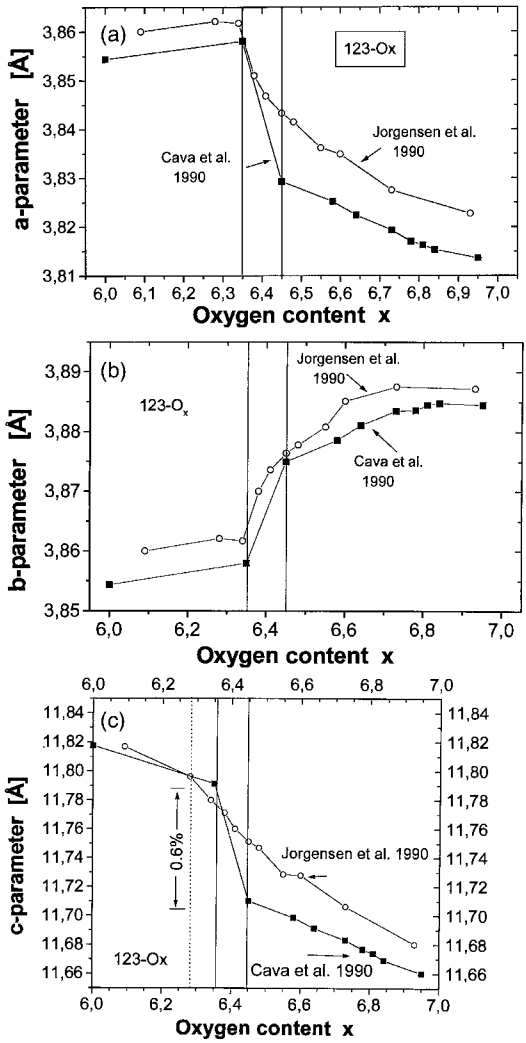

Fig. 12. Dependence of the lattice parameters on oxygen nonstoichiometry: (a) *a*-parameter; (b) *b*-parameter; (c) *c*-parameter. NPD after Cava et al. (1990) (solid squares), at $T = 5$ K (compare table 3a); Jorgensen et al. (1990b) (open circles), NPD at RT. Note the abrupt change at the phase transition ($x = 6.35$–6.45) of the Zr-gettered samples of Cava et al. The vertical shift of the two groups of data is due to the different temperatures. The vertical lines show the boundaries of changes of the lattice parameters. The onset of superconductivity for the Zr-gettered samples is $x = 6.45$, that for the quenched samples is $x \approx 6.35$.

with a much larger number of equilibrium samples and more accurately determined oxygen content show several deviations from linearity for the *a*-, *b*-, and *c*-parameters with the corresponding changes of orthorhombicity and unit cell volume near the overdoped phase (sect. 3.2.2.3 and 3.2.2.4).

The dependence of the structural parameters on the oxygen content of the gettered samples as refined by neutron diffraction in the centrosymmetric Pmmm space group for the orthorhombic and in the P4/mmm for the tetragonal phase at 5 K (Cava et al. 1990) are given in table 3a. The experiments were not aiming at the highest possible resolution but combined good resolution (D2B instrument in ILL, Grenoble) with the investigation

Table 3a
Neutron diffraction data of 123-O_x at 5 K. Structural parameters at 10 oxygen stoichiometries[a]

υ=		Oxygen stiochiometry									
		6.95	6.84	6.81	6.78	6.73	6.64	6.58	6.45	6.35	6.00
a		3.8136(1)	3.8153(1)	3.8163(1)	3.8170(1)	3.8193(1)	3.8224(1)	3.8252(1)	3.8293(1)	3.8580(1)	3.8544(1)
b		3.8845(1)	3.8848(1)	3.8845(1)	3.8936(1)	3.8835(1)	3.8811(1)	3.8786(1)	3.8750(1)	3.8580(1)	3.8544(1)
c		11.6603(3)	11.6692(3)	11.6739(3)	11.6768(3)	11.6832(2)	11.6912(3)	11.6987(3)	11.7101(4)	11.7913(3)	11.8175(4)
Ba	(*z*)	0.1843(2)	0.1856(2)	0.1859(2)	0.1862(2)	0.1867(2)	0.1873(3)	0.1877(2)	0.1878(3)	0.1931(2)	0.1944(3)
	(*B*)	0.34(4)	0.41(4)	0.25(4)	0.27(40)	0.32(3)	0.16(5)	0.43(4)	0.05(6)	0.68(6)	0.37(6)
Y	(*B*)	0.67(4)	0.41(4)	0.44(4)	0.18(4)	0.37(3)	0.18(5)	0.63(4)	0.14(6)	0.48(5)	0.15(5)
Cu(1)	(*B*)	0.44(4)	0.43(4)	0.34(4)	0.26(4)	0.29(3)	0.11(4)	0.46(4)	0.0.06(6)	0.76(5)	0.44(5)
Cu(2)	(*z*)	0.3546(2)	0.3552(1)	0.3561(1)	0.3559(1)	0.3561(1)	0.3571(2)	0.3574(1)	0.3573(2)	0.3603(2)	0.3602(2)
	(*B*)	0.22(3)	0.28(3)	0.17(3)	0.14(3)	0.23(2)	0.01(3)	0.47(3)	0.09(4)	0.59(3)	0.23(3)
O(1)	(*z*)	0.1572(2)	0.1579(2)	0.1570(2)	0.1565(2)	0.1568(2)	0.1564(2)	0.1553(2)	0.1541(3)	0.1515(3)	0.1511(3)
	(*B*)	0.65(4)	0.71(4)	0.65(4)	0.55(4)	0.68(3)	0.51(4)	0.86(4)	0.54(6)	1.06(5)	0.61(5)
O(2)	(*z*)	0.3781(2)	0.3785(2)	0.3786(2)	0.3787(2)	0.3786(2)	0.3786(2)	0.3792(2)	0.3781(3)	0.3788(2)	0.3791(2)
	(*B*)	0.55(4)	0.53(4)	0.55(4)	0.43(4)	0.50(3)	0.38(4)	0.74(4)	0.30(6)	0.59(3)	0.27(3)
O(3)	(*z*)	0.3777(2)	0.3777(2)	0.3780(2)	0.3779(2)	0.3778(2)	0.3786(3)	0.3776(2)	0.3768(4)	0.3788	0.3791
	(*B*)	0.33(4)	0.22(4)	0.25(4)	0.15(4)	0.31(3)	0.15(4)	0.62(4)	0.10(6)	0.59	0.27
O(4)	(*B*)	0.97(8)	0.72(8)	0.56(8)	0.49(8)	0.61(7)	0.65(11)	0.86(10)	0.10(18)	3.14(50)	
	(*n*)	0.475	0.420	0.405	0.390	0.375	0.320	0.290	0.225	0.175	0.000
R_I		6.57	8.14	7.32	5.61	4.46	7.54	7.28	10.95	8.06	8.57
R_P		10.42	9.32	10.61	9.83	8.03	10.92	9.50	15.51	12.63	12.93

[a] The standard deviations do not include the uncertainty in the effective neutron wavelength. After Cava et al. (1990).

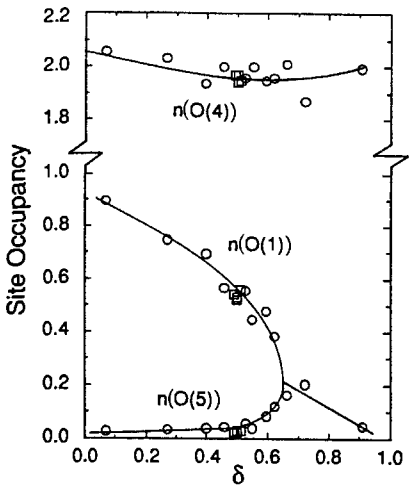

Fig. 13. Site occupancies for oxygen in the 123-O_x structure as a function of nonstoichiometry from RT neutron diffraction. $\delta \approx 7-x$ is based on the measured weight loss. Note the use of O1 for the chain sites and O4 for the apical sites. A smooth T–O transition takes place, indicating a second-order transition. This is in contrast to later experiments (Radaelli et al. (1992); cf. fig. 34, sect. 3.3). After Jorgensen et al. (1990a).

of 10 samples in the range $x = 6.00$–6.95. The highest error source is the reproducibility of the position of the samples in the beam to achieve the same wavelength. The estimated error limits are ± 0.0003 Å and are not included in the values for the lattice parameters. The calculated standard error for the oxygen occupancies is 3%. All sites were refined and with the exception of the chain oxygen O4 found fully occupied. Jorgensen et al. (1990a) found for their samples (quenched from higher temperatures in liquid nitrogen) an up to 5% occupancy of the antichain position O5 and even some vacancies for the apical oxygen (fig. 13; note that in this figure O4 is used for the apical oxygen and O1 for chain oxygen). Later work with better equilibrated samples (Radaelli et al. 1992, Böttger et al. 1996) confirmed the occupancy of O5. Single-crystal work by von Zimmermann et al. (1999) did not show O5 site occupation (sect. 5.1.1). We have, therefore, to conclude that the O5 occupancy depends sensitively on the synthesis conditions.

3.2.1.2. *Cu–O bonds.* Bond lengths at 5 K (Cava et al. 1990) are given in table 3b. As mentioned above, the change of the O-nonstoichiometry strongly affects the apical bond Cu2–O1 (Cava et al. 1988a,b, 1990). Figure 14 shows this trend and fig. 15 shows the changes of the Cu2–O2 and Cu2–O3 bonds in the superconducting planes which are appreciably smaller (Hewat 1994). The 0.6% contraction step in the c-axis (fig. 12c) translates into a 3.4% contraction of the apical bond. A further 3% contraction takes place in the superconducting region ($x > 6.4$) (fig. 14), with increasing T_c (fig. 2).

The same bond after Jorgensen et al. (1990a) is also shown in fig. 14. The influence of different synthesis conditions is again clearly seen. Although the trend of change of the bond with oxygen content is the same, differences in the slopes of the curves exist, particularly in the region of the tetragonal → orthorhombic transition at $x \approx 6.4$. The synthesis conditions of Cava et al. (1987a,b) – Zr getter, lower temperatures – and Jorgensen et al. (1990a) – quenched in liquid nitrogen from higher temperatures – are summarized in table 4 for comparison. Further discussion about the differences between the two curves in

Table 3b

Bond lengths in $YBa_2Cu_3O_x$ at 5 K together with the bond valence sums V defined by Brown and Andermatt (1985)[a]

$x=$		Oxygen stiochiometry									
		6.95	6.84	6.81	6.78	6.73	6.64	6.58	6.45	6.35	6.00
Ba	–O(1)×4	2.740(0)	2.742(0)	2.744(0)	2.745(0)	2.746(0)	2.748(1)	2.750(0)	2.752(1)	2.772(1)	2.773(1)
	–O(2)×2	2.980(3)	2.973(2)	2.972(2)	2.971(2)	2.966(2)	2.960(3)	2.963(3)	2.952(4)	2.918(3)	2.911(3)
	–O(3)×2	2.953(3)	2.944(3)	2.945(3)	2.942(3)	2.937(3)	2.942(4)	2.931(3)	2.926(4)	2.918	2.911
	–O(4)×2	2.873(2)	2.886(2)	2.890(2)	2.893(2)	2.900(2)	2.907(3)	2.912(2)	2.916(3)	2.985(2)	2.999(3)
	$-V$	2.192(7)	2.143(6)	2.121(6)	2.108(6)	2.088(5)	2.044(11)	2.020(6)	1.979(11)	1.901(8)	1.809(8)
Y	–O(2)×4	2.407(1)	2.405(1)	2.405(1)	2.403(1)	2.404(1)	2.404(1)	2.400(1)	2.407(2)	2.401(1)	2.399(1)
	–O(3)×4	2.381(1)	2.382(1)	2.381(1)	2.382(1)	2.384(1)	2.380(2)	2.389(1)	2.397(3)	2.401	2.399
	$-V$	2.905(7)	2.909(7)	2.913(7)	2.917(7)	2.905(7)	2.921(11)	2.900(7)	2.842(19)	2.849(7)	2.865(7)
Cu(1)	–O(1)×2	1.833(2)	1.843(2)	1.833(2)	1.828(2)	1.832(2)	1.829(2)	1.817(2)	1.805(4)	1.786(4)	1.786(4)
	–O(4)×2	1.942(0)	1.942(0)	1.942(0)	1.942(0)	1.942(0)	1.941(0)	1.939(0)	1.937(0)	1.929(0)	1.927(0)
	$-V$	2.378(7)	2.158(6)	2.166(7)	2.149(7)	2.057(7)	1.942(7)	1.923(7)	1.799(15)	1.774(16)	1.308(16)
Cu(2)	–O(1)×1	2.301(3)	2.302(3)	2.324(3)	2.328(3)	2.328(3)	2.347(3)	2.364(3)	2.380(4)	2.463(4)	2.471(4)
	–O(2)×2	1.927(0)	1.927(0)	1.926(0)	1.927(0)	1.928(0)	1.928(0)	1.930(0)	1.930(1)	1.941(0)	1.940(0)
	–O(3)×2	1.961(0)	1.960(0)	1.959(0)	1.959(0)	1.958(0)	1.957(1)	1.954(0)	1.951(1)	1.941	1.940
	$-V$	2.209(1)	2.212(1)	2.203(1)	2.197(1)	2.196(1)	2.187(3)	2.179(1)	2.181(6)	2.127(1)	2.134(1)
O(1)	$-V$	2.015(4)	1.991(4)	1.992(4)	1.996(4)	1.985(4)	1.975(7)	1.984(4)	1.993(11)	1.942(11)	1.937(11)
O(2)	$-V$	2.030(3)	2.040(2)	2.043(2)	2.044(2)	2.044(2)	2.050(3)	2.049(3)	2.046(8)	2.058(3)	2.072(3)
O(3)	$-V$	0.014(4)	2.023(4)	2.026(4)	2.027(4)	2.030(4)	2.036(9)	2.036(3)	2.033(10)	2.058(3)	2.072(3)
O(4)	$-V$	1.798(1)	1.770(1)	1.762(1)	1.755(1)	1.742(1)	1.730(1)	1.725(1)	1.723(1)	1.621(1)	1.604(1)
Cat	$-V$	14.08(3)	13.78(3)	13.73(3)	13.68(3)	13.53(3)	13.33(5)	13.22(3)	12.96(7)	12.68(4)	12.06(4)
Oxy	$-V$	13.83(2)	13.60(2)	13.545(2)	13.50(2)	13.39(2)	13.23(4)	13.14(2)	12.92(6)	12.68(3)	12.18(3)

[a] After Cava et al. (1990).

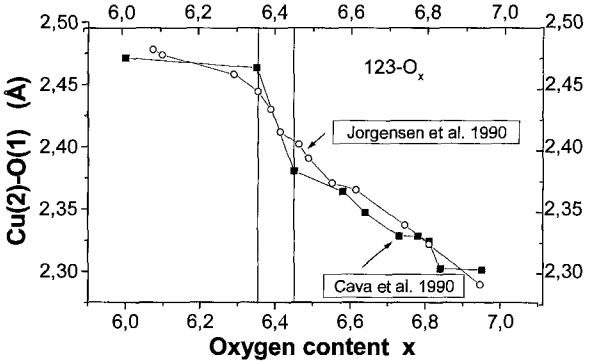

Fig. 14. Dependence of the apical bond Cu2–O1 on the oxygen nonstoichiometry. Note the abrupt change of the Zr-gettered samples (solid squares) at the T → O transition. NPD data, after Cava et al. (1990) and Hewat (1994) at $T = 5$ K, and Jorgensen et al. (1990a) (open circles) at RT.

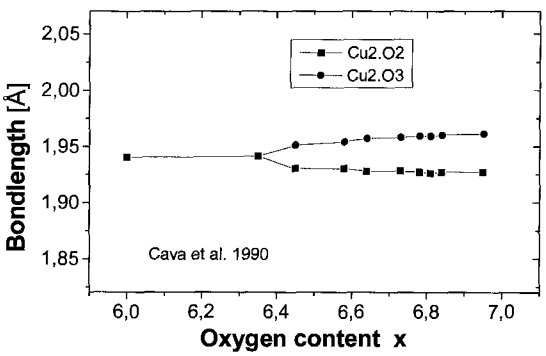

Fig. 15. Cu2–O3 and Cu2–O2 bond lengths as a function of oxygen nonstoichiometry. After Cava et al. (1990) and Hewat (1994).

Table 4
Comparison of the synthesis conditions of quenched samples

Cava et al. (1987a,b, 1990)	Jorgensen et al. (1990a)
Master batch, powder/pellets	**Master batch, powder/pellets**
Fired in air 900 and 950°C 3 days	Fired in air 960°C 1 day
Intermediate grindings.	Intermediate grinding (200mesh).
Fired in flowing O_2, 16 h at **1000°C**;	Pellets 960°C 1 day in flowing O_2;
Annealing in flowing O_2, 12 h at 500°C	Annealing **670°C** 1 day/cooling 50°C/h;
Stated composition: $x = 7.00$?	Composition (iodometric) $x = 6.93 \pm 0.01$
Impurities?	Impurities: few % green phase
Reduction of oxygen content	**Reduction**
2 days **360**–520°C with Zr foil[a] in sealed evacuated quartz ampoules;	2–4 days **520±1°C** O_2–Ar controlled atmosphere at given P_{O_2} ($1–2 \times 10^{-4}$ atm);
Quenched to RT	**Quenched to liquid nitrogen**
Oxygen determination	**Oxygen determination**
Reduction in N_2–15% H_2;	Iodometry: $\Delta x = \pm 0.01$;
Stated accuracy $\Delta x = \pm 0.02$	Thermogravimetry $\Delta x = \pm 0.02$

[a] Cava et al. (1990). 4 days at **440°C** with Zr foil; variation of stoichiometry with the amount of Zr.

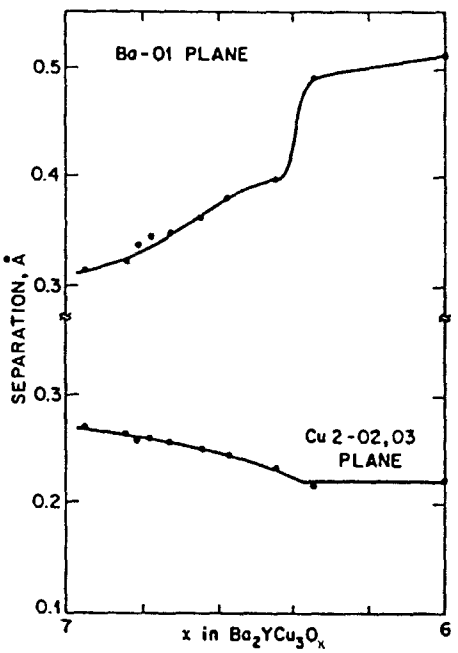

Fig. 16. Dependence of the puckering (dimpling) of the Cu2–O2,O3 plane and the Ba–O1 plane on oxygen nonstoichiometry. The separation is shown between the Ba and O1 layers, and between Cu2 and the average O2,O3 layer along the *c*-axis. We note that the relative change at the step in the Cu2–O2,O3 dimpling is 2.3% whereas the bond lengths of Cu2–O2 and Cu2–O3 (fig. 15) change very little. Also, the Ba–O1 dimpling at $x \approx 6.4$ shows a change by 24% whereas the Ba–O1 bond length changes only by 1% (fig. 18). After Cava et al. (1990).

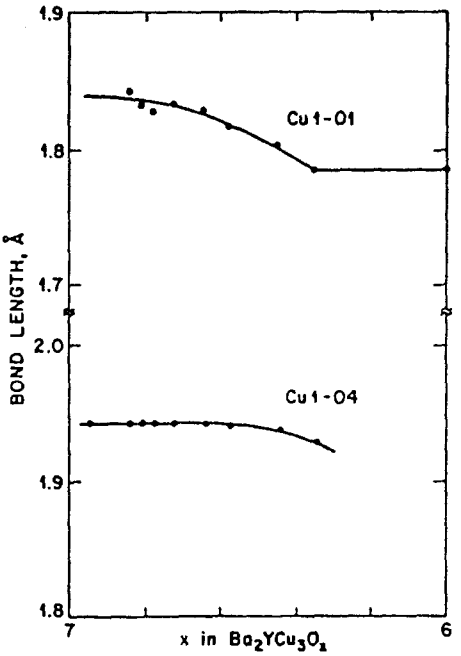

Fig. 17. Dependence of the bond lengths between Cu1 and the apical oxygen O1 and Cu1 and the chain oxygen O4 on oxygen nonstoichiometry. Whereas the effect is very pronounced in the first case (30%), it is very small in the second case. After Cava et al. (1990).

figs. 12 and 14 is given in the context of the T → O transition in sect. 3.3. The controversy about the existence of the abrupt step in the *c*-axis did not only come from the results of Jorgensen et al. (1990a) and other groups, but also from inconsistencies among the various Zr-gettered samples. Thus, Cava et al. (1988a,b) did not find this step and the onset of superconductivity at the T → O transition, but inside the orthorhombic symmetry regime. Several other groups have also found the onset of superconductivity inside the orthorhombic phase (Maletta et al. 1989, Radaelli et al. 1992). As we will see, these findings seem to be confirmed by the equilibrium samples (sect. 3.2.2.3). The explanation given by Cava et al. (1990) is that this effect depends on the annealing temperature.

Figure 16 shows the increase with oxygen doping of the dimpling Cu2–O2/O3 of the planes (i.e. spacing from Cu2 to the average O2/O3 plane). The absolute change of the

mean value of the Cu–O2 and Cu–O3 bonds (fig. 15) is 0.055 Å and the relative change is significant: 2.3%. The dependence of dimpling on the oxygen content is discussed in sects. 5.3, 6 and subsequent sections for equilibrium samples. The changes of the Cu1–O1 (apex) and Cu1–O4 (chain) bonds are shown in fig. 17. The increase is 2.63% for the former, but only 0.8% for the latter. Summing up, appreciable changes of bond lengths take place between the regime of fourfold coordination ($x > 6.35$) and twofold coordination ($x < 6.35$) where the bond length remains constant (Cava et al. 1990).

3.2.1.3. *Ba–O and Y–O bonds.* Figure 18 shows the changes of the Ba bonds to the apical oxygen O1 and the chain oxygen O4. The coordination changes stepwise again. The effect is much more pronounced in the Ba–O1 layer. The dimpling is shown in fig. 16. The bond lengths of the Ba-atoms to the oxygens of the planes O2 and O3 are shown in fig. 19. Like in the case of Cu2 (fig. 15) the orthorhombicity splits these values whereas in the tetragonal regime they overlap. Analogous is the situation for Y.

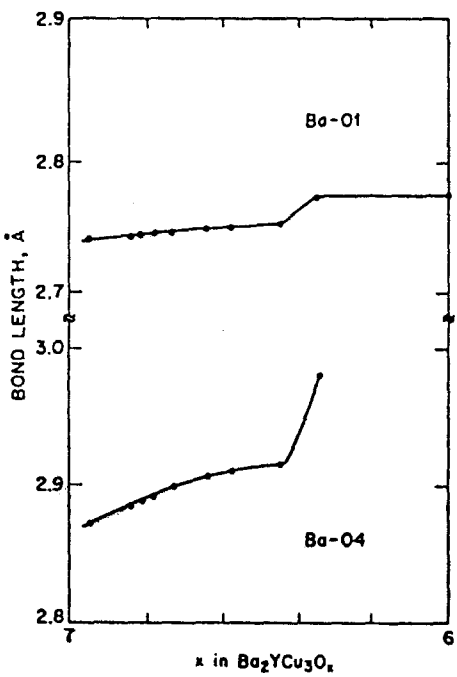

Fig. 18. Dependence of the Ba–O bond lengths on oxygen nonstoichiometry. The T → O transition is much more pronounced for the oxygen of the chains. After Cava et al. (1990).

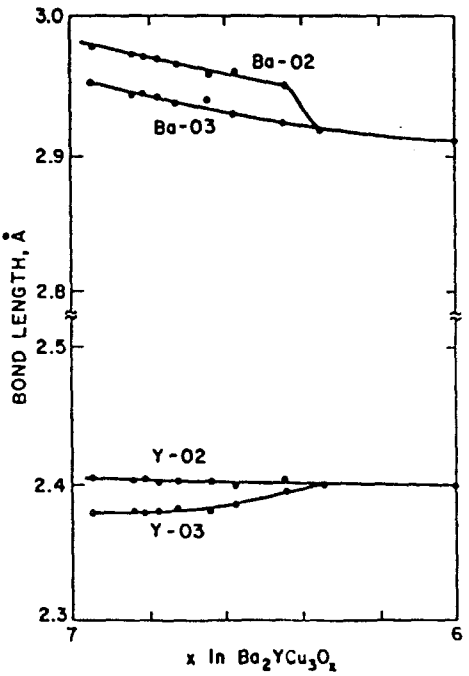

Fig. 19. Dependence of the bond lengths between Ba and Y and the plane oxygens O2 and O3 on oxygen nonstoichiometry. The splitting in the orthorhombic range is clearly seen. After Cava et al. (1990).

3.2.1.4. *Application of the Bond Valence Sum (BVS) method to 123-O_x – I.* The Bond Valence Sum (BVS) method is a *very sensitive probe* because it reacts to any change of the bond lengths of a solid. Due to this reason it is not very specific and the values it gives should be considered as good estimates of the valence *and* strain effects acting on a given atom. However, its great value is as a warning that non-ideal conditions are existing in the structure. Using a nonstoichiometric series consisting of *many* samples one can then find important trends between valence and other properties.

The idea that the strength of the bond between a given anion–cation pair in a structure can give information about the valence of the ions involved originates from Pauling (at a time where only very few crystal structures had been determined!) and is based on the idea that *higher oxidation states lead to shorter bonds*. Pauling (1929) defined a *bond strength s* for a cation–anion bond:

$$s = z/N,$$

with z the formal valence of the cation, and N the coordination number of the nearest anion neighbors (assumed to be equivalent).

Summation over the bond strengths of the cations surrounding an anion would give the anion valence. Much later, after a very large number of crystal structures had become available, it was shown that for most inorganic compounds *the sum of the bond valences around any atom lies within 0.1 of its formal oxidation state* (Brown and Shannon 1973). The historical development of the method and the contributions of Zachariasen (1931) and Brown and Andermatt (1985) are briefly discussed by Marezio and Chaillout (1994) and by Hewat (1994). Brown (1989) presented a complete study of the oxidation states and the internal stresses in 123-O_x ($x = 6.0$–7.0) using the BVS method. He pointed out that because the structure of 123-O_x is highly constrained there are some important difficulties in applying this method.

The bond valence s_{ij} between a cation i and an anion j which are at a distance R_{ij}, is given according to Brown and Andermatt (1985) by

$$s_{ij} = \exp(R_0 - R_{ij}/B),$$

where R_0 and B are constants with tabulated values. B has a typical value of 0.37 Å, and the R_0 value was taken in 123-O_x to be 1.60 Å for Cu^{1+}, 1.679 Å for Cu^{2+}, and 1.73 Å for Cu^{3+} (Brown 1989). These values arise as averages from a series of structure determinations of well-known compounds with corresponding copper valences, using the valence equation (1). From the Inorganic Crystal Structure Database Brown and Andermatt (1985) have determined average R_0 values for 750 ion pairs. Summing over all the copper–oxygen bonds ij in the copper coordination sphere, we can determine the valence of an ion (as a sum of bond valences) by solving the equation

$$V_j = \sum_j s_{ij} = \sum_j \exp\left(\frac{R_0 - R_{ij}}{0.37}\right) \tag{1}$$

With this equation Brown (1989) analyzed 13 structure determinations of 123-O_x with different x values. Initial calculations were performed for all copper as Cu^{2+}. When

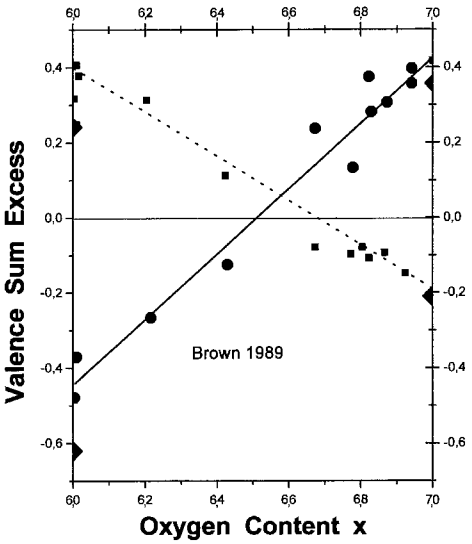

Fig. 20. Difference between the bond valence sums of the investigated nonstoichiometric 123-O_x samples and the oxidation states (per Ba_2Cu_3 formula unit) of Ba (circles, solid line) and Cu (squares, dotted line). At $x=7.0$ the Ba is too small for its cage and at $x=6.0$ it is too big. Lattice distortions will appear at both these values (see text). The diamonds show model calculations. After Brown (1989).

deviations appeared, mixtures of the various copper valences were used. With increasing oxygen content the valence sums of Y, O2, and O3 remain more or less constant (at 3.0 and 2.0 respectively) and *that of O4 increases (also of O1 and Ba).* However, although the valence sums of Cu1 and Cu2 increase with increasing oxygen content, their ratio to the expected value decreases due to the strains.

An important aspect of this investigation concerns the *internal stresses* of the 123-O_x structure and their change with oxygen nonstoichiometry. Undistorted cubic perovskites are very rare. Stresses appear in the following two cases:

(1) If the large atom A of perovskite (Ba) is too large for its cubic cage BO_3 (Cu_3O_x) then the cage is under tension and Ba under compression.

(2) If Ba is too small for the Cu_3O_x cage the opposite happens.

Brown (1978) has shown that if the difference between the valence sum determined from the crystallographic data and the ideal valence value is more than 0.2, the cubic perovskite structure is distorted by one of the following two mechanisms:

(i) When A is too large for its cage the smaller B atom is shifted in an off-center position in its octahedron. This leads to a *ferroelectric phase,* e.g., $BaTiO_3$.

(ii) When A is too small for its cage the cage contracts by a rotation of the octahedra leading to a *ferroelastic phase.*

For the application of BVS it is important to know that in the above cases the coordination sphere of the cation under tension is distorted. This can lead to a *higher valence sum without change of the average bond lengths* (Brown and Shannon 1973). Thus, *both valence changes and lattice distortions affect the BVS.*

The differences between the valence sums based on the structural data and the oxidation states of Ba and Cu – per formula unit Ba_2Cu_3 – as a function of the oxygen nonstoichiometry (Brown 1989) are shown in fig. 20. The results indicate that *oxygen-*

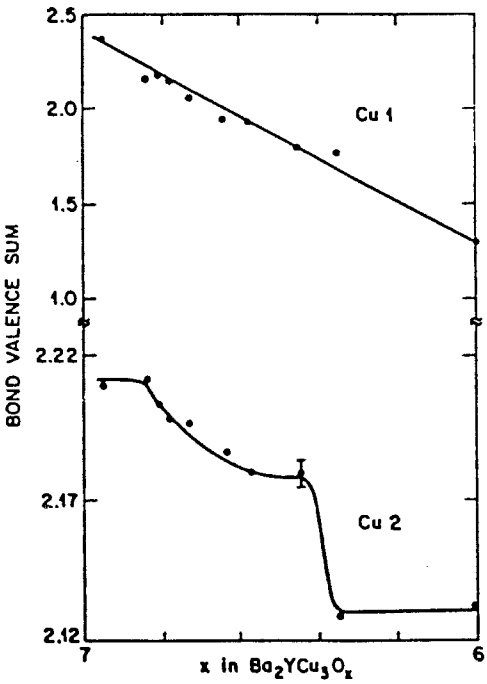

Fig. 21. Bond valence sums of Cu1 and Cu2 as a function of oxygen nonstoichiometry. Note that the BVS of Cu2 follows very nearly the shape of the $T_c(x)$ curve (fig. 2) and reflects the T → O transition and the optimally doped phase. The BVS of the chain Cu1 increases linearly due to the increase of the carriers concentration with doping. After Cava et al. (1990).

rich and oxygen-poor compositions are near to structural instability. Thus, for $x \approx 7$ the Cu_3O_x cage is smaller than the Ba ion, leading to tensile stress. This tension is partly relieved by the orthorhombic distortion (elongation of the Cu1–O4 bond = *b*-axis; increase of the average Cu2–O bond lengths by distorting the Cu2 environment). Additional relief comes also from the distribution of the smaller Cu^{3+} in the Cu2 and Cu1 sites, but the cages around the Cu ions remain too large. Brown (1989) concludes that further relief of the tension could be expected from a transformation increasing the Cu–O distances, e.g., a *ferroelectric* displacement of the copper atoms from the centers of their coordination polyhedra. For $x \approx 6$ the cage is too large for the Ba ion. The stress could be relieved if the cage would contract, e.g., by a *ferroelastic* rotation of the CuO_4 planes.

The BVS method has been extensively applied to estimate the carrier concentrations for a given T_c. For 123-O_x this is rather doubtful, due tot the existence of the two different Cu sites, as will be discussed in sect. 5.3. Cava et al. (1988a,b, 1990) have calculated with the BVS method the formal valences of the chain copper (Cu1) and the plane copper (Cu2) as a function of oxygen doping. Figure 21 shows that the Cu1 valence increases smoothly with oxygen content. Based on an ideal structure one would expect that Cu1 in 123-O_6, with its twofold coordination to the apical oxygens O1 (fig. 6), would have a formal valence of 1^+. The calculated 1.3^+ value shows the structural strains which clearly exist in the 123-O_x structure, near the O_6 stoichiometry, as Brown (1989) has shown. The ~29% linear increase with doping in the superconducting range $\sim 6.5 < x < \sim 6.9$ (~45%

for $\sim 6.0 < x < \sim 6.9$) shows the strong increase of the charge associated with the chains. On the contrary, the change of the charge associated with the planes in the superconducting range is only ~2% and shows appreciable changes of slopes.

In the range $\sim 6.0 < x < \sim 6.3$ no change of the Cu2 valence takes place. All the positive charges remain in the chains. In the range $\sim 6.35 < x < \sim 6.45$, the $T \rightarrow O$ phase transition takes place and the superconductivity sets in. At this point the Cu2 valence shows an abrupt increase with doping. After filling two-thirds of the chains with oxygen, a smooth increase follows until a final plateau in the range $\sim 6.84 < x < \sim 6.9$ is reached in the optimally doped and overdoped regime. Very interesting is the similarity between the T_c vs. x curve and the formal Cu2 valence vs. x found by Cava et al. (1988a,b, 1990), supporting the *charge-transfer from the reservoir block to the planes.* The importance of the apical bond Cu2–O1 for the charge transfer becomes apparent upon comparison of figs. 14 and 21. The contraction of the apical bond scales also very well with the increase of T_c as a function of doping.

Based on their BVS results Cava et al. (1988a,b, 1990) could conclude that the decrease of T_c from 90 to 60 K (with decreasing O content) is due to the transfer of a negative charge of $\approx 0.03e$/Cu from the chains to the planes and that the superconductivity is suppressed if further $\approx 0.05e$/Cu is transferred to the plains. These and many other results led to the now accepted general picture of the HT_c cuprates as consisting of copper–oxygen superconducting planes sandwiched between charge reservoirs.

Probably due to difficulties in synthesizing oxygen-rich samples at that time Cava et al. (1988a,b, 1990) have only one point over $x = 6.9$. The same is true for Jorgensen et al. (1990a). Thus no conclusion can be drawn from these data about the phenomena in the optimally doped and overdoped regimes (sects. 5–7).

3.2.1.5. *Mobility of oxygen, reordering at quenching.* Underdoped ($6.3 < x < 6.6$) single crystals (<2 mg) quenched in liquid nitrogen from 520°C show at room temperature, stored in air, relaxation phenomena in both their structural and their superconducting properties. Veal et al. (1990a) have found an increase of T_c up to 15 K saturating upon aging after several days. It is accompanied by a decrease of the a-axis and an increase of the b-axis (increase of orthorhombicity), leading to a decrease of the oxygen content x of the $T \rightarrow O$ transition. The structural changes were investigated by X-ray diffraction. This effect is quite interesting because it shows that *even at room temperature an appreciable mobility of the oxygen exists in the 123 lattice.* This is in contrast to the assumption that at $T < 500$°C the mobility of oxygen is frozen, an argument for investigating quenched samples.

Absorption of molecular oxygen and subsequent diffusion of atomic oxygen through the lattice seems to be too slow a process to account for this behavior. Several tests indicated that the changes were not due to absorption of additional oxygen from the air during aging (Veal et al. 1990a):

(1) The final T_c values reached by the samples depend on the stoichiometries from which they were quenched. If absorption of oxygen was taking place during aging then

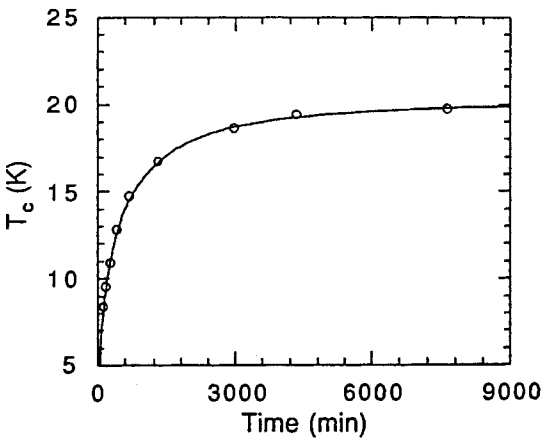

Fig. 22. $T_{c,(onset)}$ vs. annealing time at room temperature. 123-$O_{6.41}$ quenched from 500°C to liquid nitrogen. T_c increases from 0 to 20 K in ~150 h due to local rearrangements of the oxygen in the chains. After Jorgensen et al. (1990b).

probably all samples would relax to the same oxygen content (under the assumption of comparable grain interface properties).

(2) Absorption of oxygen at room temperature would be expected to cause broadening of the X-ray diffraction peaks. This was not the case.

(3) Within the rather large error limit of a gravimetric determination ($\Delta x = \pm 0.04$) no increases of the sample weight were detected.

(4) In spite of the above, it could be argued that a shell effect of absorbed oxygen might result in the increase of T_c. This was shown not to be the case because a small single crystal crushed to powder still showed the same T_c.

(5) Annealing an aged sample with $x = 6.45$ at 100°C once in flowing N_2 and once in O_2 and then quenching in liquid nitrogen, gave the same T_c's (however, both decreased by six degrees compared with the original).

Based on this evidence Veal et al. (1990a) concluded that the increase of T_c and orthorhombicity observed were due *not* to additional oxygen absorbed during aging, but to rearrangement of the oxygen in the chains. They particularly proposed short-path diffusion due to jumping from the anti-chain site O5 (statistically occupied in the tetragonal phase) to O4 during aging. This should result in changes of the hole concentration in the planes, increasing T_c and orthorhombicity in accordance with the literature (Cava et al. 1988b, Jorgensen et al. 1990a, Zaanen et al. 1988).

To investigate the oxygen rearrangement mechanism Jorgensen et al. (1990b) used NPD, characterizing their polycrystalline sample ($x = 6.415$ by iodometry) with dc magnetization as a function of the ageing time at room temperature. Starting with a $T_c = 90$ K ($6.9 < x < 7.0$) prepared after their previously published method (Jorgensen et al. 1990a), cf. table 4, they reduced the material in nitrogen containing 0.048% oxygen at 520°C for 112 h and then quenched in liquid nitrogen. The sample was zero-field cooled and then slowly warmed up in a SQUID magnetometer. Figure 22 shows the increasing T_c as a function of the aging time. The first measurement did not show superconductivity at all, but after 150 h the $T_{c,\,onset}$ had reached asymptotically 20 K, the same behavior as that

of the single crystals above (Veal et al. 1990a). NPD showed that the unit-cell volume and the lattice parameters decrease and the orthorhombicity increases (a decreases more than b) with aging time (fig. 23) as T_c increases. A comparison of figs. 22 and 23 shows that *in the initial stage these samples are orthorhombic but not superconducting,* similar to some findings on slowly cooled samples (Maletta et al. 1989, Radaelli et al. 1992) and the equilibrium samples discussed in (sect. 3.3). We note the appreciable contraction of the unit cell volume in fig. 23 (0.1%), characteristic for the increased coupling with increasing T_c due to oxygen ordering. This results from the decrease of the c-axis (0.04%) and the a-axis (0.05%). In contrast, the b-axis contracts almost three times less (0.013%) indicating that an expanding mechanism may counteract. The time-dependent increase of T_c (fig. 22) is given by the following equation, of a type often found for ionic and hopping relaxation phenomena:

$$T_c(t) = T_c(\infty) - [T_c(\infty) - T_c(0)]\exp[-(t/\tau)^{1/2}], \tag{2}$$

with t the annealing time and τ a characteristic time constant with best-fit value 386 min.

The large continuous decrease of the c-axis is a typical indication of the charge transfer in samples quenched from high temperatures (table 4, Jorgensen et al. 1990a), which do not show an abrupt step-like decrease like the Zr-gettered samples (Cava et al. 1988a,b, 1990). From the structure of the unit cell (fig. 5) we see that the c-axis is the sum of the Cu–O bond lengths and the Cu2–Cu2 spacing $2\times$(Cu1–O1 + Cu2–O1) + (Cu2–Cu2). Therefore, the contraction of the c-axis must result from the contraction of some of these bonds or spacings due to charge transfer. Figure 24 shows the dependence of these bond lengths on the aging time after quenching. The main change is the contraction of the apical bond Cu2–O1 (Cu2–O4 in fig. 24) by 0.01 Å which in spite of the small expansions of the Cu1–O1 and the Cu2–Cu2 leads to the contraction of the c-axis.

The change of the oxygen site occupancies (O1, O4, O5) during aging was found to be insufficient for explaining the increase of T_c shown in fig. 22. Thus, it was proposed (Jorgensen et al. 1990b) that it is not the long-range oxygen ordering of the chains which leads to charge transfer and the increase of T_c after aging at room temperature, but the *local oxygen ordering.* It has been argued in the literature (see e.g., Hou et al. 1990, Zaanen et al. 1988) that the local ordering of the oxygens around Cu1 (O4 and O5) influences its oxidation state via the coordination number and geometry. Roughly, these models assume that Cu1 can reach only the 2^+ oxidation state. This is the case with three, four, five or six oxygen nearest neighbors, while 1^+ is the oxidation state of Cu1 with two neighbors. A random distribution of the oxygens in the Cu1 plane leads to a maximum number of threefold coordinated Cu and therefore to a maximum of 2^+ charges. However, when ordering leads to fourfold or higher coordination, the number of 2^+ charges becomes a minimum. Then, the transfer of electrons from the planes to the chains reaches a maximum and the hole count in the planes increases. Thus, *local ordering without a net change of occupancies may lead to an increase of the hole concentration in the planes and of* T_c (Jorgensen et al. 1990b). This ordering is expected to cause an expansion of the b-axis, counteracting the general contraction of the unit cell (fig. 23). This is in agreement with the smaller contraction of the b-axis (fig. 23).

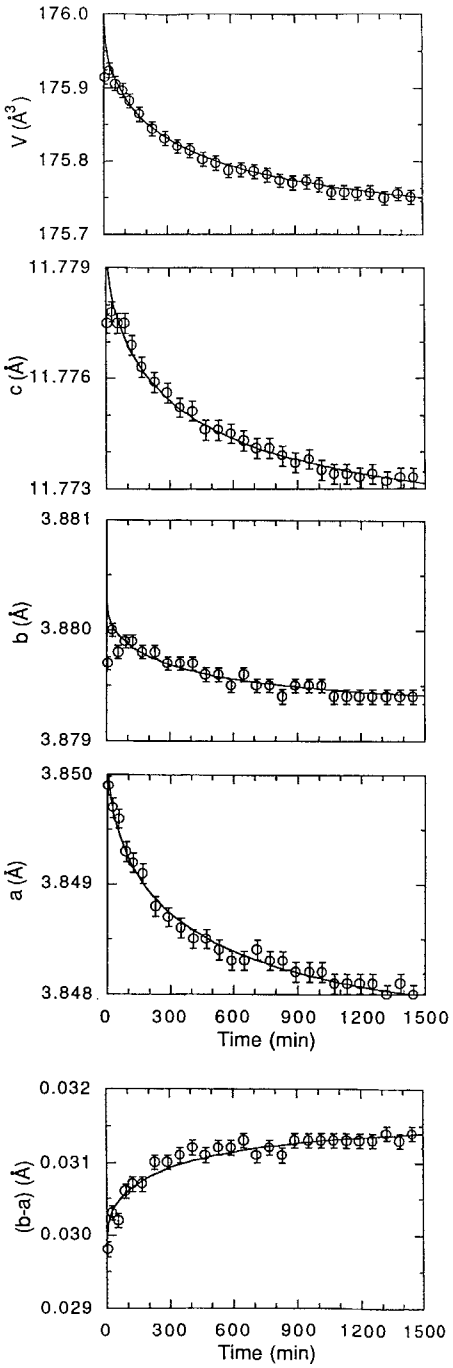

Fig. 23. Relaxation of the unit cell volume, lattice parameters, and orthorhombic strain at room temperature, after quenching from 500°C to liquid nitrogen. After Jorgensen et al. (1990b).

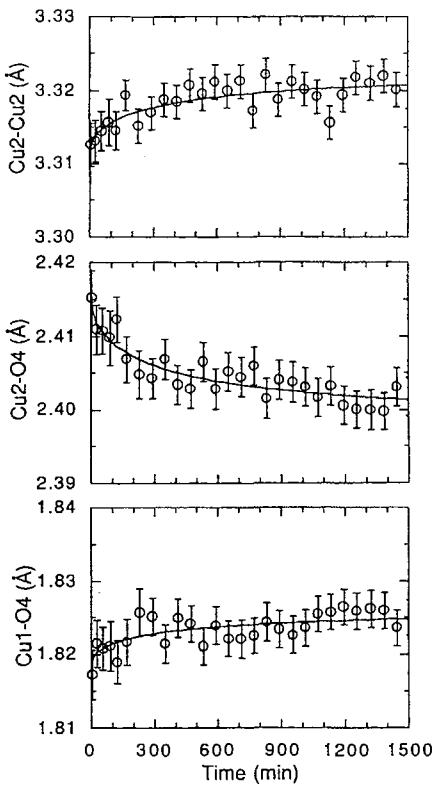

Fig. 24. Relaxation of the bond lengths under the conditions of figs. 22 and 23. Note the contraction of the apical bond with time, here denoted as Cu(2)–O(4). This is the result of charge transfer without change of the oxygen occupancies, due to change of the local oxygen ordering. After Jorgensen et al. (1990b).

Soon after, Ceder et al. (1991a) performed a Monte Carlo simulation of the above Veal and Jorgensen experiments, with the same Ising model used in the ASYNNNI model to derive the phase diagram (sect. 5.2). The results indicated that in contrast to the above, O5–O1 ordering, which is faster because it needs only nearest-neighbor jumps, dominates the initial relaxation period (~90 min). This reduces the number of Cu with oxygen coordination 3, establishes the O–I structure (fully occupied chains) and increases the number of holes in the planes. This could explain why the samples quenched from the tetragonal structure are found to be orthorhombic. In a second stage, the much longer formation of the chain ordering dominates, leading to the O–II structure with every second chain empty (O-I to O-II). According to this simulation the above ageing experiments could observe only the second stage of the ordering. The transition from the tetragonal phase (statistical distribution of O5 and O1) to the O–I phase (no O5 sites occupied) occurred during quenching. Although this result is quite interesting, we note that, as discussed in sect. 5.2, the ASYNNNI model, on which this simulation is based, was not particularly accurate in predicting structural details.

In conclusion, it can be said that the experiments of Veal et al. and Jorgensen et al. discussed above illustrate clearly the importance of the intra-chain local oxygen ordering.

Thus, chain length and inter-chain ordering in superstructures are important for charge transfer. Unfortunately, up to now a microscopic picture of exactly how charge transfer is controlled by these two parameters is lacking (cf. sects. 5.1, 5.2).

3.2.2. *Equilibrium samples with high-resolution oxygen determination*

In sect. 3.1.2 we have discussed methods leading to near equilibrium samples with oxygen content up to $x = 6.99$. These methods, combined with an oxygen determination method *10 times more accurate than iodometry* (Conder et al. 1989) and with a large number of investigated compositions, allowed to see more clearly the trends of structural, optical (Raman) and diamagnetic properties. They made possible a systematic study of the overdoped $x > 6.95$ range, and shed more light in the underdoped ($6.95 \geqslant x \geqslant 6.4$) and insulating ($6.40 \geqslant x \geqslant 6.0$) ranges of 123-$O_x$. These investigations

(1) Showed the existence of an up to then unknown *displacive transformation* between the optimally doped and the overdoped regime (sect. 6), and
(2) Gave new results about:
   - the transitions correlated with the onset of superconductivity (sect. 3.3.2);
   - a *sequence of steps* in the in-phase Raman phonon frequency (sect. 5.5),
   - *phase separation* in underdoped 123-O_x (sect. 5.5)
   - *phase separation* in oxygen-overdoped 123-O_x (sect. 7), and
   - *phase separation* in Ca-overdoped 123-$O_{6.95}$ (sect. 8).

3.2.2.1. *Lattice parameters vs. oxygen content.* Only a rough comparison can be made between the dependence of the lattice parameters on the oxygen nonstoichiometry for quenched samples (quenching from higher and lower temperatures, Zr-gettering etc.) and equilibrium samples. The reason is that the main systematic studies of the structure of 123-O_x as a function of the oxygen content using quenched samples (Jorgensen et al. 1990a, Cava et al. 1990) have investigated relatively few compositions in the range of $x \approx 6.0$–6.9. In this range, the high accuracy of the oxygen determination and the controlled near-equilibrium conditions allowed the synthesis and study of more than a hundred compositions with three different methods (table 2; Conder et al. 1994a, Kaldis 1997). In the case of CAR and BAO samples (sect. 3.1.2) more than forty equilibrium compositions each have been investigated in the above-mentioned x range. Thus, although there is good agreement in the range of the T–O transition, no comparison is possible in the overdoped region.

We note that, as mentioned in sect. 3.1.3, high-resolution oxygen determination is not valid at $x < 6.45$, i.e. in the absence of Cu^{3+} (formal valence). Samples with lower oxygen content were analyzed by iodometry and thermogravimetric analysis.

3.2.2.2. *X-ray diffractometry, $T = 300\,K$.* The lattice parameters and some bond lengths of the three different kinds of samples discussed in sect. 3.1.2 have been measured with X-ray diffraction using either a Guinier camera with internal standard (Rusiecki et al. 1990, Rusiecki and Kaldis 1991, Conder et al. 1994a) or a STOE powder diffractometer

(Krüger et al. 1997) with Ge-monochromatized Cu Ka_1 radiation ($l = 1.54098$). In the diffractometry, the parameters of the orthorhombic Pmmm space group were determined with more than 30 reflections. NIST silicon standard ($a = 5.43088$ Å) was used as an internal standard for the determination of the lattice parameters (also with the film camera). Data were recorded in transmission geometry in the $2q$ range 5–120°. Due to the low scattering power of oxygen for X-rays a refinement of the occupation of the oxygen sites was not performed. With the exception of the O4 site (chain oxygen), which was assumed to correspond to the value obtained by the volumetric oxygen analysis, all other oxygen site occupancies (including O5) had to be fixed. With the exception of Cu1 (chain copper), the metal occupancies were also fixed at 100%. The refinements converged at rather low disagreement factors between observed and measured intensities $R_I = 0.04$–0.08.

3.2.2.3. *Lattice parameters of samples with Ba carbonate precursor (CAR samples).* Figures 25a–e show the abrupt change of the X-ray lattice parameters at the T → O transition. The stepwise change of the c-axis is 0.05 Å (0.5%). The step in the equilibrium samples is slightly smaller than in the Zr-gettered samples (0.6%, fig. 12c), but possibly more narrow. Less abrupt changes appear in the other lattice parameters, with the exception of the unit cell volume as we will discuss later. The difference from the quenched samples (Jorgensen et al. 1990a) is clearly shown in the example of the c-parameter in fig. 26a, whereas the difference in the in-plane axes is smaller (fig. 26b). We can, therefore, conclude that abrupt change of the lattice constant c at the T–O transition is characteristic for near-equilibrium samples, including the Zr-gettered synthesized under the conditions of table 4. DC susceptibility measurements (fig. 27a) show superconductivity at $x \approx 6.396$ for the equilibrium samples, but small amounts of the sample become superconducting at an earlier stage (fig. 27b; see also sect. 3.3).

Another interpretation has been given by Tallon (1990) and Tallon et al. (1995) (see also review by Radaelli 1998) who proposed that the onset of superconductivity in 123-O_x appears at a certain value of the concentration of holes per Cu2 atom. As we will discuss in later sections (5.3, 8.4) this is still questionable, because good $Y_{1-y}Ca_yBa_2Cu_3O_6$ samples seem not to be superconducting (Merz et al. 1998). Tallon et al., however, had superconducting samples.

As already mentioned, although the transition appears very abrupt in the c-axis (fig. 25d) and in the unit cell volume (fig. 25e) it extends to a larger composition range 6.3–6.4(5) for the a-axis (fig. 25a) and 6.3–6.45 for the b-axis (fig. 25b). It could be argued that the transition starts at the a–b plane, the corresponding c-axis changes being too small to be seen in the 6.3–6.4 range. Synchrotron radiation measurements could clarify this point.

The total relative change of the lattice parameters in the $x = 6.0$–6.99 range is large: −1.15% for the a-axis, +0.72% for the b-axis, −1.64% for the c-axis, and −1.85% for the unit cell volume. The a- and b-parameters as well as the orthorhombicity have a linear dependence on oxygen only in the underdoped range $x = 6.5$–6.75. The large number of measured compositions allows to measure the deviation from linearity. *At $x = 6.75$ the*

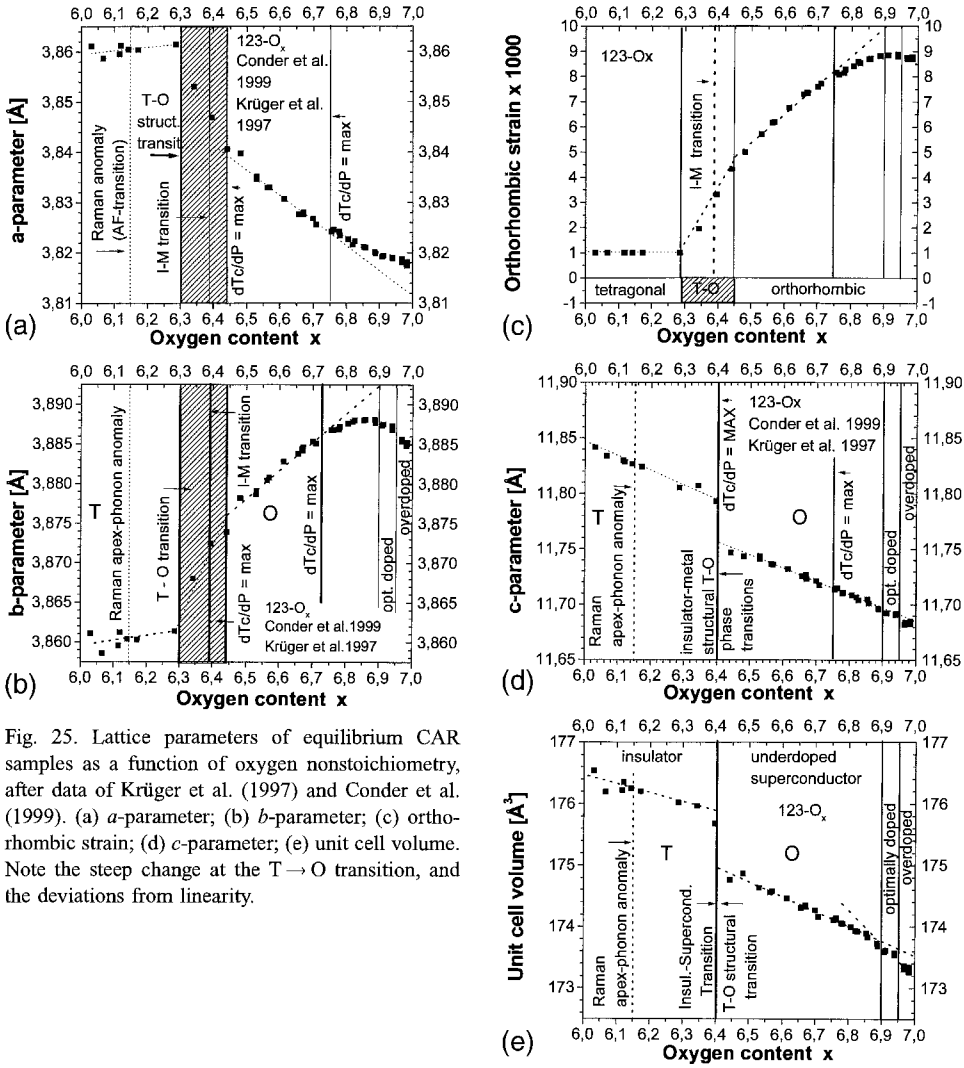

Fig. 25. Lattice parameters of equilibrium CAR samples as a function of oxygen nonstoichiometry, after data of Krüger et al. (1997) and Conder et al. (1999). (a) *a*-parameter; (b) *b*-parameter; (c) orthorhombic strain; (d) *c*-parameter; (e) unit cell volume. Note the steep change at the T → O transition, and the deviations from linearity.

x-dependence of both a- and b-parameters becomes nonlinear. As we will see, many other changes in properties appear at this composition, which is an important point of the phase diagram (sect. 5.4.2). Extrapolation of the tangent in the range $x = 6.5$–6.75 up to $x = 7$ shows the relative deviation from linearity to be +0.15% ($\Delta a = 0.006$ Å) for the *a*-axis and appreciably stronger, –0.25% ($\Delta b = 0.010$ Å), for the *b*-axis.

The *c*-axis of the CAR samples changes almost linearly with the O-content up to $x \leqslant 6.95$, opposite to the BAO and DO samples (sect. 3.2.2.4). We note that in contrast to the *a*- and *b*-axes it also does not show a change of slope at $x = 6.75$.

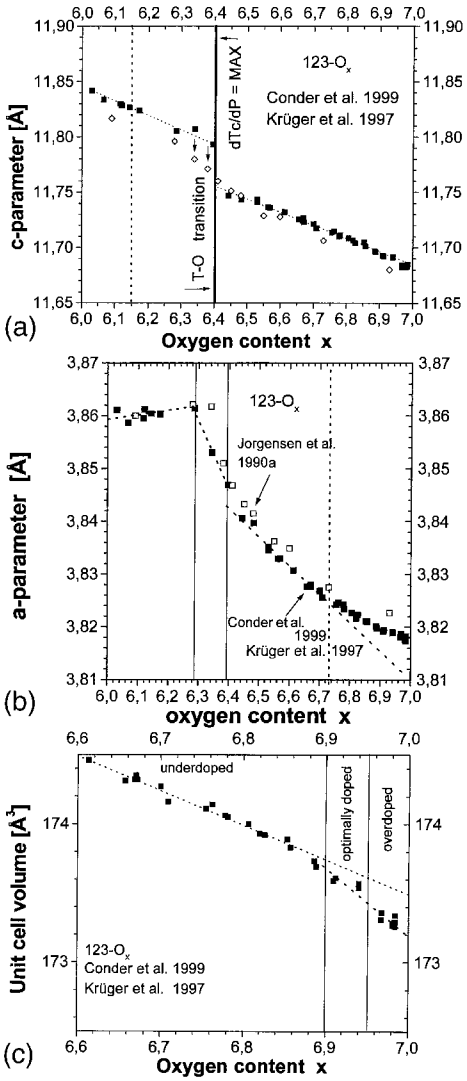

Fig. 26. (a) Comparison of the *c*-parameter doping dependence of CAR samples (XRD 300 K, solid squares; Conder et al. 1999, Krüger et al. 1997) and quenched samples (NPD 300 K, open diamonds; Jorgensen et al. 1990a) both with Ba_2CO_3 precursor. The differences near the T–O transition are underlined with arrows. (b) Comparison of the *a*-parameter doping dependence of CAR samples (XRD 300 K, solid squares; Conder et al. 1999, Krüger et al. 1997) and quenched samples (NPD 300 K, open squares; Jorgensen et al. 1990a) both with Ba_2CO_3 precursor. The differences near the T–O transition are small, however, due to the large number of samples and the exact chemical analysis, the trends in the change of slopes are better visible for the CAR samples. (c) Decrease of the unit cell volume of the CAR samples in the optimally doped and overdoped ranges, reflecting the decrease of *b*-axis due to increasing interactions (Conder et al. 1999, Krüger et al. 1997).

Other differences to fig. 12 appear in the overdoped region. The unit cell volume shows an additional decrease in the optimally doped and overdoped regions (fig. 26c) reflecting changes of the *b*- and, to a lesser extent, the *c*-parameter. The decrease of the *b*-parameter clearly seen in the overdoped region (Krüger et al. 1997), mimicks the T_c dependence on oxygen doping (fig. 25b). This shows that the *structural changes due to overdoping* which we discuss in sect. 6 and subsequent sections, *are not only limited to the c-axis but are correlated with changes in the planes.* More pronounced anomalies appear in samples synthesized without carbonate, as we discuss in sect. 3.2.2.4.

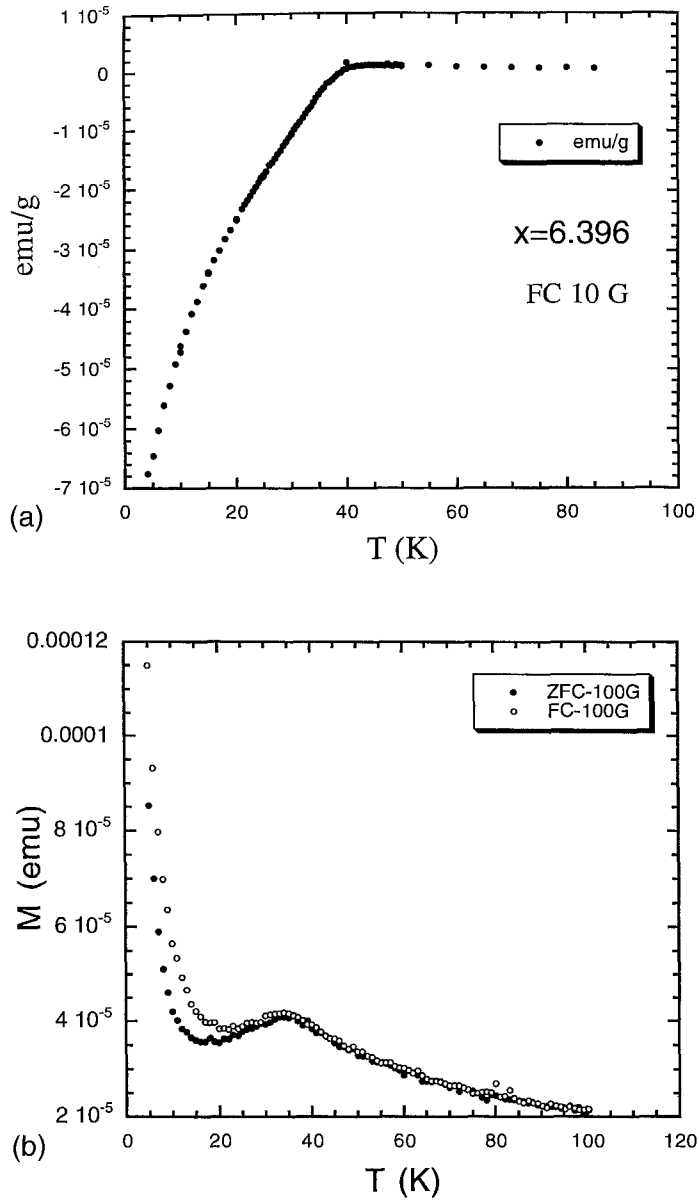

Fig. 27. (a) Diamagnetic transition clearly seen for 123-O_x with $x=6.396$. Field cooling, $H=10$ G. After A. Shengelaya (Conder et al. 1999). (b) Small amounts of the sample become superconducting already at $x=6.342$. $H=100$ G, ZFC and FC. At $H=10$ G and FC no distinct indication of superconductivity appears. After A. Shengelaya (Conder et al. 1999).

The vertical lines (solid or dotted) in figs. 25 and 26 correspond to some of the important compositions (6.15, 6.4, 6.75, 6.90, 6.95) of the phase diagram correlated to changes of several physical properties, which we discuss in detail in other sections. Here, we discuss briefly some possible reasons leading to the nonlinearity of the *a*- and *b*-lattice parameters with oxygen content:

(a) Partial occupation of the anti-chain sites O5. As already mentioned, slowly cooled samples investigated by high-resolution neutron diffraction (Radaelli et al. 1992, Böttger et al. 1996), but also in quenched samples (Jorgensen et al. 1990a), an occupancy (5%) of the O5 site has been found. The relative increase of the *a*- and decrease of the *b*-parameter starting from $x \approx 6.75$ could be in principle explained by increasing O5 and decreasing O4 occupancies in the oxygen-rich regime (Krüger et al. 1997). EXAFS investigations of these samples did not confirm up to now this assumption (Röhler et al. 1997a,b). Also single-crystal work (von Zimmermann et al. 1999) did not find O5 occupation.

(b) Nonstoichiometry of Cu1 due to the incorporation of carbonate. However, the Rietveld refinement showed the occupancy of this site to *be independent of the oxygen content,* having values between 0.93 and 0.88 (Krüger et al. 1997). The most probable reason for the deficiency of Cu1 is the carbonate traces of the order of 1000 ppm (sect. 3.1.4) found in these samples. This assumes that one carbonate impurity would hinder the substitution of several Cu1 atoms. Cu1 site defects have been observed and discussed in detail in single-crystal refinements of the double chain compound 247-O_x ($Y_2Ba_4Cu_7O_{14-x}$) (Schwer et al. 1993a,b and references therein; Krüger et al. 1994). In single crystals grown in alumina crucibles the main impurity is, however, Al-ions incorporated in the chains. Due to the higher temperatures involved, the carbonate incorporation is probably less important in single crystals. The CAR powder samples have been processed at lower temperatures (935°C) and, therefore, the main impurity is carbonate which, however, has been reduced to only ≈1500 weight ppm due to an effective expelling procedure (sect. 3.1.2). The possibility for reaction with alumina is small at these temperatures.

(c) The existence of a series of superstructures indicating long range interactions, which is discussed in sects. 5.1.1 and 5.5.2.

(d) The change of the superconducting coupling. We conclude that the changes of *the superconducting coupling* in the optimally doped and overdoped ranges (leading to the decrease of the *b*-axis mimicking the T_c vs. O curve of fig. 2) are mainly responsible for the nonlinearity of the *a*- and *b*-lattice parameters. Several experimental results support this idea: As we will see most measurements influenced by the structure do show changes of slope at $x \approx 6.75$. Thus, e.g., the pressure dependence of T_c shows a giant anomaly in this range (sect. 5.2) and the onset of the diamagnetic transition shows an abrupt step in this range. This is the range generally considered as the Ortho II → Ortho I transition, but doubt must be expressed in view of the fact that recent superstructure investigations (von Zimmermann et al. 1999) find that at RT this transition takes place at higher oxygen content (sect. 5.1). Only at higher temperatures ($T > 350$ K) is the Ortho I phase present for $x > 6.4$.

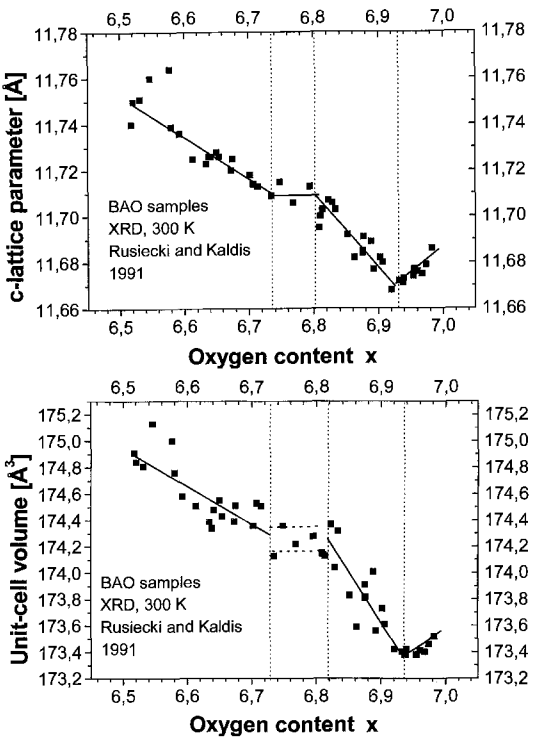

Fig. 28. (a) c-parameter of BAO-123-O_x samples (XRD, 300 K) showing a minimum at $x \approx 6.93$ near the onset of the overdoped range. This was the reason to start the investigation for a phase transformation (sect. 6). In contrast, the CAR samples show a linear behavior (cf. fig. 25d). (b) Unit cell volume of BAO-123-O_x samples (XRD, 300 K) showing the minimum at $x \approx 6.93$ near the onset of the overdoped range. The anomaly in the $x = 6.73$–6.80 range indicates the coexistence of two phases, in the range of the $T_{c,\,onset}$ transition shown in fig. 2 (hatched). After data of Rusiecki and Kaldis (1991).

3.2.2.4. *Lattice parameters of BAO and DO samples.* There are interesting differences among the lattice parameters of samples synthesized with (CAR) and without (BAO, DO) Ba carbonate as precursor (sect. 3.1.2). *The absence of carbonate as a precursor of the solid-state reaction (DO) and the expulsion of carbonate (BAO) seem to render a particular sensitivity of these samples to structural distortions (DO) and metastable phases (BAO).*

The effect is striking in the c-parameter which is almost linear for the CAR samples (fig. 25d), but shows changes of slope at $x \approx 6.75$ and $x \approx 6.80$, and a minimum at $x \approx 6.93$, for the BAO samples (Rusiecki et al. 1990, Rusiecki and Kaldis 1991) (fig. 28a). Corresponding anomalies appear for the DO samples as we will discuss later (Conder et al. 1994a, Conder and Kaldis 1995, Kaldis 1997). The minimum of the c-parameter at $x \approx 6.93$ corresponds to a displacive transformation at the onset of the overdoped region, which we will discuss in detail in sect. 6. As we have seen above for the CAR samples (sect. 3.2.2.3) in the range of $x \approx 6.75$, the deviation from linearity of the in-plane lattice parameters – seen also in the orthorhombic strain and the unit cell volume – sets in. The corresponding change of slope for the c-axis is smoothed out in the presence of carbonate, but appears clearly in the BaO samples. Figure 28a shows also that for these samples the c-parameter seems independent of doping in the $x = 6.73$–6.80 range. A lattice parameter

independent of composition indicates a two-phase region, separating two different phases. It is consistent with the anomaly in the $T_{c,\,onset}$ of fig. 2 which shows a clear step in this range. In this step, samples with $T_{c,\,onset} \approx 93$ K and $T_{c,\,onset} \approx 74$ K coexist, an indication of a *two-phase region* separating the two T_c phases (cf. fig. 45, below). Under the influence of the *a*- and *c*-parameters the unit cell volume (fig. 28b) shows this two-phase region more pronounced. However, a larger scattering of data appears in the curve of the unit cell volume due to the contributions of the in-plane lattice parameters, as we will discuss below.

Compared to the *c*-axis the in-plane lattice parameters of the BAO and DO samples show a larger scattering. They show deviations from linearity but the situation is more complex. In the first case (BAO) the number of investigated samples (45) in the 6.5–7.0 range is as large as that of the CAR samples, giving good statistics. Thus, in spite of a larger scattering of the data the changes of slope can be clearly seen.

Figure 29a shows the raw data of the *a*- vs. *x* plot fitted with a simple polynomial. As this, however, is a physical problem and not a statistical one, treatment of the data in three nonstoichiometry segments, as suggested by figs. 28a,b, seems reasonable. This is shown in fig. 29b. The linear fitting in three segments covers 75% of the samples (solid line). The remaining 25% have higher *a*-values and lie on a parallel curve (dotted line). They are probably from samples pinned in a nearly metastable state, not being able yet to reach equilibrium. Upon closer inspection of the data it can be seen that the horizontal part at the transitional range near $x = 6.75$ (cf. sect. 5.4.2) appears also in other composition ranges, as shown in fig. 29c. Assuming a reproducibility error of 0.0025 Å in the *a*-parameter (as compared to the fourth decimal point in the CAR samples, Krüger et al. 1997), due to *the metastability effects and the reproducibility of the BAO method,* it is possible to include almost all data in a tentative scheme of a series of four phases separated by two-phase regions (hatched). To avoid misunderstandings we stress that the coexistence of phases is not supported by two-phase samples. All samples are macroscopically (XRD) phase pure. It is the scattering of the *a*-values in certain *x*-ranges which tentatively implies that some of them are pinned in another metastable phase. The figure is drawn in the frame of a classical thermodynamic picture, but other models could be also applicable.

Inspection of figs. 28a and 29 shows – as mentioned already – that the scattering of data is present mainly in the in-plane lattice parameters, particularly in *a*-, which are sensitive to oxygen ordering (superstructures). Due to the lack of exhaustive characterization of the BAO samples, fig. 29c might be considered as tentative. It cannot be ignored, however, that it is qualitatively consistent with a sequence of superstructures as indicated by Raman investigations (sect. 5.5) or by recent hard X-ray investigations (sect. 5.1). This stresses the importance of systematic comparison and evaluation of the reaction mechanism of samples prepared by various methods. The yet unknown mechanisms of the various solid–vapor–liquid reactions (in mesoscopic and atomistic scale) involved in the preparation of these complex perovskites seem to be specifically sensitive to metastable and stationary states. Some, possibly under the influence of grain-interface wetting by a flux (e.g., carbonate traces at high temperatures) homogenize the reacting batch *macroscopically* (CAR method, sect. 3.1). Other synthesis reactions using BaO precursor (BAO method,

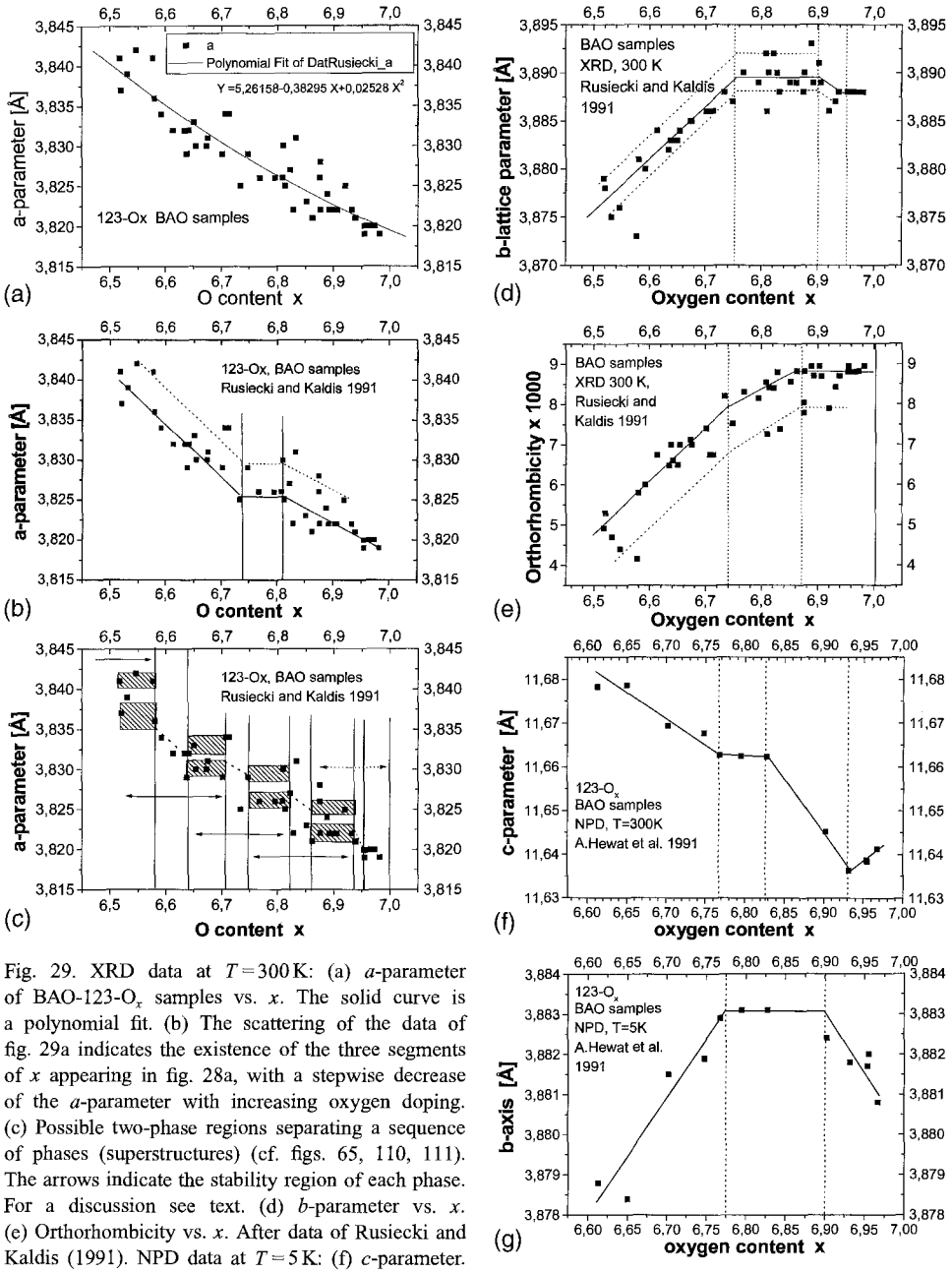

Fig. 29. XRD data at $T = 300$ K: (a) a-parameter of BAO-123-O_x samples vs. x. The solid curve is a polynomial fit. (b) The scattering of the data of fig. 29a indicates the existence of the three segments of x appearing in fig. 28a, with a stepwise decrease of the a-parameter with increasing oxygen doping. (c) Possible two-phase regions separating a sequence of phases (superstructures) (cf. figs. 65, 110, 111). The arrows indicate the stability region of each phase. For a discussion see text. (d) b-parameter vs. x. (e) Orthorhombicity vs. x. After data of Rusiecki and Kaldis (1991). NPD data at $T = 5$ K: (f) c-parameter. The minimum found by XRD is confirmed. The lower values are due to the thermal contraction at low temperatures. (g) b-parameter vs. x. The lines are guides to the eye. After data of Hewat et al. (1991).

sect. 3.1) are easier pinned (partly) in metastable states. Similar is true for the DO method using direct oxidation of the barium metal (sect. 3.1).

Figures 29d,e show the *b*-lattice parameter and orthorhombicity behavior of the BAO samples. In spite of the scattering of the data in the oxygen-rich range the decrease of the *b*-parameter in the overdoped range can be seen in fig. 29d.

The DO method (cf. sect. 3.1.2.1 and table 2) has its own fingerprint of structural anomalies, indicating a structural-pinning reaction mechanism. In spite of many grindings and annealings, reaction and phase transformation rates are probably slower, pinning the structure in metastable states. The number of samples investigated was limited (20), but, owing to the use of a better controlled closed system with higher reproducibility of the synthesis conditions, the scattering of the data was smaller than for the BAO samples and could give some additional information about the overdoped range.

Figures 30a–e show the lattice parameters vs. x of the DO samples. The spikes of these curves seem at first glance to be the result of scattering. Closer inspection shows that they coincide with the five characteristic compositions occurring at $x \approx 6.7$, 6.8, 6.9, 6.95, and 6.97. As mentioned for the BAO samples, the anomalies in the 6.7–6.8 range do appear also for $T_{c,\,onset}$ (fig. 2, hatched area) and are, therefore, associated with the superconductivity. We note that the CAR, BAO and DO curves are linear and do not show any scattering up to 6.7 (up to 6.8 for the *a*-axis). Only slight differences in slope exist in this range. At $x \approx 6.7$ however, the *b*-axis drastically changes its slope. At the onset of the optimally doped range ($x = 6.90$), all parameters (particularly *a*-) show a maximum. The same is true for the displacive transition at 6.95. Even the small anomaly at 6.97 can be attributed to an anomaly of the dimpling (Röhler et al. 1998).

Last but not least, it is very interesting to compare the behavior of the DO samples with that of the BAO samples with respect to the *c*-axis anomaly (fig. 30d). We then find that the baseline of the DO curve coincides with that of the BAO curve (dotted line) in the range $x > 6.80$. In view of the fact that method of synthesis, starting materials, apparatus, and operator were *quite different* we can conclude that this is not a mere coincidence, but these two methods do really reach states which are not attainable for the CAR samples (different activation energies), whose *c*-parameters remain higher and change linearly with x. In addition, the DO method shows characteristic spikes in the compositions of the above mentioned transitions, supporting the assumption of structural pinning.

Summing up, the lattice constants of near-equilibrium samples synthesized by three different synthesis methods indicate the possible existence of several two-phase regions (miscibility gaps), and transitions in the whole nonstoichiometric range ($x = 6.0$–6.99). We list them here:

(1) $x = 6.3$–6.45. CAR samples: structural T–O transition. It appears in this range only for the in-plane lattice parameters. For the *c*-axis it is much more abrupt and appears at $x = 6.40$ (–6.45), coinciding with the onset of superconductivity.

(2) $x = 6.75$–6.80. CAR samples: deviation from linearity of the *a*- and *b*-axis. BAO samples: change of slope of all lattice parameters; *c* and *V* independent of doping, indicating possible miscibility gap. The DO samples show also changes of slope. In

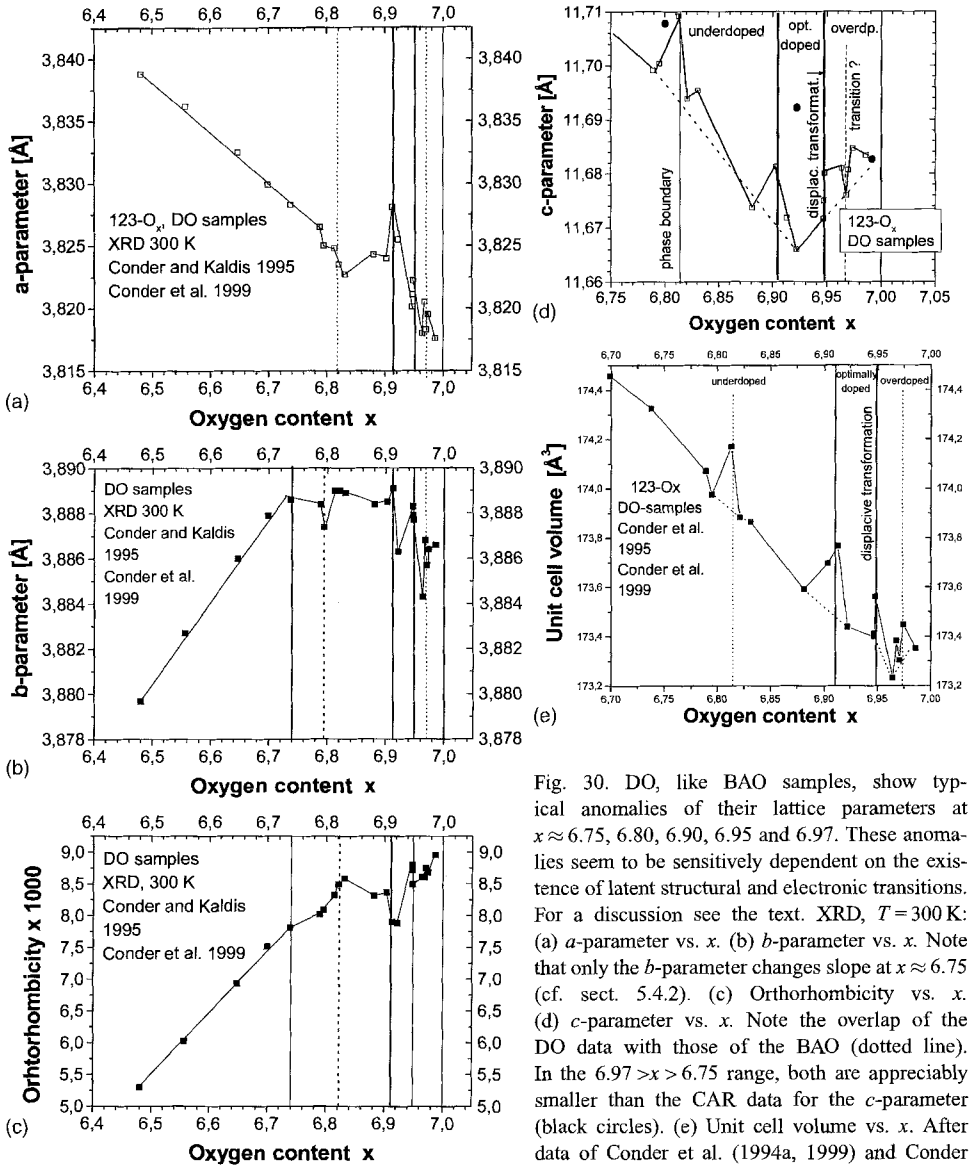

Fig. 30. DO, like BAO samples, show typical anomalies of their lattice parameters at $x \approx 6.75$, 6.80, 6.90, 6.95 and 6.97. These anomalies seem to be sensitively dependent on the existence of latent structural and electronic transitions. For a discussion see the text. XRD, $T = 300$ K: (a) a-parameter vs. x. (b) b-parameter vs. x. Note that only the b-parameter changes slope at $x \approx 6.75$ (cf. sect. 5.4.2). (c) Orthorhombicity vs. x. (d) c-parameter vs. x. Note the overlap of the DO data with those of the BAO (dotted line). In the $6.97 > x > 6.75$ range, both are appreciably smaller than the CAR data for the c-parameter (black circles). (e) Unit cell volume vs. x. After data of Conder et al. (1994a, 1999) and Conder and Kaldis (1995).

this range many changes of physical properties take place: transition of the T_c plateaus 60 → 90 K takes place, cf. fig. 2 (see also sect. 5.4.1); change of slope in uniaxial and hydrostatic pressure experiments, giant pressure effect of T_c (sect. 5.2); steps in the

in-phase phonon Raman shifts appearing at the compositions of na_0 superstructures (Raman, sect. 5.5).

(3) $x \approx 6.50$–6.99. *a*-axis BAO samples, indications for the existence of a sequence of phases separated by miscibility gaps. This would be consistent with the appearance of superstructures.

(4) $x = 6.90$. DO samples: clear anomaly (spike) of the curves vs. x, coinciding with the onset of the optimally doped phase.

(5) $x \approx 6.95$. BAO samples: *c*-axis minimum, coinciding with the displacive transformation at the onset of the overdoped phase. Triggered by these results and NPD investigations (discussed later), EXAFS measurements showed a first-order-like jump increasing the dimpling Cu2–O2,O3 (Kaldis et al. 1997b, Röhler et al. 1998), the Y–O2,O3 distance becoming smaller (sect. 6.5). As we will discuss in sect. 6.3, corresponding anomalies have been found in Raman measurements.

(6) $x = 6.95$. DO samples: spikes of the curves vs. x, coinciding with anomalies of the dimpling (cf. sect. 6.5) (Röhler et al. 1998).

The conclusion is that *the anomalies of the lattice constants – particularly for samples synthesized without carbonate – correspond to important changes of the lattice, some of them clearly related to superconductivity.* Carefully measured lattice constants in high-quality equilibrium samples combined with a high-resolution determination of oxygen is a very sensitive probe for phase boundaries and transitions. We recall that due to the high resolution of the volumetric oxygen determination (Conder et al. 1989) it is the first time that the dependence of the lattice parameters on the oxygen nonstoichiometry can be investigated so exactly and even small anomalies can be detected.

Tables 5, 6 and 7 give the values of the XRD lattice parameters at $T = 300$ K (Guinier camera, with Si standard) for the CAR, BAO and DO samples, respectively. To confirm the anomalies in the lattice parameters found by XRD, an NPD refinement was performed as a function of temperature at 12 oxygen contents. Tables 8a–d give neutron diffraction data of 12 selected BAO-sample compositions at $T = 5$ K and 300 K (Hewat et al. 1991). Figure 29f shows the *c*-parameter vs. x as measured at 5 K. Both anomalies found with XRD were confirmed, as apparent upon comparison with fig. 28a. The same is true for the *b*-parameter shown in fig. 29g, where the decrease in the overdoped range is seen more clearly than in fig. 29d. The NPD bond lengths of the BAO samples are discussed in more detail in conjunction with the dimpling transition corresponding to the minimum of the *c*-axis (sect. 6.1).

It is interesting that although the CAR samples do not show the *c*-axis anomaly at the large length scale of XRD, Raman and EXAFS investigations, which have a much smaller length scale (sect. 6), find the corresponding anomalies at RT and $T = 25$ K, respectively. We may conclude, therefore, that *the corresponding structural changes appear in the CAR samples at mesoscopic scale.* Therefore, the chemical and thermal history of the samples can mask several structural properties at the macroscopic scale, which, however, can be still detected with small length scale experimental methods. This is an important facet of the complexity of the HT_c cuprates: *the different properties between micro- and macroscopic scales.*

Table 5
Lattice parameters of CAR samples[a]

O content	*a*	*b*	Orthorhombicity	*c*	Volume
6.03	3.8611	3.8611	1	11.8417	176.53717
6.066	3.8586	3.8586	1	11.8337	176.18952
6.12	3.8612	3.8612	1	11.8285	176.34951
6.116	3.8595	3.8595	1	11.8299	176.22
6.143	3.8604	3.8604	1	11.8266	176.25
6.172	3.8603	3.8603	1	11.8237	176.2
6.286	3.8614	3.8614	1	11.8052	176.02037
6.342	3.853	3.868	1.94275	11.807	175.96449
6.396	3.8469	3.8724	3.30341	11.793	175.6772
6.442	3.8406	3.8739	4.31655	11.7466	174.76
6.482	3.8397	3.8782	4.98841	1.7432	174.87
6.53	3.8346	3.8787	5.7174	11.7437	174.63
6.53	3.8351	3.8791	5.70377	11.7407	174.63
6.563	3.8329	3.8804	6.158	11.7367	174.56
6.569	3.833	3.8808	6.19669	11.7361	174.58
6.613	3.8307	3.8828	6.7544	11.732	174.46
6.657	3.8276	3.8838	7.28791	11.7254	174.31
6.668	3.8277	3.8844	7.35208	11.7245	174.32
6.67	3.8276	3.8842	7.34	11.7268	174.35
6.671	3.828	3.8846	7.34	11.7229	174.32
6.7	3.8268	3.8853	7.5854	11.7213	174.27
6.709	3.8256	3.8851	7.7165	11.7176	174.16
6.755	3.8242	3.8868	8.1381	11.7136	174.11
6.762	3.8246	3.8868	8.06598	11.7148	174.14
6.778	3.8242	3.8869	8.13	11.7101	174.06
6.781	3.8234	3.8872	8.27	11.711	174.05
6.806	3.8227	3.8876	8.41731	11.7085	174
6.82	3.8216	3.8878	8.58692	11.7064	173.93
6.826	3.8223	3.888	8.52107	11.7041	173.92
6.853	3.8211	3.888	8.68	11.7046	173.89
6.857	3.821	3.8881	8.7	11.701	173.83
6.886	3.8201	3.8881	8.82177	11.6968	173.73
6.888	3.8198	3.8877	8.8096	11.6958	173.69
6.909	3.8192	3.8874	8.84956	11.6926	173.59
6.912	3.8194	3.8875	8.83624	11.6923	173.61
6.94	3.8189	3.8873	8.88	11.6919	173.57
6.94	3.819	3.8868	8.8	11.6909	173.54
6.967	3.8181	3.8854	8.74	11.6821	173.31
6.968	3.8187	3.8856	8.684	11.684	173.36

continued on next page

Table 5, *continued*

O content	*a*	*b*	Orthorhombicity	*c*	Volume
6.981	3.8179	3.885	8.71	11.6825	173.28
6.981	3.8179	3.8848	8.68527	11.6827	173.28
6.981	3.8177	3.8849	8.72433	11.6828	173.27
6.983	3.8177	3.8851	8.75006	11.6835	173.29
6.983	3.8174	3.885	8.77649	11.6829	173.26
6.984	3.8182	3.8852	8.7	11.685	173.34
6.984	3.8175	3.8851	8.77626	11.6841	173.29

[a] Conditions of synthesis with carbonate precursor, sect. 3.1.2). XRD at $T = 300$ K. STOE Diffractometer, use of silicon standard. Data after Krüger et al. (1997) and Conder et al. (1999).

3.3. *The T → O transition*

The difference between Zr-gettered samples quenched in air from lower temperatures (Cava et al. 1987a,b, 1990) and quenched in liquid nitrogen from higher temperatures (Jorgensen et al. 1990a) impeded in the beginning the understanding of the nature of this transition. The T → O transition was implicated in the argument on abrupt change or continuous change of the lattice parameters, the former being considered as an indication for a first-order transition and the latter as an indication for a second-order transition. The two different methods of synthesis are compared in table 4. A comparison of the lattice constants is given in fig. 12. The same difference appears also by the contraction of the apical bond which is correlated to this transition (fig. 14). As we have seen, the abrupt change of the lattice parameters at $x = 6.35$ has been *confirmed* with equilibrium CAR samples (Conder et al. 1999, fig. 25). On the other hand, NPD at *high temperatures* by Jorgensen et al. (1987b) indicated that the transition is second order.

A drawback of the work of Jorgensen et al. (1990a), as in all quenching experiments, concerns the effectivity of quenching which is never instantaneous and complete. Thus, a certain disorder will always remain in such samples. The low temperature of the quenching in air used by Cava et al. and the relatively slow gettering with zirconium probably succeeded in bringing these samples not far from thermodynamic equilibrium. Using such samples Cava et al. (1987a,b, 1990) could support and extend the T_c plateau found by Tarascon et al. (1987a). The latter reported, based on first ac susceptibility measurements, that samples prepared in flowing gas were a mixture of $T_c \approx 91$ and $T_c \approx 55$ K materials. The important contribution of Cava et al. (1987a,b) at this point was to show clearly the existence of the two "plateaus" in the T_c vs. x curve. However, some questions were raised by this work. Although their samples extended into the range $x \geqslant 6.30$, their lattice constants did not show the I–M transition, all the samples staying superconducting ($T_c \approx 27$ K at $x = 6.3$). In a later more systematic investigation, Cava et al. (1990) gettered their samples at the fixed temperature of 440°C and varied the stoichiometry by changing the amount of Zr foil (table 4). The superconductivity

Table 6
Lattice parameters of the BAO samples (Ba-oxide precursor, sect. 3.1.2)[a]

O content	*a*	*b*	Orthorhombicity	*c*	Volume
6.517	3.841	3.879	4.92	11.74	174.91
6.52	3.837	3.878	5.3	11.75	174.84
6.531	3.839	3.875	4.7	11.751	174.81
6.546	3.842	3.876	4.4	11.76	175.13
6.577	3.841	3.873	4.15	11.764	175
6.58	3.836	3.881	5.8	11.739	174.76
6.592	3.834	3.88	6	11.736	174.58
6.613	3.832	3.884	6.74	11.725	74.51
6.634	3.832	3.882	6.48	11.723	174.39
6.638	3.829	3.883	7	11.726	174.34
6.641	3.832	3.883	6.61	11.726	174.48
6.65	3.833	3.883	6.5	11.728	174.55
6.654	3.83	3.884	7	11.726	174.43
6.673	3.83	3.885	7.12	11.72	174.39
6.675	3.831	3.885	7	11.725	174.51
6.702	3.829	3.886	7.4	11.718	174.36
6.707	3.834	3.886	6.74	11.714	174.53
6.714	3.834	3.886	6.74	11.713	174.51
6.734	3.825	3.888	8.2	11.709	174.13
6.748	3.829	3.887	7.52	11.715	174.36
6.768	3.826	3.89	8.3	11.706	174.22
6.795	3.826	3.889	8.15	11.713	174.28
6.808	3.826	3.892	8.55	11.695	174.15
6.81	3.83	3.886	7.26	11.7	174.14
6.813	3.825	3.89	8.42	11.703	174.13
6.822	3.827	3.892	8.4	11.707	174.37
6.828	3.822	3.89	8.8	11.706	174.04
6.833	3.831	3.888	7.38	11.703	174.32
6.851	3.823	3.889	8.56	11.692	173.83
6.862	3.821	3.889	8.82	11.682	173.59
6.875	3.828	3.888	7.78	11.685	173.91
6.875	3.826	3.888	8.04	11.684	173.81
6.876	3.822	3.89	8.81	11.691	173.82
6.888	3.824	3.893	8.94	11.689	174.01
6.892	3.822	3.889	8.7	11.677	173.56
6.902	3.822	3.891	8.95	11.682	173.73
6.906	3.822	3.889	8.69	11.68	173.61
6.92	3.825	3.886	7.9	11.668	173.42
6.932	3.822	3.887	8.43	11.672	173.4

continued on next page

Table 6, *continued*

O content	*a*	*b*	Orthorhombicity	*c*	Volume
6.938	3.821	3.888	8.7	11.671	173.38
6.939	3.821	3.888	8.7	11.673	173.42
6.954	3.82	3.888	8.8	11.674	173.38
6.955	3.819	3.888	8.95	11.677	173.38
6.96	3.82	3.888	8.8	11.676	173.41
6.967	3.82	3.888	8.8	11.675	173.4
6.973	3.82	3.888	8.82	11.679	173.46
6.982	3.819	3.888	8.95	11.686	173.52

[a] XRD at $T = 300$ K (Guinier camera, with Si standard). After Rusiecki and Kaldis (1991).

Table 7
Lattice parameters of DO samples (Ba-metal precursor, sect. 3.1.2)[a]

O content	*a*	*b*	Orthorhombicity	*c*	Volume
6.48	3.8388	3.8797	5.29896	11.741	174.86332
6.556	3.8362	3.8827	6.02417	11.732	174.74595
6.648	3.8325	3.886	6.9314	11.7207	174.5575
6.699	3.8299	3.8879	7.51509	11.7162	174.45736
6.738	3.8283	3.8886	7.81402	11.7101	174.32507
6.789	3.8265	3.8884	8.02344	11.6992	174.07196
6.795	3.825	3.8874	8.09087	11.7004	173.97682
6.813	3.8248	3.889	8.32275	11.7092	174.17022
6.821	3.8235	3.889	8.49271	11.6939	173.88352
6.831	3.8227	3.8889	8.58447	11.6954	173.86496
6.881	3.8243	3.8884	8.31097	11.6737	173.59268
6.903	3.824	3.8885	8.36305	11.6813	173.69654
6.913	3.8281	3.8891	7.90442	11.6718	173.76817
6.922	3.8255	3.8863	7.88402	11.666	173.4389
6.947	3.8201	3.8879	8.79606	11.675	173.39905
6.947	3.8211	3.8883	8.71663	11.6717	173.41325
6.948	3.8222	3.8877	8.49557	11.6801	173.56123
6.964	3.818	3.8843	8.60782	11.681	173.23224
6.968	3.8205	3.8868	8.60223	11.676	173.38299
6.97	3.8183	3.8857	8.7487	11.6807	173.30384
6.974	3.8195	3.8864	8.68166	11.6847	173.44891
6.986	3.8176	3.8866	8.95615	11.6834	173.35226

[a] XRD at $T = 300$ K (Guinier camera, with Si standard). After Conder and Kaldis (1995)

Table 8a
NPD of $YBa_2Cu_3O_x$ at $T = 5$ K. Structural parameters (Å) as a function of x[a]

Var.		x																							
		6.967		6.954		6355		6.932		6.902		6.828		6.795		6.768		6.748		6.702		6.650		6.613	
a		3.8116	(1)	3.813	(1)	3.8138	(1)	3.8161	(1)	3.8154	(1)	3.8167	(1)	3.8181	(1)	3.8205	(1)	3.8218	(1)	3.8225	(1)	3.827	(1)	3.8253	(1)
b		3.8808	(1)	3.8817	(1)	3.882	(1)	3.8818	(1)	3.8824	(1)	3.8831	(1)	3.8831	(1)	3.8829	(1)	3.8819	(1)	3.8815	(1)	3.8784	(1)	3.8788	(1)
c		11.6413	(3)	11.6387	(3)	11.6384	(3)	11.6364	(4)	11.6452	(4)	11.6623	(3)	11.6625	(3)	11.6627	(4)	11.6677	(4)	11.6694	(4)	11.6786	(4)	11.6783	(4)
Y	(B)	0.03	(2)	0.06	(2)	0.16	(3)	0.21	(3)	0.02	(3)	0.05	(3)	0.17	(3)	0.06	(3)	0.1	(3)	0.11	(3)	0.14	(3)	0.1	(3)
Ba	(Z)	0.1824	(2)	0.1831	(2)	0.1842	(2)	0.184	(3)	0.1824	(2)	0.1847	(2)	0.1865	(2)	0.185	(3)	0.1861	(2)	0.1866	(2)	0.1876	(2)	0.1875	(3)
	(B)	0.14	(3)	0.15	(2)	0.2	(3)	0.21	(3)	0.18	(3)	0.2	(3)	0.26	(3)	0.25	(3)	0.22	(3)	0.2	(3)	0.22	(3)	0.25	(3)
Cu1	(B)	0.11	(2)	0.15	(2)	0.22	(2)	0.26	(3)	0.15	(3)	0.16	(3)	0.28	(3)	0.2	(3)	0.19	(3)	0.21	(3)	0.23	(3)	0.17	(3)
Cu2	(Z)	0.3542	(1)	0.3546	(1)	0.3552	(1)	0.3555	(1)	0.3545	(1)	0.355	(1)	0.3561	(1)	0.3554	(1)	0.3557	(1)	0.3559	(1)	0.3565	(1)	0.3562	(1)
	(B)	0.16	(2)	0.12	(2)	0.13	(2)	0.15	(2)	0.16	(2)	0.17	(2)	0.13	(2)	0.19	(2)	0.14	(2)	0.14	(2)	0.1	(2)	0.08	(2)
O1	(Z)	0.159	(2)	0.1589	(2)	0.1593	(2)	0.1592	(2)	0.1585	(2)	0.1576	(2)	0.1581	(2)	0.1572	(2)	0.1569	(2)	0.1568	(2)	0.1568	(2)	0.1566	(2)
	(B)	0.32	(3)	0.31	(2)	0.38	(3)	0.45	(3)	0.34	(3)	0.39	(3)	0.48	(3)	0.45	(3)	0.43	(3)	0.4	(3)	0.43	(3)	0.34	(3)
O2	(z)	0.3779	(2)	0.3782	(2)	0.3781	(2)	0.3777	(2)	0.3777	(2)	0.378	(2)	0.3783	(2)	0.3778	(2)	0.3778	(2)	0.3781	(2)	0.3781	(2)	0.3775	(2)
	(B)	0.23	(3)	0.24	(2)	0.28	(3)	0.29	(3).	0.24	(3)	0.2	(3)	0.26	(3)	0.2	(3)	0.13	(3)	0.13	(3)	0.16	(3)	0.12	(3)
O3	(Z)	0.3783	(2)	0.3778	(2)	0.378	(2)	0.3779	(2)	0.3782	(3)	0.3777	(2)	0.3778	(2)	0.3777	(3)	0.3779	(3)	0.3776	(2)	0.3779	(2)	0.378	(3)
	(B)	0.37	(3)	0.29	(2)	0.32	(3)	0.33	(3)	0.34	(3)	0.3	(3)	0.29	(3)	0.3	(3)	0.27	(3)	0.24	(3)	0.21	(3)	0.22	(4)
O4	(x)	0.0173	(28)	0.0171	(24)	0.0195	(26)	0.0242	(25)	0.019	(29)	0.0237	(26)	0.0245	(26)	0.0258	(26)	0.0299	(22)	0.0292	(21)	0.0325	(23)	0.0338	(23)
	(B)	0.05	(6)	0.14	(5)	0.33	(6)	0.41	(8)	0.02	(7)	0.06	(8)	0.36	(8)	0.01	(8)	0.0	(9)	0.	(8)	0.03	(10)	0.	(11)
	(n)	0.49	(1)	0.47	(1)	0.49	(1)	0.51	(1)	0.47	(1)	0.42	(1)	0.41	(1)	0.4	(1)	0.37	(1)	0.36	(1)	0.33	(1)	0.32	(1)
R_F		4.04		2.32		2.81		3.64		4.62		4.57		2.73		4.81		4.64		3.51		4.49		4.6	
R_P		6.46		5.07		5.5		5.99		7.32		7.33		5.4		7.45		7.12		5.99		7.03		7.27	
R_{WP}		8.21		6.53		7.3		7.99		9.35		9.29		7.2		9.52		9.08		7.66		8.98		9.4	
R_E		3.38		4.14		3.97		4.63		3.92		3.96		4.4		4.16		3.8		3.79		3.82		3.93	

[a] The standard deviations of the relative lattice parameters do not include the uncertainty in the effective neutron wavelength $\lambda = 1.0506(3)$. The sites were assumed fully occupied except for O4 where the oxygen occupancy (2n) was taken from the volumetric determination (Conder et al. 1989). After Hewat et al. (1991).

Table 8b
NPD of $YBa_2Cu_3O_x$ at $T = 300$ K. Structural parameters as a function of x [a]

Var.		x																							
		6.967		6.954		6355		6.932		6.902		6.828		6.795		6.768		6.748		6.702		6.650		6.613	
a		3.8195	(1)	3.8206	(1)	3.8213	(1)	3.8235	(1)	3.8229	(1)	3.824	(1)	3.8252	(1)	3.8276	(1)	3.8289	(1)	3.8295	(1)	3.8339	(1)	3.8323	(2)
b		3.8852	(1)	3.8861	(1)	3.8865	(1)	3.8866	(1)	3.8871	(1)	3.888	(1)	3.8882	(1)	3.8876	(2)	3.8868	(1)	3.8863	(1)	3.8835	(1)	3.8839	(2)
c		11.6835	(3)	11.6818	(3)	11.6833	(3)	11.6816	(4)	11.6873	(4)	11.7062	(4)	11.7077	(4)	11.706	(5)	11.7107	(5)	11.7128	(5)	11.7255	(4)	11.7234	(5)
Y	(B)	0.26	(3)	0.32	(3)	0.41	(3)	0.4	(4)	0.28	(3)	0.3	(3)	0.46	(3)	0.31	(4)	0.33	(3)	0.37	(3)	0.43	(3)	0.39	(4)
Ba	(z)	0.1834	(3)	0.1838	(2)	0.1849	(3)	0.1852	(3)	0.1837	(3)	0.1855	(3)	0.1875	(3)	0.1858	(3)	0.1869	(3)	0.1869	(2)	0.1877	(3)	0.188	(3)
	(B)	0.46	(3)	0.48	(3)	0.55	(3)	0.56	(4)	0.52	(4)	0.5	(4)	0.59	(4)	0.51	(4)	0.51	(4)	0.49	(4)	0.54	(4)	0.59	(5)
Cu1	(B)	0.32	(3)	0.34	(2)	0.46	(3)	0.47	(4)	0.41	(4)	0.41	(4)	0.55	(3)	0.48	(4)	0.43	(4)	0.49	(3)	0.55	(4)	0.5	(4)
Cu2	(z)	0.3541	(1)	0.3549	(1)	0.3555	(1)	0.3557	(1)	0.3545	(2)	0.3551	(2)	0.3569	(1)	0.3555	(2)	0.3555	(2)	0.3562	(1)	0.3562	(2)	03.563	(2)
	(B)	0.4	(2)	0.39	(2)	0.36	(2)	0.38	(3)	0.42	(3)	0.4	(3)	0.35	(2)	0.4	(3)	0.36	(3)	0.36	(3)	0.3	(3)	0.32	(3)
O1	(z)	0.158	(2)	0.1582	(2)	0.1586	(2)	0.1585	(3)	0.1581	(3)	0.1572	(3)	0.1579	(2)	0.1572	(3)	0.1568	(3)	0.1567	(2)	0.1559	(3)	0.1568	(3)
	(B)	0.58	(3)	0.62	(3)	0.66	(3)	0.72	(4)	0.64	(4)	0.69	(4)	0.8	(4)	0.79	(4)	0.72	(4)	0.75	(4)	0.76	(4)	0.71	(4)
O2	(z)	0.378	(2)	0.378	(2)	0.378	(2)	0.3781	(3)	0.3777	(3)	0.3778	(3)	0.3782	(2)	0.3779	(3)	0.378	(3)	0.378	(2)	0.3777	(3)	0.378	(3)
	(B)	0.44	(3)	0.45.	(3)	0.51	(3)	0.49	(4)	0.47	(4)	0.45	(4)	0.5	(4)	0.46	(4)	0.41	(4)	0.43	(4)	0.42	(4)	0.45	(4)
O3	(z)	0.3782	(2)	0.3777	(2)	0.3782	(2)	0.3784	(3)	0.378	(3)	0.3787	(3)	0.3786	(3)	0.3786	(3)	0.3789	(3)	0.3785	(3)	0.3791	(3)	0.3792	(3)
	(B)	0.54	(4)	0.47	(3)	0.53	(3)	0.54	(4)	0.56	(4)	0.51	(4)	0.51	(4)	0.52	(4)	0.49	(4)	0.47	(4)	0.43	(4)	0.53	(5)
O4	(x)	0.0305	(20)	0.0336	(15)	0.034	(19)	0.0349	(23)	0.0332	(21)	0.0358	(21)	0.0391	(22)	0.0359	(24)	0.0388	(21)	0.0397	(21)	0.0405	(23)	0.0414	(24)
	(B)	0.36	(8)	0.34	(7)	0.66	(8)	0.81	(10)	0.25	(9)	0.2	(10)	0.73	(11)	0.32	(11)	0.15	(11)	0.26	(11)	0.24	(12)	0.08	(13)
	(n)	0.49	(1)	0.47	(1)	0.49	(1)	0.51	(1)	0.46	(1)	0.41	(1)	0.41	(1)	0.4	(1)	0.37	(1)	0.37	(1)	0.34	(1)	0.32	(1)
R_F		4.99		3.17		3.59		4.43		5.71		5.52		3.89		5.92		5.48		4.81		5.68		5.8	
R_P		6.04		5.08		5.16		5.67		7.15		6.96		5.25		7.19		6.71		5.96		6.73		7.04	
R_{WP}		7.8		6.51		6.84		7.5		9.02		8.91		6.94		9.18		8.58		7.56		8.62		9.13	
R_E		3.27		4.11		4.		4.71		3.88		3.93		4.45		4.1		3.76		3.76		3.85		3.84	

[a] After Hewat et al. (1991).

Table 8c
NPD of $YBa_2Cu_3O_x$ at $T = 5$ K. Bond lengths (Å) as a function of x[a]

Var.		x											
		6.967	6.954	6355	6.932	6.902	6.828	6.795	6.768	6.748	6.702	6.650	6.613
Y	–O2×4	2.404 (1)	2.402 (1)	2.402 (1)	2.405 (1)	2.406 (1)	2.405 (1)	2.403 (1)	2.407 (1)	2.407 (1)	2.404 (1)	2.404 (1)	2.408 (1)
	–O3×4	2.373 (1)	2.377 (1)	2.376 (1)	2.377 (1)	2.375 (2)	2.381 (2)	2.381 (1)	2.382 (2)	2.382 (2)	2.384 (1)	2.385 (1)	2.383 (2)
Ba	–O1×4	2.731 (0)	2.733 (0)	2.734 (0)	2.735 (0)	2.734 (0)	2.739 (9)	2.741 (0)	2.741 (0)	2.743 (0)	2.744 (0)	2.746 (0)	2.746 (1)
	–O2×2	2.989 (3)	2.985 (3)	2.974 (2)	2.972 (3)	2.988 (3)	2.973 (2)	2.960 (2)	2.969 (3)	2.959 (2)	2.958 (2)	2.949 (2)	2.945 (3)
	–O3×2	2.970 (3)	2.959 (3)	2.951 (3)	2.953 (3)	2.971 (3)	2.949 (3)	2.934 (3)	2.947 (4)	2.941 (3)	2.934 (3)	2.931 (3)	2.932 (4)
	–O4	2.808 (7)	2.814 (6)	2.818 (7)	2.805 (7)	2.805 (7)	2.817 (7)	2.831 (7)	2.815 (7)	2.816 (6)	2.823 (5)	2.827 (6)	2.822 (6)
	–O4	2.896 (7)	2.901 (6)	2.917 (7)	2.928 (7)	2.902 (8)	2.936 (7)	2.954 (7)	2.946 (7)	2.967 (6)	2.970 (6)	2.990 (6)	2.992 (7)
Cu2	–O1	2.271 (3)	2.276 (3)	2.278 (3)	2.283 (3)	2.281 (3)	2.300 (3)	2.307 (3)	2.310 (3)	2.318 (3)	2.322 (3)	2.330 (3)	2.329 (3)
	–O2×2	1.924 (0)	1.925 (0)	1.924 (0)	1.924 (0)	1.925 (0)	1.926 (0)	1.925 (0)	1.927 (0)	1.927 (0)	1.927 (0)	1.929 (0)	1.927 (0)
	–O3×2	1.959 (0)	1.958 (0)	1.958 (0)	1.957 (0)	1.959 (1)	1.958 (0)	1.957 (0)	1.957 (0)	1.957 (0)	1.956 (0)	1.954 (0)	1.955 (0)
Cu1	–O1×2	1.850 (2)	1.848 (2)	1.853 (2)	1.851 (2)	1.844 (2)	1.837 (2)	1.842 (2)	1.832 (2)	1.829 (2)	1.828 (2)	1.830 (2)	1.827 (2)
Cu1	–O4	1.940 (0)	1.941 (0)	1.941 (0)	1.942 (0)	1.941 (0)	1.942 (0)	1.942 (0)	1.942 (1)	1.943 (0)	1.942 (0)	1.942 (1)	1.942 (1)

[a] After Hewat et al. (1991).

Table 8d
NPD of YBa_2Cu3O_x at $T = 300$ K. Bond lengths (Å) as a function of x[a]

Var.		x											
		6.967	6.954	6355	6.932	6.902	6.828	6.795	6.768	6.748	6.702	6.650	6.613
Y	–O2×4	2.408 (1)	2.408 (1)	2.408 (1)	2.407 (2)	2.411 (2)	2.412 (2)	2.409 (1)	2.411 (2)	2.410 (2)	2.410 (1)	2.412 (2)	2.410 (2)
	–O3×4	2.380 (1)	2.384 (1)	2.381 (1)	2.380 (2)	2.383 (2)	2.380 (2)	2.381 (2)	2.382 (2)	2.381 (2)	2.384 (2)	2.382 (2)	2.381 (2)
Ba	–O1×4	2.738 (0)	2.739 (0)	2.740 (0)	2.742 (1)	2.740 (1)	2.745 (1)	2.747 (1)	2.746 (1)	2.749 (1)	2.749 (0)	2.752 (1)	2.751 (1)
	–O2×2	2.988 (3)	2.985 (3)	2.975 (3)	2.973 (4)	2.984 (4)	2.972 (4)	2.958 (3)	2.970 (4)	2.962 (4)	2.962 (2)	2.953 (4)	2.953 (4)
	–O3×2	2.969 (3)	2.961 (3)	2.956 (3)	2.956 (4)	2.966 (4)	2.959 (4)	2.941 (4)	2.957 (4)	2.951 (4)	2.948 (3)	2.949 (4)	2.947 (4)
	–O4	2.792 (6)	2.788 (4)	2.798 (5)	2.798 (6)	2.790 (6)	2.803 (6)	2.813 (6)	2.806 (6)	2.810 (6)	2.809 (5)	2.817 (6)	2.817 (6)
	–O4	2.947 (6)	2.959 (4)	2.969 (6)	2.975 (7)	2.958 (6)	2.983 (6)	3.010 (6)	2.987 (7)	3.006 (6)	3.008 (6)	3.021 (7)	3.025 (7)
Cu2	–O1	2.289 (3)	2.296 (3)	2.299 (3)	2.302 (4)	2.294 (4)	2.315 (4)	2.328 (3)	2.320 (4)	2.325 (4)	2.335 (3)	2.347 (4)	2.337 (4)
	–O2×2	1.929 (0)	1.928 (0)	1.927 (0)	1.928 (1)	1.929 (1)	1.929 (1)	1.927 (0)	1.930 (1)	1.931 (1)	1.930 (0)	1.932 (1)	1.932 (1)
	–O3×2	1.961 (0)	1.960 (0)	1.960 (0)	1.960 (1)	1.961 (1)	1.962 (1)	1.959 (0)	1.961 (1)	1.961 (1)	1.959 (0)	1.959 (1)	1.959 (1)
Cu1	–O1×2	1.845 (2)	1.847 (2)	1.852 (2)	1.850 (4)	1.846 (4)	1.839 (4)	1.847 (2)	1.839 (4)	1.835 (4)	1.834 (2)	1.827 (4)	1.937 (4)
Cu1	–O4×2	1.945 (0)	1.946 (0)	1.946 (0)	1.946 (1)	1.946 (1)	1.947 (1)	1.948 (1)	1.947 (1)	1.948 (1)	1.948 (1)	1.947 (1)	1.947 (1)

[a] After Hewat et al. (1991).

disappeared at $x \approx 6.35$. It is a pity that the 27 K samples were not further reproduced and investigated parallel to the other samples, because a comparison would have extended our knowledge of how the solid-state reaction influences the superconducting properties.

The stepwise change of the apical bond (fig. 14) and of the BVS (fig. 21) at the transition supported the idea (Miceli et al. 1988, Cava et al. 1988a,b, 1990) that the I–M transition is coupled with the T–O transition enabling the onset of the charge transfer.

3.3.1. *The structural T → O transformation at the insulator–superconductor transition*

The order of the T → O transition has been the object of many discussions. Thus, the short-range interactions ASYNNNI model (sect. 5.2) (de Fontaine et al. 1990a,b) predicted a first-order transition and a miscibility gap at intermediate temperatures. The temperature and composition dependence of the T–O transition it predicts is in very good agreement with experiment. On the other hand, Monte-Carlo simulations (Aukrust et al. 1990) and transfer matrix scaling (Bartelt et al. 1989) predict second-order phase transitions in the whole phase diagram. Only for an Ortho II–tetragonal phase transition at zero K they predict a first-order transition.

We recall that in the first-order structural transformations the lattice deformation triggering the change of structure takes place via a large-scale motion preserving the topological integrity (lattice correspondence). A homogeneous strain drives the lattice transformation, the atoms moving in a cooperative fashion with speeds which can reach the speed of sound (*displacive transformation*). The difference to the diffusive second-order *reconstructive transformations,* where bonds to the neighboring atoms are broken and re-formed, is well known: the individual atoms diffuse to a locally favorable environment.

The appearance of a "tweed" microstructure near the transition temperature may suggest a *martensitic transformation,* which in most cases is a first-order structural transition. Such transitions are very common in low-temperature (LT) superconductor materials (Krumhansl 1992) like V_3Si and Nb_3Sn or in ceramics and alloys undergoing chemical phase separation.

An example of a displacive martensitic transformation is the square → rectangular lattice. A two-dimensional analog is the T → O transition in 123-O_x. In the basal plane of the perovskite structure the number of available oxygen sites (O4 and O5) is twice the number of oxygen atoms (O4). Both sites are statistically occupied in the tetragonal phase. When these O atoms break the twofold symmetry between the sites and occupy only the *b*-axis sites (O4) the T → O martensitic transition takes place (Kartha et al. 1995). In spite of their first-order nature, such transformations show pretransitional effects up to hundreds of degrees above the transition temperature. Figure 31 shows schematically this precursor regime. The tweed pattern of 123-O_x has been studied very well with high-resolution electron microscopy (HREM). According to Kartha et al. (1995) the driving force for the appearance of this microstructure is the disorder of the material as it nears the transformation.

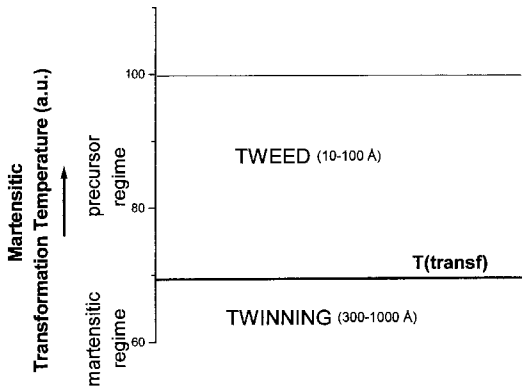

Fig. 31. Schematic diagram of the temperature fields of the tweed precursor of a martensitic transformation and of the twinned lower-temperature phase. Tweed has mesoscopic dimensions.

Although not directly connected with the 123-O_x case, it is worth mentioning here the case of $Fe_{1-x}Pd_x$, showing the extreme sensitivity of the martensitic transformations to compositional changes. The martensitic transformation for $x = 29\%$ appears at room temperature. Increasing the Pd content by 3% suppresses the transition temperature. A change of 1% in composition reduces the temperature by 100 K! This illustrates impressively how easy it is to miss a transition or misinterpret its order by assuming continuous change of e.g., the lattice parameters, if the compositions very near to it are not investigated (sect. 6). Following the ideas of Krumhansl (1992) and Kartha et al. (1995), the role of disorder in creating pretransitional phenomena can be illustrated easily with the above-mentioned Fe–Pd alloy. During the cooling of the alloy a local variation of the Pd content results, due to simple disorder *quenched-in* from higher temperatures. Small Pd-poorer regions will tend to transform to the martensitic phase already at higher temperatures. The statistical distribution of such mesoscopic domains leads to pretransitional deformations accompanying the first-order transition. Thus, the tweed theory of Kartha et al. (1995) treats the overall system as a collection of local regions interacting via the extended strain fields produced from these deformations. This cooperative behavior and the fact that tweed is not a transient state, because the disorder is always existing, are the differences to other models used earlier for the tweed of 123-O_x (Semenovskaya and Khachaturyan 1993).

Novel theoretical models (e.g. Bishop 2000), give a general frame for the importance of the elastic deformation energy which, developing long-range forces, might be more important than the Coulomb energy for HT_c superconducting oxides. Intrinsic nanoscale patterning of spin, charge and lattice degrees of freedom is considered as an important effect, which may lead to the coexistence of inhomogeneous superconductivity and magnetism.

The difficult task to find some indications that at the macroscopic scale the transition is first-order has been undertaken by Radaelli et al. (1992) using $ErBa_2Cu_3O_x$ (Er-123-O_x) slowly cooled samples, equilibrated at low temperatures (table 2). The reduction was made by equilibrating a mixture of $x = 6.9$ and $x = 6.1$ samples (cf. sect. 3.1.2.2). As do most

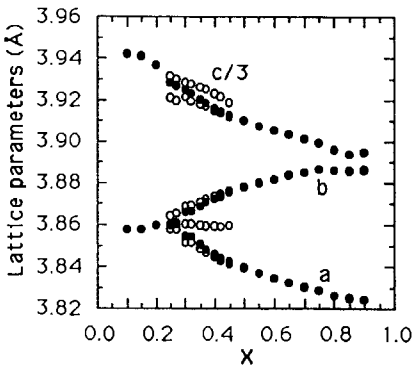

Fig. 32. Lattice parameters of Er-123-O_{6+x} as a function of oxygen nonstoichiometry. Single-phase Rietveld refinements, solid signs; two-phase refinements, open signs. The latter method shows a discontinuity of the c-axis. After Radaelli et al. (1992).

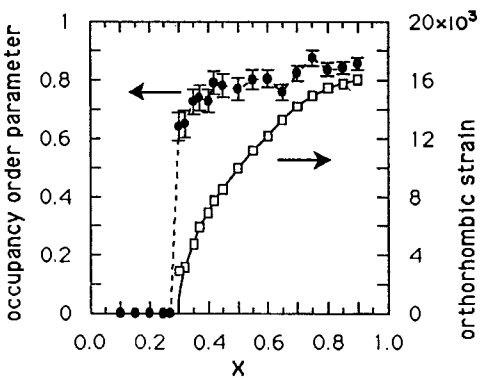

Fig. 33. Orthorhombic strain and occupancy order parameter as a function of oxygen nonstoichiometry. Extrapolation of the orthorhombic strain to zero gives the composition of the transition. The discontinuity of the order parameter indicates the first-order character of the transition. After Radaelli et al. (1992).

investigations in this field, this one suffers from an only approximate determination of oxygen by neutron diffraction ($\approx 4\%$ accuracy). However, in this particular case this is not jeopardizing the results concerning the order of the T → O transition. In fact, the work of Radaelli et al. (1992) is a highlight of diffraction work in the HT_c field. Its importance is augmented by the fact that it illustrates once more how important high-quality samples are for disentangling the properties of the HT_c superconductors. Their structure refinement with NPD showed clearly a systematic broadening of the diffraction peaks near the T → O transition, supporting earlier findings (Jorgensen et al. 1990a,b). This broadening shows two important characteristics:

– anisotropy, i.e. *hkl* dependence, as has been shown before (David et al. 1989), and
– asymmetry of the line shapes, which is independent of strain or particle size.

Agreement between calculated and experimental diffraction patterns was only achieved when both an orthorhombic and a tetragonal phase were included in the refinement.

Similar to the quenched samples of Jorgensen et al. (1990a), the slowly cooled samples of Radaelli et al. (1992) do not show the abrupt decrease of the c-axis found by Cava et al. (1990) (fig. 12) and shown by equilibrium samples (fig. 25) in single-phase Rietveld refinements. The dependences of the lattice parameters on the oxygen content are shown in fig. 32. An inflection can be seen in the c-axis in the region around $x \approx 0.35$, similar to quenched samples (Jorgensen et al. 1990a). The change from the tetragonal to the orthorhombic model in the refinement has been done by determining the composition ($x = 0.3$) of the transition via extrapolation of the orthorhombic strain to zero as shown in fig. 33. Allowing for partial occupancy of the oxygen sites around Cu1 and using isotropic temperature factors for all atoms, the peak widths were calculated with an isotropic strain parameter $\sigma 1$, including the instrumental resolution and isotropic particle-size broadening. The chain (O4) and antichain (O5) site occupancies are shown

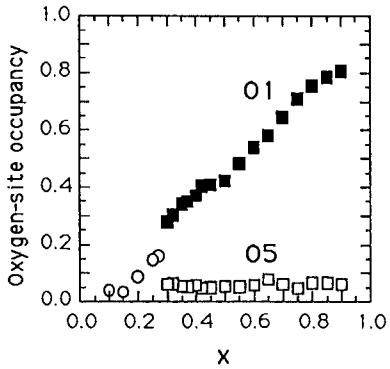

Fig. 34. Chain (O1) and anti-chain (O5) site occupancies as a function of oxygen nonstoichiometry. Note the different notation of the chain site in this figure. The transition T–O takes place abruptly, in contrast to previous investigations (cf. fig. 13). After Radaelli et al. (1992).

in fig. 34. The antichain sites are occupied to ~5%, a fact not considered by Cava et al. (1990), which has appreciable influence on the BVS calculations (Böttger et al. 1996). The occupancy of chain oxygen (O1 in Radaelli's nomenclature) shows a plateau-like deviation from linearity in the range $x \approx 6.42$–6.50. In the orthorhombic range there is no converging of the two curves but an abrupt change to tetragonal. This is opposite to the picture given by the high-temperature *in situ* measurements either at constant oxygen partial pressure (Jorgensen et al. 1987b) or at constant temperature (Shaked et al. 1989, Jorgensen et al. 1988). There, in the orthorhombic regime the O5 occupancy increases smoothly to match the O1 at the transition, a typical behavior of a second-order transition exhibited also by the samples quenched at high temperatures (fig. 13) (Jorgensen et al. 1990a). Also, the dependence on oxygen content of the oxygen-site order parameter $[n(O1)-n(O5)]/[n(O1)+n(O5)]$, which is the order parameter of the transition, shows a strong discontinuity (fig. 33) which is compatible only with a first-order phase transition. Again this is in contrast to the earlier results of Jorgensen et al. (1990a), where the plot of the two geometrical order parameters of the $T \rightarrow O$ transition [orthorhombic strain $b-a$, and chain site occupancy $n(O1)-n(O5)$] is linear and extrapolates to zero, a clear criterion for "a well behaved 2nd order transition".

The picture becomes clearer if the two order parameters, site occupancy and orthorhombic strain, are plotted one vs. the other, both for the slow-cooled samples (Radaelli et al. 1992) and for the *in situ* measured high-temperature (490°C) samples (Shaked et al. 1989, Jorgensen et al. 1988). Whereas the *in situ* data lie on a line through the origin, the line of the data from the slowly cooled Er-123-O_x samples has an intercept of 0.65! Thus, *whereas the high-temperature in situ measurements display a second-order behavior, those of the slowly cooled samples follow a first-order behavior.*

For a first-order transition we expect hysteresis resulting in a mixture of orthorhombic and tetragonal phases. Indeed, two-phase refinements by Radaelli et al. showed a larger c-lattice parameter for the tetragonal phase (fig. 32) leading to a discontinuity at the transition.

Summing up, there are several arguments supporting the idea of *a first-order $T \rightarrow O$ transition – at least at RT and lower temperatures* (Radaelli et al. 1992). According

to the theoretical considerations of Kartha et al. 1995 this is probably a *martensitic transformation.* As mentioned above (sect. 3.2.2.3), the RT X-ray lattice parameters of the equilibrium samples indicate a higher degree of complexity with the different transition widths for the *c*- and *a*-, *b*-axes (figs. 25a,b,d). A comparison of all samples (XRD, NPD at RT and LT) discussed in this review shows that the lowest x value for the appearance of the T–O transitions in the *a*- and *b*-parameters is 6.3 for equilibrium samples and 6.35 for quenched and gettered samples. The highest value for its completion is 6.45. The X-ray RT *c*-parameter of the equilibrium samples (fig. 25d) shows a more abrupt step which seems to extend only in the 6.40–6.43 range (although some small deviations from linearity appear also up to 6.5). This behavior of the *c*-parameter seems consistent with a first-order structural transition. As already mentioned, structure refinements with synchrotron radiation may clarify the situation.

The question has been asked many times whether the T–O and I–M transitions coincide, as originally suggested by Cava et al. 1990. The equilibrium samples are superconducting at $x = 6.396$, but small amounts of superconducting material appear already at $x = 6.342$ (fig. 27b). For the gettered samples the onset of superconductivity was $x = 6.45$ and for the quenched samples 6.34 can be extrapolated (Jorgensen et al. 1990b). We may conclude, therefore, that the I–M transition takes place in the course of the structural T–O transition, which may possibly follow two steps: first intra-plane ordering and then adjustment of the intra-plane spacing. Thus, the investigation of equilibrium samples seems to support the original idea of Cava et al. (1990), that the onset of superconductivity is triggered by the contraction of the apical bond.

3.3.2. *Raman investigations near the T–O transition*

Recently micro-Raman investigations (sect. 5.5, 6.2) could be extended over the whole range of insulating and superconducting 123-O_x ($7 > x > 6$) (Palles et al. 2000a, Liarokapis 2000, Liarokapis et al. 2000). As we will discuss later (sect. 5.5.1), the oxygen-site phonons show appreciable changes in the whole nonstoichiometric range. This is also true for the $x < 6.5$ range discussed here, which includes the I–M and T–O transitions. Figure 35a shows the dependence of the apex (Ag) phonon frequency on the oxygen nonstoichiometry, at RT. The figure includes data taken with three different excitation wavelengths. Strong (vertical) shifts appear in the range of the transitions ($6.3 < x < 6.45$) particularly between blue (476.2 cm^{-1}) and red (647.1 cm^{-1}), but also between green (514.5 cm^{-1}) and red excitation. This is due to resonance excitation of the 486 cm^{-1} ($x = 6.2$) and 493 cm^{-1} ($x = 6.3$–6.4) modes as discussed in the past (Liarokapis 1997).

The apex is abnormally wide, indicating the coexistence of several phases (Iliev et al. 1993, Liarokapis 1997). As will be discussed in sect. 5.5.1, a deconvolution with four Lorentzians (Palles et al. 2000a) shows the coexistence of four phases (475, 486, 493 and 502 cm^{-1}) (fig. 63), indicated in fig. 35a by the horizontal lines. We prefer (sect. 5.5.1) to show the individual data coming from the excitation of several parts of the same crystallite and also from different crystallites, in order to scout for the appearance of different phases in the same sample. Following the green excitation spectra (solid squares, fig. 35a) we find

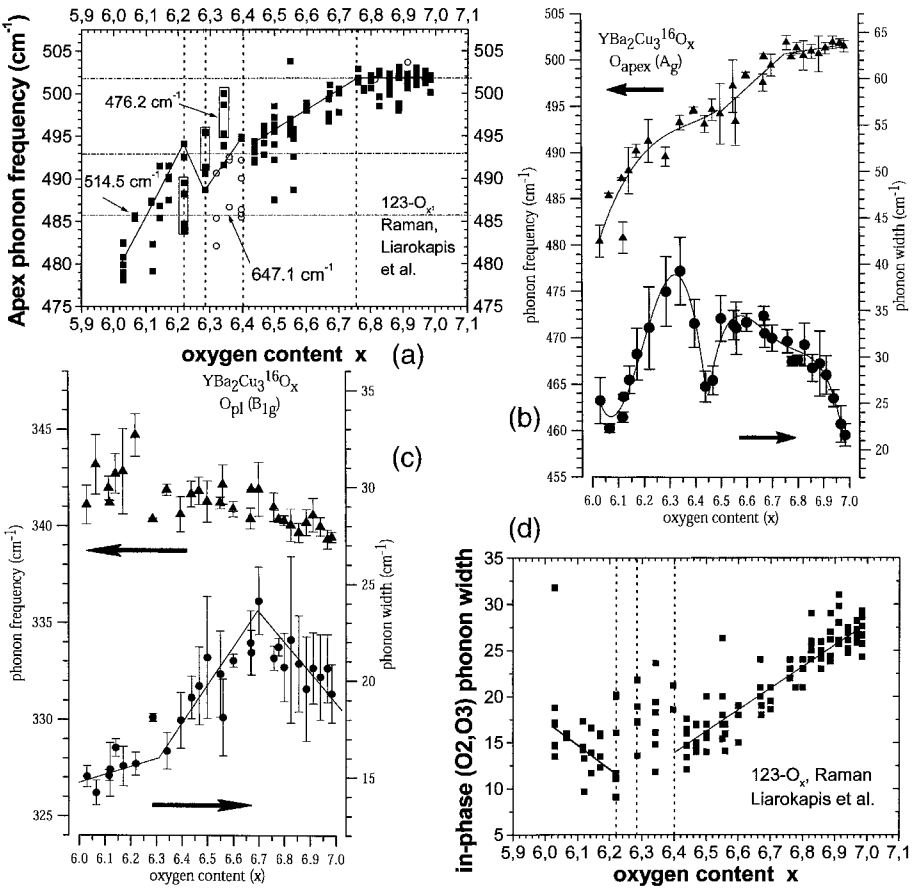

Fig. 35. (a) Changes of slope at $x \approx 6.2$, 6.3, and 6.4 of the apex phonon frequency vs. oxygen content, due to the Néel, T–O and I–M transitions (see text). Solid squares, green laser; solid squares in a frame, blue laser; open circles, red laser. Note the shifts of frequency for the compositions $x \approx 6.22$, 6.28, and 6.4 and excitation by two different wavelengths, due to resonance. The horizontal dashed–dotted lines correspond to the frequencies of the phases deconvoluted (fig. 63) from the apex width. (b) Top: Apex phonon frequency vs. x, average values over many measurements. Bottom: Apex phonon width vs. oxygen content. Note the maximum and the minima associated with the above transitions, cf. (a). The large width of the apex phonon is an indication of the coexistence of several phases (see text). (c) Abrupt discontinuity in the Raman frequency spectra vs. x of the B1g phonon (out-of-phase vibrations of the O2 and O3) at $x \approx 6.25$ (top), coinciding with the onset of the Fano coupling with the superconducting carriers shown by the increase of the width vs. x of the B1g phonon (bottom). (d) In-phase (vibrations of the O2 and O3) phonon width vs. x. See text. After Liarokapis et al. (2000).

abrupt changes of slope or discontinuities at $x \approx 6.2$, 6.3 and 6.4, indicating the existence of three transitions, two of them overlapping with the above-discussed onset of the T–O and I–M transitions.

As mentioned above, in the *small length scale* of Raman spectroscopy (sect. 5.5.1) the 486 and 493 cm^{-1} phases coexist (phase separation) in the oxygen-content range of the T–O transition. Inspection of the apex phonon width (fig. 35b) shows a sharp maximum in the range of $x \approx 6.35$, starting at $x \approx 6.15$, and followed by a sharp minimum at $x \approx 6.45$. Near $x \approx 6.0$ the apex frequency tends towards 475 cm^{-1} (fig. 35a) and, therefore, as seen from fig. 64, also a 475 cm^{-1} phase is present there, decreasing at $x \approx 6.2$ and disappearing at 6.4. Also, the magnetic properties at room temperature change at this composition range. The Néel temperature is 410 K at $x \approx 6.05$ and 250 K at $x \approx 6.34$ (Burlet et al. 2000). Linear extrapolation gives $x \approx 6.25$ for 300 K. This is where the first transition takes place in fig. 35a.

The oxygens of the planes seem also to become involved in this transition, as an abrupt decrease of the B1g phonon (O2, O3 out-of-phase vibrations along the *c*-axis) frequency takes place at $x \approx 6.25$ (fig. 35c, above). The width of this phonon also shows a sudden increase in the same region with an asymmetric Fano shape due to coupling with carriers resulting from the charge transfer (fig. 35c, below). Therefore, we reason that the onset of carriers in the planes appears at RT at the Néel temperature i.e. at $x \approx 6.25$. We may assume that these charges are the result of the formation of hole-doped clusters in a tetragonal insulating matrix, leading, with increasing doping, to the onset of the bulk T–O transition at $x \approx 6.30$ (as seen by the X-rays) (figs. 25) and the I–M transition at $x \approx 6.4$ (figs. 27).

The in-phase Ag phonon width (in-phase vibrations of O2, O3 along the *c*-axis) also shows an anomalous behavior in the range of these transitions (fig. 35d). Although the baseline shows that a minimum of the width should appear at $6.2 < x < 6.4$ the scattering of the data indicates appreciable contribution due to cluster formation or disorder. In the tetragonal phase the same phonon shows appreciable anharmonicity (Liarokapis et al. 2000), disappearing at the T–O transition at $x \approx 6.30$ and increasing again at $x > \sim 6.40$. The localization of carriers in the insulating phase seems to influence the anharmonic potentials at $x < 6.3$. The anharmonicity disappears at the structural transition. But the delocalization at $x > 6.40$ supports the anharmonicity (possible polaron formation) which, however, decreases with increasing carrier concentration to disappear at optimal doping (Liarokapis et al. 2000).

In conclusion, the above structural, optical and magnetic investigations suport the picture of three sequential transitions at RT correlated with the onset of superconductivity. The complexity is increased by the coexistence of three phases at mesoscopic scale and the possible appearance of hole-doped orthorhombic clusters in the tetragonal insulating matrix.

4. Local structure

Historically, the interest in the local structure has arisen from investigations of the non-periodic structure of liquids and particularly of amorphous solid materials. The term "local" is often used to indicate that a view of the structure is given as seen from

the atoms *inside* the solid. Several methods give information about the local structure. Among them are the "extended X-ray absorption fine structure" analysis (EXAFS) and the "pair distribution function" (PDF) analysis of neutron powder diffraction data. Neither are restricted by the symmetry conditions of diffraction. Lattice imaging and electron diffraction techniques also give information about the local structure but are subject to the laws of diffraction. As an additional disadvantage of these methods may be considered the thickness of the sample (>200 Å) which is averaging the signal over this range. Other methods giving information about the local structure are NQR and Mössbauer spectroscopy. Particularly for the former the body of literature is so large that its discussion would by far exceed the boundaries of this work.

In the previous sections we have discussed some lattice effects which are to some degree reflected in the average structure (e.g., lattice-parameter anomalies). Local deviations from the average structure become apparent in crystallographic analysis with higher Debye–Waller factors. The Debye–Waller factor of the split atom model of the chain oxygen will be discussed in sect. 4.1, and in the following subsections we will discuss the results of other methods of investigating the local structure of 123-O_x. The large number of phonon investigations, e.g., with inelastic neutron scattering is outside the scope of this materials-oriented review. A recent exhaustive reference for this field exists (Furrer 1998).

4.1. *Anomalies of the Debye–Waller factor: the split atom model of the chains*

Indications for local structure anomalies emerge from the value of the Debye–Waller factors (B) resulting from the average structure refinements. A good example in the case of the HT_c superconductors is the chain oxygen deformation.

According to the classical Debye theory for a harmonic crystal

$$B_{ii} = 8\pi u_{ii}^2$$

with u_{ii}^2 the mean square atomic displacements in the i direction, given in $Å^2$. Already Capponi et al. (1987) observed, in the structure refinement of $YBa_2Cu_3O_7$, much larger thermal vibrations of the chain oxygen O4 perpendicular to the chain (b-axis) and anomalous temperature dependence. Using anisotropic thermal vibrations in their refinement they found much better agreement. Figure 36 shows the temperature dependence of the B_{33} factor for the anomalous chain oxygen O4 compared with the normal behavior of the apical oxygen O1. In the same year these results were reproduced by two other groups (Beno et al. 1987, Beech et al. 1987). Soon, a much more accurate neutron diffraction study of oxygen-rich polycrystalline 123-$O_{6.91}$ was performed (Francois et al. 1988). A higher precision by approximately a factor of 2 was achieved mainly by including higher-order reflections. A possible constant scale error in the neutron wavelength was reduced by normalizing the unit cell volume to that established by precise X-ray measurements. This study also found the anomalously high B factors of the chain oxygen O4. They could reduce them by using, in the refinement, a split-atom structural

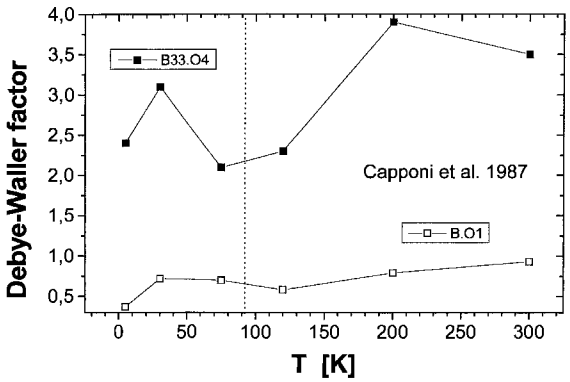

Fig. 36. Debye–Waller factors as a function of temperature. Note the much higher value and the different temperature dependence of B for the chain oxygen O4 as compared to the other oxygen atoms of the structure, e.g. B for the apical oxygen O1. After data of Capponi et al. (1987).

model for the chain. This assumes a displacement of the O4 atoms into two potential minima perpendicular to the chain at a distance ~±0.1 Å along the a-axis. Thus, the chain is certainly not linear and has probably a (randomly) disordered zig-zag shape. The justification of this model came from the resulting normal values and temperature dependence of the *isotropic* B factor.

A detwinned single crystal of 123-$O_{6.7}$ gave an X-ray refinement supporting the above findings (Wong-Ng et al. 1990). Later, an untwinned crystal of 123-$O_{6.88}$ was precisely investigated and electron density maps could be constructed by Sullivan et al. (1993). They also confirmed the anomaly of the O4 and suggested from the electron-density difference maps that a dynamic disorder rather than a static split-atom site exists. Refinements with the split-atom model or with anisotropic O4 B factors gave results similar to those of Francois et al. (1988).

Oxygen-rich single crystals ($x = 6.98$ and 6.96, $T_c = 90$–91 K) were also investigated by Schweiss et al. (1994) with high-resolution elastic neutron scattering. Their data confirm the work of Francois et al. (1988) and their split-atom model for O4. They considered this static model to be more acceptable than dynamic disorder. Probably the sample history was also important here, because Pyka et al. (1993) when performing inelastic neutron scattering in a good sample with $x = 6.95$ ($T_c = 92$ K, 95% single domain) discovered a new vibrational mode with frequency 5.1 THz = 21 meV = 170 cm^{-1} at Γ. In addition, its polarization and absence in the 123-O_6 spectra qualify it for a transverse ⟨100⟩ O4 vibration. The ratio linewidth/frequency at 0.07 was rather large, and it did not decrease appreciably at low temperatures. The rather weak temperature dependence of this peak was considered not to be evidence for an instability of the chain oxygen with its strongly temperature-dependent B factors. The increased value of the linewidth/frequency ratio can be explained either with moderate anharmonicity or with strong coupling of this phonon to electrons. Based on their elastic studies mentioned above the authors concluded that there is clear evidence for anharmonic behavior.

Anharmonicity is an important issue in the debate about the mechanism of superconductivity because it can lead to enhanced electron–lattice coupling. A brief discussion of this issue for the chains of 123 is given by Pickett (1995); the references include

many articles on this subject. A volume edited by Mihailovic et al. (1995) discusses anharmonicity in HT_cS.

4.2. *Lattice distortions: investigations of the pair distribution function (PDF)*

A detailed discussion of the PDF analysis has been given by Egami (1994), in Kaldis (1994), and by Egami and Billinge (1996). The latter is a recommended review of lattice effects on HT_c superconductors up until 1996. The Pair Distribution Function (PDF) represents the weighted probability to find an atom at a given distance from another atom. The elastic scattering part of the diffracted intensity is the sum of the Bragg diffraction intensity and the *diffuse* scattering intensity. The latter is very important for investigating the local structure because it contains information about the *non-periodic* components of the structure. The difference between the conventional crystallographic approach using the Rietveld refinement and the PDF becomes clear if we recall that the former uses only the Bragg intensity, leaving out the diffuse scattering. Thus, no aperiodic features are included in the crystallographic refinement so that an *average structure* results. On the contrary, the PDF analysis of the diffraction data renders the local structure. Another advantage of the PDF analysis is that it is not necessary to assume a certain structural model, although in fact variations of the parameters are often used to make comparisons between a calculated model and the PDF. The scattered intensity can be measured as a function of the momentum transfer $\boldsymbol{Q} = \boldsymbol{k} - \boldsymbol{k}_0$ ($\boldsymbol{k}$, scattered, $\boldsymbol{k}_0$, incident wave vectors). In measuring the PDF it is possible to reach very high $\boldsymbol{Q}$ values up to 25–30 $Å^{-1}$ (d-spacing: 0.20–0.25 Å), whereas using Cu K_a radiation only $\boldsymbol{Q} \ll 8\,Å^{-1}$ can be reached. Rietveld refinements reach $\boldsymbol{Q} < 15\,Å^{-1}$ (d-spacing: 0.4 Å).

For the field of interest of this review, these investigations brought an important result: *local lattice distortions of the order of 0.1 Å in domains of the order of 10 Å exist in HT_c superconductors,* which in contrast to some of the effects discussed in sects. 3.2.2 and 6.1 are not reflected in the average structures. This *intrinsic inhomogeneity* has nothing to do with doping defects, as it appears in chemically homogeneous materials like $YBa_2Cu_4O_8$ (124) which does not have oxygen nonstoichiometry due to the stabilization of the double chains by edge sharing (Karpinski et al. 1988, Kaldis et al. 1991). It is also present in 123-O_x with $x \approx 7.00$ which certainly does not have gross nonstoichiometric deviations. For HT_c superconductivity these effects are important in view of the similar dimensions of the coherence length, and as a possible indication for the existence of polarons. The interested reader can find a complete discussion in the review of Egami and Billinge (1996).

The lattice distortions found by the PDF investigations of Egami and coworkers in various HT_c superconductors are mainly triggered by *displacements of the oxygen atoms (surrounding the Cu atoms) along the* c-axis. However, for optimally doped 123 the results of the PDF investigations were rather ambiguous (Egami and Billinge 1996). Recently, two PDF investigations (Louca et al. 1999, Gutmann et al. 2000) have dealt with the apical bond problem in 123, the latter as a function of stoichiometry; these will be discussed in sect. 4.4. These results are related to the high-resolution ED investigations

(Etheridge 1996) discussed in the next section, and the EXAFS measurements of Röhler et al. (1997b) which we will discuss in detail in sect. 7.4.

4.3. *Distortion of the planes: high-resolution electron diffraction*

Etheridge (1996) presented a systematic in-depth ED study of nearly stoichiometric 123. Although the investigation of other oxygen contents has not yet been published by this author, we include her results in this review, as they give information about the distortions of the superconductive planes.

Several techniques have been used to achieve this result:

(1) In selected-area ED patterns *very* long exposures could discover a structured weak *diffuse* scattering (figs. 37 and 38). *Static correlated displacements* of atoms in directions nearly $\langle 2803 \rangle$ and $\langle 091 \rangle$ are proposed as the reason for this diffuse scattering. These are consistent with coupled displacements of Cu2 and the apical oxygen O1 sites in the a–b plane, which are nearest neighbors in these directions. The coupling occurs over a distance of two unit cells as illustrated in fig. 39.

(2) In *all* high-resolution electron microscopy (HREM) images of 123 published up to now an *extremely subtle modulation of the atomic contrast* can be found along some zone axes, which remained unobserved in the past. The interpretation given by Etheridge (1996) is that it results from a local perturbation of the charge density distribution along planes parallel to $\{449\}$. The oxygen pyramidal planes defined by the plane oxygens O2, O3 and the apical oxygen O1, shown in fig. 5, are parallel to these planes. The dimensions of this perturbation along the $\langle 094 \rangle$ and $\langle 904 \rangle$ directions (roughly along the c-axis) are 5 Å, and along the $\langle 110 \rangle$ directions (in the superconducting plane) 10–20 Å. Therefore, these are intersecting planes *dividing the*

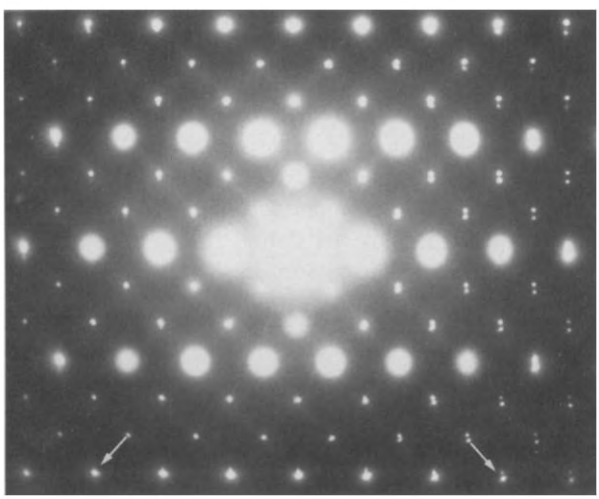

Fig. 37. Twinned orthorhombic crystallite 123-$O_{6.9}$. Selected-area ED pattern of the $\langle 111 \rangle$ zone axis. Diffuse streaks (along the arrows) parallel to $\langle 10\bar{1} \rangle^*$ and $\langle 01\bar{1} \rangle^*$. The intensity distribution of these diffuse streaks is characteristic rather for atomic displacements than for substitutions or vacancies. After Etheridge (1996).

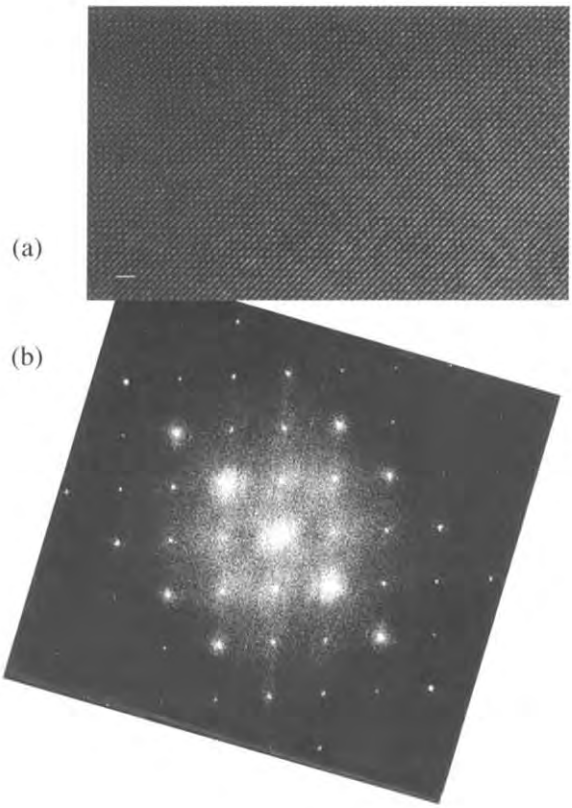

Fig. 38. (a) High-resolution electron microscopic image along the ⟨111⟩ zone axis of 123-O_x (with $x > 6.9$). The scale bar is 10 Å. (b) The corresponding Fourier transform shows diffuse scattering streaks linking Bragg reflections parallel to the $\langle 101 \rangle^*$ and $\langle 011 \rangle^*$ directions in reciprocal space. These appear also in the diffraction pattern of the same crystallite (fig. 37). After Etheridge (1996).

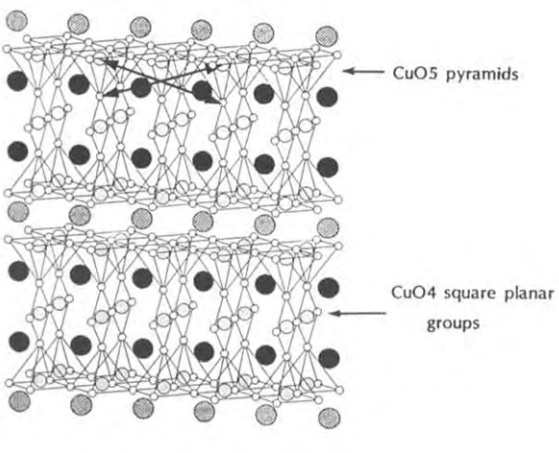

Fig. 39. Schematic average structure of 123-$O_{6.9}$ with atomic displacement vectors [28 0 3] and [28 0 $\bar{3}$] (arrows). They illustrate that the coupled displaced atoms Cu2 and O1 (apical) are two unit cells apart. The ⟨091⟩ displacement vectors are directed into the paper plane and are not shown in this figure which is only two unit cells deep. After Etheridge (1996).

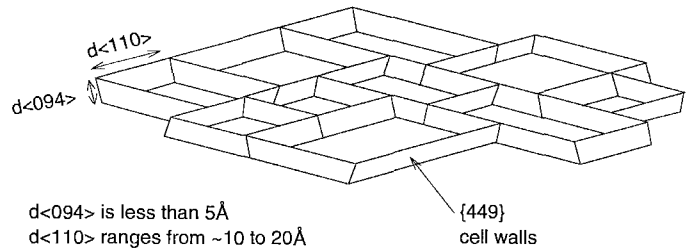

Fig. 40. Schematic illustration of the network of irregular cells, with walls parallel to {449}, partitioning the superconducting plane of 123-$O_{6.9}$. After Etheridge (1996).

superconducting planes in cells of dimensions comparable to the coherence length. The *irregular* network of these shallow dish cells is schematically shown in fig. 40. The walls of these cells are parallel to the oxygen pyramidal planes shown in the previous figure. In successive superconducting planes different patterns of cells may exist.

(3) High-resolution dark-field images suggest that adjacent cells are slightly misaligned, inducing the atomic displacements.

(4) Convergent-beam ED (CBED) patterns along the minor zone axes [011] and [101] show that the mirror planes perpendicular to the *a*- and *b*-axis are absent. This is further evidence for local symmetry breaking in the average Pmmm structure (in addition to the few oxygen vacancies, 1:25 sites).

It is important to stress that the atomic displacements found by ED (1), are consistent with the local perturbation of the charge density found in the HREM images (2). Also, the range of interaction of the displacements from (1) is consistent with the frequency of appearance of the cell walls received from (2) (Etheridge 1996).

Summing up, it can be said that the above phenomena are very feeble and need particular effort to be observed. However, it is gratifying to see that *they all independently contribute complementary evidence for the model given above (fig. 40): superconducting planes as a network of irregular cells 2–4 unit cells wide, resulting from correlated displacements of Cu2 and O1 two unit cells apart. Depending on the phase correlations of these displacements it is possible that a coupled tilting of linked arrays of the CuO_5 pyramids results* (Etheridge 1996). Etheridge stresses particularly the fact that the dark line contrast of the HREM images is present in most publications up to now and therefore it can be considered as *an intrinsic property of 123-O_7*. She also gives extended proof that the above effects have nothing to do with oxygen vacancies in the chains, irradiation damage or tweed structure phenomena.

As the origin of the cell network of the superconducting planes again *lattice strains,* already found by the BVS method (compare sect. 3.2.1.4), have to be considered. From the coarse order of the cells, *long-range* strain fields can be assumed. This supports theoretical models discussing nanoscale patterning (e.g., Bishop 2000). According to Etheridge, several effects influencing the elastic energy can be responsible for these strains:

(a) The different ideal dimensions between the Cu2–O2,O3 superconducting planes and the Cu1–O4 chains as well as Ba–O planes. It is reasonable to expect that the relaxation of the Cu2–O bonds in the superconducting plane will distort the apical site, as this is the most feeble point of the structure (Cu2–O1 is the longest bond, sect. 2).
(b) The orthorhombic strain due to the different lengths of the *a*- and *b*-parameters is responsible for the atomic displacements of the O4 chain sites found by Francois et al. (1988) (see sect. 4.2). These displacements may also influence the other bonds of Cu1 with oxygen shifting the position of the apical oxygen O1 (Etheridge 1996).

We recall that steric reasons were given also by Brown (1989) sect. 3.2.1.4 for the strains in the 123-O_x lattice. Two completely different approaches are, therefore, leading to similar conclusions.

In conclusion it can be said that electron diffraction shows complex oxygen displacements both perpendicular to (like Egami with PDF, sect. 4.2) and in the planes. The nanodomain structure of the superconducting planes found by Etheridge can be considered as a kind of crossed stripes system of *ferroelastic* origin. It triggered investigations of its influence on macroscopic transport and magnetic properties of 123-O_x (Jung et al. 2000, Darhmaoui and Jung 1996, 1998). These authors found that the temperature dependence of the critical current density depends on the disorder of the superconducting planes. Further, they were able to determine the correlation between the superfluid density at low temperature and the nanoscopic disorder in the planes of 123 thin films. They also estimated that for thin superconducting films (thickness 1500 Å, area 1 cm^2) the above-mentioned nanostructure (fig. 40) increases the surface area of the (110) face by almost *six orders of magnitude*. No wonder, therefore, that its influence is quite visible in macroscopic properties.

Out of the wealth of the distortions investigated with inelastic neutron scattering (Furrer 1998) we chose arbitrarily to mention here the recent work of McQueeney et al. (1999) and Egami et al. (2000). Reinvestigating the anomalous dispersion of the longitudinal (LO) phonons (Pintschovius and Reichardt 1998) in La–Sr cuprates this group found a discontinuity in dispersion, indicating dynamic short-range cell doubling in the CuO_2 planes along the direction of the Cu–O bond, probably a charge-ordering effect different from the stripe charge ordering. Egami et al. (2000) investigated the spatial charge inhomogeneities in manganites and cuprates. In manganites these are polarons, in cuprates the inhomogeneities have more dynamic nature and involve phonons that result in charge transfer between oxygen and copper.

4.3.1. *Nanoscale phase separation. The Phillips model*

The evidence for the existence of *nanoscopic disorder* as an *intrinsic property* of 123-O_x brought by the above-mentioned work of Etheridge, is an appreciable support for the theoretical model introduced by Phillips (1987, 1990, 1991, 1999–2001) and by Phillips and Jung (2001a,b). A main feature of this model is that in contrast to all other theoretical models for HTSC it is not based on the effective medium approximation (EMA) but is

inspired by the glassy state, an idea which had been also discussed very early by Müller et al. (1987). According to Phillips, the conventional field-theoretical models derive the properties of the material substituting the intrinsic spatial inhomogeneities by the EMA. This is supposed to include the up to now unknown but essential characteristics of the material responsible for the anomalous properties. In contrast, the model of Phillips is based on the existence of intrinsic heterogeneities resulting from nanodomains in the HTCS. This is of course an approach with special appeal to those engaged in materials research.

The importance of the nanodomains derives from breaking the CUO2 planes into *a system of metallic nanoislands and a network of semiconductive nanodomain walls* that contain a pseudogap (Phillips 1987). Thus the electrical conduction through the planes shows a pseudogap confined to a single plane. Electrical conduction is also possible outside of the planes at frequencies below the gap, via resonant tunnelling dopant centers in the semiconducting planes (Ba–O) which separate the cuprate planes. Using such zigzag filamentary paths it was possible to provide new explanations for neutron diffraction anomalies (Phillips 2000, Reichardt et al. 1989), IR (Homes et al. 1995) vibronic spectra (Phillips and Jung 2001a), and STM (Phillips and Jung 2001b, Hudson et al. 1999, Pan et al. 2000, Howald et al. 2001). Recently, an increasing consensus has emerged about the existence of intrinsic inhomogeneities in HTC superconductors leading to phase separation (e.g. Howald et al. 2001). We note that elastic energy seems to play an important role in HTSC, associated with various lattice distortions (cf. sect. 3.2.1.4, Fig. 20; sect. 4.3, Fig. 40). The well-known formation of misfit dislocations in thick epitaxial layers (Frank and van der Merwe 1949, van der Merwe 1963) offers a good analogy to the formation of the nanodomains of the superconducting planes (Phillips and Jung 2001b). With increasing thickness of the epitaxial layer, the lattice constant misfit leads to increasing stress. As the harmonic strain misfit energy increases quadratically with the layer thickness, at a certain thickness the strain exceeds the elastic limit, and misfit dislocations appear in order to decrease the elastic energy of the system. Misfit dislocations in semiconductors appear commonly by shifting a lattice half-plane. However, in case of phase separation relief of the elastic misfit can be achieved by the existence of any second phase with different lattice constant. If the energy difference of the two phases is small, the reduction of the total energy can be achieved even by a single atomic layer. The *nanoscale phase separation model* of Phillips and Jung (2001b) assumes that this is the case for the cuprates with their easily distorted perovskite structures.

4.4. *EXAFS and PDF investigations of the apical oxygen*

The Extended X-ray Absorption Fine Structure (EXAFS) is generated by the excitation of a certain atom in the unit cell, using X-ray photons with energy beyond that of the absorption edge. The *oscillating absorption pattern* from which the local structure is calculated, results from the interference of the emitted photoelectrons and those backscattered from the atomic cluster surrounding the absorbing atom. The strong scattering of electrons by atoms makes EXAFS an extremely sensitive probe of the local structure. The complexity of EXAFS spectra is the result not only of single scattering

paths but also strong contributions from multiple scattering paths. The latter enrich the spectra strongly and if they can be analyzed offer a great number of structural details on the coordination sphere around the excited atom. In addition, in EXAFS the momentum transfer for the backscattered photoelectrons is very high, reaching values higher than $16\,Å^{-1}$, and giving much more structural detail than the crystallographic Rietveld refinements. A resolution in momentum transfer of $0.1\,Å^{-1}$ in the radial distribution function of EXAFS in the range $k = 4–14\,Å^{-1}$ could be reached with Rietveld refinement only for $Q \approx 25–28\,Å^{-1}$ (Röhler 1994). *Very short length and time scales* strongly increase the importance of EXAFS investigations. *The length scale is of the order of a few Å and the time scale is of the order of* $\ll 10^{-16}$ *s* so that EXAFs will give an instantaneous picture of a dynamic effect.

A much discussed issue of the local structure investigated by EXAFS is the double-well potential of the apical oxygen (Conradson and Raistrick 1989, Mustre-de Leon et al. 1990), which is very interesting for HT_c anharmonicity models (Bishop et al. 1989). In these investigations on *c*-axis oriented powders, changes in the phase of the oscillations of the Cu K edge EXAFS spectra (beats) were observed (fig. 41) in the $12\,Å^{-1}$ range of the photoelectron momentum k. Such beats are known to appear by the superposition of two scattering atom shells situated very close to each other. As seen from fig. 41 the beats are dependent on temperature and Mustre-de Leon et al. (1990) originally found the effect to become smaller near T_c. The analysis of the spectra indicated that the beat could be due to a double-well potential at the site of the apex oxygen which was dynamically tunneling between two minima separated by 0.13 Å. The beat change at T_c would indicate that this separation was slightly diminished pushing the beat to k-values outside of the experimental range. As can be seen from fig. 14 a shift of the apical oxygen by 0.13 Å corresponds to a very large change of the oxygen content and consequently of the carrier concentration. This finding would also support the idea that dynamic instabilities of ferroelectric type are important for HT_c superconductivity (Bishop et al. 1989).

The work of Mustre-de Leon et al. could be partly supported by the results of Stern et al. (1992, 1993). They also found the beats, but no dependence on temperature or nonstoichiometry. Booth et al. (1996) later performed a systematic in-depth investigation of a single crystal and two films on different substrates and found clearly the beats for the single crystals but not for the films, supporting the findings of Stern et al. that the effect is sample dependent, but proving that grain misalignment is not responsible for it. This of course does not change the fact that experimentally the phenomenon does exist and the beat of the EXAFS spectra is clearly seen in the single crystal (fig. 41). That thin films deviate from this behavior is not astonishing. Thin films are subject to strains induced by the substrate, and the 123-O_x (1996 state of the art) still contained many more defects than the single crystals. Nevertheless, Booth et al. (1996) found that even in the films the Cu2–O1, Cu2–Cu2 and Cu1–Cu2 pairs are ~0.02 Å shorter than those found in single crystals with diffraction experiments.

Several crystallographic investigations did not show any indication for a split apex site because the corresponding DEBYE–Waller factors are not large enough (e.g., Kwei et al. 1990, Sharma et al. 1991, Sullivan et al. 1993, Schweiss et al. 1994). Egami and

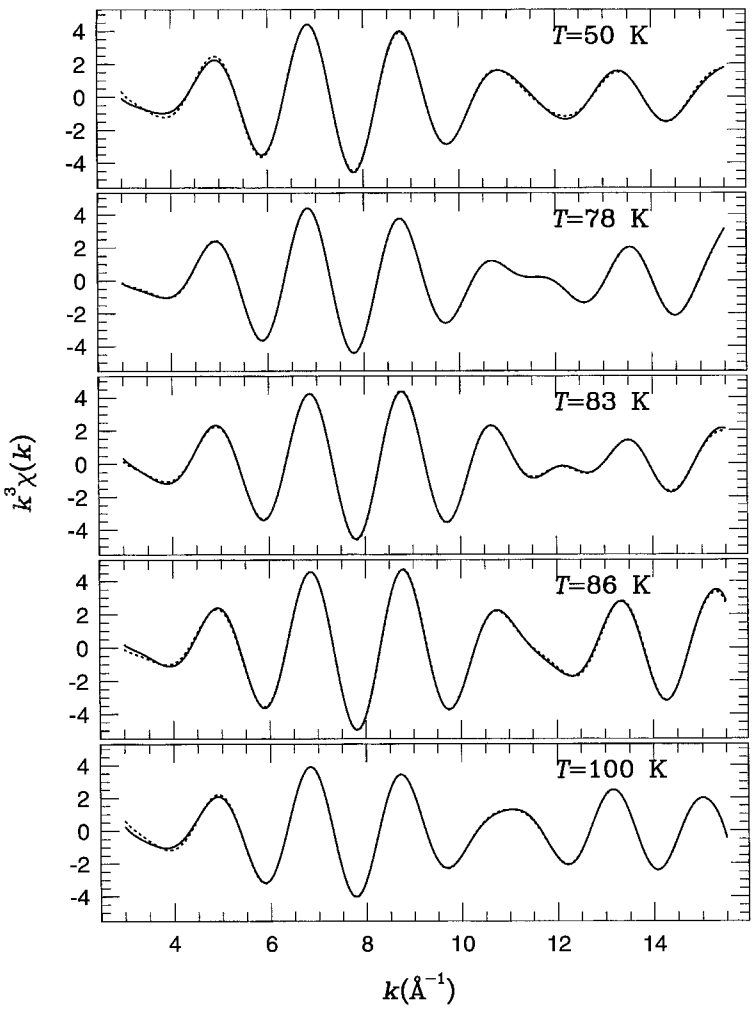

Fig. 41. EXAFS $k^3_\chi(k)$ oscillation spectra of $YBa_2Cu_{2.958}Ni_{0.042}O_{6.95}$ depicting a beat near 12 $Å^{-1}$ which was originally assumed to result from a splitting of the apex site: experimental (solid) curves at various temperatures and calculated fits (dashed) assuming the split apex site. After Booth et al. (1996).

Billinge (1996) report an unpublished PDF investigation of Billinge et al. where real space structure refinements do not show any disorder of the apical oxygen site, in agreement with the crystallographic results. Nevertheless, if in the refinement they use a split position of only 0.033 Å for Cu2 along the *c*-direction they arrive at smaller agreement factors, in accordance with the slightly elongated $Cu2_z$ thermal factor. They conclude that this is possibly an indication for inhomogeneous charge distribution in the planes, indicative of the existence of *polarons* or a microscopic *phase separation* of holes, in which case

a Cu2 atom would adjust its height along the c-axis when a localized hole was in the vicinity. These results are supported by the recent work of Gutmann et al. (2000).

Booth et al. (1996) suggested that a comparison should be made between the correlated Debye–Waller factors given by EXAFS, which give the instantaneous positions of the atoms, and the uncorrelated average over many unit cells given by diffraction. To this end they deduced, from the instantaneous deviation of the atomic position from its mean position, the average deviation in the interatomic distance of atoms A and B, the broadening parameter σ_{AB} (Debye–Waller factor), and from that a "correlation" parameter ϕ:

$$\sigma_{AB}^2 = \sigma_A^2 + \sigma_B^2 - 2\sigma_A\sigma_B\phi,$$

where σ_{AB}^2 is given by EXAFS, and σ_A^2 is given by the diffraction experiments. The expected values for ϕ are +1 for in-phase vibration of atoms (acoustic phonons), −1 for out-of-phase (optical phonon) and 0 for atoms several cells apart above the Debye temperature. Figure 42 shows the average deviation of the broadening parameters σ_{AB} as a function of temperature. Note that in the figures O4 labels the apical oxygen instead of O1. The Debye–Waller factors increase with temperature as expected from a not high Debye temperature. An exception is the Cu1–O1 bond which, due to an anomalous double peak in the region of T_c, has a much higher average value in the temperature range considered. Also, the Cu2–O1 bond reflects the anomalous behavior of the apex oxygen near T_c with a clear peak. Both Stern et al. (1993) and Kimura et al. (1993) have found anomalies of the Cu1–O1.

Booth et al. (1996) conclude that although the physics behind these oscillations of σ_{Cu1-O1} and σ_{Cu2-O1} cannot be yet finally explained, they can be interpreted as changes of the correlation of the Cu2, Cu1 and O1 positions in the lattice. In agreement with this, the correlation parameter ϕ of the Cu2–O1 pair shows clear anomalies with a stepwise decrease in the range 80–100 K (fig. 43). According to these authors it is possible that the increase of the Debye–Waller factor and the decrease of the correlation parameter may result from the appearance of a negatively correlated mode. This mode excited near T_c would counteract the correlation dominating in the remaining temperature region. Such mode could be of polaronic-hopping nature (Booth et al. 1995).

The dynamic bistability in the apex O1–Cu1–O1 cluster was modeled by Mustre-de Leon et al. (1992) by assuming tunneling of the holes between two states leading to a double-well potential due to the large polarizability of the apical O^{2-} ion; this is generally compatible with current polaron models for electron–phonon coupling. The calculations of Ranninger and Thibblin (1992) showed that with decreasing speed of hopping the PDF becomes wider and then splits. A decrease by a factor of <2 is enough to bring about this change: When the frequency of hopping of the electron exceeds that of the lightest optical phonon, obviously the lattice cannot respond and the displacement of the individual atoms remains small; at slower hopping the lattice has time to respond and the Cu and O1 atoms come nearer or move away with the polaron hopping in and out of the ligand. If the hopping frequency becomes smaller than the optical frequency two

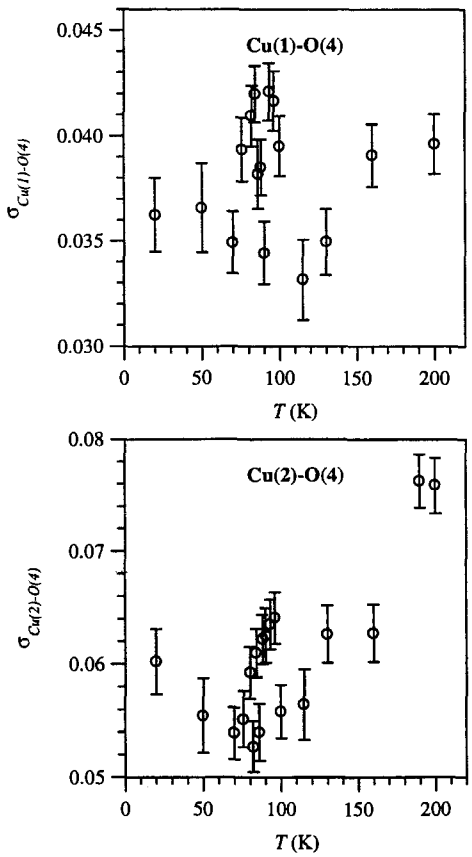

Fig. 42. The Debye–Waller factors σ_{A-B} vs. T (see text) for the single scattering (SS) paths. Only the Cu1–O4 and Cu2–O4 pairs (here, O4: apex) show anomalies near T_c. After Booth et al. (1996).

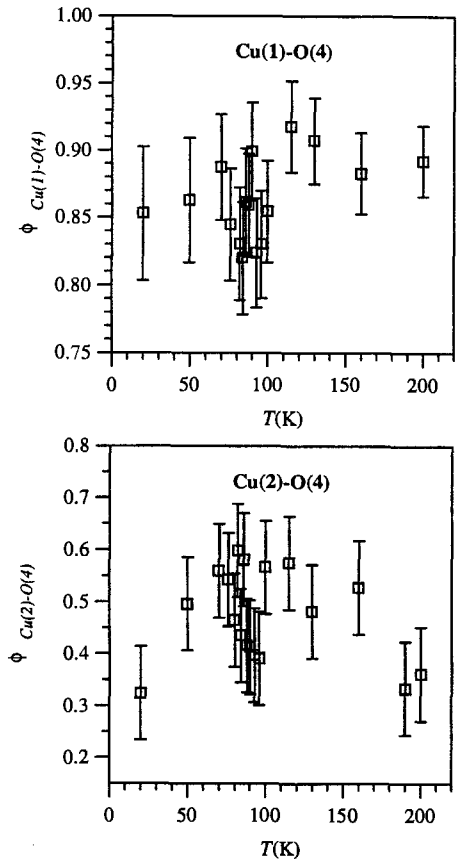

Fig. 43. Correlation parameters ϕ vs T for the Cu1–O4 and Cu1–O4 pairs show clear anomalies near T_c (see text). O4 indicates the apex site here. After Booth et al. (1996).

different pair distributions appear (= polaron absent or present). Thus, a small change in the hopping rate of the polaron could explain the difference found between the single crystal (split atom) and the film (single position). Also, the wider Debye–Waller factor of the Cu2–O1 peak compared to Cu1–O1 and its correlation parameter ~0.5 are consistent with the Ranninger model.

Optical measurements (1993 state of the art) do not seem to support the existence of a double-well potential at the apex site. As discussed in controversy (Mustre-de Leon et al. 1993, Thomsen and Cardona 1993), it should correspond to an IR mode which could not be detected up to now with IR and Raman measurements. Further, the temperature dependences of the frequency, linewidth and oscillator strength of the IR mode of the

apical oxygen have step-like discontinuities at T_c, whereas the variations in the energy levels of the double well show a singularity.

Röhler et al. (1992) have also found a step-like discontinuity near T_c in the Cu K edge EXAFS, supporting the shift of the chemical potential at the onset of superconductivity (Khomskii and Kusmartsev 1992). Analyzing the EXAFS beat structures of Mustre-de Leon et al. (1992) and Stern et al. (1993), Röhler (1994) presented a different interpretation, which is in agreement with the finding of Stern et al. that the beats disappear in the oxygen-rich range. His model calculations confirmed the existence of two Cu1–O4 bond lengths with a difference of ~0.1 Å in the EXAFS spectra, but offered an alternative explanation by a static model based on the local distortions of Cu2 caused by isolated oxygen vacancies of the chain. Nevertheless, as pointed out by Egami and Billinge, the discrepancy with the crystallographic Debye–Waller factors remains.

The calculation gives a characteristic life time of the two states of 10^{-13} s. In view of the EXAFS time scale of $\approx 10^{-15}$ s and its ability to give instantaneous pictures of the local structure, Röhler (1994) argued that no difference is expected between a two-site apex configuration resulting from dynamic bistability and one resulting from static vacancy-induced distortions. However, the instantaneous picture delivered by EXAFS also seems to be subject to yet unknown boundary conditions. This is illustrated by the valence-fluctuation phenomenon of some rare-earth ions in their solid compounds (Röhler 1994). They can be described as dynamic alloys of two different valence states of the same atom, occupying crystallographically indistinguishable sites with a fluctuation time scale of the order of 10^{-13} s. Thus, time scale and splitting of the bond lengths of the atoms in the two valence states are comparable to the double-well apex configuration discussed above. EXAFS spectra show *beats* for the "inhomogeneous" mixed valence systems where the valences are static or slowly fluctuating ($\sim 10^{-9}$ s), but they show almost no effect in "homogeneously" mixed valence systems fluctuating with $\sim 10^{-13}$ s. The reason is not known. Kohn et al. (1982) proposed that the unstable wave functions hybridize with their nearest environment.

As mentioned above, very recently two new PDF investigations on the same subject have appeared which we will briefly discuss here. In a reduced-dimensional function like the PDF a complex crystal structure like that of 123-O_x may lead to a situation where several atom pairs have overlapping bond-distance correlations. The angular averaging then leads to the loss of all information about orientation. The result is that the Cu–O pair correlations and the associated local distortions can not be resolved from those of other pairs like Y–O, Ba–O, and O–O. To overcome this difficulty Louca et al. (1999) applied the isotope Difference Pair Density Function (DPDF) analysis in two 123-$O_{6.92}$ samples made of the pure isotopes ^{65}Cu and ^{63}Cu. Due to the difference in the neutron scattering length of these isotopes, and the resulting enhancement of the scattering amplitude, this method *is a Cu-specific* PDF analogue to the EXAFS measurements at the Cu absorption edge, but possibly with higher resolution. The local atomic structure around Cu and its temperature dependence is obtained without interference from the undesirable pair correlations of Ba–O, Y–O etc. which have comparable bond distances.

Louca et al. (1999) have worked with seemingly well-characterized samples (no quenching, annealing at 400°C for 48 h), although they do not disclose lattice parameters and some other structural data. They found significant structural distortions in the superconducting planes, associated, however, mainly *with the Cu2 and not with the apical oxygen.* They also found a temperature-dependent splitting of the Cu2–O1 pair correlations. However, they could locate its origin to the Cu2 sites because, if it originated from the apical oxygen, then similar anomalies should appear in the Cu1–O1 correlations, and this was not the case. The splitting is found to be of the order of 0.25 Å, but due to technical reasons (limitation of the Fourier truncation) the authors do not consider this value reliable. They conclude that the *double Cu2–O1 peak does exist,* with $\frac{2}{3}$ of the pairs close to 2.25 Å separation and $\frac{1}{3}$ with a somewhat larger value. The authors point out that the nature of the distortion of the superconducting planes they find is consistent with the previous findings of Röhler et al. (1997a,b) about dimpling (Cu2–O2,O3) which will be discussed in detail in sect. 6. The direction of the Cu2 distortions is, therefore, parallel to the *c*-axis.

At the time the manuscript of this review was nearly completed the PDF work of Gutmann et al. (2000) appeared. As the authors note a disadvantage of their investigation compared with EXAFS is the measurement of the total PDF (disadvantages discussed above) and not of the chemical specific PDF. Gutmann et al. (2000) investigated the PDF of four different stoichiometries, $x = 6.25$, 6.45, 6.65, 6,94. Unfortunately, half of the samples were investigated in another neutron facility so that there is no quantitative agreement between the two groups of data. The authors did not find any evidence for the splitting of the apical oxygen site. However, they arrived at a slightly improved fit if the Cu2 site was split along the direction of the *c*-axis. This is interpreted as the result of charge inhomogeneities in the superconducting planes. They also discussed possible formation of stripes (see sect. 7.4).

We note here that a splitting of the apical oxygen signal is routinely seen (Haase 2000) with a novel NMR technique in 123-$O_{6.95}$ (Haase et al. 1998). At present it is not clear whether it is a static or a dynamic effect. Recently two different apex signals have been found also in $La_{2-x}Sr_xCuO_4$.

The above discussion shows the challenges which HT_c materials are issueing to all scientific disciplines involved. In view of all the difficulties discussed above, it is necessary to expand the investigations to a much wider range of oxygen contents. The present knowledge supports the existence of anomalies first observed by the Los Alamos group. After a series of investigations it is found that the source of anomalies is not the apical oxygen but the Cu2 site distortions which seem to be important for HT_c superconductivity (e.g., Andersen et al. 1995). As the work of Booth et al. (1996) indicated, the Cu–O1 pair distribution function is more complex than the originally assumed split-atom model.

A concluding remark for this section concerns the quality of the samples. In several cases sample characterization data are missing (e.g., values of lattice parameters, methods of synthesis, magnetic data), giving the unfortunate impression that when so sophisticated investigations are involved the quality of the samples does not matter!

5. Insulating, underdoped, optimally doped phases: phase diagram, phase separation and superstructures

5.1. *Phase diagram and superstructures: experiments and calculations*

More information about the superstructures will probably improve our understanding of the charge transfer mechanism. An open question is how the electronic states of the chains hybridize with those of the planes. Both the local, intra-chain oxygen order controlling the length and disorder of the chain, and the inter-chain order leading to the superstructure formation are not well known. The same is true for the relationship of oxygen disorder and the superconducting properties. As a result, only idealized models can be investigated up to now.

From the experimental point of view the difficulties are very large due to the natural limitation of the freezing mobility of oxygen.

5.1.1. *Experimental investigations: EM, XRD and ND*

The dependence of the critical temperature on the nonstoichiometric superstructures resulting from oxygen ordering of the chains was found very early. To our knowledge, the existence of the $T_c \approx 60$ K phase was first reported by Tarascon et al. (1987a) and the first two-plateau curve by Johnston et al. (1987) and Cava et al. (1987a). The shape of this curve (for slow-cooled equilibrium samples, cf. fig. 2) triggered a very large number of EM investigations which brought to light the existence of a series of superstructures.

These and several other investigations (see, e.g., in Kaldis 1990) showed at an early stage the importance of the EM (HREM and ED) investigations not only to discover superstructures, but also to give a first framework of a structural model for the XRD and NPD investigations of new structures of HT_c and related compounds. Van Tendeloo et al. (1987) discovered that, in addition to the existence of the full-chain, normal-123 structure, a_0, a $2a_0$ superstructure (every second chain empty) appeared for $x > 6.5$ if oxygen was stripped off the chains via electron-beam heating. More systematic investigations were then performed as a function of nonstoichiometry by Chaillout et al. (1988), extended later to larger series of nonstoichiometric samples (Alario-Franco et al. 1988) and followed by the discovery of the herringbone superstructures $2\sqrt{2a} \bullet 2\sqrt{2b} \bullet c$ type (at $x \approx 6.75$ and 6.25) which recently was reinvestigated and found to be due to impurities (Yakhou et al. 1996). Among the large number of other early papers dealing with EM investigations of superstructures we mention Zandbergen et al. (1987), Werder et al. (1988), Reyes-Gasga et al. (1989) and Beyers et al. (1989).

The investigation by Beyers et al. (1989) is particularly important because the authors investigated equilibrated samples, synthesized under well-controlled conditions in a solid-state ionic cell (Ahn et al. 1988), using slow cooling (18°C/h). This is in contrast to most other investigations at the time, which were performed on quenched, non-equilibrated samples. The result was increased homogeneity. Thus, with the exception of the $x = 6.65$ and 6.90 samples, *all investigated crystallites* in samples of the same stoichiometry gave reproducible electron diffraction patterns (Beyers et al. 1989). These

authors found *long-range* ordering along the *c*-direction *only* for the $2a_0$ superstructure (doubling of the *a*-axis, wavevector $(\frac{1}{2},0,0)$ which appeared in the $x=6.28$–6.61 range covering *both* insulator and superconductor fields. A *two-phase region* was found for $x=6.65$ with the $2a_0$ and an ordered superstructure with wave vector $(\frac{2}{5},0,0)$. Due to the lack of investigation of the intermediate compositions, we can assume that this two-phase region covered the range 6.61–6.71 (fig. 109). A sequence of higher superstructures with short-range ordering was found in the range $x=6.71$–6.90. At $x=6.71$ with wave vector (0.37,0,0); at $x=6.75$ with wave vector $(\frac{1}{3},0,0)$; and at $x=6.85$ and also in some crystallites of the the $x=6.90$ diffuse streaks along the *a*-direction. Again it seems reasonable to assume that the diffuse streaks extended in the range 6.85–6.90 (fig. 109).

Beyers et al. (1989) discuss their results in the frame of the Gibbs phase rule, tending to the classical picture that the plateaus of T_c are two-phase regions (miscibility gaps) and the rapidly changing T_c regions $x \approx 6.40$ and 6.80 are homogeneity ranges, i.e single phases (solid solutions with oxygen). This was illustrated (Beyers and Shaw 1989) by a schematic figure similar to fig. 45 but without the lattice parameters. Based on this thermodynamic picture the $T_{c,\,onset}$ results of fig. 2 may be interpreted as showing a sequence of superstructures in the "60 K plateau". But, there is more evidence from fig. 2 that a miscibility gap (two-phase region) appears in the $x \approx 6.75$–6.80 range. The lattice parameters – a more direct criterion for the coexistence of phases – indicate also that a series of two-phase regions appear in the superconducting range (sects. 3.2.2.3, 3.2.2.4). This picture is also supported by the results of Raman investigations (sects. 5.5.1, 5.5.2). More details are given further below and in the discussion of the important points of the T–x phase diagram (sect. 9).

The superstructures with wave vectors $\frac{2}{5}$ at $x \approx 6.65$ and 0.37 at 6.71 found by Beyers et al. (1989) were not identified. The diffuse streaks at $x \approx 6.85$ indicate a series of very similar superstructures, which were considered by de Fontaine et al. (1990a) as the result of their structure combination branching mechanism (sect. 5.2). They also considered the 0.37 as a $\frac{3}{8}$ which according to their ASYNNNI model could give a chain sequence (11011010) of full (1) and empty (0) chains.

As in EM-investigations only small parts of the sample volume can be investigated, and nonstoichiometric artifacts are easily possible due to overheating of the material by the electron beam, very early, bulk structural techniques like XRD and ND were used to prove the existence of superstructures. The $2a_0$ superstructure was observed for the first time with XRD by Flemming et al. (1988) and the $3a_0$ by Plakhty et al. (1992). Further important work with XRD was performed by Zeiske et al. (1992), Grybos et al. (1994), Plakhty et al. (1994), Schleger et al. (1995a,b), Poulsen et al. (1996), Andersen et al. (1996), E. Straube et al. (1998), and very recently with hard X-rays by von Zimmermann et al. (1999) as a function of stoichiometry, which we will discuss in detail. The first observation of the $2a_0$ with ND was reported by Zeiske et al. (1991) and of the $3a_0$ by Plakhty et al. (1995) and Schleger et al. (1995a). One of the important contributions of this XRD and ND work was to show – in contrast to the early ideas, and consistent with local-structure work (sect. 4) – that in addition to the oxygen ordering of the Cu1–O chains *appreciable relaxation of the cations is associated with the formation of*

Table 9
Antiparallel atomic displacements in the $2a_0$ (ortho-II) and $3a_0$ (ortho-III) superstructures of 123-O_x [a]

Atom	Mean position in unit cell			Atomic displacements (Å)			
				Ortho-II		Ortho-III	
	a_0	b_0	c_0	$2a_0x$	c_0z	$3a_0x$	c_0z
Y	$\frac{1}{2}$	$\frac{1}{2}$	$\frac{1}{2}$	−0.011(1)	0	−0.010(1)	0
Ba	$\frac{1}{2}$	$\frac{1}{2}$	z	0.039(1)	0	0.059(2)	0.040(2)
Cu(1)	1	0	0	0	0	−0.034(2)	0
Cu(2)	1	0	Z	0	0.015(2)	0.007(1)	0.009(1)
O(1)	1	0	Z	0	0.040(2)	0.014(1)	0.068(8)
O(2)	$\frac{1}{2}$	0	Z	0.002(1)	0	−0.006(4)	0.005(7)
O(3)	1	$\frac{1}{2}$	Z	0	0.004(1)	0.007(5)	0.010(7)
O(4)	1	$\frac{1}{2}$	0	0	0	−0.045(6)	0

[a] After Plakhty et al. (1995).

these superstructures. Table 9, after Plakhty et al. (1995), shows the antiparallel atomic displacements in the $2a_0$ (ortho-II) and $3a_0$ (ortho-III) superstructures as determined for both phases by joint profile refinement of X-ray and neutron scattering data, measured at RT, on single crystals.

Plakhty et al. (1994) have found the $2a_0$ superstructure in crystals with $6.40 \geqslant x \geqslant 6.63$ and the $3a_0$ superstructure with $6.70 \geqslant x \geqslant 6.80$. In the range $6.63 \geqslant x \geqslant 6.70$ they found a *two-phase region.* In spite of the different error margins of the determinations of oxygen content (Beyers et al., $\Delta x = \pm 0.02$, Plakhty et al. neutron refinement, $\Delta x \approx \pm 0.4$) and particularly the different thermal and chemical history of the samples, there is a partial overlap of the miscibility gaps. The miscibility gap ($2a_0 + 3a_0$) of Plakhty et al. overlapps with the two-phase region of Beyers et al. (1989) and the range of the ortho-VIII superstructure (consisting of a sequence of $2a_0$ and $3a_0$ chains) found by von Zimmermann et al. (1999), (cf. fig. 109). Their results (Plakhty et al. 1994) show for a very slowly cooled crystal ($x = 6.55$) only *short-range* order even for the $2a_0$ superstructure, with maximal anisotropic correlation lengths 240(30) Å along the b-axis, 17 Å along the a-axis [100] and 8.6 Å along the c-axis [001]. Similar domain sizes have been found before by Hohlwein (1994). Pinning of the domain walls by impurities, twinning and other defects, as well as the high activation energy for the motion of the Cu–O chains, are the reasons considered. Figure 44a shows the structures and the shifts of the various atoms in these superstructures. The oxygen ordering results in appreciable relaxations of the cations which can be seen clearly in the average crystallographic structure. The largest impact has the shift of the Ba atom. Shifts which appear in both structures include:

(a) Ba^{2+} shift towards the full chains. The x-displacement appears stronger in the $3a_0$ superstructure which has two full chains. The z-displacements in this structure are

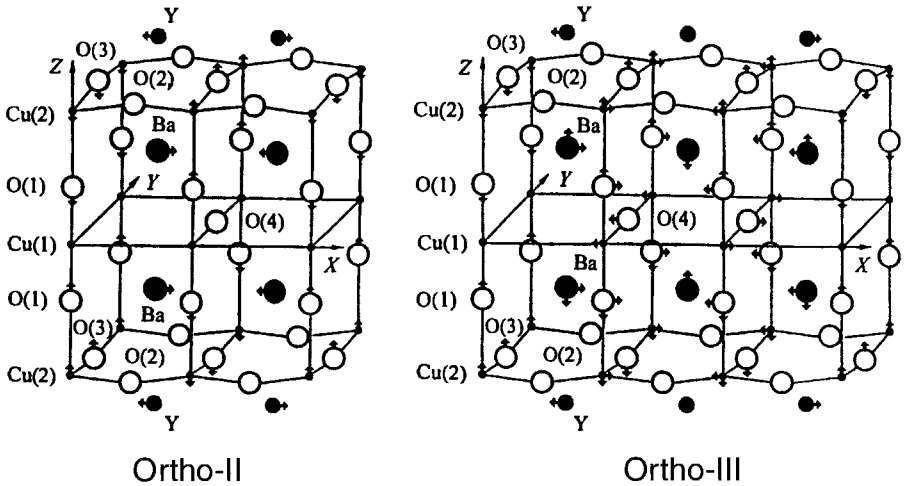

Fig. 44a. The average crystallographic structures of ortho-II and ortho-III phases. The arrows indicate the displacements of the various atoms due to the formation of the superstructures. After Plakhty et al. (1995).

larger for the Ba2 (of the central cell), which is under the influence of full chains from both sides. This results in a shift of 0.008(4) Å towards the basal plane

(b) O1 and Cu2 shift towards the empty chains in $2a_0$. In analogy it can be assumed that a similar shift of O3 appears in $3a_0$. Thus, Cu2 is displaced out of the plane already as a result of the formation of superstructures. This is interesting in conjuction with the PDF investigations discussed in sect. 4.2.

(c) Y^{3+} shift towards the empty chains. This is due partly to the shift of O3 and partly to the shift of Ba^{2+}.

It is believed that these shifts are not significantly influenced by the oxygen content (Hohlwein 1994, Plakhty et al. 1995) and the variation of temperature (Straube et al. 1998).

In the most recent single-crystal diffraction work with hard (100 KeV, penetration depth 1 mm) X-rays (von Zimmermann et al. 1999), it was found that the only true equilibrium phases with long-range order are the T (only phase appearing for $x < 6.35$) and the O a_0 ($x > 6.82$ at RT). The $2a_0$ is also a 3D phase, but with small domains – as mentioned above – appearing for $6.35 \leqslant x < 6.62$. The $3a_0$ is a 2D single phase appearing in this investigation in the range $6.72 \leqslant x \leqslant 6.82$. In addition to the $2a_0$ and $3a_0$ superstructures, they found the following superstructures or mixtures of superstructures:

(1) Ortho-V: a chain sequence (10110) resulting from the sequential ordering of $2a_0 + 3a_0$. It is a bulk 2D phase and appears in a *mixture* with $2a_0$ at a composition $x = 6.62$. This is not far away from $\frac{3}{5}$ ($x = 6.6$) which would be the ideal $5a_0$ composition. We recall that Beyers et al. (1989) observed at $x = 6.65$ (6.61–6.71) with EM the mixture of $2a_0$ and $\frac{2}{5}$ ($x = 6.4$);

(2) Ortho-VIII: a chain sequence (10110110) resulting from the sequential ordering of ortho-III and ortho-V $[3a_0 + (2a_0 + 3a_0)]$, with ideal compositions $\frac{3}{8}$ ($x = 6.375$)

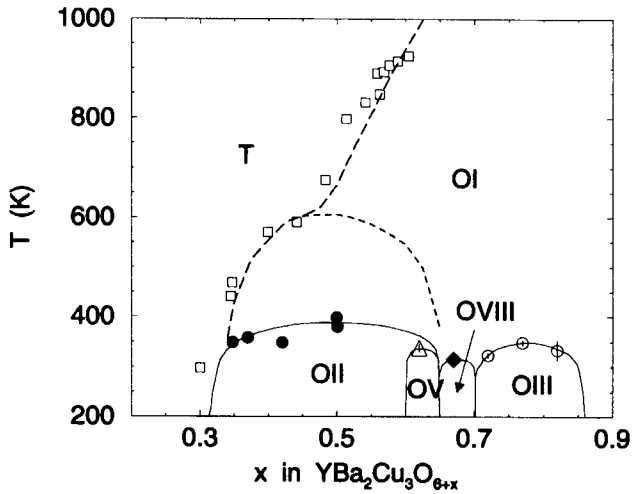

Fig. 44b. Superstructures of 123-O_x in the T–x field, as determined by hard X-ray diffraction. The larger parabolic curve (dotted line) shows the prediction of the ASYNNNI model. The experimentally determined curve lies 200 K lower. After von Zimmermann et al. (1999).

and $\frac{5}{8}$ ($x = 6.25$). The actual modulation vectors at 0.382 and 0.627 are near to these values, the phase appearing for slowly cooled crystals at $x = 6.67$. It is a bulk 2D phase. Beyers et al. (1989) found the phase (0.37,0,0) at $x = 6.71$. We note that 6.67 is approximately the range where the $4a_0$ superstructure could be expected. This superstructure has been reported only once as found by EM (Van Tendeloo and Amelinckx 1990) but was absent in the investigations of von Zimmermann et al. (1999).

The appearance of $2a_0$ and $3a_0$ sequences before the pure $3a_0$ extends the contributions of $2a_0$ up to $x = 6.72$ and makes difficult the investigation of the properties of the pure superstructures. From the point of view of phase stability, it seems reasonable that the pure $2a_0$ and $3a_0$ phases are separated by mixtures with increasing $3a_0$ content. We recall that Plakhty et al. (1994, 1995) have found in approximately the ortho-VIII range $[3a_0 + (2a_0 + 3a_0)]$ the two-phase region of $2a_0$ and $3a_0$ (cf. fig. 109a). Better crystals, even slower cooled and much longer than one-hour measurements may show even more clearly the boundaries between two-phase and single-phase regions.

A very good account of the growth history and characterization of the crystals used in this study is given by von Zimmermann et al. (1999). Using gas-volumetric equipment they can determine the oxygen content with a relative accuracy $\Delta x = 0.02$ using the ideal gas law, provided that the volume of the apparatus and the original composition of the buffer powder are exactly known. The accuracy of the method depends on this calibration. Figure 44b summarizes the phase relationships they have found. This yet incomplete T–x phase diagram is dominated by the tetragonal and the "ideal" (all chains occupied, intra-chain occupation statistical) a_0 orthorhombic structure, which appears *at higher temperatures* (above $T \approx 350$ K) down to $x > 6.35$. It is clear, therefore, that in this range

a large number of oxygen vacancies exists in all the chains of the a_0 structure. According to the authors only these two phases are true equilibrium phases and show 3D long-range order. At room temperature the a_0 orthorhombic structure appears only at $x > 6.82$.

Characteristic for the phase diagram at $x < 6.82$ are phase transitions above room temperature (< 150°C) between the a_0 orthorhombic structure and the superstructures. Transitions occur down to 30–50°C and it is possible to expect at least a tendency for such transitions even at lower temperatures. This feature accounts for many of the numerous contradictions and irreproducibilities in sample preparation and several property measurements of the last 15 years! Depending on the conditions of synthesis the activation energies for the appearance of the various superstructures will be different. The $a_0 \rightarrow 2a_0$ transition takes place upon cooling at 368 K. This is 200 K lower than predicted by the ASYNNNI model (sect. 5.2; see also fig. 44b).

As mentioned above, the single-phase, $3a_0$ superstructure has a finite-size ordering in the a–b plane. It does not appear in this work at its nominal composition $x = 6.66$ but in the range $x = 6.72$–6.82, with maximum intensity at $x \approx 6.76$. The $a_0 \rightarrow 3a_0$ transition takes place at 321 K. For both $2a_0$ and $3a_0$ superstructures the peak intensity and width freeze at $T < 35$C°. The thermal behavior of the ortho-V and ortho-VIII phases is interesting. Heating of ortho-V leads to $2a_0$, but ortho-V ($2a_0 + 3a_0$) is not yet recovered on cooling after one hour. The disappearance of the ortho-V correlations upon heating takes place in the range 50–70°C with the $2a_0$ correlations increasing simultaneously. The latter disappear near 110°C. Heating of ortho-VIII above room temperature leads to ortho-V and then to $3a_0$. Upon cooling, ortho-V is recovered in one hour. However, by longer duration of the experiments it is possible that $3a_0$ could also be recovered. The ortho-VIII superstructure peaks start broadening upon heating at $T = 42$–45°C. Above 50°C the peak position shifts to the position of ortho-V, and at 150°C has reached the position of $3a_0$. Upon cooling the scheme is reversible down to 75°C and then freezes into ortho-V (cf. fig. 44b).

Characteristic of these XRD results (von Zimmermann et al. 1999) and of several previous findings – particularly of the EM investigations of Beyers et al. (1989) – is the fact that *the superstructures appear at oxygen stoichiometries higher than their ideal compositions,* the deviations increasing with increasing number of chains. This means that *"empty" chains are partly occupied.* Von Zimmermann et al. (1999) estimate from their results an occupation of the empty chains of ~10% for the $2a_0$ superstructure and 30% for the $3a_0$ superstructure. The resulting disorder probably influences the Cu charges.

Von Zimmermann et al. (1999) discuss the possibility that this shift of compositions is due to a temperature-dependent tilting of the phase boundary lines. Possibly then, at low temperatures the compositions of the superstructures could be near the ideal values. However, due to the very slow oxygen ordering kinetics, already near room temperature when the superstructures become stable during cooling, the phase diagram is frozen. *The freezing temperature for the chain movements was estimated to be 313 K, and that for the individual oxygen jumps to be 250 K.* This latter temperature was estimated from the time-dependent increase of T_c for quenched samples at these temperatures (cf. sect. 3.2.1.5).

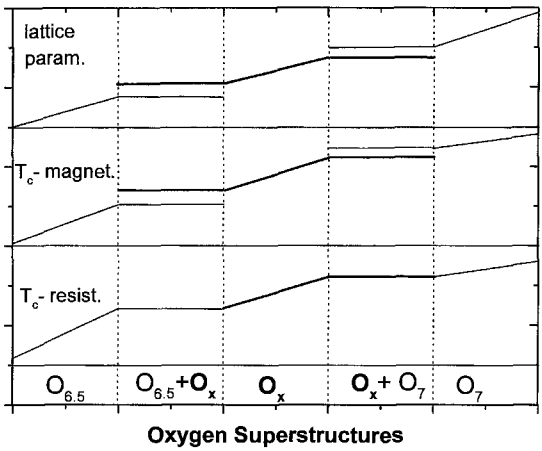

Fig. 45. Schematic to illustrate that the two plateaus of the T_c vs. x curve of 123-O_x could be explained by a classical picture of miscibility gaps. One superstructure is sufficient to explain the two plateaus. Based partly on a figure of Beyers and Shaw (1989).

The above investigations also touch the problem of the *chemical phase separation.* Beyers et al. (1989) interpreted the coexistence of the $2a_0$ and $(\frac{2}{5},0,0)$ superstructures at $x \approx 6.65$ as a phase separation leading to the $T_c = 60$ K plateau. This idea was partly inspired by the early theoretical work of Khachaturyan and Morris (1988) and Khachaturyan et al. (1988), which alone at that time could account for the superstructures observed. These authors considered the superstructures as metastable transients that precede the *spinodal decomposition* into the main stable phases tetragonal at $x = 6.0$ and orthorhombic a_0 at $x = 7.0$. We believe that in view of the complexity of this system, *the possibility of miscibility gaps does exist.* As already mentioned, Beyers and Shaw (1989) discussed a decomposition between the superstructure phases $x = 6.5$ and O_x and the stoichiometric structure $x = 7.0$, and considered the T_c changes in the possibly existing miscibility gaps between these phases. Figure 45 (based partly on a figure of Beyers and Shaw 1989) shows the consequences for the change in lattice parameter and in T_c as a function of the oxygen nonstoichiometry. As expected from the phase rule, in the two-phase regions of the miscibility gaps the properties of the coexisting phases are fixed because the oxygen content is fixed (pseudobinary system $YBa_2Cu_3O_x$–O_2). The figure shows that phase separation due to two miscibility gaps would be sufficient to explain the existence of the two "plateaus" at $T_c = 60$ and 90 K. As mentioned above, the investigation of equilibrium samples (lattice parameters) seem to be consistent with the Gibbs phase rule picture.

Von Zimmermann et al. (1999) discuss kinetic reasons for the explanation of the coexistence of $2a_0$ and ortho-V at $x = 6.62$. Based on their studies of oxygen ordering kinetics (Schleger et al. 1995a,b, Käll et al. 1999), and the lower transition temperatures (95°C and 50°C), they point out that the formation kinetics of ortho-V are much slower than those of $2a_0$. Thus, the coexistence of $2a_0$ with ortho-V could be the result of freezing mobility before equilibrium is reached.

The phase diagram of fig. 44b does not comply with the phase rule in its present form. Comparison with phase diagrams of the type of fig. 1 makes this even clearer. Although both diagrams cover the subsolidus field, the study of the hydride phases can be extended down to liquid-nitrogen temperatures due to the much higher mobility of hydrogen. Most obvious difference between the two diagrams is the absence of two-phase regions (miscibility gaps) or phase-transition lines separating the superstructure ranges in the 123 diagram. Von Zimmermann et al. (1999) point out themselves that their phase diagram is not yet complete. Their conclusion is that the superstructures they studied are not equilibrium phases and it is possible that in more perfect crystals and with *longer annealing times* a more complex spectrum of superstructures may appear. We may add that much more insight could be gained by investigating a much larger number of compositions. Study of the trends could then contribute appreciably to a better understanding of the phase diagram. Thus, although the diagram of fig. 44b is the result of the most advanced diffraction study (up to 1999) it possibly gives only some of the phases involved and not their complete relationships. After discussing the changes of structural and some physical properties as a function of oxygen nonstoichiometry we will combine, in sect. 9, all the experimental results we have discussed in this review in a tentative T–x phase diagram.

Associated with the problem of the equilibration is that of finite-range order. This is particularly important for the $2a_0$ superstructure with its 3D short-range order and the largest stability region. Schleger et al. (1995a,b) have suggested that this short-range order is due to the formation of anti-phase boundaries which limit the growth of the $2a_0$ domains. Impurity defects stabilize the anti-phase boundaries and slow down the moving of long Cu–O chains limiting the domain growth. The results of von Zimmermann et al. (1999) and Käll et al. (1999) support these ideas. The question arises here whether these phase boundaries are also associated with the *stripes* which recently have been found to exist also in 123-O_x (sect. 7.4). Anyway, the short-range order is consistent with the nanoscale phase separation model (sect. 4.3.1).

The small 2D domains of the short-range superstructures $3a_0$, ortho-V and ortho-VIII may also suggest that *a random faulting sequence $2a_0$ and $3a_0$* underlies the ordering mechanism. This simple model has been suggested a long time ago by Khachaturyan and Morris (1990) who have calculated structure factors qualitatively similar to those measured now by von Zimmermann et al. (1999). Von Zimmermann et al. (1999), however, believe that this finite order is due to the sluggish kinetics of oxygen at low temperatures. The ortho-V and ortho-VIII superstructures are formed only by very slow cooling, indicating that *long-range interactions become strong only at low temperatures.* Model simulations (Jensen et al. 1997, Mønster et al. 1999) indicate also that long-range interactions are necessary for the superstructures to form. Thus, according to the authors, the slow oxygen ordering kinetics for moving long chains at low temperatures are the reason for the small domains of these large crystallographic cells.

The phase diagram of fig. 44b, in its present form, leads to following conclusion. The 60 K "plateau" ($x \approx 6.6$–6.75, fig. 2) of T_c corresponds to the stability range **not** of the

single-phase $2a_0$ superstructure, but to a series of single phases and mixtures of phases whose structural units are the $2a_0$ and $3a_0$ sequences:

$$2a_0\,(x \approx 6.6) \bullet 2a_0 + \text{ortho-V}\,(x \approx 6.65) \bullet \text{ortho-VIII}\,(x \approx 6.70) \bullet 3a_0.$$

It is a matter of interpretation whether one follows the Gibbs picture with miscibility gaps or the ASYNNNI model based on the CVM method and discussed in sect. 5.2. The first was followed by Beyers and Shaw (1989), and the results of the lattice constants of equilibrium samples seem to support it. The ASYNNNI model is nearer to the ideas of von Zimmermann et al. Much more work (with many more stoichiometric compositions) is necessary to find out whether there are miscibility gaps between ortho-V, ortho-VIII and $3a_0$. Also, the single-phase character of the ortho-V and ortho-VIII phases should possibly be better supported.

The transition between the two plateaus appears in the boundary of the phases $3a_0$ and a_0. The question whether this is a miscibility gap or a transition between two phases with different chain sequences cannot be answered with certainty at the present stage of knowledge. However, the important fact remains that in this range ($x \approx 6.75$–6.80) many physical and structural properties change, indicating a correlation between superstructure ordering and superconductivity. This multiphase transition region between plateaus is consistent (a) with the T_c measurements of equilibrium samples (fig. 2), indicating a mixture of phases (hatched areas), and (b) with the horizontal parts of the lattice parameters vs. x curves of the BAO samples (figs. 28 and 29). That the a-lattice parameter shows several such plateaus is not surprising in view of the slow kinetics and the extreme sensitivity to the chemical and thermal history. A detailed discussion of the changes in structural and physical properties appearing at $x \approx 6.75$–6.80 will be given in sect. 5.4.2.

5.2. *Model calculations*

In view of the complexity of the pseudobinary $YBa_2Cu_3O_x$–O_2 phase diagram ,the task for the theory is extremely difficult. In the optimism of the first hour, simple *lattice gas* models were proposed soon after the discovery of high-temperature superconductivity. They were based on the assumptions that the system can be described as a lattice of *oxygen atoms only* interacting with either long- or short-range potentials (independent of oxygen content and temperature). The "equilibrium" states may be obtained either by calculations with the mean-field approximation or by Monte Carlo simulations. Rather unexpectedly, this approach did help to some degree in predicting phase-diagram properties. Improved versions of the ASYNNNI model helped to increase our knowledge about superstructures and ordering mechanisms important for the electronic structure and the charge transfer. A detailed discussion of these models is outside the scope of this review. We discuss only some of the highlights of the ASYNNNI model which are of interest for experimental phase-diagram investigations. They illustrate the great complexity of the superstructure picture.

The first two models followed quite different approaches. Khachaturyan and Morris (1988) calculated the T–x phase diagram in the mean-field approximation using *long-range* interaction potentials of the oxygens in the basal a–b plane defined by the chains (Cu1/O4/O5). The long-range interactions include strain effects and describe the mesoscopic ordering (twin formation). As mentioned above, Khachaturyan and Morris (1990) suggested a simple mechanism of formation of the superstructures which produced structure factors to some degree similar to those recently measured. These ideas led, however, also to the conclusion that the diffuse scattering is the result of interstitial defects in the b–c plane, which has not been verified experimentally up to now. Von Zimmermann et al. (1999) point out that the observed oxygen ordering has 2D character as it results from the defects of the a–b basal plane $Cu1O_x$, and that it has domain sizes much smaller than the twin domains.

The other early model (ASYNNNI, de Fontaine et al. 1987), followed the opposite approach, using *short-range* effective pair interactions; despite its simplicity it succeeded in accounting correctly for the formation of the chains, the appearance of the tetragonal and orthorhombic phases, and the locus of their transition in the T–x phase diagram. It also succeeded in predicting superstructures but – as we have seen above (sect. 5.1.1) – it gave a quite erroneous critical temperature for the ortho-II phase.

The *effective pair interactions* V_n are deduced from the general effective cluster interactions (Sanchez et al. 1984) using the *cluster variation method* (CVM) approximation. Thus for the basal plane of 123-O_x (Cu1–O, mirror plane of the structure) the effective O–O pair interactions are given by the linear combination of the total energies:

$$V_n = \tfrac{1}{4}(W^{(n)}_{\mathrm{O\,O}} + W^{(n)}_{\square\,\square} - W^{(n)}_{\mathrm{O}\,\square} - W^{(n)}_{\square\,\mathrm{O}}), \tag{3}$$

with O the occupied oxygen sites and □ the empty oxygen sites, $W^{(n)}_{\mathrm{O\,O}}$ the total energy average over all configurations of □ and O having two occupied O sites in nth-neighbor pair position, and similar definitions for other $W^{(n)}$'s. The energies W have values on the order of the cohesive energy of the materials and can be calculated by quantum-mechanical methods. The effective pair interactions V, however, are small differences of large numbers and orders of magnitudes smaller than the W's (de Fontaine et al. 1992).

In the work of de Fontaine et al. the oxygen configurational statistics are modeled using a 2D Ising (lattice gas) model of the basal plane considering three interpenetrating square lattices (fig. 46a): (a) of the Cu1 atoms (assumed to be always fully occupied), (b) of the O4 and c) of the O5 oxygen atoms. In the tetragonal phase the latter two sublattices are occupied randomly, and in the orthorhombic stoichiometric material ($x = 7$) one (O4) is fully occupied and one (O5) is assumed to be empty. The model considers only the O–O asymmetric interactions up to next-nearest neighbors (NNN). This is denoted also by the name: Asymmetric Next-Nearest Neighbor Ising model (ASYNNNI). As mentioned above, the interaction potentials are considered to be *independent* of T and x. Three *effective* pair interactions (not pair potentials) were considered in the original model, all inside the basal a–b plane divided into two sublattices (O4 and O5):

– V_1 couples the two oxygen sublattices of O4 and O5 and is the *inter-sublattice* nearest-neighbor (NN) interaction. The experimental fact that Cu1–O4 chains are formed in the

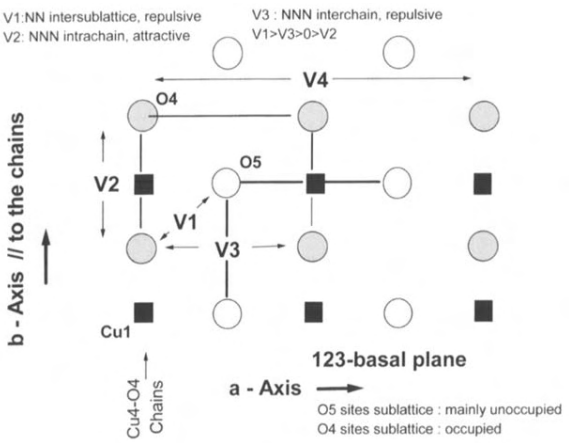

Fig. 46a. Schematic illustration of the three sublattices Cu1 (solid squares), O4 (gray circles) and O5 (open circles) and the interaction potentials V used in the ASYNNNI model. For a discussion see the text.

structure shows that this interaction is a *strong Coulomb repulsion,* i.e. clearly positive. The other two interactions are intra-sublattice NNN less strong interactions.

- V_2 is the *intra-chain* (NNN) interaction between two O4 atoms mediated by a Cu1 atom. It is an *attractive covalent interaction* which together with V_1 force the O4 on their chain sites and keep the O5 sites nearly empty at $x > 6.35$ and lower temperatures.
- V_3 is a weaker *Coulomb repulsive inter-chain* (NNN) interaction which stabilizes the $2a_0$ superstructure. The anisotropy of the model is introduced with the inequality $V_2 \neq V_3$, which also from a phenomenological point of view is rather clear. To account for the existing higher-order superstructures a series of interactions along the a-axis $V_3 = J_1, J_2, J_3, \ldots$ (corresponding to higher neighbors) have been introduced (e.g., V_4 in fig. 46a).

Stability and ground-state analysis (de Fontaine et al. 1987, 1990a,b, Inoue et al. 1987, Wille et al. 1988) indicated the relative magnitude and sign of these effective interactions to be

$$V_1 > V_3 > 0 > V_2. \tag{4}$$

This inequality expresses the fact that only the 4-fold square planar or the 2-fold apical Cu1–O coordination are favorable in the frame of the model [fig. 46b, (a) and (c)]. Other theoretical calculations have shown that the 3-fold coordination [fig. 46b, (b)] has higher energy (Burdett and Kulkarni 1989) and decreases the hole count in the planes and T_c (Ceder et al. 1991b). We note that, nevertheless, this coordination appears at the ends of chain fragments. Ignoring the intra-chain disorder is one of the drawbacks of this model.

First-principle total energy calculations (Sterne and Wille 1989) gave absolute values for the effective pair interactions $V_1/k_B = 4278\,K$, $V_2/k_B = 1488\,K$, and $V_3/k_B = 682\,K$. Using their data, Ceder et al. (1990) were able to propose a phase diagram with a real temperature scale in K. The boundaries of this diagram which were in agreement with the experimental results are the T → O transition and its temperature dependence. Figure 47a

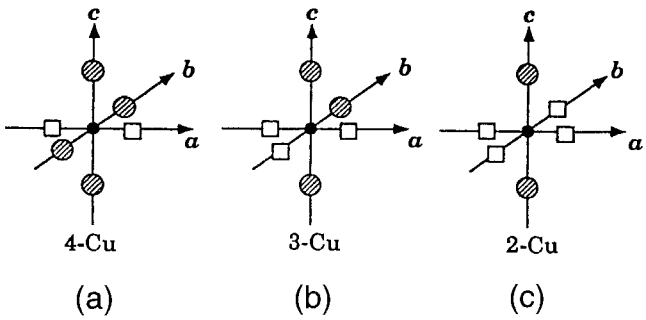

Fig. 46b. Cu1-oxygen coordinations discussed by the ASYNNNI model. For a discussion see the text. After de Fontaine et al. (1992).

shows the T–x phase diagram of de Fontaine et al. (1990a) derived *without* fitting any parameter, and the experimental values measured by Andersen et al. (1990). However, the same group (von Zimmermann et al. 1999) recently showed (fig. 44) that the high-temperature boundary of the OII phase lies 200°C lower than theoretically predicted. This indicates on the one hand the appreciable achievements, and on the other hand the limitations of this model and the degree of its usefulness for experimental research.

De Fontaine et al. (1990a,b) derived a family of superstructures with a *structure combination branching mechanism.* They used the linear chain Ising model to investigate the quasi-1D interchain ordering. Assuming *lack of intrachain modulations and disorder,* but fully formed (identical) chains, they investigated the repulsive interactions along the a-axis direction beyond V_3. These long-range interactions follow a convexity relation and can be obtained by a structure combination branching mechanism (de Fontaine 1984). The ground states of these quasi-1D superstructures, stabilized by convex interactions, are established by stepwise combination of the ortho-I and ortho-II structures (Level I) (fig. 47b). Thus, combination of full chains $\langle 1 \rangle$ and every second chain full $\langle 10 \rangle$ results in $\langle 110 \rangle$ or ortho-II structure, the combination $\langle 10 \rangle$ and $\langle 110 \rangle$ results in $\langle 11010 \rangle$, that of $\langle 1 \rangle$ and $\langle 110 \rangle$ in $\langle 1110 \rangle$ or ortho-III structures, etc. At Level IV, four new superstructures are predicted with sequence of chains $\langle 1101010 \rangle$ (approximately in the concentration range 6.5–6.6), $\langle 11011010 \rangle$ (approximately in 6.6–6.65), $\langle 1110110 \rangle$ (approximately in 6.68–6.74), $\langle 11110 \rangle$ (approximately in 6.78–6.98), and $\langle 1 \rangle$ above $x = 6.92$. Higher-level superstructures are expected to appear as the temperature decreases. As the long-range interactions become less and less strong with the decreasing oxygen mobility at lower temperatures, random mixtures of the 1D structures of the previous level should appear. We note that that these *idealized* "full–empty" chain superstructures considering only 2D O–O interactions have not been observed up to now, with the exception of the ortho-II ($2a_0$) and ortho-III ($3a_0$).

The above superstructures are considered to be modulations of the same phase, rather than separate phases. Therefore, according to this model, no two-phase regions in the Gibbs sense are expected at the predicted boundaries. The CVM approximation predicted the T–OII and $\overline{\text{O}}$I–OII transitions to be first-order. The two-phase regions are shown by

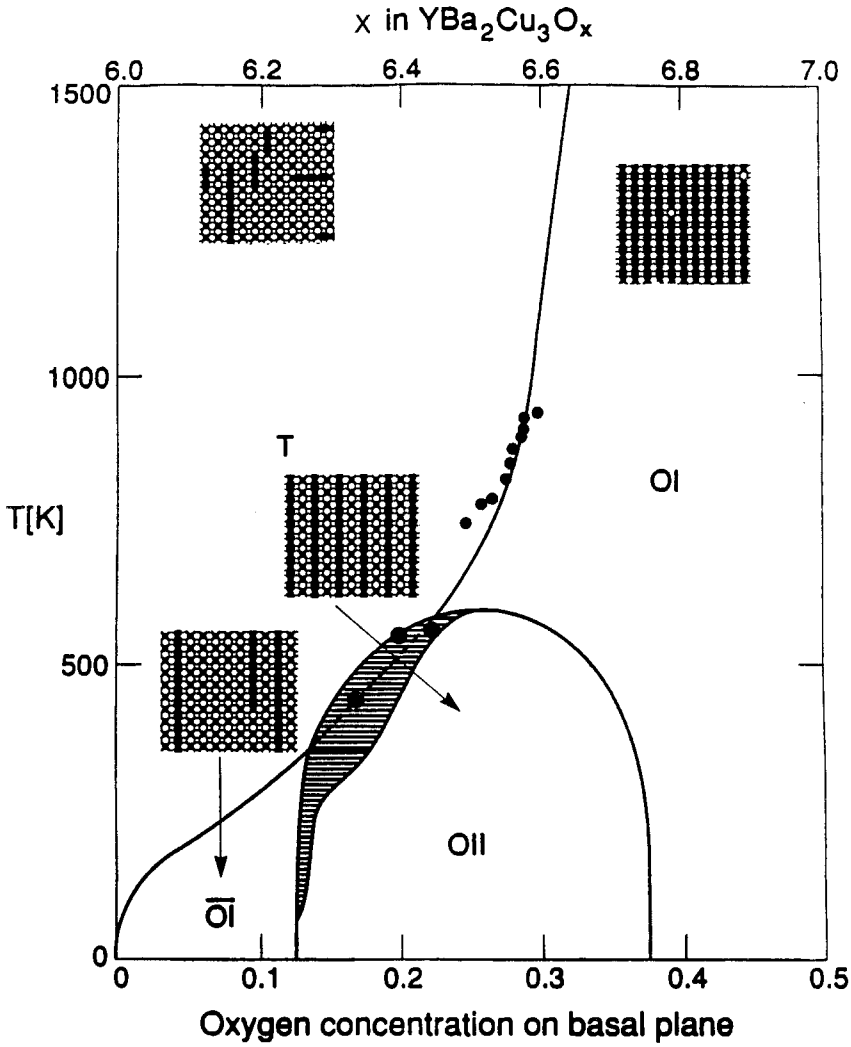

Fig. 47a. Pseudo-binary T–x phase diagram of $YBa_2Cu_3O_x$ calculated with the CVM approximation. The small solid circles are the experimental data of Andersen et al. (1990). The inserts are schematic illustrations of the 2D superstructures of the basal plane obtained from Monte Carlo simulations. Large solid circles, oxygen; small solid circles, Cu1 (large and small solid circles form the black chains); open circles, vacant sites. After de Fontaine et al. (1992). The measurements of the phase boundary of the T–O transition are in good agreement with the theory. However, comparison with fig. 45 shows that the calculated critical temperature of the ortho-II phase (~570 K) is much higher than the value recently found [~370 K, von Zimmermann et al. (1999)].

the tie lines in fig. 47a. However, transfer matrix calculations and Monte Carlo simulations do not show any first-order transitions (Bartelt et al. 1989, Aukrust et al. 1990). A useful review about the ASYNNI model is given by de Fontaine et al. (1990a, 1992).

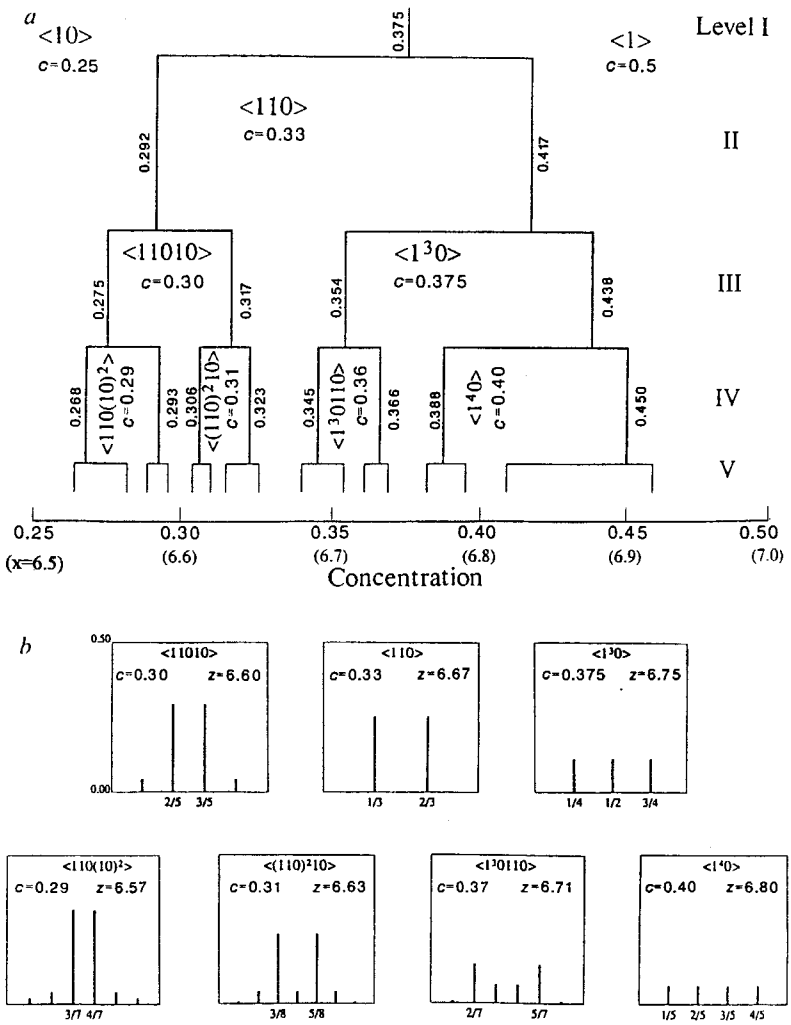

Fig. 47b. (a) Branching algorithm for quasi-1D superstructures of the basal plane of $YBa_2Cu_3O_x$. The symbols 1 and 0 denote oxygen-full and -empty chains. The concentration scale x is given together with the basal plane coverage. (b) Diffraction patterns (Fourier amplitude-squared) along (h00) of the superstructures existing on Level IV (levels I → V, decreasing temperature; z, oxygen content x). Superstructures appear at $x = 6.57$, 6.60, 6.63, 6.67, 6.71, 6.75, 6.80. After de Fontaine et al. (1990b).

Although the ASYNNNI model reproduces excellently the temperature and composition dependence of the O–T transition and the existence of the O-II phase, as we have seen it is 200 K wrong in the prediction of the O-I to O-II transition temperature. Further, it does not account for the appearance of the up to now *observed* higher superstructures (O-V and O-VIII, sect. 5.1.1) and it predicts always long-range order

of the superstructures, instead of the short-range order found. In view of the extreme complexity of the 123-O_x superstructures it is clear that one cannot expect much more from such simple models. An intrinsic drawback of the model is that it is based only on the order of the oxygen sublattice. However, as shown by structural investigation, appreciable cation relaxations seem to be necessary for the stabilization of the superstructures (cf. table 9, fig. 44a). A series of publications have tried to compensate the various drawbacks of the ASYNNNI model. Andersen and coworkers have experimented with several extensions of the model (cf. references in von Zimmermann et al. 1999). Schleger et al. (1994) introduced the charge and spin degrees of freedom of the itinerant carriers and considered the entropy contributions resulting from them. The agreement with experiment is very good.

In conclusion it can be said that, even with the above-mentioned drawbacks, the ASYNNNI model has considerably helped to understand the difficulties of the superstructure problem. The delicate balance resulting from eqs. (3) and (4) indicates the strong dependence on preparation conditions to be expected. The complexity of superstructures dictates extremely slow cooling and low-temperature annealing. Here, however, the freezing of the mobility of oxygen puts a natural limitation.

Another interesting topic is the structure combination branching mechanism. As the relaxation of the cationic lattice and the disorder of the chains is not taken into consideration even if the method is thermodynamically sound, the predictions can be only be correct to a certain degree. The appearance of ortho-V and ortho-VIII in the structure as found by von Zimmermann et al. (1999) with different chain sequences than those predicted above show that simple "telescoping" of the oxygen is not enough. Thus, in our opinion the question about the existence of miscibility gaps separating the various superstructures still remains open. Independently of the partial validity of the branching mechanism of de Fontaine, with decreasing differences of the energies of the various superstructures the system comes near to a random distribution of chains. In view of the small driving force and the low mobility of oxygen, the experimental proof of the miscibility gaps becomes then very difficult. On the other hand, the relaxation of the cationic sublattice may increase the involved interactions so that miscibility gaps can be seen.

5.3. *T_c dependence on nonstoichiometry and hole concentration: applications of the BVS method – II*

The strong dependence of the temperature of the diamagnetic transition on the carrier concentration was one of the first subjects to be investigated after the discovery of HT_c superconductivity. Shafer and Penney (1990), who were among the first to investigate this subject, found a parabolic dependence of T_c on the hole concentration and wrote the first review on the subject. The parabolic dependence was further supported by Tokura et al. (1988), Torrance et al. (1988) and Torrance and Metzger (1989). Later Whangbo and Torrardi (1990) showed that this applies to all p-type superconductors. Tokura et al. investigated a large number of substituted 123 compounds of the general

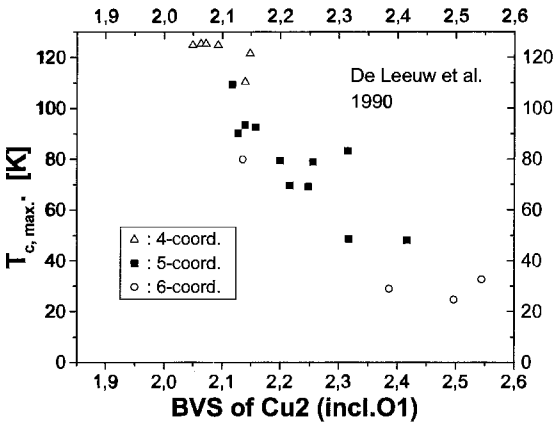

Fig. 48. Correlation between the maximum $T_{c,max}$ of 19 superconductors and the bond valence sum of the Cu2 atom. This correlation exists if not only O2 and O3 but also the apical oxygen O1 are included in the calculation. After de Leeuw et al. (1990).

formulae $Y(La_xBa_{1-x})_2Cu_3O_y$ and $(Y_xCa_{1-x})Ba_2O_y$ each with a different total charge of *non-copper* cations Q. Knowing that the degree of oxidation, which they put equivalent to the *average charge p per bond*, is very important for these materials, Torrance et al. (1988) measured it approximately by iodometric titration. From Q and p they could estimate indirectly the oxygen content y from the simple electroneutrality condition

$$Q + 3(2 + p) = 2y, \tag{5}$$

and they could show that the changes of T_c found by variation of the oxygen content (Engler et al. 1987, Tarascon et al. 1987b, Johnston et al. 1987, Cava et al. 1987a) are due to changes of the charge in the $[Cu–O]^{p+}$ bonds.

Studies of a series of well-characterized samples as a function of nonstoichiometry showed the existence of a maximum of T_c at $\sim x = 6.92$ (Graf et al. 1990, Rusiecki et al. 1990). Also, at this composition range the anomaly of the c-axis (fig. 28a) was found by Rusiecki et al. (1990), which was the first evidence for the existence of different materials properties in the then scarcely investigated *overdoped* range. Claus et al. (1992a) made the first T_c vs. x investigation of the overdoped region with estimated x values, and measured a few compositions with lower T_c. Just before the manuscript was finalized a paper containing a brief summary of the rather large literature concerning T_c vs. x or hole concentration (Schlachter et al. 1999) came to the attention of the author. The interested reader can find in its introduction references in addition to those discussed in this review.

Very popular among crystallographers and materials scientists for the estimation of the hole density is the *empirical* BVS method (sect. 3.2.1.4). Starting from the work of Brown (1989), de Leeuw et al. (1990) considered separately the bond valences of copper and oxygen in the planes. They demonstrated a correlation between the maximum $T_{c,max}$ and the in-plane bond valence sum of Cu2 and of O_p for 19 superconductors, whose structures were known at the time (fig. 48). In the V_{Cu2} they included the oxygen contributions both from the O_p (O2, O3) and apical oxygens (O1). The correlation disappears if the apical oxygens are not considered. The work of de Leeuw et al. demonstrated clearly that the

valences calculated with *BVS* are relevant to superconductivity and proposed a method to calculate the hole densities of the planes. Figure 48 shows that V_{Cu2} decreases with increasing $T_{c,max}$.

Extending the work of de Leeuw et al., Tallon (1990) proposed to use, instead of V_{Cu2} or V_0, their sum and difference as independent variables, due to the fact that the holes have a hybrid copper–oxygen character:

$$p \approx V_- = (V_{Cu2} - 2) + (2 - V_{O2}) + (2 - V_{O3}) = 2 + V_{cu2} - V_{O2} - V_{O3}, \tag{6}$$

$$V_+ = (2 - V_{O2}) + (2 - V_{O3}) - (V_{Cu2} - 2) = 6 - V_{cu2} - V_{O2} - V_{O3}, \tag{7}$$

with $V_{Cu2} - 2$ the excess charge on Cu2, and $2 - V_{O_p}$ the excess charge on each oxygen of O2 and O3.

V_- is a parameter for the change of hole density in the planes and it becomes zero for Cu^{2+} and O^{2-}. Tallon (1990) argued that an advantage of V_-, compared to the valence sum of copper V_{Cu2}, is its relative insensitivity to internal stresses as the effects on copper and oxygen would tend to cancel each other. V_- is mainly sensitive to shifts of the oxygens O1, O2, O3 out-of-plane, as the in-plane bond sums cancel each other.

V_+ is a parameter for the shift of holes from Cu to O along the Cu–O bonds *in the planes* (distribution of charge between Cu and O). Contrary to V_- it is sensitive to strain, the effects on Cu and O adding to each other. This is meaningful only outside the range of the charge shift very near to oxygen (localization, semiconductivity) or very near to copper.

Plotting T_c vs. V_- results in the well-known parabolic curve in agreement with the earlier results of Shafer et al. (1988), Shafer and Penney (1990), Tokura et al. (1988), Torrance et al. (1988), and Groen et al. (1990) with a maximum near ~0.17 holes/Cu atom. Based on the data for $La_{2-x}Sr_xCuO_4$ and the Bi family, Presland et al. (1991) described the parabola with

$$\frac{T_c}{T_{c,max}} = 1 - 82.6(p - 0.16)^2, \tag{8}$$

which was considered as a generalized *empirical* equation of the approximately parabolic dependence of T_c on the number of holes p per Cu2 atom. They claimed that it applies for all the p-type superconductors, the more recent studies converging to a maximum at $p \approx 0.16$. However, it is difficult to incorporate 123 in this picture because there is no direct method for the measurement of p in 123 as a function of the nonstoichiometry x, due to the existence of two different Cu valences. To overcome this difficulty Tallon et al. (1995) had an interesting idea, which, however, had a doubtful experimental confirmation.

In $Y_{1-x}Ca_xBa_2Cu_3O_6$ with all oxygen removed from the chains (cf. fig. 46b, part c) the Cu1 atoms can be considered to be in the Cu^{1+} valence state. In this case we have for the planes $p \approx x/2$, i.e. if V_- for the undoped 123-O_6 becomes zero, only the holes from the Ca doping still exist (the question not asked at the time is whether these holes contribute

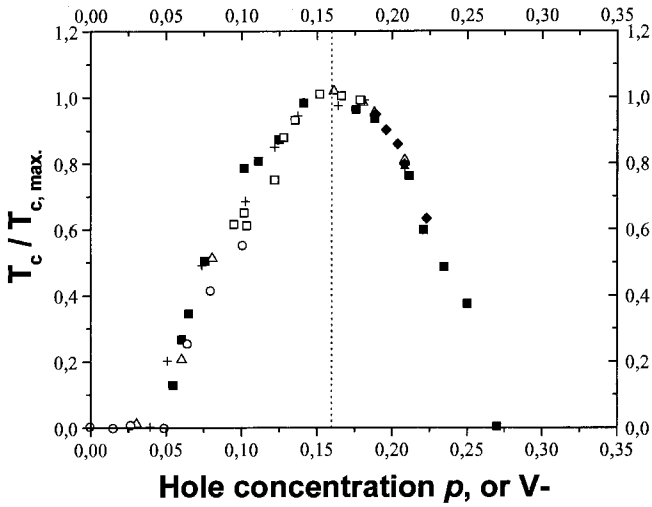

Fig. 49. Generic parabola for normalized T_c vs hole concentration based on BVS calculations, for $La_{1-x}Sr_xCu_2O_4$ and $Y_{1-x}Ca_xBa_2Cu_3O_{7-\delta}$ after Tallon et al. (1995). The validity for the Y-compound is based on the assumption that $7-\delta=6.0$ samples, completely stripped of their chain oxygen, are still superconducting. As shown in fig. 51 this is doubtful. Open circles: $Y_{1-x}Ca_xBa_2Cu_3O_6$ from $p=x/2$. Open squares: from $p=V_-$ in $YBa_2Cu_3O_{7-\delta}$ with different δ. Solid diamonds: from $p=V_-$ of $Y_{1-x}Ca_xBa_2Cu_3O_{7-\delta}$ with $\delta\approx 0.04$ and different x. + symbols: from $p=V_-$ of $Y_{1-x}Ca_xBa_2Cu_3O_{7-\delta}$ with $x=0.1$ and different δ. Solid squares: $La_{2-x}Sr_xCuO_4$. Open triangles: $La_{2-x}Sr_xCaCu_2O_6$.

to superconductivity). In this way, if the exact stoichiometry is known also the hole density will be known. What these authors overlooked was that not the hole density, but the *mobile hole density* is relevant here. As we will discuss below, this is supported by recent results.

According to Presland et al. (1991), Ca_y-123-O_6 and Y-123-O_x follow the generic parabola of eq. (8) shown in fig. 49. Using the $p=x/2$ and $p=V_-$ relations the dependence of the hole concentration on doping for both 123-O_x and Ca(10%)-123-O_x was calculated. The dependence shown in fig. 50 should be a rather smooth function with a change of slope at $x\approx 6.4$ and a saturation at $x<6.3$ for Ca-123-O_x. *In spite of the opinion of the authors, the curve for $x=0$ (0% Ca) is not smooth* and shows clearly that a discontinuity appears. The authors argue that even if they use for the calculation of $p=V_-$ the data of Cava et al. (1990), which as we have seen (sect. 3.2.2) show the abrupt step of Cu-BVS near the T → O transition, the curve remains smooth without an abrupt change near $x=6.5$. Tallon et al. (1995) and Tallon (1990) conclude that this is an indication that, independently of the existence of an oxygen superstructure or of substitutional Ca doping, the process of excitation for the underdoped and overdoped regime remains the same.

The above results of Tallon et al. concerning the Ca-doping are *questionable* both from the point of view of the quality of the samples and the physics of Ca dopings. According to Röhler et al. (1999b), at least for fully oxygenated Ca-123-$O_{6.95}$, it is not the Ca introducing additional carriers, but the dilution of the Y-123-O_x which leads to the decrease of T_c (sect. 8.4)! Further, as Merz et al. (1998) have shown, $Y_{1-x}Ca_xBa_2Cu_3O_6$

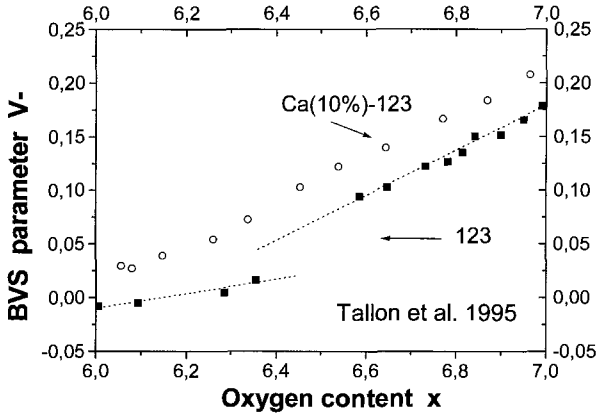

Fig. 50. Bond valence sum parameter V_- vs oxygen deficiency δ for $Y_{1-x}Ca_xBa_2Cu_3O_{7-\delta}$ with Ca contents $x=0$ and $x=0.1$. After Tallon et al. (1995). The $x=0$ curve does show a discontinuity (see text).

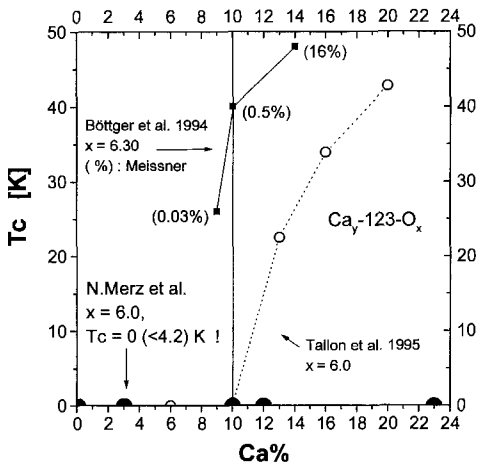

Fig. 51. T_c vs. Ca doping for $Y_{1-y}Ca_yBa_2Cu_3O_6$ from data of Tallon et al. (1995) and Merz et al. (1998) together with some unpublished $O_{6.3}$ data of Böttger and Kaldis (1994). All Ca compositions of Merz et al. *are not superconducting.* The $O_{6.3}$ samples of Böttger and Kaldis show low Meissner effect, indicating that some of them *are not really superconducting.*

is not superconducting for most relevant Ca concentrations (0, 3, 10, 12, 23%). Figure 51 shows the T_c's found as a function of the Ca concentration for $Y_{1-x}Ca_xBa_2Cu_3O_6$ by Tallon et al. (1995) and Merz et al. (1998), together with unpublished results of Böttger and Kaldis (1994) for three $O_{6.3}$ samples with exactly determined oxygen content (sect. 3.1.3). We see that even at $x=6.30$ some samples show marginal superconductivity with *very small* Meissner effect.

Several problems arise from the preparation of such samples. Thus, Tallon found difficulties because Ca substituted both the Y- and the Ba-site in his polycrystalline samples. Oxygen-rich, equilibrium, polycrystalline samples do not have this problem, as NPD (Böttger et al. 1996) and Ca-EXAFS (Röhler et al. 1999a) have clearly shown. In single crystals, however, this problem does appear (Böttger et al. 1997, Schlachter et al. 1999). Tallon et al. (1995) used high temperatures for the synthesis (up to 1000°C) in pure oxygen and cooled slowly. The Ca content was known to the authors only from,

unfortunately unpublished, neutron diffraction data. The oxygen content was known for most samples from the weight changes (probably $\Delta x \approx \pm 0.2$–0.4?), and only in a few cases from iodometric titration. Probably, the samples of Tallon et al. did have oxygen contents >6.0 and/or very small Meissner effect.

But also from the BVS point of view several arguments have appeared recently against the concept of Tallon (eqs. 6, 7). The assuption was made by Tallon that the BVS directly gives the actual charge on the ion (Chmaissem et al. 2001). This approach differs from that of Brown (1989, 1991) who did not use both the BVS of Cu2 and that of O_p, but only that of Cu2, after making corrections for internal strains. Brown used the fraction of Cu^{3+} in the Cu2 plane and considered them to give the hole concentration in the planes. Chmaissem et al. (2001) compared these two different calculations for 123-O_x and $(Ca_xLa_{1-x})(Ba_{1.75-x}La_{0.25+x})Cu_3O_y$. Following Brown (1989, 1991) they use the fraction ξ of Cu^{3+} in the Cu2 plane, the fraction of the Cu^{2+} ions being $(1-\xi)$. The average charge (oxidation state)/Cu ion is:

$$V_{avg} = 3\xi + 2(1-\xi) = 2 + \xi. \tag{9a}$$

This average charge should be equal to the sum of the bond valences of Cu^{2+}, $V^{(2+)} = BVS^{+2}_{Cu}$, and of Cu^{3+}, $V^{(3+)} = BVS^{+3}_{Cu}$,

$$V_{avg} = \xi V^{(3+)} + (1-\xi)\, V^{(2+)}. \tag{9b}$$

From eqs. (9a) and (9b) we arrive at

$$\xi = \frac{V^{(2+)} - 2}{V^{(2+)} + 1 - V^{(3+)}}. \tag{10}$$

Similarly a $\xi^{(1)}$ fraction can be defined for the Cu^{+1} in the chains

$$\xi^{(1)} = \frac{V^{(2+)} - 2}{V^{(2+)} + 1 - V^{(1+)}}. \tag{11}$$

Chmaissem et al. (2001) found that the calculations of the BVS in the past (Tallon 1990, Cava et al. 1990, Böttger et al. 1996, Karppinen and Yamauchi 1999) have not considered the presence of Cu^{+1} ($\xi = \xi^{(1)} = 0$). Eckstein and Kuper (1999) have recently used eqs. (10–11) to calculate from the data of Cava et al. (1990) the V_- for optimally doped 123. Tallon (1990) and Tallon and Cooper (1993) have calculated with $\xi = 0$, $p \approx V_- \approx 0.16$ and Karppinen and Yamauchi (1999) calculated $V_- = 0.99$. Eckstein and Kuper (1999) found for optimally doped 123 $V_- \approx 0.105$, showing that *there is no universal value.* According to them the discrepancies arise from the inconsistent use of $\xi = 0$. Chmaissem et al. (2001) calculated from the data of Cava et al. (1990) for oxygen-rich 123 the hole concentration C of the Cu2 plane using the method of Tallon with $\xi = 0$, the method of Tallon with $\xi \neq 0$ and the method of Brown. The results are

Table 9a
Calculation of the p and C values by Chmaissem et al. (2001), using the BVS method of Brown (1989, 1991), Tallon (1990) and Tallon and Cooper (1993), based on the experimental data of Cava et al. (1990)[a]

	Oxygen concentration x			
	6.95	6.84	6.81	6.78
T_c	90	88	86	80
p^{Brown}	0.264	0.238	0.222	0.207
$p^{\xi=0}$ Tallon	0.105	0.089	0.075	0.068
$p^{\xi\neq0}$ Tallon	0.165	0.150	0.135	0.125
C^{Brown} (%)	53.9	58.8	69.8	71.3
$C^{\xi=0}$ Tallon (%)	23.0	23.3	26.1	24.3
$C^{\xi\neq0}$ Tallon (%)	36.7	44.1	43.4	44.6

[a] After Chmaissem et al. (2001). For a discussion see the text.

shown in table 9a, and should be compared with the experimental findings of Zhu and Tafto (1997) who have used a novel electron diffraction method and found close to optimal doping $C = 76 \pm 8\%$. The results of the method used by Brown are the highest and nearest to the experimental results. The differences of the method used by Tallon when using $\xi = 0$ and $\xi \neq 0$ are also clear.

In view of all the results discussed above *the validity of a universal parabolic dependence of T_c vs hole concentration including 123 (fig. 48) is questionable.*

5.4. *Pressure dependence of T_c as a function of nonstoichiometry: giant dT_c/dP effects at $x \approx 6.75$ and $x \approx 6.4$*

Pressure increases the charge transfer between planes and chains because it reduces their distance and, therefore, changes the hole concentrations. This effect is analogous to the change by variation of nonstoichiometry. Thus, variation of pressure gives an additional degree of freedom to study lattice effects driven by changes of nonstoichiometry.

One of the first groups who recognized and exploited the pressure effects in HT_cS was that of C.W. Chu (Wu et al. 1987). From the strong T_c increase with pressure they had measured for the La compound of Bednorz and Müller (1986) they got the inspiration for the discovery of $YBa_2Cu_3O_{7-x}$ which strongly enhanced the HT_c research.

In principle, one would expect in the complicated perovskite structure of 123-O_x pressure induced phase transitions, due to the large number of structural degrees of freedom or at least atomic rearrangements under pressure, shedding some light in the problem of superstructures. Indeed, pressure investigations do illuminate – among other properties – the peculiarities of the structure of HT_cS and to some degree its influence on T_c. This is understood if we consider how the 123-O_x structure reacts to pressure.

As discussed earlier (sect. 2) the coordination polyhedra of the metallic atoms in the 123-O_x structure are the CuO_5 pyramids of Cu2, the YO_8 polyhedra between two

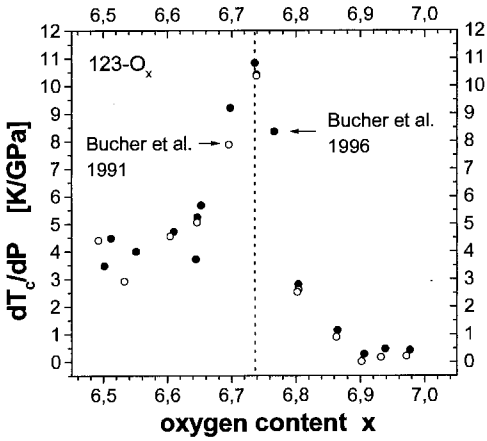

Fig. 52. Giant pressure effect in the pressure dependence of T_c as a function of oxygen nonstoichiometry x in $YBa_2Cu_3O_x$. After data of Bucher et al. (1990–1992, 1996).

neighboring superconducting planes, the BaO_{10} polyhedra and the CuO_4 squares of Cu1. $\frac{1}{4}$ of the unit cell volume lies between the two neighboring superconducting planes, but only half of this volume is filled with the YO_8 coordination polyhedra. Thus, the compressibility along the c-axis should be appreciably higher than along the a- and b-axis. This is exactly what the experiment finds. At a pressure of e.g., 10 GPa: $\Delta V/V = 6\%$, $\Delta c/c = 3.0\%$, $\Delta a/a = 1.4\%$, and $\Delta b/b = 1.7\%$ (Schilling and Klotz 1992). The question arises what pressure effects on the superconducting properties are expected when the oxygen nonstoichiometry changes. With the removal of oxygen from the chains the apical bond increases so that the coupling between chains and planes decreases. This leads to an increase of the c-axis and increased compressibility in the c-direction, as well as a decrease of T_c. Application of pressure, therefore, leads to a decrease of the apical bond and increase of T_c. This has been shown to apply, e.g., for the double chain compound $YBa_2Cu_4O_8$ (Kaldis et al. 1989, Nelmes et al. 1990).

Most interesting is that the pressure dependence of T_c, dT_c/dP, does not change linearly with nonstoichiometry but shows *two giant anomalies* in the underdoped regime at $x \approx 6.7$ and $x \approx 6.4$. The first effect can be seen in fig. 52 *increasing* dT_c/dP *by a factor of 22 (!)* from 0.5 K/GPa at $x \geqslant 6.9$ to 11 K/GPa at $x = 6.75$. The maximum lies between two different oxygen content regions, one with a small pressure effect, 0.5 K/GPa, corresponding to the oxygen-rich, high-T_c samples (90 K) at $x \geqslant 6.9$ and one with 4.5–5.0 K/GPa corresponding to the lower T_c plateau (60 K) with less oxygen ($6.50 < x < 6.66$).

This giant pressure effect appears in the narrow range where the T_c vs. x curve has the highest slope and the onset of the diamagnetic transition vs. x (fig. 2, $x = 6.75$) shows a large step at this composition, where a phase boundary appears (cf. sect. 5.1.1). Figure 53 shows the earlier measurements by Murata et al. (1989) and Medvedeva et al. (1990) (up to 8 K/GPa). Although the high-pressure effects have been measured by these authors, their oxygen contents were not exactly determined and the homogeneity of their samples has been questioned, so that confusion existed about the exact dependence on

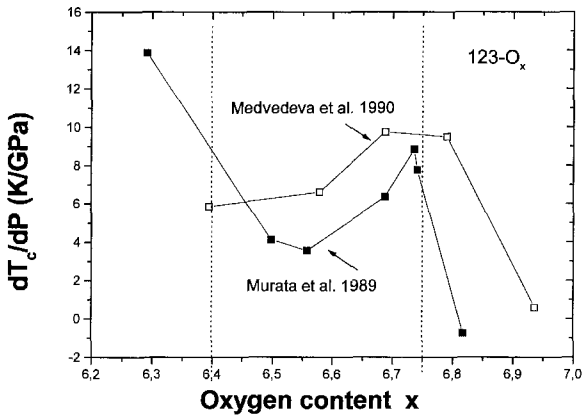

Fig. 53. First measurements of the dT_c/dP effect shown in fig. 51: solid triangles, Murata et al. (1989); open triangles, Medvedeva et al. (1990). The stoichiometries of Medvedeva et al. were in error.

nonstoichiometry. Medvedeva et al. (1990) found a wide quasi-parabolic $dT_c/dP(x)$ curve and not the sharp maximum found by Bucher et al. (1991).

Using high-resolution volumetric oxygen analysis (sect. 3.1.3) and high-quality BAO samples (sect. 3.1.2), Bucher et al. (1990) and Rusiecki et al. (1990) found at first a large increase of dT_c/dP with x (from 0.2 to 4.2 K/GPa). Upon investigation of more samples they soon after (Bucher et al. 1991, 1992) found the maximum dT_c/dP change at $x = 6.75$ (fig. 52) and proposed that *an electronic or structural transition is probably the reason for this giant pressure effect.*

A neutron diffraction study under pressure was performed by Jorgensen et al. (1990c), but unfortunately only for $x = 6.60$ and $x = 6.93$, so that the composition range of the giant pressure effect was not probed. Only small changes of the lattice parameters were observed for the compositions investigated. However, it is possible that even if the correct compositions are investigated a structural effect – appearance of superstructures or a phase transition – cannot be observed at the macroscopic length scale of neutron diffraction ($\geqslant$500 Å). In fact, micro-Raman measurements with their small length scale (sect. 5.5) do show a strong change in the behavior of the apex phonon at $x = 6.75$.

Almasan et al. (1992) confirmed and expanded the experimental results of Rusiecki et al. (1990) and Bucher et al. (1990) using single crystals and also investigating lower oxygen contents. They found, however, as did Murata et al. (1989), that at lower oxygen content ($x < 6.4$) a further increase of dT_c/dP takes place up to 7 K/GPa and considered a step-like curve with two plateaus (fig. 54). Using the pressure-induced charge transfer model (PICTM) they proposed an inverted parabolic dependence of T_c on Δn_h. A problem of this phenomenological model is that it considers only the linear charge transfer along the c-axis, while the results of thermal expansivity (Kraut et al. 1993) and also theoretical considerations (Pickett 1997) show that the in-plane axis behavior is important for the $x = 6.75$ anomaly (sect. 5.4.1).

Bucher et al. (1991, 1992) measured more compositions and were able to show that there is no plateau in the region $6.4 \leqslant x \leqslant 6.8$, but a very narrow giant maximum (fig. 52). Weber et al. (1992) and Benischke et al. (1992) reproduced these results. Their lower

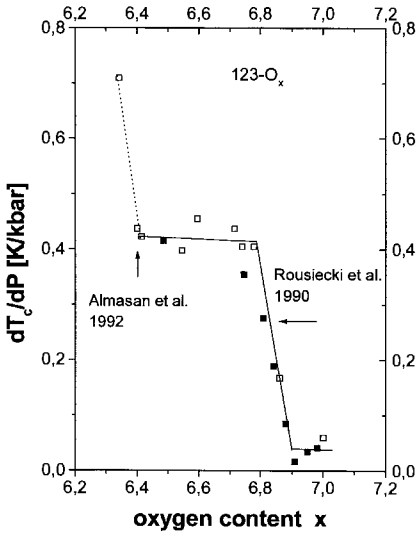

Fig. 54. Pressure dependence of (resistive) dT_c/dP as a function of nonstoichiometry (left-hand axis). After Almasan et al. (1992). Solid squares, Rusiecki et al. (1990).

value of the dT_c/dP maximum (7 compared to the 10.5 k/GPa of Bucher et al. 1991) could be due to the different temperatures at which pressure had been applied. They applied pressure to the sample *after it had been cooled* to low temperatures in order to avoid oxygen-ordering effects. An interesting result of Benischke et al. (1992) was the differentiation between the "true" pressure effect of their polycrystalline material and the pressure effect due to the weak links. For the large change of dT_c/dP with pressure as a function of nonstoichiometry (fig. 52) no explanation could be given. However, the fact that their measurements were made at low temperatures indicate that oxygen-ordering effects of the type found by Veal et al. (1990b) are not responsible for the maximum at $x \approx 6.75$.

To investigate the role of oxygen-ordering effects for the composition $x \approx 6.75$ the same group (Metzger et al. 1993) performed measurements both on polycrystalline samples and on single crystals prepared with a similar thermal history. Utilizing measurements at low and high temperatures they separated the two main contributions to dT_c/dP: the intrinsic pressure effect (7.4 K/GPa) which excludes oxygen ordering via diffusion and is measured at low temperatures, and the oxygen-ordering effect (4.1 K/GPa) by diffusion which can be measured at $T > 240$ K. Their sum 11.5 K/GPa was higher than the results of Bucher et al. (1991) (10.5 K/GPa) and Medvedeva et al. (1990) (10 K/GPa). They concluded that higher oxygen ordering (inter- and intra-chain) is energetically favored when pressure is applied, the oxygens being pushed together. They also showed that ordering effects due to pressure and temperature appear at $T > 240$ K, which seems reasonable in view of the smaller volume of the ordered samples. The effect of application of pressure on T_c shows a *relaxation* to an "equilibrium" value with a characteristic time constant. In view of the complexity of the pressure effect on T_c, it may be questioned whether the system reaches a true equilibrium state and not a *stationary state.* In any case, the process

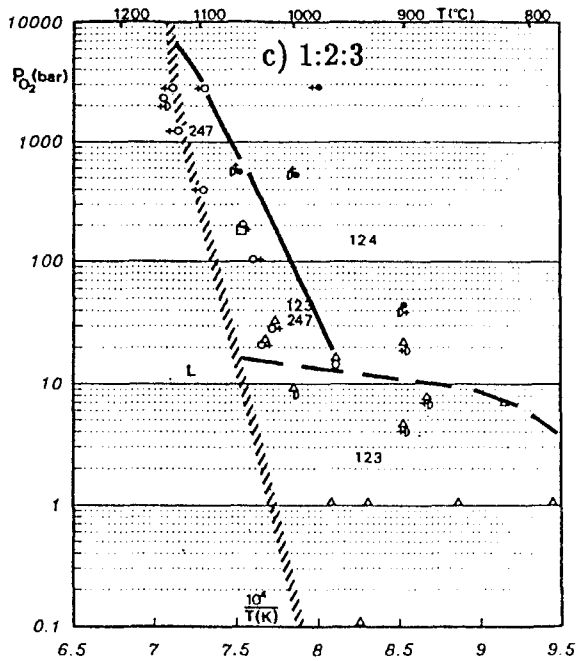

Fig. 55. *P–T* cross section of the pseudo-binary *P–T–x* phase diagram of 123-O_x. The stability field of the 123 phase is smaller than shown. Slow decomposition kinetics do not allow the exact determination of the phase boundary with the 124 phase. After Karpinski et al. (1991).

appears reversible and the original T_c value is reached again after sufficient annealing time at room temperature (Metzger et al. 1993).

In a continuation of this work Fietz et al. (1996) expanded their investigation systematically to both the underdoped, $x > 6.4$, and the overdoped regime using polycrystalline and single-crystalline samples. It is rather doubtful whether the claimed $x = 7$ has really been reached, in view of the lack of a high-resolution *direct* oxygen determination. Reduction of the samples was performed by annealing at various temperatures and partial pressures of oxygen, and the oxygen content was always estimated thermodynamically. To bypass the difficulties caused by the extremely slow oxidation of oxygen-rich single crystals they annealed under 200 bar oxygen pressure. The same was done for the oxygen-rich polycrystalline samples. As this method is now generally applied in order to increase the low oxygen content of single crystals, it is worth noting that, as shown by Karpinski et al. (1991) in the quasi-binary *P–T–x* phase diagram of $YBa_2Cu_3O_x$ (fig. 55), this pressure lies outside the stability region of 123-O_x up to temperatures of 1050°C. Thus, depending on the temperature and duration of the annealing as well as the rate of the diffusion kinetics, it is possible that this treatment introduces into 123 various defects, e.g., double chain fragments, which are the structural units of the 124 and 247 phases (Kaldis et al. 1991). To our knowledge, no systematic characterization by EM and high-resolution synchrotron radiation methods (e.g., Qadri et al. 1997) of such pressure-loaded crystals has been done up to now.

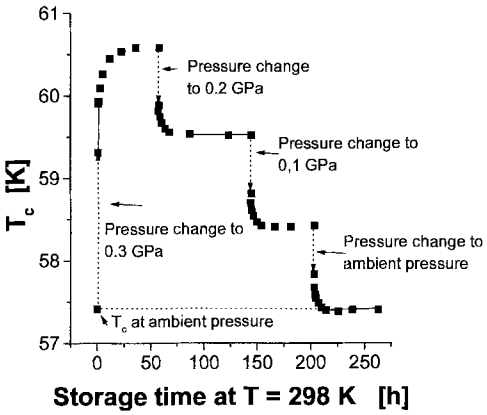

Fig. 56a. T_c thermal relaxation at 298 K of a single-crystal 123-$O_{6.58}$. For every pressure, T_c is measured at least 8 times after different storage periods at 298 K. After Fietz et al. (1996).

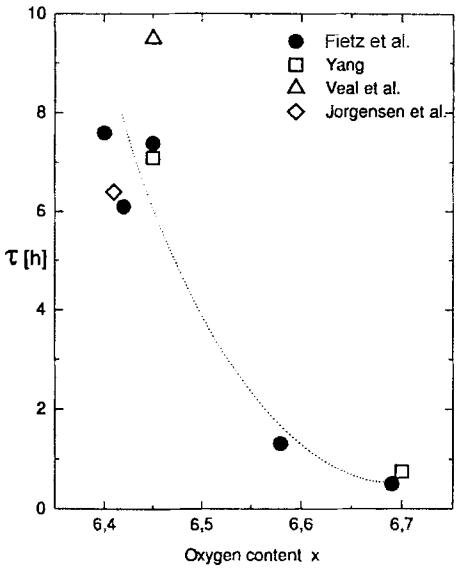

Fig. 56b. Dependence of the time constant on the oxygen stoichiometry. The curve follows eq. (2) of Jorgensen et al. (1990b) and Veal et al. (1990b). Open squares: Yang (1992). After Fietz et al. (1996).

Thermal relaxation of the samples under pressure at *room temperature* (Fietz et al. 1996) for sufficient time gives the total pressure effect consisting of the intrinsic and the oxygen-ordering pressure effect

$$\frac{dT_c}{dP} = \left(\frac{dT_c}{dP}\right)_i + \left(\frac{dT_c}{dP}\right)_O .$$

The thermal relaxation to the equilibrium value under a given pressure, $T_{c,Pi}$ is shown for a single crystal with $x \approx 6.58$ in fig. 56a. After each pressure change at least 8 annealings at room temperature were performed and the T_c was measured. The sample remained under pressure through all the thermal cycling. Figure 56b shows the time constant τ of the T_c relaxation under pressure at $T = 298$ K as a function of oxygen stoichiometry and the agreement with the relaxation law (2) of the thermally quenched samples by Jorgensen et al. (1990b) and Veal et al. (1990b) discussed in sect. 3.2.1.5. The trend is clear: τ decreases strongly with increasing oxygen content. Figure 57 shows the changes of the pressure-induced T_c changes (dT_c/dP) with oxygen stoichiometry for annealings at 298 and 100 K (Fietz et al. 1996) in order that intrinsic pressure effect and relaxation effects due to oxygen ordering can be differentiated. Two important results can be seen:

(a) The anomaly at $x \approx 6.7$ appears at both temperatures (appreciably reduced at 100 K) indicating that it has also a non-diffusional component. From the 11 K/GPa at $T = 298$ K, 6 K/GPa remain at $T = 100$ K.

(b) A giant pressure effect appears at $x < 6.5$ (30 K/GPa) which is probably due to diffusional oxygen ordering and, therefore, does not appear at lower temperatures.

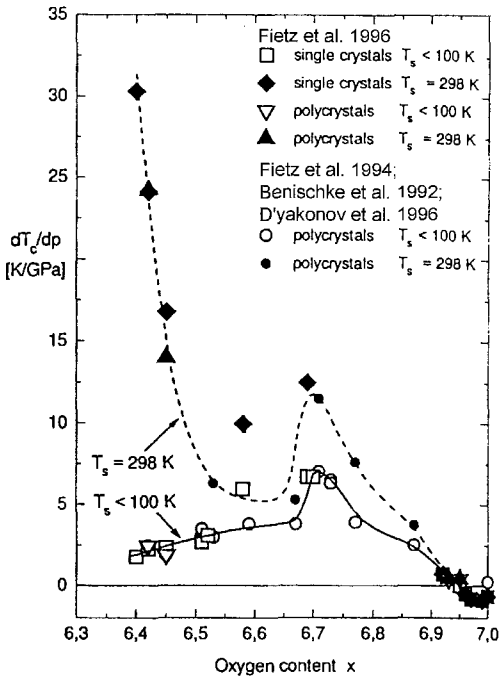

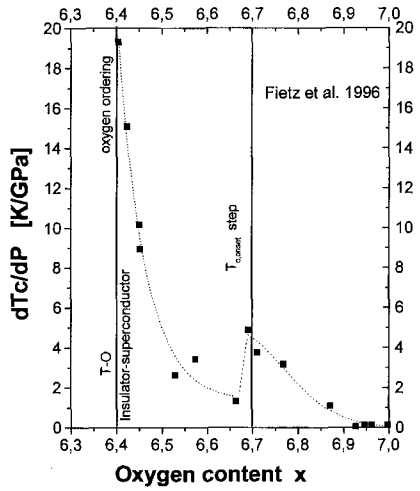

Fig. 58. Pressure dependence of T_c due to oxygen-ordering effects as a function of nonstoichiometry of 123-O_x. After data of Fietz et al. (1996).

Fig. 57. T_c dependence on pressure as a function of nonstoichiometry. Solid symbols, total pressure effect (intrinsic and oxygen ordering) after annealing at room temperature. Open symbols, intrinsic pressure effect after annealing at 100 K. Data from Fietz et al. (1994, 1996), Benischke et al. (1992) and D'yakonov et al. (1996). After Fietz et al. (1996).

This justifies the first results of Murata et al. (1989) which have shown this effect (fig. 53) as well as the results of Almasan et al. (1992) at $x < 6.4$ (fig. 54).

The above measurements of dT_c/dP were performed at the various T_c temperatures and then brought to RT so that an additional pressure effect must be considered due to the fixed volume of the He used as pressure medium. Figure 58 shows the effective pressure effect due to oxygen ordering. For $x > 6.93$ (overdoped phase) no oxygen ordering takes place. With almost 5 K/GPa, oxygen ordering seems to be involved both in the $x = 6.75$ effect and in the vicinity of the T → O phase transition, where, with the high number of vacancies in the chains, the effect becomes very large. The particular properties of the $x = 6.75$ composition will be discussed in sect. 5.4.2.

The giant pressure effect reported by Fietz et al. (1996) at $x \approx 6.4$ is 30 K/GPa, a factor of 2 larger than that found by Murata et al. (1989) at the same composition, and by far the largest pressure effect on T_c ever found. It illustrates dramatically the importance of oxygen ordering under pressure for T_c. It is peculiar that this effect is scarcely known. It is reversible, disappearing via a relaxation process (like that of fig. 56a) when the pressure

is reduced to ambient. Ordering by diffusion in the T–O phase transition (cf. sect. 3.3.1) indicates rather a second-order transition than a martensitic transformation.

5.4.1. *Uniaxial pressure investigations dT_c/dP_i as a function of nonstoichiometry*

Further proof for the complexity of structural effects in 123-O_x, as well as an alternative explanation for the giant effect at $x=6.75$, came from uniaxial pressure investigations of dT_c/dP via thermal expansion experiments (Meingast et al. 1991, Kraut et al. 1993) or direct uniaxial pressure in magnetization experiments (Welp et al. 1992). Particularly Kraut et al. performed their investigations at four different oxygen contents.

For a second order phase transition like that of the normal → superconducting state the pressure dependence of the transition temperature is related to the anomalies of the thermal expansion and the specific heat via the Ehrenfest relation:

$$\frac{dT_c}{dP_i} = \frac{\Delta\alpha_i V_m}{\Delta C_p/T_c},$$

with $\Delta\alpha_i = \alpha_s - \alpha_n$ the difference of the thermal expansivities in the normal and the superconducting states at T_c, $\Delta C_p/T_c$ the difference of the normal- and superconducting-state specific heats at T_c, and V_m the molar volume. Thus, by measuring $\Delta\alpha_i$ for the three crystallographic axes $i=a, b, c$ and knowing the specific heat and molar volume, the uniaxial pressure dependencies of T_c can be calculated. One can reconstruct also the hydrostatic pressure effect by adding the three components dT_c/dP_i along the three crystallographic axes. Meingast et al. (1991), and Kraut et al. (1993) measured the thermal expansivities of single crystals in the three crystallographic directions, using ultrahigh-resolution capacitance dilatometry. Welp et al. (1992) measured directly the effect of the uniaxial stresses on a.c. susceptibility and confirmed the results of Meingast et al. (1991) (calculated from the thermal expansions) for one oxygen-rich single crystal.

The main results of these investigations are:

(a) The uniaxial pressure along the *c*-axis follows the pressure-induced charge transfer model (PICTM) – pressure increases the carrier concentration in a similar manner as oxygen. dT_c/dP_c is, therefore, strongly dependent on oxygen content and decreases with increasing concentration of holes, n_h. Near the optimal doping it reaches a value of zero, then in the overdoped region negative values, because further increase of carriers decreases T_c. This agreement with the charge-transfer model between chains and planes due to doping is expected, because as mentioned earlier, the largest changes in bond length appear, both for oxygen doping and under pressure, for bonds parallel to the *c*-axis.

(b) PICTM cannot explain why this is not the case for the calculated dT_c/dP_a and dT_c/dP_b. They show *opposite sign* and have *large values at high oxygen content* (fig. 60b). By canceling each other they induce the low values of the hydrostatic pressure effect in the overdoped regime (cf. sect. 5.4 and fig. 52). This anisotropy of the *a*–*b* plane is clearly apparent from the data of fig. 59 for single crystals. The pressure effect is nearly independent of oxygen doping for the *b*-axis, in contrast to the *c*-axis, with the

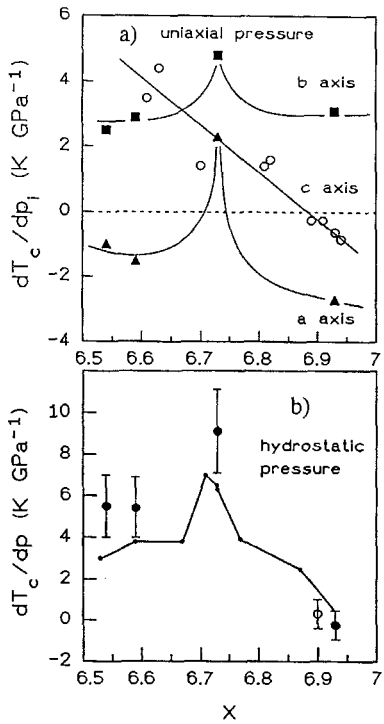

Fig. 59. (a) Uniaxial pressure changes of T_c as a function of stoichiometry in 123-O_x, calculated from thermal expansivities of single crystals. We note the strong linear x dependence of dT_c/dP_c along the c-axis, and the nearly x-independent dT_c/dP_b. dT_c/dP_a and dT_c/dP_b show strong anomalies at $x \approx 6.75$. (b) Comparison of the directly measured hydrostatic pressure (solid circles, Kraut et al. 1993; open circles, Benischke et al. 1992) and the sum of the calculated uniaxial pressures (solid line, Meingast et al. 1991). After Kraut et al. (1993).

exception of $x = 6.75$. This striking new feature sheds new light on the discussion of the above section (sect. 5.4) and indicates that the PICTM is not sufficient to explain these effects, because not only the effects parallel to c-axis are important for T_c, but also *additional pressure effects.* In particular, it shows that dT_c/dP_a and dT_c/dP_b are strongly coupled to the orthorhombic distortion at low temperatures and *constant* oxygen content.

(c) Even more interesting is the finding that *both* dT_c/dP_a and dT_c/dP_b show large positive values at the anomaly of $x \approx 6.75$. We recall that the actually measured data are $\Delta\alpha_i$, i.e. thermal expansivities at the superconductive transition temperature T_c. *The expansivity anomalies at T_c, along the a-axis, change their sign for samples with $x \approx 6.73$* as shown in fig. 60. Thus, at this composition the a-axis expands at T_c, like the b-axis, whereas in all other measured compositions it contracts. We recall that the a-axis is sensitive to the formation of superstructures, and as we have seen (sect. 5.1–5.2) this anomaly lies near the boundary of the $3a_0$–a_0 transition. This would be consistent with the idea that structural effects trigger the large and abrupt oxygen-dependent change of dT_c/dP_a (from −2 to +2 K/GPa at $x \approx 6.75$, in fig. 59a) (Bucher et al. 1991, 1992, 1996, Rusiecki et al. 1990). A more specific explanation by Kraut et al. (1993) is discussed in the next section.

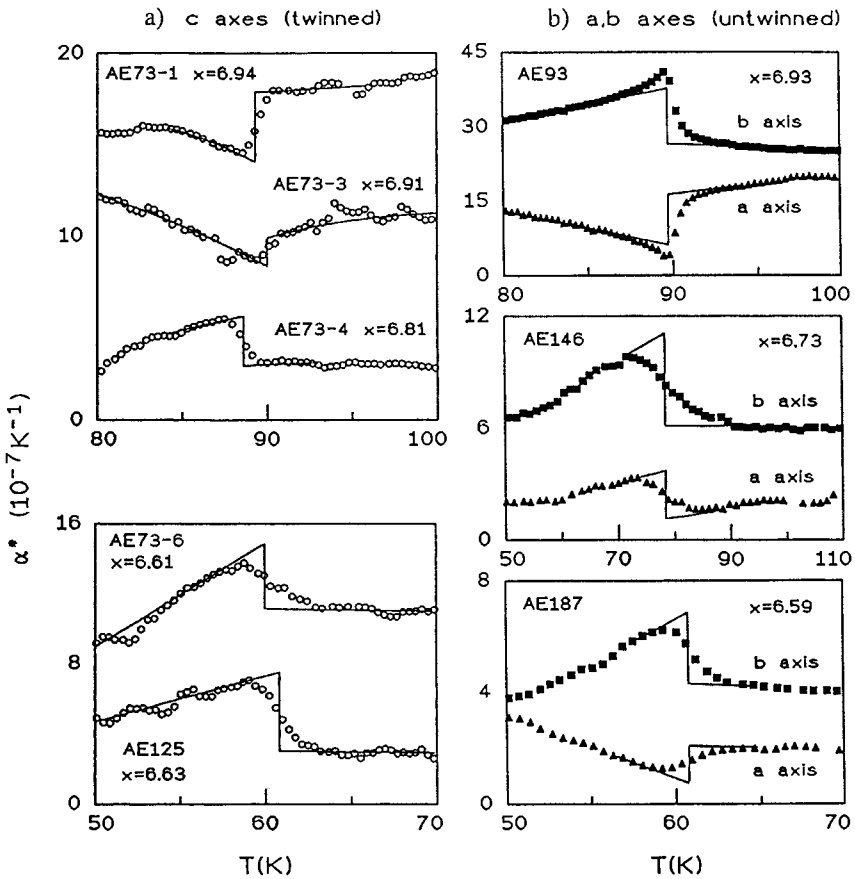

Fig. 60. Anomalies of the thermal expansivities at T_c (a) along the c-axis and (b) along the b- and a-axes of single crystals of 123-O_x, after subtracting the background. Note the sign changes of the a-axis at $x \approx 6.75$ and of the c-axis near optimal doping. The scales of the vertical axes are not the same and some data are shifted vertically for clarity. After Kraut et al. (1993).

5.4.2. *The structural, optical and magnetic anomalies at $x \approx 6.75$*

After all these investigations the question arises again what is the nature of the effect at $x = 6.75$ (Bucher et al. 1991). Fietz et al. (1996) exclude a diffusional process because oxygen motion effects have time constants which increase strongly at $T \leqslant 240$ K. This is supported by findings in the literature (sect. 3.2.1.5). Thus, Veal et al. (1990b) found for an $x \approx 6.45$ sample an increase of the time constant from 0.25 to 229 days already by decreasing the annealing temperature from 25°C to 0°C, and Lavrov (1992) with conductivity found an abrupt onset of oxygen ordering above 250 K. However, latent structural and/or electronic phase transitions or cross-overs can induce structural and electronic anomalies even at very low temperatures. This explanation was proposed by

Bucher et al. (1990–1992, 1996) and (Rusiecki et al. 1990); ideas in the same vein were presented by Metzger et al. (1993) and Fietz et al. (1996). They consider atomic displacements or tilting of structural elements with a low activation energy as the possible reason for this effect. Pressure-dependent reorganization of the charge distribution due to ordering of chain fragments was proposed by Kraut et al. (1993).

We summarize here the anomalies of the structural and physical properties accompanying the giant dT_c/dP change at $x = 6.75$:

(a) Lattice parameters. From figs. 25a,b (sect. 3.2.2.1) we see that the deviation from linearity takes place in both cases near $x = 6.75$, leading to a relative decrease of the b-parameter and a relative increase of the a-parameter. These changes culminate in the increase of tetragonality at $x = 6.95$, where the displacive phase transformation takes place (sect. 6) and the b-axis decreases. The corresponding decrease of the orthorhombicity indicates that, possibly, already at $x \approx 6.75$ the negative interactions start, leading to the decrease of T_c in the overdoped phase (see also point c). The suggestion that the results of fig. 25 could be due to an increase of the O5 occupancy (Krüger et al. 1997) does not seem to be supported by EXAFS. Also, von Zimmermann et al. (1999) did not find O5 occupation.

(b) Magnetization measurements/Superstructures. It is well known that the T_c vs. x curve shows a strong change of slope from the so-called 60 K to the 90 K plateau at $x = 6.75$. The abrupt change of the onset temperature (fig. 2) illustrates this even more clearly. As discussed in sect. 5.1.1 this is the locus of a miscibility gap or of several phase boundaries (cf. fig. 109), supporting the above-mentioned idea of a specific feature of the structural phase diagram. A hard X-ray phase diagram (fig. 44b) shows, in this oxygen content range, the $3a_0$–a_0 phase boundary. These superstructures have different a-axis lengths.

(c) Raman measurements. An important change takes place at $x \approx 6.75$ in the apex frequency, sect. 5.5.1 (fig. 61). *In the range $7.0 \geqslant x \geqslant 6.75$ the apex phonon frequency becomes independent of the oxygen content,* in contrast to the underdoped region. Liarokapis (1997, 2000) measured the Fano asymmetry of the in-phase B_{1g} phonon as a function of the oxygen doping. This asymmetry results from a coherent interference of light scattered by the continuous free carrier spectra and the discrete phonon spectra. The coupling to the carriers (fig. 35c) peaks at $x \approx 6.7$. Both results support the above-mentioned beginning of overdoping at this composition. Liarokapis et al. (2000) measured also the anharmonicity of the oxygen phonons in the whole range $6.03 < x < 7.0$, and found that particularly for apex the maximum appears at $x \approx 6.7$. This will, possibly, activate the discussion about polaron formation.

(d) Pressure-dependent charge redistribution. Pressure-induced ordering in the basal plane cannot be concluded from the results of Kraut et al. (1993) since they have not been obtained by application of pressure. They adopt an alternative explanation for the anomalies of their thermal expansivity measurements and their calculated uniaxial pressure changes of dT_c/dP along the three crystallographic axes. Short chain segments have energy levels above the Fermi level and, therefore, they cannot contribute to the charge transfer (Burdett 1992). For chains with a critical size

($x \approx 6.73$), the energy bands may shift strongly with pressure, leading to a large pressure-induced charge redistribution, which takes place mainly along the *a*- and *b*-axes, being thus *different* to the commonly known charge transfer along the *c*-direction. The above-mentioned presence of the superstructure phase boundaries may enhance this redistribution.

The pressure-dependent charge redistribution is also supported from theoretical calculations of the effect of uniaxial pressure on the band structure of stoichiometric $YBa_2Cu_3O_7$ (Pickett 1997). The results do not show any charge transfer from the chains to the planes under pressure, which is in agreement with the very small pressure effect on T_c for this stoichiometry. There is, however, a charge redistribution inside the superconducting planes due to relative changes in the potentials of the Cu2, O2 and O3 ions. It is generally accepted that at low doping levels the holes go to the Cu2 ions and their four O NN (Zhang–Rice singlets). With increasing doping there is a shift of positive charge towards the oxygens, increasing T_c. This trend is consistent with the increasing charge on O2, O3 with uniaxial pressure along the *b*-axis.

In conclusion, the $x \approx 6.75$ composition is an important point of the phase diagram where structural, magnetic and optical properties show appreciable changes.

5.5. *Raman scattering as a function of nonstoichiometry – I*

5.5.1. *The apex Raman phonon and phase separation*

Very interesting in this context are the results of micro-Raman scattering on individual single crystallites of equilibrium samples (Liarokapis 1997, Kaldis et al. 1997b) as a function of nonstoichiometry. Some aspects have already been discussed briefly in sect. 3.3.1. A major advantage of Raman scattering is its great sensitivity to the appearance of new phases as *it takes only a few atoms to form a new phonon.* The reason is that the frequency of the Raman mode of the vibrations of mainly one type of atoms is much stronger influenced by interactions of these atoms with their nearest neighbors than with their next-nearest neighbors (e.g., Iliev et al. 1993). Thus, an effect appearing in approximately 20 atoms (micro domains < 40 Å) can still be detected. This should be compared with the 500–1000 Å length scale of the X-ray diffraction methods. Of course this ideal resolution of the Raman scattering may be decreased from case to case due to experimental limitations like, e.g., the laser beam cross-section.

Several results of Raman investigations on equilibrium samples have been reported recently (Poulakis et al. 1996, Liarokapis 1997, 1999, Liarokapis et al. 2000, Palles et al. 2000a). The measurements were performed on individual microcrystallites (platelets) using a T64000 triple Jobin–Yvon spectrometer with a microscope, in the scattering configurations $yy(zz)\acute{y}$ and $y(xx)\acute{y}$. In these directions the *z*-axis coincides with the crystallographic *c*-axis perpendicular to the platelets. Looking at individual platelets with polarized light it is possible to select properly oriented crystallites for micro-Raman measurements. For 29 compositions in the range $6.020 \leqslant x \leqslant 6.984$ several (up to 10) crystallites have been studied from each composition.

An advantage of the micro-Raman method is that probing very small crystallites (>5 μm) or several parts of larger crystallites can give a good statistic of the various phases appearing in a certain composition range. Owing to the very cautious cooling of the samples used to reach equilibrium and their very good reproducibility, variations of the Raman signal could be attributed largely to phase changes. An appreciable statistic, the investigation of a large composition range, and the high-resolution determination of the oxygen content allowed to differentiate changes of the signal due to reproducibility and *due to phase changes*. Thus, it is more instructive not to take the average signal of all crystallites having the same composition, but to plot the value of each individual measured. This shows possibly existing centers of weight inside the normal scattering of the data, indicating the existence of other phases. Thus, in addition to being very useful for the characterization of the phase purity of the samples, inspection of the individual data allows scouting for possible phase separation or phase transitions occurring at certain compositions. We will illustrate this point later, especially with figs. 62 and 64. In the following figures *all* measured data are shown. This enables the reader to have a realistic impression of the degree of homogeneity that even good samples have. The samples used in these investigations were CAR equilibrium samples (sect. 3.1.2) which show extremely small scattering in their lattice parameters (sect. 3.2.2.3).

An important message emanating from these investigations is that the Raman phonons of equilibrium samples show appreciable deviations from the linear dependence on oxygen doping found in the past (for reviews, see Thomsen 1991 and Thomsen and Cardona 1994). Figure 61 shows the Raman frequency shifts of the apex phonon as a function of the nonstoichiometry (Poulakis et al. 1996, Liarokapis 1997, Liarokapis et al. 2000, Palles et al. 2000a). Contrary to earlier investigations (MacFarlane et al. 1988, Thomsen and Cardona 1994) which found a linear dependence using a rather small number of compositions, a nearly linear increase with oxygen in the insulating range exists only up to the RT Néel transition ($6.0 < x < 6.2$, cf. sect. 3.3.1) and then in the superconducting range only for $6.4 < x < 6.75$. The hardening of the apex phonon is due to the decrease of the apical bond with oxygen doping (cf. figs. 14, 66). Above the phase boundaries at $x = 6.75$ the apex frequency becomes *independent* of the oxygen doping. In this range the charge transfer nears saturation and the frequency remains constant, although the Cu2–O1 bond length is still decreasing (fig. 14). The structural changes starting at $x > 6.75$ were discussed in sect. 5.4.2. A relative decrease of the orthorhombicity starts at this doping level which is actually leading to a saturation in the optimally doped region and to an absolute decrease in the overdoped range, mimicking T_c (fig. 25c). Also, the width of the out-of-phase-phonon B_{1g} shows a decrease of the coupling with the superconducting carriers starting at $x = 6.7$ (fig. 35c), indicating the onset of negative interactions. Figure 61 shows that the apex phonon frequency clearly reflects the transformations and changes at $x \approx 6.22$, 6.28, 6.40 and 6.75. The first three are correlated with the onset of superconductivity, as discussed in sect. 3.3.1.

Figure 62 shows the width of the apex phonon vs oxygen doping after Poulakis et al. (1996), and Liarokapis et al. (2000). The lines are a guide to the eye and are joining the extreme values. The statistical average for each composition is shown in fig. 35b.

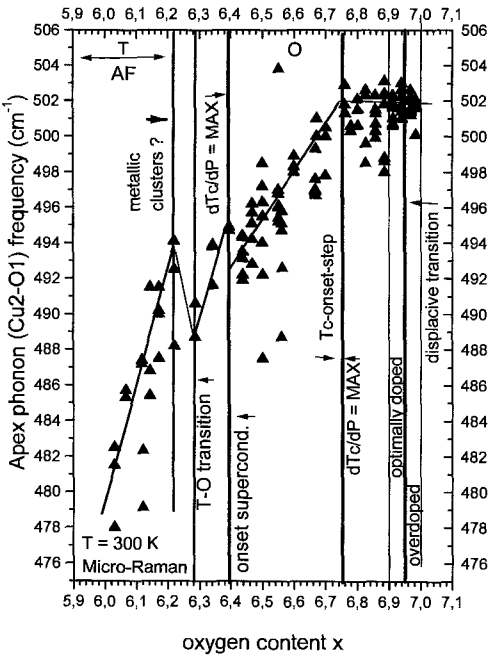

Fig. 61. Dependence of the apex phonon (Cu2–O1, A_g) frequency on oxygen stoichiometry. Five regions appear to exist (cf. fig. 35a); the slope changes take place at the characteristic oxygen contents $x = 6.22$, 6.30, and 6.75. After data of Poulakis et al. (1996), Palles et al. (2000a) and Liarokapis et al. (2000).

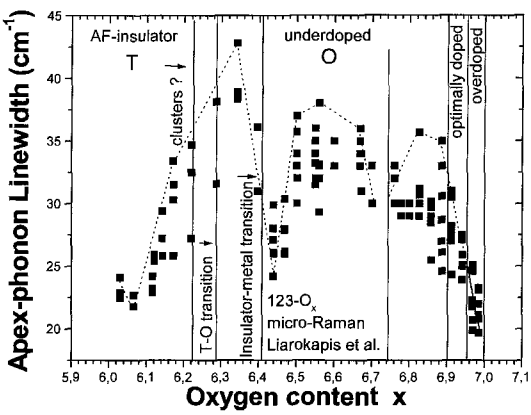

Fig. 62. Apex phonon width as a function of nonstoichiometry. Note the two maxima at $x = 6.35$ and 6.56 and the minima at $x = 6.0$–6.15, 6.43, and 6.95–6.99. After Poulakis et al. (1996), Palles et al. (2000a) and Liarokapis et al. (2000).

The anomalous width of the apex phonon led previous investigators (Iliev et al. 1993) to deconvolute, with three Lorentzians, the spectra of one underdoped single crystal ($x \approx 6.4$). They concluded that *phase separation at mesoscopic scale* was present and attributed the Lorentzians with peak intensities at 500, 488 and 474 cm^{-1} and constant width to the coexistence of the ortho-I, ortho-II and tetragonal phases. Poulakis et al. (1996), Liarokapis (1997, 2000), Palles et al. (2000a) and Liarokapis et al. (2000) investigated a very large number of crystallites of many CAR equilibrium samples in the

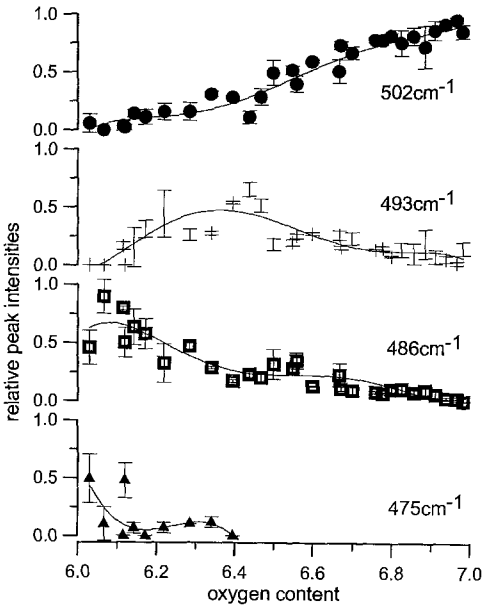

Fig. 63. Deconvolution of the apex phonon width in four Lorentzians with 502, 493.5, 486 and 475 cm^{-1} (see text). After Palles et al. (2000a) and Liarokapis et al. (2000).

whole nonstoichiometric region ($6.0 < x < 7.0$). After trying several fits they concluded that the experimental curve could be very well fitted with four Lorentzians with constant width independent of doping. The deconvolution gave for the four Lorentzians the frequencies 502, 493, 486 and 475 cm^{-1}. The relative intensities of these four apex phases are shown in fig. 63. At each oxygen content the sum of the four intensities is 100%. Figures 35a and 64 show the above frequencies (horizontal dotted–dashed lines). From these figures the composition range of these phases can be approximately derived. It can be seen that:

- The 502 cm^{-1} mode dominates the oxygen-rich superconducting regime (optimally doped, overdoped) where the other modes are practically zero. It can be, therefore, assigned to the stoichiometric phase with ortho-I structure (a_0).
- The 493 cm^{-1} mode has its maximum intensity at $x = 6.47$, which is consistent with figs. 35a and 64. It extends its maximum in a large range which is consistent with the ortho-II phase ($2a_0$ superstructure) in the phase diagram of fig. 44b, and with the lattice parameters (figs. 25a,b).
- There is no indication that the 486 cm^{-1} mode corresponds to the ortho-II phase as proposed by Iliev et al. (1993). As shown in fig. 35a this phase comes in resonance by red excitation in the range $6.3 < x < 6.4$. In some samples traces of it appear up to $x = 6.56$ (figs. 35a, 64), and it seems to show magnetic response (Liarokapis et al. 2000). Thus, it is probably not the ideal tetragonal, but rather a coexisting disordered phase with rather wide stability range. Samples treated with a 5.5 T magnetic field

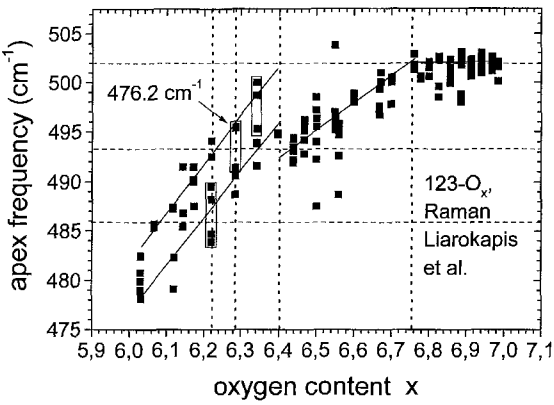

Fig. 64. Coexistence of apex phases as seen from the Raman shifts. With the exception of the framed data, which were obtained with blue laser excitation (476.2 cm^{-1}), for all other data green laser excitation (514.5 cm^{-1}) was been used. For details see the text. After data of Liarokapis et al. (2000).

show a decrease of frequency in the range $x < 6.5$ where this phase dominates. It could possibly be the phase of the hole-doped clusters (sect. 3.3.2).

– The 475 cm^{-1} could be the ideal tetragonal O_6 without oxygen in the chains. It coexists near 6.0 with the 486 cm^{-1} and disappears at the I–M transition ($x \approx 6.4$).

The apex phonon frequency vs oxygen content is a good example to illustrate the additional information that can be acquired about the material by the inspection of individual data as compared to their statistical average, provided that material with high reproducibility is used (like the CAR samples, sect. 3.2.2.3). Figure 64 shows the apex phonon-frequency data of the green (514.5 cm^{-1}) and blue (476.2 cm^{-1}) excitations (cf. fig. 35a). The latter are framed for recognition. Even if we discard the green excitation data at the same compositions with the blue excitation, the splitting of the individual data of most samples shows the coexistence of two phases, whereas fig. 35b gives no such indication at all.

In conclusion, Raman investigations show the *coexistence of several phases* in 123-O_x, with fractions changing as a function of the nonstoichiometry. As these investigations probe the local level of the atoms, this effect is not due to a macroscopic phase separation obeying the T–x phase diagram and discussed in sects. 5.1 and 5.2. It is a microscopic effect showing rather a kind of physical *phase separation* in phases only partly represented in the macroscopic phase diagram. Physical phase separation has been discussed since many years, particularly for the La cuprates (Müller and Benedek 1992, Sigmund and Müller 1994, Mihailovic et al. 1995, Kaldis et al. 1997a, Bianconi and Saini 1997, 2000).

5.5.2. *The steps in the in-phase phonon frequency*

Figure 65 shows the individual crystallite measurements of the O2, O3 in-phase vibration mode parallel to the c-axis (A_g phonon) as a function of the oxygen content. In this section we will discuss only the effects appearing in the underdoped phase $6.03 \leqslant x \leqslant 6.89$. The results of the overdoped phase will be discussed in sect. 7.4, and the T–x phase diagram in sect. 9. The in-phase phonon shows a large dependence on the oxygen content of the chains (doping due to charge transfer), its frequency decreasing strongly with

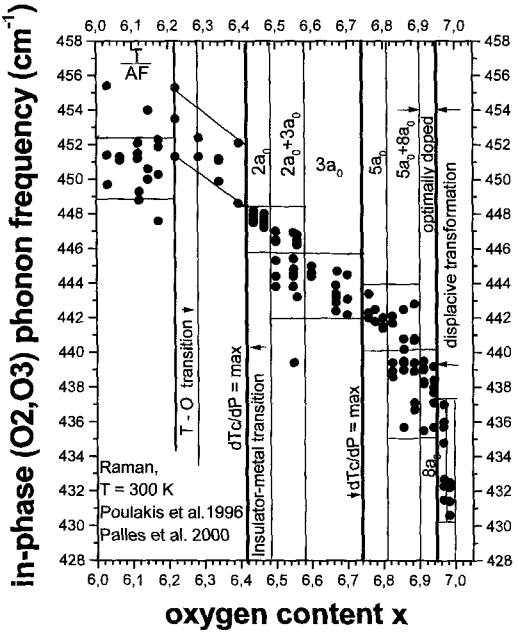

Fig. 65. O2,O3 in-phase vibration (A_g phonon) vs. oxygen doping, measured with micro-Raman on individual monocrystallites. A strong softening of the phonon appears in the overdoped range where neutron diffraction (Conder et al. 1994a) has shown a discontinuity in the Cu2–O2,O3 bond (dimpling) (cf. fig. 66a). The trends are visible, showing phase boundaries indicated by vertical and horizontal lines (see text). After data of Poulakis et al. (1996) and Palles et al. (1996, 2000a).

increasing x (Poulakis et al. 1996), as the dimpling increases. A shift of ~6% (456 → 430 cm^{-1}) takes place in the range $6.03 \leqslant x \leqslant 6.984$ with increasing oxygen doping as the *dimpling* increases (fig. 66a, sect. 6.2). A sharp softening of this phonon takes place in the overdoped region (sect. 7.4). In contrast, an increase in frequency of ~5% (478 → 503 cm^{-1}) takes place for the apex phonon in the same range ($6.0 \leqslant x \leqslant 7.0$) (fig. 61) as the apex bond decreases (fig. 66b). As mentioned above (sect. 5.5.1), for $x \geqslant 6.7$ the frequency of the apex phonon remains constant.

The antiferromagnetic transition at $x = 6.22$ is clearly seen with a discontinuity, and from this doping level the frequency starts to decrease with increasing oxygen content (fig. 65). This is consistent with the conclusion drawn in sect. 3.3.1 that doping of the planes starts at $x = 6.22$. Similar to the in-phase phonon width (fig. 35d), the frequency also shows a strong splitting of the data of each sample in the $6.2 < x < 6.4$ range, indicating the coexistence of phases.

As can be seen from fig. 65 (cf. figs. 110, 111), the Raman shifts of the O2, O3 in-phase mode (characteristic for the dimpling of the planes, sect. 6.5, figs. 76, 77) *soften stepwise* for dopings $x > 6.4$, forming, with increasing oxygen content, a descending staircase with step height 2–4 cm^{-1} (Kaldis et al. 1997b). As the masses of the atoms involved do not change, a straightforward explanation would be a stepwise increase of the distance between the oxygens of the planes O2,O3 and Cu2. The increasing trend of Cu2–O2,O3 distance with oxygen content has been shown by neutron diffraction (Conder et al. 1994a, Hewat et al. 1991) (fig. 66b) and confirmed by EXAFS measurements (Röhler et al. 1997a,b, Kaldis et al. 1997b) (figs. 76, 77). But local probe measurements (e.g., EXAFS)

at compositions sufficiently near to prove possibly existing stepwise changes of dimpling are not yet existing. It is very interesting that the compositions at which the softening steps appear in fig. 65 correspond approximately to the ideal oxygen contents of a na_0 superstructure series (Kaldis et al. 1997b), the first members of which were found in the past by ED and HREM. Interactions of the plane oxygens with the chain occupancy is a very complex subject and presently not easy to understand. Anyway, the experimental fact remains, so that an *interaction between the stepwise softening of the dimpling in the planes and the ordering of the chains* should be considered. A staircase of *"dimpling-chain superstructures"* which could become visible due to the small length scale of the Raman scattering and the high resolution of the oxygen content, would support and extend the picture of the various superstructures of the underdoped 123-O_x, which has been discussed from the early days of HT_c superconductivity (sect. 5.1.1). The staircase of fig. 65 suggests the superstructure series $n_{j-2} + n_{j-1} = n_j$ ($2a_0$, $3a_0$, $5a_0$, $8a_0$, ..., na_0), which in the picture of classical thermodynamics should be separated by *miscibility gaps* (two-phase regions, e.g., $2a_0 + 3a_0$, $5a_0 + 8a_0$) or phase transitions ($3a_0 \rightarrow 5a_0$). We note that such superstructures, if they existed, would probably have, above $3a_0$, different chain sequences than those experimentally found by von Zimmermann et al. (1999) (sect. 5.1.1). However, no direct structural evidence exists up to now for the na_0 series with $n > 3$. In principle, it is possible that only the corresponding phononic and electronic states exist, leading to the steps of the in-phase phonon at given doping levels, without measurable change of structure. It is also possible that these steps are associated with the organization of stripes.

The in-phase phonon frequency steps appearing at the compositions corresponding to the superstructures are shown in figs. 110 and 111 with an extended x scale (see sect. 9). The data are divided by horizontal and vertical lines defining the oxygen content of the in-phase steps. Thus, we see that, e.g., the data in the range 6.60–6.75 (fig. 110) have a scattering of ~3 cm^{-1} (442–445) which is practically independent of the oxygen content and the origin of the batch. There are also data in the range 6.42–6.50 with a scattering of 2 cm^{-1} (446–448) independent of x (in the range of 1 cm^{-1}). The actual steps appear at 6.50 and 6.56, rather clearly indicating the two-phase field (miscibility gap). The assignment to the superstructures offers itself, as these fields coincide fairly well with the compositions corresponding to the above superstructure series. These are indicated by the asterisks in the lower part of the diagram. Thus, the phase fields we just considered would correspond to the $2a_0$ and $3a_0$ superstructures and a miscibility gap between them.

These two superstructures have been detected originally with ED and were made visible with the nanoscale resolution of HREM. In fact, these and other chain-superstructures have been detected by HREM as defects in samples of various chemical and thermal histories[2]. Later, the above two first members of this series could be studied in single crystals of the corresponding oxygen contents with XRD and ND (sect. 5.1.1).

Figures 110 and 111 imply that, possibly, the high-quality equilibrium samples (sect. 3.1.2) used in this investigation, combined with the high-resolution determination

[2] We recall, however, that HREM cannot directly see oxygen and that the superstructure is deduced from changes of the heavy metal patterns which have strong contrast (e.g., Van Tendeloo and Amelinckx 1990).

of the oxygen content (sect. 3.1.3) enabled the Raman investigations to probe such "phase relationships". As we already discussed (sect. 5.1.1), high-resolution diffraction experiments with synchrotron radiation have recently shown (in addition to $2a_0$ and $3a_0$) the existence not of the $5a_0$ and $8a_0$ superstructures with every 5th or every 8th chain empty (which would indicate very long range interactions), but of the ortho-V $(2a_0+3a_0)$ and ortho-VIII $[(2a_0+3a_0)+3a_0]$ superstructures with chain sequences (10110) and (10110110) in bulk crystals (von Zimmermann et al. 1999). With the exception of $2a_0$, the other superstructures appear in small 2D domains.

It should be stressed that the structural work up to now could resolve only chain ordering. *It is the Raman results which indicate the possible interaction between stepwise dimpling changes and chain ordering,* as their oxygen contents seem to coincide. We also note that in view of these complex superstructures and their two-dimensional, possibly non-equilibrium character in bulk crystals (von Zimmermann et al. 1999), it is to be expected that even for small differences of the chemical and thermal history of the samples, different "thermodynamic" relationships may be found. Even small activation energies may pin the system, leading to *stationary states* which are not necessarily in thermodynamic equilibrium. Differences are expected between microcrystallites and bulk crystals which are much more difficult to equilibrate. With both total history of the samples and length scale of the detection method different, also the compositions which appear in the phase diagram may be different. This is already demonstrated with the differences in the phase sequence appearing in figs. 44b and 65, as well as with the phase diagrams of figs. 110 and 111.

An important question which cannot be answered at present is the influence of these "dimpling-chain superstructures" (Kaldis et al. 2000a) on superconductivity. One can speculate that possibly the characteristic dimensions of these superstructures are important for increasing the superconductive coupling. Also, it is possible that the lamellar nanoscale character of the full–empty sequences of chains in these superstructures may lead to the formation of stripes, which have been shown to exist also in 123-O_x (cf. sect. 7.5). Dimpling-chain interactions may possibly be understood better using the ideas of Andersen et al. (1995).

In conclusion, whereas in the in-phase O2,O3 phonon frequency vs x curve steps can be resolved corresponding to compositions of a chain-superstructure series, no such effect can be seen in the apex phonon. If a staircase of phases existed, as indicated by the in-phase phonon steps, it would divide the superconducting range of 123-O_x in alternating zones of phase-separated material.

6. Overdoped phase – I: displacive martensitic transformation

6.1. *Overdoped phase investigated with equilibrium samples and high resolution volumetric analysis*

As mentioned already, the overdoped phase has been comparatively less investigated in the past, from the point of view of the materials research. In view of the fact

that in 123-O_x the overdoped range covers only a very narrow stoichiometric range ($\Delta x_{overd} \approx 6.984–6.950 = 0.034$), the difficulty to adjust the oxygen content by (the so popular) quenching, and the uncertainty about the exact oxygen content due to the use of rather crude methods of oxygen determination ($\Delta x = 0.1–0.01$) have appreciably limited the number of overdoped samples investigated. In most cases T_c is used as a relative measure of x.

Using equilibrium conditions for the slow reduction of oxygen in 123-O_x samples with yttrium metal of exact known weight, the oxygen content can be adjusted to better than within $\Delta x_{cont} = 0.01$ (sect. 3.1.2.1). The use of volumetric analysis (sect. 3.1.3) then allows the determination of oxygen with the extremely high accuracy of $\Delta x = \pm 0.001$. In this way even in the very narrow overstoichiometric phase a series of samples can be synthesized without particular difficulty. This has allowed a systematic investigation of these samples with structural (average and local structure with XRD, ND, EXAFS), magnetic and optical (Raman) measurements.

6.2. *Dimpling (Cu2–O2,O3) transition at the onset of the overdoped regime: neutron diffraction*

In a previous section we have discussed the c-axis anomaly found first for BAO *equilibrium samples* by X-ray diffraction at the onset of the overdoped regime $x = 6.92$ (sect. 3.2.2.4, fig. 29; Rusiecki et al. 1990). This effect was reproduced by Nakazawa et al. (1994). Possibly, Claus et al. (1992b) may have seen it also (sect. 7.1). In order to additionally verify this effect, and particularly to find the changes of bond lengths corresponding to this anomaly, an investigation of a series of 12 typical BAO samples in the range $6.62 \leqslant x \leqslant 6.98$ was performed by high-resolution neutron diffraction at ILL, Grenoble (Conder et al. 1994a, Kaldis 1997). Figure 66 shows the results of these measurements (Hewat et al. 1991). The corresponding data are given in table 8 (sect. 3.2.2.4). *The minimum of the c-axis* (fig. 29) *could be verified also by neutron diffraction* (fig. 29f). It was also found to be the result of an abrupt discontinuity appearing at the onset of the overdoped regime in the Cu2–O2,O3 separation along the c-axis (dimpling), see fig. 66a. This effect is also accompanied by a small anomaly of the apical bond (fig. 66b). We note that the details of the anomaly shown in fig. 66a (NPD) are characteristic for the BAO samples. The corresponding anomaly of the dimpling of the CAR samples (EXAFS, fig. 76) is slightly different.

Figures 7 (sect. 2) and 70 (sect. 6.4) show the dimpling of the superconducting planes. The average of the two O2 and O3 positions, which increases with increasing oxygen content, changes slope abruptly at $x \approx 6.95$ (fig. 66a). This abrupt change of dimpling indicates the existence of a structural phase transition at the onset of the overdoped regime. As already mentioned (sect. 5.5.2) and discussed below, this transition was shown to exist also by subsequent Raman (sect. 6.3) and EXAFS investigations (fig. 76, sect. 6.4). We note that according to fig. 66a the increasing Cu2–O2,O3 separation scales with the increasing T_c, up to the onset of the overdoped phase. The scaling of dimpling with T_c has been found also for Ca-123 (Böttger et al. 1996), a clear additional correlation between structure and superconductivity.

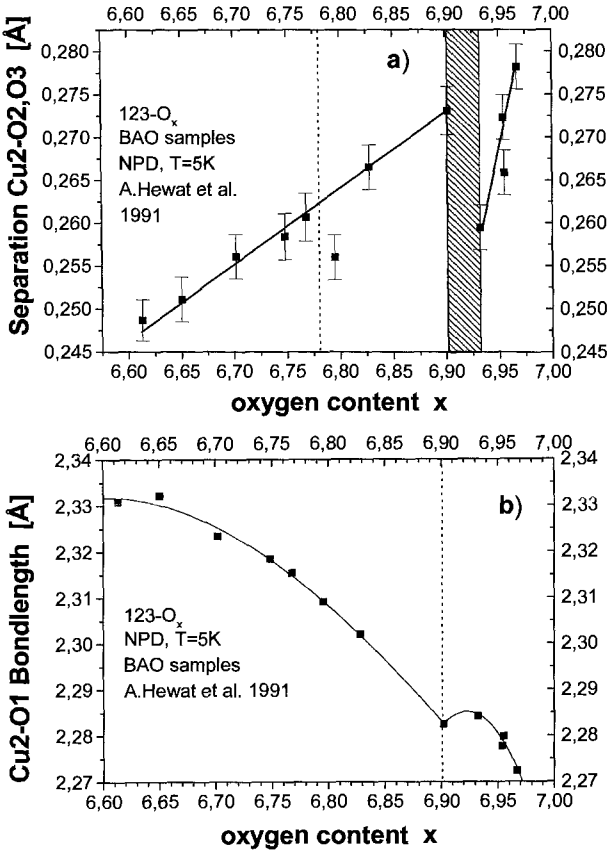

Fig. 66. High-resolution neutron diffraction at $T = 5$ K of BAO samples (sect. 3.2.2.4). (a) With increasing oxygen content the dimpling increases. The dimpling anomaly corresponds to the c-axis anomaly (fig. 29f) at $x = 6.93$, earlier found using X-rays by Rusiecki et al. (1990), cf. fig. 28a. (b) The apical bond shows only a very small anomaly. After Conder et al. (1994a) and Hewat et al. (1991).

6.3. *Raman scattering as a function of nonstoichiometry – II. Softening of the in-phase O2,O3 phonon*

Raman measurements on underdoped and insulating equilibrium samples were discussed in sect. 5.5 and sect. 3.3.2 respectively. In the overdoped region the largest Raman shift as a function of the nonstoichiometry appears for the O2,O3 in-phase vibration mode (A_g phonon). As discussed in sect. 5.5, fig. 65 shows the dependence of the Raman frequency of the O2,O3 in-phase A_g phonon on the oxygen content. In the optimally doped and overdoped phase a decrease of the phonon frequency by 8 cm^{-1} ($\approx 30\%$ of the total change) takes place. Near the onset of the overdoped regime ($x \approx 6.95$) an abrupt softening (45% of the highest value at $x = 6.44$) takes place for CAR samples. $x \approx 6.95$ is very near to the stoichiometry of the appearance in the BAO samples of the minimum in

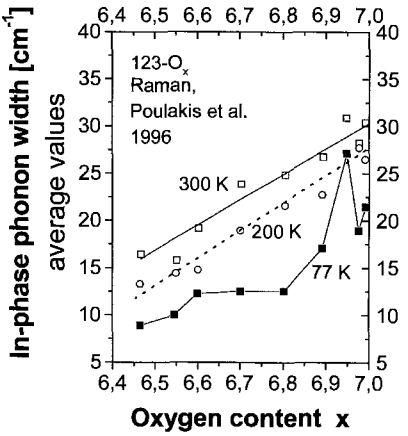

Fig. 67. Temperature dependence of the Raman in-phase (O2,O3) phonon width vs. oxygen content. Note the abrupt increase of the width at 77 K for $6.9 < x < 7.0$, indicating the onset of a structural phase transition. After Poulakis et al. (1996).

the *c*-axis as found by XRD (Rusiecki et al. 1990; see sect. 3.2.2.4, fig. 29) and NPD, and of the abrupt discontinuity in the Cu2–O2/O3 bond discussed above (sect. 6.1, fig. 66a, Conder et al. 1994a). As there is no correlation of this effect with other phonon modes, it becomes clear that the reason must be the structural transition corresponding to the abrupt change of the dimpling (Cu2–O2,O3 bond). This is also supported by the temperature dependence of the width of the in-phase phonon which at $T \leqslant 160$ K shows a widening with an abrupt maximum at $6.9 < x < 7.0$ (fig. 67). A study of the local structure by EXAFS (sect. 6.4) confirmed the existence of this structural transition and showed some important aspects of the structural mechanism.

Contrary to the above behavior of the in-phase A_g phonon, the out-of-phase vibration of the O2,O3 (B_{1g} phonon) is not affected both in frequency and in width by the change of the oxygen content (fig. 35c).

6.4. *Local structure of the planes: EXAFS in the optimally doped and overdoped regimes*

The EXAFS investigations of the apical oxygen were discussed in sect. 4.4. Here we discuss the local structure of the planes in conjunction with the displacive martensitic transformation at the onset of the overdoped phase.

Röhler has systematically investigated in the last few years the local structure of equilibrium samples of 123-O_x as a function of nonstoichiometry (Röhler et al. 1997a,b, 1998) using yttrium K edge EXAFS. The dependence on the oxygen content was measured in the $x = 6.801$–6.984 and $T = 20$–300 K range, originally with 4 (Röhler et al. 1997a), then with 6 (Röhler et al. 1997b) and finally with 10 stoichiometries (Röhler et al. 1998). The results show *appreciable displacements of the Cu2 atoms in the superconducting planes,* which induce distortions of the O2,O3 oxygen and sensitive changes of dimpling, culminating in the transition between the optimally doped and overdoped phases. For optimal doping the distortions of the CuO_2 planes become smallest

and also temperature independent in the superconducting regime ($T < 80$ K). Also, as a function of temperature clear local structure anomalies were found both at T_c and at the spin-gap opening temperature (≈ 160 K).

The principles of EXAFS have been discussed in sect. 4.4. For the investigation of the local structure of 123-O_x as a function of oxygen nonstoichiometry, Röhler et al. (1997a,b) used the Y atom for photoexcitation, due to its excellent view of the $Cu2O_2$ superconducting planes. This is because, as we recall, the Y layer is situated between two adjacent $Cu2O_2$ planes (figs. 4 and 5). Further, according to previous diffraction studies the Y site moves much less than the Ba site upon changing the oxygen nonstoichiometry (table 9, sect. 5.1.1). In contrast, Cu-EXAFS has the great disadvantage of two non-equivalent copper sites which makes the analysis of the spectra much more complicated. Y-EXAFS has only the drawback that it does not face the very interesting apex site which reacts sensitively to the charge transfer between chains and planes. Figure 68 shows the scattering atomic cluster with diameter ≈ 16 Å centered at the Y atom. The single scattering paths Y–O2,O3 to the nearest neighbors, and Y–Cu2 to the next-nearest neighbors, as well as the multiple scattering paths Y–Cu2–Ba and Y–O2,O3–Ba are shown with arrows. The apical oxygen (tip of the pyramid) does not belong to this two-shell cluster, but it is shown for clarity.

The important single backscattering (SS) and multiple backscattering (MS) paths are:
- Y–O2, Y–O3 (SS)
- Y–Cu2 (SS)
- Y–Cu2–Ba (SS, MS)
- Y–O2–Ba, Y–O3–Ba (SS, MS)
- Y–O2–Cu2, Y–O3–Cu2 (MS)
- Y–O2–O3 (MS)

In the multiscattering paths, the smaller the angle between the two legs the more effective is the signal. Figure 69 shows the Yttrium K EXAFS of 123-O_x at $T = 90$ K, with parameter the oxygen stoichiometry ($6.806 \leqslant x \leqslant 6.984$). The moduli of the Fourier transforms $|\mathrm{FT}(\chi\kappa^2)|$ for various stoichiometries, as obtained from the interference patterns in the photoelectron momentum window $\kappa = 2$–16 Å^{-1}, are plotted together. $\chi\kappa$ is the Fourier transform of an effective radial PDF $\rho(R)$ which contains the structural information and the physics of electron scattering: $\rho(R)\,\mathrm{d}r \approx$ probability of finding an atom within a sphere with radius $R + \mathrm{d}R$ around the absorbing Y atom. R_{eff} is the effective path length, $R = r_{\mathrm{tot}}/2$ with r_{tot} the total length of the MS path. From the depicted R_{eff} range the 5 strongest peaks have been analyzed in detail.

As we discussed in sect. 2 (fig. 7) the CuO_2 superconducting planes are not flat but have an appreciable dimpling, clearly shown in fig. 70. On average, the planes consisting of the O2/O3 (110) rows lie 0.27 Å higher along the c-axis than the Cu2 planes. In addition, the oxygen rows O2 and O3 lie on two different levels, and have different thermal vibrations, both resulting from the orthorhombic symmetry of the superconducting 123-O_x structure. In the unit cell the O2,O3 layers are nearest to the Y layer and the Cu2 layers are nearest to the Ba layer. This separation between the oxygen and copper layers results in 0.8 Å difference in the length of the average Y–O2/O3 and Y–Cu2 bond lengths.

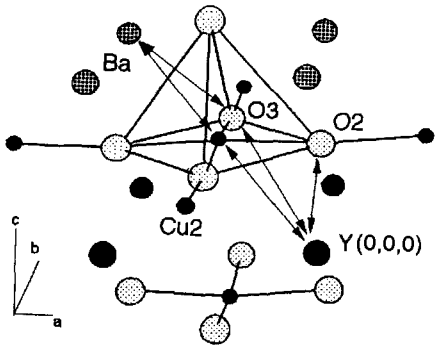

Fig. 68. Y-EXAFS. Scattering atomic cluster centered at the Y atom with diameter ~16 Å. It includes parts of two adjacent CuO_2 layers separated by the Y layer, as well as the Y–Ba block. The CuO_5 pyramid with the apical oxygen is shown for clarity. The single scattering paths to the nearest neighbors, O2,O3, and next-nearest neighbors, Cu2, as well as the multiscattering paths to Ba are shown schematically by arrows. After Röhler et al. (1997a,b).

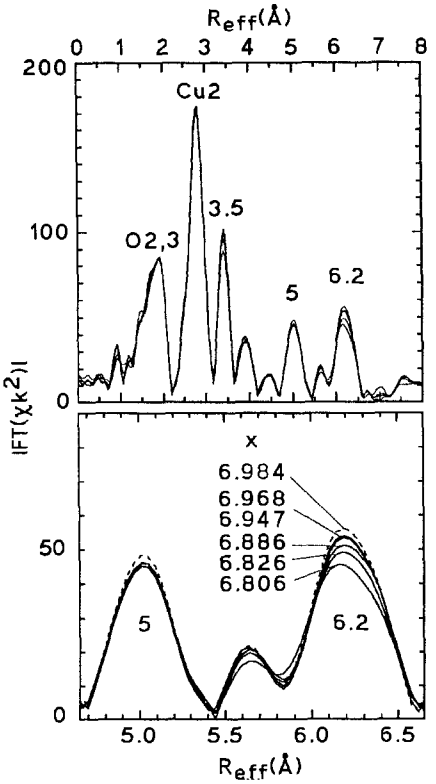

Fig. 69. (a) Fourier transforms from the Y K EXAFS interference patterns (using the photoelectron momentum window $\kappa = 2$–16 Å^{-1}) with parameter the oxygen stoichiometry at $T = 90$ K. (b) Magnification of the "6.2" and "5" peaks. After Röhler et al. (1999a).

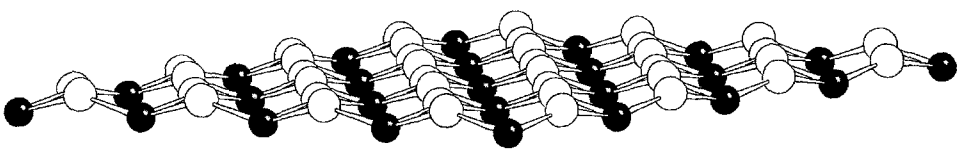

Fig. 70. Top-side view along the Cu2–Cu2 (110) rows of the $Cu2O_2$ superconducting planes of the 123-O_x structure, schematically illustrating their dimpling. The copper rows lie lower than the oxygens. Inside the O2,O3 rows there is a difference in height of the O2 (lower) and O3 (higher) sites. It shows clearly that the superconducting planes consist of three stacked layers (cf. figs. 7 and 15).

Therefore, their SS signals are clearly separated in the high-resolution EXAFS spectra of fig. 69. Diffraction work has shown that the Y–O2/O3 average bond length is 2.40 Å and depends feebly on the temperature but strongly on the oxygen content (Capponi et al. 1987, Francois et al. 1988, Jorgensen et al. 1990a, Schweiss et al. 1994). Change of stoichiometry from 6.6 to 6.97 leads, at 5 K, to a contraction of the average Y–O2/O3

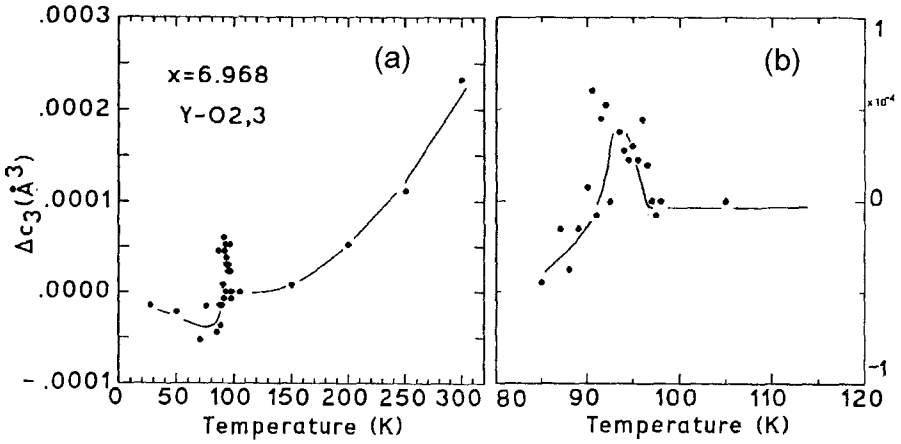

Fig. 71. Mean cubic relative displacements Δc_3 vs. temperature of the highly overdoped sample $x = 6.968$, relative to $T = 100$ K, to quantify the anharmonicity of the Y–O2,O3 bonds near T_c. (a) and (b): two different scales. After Röhler et al. (1997a).

by 0.04 Å (Hewat et al. 1991, Conder et al. 1994a) and Δ(Y–O2) – Δ(Y–O3) $\approx$ 0.02 Å (Cava et al. 1990) (fig. 19).

The two nearest- and next-nearest-neighbor peaks "O2,O3" and "Cu2" could be analyzed quantitatively. Fitting of the Y–O2,O3 peak was not possible using harmonic approximations, due to *either strong disorder and/or strong anharmonicity.* The anharmonicity of the radial distribution function of the Y–O2,O3 was expressed by the mean cubic relative displacements Δc_3 which describe deviations from the Gaussian radial distribution function. Their plot vs. temperature shows a clear singularity at T_c (fig. 71). The mean-squared relative displacement due to small harmonic disorder of thermal/static origin, $\sigma^2 = (R - R_0)^2$, was found to be independent of the oxygen content in the range 6.801–6.947 but decreased appreciably (20%) for high overdoping, 6.984 (Röhler et al. 1997a).

The Y–Cu2 peak does not show such effects. The crystallographic structure gives an Y–Cu2 bond length of ~2.2 Å and no orthorhombic split. Neutron resonance spectroscopy has shown the absence of anomalous copper vibrations in the range 10–300 K for $x \approx 6.2$ and $x \approx 7$ (Hecker et al. 1994). The pair distribution function from a harmonic fit has a nearly Gaussian form. *The bond lengths Y–Cu(2) are in the range of 20–100 K independent of oxygen content and temperature.* Nevertheless, the temperature dependence of the mean-squared deviations $\sigma^2(T)$ shows a deviation from the harmonic contribution to the Debye–Waller factor, with a clear step at 80 K and onset at T_c (fig. 72b).

The peaks at 3.5, 5 and 6.2 Å are mixtures of single and multiscattering paths and due to their complexity they could be analyzed only qualitatively (Röhler et al. 1998):
Peak "3.5": Y–Ba, Y–O2–O3, Y–O2–Cu2, Y–O3–Cu2, Y–Y, Y–Y
Peak "5": Y–Ba, Y–O2–Ba, Y–O2–Ba–O2, Y–Ba, Y–O3–Ba, Y–O3–Ba–O3, Y–Y
Peak "6.2": Y–Ba, Y–Cu2–Ba, Y–Cu2–Ba–Cu2

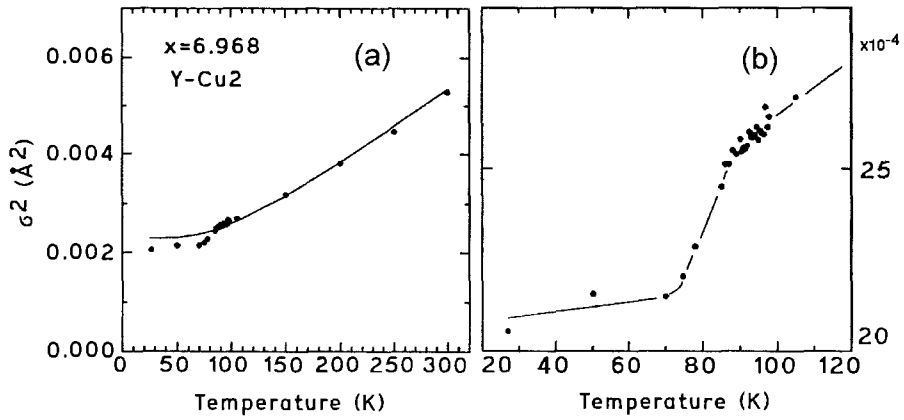

Fig. 72. Mean-squared displacements of Y–Cu2 σ^2 vs. temperature: (a) the line is a fit of the harmonic model of lattice vibrations; (b) magnification of the superconducting regime. The line is a guide to the eye. After Röhler et al. (1997a).

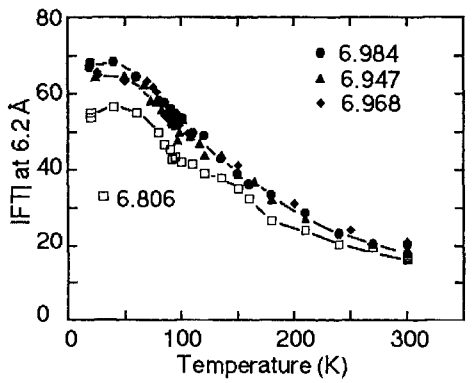

Fig. 73. Temperature dependence of the Fourier transform modulus at the maximum of the "6.2" peak, with as parameter the oxygen content. The underdoped sample shows two steps at 160 K and 100 K. After Röhler et al. (1997a).

Figure 73 shows the temperature dependence of the Fourier transform modulus at the maximum of the "6.2" peak, with oxygen stoichiometry as parameter. There is no appreciable dependence on the oxygen nonstoichiometry except for the relatively underdoped sample (6.806) which shows a weaker temperature dependence (−15%) with a broad maximum at 40 K and forms a staircase with steps at $T \approx 160$ K and nearly 100 K.

A comparison of the scattering paths of the "6.2" and "5" peaks reveals appreciable similarities because they both contain Y–Ba configurations, but in peak "5" the intermediate atoms are the orthorhombically split O2 and O3 with shorter average scattering length and larger bridging angle.

Peak "5" is nearly independent of nonstoichiometry in the temperature range 80–300 K. This indicates that the average position of the oxygen layer O2/O3 is nearly independent for $x = 6.801$–6.984. The heavily overdoped sample (6.984) shows a higher signal for $T < 80$ K (10% at 40 K).

The temperature and oxygen concentration dependencies of the maxima of peaks "3.5" and "6.2" are highly correlated. They both have a relatively weaker, staircase-like temperature dependence of the underdoped sample and a similar temperature dependence of the overdoped samples at $T > 80$ K. A difference is that the overdoped samples of "3.5" show a well-developed plateau in the 100–130 K range and a clear step at 100 K.

Model calculations neglecting vibrational displacements by Röhler et al. (1998) could qualitatively reproduce the Fourier transform spectra found experimentally. The main assumption has been that *with changing oxygen nonstoichiometry Cu2 moves along the c-axis,* neglecting vibrational displacements. This work allowed to understand better the influence of the Cu2 shifts on the spectra.

The main results emanating from these EXAFS investigations (Röhler et al. 1997a,b, 1998) are:

- Y–Cu2 spacing. The experiment shows that the Y–Cu2 bonds are independent of oxygen nonstoichiometry. On the other hand, the model calculations of Röhler et al. (1998) show that with increasing Cu2–O2,O3 spacing (increasing oxygen content) peak "5" remains unaffected, the heights of peaks "3.5" and "6" increase (both in good agreement with the experiment) but the position of the "Cu2" peak is also shifted. The latter seems to contradict the experiment. This discrepancy is solved if it is assumed that the shift of Cu2 along the *c*-axis takes place *under constant Y–Cu2* ***bond length***. Under this condition *the Y–Cu2* ***separation*** *(along the c-axis) increases with oxygen content only if the Cu2 atoms are allowed to rotate around the central Y sites in the [111] plane of the Y–Ba blocks.* This results in an expansion/contraction of the cationic sublattices of Y, Cu2, and Ba along [110], in agreement with the contraction of the *a*-parameter and the expansion of the *b*-parameter with increasing oxygen content found by X-ray diffraction of equilibrium samples (Conder et al. 1994a, Krüger et al. 1997, Kaldis et al. 1997a), discussed in sect. 3.2.2.3.

  Figure 74a schematically illustrates these distortions with exaggerated orthorhombicity. The smaller *a*/larger *b* configuration corresponds to the optimally doped *a*–*b* plane, and the opposite to the underdoped. The arrows show the three-body scattering configuration Y–Cu2–Ba of the "6.2" peak. A side view of the [110] cross-section along the *c*-axis, fig. 74b demonstrates how under constant Y–Cu2 bond length the separation between Y layer and Cu2 layer increases by δz and the scattering angle decreases by 2°. With doping the orthorhombicity increases and the rotation around Y shifts Cu2 lower along the *c*-axis, thus increasing the Y–Cu2 separation.

  Further conclusions about the Y–Cu2 pair are that in the normal state they vibrate harmonically, but in the superconducting state their vibrations are frozen. Symmetry-breaking lattice distortions do not exist in the Cu2 sublattice.
- Y–O2,O3 spacing. Its dependence on nonstoichiometry is controlled from the two conditions: Y–Cu2 bond length constant (see above) and peak "5" practically independent of nonstoichiometry (experiment). As already mentioned, this peak has very strong contributions from the Y–O2,O3–Ba MS paths. From Figure 75a it can be seen that the changes of the Y–Ba block with nonstoichiometry influence these scattering paths. Varying the Y–O2,O3 distances inside the rather large error margins

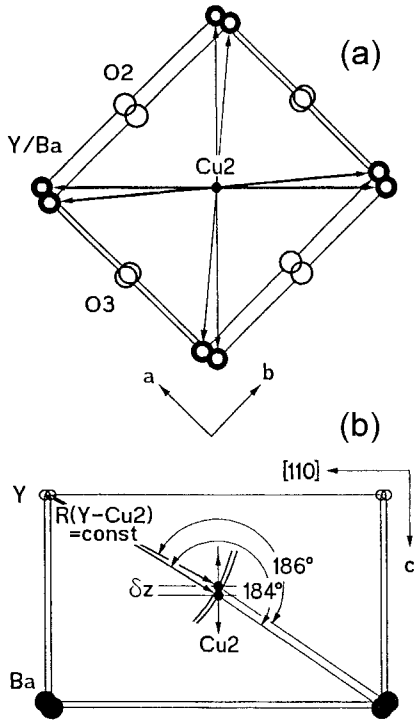

Fig. 74. (a) Top view of the Y (upper)–Ba (lowest) layers with Cu2 and O2,O3 between them (Y, small open spheres; Ba, large black spheres; O, large open spheres). The geometry of the underdoped and optimally doped cells of 123-O_x are overplotted. The increase of the orthorhombicity with oxygen doping is exaggerated (small *a*-large *b*-axis optimally doped). The Y–Cu2–Ba scattering paths (peak "6.2") are indicated by arrows. (b) Cross-section along [110] with constant Y–Cu2 bond lengths to illustrate the rotation of Cu2 with increasing doping, leading to an increase of the Y–Cu2 separation by δz. After Röhler et al. (1997a).

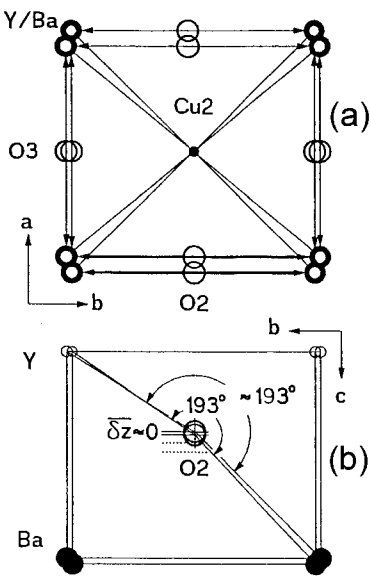

Fig. 75. (a) The same cell as in fig. 74a, rotated by 45°. The arrows show here the Y–O2,O3–Ba scattering paths (peak "5"). (b) Analogous cross-section as in fig. 74b, along [010] with the Y–O2,O3–Cu2 forward scattering angle fixed at ~13° on doping. As can be seen, doping does not shift the oxygens along the *c*-axis ($\delta z \approx 0$) but along the *a*- (cf. a) and *b*-axes, the Y–O2,O3 bond lengths changing in the frame of the orthorhombic distortion. The dashed horizontal lines show the expansion of Cu2 along the *c*-axis. After Röhler et al. (1997a).

(~1%) of the harmonic single-shell analysis of the "O2,O3" peak, and restricting the O2,O3 displacements only along the *c*-axis, two possibilities may be considered: fixed forward scattering angle or fixed *average* Y–O2,O3 distance. In the first case the O2,O3 displacements along *c* are very small as shown in fig. 75b.

In the second case these displacements and, therefore, the changes of the forward scattering angle become appreciable (fig. 75b), shifting the height of the "5" peak outside the experimental findings. The O2 and O3 move along the *a*- and *b*-axes according to the orthorhombic distortion.

We note the strong anharmonicity and/or disorder of the Y–O2,O3 bonds mentioned above. In addition, the shapes of the "O2,O3" and "5" peaks in the calculated Fourier transform spectra have some differences to those found experimentally. This indicates also that *the ideal geometry of the Y–O2,O3 cluster used in the calculations is not correct and that this cluster is distorted.* Finally, Röhler concludes from this analysis that, contrary to the Cu2 sublattice, symmetry-breaking distortions (e.g., of the antiferro type) would be allowed in the O2,O3 layer.

– Cu–O2,O3 spacing. As we have seen, peak "5" contains nearly collinear Y–O2,O3–Ba multiscattering paths (deviation 13°) and peak "6.2" even more collinear Y–Cu–Ba (deviation 4°). Therefore, a very small variation of the forward scattering geometry will have very strong influence on the effective amplitudes (Röhler and Crüsemann 1995). Calculations with the FEFF6 code (Zabinsky et al. 1995) show that the maximum of the "6.2" peak varies almost linearly with the *c*-displacements of Cu2 (Röhler et al. 1997b). In view of the fact that both scattering paths involve the same Ba layer, the dependence on nonstoichiometry and temperature can be taken from the ratio of the Fourier transforms of these two peaks. The results are shown in the next section.

As discussed above, the peaks "5" and "6.2" have quite different dependencies on the oxygen nonstoichiometry. The almost negligible change of peak "5" for $x < 6.95$ indicates that the vertical position of O2,O3 is not influenced by the nonstoichiometry in the underdoped and optimally doped regime. The increase of peak "6" shows that *the Cu2 atoms do shift appreciably towards the Ba layer, moving out of the plane.* The overall increase of this peak corresponds to a relative displacement of Cu2 by $\delta R = 0.051$ Å.

6.5. *The displacive martensitic transformation in the overdoped regime of 123-O_x*

The use of equilibrium samples (cf. sect. 3.1.2) and the high resolution of the volumetric oxygen analysis (sect. 3.1.3) allowed a systematic investigation of the optimally doped and overdoped regime of 123-O_x up to $x = 6.984$. We recall briefly the steps discussed in previous sections which led to the discovery of the displacive martensitic transformation.

A minimum of the *c*-axis in the oxygen-rich region $x = 6.925$ (fig. 28a, sect. 3.2.2.4), found only for the BAO and DO equilibrium samples by XRD (sect. 3.1.2), was confirmed by ND (fig. 29f) and was found to result from an abrupt discontinuity of the dimpling (Cu2–O2/O3) of the superconducting planes (fig. 66a) indicating the existence of a phase transition (sect. 6.2). Micro-Raman investigations (statistical average of many crystallites)

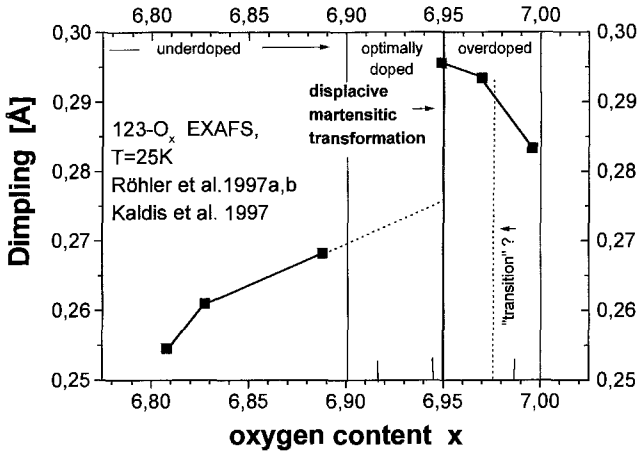

Fig. 76. Dimpling O2/O3–Cu2 as a function of x (after Röhler et al. 1997a,b and Kaldis et al. 1997b). Note the abrupt first-order jump at the onset of the overdoped regime, $x = 6.947$, which has been completely confirmed by later measurements (Röhler et al. 1998). Note that without the two points in the range $x = 6.95$–6.97 the transition step would have been missed.

showed that one of the phonons corresponding to dimpling, the A_g phonon of the in-phase vibrations of O2 and O3 ($\| c$-axis), showed a strong softening at $x = 6.950$ (figs. 65, 79) (sect. 6.2, Poulakis et al. 1996). EXAFS found *a discontinuity* there (Röhler et al. 1997a,b) (sect. 6.4), and finally when 10 samples with different oxygen contents could be measured (Röhler et al. 1998), *a steep first-order-like jump appeared in the dimpling* (fig. 76). These last measurements have been performed recently at four additional compositions, three indicated on the x-axis and one at 6.95. They completely support the above figure.

From fig. 77 we see the structural changes leading to this transformation. With increasing oxygen content the Y–Cu2 separation increases (with the Cu2 moving on a sphere of *constant* Y–Cu2 radius, cf. fig. 74) by the shift of Cu2 towards the Ba layer. For $x < 6.950$ the positions of O2 and O3 remain practically unaffected. It is in the overdoped regime that the O2, O3 move away from Y. As in this range the a-axis increases, and the b-axis decreases (figs. 25a,b) increasing the tetragonality of the unit cell, this transition is considered to be a *martensitic transformation* of 123-O_x (Kaldis et al. 1997b).

Closer inspection of the spikes of the lattice parameters vs. x of the DO samples (sect. 3.2.2.4), in particular those of the c-axis or of the unit cell volume, shows a striking similarity to the changes of dimpling shown in fig. 76, for CAR samples. Figure 30d illustrates this unexpected behavior of the c-axis at larger magnification. The minimum of the DO c-axis corresponds to the optimally doped phase. The step at $x = 6.95$ corresponds to the onset of the overdoped phase and the martensitic transformation. There is a sharp spike at $x = 6.970$ corresponding to the O2,O3 shift in the opposite direction (away from yttrium) (fig. 77), strongly decreasing the dimpling. Unfortunately, no data point exists in the range $6.970 < x < 6.980$ to judge the slope of the dimpling in this range. One could

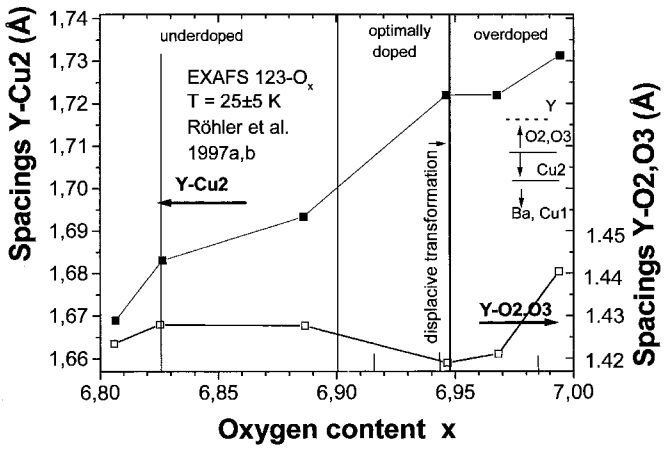

Fig. 77. Variation of the spacings Y–Cu2 and Y–O2,O3 with oxygen nonstoichiometry. Note the abrupt jump of the average O2,O3 position towards Cu2. In the underdoped regime, increasing distance of O2,O3 from Cu2 scales with increasing T_c. After Röhler et al. (1997a,b, 1998) and Kaldis et al. (1997b). On the right, the movements of the atoms along the c-axis are shown schematically. The Cu2 atoms move out of the superconducting plane.

argue that the position of the spikes (fig. 30d) in the lattice parameters of the DO samples is an extreme coincidence. Some arguments against this were presented in sect. 3.2.2.4.

The transition at $x = 6.95$ underlines the change of mechanism from the optimally doped superconductor to the "bad" metal in the overdoped region. An important characteristic of this transition is its influence on the magnetization. As we will discuss in sect. 7.1 a splitting of the diamagnetic transition has been observed by many laboratories for oxygen-rich samples. For the equilibrium samples discussed here this splitting appears without exception at $x = 6.949$, exactly at the doping leading to the martensitic transformation at the onset of the overdoped phase (Kaldis et al. 1997b). Thus, this transition can be considered as the onset *boundary of the phase-separated overdoped phase* where the T_c decreases with nonstoichiometry.

Recently, Emerson et al. (1999) have confirmed with careful specific-heat measurements previous findings of Nakazawa and Ishikawa (1989) and Moler et al. (1997) that in the overdoped regime a sharp increase of the Debye temperature takes place. This is shown in fig. 78. In their estimated oxygen content scale the abrupt increase of the Debye temperature takes place at $x \approx 6.98$. In view of the fact that the oxygen determination was indirect, it seems reasonable to assume that this effect is related to the displacive martensitic transformation ($x = 6.95$, determined directly, with high accuracy, sect. 3.1.3) and the series of structural phenomena which accompany it in the overdoped region: the abrupt decrease of the unit-cell volume (fig. 25e), the decrease of the b-axis, the decrease of the orthorhombicity (figs. 25b,c) and the minimum of the c-axis (Rusiecki et al. 1990) (fig. 28a).

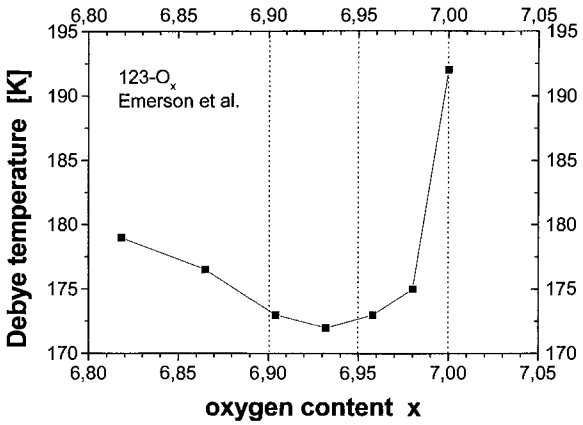

Fig. 78. Sudden increase of the Debye temperature at $x \approx 6.95$, from specific heat measurements. After data of Emerson et al. (1999).

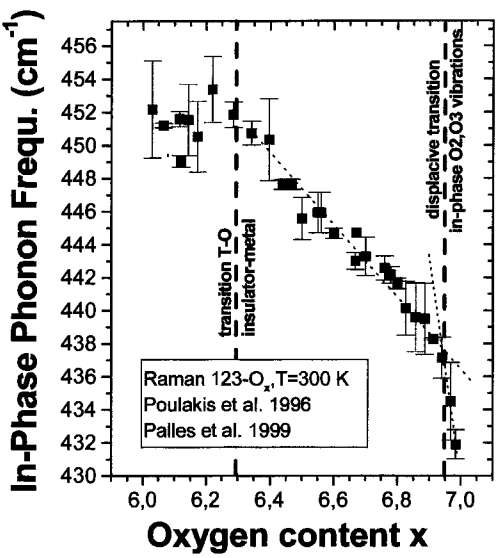

Fig. 79. Raman in-phase phonon frequency vs. x. Average values from 5–10 crystallites at each composition. Compare with fig. 65 showing the individual measurements. The onset of the abrupt softening of the phonon is clearly seen at the transition stoichiometry ($x = 6.95$). After Poulakis et al. (1996), Palles (2000) and Palles et al. (2000a).

Another change of properties influencing the Debye temperature is the above-mentioned softening of the Raman in-phase phonon, already at room temperature, accompanying this transition (figs. 79, 65) and the independence of the apex phonon (fig. 61) in the overdoped regime. We note also that these structural changes may have important implications for the physics of HT_c (Röhler 2000a). According to Andersen et al. (1995) the shifts of Cu2 and O2,O3 out of the plane influence the band structure in the vicinity of the Fermi level.

7. Overdoped phase – II: phase separation in 123-O_x

7.1. *The splitting of the diamagnetic transition in the overdoped regime*

Although theoretical models of phase separation due to the separation of spin and charge appeared very early (Gor'kov and Sokol 1987), the research concentrated on La cuprates, and only very recently has appreciable experimental evidence appeared about the existence of stripes in 123-O_x. The phase-separation literature has been reviewed in a series of volumes edited by Müller and Benedek (1992), Sigmund and Müller (1994), Mihailovic et al. (1995), Kaldis et al. (1997a), and Bianconi and Saini (1997, 2000). Most of this work is based on the proximity of the superconductor and antiferromagnetic insulator states in the HT_c cuprates. A system of doped holes in an antiferromagnetic insulator matrix tends to phase-separate.

Historically, the first indication from materials research for the existence of an overdoped regime came with the finding of a maximum of T_c (Graf et al. 1990, Rusiecki et al. 1990) and with the c-axis anomalies discussed in sect. 3.2.2.4 (Rusiecki et al. 1990). More data were presented later by Claus et al. (1992a,b). However, in the earlier literature there is a series of indications for several anomalies of the oxygen-rich samples.

Splitting of the specific-heat peak for oxygen-rich samples has been observed in long-annealed unquenched samples as early as the Interlaken Conference, by Ishikawa et al. (1988a,b). Figure 80 shows their first results with two transitions at $T \approx 88.5$ K and 91.3 K. A similar splitting was found in the resistive and magnetic transitions, leading them to the conclusion that both peaks correspond to superconducting transitions involving substantial fractions of the sample volume. Further results of this group will be discussed below. Also, work on single crystals by other groups gave similar results (Inderhees et al. 1988, Butera 1988).

Phase separation in two orthorhombic phases with $x \approx 7.0$ and 6.7 but common orientation was found with XRD high-resolution scans in a triple-axis spectrometer using Ge (111) crystals as monochromator and analyzer (YouHoydoo et al. 1988).

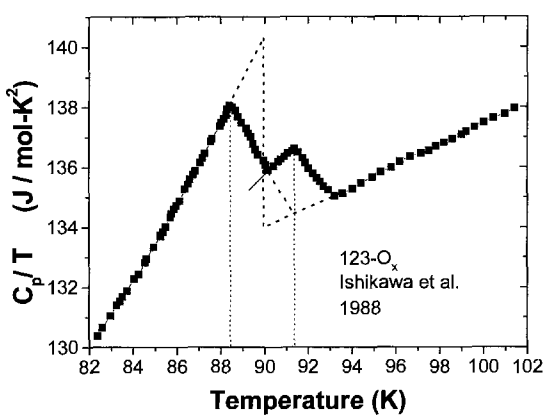

Fig. 80. Specific heat C_p/T as a function of temperature for an oxygen-rich sample with two distinct peaks ($\Delta C_p/T = 3$ K). This splitting was found also in the resistive and magnetic transitions. The figure was schematically reconstructed, not considering all measured data. After Ishikawa et al. (1988a).

Loram et al. (1991) investigated the specific heat of oxygen-rich samples as a function of nonstoichiometry. Using a high-precision differential technique, with as reference a $YBa_2(Cu_{0.93}Zn_{0.7})_3O_x$ sample to suppress the large phonon term, they found that their highly oxygenated 123-O_x ($x \approx 7$) samples showed a double transition in the range of $x \geqslant 6.95$. The splitting changed systematically with x and was present *in all samples*. At $x \approx 7$ two peaks were observed at $T_{c1} \approx 88$ K and $T_{c2} \approx 92.5$ K in 4 samples from three different laboratories. Resistivity measurements showed similar effects. These authors also considered the specific-heat anomaly to be a *bulk effect* and to be definitive evidence for a multicomponent order parameter. Several arguments support a bulk effect (Loram et al. 1991):

- The comparable magnitudes of the anomalies at T_{c1} and T_{c2} show that each of them is connected with approximately half the sample volume. The authors explicitly reject the existence of minority (impurity) phases with a different T_c than the bulk, or nucleation of superconductivity on grain or twin boundaries.
- The sharp anomalies are not consistent with a spread of T_c due to inhomogeneities in the oxygen distribution and with the sequence in which the measurements were performed (first $x \approx 7.0$, then 6.50, then 6.75).
- As *the resistivity onset of the diamagnetic transition coincides with* T_{c2} it is clear that the long-range order of superconductivity starts at this temperature. As the resistive transition is finished at $T > T_{c1}$ the authors conclude that the long-range order is fully established at this temperature.

As a possible explanation of this phenomenon the authors consider, in the case of non s-wave pairing, the coupling between the superconducting order parameter with an environment of different symmetry and propose that it may lead to two different T_c's dependent on the crystallographic direction. Thus, T_{c1}, which changes with the chain oxygen, may be the transition temperature for c-axis superconductivity while T_{c2}, which seems rather independent of oxygen, may be the transition temperature for the superconductivity of the planes.

The crystallographic phase separation (chemical phase separation) (YouHoydoo et al. 1988) reappeared in the work of Claus et al. (1992b). They found that single crystals with $x > 6.92$ had split c-axis with slightly different c-parameters. The corresponding resistive and (dc) diamagnetic transitions show the two-step behavior of Loram et al. (1991), but their specific heat did not show the two peaks. For the structural investigation they used a two-axis goniometer and recorded Θ–2Θ XRD spectra in the Bragg–Brentano focusing geometry. Only c-axis reflections ($00l$) could be measured for $l = 2$–14. The absolute accuracy of the c-axis parameter was estimated to be rather low, ~0.01 Å. A narrow rocking curve (~0.025 FWHM) was measured for one crystal; other crystals had much broader rocking curves corresponding to misorientations of 0.5°, and some showed several peaks indicating that they consisted of several grains with similar misorientations. However, each of these grains (~6) could be measured individually. The crystals were thermally treated under known conditions to reach oxygen contents near 6.92 and then 6.94 reversibly and were measured in the two states. Figures 81a,b show the lattice constants and the relative intensities of the crystal parts, with larger c-parameter

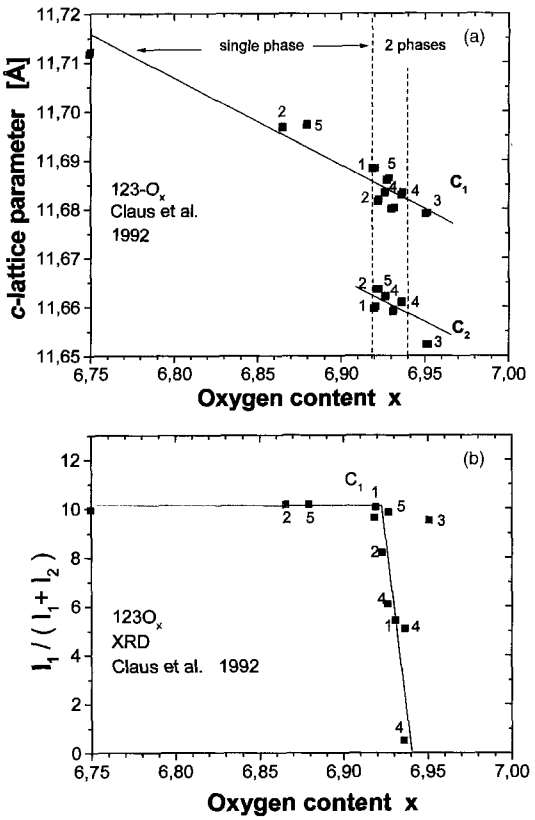

Fig. 81. (a) Splitting of the XRD c-lattice parameters for crystals reversibly oxygenated and deoxygenated between $x \approx 6.92$ and 6.94. At $x < 6.92$ the lattice constants follow the normal x dependence (C_1). At $x > 6.92$ the splitting starts (C_2). (b) Relative intensities of the (0013) diffraction line of the part of the crystals with the larger c-parameter (C_1). Above oxygen content 6.94 (C_1) the intensity disappears reversibly with the oxygen content. The numbers show measurements on the same crystal. After Claus et al. (1992b).

C_1 at $x \leqslant 6.92$ and smaller C_2 at $x \geqslant 6.92$. From fig. 81a we see a miscibility gap, two phases coexisting in the 6.92–6.95 range. From fig. 81b we see that the intensity of the larger (C_1) disappears – as expected – with increasing x, after we cross the miscibility gap. This is the classical picture of phase rule thermodynamics. In view of the estimated oxygen contents they used, it is possible that these figures illustrate the c-parameter anomaly (fig. 28a) and the displacive phase transformation found at the onset of the overdoped region at $x = 6.95$ (Rusiecki et al. 1990, Conder et al. 1994a, Kaldis 1997, Kaldis et al. 1997b, Röhler et al. 1998), which also lead to phase separation. Possibly due to hysteresis, the grains of the various crystallites measured above could be frozen at different stages of the transition and the minimum of the c-parameter could show, therefore, different dimplings and c-parameters. Figures 81a,b also remind of the miscibility gaps tentatively proposed for the a-parameter of the BAO samples (fig. 29c).

7.2. *The shell model*

Soon after the work of Loram et al. (1991) and before the work of Claus et al. (1992a,b) Nakazawa finished his Ph.D. thesis (Nakazawa 1991) at Tokyo University. This thesis

summarized and discussed the numerous investigations performed since 1987 by the Ishikawa group, with particular care for the quality of the material (e.g., Ishikawa et al. 1988a,b). The highlights of this thesis were published later (Nakazawa et al. 1994). These authors were, therefore, the first to show that improvement of the sample preparation by avoiding quenching and by the use of low-temperature annealing allows the development of the two specific-heat peaks at T_c (fig. 80), and were also among the few teams at that time which measured directly the oxygen content of *each* of their samples by iodometry (Nakazawa 1991, Nakazawa et al. 1994). They also developed the shell model we will discuss below (Nakazawa 1991, Nakazawa and Ishikawa 1991).

An extensive investigation of the specific heat and the a.c. susceptibility as a function of the annealing temperature of polycrystalline samples was presented by Janod et al. (1993). They found for all investigated samples the double peaks for annealing temperatures 350–550°C, except for 460°C. It is unfortunate that their expertise in specific-heat and ac-susceptibility measurements could not be supported by accurate determination of the oxygen content of each sample. They did not measure the oxygen of the samples they used for specific-heat and susceptibility measurements, but that of another series of samples which showed a smaller splitting. Thus, all the figures of this work have only the annealing temperatures as parameters, and only the T_c vs. x shows estimated oxygen contents based on the work of Claus et al. (1992a), which in turn also used thermodynamically estimated oxygen contents. Further, no investigation of the change of the lattice constants with oxygen was presented, which would trace the trends of structural changes. Nevertheless, the work of Janod et al. (1993) is an important contribution to the splitting of the diamagnetic transition because it supports and extends the experimental findings of Ishikawa et al. (1988a,b), Nakazawa (1991) and Loram et al. (1991):

(a) that careful straightforward synthesis with low-temperature annealings leads to two very well-developed peaks at T_c, and
(b) that both peaks correspond to superconducting transitions and to substantial superconducting volumes of the sample, reversible with oxygen change.

The two peaks of the specific heat of 5 samples annealed at 300°C for 240 h appear at two critical temperatures $T_{c1} = 87$ K and $T_{c2} = 92$ K, corresponding to 40% and 60% of the sample volume. With increasing annealing temperature a cross-over of T_{c1} and T_{c2} takes place in the samples of Janod et al., as shown in fig. 82, but unfortunately we do not know exactly the corresponding change of the oxygen or carrier concentration. The authors claim that they have reached an oxygen content of $x = 7.0$ under 100 bar of oxygen and refer to a Russian team who have reached $x = 7.2$. It is questionable whether such samples are homogeneous at mesoscopic scale, due to the T–x phase diagram shown in fig. 55 (Karpinski et al. 1991) and discussed in sect. 5.4. Also one would like to know more about the accuracy of the indirect methods used for such oxygen determinations.

Janod et al. (1993) propose the same model as Nakazawa (1991), namely that the grains of the sample consist of a surface layer (shell) with higher oxygen content and lower T_c, and a core with lower oxygen content and higher T_c. Nakazawa's model is based on the lattice-constant anomalies reported earlier (Rusiecki et al. 1990) for $x = 6.92$, which he could reproduce in carefully synthesized low-temperature-annealed samples: a minimum

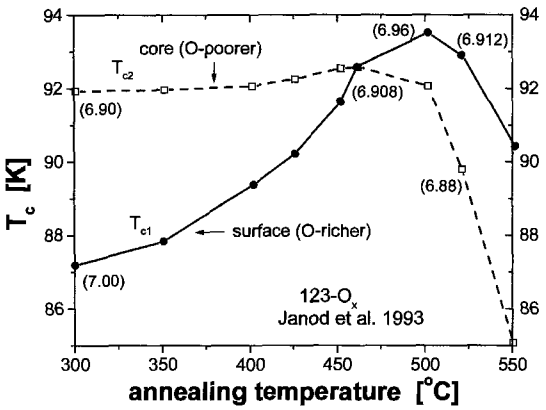

Fig. 82. Evolution of T_{c1} and T_{c2} with annealing temperature. After data of Janod et al. (1993). The authors propose that T_{c1} corresponds to an oxygen-rich shell on the surface of the grains and T_{c2} to an oxygen-poor core of the grains.

of the c-parameter and a maximum of the orthorhombicity (Nakazawa et al. 1994). Based on these structural changes Nakazawa proposes that in the surface layer of the grains with $x > 6.90$, O5 sites are occupied, which decreases T_c. In fact, the same argument has been used later by Krüger et al. (1997) to explain the changes of the lattice constants in the overdoped regime, but this could not be proven experimentally up to now (sect. 5.4.2). However, in order that the Nakazawa/Ishikawa/Janod et al. shell model is valid, the surface layer has to strongly reduce the diffusion of the oxygen through the surface to the core of the grains. As we will discuss in the next section, this is not the case (Conder et al. 1994a,b).

7.2.1. *Oxygen diffusion in the grains: no surface barrier*

In order to test the above "shell" model, the diffusion rate of oxygen in 123-O_x grains at 320°C was calculated for various grain sizes, using measured diffusion coefficients (Conder et al. 1994b). Self-diffusion coefficients were measured in thermogravimetric studies of the oxygen isotope exchange (Conder et al. 1993). The chemical diffusion coefficient D was calculated from the self-diffusion coefficient D^* using the equation

$$D = D^* F h, \tag{12}$$

with an estimated thermodynamic factor F and the Haven factor h which has a value near unity (Salomons and de Fontaine 1990).

Due to the strong anisotropy of the oxygen diffusion coefficient in 123-O_x a one-dimensional bilateral diffusion model (Schmalzried 1981) was used for the calculation of D (Conder et al. 1993). From the solution of Fick's second law the total concentration of the diffusing oxygen was obtained. This is equivalent to the diffusion progress α, which is 0 at the beginning and 1 at the end of the diffusion process. This parameter has been determined directly from thermogravimetric weight-change measurements (Conder et al. 1993, Krüger et al. 1993) of the oxygen isotope exchange $^{18}O \rightarrow {}^{16}O$ at very low temperatures (225–290°C, thermobalance resolution 1 μg). The experimental results

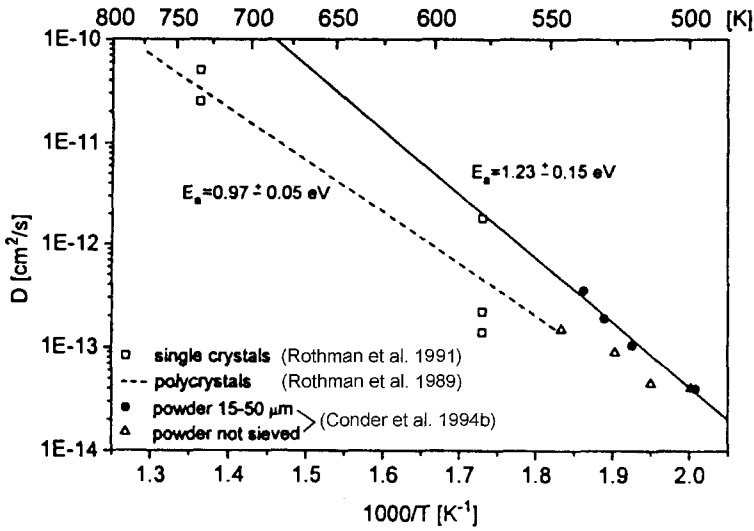

Fig. 83. Arrhenius plot of the oxygen tracer self-diffusion coefficient D^*. Comparison of the data of Conder et al. (1994b) with those of Rothman et al. (1989, 1991). After Conder et al. (1994b).

showed that at these temperatures only the O4 sites of the chains are exchanged, justifying the use of a one-dimensional model (Conder et al. 1993). As in these experiments the oxygen content remains constant, the tracer-diffusion (self-diffusion) coefficients can be calculated from isothermal runs. To receive as high an oxygen content as possible, the synthesis method of sect. 3.2.1 (table 2, CAR method) was extended by an additional annealing at 320°C for **300 h** in 1 bar of oxygen or in other samples by slow cooling down to 500°C with 5°C/h and then by **4°C/h** down to room temperature.

The oxygen tracer coefficient D^* was calculated for many values of α obtained from the isotope-exchange experiments at different temperatures. Satisfactory constant values near 10^{-13} cm^2/s were obtained in the vicinity of 250°C. Arrhenius plots are shown in fig. 83 including the data of Rothman et al. (1989, 1991). We note that their data have been based on secondary ion mass spectroscopy (SIMS), taking depth profiles of the tracer in the sample. Conder et al. (1994b) from their high-resolution thermogravimetric measurements obtained the value $E_a = 1.23 \pm 0.15$ eV at low temperatures for powder samples with grain size 15–50 μm. To calculate the chemical diffusion coefficient from eq. (12), the thermodynamic factor F must be known.

F is given by (Murch 1980, Salomons and de Fontaine 1990)

$$F = 0.5 \frac{\mathrm{d}\ln(p_{O_2}/p^0_{O_2})}{\mathrm{d}\ln(7-x)}, \tag{13}$$

with p_{O_2} the oxygen pressure and $7-x$ the oxygen content of the sample. Therefore, F can be calculated from the slope of the 123 equilibrium isotherms in the $\ln(p_{O_2})$–$\ln(7-x)$ coordinates measured earlier (Conder et al. 1992). Using the value $F = 20$

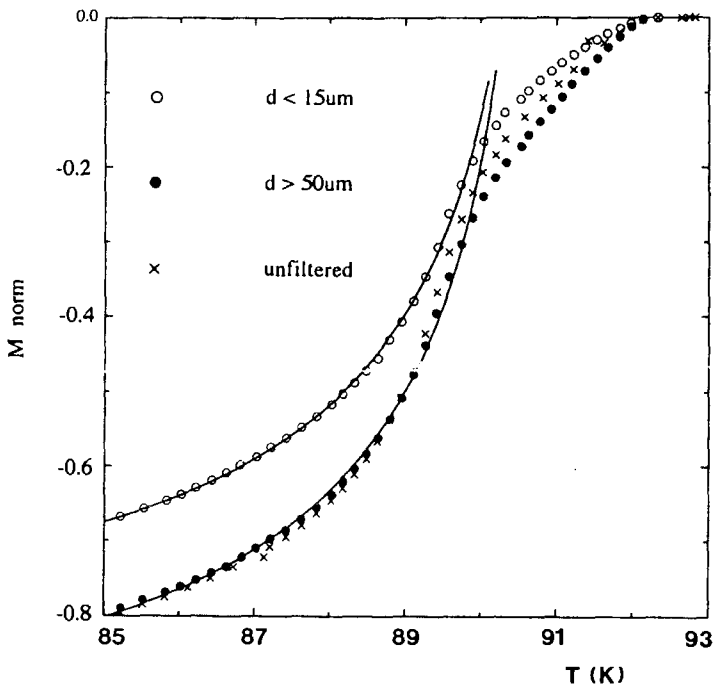

Fig. 84. Magnetization curves vs. T for three samples, two of them resulting from sieved fractions of the first, after grinding. Solid lines are Shoenberg fits (cf. sect. 7.3). (a) Equilibrium sample (crosses), $T_{c,onset} = 92.2$ K. (b) Sieved fraction with grains <15 μm (open circles). (c) Sieved fraction with grains >50 μm (solid circles). No changes of $T_{c1} = T_{c,onset} = 92.2$ K and $T_{c2} = 90.2$ K with grinding or grain size were found (see text). After Conder et al. (1994a,b).

(corresponding to $x = 6.93$) the chemical diffusion coefficient for 320°C was found to be $D = 8 \times 10^{-11}$ cm^2/s.

With these values, grains up to 100 μm should be completely oxidized after annealing at 320°C for 300 h. Using the data of Rothman et al. (1989, 1991) with $F = 20$ one calculates a chemical diffusion coefficient $D = 1.4 \times 10^{-11}$ cm^2/s. With this smaller value which does not correspond to equilibrium samples the grains remain homogeneous up to 50 μm. 100 μm grains would show only a difference $\Delta x = 0.02$ between surface and center.

To confirm these calculations directly with magnetization experiments an oxygen-rich sample ($T_{c,onset} = T_{c1} = 92.2$ K) was measured and then fractionated with ultra-sound sieving equipment to three fractions of different grain sizes. The magnetization of the two extreme fractions with grain size $d < 15$ μm and $d > 50$ μm was measured again and is shown in fig. 84. From the fit in the temperature regime $T < 88$ K (see sect. 7.3) it is found that the broadening of the transition at $T > 88$ K – leading to two T_c's – is observed for both fractions in the same temperature range, both fractions having an identical $T_{c2} = 90.2$ K. The second fit parameter R/λ_0 (eq. 15, sect. 7.3) for the fraction $d > 50$ μm is ~3 times larger than that for $d < 15$ μm, in agreement with the grain sizes.

This shows that both fractions have grains with identical magnetic properties. The small difference in the shape of the magnetization curves is, therefore, due only to the different grain sizes and not to different superconducting properties of the grains. The Shoenberg equation (Shoenberg 1940) (eq. 14, sect. 7.3) fits the magnetization curves of both grain sizes (fig. 84) very well, but only in the $T < 89.9$ K regime. This means that the anomalous magnetization behavior near T_c is not due to an inhomogeneous oxygen distribution in the grains, because this would have been different for different grain sizes also for $T < 89.9$ K (Conder et al. 1994b). The above magnetic and thermodynamic investigations show that the "shell" model cannot be used to explain the splitting of the diamagnetic transition.

7.3. *The splitting of the diamagnetic transition as a function of the exact oxygen content: indication for phase separation*

The magnetic and structural investigations started by Rusiecki et al. (1990) were continued in the following years and as mentioned in sect. 6 led to the discovery of the displacive martensitic transformation at the onset of the overdoped range (Conder et al. 1994a, Kaldis 1997, Kaldis et al. 1997b, Röhler et al. 1998). The magnetization of more than 150 samples analyzed with high-resolution volumetric analysis, $\Delta x = 0.001$ (Conder et al. 1989), has been measured, and some T_c values are shown in fig. 2 and were reported in several occasions (Schwer et al. 1993a, Conder et al. 1994a, Kaldis 1997). At this point we concentrate on the overdoped regime. As fig. 85 shows, the splitting of the diamagnetic transition starts for equilibrium samples precisely at $x = 6.950$, i.e., at the onset of the overdoped regime coinciding with the martensitic transformation (sect. 6). This

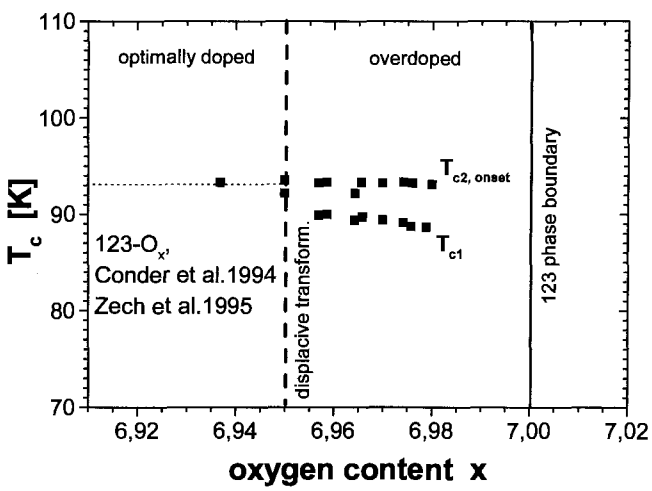

Fig. 85. Splitting of the diamagnetic transition of 123-O_x at $x \geqslant 6.950$, indicating the phase separation of the overdoped phase. $T_{c1} = T_{c,\,optim.\ doped}$ remains practically unchanged with x, whereas T_{c2} decreases with x. The onset of the splitting coincides with the displacive martensitic transformation (sect. 6.4) at the onset of the overdoped phase. After data of Conder et al. (1994a) and Zech et al. (1995a,b).

splitting has been found for *all investigated samples* with $x \geqslant 6.950$. DC magnetization measurements have been performed with a SQUID magnetometer on *cold-pressed* powder samples (to avoid recrystallization of surface grains when sintering ceramic pellets) sealed under vacuum between two quartz rods in quartz ampoules (internal diameter 3 mm) (Zech et al. 1995a).

High-precision field-cooled (FC) measurements were performed while cooling down from $T > T_c$ with an external field $H = 10$ Oe. Measurements at very small temperature intervals (down to every 0.5 K) were taken in order to clearly expose changes of slopes. We recall that FC magnetization measures the field repulsion of the single grains, in contrast to zero-field cooling (ZFC) which measures the screening of the applied field and therefore, the superconducting properties of the entire sample surface. Figure 8 shows typical magnetization measurements for an optimally doped sample ($x = 6.912$) and an overdoped sample with $x = 6.974$. A two-parameter fit with the Shoenberg model is shown by the solid line. This simple model describes the flux expulsion of small grains with diameter comparable to the penetration depth (Shoenberg 1940) according to the equation

$$M(T)_{\text{norm}} = 1 - 3\frac{\lambda(T)}{R}\coth\left(\frac{R}{\lambda(T)}\right) - 3\left(\frac{\lambda(T)}{R}\right)^2, \tag{14}$$

with M_{norm} the normalized magnetization, R the radius of the grains, and $\lambda(T)$ the London penetration depth. For the fitting the two-fluid approximation was used:

$$\lambda(T)^2 = \frac{\lambda(T)_0^2}{(1 - T/T_c)^4}, \tag{15}$$

with $\lambda_0 = \lambda(T = 0\,\text{K})$. The only fitting parameters are T_c and R/λ_0 (Zech et al. 1995b). Figure 8 (curve a, $x = 6.912$) shows an excellent fit up to T_c, with eq. (14), for the optimally doped samples. It also shows that for overdoped samples (curve b) an excellent fit is possible, but only up to a lower temperature where a broadening of the transition takes place due to change of curvature. For the overdoped sample with $x = 6.974$, eq. (14) describes the magnetization for $T < 89$ K. An extrapolation of the fit up to $M(T) = 0$ gives a $T_{c1} = 89$ K clearly different from the onset of the diamagnetic signal at $T_{c2} = 92.2$ K. We recall that these are very near to the values found by the specific-heat measurements of Ishikawa et al. (1988a,b), Loram et al. (1991), and the crystallographic splitting (Claus et al. 1990; sect. 7.1).

This effect shows the existence of two systems with different critical temperatures. In the underdoped and optimally doped phases only one transition temperature (T_c) is found. As fig. 85 indicates, the T_{c2} values fit without discontinuity to the optimally doped T_c values. The lower T_{c1} values in the overdoped range decrease with x so that, e.g., $\Delta T_c \approx 3.5$ K at $x = 6.976$. More details about the splitting can be seen in fig. 86, showing the susceptibility curve of a $x = 6.990$ sample synthesized with ^{18}O. Also drawn is the susceptibility curve of the same sample after a site-selective isotope exchange with ^{16}O

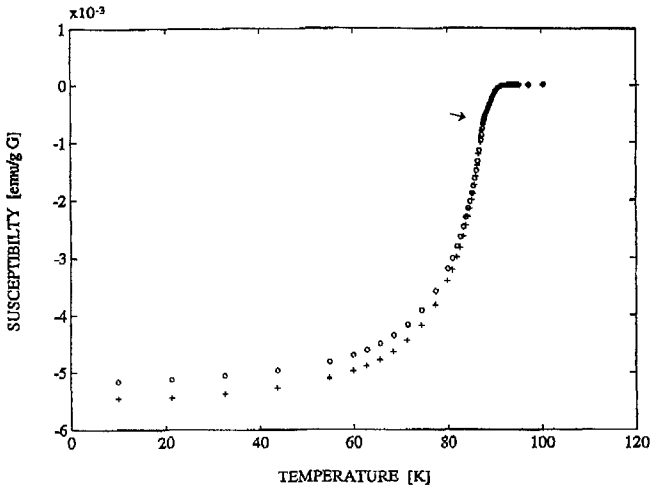

Fig. 86. Morphology of the magnetization curve of an equilibrium sample due to the splitting of the diamagnetic transition. The arrow shows the change of curvature. Open circles, $YBa_2Cu_3^{18}O_{6.990}$. Crosses, the same sample after site-selective isotope exchange with ^{16}O which slightly increased the O content to 6.991. After data of Zech et al. (1995a) and Conder et al. (1994a).

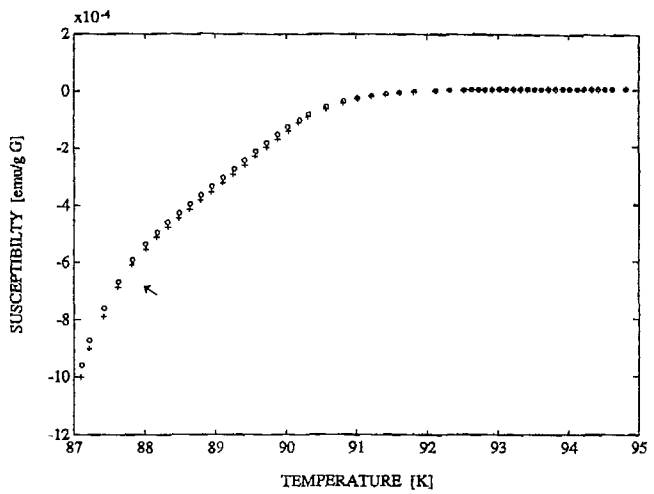

Fig. 87. Magnification of the curves of fig. 86 to show the extreme reproducibility of the equilibrium samples even after the series of manipulations necessary for the isotope exchange. The arrow shows the temperature of the change of curvature. After data of Zech et al. (1995a).

and a slight increase of oxygen content to $x = 6.991$. The change of slope leading to T_{c2} is clearly shown (arrow). Figure 87 shows a magnification of the two curves of fig. 83 in the higher temperature range. As can be seen, *the reproducibility of the sample in spite of the manipulations for the isotope exchange is extremely high,* the small change

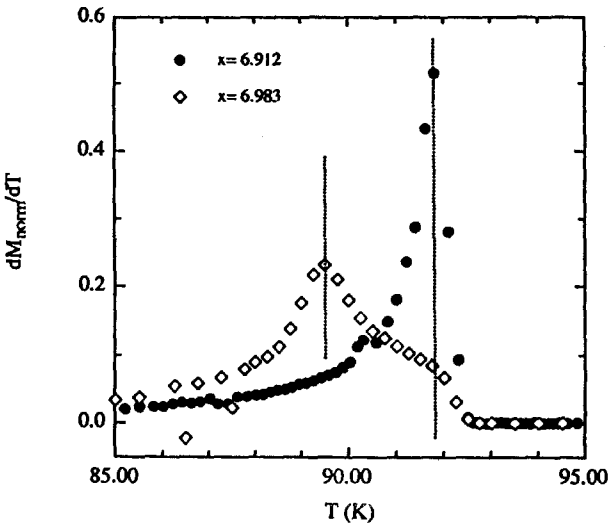

Fig. 88. Derivatives of the magnetization curves showing the position of the T_c's.The optimally doped sample ($x=6.912$) does not show the splitting. The overdoped sample ($x=6.983$) does show the splitting with $T_{c2} \approx T_{c,opt} \approx 91.8$ K and $T_{c1} = 89.5$ K. After Conder et al. (1994a).

being due to the actual isotope effect (Zech et al. 1995a,b). The flat part of the curve starts at ~88 K. If a large number of temperature measurements exists, then the first derivative of the curve can determine to high accuracy the two T_c values. Figure 88 shows the derivative peak (dM_{norm}/dT) of an optimally doped sample ($x=6.912$) and an overdoped sample ($x=6.983$). The latter clearly shows the two T_c's: $T_{c2}=91.8$ K, almost overlapping with the T_c-optimal, and $T_{c1}=89.5$ K, the T_c decreasing with doping. As to the reason for this splitting we have seen in sect. 7.1 the ideas of Loram et al. (1991). Another possibility is that the appearance of two transition temperatures is due to the existence of a pseudogap (T^*) which appears mainly in the c-axis properties (resistivity, optical conductivity etc.) (see, e.g., Uchida 1997). We recall that the splitting of the diamagnetic transition occurs at the displacive transformation at $x=6.95$ (sect. 6.5), which is associated with structural changes along the c-axis (dimpling) (Conder et al. 1994a, Röhler et al. 1997a,b).

The splitting of the diamagnetic transition shows the existence of *physical phase separation* in the overdoped phase. Roughly, the stability of the optimally doped phase is such that the material tends to retain it in cluster form even in the overdoped range. Thus the $T_{c2,\,onset}$ stays constant near the value of the $T_{c,\,optimal}$. We will see that in the much wider Ca-123 "overdoped" range the effect is present to a much larger extent.

7.4. *Phase separation due to stripe formation: separation of spin and charge*

As mentioned at the beginning of sect. 7, a system of doped holes in an antiferromagnetic insulator matrix tends to phase-separate. We have seen above the splitting of the

diamagnetic transition in the O-overdoped phase, as evidence for the existence of phase separation. Before we review similar phenomena in the Ca-doped 123, we discuss briefly some experimental results concerning stripe formation in 123. One form of phase separation is the formation of stripes by the doped holes, separating hole-free, insulating, antiferromagnetic domains.

The theory of the *stripe-phase model* is based on the theoretical work of Emery et al. (1990) and Zaanen and Gunnarsson (1989). First experimental proof of the existence of stripes in La cuprates and possibly other HT_c cuprates came from the ingenious work of Tranquada et al. (1995) and, starting from another point, the work of Bianconi and Missori (1994) proposing the existence of quantum wires in a Wigner polaron crystal.

The theoretical work of Emery et al. and Zaanen and Gunnarsson predicted the dynamic behavior of stripes and *the existence of cross-overs or phase transitions as a function of temperature.* As this behavior should be reflected in the lattice properties of the HT_c cuprates, Sharma et al. (2000) used MeV helium ions channeling spectrometry to probe the existence of incoherent lattice fluctuations in 123-O_x at three different stoichiometries. This ultrafast real space probe has a response of $<10^{-17}$ seconds and can detect, in single crystals, static and dynamic uncorrelated atomic displacements with sub-picometer resolution. Estimations of the spin-fluctuation frequencies in La-214 indicate strong temperature dependence in the range of 10^{-13} s at RT and 10^{-10} s at low temperatures, a time scale very well covered by the above method. For channeling to occur, the accelerated He ions are directed along a main crystallographic direction and undergo a sequence of glancing collisions with close-packed lattice elements (chains or planes).

Many parameters influence the critical angle for channeling and are reflected on the measured full width at half maximum (FWHM) of the channeling angular scan. Most important – and very specific for the goal of this experiment – are incoherent displacements of the atoms from their regular lattice sites. Coherent displacements like those of thermal expansion are less important. Other important parameters are, e.g., the energy of the ions, the atomic numbers of the impinging and scattering ions, the interatomic spacing, and the electron screening potential.

Sharma et al. (2000) used for their experiment single crystals with $\Delta T_c < 1$ K. Variation of the oxygen content was achieved with annealing in O_2/N_2 gas mixtures. Rutherford backscattering was measured between 300 and 30 K as a function of the tilt angle about the [001] axis of the crystals to determine the non-channeled amount of incident ions. The atomic displacements were extracted from the measured FWHM and were found to be appreciably larger than the Debye thermal vibration component. Subtraction of this thermal background led to the *excess atomic displacements* $u_{ex.}$ whose dependence on temperature with as parameter the oxygen nonstoichiometry are given in fig. 89. All three investigated stoichiometries with $T_c = 45$, 65 and 92.5 K show appreciable changes of slope at three different temperatures T_1, T_2 and T_3, indicating cross-over or phase transitions, with values varying with the oxygen nonstoichiometry. For all investigated stoichiometries $T_3 \approx T_c$ and the T_1 and T_2 are located in the normal state. The changes of the excess atomic displacements are most pronounced for the optimally doped samples (bottom), where the characteristic temperatures have the values $T_1 \approx 230$ K, $T_2 \approx 150$ K.

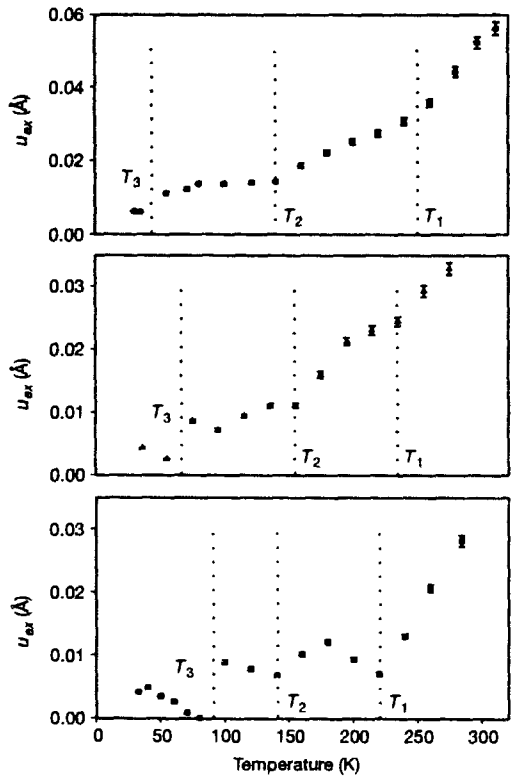

Fig. 89. Excess atomic displacements u_{ex} measured by ion channelling. Temperature dependence for three different stoichiometries, $T_c = 45$ K (top), 65 K and 92.5 K (bottom). The three characteristic temperatures support the "stripe phase model" (see text). After Sharma et al. (2000).

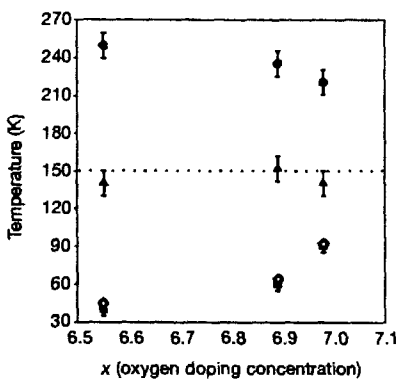

Fig. 90. Dependence of the characteristic temperatures of fig. 89 on the oxygen doping. T_1, circles; T_2, triangles; T_3, squares; T_c, open diamonds. After Sharma et al. (2000).

Figure 90 shows the dependence of T_1, T_2 and T_3 on the oxygen doping. A slight dependence is found for T_1, nearly independence for T_2 and the T_c dependence for T_3.

Sharma et al. (2000) discuss their results in conjunction with the stripe-phase scenario (Emery et al. 1997). The assignment of T_1 to the stripe formation temperature where

the holes segregate into stripes is not straightforward. The slight dependence on oxygen doping of T_1 is in contrast with a more pronounced dependence predicted by this model or with the excitation energy gap from Giaever tunneling and photoemission measurements (Deutscher 1999). The authors point out, however, that the lattice fluctuations they study with channeling are charge fluctuations. On the other hand the tunneling and photoemission experiments detect fermions with both charge and spin. The difference between the channeling data and these experiments indicate that different energy scales are associated with the spin and charge quantum numbers in the normal state. One may, therefore, conclude that a non Fermi-liquid scenario with spin–charge separation is valid.

The assignment of T_1 as *the stripe formation temperature* helps to understand the increase of $u_{ex.}$ with decreasing temperature (maximum between T_1 and T_2, fig. 89, bottom). Bianconi et al. (1996) have found that the formation of stripes leads to two different regions having different lattice constants. Two different lattice constants would enhance the excess displacements. With further decrease of temperature, $u_{ex.}$ decreases until it reaches T_2.

The lack of x dependence of T_2 is in very good agreement with the *temperature for pairing within a single stripe* predicted by Emery et al. (1997) or the pseudo-gap temperature found experimentally (Batlogg and Emery 1996) at nearly 150 K. This would mean that an increase of $u_{ex.}$ should be expected at lower temperatures when superconductivity sets on in the individual stripes. This is shown in fig. 89 (bottom). At $T_c = T_3$ we expect an increased coherence of the lattice and this is manifested in an abrupt drop in $u_{ex.}$. The increase at $T < T_3$ can be assigned to spin-fluctuation dynamics, an indication of slowing boundary fluctuations which can be followed easier by the lattice. This work of Sharma et al. (2000) supports the *spin–charge separation* scenario as the superconducting properties of 123-O_x evolve with oxygen doping.

Additional support for the *stripe-phase* scenario is coming from neutron scattering experiments by Mook et al. (2000), culminating a series of important papers by this group (Mook et al. 1993). Thus Dai et al. (1998) and Mook et al. (1998) were able to show the appearance of spin fluctuations, and Mook and Dogan (1999) that of charge fluctuations, supporting the existence of a *dynamic* stripe phase in 123-O_x crystals with high T_c. The interpretation of these results was, however, ambiguous due to the fact that the magnetic fluctuations due to the spins had a fourfold satellite pattern at incommensurate points around the $(\frac{1}{2}, \frac{1}{2})$ magnetic reciprocal lattice position, which allowed also the possibility of nested Fermi surface. On the other hand, for a 1D stripe phase only one set of satellites is expected. Tranquada et al. (1995) and Tranquada (1998) proposed that the fourfold symmetry could be the result of stripes alternating in direction for consecutive planes along the c-axis.

Mook et al. (2000) solved this problem after recognizing that the fourfold symmetry is the result of the twinning of the large crystal (25 g) they were using in the past. By applying pressure they could partially de-twin a smaller crystal and discriminate the single sets of satellites resulting from the two twin orientations. They showed for 123-$O_{6.6}$ that the incommensurate magnetic scattering has a 1D modulation vector. Based on this result Mook et al. (2000) revisited their results on charge fluctuations obtained by investigation

of the phonon spectra (Mook and Dogan 1999). They were able to show that these results also are consistent with 1D charge fluctuations.

The work of Sharma et al. (2000) and Mook et al. (2000) supports the dynamic stripe theory against the Fermi-liquid approach (Zaanen 2000). For materials research it is important to know that stripe phases appear also in 123-O_x, in order to scout for possible mesoscopic structural indications of their presence as a function of nonstoichiometry.

8. Overdoped phase – III: phase separation in the Ca-overdoped regime, Y(Ca)-123-O_x

Already at the beginning of the HT_c era, Ca doping was assumed to increase the carrier concentration in 123-O_x (Tokura et al. 1988). Using the simple electroneutrality condition discussed in sect. 5.1,

$$Q + 3(2 + p) = 2y, \tag{5}$$

they assumed – and after them a whole series of other authors (sect. 5.1, e.g., Tallon et al. 1995) – that the decrease of the positive charge due to the substitution of Y^{3+} by Ca^{2+} will result in a linear decrease of the oxygen content. In all these investigations, the decrease of T_c was considered as the only evidence for overdoping.

All these studies of Ca-doped 123-O_x in the literature have been performed on samples that had not been fully oxygenated, and *none was supported by a direct chemical analysis of the oxygen content* with a high-resolution method. Böttger et al. (1996) presented the first systematic study on *fully oxygenated samples* with neutron diffraction.

The samples have been synthesized by a solid-state reaction, similar to the CAR samples (sect. 3.1.2) to achieve maximal oxygen loading. Stoichiometric parts of high-purity powders (Y_2O_3, $CaCO_3$, $BaCO_3$, CuO) were mixed in ethanol and homogenized in a ball mill, then dried for one day (100°C). The mixture was subsequently annealed in air at temperatures 860°C (to avoid formation of eutectics), 870 and 885°C for 16 h. Further annealing in flowing oxygen at 900°C (8 h), 920°C (8 h), 950°C (70 h), and 960°C (30 h) was performed in order to expel as completely as possible the carbonate traces. To improve the oxygen diffusion and homogeneity, thorough grindings were performed between these annealings. To achieve maximum oxygen contents a *very slow cooling rate (4°C/h)* was used from 500°C to room temperature.

A structure refinement (XRD and NPD) as a function of the Ca and oxygen content has been performed on 11 Ca-doped compositions (Ca 2–20%) reaching up to the solubility phase boundary (20%) and one highly O-overdoped sample (table 10). The decrease of T_c down to 55 K and two significant structural changes with increasing Ca-content,

– a large increase of the apical bond by 1.25%, and
– a decrease of the orthorhombic strain by 30%,

supported the generally accepted picture of overdoping.

8.1. *Oxygen content: the A and B states*

In the first exact investigation of the oxygen content (Böttger et al. 1996) using high-resolution volumetric determination (sect. 3.1.3), the linear dependence of the oxygen content on Ca doping was proven not to be correct (Kaldis 1997). As mentioned earlier, this powerful analytical method has a very high accuracy, $\Delta x = \pm 0.001$, due to calibration with the coulometric decomposition of water; it allowed, therefore, for the first time an exact investigation of the dependence of the oxygen content on the Ca doping. Figure 91 shows this dependence which strongly deviates from the dotted line predicted by eq. (5) (Tokura et al. 1988) as shown recently (Kaldis 1997). This result shows that *in spite of the large Ca doping the oxygen content decreases only slightly and oscillates between two "states" A* ($x = 6.980$) *and B* ($x = 6.966$). Thus, starting with an oxygen-overdoped (O-O) 123 material having a very high oxygen content, $x = 6.994$ at (0% Ca), the oxygen content at 17% Ca reaches only $x = 6.952$ instead of the expected 6.905 (the 20% Ca samples were not analyzed due to a small amount of a second phase found by X-ray diffractometry). *Almost all of the decrease of oxygen in the range 0–15% Ca is reached already at 2% Ca.* It is also interesting that the phase boundaries of the overdoped phases are approximately the same ($x \approx 6.95$ and 6.98) both for the Ca-overdoped and the O-overdoped samples, fig. 92. Application of oxygen pressure (100 bar at 900 K) on the oxygen-poor state B (at 10% Ca) ($x = 6.96$) shows that it can be further oxidized. This oxidation stops exactly at the A state ($x = 6.98$), indicating that this is the state with the highest possible oxygen content, which the B states tend to reach (fig. 93). For Ca% $\geqslant$ 15

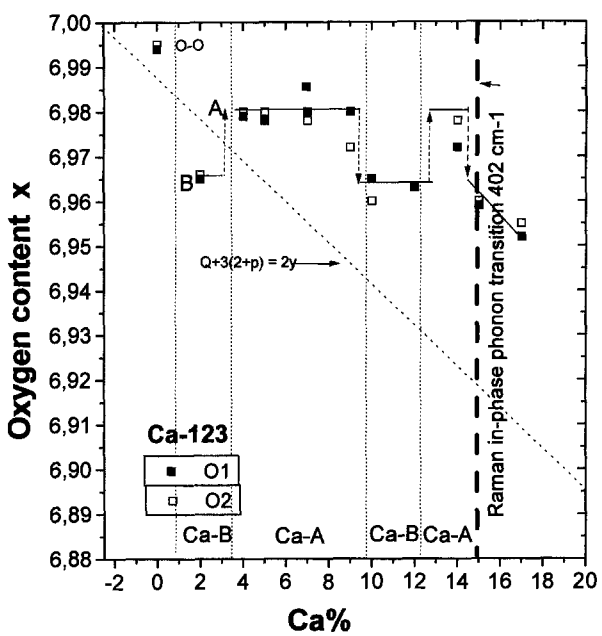

Fig. 91. Change of the O content x of $Y_{1-y}Ca_yBa_2Cu_3O_x$ (Ca-123-O_x) with Ca%. This is the first direct oxygen determination in the literature for this system. The assumption that the linear relation of eq. (5) is valid, is not correct (see text). The linear dependence used in the literature is also shown (diagonal dotted line). After Kaldis (1997) and Kaldis et al. (2000b).

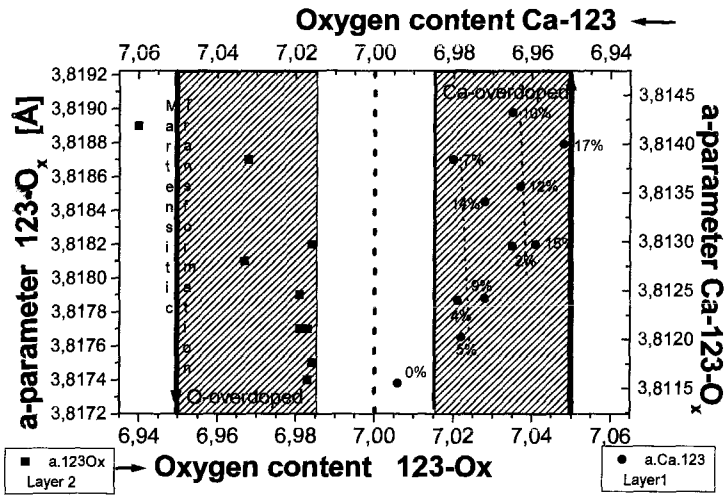

Fig. 92. Oxygen-poor phase boundaries of the overdoped phases 123-O_x and Ca-123-O_x in the example of the a-parameter: bold vertical axes at $x \approx 6.95$. Oxygen-rich phase boundaries at $x \approx 6.98$. Lower x-axis: oxygen content of 123-O_x. Upper x-axis: oxygen content of Ca-123-O_x. The oxygen has been directly determined with ± 0.001 accuracy. After Kaldis et al. (2000b).

the oxygen content seems to follow the slope of eq. (5). The oxygen content of the Ca-free sample (oxygen-overdoped, O-O state), synthesized under the same conditions, is appreciably higher (6.994). We also note that in fig. 93 and table 10 a hysteresis appears for the A → B transitions at 9–10 and 14% Ca.

In view of these unexpected results of the near independence of the oxygen content on the Ca doping, the question of the homogeneity of the samples must be discussed. It is known from the literature that it is very difficult to obtain homogeneous Ca-doped 123 samples, one of the problems being the substitution of Ca both for Y and Ba (Buckley et al. 1991). The substitution site depends on the chemical history of the samples. Thus, polycrystalline samples *slowly cooled* (Böttger et al. 1996) show, up to 20 wt% Ca, *no substitution of the Ba site.* This has been confirmed for the same samples by Röhler et al. (1999a) with Ca-EXAFS. On the other hand, single crystals, probably contaminated with some Al, do show, above 11 wt% Ca, substitution of both the Y and Ba sites (Böttger et al. 1997). Similar results have been achieved for single crystals grown in zirconia crucibles by Schlachter et al. (1999). This anomalous dissolution can be explained with the percolation limit of the Ca-123 clusters (sect. 8.3.1), which overlaps with 11%. Obviously for single crystals, a segregated phase with higher Y substitution is less energetically favourable than a combined Y and Ba substitution.

Rietveld refinement with XRD is a very sensitive method for differentiating between Ca and Ba or Y, because the numbers of electrons are quite different: $Z = 20$ (Ca), 39 (Y) and 56 (Ba). Combined NPD and XRD also clearly show that slowly cooled, highly oxygenated, polycrystalline samples are single phase up to 17 wt% Ca. A small amount

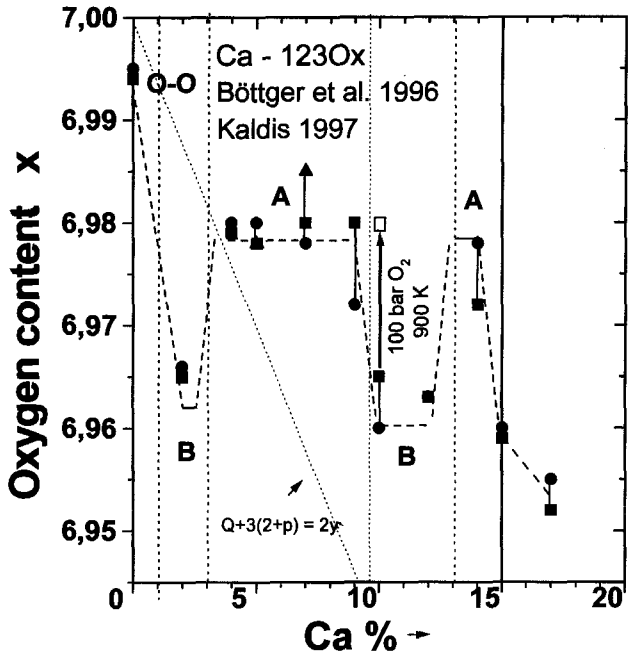

Fig. 93. Oscillatory change of oxygen content vs. Ca%, as determined with high-resolution oxygen analysis. Application of O pressure (100 bar of O_2 at 900 K) on the oxygen-poor state B leads to its oxidation to the A state (arrow, 10% Ca). Note hysteresis phenomena near the A–B transitions, with increasing Ca%. The dotted and dashed lines are guides to the eye. After Böttger et al. (1996), Kaldis (1997) and Kaldis et al. (2000b).

of a second phase appears at 20%. The Ca content is unambiguously determined with these structural investigations (within 4%) and in agreement with the composition of the starting material. The incorporation of Ca is further demonstrated by the above-mentioned strong decrease of T_c and the expansion of the apical bond. We note, however, that the diffraction and magnetic measurements have large length scales.

Microprobe analyses of cold-pressed tablets have been performed for the 9% and 14% Ca compositions where the A–B changes appear and the O analysis (table 10) shows some scattering. For comparison the 4% and 17% Ca samples were also investigated, together with the undoped (0%) sample. The results followed the calculated changes of the Y, Ba and Cu contents with increasing Ca doping for substitution of the Y by Ca (figs. 94–96). The spread in the measured values for a given Ca content shows the degree of homogeneity of the metal sublattice. The deviations are negative for Ba and Y contents and are limited to 3% or less. In fact, deviations of 1.5–3% appear only for the 9% and 14% Ca compositions near the transitions of the oxygen content A $\rightleftarrows$ B (fig. 93), the 4% and 17% compositions having much smaller deviations (0.6–0.7 and 0.1–0.5% respectively) supporting a hysteresis associated with these transitions. In addition, for the Cu content a small systematic negative deviation is found (fig. 96), possibly due to the well-known Cu1 defects. Some slight excess of Cu exists in the transition compositions

Table 10
Volumetric determination of oxygen (Conder et al. 1989) in Ca-doped 123[a]

Ca content (%)		Oxygen determination		
		1st Analysis	2nd Analysis	3rd Analysis
0		6.994±0.001	6.995	
2	B → A	6.965	6.966	
4		6.979	6.980	
5		6.978	6.980	6.978
7		6.980	6.978	6.985
9	A → B	6.980	6.972	
10		6.965	6.960	
12	B → A	6.963	6.963	
14	A → B	6.972	6.978	
15		6.959	6.960	
17		6.952	6.955	
20		–	–	

[a] All samples were analyzed twice, except two analyzed three times. After data of Böttger et al. (1996).

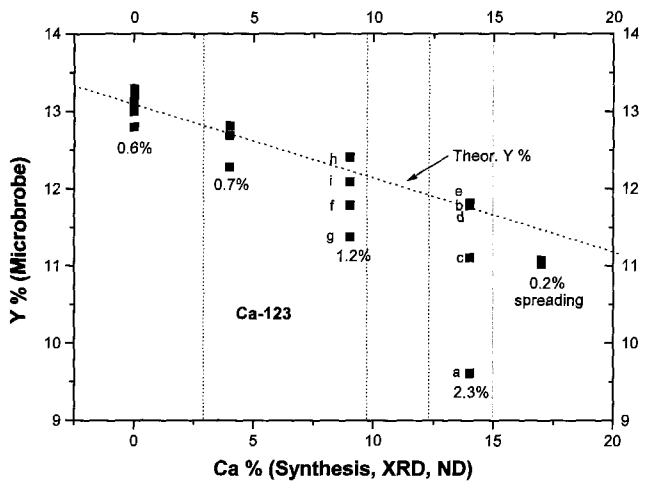

Fig. 94. Microprobe analysis for Y as a function of Ca content. The theoretical Y content and the spreading of data for each Ca content are also given. Note increased spreading near the transitions. After Kaldis et al. (2000b).

(9, 14% Ca; A) which are compensated by slightly less Ba and Y. This nonstoichiometric disorder is small enough to evade detection by the structure refinements and the EXAFS investigations. Further discussion of the disorder of these samples due to ageing in sect. 8.3.1.

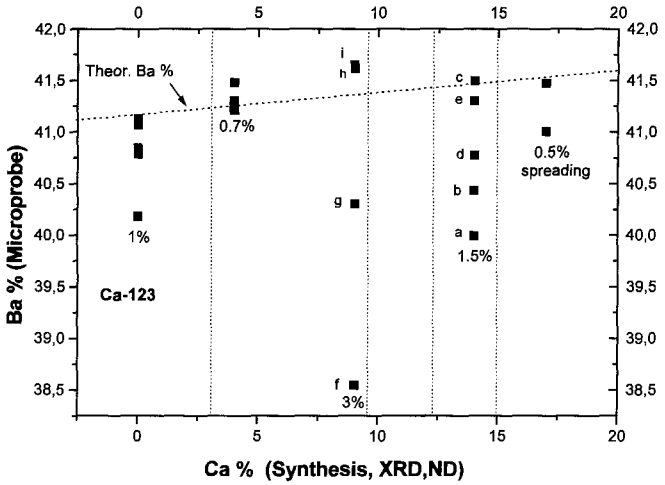

Fig. 95. Same as fig. 94, but for Ba content (see text). After Kaldis et al. (2000b).

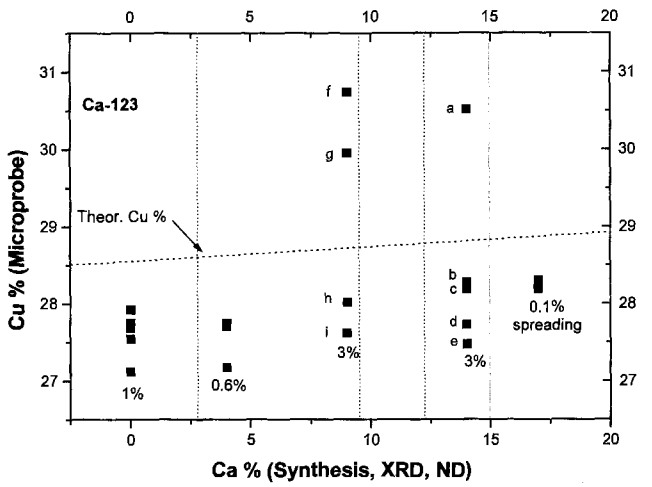

Fig. 96. Same as figs. 94 and 95, but for Cu content (see text). After Kaldis et al. (2000b).

The instabilities leading to the changes between the states A and B (figs. 91 and 93) were considered to be a kind of phase transitions (Kaldis 1997). The compositions at which they appear are marked in all figures by vertical dotted lines. Figures 91 and 93 do not show the average of the analytical oxygen determinations of each sample, as usual in the literature, but the results of the individual determinations for each batch (see also table 10). Owing to the high accuracy of the analytical method deviations above the analytical error $\Delta x = \pm 0.001$ tend to indicate statistical deviations in the homogeneity of the batches. Whereas very good agreement is achieved between the two oxygen

determinations for most samples, indicating good oxygen homogeneity, clear deviations are found near 9–10% Ca and at 14% Ca, in agreement with the nonstoichiometric disorder found by the microprobe investigations. This spreading of the data can be attributed to hysteresis associated with the A $\rightleftarrows$ B transitions.

Additional support for the existence of transitions or cross-overs associated with the change of O content is the fact that miscibility gaps could not be traced up to now with XRD and ND (Böttger et al. 1996). It seems, therefore, probable that B $\rightarrow$ A transitions take place in the ranges 2–4% and 12–14% Ca and A $\rightarrow$ B transitions in the ranges 9–10% and 14–15% Ca. The solid or dashed lines and arrows (guides to the eye) joining the data in figs. 91 and 93 illustrate this possibility.

The question arises now, what is the reason for the unexpected deviation of the oxygen content from the predictions of the electroneutrality condition? Inspection of eq. (5) shows that changes of the oxygen content may arise for two reasons: either changes of the charge of the cations or of the charge per $(Cu–O)^{+p}$ pair. Taking into consideration the anomalous incorporation of Ca into the lattice, discussed in sects. 8.3 and 8.4, it seems possible that such changes appear due to *screening effects of the charge of* Ca^{2+}. Variations of this screening with increasing Ca content may lead to the A$\leftrightarrow$B changes of the oxygen content. The spreading appearing in the oxygen and heavy-metal contents (figs. 94–96) at these changes, can be considered to result from the hysteresis of phase transitions triggered by the variation of the *effective* Ca^{2+} charge. These transitions and the general deviation of the experimental curve from eq. (5) would then be associated with changes of the localization of holes with Ca doping (sects. 8.3, 8.4) which could proceed stepwise. Thus, the A $\rightleftarrows$ B transitions may be attributed to slightly different oxygen ordering configurations triggered by the Ca distribution. It is due to the extreme accuracy of the oxygen determination that they can be detected.

8.2. *Structural, optical and magnetic characterization of Ca-123-O_x*

In view of the extreme resolution of the oxygen determination, $\Delta x = \pm 0.001$, due to the coulometric calibration (Conder et al. 1989), it is clear that many physical measurements do not have the necessary resolution to trace effects of that order. In characterizing the properties of the Ca-doped samples, the only ones "fully" oxygenated in the literature, it is reasonable to look also for indications of the existence of the A and B oxygen content states.

8.2.1. *Structural characterization*

Plotting structural parameters and some bond lengths vs. oxygen content leads to segregation of the data into two groups corresponding to the A and B states of figs. 91 and 93. Figures 97a–c show the dependence of the *a*-, *b*- and *c*-parameters (Böttger et al. 1996) on the oxygen content (Kaldis et al. 2000b), and figs. 98a–c show their dependence on the Ca content (Böttger et al. 1996).

In fig. 97 there is not much scatter in the data of each group, almost none for the *c*-axis. In fact, the linear scaling of the lattice parameters with the two groups of oxygen

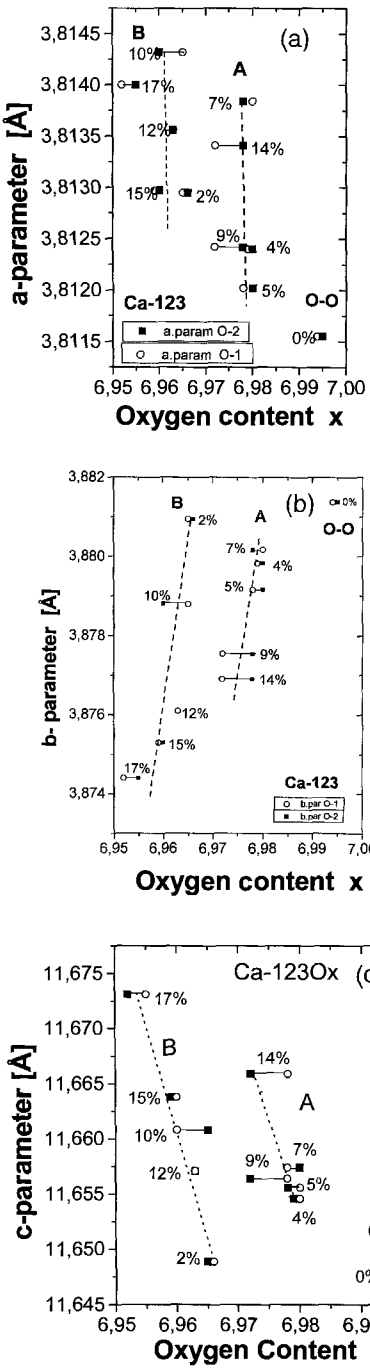

Fig. 97. (a) *a*-parameter of Ca-123-O_x as a function of oxygen content *x*, for various Ca contents (given in %). (b) *b*-parameters. (c) *c*-parameters. Note the good scaling with oxygen content. The data segregate into two groups corresponding to A and B. Circles (squares): 1st (2nd) O determination. After Kaldis et al. (2000b).

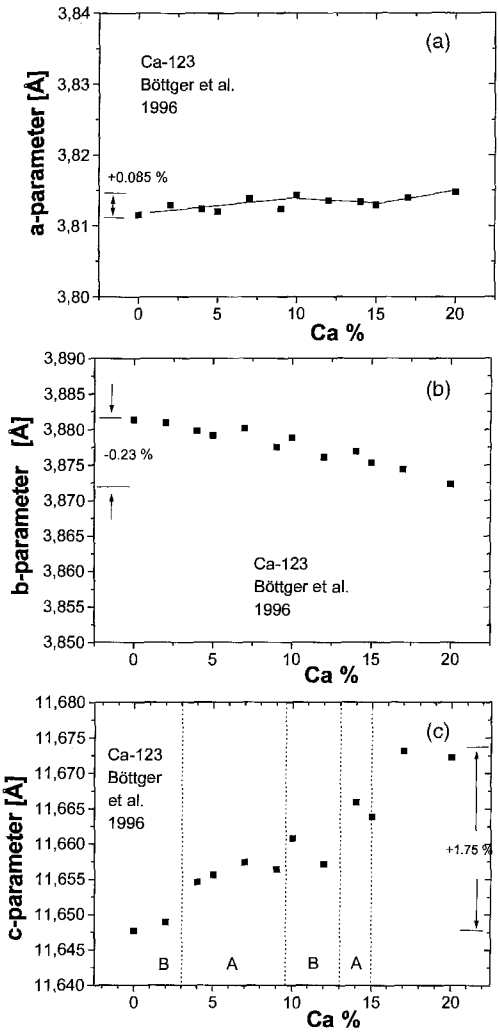

Fig. 98. Lattice parameters of Ca-123-O_x vs. Ca%: (a) *a*; (b) *b*; (c) *c*. Note that *a* is almost independent of Ca%, *b* changes little, and only *c* increases appreciably (cf. table 6; see text). After data of Böttger et al. (1996).

Table 11
Relative changes of the lattice parameters and apical bond with doping

Doping	Relative change (%)			
	a-parameter	*b*-parameter	*c*-parameter	Apical bond
123-O_x	−1.15	+0.5	−1.45	−7.6
Ca-123O_x	+0.085	−0.23	+1.75	+2.8

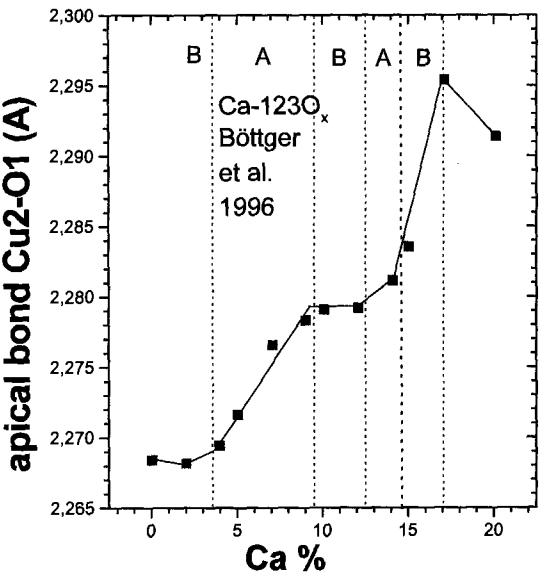

Fig. 99. Change of the apical bond with Ca%. Slope changes at the A–B transitions (vertical dotted lines) can be seen at 4, 9, 12, 14 and 17% Ca. After data of Böttger et al. (1996).

content (A and B) is remarkable. Figure 98 shows the expected opposite trends to the O doping shown in fig. 26, supporting the current ideas of overdoping. It is interesting to note that the *relative changes* of the lattice parameters with doping are appreciably different for Ca doping (0–20%) and O doping ($x = 6.5$–7.0) as shown in table 11. We may, therefore, conclude that Ca doping, in contrast to O doping, affects only slightly the *a*-axis, to some degree the *b*-axis, and *more strongly the c-axis.* This shows rather small interaction with the superconducting planes and the oxygens in general. The expansion of the *c*-axis is also due to the larger Ca ion. The apical bond is also less affected by the Ca doping. An influence of the A and B states may be seen in the plot of the apical bond vs. Ca% (fig. 99), a bond length crucial for the charge transfer (sect. 3.2.1). Five different ranges appear which seem to be related to the B and A states (vertical dotted lines). The increase of the apical bond is interrupted in the range 10–14% Ca and continues with higher slope at >14% Ca. As we will see, changes in the 14–15% range appear in most properties (magnetic, Raman, EXAFS).

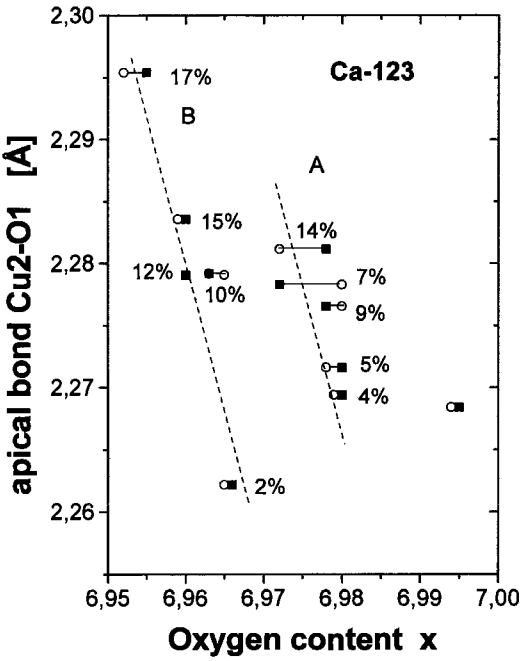

Fig. 100. Scaling of the apical bonds with oxygen content for various Ca%. The data segregate very well into the B and A groups. Structural data from NPD at 1.5 K (Böttger et al. 1996). After Kaldis et al. (2000b).

Similar to the lattice parameters also the apical bond scales very well linearly with oxygen (fig. 100).

8.2.2. *Raman characterization*

The advantages of micro-Raman measurements for such investigations were discussed in sect. 5.5. We mention here that not only macroscopic but partly *mesoscopic statistics of the distributions of phases as a function of the dopant* become available.

Recent micro-Raman investigations of these samples (Palles 2000, Palles et al. 2000b) showed the existence of phase separation with Ca doping. Several new modes were observed, some scaling with Ca content and some scaling with oxygen content, indicating phase separation. In addition to the well-known B_{1g} mode (out-of-phase vibrations of the plane oxygens O2 and O3) at 340 cm^{-1}, another mode with the same symmetry appears at ~322 cm^{-1}; its intensity increases with Ca content.

More interesting in the present context are the changes appearing in the A_g phonon (in-phase vibrations of O2, O3). As we have discussed earlier, this phonon is associated with the dimpling of the superconducting planes which undergoes appreciable changes in the oxygen-overdoped range of 123-O_x (sect. 6). In addition to the main in-phase mode at 429 cm^{-1} a new mode appears at ~402 cm^{-1}; its intensity increases also almost linearly with Ca content. But it is the main in-phase mode which seems to reflect the changes between the A and B states:

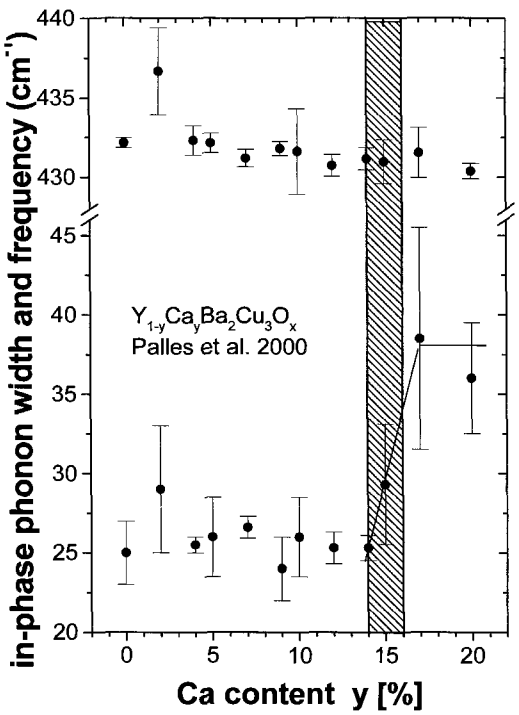

Fig. 101. Raman in-phase phonon (O2,O3 vibrations) width vs. Ca%. Note the abrupt increase of width above 15% Ca. After Palles (2000) and Palles et al. (2000b).

- Its width increases appreciably above ~14–15% Ca due to an increasing contribution of the 402 cm^{-1} mode, indicating the possible existence of a phase transition coinciding with the last A → B transition and the end of the oxygen content oscillations (figs. 91, 93). Figure 101 shows this effect.
- Particularly at low temperatures a splitting appears which could be fitted with three Lorentzians at 402, 429 and 439 cm^{-1}. The relative intensity of the main in-phase phonon peak 429 cm^{-1} to that of the 429+439 peaks seems to scale with the oxygen-content variations between the states A and B but not with the Ca content. Figure 102 shows this dependence of the relative amplitude on Ca%. Five to seven crystallites have been measured from each Ca composition. Clearly the relative intensity does not scale with the Ca content, but it seems to scale fairly well with the oxygen content (figs. 91, 93). The frame of the dotted and solid lines and the arrows shows an idealized behavior which is compared with the data, and it is only a guide to the eye. Again, the spreading of the values for different crystallites of the same Ca content at 10, 12 and 15% Ca exists, which can be attributed to hysteresis and pinning effects due to the existence of transitions between the A and B states (see sect. 8.1).

Additional evidence exists for the transition at 14–15% Ca (the last A–B transition) from other measurements:

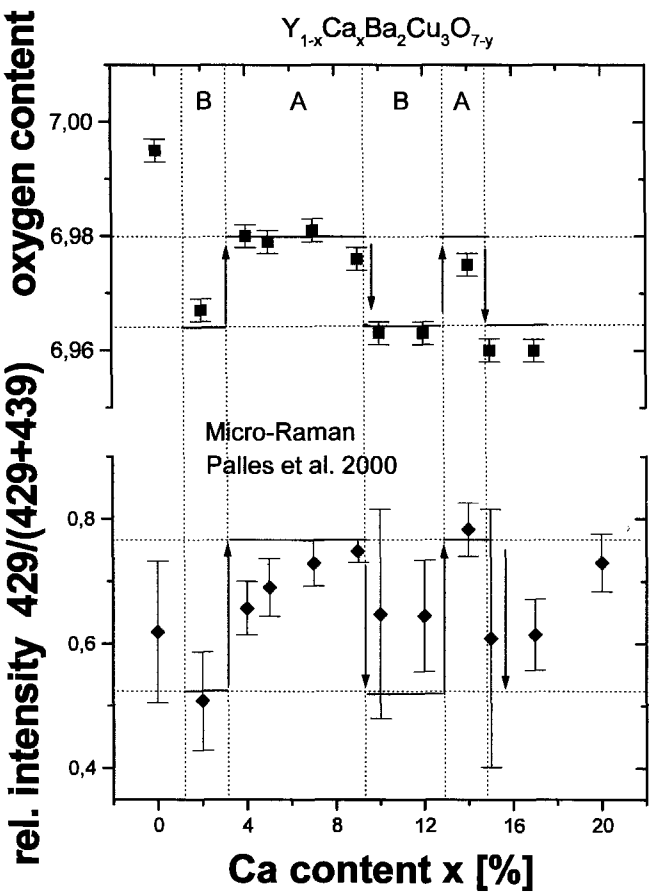

Fig. 102. Upper part: oxygen content vs. Ca%. Lower part: comparison of the relative intensity of the Raman in-phase modes 429/(429+439) vs. Ca% with the A–B transitions of the oxygen content. The 439 cm^{-1} mode is a new mode appearing with the Ca doping; however, it does not scale with Ca and it seems to scale with O. After Palles (2000) and Palles et al. (2000b).

- The apex phonon width shows an appreciable increase at 15% Ca due to the appearance of new modes.
- The T_c vs Ca% shows an anomaly in this range (see below).
- The dimpling (Cu2–O2,O3) vs Ca% shows a transition both in neutron diffraction (Böttger et al.) and EXAFS (Röhler et al. 1999b) measurements (see below). The latter changes slope at 9% and 15% Ca.

8.2.3. *Magnetic characterization*

As discussed earlier (sect. 7.1), oxygen-overdoped 123 shows two critical temperatures (see e.g., fig. 85). The same effect is observed in Ca-123 (Kaldis et al. 2000b).

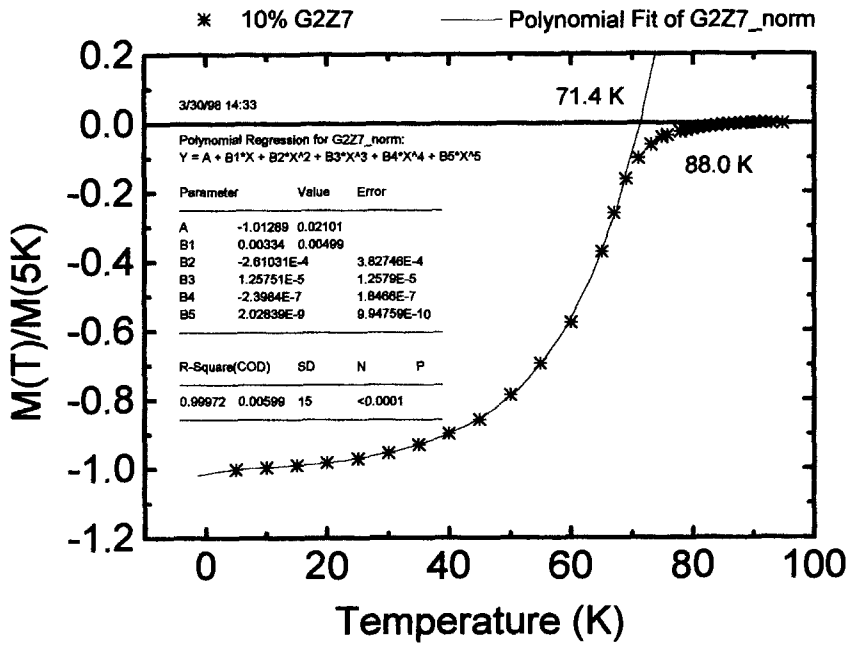

Fig. 103. Normalized magnetization curve for Ca-123-O_x with 10% Ca. The onset $T_{onset} = T_{c2}$ is 88.0 K. Polynomial fitting results in $T_{c1} = 71.4$ K. After Rossel et al. (1999) and Kaldis et al. (2000b).

Figure 103 shows a typical normalized magnetization curve for 10% Ca. The change of curvature at the higher temperature range leading to a second T_c (T_{c1}) is clearly seen (cf. figs. 86, 87). Due to the wider transitions of the Ca-doped samples, T_{c2} was not determined by the Shoenberg method (Zech et al. 1994, cf. sect. 7.3) but by a polynomial regression (Rossel et al. 1999). In this particular case, the onset temperature was found to be $T_{c,\,onset} \equiv T_{c2} = 88.0$ K, and the fitting gave $T_{c1} = 71.4$ K. Figure 104 shows the dependence of both these temperatures on the Ca content. Whereas T_{c1} changes drastically down to 47 K, T_{c2} remains near the T_c value of the oxygen optimally doped and overdoped 123 region, changing very little even for large Ca concentrations. As discussed in sect. 7.3 the appearance of two T_c's is evidence for phase separation. It can be argued that similarly to the O-overdoped region, the optimally doped phase is thermodynamically more stable and it continues to exist even under higher overdoping leading to *physical phase separation* in optimally doped and overdoped clusters. It is interesting to compare the T_c of fig. 105 with the corresponding one for oxygen-overdoped 123 (fig. 85). The onset temperature T_{c2} remains also constant in the range $x > 6.95$ and has the same values for both the oxygen-overdoped and the Ca-doped ranges. The splitting of the diamagnetic transition in the Ca-doped phase, similar to the O-overdoped phase, is a strong indication for *physical phase separation.* We note that if chemical phase separation were present, then the T_c's should form plateaus like those of fig. 45.

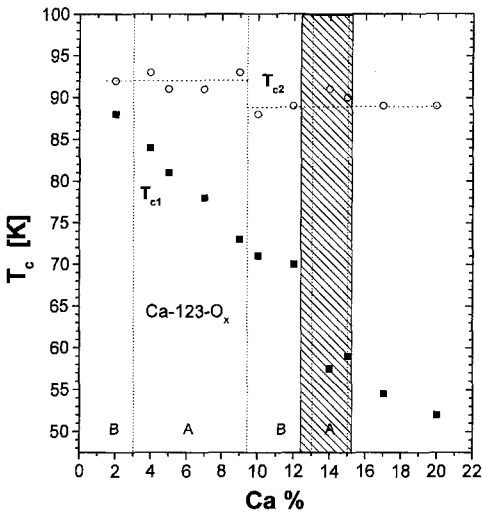

Fig. 104. T_{c1} and T_{c2} as a function of Ca%. $T_{c2,onset}$ is almost independent of the Ca doping, behaving similarly to oxygen-overdoped 123-O_x and having approximately the same value (cf. fig. 85). T_{c2} decreases strongly, and shows a strong anomaly at ~13–15% Ca (hatched area). At this concentration the width of both in-phase and out-of phase phonons increases and the dimpling change of slope takes place (EXAFS). The strong splitting of the diamagnetic transition of Ca-123-O_x indicates the existence of physical phase separation in the Ca-doped phase, similar to the O-overdoped phase. After Kaldis et al. (2000b).

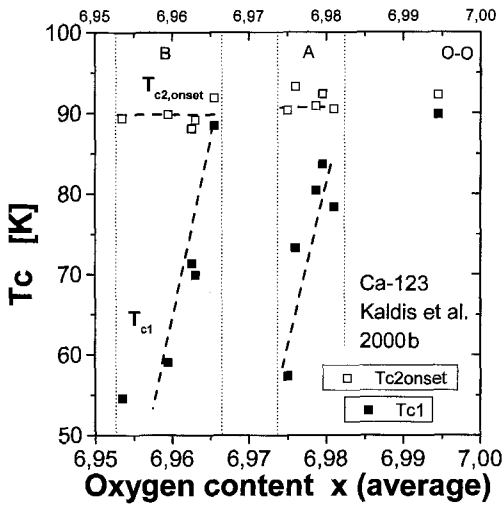

Fig. 105. T_{c1} and T_{c2} dependence on oxygen content of the 11 Ca-doped samples of fig. 104. The data scale linearly in A and B groups, showing a correlation of the A and B states with T_c. After Kaldis et al. (2000b).

The T_{c1} curve (fig. 104) shows clear anomalies with a discontinuity in the range 13–15% Ca (hatched area) which coincides with the B → A transition at 13–14% and A → B at 14–15% (cf. fig. 93), the abrupt increase of the in-phase phonon width (fig. 101) and of the apex phonon width due to the appearance of new modes. This is additional support for the phase-separation scenario. Figure 105 shows the dependence of T_c on oxygen content. Both T_{c1} and T_{c2} scale with oxygen and the data segregate in the two states A and B, indicating a correlation to superconductivity.

Figure 106 shows that the relative intensity of the Raman in-phase mode ratio 429/(429+439) (cf. fig. 102) scales well with T_{c2}, indicating that the splitting of the

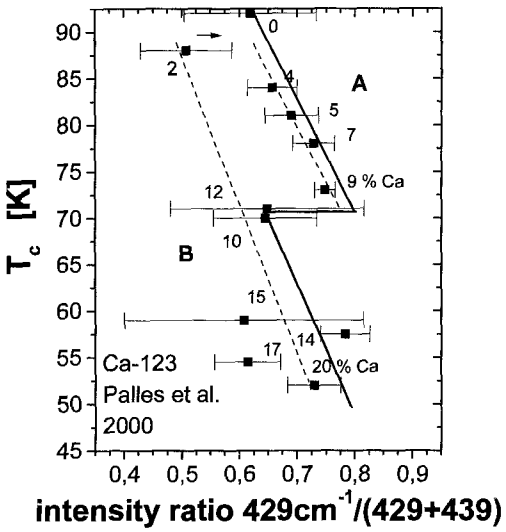

Fig. 106. Dotted lines: T_c scaling with the Raman intensity ratio 429/(429+439), of the samples belonging to groups A and B (cf. fig. 102) (see text). After Palles (2000).The solid curve connecting the data is discussed in sect. 8.3.1.

in-phase phonon is related to superconductivity. Also, this figure which is not directly related to the oxygen content, shows a good scaling of T_c with the data corresponding to the A group (4, 5, 7, 9% Ca) and a fairly good one with those corresponding to the B group. The correlation of fig. 106 is the only one where the 14% sample is grouped with the B group instead of A, indicating that the investigated crystallites have already performed the transition to B. This is an important fact, which supports the reactivity of the compositions at the A–B transitions.

Up to now the decrease of T_c due to doping with Ca was considered in the literature to be due to the increase of the hole carriers. A possible *localization* of these carriers, as we will discuss in sect. 8.4, was not taken into consideration.

8.3. *EXAFS investigations*

To investigate the controversial mechanism of Ca incorporation in 123, Y-EXAFS investigations have been performed in the same samples (Röhler et al. 1999a,b). Figure 107 shows the dependence of dimpling as a function of Ca content resulting from the EXAFS and the previous NPD (Böttger et al. 1996) investigations. A wide step-like decrease of dimpling appears at 9% Ca and ends at 14% Ca (both compositions of A–B transitions), which could not be so clearly resolved with neutron diffraction. However, the total change of dimpling is the same for both methods. Thus, these measurements also support the existence of the A and B states, but put a questionmark to the number of transitions. This will be discussed in sect. 8.3.1.

The EXAFS results concerning the incorporation of Ca were completely unexpected. Up to $R_{\text{eff}} \approx 5$ Å the EXAFS spectra of 123 show *no substantial difference with or without*

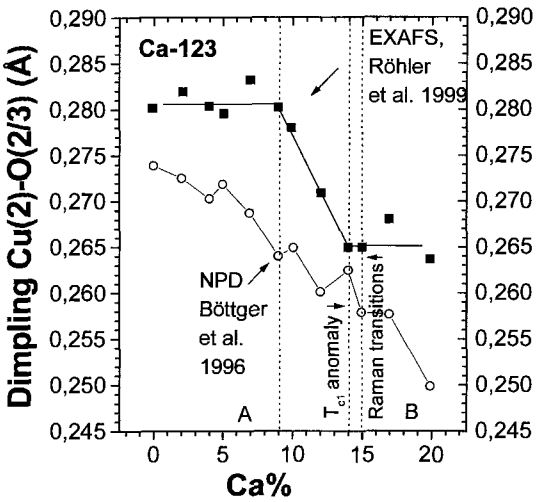

Fig. 107. Y-EXAFS investigation of the dimpling (Cu2–O2,O3) vs. Ca%. The decrease of dimpling changes slope at 9% and 14% Ca. After Röhler et al. (1999b). The transition at 14% is clearly supported by the Raman data (cf. fig. 101) and the T_c data (cf. fig. 104). For comparison the neutron diffraction data of Böttger et al. (1996) are also shown.

Ca doping. The question arises, therefore, where does the Ca enter into the Y-123-O_x lattice and in what electronic state?

- As mentioned already, both neutron diffraction (Böttger et al. 1996) and EXAFS (Röhler et al. 1999a) have shown clearly – in contrast to the findings of Buckley et al. (1991) – that in equilibrium, polycrystalline, fully oxygenated samples Ca substitutes only for Y. For single crystals, which have a completely different chemical and thermal history, Ca substitutes for Y and Ba at higher concentrations (>11% Ca) (Böttger et al. 1996, Schlachter et al. 1999).
- In view of the strong decrease of T_{c1} with Ca doping and the neutron-diffraction evidenced dissolution in the lattice (e.g., *c*-lattice parameter change) it has to be concluded that Ca is dissolved in the 123-O_x lattice but in *monodisperse* conformation, i.e. with only Y as nearest and next-nearest neighbors (Röhler et al. 1999b). This could be possible in principle up to 25% Ca, but strongly disordered Ca ions segregate in clusters of up to 4 NN. Unfortunately, model calculations show that these clusters can be resolved by Ca-EXAFS but only for measurements with photoelectron momentum $k \geqslant 12\,\text{Å}^{-1}$ (Röhler et al. 1999a). This work is presently planned.

The simplest straightforward model proposed by Röhler et al. is Ca-substituted 123 cells surrounded by the NN Y-substituted cells forming cross-like clusters of 5 distorted cells. Figure 108 illustrates this model for increasing Ca content. Röhler et al. (1999b) pointed out that if the single Ca ions percolate in a random way, the critical value for a square two-dimensional lattice would be in accordance with existing models (Stauffer and Aharony 1995), ~60% Ca. For the cross-like 5-cell clusters the critical percolation value would be five times smaller, i.e. ~12%. This is in fairly good agreement with the dimpling changes in the 9–14% Ca (fig. 107) range and also with the increases of the width of the Raman in-phase and out-of-phase phonons at ~15% Ca, found in the same samples by Palles (2000) and Palles et al. (2000b) (fig. 101). It is also in agreement

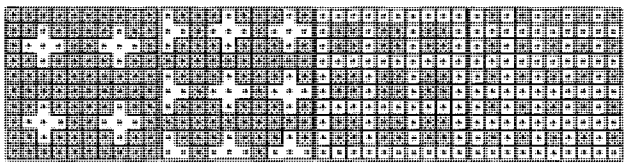

Fig. 108. Model for the monodisperse dissolution of Ca-123 in an Y-123 matrix so that all NN are Y-123. Clusters in the form of crosses, consisting of 4 distorted molecules of Y-123 surrounding 1 molecule of Ca-123 are proposed. A percolation is expected at ~12% Ca. This is in good agreement with the experiment (fig. 107). Based on this model one would expect that the holes introduced by the Ca^{2+} into the Y^{3+} matrix will be screened by the Y-123 NN. After Röhler et al. (1999b).

with the oxygen-content results (fig. 93) which show A–B transitions at 9% and 14% Ca and an end of the transitions at 15% Ca followed by a stronger decrease of oxygen. Last but not least, the dimpling change at 14% Ca is in excellent agreement with the step in T_{c2} at 14% Ca (fig. 104) showing the influence of Ca percolation on the decrease of T_c.

More information on the mechanism of the incorporation of Ca in 123 could be expected if Ca-EXAFS investigations at $k \geqslant 12\,\text{Å}^{-1}$ are performed.

8.3.1. *The A–B transitions and ageing effects*

We may now draw the balance of the correlations of the various properties of the material with the A–B transitions:

(a) Large-length-scale methods, XRD, NPD: The lattice parameters a and b change very little with Ca doping. The main change is in the c-parameter which hardly reflects the A–B transitions. The transitions become more visible in the apical bond (fig. 99) where changes of slope take place at 3–4, 9–10, 12–14, and 17–20% Ca. Plotted vs. oxygen, most structural data scale with groups A and B. The magnetization measurements T_{c1} show clearly anomalies in the range of the transitions at 12–14 and 14–15% Ca. Deviations seem also to exist in the range of the 9–10% Ca transition.

(b) Small-length-scale methods: Raman investigations give appreciable evidence for the existence of A–B transitions. At 15% Ca, splitting of the phonons characteristic for the vibrations ($\|$ c-axis) of the plane oxygens O2,O3 (dimpling), out-of-phase O2,O3 (B1g) and in-phase (Ag) (fig. 101), takes place. The latter ($439\,\text{cm}^{-1}$) splits into 429 and 439 and their relative intensity scales fairly well with the oxygen content (fig. 102).

On the other hand, as we have seen above, EXAFS show transitions only at 9% and 14% Ca. Small deviations of the data at 2%, 7% and 17% Ca are too small to be considered, although some appear also in NPD. A full reconciliation of all data would be achieved if the oxygen content of 2% Ca (B state) would be shifted to that of 4% (A state), and the 14% (A) in the opposite direction (figs. 91, 93). An error in the very well reproduced oxygen content (table 10) does not seem possible, as hundreds of measurements have shown up to now, with this extremely accurate analytical method (sect. 3.1.3). In view of the fact that each analysis uses 100 mg of material,

the above results represent the statistical average of 200 mg which is representing the average bulk properties of the sample. More suitable for an explanation seems the ageing of the samples. The oxygen analysis, XRD and magnetization measurements (without the 14% sample) have been performed nearly at the same time (Böttger 1994). The NPD which is the origin of the structural data presented here, was performed in 1995 (Böttger et al. 1996), and did not show any difference from the XRD data. The Raman measurements were performed in 1997, the microprobe measurements and the EXAFS in 1998. Additional magnetic measurements have been performed later (Rossel et al. 1999) to check the quality of the samples (these gave T_c changes not larger than 1 K), and to determine the T_c of the 14% sample. It seems, therefore, reasonable to assume that during this time some changes in the oxygen composition and the disorder of the samples in the transition ranges could take place. Thus, whereas the analysis, the structural properties and the magnetization (without 14%) give the original picture of the properties, subsequent changes of the samples are mirrored in the other measurements. Particularly vulnerable seem the transition compositions (figs. 91, 93) because, as we have seen in the example of the 10% sample, they can be further oxidized. This would explain why no substantial change has been found with EXAFS for the 2% composition.

The case of the 14% sample is more obvious. The microprobe analysis (figs. 94–96) shows that, at least after four years of ageing, this sample and that with 9%, in both of which EXAFS finds a change of slope, have a certain cationic disorder: an Y and Ba deficiency, compensated in some parts of the samples by more copper. The origin of this disorder is probably intrinsic, as already the difference in the two oxygen determinations (table 10) of these samples indicates. We have attributed this disorder to hysteresis in the A–B transitions involved. Therefore, it is reasonable to assume that given enough time this transition will proceed through the bulk of the sample. Then, with the 2% sample developing an $x \approx 6.98$ and the 14% sample an $x \approx 6.96$ the present picture of the samples, as given e.g., by fig. 106, would correspond to the solid zig-zag line with one A–B transition. Similar curves can be drawn also for other curves plotted vs. oxygen. The assumption of an ageing process is also supported by the appreciable scattering of the Raman data in the samples of 9% and 15% Ca composition.

Summing up: EXAFS and NPD show that a decrease of the dimpling takes place between A and B, starting at 9% Ca and ending at 14%. This is the percolation process of the *monodispersely dissolved* Ca which ends at Ca $\geqslant$ 14%. NPD and XRD show that the contraction of the apical bond ceases during this percolation. This shows consistency between older and recent measurements, and gives an explanation for two A–B transitions. The other transitions appear in the oxygen determination and the linear scaling of the NPD and XRD data vs. oxygen content. Their appearance is possibly the result of *Ca ordering in the monodisperse solution.* This process influences the mobility of the holes introduced by Ca. If they are trapped (Röhler et al. 1999b, Merz et al. 1998, Nücker 1999), as will be discussed in the next section, then it is possible that the oxygen content remains constant. Depending on the screening of Ca charge resulting from the conformation of its dissolution in the lattice (see above), variations of this charge may result, leading to changes of oxygen and the A–B transitions (cf. sect. 8.1).

8.4. *Ca doping and localized carriers*

From the beginning of the HT_c era it has been assumed that Ca increases the carrier concentration, their negative interaction leading to a decrease of T_c (e.g., Tokura et al. 1988, Tallon et al. 1995, Bernhard and Tallon 1996). The picture emanating from the above-mentioned work of Röhler et al. (1999a,b) could be quite different: From the cloud of Y cells surrounding the Ca cells of fig. 108 it can be assumed that the holes introduced by Ca^{2+} doping are trapped and remain localized. Therefore, not additional carriers introduced by the Ca are responsible for the decrease of the T_c, but *the decrease of the superconducting carriers due to decreasing Y-123O_x* as the substitution with Ca increases. In case of no dissolution of Ca-123 in the Y-123 matrix (chemical phase separation) the two T_c's would be observed to form plateaus (cf. fig. 45).

The exact oxygen determination of the Ca-123 samples (the first ever made) which led to the finding that A and B states have less effective charge of Ca than had always been assumed, gives a very important support to the above picture of Röhler et al. (1999b): different screenings of the Ca charge at compositions lower or higher than the percolation limit (monodispersely dissolved Ca in the 123 lattice).

Islands of Ca-123 in the Y-123 matrix (fig. 108) are in general agreement with physical *phase separation* shown by the magnetic and Raman measurements, the similar behavior of the O-overdoped 123-O_x phase (sect. 7), the general scenario of the two-component picture of Gor'kov and Sokol (1987) discussed later by Mihailovic and Müller (1997), and the literature of phase separation. The stability of the optimally doped 123-O_x phase leads to a segregation of an optimally doped superconducting matrix (Y-123) with itinerant carriers and non-superconducting clusters with localized carriers (Ca-123).These results may change our understanding of the mechanism of Ca overdoping, and probably also of the validity for 123 of the "universal" T_c vs. doping parabola (Tallon et al. 1995, Bernhard and Tallon 1996) so frequently cited.

Another very interesting investigation of Ca-123 supporting the localization of carriers and the two-component picture (Mihailovic and Müller 1997) was performed by Merz et al. (1998). They used polarization-dependent near-edge X-ray absorption fine structure (NEXAFS) measurements to investigate the unoccupied electronic structure of Ca-123-O_x samples with various degrees of Ca and oxygen doping. The investigations were performed on detwinned single crystals. Their results have shown that, as expected from the immediate vicinity of Y to the CuO_2 planes, the holes produced by the substitution with Ca appear only in the planes. This is in agreement with optical measurements by Widder et al. (1996). Independently of the Ca or oxygen doping the holes either in the planes or in the chains are associated with *oxygen sites only.* On the other hand, oxygen doping increases the number of holes both at the chain site O4 *and the apical site O1* and introduces again superconductivity in oxygen-depleted Ca-123 samples. Further, Merz et al. (1998) find that superconductivity appears only *if* ***both*** *the CuO_2 planes and the CuO_3 chains – particularly the apex sites – have an appropriate number of holes.* As Ca doping increases only the number of holes of the planes, and Ca-123 samples with depleted oxygen content do not show any superconductivity at all –

Table 12
Stoichiometry and superconductivity of *tetragonal* $Y_{1-y}Ca_yBa_2Cu_3O_x$, see also fig. 51[a]

Ca content y	O content x	Meissner (%)	T_c(90%) (K)
0	6.18	0.02	79
0.09	6.29	0.03	26
0.10	6.29	0.5	40
0.14	6.30	16	48

[a] After data of Böttger and Kaldis (1994).

independently of the number of holes in the planes – they conclude that only a proper balance of Ca doping and O doping may lead to a $T_{c,max}$ by establishing *optimal hole numbers both on the Cu2 planes and the apical sites.*

Further NEXAFS investigations on the unoccupied electronic structure of p-doped HT_c superconductors with the apex site substituted by halogen atoms (F, Cl) seem to support the above findings, provided that the homogeneity of the samples is proven (Nücker 1999). Also, in analogy to the above, in oriented single crystals of the ladder compounds $(Sr,Ca,Y)_{14}$, Merz et al. (1998) could study spectral features corresponding to hole states on both the chain and ladder sites. Their results show that the holes reside mainly on the oxygens of the chains. The results of this work give *a new charge-transfer picture and underline the importance of the apex site for superconductivity.*

Merz et al. (1998) find that Ca-doped oxygen-depleted 123-O_6 samples *are not superconducting,* in clear *contrast* to the findings of Bernhard and Tallon (1996) and Tallon et al. (1995). Whereas the earlier literature (e.g., Greaves and Slater 1989) reports superconductivity in such samples, more recent work (Hejtmanek et al. 1996) finds no superconductivity. The explanation for these discrepancies is probably the very small Meissner effect. Böttger (1994) and Böttger and Kaldis (1994) have found that whereas small steps appear in the magnetization curves, the Meissner fraction even for some Ca_y-123-$O_{6.3}$ samples is very small, so that practically most such samples are not superconducting (fig. 51). Table 12 shows their findings. These strongly O-depleted samples are of course all tetragonal.

Merz et al. (1998) can simply explain the unexpected decrease of $T_{c,max}$ found earlier by Bernhard and Tallon (1996) and Tallon et al. (1995) with increasing Ca doping for samples with optimally doped planes. The increase of carriers with Ca doping must be counterbalanced with a decrease of the O doping. The latter reduces the holes on the apical site and decreases the $T_{c,max}$. On the contrary, increase of the O doping increases both the hole population on the apical site and on the planes. As the latter become overdoped the T_c is lowered.

In conclusion, recent investigations of the 123 Ca overdoping reveal a much more complex picture consisting of alloying superconducting 123 with a non-superconducting substance (Ca-123 molecules with localized Ca-induced hole carriers) supporting once more physical phase separation.

Thus, *physical phase separation* does not appear only at the onset of superconductivity. In various forms it is also present in the oxygen-underdoped and -overdoped phases, as well as in the Ca-doped phase. It is probably an important characteristic of HT_c superconductivity.

9. Significant points of a doping-dependent phase diagram 123-O_x ($6.0 < x < 7.0$)

Starting from characteristic changes of the X-ray lattice parameters cleared from possible sample irreproducibilities by the high-accuracy oxygen analysis, it is not difficult to find that also some structural, optical and magnetic properties of 123-O_x show appreciable changes near these oxygen contents. Even more sensitive to some of these oxygen contents appear to be the oxygen Raman phonons. The conclusion is that these compositions are significant points in the T–x phase diagram and may help to illuminate further the correlation between structural and physical properties.

Figure 109 summarizes the appearance of such changes vs. x in structural (average structure XRD and ND, and local structure EM, EXAFS), magnetic (under normal and high pressure), and optical (Raman) measurements for polycrystalline samples and single

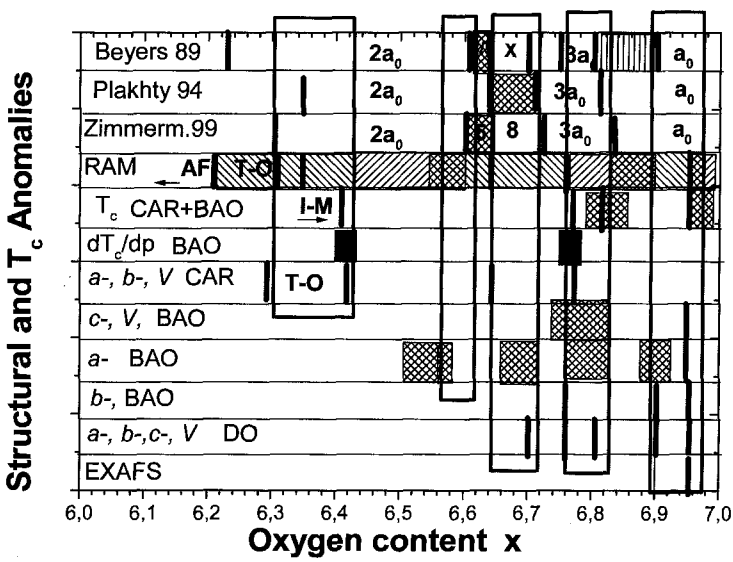

Fig. 109. Schematic illustration of phase relationships, structural transitions and T_c anomalies appearing in the nonstoichiometric range of 123-O_x. First row: EM investigations of Beyers et al. (1989). Second row: XRD and NPD on poly- and single-crystalline samples, after Plakhty et al. (1994, 1995). Third row: Hard X-ray single-crystal refinements of superstructures, after von Zimmermann et al. (1999). Fourth and fifth rows: T_c under normal and higher pressures, measured in equilibrium samples. Sixth to tenth rows: phase relationships deduced from lattice parameters of slowly cooled samples (preparation methods described in sect. 3.1.2.2). Eleventh row: EXAFS results after Röhler et al. (1997a,b, 1998).

crystals. The individual investigations have been discussed in detail throughout this review.

Although the various phases and transitions depend on the method of preparation, five concentration regions include most observed anomalies.

(a) The T–O transition appears in the range of ~6.3–6.4 depending on the investigated samples and the method used. For CAR samples the onset of the transition appears at $x = 6.3$, supported by micro-Raman on individual crystallites. Deconvolution of the apex-phonon width indicates the coexistence of *two* phases. The I–M transition (onset $x = 6.4$) seems correlated to the structural transformation.

(b) At the other end of the nonstoichiometric range (optimally doped and overdoped), changes of slope of the lattice parameters follow the onset of the optimally doped T_c plateau at $x = 6.90$. Also, changes of slope of the c-lattice parameter, ND and EXAFS manifest clearly the existence of a displacive transformation at $x = 6.95$. This transition separates the optimally doped phase of 123-O_x, which is its thermodynamically stablest form, from the *phase-separated* overdoped phase (as demonstrated from the splitting of the diamagnetic transition with onset $x = 6.95$).

(c) In the intermediate range the chain superstructures appear. The 1D character of their chains may be important for the formation of *stripes* and the superconducting interactions in general. For this reason their investigation is of importance. Originally discovered by EM, the $2a_0$ and $3a_0$ have been studied now by XRD and ND and their structure is appreciably well known. Whereas the $2a_0$ is a 3D structure, the higher members are only 2D superstructures appearing as domains of the basal (a–b) plane. Higher superstructures (ortho-V and ortho-VIII) found with XRD are only combinations of the $2a_0$ and $3a_0$. *Long-range interactions* must exist, however, forming combinations up to eight chains. These superstructures are presently considered to be metastable. Therefore, as their appearance depends on a delicate balance of various interactions, it is expected that it will be strongly influenced by the history of the samples. Two models for the generation of superstructures have been used: The classical Gibbs thermodynamics predict single-phase regions separated by two-phase regions (miscibility gaps), and the cluster variation method (CVM) uses geometrical criteria to predict a combination of parent superstructures leading to sequences of empty–full chains, without separating two-phase regions. The latter are of course difficult to prove experimentally with single crystals. Depending on the complexity of the phase diagram at high temperatures additional segregation phenomena are imposed during crystal growth. Up to now, the sequence of superstructures $2a_0$, ortho-V, ortho-VIII, and $3a_0$ have been found (single crystals near RT) without the separating two-phase regions. Lattice constants of samples resulting from one preparation method (BAO) do show horizontal parts, indicative of two phase regions, although no coexisting phases could be traced by XRD. Finally, the in-phase phonon shows steps near compositions where the na_0 superstructure series should appear. These steps seem to be separated by two-phase regions. The actual structure of these phases is not known. Also, it is not known if

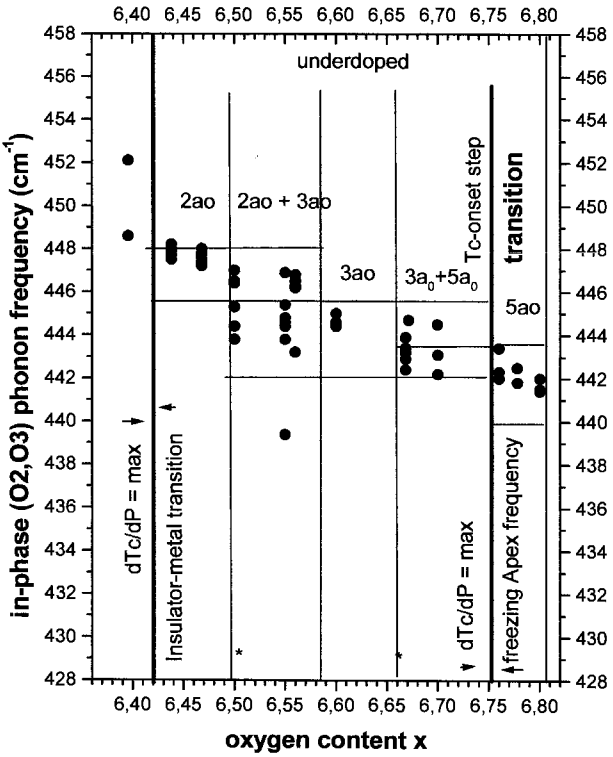

Fig. 110. In-phase phonon frequency (Raman shifts) vs. oxygen content x for $6.40 < x < 6.80$. The construction of the phase fields is discussed in sect. 5.5.2. After Kaldis et al. (2000b) with data of Poulakis et al. (1996) and Palles et al. (2000a).

these steps correspond to changes of structure or some other property, taking place at the na_0 oxygen contents.

As shown in fig. 109, phase boundaries and two-phase regions consistently appear roughly in the ranges $x \approx 6.6$, 6.7 and 6.8. As an example, we discuss here the tentative sequence of "dimpling-chain-superstructures" and construct a more detailed T–x structural phase diagram based on the room-temperature (RT) Raman measurements of the in-phase (O2,O3 vibrations $\parallel$ c-axis) phonon frequency vs. oxygen stoichiometry, and complemented by the results of structural (RT and LT), and magnetic (LT) measurements. We note once more that most of the data leading directly or indirectly to this phase diagram have been measured in large series of equilibrium samples (sect. 3.2.2) analyzed with high-accuracy oxygen volumetric analysis.

The apex and in-phase phonon vs. x diagrams (micro-Raman sect. 5.5) are shown in figs. 61, 64 and 65, and the in-phase phonon in expanded scale ($x > 6.40$) in figs. 110 and 111, respectively. The significant points of the phase diagram appear in the following oxygen contents referring to these figures:

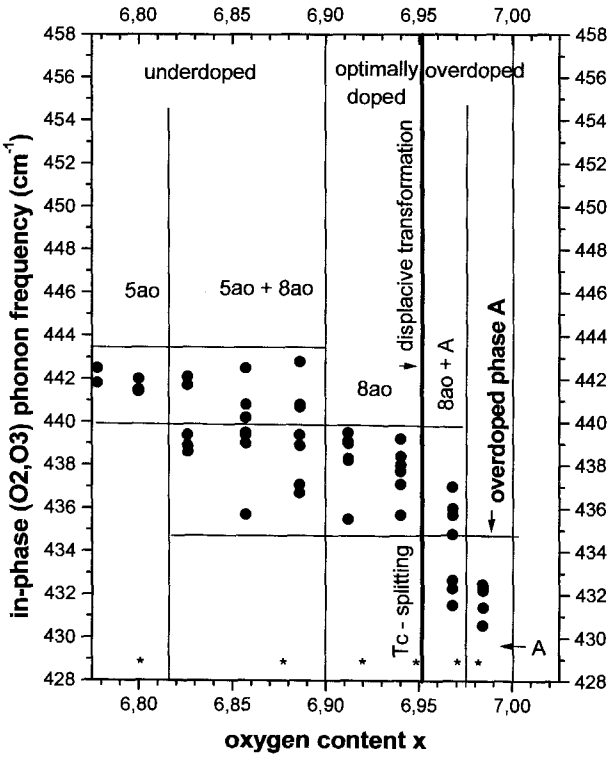

Fig. 111. Same as fig. 110, but for $6.80 < x < 7.00$. After Kaldis et al. (2000b) with data of Poulakis et al. (1996) and Palles et al. (2000a).

$x = 6.20$

Mesoscopic, RT

Micro-Raman: The Raman *apex phonon* frequency (figs. 61, 64), which – from the structure view point – is expected to be both sensitive to chain and plane changes, shows at this composition an abrupt softening with decreasing oxygen content indicating a transition inside the insulator regime. This is attributed to the AF transition at RT. The width changes also, indicating the coexistence in the whole $6.0 < x < 7.0$ range of four different phases (fig. 63). Probably *physical phase separation*, as the X-ray investigations (cf. fig. 25) up to now do not show structural changes. It is possible that the appearance of the metallic clusters takes place at 6.20 and the percolation leading to the superconducting phase at 6.40. More compositions and synchrotron radiation investigations are needed to clarify the structural picture.

$x = 6.30$

Macroscopic, RT

Structure: In the range $x = 6.30$–6.40 the *a*- and *b*-lattice parameters show a *widening* (figs. 25a,b) due to the onset of the $T \rightarrow O$ transition at 6.30.

$x = 6.40$

Macroscopic, LT

Superconductivity: The *insulator–superconductor transition* takes place near this composition probably as a result of the percolation of the hole doped clusters. At $x = 6.342$ small amounts of the material become superconducting (fig. 27b).

Superconductivity under pressure: A giant dT_c/dP effect has been measured at RT (sect. 5.4) indicating an increased compressibility at the T–O transition due to the half-filled chains and strong oxygen-ordering effects. The effect disappears at LT where the mobility of oxygen freezes (fig. 58).

Mesoscopic/microscopic, RT

Raman: Both apex and in-phase phonons show smaller changes of slope, but much less abrupt and significant than at $x = 6.20$.

Macroscopic, RT–LT

Structure: The structure reacts at the onset of superconductivity with an abrupt decrease of the *c*-axis (sect. 3.2, figs. 12c, 25d, 25e) and the apical bond (fig. 14).

$x = 6.4$–6.5

Mesoscopic/microscopic, RT

Raman: The statistics of the microcrystallites indicate the existence of two steps of the in-phase phonon (O2–O3) frequency (one between 6.40–6.43 and another at 6.50) nearly overlapping with the range of the $2a_0$ chain superstructure (fig. 110 and sect. 5.5.2).

Macroscopic, RT–LT

Structure: Single crystal Rietveld refinement in bulk single crystals shows the onset of $2a_0$ at $x \approx 6.35$ (fig. 44, sect. 5.1.1).

$x = 6.5$–6.6

Mesoscopic/microscopic, RT

Raman: The statistics of the microcrystallites show two steps in the in-phase phonon (O2–O3) frequency (one at 6.50 and another between 6.57–6.60) where two in-phase "phases" coexist. In a na_0 series of superstructures this could be the range of the $2a_0$–$3a_0$ miscibility gap (coexistence of the two superstructure phases) (fig. 110, sect. 5.5.2), *the frequencies of each phase remaining constant with x* as expected from the phase rule.

$x = 6.58$–6.66

Mesoscopic/microscopic, RT

Raman: in-phase phonon frequency indicates a single phase. The stoichiometry of the $3a_0$ superstructure is $x = 6.66$ (small asterisk in lower part of fig. 110).

$x = 6.66$–6.75

Mesoscopic/microscopic, RT

Raman: in-phase phonon frequency indicates a "two-phase" region, possibly $(3a_0 + 5a_0)$, between the $3a_0$ and $5a_0$ compositions.

$x = 6.75$–6.78

Macroscopic, LT, RT

Superconductivity: The T_c-onset shows a step (fig. 2) and a miscibility gap.

Superconductivity under pressure: Another giant maximum of dT_c/dP appears at this oxygen content (fig. 52) indicating an important transition or cross-over (sect. 5.4).
Structure: The *a*- and *b*-parameters start to deviate from linearity (fig. 25a–c).
Mesoscopic/microscopic LT, RT
Raman: The *apex phonon frequency becomes independent of the oxygen content* (fig. 61). The in-phase phonon indicates a phase boundary (transition). From stoichiometry it could be the boundary between the two-phase region ($3a_0 + 5a_0$), and the $5a_0$ superstructures (fig. 110), (sect. 5.4.2).

$x = 6.75$–6.82
Mesoscopic/microscopic, RT
Raman: In-phase phonon frequency shows a single phase behavior. The composition of the $5a_0$ superstructure would be $x = 6.80$ (fig. 111).

$x = 6.82$
Macroscopic, RT
Structure: Spikes in the unit cell volume, *c*-axis (and the other lattice parameters) of DO samples, figs. 30.
Mesoscopic/microscopic, RT
Raman: Onset of a "two-phase" region. From here on the stoichiometries of the na_0 superstructures do not follow exactly the sequence of the in-phase phases (fig. 111).

$x = 6.82$–6.90
Mesoscopic/microscopic, RT, LT
Raman: In-phase phonon frequency "two-phase" regions. The ideal stoichiometry of the $8a_0$ lies with 6.875 inside this range. In case of actual superstructures this would mean disorder: vacancies in the chains shifting the appearance of the superstructures at higher compositions (sect. 5.1.1). From the sequence, it could be a miscibility gap $5a_0$+$8a_0$ (fig. 111).
Local structure EXAFS ($T = 25$ K): Y–O2,O3 spacing remains rather independent of oxygen doping in this range (fig. 77).

$x = 6.90$
Macroscopic, LT
Superconductivity: Onset *optimally doped* region, $T_{c,max}$ plateau.
Structure: Anomalies of unit cell volume and *c*-axis of DO samples (figs. 30).
Mesoscopic/microscopic, RT, LT
Raman: In-phase phonon frequency, transition from two-phase region to a single phase region. Analogy to a phase boundary between $5a_0 + 8a_0$ and $8a_0$ superstructures (fig. 111).
Local structure EXAFS ($T = 25$ K): Onset of stronger increase of dimpling (fig. 76).

$x = 6.92$
Structure: Theoretical composition of a $13a_0$ superstructure!

$x = 6.95$
Macroscopic, RT, LT
Superconductivity: Onset of *overdoped* region.

Magnetism: Splitting diamagnetic transition (T_{c1}, T_{c2}), fig. 85.

Structure RT and LT: *c*-axis and unit cell volume anomaly BAO, DO and CAR samples (XRD, ND; figs. 26c, 29f, 30). Dimpling (Cu2–O2,O3) discontinuity neutron diffraction (fig. 66a).

Mesoscopic/microscopic, RT

Raman RT: Abrupt softening in-phase phonon (fig. 79).

Mesoscopic, RT

Local structure EXAFS ($T = 25$ K): Dimpling abrupt increase (fig. 76) due to jump of the O2,O3 plane away from the Cu2 plane.

Displacive martensitic transformation (sect. 6.4).

$x = 6.95$–6.97

Mesoscopic/microscopic, RT, LT

Raman RT: In-phase phonon possibly indicates a "two-phase" region. Analogy with $8a_0 + A$, the overdoped phase (fig. 111).

Local structure EXAFS ($T = 25$ K): Dimpling remains constant in this doping range (fig. 76).

$x = 6.97$

Macroscopic, RT

Structure: Unit-cell volume and *c*-axis anomalies (XRD, fig. 30).

Local structure EXAFS ($T = 25$ K): Dimpling abruptly decreases due to shift of the O2,O3 plane towards the Cu2 plane (fig. 76). Spike in the DO lattice parameters.

Mesoscopic, RT

Raman: In-phase phonon indicates the stability region of the *overdoped phase A* (fig. 110).

In the above, the compositions of superstructures have been calculated from the sequence $n_{j-2} + n_{j-1} = n_j$ for the superstructures $2a_0$, $3a_0$, $5a_0$, $8a_0$, ..., na_0 with increasing O content, as has been proposed in the past (Kaldis et al. 1997b). In figs. 110 and 111 the asterisks in the lower part show oxygen contents for such superstructures. Above $5a_0$, shifts of the compositions start. The existence of higher chain superstructures has now been experimentally proven also for bulk single crystals (von Zimmermann et al. 1999) but with other sequences. As already mentioned, the overlap of the composition fields of (a) the experimentally found $2a_0$, $3a_0$, and the extrapolated $5a_0$, $8a_0$ (... na_0) members of this sequence with (b) the compositions of in-phase phonon steps ("phases"), as well as the appearance between them of "two-phase steps", brought up the possible existence of "dimpling-chain" superstructures (sect. 5.1.1). If such superstructures do exist, it would be interesting to study their properties. Their characteristic lengths might be important for superconductivity.

9.1. *A T–x phase diagram for 123-O_x*

Combining the above significant points of the phase diagrams of figs. 110, and 111 with elements of the structural phase diagram of von Zimmermann et al. (1999) above RT, we can construct a schematic T–x phase diagram for 123-O_x, as shown in fig. 112.

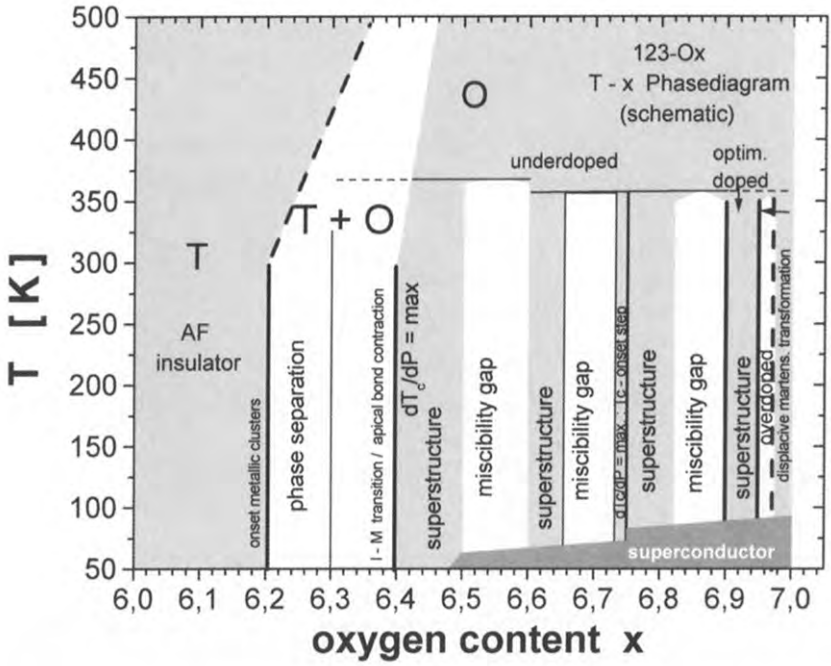

Fig. 112. Proposed T–x phase diagram for 123-O_x. After Kaldis et al. (2000b).

We adopt the high-temperature phase boundary of $T \rightarrow O$ and the temperature of transformation of the superstructures to the orthorhombic basic ortho-I (O) structure from von Zimmermann et al. (1999), but we use the sequence of superstructures indicated by the Raman in-phase data, shown in figs. 110 and 111. We obtain a sequence of single-phase superstructure regions with intermediate regions of phase separation (miscibility gaps) at mesoscopic/microscopic scale. Presently, due to lack of experimental investigations, a mechanism of the coupling of dimpling to the superstructure chains is not known. Theoretical investigations like those of Andersen et al. (1995) may shed more light on this problem (Röhler 2000b).

Due to the small scale of fig. 112 the decrease of T_c in the overdoped range is not shown. Also the critical points of the phase-separated regions are kept rather flat due to lack of knowledge of their properties.

It is interesting now to compare this diagram with that of La_2CuO_{4+y} (Wells et al. 1997), even if some details have changed in the meantime (fig. 113). Both phase diagrams show a normal state interrupted by a sequence of phase-separated regions. In between appear single-phase oxygen-intercalated structures with changing characteristic lengths. The superconducting states appear in these regions at lower temperatures. In both phase diagrams we have *a sequence of structural instabilities modulating the normal and superconducting states.* It is possible that this is a generic element of the phase diagram of HT_c cuprates.

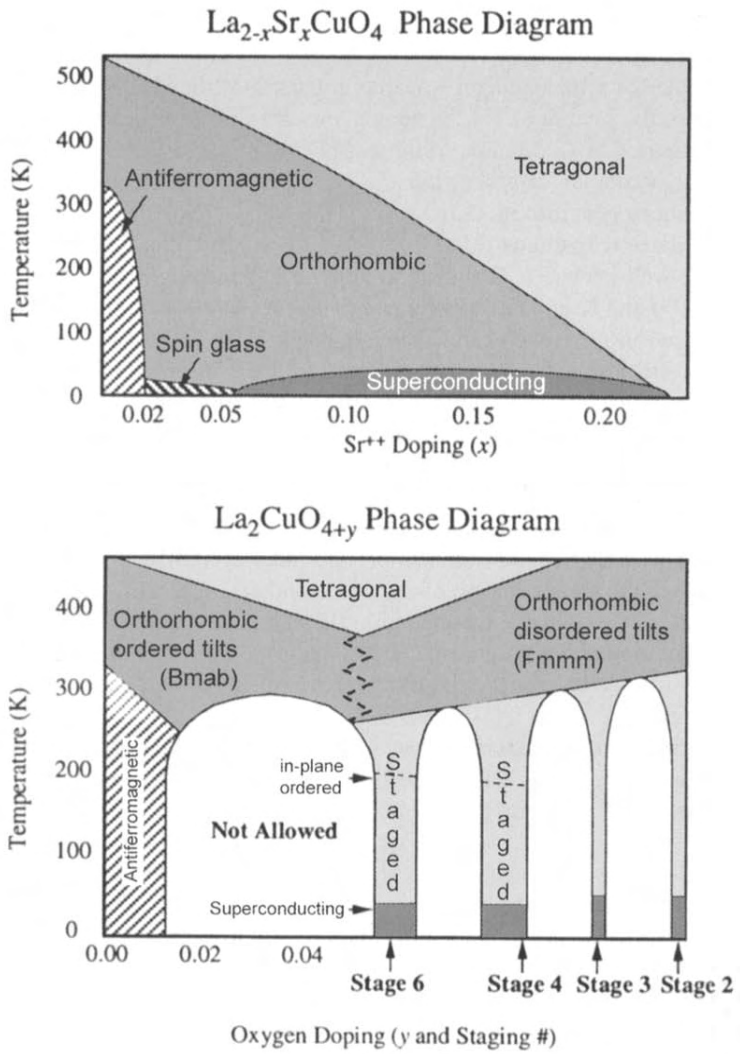

Fig. 113. T–x phase diagram for La cuprates. After Wells et al. (1997).

In the phase diagram of fig. 113 several types of stripes have been found, following the ingenious discovery of stripes by Tranquada et al. (1995) and the concept of quantum wires (Bianconi and Missori 1994). Whereas for the La cuprates a *folklore* of stripes have been reported by many authors, up to very recently, this type of phase separation has not been experimentally proven for 123. Very recently, however, two papers (Sharma et al. 2000, Mook et al. 2000) have presented evidence that stripes do exist also in 123-O_x (sect. 7.4).

Summary

After five decades of semiconductor research in pursuit of the ideally homogeneous and perfect material, the picture of HT_c materials emanates as intrinsically inhomogeneous. This review has tried to show some of these aspects:

(A) There is a wealth of data showing the existence of important lattice effects and intrinsic inhomogeneities in 123-O_x.

(1) **Five phase transitions exist:**

- The well-known T–O transition at $x = 6.4$, which according to Kartha et al. (1995) and Krumhansl (1992) is a first-order martensitic transformation. Also a neutron diffraction refinement (Radaelli et al. 1992) concludes that it is a first-order structural transition (sect. 3.2.1). The onset of superconductivity (I–M transition) takes place inside the composition range of the T–O transition (fig. 25d,e) and the latter triggers the former, as originally proposed by Cava et al. (1990). The ideas of a universal hole count for all cuprates to become superconducting (Tallon et al.) are doubtful for 123-O_x because their proof was based on questionable samples (sect. 5.3, 8.4). Recent structural data on very slowly cooled equilibrium samples (Conder et al. 1999; sect. 3.2.2) support clearly the abrupt change of the *c*-axis and apical bond found earlier by Cava et al. (1990). Charge transfer from the chains to the planes is coupled to this *c*-axis contraction. A giant dT_c/dP effect is measured at this composition which seems to be correlated with the oxygen ordering taking place at this transition (sect. 5.4).

  Raman investigations show another transition or cross-over at the Néel temperature ($x = 6.22$). Deconvolution of the apex-phonon width shows the coexistence of four phases in the nonstoichiometric range of 123. It is possible that physical phase separation starts at $x = 6.22$ with the formation of hole-doped islands in an AF matrix (sect. 3.3.2), the percolation to the superconducting phase taking place at $x \approx 6.40$.
- A fourth latent transition or cross-over takes place at $x = 6.75$. At this composition the *a*- and *b*-lattice parameters deviate from linearity, and orthorhombicity, mimicking T_c, starts saturating (figs. 25a–c). It is possible, therefore, that this composition marks the start of the negative interactions leading to a decreasing T_c in the overdoped phase. Structurally, these changes are mainly in the planes, but have appreciable influence on the apex phonon frequency which for $x > 6.75$ becomes independent of doping (although its bond length is further decreasing). The most pronounced physical effect is the giant dT_c/dP increase (sect. 5.4), which is also connected with thermal expansion anomalies of the *a*-axis near T_c (sect. 5.4.2).
- A fifth transition exists at the onset of the overdoped phase, $x = 6.95$. This is a displacive transformation (Kaldis et al. 1997b) followed by a decrease of orthorhombicity and a stepwise decrease of the *b*-axis (fig. 25b), but most importantly by an abrupt increase of dimpling (sect. 6). This transition is

the boundary of the phase-separated overdoped phase. This is supported by the splitting of the diamagnetic transition to $T_{c2,\,onset}$ (almost independent of oxygen doping) and T_{c1}, and also by Raman measurements. The physical phase separation is probably due to overdoped islands in a matrix of the optimally doped phase. Thus, *both ends of the superconducting field seem to be phase-separated* ($6.15 < x < 6.40$, and $6.95 < x < 7.00$). The $T_{c2,\,onset}$ appears with the same value in the Ca-doped 123 (see below). The transitions at $x = 6.75$ and 6.95 lead to changes parallel to the c-axis, but are induced by changes of orthorhombicity. The latter is triggered by displacement of O2,O3 parallel to the c-axis and away from Cu2 (which moves out of the planes).

(2) *Several lattice distortions have been found in the underdoped and optimally doped fields.*
- PDF (sect. 4.2) shows that in the local structure, shifts of 0.1 Å of the oxygen sites appear along the c-axis in domains of ~10 Å. The question arises whether this is the result of the presence of polarons or some kind of stripes, as was shown to be the case for the La cuprates.
- Electron diffraction shows correlated displacements of Cu2 and O1 in the a–b plane (sect. 4.3), leading to local perturbation of charge density roughly parallel to the c-axis, supporting the results of PDF. These perturbations form a network of cells in the a–b plane with nanoscopic dimensions, comparable with the coherence length. The reason for these distortions is the *strain field,* which has been shown to exist also with the bond valence sum method in the 123-perovskite lattice (sect. 3.2.1.4). These results support the nanoscale phase separation model of Phillips and Jung (2001a,b) (sect. 4.3.1).
- Y-EXAFS shows displacements of the O2,O3 and Cu2 atoms parallel to the c-axis, inducing distortions of the dimpling. Lattice distortions appear also both at T_c and the spin-gap opening temperature.

(B) A large number of experiments support the existence of several fields of phase separation. We have mentioned under (1) and (2) the physical phase separation at the two boundaries of the superconducting regime. In the underdoped range a kind of phase-rule obeying phase separation in mesoscopic scale can be considered, due to the existence of a series of in-phase phonon-frequency steps ("phases"), appearing at compositions where also the chain superstructures appear. This puts the question about the existence of *dimpling-chain superstructures,* where the chain-ordering phenomena would be correlated with the dimpling Raman shifts parallel to the c-axis (sect. 5.5.2). (figs. 110, 111).

(C) A bag full of interesting and unexpected complexities is the case of Ca-doped 123-O_x. The structural data and the T_c change give the impression of classical overdoping: c-axis and apical bond increasing, T_c decreasing with Ca doping. A thorough inspection of the magnetization data of fully oxygenated samples shows that there also is a strong diamagnetic splitting and, therefore, phase separation following the pattern of the O-overdoped 123, and supported by the appearance of new Raman modes (sect. 8.2). $T_{c2,\,onset}$ has the same value as for optimally O-doped $123O_{6.92}$

and is almost independent of Ca doping, T_{c1} decreases strongly with Ca doping. The question about the local structure opens Pandora's box. Y-EXAFS sees, up to $R_{eff} \approx 5$ Å, almost no changes in the spectra and at higher Ca doping something like amorphisation. A model accommodating these difficulties (sect. 8.4) is the *monodisperse dissolution* of Ca-123 molecules in the lattice (Röhler et al. 1999b). This is expected to lead to localization of the holes introduced by Ca, the carriers screened by the locally distorted Y-123 cells surrounding the Ca-123. Then, the overdoping does not come from the holes doped by Ca but by the decreasing Y-123 contributions to the superconducting carriers with increasing Ca content.

Not only may all of these be wrong in our picture of Ca-123. The assumption of linear dependence of O content on Ca% is also wrong (sect. 8.1). Up to 17% Ca very little oxygen is lost, not supporting the classical picture of substitution, except if the Ca holes are not available to the lattice. And last but not least, Ca-123O_6 which has been used to support the adoption of the parabolic dependence of T_c on the carrier concentration for 123 (Tallon et al. 1995) is not superconducting! 123O_6 doped with 5 different Ca compositions (0–22%) was found not to be superconducting (fig. 51) as discussed in sect. 8.4 (Merz et al. 1998).

Summing up we can say that from the structural point of view the *lattice strains* are very important, leading to most of the local structure effects. The above is a list of *experimental* facts, which depending on the theoretical model can be interpreted differently. The ultimate goal of this review is to bring these facts to the attention of the reader (or remind some of them). Because whatever their interpretation may be, *these experimental facts should not be overlooked.*

Acknowledgments

Many thanks are due to Professor J. Röhler for critically reading the manuscript, to Professors K.A. Müller, H. Keller, E. Liarokapis, and J. Röhler for many fruitful discussions, and to Professor E. Liarokapis and Drs G. Böttger, K. Conder, P. Fischer, A.W. Hewat, J. Karpinski, I. Mangelshots-Loquet, D. Palles, Ch. Rossel, S. Rusiecki, H. Schwer, A. Shengelaya and D. Zech for longstanding collaborations and/or permission to use some yet unpublished data. For the discussion of the phase relationships of 123-O_x and the scouting for phase-separation phenomena the input of the Raman investigations as a function of nonstoichiometry was found to be an invaluable asset. My particular thanks go to Professor E. Liarokapis and his collaborators for these important contributions. Last but not least the technical support of E. Jilek, S. Mollet and A. Wisard over the years is gratefully acknowledged.

Permissions for publication of figures and/or preprints and reprints have been received from Dr. N.H. Andersen, Prof. F. Bridges, Dr. P. Burlet, Prof. R. Cava, Prof. T. Egami, Dr. J. Etheridge, Dr. W.H. Fietz, Prof. L.H. Greene, Dr. J.D. Jorgensen, Dr. C. Meingast, Dr. S.B. Qadri, Prof. R.P. Sharma, and Dr. J. Tallon. The author acknowledges this with pleasure.

The experimental work from the author's laboratory reported here has been supported in the past by the Swiss National Science Foundation (National Program of Superconductivity) and the ETH. The author wishes to aknowledge this crucial support.

References

Ahn, B.T., T.M. Gür, R.A. Huggins, R. Beyers, E.M. Engler, P.M. Grant, S.S.P. Parkin, G. Lim, M.L. Ramirez, K.P. Roche, J.E. Vazquez, V.Y. Lee and R.D. Jacowitz, 1988, Physica C **153–155**, 590–593.

Ahn, B.T., V.Y. Lee, R. Beyers, T.M. Gür and R.A. Huggins, 1990, Physica C **167**, 529.

Alario-Franco, M.A., C. Chaillout, J.J. Capponi, J. Chenavas and M. Marezio, 1988, Physica C **156**, 455.

Almasan, C.C., S.H. Hahn, B.W. Lee, L.M. Paulius, M.B. Maple, B.W. Veal, J.W. Downey, A.P. Paulikas, Z. Fisk and J.E. Schirber, 1992, Phys. Rev. Lett. **69**, 680.

Andersen, N.H., B. Lebech and H.F. Poulsen, 1990, in: High T_c Superconductor Materials, Proc. E-MRS Symposium, Strassbourg, France, eds H. Habermeier, E. Kaldis and J. Schoenes, J. Less-Common Met. **164–165**, 124–131.

Andersen, N.H., et al., 1996, Annual Progress Report Risø-R-933(EN) (Risø Nat. Laboratory, Denmark) p. 43.

Andersen, O.K., A.I. Liechtenstein, O. Jepsen and F. Paulsen, 1995, J. Phys. Chem. Solids **12**, 1573.

Appelman, E.H., L.R. Morss, A.M. Kini, U. Geiser, A. Umezawa, G.W. Crabtree and K.D. Carlson, 1987, Inorg. Chem. **26**, 3237.

Aukrust, T., M.A. Novotny, P.A. Rikvold and D.P. Landau, 1990, Phys. Rev. B **41**, 8772.

Bartelt, N.C., T.L. Einstein and L.T. Wille, 1989, Phys. Rev. B **41**, 10759.

Batlogg, B., and V.J. Emery, 1996, Nature **382**, 20.

Bednorz, J.G., and K.A. Müller, 1986, Z. Phys. B **64**, 189.

Beech, F., S. Miraglia, A. Santoro and R.S. Roth, 1987, Phys. Rev. B **35**, 8778.

Benischke, R., T. Weber, W.H. Fietz, J. Metzger, K. Grube, T. Wolf and H. Wühl, 1992, Physica C **203**, 293.

Beno, M.A., L. Soderholm, C.W. Capone, D.G. Hinks, J.D. Jorgensen, J.D. Grace, I.K. Schuller, C.U. Segre and K. Zhang, 1987, Appl. Phys. Lett. **51**, 57.

Bernhard, C., and J.L. Tallon, 1996, Phys. Rev. B **54**, 10201

Beyers, R., and T.M. Shaw, 1989, The structure of $Y_1Ba_2Cu_3O_{7-\delta}$ and its derivatives, in: Solid State Physics, Vol. 42, eds H. Ehrenreich and D. Turnbull (Academic Press, New York) pp. 135–312.

Beyers, R., E.M. Engler, P.M. Grant, S.S.P. Parkin, G. Lim, M.L. Ramirez, K.P. Roche, J.E. Vazquez, V.Y. Lee, R.D. Jacowitz, B.T. Ahn, T.M. Gür and R.A. Huggins, 1987, Mater. Res. Soc. Symp. Proc. **99**, 77.

Beyers, R., B.T. Ahn, G. Gorman, V.Y. Lee, S.S.P. Parkin, M.L. Ramirez, K.P. Roche, J.E. Vazquez, T.M. Gür and R.A. Huggins, 1989, Nature **340**, 619.

Bianconi, A., and M. Missori, 1994, The coupling of a Wigner polaronic charge density wave with a Fermi liquid – A possible pairing mechanism in HT_c superconductors, in: Phase Separation in Cuprate Superconductors, eds E. Sigmund and K.A. Müller (Springer, Berlin).

Bianconi, A., and N.L. Saini, eds, 1997, Proc. Int. Conf. on Stripes, Lattice Instabilities, and High-T_c Superconductivity, December 1996, Rome, Italy, J. Superconductivity **10**, 267–466.

Bianconi, A., and N.L. Saini, eds, 2000, Stripes and Related Phenomena, Proc. 2nd Int. Conf. on Stripes, Lattice Instabilities, and High-T_c Superconductivity, June 1998, Rome, Italy (Kluwer Academic/Plenum, Dordrecht/New York).

Bianconi, A., A. Congiu Castellano, M. de Santis, P. Rudolph, P. Lagarde, A.M. Flank and A. Marcelli, 1987, Solid State Commun. **63**, 1009.

Bianconi, A., N.L. Saini, A. Lanzara, M. Missori, T. Rossetti, H. Oyanagi, H. Yamaguchi, K. Ota and T. Ito, 1996, Phys. Rev. Lett. **76**, 3412.

Bischof, R., E. Kaldis and I. Latsis, 1983, J. Less-Common Met. **94**, 117.

Bishop, A.R., 2000, lecture at Proc. 2nd Int. Conf. on Stripes, Lattice Instabilities, and High-T_c Superconductivity, June 1998, Rome, Italy.

Bishop, A.R., R.L. Martin, K.A. Müller and Z. Tesanovic, 1989, Z. Phys. B **76**, 17.

Booth, C.H., F. Bridges, E.D. Bauer, G.G. Li, J.B. Boyce, T. Claeson, C.H. Chu and Q. Xiong, 1995, Phys. Rev. B **52**, 15745.

Booth, C.H., F. Bridges, J.B. Boyce, T. Claeson, B.M. Lairson, R. Liang and D.A. Bonn, 1996, Phys. Rev. B **54**, 9542.

Bordet, P., C. Chaillout, T. Fournier, M. Marezio, E. Kaldis, J. Karpinski and E. Jilek, 1993, Phys. Rev. B **47**, 3465

Böttger, G., 1994, Diploma Thesis (University of Leipzig).

Böttger, G., and E. Kaldis, 1994, unpublished.

Böttger, G., I. Mangelshots, Ch. Krüger, E. Kaldis and P. Fischer, 1996, J. Phys.: Condens. Matter **8**, 8889.

Böttger, G., H. Schwer, E. Kaldis and K. Bente, 1997, Physica C **275**, 198.

Brown, I.D., 1978, Chem. Soc. Rev. **7**, 359.

Brown, I.D., 1989, J. Solid State Chem. **82**, 122.

Brown, I.D., 1991, J. Solid State Chem. **90**, 155.

Brown, I.D., and D. Andermatt, 1985, Acta Crystallogr. B **41**, 244.

Brown, I.D., and R.D. Shannon, 1973, Acta Crystallogr. A **29**, 266.

Bucher, B., J. Karpinski, E. Kaldis and P. Wachter, 1990, Pressure dependence of T_c and anisotropic features in the family $Y_2Ba_4Cu_{6+n}O_{14+n}$, in: High T_c Superconductor Materials, Proc. E-MRS Symposium, Strassbourg, France, eds H. Habermeier, E. Kaldis and J. Schoenes, J. Less-Common Met. **164–165**, 20–30.

Bucher, B., E. Kaldis, S. Rusiecki and P. Wachter, 1991, in: Abstract Book, XIII AIRAPT Conference, Bangalore, India, October 1991.

Bucher, B., E. Kaldis, S. Rusiecki and P. Wachter, 1992, Pressure dependence of T_c in the family YBaCuO, in: Proc. XIII AIRAPT Conf., Bangalore, India, 1991 (Oxford University Press, New Delhi).

Bucher, B., E. Kaldis, Ch. Krüger and P. Wachter, 1996, Europhys. Lett. **34**(5), 391.

Buckley, R.G., D.M. Pooke, J.L. Tallon, M.R. Presland, N.E. Flower, M.P. Staines, H.L. Johnson, M. Meylan, G.V.M. Williams and M. Bowden, 1991, Physica C **174**, 383.

Burdett, J.K., 1992, Physica C **191**, 282.

Burdett, J.K., and G.V. Kulkarni, 1989, Phys. Rev. B **40**, 8708.

Burlet, P., J.Y. Henry and L.P. Regnault, 2000, Physica C **296**, 205.

Butera, R.A., 1988, Phys. Rev. B **37**, 5909.

Capponi, J.J., C. Chaillout, A.W. Hewat, P. Lejay, M. Marezio, N. Nguyen, B. Raveau, J.L. Soubeyroux, J.L. Tholence and R. Tournier, 1987, Europhys. Lett. **3**, 1301.

Cava, R.J., B. Batlogg, C.H. Chen, E.A. Rietman, S.M. Zahurak and D. Werder, 1987a, Phys. Rev. B **36**, 5719.

Cava, R.J., B. Batlogg, C.H. Chen, E.A. Rietman, S.M. Zahurak and D. Werder, 1987b, Nature **329**, 423.

Cava, R.J., B. Batlogg, S.A. Sunshine, T. Siegrist, et al., 1988a, Physica C **153–155**, 560.

Cava, R.J., B. Batlogg, K.M. Rabe, E.A. Rietman, P.K. Gallagher and L.W. Rupp Jr, 1988b, Physica C **156**, 523.

Cava, R.J., A.W. Hewat, E.A. Hewat, B. Batlogg, M. Marezio, K.M. Rabe, J.J. Krajewski, W.F. Peck Jr and L.W. Rupp Jr, 1990, Physica C **165**, 419.

Ceder, G., M. Asta, W.C. Carter, M. Kraitchman, D. de Fontaine, M.E. Mann and M. Sluiter, 1990, Phys. Rev. B **41**, 8698.

Ceder, G., R. McCormack and D. de Fontaine, 1991a, Phys. Rev. B **44**, 2377.

Ceder, G., M. Asta and D. de Fontaine, 1991b, Physica C **177**, 106.

Chaillout, C., and J.P. Remeika, 1985, Solid State Commun. **56**, 833.

Chaillout, C., M.A. Alario-Franco, J.J. Capponi, J. Chenavas, P. Strobel and M. Marezio, 1988, Solid State Commun. **65**, 283.

Chmaissem, O., Y. Eckstein and C.G. Kuper, 2001, Phys. Rev. B **63**, 174510.

Claus, H., S. Yang, A.P. Paulikas, J.W. Downey and B.W. Veal, 1990, Physica C **171**, 205.

Claus, H., M. Braun, A. Erb, K. Röhberg, B. Runtsch, H. Wühl, G. Bräuchle, P. Schweiss, G. Müller-Vogt and H. v. Löhneysen, 1992a, Physica C **198**, 42.

Claus, H., U. Gebhardt, G. Linker, K. Röhberg, S. Riedling, J. Franz, T. Ishida, A. Erb, G. Müller-Vogt and H. Wühl, 1992b, Physica C **200**, 271.

Conder, K., 1999, private communication.

Conder, K., 2000, Oxygen Exchange in the Superconductors of the YBaCuO Family, Habilitationsschrift (Department of Materials Sciences, ETH, Zurich).

Conder, K., and E. Kaldis, 1989, J. Less-Common Met. **146**, 205.

Conder, K., and E. Kaldis, 1995, unpublished.

Conder, K., and Ch. Krüger, 1996, Physica C **269**, 92.

Conder, K., S. Rusiecki and E. Kaldis, 1989, Mater. Res. Bull. **24**, 581.

Conder, K., Wang Longmei, E. Boroch and E. Kaldis, 1991, Eur. J. Solid State Inorg. Chem. **28**, 487.

Conder, K., J. Karpinski, E. Kaldis, S. Rusiecki and E. Jilek, 1992, Physica C **196**, 164.

Conder, K., E. Kaldis, M. Maciejewski, K.A. Müller and E.F. Steigmeier, 1993, Physica C **213**, 282.

Conder, K., D. Zech, Ch. Krüger, E. Kaldis, H. Keller, A.W. Hewat and E. Jilek, 1994a, Indications for a phase separation in $YBa_2Cu_3O_{7-x}$, in: Proc. Int. Workshop on Phase Separation, September 1993, eds E. Sigmund and K.A. Müller (Springer, Berlin) Part V, Phase Separation in Cuprate Superconductors, pp. 210–224.

Conder, K., Ch. Krüger, E. Kaldis, D. Zech and H. Keller, 1994b, Physica C **225**, 13.

Conder, K., H. Schwer, A. Shengelaya and E. Kaldis, 1999, to be published.

Conradson, S.D., and I.D. Raistrick, 1989, Science **243**, 1340.

Dai, P., H.A. Mook and F. Dogan, 1998, Phys. Rev. Lett. **80**, 1738.

Darhmaoui, H., and J. Jung, 1996, Phys. Rev. B **53**, 14621.

Darhmaoui, H., and J. Jung, 1998, Phys. Rev. B **57**, 8009.

David, W.I.F., O. Moze, F. Licci, F. Bolzoni, R. Cywinski and S. Kilcoyne, 1989, Physica B **156–157**, 884.

de Fontaine, D., 1984, J. Phys. A **17**, L713-L717.

de Fontaine, D., L.T. Wille and S.C. Moss, 1987, Phys. Rev. B **36**, 5709.

de Fontaine, D., G. Ceder and M. Asta, 1990a, in: High T_c Superconductor Materials, Proc. E-MRS Symposium, Strassbourg, France, eds H. Habermeier, E. Kaldis and J. Schoenes, J. Less-Common Met. **164–165**, 108–123.

de Fontaine, D., G. Ceder and M. Asta, 1990b, Nature **343**, 544.

de Fontaine, D., M. Asta, G. Ceder, R. McCormack and G. Van Tendeloo, 1992, Europhys. Lett. **19**, 229–234.

de Leeuw, D.M., W.A. Groen, L.F. Feiner and E.E. Havinga, 1990, Physica C **166**, 133.

Deutscher, G., 1999, Nature **397**, 410.

Domanges, B., M. Hervieu and B. Raveau, 1993, Physica C **207**, 65.

D'yakonov, V.P., I.M. Fita, G.G. Levchenko and V.I. Markovich, 1996, Phys. Solid State **38**, 458.

Eckstein, Y., and C.G. Kuper, 1999, Physica B **284–288**, 404.

Egami, T., 1994, Local structural distortion: implication to the mechanism of HT_c superconductivity, in: Materials and Crystallographic Aspects of HT_c-Superconductivity, NATO-ASI Series E Vol. 263, ed. E. Kaldis (Kluwer Academic Publishers, Dordrecht) pp. 45–64.

Egami, T., and S.J.L. Billinge, 1996, Lattice effects in high-T_c superconductors, in: Physical Properties of High Temperature Superconductors, Vol. V, ed. D.M. Ginsberg (World Scientific, Singapore) pp. 1–109.

Egami, T., Y. Petrov and D. Louca, 2000, J. Superconductivity **13**, 709.

Emerson, J.P., D.A. Wright, B.F. Woodfield, J.E. Gordon, R.A. Fischer and N.E. Phillips, 1999, Phys. Rev. Lett. **82**, 1546.

Emery, V.J., S.A. Kivelson and H.Q. Lin, 1990, Phys. Rev. Lett. **64**, 475.

Emery, V.J., S.A. Kivelson and O. Zachar, 1997, Phys. Rev. B **56**, 6120.

Engler, E.M., et al., 1987, J. Am. Chem. Soc. **109**, 2848.

Etheridge, J., 1996, Philos. Mag. **73**, 643.

Eyring, L., 1979, The binary rare earth oxides, in: Handbook on the Physics and Chemistry of Rare Earths, Vol. 3, eds K.A. Gschneidner Jr and L. Eyring (North-Holland, Amsterdam) ch. 27.

Farneth, W.E., R.K. Borida, E.M. McCarron III, M.K. Crawford and R.B. Flippen, 1988, Solid State Commun. **66**, 953.

Fietz, W.H., J. Metzger, T. Weber, K. Grube and H.A. Ludwig, 1994, AIP Conf. Proc. **309**(Part I), 703.

Fietz, W.H., R. Quenzel, H.A. Ludwig, K. Grube, S.I. Schlachter, F.W. Hornumg, T. Wolf, A. Erb, M. Kläser and G. Müller-Vogt, 1996, Physica C **270**, 258.

Flemming, R.M., L.F. Schneemeyer, P.K. Gallagher, B. Batlogg, L.W. Rupp and J.V. Waszczak, 1988, Phys. Rev. B **37**, 7920.

Francois, M., A. Junod, K. Yvon, A.W. Hewat, J.J. Capponi, P. Strobel, M. Marezio and P. Fischer, 1988, Solid State Commun. **66**, 1117.

Frank, F.C., and J.H. van der Merwe, 1949, Proc. R. Soc. A **198**, 205; **200**, 125.

Furrer, A., ed., 1998, Neutron Scattering in Layered Copper-Oxide Superconductors, Vol. 20 of Physics and Chemistry of Materials with Low-Dimensional Structures (Kluwer Academic Publishers, Dordrecht).

Gallagher, P.K., H.M. O'Bryan, S.A. Sunshine and D.W. Murphy, 1987, Mater. Res. Bull. **22**, 995.

Gallagher, P.K., G.S. Grader and H.M. O'Bryan, 1988, Mater. Res. Bull. **23**, 1491.

Ginsberg, D.M., ed., 1990–95, Series: Physical Properties of High Temperature Superconductors (World Scientific, Singapore).

Goodenough, J.B., and M. Longo, 1970, in: Landolt–Berstein Group II, Vol. **4a**, eds K.-H. Hellwege and A.M. Hellwege (Springer, Berlin) ch. 3a.

Gor'kov, L.P., and A.V. Sokol, 1987, JETP Lett. **46**, 420.

Graf, T., 1991, Ph.D. Thesis No. 2480 (University of Geneva, Imprimerie Nationale) p. 18.

Graf, T., G. Triscone and J. Müller, 1990, J. Less-Common Met. **159**, 349.

Greaves, C., and P.R. Slater, 1989, Supercond. Sci. Technol. **2**, 5.

Greaves, C., and P.R. Slater, 1991, Physica C **175**, 172.

Groen, W.A., D.M. de Leeuw and L.F. Feiner, 1990, Physica C **165**, 55.

Grybos, J., D. Hohlwein, Th. Zeiske, R. Sonntag, F. Kubanek, K. Eichhorn and Th. Wolf, 1994, Physica C **220**, 138.

Gutmann, M., S.J.L. Billinge, E.L. Brosha and G.H. Kwei, 2000, Phys. Rev. B **61**, 11762.

Haase, J., 2000, private communication (Physics Department, University of Stuttgart).

Haase, J., N.J. Curro, R. Stern and C.P. Slichter, 1998, Phys. Rev. Lett. **81**, 1489.

Harris, D.C., 1990, The Chemistry of Superconductor Materials (Noyes Publications, Park Ridge, NJ).

Harris, D.C., M.E. Hills and T.A. Vanderah, 1987, J. Chem. Ed. **64**,847.

Hecker, N.E., H.A. Mook, J.A. Harvey, N.W. Hill, M.C. Moxon and J.A. Golovchenko, 1994, Phys. Rev. B **50**, 16129.

Hejtmanek, J., Z. Jirak, K. Knizek, M. Dlouha and S. Vratislav, 1996, Phys. Rev. B **54**, 16226.

Hewat, A.W., 1994, Neutron powder diffraction on the ILL high flux reactor and high T_c superconductors, in: Materials and Crystallographic Aspects of HT_c-Superconductivity, ed. E. Kaldis, NATO ASI Series E, Vol. 263 (Kluwer Academic Publishers, Dordrecht) pp. 17–44.

Hewat, A.W., E. Kaldis, S. Rusiecki, P. Fischer and E. Jilek, 1991, unpublished data.

Hohlwein, D., 1994, Superstructures in 123 compounds, in: Materials and Crystallographic Aspects of HT_c-Superconductivity, ed. E. Kaldis, NATO ASI Series E, Vol. 263 (Kluwer Academic Publishers, Dordrecht) pp. 65–81.

Homes, C.C., T. Timusk, D.A. Bonn, R. Liang and W.N. Hardy, 1995, Can. J. Phys. **73**, 663.

Hou, C.J., A. Manthiram, L. Rabenberg and J.B. Goodenough, 1990, J. Mater. Res. **5**, 9.

Howald, C., P. Fournier and A. Kapitulnik, 2001, LANL cond-mat/0101251.

Hudson, E.W., S.H. Pan, A.K. Gupta, K.W. Ng and J.C. Davis, 1999, Science **285**, 88.

Hume, D.N., and I.M. Kolthoff, 1944, Ind. Eng. Chem. Anal. Ed. **16**, 103.

Iliev, M., C. Thomsen, V. Hadjiev and M. Cardona, 1993, Phys. Rev. B **47**, 12341.

Inderhees, S.E., M.B. Salamon, N.D. Goldenfeld, J.P. Rice, B.G. Pazol, D.M. Ginsberg, J.Z. Liu and G.W. Crabtree, 1988, Phys. Rev. Lett. **60**, 1178.

Inoue, M., T. Takemori and T. Sakuda, 1987, Jpn. J. Appl. Phys. **26**, L2015.

Ishikawa, M., Y. Nakazawa, T. Takabatake, A. Kishi, R. Kato and A. Maesono, 1988a, Physica C **153–155**, 1089.

Ishikawa, M., Y. Nakazawa, T. Takabatake, A. Kishi, R. Kato and A. Maesono, 1988b, Solid State Commun. **66**, 201.

Jacobson, A.J., J.M. Newsam, D.C. Johnston, D.P. Goshorn, J.T. Lewandowski and M.S. Alvarez, 1989, Phys. Rev. B **39**, 254.

Janod, E., A. Junod, T. Graf, K.-Q. Wang, G. Triscone and J. Müller, 1993, Physica C **216**, 129.

Jensen, D.M., T. Fiig, N.H. Andersen and P.-A. Lindgård, 1997, Annual Progress Report, Solid State Physics, Risø-R-933(EN) (Risø Nat. Laboratory, Denmark) p. 44.

Johnston, D.C., A.J. Jacobson, J.M. Newsam, J.T. Lewandowski, D.P. Goshorn, D. Xie and W.B. Yelon, 1987, in: Chemistry of High-Temperature Superconductors, ACS Symposium, August 1987, eds D.L. Nelson, M.S. Whittingham and T.F. George, ACS Symposium Series, Vol. 351 (American Chemical Society, Washington, DC) p. 136.

Jorgensen, J.D., B.W. Veal, W.K. Kwok, G.W. Crabtree, A. Umezawa, L.J. Nowicki and A.P. Paulikas, 1987a, Phys. Rev. B **36**, 5731.

Jorgensen, J.D., M.A. Beno, D.G. Hinks, L. Soderholm, K.J. Volin, R.L. Hitterman, J.D. Grace, I.K. Schuller, C.U. Segre, K. Zhang and M.S. Kleefish, 1987b, Phys. Rev. B **36**, 3608.

Jorgensen, J.D., H. Shaked, D.G. Hinks, B.W. Veal, A.P. Paulikas, L.J. Nowicki, G.W. Crabtree, H. Claus, W.K. Kwok, L.H. Nunez and H. Claus, 1988, Physica C **153–155**, 578.

Jorgensen, J.D., B.W. Veal, A.P. Paulikas, L.J. Nowicki, G.W. Crabtree, H. Claus and W.K. Kwok, 1990a, Phys. Rev. B **41**, 1863.

Jorgensen, J.D., S. Pei, P. Lightfoot, H. Shi, A.P. Paulikas and B.W. Veal, 1990b, Physica C **167**, 571.

Jorgensen, J.D., S. Pei, P. Lightfoot, D.G. Hinks, B.W. Veal, B. Dabrowski, A.P. Paulikas, R. Kleb and I.D. Brown, 1990c, Physica C **171**, 64.

Jung, J., B. Boyce, H. Yan, M. Abdelhadi, J. Skinta and T. Lemberger, 2000, J. Superconductivity **13**, 753.

Kaldis, E., ed., 1990, Solid State Chemistry of High-T_c Superconductors – Materials and Characterization, Eur. J. Solid State & Inorg. Chem. (Gauthier-Villars, Paris) **27**.

Kaldis, E., ed., 1994, "Materials and Crystallographic Aspects of HT_c-Superconductivity", NATO ASI Series E, Vol. 263 (Kluwer Academic Publishers, Dordrecht).

Kaldis, E., 1997, Lattice instabilities, structural anomalies and phase transitions in $Y_{1-y}Ca_yBa_2Cu_3O_x$ Phases, in: Ten Years after the Discovery, Workshop on High-Tc Superconductivity, August 1996, Delphi, Greece, eds E. Kaldis, E. Liarokapis and K.A. Müller, NATO ASI Series E, Vol. 343 (Kluwer Academic Publishers, Dordrecht) pp. 411–446.

Kaldis, E., and B. Fritzler, 1982, Valence and phase instabilites in $TmSe_x$ crystals, in: Progress in Solid State Chemistry, Vol. 14, eds G.M. Rosenblatt and W.L. Worrell (Pergamon Press, Oxford) pp. 95–139.

Kaldis, E., P. Fischer, A.W. Hewat, E.A. Hewat, J. Karpinski and S. Rusiecki, 1989, Physica C **162**, 524.

Kaldis, E., J. Karpinski, S. Rusiecki, B. Bucher, K. Conder and E. Jilek, 1991, Physica C **185–189**, 190.

Kaldis, E., E. Liarokapis and K.A. Müller, eds, 1997a, Ten Years after the Discovery, Proc. Workshop on High-Tc Superconductivity 1996, NATO Advanced Study Institute, August 1996, Delphi, Greece, NATO ASI Series E, Vol. 343 (Kluwer Academic Publishers, Dordrecht).

Kaldis, E., J. Röhler, E. Liarokapis, N. Poulakis, K. Conder and P.W. Loeffen, 1997b, Phys. Rev. Lett. **79**, 4894.

Kaldis, E., E. Liarokapis, N. Poulakis, D. Palles and K. Conder, 2000a, in: Stripes and Related Phenomena, Proc. 2nd Int. Conf. on Stripes, Lattice Instabilities, and High-T_c Superconductivity, June 1998, Rome, Italy, eds A. Bianconi and N.L. Saini (Kluwer Academic/Plenum, Dordrecht/New York) p. 211.

Kaldis, E., et al., 2000b, to be published.

Käll, M., M. von Zimmermann, N.H. Andersen, J. Madsen, T. Frello, O. Schmidt, H.F. Poulsen, J.R. Schneider and Th. Wolf, 1999, unpublished (Risø Nat. Laboratory, Denmark).

Karen, P., and A. Kjekshus, 1991, J. Solid State Chem. **94**, 298.

Karpinski, J., E. Kaldis, S. Rusiecki, B. Bucher and E. Jilek, 1988, Nature **336**, 660.

Karpinski, J., S. Rusiecki, E. Kaldis and E. Jilek, 1991, High oxygen pressure investigations in the $Y_2Ba_4Cu_{6+n}O_{14+n}$ Family, in: Proc. HIP-3 Conference, Osaka, June 1991, ed. M. Koizumi (Elsevier, Amsterdam).

Karppinen, M., and H. Yamauchi, 1999, Philos. Mag. B **79**, 343.

Karppinen, M., A. Fukuoka, L. Niinistö and H. Yamauchi, 1996, Supercond. Sci. Technol. **9**, 121.

Kartha, S., J.A. Krumhansl, J.P. Sethna and L.K. Wickham, 1995, Phys. Rev. B **52**, 803.

Keller, S.W., K.J. Leary, A.M. Stacy and J.N. Michaels, 1987, Mater. Lett. **5**, 357.

Khachaturyan, A.G., and J.W. Morris, 1988, Phys. Rev. Lett. **61**, 215.

Khachaturyan, A.G., and J.W. Morris, 1990, Phys. Rev. Lett. **64**, 1989.

Khachaturyan, A.G., S.V. Semenovskaya and J.W. Morris, 1988, Phys. Rev. B **37**, 2243.

Khomskii, D., and F.V. Kusmartsev, 1992, Phys. Rev. B **52**, 803.

Kimura, H., H. Oyanagi, T. Terashima, H. Yamaguchi, Y. Bando and J. Mizuki, 1993, Jpn. J. Appl. Phys. **32–2**, 584.

Kohn, W., T.K. Lee and Y.R. Lin-Liu, 1982, Phys. Rev. B **25**, 3557.

Kraut, O., C. Meingast, G. Bräuchle, H. Claus, A. Erb, G. Müller-Vogt and H. Wühl, 1993, Physica C **205**, 139.

Krüger, Ch., K. Conder and E. Kaldis, 1993, Physica C **213**, 219.

Krüger, Ch., H. Schwer, J. Karpinski, K. Conder, E. Kaldis, C. Rossel and M. Maciejewski, 1994, Z. Anorg. Allg. Chemie **620**, 1932.

Krüger, Ch., K. Conder, H. Schwer and E. Kaldis, 1997, J. Solid State Chem. **134**, 356.

Krumhansl, J.A., 1992, Fine scale mesostructures in superconducting and other materials, in: Lattice Effects in High-T_c Superconductors, eds Y. Bar-Yam, T. Egami, J. Mustre-de Leon and A.R. Bishop (World Scientific, Singapore) pp. 503–516.

Kwei, G.H., A.C. Larson, W.L. Huts and J.L. Smith, 1990, Physica C **169**, 217.

Lavrov, A.N., 1992, Phys. Lett. A **168**, 71.

Liarokapis, E., 1997, Raman scattering in YBCO compounds, in: Ten Years after the Discovery, Workshop on High-Tc Superconductivity, August 1996, Delphi, Greece, eds E. Kaldis, E. Liarokapis and K.A. Müller, NATO ASI Series E, Vol. 343 (Kluwer Academic Publishers, Dordrecht) pp. 447–468.

Liarokapis, E., 1999, Physica C **317–318**, 270.

Liarokapis, E., 2000, Physica C **341–348**, 2185.

Liarokapis, E., et al., 2000, to be published.

Lindemer, T.B., C.R. Hubbard and J. Brynestad, 1990, Physica C **167**, 312.

Loram, J.W., J.R. Cooper and K.A. Mirza, 1991, Supercond. Sci. Technol. **4**, S391.

Louca, D., G.H. Kwei, B. Dabrowski and Z. Bukowski, 1999, Phys. Rev. B **60**, 7558.

Macejewski, M., A. Baiker, K. Conder, Ch. Krüger, J. Karpinski and E. Kaldis, 1994, Physica C **227**, 343.

MacFarlane, R.M., H.J. Rosen, E.M. Engler, R.D. Jacowitz and V.Y. Lee, 1988, Phys. Rev. B **38**, 284.

Maletta, H., E. Pörschke, B. Rupp and P. Meuffels, 1989, Z. Phys. B **77**, 181.

Marezio, M., and C. Chaillout, 1994, A classification of the copper oxide superconductors and the relationship between the Cu valence and the superconducting properties, in: Materials and Crystallographic Aspects of HT_c-Superconductivity, ed. E. Kaldis, NATO ASI Series E, Vol. 263 (Kluwer Academic Publishers, Dordrecht) pp. 3–16.

McQueeney, R.J., Y. Petrov, T. Egami, M. Yethiraj, G. Shirane and Y. Endoh, 1999, Phys. Rev. Lett. **82**, 628.

Medvedeva, I.V., Y.S. Bersenev, B.A. Gizhevsky, N.M. Chebotaev, S.V. Naumov and G.B. Demishev, 1990, Z. Phys. B **81**, 311.

Meingast, C., O. Kraut, T. Wolf, H. Wühl, A. Erb and G. Müller-Vogt, 1991, Phys. Rev. Lett. **67**, 1634.

Merz, M., N. Nücker, P. Schweiss, S. Schuppler, C.T. Chen, V. Chakarian, J. Freeland, Y.U. Idzverda, M. Kläser, G. Müller-Vogt and Th. Wolf, 1998, Phys. Rev. Lett. **80**, 5192.

Metzger, J., T. Weber, W.H. Fietz, K. Grube, H.A. Ludwig, T. Wolf and H. Wühl, 1993, Physica C **214**, 371.

Miceli, P.F., J.M. Tarascon, L.H. Greene, P. Barboux, F.J. Rotella and J.D. Jorgensen, 1988, Phys. Rev. B **37**, 5932.

Mihailovic, D., and K.A. Müller, 1997, in: Ten Years after the Discovery, Workshop on High-Tc Superconductivity, August 1996, Delphi, Greece, eds E. Kaldis, E. Liarokapis and K.A. Müller, NATO ASI Series E, Vol. 343 (Kluwer Academic Publishers, Dordrecht).

Mihailovic, D., G. Ruani, E. Kaldis and K.A. Müller, eds, 1995, Anharmonic Properties of High-T_c Cuprates (World Scientific, Singapore).

Moler, K.A., et al., 1997, Phys. Rev. B **55**, 3954.

Monod, P., M. Ribault, F. D'Yvoire, J. Jegoudez, G. Collin and A. Revcolevschi, 1987, J. Phys. (Paris) **48**, 1369.

Mønster, D., P.-A. Lindgård and N.H. Andersen, 1999, unpublished.

Mook, H.A., and F. Dogan, 1999, Nature **401**, 145.

Mook, H.A., Y. Yethiraj, G. Aeppli, T.E. Mason and T. Armstrong, 1993, Phys. Rev. Lett. **70**, 3490.

Mook, H.A., et al., 1998, Nature **395**, 580.

Mook, H.A., P. Dai, F. Dogan and R.D. Hunt, 2000, Nature **404**, 729.

Müller, K.A., 1994, Recipe for high-T_c transition-metal chalcogenides, in: Phase Separation in Cuprate Superconductors, eds E. Sigmund and K.A. Müller (Springer, Berlin) pp. 1–11.

Müller, K.A., and G. Benedek, 1992, Phase Separation in Cuprate Superconductors (World Scientific, Singapore).

Müller, K.A., K.W. Blazey, J.G. Bednorz and M. Takashige, 1987, Physica B **148**, 149.

Murata, K., Y. Honda, H. Oyanagi, Y. Nishihara, H. Ihara, N. Terada, R. Sugise, M. Hirabayashi, M. Tokumoto and Y. Kimura, 1989, MRS Int. Meeting on Advanced Materials, **6**, 681.

Murch, G.E., 1980, Atomic Diffusion Theory in Highly Defective Solids, Vol. 6 of Diffusion and Defect Monograph Series (Trans Tech, Aedersmannsdorf).

Mustre-de Leon, J., S.D. Conradson, J. Batistic and A.R. Bishop, 1990, Phys. Rev. Lett. **65**, 1678.

Mustre-de Leon, J., J. Batistic, A.R. Bishop, S.D. Conradson and S.A. Trugman, 1992, Phys. Rev. Lett. **68**, 3236.

Mustre-de Leon, J., J. Batistic, A.R. Bishop, S.D. Conradson and I.D. Raistrick, 1993, Phys. Rev. B **47**, 12322.

Nakazawa, Y., 1991, Ph.D. Thesis (Prof. M. Ishikawa; Institute of Solid State Physics, University of Tokyo).

Nakazawa, Y., and M. Ishikawa, 1989, Physica C **162–164**, 83.

Nakazawa, Y., and M. Ishikawa, 1991, private communication.

Nakazawa, Y., J. Takeya and M. Ishikawa, 1994, Physica C **225**, 71.

Narlikar, A., ed., since 1990, Series: Studies of High Temperature Superconductors (Nova Science Publisher, New York).

Nelmes, R.J., J.S. Loveday, E. Kaldis and J. Karpinski, 1990, Physica C **172**, 311.

Nücker, N., 1999, Seminar lecture, Seminar for Superconductivity, 2 February 1999, Laboratorium für Festkörperphysik, ETH, Zurich.

Nücker, N., J. Fink, B. Renker, D. Ewert, C. Politis, P.J.W. Weijs and J.C. Fuggle, 1987, Z. Phys. B **67**, 9.

Nücker, N., J. Fink, J.C. Fuggle, P.J. Durham and W.M. Temmerman, 1988, Phys. Rev B **37**, 5158.

Palles, D., 2000, Ph.D. Thesis (Department of Physics, National Technical University, Athens).

Palles, D., N. Poulakis, E. Liarokapis, K. Conder, E. Kaldis and K.A. Müller, 1996, Phys. Rev. B **54**, 6721.

Palles, D., N. Poulakis, E. Liarokapis, K. Conder and E. Kaldis, 2000a, Physica C **341–348**, 2163.

Palles, D., D. Lampakis, G. Böttger, E. Liarokapis and E. Kaldis, 2000b, Physica C **341–348**, 2149.

Pan, S.H., E.W. Hudson, K.M. Lang, H. Elsaki, S. Uchida and J.C. Davis, 2000, Nature **403**, 746.

Pauling, L., 1929, J. Am. Chem. Soc. **51**, 1010.

Phillips, J.C., 1987, Phys. Rev. Lett. **59**, 1856.

Phillips, J.C., 1990, Phys. Rev. B **41**, 8968.

Phillips, J.C., 1991, Phys. Rev. B **43**, 11415.

Phillips, J.C., 1999, Philos. Mag. B **79**, 1477.

Phillips, J.C., 2000, Philos. Mag. B **80**, 1773.

Phillips, J.C., 2001, Philos. Mag. B **81**, 35.

Phillips, J.C., and J. Jung, 2001a, Phys. Rev. B, submitted. LANL cond-mat/0103167.

Phillips, J.C., and J. Jung, 2001b, Philos. Mag. B, in press.

Pickett, W.E., 1995, Anharmonic oxygen displacements in $La_{2-x}(Sr,Ba)_xCuO_4$ planes and in $YBa_2Cu_3O_7$ chains, in: Proc. Int. Workshop on Anharmonic Properties of High-T_c Cuprates, Bled, Slovenia, September 1994, eds D. Mihailovic, G. Ruani, E. Kaldis and K.A. Müller (World Scientific, Singapore) pp. 159–170.

Pickett, W.E., 1997, Physica C **289**, 51–62.

Pintschovius, L., and W. Reichardt, 1998, Phonon dispersion and phonon density states in copper–oxide superconductors, in: Neutron Scattering in Layered Copper-Oxide Superconductors, ed. A. Furrer, Vol. 20 of Physics and Chemistry of Materials with Low-Dimensional Structures (Kluwer Academic Publishers, Dordrecht).

Plakhty, V., A. Stratilatov, Yu. Chernenkov, V. Fedorov, S.K. Sinha, C.L. Loong, G. Gaulin, M. Vlasov and S. Moshkin, 1992, Solid State Commun. **84**, 639.

Plakhty, V., B. Kviatkovsky, A. Stratilatov, Yu. Chernenkov, P. Burlet, J.Y. Henry, C. Martin, E. Ressouche, J. Schweizer, F. Yakhou, E. Elkaim and J.P. Lauriat, 1994, Physica C **235–240**, 867–868.

Plakhty, V., P. Burlet and J.Y. Henry, 1995, Phys. Lett. A **198**, 256.

Poulakis, N., D. Palles, E. Liarokapis, K. Conder, E. Kaldis and K.A. Müller, 1996, Phys. Rev. B **53**, R534.

Poulsen, H.F., M. von Zimmermann, J.R. Schneider, N.H. Andersen, P. Schleger, J. Madsen, R. Hadfield, H. Casalta, R. Liang, P. Dosanjh and W.N. Hardy, 1996, Phys. Rev. B **53**, 15335.

Presland, M.R., J.L. Tallon, R.G. Buckley, R.S. Liu and N.E. Flower, 1991, Physica C **176**, 95.

Pyka, N., W. Reichardt, L. Pintschovius, S.L. Chaplot, P. Schweiss, A. Erb and G. Müller-Vogt, 1993, Phys. Rev. B **48**, 7746.

Qadri, S.B., E.F. Skelton, M.S. Osofsky, V.M. Browning, J.Z. Hu, P.R. Broussard, M.E. Reeves and W. Prusseit, 1997, Physica C **282–287**, 93.

Radaelli, P.G., 1998, Structural anomalies, oxygen ordering and superconductivity in $YBa_2Cu_3O_{6+x}$, in: Neutron Scattering in Layered Copper-Oxide Superconductors, ed. A. Furrer, Vol. 20 of Physics and Chemistry of Materials with Low-Dimensional Structures (Kluwer Academic Publishers, Dordrecht).

Radaelli, P.G., C.U. Segre, D.G. Hinks and J.D. Jorgensen, 1992, Phys. Rev. B **45**, 4923.

Ranninger, J., and U. Thibblin, 1992, Phys. Rev. B **45**, 7730.

Raveau, B., M. Huve, A. Maignan, M. Hervieu, C. Michel, B. Domanges and C. Martin, 1993, Physica C **299**, 163.

Reichardt, W., N. Pyka, L. Pintschovius, B. Hennion and G. Collin, 1989, Physica C **162–164**, 464.

Reyes-Gasga, J., T. Krekels, G. Van Tendeloo, J. Van Landuyt, S. Amelinckx, W.H.M. Bruggink and H. Verweij, 1989, Physica C **159**, 831.

Röhler, J., 1994, Evidence from EXAFS for an axial oxygen centered lattice instability in $YBa_2Cu_3O_{7-\delta}$, in: Materials and Crystallographic Aspects of HT_c-Superconductivity, ed. E. Kaldis,

NATO-ASI Series E, Vol. 263 (Kluwer Academic Publishers, Dordrecht) pp. 353–372.

Röhler, J., 2000a, Physica C **341–348**, 2151. LANL cond-mat0003116.

Röhler, J., 2000b, Physica B **284–288**, 1041–1042. LANL cond-mat/9906432.

Röhler, J., and R. Crüsemann, 1995, Multiple scattering analysis of Cu-K EXAFS in $Bi_2Sr_{1.5}Ca_{1.5}Cu_2O_{8+\delta}$, in: Proc. Int. Workshop on Anharmonic Properties of High-T_c Cuprates, Bled, Slovenia, September 1994, eds D. Mihailovic, G. Ruani, E. Kaldis and K.A. Müller (World Scientific, Singapore) pp. 86–94.

Röhler, J., A. Larish and R. Schäfer, 1992, Physica C **191**,57.

Röhler, J., P.W. Loeffen, S. Müllender, K. Conder and E. Kaldis, 1997a, Local structure studies of the underdoped–overdoped transition in $YBa_2Cu_3O_x$, in: Ten Years after the Discovery, Proc. Workshop on High-Tc Superconductivity 1996, eds E. Kaldis, E. Liarokapis and K.A. Müller, NATO ASI Series E, Vol. 343 (Kluwer Academic Publishers, Dordrecht) pp. 469–502.

Röhler, J., P.W. Loeffen, K. Conder and E. Kaldis, 1997b, Physica C **282–287**, 182–185.

Röhler, J., et al., 1998, unpublished.

Röhler, J., E. Rose, J.B. Philip, T. Lipinski, G. Böttger and E. Kaldis, 1999a, Annual Report (HASYLAB).

Röhler, J., C. Friedrich, T. Granzow, E. Kaldis and G. Böttger, 1999b, Phase separation in overdoped $Y_{1-0.8}Ca_{0-0.2}Cu_3O_{6.96-6.98}$, in: HTS99 Miami, January 1999, eds S.E. Barnes, J. Ashkenasi, J.L. Cohn and F. Zuo, AIP Conf. Proc. **483**, 320–323. LANL cond-mat/9902030.

Rossel, C., et al., 1999, unpublished results (IBM Zurich Research Laboratory).

Rothman, S.J., J.L. Routbort and J.E. Baker, 1989, Phys. Rev. B **40**, 8852.

Rothman, S.J., J.L. Routbort, U. Welp and J.E. Baker, 1991, Phys. Rev. B **44**, 2326.

Rusiecki, S., and E. Kaldis, 1991, unpublished work (ETH, Zurich).

Rusiecki, S., B. Bucher, E. Kaldis, E. Jilek, J. Karpinski, C. Rossel, B. Pümpin, H. Keller, W. Kündig, T. Krekels and G. Van Tendeloo, 1990, in: High T_c Superconductor Materials, Proc. E-MRS Symposium, Strassbourg, France, eds H. Habermeier, E. Kaldis and J. Schoenes, J. Less-Common Met. **164–165**, 31–38.

Salomons, E., and D. de Fontaine, 1990, Phys. Rev. B **41**, 11159.

Sanchez, J.M., F. Ducastelle and D. Gratias, 1984, Physica A **128**, 334.

Schilling, J.S., and S. Klotz, 1992, in: Physical Properties of High Temperature Superconductors, Vol. III, ed. D.M. Ginsberg (World Scientific, Singapore) p. 59.

Schlachter, S.I., W.H. Fietz, K. Grube, Th. Wolf, B. Obst, P. Schweiss and M. Kläser, 1999, Physica C **328**, 1–13.

Schleger, P., W.N. Hardy and H. Casalta, 1994, Phys. Rev. B **49**, 514.

Schleger, P., R. Hadfield, H. Casalta, N.H. Andersen, H.F. Poulsen, M. von Zimmermann, J.R. Schneider, R. Liang, P. Dosanjh and W.N. Hardy, 1995a, Phys. Rev. Lett. **74**, 1446.

Schleger, P., H. Casalta, R. Hadfield, H.F. Poulsen, M. von Zimmermann, N.H. Andersen, J.R. Schneider, R. Liang, P. Dosanjh and W.N. Hardy, 1995b, Physica C **241**, 103.

Schmalzried, H., 1981, Solid State Reactions (Verlag Chemie, Weinheim).

Schweiss, P., W. Reichardt, M. Braden, G. Collin, G. Heger, H. Claus and A. Erb, 1994, Phys. Rev. B **49**, 1387.

Schwer, H., J. Karpinski, K. Conder, Ch. Krüger, E. Kaldis and C. Rossel, 1993a, 249.

Schwer, H., E. Kaldis, J. Karpinski and C. Rossel, 1993b, Physica C **211**, 165.

Semenovskaya, S.V., and A.G. Khachaturyan, e.g.: 1993, Physica D **66**, 205.

Shafer, M.W., and T. Penney, 1990, Hole, T_c relationships in superconducting oxides, in: Solid State Chemistry of High-T_c Superconductors – Materials and Characterization, ed. E. Kaldis, Eur. J. Solid State & Inorg. Chem. (Gauthier-Villars, Paris) **27**, 191–220.

Shafer, M.W., R.A. De Groot, M.M. Plechaty and G.J. Scilla, 1988, Physica C **153–155**, 836.

Shaked, H., J.D. Jorgensen, J. Faber, D.G. Hinks and B. Dabrowski, 1989, Phys. Rev. B **39**, 7363.

Sharma, R.P., F.J. Rorella, J.D. Jorgensen and L.E. Rehn, 1991, Physica C **174**, 409.

Sharma, R.P., S.B. Ogale, Z.H. Zhang, J.R. Liu, W.K. Chu, B. Veal, A. Paulikas, H. Zheng and T. Venkatesan, 2000, Nature **404**, 736.

Shoenberg, D., 1940, Proc. R. Soc. London Ser. A **175**, 49.

Sigmund, E., and K.A. Müller, eds, 1994, Phase Separation in Cuprate Superconductors (Springer, Berlin).

Stauffer, D., and A. Aharony, 1995, Perkolationstheorie: eine Einführung (VCH, Weinheim, Germany) p. 18.

Stern, E.A., M. Qian, Y. Yacoby, S.M. Heald and H. Maeda, 1992, Unusual copper environment in $YBa_2Cu_3O_{7-\delta}$ superconductors as found by XAFS, in: Proc. Conf. Lattice Effects in High T_c Superconductors, eds Y. Bar-Yam, T. Egami, J. Mustre-de Leon and A.R. Bishop (World Scientific, Singapore) p. 51.

Stern, E.A., M. Qian, Y. Yacoby, S.M. Heald and H. Maeda, 1993, Physica C **209**,331.

Sterne, P., and L.T. Wille, 1989, Physica C **162–164**, 223.

Straube, E., D. Hohlwein and F. Kubanek, 1998, Physica C **295**, 1.

Sullivan, J.D., P. Bordet, M. Marezio, K. Takenaka and S. Uchida, 1993, Phys. Rev. B **48**, 10638.

Swaminathan, K., J. Janaki, G.V.N. Rao, O.M. Sreedharan and T.S. Radhakrishnan, 1988, Mater. Lett. **6**, 265.

Takayama-Muromachi, E., Y. Uchida, M. Ishi, T. Tanaka and K. Kato, 1987, Jpn. J. Appl. Phys. **26**, L1156.

Tallon, J.L., 1990, Physica C **168**, 85.

Tallon, J.L., and J.R. Cooper, 1993, in: Advances in Superconductivity, Vol. V, eds Y Bando and H. Yamaguchi (Springer, Tokyo) p. 339.

Tallon, J.L., C. Bernhard, H. Shaked, R.L. Hitterman and J.D. Jorgensen, 1995, Phys. Rev. B **51**, 12911.

Tarascon, J.M., W.R. McKinnon, L.H. Greene, G.W. Hull, B.G. Bagley, E.M. Vogel and Y. La Page, 1987a, Proc. 1987 MRS Spring Meeting, April 1987, eds D.V. Gupser and M. Schluter (Materials Research Society, Pittsburg, PA) Vol. EA-11, p. 65.

Tarascon, J.M., P. Barboux, B.G. Bagley, L.H. Greene, W.R. McKinnon and G.W. Hull, 1987b, in: Chemistry of High-Temperature Superconductors, ACS Symposium, August 1987, eds D.L. Nelson, M.S. Whittingham and T.F. George, ACS Symposium Series, Vol. 351 (American Chemical Society, Washington, DC) p. 198.

Tetenbaum, M., B. Tani, B. Czech and M. Blander, 1989, Physica C **158**, 377.

Thomsen, C., 1991, in: Light Scattering in Solids, Vol. VI, eds M. Cardona and G. Güntherodt (Springer, Berlin).

Thomsen, C., and M. Cardona, 1993, Phys. Rev. B **47**, 12320.

Thomsen, C., and M. Cardona, 1994, in: Physical Properties of High Temperature Superconductors, Vol. 5, ed. D.M. Ginsberg (World Scientific, Singapore).

Tokura, Y., J.B. Torrance, T.C. Huang and A.I. Nazzal, 1988, Phys. Rev. B **38**, 7156.

Torrance, J.B., and R.M. Metzger, 1989, Phys. Rev. Lett. **63**, 1515.

Torrance, J.B., Y. Tokura, A.I. Nazzal, A. Benzike, T.C. Huang and S.S.P. Parkin, 1988, Phys. Rev. Lett. **61**, 1127.

Tranquada, J.M., 1998, Physica B **241–243**.

Tranquada, J.M., B.J. Sternlieb, J.D. Axe, Y. Nakamura and S. Uchida, 1995, Nature **375**, 561.

Uchida, S., 1997, Physica C **282–287**, 12.

van der Merwe, J.H., 1963, J. Appl. Phys. **34**, 117, 123.

Van Tendeloo, G., and S. Amelinckx, 1990, in: High T_c Superconductor Materials, Proc. E-MRS Symposium, Strassbourg, France, eds H. Habermeier, E. Kaldis and J. Schoenes, J. Less-Common Met. **164–165**, 92.

Van Tendeloo, G., H.W. Zandbergen and S. Amelinckx, 1987, Solid State Commun. **63**, 603.

Veal, B.W., H. You, A.P. Paulikas, H. Shi, Y. Fang and J.W. Downey, 1990a, Phys. Rev. **42**, 4770.

Veal, B.W., A.P. Paulikas, Hoydoo You, H. Shi, Y. Fang and J.W. Downey, 1990b, Phys. Rev. B **42**, 6305.

von Zimmermann, M., T. Frello, N.H. Andersen, J. Madsen, M. Käll, O. Schmidt, T. Niemöller, J.R. Schneider, H.F. Poulsen, Th. Wolf, R. Liang, P. Dosanjh and W.N. Hardy, 1999, preprint LANL cond-matter/9906251, submitted to Phys. Rev. B, April 7th, 1999 (to be published in revised form).

Wada, T., H. Yamauchi and S. Tanaka, 1992, J. Am. Chem. Soc. **75**, 1705.

Wang, J., I. Monot, M. Hervieu, J. Provost and G. Descardin, 1996, Supercond. Sci. Technol. **9**, 69.

Weber, T., R. Benischke, W.H. Fietz, J. Metzger and T. Wolf, 1992, in: Proceedings DPG TT11.19, Spring Meeting Deutsche Physikalische Gesellschaft, Regensburg, Germany.

Wells, B.O., Y.S. Lee, M.A. Kastner, R.J. Christianson, F.C. Chou and R.J. Birgeneau, 1997, in: Ten Years after the Discovery, Workshop on High-Tc Superconductivity, August 1996, Delphi, Greece, eds E. Kaldis, E. Liarokapis and K.A. Müller, NATO ASI Series E, Vol. 343 (Kluwer Academic Publishers, Dordrecht) pp. 349–370.

Welp, U., M. Grimsditch, S. Fleshler, W. Nessler, J. Downey, G.W. Crabtree and J. Guimpel, 1992, Phys. Rev. Lett. **69**, 2130.

Werder, D.J., C.H. Chen, R.J. Cava and B. Batlogg, 1988, Phys. Rev. B **38**, 5130.

Whangbo, M.-H., and C.C. Torrardi, 1990, Science **249**, 1143.

Widder, K., et al., 1996, Physica C **267**, 254.

Wille, L.T., A. Berera and D. de Fontaine, 1988, Phys. Rev. Lett. **60**, 1065.

Wong-Ng, W., F.W. Gayle, D.L. Kaiser, S.F. Watkins and F.R. Fronczek, 1990, Phys. Rev. B **41**, 4220.

Wu, W.K., J.R. Ashburn, C.J. Torng, P.H. Hor, R.L. Meng, L. Gao, Z.J. Huang, Y.Q. Wang and C.W. Chu, 1987, Phys. Rev. Lett. **58**, 908.

Yakhou, F., V. Plakhty, A. Stratilatov, P. Burlet, J.P. Lauriat, E. Elkaim, J.Y. Henry, M. Vlasov and M. Moshkin, 1996, Physica C **261**, 315–322.

Yang, S., 1992, Ph.D. Thesis (University of Illinois, Chicago, IL).

You, Hoydoo, J.D. Axe, X.B. Kan, S. Hashimoto, S.C. Moss, J.Z. Liu, G.W. Crabtree and D.J. Lam, 1988, Phys. Rev. B **38**, 9213.

Zaanen, J., 2000, Nature **404**, 714.

Zaanen, J., and O. Gunnarsson, 1989, Phys. Rev. B **40**, 7391.

Zaanen, J., A.T. Paxton, O. Jepsen and O.K. Andersen, 1988, Phys. Rev. Lett. **60**, 2685.

Zabinsky, S.I., J.J. Rehr, A. Ankudinov, R.C. Albers and M.J. Eller, 1995, Phys. Rev. **B 52**, 2995.

Zachariasen, W.H., 1931, Z. Kristallogr. **80**, 137.

Zandbergen, H.W., G. Van Tendeloo, T. Okabe and S. Amelinckx, 1987, Phys. Status Solidi **103**, 45.

Zech, D., H. Keller, K. Conder, E. Kaldis, E. Liarokapis, N. Poulakis and K.A. Müller, 1994, Nature **371**, 681.

Zech, D., K. Conder, H. Keller, E. Kaldis, E. Liarokapis, N. Poulakis and K.A. Müller, 1995a, unpublished data.

Zech, D., K. Conder, H. Keller, E. Kaldis, E. Liarokapis, N. Poulakis and K.A. Müller, 1995b, Total and site-selective oxygen isotope effect in $YBa_2Cu_3O_x$, in: Proc. Int. Workshop on Anharmonic Properties of High-T_c Cuprates, Bled, Slovenia, September 1994, eds D. Mihailovic, G. Ruani, E. Kaldis and K.A. Müller (World Scientific, Singapore) pp. 18–29.

Zeiske, Th., R. Sonntag, D. Hohlwein, N.H. Andersen and T. Wolf, 1991, Nature **353**, 542.

Zeiske, Th., D. Hohlwein, R. Sonntag, F. Kubanek and T. Wolf, 1992, Physica C **194**, 1.

Zhu, Y., and J. Tafto, 1997, Philos. Mag. B **75**, 785.

Handbook on the Physics and Chemistry of Rare Earths
Vol. 31
edited by K.A. Gschneidner, Jr., L. Eyring and M.B. Maple

Chapter 196

FLUX PINNING

Harald W. WEBER
Atomic Institute of the Austrian Universities, Vienna, Austria

Contents

1. Introduction

Try to count the number of publications on flux pinning in (R)$Ba_2Cu_3O_{7-\delta}$ (R-123), e.g. in the High-T_c Update (1987–2000) or in one of the more recently established databases (e.g., Superconductivity Database 1996), and you will realise that a comprehensive review of data accrued in these past fifteen years since the discovery of high-temperature superconductivity by Bednorz and Müller (1986) is just not feasible. Any solution of this problem will, therefore, necessarily contain a significant amount of personal views and preferences of the author as well of his (not unlimited) awareness of published work, and is certainly not aimed at a classification of research into better or lesser categories. The choices that had to be made were facilitated to a certain extent by the recently growing interest in the mixed-state properties in the $J_c \to 0$ limit (cf. the Workshops on Flux Dynamics 1994–2000), i.e., the behaviour of the flux line lattice under (nearly) zero flux pinning conditions, and matters of flux lattice melting involving a first- or a second-order phase transition (e.g. Welp et al. 1996, Schilling et al. 1996, Roulin et al. 1996). These subjects are not considered below, except for a brief reference in sect. 2. Furthermore, an extensive review of flux pinning effects by "weak" collectively acting defects is available (Blatter et al. 1994), which does not need to be repeated, but will be referred to and compared with "strong" pinning characteristics in sect. 3. Work on ceramics, whose flux-pinning characteristics are strongly influenced by the details of the grain arrangement and, correspondingly, by the nature of the resulting weak link structures, sheds little light on

the intrinsic flux-pinning properties and will, therefore, not be emphasised. As a result, the main thrust of this article will be placed on those flux-pinning effects which result in high critical current densities J_c even at high temperatures and in high magnetic fields; i.e., I will focus on those aspects of flux pinning which lead to applications of R-123 materials at or near the boiling temperature of liquid nitrogen. A further restriction that seems to be appropriate in view of the extensive literature, will refer to the chemical substitutions of the parent substance Y-123; i.e., we will mainly consider Nd substitutions, since the preparation processes and defect structures of this compound have been studied in most detail up to the present time.

Hence, this article will be organised in the following way. After a brief review of the mixed-state properties and the nature of the flux-line lattice in sect. 2, I will address some characteristic features of weak and strong flux pinning depending on the nature of the defects responsible for pinning. Section 4 will be devoted to a discussion of experimental techniques commonly employed to assess the critical current densities in the various forms of material; i.e., single crystals, melt-textured monoliths or thin films and tapes. Section 5 presents an overview of a special feature in the magnetisation curve, which seems to be dominated by the "as-grown" defect structure in single-crystalline and melt-processed 123 materials, and which is commonly referred to as the "fishtail effect" because of a characteristic dip in the magnetisation curve both in increasing and in decreasing fields. It should, however, more correctly be described as an anomalous *increase* of J_c with magnetic field in between field ranges below and above the "anomaly", where J_c decreases with field – as expected from conventional flux-pinning considerations. Section 6 will then discuss the nature of intentionally introduced artificial defects, which are either produced by certain processing conditions (such as the addition of excess Y_2BaCaO_5 – Y-211 – in melt-textured materials) or develop "automatically" during the growth process (as in R-123 thin films) or have to be introduced artificially by suitable types of radiation. The results of these procedures and the corresponding flux-pinning action of these various defect structures will be presented in the form of selected examples in sects. 7 and 8, where the resulting critical current densities, the irreversibility lines, the remnant magnetisation as well as the levitation forces will be presented. I will conclude with a brief summary in sect. 9.

2. The mixed-state phase diagram

The basic features of the mixed-state phase diagram have been established many years ago by Abrikosov (1957) on the basis of Ginzburg–Landau (1950) theory. It strictly refers to thermodynamic equilibrium conditions and to a "perfect"; i.e., totally homogeneous and defect-free, superconducting material. As shown in fig. 1, three phases can be established depending on the magnitude of the magnetic field: the Meissner state (Meissner and Ochsenfeld 1933), which is characterised by complete flux expulsion and is stable below the lower critical magnetic field H_{c1}; the normal conducting state, in which the magnetic field penetrates the sample completely and homogeneously above the upper critical

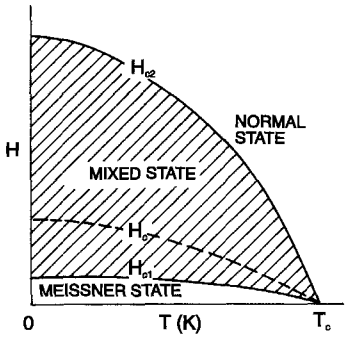

Fig. 1. Mixed state phase diagram of conventional type-II superconductors.

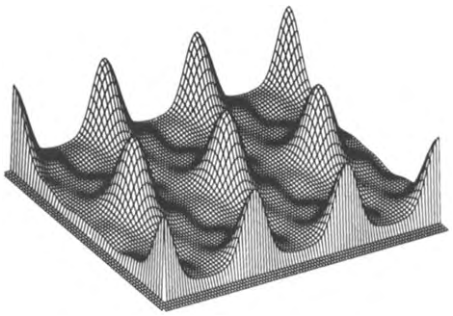

Fig. 2. Three-dimensional view of the flux line lattice in niobium, as determined from neutron diffraction (Weber et al. 1973).

field H_{c2}; and, in between, the mixed state, which is characterised by the coexistence of superconductivity and some magnetic-field containing regions. The clarification of the microscopic nature of this state was certainly one of the most fascinating tasks in superconductivity since the theoretical prediction by Abrikosov (1957) that it consisted of a quantized array of magnetic flux quanta ($\phi_0 = h/2e$) forming a regular two-dimensional lattice of straight "flux lines", arranged parallel to the magnetic field direction and each surrounded by a set of supercurrents circulating around the centres of the flux line cores in closed loops ("vortices"). The experimental verification of this prediction took almost 10 years, and was achieved by neutron diffraction (Cribier et al. 1964, Schelten et al. 1971, Weber et al. 1973) and by the "decoration technique" (Träuble and Eßmann 1966). A three-dimensional view of such an undisturbed flux-line lattice at low magnetic fields is shown in fig. 2 (Weber et al. 1973); a comprehensive review of the subject was prepared by Brandt (1995).

Since all of the high-temperature superconductors (HTS) belong to the same class of superconductivity – they are type-II superconductors – not too many changes in the mixed-state phase diagram were expected initially. However, this turned out to be an oversimplification and, in fact, an erroneous assumption. The number of phase diagrams that has appeared in the literature during the past few years is uncountable; an example pertaining to Y-123 is shown in fig. 3 (Blatter et al. 1994). However, before going into the details of this figure, a few words of caution seem to be appropriate. As pointed out in the last paragraph, the mixed-state phase diagram of fig. 1 strictly refers to the thermodynamic equilibrium state and is, by definition, only valid for a superconductor in which the flux lines are subjected *only* to the repulsive interactions between them, but flux-pinning interactions between defects and the flux-line lattice, which would render the free energy of the system position dependent, do not exist. This condition cannot be met by high-temperature superconducting materials up to the present, since structural defects are always present, although their pinning forces may become extremely small or negligible, at least at high temperatures. The pinning force is strongly dependent on the material under consideration, i.e. the apparent reversible regime in the phase

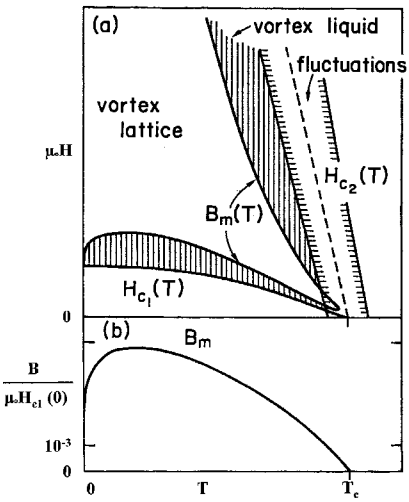

Fig. 3. Mixed-state phase diagram of high-temperature superconductors (Blatter et al. 1994): (a) phase diagram with parameters chosen to represent Y-123; (b) enlarged view of the low-field melting line.

diagram may range from $\sim 0.4 \leqslant t = T/T_c \leqslant 1.0$, e.g., for $Bi_2Sr_2CaCu_2O_8$ (Bi-2212), to $\sim 0.85 \leqslant t \leqslant 1.0$ for Y-123. At lower temperatures, very strong flux pinning can prevail. Therefore, a large number of published phase diagrams suffer from the drawback that the phase boundary lines have to be extracted from data which are clearly affected by flux pinning, or even worse, that "phase boundaries" are added, which are not related to the thermodynamic state at all, but exclusively determined by the strength of the pinning potential ("irreversibility line", Malozemoff et al. 1988).

Turning to fig. 3, the most important changes in the thermodynamics of the phase diagram are to be found at high temperatures. First, the traditional "mean-field" description of the phase transition into the normal conducting state, marking a single well-defined transition line for $H_{c2}(T)$, is blurred by fluctuations (e.g., Tesanovic 1991). At lower temperatures, the vortex liquid becomes thermodynamically stable, then turns into a vortex solid (the flux-line lattice) under a first- or a second-order phase transition, depending on sample purity and residual defect structures (such as twin boundaries). This part of the phase diagram is, in any case, characterised by large vortex phase fluctuations, particularly in the more two-dimensional superconductors, such as Bi-2212 (e.g., Bulaevskii et al. 1992, Koshelev 1994). The remaining overwhelming part of the phase diagram is then occupied by the flux-line lattice (note that the order of magnitude of $H_{c2}(0)$ is a few tens to a few hundreds T, whereas $H_{c1}(0)$ is only a few mT). The lower boundary lines shown in fig. 3 are certainly subject to discussion, since they have to be extracted from strongly pinning-dominated measurements. Considering the huge amount of work put into the assessment of the lower critical field at low temperatures (see, e.g., the review by Meilikhov and Shapiro 1991, and a recent paper on the subject by Böhmer et al. 1997), the "re-entrant" melting behaviour just above H_{c1} may or may not exist, but is certainly hard to prove experimentally under true thermodynamic equilibrium conditions as stipulated before.

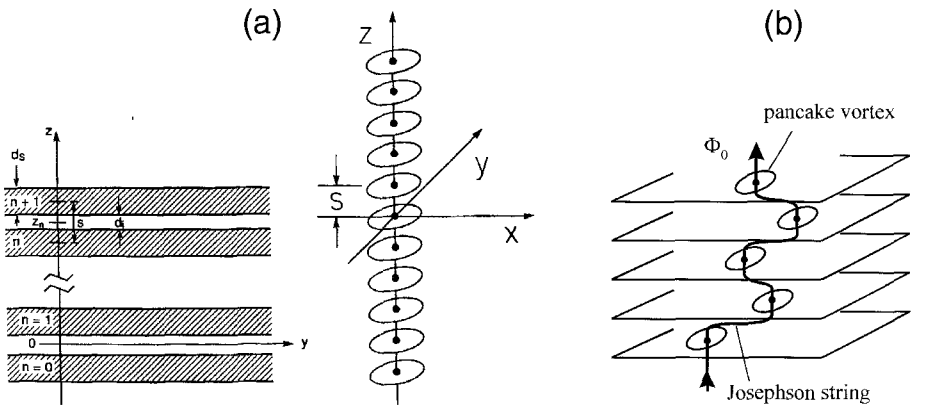

Fig. 4. Pancakes in high-temperature superconductors: (a) stack of aligned pancakes for $H \| c$ (Clem 1991); (b) decoupled pancakes in a strongly two-dimensional HTS (Blatter et al. 1994).

An additional phase boundary line must be added at relatively low fields, which refers to the nature of the flux line itself and which is again of special importance for the low-dimensional materials, although some indications for its relevance also in Y-123 (predominantly at low temperatures, where the c-axis coherence length is very small) were deduced by Schalk et al. (1992a, 1994) from measurements of the angular dependence of J_c in Y-123 thin films and the corresponding analysis in terms of the pinning potential. In essence, the layered character of the superconductors leads to a break-up of the straight (continuously connected) flux line into a series of layers carrying the supercurrents alternated by "blocking layers", which may either be non-superconducting (in the extreme two-dimensional case, Lawrence and Doniach 1971) or only weakly superconducting. These superconducting layers form stacks of "pancakes" (Pearl 1964, Clem 1991, Bulaevskii et al. 1992), which are coupled by magnetic interactions and by Josephson strings, thus aligning them along the field direction much in the same way as a regular flux line (cf. fig. 4a). However, as the field increases, the correlation between the pancakes becomes weaker and they finally decouple (fig. 4b) at a certain field H_{DC}, which could be directly observed in neutron diffraction experiments on Bi-2212 single crystals (Cubitt et al. 1993). This "decoupling" line, which is fairly independent of temperature, finally joins the melting line at elevated temperatures and certainly represents a thermodynamic equilibrium phase boundary that is related to the nature of the magnetic microstructure. Obviously, the question of whether or not a continuously connected flux line or a set of independent pancakes determines the magnetic microstructure of the mixed state, will play a significant role for flux pinning. Apart from details of the flux-pinning interaction (cf. sect. 3), one important issue was pointed out early on by Kes et al. (1990), i.e., that the response of decoupled pancakes will always be determined entirely by the c-axis component of the magnetic field.

The discussion so far has been tacitly based on the assumption that the magnetic field is directed parallel to the crystallographic c-axis of the superconductor. If we drop

this assumption, the general shape of the phase diagram is modified only moderately. The corresponding upper critical fields H_{c2} will be much higher, the lower critical fields H_{c1} lower by the same factor, although not too much is known, mainly because of experimental problems which would require sample alignments of better than 1° in most cases. However, the magnetic microstructure is changed and this is again more pronounced in the case of two-dimensional materials. The first striking effect, occurring also in nearly three-dimensional materials, was predicted by Tachiki and Takahashi (1989) early on and is related to the formation of the flux-line lattice. Because of the "normal-conducting" flux-line core, the lattice will gain energy if the flux lines are located on weaker superconducting or, even better, normal conducting regions. These are present in all HTS in a more or less pronounced form due to the existence of the "blocking layers", which are characterised by a (slight) suppression of the order parameter. Hence, the flux lines will automatically move to these regions, i.e., into the space between the fully superconducting CuO_2 planes ("*a*,*b*"-planes), thus preventing the formation of a regular long-range ordered flux-line lattice of hexagonal or square symmetry. Instead, they will form chains in between the CuO_2 planes, which were indeed observed by decoration experiments (Dolan et al. 1989, Gammel et al. 1992). This is called the "intrinsic pinning" effect and falls into the category of thermodynamic equilibrium phenomena. The second effect only plays a role in truly two-dimensional materials, where the blocking layer is sufficiently thick and prevents the formation of a finite order parameter. In this case, the circulating supercurrents forming the flux lines are completely suppressed and replaced by Josephson currents with different dimensions and physical properties (Clem and Coffey 1990). Obviously, this change of the magnetic microstructure ("Josephson vortex") will also have a significant impact on the flux pinning properties in two-dimensional HTS materials.

3. Weak versus strong flux pinning

The basics of flux pinning were comparatively simple in the metallic low-temperature superconductors, since "strong pinning" prevailed in most cases, i.e., the pinning potentials were deep and matters of thermal activation were not too important because of the low temperatures involved (cf., e.g., Campbell and Evetts 1972, Ullmaier 1975, Weber and Hittmair 1979). It was, therefore, possible to model the elementary flux-pinning interaction between a certain defect and a single flux line fairly successfully, but the summation of these individual forces (p_m) to obtain the bulk volume pinning force $\boldsymbol{P}_V = -\boldsymbol{J}_c \times \boldsymbol{B}$, and hence the critical current density, or – more correctly – vice versa, turned out to be tedious (e.g., Labusch 1969, Dew-Hughes 1971, 1974). Most of this work on "model systems", i.e., homogeneous superconductors with just one type of deliberately introduced defects, indicated that the summation was in between the "direct" summation law, where the individual elementary pinning forces p_m were just multiplied by the defect density and added up, and the "statistical" summation, which predicted a quadratic dependence of the bulk pinning force on p_m. Also, at that time, Larkin and

Ovchinnikov (1974, 1979) proposed the "collective" pinning theory, which introduced certain collective actions of several defects over a certain correlation length or volume for the first time, a theory that represents the basis for most flux-pinning considerations in high-temperature superconductors because of their generally "weak" pinning potentials.

In order to put these general remarks onto a more quantitative basis, three characteristic parameters and their actual magnitudes in low- versus high-temperature superconductors have to be considered. First, the critical current density J_c can never exceed a certain maximum value, which is defined by the material-dependent "depairing" current; i.e., the maximum loss-free current $J_{c,max}$ the superconductor can sustain before breaking up the Cooper pair correlation. Since $J_{c,max} \propto H_c/\lambda$, i.e., proportional to the thermodynamic critical field divided by the magnetic field penetration depth λ, the intrinsic material dependence is obvious and provides at the same time a natural distinction between low- and high-temperature superconductors, since H_c is relatively large (in particular compared to the upper critical field) and λ is relatively small in the former case, whereas the opposite is true in the latter. Thus, $J_c/J_{c,max}$ will be of the order of 10^{-1} for conventional superconductors versus $<10^{-3}$ in HTS. Second, we are concerned with high operating temperatures in the case of HTS, which render thermal fluctuations far more important and lead to thermally activated depinning or melting. This effect is conveniently characterised by the Ginzburg number Gi (e.g., Blatter et al. 1994), which is proportional to the square of T_c divided by the square of the minimum condensation energy ($\propto H_c^2 \xi^3 \varepsilon$, where ξ is the coherence length and ε is the mass anisotropy parameter, $(m_{a,b}/m_c)^{1/2}$). Numbers for Gi dramatically emphasise the problem: $\mathrm{Gi} \approx 10^{-8}$ in low-temperature superconductors, but $\mathrm{Gi} \approx 10^{-2}$ in HTS. Third, even quantum fluctuations affect the phase diagram (cf. sect. 2) and can add to the creep behaviour of the vortices. This effect differs in low- and high-temperature superconductors by a factor on the order of 100. Finally, since all of the above three effects are strongly affected by anisotropy (either through λ or directly through the anisotropy parameter ε), all flux-pinning effects in the HTS will depend on the directions of magnetic field and current flow with respect to the crystallographic axes in the material.

The difference between strong pinning and weak collective pinning can be visualised as follows (fig. 5). In the first case, a defect with a diameter of at least $2\xi(T)$ is required to provide the flux line with the highest possible energy gain by saving the condensation energy of the ("normal conducting") flux line core ($\mu_0 H_c^2/2$ per unit volume). In the best case, the defect should, therefore, be normal conducting itself, but superconducting inclusions with significantly different thermodynamic properties of their superconducting state (compared to the surrounding matrix) will also serve the purpose. The latter is often referred to as $\Delta T_c, \Delta H_{c2}$, or $\Delta\ell$-pinning, where ℓ is the electron mean free path, which primarily affects the Ginzburg–Landau parameter κ and the upper critical field H_{c2} (Campbell and Evetts 1972, Freyhardt 1971a, Antesberger and Ullmaier 1974, Adaktylos and Weber 1977). Depending on the size and the shape of the defect, the energy gain of the flux line reaches its maximum for normal-conducting inclusions and is given by the condensation energy multiplied by the length of the defect along the field direction and by the cross-sectional area of the flux-line core or of the defect in the plane perpendicular

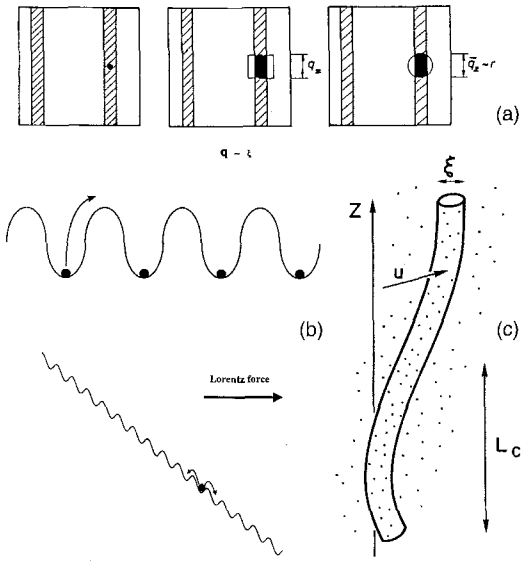

Fig. 5. Flux pinning in superconductors: (a) strong pinning through the core interaction by normal conducting precipitates of various shapes; (b) schematic view of the pinning potentials without (top panel) and under the action of a Lorentz force (bottom panel); (c) schematic view of pinning of a single flux line by the collective action of many small point pinning centres (after Ullmaier 1975).

to the field. This energy represents an upper limit of the pinning potential for $H \rightarrow 0$, which will, of course, in general decrease with temperature and magnetic field. At fixed temperature, the Lorentz force $\boldsymbol{P}_L$ acting on the flux lines will shift their spatial distribution and result in a "wash-board"-like arrangement of pinning potentials (fig. 5b) leading eventually to depinning for $\boldsymbol{P}_L = -\boldsymbol{P}_V$. Since this "critical state" equation does not refer to a thermodynamic equilibrium situation, depinning is always assisted by any energy transfer to the system, in particular thermal energy, as was pointed out by Anderson (1962) early on ("flux creep").

Contrary to the above, weak pinning prevails if the defect structure consists of a large number of very small defects ("point" pinning centres), the spatial distribution of which *must* fluctuate over a certain volume. In this case (fig. 5c), the entire ensemble of these defects interacts collectively with the flux line (we consider again the limit $H \rightarrow 0$) and exerts a pinning force over distances on the order of ξ in the plane perpendicular to the field and of the "correlation length" L_c along the field direction, which is largely determined by the elastic properties of the flux line. The actual scales of fig. 5c are more appropriate for the low-temperature superconductors, because ξ is rather large compared to the defect sizes, but the general picture remains the same in high-temperature superconductors, if the defect size does not exceed 0.5–1 nm, i.e., is clearly smaller than ξ. If we now increase the magnetic field, the usual interactions between the flux lines will start to play a role and lead to a change in the "correlation volume"; i.e., the coherence length ξ in the above flux-pinning considerations has to be replaced by the "transverse correlation length", R_c. As a consequence, several flux lines can be pinned simultaneously by the same ensemble of defects (collective pinning of three-dimensional flux-line bundles).

Under the influence of thermal activation, a rich variety of scenarios can emerge, which has been described by Blatter et al. (1994) in much detail. In general, the critical current density will decrease more rapidly with temperature and the character of the flux line lattice can change into a "glassy state". In addition, the dynamics of the system change and the pinning potentials depend on current density in a non-linear way (in contrast to the original flux creep model by Anderson 1962). If we consider the lower-dimensional high-temperature superconductors, where the continuous flux line breaks up into pancakes, as discussed in sect. 2, individual single-pancake pinning, individual pinning of stacks of pancakes, collective pinning of two-dimensional bundles and/or collective pinning of three-dimensional bundles can take place. Furthermore, transitions between these possibilities may occur depending on the size of the coherence length $\xi(T)$, which grows with rising temperature and may, therefore, lead to stronger coupling across the blocking layers ($H \parallel c$) and, hence, to a more three-dimensional behaviour at elevated temperatures. In all cases, (collective) creep or even thermally assisted flux flow (Kes et al. 1989) prevails and affects the data obtained from experiment, an issue that will be addressed in the following section.

In conclusion, as pointed out in the introduction, the results to be presented in sects. 5–8 are not aimed at a detailed discussion of these fundamental aspects of flux pinning and flux dynamics, but rather at possibilities to improve J_c in the 123 superconductors. We must be aware of the fact, however, that the "J_c's" quoted in the literature often do not refer to the "true" critical current densities, since the data are affected by creep and relaxation, and should rather be quoted as shielding current densities J_s. Furthermore, we will refrain from judgements of the nature of the boundary line, where J_s goes to zero, and will refer to it as the irreversibility line. This characteristic parameter is subject to the same restrictions as mentioned above; i.e., sensitive to the resolution of the experiment and its time scale. It is useful to note that the shape of this curve ($H \parallel c$) follows a power law (with an exponent of 1.5) for more three-dimensional HTS, as predicted by Malozemoff et al. (1988) on the basis of a depinning argument, but an exponential law for two-dimensional systems, as shown schematically in fig. 6.

4. Experimental techniques

J_c and the irreversibility line can be measured with several techniques, but we are usually not completely free to choose among them, since the form of the material under investigation imposes certain constraints, which can only be met by one or several special techniques. In principle, J_c is always determined from the critical state equation

$$\boldsymbol{P}_L = \boldsymbol{J}_c \times \boldsymbol{B} = (\mathrm{rot}\,\boldsymbol{H} \times \boldsymbol{B}) = (\mathrm{rot}\,\boldsymbol{B} \times \boldsymbol{B})\frac{\partial H}{\partial B} = -\boldsymbol{P}_V, \tag{1}$$

where $\partial H/\partial B$ can be set equal to 1 in HTS. Hence, the critical current density can be assessed from a direct transport critical current measurement or, magnetically, from the

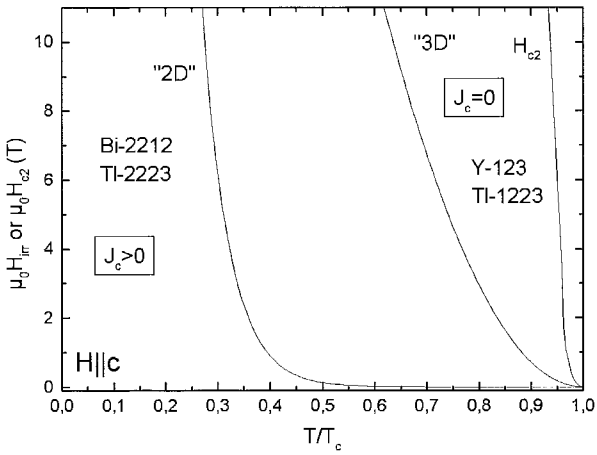

Fig. 6. Schematic representation of the irreversibility lines in HTS. The "3D" case corresponds to a power-law dependence of H_{irr} on temperature, the "2D" case to an exponential dependence.

corresponding flux-density gradient built up by the pinning centres. The latter is usually not directly accessible and must be evaluated from models, in most cases from the Bean model (Bean 1962).

Direct transport measurements are generally employed on thin films, tapes and coated conductors. They quickly reach their natural limits as the currents go up and/or the cross-section of the conductor increases. They are fast, i.e., can be started immediately after the magnetic field is set, and trace the I–V characteristics, which is of course most valuable if flux creep or thermally assisted flux flow (Kes et al. 1989) prevails, because the electric field is directly determined. On the other hand, J_c must be defined by a criterion; e.g., 1 μV/cm. It will be affected by the presence of stabilising materials, the silver tube or conducting substrates, and thus generally refers to the "overall" J_c, which can be converted to the critical current density of the superconductor if the shape and the volume fraction of the superconducting material are known.

Magnetic methods are required for single crystals (because of their generally very small size, the corresponding contact problems and the huge critical currents) and for melt-textured bulks (because of their enormous current requirements). Several possibilities are available: dc and ac techniques, and among the dc methods "global" and more "local" techniques. Starting with the global dc techniques, Superconducting Quantum Interference Devices (SQUID's) have been used most extensively, followed by Vibrating Sample Magnetometers (VSM's). In both cases, the magnetic moment of the sample is measured as a function of magnetic field, but the "timing" of the experiment can vary by orders of magnitude. Taking, e.g., the custom-built high-field (8 T) SQUID operated by our group, the settling time of the instrument after applying a certain magnetic field amounts to about 10 minutes followed by the measuring cycle (where the sample is slowly moved up and down in a set of pick-up coils), which takes at least another 5 min. Therefore, if strong creep prevails, we obtain information on the magnetic moments after a relaxation period of 10 min and then averaged over an additional period of 5 min (Kritscha

et al. 1990a). On the contrary, the VSM can collect data in continuously (but slowly) changing external fields and, therefore, provides data in a different "time window" of the relaxation process. In both cases, the moment m is then converted into the magnetisation, $M = m/V$, where V is the sample volume, plotted as a function of the external field and used to calculate the critical current densities via the Bean model and/or its extensions for finite geometry and demagnetisation effects (Gyorgy et al. 1989, Sauerzopf et al. 1990, Wiesinger et al. 1992a, cf. also Brandt 1995, 1996, and references therein). The third global technique, to be discussed briefly, is torque magnetometry, and I take the example of a capacitance torquemeter (Griessen et al. 1977). Here, the torque $\boldsymbol{\tau}$ exerted on a superconducting sample with a magnetic moment $\boldsymbol{m}$ in an external magnetic field $\boldsymbol{H}_e$ is given by $\boldsymbol{\tau} = \boldsymbol{m} \times \mu_0 \boldsymbol{H}_e = m\mu_0 H_e \sin\,\alpha$, where $\alpha = \alpha(\boldsymbol{m}, \mu_0 \boldsymbol{H}_e)$ is the angle between the magnetic moment and the external field. Obviously, the torque disappears if the moment is parallel to the field direction. A certain disadvantage is the necessity of applying the field out of the main crystallographic directions (e.g., at an angle of 5° with respect to the c-axis) and the requirement of re-calibration at each temperature. All further procedures are the same as above, i.e., the moment is extracted from the data, converted into the magnetisation and evaluated in terms of certain models to obtain J_c. The main advantage of measuring the torsion with a capacitance lies in its very high sensitivity and, in particular, in its very fast response. Hence, magnetisation relaxation can be studied at a very early stage and, if combined with a fast sweeping magnet, be extended to the so-called dynamic relaxation regime, a concept that was originally introduced by Pust et al. (1990) and explored in much detail by the group at the Vrije Universiteit (VU) Amsterdam (Quaford et al. 1992, Lensink 1993, Schnack 1995, van Dalen 1995).

Of course, an important question should be asked immediately; i.e., what do we really extract from such magnetic measurements in terms of the critical current density? This matter was addressed by Werner et al. (Werner et al. 1996, Werner 1997), who started to compare experimental results on the same single crystal, but obtained from different techniques. An example comparing torque and SQUID magnetometry on an Yb-123 single crystal ($H \parallel c$) is shown in fig. 7, where the shielding current density J_s is plotted versus the induction B in the crystal (Werner et al. 1996), as evaluated form a modified Bean model (Wiesinger et al. 1992a). Details of the shape of the J_s–B curve are not of interest right now, but will be considered in sect. 5. The uppermost five curves show the dynamic relaxation response obtained by torque magnetometry under different field sweep rates. The curves marked by the symbols refer to conventional relaxation after 10 and 15 minutes, respectively, starting at several fields from the uppermost curve (40 mT/s), and the bottom solid line shows the data taken by the 8 T SQUID under the conditions mentioned above. Apart from the very nice agreement between the conventional and the dynamic relaxation rates (Werner et al. 1996), the data obtained from the torque and the SQUID at comparable relaxation times are very close and demonstrate the feasibility of such magnetic measurements and of the evaluation methods for obtaining reliable data on the current density J_s.

Turning next to more "local" techniques, the magneto-optical Faraday effect will be discussed first (Alers 1957, Kirchner 1968, Huebener et al. 1972, Koblischka and

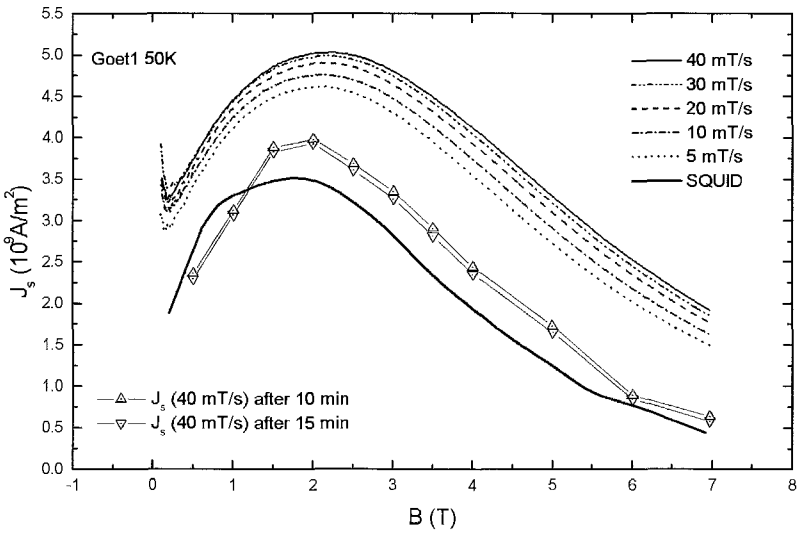

Fig. 7. Comparison of experimental data obtained by SQUID and by torque magnetometry on the same single crystal (Werner 1997).

Wijngaarden 1995, Wijngaarden et al. 1996). Here, the penetration of the flux front into, e.g., a single crystal is traced by the rotation of the polarisation vector of linearly polarised light when passing through a certain "magneto-optical" layer (e.g., a thin film of EuSe). The parts of the layer which are subjected to a magnetic field will provide us with a different image compared to the field-free regions (dark versus bright, depending on the set-up of the polarisation analyser) with a spatial resolution on the order of 0.5 μm. The magnetic resolution depends on the magneto-optical layer used for the experiment, but is generally on the order of 5 mT, and the time resolution is immediate. Two important conclusions can be drawn from such an experiment. First, the visual inspection of the flux penetration process leads to a crucial check of the models employed for the above evaluations of the magnetisation curves in terms of J_c. As shown in fig. 8, all the general features of the Bean model in its modified form for a finite geometry are beautifully confirmed by experiment along the entire magnetisation loop from 0 to +7 T to zero and then to −2 T. Thus, evaluations of J_c as described above are feasible and lead to the right answers. Second, the details of the flux patterns, in particular the local distributions of the field H_z at the sample surface, can be converted accurately into the current patterns (Wijngaarden et al. 1996) and thus provide us with more local information on the critical current density than the global techniques described above.

The latter also holds for the last dc technique I will discuss in the following, i.e., the application of multi-Hall-probe arrays for the direct recording of the flux density gradients along the radius of a superconductor. It was invented about 25 years ago (Weber et al. 1976, Adaktylos et al. 1977), forgotten, and re-invented (Majer et al. 1996), although with significantly improved technology. In this case, an array

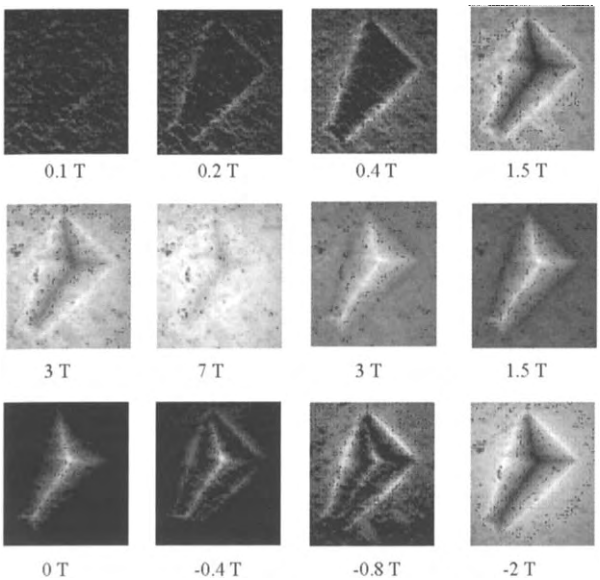

Fig. 8. Magnetisation loop ($0 \rightarrow 7 \rightarrow 0 \rightarrow -2$ T) recorded by the magneto-optical Faraday effect on a single crystal (Werner 1997).

of approximately 10–15 very small Hall probes (e.g., $10 \times 10\,\mu m^2$) are manufactured from GaAs/AlGaAs heterostructures and arranged at equal spacing of, say, $100\,\mu m$. The Hall voltages, therefore, directly display the flux profile, i.e., the z-component of the local induction at the sample surface. This can again be converted into critical current densities with similar algorithms as in the case of the magneto-optical Faraday effect. The advantages of this technique are manifold. First, the spatial resolution can be adjusted to the experimental requirements (active areas of $1 \times 1\,\mu m^2$ have been achieved and the spacing can be made according to sample size and/or the type of experimental investigation envisaged). Second, the time resolution is immediate, and the system can also be operated under ac conditions. Third, magnetisation loops or relaxation measurements can be made at any of the available positions "within" the sample. Of course, the amount of data handling is quite extensive, in particular since the individual Hall probes may require individual calibrations (deviations of their field response from linearity) and re-calibrations at different temperatures.

Many novel experiments based on this technique have been reported in the literature (e.g., Abulafia et al. 1995, 1996, Yeshurun et al. 1996, Doyle et al. 1997). For the purpose of this section, I wish to concentrate on two results, which are shown in fig. 9 (Werner 1997). First, the flux profile (fig. 9a) obtained at a certain external field (~280 mT, 60 K) again shows all the characteristic Bean-like features and a (smeared-out) increase of the field at the sample edge as expected from demagnetisation. Second, the comparison between the local Hall-probe measurement and SQUID magnetometry (fig. 9b) is as favourable as in the case of torque magnetometry, i.e., the current densities J_s deduced

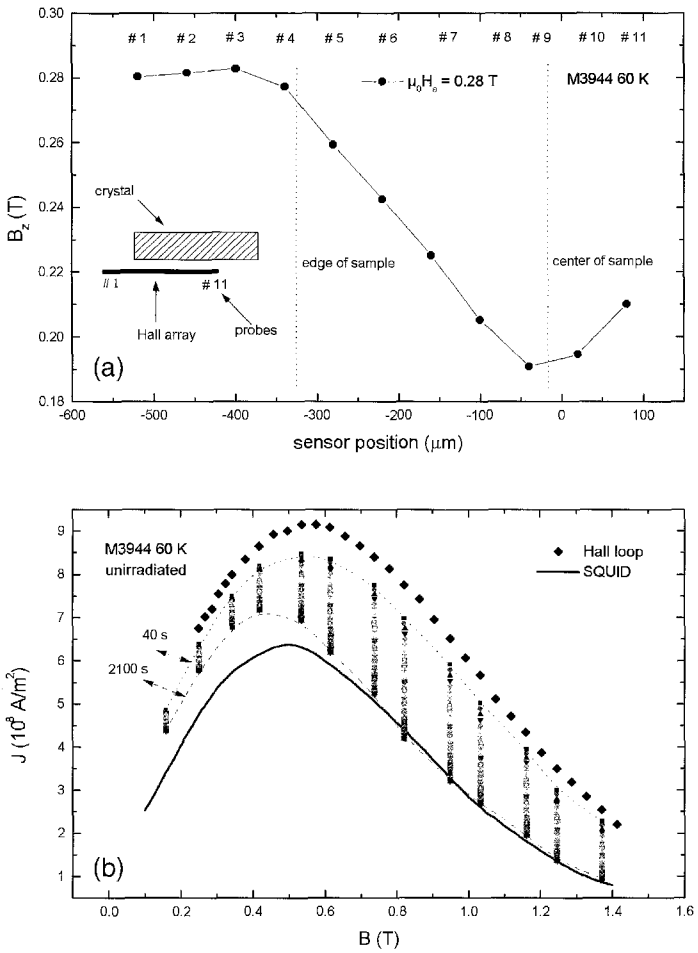

Fig. 9. (a) Measurement of the flux profile in a single crystal with a multi-Hall-probe array: B_z versus sensor position (Werner 1997). (b) Comparison of experimental data obtained by SQUID and Hall probe magnetometry on the same single crystal (Werner 1997).

from both kinds of experiment agree very well and, therefore, confirm the basic concepts of these techniques.

The last technique to be discussed in the context of J_c measurements is an ac method proposed by Campbell (1969) and modified by Rollins et al. (1974), which is particularly well suited for measurements on bulk samples; e.g., melt-textured HTS. A schematic view of its basic principles is shown in fig. 10. Assume that a Bean-like flux profile has been established by a certain dc field well above the full penetration field. If a small ac ripple field of amplitude h_{ac} is superimposed parallel to the dc field, the flux profile near the sample surface is modified accordingly (as shown by the shaded area in fig. 10). With

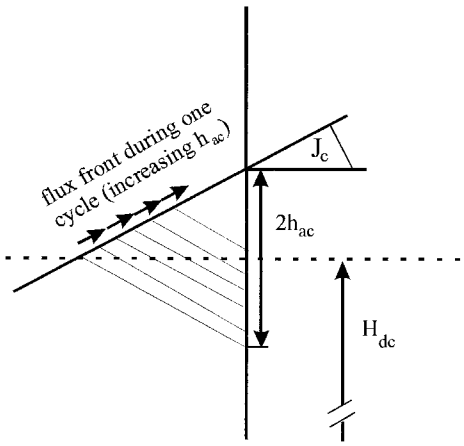

Fig. 10. Schematic representation of the flux front near the sample surface upon superimposing an ac ripple field of amplitude h_{ac} onto a large dc field H_{dc} (Frischherz et al. 1995).

increasing h_{ac} the "modified" flux profile moves further into the interior of the sample and eventually affects the entire flux-density gradient. Hence, the idea of such a "flux profile" experiment consists of measuring the induced voltages in a set of compensated pick-up coils (one containing the sample) as a function of ac amplitude at constant dc field and temperature. The in-phase signal S_{in} of the lock-in amplifier in the superconducting state is given by

$$S_{in} = \frac{\alpha'(a+b)}{J_c} h_{ac}^2 + \beta h_{ac} + \gamma = \alpha h_{ac}^2 + \beta h_{ac} + \gamma, \tag{2}$$

where α', β, and γ are instrumental constants and a, b are the geometrical dimensions of a rectangular sample in the plane perpendicular to the field ($c \gg a,b$; $H \parallel c$). $S_{in}(h_{ac})$ is then fitted to a parabola to obtain α and the critical current density is calculated from

$$J_c = \frac{S_n}{h_{ac}} \frac{a+b}{\alpha ab}, \tag{3}$$

where S_n/h_{ac} is the slope of the signal in the normal conducting state. In practice, both the real and the imaginary part of the signal are measured at the same time, the frequency is kept relatively low (9 Hz), and the amplitude is varied between 0 and 10–20 mT. The latter can be avoided, if the version introduced by Rollins et al. (1974) is employed, where signal averaging and phase-sensitive signal analysis at a fixed ac field amplitude are sufficient. In principle, this method is very well suited to determine critical current densities in large samples, unless the flux profiles become too steep to be noticeably changed by the ac field over a significant penetration range into the interior of the sample (such as for instance in melt-textured samples at 4.2 K). A comparison with SQUID magnetometry (Frischherz et al. 1995) leads to similar results as shown in figs. 7 and 9 for torque and Hall probe arrays; i.e., J_c as deduced from this ac technique is larger (because of its fast response) than that obtained from a SQUID experiment (by a factor of up to 2, depending on relaxation).

To conclude this section, a few words on the experimental assessment of the irreversibility lines seem to be appropriate. As pointed out in much detail above, the timing ("time window") of the experiment represents a decisive factor for the apparent magnitude of J_c. Since we are now looking for methods to determine the exact location in the H,T plane, where J_c becomes zero, the timing will again play a crucial role. In addition, the criterion $J_c = 0$ is extremely ill defined, since it entirely depends on the resolution of the experimental technique employed. I will choose two examples (SQUID magnetometry and ac susceptibility) to demonstrate the salient features of the problem.

In the dc case, there are two ways of determining the irreversibility line: one is to sweep the magnetic field at constant temperature and take the point where the loop closes, i.e., the hysteretic behaviour disappears (fig. 11a), the other is to sweep the temperature at constant field and take the point where the zero-field-cooled (ZFC) and the field-cooled (FC) branches merge (fig. 11b). The latter is more frequently used, because it is generally easier and faster to vary the temperature in small increments. Obviously the results will be quite arbitrary, since the curves always merge tangentially and will strongly depend on the resolution of the set-up and the time scale chosen. Distinct improvements can be achieved by noting that the measuring principle involves a movement of the sample between the set of pick-up coils in a slightly inhomogeneous field, which can be visualised to be equivalent to the superposition of a small ac field and which results in a distortion (fig. 12) of the SQUID signal response curves, if dissipative processes ("hysteresis losses") set in (Kritscha et al. 1990a, Suenaga et al. 1992, Sauerzopf et al. 1992). In this way, the "$J_c = 0$"-criterion can be approximated by 10^4–10^5 A m^{-2} (depending on sample size). If this more sensitive criterion is used, all differences, mentioned occasionally in the literature, between the "loop" and the ZFC–FC experiments disappear, thus confirming equilibrium conditions in both cases (Kritscha et al. 1991).

Even more commonly used are ac techniques, which are based on the detection of energy losses of the superconductor, much in the same way as discussed above for the signal distortion in the SQUID (for reviews, cf. Clem 1992, Frischherz et al. 1995, Gömöry 1997). A wealth of information on the frequency and amplitude dependence of χ' and χ'' has been accrued for all kinds of HTS and for magnetic field orientations parallel and perpendicular to the crystallographic c-axis. The main points are the following. If the superconductor is in the critical state, a peak in the out-of-phase signal χ'' occurs, when the flux front reaches the centre of the sample. Of course, this peak indicates the presence of a certain critical current density J_c (which is given in the simplest case of an infinite cylinder by h_{ac}/r) and, therefore, defines a certain sample-dependent J_c criterion (of similar order as in the above dc case, i.e., 10^5 A m^{-2}). On the other hand, if strong flux creep prevails, e.g., thermally assisted flux flow, χ'' will also show a peak (Geshkenbein et al. 1991) at a certain flux flow resistivity ρ_{TAFF}, which is given by $\rho_{TAFF}(H,T) = \mu_0 \pi \nu r^2$ (ν is the excitation frequency, r the sample radius). Since in most cases of interest, both effects will contribute to the experiment at the same time, we expect a certain amplitude dependence (from the critical state equation) and a certain frequency dependence from flux creep or flow. Although the analysis is obviously not trivial, the peak of χ'' is still often used to characterise the irreversibility point because

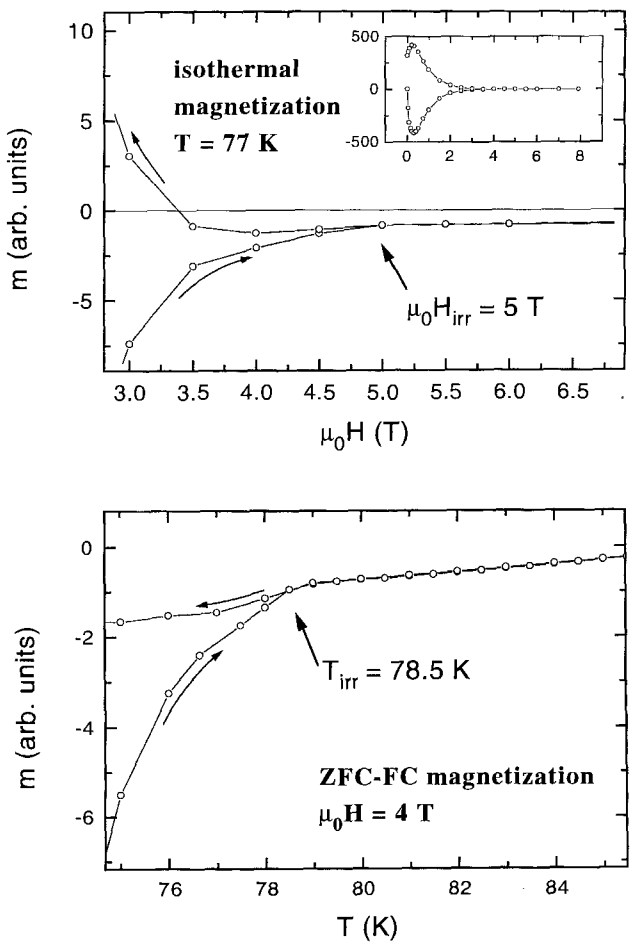

Fig. 11. "Standard" methods to determine the irreversibility line from dc measurements on single crystals (Frischherz et al. 1995): (a) Isothermal magnetisation ("closing" of the loop); zero-field-cooled/field-cooled magnetisation ("opening" of the branches).

of the relatively high experimental accuracy with its determination (fig. 13). Alternatives are extrapolations of the loss signal to zero at high temperatures (Yacobi et al. 1992), an extrapolation of the in-phase signal χ' to zero at high temperatures, or the analysis of higher harmonics, where again the peak or extrapolations can be employed. A comparison of these various evaluation possibilities is shown in fig. 13 (Wacenovsky 1993) for a melt-textured Y-123 sample. Taking the example of 1 T, the peaks of χ'' and of the third harmonic lead to the same irreversibility temperature T_{irr}, and the same holds for the extrapolations of χ' and of the third harmonic, the difference being ~0.5 K. A more

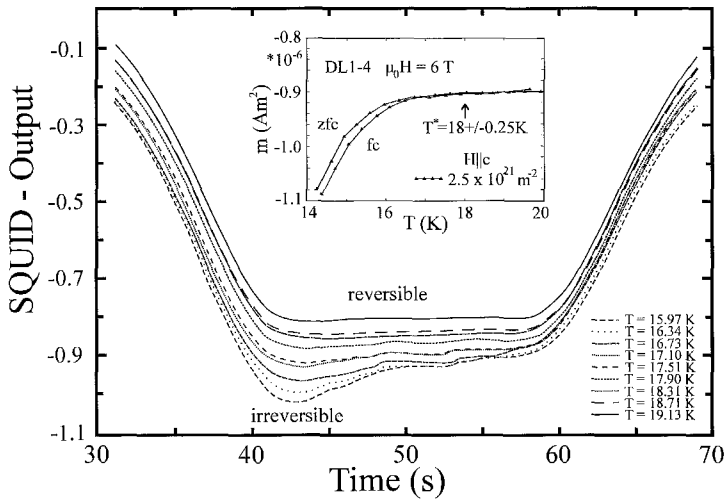

Fig. 12. Distortion of the SQUID output signals by hysteresis effects in a single crystal (Kritscha 1991).

complete comparison of data obtained at different frequencies and field amplitudes (peak in χ'', extrapolation of χ'' to zero: "onset") as well as by SQUID magnetometry is shown in fig. 14, again for a melt-textured Y-123 sample (Frischherz et al. 1995). Systematic dependencies are found in all cases, including the SQUID measurement, the "frequency" in the latter case being determined from the speed of the sample movement between the pick-up coils. In summary, if the frequencies and the ac amplitudes are kept low, the differences between the various experimental parameters lead to discrepancies in T_{irr} on the order of 1 K.

In conclusion, sufficient control of the experimental parameters and a critical assessment of the characteristics of each techniques will in general lead to reliable data both on the current densities and the irreversibility lines. Direct comparisons of published data are still difficult, in particular when the experimental parameters are not explicitly specified.

5. A flux-pinning anomaly: the "fishtail" effect

It may appear strange to start the discussion of flux-pinning results with an "anomaly", but almost every 123 single crystal, many other high-T_c single crystals (such as, e.g., Tl-1223) and several melt-textured materials (e.g., Nd-123) show the so-called "fishtail" effect, which was given this name because of a characteristic dip in the magnetisation curve (fig. 15a, Däumling et al. 1990). The development of the "second peak" is obviously related to an anomalous increase of the critical current density with magnetic field. However, it turned out soon (fig. 15b, upper panel) that such a dip is not a necessary prerequisite of the J_c anomaly, since it can be masked in a magnetisation curve (Kritscha

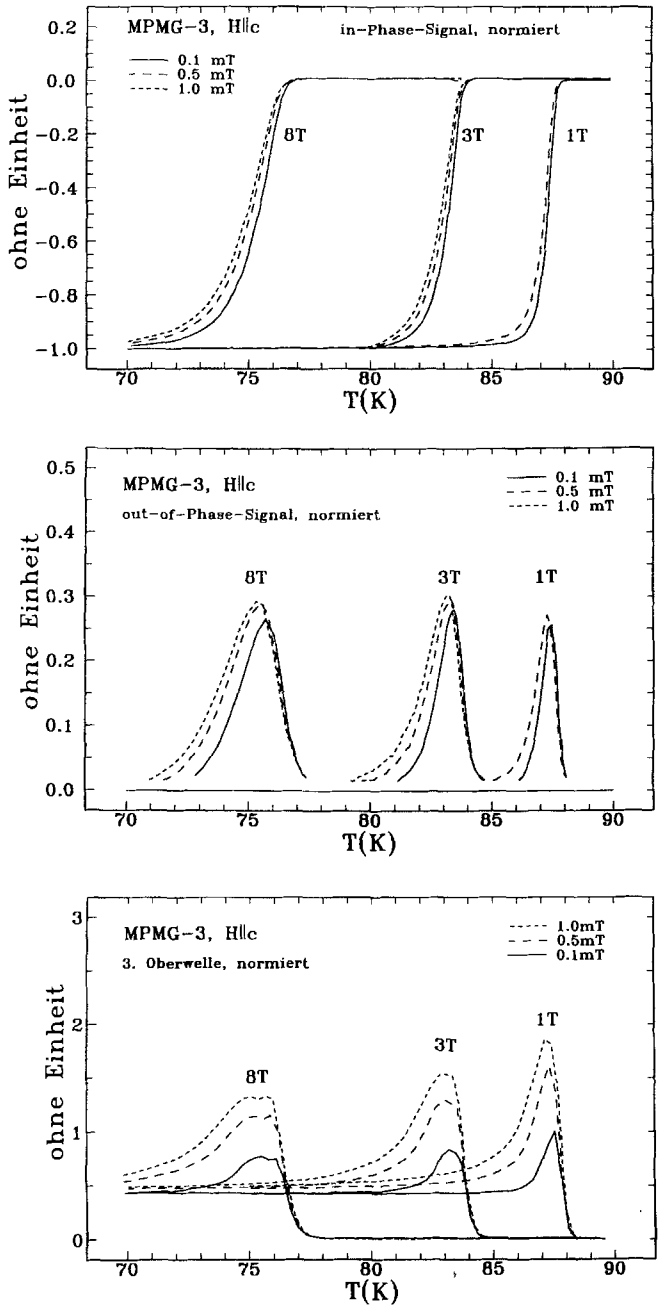

Fig. 13. Measurement of the ac susceptibility on a melt-textured superconductor (Wacenovsky 1993). Top panel: in-phase signal; middle panel: out-of-phase signal; bottom panel: third harmonic.

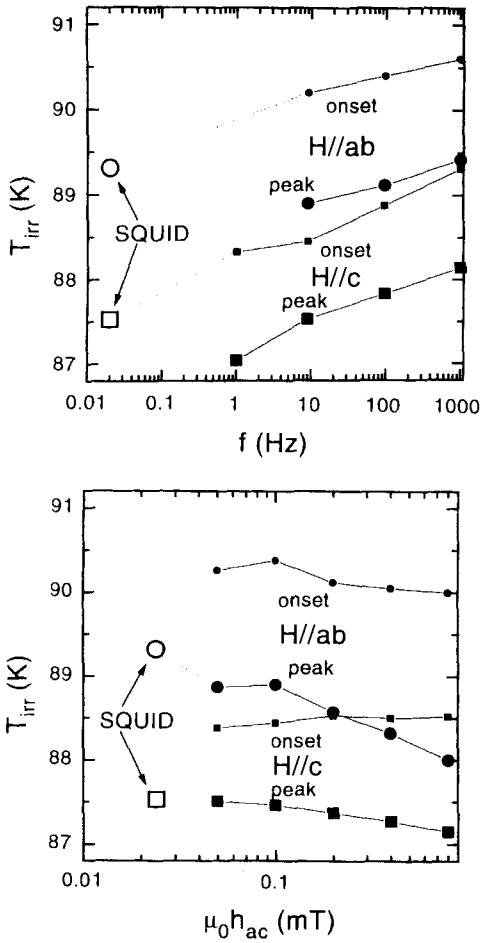

Fig. 14. Irreversibility temperatures as a function of (top) frequency and (bottom) amplitude of the ac ripple field. The open symbols denote the quasi-static conditions of SQUID magnetometry; for details cf. the text (Frischherz et al. 1995).

1991) by sample-dependent combinations of size and critical current density (according to the Bean model), i.e., the central issue is the *increase* of J_c with increasing magnetic field (lower panel).

Such an increase of J_c with increasing field was occasionally seen in low-temperature superconductors, and at least three different mechanisms were identified, depending on the nature of the defects. The first mechanism prevails whenever an *ordered* defect structure occurs, i.e., the defect spacing d is constant throughout the superconductor. Then, whenever d equals the lattice parameter a_0 of the flux-line lattice or multiples of a_0, "matching" occurs and peaks in the pinning force or the critical current density are found. A nice example of these matching peaks was reported by Hillmann and Hauck (1972) for ordered precipitates in NbTi. In view of the underlying mechanism, the peaks always occur at the same induction B (which determines the lattice parameter) and are,

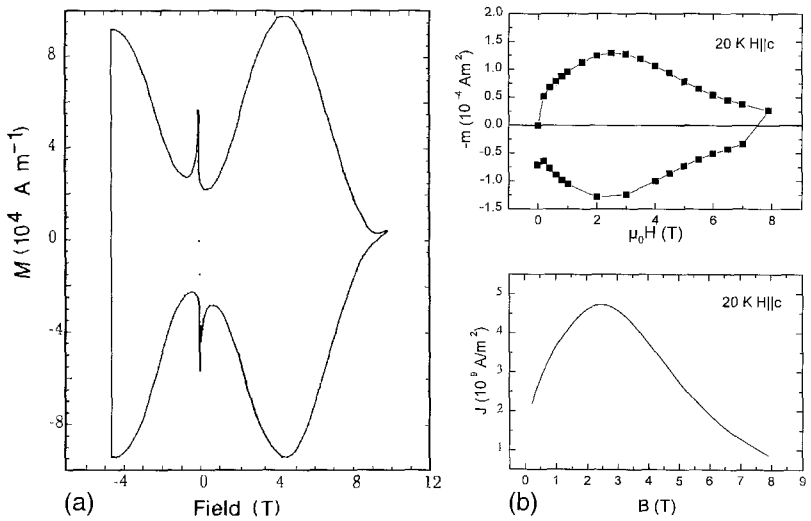

Fig. 15. Fishtail anomaly in 123 single crystals: (a) magnetisation loop showing a characteristic dip (Däumling et al. 1990): (b, top panel) magnetisation loop without a dip and (bottom panel) $J_c(B)$ dependence evaluated from the data of the top panel (Werner 1997).

therefore, temperature *independent.* Another mechanism was experimentally investigated by Evetts and Wade (1970), who studied a superconductor with a well-defined number of superconducting inclusions of (slightly) different superconductive properties. Since the elementary pinning force is, in this case, proportional to the difference between the reversible magnetisation of each compound, ΔM_{rev}, the pinning force will decrease with magnetic field, go to zero (when $\Delta M_{rev} = 0$; i.e., where the two reversible magnetisation curves cross) and increase again at higher fields before finally dropping to zero near H_{c2} of the matrix. This mechanism leads to a dip in the magnetisation curve followed by a broad maximum. Since the reversible superconductive properties of both phases depend on temperature, the peak itself will also be temperature *dependent,* in contrast to the first case. The third mechanism, which often leads to sharp peaks near H_{c2} in nearly reversible superconductors, is related to the smallness of c_{66}, the shear modulus of the flux-line lattice, near H_{c2}, and can be understood in terms of collective pinning theory. A particularly complete study of this effect was made by Meier-Hirmer et al. (1985) using radiation-induced point defects in V_3Si single crystals, which varied in their concentration by more than three orders of magnitude. As shown in fig. 16, sharp peaks develop near H_{c2} in the initial state and at low defect concentrations, which then start to broaden and to shift to lower fields prior to disappearing at high defect concentrations. Very good agreement with the static collective pinning theory (Larkin and Ovchinnikov 1979) was found at low defect concentrations, whereas the J_c–B dependence at the highest defect concentration was attributed to plastic flow of the flux lines (Kramer 1973).

According to these considerations, the first model for the "fishtail" anomaly in HTS single crystals (Däumling et al. 1990) was based on the assumption that oxygen-

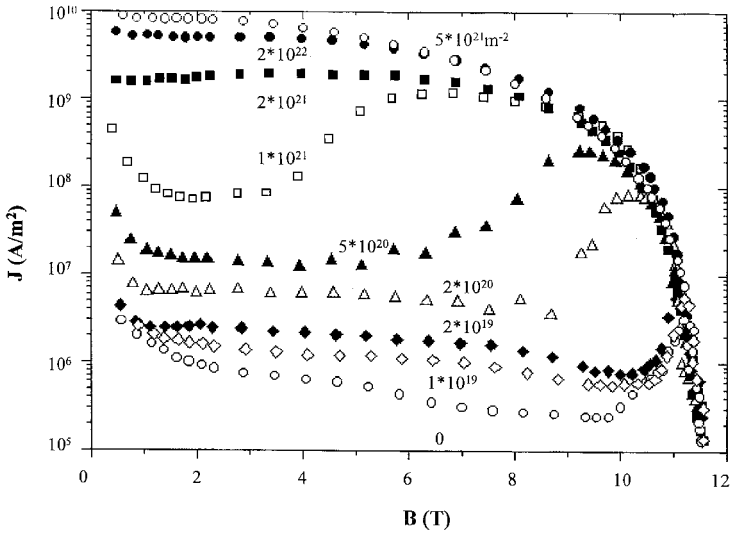

Fig. 16. Dependence of the persistent currents on magnetic field in a V_3Si single crystal as a function of neutron fluence (Meier-Hirmer et al. 1985).

deficient parts of the superconductor with distinctly lower transition temperatures into the superconducting state (cf., e.g., the T_c–δ phase diagram of Y-123, Jorgensen et al. 1988, 1990, Cava et al. 1990, Breit et al. 1995) were the responsible defects, which would turn normal conducting at a certain temperature and magnetic field far below the transition temperature T_c of the single crystal and would, thus, be "switched on automatically" by the increasing magnetic field along the magnetisation loop. In addition, the appearance of "granularity" at higher magnetic fields had to be invoked in the early studies (Däumling et al. 1990, Zhukov et al. 1993, Cohen et al. 1993), an argument that might have been applicable at that stage, but was later contradicted by transport measurements (Gordeev et al. 1994) showing a "fishtail" effect of J_c, and by magneto-optical studies of the flux penetration patterns (cf., e.g., fig. 8) in single crystals of better quality. Moreover, de Groot et al. (1991) pointed out that the fishtail anomaly did not disappear after extended oxygenation treatments, an observation that shed doubt on the entire idea of this mechanism being responsible for the fishtail.

As a consequence, alternative models focusing mainly on the dynamics of the flux-line lattice, possible transitions between single-vortex pinning or pinning of small versus large bundles, and possible transitions between two- and three-dimensional vortex structures were proposed. (Actually, a very similar feature in the magnetisation curve of strongly two-dimensional HTS, such as Bi-2212 or Tl-2223, which is sometimes called the "arrowhead" feature, might be caused by field-induced decoupling of pancakes, cf. sect. 2, and therefore not be related to the fishtail in 123 HTS, cf. also below). For instance, Krusin-Elbaum et al. (1992) and Civale et al. (1994a) studied magnetisation curves and relaxation, analysed their data in terms of a transition between a single-vortex pinning

regime and collective pinning of vortex bundles, and included the collective creep concept (Feigel'man et al. 1989, 1991). The corresponding normalised relaxation rate, S, looked like the mirror image of the magnetisation curve (or the J_s–H dependence) and the initial drop of the magnetisation was, therefore, attributed to the vortex dynamics, i.e., faster relaxation in the low-field regime, which differ under different pinning scenarios. These findings were soon questioned (Zhukov et al. 1994, Yeshurun, et al. 1994) based on careful measurements of the field dependence of S. These authors pointed out that the minimum of S was usually observed at fields significantly *below* the peak field of the fishtail, i.e. S was *not* the mirror image of M, and that a qualitatively similar relaxation behaviour occurred in crystals with and without the fishtail feature. The alternative explanations, however, differ, although both aim at a static origin of the anomaly in Y-123. Zhukov et al. (1994) favour changes in the elastic properties of the flux-line lattice and/or decoupling of flux lines into pancakes, which could also be associated with a decrease of the collective pinning correlation length resulting in an increase of J_c. (Decoupling into pancakes *above* 40 K would be inconsistent with data by Schalk et al. (1994), which were obtained on Y-123 thin films). Based on comparisons with Bi-2212, Yeshurun et al. (1994) pointed out that the "effective" time scales accessible to experiment differ largely between the two materials (because of their strongly different collective pinning activation energies U_c, Ginzburg numbers and depairing current densities; cf. sect. 3), and that the anomaly would still be present in YBCO for $t=0$, but not in BiSSCO. Evidence for the dynamic nature of the fishtail was obtained by van Dalen et al. (1995), who employed torque magnetometry on twin-free Dy-123 single crystals and evaluated their data in terms of the so-called general inversion scheme ("GIS", Schnack et al. 1993). The latter is based on the assumptions that the temperature and the current dependence of the activation energy can be separated and that U_c and the true critical current density J_c are connected by a power law. Such an analysis showed a smoothly decreasing dependence of the true J_c with field, which was interpreted as a clear sign for the dynamic origin of the fishtail; i.e., field-dependent relaxation rates and reduced activation energies at low fields. From the relatively weak field dependence of J_c, the authors conclude, furthermore, that the single-vortex pinning regime always prevails and no cross-overs occur. The most recent dynamic picture to be presented comes from measurements of the time evolution, $\partial B/\partial t$, of the local induction with Hall probe arrays (Abulafia et al. 1996), which can be analysed in terms of the vortex velocity $\boldsymbol{v}$ ($\boldsymbol{v}=\boldsymbol{v}_0 \exp[-U/kT]$) and, hence, in terms of a pinning potential U/kT without further assumptions about the creep mechanisms. The authors found a characteristic change in the slope of U/kT versus J at the peak field. This cross-over was related to a change in the creep mechanism at the peak field; i.e., collective creep prevails below the peak field, but a dislocation-mediated mechanism of plastic creep (Geshkenbein et al. 1989, Hirth and Lothe 1982) takes over at higher fields.

With the advent of a new generation of Y-123 single crystals of extremely high purity, and in view of a thorough study of the fishtail and its angular dependence in several 123 single crystals, the original proposal by Däumling et al. (1990) of oxygen-deficient clusters being responsible for the enhancement of J_s received strong

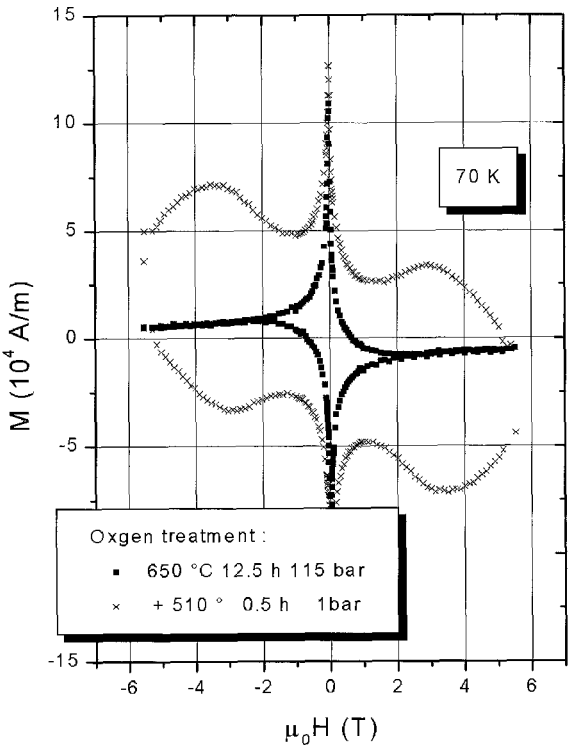

Fig. 17. Reversible introduction and removal of the fishtail anomaly in Y-123 single crystals by oxygen treatments (Erb et al. 1997).

experimental support. In the first case, the application of the new (non-reactive) crucible material $BaZrO_3$ (Erb et al. 1995, 1996a) and high-pressure oxygenation at 100 bar (Däumling et al. 1996) led to a complete disappearance of the fishtail (Erb et al. 1996b). Moreover, low-pressure post-annealing followed again by the initial oxygenation procedure allowed to reversibly introduce and take out the anomaly, as shown in fig. 17 (Erb et al. 1997). Similar treatments of less pure single crystals failed. Consequently, the authors argue that in the high-purity case and under optimal doping conditions ($\delta = 0.09$), two different situations prevail depending on the oxygenation process. Upon high-temperature/pressure oxygenation, the remaining oxygen-deficient unit cells are statistically distributed, whereas clustering of these unit cells occurs under low-temperature/pressure annealing conditions due to a smaller entropy term in the free energy (Vargas and Larbalestier 1992). These clusters will then have certain superconductive properties (depending on their local value of δ), can be made normal conducting by certain magnetic fields – as described in the beginning of this section – and lead to the fishtail. On the contrary, clustering will always occur in less pure single crystals near and around the local impurity atoms, thus preventing the removal of the fishtail even under high-temperature/pressure oxygenation conditions. Of course, details of the above

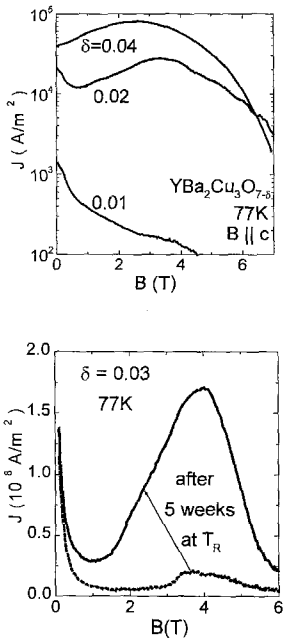

Fig. 18. Dependence of the fishtail anomaly on (top panel) the global oxygen deficiency δ and (bottom panel) oxygen clustering due to the finite mobility of oxygen at room temperature (Küpfer et al. 1996).

arguments will have to be supported by further experimental evidence, but this is just a matter of time considering the recent pace of these developments.

The second piece of evidence for oxygen-deficient lattice cells being responsible for the fishtail anomaly comes from a careful investigation of the angular dependence of the magnetic moments in twin-free and twinned single crystals at various levels of the oxygen-deficiency parameter δ (Küpfer et al. 1996, 1997). Leaving the influence of the twins aside for the moment (which lead to their own J_s peak, cf. sect. 6.2) and concentrating on the results in twin-free crystals, both the development and the enhancement of the fishtail anomaly with increasing δ were reported as well as a substantial increase of the peak height after extended annealing at room temperature (fig. 18). The first was explained by the increasing number of oxygen defects, the second by small-scale diffusion processes in the oxygen system, which favour the formation of clusters. Since the number of defects is a crucial parameter in the static collective pinning theory and because of the full experimental analogy to the above-mentioned study of point pinning centres in V_3Si single crystals (cf. fig. 16), the fishtail is proposed to be due to collective pinning by these oxygen-deficient clusters followed by plastic vortex interaction above the peak field. For further details regarding the discussion of relaxation and $J_c(B,T)$ scaling we refer to the papers by Küpfer et al. (1997) and by Meier-Hirmer et al. (1985).

That the global oxygen deficiency is rather unimportant, but local clustering essential, is also confirmed by a systematic investigation of Y-123 single crystals with T_c's ranging

from 14.0 to 92.8 K (Brandstätter et al. 1996, 1998a). Fishtails are found in all cases (maybe with the exception of the crystals with a T_c of 14 and 21.8 K). If we consider crystals with very similar δ, e.g., with T_c's of 92.8, 92.1 and 90.2 K, the peak fields move from 3.5 to 9.5 and back to 4 T and the corresponding J_c's are 1.5, 1.8 and 2.6×10^9 A m^{-2} ($H \parallel c$, T = 50 K), respectively, i.e., clearly more dependent on the local arrangement of the oxygen atoms than on the global δ. In addition, the cross-over from 3D flux lines to 2D pancakes, which can be observed from the appearance of a crossing point in the $m(T)$ curves or from the functional dependence of the irreversibility line on temperature, does not substantially alter the fishtail effect.

To conclude this section, results on substituted 123 superconductors will be briefly summarised. Firstly, it turned out that due to special processing techniques under reduced oxygen pressure very high T_c's and sharp transitions were obtainable in light-R substituted superconductors, such as Nd, Sm and Eu and mixtures thereof (Yoo et al. 1994, Murakami et al. 1994, 1996). Both single crystals and melt-textured materials were produced in this way, but the details of the processing conditions depend on the substitution element in a critical way (e.g., Wolf et al. 1997). Partly because of its record T_c of ~96 K and partly due to the enormous fishtail effect, Nd-123 shows exceedingly high irreversibility lines, the irreversibility field ($H \parallel c$) at 77 K reaching ~13 T (Wolf et al. 1997). As to the nature of the pinning mechanism responsible for the fishtail anomaly, mostly static pinning scenarios have been proposed. Whereas Wolf et al. (1997) analyse their data much in the same way as described above for Y-123, and ascribe the fishtail to oxygen-deficient clusters (in addition to considering pinning by Nd-422 precipitates and by twin boundaries), Chikumoto and Murakami (1996) and Murakami et al. (1996) propose a Nd–Ba anti-site exchange mechanism leading to Nd-rich regions with diameters of 20–50 nm embedded in the Nd-123 matrix with a chemical composition close to 123. The clusters [Nd(Nd,Ba)$_2$Cu$_3$O$_{7-\delta}$], which were observed by TEM (Egi et al. 1995) and by STM (Ting et al. 1997), are then assumed to have weaker superconducting properties and to turn normal at the peak field. Only small influences of the size and concentration of 422-precipitates on the peak field are found (Yoo et al. 1995). However, the introduction of artificial pinning centres into melt-textured Nd-123 through neutron irradiation (cf. sect. 6.3), led to a complete disappearance of the fishtail peak (Weber 1996), i.e., to a smooth $J_c(B)$ dependence, with low-field critical current densities near 2×10^9 A m^{-2} as compared to 1.5×10^8 A m^{-2} prior to irradiation ($H \parallel c$ at 77 K). Similar trends had been observed before (Sauerzopf et al. 1995) on irradiated Y-123 single crystals both for $H \parallel c$ and for $H \parallel a,b$. An additional feature, i.e., the recent observation of temperature-*independent* second peaks at low fields (around 2 T) in Nd-123 single crystals processed under reduced oxygen pressure (Murakami et al. 1996), confirms the complicated interplay of different flux-pinning mechanisms to the measured field and temperature dependence of J_c (in agreement with the observations of Küpfer et al. 1997 and Wolf et al. 1997).

In summary, oxygen-deficient clusters seem to play a crucial role for the understanding of the "fishtail" effect in 123 HTS, although additional micro-structural work will be required for a more quantitative analysis of the flux pinning and depinning mechanisms.

6. Flux pinning by artificial pinning centres

The optimisation of the defect structure for flux pinning has, of course, been a major goal since the discovery of HTS. However, this turned out to be extremely tedious, in particular if metallurgical (processing) procedures were to be employed. Remarkable exceptions are the formation of normal-conducting inclusions in melt-textured R-123, such as the 211-precipitates in Y-123 or the 422-precipitates in Nd-123, or other additions such as CeO_2, Pt, or MgO. Extended oriented planar defects are twin boundaries in all forms of R-123, dislocation chains (which seem to form naturally during the growth of R-123 thin films), and arrays of stacking faults, which form predominantly in melt-textured 123 materials. Most successful, however, was the application of radiation techniques, where strongly pinning defects could be achieved by certain interactions of radiation with matter, such as spherical statistically distributed defect cascades (fast neutrons), oriented arrays of cylindrical amorphous defects ("columnar tracks", heavy ions of very high energy) or randomly oriented cylindrical fission tracks (GeV-proton-induced fission in Bi- and Hg-based materials or thermal-neutron-induced fission of U additions to Y-123 and Bi-2223).

The nature and, if available, the most likely pinning mechanisms of these defects will be reviewed in this section, while the impact of these defects on the critical current densities and the location of the irreversibility line will be mostly presented in sect. 7.

6.1. *Normal-conducting inclusions*

Several reviews of the subject have been prepared (e.g. Murakami 1992, Salama et al. 1993, McGinn 1995, Sandiumenge et al. 1997), which do not only address the formation of the 211-particles ("green phase") in melt-textured 123 materials, but also the complexity of the defect microstructure, in general, which consists of twin planes, stacking faults, micro-cracks, sub-grain boundaries, minority phases etc., all coexisting in the matrix and each contributing to the bulk pinning properties in a different way. The 211-precipitates themselves (Jin et al. 1988, Zhu et al. 1991) were initially found to be very large (with diameters on the order of 20 μm), which required modifications of their growth conditions to render them suitable for flux pinning (2ξ is only ~4 nm at 77 K, $H \parallel c$, in Y-123). A description of various processes developed to achieve the required refinement of the size distribution of the precipitates can be found in the above review articles. An example of recent results obtained on directionally solidified Y-123/Y-211 composites is shown in fig. 19 (Sandiumenge et al. 1997). In this case (material with 15 wt% 211 precursor and 1 wt% CeO_2 addition), the sizes follow a log-normal distribution with the position of the maximum at 0.4 μm; i.e., a factor of 50 down from the first results quoted above.

Next, we have to address the question of whether or not these precipitates are directly responsible for flux pinning and, if so, through which mechanism. Normal-conducting precipitates are, of course, the first choice for strong pinning centres (cf. sect. 3), but their size should be comparable to the coherence length. From earlier work on low-temperature superconductors (Coote et al. 1972), we know, however, that sharp interfaces between

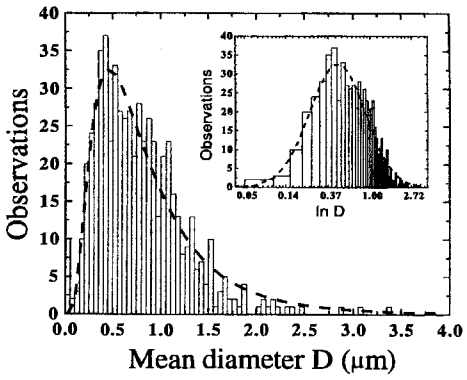

Fig. 19. Log-normal distribution of precipitate sizes in a directionally solidified Y-123/Y-211 composite; the position of the maximum is found at 0.4 μm (Sandiumenge et al. 1997).

the matrix and large precipitates will lead to a substantial elementary pinning force, since the order parameter varies abruptly over a short distance and thus leads to a steep gradient of the pinning potential, which determines the pinning force. Consequently, surface pinning at the matrix–precipitate interface was proposed to be responsible for the high critical current densities achievable in these materials (Murakami et al. 1992). Employing in addition the direct summation of elementary pinning forces, which is reasonable in the case of strong pinning, the resulting critical current densities are proportional to $N_p d^2$ (where N_p is the number of precipitates per unit volume and d is their diameter). The latter is equivalent to V/d, where $V \approx N_p\, d^3$ is the volume fraction of the 211-phase, and represents the effective surface area between the precipitates and the 123 matrix. Thus, by changing the volume fraction and the average size of the precipitates and plotting the resulting J_c versus V/d, the pinning mechanism can be identified (Murakami 1992), as shown in fig. 20 (Sandiumenge et al. 1997). Very good agreement with the predicted V/d dependence is found at relatively low fields (<1.5 T) and high temperatures, i.e., exactly under conditions where we expect a predominance of single-vortex pinning by strongly pinning defects. Indeed, other pinning centres and/or other flux-line configurations become more dominant in other field and temperature ranges, as discussed by Sandiumenge et al. (1997) in much detail. Returning to the pinning action of the interfaces, some concern was expressed about the validity of this argument, since phase boundaries tend to attract impurities, which could then in turn be responsible for flux pinning, e.g., through the $\Delta\ell$ effect. However, the corresponding TEM images (e.g., fig. 21) did not provide any evidence for impurity agglomerations or strain at the interfaces. Lastly, it could be argued that the large 211-precipitates, which are readily observed by polarised light microscopy and are used for assessing the size distributions, such as in fig. 19, might be accompanied by smaller-sized, say 30 nm, particles, which are not seen in the microscope, but would be suitable for pinning directly via the core interaction rather than via the surface pinning mechanism. This would, however, lead to a different dependence of J_c on V/d.

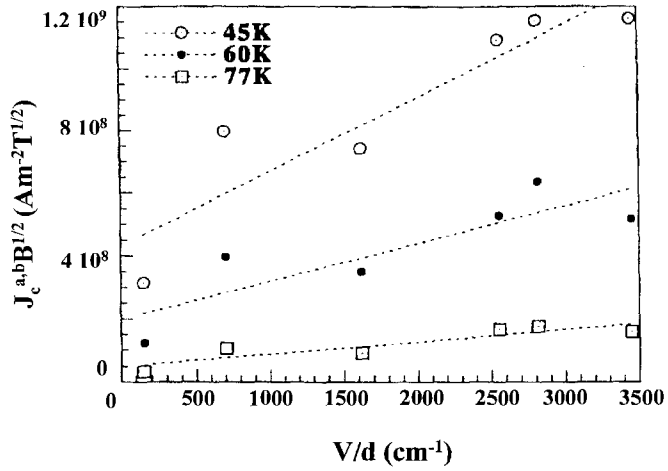

Fig. 20. J_c versus the effective surface area of Y-211 precipitates in the 123 matrix. The observed linear dependence at low fields and high temperatures confirms single-vortex pinning at the interfaces and direct summation (Sandiumenge et al. 1997).

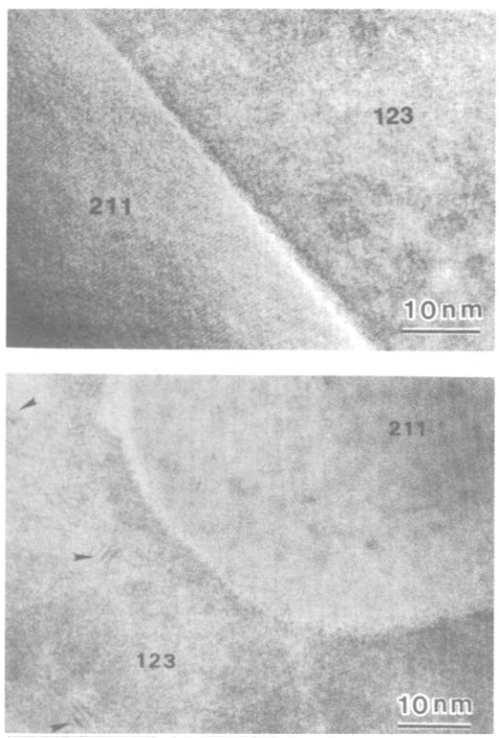

Fig. 21. High-resolution TEM images of 211–123 interfaces (from Murakami 1992, p. 92). Note that the interfaces are clean.

6.2. *Extended planar defects*

In this subsection, I will discuss defects such as twin boundaries, stacking faults, dislocations, dislocation chains, and nano-rods, which are not always introduced artificially, but sometimes develop naturally during the growth of the 123-phase (such as twin boundaries in all forms of 123 materials, stacking faults in melt-textured materials, and dislocation chains in epitaxial thin films). Again, a huge number of papers has been devoted to each of them, from which I will select a few for demonstrating their flux-pinning effect.

The first and most widely investigated defect certainly is the formation of the twin boundary structure in the R-123 system, which is caused by the necessary phase transformation from the tetragonal to the orthorhombic crystal structure during processing and serves the purpose of relieving the resulting strains by occasional interchanges of the crystallographic [100] and [010] directions. The resulting {100} twin planes are extended planar defects, which go right through the whole thickness of single crystals along the *c*-direction, but may be arranged in completely different ways depending on growth conditions. In addition to their obvious dependence on the oxygen content (the orthorhombicity becomes smaller with increasing δ), influences of certain substitutions, e.g., Fe doping (Wördenweber et al. 1989), or of the presence of 211-precipitates (Müller and Freyhardt 1996), were reported. Two examples obtained by polarised-light microscopy on Y-123 single crystals are shown in fig. 22, one referring to a dense cross-linked pattern, the other to an arrangement of a few parallel twins. Extensive structural investigations (e.g., Zhu 1995) clearly demonstrate structural disorder associated with each boundary, which will lead to flux pinning along the entire length of the boundary, i.e., an extended planar defect, which will prevent flux motion across it.

Evidence for flux pinning by twin boundaries came predominantly from transport measurements on single crystals and thin films. A nice example, reported for a single crystal with preferential twin boundary orientations along the [110] and the [1$\bar{1}$0] directions (Kwok et al. 1990a, 1991a), is shown in fig. 23. Here, the magnetic field is kept parallel to the *a,b* plane and the sample is rotated in such a way that the transport current I is at certain angles θ with respect to the field direction. The angle $\theta = 0°$, therefore, corresponds to a force-free configuration with $H \parallel I$, where the Lorentz force

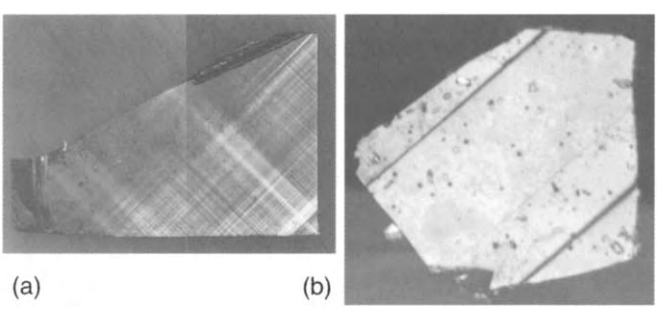

Fig. 22. Twin patterns in Y-123 single crystals, as observed by polarised light microscopy (Werner 1997): (a) dense cross pattern; (b) individual unidirectional twins.

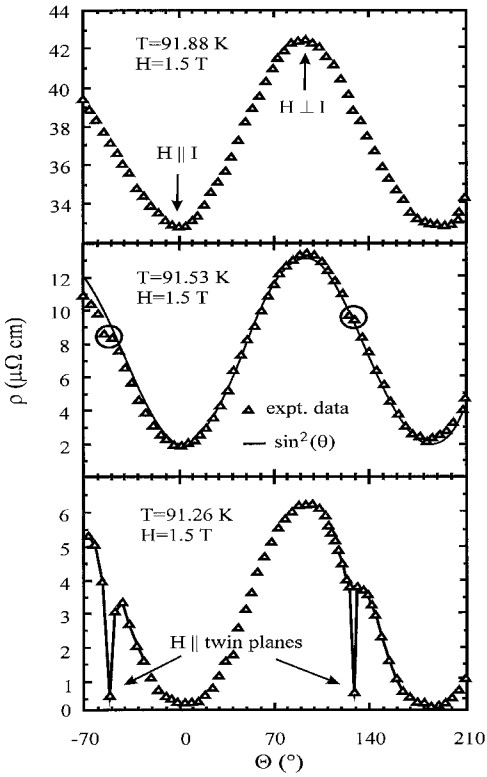

Fig. 23. Angular dependence of the resistivity in an Y-123 single crystal at three temperatures. The circles in the middle panel show the onset of pinning by the twin planes, which becomes fully developed in the bottom panel (Kwok et al. 1990a).

goes to zero leading to a minimum in the resistivity ρ ($\theta = 0°$, $\theta = 180°$). Sharp decreases of ρ, about 2° wide, occur at angles of −45° and 45° from the maximum ($\theta = 90°$), i.e., whenever the field is aligned parallel to the twin planes ([110] and [1$\bar{1}$0]) and flux pinning by the twin boundaries becomes effective. However, details of this angular dependence were soon found to be sample dependent (Kwok et al. 1990b, 1991a), i.e., influenced by the presence or absence of additional defect structures. Transport measurements of J_c on Y-123 thin films (Roas et al. 1990) provided evidence for flux pinning by extended planar defects, which were assumed to be twin planes or stacking faults. In these experiments, the condition $H \perp I$, i.e., the maximum Lorentz force, was always maintained and the sample rotated under this condition from $H \parallel a,b$ ($\theta = 0°$) to $H \parallel c$ ($\theta = 90°$). The corresponding angular dependence of J_c shows extremely sharp maxima for $H \parallel a,b$, which are attributed to the intrinsic pinning effect (Tachiki and Takahashi 1989), but a broader second maximum for $H \parallel c$, which can only be explained by the presence of extended defects growing along the c-axis. Contrary to the above assumption of twin planes being responsible for pinning in the case $H \parallel c$, Schalk et al. (1996) proposed a novel extended defect structure, i.e., *dislocation chains* along the c-axis, based on a thorough study of the growth conditions following various processing routes in Y-123 thin

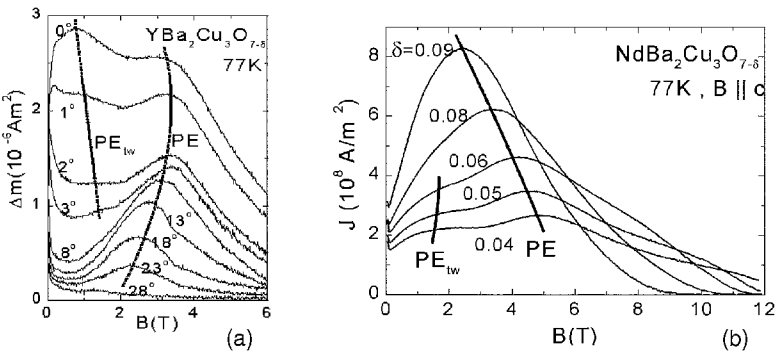

Fig. 24. Twin boundary pinning in Y- and Nd-123 single crystals as deduced from magnetic measurements: (a) Angular dependence of Δm at various angles near to the c-direction; note that twin boundary pinning (PE_{tw}) disappears for misalignment angles above 8° (Küpfer et al. 1996). (b) Persistent currents as a function of field for various oxygen deficiencies δ; note that PE_{tw} disappears for $\delta > 0.08$ (Wolf et al. 1997).

films. The experiments consisted of employing scanning tunnelling microscopy (STM) to determine the growth patterns first and then of measuring transport J_c's on patterned parts of these samples to assess their superconductive properties and to establish a correlation with their microstructure. In contrast to the generally small density of growth spirals and associated screw dislocations (Gerber et al. 1991, Mannhart et al. 1992), which are usually found to be on the order of 10^{12} m^{-2}, the dislocation chains, formed as a consequence of the cluster-like deposition and the two-dimensional growth mode, can be spaced as closely as a few 10 nm apart, thus leading to higher defect densities by about three orders of magnitude, which renders them suitable for flux pinning, even at high magnetic fields, and additionally results in similarly broad peaks for $H \parallel c$, as found by Roas et al. (1990). The above number of 10^{15} dislocations per m^2 has recently been confirmed experimentally in a TEM study of highly bi-axially oriented Y-123 thin films (Svetchnikov et al. 1997).

Returning to flux pinning by twin boundaries, the interplay of this mechanism with that exerted by other defects will be discussed on two examples. First, transport measurements on twinned and detwinned single crystals clearly showed the interplay with intrinsic pinning and the "lock-in" transition (Feinberg and Villard 1990) of the flux lines in the magnetoresistivity close to T_c (Kwok et al. 1991b). From the differences in the angular dependence of the resistivity drop (the one related to intrinsic pinning is extremely sharp, ~0.3° wide), the authors were able to determine the onset temperatures and fields in the vicinity of H_{c2}, at which each of these mechanisms becomes effective. Magnetic measurements on single crystals and melt-textured Y- and Nd-123 (Küpfer et al. 1996, 1997, Wolf et al. 1997) address the interplay of twin boundary pinning, the fishtail anomaly (cf. sect. 5) and/or intrinsic pinning. From measurements of the angular dependence of the hysteresis widths Δm of the magnetisation curves, the authors were able to define a second peak (or a shoulder) at lower fields (fig. 24), which is most pronounced for $H \parallel c$, i.e., the currents flowing in the a,b plane, and disappears for misalignment angles above ~8°. Such peaks are observable only when the

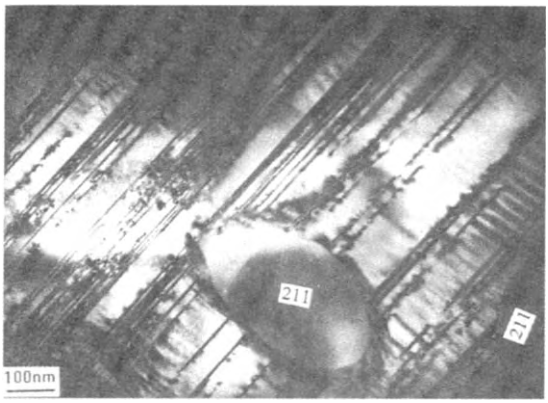

Fig. 25. TEM image of stacking faults near 211-precipitates in melt-processed Y-123 (Zhang et al. 1995a).

competing pinning interactions become small, e.g., collective pinning by point defects of relatively low concentration at higher temperatures. Furthermore, these twin boundary peaks disappear with increasing oxygen deficiency δ, which was explained by the increasing strength of collective pinning due to the enhanced number of point defects, i.e., statistically distributed oxygen-deficient lattice cells.

In summary, the question of whether or not twin planes are strongly pinning defects, is certainly not easily answered. In my opinion they are *not,* because they were shown to be effective only for flux lines closely aligned to preferentially oriented twins (otherwise, only the crossing points would act as pinning centres). Theoretical estimates of the role of twin-boundary pinning in melt-textured materials support this from a practical point of view (Fujimoto et al. 1992). Indeed, twin planes could actually serve the opposite purpose by providing "channels" of easy vortex motion (Oussena et al. 1995) and thus eventually develop into a "weak link" at higher magnetic fields, as was recently observed by the magneto-optical technique on a single crystal containing only one major twin boundary (Werner 1997).

The next type of extended planar defects to be discussed are stacking faults and dislocations, which play a major role in melt-textured materials. TEM observations of stacking faults in Y-123 (Zandbergen et al. 1988) proved them to basically consist of CuO double chain layers. Their formation can proceed under different mechanisms (Rabier et al. 1993, Gu et al. 1993, Zhang et al. 1995a, Sandiumenge et al. 1995), which depend again on details of the processing conditions (such as temperature and oxygenation procedure) and can lead to large arrays extending over several tens of nm to several μm. An example of such an array is shown in fig. 25 (Zhang et al. 1995a). In addition, dislocations are generally found to be associated with the stacking faults. Dislocations are otherwise introduced into melt-textured materials artificially, e.g., by hot isostatic pressing or by high-temperature uniaxial compression (Selvamanickam et al. 1993, Martínez et al. 1996), and into single crystals by high-temperature indentation (Yoshida et al. 1990). In all cases, the high temperatures needed for these special processing conditions severely affect the "as-grown" properties of the superconductors, i.e., require post-processing

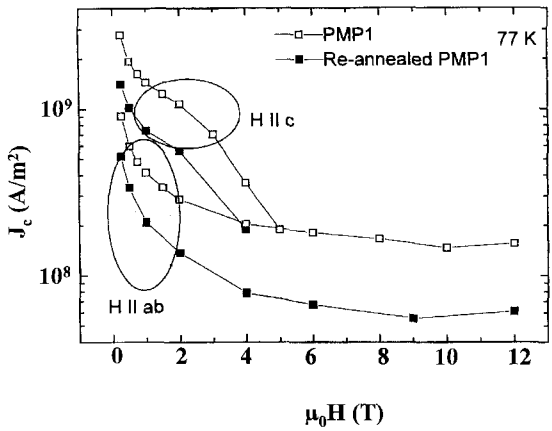

Fig. 26. Field dependence of the critical current densities in melt-processed Y-123 in the as-grown and in the re-annealed state. The reduction of J_c is related to the reduction of the number of stacking faults by three orders of magnitude (Zhang et al. 1995b).

oxygenation treatments, which in turn affect the newly introduced defect structures. Hence, an analysis of the flux-pinning action of these defects is extremely complicated.

Flux pinning by dislocations has been well established in the metallic superconductors (Kramer and Bauer 1967, Freyhardt 1971b, Dew-Hughes and Witcomb 1972, cf. also the monographs by Campbell and Evetts 1972 and by Ullmaier 1975). The elementary pinning force critically depends on the type of dislocation (screw dislocations parallel or perpendicular to the flux lines, edge dislocations, etc.). Core pinning by dislocations in melt-textured HTS was recently considered by Ullrich et al. (1993), who calculated the pinning potential under the assumption of a line defect (dislocation plus the surrounding strain field) with a reduced order parameter and employed direct summation with the dislocation density N_d.

As pointed out above, no "model" systems are available for studies of flux pinning by these defects on their own, since they are always accompanied by other strongly pinning defects. However, Zhang et al. (1995b) reported on a special annealing experiment of "powder-melt-processed" Y-123 (Zhou et al. 1990), which allowed stacking faults and most of the dislocations to be removed without nominally changing the remaining defect structure. The corresponding reduction of J_c, which was also accompanied by reductions of the irreversibility lines for both field orientations, is shown in fig. 26; it was explained by the strongly reduced number of stacking faults (from 10^6 cm^{-1} to about 10^3 cm^{-1} according to TEM images).

Finally, I wish to mention the possibility of introducing artificial extended objects, such as nano-tubes or nano-rods, although this has not been applied to 123 materials so far. The first report came from Fossheim et al. (1995), who embedded carbon nano-tubes into ceramic Bi-2212 superconductors and found some enhancements of flux pinning from magnetisation measurements. More recently, MgO nano-rods were introduced into Bi-2212, Tl-2223 and Bi-2223 (Yang and Lieber 1996, 1997), which seem to be advantageous because of their chemical inertness and which allowed good texturing of the superconductors.

6.3. *Radiation-induced defects*

Extended defects can be produced in all classes of HTS by radiation techniques, if the interaction of the particles with the constituents of the superconductor is sufficiently strong, i.e., the primary knock-on atom has energies above ~1 keV in the case of elastic nuclear interactions, or the interaction occurs electronically and leads to amorphisation of the material over extended areas. I will discuss in the following the most important types of radiation suitable for the production of extended defects and the nature of these defects, which was established in most cases by TEM.

The first indication of strong flux-pinning enhancements came from *fast neutron irradiation* of Y-123 single crystals (Umezawa et al. 1987). Since the samples are exposed to this kind of radiation in a reactor, the experimental conditions for an assessment of the neutron-induced defects were quite difficult. Therefore, transmission electron microscopy was employed in two stages: first by simulating the defect production by fast neutrons through in-situ irradiation with suitable ions (e.g., Kr or Xe with an energy of 50 or 85 keV), and second, by directly exposing TEM samples to various reactor neutron spectra and fluences (Frischherz et al. 1993, 1994). The results may be summarised as follows. Collision cascades were identified to be the major defect, with sizes ranging from below 1 nm (the resolution limit of conventional TEM) up to 5 nm, the average defect diameter being 2.5 nm. They are surrounded by an inwardly directed (vacancy) strain field, which renders the total defect size an approximately spherical volume with a diameter of 6 nm on average. The density of cascades was found to be $5\times10^{22}\,\mathrm{m}^{-3}$ at a fluence of $10^{22}\,\mathrm{m}^{-2}$ ($E>0.1$ MeV) and to scale linearly with fast neutron fluence. They remained stable at temperatures up to at least 400°C. High-resolution images of simulated (Xe irradiation) or neutron-induced defects showed mostly amorphous, but in some cases re-crystallised, defect structures, thus confirming their suitability for flux pinning. A high-resolution TEM image of such a defect is shown in fig. 27 (Weber 1996).

As mentioned above, fast neutron irradiation is usually performed in fission reactors, which provide a characteristic distribution of neutron energies (cf., e.g., Weber et al. 1986). Fast neutrons with energies above 0.1 Mev, which are mainly responsible for cascade production because of their ability to transfer sufficient energy to the primary knock-on atoms, represent only a minor fraction of the neutrons interacting with the superconductor. These lower-energy neutrons create point defects (Frenkel pairs) and defect clusters of smaller size. Oxygen, being the lightest constituent of the system, is preferentially displaced, resulting in a certain additional disordering of the oxygen subsystem and, hence, in a depression of T_c. This effect and the influence of annealing steps, which lead to an enhanced mobility of the oxygen atoms, were reported by Sauerzopf et al. (1997); their results are shown in fig. 28. Accompanying model calculations (Trushin et al. 1996) revealed that vacancies in the CuO chains were mainly responsible for the observed effects. Hence, neutron irradiation leads in general to complicated interactions of the newly introduced defects with the pre-irradiation defect structure.

This interplay between "new" and "as-grown" defect structures also plays a major role when critical current densities and irreversibility lines are analysed and related to flux-

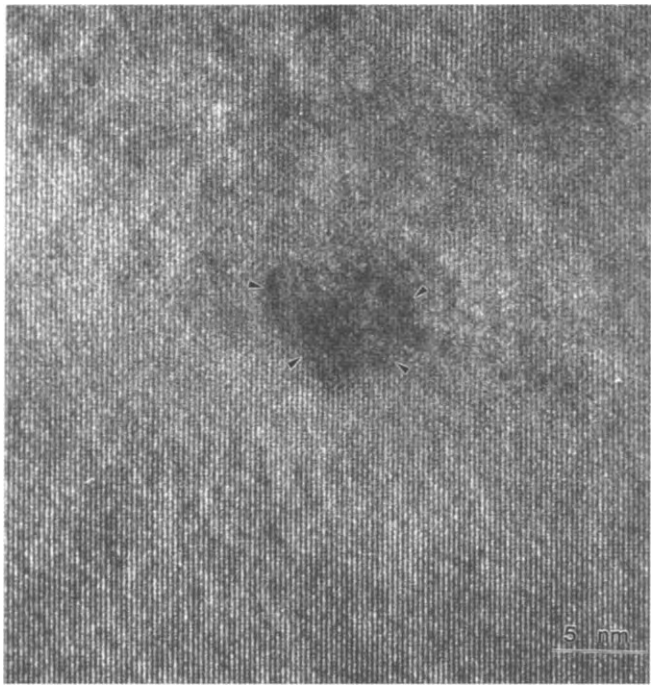

Fig. 27. High-resolution TEM image of a fast-neutron-induced collision cascade in Y-123 (Weber 1996).

pinning mechanisms in 123-superconductors. From the size of the collision cascades, which matches almost exactly the flux-line diameter at 77 K, we expect strong pinning at elevated temperatures (through the core pinning interaction). This is confirmed (e.g., Sauerzopf et al. 1995) by the huge enhancements of J_c in 123 single crystals and the observed upward shifts of the irreversibility line ($H \parallel c$). However, (low-energy) proton irradiation, which produces mainly point defects or small point-defect clusters, also results in considerable J_c enhancements (Civale et al. 1990), although without the accompanying change of the irreversibility line. Hence, the question of which defects contribute to what extent to flux pinning in the case of neutron irradiation needs to be addressed. This was done in several steps (Wiesinger et al. 1992b, Vlcek et al. 1992, 1993, Sauerzopf 1998), the basic idea being related to the differences in mobility between point defects and cascades upon exposing the material to annealing cycles at elevated temperatures (note that the cascades remain unaffected up to temperatures of at least 400°C, cf. above, Frischherz et al. 1994). It turns out (Sauerzopf 1998), that the contribution to $J_c(H \parallel c)$ of smaller defects is significant as long as the concentration of the strong pinning centres is small, i.e., at low neutron fluences, and can be completely removed by an annealing step at 250°C. On the other hand, the increase of J_c (after annealing, i.e., after removal of the additional point defects) is linearly correlated with the concentration of the cascades and becomes the only relevant contribution at

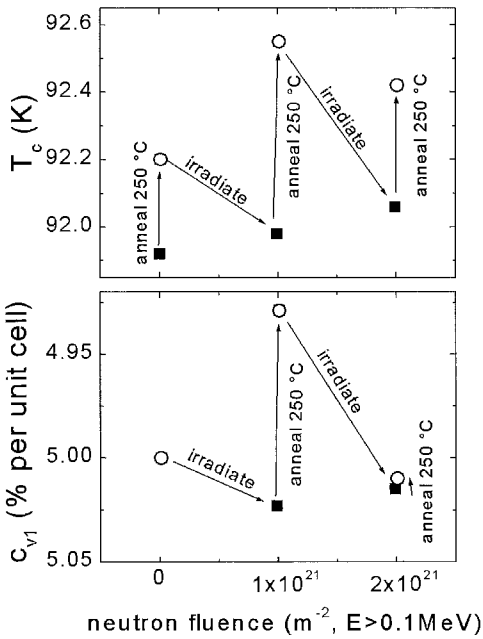

Fig. 28. Influence of neutron irradiation and annealing on the transition temperature T_c of Y-123 single crystals. The lower panel shows results of model calculations, which relate the above changes predominantly to the formation and removal of additional vacancies in the CuO chains (Sauerzopf et al. 1997, Trushin et al. 1996).

cascade concentrations of around 2×10^{22} m^{-3}. For $H \parallel a,b$, i.e., when current flow along the crystallographic c-direction is involved, the situation becomes more complicated due to the presence of intrinsic pinning effects and due to changes of the material anisotropy caused by the introduction of scattering centres, i.e., the additional point defects.

Another (and equally or even more) effective irradiation technique was introduced by several groups (Civale et al. 1991, Konczykowski et al. 1991, Gerhäuser et al. 1992, Hardy et al. 1992) and is based on a completely different interaction mechanism with matter, i.e., the electronic energy loss of *heavy ions of very high energy,* e.g., 5 GeV Pb or 1 GeV Au ions (for a review, see Civale 1997). In this case, the damage process leads to complete disorder (amorphisation) of the material *along* the direction of the incident particles, i.e., to the formation of "columnar tracks". Hence, the defect production is completely different from that of fast neutrons, in particular also with regard to their arrangement; i.e., we find perfect alignment of the tracks along the particle direction as opposed to a statistical distribution in the case of fast neutrons. This situation is shown schematically in fig. 29 (adapted from Kraus et al. 1994a), where the interaction of charged particles with matter and the corresponding defect production are depicted for ions of different mass and energy. It should be noted that the production of continuous columnar tracks requires an electronic stopping power S_e of at least 20 keV/nm (in Y-123): for lower S_e oriented (nearly continuous) "strings of beads" are formed, and for still lower S_e individual amorphous defect areas along the particle trajectory. As a consequence, the pinning action of the tracks is, in general, strongly anisotropic, and it is optimal for tracks oriented

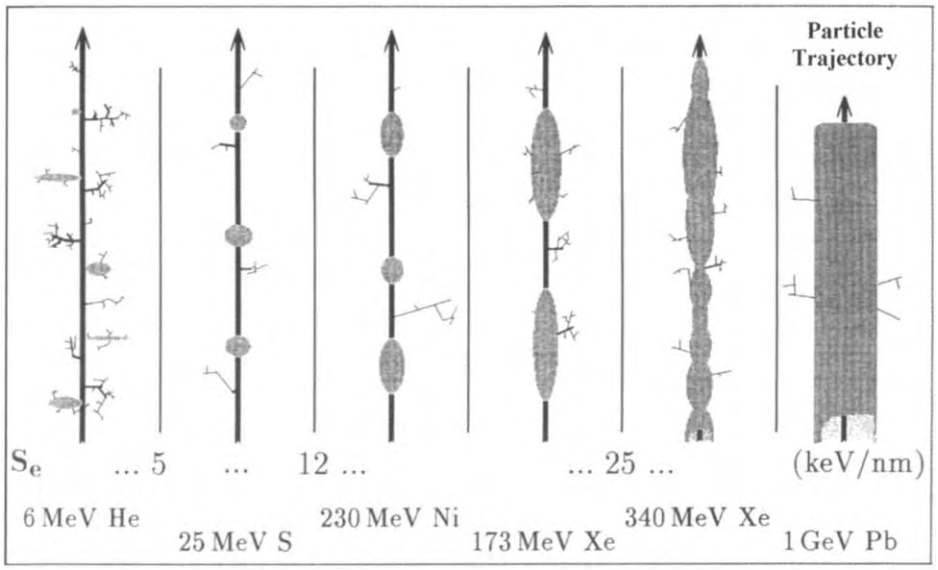

Fig. 29. Schematic representation of the defect formation upon ion irradiation. S_e denotes the electronic energy loss (stopping power), the numbers are only approximate (adapted from Kraus et al. 1994a).

parallel to the magnetic field direction. In this case, vast improvements of J_c and shifts of the irreversibility line were reported, which go far beyond those achievable with collision cascades. Further fundamental work that allows one to probe details of the magnetic microstructures, e.g., the question of forming flux lines or pancakes, was done on Y-123 and Bi-2212 thin films (Holzapfel et al. 1993, Kraus et al. 1994a) and should be mentioned here as an example of research on flux-line dynamics and the nature of the vortex-solid structures evolving under "correlated" disorder as provided by the columnar tracks (Civale 1997).

Again, the defects were investigated carefully by TEM (e.g., Hardy et al. 1991, Zhu et al. 1993). It turns out that each particle leads to the creation of a track, which is roughly cylindrical in shape with a diameter on the order of 5–10 nm (fig. 30) and has an amorphous interior. If the energy of the incident particles is below optimum, i.e., the stopping power falls below a certain material-specific value, the shape of the defect along the trajectory becomes inhomogeneous as shown schematically in fig. 29. In all cases, and even with the highest energies employed so far, the thickness accessible for these types of radiation-induced defects is limited to a few tens of μm. This is certainly the most serious disadvantage of the technique. The other drawback, viz. the preferential orientation of the tracks, can be at least partially removed by forming "splayed" tracks (Civale et al. 1994b), but the distribution will of course never be random and, therefore, never effective for arbitrary orientations of the magnetic field.

The final possibility for introducing extended defects into high-temperature superconductors by radiation was proposed and tested on ceramics quite early on (Fleischer et al.

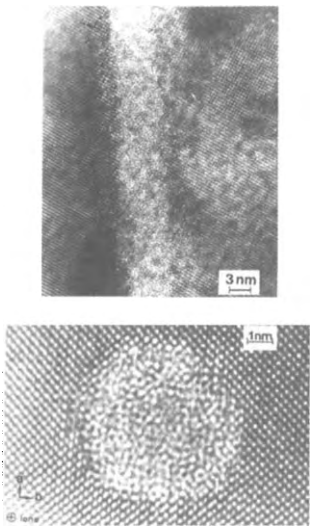

Fig. 30. TEM images of heavy-ion-induced columnar tracks in Y-123 single crystals. The top panel shows the amorphous (cylindrical) defect zone along the particle trajectory, the bottom panel views the defect from the top. 5.3 GeV Pb ion irradiation to a fluence of $6\times10^{15}\,m^{-2}$ (Hardy et al. 1991).

1989) and consists of introducing *fission tracks* into the material, either by adding small amounts of fissionable nuclei, e.g., ^{235}U, and exposing the superconductor to a beam of thermal neutrons (Weinstein et al. 1993, 1994), or by direct fission of suitable nuclei of the superconducting material, e.g., ^{209}Bi or ^{200}Hg, by very-high-energy protons (Krusin-Elbaum et al., 1994).

In the latter case, 800 MeV protons were employed by Krusin-Elbaum et al. (1994) to induce *fission* of the ^{209}Bi nuclei in Bi-2212 and -2223 tapes, and more recently of Hg nuclei in Hg-based 1212 ceramics. The corresponding fission products, such as Xe or Kr, have sufficient energy to produce columnar defects in much the same way as discussed above. However, due to the statistical nature of the fission locations, the directions of the columnar tracks are random, i.e., the desired splay of these extended defects is automatically achieved. TEM on such an irradiated Bi-2212 tape showed columnar defects with diameters of 7 nm and lengths in excess of 6 μm, which is found to be consistent with the expected total range of columnar defect production by the fission tracks of 7 μm for 80 MeV Xe and of 12 μm for 100 Mev Kr. The results confirm the beneficial effects of these defects on the critical current densities, the irreversibility lines as well as the creep behaviour. Obviously, more work is still needed to assess the potential of this kind of radiation treatment. However, in view of the enormous penetration range of such high-energy protons into the superconductors, the most serious limitation of the track formation as discussed in the previous paragraph is clearly removed.

The second possibility (Weinstein et al. 1993, 1994) is based on *adding small amounts of fissionable nuclei*, such as ^{235}U, to the superconductor prior to processing, and to expose the final product to a beam of *thermal* neutrons, thus inducing fission of the added uranium and creating fission tracks in much the same way as discussed in the last paragraph. Thermal neutrons have a very large penetration range in all superconductors

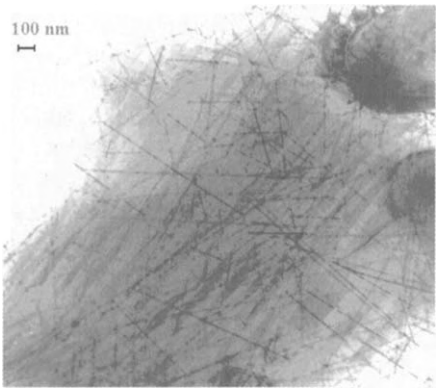

Fig. 31. TEM image of fission tracks created by thermal-neutron-induced fission of ^{235}U admixtures to melt-processed Y-123 (Weinstein et al. 1998).

of interest and are, in addition, much more readily available and of beam sizes even suitable for processing of components, if desired. The fission products are well known in this case, they have a total energy of 160–180 MeV and create columnar defects of isotropic distribution, again with a diameter of ~10 nm and lengths on the order of 10 μm. Due to the relatively low energy of the fission products, the defects usually have the character of the above-mentioned "strings of beads" (fig. 31, from Weinstein et al. 1998). In the specific case of melt-textured Y-123, detailed studies of the chemistry and the phase formation during processing revealed the formation of a stable U–Pt–Y–Ba–O compound, which is dispersed in the matrix in the form of extended particles with sizes of ~300 nm. Consequently, all of the fission tracks originate from these clusters and form three-dimensional "star-like" patterns in the matrix. However, if we consider their flux-pinning action, projections of these three-dimensional defect structures onto the plane perpendicular to the applied field, i.e., into the symmetry plane of the flux-line lattice, must be made, which turn out to result in effective defect sizes with diameters of 10–20 nm, i.e., quite similar to (about twice as large as) those created by fast neutron irradiation (Eisterer et al. 1998). Indeed, first results of the exposure of U-doped melt-textured Y-123 monoliths to thermal neutron irradiation confirm the similarity of the J_c enhancements to those obtained upon introducing collision cascades by fast neutrons. Some of these results will be presented in sect. 7. However, if we aim at the optimisation of large pellets, e.g., for maximum trapped-field conditions (cf. sect. 8), the sizes of these pellets may easily surpass the space limitations of fast neutron irradiation facilities, which renders U-doping followed by *thermal* neutron irradiation an unchallenged tool for this purpose (due to the much less stringent spatial restrictions in the latter case).

Finally, I wish to point out that alternative suggestions for doping the superconductors, e.g., by adding Li to the material and relying on the Li(n,α) reaction (Zhao et al. 1992), do not fall into the category of radiation treatments to be discussed in this context, since the resulting defects are too small to act as effective strong pinning centres.

In summary, various possibilities of introducing artificial defect structures into all families of high-temperature superconducting materials have been explored during the past few years, only a few of them being effective for enhancing their flux-pinning

properties at high temperatures and magnetic fields. Among them, some techniques are more suitable for fundamental studies of the flux-line-defect interactions (fast neutrons, columnar tracks), others seem to be promising also from an applied point of view (fast neutrons because of the statistical defect distribution and the large penetration range, fission tracks for the same reasons, but in Y-123 only, if the preparational aspects, i.e., successful admixing of the doping elements without property degradation, can be solved, as has been demonstrated for Y-123). Both fast-neutron and thermal-neutron irradiation do not seem to represent a major problem for materials and applications which do not require a silver sheath, as far as the induced radioactivity of the superconductors is concerned. Silver, however, activates badly under a thermal neutron environment, which might make other radiation treatments, such as proton-induced fission, more attractive in this case.

7. Critical current densities and irreversibility lines

Published results on J_c and on the irreversibility lines in R-123 superconductors would presumably fill a few books as of today. Moreover, the caveats addressed in sect. 4 and our own experience with data on hundreds of samples prevent me from trying to chase for "record" J_c's and the "highest" irreversibility lines in the literature. I will rather choose a few examples, preferably on systems which allow the experiment to be done on the same sample prior to and following a certain treatment, in order to make sure that the defect structure for flux pinning remains otherwise (almost) unchanged. The point here is rather to show along which lines flux pinning can be optimised. Some of these aspects were already presented in the preceding sections, the main emphasis here will be to expand on the actual J_c's and the irreversibility lines.

As the first example, I take the influence of oxygen deficiency. It is tempting to expect that (small) deviations from optimal doping will lead to additional point defects, which should add to flux pinning. In addition, the enormous change of the superconducting parameters upon reducing the global oxygen content (the anisotropy parameter increases by a factor of ~20 by reducing T_c from 92 to 20 K, Chien et al. 1994) will make this system ideally suited for studying dimensionality effects on flux pinning. These issues were addressed in grain-aligned ceramics, thin films, single crystals and melt-textured bulk samples (Seidler et al. 1991, Feenstra et al. 1992, Gray et al. 1992, Ossandon et al. 1992a,b, Thompson et al. 1992, 1994, Jones et al. 1993, Wisniewski et al. 1994, 1996, Brandstätter et al. 1996, 1998a, van Dalen et al. 1996, Samadi Hosseinali et al. 1997).

The first conjecture is ruled out by all data on all forms of 123 superconductors, i.e., it turns out that J_c decreases immediately if δ starts to deviate from its optimum value. This is illustrated in fig. 32, where J_c is plotted as a function of magnetic field in melt-textured Y-123 superconductors ($H \parallel c$) with transition temperatures between 92.4 and 45.8 K (Wisniewski et al. 1996). The data deliberately refer to very low temperatures (5 K in this case), in order to minimise the influence of variations in T_c. A very similar behaviour is found for the irreversibility lines (IL's) as shown in fig. 33 for $H \parallel c$, i.e.,

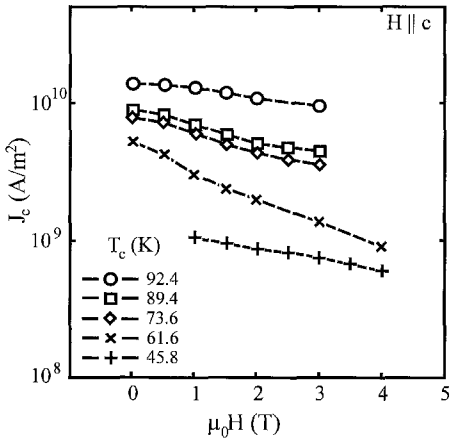

Fig. 32. Critical current densities versus applied field (at 5 K) in melt-textured Y-123 bulk superconductors ($H \parallel c$) with various degrees of oxygen deficiency (Wisniewski et al. 1996).

they start to move to lower fields and temperatures immediately upon changing δ. As suggested by Almasan et al. (1992), a scaling invariance of the IL's can be found, if the irreversibility fields H_{irr} are normalised by a certain scaling field H^+, which is defined as H_{irr} at $T/T_c = 0.6$ (fig. 33b). This shows that the data follow the power law $H_{irr} = \beta[1-(T/T_c)]^{1.5}$ at high temperatures, indicative of flux-line depinning (Malozemoff et al. 1988), but at lower temperatures turn into an increasingly exponential behaviour with decreasing T_c, which is characteristic of 2D magnetic microstructures. In fact, careful measurements of the magnetic moments on oxygen-deficient single crystals in the reversible regime show a crossing point of the $m(T)$ curves at various fields, beginning with $\delta = 0.32$ (Brandstätter et al. 1998a), which is considered to be the signature of vortex fluctuations in 2D superconductors (Bulaevskii et al. 1992, Koshelev 1994, Brandstätter et al. 1997). However, even in the 2D regime, say around the 60 K plateau, a variation of δ does not lead to enhancements of J_c, i.e., the role of point defects is marginal also under these circumstances. (Note, however, that extended room-temperature annealing may lead to the formation of clusters due to oxygen mobility and contribute to flux pinning in this way, as discussed in sect. 5.)

In summary, the change of flux pinning in O-deficient Y-123 seems to be primarily due to the gradual transition from 3D flux lines to 2D pancakes. In addition, as discussed in much detail by Thompson et al. (1994), the reversible mixed-state parameters (such as the condensation energy) degrade in a similar way as T_c resulting in a reduced pinning capability through this fundamental effect. An interesting analysis of critical current densities and relaxation rates in O-deficient thin films (van Dalen et al. 1996) allows the flux-pinning mechanism to be identified by employing the general inversion scheme (Schnack et al. 1993, cf. also sect. 5). The temperature dependence (fig. 34) of the (unrelaxed) critical current densities in several O-deficient systems (with δ varying from 0 to 0.4) can be described by defining a single disorder parameter in the framework of $\Delta\ell$ pinning (cf. sect. 3) of 3D single vortices, where ℓ is the mean free path of the

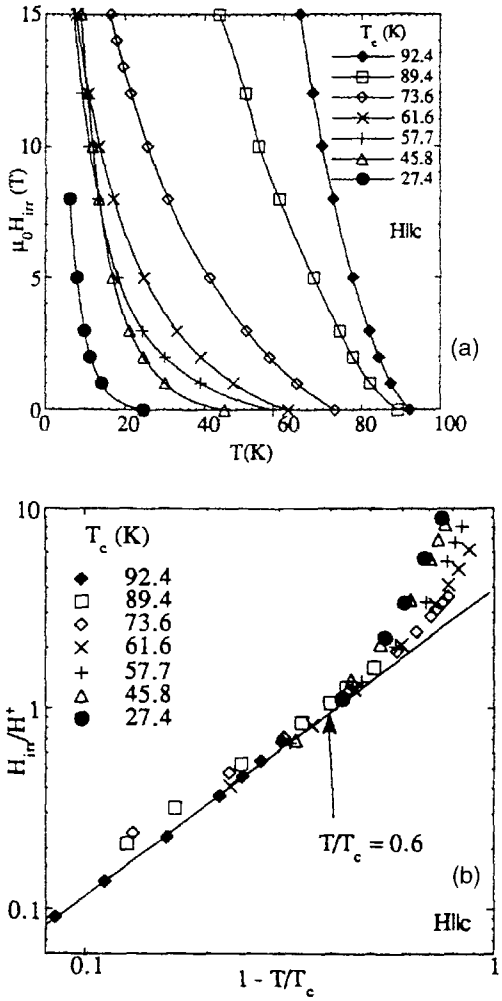

Fig. 33. Irreversibility lines in melt-textured Y-123 bulk superconductors ($H \parallel c$) with various degrees of oxygen deficiency (Wisniewski et al. 1996): (a) H_{irr} versus temperature; (b) normalised H_{irr} versus $[1-(T/T_c)]$.

charge carriers. Alternative mechanisms, such as ΔT_c pinning or pinning by individual oxygen defects, are incompatible with the experimental data.

The second example is still related to the issue of point defects and will briefly describe two experiments. In the first, advantage is taken of the (scarce) availability of isotopically pure rare earths, which are then synthesised to form 123-ceramics. For instance, in the case of Gd, two isotopes can be used, ^{155}Gd and ^{160}Gd, which have tremendously different absorption cross sections for thermal neutrons ($\sigma = 61.000$ b and $\sigma = 0.77$ b, respectively). Hence, if ^{155}Gd is exposed to a thermal neutron beam, each thermal neutron will be absorbed and will produce a Gd recoil atom having a recoil energy of 180 eV. According to TRIM calculations (Biersack and Haggmark 1980) this recoil will result on average

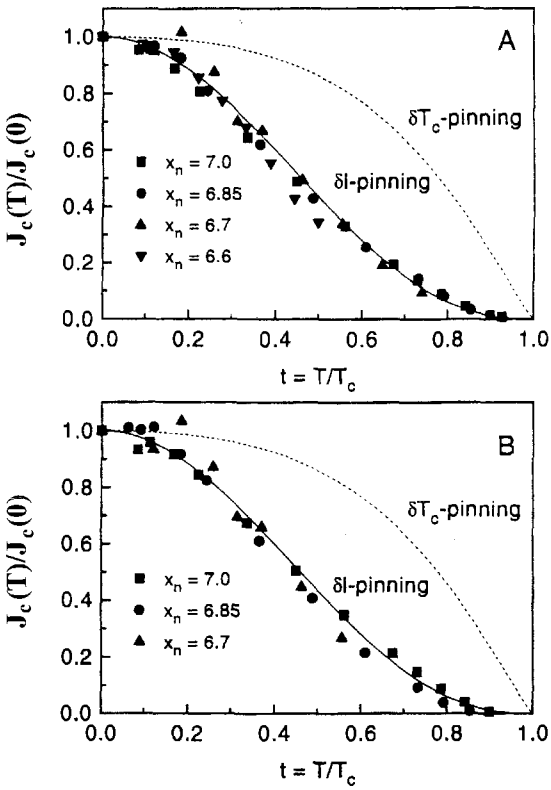

Fig. 34. "True" critical current densities in various oxygen-deficient thin films versus reduced temperature. The solid lines correspond to flux pinning due to spatial fluctuations of the mean free path and the dashed line to pinning due to spatial variations of the transition temperature (van Dalen et al. 1996).

in the formation of 2.7 point defects per Gd recoil, i.e. will lead to the formation of randomly distributed Frenkel pairs (strictly point defects). On the contrary, a reference sample containing ^{160}Gd should be practically unaffected by the thermal neutron beam. Two sets of experiments along these lines have been reported so far (Brezgunov et al. 1990, Sickafus et al. 1992), but both were not "clean" in a strict sense, because they did not employ "purely" thermal neutrons, but rather the full neutron spectrum with and without a Cd shield, i.e., all neutrons except for the thermals in the first case, and all neutrons in the latter. Hence, the contribution of the high-energy neutrons (cf. sect. 6.3) had to be subtracted in some complicated way. A new experiment with an extremely well thermalised neutron beam (i.e. a Cd ratio of about 500) was made over a period of four years (due to the very low flux density resulting from a pure thermal neutron beam; Brandstätter et al. 1998b) and confirmed the marginal role of point defects in an unambiguous way. Approximately 5×10^{25} point defects per m^3 (an unknown amount of them may have recombined immediately) were necessary to enhance J_c in ^{155}Gd-123 by 50% (10 K, 0.3 T), and J_c has reached 2.2×10^9 A m^{-2} (10 K, 1 T) at twice this defect concentration, up by a factor of ~2 compared to the unirradiated state. The ceramic sample containing ^{160}Gd did not show any changes of T_c or J_c.

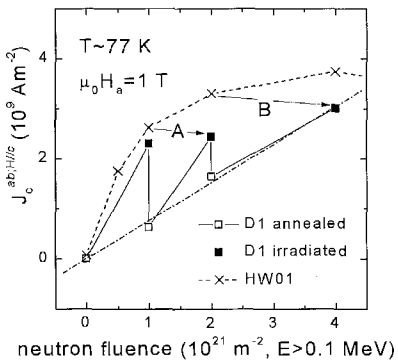

Fig. 35. Critical current density ($H \parallel c$) at 77 K of an Y-123 single crystal as a function of fast neutron fluence. The crosses refer to sequential irradiation without annealing, the solid symbols to sequential irradiation prior to annealing, and the open symbols to the results after annealing (Sauerzopf 1998).

Similarly small effects on J_c were found upon irradiating Y-123 single crystals (at low temperature or room temperature) with 1 MeV electrons (Giapintzakis et al. 1992, 1994a,b) to very high fluences (up to 10^{24} m^{-2}). In this case, mainly O and/or Cu atoms from the CuO_2 planes are displaced, leading again to the formation of Frenkel pairs. Apart from the small effects on J_c, systematic increases of the normal-state resistivity were found, which fit well into the picture of radiation-induced disorder and its consequences for charge-carrier scattering.

The next example will address the improvement of critical current densities and irreversibility lines by statistically distributed spherical defects, such as those introduced by fast neutron irradiation. The basic principles have already been discussed in sect. 6.3, in particular also the complicated interactions between the radiation-induced point defects (T_c depression, reduction of material anisotropy due to isotropically distributed scattering centres) and the as-grown defect structure, flux pinning by small defect clusters and by large cascades, as well as the role of defect mobility at ambient temperature or upon annealing at elevated temperatures (Sauerzopf et al. 1995, Sauerzopf 1998). Some of the salient features are summarised in fig. 35, where J_c^{ab} is plotted versus fast-neutron fluence for two Y-123 single crystals. The crosses refer to sequential irradiation without intermediate annealing, i.e., to the flux-pinning action of both the small clusters and the larger collision cascades, whereas the squares show the same irradiation treatment, but interrupted by annealing cycles at 250°C after each irradiation step. Starting from very low J_c's in these single crystals, both kinds of defects initially enhance J_c, but the strongly pinning cascades take over after reaching a significant concentration ($\sim 2\times10^{22}$ m^{-3}). Note also that J_c varies linearly with cascade concentration. The increase of critical current densities in single crystals is generally high (by factors on the order of 100), and the values of J_c can reach those of thin films, as shown in fig. 36. Due to the statistical arrangement of the newly introduced defects, enhancements of J_c are also observed for other orientations of the magnetic field, in particular of course for $H \parallel a,b$. In this case, magnetic measurements only allow one to deduce the critical current density J_c^c. The relative contributions of smaller and larger defects are depicted in fig. 37. Less dramatic effects are found in melt-textured bulk materials, but even factors

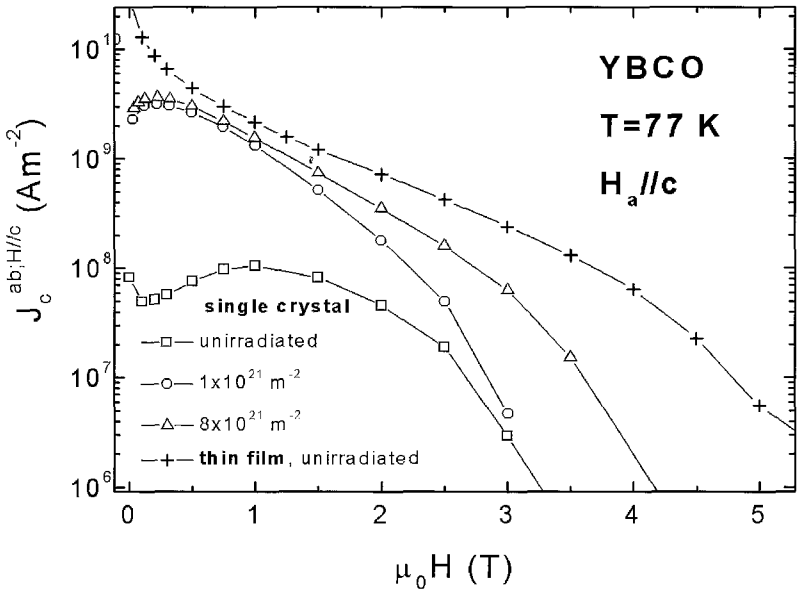

Fig. 36. Comparison of critical current densities in Y-123 thin films and single crystals, in the latter case at various fast neutron fluences.

on the order of 10 can be considered to be of significant technological importance in this case. First results on a Nd-123 monolith are shown in fig. 38 (Kern 1997, Weber 1996), which demonstrate the feasibility of J_c's well above 10^9 A m^{-2} at low fields and still above 10^8 A m^{-2} at 6 T. Although the irreversibility lines are rarely found to change upon irradiation in melt-textured materials (due to the presence of strongly pinning defects in the pristine samples), some small effects still occur in Nd-123, leading to an irreversibility field of ~11 T at 77 K ($H \parallel c$), very close to the best result reported so far for melt-textured specimens exposed to high-pressure oxidation (Wolf et al. 1997). Only the exposure of R-123 thin films to fast neutron irradiation has generally led to negative results (Schalk et al. 1992b), which has been attributed to the optimised pre-irradiation defect configurations that are being formed during the growth process. In fact, irradiation to various fluences has always left the critical currents nearly unchanged except for those transport measurements in which both the field and the current were oriented in the *a,b* planes (but still perpendicular to each other). In this case (fig. 39, Schalk 1992), J_c drastically decreases (for H parallel to the planes), which is taken as the signature of disorder-induced weakening of the intrinsic pinning effect.

Melt-textured materials (Y-123, Nd-123) with U admixtures represent a highly promising system for high-J_c applications due to the possibility of forming randomly oriented fission tracks (cf. sect. 6.3). Results on the critical current densities (taken by the flux-profile technique, i.e. in the nearly unrelaxed state) are shown in fig. 40 (Weinstein et al. 1998, Eisterer et al. 1998). J_c following thermal neutron irradiation to the optimal

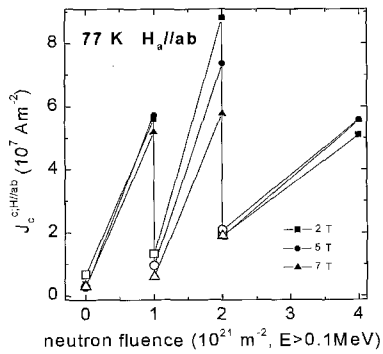

Fig. 37. Critical current density along the crystallographic c-direction ($H \parallel a,b$) of an Y-123 single crystal as function of fast neutron fluence. Open symbols refer to results after annealing (Sauerzopf 1998).

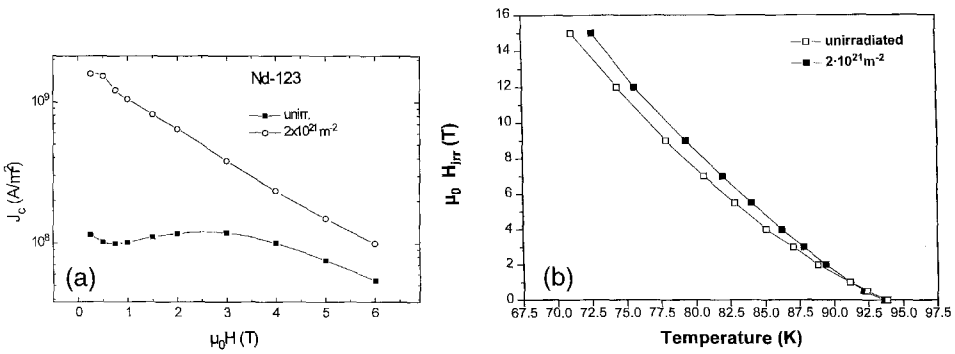

Fig. 38. Fast neutron irradiation of a Nd-123 melt-textured superconductor (Kern 1997): (a) critical current density ($H \parallel c$) versus field at 77 K (prior to and following irradiation to a fluence of 2×10^{21} m^{-2}, $E > 0.1$ MeV); (b) irreversibility lines for $H \parallel c$, same conditions as above.

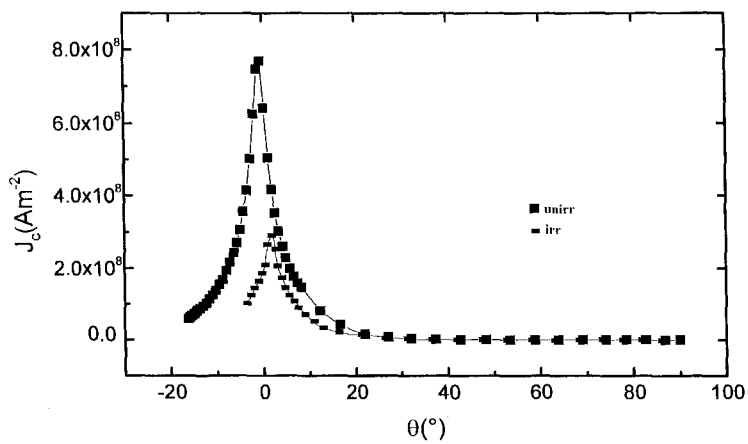

Fig. 39. Fast neutron irradiation of Y-123 thin films, $H \parallel a,b$: $\theta = 0$ (Schalk 1992).

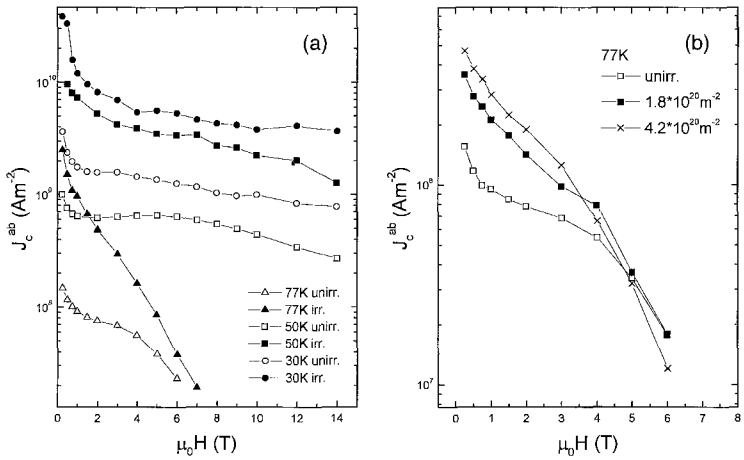

Fig. 40. (a) Critical current densities ($H \parallel c$) in melt-textured Y-123 with an admixture of 0.3 wt% uranium at various temperatures. The open symbols refer to a reference sample, the solid symbols to a sample exposed to a thermal neutron fluence of 4×10^{20} m^{-2} (Weinstein et al. 1998). (b) Sequential thermal neutron irradiation of a melt-textured Y-123 superconductor with an admixture of 0.3 wt% uranium. Critical current densities ($H \parallel c$) versus field at 77 K (open squares: unirradiated, solid squares: 1.8×10^{20} m^{-2}, crosses: 4.2×10^{20} m^{-2}, Eisterer et al. 1998).

fluence (4×10^{20} m^{-2}) for this particular U content (0.3 wt%) is shown in fig. 40a at three temperatures and compared to typical data prior to irradiation. The resulting J_c's are superior to any previously reported data. More systematic work has started only recently; the evolution of J_c at 77 K with thermal neutron fluence for a material with a U content of 0.3 wt% is shown in fig. 40b.

With the next example I will return to more fundamentally oriented studies, although the results on J_c are spectacular in some cases. Exposure of Y-123 single crystals to heavy-ion irradiation has led to a wealth of information, which can be briefly summarised as follows. First, the critical current densities are enormously enhanced, particularly at high temperatures where the as-grown defects lose their pinning capability. An example referring to 580 MeV Sn ion irradiation at an angle of 2° with respect to the crystallographic c-axis is shown in fig. 41 (Civale et al. 1991). The ion fluence is expressed (rather inconveniently) by the so-called "matching field" B_Φ, i.e., the field at which the density of flux lines matches the density of the induced columnar tracks. (Since each incoming ion creates one such defect, a fluence of, say, 3×10^{15} m^{-2} corresponds to $B_\Phi = 6$ T). The results of fig. 41 confirm the huge increase of J_c, particularly at 77 K (note the open squares near $J_c = 0$ in the unirradiated state). The dotted line indicates the effect of proton irradiation on a similar crystal (Civale et al. 1990), which is characteristic of the flux-pinning action of small point-defect clusters. Clearly, the additional number of small defects also contributes to J_c, but the irreversibility line remains unchanged. On the contrary, upward shifts of the IL occur upon heavy-ion irradiation (fig. 42, Civale and Krusin-Elbaum 1997) with no hint of saturation, indicating the presence of flux-

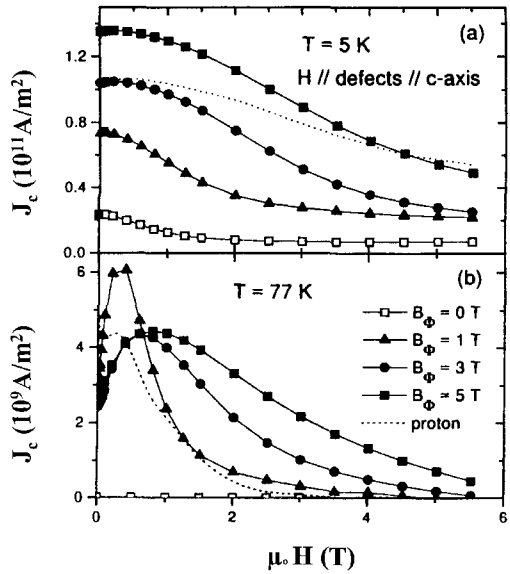

Fig. 41. Critical current densities ($H \parallel c$) as a function of field in an Y-123 single crystal irradiated with 580 MeV Sn ions to various fluences (expressed by the matching fields B_Φ): (a) 5 K, (b) 77 K. For comparison, the largest J_c's obtained by proton irradiation of a similar crystal are shown by the dotted lines (Civale 1997).

pinning centres with strongly enhanced pinning potentials, in agreement with the first observation of this kind reported by Kritscha et al. (1990b) for fast-neutron-irradiated Bi-2212 single crystals. However, care must be taken at higher fluences, since some deterioration of the superconducting matrix, as indicated, e.g., by a T_c depression, cannot be avoided and the amount of non-superconducting material will become of increasing significance (recall that a single columnar track has a diameter of ~10 nm and extends through the entire thickness of the crystal, i.e. 10 to a maximum of 100 μm). Finally, irradiation experiments on single crystals, thin films and multilayers should be mentioned, where the incident beam strikes the sample at a certain angle with respect to the main crystallographic directions (Civale et al. 1991, 1992, Hardy et al. 1996, Holzapfel et al. 1993, Kraus et al. 1994b, Schmitt et al. 1991). First, single crystals irradiated at an angle of 30° from the c-axis (580 MeV Sn ions) and magnetised at angles of +30° or −30° from the c-axis show an enormous difference in flux pinning at high temperatures (fig. 43a), since the flux lines are aligned parallel to the tracks in one case and cross the tracks under an angle of 60° in the other case. This large unidirectional anisotropy nicely confirms the existence of a 3D flux-line lattice at high temperatures. In addition, the significant differences in the hysteresis loops at high fields demonstrate the role of the defect – flux-line lattice orientation for the pinning potential and the irreversibility line. The fact that the enhancements of J_c are nearly the same for both orientations at low temperatures, is in agreement with many other results and confirms the role of flux pinning by the as-grown defect structure at these temperatures. Under more general geometrical conditions (e.g., Hardy et al. 1996) or upon rotating the single crystal with respect to the magnetic field direction (e.g., Kolesnik et al. 1997), a "lock-in" of the flux line at the defect orientation

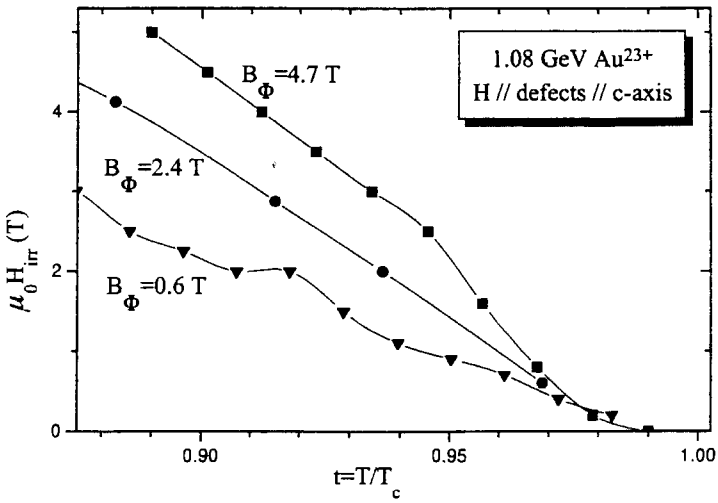

Fig. 42. Shift of the irreversibility line ($H \parallel c$) in an Y-123 single crystal following 1.08 GeV Au ion irradiation to various fluences (Civale and Krusin-Elbaum 1997).

or the *a,b* planes (Feinberg and Villard 1990, Feinberg 1992) and/or the formation of kinks and "stair-case" patterns had to be invoked. Similar conclusions were drawn from transport measurements on thin films, which were irradiated parallel to the *c*-direction and under angles of 30° and 60° from the *c*-axis (fig. 43b). The angular dependence of J_c shows in all cases a pronounced maximum for H parallel to the tracks, which can even exceed the intrinsic pinning maximum for $H \parallel a,b$. However, if an Y/Pr-123 multilayer is exposed to the same treatment (fig. 43c), the correlation with the track direction is lost, the intrinsic pinning peak reduced (in agreement with the situation depicted in fig. 39) and J_c otherwise generally enhanced. This can only be understood if the 3D flux-line lattice is replaced by a 2D pancake structure (due to the intermittent normal-conducting Pr-123 layers), which are pinned and depinned independently (in the same way as in other 2D materials such as Bi-2212) and, therefore, do not correlate with preferential defect orientations.

To conclude this section, I wish to just show – without comments – the reward of many years of work, which should allow us to proceed with applications of Y-123 materials in all those areas that require conductors in the form of tapes or wires, i.e., the successful development of coated conductors. In view of all the favourable properties of this class of high-temperature superconductors, i.e., their high irreversibility line, their correlated flux-line lattice, the flux-pinning properties, etc., which all manifest themselves at their best in Y-123 thin films, the fabrication of thick films on technical substrates without significant weak link problems is to be considered as a major breakthrough in the field (e.g., Norton et al. 1996, Freyhardt et al. 1997). Figure 44 demonstrates that the best J_c–B characteristics achieved so far for Y-123 thin films are nearly matched by the coated conductors and thus provide us with means of producing long lengths (although at present over unacceptably

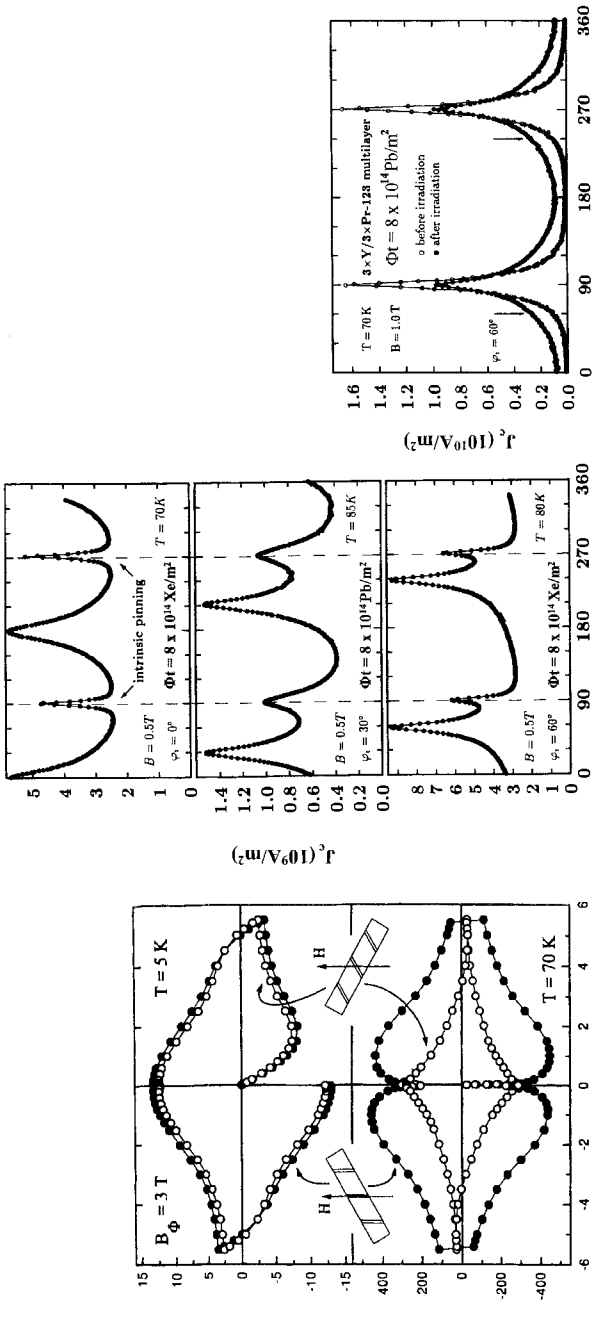

Fig. 43. Effects of heavy-ion irradiation under different angles on flux pinning in Y-123 superconductors: (a) hysteresis loops at (top) 5 K and (bottom) 70 K of an Y-123 single crystal irradiated with 580 MeV Sn ions under an angle of 30° with respect to the *c*-axis and measured with the field at +30° or −30° from the *c*-axis (cf. the schematic of the field and track orientations, from Civale 1997); (b) angular dependence of the transport critical current densities in Y-123 thin films irradiated under various angles with respect to the *c*-axis (top: parallel to the *c*-axis, 340 MeV Xe; middle: 30°, 770 MeV Pb; bottom: 60°, 340 MeV Xe; from Kraus et al. 1994b); (c) angular dependence of the transport critical current densities in an Y-123/Pr-123 multilayer system irradiated by 770 MeV Pb ions under an angle of 30° with respect to the *c*-axis (Kraus et al. 1994b).

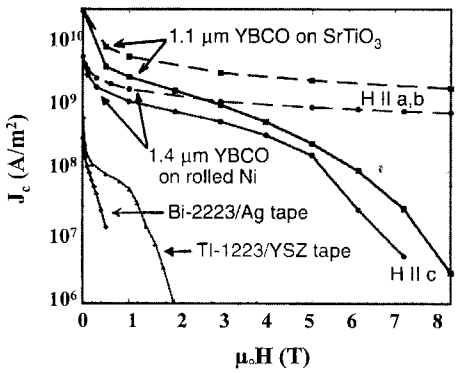

Fig. 44. Transport critical current densities in a coated conductor (1.4 μm Y-123 on rolled Ni) compared to results on Y-123 thin films on $SrTiO_3$, Ag-sheathed Bi-2223 tapes and Tl-1223 on YSZ tapes (Norton et al. 1996).

long periods of time) of high-J_c material on planar or curved substrates. Progress in this field has been so rapid that any further discussion would be outdated by the time this article goes into print.

8. Field mapping and levitation forces

Field mapping of the remnant magnetisation and measurements of the levitation forces have established themselves as rather independent topics with strong emphasis on application-oriented aspects. These experiments are performed exclusively on melt-textured superconductors and are aimed at optimising the trapped field. This can obviously be achieved by the highest possible J_c, but requires at the same time the largest possible sample size [because $M_{irr}(H=0)$ is directly proportional to this parameter]. Hence, there is not much to add in the context of this article, since the ways and possibilities of enhancing J_c have been outlined in the preceding sections and the technical issues related to the fabrication of large "single-grain" pellets are addressed in other chapters of this book. Nevertheless, I wish to add a few comments, in particular on the experimental aspects of the field-mapping procedures, which are sometimes treated rather casually in the literature. An early overview of the subject can be found in the monograph by Murakami (1992, chapter 14); fundamental general aspects have been discussed by Brandt (1989); and more recent developments have been compiled in conference proceedings, e.g., EUCAS '95 (Dew-Hughes 1995), Low Temperature Engineering and Cryogenics Conference '96 (Scurlock 1997), or ASC '97 (Clark 1997).

The general task is to magnetise the sample to at least twice the full Bean penetration field (to ensure uniform and maximal flux density gradients after demagnetisation), to reduce the external field to zero and to measure either the distribution of the trapped magnetic induction or the force exerted on some permanent magnet. Each of these steps can be done in different ways, which should in principle lead to identical results, but can be subject to subtle external effects. The magnetisation of the sample ("activation") can either be done by field cooling to the desired temperature (in general 77 K) or by

raising the field at this temperature. The latter may have some advantages, since large-bore superconducting magnets can be avoided and pulsed devices used instead. However, in this case, a detailed analysis of the pulse time and the required magnitude of the field are essential (Gruss et al. 1999, Fujimoto et al. 1997, Morikawa and Tsuchimoto 1997), in order to achieve the fully penetrated state. Furthermore, cracking under the enormous forces represents a major problem that was shown to not only depend on the static parameters, but also on the dynamics of the process (Ren et al. 1995, Weinstein et al. 1996, Fuchs et al. 1996). This may actually represent the most serious limitation for further progress in the field.

Once the remnant state is established, field mapping is usually done by a scanning Hall probe device on an x–y sledge, which can be computer-controlled for automatic data acquisition (e.g. Nagashima et al. 1997). A typical example is shown in fig. 45 (Novak 1998), which demonstrates a uniform Bean-like field profile over a pellet with a diameter of 25 mm and a thickness of 13.6 mm (fig. 45a). This confirms in a qualitative manner that the supercurrent flow is everywhere unimpeded by weak links, that the activation had been done correctly into the fully penetrated state, and that the application of the Bean model will be well justified. For a quantitative analysis of the maximum trapped field B_{max} and the associated critical current densities, numerical calculations require due consideration of a number of issues, which are only rarely mentioned in the literature. First, of course, the exact geometry of the system has to be used in the calculations (plate versus disk). Second, the properties of the Hall probe device have to be considered (the size and the shape of the probe will determine a certain amount of spatial averaging of the profile, which could mask small-scale inhomogeneities of the material). Third, the thickness of the Hall probe and its coating or substrate will determine the size of the gap between the surface of the superconductor and the measuring device (the same problem will also be caused by non-planar surfaces of the pellet or a variable sample thickness over the diameter). And finally, the time scale of the experiment has to be specified because of thermal activation and the corresponding relaxation of the profile. As an example, the influence of the gap size is demonstrated in fig. 45b. This suggests that the B_{max} "extrapolated" to a gap size of zero would be most adequate. Furthermore, an explicit determination of the time dependence of B_{max} would be highly desirable. Although this is often quoted in the literature to nicely follow a logarithmic law and to be approximately 5% per decade (e.g., Weinstein et al. 1996, see also fig. 45c), it could be worthwhile to use a certain "prescription", say $t = 1.000$ s, for specifying B_{max}. Finally, in particular when addressing large thick pellets, it can be very useful to check the sample on both sides, since cracks or other major imperfections may not go right through the entire material thickness (cf. fig. 45d, which refers to the "bottom" side of an otherwise "normal" sample). A consistency check of the above can be made by measuring the magnetisation of the sample by SQUID, vibrating sample magnetometry or other techniques, which is also sometimes used to assess J_c as an input parameter for the above numerical calculations. Good agreement is found on small samples. However, this can only be of limited relevance at present, since the pellet sizes of interest, at up to 50 mm diameter, by far exceed the spatial capabilities of the magnetometers.

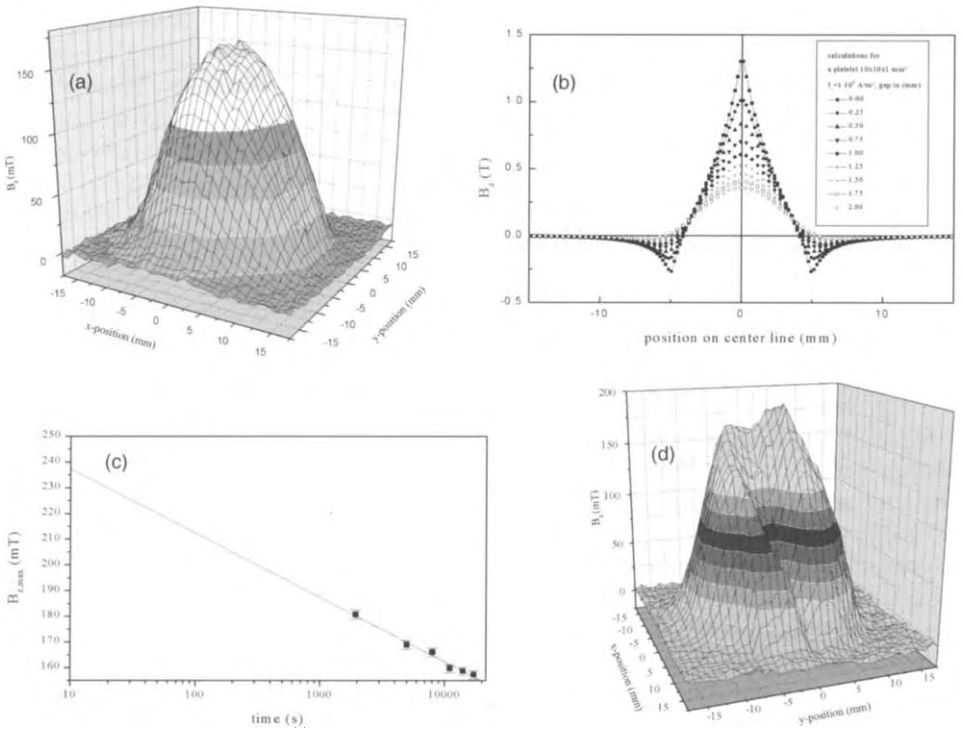

Fig. 45. Field mapping of the remnant magnetisation in large Y-123 pellets (Novak 1998): (a) flux profile at 77 K in a pellet with a diameter of 25 mm and a thickness of 13.6 mm, activated at 77 K and 2 T (gap: 0.5 mm); (b) influence of the gap size on the trapped field in a rectangular platelet with dimensions $10\times10\times1$ mm^3; (c) influence of the relaxation at 77 K on the maximum trapped field (activation at 77 K in a field of 2 T); (d) flux profile showing the influence of a crack on the bottom of a pellet with a diameter of 25 mm and a thickness of 13.6 mm, activated at 77 K and 2 T (gap: 0.6 mm).

Further recent work refers to the analysis of trapped fields when several pellets are stacked together (e.g. Nagashima et al. 1997), to possibilities of reducing flux creep by special procedures (Liu et al. 1995, Weinstein et al. 1996, Levin et al. 1998), and to enhancements of J_c by radiation techniques (Weinstein et al. 1996, 1998, Eisterer et al. 1998, Novak 1998). Successful reductions of the creep rate were achieved by post-activation cooling by several degrees or by cooling the sample still during activation. Record trapped fields of 10.1 T at 42 K could be achieved in this way and maintained nearly unchanged for more than three hours (Weinstein et al. 1996). Alternatively, heat pulses were reported to reduce creep in (Y,Pr)-123 single crystals (Levin et al. 1998). Enhancements of J_c by statistically distributed fission tracks (Weinstein et al. 1998) led to an increase of B_{max} by factors of ~5 at 77 K in Y-123 pellets of 20 mm diameter and 8 mm thickness. Similar results were obtained upon fast neutron irradiation of Y- and Sm-123 plates ($10\times10\times1$ mm^3), cf. fig. 46.

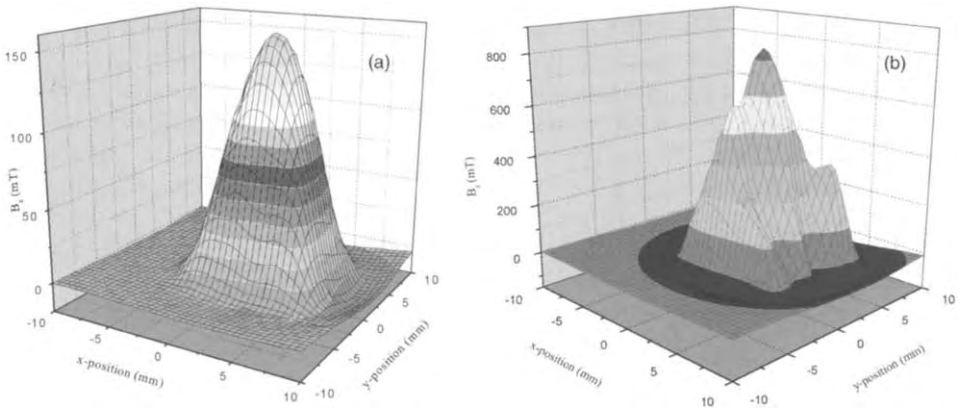

Fig. 46. Trapped-field distribution at 77 K in a rectangular platelet with dimensions $10\times10\times1$ mm^3, activated at 77 K in a field of 2 T and extrapolated to gap zero (Novak 1998): (a) trapped-field distribution in the unirradiated state: $B_{z,\max} = 156$ mT; (b) trapped-field distribution in the irradiated state (fast neutron fluence: 2×10^{21} m^{-2}, $E > 0.1$ MeV): $B_{z,\max} = 812$ mT.

With regard to measurements of the levitation forces, many of the above comments apply in a similar way. Crucial parameters are again J_c, B_{max}, the size and thickness of the superconductor, the distance between superconductor and magnet, and, in addition, the magnet material, the size of the magnet, the relative size of the superconductor versus the size of the magnet, etc. For more details, cf., e.g., Murakami (1992), Campbell and Cardwell (1997), Teshima et al. (1997).

9. Summary

As stated in the introduction of this article, I have tried to focus my review of published work on flux pinning in R-123 superconductors on those aspects which are in principle suited for achieving high critical current densities in these materials. We should not forget at this stage that – although discovered among the first high-temperature superconducting materials – R-123 superconductors still hold the highest potential for high critical current densities at the boiling temperature of liquid nitrogen among all other members in the family of the cuprates, and are potentially challenged in this respect only by Tl-1223 or Hg-1223, if suitable processing technologies can be developed. This unmatched performance at high temperatures is primarily related to the (nearly) three-dimensional character of superconductivity, which allows the formation of a 3D flux-line lattice and, consequently, facilitates pinning by a given crystallographic defect structure in comparison to the (more) 2D superconductors forming flux-line segments (pancakes) of comparatively high mobility under a Lorentz force.

The main issue that will require close attention, also in the foreseeable future, is the optimisation of the defect structures for flux pinning. The record performance of R-123

thin films can still be understood only partly in terms of the underlying defect structures, but has been approached recently by the fabrication technologies for coated conductors, which are in principle not too different from thin-film growth techniques, and have led to success by avoiding the formation of grain boundaries with too large grain-boundary angles. Obviously, this crystallographic defect has to be avoided, and my best guess about the most likely defect structure in the thin films is the formation of a dense array of extended planar defects along the crystallographic *c*-direction. The growth conditions of other forms of R-123 superconductors are too different to allow a one-to-one projection of these defects in these cases. Important defect structures for flux pinning in single crystals and melt-textured materials seem to be clusters of oxygen-deficient lattice cells, normal-conducting precipitates, and arrays of stacking faults, but their control is rather tedious and in many cases determined by the growth conditions. A remarkable exception is provided by radiation techniques, which allow, under certain conditions, extremely well-controlled modifications of the defect structures for flux pinning, and have led to record J_c's both in single crystals and in melt-textured materials. The extent to which they may be useful for applications, is still under discussion, and certainly depends on the envisaged application.

It is safe to state, in conclusion, that progress with our understanding of issues related to improve flux pinning in R-123 superconductors has been breathtaking over the past decade, and will certainly remain in the focus of further research, particularly with respect to all micro- and nano-structural aspects of material properties and defect configurations.

Acknowledgements

I am pleased to acknowledge the continuous, most fruitful and scientifically challenging cooperation with Dr. Franz M. Sauerzopf during the past (many) years, who also proved to be indispensable for the day-to-day operation of and the working atmosphere in a group of up to 25 members. The contributions of many brilliant undergraduate and graduate students as well as of post-doctoral fellows to the research activities described in this article are gratefully acknowledged. Furthermore, I wish to thank many colleagues from abroad, who contributed to our research in various ways, in particular Professor H.C. Freyhardt, Göttingen, Dr. M. Murakami, Tokyo, Dr. M.A. Kirk and Dr. B.W. Veal, Argonne, Professors R. Weinstein and K. Salama, Houston, Professor D. Bäuerle, Linz, Professor R. Griessen, Amsterdam, Professor P. Kes, Leiden, and Professor Y. Yeshurun, Ramat-Gan. I also wish to thank many colleagues for their willingness to provide me with original data or graphic files of some of their figures reproduced in this article. In conclusion, I wish to thank the Austrian Science Foundation, Vienna, for funding more than ten research projects on HTS, and the European Union for funding two Brite Euram projects and two networks on the subject (HCM and TMR).

References

Abrikosov, A.A., 1957, Sov. Phys. JETP **5**, 1174.

Abulafia, Y., A. Shaulov, Y. Wolfus, R. Prozorov, L. Burlachkov and Y. Yeshurun, 1995, Phys. Rev. B **75**, 2404.

Abulafia, Y., A. Shaulov, Y. Wolfus, R. Prozorov, L. Burlachkov, Y. Yeshurun, D. Majer, E. Zeldov, H. Wühl, V.B. Geshkenbein and V.M. Vinokur, 1996, Phys. Rev. Lett. **77**, 1596.

Adaktylos, I., and H.W. Weber, 1977, Philos. Mag. **35**, 983.

Adaktylos, I., E. Schachinger and H.W. Weber, 1977, J. Low Temp. Phys. **26**, 533.

Alers, P.B., 1957, Phys. Rev. **105**, 104.

Almasan, C.C., M.C. de Andrade, Y. Dalichaouch, J.J. Neumeier, C.L. Seaman, M.B. Maple, R.P. Guertin, M.V. Kuric and J.C. Garland, 1992, Phys. Rev. Lett. **69**, 3812.

Anderson, P.W., 1962, Phys. Rev. Lett. **9**, 309.

Antesberger, G., and H. Ullmaier, 1974, Philos. Mag. **29**, 1101.

Bean, C.P., 1962, Phys. Rev. Lett. **8**, 250.

Bednorz, J.G., and K.A. Müller, 1986, Z. Phys. B **64**, 189.

Biersack, J.P., and L.G. Haggmark, 1980, Nucl. Instrum. Methods **174**, 257.

Blatter, G., M.V. Feigel'man, V.B. Geshkenbein, A.I. Larkin and V.M. Vinokur, 1994, Rev. Mod. Phys. **66**, 1125.

Böhmer, C., G. Brandstätter and H.W. Weber, 1997, Supercond. Sci. Technol. **10**, A1.

Brandstätter, G., F.M. Sauerzopf, H.W. Weber and B.W. Veal, 1996, Czech. J. Phys. **46**(S3), 1681.

Brandstätter, G., F.M. Sauerzopf and H.W. Weber, 1997, Phys. Rev. B **55**, 11693.

Brandstätter, G., F.M. Sauerzopf, H.W. Weber and B.W. Veal, 1998a, in: Critical Currents in Superconductors for Practical Applications, eds L. Zhou, H.W. Weber, E.W. Collings (World Scientific, Singapore) p. 325.

Brandstätter, G., M.C. Frischherz, L. Kratzwald, H.W. Weber and A.E. Petrov, 1998b, Physica C **307**, 197.

Brandt, E.H., 1989, Science **243**, 349.

Brandt, E.H., 1995, Rep. Prog. Phys. **58**, 1465.

Brandt, E.H., 1996, Phys. Rev. B **54**, 4246.

Breit, V., P. Schweiss, R. Hauff, H. Wühl, H. Claus, H. Rietschel, A. Erb and G. Müller-Vogt, 1995, Phys. Rev. B **52**, R15727.

Brezgunov, M.M., S.V. Belogurov, A.E. Petrov, A.N. Karpov, I.V. Kudrenitskis, V.N. Kovalev, E.N. Kurkin, A.A. Makletsov, Yu.G. Morozov and M.D. Nersesyan, 1990, Superconductivity **3**, 843.

Bulaevskii, L.N., M. Ledvij and V.G. Kogan, 1992, Phys. Rev. Lett. **68**, 3773.

Campbell, A.M., 1969, J. Phys. C **2**, 1492.

Campbell, A.M., and D.A. Cardwell, 1997, Cryogenics **37**, 567.

Campbell, A.M., and J.E. Evetts, 1972, Critical Currents in Superconductors (Taylor & Francis, London).

Cava, R.J., A.W. Hewat, E.A. Hewat, B. Batlogg, M. Marezio, K.M. Rabe, J.J. Krajewski, W.F. Peck Jr and L.W. Rupp Jr, 1990, Physica C **165**, 419.

Chien, T.R., W.R. Datars, B.W. Veal, A.P. Paulikas, P. Kostić, C. Gu and Y. Jiang, 1994, Physica C **229**, 273.

Chikumoto, N., and M. Murakami, 1996, in: Proc. 10th Anniversary HTS Workshop on Physics, Materials and Applications, eds B. Batlogg, C.W. Chu, W.K. Chu, D.U. Gubser and K.A. Müller (World Scientific, Singapore) pp. 139–142.

Civale, L., 1997, Supercond. Sci. Technol. **10**, A11.

Civale, L., and L. Krusin-Elbaum, 1997, Phys. Rev. Lett. **78**, 1829.

Civale, L., A.D. Marwick, M.W. McElfresh, T.K. Worthington, A.P. Malozemoff, F. Holtzberg, J.R. Thompson and M.A. Kirk, 1990, Phys. Rev. Lett. **65**, 1164.

Civale, L., A.D. Marwick, T.K. Worthington, M.A. Kirk, J.R. Thompson, L. Krusin-Elbaum, Y.R. Sun, J.R. Clem and F. Holtzberg, 1991, Phys. Rev. Lett. **67**, 648.

Civale, L., T.K. Worthington, L. Krusin-Elbaum, A.D. Marwick, F. Holtzberg, J.R. Thompson, M.A. Kirk and R. Wheeler, 1992, J. Met. **44**, 60.

Civale, L., L. Krusin-Elbaum, J.R. Thompson and F. Holtzberg, 1994a, Phys. Rev. B **50**, 7188.

Civale, L., L. Krusin-Elbaum, J.R. Thompson, R. Wheeler, A.D. Marwick, M.A. Kirk, Y.R. Sun, F. Holtzberg and C. Feild, 1994b, Phys. Rev. B **50**, 4102.

Clark, A.F., ed., 1997, IEEE Trans. Appl. Supercond. **7**.

Clem, J.R., 1991, Phys. Rev. B **43**, 7837.

Clem, J.R., 1992, in: Magnetic Susceptibility of Superconductors and Other Spin Systems, eds R.A. Hein, T.L. Francavilla and D.H. Liebenberg (Plenum, New York) p. 177.

Clem, J.R., and M.W. Coffey, 1990, Phys. Rev. B **42**, 6209.

Cohen, L.F., J.R. Laverty, G.K. Perkins, A.D. Caplin and W. Assmus, 1993, Cryogenics **33**, 352.

Coote, R.I., J.E. Evetts and A.M. Campbell, 1972, Can. J. Phys. **50**, 421.

Cribier, D., B. Jacrot, L.M. Rao and B. Farnoux, 1964, Phys. Lett. **9**, 106.

Cubitt, R., E.M. Forgan, G. Yang, S.L. Lee, D.McK. Paul, H.A. Mook, M. Yethiraj, P.H. Kes, T.W. Li, A.A. Menovsky, Z. Tarnawski and K. Mortensen, 1993, Nature **365**, 407.

Däumling, M., J.M. Seuntjens and D.C. Larbalestier, 1990, Nature **346**, 332.

Däumling, M., A. Erb, E. Walker, J.Y. Genoud and R. Flükiger, 1996, Physica C **257**, 371.

de Groot, P.A.J., Y. Zhu-An, R. Yanru and S. Smith, 1991, Physica C **185**, 2471.

Dew-Hughes, D., 1971, Rep. Prog. Phys. **34**, 821.

Dew-Hughes, D., 1974, Philos. Mag. **30**, 293.

Dew-Hughes, D., ed., 1995, Applied Superconductivity 1995, IOP Conf. Ser. **148**.

Dew-Hughes, D., and M.J. Witcomb, 1972, Philos. Mag. **26**, 73.

Dolan, G.J., F. Holtzberg, C. Feild and T.R. Dinger, 1989, Phys. Rev. Lett. **62**, 2184.

Doyle, R.A., B. Khaykovich, M. Konczykowski, E. Zeldov, N. Morozov, D. Majer, P.H. Kes and V. Vinokur, 1997, Physica C **282–287**, 323.

Egi, T., J.G. Wen, K. Kuroda, H. Unoki and N. Koshizuka, 1995, Appl. Phys. Lett. **67**, 2406.

Eisterer, M., S. Tönies, W. Novak, H.W. Weber, R. Weinstein and R.P. Sawh, 1998, Supercond. Sci. Technol. **11**, 1101.

Erb, A., E. Walker and R. Flükiger, 1995, Physica C **245**, 245.

Erb, A., E. Walker and R. Flükiger, 1996a, Physica C **258**, 9.

Erb, A., J.Y. Genoud, F. Marti, M. Däumling, E. Walker and R. Flükiger, 1996b, J. Low Temp. Phys. **105**, 1023.

Erb, A., E. Walker, J.Y. Genoud and R. Flükiger, 1997, Physica C **282–287**, 2145.

Evetts, J.A., and J.M.A. Wade, 1970, J. Phys. Chem. Solids **31**, 973.

Feenstra, R., D.K. Christen, C.E. Klabunde and J.D. Budai, 1992, Phys. Rev. B **45**, 7555.

Feigel'man, M.V., V.B. Geshkenbein, A.I. Larkin and V.M. Vinokur, 1989, Phys. Rev. Lett. **63**, 2301.

Feigel'man, M.V., V.B. Geshkenbein and V.M. Vinokur, 1991, Phys. Rev. B **43**, 6263.

Feinberg, D., 1992, Physica C **194**, 126.

Feinberg, D., and C. Villard, 1990, Phys. Rev. Lett. **65**, 919.

Fleischer, R.L., J.R. Hart Jr, K.W. Lay and F.E. Luborsky, 1989, Phys. Rev. B **40**, 2163.

Fossheim, K., E.D. Tuset, T.W. Ebbesen, M.M.J. Treacy and J. Schwartz, 1995, Physica C **248**, 195.

Freyhardt, H.C., 1971a, Philos. Mag. **23**, 369.

Freyhardt, H.C., 1971b, Philos. Mag. **23**, 345.

Freyhardt, H.C., J. Hoffmann, J. Wiesmann, J. Dzick, K. Heinemann, A. Isaev, F. Garcia-Moreno, S. Sievers and A. Usoskin, 1997, IEEE Trans. Appl. Supercond. **7**, 1426.

Frischherz, M.C., M.A. Kirk, J.P. Zhang and H.W. Weber, 1993, Philos. Mag. A **67**, 1347.

Frischherz, M.C., M.A. Kirk, J. Farmer, L.R. Greenwood and H.W. Weber, 1994, Physica C **232**, 309.

Frischherz, M.C., F.M. Sauerzopf, H.W. Weber, M. Murakami and G.A. Emel'chenko, 1995, Supercond. Sci. Technol. **8**, 485.

Fuchs, G., G. Krabbes, P. Schätzle, P. Stoye, T. Staiger and K.-H. Müller, 1996, Physica C **268**, 115.

Fujimoto, H., K. Taguchi, M. Murakami, N. Nakamura and N. Koshizuka, 1992, Cryogenics **32**, 954.

Fujimoto, H., K. Kawano, T. Higuchi, K. Nagashima and M. Murakami, 1997, Physica C **282–287**, 2327.

Gammel, P.L., D.J. Bishop, J.P. Rice and D.M. Ginsberg, 1992, Phys. Rev. Lett. **22**, 3343.

Gerber, C., D. Anselmetti, J.G. Bednorz, J. Mannhart and D.G. Schlom, 1991, Nature **350**, 279.

Gerhäuser, W., G. Ries, H.W. Neumüller, W. Schmidt, O. Eibl, G. Saemann-Ischenko and S. Klaumünzer, 1992, Phys. Rev. Lett. **68**, 879.

Geshkenbein, V.B., A.I. Larkin, M.V. Feigel'man and V.M. Vinokur, 1989, Physica C **162–164**, 239.

Geshkenbein, V.B., V.M. Vinokur and R. Fehrenbacher, 1991, Phys. Rev. B **43**, 3748.

Giapintzakis, J., M.A. Kirk, W.C. Lee, J.P. Rice, D.M. Ginsberg, I.M. Robertson and R.L. Wheeler, 1992, in: Layered Superconductors: Fabrication, Properties and Applications, MRS Symp. Proc. **275**, eds D.T. Shaw, C.C. Tsuei, T.R. Schneider and Y. Shinohara (MRS, Pittsburgh) pp. 741–746.

Giapintzakis, J., D.M. Ginsberg, M.A. Kirk and S. Ockers, 1994a, Phys. Rev. B **50**, 15967.

Giapintzakis, J., R.L. Neiman, D.M. Ginsberg and M.A. Kirk, 1994b, Phys. Rev. B **50**, 16001.

Ginzburg, V.L., and L.D. Landau, 1950, Zh. Eksp. Teor. Fiz. **20**, 1064.

Gömöry, F., 1997, Supercond. Sci. Technol. **10**, 523.

Gordeev, S.N., W. Jahn, A.A. Zhukov, H. Küpfer and T. Wolf, 1994, Phys. Rev. B **49**, 21.

Gray, K.E., D.H. Kim, B.W. Veal, G.T. Seidler, T.F. Rosenbaum and D.E. Farrell, 1992, Phys. Rev. B **45**, 10071.

Griessen, R.P., M.J.G. Lee and D.J. Stanley, 1977, Phys. Rev. B **16**, 4385.

Gruss, S., G. Fuchs, G. Krabbes, P. Schätzle, J. Fink, K.-H. Müller and L. Schultz, 1999, IEEE Trans. Appl. Supercond. **9**, 2070.

Gu, H., C. Colliex, S. Senoussi, C. Aguillon-Levillain and P. Manuel, 1993, Philos. Mag. A **68**, 19.

Gyorgy, E.M., R.B. van Dover, K.A. Jackson, L.F. Schneemeyer and J.V. Waszczak, 1989, Appl. Phys. Lett. **55**, 283.

Hardy, V., D. Groult, M. Hervieu, J. Provost, B. Raveau and S. Bouffard, 1991, Nucl. Instrum. Methods B **54**, 472.

Hardy, V., D. Groult, J. Provost and B. Raveau, 1992, Physica C **190**, 289.

Hardy, V., A. Wahl, S. Hebert, A. Ruyter, J. Provost, D. Groult and C. Simon, 1996, Phys. Rev. B **54**, 656.

High-T_c Update, 1987–2000, published bi-weekly by the US DOE, Ames Laboratory, USA, see also http://www.iitap.iastate.edu/htcu/htcu.html.

Hillmann, H., and D. Hauck, 1972, in: Proc. Applied Superconductivity Conf. (Annapolis), eds H.M. Long and W.F. Gauster (IEEE, New York) p. 429.

Hirth, J.P., and J. Lothe, 1982, Theory of Dislocations (Wiley, New York) ch. 15.

Holzapfel, B., G. Kreiselmeyer, M. Kraus, G. Saemann-Ischenko, S. Bouffard, S. Klaumünzer and L. Schultz, 1993, Phys. Rev. B **48**, 600.

Huebener, R.P., R.T. Kampwirth and V.A. Rowe, 1972, Cryogenics **12**, 100.

Jin, S., T.H. Tiefel, R.C. Sherwood, M.E. Davis, R.B. van Dover, G.W. Kammlott, R.A. Fastnacht and H.D. Keith, 1988, Appl. Phys. Lett. **52**, 2074.

Jones, E.C., D.K. Christen, J.R. Thompson, R. Feenstra, S. Zhu, D.H. Lowndes, J.M. Philips, M.P. Siegal and J.D. Budai, 1993, Phys. Rev. B **47**, 8986.

Jorgensen, J.D., H. Shaked, D.G. Hinks, B. Dabrowski, B.W. Veal, A.P. Paulikas, L.J. Nowicki, G.W. Crabtree, W.K. Kwok, L.H. Nunez and H. Claus, 1988, Physica C **153–155**, 578.

Jorgensen, J.D., B.W. Veal, A.P. Paulikas, L.J. Nowicki, G.W. Crabtree, H. Claus and W.K. Kwok, 1990, Phys. Rev. B **41**, 1863.

Kern, C., 1997, Diploma Thesis (Technical University of Vienna).

Kes, P.H., J. Aarts, J. van den Berg, C.J. van der Beek and J.A. Mydosh, 1989, Supercond. Sci. Technol. **1**, 242.

Kes, P.H., J. Aarts, V.M. Vinokur and C.J. van der Beek, 1990, Phys. Rev. Lett. **64**, 1063.

Kirchner, H., 1968, Phys. Lett. **26A**, 651.

Koblischka, M.R., and R.J. Wijngaarden, 1995, Supercond. Sci. Technol. **8**, 199.

Kolesnik, S., H.W. Weber, T. Skoskiewicz, M. Sawicki and W. Sadowski, 1997, Physica C **282–287**, 1961.

Konczykowski, M., F. Rullier-Albenque, E.R. Jacoby, A. Shaulov, Y. Yeshurun and P. Lejay, 1991, Phys. Rev. B **44**, 7167.

Koshelev, A.E., 1994, Phys. Rev. B **50**, 506.

Kramer, E.J., 1973, J. Appl. Phys. **44**, 1360.

Kramer, E.J., and C.L. Bauer, 1967, Philos. Mag. **15**, 1189.

Kraus, M., M. Leghissa and G. Saemann-Ischenko, 1994a, Phys. Bl. **50**, 333.

Kraus, M., G. Kreiselmeyer, J. Daniel, M. Leghissa, G. Saemann-Ischenko, B. Holzapfel, P. Kummeth, R. Scholz and L.Ya. Vinnikov, 1994b, Nucl. Instrum. Methods B **89**, 307.

Kritscha, W., 1991, Ph.D. Thesis (Technical University of Vienna).

Kritscha, W., F.M. Sauerzopf and H.W. Weber, 1990a, Physica B **165–166**, 109.

Kritscha, W., F.M. Sauerzopf, H.W. Weber, G.W. Crabtree, Y.C. Chang and P.-Z. Jiang, 1990b, Europhys. Lett. **12**, 179.

Kritscha, W., F.M. Sauerzopf, H.W. Weber, G.W. Crabtree, Y.C. Chang and P.-Z. Jiang, 1991, Physica C **199**, 15.

Krusin-Elbaum, L., L. Civale, V.M. Vinokur and F. Holtzberg, 1992, Phys. Rev. Lett. **69**, 2280.

Krusin-Elbaum, L., J.R. Thompson, R. Wheeler, A.D. Marwick, C. Li, S. Patel, D.T. Shaw, P. Lisowski and J. Ullmann, 1994, Appl. Phys. Lett. **64**, 3331.

Küpfer, H., A.A. Zhukov, A. Will, W. Jahn, R. Meier-Hirmer, T. Wolf, V.I. Voronkova, M. Kläser and K. Saito, 1996, Phys. Rev. B **54**, 644.

Küpfer, H., T. Wolf, A.A. Zhukov, C. Lessing, W. Jahn and R. Meier-Hirmer, 1997, Advances in superconductivity, in: New Materials, Critical Currents & Devices, eds R. Pinto, S.K. Malik, A.K. Grover and P. Ayyub (New Age International Limited Publishers, New Delhi) p. 291.

Kwok, W.K., U. Welp, G.W. Crabtree, K.G. Vandervoort, R. Hulscher and J.Z. Liu, 1990a, Phys. Rev. Lett. **64**, 966.

Kwok, W.K., U. Welp, K.G. Vandervoort, Y. Fang and G.W. Crabtree, 1990b, Appl. Phys. Lett. **57**, 1.

Kwok, W.K., U. Welp, S. Fleshler, K.G. Vandervoort, G.W. Crabtree, J.Z. Liu, J. Brooks, J. Hettinger and S.T. Hannahs, 1991a, Supercond. Sci. Technol. **4**, S106.

Kwok, W.K., U. Welp, V.M. Vinokur, S. Fleshler, J. Downey and G.W. Crabtree, 1991b, Phys. Rev. Lett. **67**, 390.

Labusch, R., 1969, Cryst. Lattice Defects **1**, 1.

Larkin, A.I., and Yu.N. Ovchinnikov, 1974, Sov. Phys. JETP **38**, 854.

Larkin, A.I., and Yu.N. Ovchinnikov, 1979, J. Low Temp. Phys. **34**, 409.

Lawrence, W.E., and S. Doniach, 1971, in: Proc. 12th Int. Conf. on Low Temperature Physics, ed E. Kanda (Keigaku, Tokyo) p. 361.

Lensink, J.G., 1993, Ph.D. Thesis (Vrije Universiteit, Amsterdam).

Levin, G.A., C.C. Almasan, D.A. Gajewski and M.B. Maple, 1998, Appl. Phys. Lett. **72**, 112.

Liu, J., R. Weinstein, Y. Ren, R.P. Sawh, C. Foster and V. Obot, 1995, in: Proc. 1995 Int. Workshop on Superconductivity (Maui), eds S. Tanaka and J.M. Phillips (ISTEC, Tokyo) p. 353.

Majer, D., E. Zeldov, H. Shtirkman and M. Konczykowski, 1996, in: Coherence in High Temperature Superconductors, eds G. Deutscher and A. Revcolevschi (World Scientific, Singapore) pp. 271–291.

Malozemoff, A.P., T.K. Worthington, Y. Yeshurun, F. Holtzberg and P.H. Kes, 1988, Phys. Rev. B **38**, 7203.

Mannhart, J., D. Anselmetti, J.G. Bednorz, C. Gerber, K.A. Müller and D.G. Schlom, 1992, Supercond. Sci. Technol. **5**, S125.

Martínez, B., F. Sandiumenge, N. Vilalta, S. Piñol, X. Obradors and J. Rabier, 1996, J. Appl. Phys. **80**, 5515.

McGinn, P., 1995, in: High Temperature Superconducting Materials Science and Engineering, ed D. Shi (Elsevier, Amsterdam) ch. 8, pp. 345–382.

Meier-Hirmer, R., H. Küpfer and H. Scheurer, 1985, Phys. Rev. B **31**, 183.

Meilikhov, E.Z., and V.G. Shapiro, 1991, Superconductivity **4**, 1353.

Meissner, W., and R. Ochsenfeld, 1933, Naturwissenschaften **21**, 787.

Morikawa, K., and M. Tsuchimoto, 1997, Physica C **282–287**, 1863.

Müller, U., and H.C. Freyhardt, 1996, Philos. Mag. Lett. **73**, 63.

Murakami, M., ed., 1992, Melt Processed High Temperature Superconductors (World Scientific, Singapore).

Murakami, M., K. Yamaguchi, H. Fujimoto, N. Nakamura, T. Taguchi, N. Koshizuka and S. Tanaka, 1992, Cryogenics **32**, 930.

Murakami, M., S.I. Yoo, T. Higuchi, N. Sakai, J. Weltz, N. Koshizuka and S. Tanaka, 1994, Jpn. J. Appl. Phys. **33**, L715.

Murakami, M., S.I. Yoo, N. Sakai, K. Sawada, T. Higuchi and N. Chikumoto, 1996, in: Critical Currents in Superconductors, eds T. Matsushita and K. Yamafuji (World Scientific, Singapore) pp. 57–62.

Nagashima, K., T. Higuchi, J. Sok, S.I. Yoo, H. Fujimoto and M. Murakami, 1997, Cryogenics **37**, 557.

Norton, D.P., A. Goyal, J.D. Budai, D.K. Christen, D.M. Kroeger, E.D. Specht, Q. He, B. Saffian, M. Paranthaman, C.E. Klabunde, D.F. Lee, B.C. Sales and F.A. List, 1996, Science **274**, 755.

Novak, W., 1998, Diploma Thesis (Technical University of Vienna).

Ossandon, J.G., J.R. Thompson, D.K. Christen, B.C. Sales, H.R. Kerchner, J.O. Thomson, Y.R. Sun, K.W. Lay and J.E. Tkaczyk, 1992a, Phys. Rev. B **45**, 12534.

Ossandon, J.G., J.R. Thompson, D.K. Christen, B.C. Sales, Y.R. Sun and K.W. Lay, 1992b, Phys. Rev. B **46**, 3050.

Oussena, M., P.A.J. de Groot and S.J. Porter, 1995, Phys. Rev. B **51**, 1389.

Pearl, J., 1964, Appl. Phys. Lett. **5**, 65.

Pust, L., J. Kadlecova, M. Jirsa and S. Durcok, 1990, J. Low Temp. Phys. **78**, 179.

Quaford, M., K. Heeck, J.G. Lensink, R.J. Wijngaarden and R. Griessen, 1992, Rev. Sci. Instrum. **63**, 5526.

Rabier, J., P.D. Tall and M.F. Denanot, 1993, Philos. Mag. A **67**, 1021.

Ren, Y., R. Weinstein, J. Liu and R.P. Sawh, 1995, Physica C **251**, 15.

Roas, B., L. Schultz and G. Saemann-Ischenko, 1990, Phys. Rev. Lett. **64**, 479.

Rollins, R.W., H. Küpfer and W. Gey, 1974, J. Appl. Phys. **45**, 5392.

Roulin, M., A. Junod and E. Walker, 1996, Science **273**, 1210.

Salama, K., V. Selvamanickam and D.F. Lee, 1993, in: Proc. and Properties of High T_c Superconductors, Vol. 1, ed S. Jin (World Scientific, Singapore) ch. 5, pp. 155–211.

Samadi Hosseinali, G., H.W. Weber, E. Stangl, S. Proyer and D. Bäuerle, 1997, Physica C **282–287**, 2147.

Sandiumenge, F., N. Vilalta, S. Piñol, B. Martínez and X. Obradors, 1995, Phys. Rev. B **51**, 1994.

Sandiumenge, F., B. Martínez and X. Obradors, 1997, Supercond. Sci. Technol. **10**, A93.

Sauerzopf, F.M., 1998, Phys. Rev. B **57**, 10959.

Sauerzopf, F.M., H.P. Wiesinger and H.W. Weber, 1990, Cryogenics **30**, 650.

Sauerzopf, F.M., H.P. Wiesinger, H.W. Weber, G.W. Crabtree, M.C. Frischherz and M.A. Kirk, 1992, Supercond. Sci. Technol. **5**, S105.

Sauerzopf, F.M., H.P. Wiesinger, H.W. Weber and G.W. Crabtree, 1995, Phys. Rev. B **51**, 6002.

Sauerzopf, F.M., M. Werner, H.W. Weber, R.A. Suris, V.S. Kharlamov and Yu.V. Trushin, 1997, Physica C **282–287**, 1333.

Schalk, R.M., 1992, Ph.D. Thesis (Technical University of Vienna).

Schalk, R.M., H.W. Weber, Z.H. Barber, P. Przyslupsky and J.E. Evetts, 1992a, Physica C **199**, 311.

Schalk, R.M., H.W. Weber, Z.H. Barber, C.E. Davies, J.E. Evetts, R.E. Somekh and D.H. Kim, 1992b, Supercond. Sci. Technol. **5**, S224.

Schalk, R.M., G. Samadi Hosseinali, H.W. Weber, S. Proyer, P. Schwab, D. Bäuerle and S. Gründorfer, 1994, Phys. Rev. B **49**, 3511.

Schalk, R.M., K. Kundzins, H.W. Weber, E. Stangl, S. Proyer and D. Bäuerle, 1996, Physica C **257**, 341.

Schelten, J., H. Ullmaier and W. Schmatz, 1971, Phys. Status Solidi **B 48**, 619.

Schilling, A., R.A. Fisher, N.E. Phillips, U. Welp, D. Dasgupta, W.K. Kwok and G.W. Crabtree, 1996, Nature **382**, 791.

Schmitt, P., P. Kummeth, L. Schultz and G. Saemann-Ischenko, 1991, Phys. Rev. Lett. **67**, 267.

Schnack, H.G., 1995, Ph.D. Thesis (Vrije Universeit, Amsterdam).

Schnack, H.G., R. Griessen, J.G. Lensink and H.H. Wen, 1993, Phys. Rev. B **48**, 13178.

Scurlock, A.G., ed., 1997, Cryogenics **37**(10).

Seidler, G.T., T.F. Rosenbaum, D.L. Heinz, J.W. Downey, A.P. Paulikas and B.W. Veal, 1991, Physica C **183**, 333.

Selvamanickam, V., M. Mironova, S. Son and K. Salama, 1993, Physica C **208**, 238.

Sickafus, K.E., J.O. Willis, P.J. Kung, W.B. Wilson, D.M. Parkin, M.P. Maley, F.W. Clinard Jr, C.J. Salgado, R.P. Dye and K.M. Hubbard, 1992, Phys. Rev. B **46**, 11862.

Suenaga, M., D.O. Welch and R.C. Budhani, 1992, Supercond. Sci. Technol. **5**, S1.

Superconductivity Database, 1996, ETL, ISTEC, Japan, http://www.aist.go.jp/RIODB/sprcnd_etl/.

Svetchnikov, V.L., V.M. Pan, C. Traeholt and H.W. Zandbergen, 1997, IEEE Trans. Appl. Supercond. **7**, 1396.

Tachiki, M., and S. Takahashi, 1989, Solid State Commun. **70**, 291.

Tesanovic, Z., 1991, Phys. Rev. B **44**, 12635.

Teshima, H., M. Sawamura, M. Morita and M. Tsuchimoto, 1997, Cryogenics **37**, 505.

Thompson, J.R., D.K. Christen, Y.R. Sun, H.R. Kerchner, J.E. Tkaczyk and K.W. Lay, 1992, Cryogenics **32**, 982.

Thompson, J.R., J.G. Ossandon, D.K. Christen, R. Feenstra, B.C. Sales, H.R. Kerchner, E.C. Jones and Y.R. Sun, 1994, in: Critical Currents in Superconductors, ed H.W. Weber (World Scientific, Singapore) pp. 70–75.

Ting, W., T. Egi, R. Itti, K. Kuroda, N. Koshizuka and S. Tanaka, 1997, Appl. Phys. Lett. **70**, 770.

Träuble, H., and U. Eßmann, 1966, Phys. Status Solidi **18**, 813.

Trushin, Yu.V., B.J. Ber, V.S. Kharlamov and E.E. Zhurkin, 1996, J. Nucl. Mater. **233–237**, 991.

Ullmaier, H., 1975, Irreversible Properties of Type II Superconductors (Springer, Berlin).

Ullrich, M., D. Müller, W. Mexner, M. Steins, K. Heinemann and H.C. Freyhardt, 1993, Phys. Rev. B **48**, 7513.

Umezawa, A., G.W. Crabtree, J.Z. Liu, H.W. Weber, W.K. Kwok, L.H. Nunez, T.J. Moran, C.H. Sowers and H. Claus, 1987, Phys. Rev. B **36**, 7151.

van Dalen, A.J.J., 1995, Ph.D. Thesis (Vrije Universiteit, Amsterdam).

van Dalen, A.J.J., M.R. Koblischka, R. Griessen, M. Jirsa and G. Ravi Kumar, 1995, Physica C **250**, 265.

van Dalen, A.J.J., R. Griessen, S. Libbrecht, Y. Bruynseraede and E. Osquiguil, 1996, Phys. Rev. B **54**, 1366.

Vargas, J.L., and D.C. Larbalestier, 1992, Appl. Phys. Lett. **60**, 1741.

Vlcek, B.M., M.C. Frischherz, S. Fleshler, U. Welp, J.Z. Liu, J. Downey, K.G. Vandervoort, G.W. Crabtree and M.A. Kirk, 1992, Phys. Rev. B **46**, 6441.

Vlcek, B.M., H.K. Viswanathan, M.C. Frischherz, S. Fleshler, K.G. Vandervoort, J. Downey, U. Welp, M.A. Kirk and G.W. Crabtree, 1993, Phys. Rev. B **48**, 4067.

Wacenovsky, M., 1993, Ph.D. Thesis (Technical University of Vienna).

Weber, H.W., 1996, in: Proc. 10th Anniversary HTS Workshop on Physics, Materials and Applications, eds B. Batlogg, C.W. Chu, W.K. Chu, D.U. Gubser and K.A. Müller (World Scientific, Singapore) pp. 163–166.

Weber, H.W., and O. Hittmair, 1979, Supraleitung (Thiemig Verlag, München).

Weber, H.W., J. Schelten and G. Lippmann, 1973, Phys. Status Solidi **B 57**, 515.

Weber, H.W., G.P. Westphal and I. Adaktylos, 1976, Cryogenics **16**, 39.

Weber, H.W., H. Böck, E. Unfried and L.R. Greenwood, 1986, J. Nucl. Mater. **137**, 236.

Weinstein, R., Y. Ren, J. Liu, I.G. Chen, R.P. Sawh, C. Foster and V. Obot, 1993, in: Proc. Int. Symp. on Superconductivity (Hiroshima), eds T. Fujita and Y. Shiohara (Springer, Berlin) p. 855.

Weinstein, R., J. Liu, Y. Ren, I.G. Chen, V. Obot, R.P. Sawh, C. Foster and A. Crapo, 1994, in: Proc. 1994 Int. Workshop on Superconductivity (Kyoto, Japan), eds S. Tanaka and T. Matsushita (ISTEC, Tokyo) p. 39.

Weinstein, R., J. Liu, Y. Ren, R.P. Sawh, D. Parks, C. Foster and V. Obot, 1996, in: Proc. 10th Anniversary HTS Workshop on Physics, Materials and Applications, eds B. Batlogg, C.W. Chu, W.K. Chu, D.U. Gubser and K.A. Müller (World Scientific, Singapore) pp. 625–628.

Weinstein, R., R.P. Sawh, Y. Ren, M. Eisterer and H.W. Weber, 1998, Supercond. Sci. Technol. **11**, 959.

Welp, U., J.A. Fendrich, W.K. Kwok, G.W. Crabtree and B.W. Veal, 1996, Phys. Rev. Lett. **76**, 4809.

Werner, M., 1997, Ph.D. Thesis (Technical University of Vienna).

Werner, M., F.M. Sauerzopf, H.W. Weber, A. Hoekstra, R. Surdeanu, R.J. Wijngaarden, R. Griessen and K. Winzer, 1996, in: Critical Currents in Superconductors, eds T. Matsushita and K. Yamafuji (World Scientific, Singapore) pp. 203–206.

Wiesinger, H.P., F.M. Sauerzopf and H.W. Weber, 1992a, Physica C **203**, 121.

Wiesinger, H.P., F.M. Sauerzopf, H.W. Weber, H. Gerstenberg and G.W. Crabtree, 1992b, Europhys. Lett. **20**, 541.

Wijngaarden, R.J., H.J.W. Spoelder, R. Surdeanu and R. Griessen, 1996, Phys. Rev. B **54**, 6742.

Wisniewski, A., M. Baran, C. Czurda, H.W. Weber, P.X. Zhang and L. Zhou, 1994, in: Critical Currents in Superconductors, ed H.W. Weber (World Scientific, Singapore) pp. 447–450.

Wisniewski, A., C. Czurda, H.W. Weber, M. Baran, M. Reissner, W. Steiner, P.X. Zhang and L. Zhou, 1996, Physica C **266**, 309.

Wolf, T., A.C. Bornarel, H. Küpfer, R. Meier-Hirmer and B. Obst, 1997, Phys. Rev. B **56**, 6308.

Wördenweber, R., G.V.S. Sasty, K. Heinemann and H.C. Freyhardt, 1989, J. Appl. Phys. **65**, 1648.

Workshops on Flux Dynamics, 1994–2000, Workshops held in Palaiseau, Lake Forest, Shoresh, Monte Verita, Hachimantai, Palo Alto, Lunteren.

Yacobi, E.R., A. Shaulov, Y. Yeshurun, M. Konczykowski and F. Rullier-Albenque, 1992, Physica C **199**, 15.

Yang, P., and C.M. Lieber, 1996, Science **273**, 1836.

Yang, P., and C.M. Lieber, 1997, Appl. Phys. Lett. **70**, 3158.

Yeshurun, Y., E.R. Yacobi, L. Klein, L. Burlachkov, R. Prozorov, N. Bontemps, H. Wühl and V.M. Vinokur, 1994, in: Critical Currents in Superconductors, ed H.W. Weber (World Scientific, Singapore) pp. 237–239.

Yeshurun, Y., A.P. Malozemoff and A. Shaulov, 1996, Rev. Mod. Phys. **68**, 3.

Yoo, S.I., N. Sakai, H. Takaichi, T. Higuchi and M. Murakami, 1994, Appl. Phys. Lett. **65**, 633.

Yoo, S.I., M. Murakami, N. Sakai, T. Ohyama, T. Higuchi, M. Watahiki and M. Takahashi, 1995, J. Electron. Mater. **24**, 1923.

Yoshida, T., K. Kuroda and H. Saka, 1990, Philos. Mag. A **62**, 573.

Zandbergen, H.W., R. Gronsky, K. Wang and G. Thomas, 1988, Nature **331**, 596.

Zhang, P.X., L. Zhou, P. Ji, W.M. Bian, X.Z. Wu and Z.H. Lai, 1995a, Supercond. Sci. Technol. **8**, 15.

Zhang, P.X., H.W. Weber and L. Zhou, 1995b, Supercond. Sci. Technol. **8**, 701.

Zhao, Y.J., J.R. Liu, R.L. Meng and W.K. Chu, 1992, Physica C **198**, 256.

Zhou, L., P.X. Zhang, P. Ji, K.G. Wang, J.R. Wang and X.Z. Wu, 1990, Supercond. Sci. Technol. **3**, 490.

Zhu, Y., 1995, in: High Temperature Superconducting Materials Science and Engineering, ed D. Shi (Elsevier, Amsterdam) ch. 5, pp. 199–258.

Zhu, Y., H. Zhang, H. Wang and M. Suenaga, 1991, J. Mater. Res. **6**, 2507.

Zhu, Y., Z.X. Cai, R.C. Budhani, M. Suenaga and D.O. Welch, 1993, Phys. Rev. B **48**, 6436.

Zhukov, A.A., H. Küpfer, S.A. Klestov, V.I. Voronkova and V.K. Yanovsky, 1993, J. Alloys & Compounds **195**, 479.

Zhukov, A.A., H. Küpfer, S.N. Gordeev, W. Jahn, T. Wolf, V.I. Voronkova, A. Erb, G. Müller-Vogt, H. Wühl, H.-J. Bornemann, K. Salama and D.F. Lee, 1994, in: Critical Currents in Superconductors, ed. H.W. Weber (World Scientific, Singapore) pp. 229–232.

Handbook on the Physics and Chemistry of Rare Earths
Vol. 31
edited by K.A. Gschneidner, Jr., L. Eyring and M.B. Maple

Chapter 197

MAGNETORESISTANCE AND HALL EFFECT

C.C. ALMASAN[1] and M.B. MAPLE[2]
[1]*Department of Physics, Kent State University, Kent, OH 44242, USA;*
[2]*Department of Physics and Institute for Pure and Applied Physical Sciences, University of California, San Diego, La Jolla, CA 92093, USA*

Contents

List of symbols and acronyms

a	intervortex distance
c_L	Lindemann number
FC	field-cooled
H	applied magnetic field
H_{c1}	lower critical field
H_{c2}	upper critical field
H_{irr}	irreversibility line
J_c	critical current density
l	transport mean free path
M	magnetization
n_H	Hall carrier number
R	resistance
R_H	Hall coefficient
s	interlayer distance
T	temperature
T_c	critical temperature
T/T_c	reduced temperature
T^*	irreversibility temperature
T_N	Néel temperature
U	pinning potential
$\langle u^2 \rangle_{th}$	mean-squared thermal vortex fluctuation displacement
V	volume of unit cell
V_H or V_{xy}	Hall voltage
V_{xx}	longitudinal voltage
WHHM	Werthamer–Helfand–Hohenberg–Maki
ZFC	zero-field-cooled
γ	anisotropy parameter
Δ	magnitude of maximum value of the negative Hall resistivity
θ_H	Hall angle
κ	Ginzburg–Landau parameter
λ	penetration depth
λ_{so}	spin–orbit scattering parameter
ξ	coherence length

ρ	resistivity	σ_{xy}^{n}	normal-state contribution to Hall conductivity
ρ_{yx}	off-diagonal matrix elements of the resistivity tensor	τ_{H}	cycloton relaxation lifetime
σ_{xy}	Hall conductivity	τ_{tr}	transport scattering lifetime
σ_{xy}^{s}	superconducting contribution to Hall conductivity	χ	magnetic susceptibility
		ϕ_0	magnetic flux quantum

1. Introduction

One of the most important and challenging problems in condensed matter physics is the occurrence of superconductivity at high temperatures in the layered copper oxide compounds. Both the superconducting and normal-state properties of these materials are highly unusual and appear to be inextricably linked to one another. A rich and complex temperature vs. carrier concentration phase diagram has been established from experimental investigations of a number of copper oxide systems. Regions in this phase diagram that have been identified up to this point contain antiferromagnetism, superconductivity, intra- and inter-CuO_2 plane insulator–metal transitions, Fermi and non-Fermi liquid behavior, a normal phase characterized by a pseudogap, spatially inhomogeneous static and dynamic charge and spin "stripe" phases, and, possibly, a quantum critical point. In the superconducting state, the magnetic field vs. temperature phase diagram has been found to contain a plethora of vortex phases and phenomena, including the melting of vortex lattice and glass phases, activated and quantum flux creep, decoupling of vortices in adjacent CuO_2 planes, "peak effects" in the critical current density, dynamic vortex phases, etc. In this chapter, we review magnetoresistance and Hall-effect measurements on high-T_c cuprate superconductors in both the normal and superconducting states that address several issues: for the normal state, the temperature dependence of the Hall coefficient R_H and the cotangent of the Hall angle $\cot\Theta_H$; for the superconducting state, the temperature dependence of the upper critical field H_{c2} and irreversibility line H^* as well as the anomalous sign change of the Hall effect near the superconducting critical temperature T_c. These measurements provide important information regarding the electronic structure and excitations that underly the normal and superconducting properties, fundamental superconducting state parameters, as well as vortex pinning and dynamics for these remarkable materials.

2. Upper critical field and irreversibility line of cuprate superconductors

The performance of high-temperature superconductors in magnetic fields is intimately related to the upper critical field $H_{c2}(T)$, the irreversibility line $H_{irr}(T)$, and the critical current density $J_c(H,T)$. The $H_{c2}(T)$ curve defines the region in the H–T plane in which superconductivity occurs and provides information about the nature and origin of superconductivity (i.e., spin and orbital angular momenta of the pairs, pairing mechanism)

and certain parameters such as the superconducting coherence length ξ and spin–orbit scattering parameter λ_{so}. The $H_{irr}(T)$ curve delineates the superconducting region in the H–T plane in which $J_c \neq 0$ and the magnetization $M(H,T)$ exhibits irreversible behavior. This curve contains information about the phases and dynamics of the vortices in the mixed state between $H_{c1}(T)$, the lower critical field, and $H_{c2}(T)$ (e.g., melting of vortex lattice or glass phases, activated flux motion, coupling between pancake vortices in adjacent conducting CuO_2 planes), as well as relevant parameters such as ξ, the penetration depth λ, and the pinning potential U, depending on the model used to describe $H_{irr}(T)$.

2.1. *Upper critical field*

In the early stages of research on high-T_c oxide superconductors, the $H_{c2}(T)$ curve was generally inferred from measurements of resistive superconducting transition curves in magnetic fields. As an example, the inset of fig. 1 depicts the normalized electrical resistivity $\rho/\rho(100\,\mathrm{K})$ vs. temperature for a polycrystalline sample of $YbBa_2Cu_3O_{7-\delta}$ in various applied magnetic fields between 0 and 9 T (Maple et al. 1987). The $H_{c2}(T)$ data were obtained by defining T_c in the applied field as the temperature at which ρ drops to 0.5 of its extrapolated normal-state value. Figure 1 shows two $H_{c2}(T)$ curves that have been fitted to the $H_{c2}(T)$ data between 0 and 9 T that are derived from the standard Werthamer, Helfand, Hohenberg, and Maki (WHHM) theory (Maki 1966, Werthamer, Helfand and Hohenberg 1966) for conventional type-II superconductors in the limits of complete ($\lambda_{so}=0$) and zero ($\lambda_{so}=8$) paramagnetic limitation. In 1989, Nakao et al. (1989) estimated that $H_{c2}^{\parallel c}(0)=40\pm5$ T and $H_{c2}^{\perp c}(0)=110\pm10$ T from their measurements of hysteretic M–H curves in pulsed magnetic fields above 100 T on single-crystal specimens of $YBa_2Cu_3O_{7-\delta}$. Electrical resistivity measurements in megagauss magnetic fields were reported by Goettee et al. (1994) on $YBa_2Cu_3O_{7-\delta}$ epitaxial

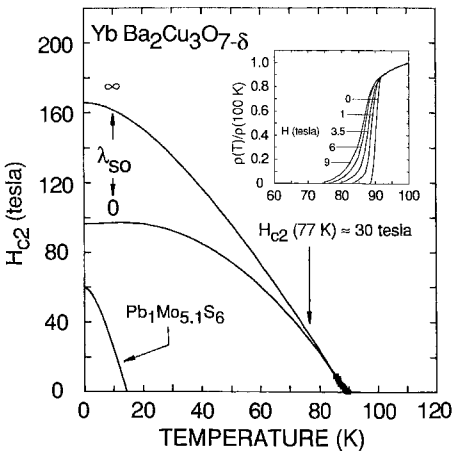

Fig. 1. Upper critical field $H_{c2}(T)$ curves extrapolated in accord with standard WHHM theory from resistively measured $H_{c2}(T)$ data for $YbBa_2Cu_3O_{7-\delta}$ in magnetic fields up to 9 tesla. Inset: Normalized electrical resistivity $\rho/\rho(100\,\mathrm{K})$ vs. T in magnetic fields up to 9 T. From Maple et al. (1987).

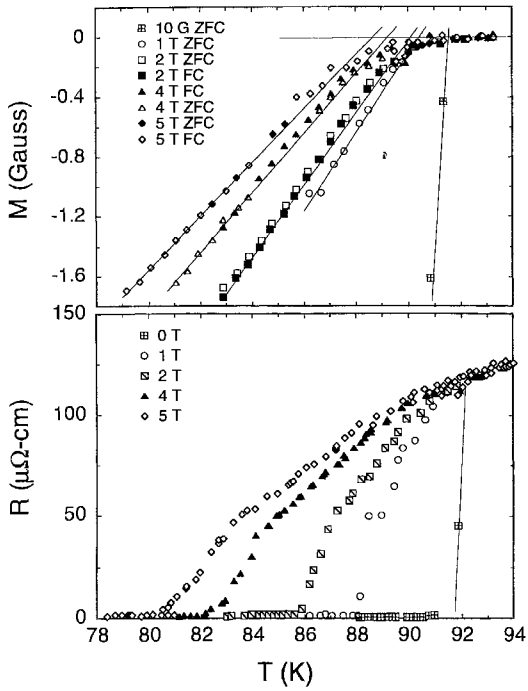

Fig. 2. Upper panel: Temperature dependence of the magnetization of $YBa_2Cu_3O_{7-\delta}$, measured in different magnetic fields oriented perpendicular to the CuO_2 planes for zero-field-cooled (ZFC) and field-cooled (FC) measurements. Lower panel: Resistive transition curves for $YBa_2Cu_3O_{7-\delta}$, measured in the same fields as in the upper panel. From Welp et al. (1989).

films. The determination of the $H_{c2}(T)$ curve with high values of T_c and $H_{c2}(0)$ from magnetoresistance measurements is, in general, complicated by pronounced broadening of the resistive transition in a magnetic field, which has been attributed to "giant" flux flow (Malozemoff et al. 1988, Tinkham 1988) and/or fluctuation effects in these materials. It has even been conjectured that the resistively determined boundary in the $H-T$ plane may be related more to the irreversibility line than to $H_{c2}(T)$.

Finnemore et al. (1987) were the first to emphasize that $H_{c2}(T)$ and related thermodynamic parameters for high-T_c oxide superconductors can, in principle, be extracted from measurements of the field and temperature dependence of the reversible magnetization $M(H,T)$ using the linear Abrikosov result (Tinkham 1996)

$$4\pi M(H,T) = -\frac{1}{(2\kappa^2 - 1)\beta_A}(H_{c2} - H), \tag{1}$$

where $\kappa \equiv \lambda/\xi$ is the Ginzburg–Landau parameter, λ is the penetration depth, ξ is the coherence length, $\beta_A = 1.16$ is the parameter for a hexagonal flux line lattice, and H is the applied magnetic field. Shown in fig. 2 is a plot of the temperature dependence of both the reversible magnetization and resistance measured in different magnetic fields applied perpendicular to the CuO_2 planes of $YBa_2Cu_3O_{7-\delta}$ single crystals (Welp et al. 1989). These reversible magnetization measurements reflect an equilibrium state and, therefore, are not complicated by effects arising from flux motion, as encountered in

the magnetoresistance measurements. The superconducting critical temperature $T_c(H)$ is defined as the intercept of the extrapolation of the reversible magnetization in the superconducting state with the normal-state base line. The authors have shown that values of H_{c2} and the critical-field slopes for $YBa_2Cu_3O_{7-\delta}$ single crystals, determined from these $M(H,T)$ data, are about 3 to 4 times larger, depending on the field direction, than those determined resistively.

The drawback of the method just described is the following: eq. (1) gives field-independent slopes for the $M(H,T)$ curves, i.e.,

$$4\pi \left(\frac{\partial M}{\partial T}\right)_H = -\frac{1}{(2\kappa^2 - 1)\beta_A}\frac{dH_{c2}}{dT}. \tag{2}$$

On the other hand, fig. 2 clearly shows that the slopes $(\partial M/\partial T)_H$ are field dependent. This implies that the lower temperature region on the reversible $M(H,T)$ curves lies outside the Abrikosov linear regime and, therefore, an analysis of these data in terms of the linear Abrikosov theory is not satisfactory. Most of the high-T_c oxide superconductors have field-dependent slopes $(\partial M/\partial T)_H$ in the linear regime and suffer from this drawback.

The mean-field theoretical model developed by Hao and Clem allows the anisotropic superconducting state thermodynamic parameters to be determined from measurements of $M(H,T)$ outside of the linear Abrikosov regime (Hao et al. 1991); their model reduces to the Abrikosov linear region only in the vicinity of the transition. However, the determination of the mean-field upper critical field curve $H_{c2}(T)$ is further complicated by the enhanced effect of thermodynamic fluctuations of the order parameter as a result of the very short coherence length, large anisotropy, and high T_c of the layered oxide superconductors. This presence of thermodynamic fluctuations is readily apparent in magnetoresistance $R(H,T)$ and dc magnetization measurements on these materials. Welp et al. (1991) were the first to determine the mean-field critical temperatures $T_c(H)$ with the magnetic field H applied parallel ($H \parallel c$) to the c-axis for a single-crystal specimen of $YBa_2Cu_3O_{7-\delta}$ from an analysis of $R(H,T)$ and $M(H,T)$ data using the Ginzburg–Landau fluctuation theory for layered superconductors within the Hartree approximation in the high-magnetic-field limit (Ullah and Dorsey 1991).

In contrast to the cuprates with high values of T_c and $H_{c2}(0)$, where only the slope of the upper critical field near T_c, $(dH_{c2}/dT)_{T_c}$, could be determined, in the cuprates with low values of T_c and $H_{c2}(0)$ [e.g., electron-doped $Ln_{2-x}Ce_xCuO_{4-y}$ (Ln = Pr, Nd, Sm), hole-doped $Tl_2Ba_2CuO_6$, $Y_{1-x}Pr_xBa_2Cu_3O_{7-\delta}$, and $Bi_2Sr_2CuO_y$ compounds], a large part of the H–T phase diagram can be explored for values of T and H that are readily experimentally accessible. This renders the low-T_c cuprates attractive candidates for studies of the T-dependence of H_{c2} and of the nature of the H–T phase diagram.

A general feature of the low-T_c cuprates is the striking nearly parallel shift of the resistive superconducting transition curves to lower temperatures with increasing H for both $H \parallel c$ and $H \perp c$, with a transition width that remains essentially constant, as in conventional superconductors. Shown in figs. 3a and 3b are the resistive transition curves of an electron-doped $Sm_{1.85}Ce_{0.15}CuO_{4-y}$ single crystal ($T_c \approx 11.4$ K) in magnetic

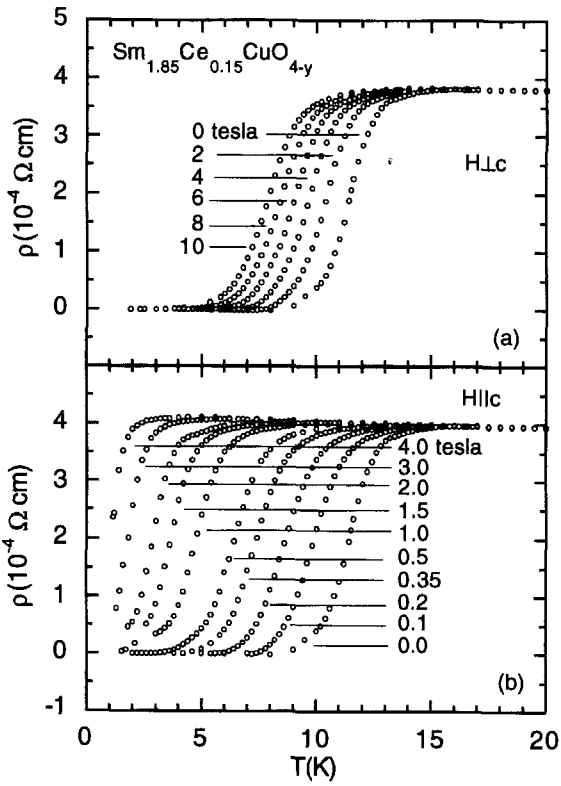

Fig. 3. Electrical resistivity ρ vs. temperature T for a $Sm_{1.85}Ce_{0.15}CuO_{4-y}$ single crystal in applied magnetic fields up to 10 T with (a) $H \perp c$ and (b) $H \parallel c$. Taken from data reported by Dalichaouch et al. (1990).

fields $H \perp c$ and $H \parallel c$, respectively (Dalichaouch et al. 1990). The absence of the field-induced broadening of the transition width with increasing H is, indeed, quite evident. Consequently, it has been argued that the value of H_{c2} is well-defined in this case (Hidaka and Suzuki 1989, Dalichaouch et al. 1990, Suzuki and Hikita 1990) and, hence, is not affected by flux flow.

A striking feature of the resistively determined upper critical field H_{c2}, however, is its unusual temperature dependence; i.e., the $H_{c2}(T)$ curve has strong positive curvature over a wide temperature range and appears to diverge as $T \rightarrow 0$. This unusual behavior of the resistively determined $H_{c2}(T)$ has been reported for different cuprate superconductors including the electron-doped materials $Ln_{1.85}Ce_{0.15}CuO_{4-y}$ (Ln = Pr, Nd, Sm) (Dalichaouch et al. 1990, de Andrade et al. 1991, Hidaka and Suzuki 1989), the underdoped compounds $R_{1-x}Pr_xBa_2Cu_3O_{7-\delta}$ (R = Y, Gd) (Maple et al. 1994, Iwasaki et al. 1990) and $YBa_2Cu_{3-x}Zn_xO_{7-\delta}$ (Walker et al. 1995), and the overdoped compounds $Tl_2Ba_2CuO_6$ (Mackenzie et al. 1993) and $Bi_2Sr_2CuO_6$ (Osofsky et al. 1993). This is in contrast with the $H_{c2}(T)$ curve of conventional superconductors which has negative curvature and saturates at a constant value as $T \rightarrow 0$. Interestingly, an $H_{c2}(T)$ curve with

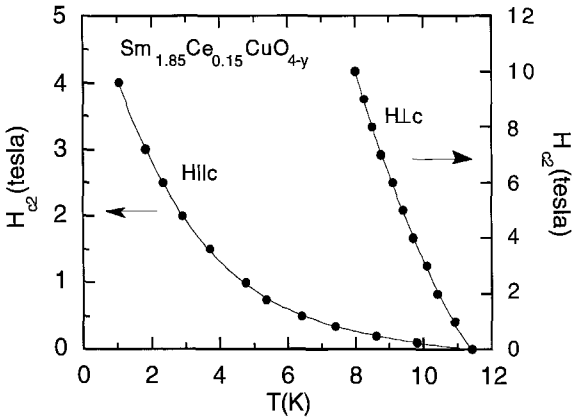

Fig. 4. Upper critical magnetic fields $H_{c2}(T)$ of a $Sm_{1.85}Ce_{0.15}CuO_{4-y}$ single crystal determined from $\rho(H,T)$ measurements in applied magnetic fields $H \parallel c$ and $H \perp c$. Solid lines are guides to the eye. From Dalichaouch et al. (1990).

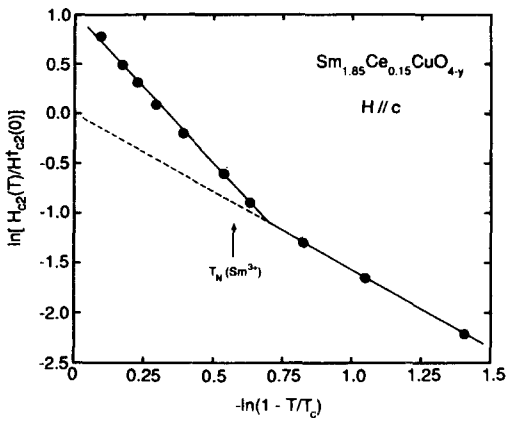

Fig. 5. $\ln[H_{c2}(T)/H^{\perp}_{c2}(0)]$ vs. $-\ln(1-T/T_c)$ plot of the data from fig. 3 for $Sm_{1.85}Ce_{0.15}CuO_{4-y}$ with $H \parallel c$, where $H^{\perp}_{c2}(0) = 1.83$ T. $T_N(Sm^{3+})$ indicates the Néel temperature below which the Sm^{3+} ions order antiferromagnetically. The straight lines represent least-squares fits to the data. From Dalichaouch et al. (1990).

positive curvature has also been observed for organic superconductors (Oshima et al. 1988).

An example of $H_{c2}(T)$ curves obtained from the $\rho(T,H)$ measured in two orientations of the applied magnetic field is shown in fig. 4 for $Sm_{1.85}Ce_{0.15}CuO_{4-y}$ (Dalichaouch et al. 1990). The data reveal a large anisotropy with H_{c2} largest for $H \perp c$, typical of layered compounds. Both curves have positive curvature throughout the entire temperature range of the measurements. The more rapid increase of H_{c2} below 5 K for $H \parallel c$ was attributed to antiferromagnetic ordering of the Sm^{3+} ions, since the increase in $H_{c2}(T)$ occurs near the Néel temperature $T_N = 4.8$ K and a similar effect occurs in the antiferromagnetic superconductor $SmRh_4B_4$ (Dalichaouch et al. 1990). This rapid increase of $H_{c2}(T)$ below 5 K is better illustrated by the ln–ln plot of fig. 5 (Dalichaouch et al. 1990), in which the

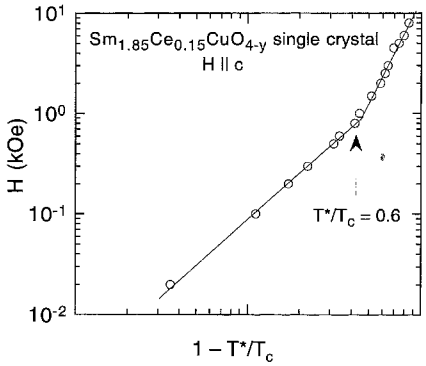

Fig. 6. Log–log plot of the applied magnetic field H vs. $(1-T^*/T_c)$, where T^* is the irreversibility temperature and T_c is the superconducting critical temperature for $Sm_{1.85}Ce_{0.15}CuO_{4-y}$. The solid lines represent least-squares fits to the data. From Almasan et al. (1991).

normalized upper critical field, $H_{c2}(T)/H_{c2}^{\dagger}(0)$, is shown as a function of $1-T/T_c$ for $H \parallel c$. The plot shows that H_{c2} has the following power-law temperature dependence:

$$H_{c2}(T) = H_0 \left(1 - \frac{T}{T_c}\right)^m, \tag{3}$$

with $m = 1.6$ for $5.7 \leqslant T \leqslant 11.4$ K $(0.5 \leqslant T/T_c \leqslant 1)$ and $m = 3$ for $T < 5.7$ K $(T/T_c = 0.5)$.

It was previously suggested that positive curvature of the resistively determined $H_{c2}(T)$ curve may be a general property of high-T_c cuprate superconductors (Cooper, Loram and Wade 1995, Ovchinnikov and Kresin 1995, 1996, Abrikosov 1997). However, the T-dependence of the resistively determined $H_{c2}(T)$ curve was interpreted as a measure of the T-dependence of the irreversibility line (Almasan et al. 1992a). Indeed, the irreversibility line $H_{irr}^{M}(T)$ extracted from zero-field-cooled and field-cooled dc magnetization M measurements on another $Sm_{1.85}Ce_{0.15}CuO_{4-y}$ single crystal ($T_c \approx 20$ K) for $H \parallel c$ measured in various magnetic fields has also positive curvature and the same power-law behavior, with a change in the value of the exponent from $m \approx 3/2$ for $0.6 \leqslant T/T_c \leqslant 1$ to a more rapid temperature dependence for $T/T_c \leqslant 0.6$ (Almasan et al. 1991) (see fig. 6). This result suggests that the $H-T$ line extracted from the $R(H,T)$ measurements on the $Sm_{1.85}Ce_{0.15}CuO_{4-y}$ single crystals with $H \parallel c$ (fig. 4) is related to the irreversibility line (since it has the same temperature dependence) even for the lower-T_c electron-doped cuprates. In fact, flux-relaxation measurements on a $Sm_{1.85}Ce_{0.15}CuO_{4-y}$ single crystal (Almasan et al. 1991) revealed that the activation energies are comparable to those of the hole-doped $YBa_2Cu_3O_{7-\delta}$ superconductor (Malozemoff 1989), implying a similar degree of flux motion in both systems. The much weaker broadening observed in the field-dependent resistive transitions in the electron-doped copper oxides would appear to be a result of their lower critical temperatures, not higher pinning energies (Almasan et al. 1991).

The main question to be addressed next is the following: if the resistively determined $H-T$ curve even in the low-T_c cuprates is not $H_{c2}(T)$, than how can one determine $H_{c2}(T)$? In an attempt to determine $H_{c2}(T)$ of the $Sm_{1.85}Ce_{0.15}CuO_{4-y}$ compound, Han et al. (1992) analyzed the $R(H,T)$ data in terms of the Ginzburg–Landau fluctuation theory

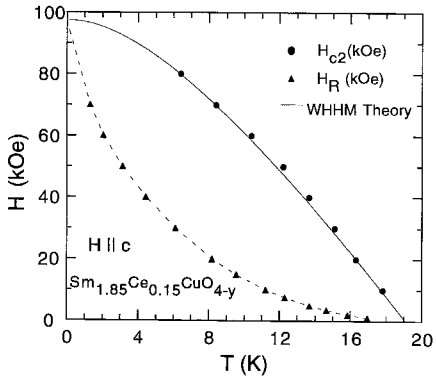

Fig. 7. Upper critical field $H_{c2}(T)$ for $Sm_{1.85}Ce_{0.15}CuO_{4-y}$ determined from a fluctuation analysis of $R(T,H)$ data (solid circles). The $H_{c2}(T)$ curve was calculated from the WHHM theory (solid line) and fitted to the $H_{c2}(T)$ data, while the irreversibility line $H_R(T)$ was inferred from $R(T,H)$ measurements (solid triangles). From Han et al. (1992).

for layered superconductors (Ullah and Dorsey 1991) within the Hartree approximation in the high-magnetic-field limit. As shown by fig. 7, in contrast to the resistively determined $H-T$ line, which we now refer to as $H^{R}_{irr}(T)$, the $H_{c2}(T)$ curve extracted with this analysis exhibits negative curvature down to reduced temperatures $T/T_c \approx 0.3$ and is in excellent agreement with the WHHM theory for conventional type-II superconductors, without paramagnetic limiting effects (i.e., with the spin–orbit scattering parameter $\lambda_{so} = \infty$). The values of the initial slope $(dH_{c2}/dT)_{Tc} = -7.38$ kOe/K, the in-plane coherence length $\xi_{ab}(0) = 48.4$ Å, and $H_{c2}(0) = 97.6$ kOe derived from the fluctuation analysis are in reasonable agreement with the values previously obtained by fitting the mean-field Hao–Clem variational model (Hao et al. 1991) to reversible-magnetization data for $Sm_{1.85}Ce_{0.15}CuO_{4-y}$ below T_c and outside of the fluctuation region (Almasan et al. 1992b).

2.2. *Irreversibility line*

2.2.1. *Scaling invariance and universality*

A cross-over in both $H^{M}_{irr}(T)$ and $H^{R}_{irr}(T)$ from an approximate $(1-T/T_c)^{3/2}$ dependence near $T/T_c \approx 1$ to a more rapid dependence at lower reduced temperatures was first observed in the electron-doped superconductor $Sm_{1.85}Ce_{0.15}CuO_{4-y}$ (Dalichaouch et al. 1990, Almasan et al. 1991, de Andrade et al. 1991), as described above, and subsequently, in both electron-doped (Bud'ko et al. 1990, Sumarlin et al. 1992) and hole-doped compounds, the latter including oxygen-deficient $YBa_2Cu_3O_x$ (Seidler et al. 1991) and $Bi_2Sr_2CaCu_2O_{8+\delta}$ (Kadowaki and Mochiku 1992). The main question was whether the cross-over phenomenon is an intrinsic property of cuprate superconductors (e.g., related to some universal dynamical process involving flux-line mobility or to a dimensional cross-over in the vortex glass/liquid) or a material-dependent effect (e.g., resulting from a sample-dependent distribution of pinning potentials). Almasan et al. (1992a) addressed this issue through measurements of the T-dependence of $H^{R}_{irr}(T)$ in $Y_{1-x}Pr_xBa_2Cu_3O_{6.97}$, a system in which T_c can be systematically reduced from 92 K to 0 K by varying the Pr concentration. On the various resistive transition curves, $T^{R}_{irr}(H)$ was taken to be the

temperature at which $R(H,T)$ drops to 50% of its extrapolated normal-state value. The data shown in fig. 8a were obtained by applying a scaling procedure to the $H^{R}_{irr}(T)$ data extracted from the $R(H,T)$ curves; for each specimen, $H^{R}_{irr}(T)$ was normalized by the cross-over field $H^{\dagger}(x)$, defined to be the value of $H^{R}_{irr}(T)$ at $T/T_c = 0.6$. It is evident that the normalized $H^{R}_{irr}(T)$ data for all x values collapse onto a single curve. The data in the low-field and high-temperature regime follow a power-law dependence with $m \approx 3/2$. In the high-field regime and for $T/T_c \leqslant 0.6$, there is a clear departure of the data from the low-field power law; $H^{R}_{irr}(T)/H^{\dagger}(x)$ varies more rapidly than $m = 3/2$ in this regime, although it is not possible to deduce an explicit power-law dependence. Although the 50% criterion for defining $T^{R}_{irr}(H)$ was arbitrarily chosen in the above analysis, similar results were obtained using the criteria $R/R_n = 10\%$ or 90%, where R_n is the extrapolated normal-state resistance.

Having established the scaling relation for $Y_{1-x}Pr_xBa_2Cu_3O_{6.97}$, the universality of the scaling conjecture was then tested (Almasan et al. 1992a) by applying it to previously published results on other cuprate systems, notably $Sm_{1.85}Ce_{0.15}CuO_{4-y}$ (Almasan et al. 1991, de Andrade et al. 1991; see fig. 8b), oxygen-deficient $YBa_2Cu_3O_x$ (Seidler et al. 1991; see fig. 8c) and $Bi_2Sr_2CaCu_2O_{8+\delta}$ (Kadowaki and Mochiku 1992; see fig. 8d). In each figure, the magnetic field is normalized by a characteristic field $H^{\dagger}$, which is defined to be the value of H^{M}_{irr} (or H^{R}_{irr} or H^{χ}_{irr}, the irreversibility line inferred from magnetic susceptibility χ measurements) at $T/T_c = 0.6$. In all cases, Almasan et al. (1992a) found virtually identical scaling behavior, with a cross-over feature in the universality line occurring at $T/T_c \approx 0.6$. This result also suggests that the absence of the cross-over in the irreversibility line of fully oxygenated $YBa_2Cu_3O_{7-\delta}$ is merely a consequence of measurements having not been performed at sufficiently strong magnetic fields for that system.

Osofsky et al. (1993) and Mackenzie et al. (1993) reported $R(H,T)$ measurements on $Bi_2Sr_2CuO_y$ thin films and $Tl_2Ba_2CuO_6$ single crystals, respectively, and argued that the $H-T$ curves extracted from the magnetoresistance measurements represent $H_{c2}(T)$. However, the application of the scaling procedure described above to their $H-T$ data reveals that the scaling relation is obeyed here too, as well as the presence of the cross-over in $H^{R}_{irr}(T)$ at $T/T_c \approx 0.6$ (see figs. 8d,e).

2.2.2. *Origin of the cross-over behavior*

Schilling et al. (1993) observed a cross-over in the irreversibility line measured with $H \parallel c$ on single-crystal specimens of a $Bi_2Sr_2CaCu_2O_8$ superconductor from a parabolic temperature dependence, $H = H_0(1 - T/T_c)^2$, near T_c to an exponential dependence, $H \sim \exp(\text{const}/T)$, at larger H and $T/T_c \leqslant 0.5$. They argued that the two regimes reflect a cross-over from essentially three-dimensional (3D) vortex fluctuations near T_c to quasi-two-dimensional (2D) vortex fluctuations for $H \geqslant H_{cr} \approx 4\phi_0/s^2\gamma^2$ and low temperatures, where s is the interlayer distance, $\gamma = \lambda_c/\lambda_{ab}$ is the anisotropy parameter, and ϕ_0 is the magnetic flux quantum.

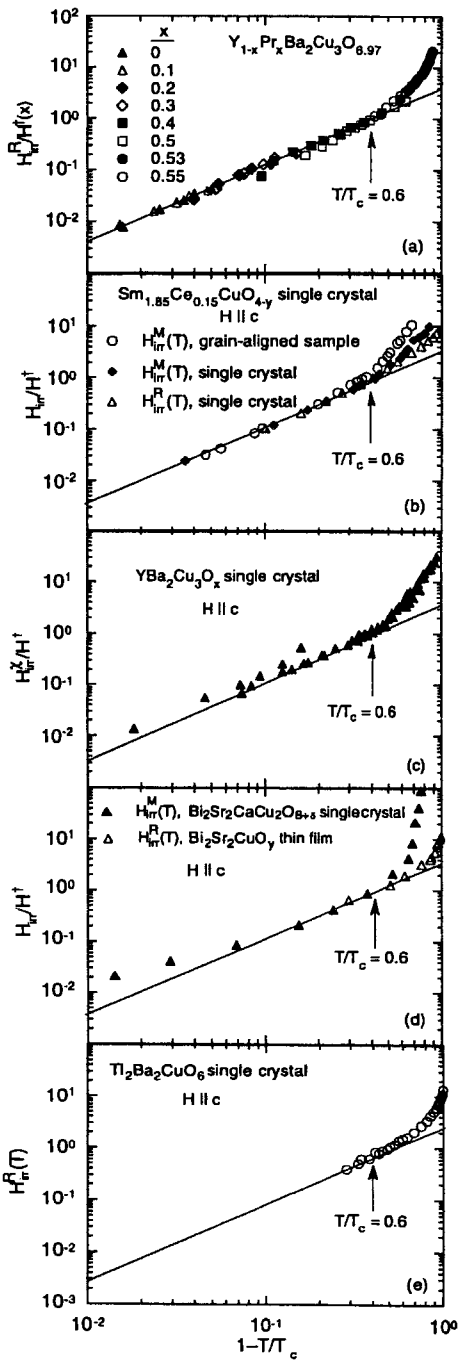

Fig. 8. Log–log plots of (a) $H_{\rm irr}^{\rm R}$, normalized to a characteristic field $H^{\dagger}(x)$, for polycrystalline $Y_{1-x}Pr_xBa_2Cu_3O_{6.97}$ (data from Almasan et al. 1992a), (b) $H_{\rm irr}^{\rm M}$ and $H_{\rm irr}^{\rm R}$, normalized to a characteristic field $H^{\dagger}$, for a grain-aligned sample and two single crystals of $Sm_{1.85}Ce_{0.15}CuO_{4-y}$ with $H \parallel c$ (data from Almasan et al. 1991 and de Andrade et al. 1991), (c) $H_{\rm irr}^{x}/H^{\dagger}$ for a single crystal of $YBa_2Cu_3O_x$ (data from Seidler et al. 1991), (d) $H_{\rm irr}^{\rm M}/H^{\dagger}$ and $H_{\rm irr}^{\rm R}/H^{\dagger}$ for a single crystal of $Bi_2Sr_2CaCu_2O_{8+\delta}$ and a $Bi_2Sr_2CuO_y$ thin film, respectively (data from Kadowaki and Mochiku 1992 and Osofsky et al. 1993), and (e) $H_{\rm irr}^{\rm R}$ for a $Tl_2Ba_2CuO_6$ single crystal (data from Mackenzie et al. 1993), all vs. $1-T/T_c$. From Almasan et al. (1992a).

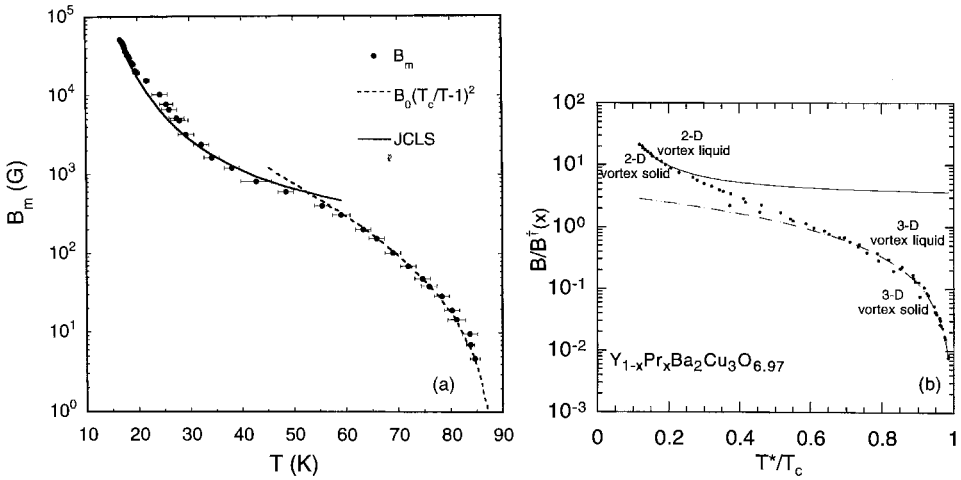

Fig. 9. (a) Vortex-lattice melting temperatures for $Bi_2Sr_2CaCu_2O_8$ (Schilling et al. 1993) and (b) $H/H^{\dagger}(x)$ vs. T/T_c for $Y_{1-x}Pr_xBa_2Cu_3O_{7-\delta}$ (Almasan and Maple 1996), both on logarithmic field scales. The solid lines correspond to a fit according to eq. (5). The dashed line in fig. 9a is a quadratic fit, while that in 9b is a power-law fit.

For $H \gg H_{cr}$, the mean-squared thermal vortex fluctuation displacement $\langle u^2 \rangle_{th}$ in Josephson-coupled layers is given by

$$\langle u^2 \rangle_{th} = \frac{8\pi\lambda_{ab}^2 k_B T}{\phi_0 s H} \ln\left(\frac{Hs^2\gamma^2}{\phi_0}\right). \tag{4}$$

Assuming that $\langle u^2 \rangle_{th}$ dominates possible quantum fluctuations, Schilling et al. (1993) used the phenomenological Lindemann melting criterion (Lindemann 1910) to describe the experimentally observed irreversibility line in terms of vortex-lattice melting; i.e.,

$$\langle u^2 \rangle \approx \langle u^2 \rangle_{th} = c_L^2 a^2 \approx \frac{c_L^2 \phi_0}{H}, \tag{5}$$

where a is the intervortex distance and c_L is the Lindemann number. For $H \ll H_{cr}$, the Lindemann criterion applied to 3D vortex fluctuations predicts a quadratic T-dependence of the irreversibility line. Almasan and Maple (1996) applied the 3D and 2D vortex-fluctuation criteria to the $Y_{1-x}Pr_xBa_2Cu_3O_{6.97}$ $H_{irr}^{R}(T)$ data. Plotted in fig. 9 on a logarithmic field scale is (a) the vortex-lattice melting temperatures $B_{irr}^{m}(T)$ for $Bi_2Sr_2CaCu_2O_8$ (Schilling et al. 1993) and (b) $B_{irr}^{R}/B^{\dagger}(x)$ vs. T/T_c for the $Y_{1-x}Pr_xBa_2Cu_3O_{6.97}$ system, where $B^{\dagger}(x)$ is the cross-over field defined above (Almasan and Maple 1996). The solid lines in both figures correspond to a fit according to eq. (5). The dashed line in fig. 9a is a quadratic fit to the data near T_c, while the dashed line in fig. 9b is a power-law fit of the form $B_{irr}^{R}/B^{\dagger}(x) \propto (1 - T/T_c)^m$ with $m = 1.45$. Recently, Blatter and Ivlev (1993) have shown that the shape of the melting line can be approximated by a power law with an exponent $m = 1.45$ if quantum fluctuations are included along with the thermal fluctuations

in the displacement amplitude (eq. 5). Hence, a possible explanation of the discrepancy between the thermal fluctuation result $m=2$ and the experimental observation $m \approx 1.5$ for the $Y_{1-x}Pr_xBa_2Cu_3O_{6.97}$ system as well as for other compounds (e.g., $YBa_2Cu_3O_x$ and $Sm_{1.85}Ce_{0.15}CuO_{4-y}$) could be that in these systems the quantum fluctuations are important. However, in the Bi- and Tl-based compounds, the thermal fluctuations are enhanced due to the weak interlayer coupling, while the quantum fluctuations remain essentially unchanged; hence, the quantum correction is less important and the data are better described by a power law with exponent $m=2$.

3. Hall-effect studies of cuprate superconductors

3.1. *Anomalous sign change in the vicinity of T_c*

The Hall effect in the mixed state of the high-temperature superconductors is one of the most puzzling and controversial transport phenomena exhibited by these materials. In particular, a lot of effort has been devoted to developing an understanding of the unusual sign change of the Hall voltage V_H just below the superconducting transition temperature of a wide variety of superconducting materials (Galffy and Zirngiebl 1988, Hagen et al. 1990a, Wang and Ting 1991).

Typical Hall voltage V_{xy} vs. applied magnetic field B data in the neighborhood of T_c for a $YBa_2Cu_3O_{7-\delta}$ single crystal, measured with B parallel to the c-axis, are shown in fig. 10 (Almasan et al. 1994a). In general, the Hall voltage V_{xy} is obtained from the antisymmetric part of the transverse voltage (measured while sweeping the applied magnetic field at constant temperature) under magnetic field reversal. Here, T_c is defined as the lowest temperature at which V_{xy} is linear in B and extrapolates to zero for $B=0$, as is characteristic of the normal state. While V_{xy} is positive and linear in B for $T > T_c$, it displays the "negative Hall anomaly" a few degrees below T_c; i.e., with increasing B, V_{xy} is zero for low values of B, decreases to negative values, passes through a minimum,

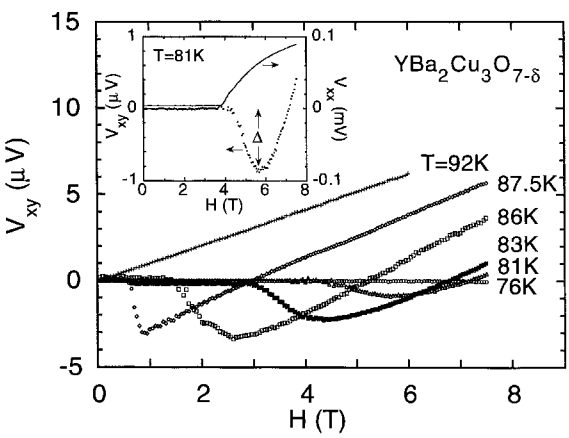

Fig. 10. Hall voltage V_{xy} vs. applied magnetic field H for an $YBa_2Cu_3O_{7-\delta}$ single crystal with $H \parallel c$ at several temperatures in the neighborhood of T_c. Inset: Hall voltage V_{xy} and longitudinal voltage V_{xx} vs. H at 81 K. From Almasan et al. (1994a).

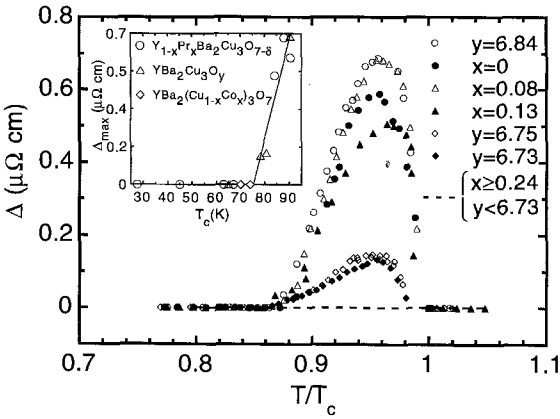

Fig. 11. Magnitude of the maximum, Δ, of $\rho_{xy}(H)$ for $Y_{1-x}Pr_xBa_2Cu_3O_{7-\delta}$, $YBa_2Cu_3O_x$, and $YBa_2(Cu_{1-x}Co_x)_3O_{7-\delta}$ single crystals, taken at different temperatures, vs. reduced temperature T/T_c. The data exhibit a maximum Δ_{max} which is plotted in the inset as a function of T_c. Also shown in the inset are two data points for $YBa_2(Cu_{1-x}Co_x)_3O_{7-\delta}$. From Almasan et al. (1995).

crosses zero, and then becomes positive for values of B lower than $B_{c2}(T)$. The region of negative V_{xy} shifts to higher fields at lower temperatures. Shown in the inset to fig. 10 are V_{xy} and the longitudinal voltage V_{xx} vs. B, measured at 81 K. The onset of the negative Hall signal occurs at a slightly higher field than the onset of V_{xx}, while the negative V_{xy} extends over a region where V_{xx} increases rapidly with increasing field.

Similar V_{xy} vs. B profiles were reported in most of the other *optimally doped* hole-like charge carrier cuprates: e.g., $YBa_2Cu_3O_{7-\delta}$ (Galffy and Zirngiebl 1988, Iye, Nakamura and Tamegai 1989, Hagen et al. 1990a, Chien et al. 1991a, Luo et al. 1992, Rice et al. 1992, Kunchur et al. 1994), $Bi_2Sr_2CaCu_2O_x$ (Iye, Nakamura and Tamegai 1989, Zavaritsky, Samoilov and Yurgens 1991), and $Tl_2Ba_2CaCu_2O_8$ (Hagen et al. 1991a, Samoilov, Ivanov and Johansson 1994), and electron-like cuprates $Nd_{1.85}Ce_{0.15}CuO_{4-y}$ (aside from the overall sign which is reversed) (Hagen et al. 1993). The existence of a similar Hall anomaly in both n- and p-type materials provides a useful test for theoretical models of the $V_{xy}(B)$ dependence. Additionally, similar V_{xy} vs. B profiles were reported in $YBa_2Cu_3O_7/PrBa_2Cu_3O_7$ multilayers (Qiu et al. 1995) and $(YBa_2Cu_3O_{7-\delta})_n/(PrBa_2Cu_3O_{7-\delta})_m$ superlattices (Kebin, Yuheng and Adrian 1996).

In addition, similar V_{xy} vs. B profiles have been observed in some underdoped cuprates; e.g., $Y_{1-x}Pr_xBa_2Cu_3O_{7-\delta}$ single crystals with $0 \leqslant x < 0.13$ (Jia et al. 1993) and $YBa_2Cu_3O_{7-\delta}$ with 1 or 2% of the Cu atoms replaced by Co (Neiman et al. 1995), while only a positive Hall signal has been observed in other underdoped cuprates; e.g., $YBa_2Cu_3O_{7-\delta}$ with 3 or 4% of the Cu atoms replaced by Co (Ginsberg and Dudey 1993, Neiman et al. 1995). A systematic study of the evolution of the magnitude of the maximum value of the negative Hall resistivity ρ_{xy} with T_c has been carried out by Almasan et al. (1995) on two cuprate systems, $Y_{1-x}Pr_xBa_2Cu_3O_{7-\delta}$ and $YBa_2Cu_3O_y$, over a wide range of doping in order to determine if there is a correlation between the negative Hall anomaly and the doping level. Figure 11 is a plot of the magnitude of the maximum value Δ of the negative Hall resistivity ρ_{xy}, extracted from ρ_{xy} vs. B curves (see the inset to fig. 10 for the definition of Δ), vs. the reduced temperature T/T_c for

underdoped $Y_{1-x}Pr_xBa_2Cu_3O_{7-\delta}$ and $YBa_2Cu_3O_y$ single crystals (Almasan et al. 1995). The Pr content was estimated by comparing the transition temperatures of the single crystals to those of high-quality polycrystalline samples (Maple et al. 1992, Paulius et al. 1994). The legend lists the samples in decreasing order of T_c. For $x=0$, a similar result was reported by Luo et al. (1992) for epitaxial $YBa_2Cu_3O_7$ films. The two interesting features of all these curves are: (1) for both systems, Δ is nonzero over the same reduced temperature range ($0.87 < T/T_c \leqslant 1$) with the onset of pinning occurring at $T/T_c \approx 0.87$ for all the single crystals of $Y_{1-x}Pr_xBa_2Cu_3O_{7-\delta}$ with $0 \leqslant x < 0.13$ and $YBa_2Cu_3O_y$ with $6.73 < y \leqslant 6.84$, and (2) Δ_{max} scales with T_c and decreases monotonically, as shown in the inset. A linear fit of the Δ_{max} vs. T_c data with $\Delta_{max} \neq 0$ extrapolates to $\Delta_{max}=0$ at $T_c = 75.2$ K. This suggests that ρ_{xy} would not display the negative anomaly for samples with $T_c < 75$ K. With few exceptions (Manson et al. 1996), the data available in the literature seem to agree with this finding (Ginsberg and Dudey 1993, Neiman et al. 1995). Certainly, the criterion used to define T_c is an important factor in this analysis.

With regard to feature (1), it is intriguing to note that the reduced temperature $T/T_c \approx 0.87$, below which Δ vanishes, is very close to the value of $T/T_c \approx 0.85$ reported by Budhani, Holstein and Suenaga (1994) from resistivity measurements on $Tl_2Ba_2CaCu_2O_8$ heavy-ion-irradiated epitaxial films, below which pinning by columnar defects inhibits flux motion and, hence, dissipation. Although the depinning temperature varies from material to material, these results suggest that the onset of pinning occurs at the same reduced temperature, at least in the three systems mentioned, regardless of the nature of the pinning site (point or columnar defects).

A survey of the literature (Hagen et al. 1993) has indicated that, in general, the anomalous Hall behavior is present among moderately clean superconductors ($l/\xi \approx 0.5$–5, where l is the transport mean free path and ξ is the coherence length), but does not occur in either the very clean ($l/\xi \gg 1$) or dirty ($l/\xi \ll 1$) limits. Colino et al. (1994) have reached the same conclusion by studying epitaxial $RBa_2Cu_3O_{7-\delta}$ (R = Eu, Ho) thin films with the c- or a-axis perpendicular to the film plane. Hence, the parameter l/ξ seems to largely determine whether or not the Hall anomaly is observed. Recently, it has been shown theoretically that, indeed, in the very clean limit, the Hall conductivity is similar to that for the normal state in the limit of high fields, while, in the moderately clean case, the sign of the Hall effect in the mixed state may differ from that in the normal state depending on the detailed structure of the Fermi surface (Kopnin and Lopatin 1995); therefore, these authors have concluded that the sign reversal is very sensitive to the details of the Fermi surface structure, the doping level, and the impurity content.

Several interpretations have been offered to explain the sign reversal of the Hall voltage of the mixed state. Freimuth, Hohn and Galffy (1991) attributed the sign reversal to the large thermoelectric effects in the mixed state. Harris, Ong and Yan (1993) reported the observation of opposite Hall signs for vortices perpendicular and parallel to the CuO_2 layers of $YBa_2Cu_3O_{7-\delta}$ single crystals. The competition between the two opposing Magnus forces acting on interlayer segments and pancakes which form the vortex line, respectively, led them to an explanation of the negative Hall anomaly in terms

of "pancake" vortices which lie in the CuO_2 planes and are linked by interlayer segments which reside in between and parallel to the CuO_2 planes. Another point of view, which has lately attracted more supporters, is that this behavior is an intrinsic property (Hagen et al. 1990a,b, 1991a,b, 1993, Almasan et al. 1995) and should have an explanation in terms of the general theory of flux motion in type-II superconductors. This is corroborated by the fact that the sign reversal was observed earlier for conventional V and Nb superconductors (Niessen, Staas and Weijsenfeld 1967, Noto, Shinzawa and Muto 1976). The observed field independence of the sign-reversing Hall angle (in the isolated vortex limit $B \rightarrow 0$) in $Bi_2Sr_2CaCu_2O_x$ and $Tl_2Ba_2CaCu_2O_8$ (Hagen et al. 1991a, Zavaritsky, Samoilov and Yurgens 1991) which is expected in the vortex dynamics picture but not within other models, is strong evidence for such an intrinsic origin of the Hall anomaly. The close similarity of the profiles of fig. 11 and the monotonic evolution of Δ_{max} with T_c for the underdoped $Y_{1-x}Pr_xBa_2Cu_3O_{7-\delta}$ and $YBa_2Cu_3O_y$ systems indicate also that the negative anomaly has an intrinsic origin (Almasan et al. 1995). Additionally, measurements of $\rho_{xy}(H)$ in the mixed state of $Nd_{1.85}Ce_{0.15}CuO_{4-y}$ (Hagen et al. 1993) provide support for the flux-dynamics interpretation, as well as evidence against thermoelectric models (Freimuth, Hohn and Galffy 1991) which attempt to explain the Hall anomaly in the mixed state of the cuprates.

The early theories of flux motion (Bardeen and Stephen 1965, Nozières and Vinen 1966) considered the Hall effect in the mixed state as being produced by normal electrons in the vortex cores and thus predicted an effect of the same sign as in the normal state. The first microscopic calculations of the flux-flow Hall effect in clean superconductors used a simple parabolic spectrum of electrons with a single effective mass, and could not provide a comprehensive picture of the sign of the Hall effect (Kopnin and Kravtsov 1976a,b). Further progress has been made only recently on the basis of time-dependent Ginzburg–Landau equations derived for a gapless superconductor in the dirty limit (Dorsey 1992, Kopnin, Ivlev and Kalatsky 1993). The main result is that the sign reversal can be intrinsic and depends on the details of the structure of the normal-state electronic spectrum. This conclusion was further confirmed by microscopic calculations for dirty superconductors (Larkin and Ovchinnikov 1995). This picture has found experimental confirmation (Jones, Christen and Sales 1994, Kunchur et al. 1994, Samoilov, Ivanov and Johansson 1994). Very recently, within a phenomenologinal analysis, Feigel'man et al. (1994) and Khomskii and Freimuth (1995) considered an additional contribution to the Hall effect due to the positive difference between the electron density at the center of the vortex core and that far outside the vortex. This contribution has a sign that is opposite to that of the conventional one and can cause a sign change. Hence, these researchers interpret the sign change in terms of broken particle–hole symmetry and obtain good agreement with the experimental signatures (Hagen et al. 1993) of this effect. Van Otterlo et al. (1995) have recently presented a microscopic derivation of the equation of motion for a vortex in a superconductor. They have obtained a coherent view of the vortex dynamics in which both hydrodynamics and the vortex core contribute to the forces acting on a vortex. The competition between these two provides an interpretation of the observed sign change in the Hall angle in superconductors with mean free path l of the order of the coherence

length ξ in terms of broken particle–hole symmetry in the electronic band structure, yielding a unifying description of the physics involved.

Other theoretical explanations for this anomaly have also been put forward. Ferrell (1992) proposed that the negative Hall sign arises from the "upstream" force exerted by backflow of quasiparticles on the core, two-band models were proposed by Hirsch and Marsiglio (1991) while Wang and Ting (1991) and Wang, Jinming and Ting (1994) have proposed that the sign reversal results from the interaction of moving vortices with imperfections of the crystal structure. However, this latter proposal is refuted by several experimental findings (Budhani, Liou and Cai 1993, Almasan et al. 1995). Specifically, the suppression of Δ_{max} with decreasing T_c [see inset to fig. 11] suggests that the negative Hall anomaly is not due to flux pinning since, in $Y_{1-x}Pr_xBa_2Cu_3O_{7-\delta}$ with low x values, the pinning potential increases with increasing x (decreasing T_c) (Paulius, Almasan and Maple 1993). Within the context of flux-pinning models, this would produce an increase in the magnitude of the negative Hall voltage. Also, the reported decrease in the magnitude of the Hall effect sign anomaly of $Tl_2Ba_2Ca_2Cu_3O_{10}$ thin films with increasing defect concentration through heavy-ion irradiation (Budhani, Liou and Cai 1993) is inconsistent with the attempt to explain the negative Hall anomaly in terms of the presence of pinning forces in the sample.

Although Hall-effect results for superconductors have traditionally been expressed in terms of the Hall coefficient R_H, the Hall angle θ_H, and the off-diagonal matrix elements of the resistivity tensor ρ_{yx}, it is of particular interest to discuss the Hall effect in the mixed state in terms of σ_{xy}, since Vinokur et al. (1993) pointed out that this quantity should be independent of the disorder in the sample. Ullah and Dorsey (1991), Dorsey (1992), Kopnin, Ivlev and Kalatsky (1993) and Geshkenbein et al. (1994) have shown that within the time-dependent Ginzburg–Landau formalism, the Hall conductivity in the superconducting state can be expressed as the sum of superconducting, σ_{xy}^s, and normal, σ_{xy}^n, contributions:

$$\sigma_{xy} = \sigma_{xy}^s + \sigma_{xy}^n = \frac{C_1}{B} + C_2 B, \tag{6}$$

where

$$\sigma_{xy} = \frac{\rho_{yx}}{\rho_{xx}\rho_{yy} - \rho_{xy}\rho_{yx}} = \frac{V_{xy}d/I}{\rho_{xx}\rho_{yy} - \rho_{xy}\rho_{yx}}, \tag{7}$$

with d the thickness of the sample, I the applied current, and ρ_{ij} $(i,j=x,y)$ the matrix elements of the resistivity tensor. In eq. (6), σ_{xy}^s arises from the motion of the magnetic vortices, while σ_{xy}^n is associated with the motion of the quasiparticles in the vortex cores. If the Hall currents produced by the motion of the vortices and the quasiparticles (C_1 and C_2, respectively) have opposite signs, then the Hall effect can change sign as B is varied, as observed experimentally. The sign of σ_{xy}^n is the same as the sign in the normal state. However, the factors that fix the sign of σ_{xy}^s are not yet understood. Although a few microscopic calculations have addressed this issue (Vinokur et al. 1993,

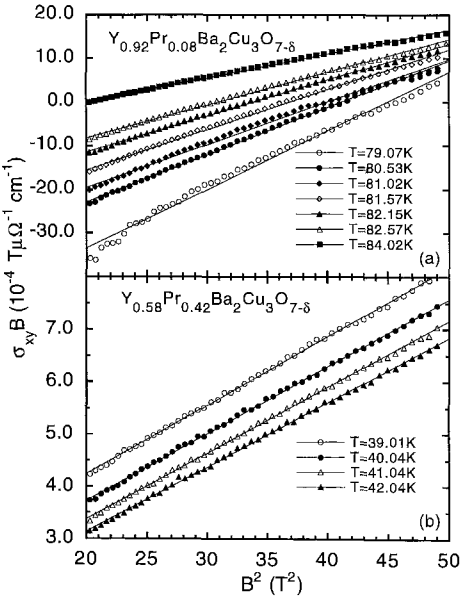

Fig. 12. $\sigma_{xy}B$ vs. B^2 data for (a) $Y_{0.92}Pr_{0.08}Ba_2Cu_3O_{7-\delta}$ and (b) $Y_{0.58}Pr_{0.42}Ba_2Cu_3O_{7-\delta}$ single crystals measured at different temperatures. The solid lines are fits to the data with eq. (6). From Almasan et al. (1995).

Feigel'man et al. 1994, Kopnin 1996), there is considerable uncertainty about why, in certain cuprates, σ_{xy}^{s} is negative while σ_{xy}^{n} is positive. Several groups have used eq. (6) to analyze the Hall conductivity data of different high-temperature superconductors in order to ascertain whether eq. (6) provides a satisfactory description of the $\sigma_{xy}(B)$ data, and, if it does, to determine how the two coefficients C_1 and C_2 depend on temperature and doping.

Figures 12a and 12b are typical plots of $\sigma_{xy}B$ vs. B^2 for specimens which do and do not, respectively, display the negative Hall anomaly. These graphs depict data taken on single crystals of $Y_{0.92}Pr_{0.08}Ba_2Cu_3O_{7-\delta}$ (fig. 12a) and $Y_{0.58}Pr_{0.42}Ba_2Cu_3O_{7-\delta}$ (fig. 12b) at various temperatures $T < T_c$ and in applied magnetic fields $B_m \leqslant B \leqslant 5$ T, where B_m is the field below which the Hall resistivity starts bending over, presumably due to flux pinning (Almasan et al. 1995). Also shown in the figures are straight-line fits of eq. (6) to the data which give values for the coefficients C_1 and C_2 which are independent of B but dependent on T. Whereas $C_1 < 0$ and $C_2 > 0$ in fig. 12a, C_1 and C_2 are both positive in fig. 12b, consistent with the presence of the negative Hall anomaly in ρ_{xy} of the sample (fig. 12a) or its absence (fig. 12b).

The results for the $Y_{0.92}Pr_{0.08}Ba_2Cu_3O_{7-\delta}$ single crystal are similar to those obtained on other single crystals which display the Hall anomaly in the mixed state; i.e., $YBa_2Cu_3O_{7-\delta}$ (Clinton et al. 1995, Ginsberg and Manson 1995, Harris et al. 1995) and $Nd_{1.85}Ce_{0.15}CuO_4$ (Lobb et al. 1994, Clinton et al. 1995). However, the Hall conductivity data for $YBa_2Cu_3O_y$ ($y = 6.84, 6.75$) single crystals (Almasan et al. 1995) and $La_{2-x}Sr_xCuO_4$ thin films (Matsuda et al. 1995), which also display the negative Hall anomaly, are described well by the time-dependent Ginzburg–Landau formalism with

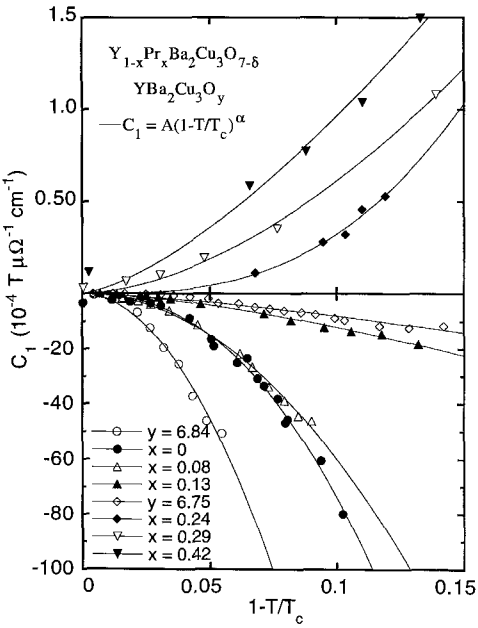

Fig. 13. Coefficient C_1 vs. $1-T/T_c$, for six $Y_{1-x}Pr_xBa_2Cu_3O_{7-\delta}$ and two $YBa_2Cu_3O_y$ single crystals with different values of x and y. The samples with $x=0.13$ and $y=6.84$ and 6.75 display the negative sign anomaly while those with $x>0.13$ do not. The solid lines represent power-law behavior indicated in the figure. From Almasan et al. (1995).

an additional constant term C_3 included in eq. (6). It seems that the C_3 term becomes important with increasing anisotropy. On the other hand, the Hall conductivity data for $Tl_2Ba_2CaCu_2O_8$ and $Bi_2Sr_2CaCu_2O_{8+\delta}$, which display the negative Hall anomaly, are described well by eq. (6) with $C_2=0$ and an additional constant term C_3 (Samoilov, Ivanov and Johansson 1994). The $\sigma_{xy}(B)$ data for $YBa_2Cu_3O_y$ ($y=6.73, 6.65$) show an even more complicated field dependence which seems to be sample dependent (Almasan et al. 1995). The results of fig. 12b are similar to those obtained on specimens which do not display the negative anomaly; i.e., single crystals of $YBa_2Cu_3O_{7-\delta}$ with 3% and 4% of the Cu atoms replaced by Co (Ginsberg and Dudey 1993, Neiman et al. 1995) and single crystals of $La_{1.83}Sr_{0.17}CuO_4$ (Harris et al. 1995).

There have been several studies which report the temperature dependence of the two coefficients C_1 and C_2 for different cuprate superconductors. As discussed below in more detail, these results seem to indicate that C_1 has the same behavior in most of the cuprates studied while the behavior of C_2 is sample and/or system dependent; i.e., the power-law temperature dependence of C_1 is the same for all the specimens studied with an exponent α decreasing as the samples are more underdoped, while C_2 displays temperature dependences which differ from system to system.

Shown in fig. 13 is a plot of C_1 vs. $1-T/T_c$ for six $Y_{1-x}Pr_xBa_2Cu_3O_{7-\delta}$ and two $YBa_2Cu_3O_y$ single crystals with different values of x and y (Almasan et al. 1995). The legend lists the samples in order of decreasing T_c. In the superconducting state, the coefficient C_1 follows a systematic trend with T_c and is negative (positive) for samples which display (do not display) the negative ρ_{xy} anomaly. Over the same reduced temperature,

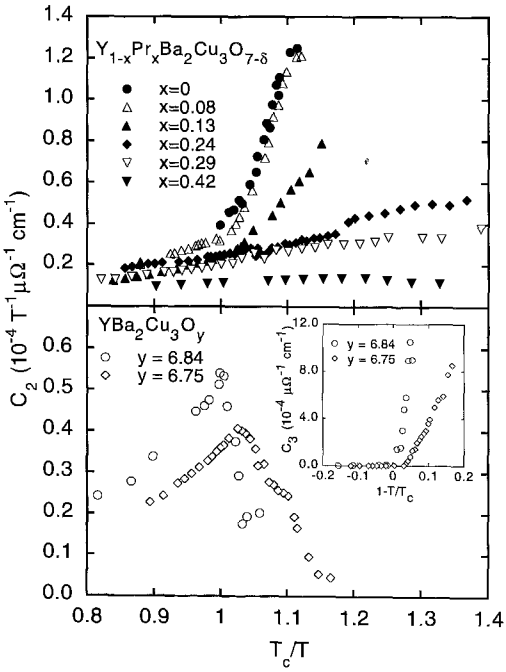

Fig. 14. Coefficient C_2 vs. T_c/T, for six $Y_{1-x}Pr_xBa_2Cu_3O_{7-\delta}$ and two $YBa_2Cu_3O_y$ single crystals with different values of x and y. Inset: C_3 vs. $1-T/T_c$. From Almasan et al. (1995).

the magnitude of C_1 is much larger for the samples which exhibit the negative anomaly (note the change in scale for $C_1<0$ and $C_1>0$ in fig. 13) with an equally good fitting of the data to eq. (6) for low and high values of x (see figs. 12a,b). The coefficient C_1 was found to have the form $C_1=A(1-T/T_c)^{\alpha}$ with the exponent α decreasing with increasing doping level; α ranges from 2.3±0.07 for $y=6.84$ to 1.4±0.07 for $y=6.75$, in the range of x and y where $C_1<0$, and from 2.8±0.05 for $x=0.24$ to 1.4±0.06 for $x=0.42$, in the range of x where $C_1>0$. As expected, C_1 vanishes within experimental error for $T \geqslant T_c$.

Ginsberg and his collaborators have found that for $YBa_2(Cu_{1-x}Co_x)_3O_{7-\delta}$ ($x=0$, 0.01, 0.02, and 0.03) single crystals (Ginsberg and Manson 1995, Neiman et al. 1995), detwinned $Y_{1-x}Pr_xBa_2Cu_3O_{7-\delta}$ single crystals (Manson et al. 1996), and $YBa_2(Cu_{1-x}Ni_x)_3O_{7-\delta}$ single crystals (Jin-Tae, Giapintzakis and Ginsberg 1996), the coefficient C_1 follows the same power law temperature dependence as presented above for twinned single crystals of $Y_{1-x}Pr_xBa_2Cu_3O_{7-\delta}$. The exponent α has a value of 2 for all the samples of $YBa_2(Cu_{1-x}Co_x)_3O_{7-\delta}$ studied, within experimental uncertainty, with a hint that it may be increasing with increasing cobalt concentration, while the value of α for Pr and Ni doping decreases with increasing doping level.

Figure 14 contains a plot of C_2 vs. T_c/T for six $Y_{1-x}Pr_xBa_2Cu_3O_{7-\delta}$ (upper panel) and two $YBa_2Cu_3O_y$ (lower panel) single crystals; the inset of the lower panel is a plot of C_3 vs. $1-T/T_c$ for the two $YBa_2Cu_3O_y$ single crystals. For $Y_{1-x}Pr_xBa_2Cu_3O_{7-\delta}$, C_2 in the superconducting state is positive and approximately proportional to T_c/T for all x values with a slope which decreases with increasing x, while, in the normal

state, C_2 is positive, small, and has a weaker temperature dependence relative to the superconducting state (see upper panel). For the two $YBa_2Cu_3O_y$ single crystals, C_2 increases with decreasing T, displays a maximum for $T = T_c$, and then decreases with decreasing T (see lower panel). The coefficient C_3 is positive in the superconducting state and decreases with increasing T to zero within experimental error at $T = T_c$ (see inset). On the other hand, Ginsberg and coworkers have found that $C_2 = a + b(1 - T/T_c)$ for $YBa_2(Cu_{1-x}Co_x)_3O_{7-\delta}$ single crystals (Ginsberg and Manson 1995, Neiman et al. 1995), while $C_2 = a + b(1 - T/T_c)^2$ for detwinned $Y_{1-x}Pr_xBa_2Cu_3O_{7-\delta}$ single crystals (Manson et al. 1996) and $YBa_2(Cu_{1-x}Ni_x)_3O_{7-\delta}$ single crystals (Jin-Tae, Giapintzakis and Ginsberg 1996).

3.2. *Scaling behavior*

An interesting scaling behavior between the Hall resistivity ρ_{xy} and the longitudinal resistivity ρ_{xx}, $\rho_{xy} \propto \rho_{xx}^{\beta}$, has been observed with the scaling exponent $\beta \approx 2$ in $Bi_2Sr_2CaCu_2O_8$ single crystals (Samoilov 1993), $Tl_2Ba_2CaCu_2O_8$ (Samoilov, Ivanov and Johansson 1994) and $Tl_2Ba_2Ca_2Cu_3O_{10}$ (Budhani, Liou and Cai 1993) films, and $(YBa_2Cu_3O_{7-\delta})_n/(PrBa_2Cu_3O_{7-\delta})_m$ superlattices (Kebin, Yuheng and Adrian 1996) and $YBa_2Cu_3O_{7-\delta}/PrBa_2Cu_3O_{7-\delta}$ multilayers (Qiu et al. 1995), and $\beta = 1.5$–2.0 in $YBa_2Cu_3O_{7-\delta}$ films (Luo et al. 1992, Kang et al. 1996). The scaling behavior $\rho_{xy} \propto \rho_{xx}^2$ has been observed in the regime of *positive* Hall effect for some cuprates and *negative* Hall resistivity for other cuprates. Kebin, Yuheng and Adrian (1996) have found that the sign anomaly in $(YBa_2Cu_3O_{7-\delta})_n/(PrBa_2Cu_3O_{7-\delta})_m$ superlattices diminishes and even disappears with decreasing $YBa_2Cu_3O_{7-\delta}$ layer thickness, i.e., increasing anisotropy, while the scaling behavior holds for all the samples, regardless of the anisotropy value, with some variation in the exponent ($\beta = 1.6$–2.0). On the other hand, Wang, Yang and Horng (1997) have found that the sign reversal of the Hall coefficient of $(YBa_2Cu_3O_{7-\delta})_n/(PrBa_2Cu_3O_{7-\delta})_m$ superlattices diminishes with decreasing $YBa_2Cu_3O_{7-\delta}$ layer thickness or increasing $PrBa_2Cu_3O_{7-\delta}$ layer thickness, while the exponent β is magnetic-field dependent and is larger for a $(YBa_2Cu_3O_{7-\delta})_n/(PrBa_2Cu_3O_{7-\delta})_m$ superlattice with a thinner $YBa_2Cu_3O_{7-\delta}$ layer. All these findings seem to rule out a possible link between scaling and sign change of the Hall resistivity.

An example of the scaling between the Hall and longitudinal resistivities is shown in fig. 15, a log–log plot of Hall resistivity $|\rho_{xy}|$ vs. longitudinal resistivity ρ_{xx} of an epitaxially grown $YBa_2Cu_3O_7$ film (Luo et al. 1992). The data shown were obtained for temperature sweeps at two magnetic field values of 1.4 and 3.7 T. The data display the power-law relationship in the negative Hall regime, with the exponent $\beta = 1.7 \pm 0.2$ for both fields. The cusp is an artifact of the absolute value $|\rho_{xy}|$, corresponding to where $\rho_{xy}(T)$ passes through zero. The power-law relationship breaks off abruptly at high temperatures, perhaps signaling the transition to flux flow and/or the normal state. Similar results were obtained for all the other cuprate superconductors for which the scaling relationship was observed.

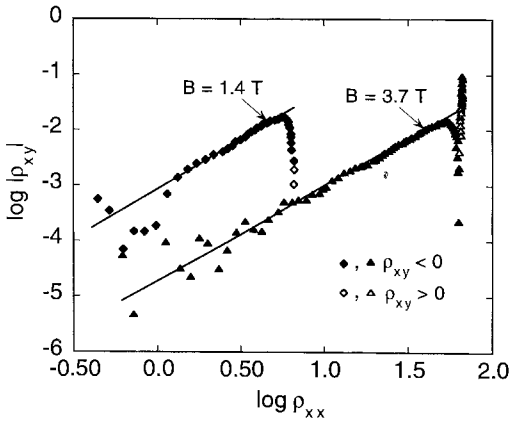

Fig. 15. Log–log plot of $|\rho_{xy}|$ vs. ρ_{xx} data for epitaxial $YBa_2Cu_3O_7$ films obtained for temperature sweeps at two magnetic field B values. Units for ρ are $\mu\Omega$ cm. The straight lines are fits of the data with $|\rho_{xy}| \propto \rho_{xx}^{\beta}$, where $\beta = 1.7 \pm 0.2$ for both fields. From Luo et al. (1992).

Dorsey and Fisher (1992) showed that the scaling behavior $\rho_{xy} = A\rho_{xx}^{\beta}$ is a general feature near the vortex-glass transition, but they were not able to obtain an exact value of the scaling exponent. A model proposed by Vinokur et al. (1993) suggests that the scaling exponent should be 2 in the thermally assisted flux flow region regardless of the pinning strength. Their analysis suggests that the scaling behavior is of a different origin than the sign change in the Hall resistivity. This is consistent with the experimental data of Luo et al. (1992), Samoilov (1993) and Kebin, Yuheng and Adrian (1996) discussed above. The results of Vinokur and coworkers are in fair agreement with scaling exponents of both weakly pinned systems; i.e., $Bi_2Sr_2CaCu_2O_8$ crystals ($\beta = 2.0 \pm 0.1$) (Samoilov 1993), and rather strongly pinned systems; i.e., heavy-ion-irradiated $Tl_2Ba_2Ca_2Cu_3O_{10}$ films ($\beta = 1.85 \pm 0.1$) (Budhani, Liou and Cai 1993), but not with the recent results on heavy-ion-irradiated $YBa_2Cu_3O_{7-\delta}$ ($\beta = 1.5 \pm 0.1$) (Kang et al. 1996). On the other hand, Wang, Jinming and Ting (1994) modified their earlier work (Wang and Ting 1991) to develop a unified theory of the Hall effect, including both the pinning effect and the thermal fluctuations. Wang, Jinming and Ting (1994) explain the scaling behavior and the anomalous sign reversal of the Hall effect by taking into account the backflow current due to pinning. In their model, the scaling exponent changes from 2 to 1.5 as the pinning strength increases. In agreement with this theory, Kang et al. (1996) have found that the scaling exponent of $YBa_2Cu_3O_{7-\delta}$ single crystals changes from 2 to 1.5 as the pinning strength increases through heavy-ion irradiation, while Kang et al. (1997) have found that for $HgBa_2CaCu_2O_{6+\delta}$, β increases from 1.5 ± 0.1 to 1.9 ± 0.1 as the magnetic field increases from 1 to 5.5 T. The authors suggest that these latter results indicate that the pinning strength decreases with increasing magnetic field.

3.3. *Normal-state Hall effect*

Among the normal-state transport properties of the high-temperature cuprate superconductors, the Hall effect remains one of the most difficult to explain. In the majority of the cuprates, the Hall coefficient R_H falls monotonically with increasing temperature. The

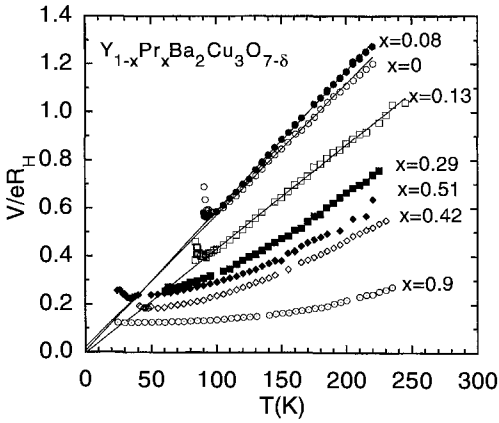

Fig. 16. Temperature dependence of the Hall carrier number $n_H = V/eR_H$ for $Y_{1-x}Pr_xBa_2Cu_3O_{7-\delta}$ single crystals with different x values. The fact that the data for two pairs of x values ($x=0$, x = 0.08, and $x=0.42$, x = 0.51) are out of sequence in the V/eR_H vs. T plot, but are not in the $\cot(\Theta_H)$ vs. T^2 plot (see fig. 17), could be a result of the error in measuring the thickness of these crystals. The $x=0.9$ value represents the nominal composition, while the x values of the superconducting samples were estimated by comparing the T_c's of the crystals with those of high-quality polycrystalline samples. From Maple et al. (1994).

pronounced temperature dependence of R_H is in sharp contrast with the behavior of R_H in conventional metals with complicated Fermi surfaces such as Cu, Ag, Ca, Mg. In these elements, R_H becomes insensitive to temperature when the temperature exceeds ~$0.3\Theta_D$, where Θ_D is the Debye temperature. Yet another puzzling feature of the Hall effect is the sensitivity of the anomalous temperature dependence to in-plane disorder. Replacement of Cu by magnetic ions such as Co, Fe, or Ni or by nonmagnetic Zn reduces the slope of the Hall carrier number $n_H \equiv V/eR_H$ (V is the unit-cell volume) vs. T as T_c is suppressed (Clayhold et al. 1989). A similar behavior has also been observed in underdoped $Y_{1-x}Pr_xBa_2Cu_3O_{7-\delta}$ (Wu et al. 1992, Almasan et al. 1994a,b) and in Ni-doped $La_{2-x}Sr_xCuO_4$ (Clayhold et al. 1989).

An example of the temperature dependence of n_H and its evolution with doping is shown in fig. 16 in which $n_H(T)$ data are displayed for the $Y_{1-x}Pr_xBa_2Cu_3O_{7-\delta}$ system with different x values (Maple et al. 1994). Notice that $n_H(T)$ is positive and, for $x \leqslant 0.13$, shows a remarkably linear temperature dependence in the normal state in the range $100\,K \leqslant T \leqslant 250\,K$ and actually extrapolates to zero at $T = 0\,K$. Similar results were obtained on other optimally doped $YBa_2Cu_3O_{7-\delta}$ specimens (Clayhold et al. 1989, Iye, Nakamura and Tamegai 1989, Rice et al. 1991, Wu et al. 1992). The upturn just above T_c was interpreted as a signature of superconducting fluctuations (Rice et al. 1991). With increasing x, the temperature range of the linear dependence of $n_H(T)$ is reduced and the overall magnitude of $n_H(T)$ decreases monotonically (Jia et al. 1992, Wu et al. 1992, Maple et al. 1994). Also, the temperature dependence of n_H appears to become less pronounced with increasing x. A similar behavior of $n_H(T)$ with doping was observed in other underdoped cuprates; e.g., Ni-doped ceramics (Clayhold et al. 1989) and $YBa_2Cu_{3-x}Zn_xO_{7-\delta}$ single crystals (Chien, Wang and Ong 1991b).

Several interpretations were given of the observed linear temperature dependence of the in-plane resistivity and Hall carrier number. Although a strong temperature dependence is possible in a two-band model provided that the scattering rates are different in these two bands, a linear T-dependence requires precise cancellation between electron and

hole contributions. This is highly unlikely to happen in all cuprate superconductors. Magnetic skew scattering is another mechanism that can cause a strongly temperature-dependent Hall effect (Fiory and Grader 1988), as reported in some heavy-fermion systems (Fert and Levy 1987) and ferromagnetic alloys (Rhyne 1968 and Bergmann 1979). Localized magnetic moments in these systems scatter conduction electrons asymmetrically, causing an anomalous contribution to the Hall effect. However, the fact that the low-temperature Hall resistivity does not saturate argues against such an explanation. In the Luttinger-liquid model of Anderson (1990) the intrinsic electronic degrees of freedom (i.e., charge and spin) are decoupled in the CuO_2 planes, with each described by an independent excitation, holons and spinons, with the latter forming the Fermi surface. Anderson (1991) proposed a scenario for understanding the observed linear temperature dependence of ρ_{xx} and the Hall carrier number $n_H = V/eR_H$ in the normal state of copper oxide superconductors by distinguishing between the relaxation rates for carrier motion normal to the Fermi surface (transport scattering rate $1/\tau_{tr}$, as measured in normal-state resistivity) and parallel to it (cyclotron relaxation rate $1/\tau_H$, as involved in Hall effect) if the transport properties are governed by two scattering times. According to his picture, one transport lifetime (τ_{tr}) determines the longitudinal resistivity ($\sigma_{xx} \propto \tau_{tr}$), while both τ_{tr} and τ_H determine the Hall conductivity ($\sigma_{xy} \propto \tau_{tr}\tau_H$). The transport scattering rate $1/\tau_{tr}$ is linear in T while the transverse relaxation rate $1/\tau_H$, determined by spinon–spinon scattering, varies as T^2, like any other fermion–fermion interaction. Thus, $\sigma_{xy} \propto \tau_{tr}\tau_H \propto 1/T^3$. Since the Hall angle $\Theta_H = \tan^{-1}(\sigma_{xy}/\sigma_{xx}) \propto 1/\tau_H$, the cotangent of the Hall angle $\cot\Theta_H = \rho_{xx}/R_H H$ is then given by

$$\cot\Theta_H = AT^2 + B, \tag{8}$$

where A is related to the spinon bandwidth and B is a constant additive term due to magnetic impurity scattering. On the other hand, using the nearly antiferromagnetic Fermi-liquid description of planar quasiparticles, Stojkovic and Pines (1996) have shown that the anomalous temperature dependence of the resistivity and Hall coefficient and the quadratic temperature dependence of the Hall angle (eq. 8) can be the result of highly anisotropic scattering at different regions of the Fermi surface.

Equation (8) was initially found to hold for $YBa_2Cu_{3-x}Zn_xO_{7-\delta}$ single crystals by Chien, Wang and Ong (1991b). It has subsequently been confirmed for a large number of systems including: Tl cuprates (Kubo and Manako 1992), $YBa_2Cu_{3-x}Co_xO_{7-\delta}$ (Carrington et al. 1992), $YBa_2Cu_{3-x}Fe_xO_{7-\delta}$ (Lan et al. 1994), $Y_{1-x}Pr_xBa_2Cu_3O_{7-\delta}$ (Wu et al. 1992, Xiong, Xiao and Wu 1993, Almasan et al. 1994a), oxygen-deficient $YBa_2Cu_3O_y$ (Xiong, Xiao and Wu 1993, Almasan et al. 1994b), $La_{1.85}Sr_{0.15}Cu_{1-x}A_xO_4$ (A = Fe, Co, Ni, Zn, Ga) (Gang, Peng and Cieplak 1992), and $HgBa_2CaCu_2O_{6+\delta}$ (Harris et al. 1994). In sharp contrast to the complicated $\rho_{xx}(T)$ and $n_H(T)$ in different systems, eq. (8) seems to be universal in every system with different doping levels.

Shown in fig. 17 is a plot of $\cot\Theta_H$ vs. T^2 calculated for a field of 6 T for $Y_{1-x}Pr_xBa_2Cu_3O_{7-\delta}$ single crystals (Almasan et al. 1994a). Typically, in the optimally doped $YBa_2Cu_3O_{7-\delta}$ (Chien, Wang and Ong 1991b, Xiong, Xiao and Wu 1993), the

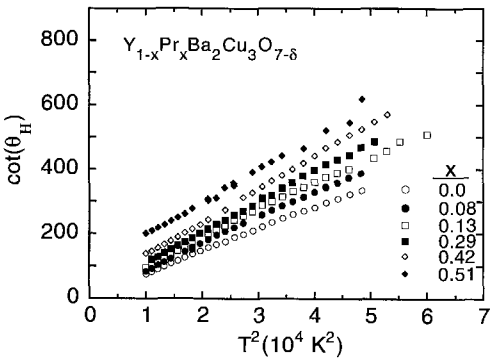

Fig. 17. Cotangent of Hall angle $\cot(\Theta_H)$ vs. T^2 of $Y_{1-x}Pr_xBa_2Cu_3O_{7-\delta}$ single crystals with $B = 6$ T and $B \| c$. From Almasan et al. (1994a).

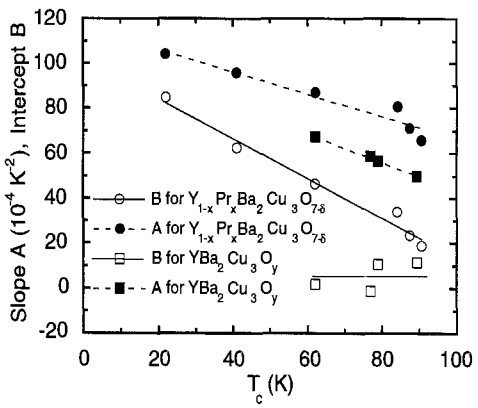

Fig. 18. Slope A and intercept B vs. T_c for $Y_{1-x}Pr_xBa_2Cu_3O_{7-\delta}$ and $YBa_2Cu_3O_y$ single crystals with $B = 6$ T and $B \| c$. From Almasan et al. (1994b).

T^2-dependence is observed in the temperature range 120–200 K. As the samples become more underdoped and the in-plane disorder increases (with increasing x), the range of the T^2-dependence moves towards higher temperatures.

Figure 18 contains a plot of the values obtained for the slope A and the intercept B [determined by fitting the data of fig. 17 and similar data for oxygen-deficient $YBa_2Cu_3O_y$ with eq. (8)] vs. T_c (Almasan et al. 1994b). Both A and B increase linearly with decreasing T_c in $Y_{1-x}Pr_xBa_2Cu_3O_{7-\delta}$, while in $YBa_2Cu_3O_y$ only A changes with oxygen content while B stays constant. There are two interesting points to be made here: first, A is sensitive to carrier concentration, as predicted by Anderson (1991) and, second, the linear correlation between T_c and A revealed here implies a close relationship between the Hall effect and the superconducting mechanism. Xiong, Xiao and Wu (1993) reported a similar relationship between A and B, and T_c for epitaxial films of $Y_{1-x}Pr_xBa_2Cu_3O_{7-\delta}$, while Hall effect measurements of $Y_{1-x}Pr_xBa_2Cu_3O_{7-\delta}$ single crystals by Wu et al. (1992) revealed that only B increases with decreasing T_c while A remains constant within experimental resolution. Hall-effect measurements on $YBa_2Cu_{3-x}Zn_xO_{7-\delta}$ single crystals performed by Chien, Wang and Ong (1991b) have shown that Zn doping, which introduces a local spin-$\frac{1}{2}$ impurity (Xiao et al. 1990) (bound spinon) into the CuO_2 plane, only

changes B proportional to x while maintaining a constant slope A. Therefore, the behavior of $\cot\Theta_H$ can be classified in three groups: (i) varying slope A and constant B, as in $YBa_2Cu_3O_y$; (ii) varying B and constant slope A, as in all Cu-site doped systems; and (iii) both varying A and B, typified by $Y_{1-x}Pr_xBa_2Cu_3O_{7-\delta}$.

4. Summary and conclusions

In this chapter, we have reviewed magnetoresistance and Hall effect measurements on high-T_c cuprate superconductors in both the normal and superconducting states that address several issues: for the normal state, the temperature dependence of the Hall coefficient R_H and the cotangent of the Hall angle $\cot\Theta_H$; for the superconducting state, the temperature dependence of the upper critical field H_{c2} and irreversibility line H^* as well as the anomalous sign change of the Hall effect near T_c. Scaling behavior, dimensional cross-over phenomena, and relevant theoretical models were also discussed. These measurements have provided important information regarding the electronic structure and excitations that underly the normal and superconducting properties, fundamental superconducting-state parameters, as well as vortex pinning and dynamics of these remarkable materials. Magnetotransport studies, including those reviewed herein and many others outside the scope of this article, have proven to be very useful in probing the physics of the normal and superconducting states of the high-T_c cuprate superconductors.

Acknowledgments

We would like to thank Cassandra Rayt (UCSD) for preparing several figures for this article. This work was supported by the National Science Foundation under Grant Nos. DMR-9601839 and DMR-9801990 at Kent State University, and the U.S. Department of Energy under Grant No. DE-FG03-86ER-45230 at University of California at San Diego.

References

Abrikosov, A.A., 1997, Phys. Rev. B **56**, 5112.

Almasan, C.C., and M.B. Maple, 1996, Phys. Rev. B **53**, 2882.

Almasan, C.C., C.L. Seaman, Y. Dalichaouch and M.B. Maple, 1991, Physica C **174**, 93.

Almasan, C.C., M.C. de Andrade, Y. Dalichaouch, J.J. Neumeier, C.L. Seaman, M.B. Maple, R.P. Guertin, M.V. Kuric and J.C. Garland, 1992a, Phys. Rev. Lett. **69**, 3812.

Almasan, C.C., S.H. Han, E.A. Early, B.W. Lee, C.L. Seaman and M.B. Maple, 1992b, Phys. Rev. B **45**, 1056.

Almasan, C.C., S.H. Han, K. Yoshiara, M. Buchgeister, B.W. Lee, L.M. Paulius, D.A. Gajewski and M.B. Maple, 1994a, Physica B **199–200**, 288.

Almasan, C.C., S.H. Han, K. Yoshiara, M. Buchgeister, D.A. Gajewski, J. Herrmann, A.P. Paulikas, G. Chun, B.W. Veal and M.B. Maple, 1994b, Physica C **235–240**(Part 5), 3119.

Almasan, C.C., S.H. Han, K. Yoshiara, M. Buchgeister,

D.A. Gajewski, L.M. Paulius, J. Herrmann, M.B. Maple, A.P. Paulikas, G. Chun and B.W. Veal, 1995, Phys. Rev. B **51**, 3981.

Anderson, P.W., 1990, Phys. Rev. Lett. **64**, 1839.

Anderson, P.W., 1991, Phys. Rev. Lett. **67**, 2092.

Bardeen, J., and M.J. Stephen, 1965, Phys. Rev. A **140**, 1197.

Bergmann, G., 1979, Phys. Today **32**, 25.

Blatter, G., and B. Ivlev, 1993, Phys. Rev. Lett. **70**, 2621.

Budhani, R.C., S.H. Liou and Z.X. Cai, 1993, Phys. Rev. Lett. **71**, 621.

Budhani, R.C., W.L. Holstein and M. Suenaga, 1994, Phys. Rev. Lett. **72**, 566.

Bud'ko, S.L., A.G. Gapotchenko, A.E. Luppov, E.A. Early, M.B. Maple and J.T. Markert, 1990, Physica C **168**, 530.

Carrington, A., A.P. Mackenzie, C.T. Lin and J.R. Cooper, 1992, Phys. Rev. Lett. **69**, 2855.

Chien, T.R., T.W. Jing, N.P. Ong and Z.Z. Wang, 1991a, Phys. Rev. Lett. **66**, 3075.

Chien, T.R., Z.Z. Wang and N.P. Ong, 1991b, Phys. Rev. Lett. **67**, 2088.

Clayhold, J., N.P. Ong, Z.Z. Wang, J.M. Tarascon and P. Barboux, 1989, Phys. Rev. B **39**, 7324.

Clinton, T.W., A.W. Smith, Q. Li, J.L. Peng, R.L. Greene, C.J. Lobb, M. Eddy and C.C. Tsuei, 1995, Phys. Rev. B **52**, R7046.

Colino, J., M.A. Gonzalez, J.I. Martin, M. Velez, D. Oyola, P. Prieto and J.L. Vincent, 1994, Phys. Rev. B **49**, 3496.

Cooper, J.R., J.W. Loram and J.M. Wade, 1995, Phys. Rev. B **51**, 6179.

Dalichaouch, Y., B.W. Lee, C.L. Seaman, J.T. Markert and M.B. Maple, 1990, Phys. Rev. Lett. **64**, 599.

de Andrade, M.C., C.C. Almasan, Y. Dalichaouch and M.B. Maple, 1991, Physica C **184**, 378.

Dorsey, A.T., 1992, Phys. Rev. B **46**, 8376.

Dorsey, A.T., and M.P.A. Fisher, 1992, Phys. Rev. Lett. **68**, 694.

Feigel'man, M.V., V.B. Geshkenbein, A.I. Larkin and V.M. Vinokur, 1994, Physica C **235–240**(Part 5), 3127.

Ferrell, R.K., 1992, Phys. Rev. Lett. **68**, 2524.

Fert, A., and P.M. Levy, 1987, Phys. Rev. B **36**, 1907.

Finnemore, D.K., R.N. Shelton, J.R. Clem, R.W. McCallum, H.C. Ku, R.E. McCarley, S.C. Chen, P. Klavins and V. Kogan, 1987, Phys. Rev. B **35**, 5319.

Fiory, A.T., and G.S. Grader, 1988, Phys. Rev. B **38**, 9198.

Freimuth, A., C. Hohn and M. Galffy, 1991, Phys. Rev. B **44**, 10396.

Galffy, K., and E. Zirngiebl, 1988, Solid State Commun. **68**, 929.

Gang, X., X. Peng and M.Z. Cieplak, 1992, Phys. Rev. B **46**, 8687.

Geshkenbein, V.B., A.I. Larkin, J.M. Harris, N.P. Ong and Y.F. Yan, 1994, Phys. Rev. Lett. **73**, 609.

Ginsberg, D.M., and R.L. Dudey, 1993, Physica A **200**, 351.

Ginsberg, D.M., and J.T. Manson, 1995, Phys. Rev. B **51**, 515.

Goettee, J.D., J.S. Brooks, W.J. Skocpol, J.L. Smith, D.G. Rickel, B.L. Freeman, C.M. Fowler, P.M. Mankiewich, E.I. De Obaldia and M.L. O'Malley, 1994, Physica B **194–196**, 1805.

Hagen, S.J., C.J. Lobb, R.L. Greene, M.G. Forrester and J.H. Kang, 1990a, Phys. Rev. B **41**, 11630.

Hagen, S.J., C.J. Lobb, R.L. Greene, M.G. Forrester and J. Talvacchio, 1990b, Phys. Rev. B **42**, 6777.

Hagen, S.J., C.J. Lobb, R.L. Greene and M. Eddy, 1991a, Phys. Rev. B **43**, 6246.

Hagen, S.J., C.J. Lobb, R.L. Greene and M. Eddy, 1991b, Physica C **185–189**(Part 3), 1769.

Hagen, S.J., A.W. Smith, M. Rajeswari, J.L. Peng, Z.Y. Li, R.L. Greene, S.N. Mao, X.X. Xi, S. Bhattacharya, L. Qi and C.J. Lobb, 1993, Phys. Rev. B **47**, 1064.

Han, S.H., C.C. Almasan, M.C. de Andrade, Y. Dalichaouch and M.B. Maple, 1992, Phys. Rev. B **46**, 14290.

Hao, Z., J.R. Clem, M.W. McElfresh, L. Civale, A.P. Malozemoff and F. Holtzberg, 1991, Phys. Rev. B **43**, 2844.

Harris, J.M., N.P. Ong and Y.F. Yan, 1993, Phys. Rev. Lett. **71**, 1455.

Harris, J.M., H. Wu, N.P. Ong, R.L. Meng and C.W. Chu, 1994, Phys. Rev. B **50**, 3246.

Harris, J.M., N.P. Ong, P. Matl, R. Gagnon, L. Taillefer, T. Kimura and R. Kitazawa, 1995, Phys. Rev. B **51**, 12053.

Hidaka, Y., and M. Suzuki, 1989, Nature (UK) **338**, 635.

Hirsch, J.E., and F. Marsiglio, 1991, Phys. Rev. B **43**, 424.

Iwasaki, H., Y. Dalichaouch, J.T. Markert, G. Nieva, C.L. Seaman and M.B. Maple, 1990, Physica C **169**, 146.

Iye, Y., S. Nakamura and T. Tamegai, 1989, Physica C **159**, 616.

Jia, Y.X., J.Z. Liu, A. Matsushita, M.D. Lan, P. Klavins and R.N. Shelton, 1992, Phys. Rev. B **46**, 11745.

Jia, Y.X., J.Z. Liu, M.D. Lan and R.N. Shelton, 1993, Phys. Rev. B **47**, 6043.

Jin-Tae, K., J. Giapintzakis and D.M. Ginsberg, 1996, Phys. Rev. B **53**, 5922.

Jones, E.C., D.K. Christen and B.C. Sales, 1994, Phys. Rev. B **50**, 7234.

Kadowaki, K., and T. Mochiku, 1992, Physica C **195**, 127.

Kang, W.N., D.H. Kim, S.Y. Shim, J.H. Park, T.S. Hahn, S.S. Choi, W.C. Lee, J.D. Hettinger, K.E. Gray and B. Glagola, 1996, Phys. Rev. Lett. **76**, 2993.

Kang, W.N., S.H. Yun, J.Z. Wu and D.H. Kim, 1997, Phys. Rev. B **55**, 621.

Kebin, L., Z. Yuheng and H. Adrian, 1996, Phys. Rev. B **53**, 8608.

Khomskii, D.I., and A. Freimuth, 1995, Phys. Rev. Lett. **75**, 1384.

Kopnin, N.B., 1996, Phys. Rev. B **54**, 9475.

Kopnin, N.B., and V.E. Kravtsov, 1976a, JETP Lett. **23**, 578.

Kopnin, N.B., and V.E. Kravtsov, 1976b, Pis'ma Zh. Eksp. Teor. Fiz. **23**, 631.

Kopnin, N.B., and A.V. Lopatin, 1995, Phys. Rev. B **51**, 15291.

Kopnin, N.B., B.I. Ivlev and V.A. Kalatsky, 1993, J. Low Temp. Phys. **90**, 1.

Kubo, Y., and T. Manako, 1992, Physica C **197**, 378.

Kunchur, M.N., D.K. Christen, C.E. Klabunde and J.M. Phillips, 1994, Phys. Rev. Lett. **72**, 2259.

Lan, M.D., J.Z. Liu, Y.X. Jia, Z. Lu and R.N. Shelton, 1994, Phys. Rev. B **49**, 580.

Larkin, A.I., and Yu.N. Ovchinnikov, 1995, Phys. Rev. B **51**, 5965.

Lindemann, F., 1910, Z. Phys. **11**, 69.

Lobb, C.J., T.W. Clinton, A.W. Smith, L. Wu, L. Qi, J.L. Peng, R.L. Greene, M. Eddy and C.C. Tsuei, 1994, Appl. Supercond. (UK) **2**, 631.

Luo, J., T.P. Orlando, J.M. Graybeal, X.D. Wu and R. Muenchausen, 1992, Phys. Rev. Lett. **68**, 690.

Mackenzie, A.P., S.R. Julian, G.G. Lonzarich, A. Carrington, S.D. Hughes, R.S. Liu and D.C. Sinclair, 1993, Phys. Rev. Lett. **71**, 1238.

Maki, K., 1966, Phys. Rev. **148**, 362.

Malozemoff, A.P., 1989, Macroscopic magnetic properties of high temperature superconductors, in: Physical Properties of High Temperature Superconductors, Vol. 1, ed. D.M. Ginsberg (World Scientific, Singapore) p. 71.

Malozemoff, A.P., T.K. Worthington, Y. Yeshurun, F. Holtzberg and P.H. Kes, 1988, Phys. Rev. B **38**, 7203.

Manson, J.T., J. Giapintzakis, A.I. Schegolev and D.M. Ginsberg, 1996, Phys. Rev. B **54**, 10155.

Maple, M.B., Y. Dalichaouch, J.M. Ferreira, R.R. Hake, B.W. Lee, J.J. Neumeier, M.S. Torikachvili, K.N. Yang, H. Zhou, R.P. Guertin and M.V. Kuric, 1987, Physica B&C **148B+C**, 155.

Maple, M.B., B.W. Lee, J.J. Neumeier, G. Nieva, L.M. Paulius and C.L. Seaman, 1992, J. Alloys & Compounds **181**, 135.

Maple, M.B., C.C. Almasan, C.L. Seaman, S.H. Han, K. Yoshiara, M. Buchgeister, L.M. Paulius, B.W. Lee, D.A. Gajewski, R.F. Jardim, C.R. Fincher Jr, G.B. Blanchet and R.P. Guertin, 1994, J. Supercond. **7**, 97.

Matsuda, Y., T. Nagaoka, G. Suzuki, K. Kumagai, M. Suzuki, M. Machida, M. Sera, M. Hiroi and N. Kobayashi, 1995, Phys. Rev. B **52**, R15749.

Nakao, K., N. Miura, K. Tatsuhara, H. Takeya and H. Takei, 1989, Phys. Rev. Lett. **63**, 97.

Neiman, R.L., J. Giapintzakis, D.M. Ginsberg and J.M. Mochel, 1995, J. Supercond. **8**, 383.

Niessen, A.K., F.A. Staas and C.H. Weijsenfeld, 1967, Phys. Lett. **25A**, 33.

Noto, K., S. Shinzawa and Y. Muto, 1976, Solid State Commun. **18**, 1081.

Nozières, P., and W.F. Vinen, 1966, Philos. Mag. **14**, 667.

Oshima, K., H. Urayama, H. Yamochi and G. Saito, 1988, Physica C **153**, 1148.

Osofsky, M.S., R.J. Soulen Jr, S.A. Wolf, J.M. Broto, H. Rakoto, J.C. Ousset, G. Coffe, S. Askenazy, P. Pari, I. Bozovic, J.N. Eckstein and G.F. Virshup, 1993, Phys. Rev. Lett. **71**, 2315.

Ovchinnikov, Y.K., and V.Z. Kresin, 1995, Phys. Rev. B **52**, 3075.

Ovchinnikov, Y.K., and V.Z. Kresin, 1996, Phys. Rev. B **54**, 1251.

Paulius, L.M., C.C. Almasan and M.B. Maple, 1993, Phys. Rev. B **47**, 11627.

Paulius, L.M., B.W. Lee, M.B. Maple and P.K. Tsai, 1994, Physica C **230**, 255.

Qiu, X.G., G. Jakob, V.V. Moshchalkov, Y. Bruynseraede and H. Adrian, 1995, Phys. Rev. B **52**, 12994.

Rhyne, J.J., 1968, Phys. Rev. **172**, 523.

Rice, J.P., J. Giapintzakis, D.M. Ginsberg and J.M. Mochel, 1991, Phys. Rev. B **44**, 10158.

Rice, J.P., N. Rigakis, D.M. Ginsberg and J.M. Mochel, 1992, Phys. Rev. B **46**, 11050.

Samoilov, A.V., 1993, Phys. Rev. Lett. **71**, 617.
Samoilov, A.V., Z.G. Ivanov and L.G. Johansson, 1994, Phys. Rev. B **49**, 3667.
Schilling, A., R. Jin, J.D. Guo and H.R. Ott, 1993, Phys. Rev. Lett. **71**, 1899.
Seidler, G.T., T.F. Rosenbaum, D.L. Heinz, J.W. Downey, A.P. Paulikas and B.W. Veal, 1991, Physica C **183**, 333.
Stojkovic, B.P., and D. Pines, 1996, Phys. Rev. Lett. **76**, 811.
Sumarlin, I.W., S. Skanthakumar, J.W. Lynn, J.L. Peng, Z.Y. Li, W. Jiang and R.L. Greene, 1992, Phys. Rev. Lett. **68**, 2228.
Suzuki, M., and M. Hikita, 1990, Phys. Rev. B **41**, 9566.
Tinkham, M., 1988, Phys. Rev. Lett. **61**, 1658.
Tinkham, M., ed., 1996, Introduction to Superconductivity (McGraw-Hill, New York).
Ullah, S., and A.T. Dorsey, 1991, Phys. Rev. B **44**, 262.
Van Otterlo, A., M.V. Feigel'man, V.B. Geshkenbein and G. Blatter, 1995, Phys. Rev. Lett. **75**, 3736.
Vinokur, V.M., V.B. Geshkenbein, M.V. Feigel'man and G. Blatter, 1993, Phys. Rev. Lett. **71**, 1242.
Walker, D.J.C., O. Laborde, A.P. Mackenzie, S.R. Julian, A. Carrington, J.W. Loram and J.R. Cooper, 1995, Phys. Rev. B **51**, 9375.
Wang, L.M., H.C. Yang and H.E. Horng, 1997, Phys. Rev. Lett. **78**, 527.
Wang, Z.B., D. Jinming and C.S. Ting, 1994, Phys. Rev. Lett. **72**, 3875.
Wang, Z.D., and C.S. Ting, 1991, Phys. Rev. Lett. **67**, 3618.
Welp, U., W.K. Kwok, G.W. Crabtree, K.G. Vandervoort and J.Z. Liu, 1989, Phys. Rev. Lett. **62**, 1908.
Welp, U., S. Fleshler, W.K. Kwok, R.A. Klemm, V.M. Vinokur, J. Downey, B. Veal and G.W. Crabtree, 1991, Phys. Rev. Lett. **67**, 3180.
Werthamer, N.R., E. Helfand and P.C. Hohenberg, 1966, Phys. Rev. **147**, 295.
Wu, J., J.L. Peng, S.J. Hagen and R.L. Greene, 1992, Phys. Rev. B **46**, 8694.
Xiao, G., M.Z. Cieplak, J.Q. Xiao and C.L. Chien, 1990, Phys. Rev. B **42**, 8752.
Xiong, P., G. Xiao and X.D. Wu, 1993, Phys. Rev. B **47**, 5516.
Zavaritsky, N.V., A.V. Samoilov and A.A. Yurgens, 1991, Physica C **180**, 417.

Handbook on the Physics and Chemistry of Rare Earths
Vol. 31
edited by K.A. Gschneidner, Jr., L. Eyring and M.B. Maple

Chapter 198

NEUTRON SCATTERING STUDIES OF SPIN FLUCTUATIONS IN HIGH-TEMPERATURE SUPERCONDUCTORS

T.E. Mason*
University of Toronto, Department of Physics, 60 St. George St., Toronto, ON M5S 1A7, Canada, and Spallation Neutron Source, Oak Ridge National Laboratory, Oak Ridge, TN 37831, USA

Contents

List of symbols and acronyms

c	spin-wave velocity
$f(\boldsymbol{Q})$	magnetic form factor
$\hbar\omega$	neutron energy transfer
$J_{\parallel}$	nearest-neighbour antiferromagnet exchange constant
$J_{\perp}$	interlayer exchange constant
k (k')	incident (scattered) neutron wave vector
$\boldsymbol{Q}$	momentum transfer
$S^{\alpha\beta}(\boldsymbol{Q},\omega)$	magnetic scattering function
Z_c, Z_χ	quantum renormalization parameters for exchange constant and magnetic response
Γ	inverse lifetime
κ	inverse correlation length
μ_B	Bohr magneton
ξ	correlation length
(π,π)	antiferromagnetic zone center for CuO_2 planes
$\frac{d^2\sigma}{d\Omega\, dE}$	partial differential cross-section
$\chi''(\boldsymbol{Q},\omega)$	imaginary part of the generalized magnetic susceptibility

* Present Address: Spallation Neutron Source, Oak Ridge National Laboratory, Oak Ridge, TN, 37831, USA.

Introduction

Soon after the discovery of high-temperature superconductors in 1986 it was realised that superconductivity occurred in close proximity to antiferromagnetic ordering of the spin-$\frac{1}{2}$ Cu^{2+} moments present in the CuO_2 planes which typify the high-T_c superconductors. The dynamics of these spins, both in the undoped, insulating parent compounds and in the doped, metallic, superconductors represent an intriguing topic of study, in the former case as an example of a low-dimensional quantum antiferromagnet and in the latter case as a strongly correlated metal. This chapter deals with neutron scattering studies of the spin fluctuations in the CuO_2 planes; as such, the rare earths that form an important constituent of almost all high-T_c materials are viewed as somewhat passive spectators. The fact that many candidate theories of high-temperature superconductivity include spin fluctuations as a central feature of the mechanism for superconductivity increases the importance of obtaining a detailed picture of the energy, momentum, temperature, and doping dependence of the magnetic dynamics of the cuprates. Furthermore, many of the anomalous normal-state properties of the doped cuprates are likely related to the proximity of antiferromagnetism in the phase diagram and the manifestation of this instability in the excitations. Even in the absence of a magnetic mechanism for high-temperature superconductivity the spin fluctuations are an important degree of freedom of the quasiparticles which form the superconducting condensate and therefore a probe of the nature of that transition.

Information about spin excitations may be inferred indirectly from bulk measurements such as magnetic susceptibility or heat capacity (see, for example, ch. 200). Nuclear magnetic resonance provides a more microscopic probe of the low-energy spin fluctuations and can provide some information about the momentum dependence when several different nuclear sites are compared. Raman spectroscopy (ch. 203) can measure the two-magnon cross-section and therefore is sensitive to the energy scale over which magnetic excitations occur and its evolution with doping or temperature. The most detailed probe of spin dynamics is inelastic neutron scattering (for a recent overview see Aeppli et al. 1997a), the topic of the present chapter. Because of its magnetic moment the neutron is sensitive to magnetic moments in solids. It is a weakly interacting, non-perturbing probe with a well-understood cross-section that is directly proportional to the static and dynamic spin correlation functions. Elastic neutron scattering can be used to determine the arrangement of spins in an ordered magnetic state (see, for example, ch. 199 describing the 4f magnetic ordering that occurs in many of the rare-earth cuprate superconductors). Inelastic neutron scattering can probe crystal field excitations (ch. 194 of volume 30 of this Handbook) as well as the collective excitations of spins, ordered or disordered. While the neutron is in many respects an ideal probe of magnetism in solids it has the drawback that neutron sources are relatively weak (even the highest flux neutron source produces fewer neutrons than a bench-top Cu-Kα X-ray tube). As a result, very large single crystals (of order 1 cm^3 or bigger) are required to measure the weak cross-section inherent in any inelastic experiment. For the high-T_c materials this situation is made more difficult by the small spin quantum number ($\frac{1}{2}$) and the large energy scale over which spin

fluctuations exist (hundreds of meV). These limitations mean that only two systems have been studied with inelastic neutron scattering in any detail, $La_{2-x}(Sr,Ba)_xCuO_4$ (214) and $YBa_2Cu_3O_{7-x}$ (123). There have been some studies of spin fluctuations in other high-T_c systems [for example Pr and Nd 214; see, e.g., Matsuda et al. (1993) and Ivanov et al. (1995)]; however, the antiferromagnetic spin waves are not qualitatively different from those observed in La 214 and the experimental difficulties of small crystals have precluded any detailed study of superconducting samples. Neutron scattering studies of 4f antiferromagnetic ordering in the rare-earth high-T_c superconductors are discussed in ch. 199 of this volume. Following a brief summary of the neutron scattering cross-section the 214 and 123 systems are discussed, in turn, with the spin fluctuations in the superconductors as the main emphasis.

1. Neutron scattering cross-section

Because of its magnetic moment the neutron can couple to moments in solids via the dipolar force. The energies and wavelengths of thermal and cold neutrons are well matched to the energy and length scales of most condensed-matter systems. In the case of high-temperature superconductors, the characteristic energy of the spin fluctuations is determined by the superexchange interaction between nearest-neighbour copper spins. This is typically ~150 meV so a complete characterisation of the magnetic dynamics requires the use of higher-energy sources such as those found at spallation neutron sources or a reactor hot source. We will briefly review the formalism that describes magnetic neutron scattering. For a detailed treatment of the neutron scattering cross-section, there are some excellent texts which can serve as an introduction (Squires 1978) or a more comprehensive exposition (Lovesey 1984).

The partial differential cross-section for magnetic neutron scattering, which measures the probability of scattering per solid angle per unit energy, is

$$\frac{\mathrm{d}^2\sigma}{\mathrm{d}\Omega\,\mathrm{d}E} = \frac{k'}{k}\frac{N}{\hbar}(\gamma \cdot r_0)\,|f(\boldsymbol{Q})|^2 \sum_{\alpha\beta}\left(\delta_{\alpha\beta} - \widehat{Q}_\alpha\widehat{Q}_\beta\right) S^{\alpha\beta}(\boldsymbol{Q},\omega), \tag{1}$$

where k (k') is the incident (scattered) neutron wavevector, N is the number of moments, $\gamma r_0 = 5.391$ fm is the magnetic scattering length, $f(\boldsymbol{Q})$ is the magnetic form factor (analogous to the electronic form factor appearing in the X-ray scattering cross-section), $\boldsymbol{Q}$ is the momentum transfer, ω is the energy transfer, and the summation runs over the Cartesian directions. $S^{\alpha\beta}(\boldsymbol{Q},\omega)$ is the magnetic scattering function which is proportional to the space and time Fourier transform of the spin–spin correlation function.

If the incident and scattered neutron energies are the same (elastic scattering) then the correlations at infinite time are being probed and, in a magnetically ordered material, the scattering function will contain delta functions at the wavevectors corresponding to magnetic Bragg reflections. The $(\delta_{\alpha\beta} - \widehat{Q}_\alpha\widehat{Q}_\beta)$ term in the cross-section means that neutrons probe the components of spin perpendicular to the momentum transfer, $\boldsymbol{Q}$.

If there is no analysis of the scattered neutron energy then (within the static approximation) the measured intensity is proportional to the Fourier transform of the instantaneous correlation function which is essentially a snapshot of the spin correlations in reciprocal space. At non-zero energy transfer, the spin dynamics of the system under study are probed. In a magnetically ordered system of localised spins, the elementary magnetic excitations are spin waves.

The fluctuation–dissipation theorem relates the correlations to absorption; in other words, the scattering function is proportional to the imaginary part of a generalised ($\boldsymbol{Q}$ and ω dependent) susceptibility, $\chi''(\boldsymbol{Q},\omega)$. In the zero-frequency, zero-wavevector limit, the real part of the generalised susceptibility is the usual DC susceptibility measured by magnetisation. In a metal, the elementary excitations are electron–hole pairs. Since it is possible to excite an electron–hole pair by promoting a quasiparticle from below the Fermi surface to above the Fermi surface, and at the same time flip its spin, neutrons can be used to probe the low-energy excitations of a metal. The generalised susceptibility (for a non-interacting metal) is just the Lindhard susceptibility that can be calculated from the band structure.

2. Insulating cuprates

2.1. *Antiferromagnetism in La_2CuO_4*

The high-T_c superconductors are complex materials displaying, in a single sample, diverse phenomena that have been active topics of research in condensed matter physics for the last thirty years. They are oxides of copper having perovskite crystal structures, generally tetragonal at high temperatures and orthorhombic at low temperatures. The importance of magnetism in the undoped, insulating, parent compounds was confirmed quite soon after the initial discovery of superconductivity in $La_{2-x}Ba_xCuO_4$ when Vaknin et al. (1987) showed, using neutron powder diffraction, that anomalies seen in the magnetic susceptibility of La_2CuO_{4-y} (Johnston et al. 1987) were due to a transition to a three-dimensional, long-range, ordered, antiferromagnetic state. The Cu^{2+} ions of the CuO_2 sheets that typify this class of materials are coupled via an antiferromagnetic superexchange interaction that is considerably stronger between nearest-neighbour copper spins in the nearly square CuO_2 planes than perpendicular to them. This leads to effectively two-dimensional magnetic behaviour; the transition to long-range 3D order occurs due to the weak interplane interaction which is not large enough to affect the spin dynamics very significantly.

Figure 1 shows the weak superlattice reflection observed below T_N by Vaknin et al. (1987) in their unpolarized neutron powder diffraction measurements. The lower panel shows how this peak, which corresponds to the unit cell doubling of a simple $+-$ arrangement of nearest-neighbour spins on a square lattice, develops below T_N (the actual value of T_N depends on the oxygen doping, y – it is 220 K for the sample used in fig. 1). The fact that this reflection is magnetic in origin was subsequently confirmed by

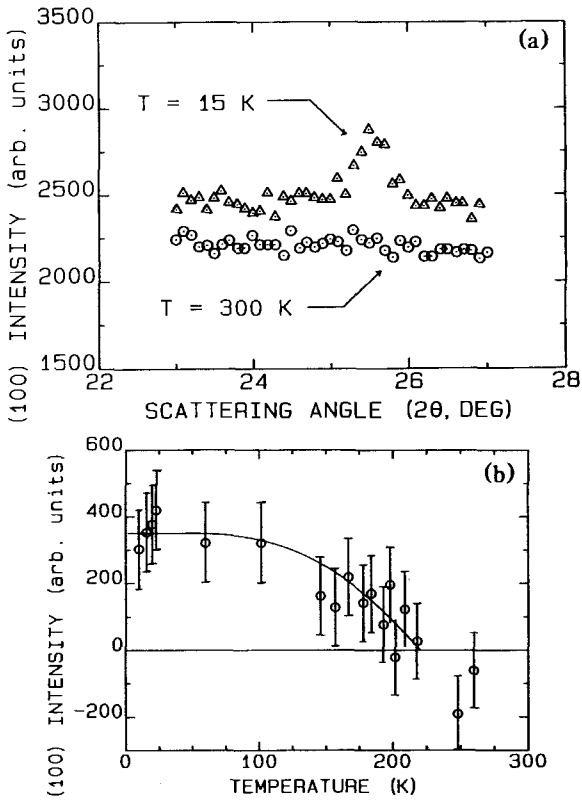

Fig. 1. Antiferromagnetic ordering observed in La_2CuO_{4-y} by unpolarized powder neutron diffraction. The top panel shows the (100) peak which appears below T_N (=220 K), and the bottom panel shows the temperature dependence of the Bragg intensity. From Vaknin et al. (1987).

polarised neutron measurements (Mitsuda et al. 1987). The ordered moment corresponds to $0.4\mu_B$/Cu. The ordering wavevector, (100) in orthorhombic notation or (π,π) in units of the dimensionless 2D reciprocal lattice, corresponds to the Fermi surface nesting instability of the 2D square lattice from which the low-temperature structure is derived.

A variety of experimental techniques have been used to establish the behaviour of $La_{2-x}(Sr,Ba)_xCuO_4$ as holes are introduced into the CuO_2 planes by replacing La with Sr or Ba. Figure 2 summarises the results for Sr doping. Initially the effect of doping is to reduce T_N, which vanishes beyond $x \approx 0.03$. There is a region of spin-glass behaviour before. For doping levels in the range 0.07–0.25, superconductivity occurs with a maximum T_c of ~ 39 K for $x = 0.15$. Because the $3d^9$ ionic configuration of Cu^{2+} has an effective spin-$\frac{1}{2}$ ground state with no orbital angular momentum, La_2CuO_4 is an excellent realisation of a 2D square lattice Heisenberg antiferromagnet that corresponds to a low-dimensional quantum Hamiltonian which, before the advent of high T_c, was not understood. There is a small spin anisotropy due to antisymmetric exchange; an indication of the extent to which this causes deviation from Heisenberg symmetry can be seen in the small canting (~0.003 rad) of the spins out of the CuO_2 plane (Kastner et al. 1988). Because it is such an excellent realisation of a model quantum magnet, experiments on

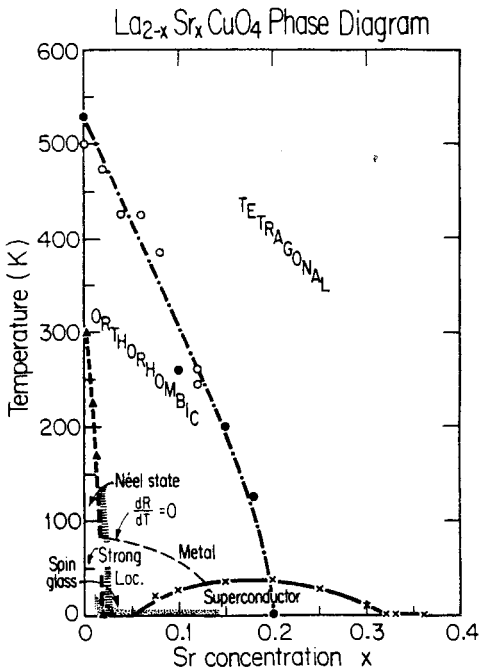

Fig. 2. Phase diagram for $La_{2-x}Sr_xCuO_4$ showing the phase boundaries for the tetragonal–orthorhombic, paramagnetic–antiferromagnetic, and normal–superconducting phase transitions as a function of temperature and doping. From Keimer et al. (1992).

La_2CuO_4 have been crucial as a test of theories that purport to explain this system. La_2CuO_4 is now probably the most completely characterised model magnetic system in existence. The spin dynamics and critical scattering have been quantitatively measured and understood over an unprecedented range of energy and temperature.

2.1.1. *Spin waves*

The lamellar structure of the high-T_c oxides suggests that the magnetic properties of the spin-$\frac{1}{2}$ moments in the CuO_2 planes will be quasi-two-dimensional, as is the case for isostructural magnetic materials such as K_2NiF_4 and K_2MnF_4 (Birgeneau, Als-Nielsen and Shirane 1977). The appropriate magnetic Hamiltonian for such a system is that of weakly coupled planes of Heisenberg spins:

$$H = \sum_{ij} J_{\parallel} \boldsymbol{S}_i \cdot \boldsymbol{S}_j + \sum_{ij'} J_{\perp} \boldsymbol{S}_i \cdot \boldsymbol{S}_{j'}. \tag{2}$$

The first term represents the coupling between nearest-neighbour Cu spins in the same CuO_2 plane. This is the dominant interaction and, neglecting the inter-layer coupling described by the second term in eq. (2), yields the Hamiltonian of a (nearly) square lattice Heisenberg antiferromagnet. One notable feature of La_2CuO_4 is that it is the first good example of a Heisenberg (i.e., isotropic) spin-$\frac{1}{2}$ system in two dimensions studied in any detail. Unlike systems with an Ising anisotropy, there is no phase transition to a long-range

ordered state at finite temperature expected for Heisenberg spins. The ordering below T_N that occurs in La_2CuO_4 and other high-T_c compounds is driven by the weak interplane interaction that eventually leads to 3D ordering.

Well below T_N, in the zero-temperature limit, the excitations out of the antiferromagnetically ordered ground state of eq. (2) are spin waves. Neglecting interlayer coupling, conventional spin-wave theory in the classical (large-S) limit predicts a dynamic susceptibility (as measured by inelastic neutron scattering) of the form

$$\chi''(\boldsymbol{Q}, \omega) = Z_\chi \pi g^2 \mu_B^2 S \left(\frac{1 - \gamma(\boldsymbol{Q})}{1 + \gamma(\boldsymbol{Q})} \right)^{1/2} \delta(\hbar\omega \pm \hbar\omega(\boldsymbol{Q})), \tag{3}$$

where

$$\hbar\omega(\boldsymbol{Q}) = 2J_{\|} \left[1 - \gamma^2(\boldsymbol{Q}) \right] \tag{4}$$

and $\gamma(\boldsymbol{Q}) = \cos(\pi h)\cos(\pi l)$. Equation (3) includes a parameter, Z_χ, which reflects the renormalization of the magnetic response compared to the classical theory due to the fact that S is not large and the Néel state is not a good approximation of the ground state. There is also a renormalization of the energy scale of the spin waves such that the exchange constant deduced from measurements of the spin-wave dispersion relation, $J_{\|}^*$, is related to that appearing in eq. (2) via $J_{\|}^* = Z_c J$. In the case of the $S = \frac{1}{2}$ square-lattice antiferromagnet Singh (1989) and Igarashi (1992a,b) have estimated $Z_c = 1.18$ and $Z_\chi = 0.51$ based on a $1/S$ expansion. Since neutron scattering measures only the effective dispersion, it cannot be used to determine Z_c. However, by placing intensity measurements on an absolute scale, Z_χ can be measured directly.

Initial attempts to measure the spin waves in La_2CuO_4 were frustrated by the very large value of the exchange constant $J_{\|}$, a consequence of the strong superexchange path between Cu^{2+} ions via the planar O. This implies that the slope of the dispersion relation, or spin-wave velocity, is very steep compared to magnetic systems typically studied using thermal neutron, triple-axis spectroscopy. For energy transfers below ~50 meV, which are easily accessed by a reactor-based, thermal neutron instrument the two counter-propagating spin-wave modes emerging from an antiferromagnetic reciprocal lattice point are not sufficiently well separated in momentum space to be resolved due to the finite instrumental resolution. For this reason, measurements such as those shown in fig. 3 were only able to place a lower bound on the spin-wave velocity (and, hence, exchange constant $J_{\|}$) of >400 meV Å (Shirane et al. 1987, Endoh et al. 1988, Yamada et al. 1989). In order to access energy transfers large enough to separately resolve the spin waves, an intense source of high-energy neutrons, such as that available at the "hot source" at the Institut Laue–Langevin, is required. A "hot source" consists of a block of graphite that is heated to a temperature much above the ambient temperature of the heavy water that acts a moderator for most of the neutrons. The neutrons that come to thermal equilibrium within the hot source have a Maxwellian distribution characterised by a temperature of 2000 K, as opposed to 300 K for the reactors thermalized in the

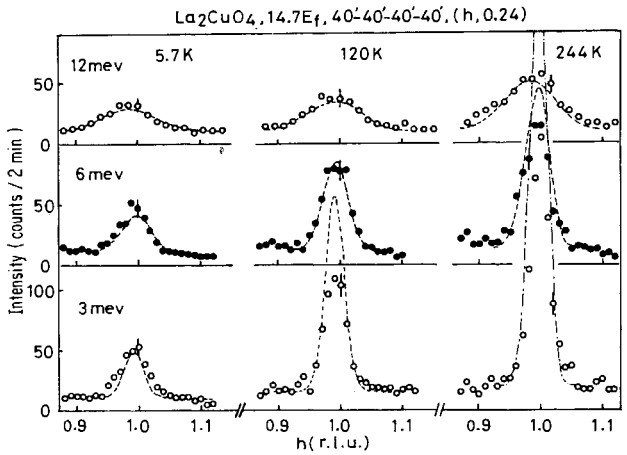

Fig. 3. Thermal triple-axis constant-energy-transfer scans through the antiferromagnetic zone center, (100), at selected temperatures below T_N, for La_2CuO_4. The dashed lines show fits to conventional spin wave theory convolved with the spectrometer resolution. In all cases, the observed peaks are unable to resolve the counter-propagating spin wave modes. This type of measurement can only place a lower bound (650 meV Å) on the spin-wave velocity. From Yamada et al. (1989).

heavy water. By allowing measurements to higher energy transfers the spin-wave velocity can be unambiguously determined from the location of resolved spin-wave peaks in constant-energy scans (see fig. 4) (Aeppli et al. 1989, Hayden et al. 1990). In order to fully determine the parameters of the magnetic Hamiltonian that describes the excitations in La_2CuO_4, it is necessary to measure spin-wave excitations throughout the Brillouin zone. This can only be done using the special characteristics of a spallation neutron source that has a spectrum of undermoderated neutrons extending beyond the thermal and hot range. Figure 5 shows the zone-boundary magnon for La_2CuO_4 measured on the HET spectrometer at ISIS along with the full dispersion relation obtained from the HET and IN1 measurements (Hayden et al. 1991b). In addition to determining the exchange constant, $J_{\|}^{*} = 153 \pm 4$ meV (corresponding to a J of 135 meV), these measurements, via the ratio of the zone-boundary magnon energy to the spin-wave velocity (850 meV Å), place an upper bound on the next-nearest-neighbour exchange constant at 9 meV. In addition, the width of observed zone-boundary magnon places a lower bound on the spin-wave lifetime of 9.3×10^{-13} s.

More recent measurements of the spin waves in La_2CuO_4 over the full Brillouin zone have been placed on an absolute scale (Hayden et al. 1996a, 1998; see also sect. 4.1.2), allowing a determination of the quantum renormalization of the magnetic response. Quantitative analysis of the intensity of the spin-wave response yields an estimate of $Z_\chi = 0.39 \pm 0.1$, in reasonable agreement with the calculation of Igarashi (1992a,b). Taken together, the inelastic neutron scattering studies of La_2CuO_4 provide a quantitative verification of the applicability of renormalized spin-wave theory and a determination of the parameters of the magnetic Hamiltonian (eqs. 2–4) that describes this material.

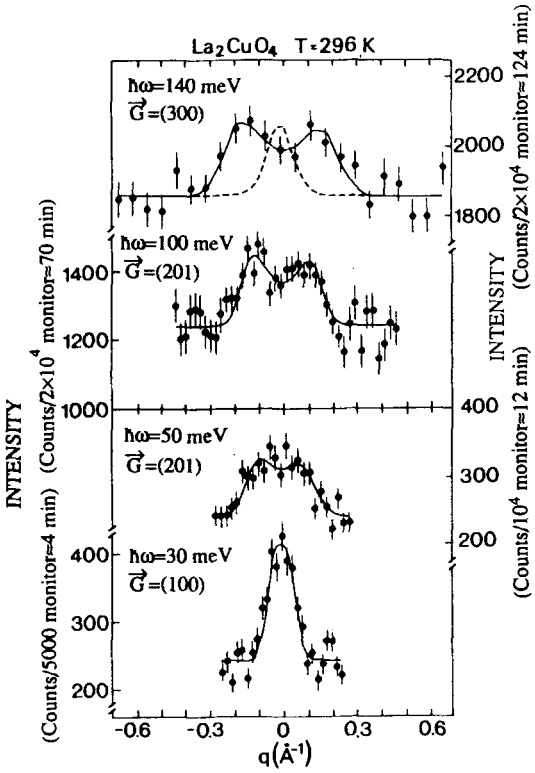

Fig. 4. Constant-energy scans through the counter-propagating spin wave modes of La_2CuO_4. Using higher-energy neutrons available at a "hot source", it is possible to measure the spin waves at frequencies where the two branches emerging from (100) and equivalent positions are separable, allowing a determination of the spin wave velocity. The dashed line in the upper scan shows the resolution-limited response, while the solid curves are the results of fits to a resolution-convolved spin wave spectrum with a velocity of 850 meV Å. From Hayden et al. (1990).

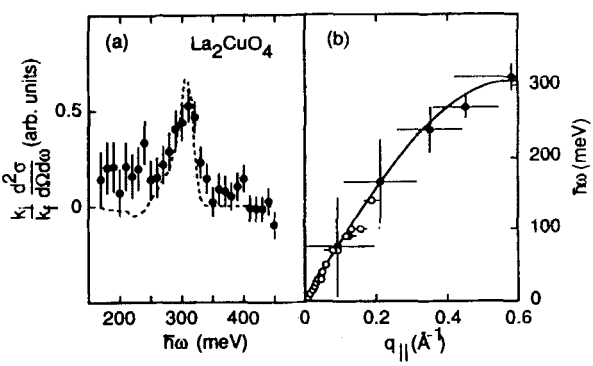

Fig. 5. Zone-boundary magnon and spin wave dispersion of La_2CuO_4. Spallation neutron sources have sufficient undermoderated epithermal neutrons to permit measurements with incident neutron energies up to 2 eV, making it possible to access high enough energy transfer to observe the zone-boundary magnon mode in La_2CuO_4 (panel a) at 312 meV. The time-of-flight data obtained on HET at ISIS (solid circles) combined with the triple-axis measurements shown in fig. 4 (open circles) were used to determine the full dispersion relation for the spin waves (panel b). From Hayden et al. (1991b).

The spin dynamics of La_2CuO_4 are not dramatically affected by the Néel transition, a reflection of the fact that there are quite long-range 2D correlations in the paramagnetic state (see below). The three-dimensional ordering is driven by the weak inter-layer coupling and has little effect on the intra-layer dynamics for energies comparable to J^* beyond introducing a modest 3.6±2.9 meV damping (at 320 K, Hayden et al. 1990). At low (<5 meV) energies, there is a manifestation of the transition to the paramagnetic state in the form of an additional, quasielastic contribution to the cross-section which has a width of 1.5±0.4 meV, in good agreement with expectations (Grempel 1988). This contribution is due to spin-wave interactions and is also consistent with numerical simulations (Tyc et al. 1989). For energies $\hbar\omega \geqslant \hbar c\xi^{-1}$, renormalized spin-wave theory gives an excellent account of the dynamics, even in the paramagnetic state.

2.1.2. *Paramagnetic critical scattering*

The properties of a magnetic system close to an instability such as an antiferromagnetic ordering transition are characterised by divergences in various physical properties. Neutron scattering can access several of the important parameters through the energy-integrated cross-section, or critical scattering, which is proportional to the Fourier transform of the instantaneous spin–spin correlation function (for a detailed discussion see Collins 1989). Of course, one can numerically integrate the measured inelastic cross-sections described in sect. 2.1.1; however, this is not as efficient as performing the energy integration experimentally by detecting scattered neutrons without energy analysis. This is accomplished on a triple-axis spectrometer by operating in the two-axis mode, without an analyser crystal. Two-axis mode will measure the desired energy-integrated cross-section only if the variation in momentum transfer for varying final energy can be neglected, the so-called static approximation. For a two-dimensional system, this can be assured by choosing the experimental geometry such that the final wavevector of the scattered neutrons is perpendicular to the planes (in this case the cross-section is integrated at constant in-plane wavevector; Birgeneau et al. 1977). This geometry is typically employed in studies of the critical scattering in high-T_c cuprates. Provided the incident neutron energy is high enough to span the range of important energy transfers, the instantaneous spin correlations are probed. Proper integration is an important consideration for La_2CuO_4 given the large exchange energy; calculations based on the cross-section expected for pure La_2CuO_4 suggest there is not a problem in this case or for lightly doped cuprates using conventional techniques (Keimer et al. 1992). The measured neutron intensity is typically a Lorentzian centered on the ordering wavevector, (100) or (π,π), with a height proportional to the staggered susceptibility and width proportional to the inverse correlation length. Figure 6 shows results obtained above T_N for La_2CuO_4 by Keimer et al. (1992).

Aside from a region of temperature extremely close to the 3D phase transition, the antiferromagnetic correlations in La_2CuO_4 are essentially two-dimensional in character due to the very large anisotropy in the magnetic interactions in the Hamiltonian (eq. 2). The $\boldsymbol{Q}$-dependent static susceptibility of the 2D $S=\frac{1}{2}$ Heisenberg antiferromagnet has

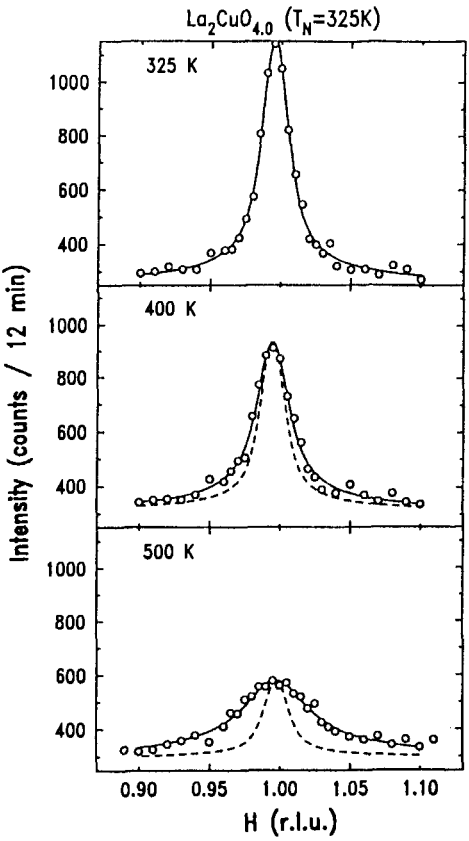

Fig. 6. Paramagnetic critical scattering in La_2CuO_4. Energy-integrating scans across the two-dimensional rod of scattering measure the Fourier transform of the instantaneous spin–spin correlation function in La_2CuO_4 above T_N. The peak width (corrected for finite instrumental resolution) is the inverse correlation length for antiferromagnetic spin fluctuations. The dashed lines show the experimental resolution function, and the solid lines are the results of fits to a Lorentzian lineshape convolved with the resolution for three different temperatures. From Keimer et al. (1992).

been treated in detail by Chakravarty et al. (1989) and Hasenfratz and Niedermayer (1991). In the regime governed by the antiferromagnetic instability (the renormalized classical region), the temperature dependence of the correlation length is determined by the exchange interaction according to the expression

$$\frac{\xi}{a} = 0.493 e^{1.15J/T}\left[1 - 0.43\left(\frac{T}{J}\right) + O\left(\frac{T}{J}\right)^2\right]. \tag{5}$$

Figure 7 shows a comparison between this prediction and the measured inverse correlation length for La_2CuO_4 between T_N and 800 K (Birgeneau et al. 1995). The value of J extracted from the low-temperature spin-wave measurements is used in the comparison so there are no adjustable parameters. There is very good agreement over the range of temperatures probed with the renormalized classical predictions, perhaps to a greater extent than might be expected based on the range over which the theory is likely to be valid. Additional studies on another realisation of the spin-$\frac{1}{2}$ 2D Heisenberg

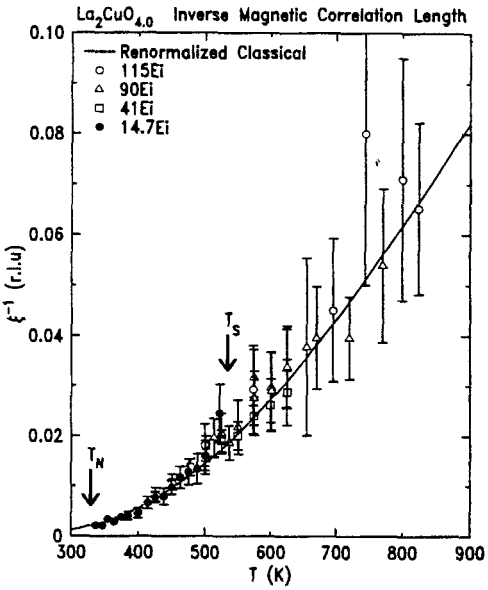

Fig. 7. Inverse correlation length extracted from fits to two-axis, energy-integrating scans through the antiferromagnetic position (see fig. 6). The line is the result of a fit to the renormalized classical theory described in the text. From Birgeneau et al. (1995).

antiferromagnet with a smaller J have covered an even wider range of T/J and found similar good agreement (Greven et al. 1994, 1995). There is also no evidence for a cross-over to a quantum-critical regime as suggested based on the NMR measurements of Imai et al. (1993). Somewhat perplexingly, given the excellent agreement for the correlation length, the temperature dependence of the staggered susceptibility (peak intensity) is described by $S(0) \sim \xi^2$, not the expected $S(0) \sim \xi^2 T^2$.

2.2. *Lightly doped* $La_{2-x}(Sr,Ba)_xCuO_4$

Doping La_2CuO_4 by replacing La with Sr or Ba introduces holes in the CuO_2 planes, eventually leading to an insulator–metal transition and a superconducting ground state. In addition to the changes in the charge transport, the low-energy magnetic properties are modified by these impurities. The Néel temperature is rapidly suppressed by introduction of these impurities due to the frustration associated with a hole that substitutes a ferromagnetic bond for an antiferromagnetic one. Beyond $x \approx 0.015$ there is no longer a long-range ordered antiferromagnetic state at low temperatures. The range $0.015 \leqslant x \leqslant 0.05$ is characterised by carrier localization below ~100 K and two-dimensional spin glass freezing (Harshman et al. 1988, Sternlieb et al. 1990). Despite the absence of long-range order at these intermediate doping levels, there are still strong antiferromagnetic correlations as evidenced by peaks in the energy-integrated neutron cross-sections at the same position, (π,π), as in undoped La_2CuO_4 (Keimer et al. 1992). Qualitatively, the results are similar to those described in sect. 2.1.2 for the paramagnetic state of La_2CuO_4, although the inverse correlation length does not vanish:

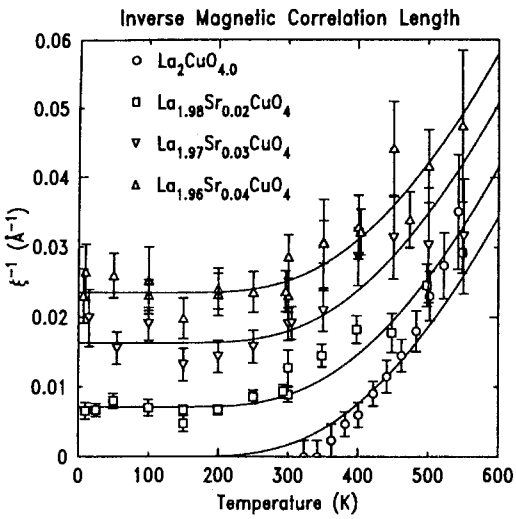

Fig. 8. Inverse magnetic correlation length for antiferromagnetic spin fluctuations in lightly doped $La_{2-x}Sr_xCuO_4$. The lines are based on a simple model in which the zero-temperature limit of κ is governed by the doping, and the temperature dependence is derived from the renormalized classical expression (eq. 5). From Keimer et al. (1992).

the decrease that occurs on cooling saturates at a doping-dependent value (see fig. 8). The increase in κ with temperature follows the same renormalized classical form (eq. 5) as the undoped material, leading to a simple description where the antiferromagnetic correlations in $La_{2-x}Sr_xCuO_4$ are characterised by an inverse correlation length that varies as $\kappa(x,T)=\kappa(x,0)+\kappa(0,T)$, with $\kappa(x,0)$ varying as $\left(a/\sqrt{x}\right)^{-1}$ and $\kappa(0,T)$ following the Hasenfratz–Niedermayer expression. The form of the zero-temperature inverse correlation length implies that the growth of correlations is limited by the mean spacing between impurities.

The shorter characteristic length scale associated with lightly doped La_2CuO_4 is also seen in the magnetic dynamics. As the energy transfer is increased, scans at constant energy remain centered on the (π,π) position with a width that is always broader than the instrumental resolution (Hayden et al. 1991a). The width, an inverse length scale characteristic of times $\sim 1/\omega$, increases linearly with energy transfer. This occurs much more rapidly than would be seen if the velocity of propagation were the same as spin waves in La_2CuO_4: there is a softening to approximately 60% of this value for the $La_{1.95}Ba_{0.05}CuO_4$ sample studied by Hayden et al. (1991a). The momentum dependence is not significantly modified by raising the temperature to above the spin-glass transition and beyond. The energy dependence of the local ($\boldsymbol{Q}$-integrated) susceptibility is sensitive to temperature at low energies. Figure 9 shows some data extracted from constant-$\boldsymbol{Q}$ scans (which are a good measure of the $\boldsymbol{Q}$-integrated cross-section over the limited range of ω probed) which are well described by the form

$$\chi_0''(\omega) = A\tan^{-1}\left(\frac{\omega}{\Gamma}\right). \tag{6}$$

Above the cross-over from localized to conducting transport ($T \approx 50\,\mathrm{K}$), the inverse lifetime Γ satisfies $\Gamma \sim T$. This implies that the spin dynamics exhibit ω/T scaling, a result

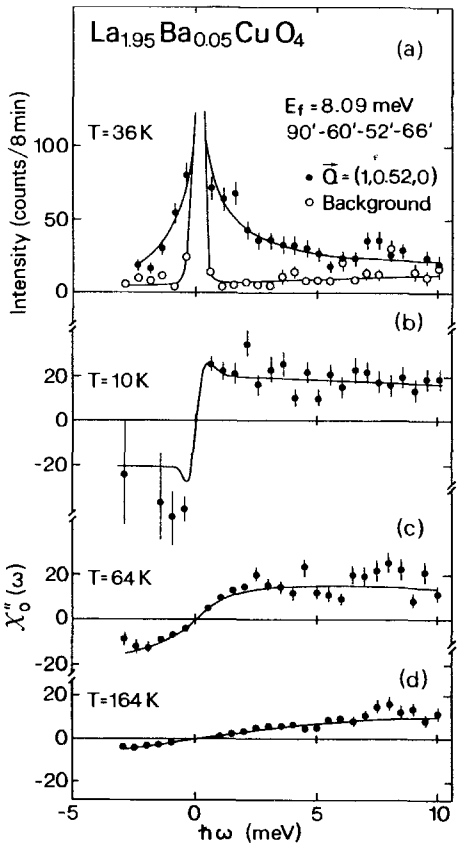

Fig. 9. Constant-Q scans at various temperatures for $La_{1.95}Sr_{0.05}CuO_4$. Panel (a) shows the intensity at a 2D antiferromagnetic wave vector and displaced away in reciprocal space, to provide a measure of the background. Panels (b)–(d) show the measured energy-dependent response obtained by correcting the raw data for the background and thermal factor. The lines are fits to the single-site response discussed in the text. From Hayden et al. (1991a).

also found by Keimer et al. (1991, 1992) where the inclusion of data at low temperatures, below which logarithmic resistivity is seen, necessitates the inclusion of a higher-order, ω/T^3, term. This sort of scaling form for the imaginary generalised susceptibility is consistent with the marginal Fermi liquid hypothesis which has been used to account for many of the anomalous normal-state properties of the cuprates (Varma et al. 1989). The overall form taken by the temperature evolution of $\chi''(\boldsymbol{Q},\omega)$ indicates that the relaxation rate probed by Cu NMR is driven by the inverse lifetime, Γ, not by the correlation length, ξ, as derived from scaling arguments (Millis et al. 1990).

2.3. *Antiferromagnetism in $YBa_2Cu_3O_{6+x}$*

The $YBa_2Cu_3O_{6+x}$ system is the most extensively studied of all of the families of high-temperature superconductors, and has also been the topic of ongoing examination by inelastic neutron scattering. In this material, the antiferromagnetically ordered parent compound is $YBa_2Cu_3O_6$. Superconductivity occurs when holes are introduced into the

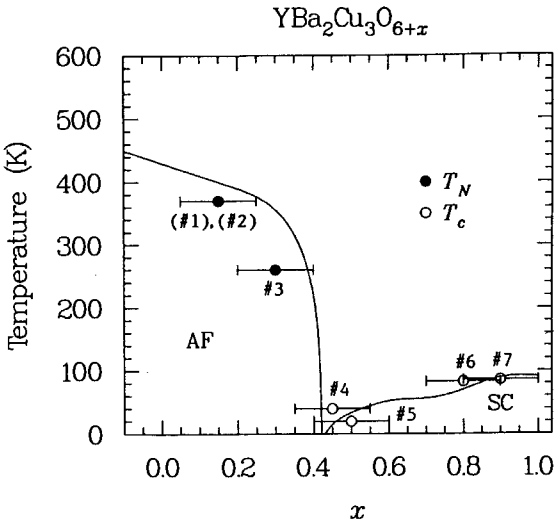

Fig. 10. Phase diagram of $YBa_2Cu_3O_{6+x}$ showing the doping dependence of the antiferromagnetic and superconducting transitions. From Tranquada et al. (1989).

CuO_2 planes by adding additional oxygen. The rough phase diagram in fig. 10 shows the suppression of T_N and the onset of superconductivity which occurs for $x \approx 0.45$.

The magnetic dynamics of the Cu^{2+} moments in insulating $YBa_2Cu_3O_{7-x}$ are governed by the same Hamiltonian as La_2CuO_4(eq. 2). The principal difference has its origin in one of the distinguishing structural features of $YBa_2Cu_3O_{6+x}$, the CuO_2 bilayers. The close spacing of the CuO_2 planes in a bilayer (3.2 Å) gives rise to an inter-layer, intra-bilayer coupling ($J_\perp \neq 0$). The inter-bilayer coupling is much smaller and can be neglected. The presence of the second term in the Hamiltonian leads to two branches in the spin-wave dispersion which differs according to whether spins in adjacent layers rotate in the same ("acoustic") or different ("optic") directions (Tranquada et al. 1989). The dynamical susceptibility for the acoustic mode is

$$\chi''_{ac}(\boldsymbol{Q},\omega) = Z_\chi \pi g^2 \mu_B^2 S \left(\frac{1-\gamma(\boldsymbol{Q})+J_\perp/J_\parallel}{1+\gamma(\boldsymbol{Q})}\right)^{1/2} \sin^2\left(\frac{\pi \Delta z l}{c}\right) \delta\left(\hbar\omega \pm \hbar\omega_{ac}(\boldsymbol{Q})\right), \tag{7}$$

and that for the optic mode is

$$\chi''_{op}(\boldsymbol{Q},\omega) = Z_\chi \pi g^2 \mu_B^2 S \left(\frac{1-\gamma(\boldsymbol{Q})}{1+\gamma(\boldsymbol{Q})+J_\perp/J_\parallel}\right)^{1/2} \cos^2\left(\frac{\pi \Delta z l}{c}\right) \delta\left(\hbar\omega \pm \hbar\omega_{op}(\boldsymbol{Q})\right). \tag{8}$$

The dispersion relations for the two modes are

$$\hbar\omega_{\substack{ac\\op}}(\boldsymbol{Q}) = 2J_\parallel \left\{1-\gamma^2(\boldsymbol{Q})+J_\perp/J_\parallel\,[1 \pm \gamma(\boldsymbol{Q})]\right\}^{1/2}, \tag{9}$$

where $\gamma(\boldsymbol{Q}) = \frac{1}{2}[\cos(2\pi h)+\cos(2\pi k)]$ and the separation of the CuO_2 planes in a bilayer, $\Delta z = 3.2$ Å (following conventional usage reciprocal space for $YBa_2Cu_3O_{6+x}$ is labelled

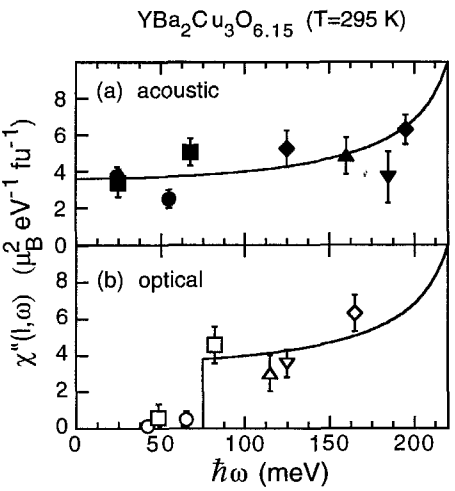

Fig. 11. Energy dependence of the local susceptibility of $YBa_2Cu_3O_{6.15}$ for the (a) acoustic and (b) optic spin-wave modes. The optic mode gap of 74 meV implies an inter-planar coupling of ~11 meV. From Hayden et al. (1998).

according to the tetragonal notation in which the antiferromagnetic ordering occurs at wavevectors related to $(\frac{1}{2},\frac{1}{2},l)$, equivalent to (π,π) in the notation of the 2D square lattice reciprocal space). The inter-planar coupling does not introduce any dispersion along the c-axis; however, the $\sin^2$ and $\cos^2$ modulations can be used to distinguish between the two modes (for a more detailed treatment of the spin-wave theory, including additional, smaller, terms in the Hamiltonian, see Tranquada et al. 1989).

The optic mode gap at the magnetic zone center has a magnitude given by $\hbar\omega_g = 2\sqrt{J_\perp J_\parallel}$, the inter-layer coupling is weak, but the intra-layer superexchange is comparable to the value found for La_2CuO_4. Due to the relatively large value of $J_\parallel$, initial studies of $YBa_2Cu_3O_{6+x}$ for antiferromagnetic compositions were not able to probe high enough frequencies to resolve the acoustic spin wave or observe the optic mode gap. Estimates of the in-plane antiferromagnetic exchange extracted from resolution-corrected fits to unresolved spin waves ranged from 80 meV to 200 meV (Rossat-Mignod et al. 1988, 1991, Tranquada et al. 1989, Shamoto et al. 1993). The high-energy spin waves in $YBa_2Cu_3O_{6.15}$ have now been resolved using the HET spectrometer (Hayden et al. 1996b, 1998) and yield a value of the exchange constant, $J_\parallel^* = 125\pm5$ meV, obtained from measurements of the spin waves throughout the Brillouin zone. This is consistent with the value extracted from the interpretation of two-magnon Raman scattering (Singh et al. 1989). The same experiment also determined the quantum renormalization of the spin-wave amplitude and found $Z_\chi = 0.4\pm0.1$, in agreement with the La_2CuO_4 data (Hayden et al. 1996a) and the $1/S$ expansion (Igarashi 1992a,b). The optic mode, corresponding to out-of-phase motion of spins in adjacent layers of a bilayer, has also been observed by both reactor-based (hot source) triple-axis (Reznik et al. 1996) and spallation source time-of-flight (Hayden et al. 1996b) techniques. Figure 11 shows the energy dependence of the local susceptibility for values of c-axis momentum transfer chosen to probe the acoustic and optic mode response. The observed gap energy of 74 ± 5 meV implies bilayer coupling

close to band-theory calculations (Anderson et al. 1995) but about twice as large as the values obtained for $Y_2Ba_4Cu_7O_{15}$ (Stern et al. 1995) and $Bi_2Sr_2Ca_2Cu_3O_{10}$ (Statt et al. 1997) using spin-echo double resonance (a nuclear magnetic resonance technique).

As was the case for La_2CuO_4, renormalized spin-wave theory gives a good description of the magnetic dynamics of antiferromagnetic $YBa_2Cu_3O_{6+x}$. The magnetic Hamiltonian for both compounds is the same (eq. 2) 2D spin-$\frac{1}{2}$ Heisenberg antiferromagnet. However, the bilayer nature of the $YBa_2Cu_3O_{6+x}$ structure introduces an additional energy scale into the problem that is manifested in the optic spin-wave modes. The exchange energy between nearest-neighbour spins within a CuO_2 plane is somewhat smaller than that found in La_2CuO_4, possibly reflecting the larger lattice constant. The coupling between layers in a bilayer is roughly 10% of the in-plane exchange.

3. Superconducting $La_{2-x}Sr_xCuO_4$

Doping the single-layer system $La_{2-x}Sr_xCuO_4$ to compositions where superconductivity occurs produces dramatic changes in the energy, momentum, and temperature dependence of the magnetic excitations. Although it does not possess a particularly high T_c at optimal doping (~39 K), it has been extensively studied because of the relative simplicity of its crystal structure, without bilayers and chains, and the availability of reasonable large single crystals (grown by the travelling solvent zone method) which exhibit bulk superconducting transitions with T_c values close to those observed in the best powder samples.

3.1. *Normal-state spin fluctuations*

The normal states of the metallic cuprates are, in many respects, as anomalous as their superconducting state. The spin fluctuations at low energies in $La_{2-x}Sr_xCuO_4$ undergo a qualitative change once the doping is sufficiently large to induce metallic behaviour at low temperatures. The mean impurity-spacing-limited, finite correlation length, antiferromagnetic response described in sect. 2.2 is replaced by an incommensurate magnetic structure which, for short time scales, has a much longer characteristic length.

3.1.1. *Low-energy incommensurate response*

The low-energy spin dynamics of $La_{2-x}Sr_xCuO_4$ undergo a qualitative change as the doping level exceeds that required to produce metallic conductivity (and, ultimately, superconductivity). The broad, commensurate response of the lightly doped compositions (see sect. 2.2) is replaced by an incommensurate response peaked at wavevectors displaced from the antiferromagnetic wavevector, (π,π). The first indications of this were observed for samples with $x=0.11$ and $x=0.15$ (Birgeneau et al. 1989, Shirane et al. 1989, Thurston et al. 1989). The limitations of sample size and quality prevented determination of the location of the peak response in the planar reciprocal lattice, the temperature dependence and effect of superconductivity, and the lack of interplanar correlations.

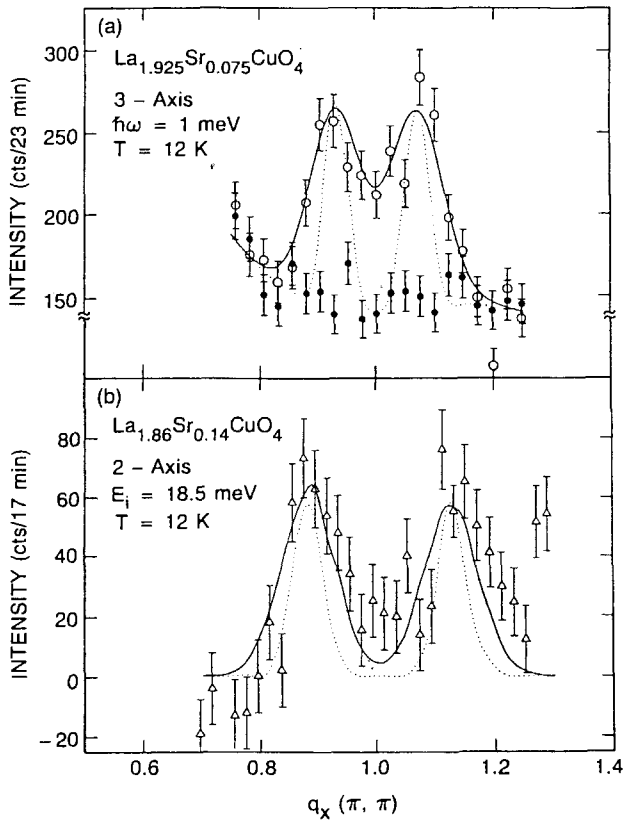

Fig. 12. Low-energy incommensurate magnetic response in metallic $La_{2-x}Sr_xCuO_4$ for two compositions ($x=0.075$ and $x=0.14$). The data are scans in momentum transfer through two of the four peaks that appear at $(\pi,\pi)\pm\delta(\pi,0)$ and $(\pi,\pi)\pm\delta(0,\pi)$. The upper panel is for an energy transfer of 1 meV, while the lower is energy-integrated using an incident neutron energy of 18.55 meV. From Cheong et al. (1991).

Later work by Cheong et al. (1991) showed that the magnetic response was peaked at wavevectors $(\pi,\pi)\pm\delta(\pi,0)$ and $(\pi,\pi)\pm\delta(0,\pi)$ in the notation of the 2D square reciprocal lattice (see fig. 12). The magnitude of the incommensuration, δ, scales approximately as $2\times$ and the intensity is rapidly suppressed as the temperature was raised to 100 K. In addition, superconductivity resulted in dramatic changes in the low-energy excitations described in sect. 3.2. The peaks are quite sharp in momentum space, indicating that on time scales comparable to the inverse of the frequencies probed (1–15 meV) the correlations exist over distances larger than the mean spacing between impurities which limits the static correlations in lightly doped $La_{2-x}Sr_xCuO_4$. The doping dependence of the incommensuration has been studied over a wider range of compositions by Petit et al. (1997) and Yamada et al. (1998). The dependence, shown in fig. 13, is similar to that of T_c (see fig. 2), although there are samples with no superconducting transition

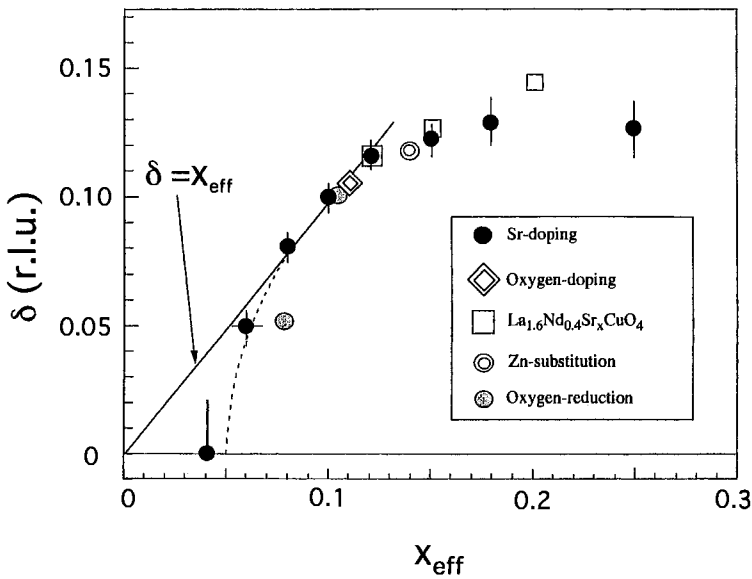

Fig. 13. Incommensurability, δ, of the spin fluctuations in $La_{2-x}Sr_xCuO_4$ and related systems, plotted as a function of the effective doping level. The magnitude of the incommensuration scales in roughly the same way as the superconducting transition temperature with doping. From Yamada et al. (1998). Note that the notation used to describe the location of the peaks in this figure (and the original reference) differs from that used in the text by a factor of 2.

that have an incommensurate response, indicating that it is not uniquely present in superconductors. Note that the notation used in fig. 13 and Yamada et al. (1998) is different from that of Petit et al. (1997) and Cheong et al. (1991); hence, the differing scale of the incommensuration, $\delta \sim x$: the data are all consistent. The most notable feature of the behaviour seen in fig. 13 is the abrupt change from commensurate to incommensurate fluctuations for $x \approx 0.06$, making it coincident with the metal–insulator transition. There is also a saturation of δ beyond optimal doping ($x = 0.14$–0.17). Full exploration of higher doping has been precluded by the increasing difficulty of growing homogeneous single crystals with $x > 0.2$.

The origin of incommensurate spin fluctuations occurring as a result of the introduction of holes into the CuO_2 planes of La_2CuO_4 can be explained by a variety of models. The fact that the incommensurate response develops abruptly as the metallic compositions are encountered suggests that it might be a manifestation of the Fermi surface. Incommensurate peaks in the dynamical susceptibility occur quite naturally for a 2D square lattice metal away from half filling and can be calculated on the basis of a tight-binding model of the band structure (Bulut et al. 1990, Bénard et al. 1993, Littlewood et al. 1993, Si et al. 1993, Tanamoto et al. 1994). This description has the virtue that it leads to a simple interpretation of the effects of superconductivity on the spin fluctuations. However, there is not yet detailed agreement between the experiments and

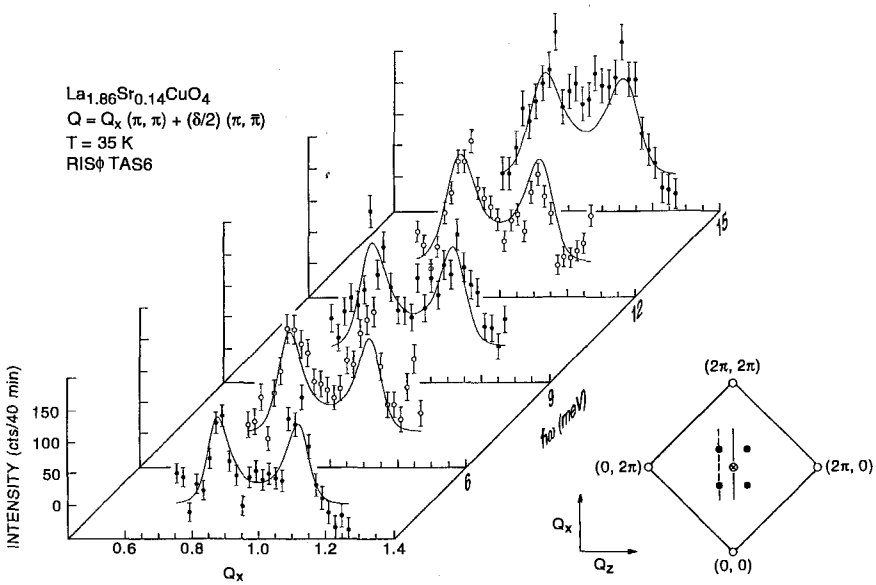

Fig. 14. Energy and momentum dependence of the incommensurate spin fluctuations in the normal state of $La_{1.86}Sr_{0.14}CuO_4$. The inset in the lower left shows the scan trajectory in the 2D square lattice momentum space (dashed line). The low-frequency incommensurate response broadens with increasing energy, merging into a broad commensurate feature as the energy is increased beyond ~15 meV. From Mason et al. (1992).

calculations in either the normal or superconducting state. An alternative view is that the incommensurate peaks are a consequence of commensurate antiferromagnetic correlations within stripes delineated by the ordering of the charged holes (Emery and Kivelson 1993, Zaanen and Gunnarsson 1989). Static charge and spin ordering of this type occurs in doped La_2NiO_4 and Nd-doped $La_{2-x}Sr_xCuO_4$ (for a recent review, see Tranquada 1998). For superconducting $La_{2-x}Sr_xCuO_4$ there is no static order, and attempts to observe charge peaks related to the incommensurate magnetic peaks have not been successful to date. However, the similar wavevector of the magnetic modulations in the ordered systems to the incommensurate peak positions in the superconducting compounds is suggestive. Descriptions taking the antiferromagnetic parent compound as a starting point and introducing frustration with the holes can also lead to incommensurate instabilities (Aharony et al. 1988, Shraiman and Siggia 1989).

The evolution of the incommensurate response as the energy is increased is summarised in fig. 14 which shows scans through two of the four incommensurate peaks in $La_{1.86}Sr_{0.14}CuO_4$ at 3.5, 6, 9, 12, and 15 meV at 35 K (just above T_c). The incommensurate peaks are well defined at lower energies but broaden with increasing energy; the scan at 15 meV no longer displays well-resolved incommensurate features. Qualitatively, this (E,Q) dependence is very similar to that observed in Cr and Cr alloys above the spin density wave (SDW) transition (Noakes et al. 1990). The lines in fig. 14 are the results of a fit to a functional form proposed by Sato and Maki (1974) to describe Cr (modified in

this case to take account of the two-dimensional nature of the incommensurate magnetism in $La_{2-x}Sr_xCuO_4$).

More recent results (Aeppli et al. 1997b) with better signal/noise and improved counting statistics have shown that this simple, mean-field, model is not sufficient to simultaneously describe the momentum and energy dependence of the spin fluctuation in the normal state of $La_{1.86}Sr_{0.14}CuO_4$. However, the general trend of the low-energy peaks to merge into a broad, flat-topped, commensurate response at higher energies (which also occurs in the Cr systems) is captured. Beyond ~25 meV, the incommensurate character of the magnetic response disappears (Petit et al. 1997), although the very interesting regime where this incommensurate–commensurate collapse occurs has not been extensively explored due to the presence of optical phonons, making unpolarized measurements unreliable. The high-energy response, which in many respects resembles that of La_2CuO_4, will be discussed in sect. 4.1.2. For energies below 15 meV, the spin dynamics are well described by a generalisation of the Sato and Maki (1974) form:

$$S(\boldsymbol{Q},\omega) = \frac{[n(\omega)+1]\cdot\chi''_{\mathrm{P}}(\omega,T)\cdot\kappa^4(\omega,T)}{\left[\kappa^2(\omega,T)+R(\boldsymbol{Q})\right]^2}, \tag{10}$$

where

$$R(\boldsymbol{Q}) = \frac{\left[\left(q_x-q_y\right)^2-(\pi\delta)^2\right]^2+\left[\left(q_x+q_y\right)^2-(\pi\delta)^2\right]^2}{2\left(2a_0\pi\delta\right)^2} \tag{11}$$

is a function, with the full symmetry of the reciprocal lattice and dimensions of $|\boldsymbol{Q}|^2$, which is positive except at zeroes, coinciding with the incommensurate peak positions. The parameters $\kappa(\omega,T)$ and $\chi''_{\mathrm{P}}(\omega,T)$ describe the frequency- and temperature-dependent inverse length scale and peak susceptibility, respectively. This form was chosen because it provided a good description of the data (when corrected for resolution effects) over a wide range of temperature (35–350 K) and energy (1–15 meV). In particular, the strong $1/q^4$ drop-off in intensity away from the incommensurate peaks is required to describe the lower-temperature data (a Lorentzian does not work). In addition, the shape of $R(\boldsymbol{Q})$ reproduces the tendency of the data to exhibit extra intensity between the incommensurate peaks, particularly as the energy (or temperature) is increased.

The results of this analysis are summarised in fig. 15 which shows the evolution of the inverse length scale $\kappa(\omega,T)$ plotted against temperature and energy added in quadrature for energies between 2.5 and 15 meV and temperatures between 35 and 350 K. All of the data follow the simple form

$$\kappa^2 = \kappa_0^2 + a_0^{-2}\left[(k_{\mathrm{B}}T/E_T)^2+(\hbar\omega/E\omega)^2\right]^{1/Z}, \tag{12}$$

where $Z=1$, κ_0=0.034 Å^{-1}, and $E_T=E_\omega=47$ meV (~$J/3$), shown as a solid line. The inset in the upper right of fig. 15 shows the variation of the low-frequency limit of $\chi''_{\mathrm{P}}/\omega$ with

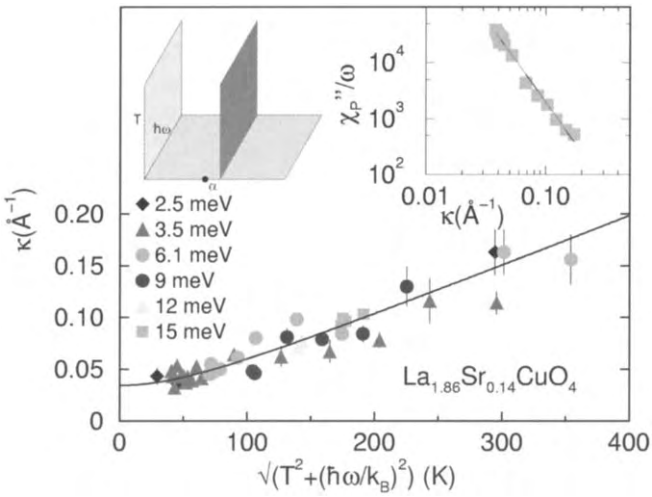

Fig. 15. Temperature dependence of the inverse length scale, $\kappa(\omega,T)$ at various fixed energy transfers plotted against temperature and energy, added in quadrature. The solid line corresponds to a $Z=1$ quantum-critical description of the data. The graph in the upper right shows the κ^{-3} variation of the peak incommensurate response. The schematic phase diagram in the upper left depicts a 3D phase space with a quantum-critical point at α. The experiments take place in the dark vertical plane slightly displaced in phase space from the critical point. From Aeppli et al. (1997b).

κ which obeys a power law $\kappa^{-\delta}$ with $\delta=3$. The (ω,T) scaling, dynamical exponent $Z=1$, and $\delta=(2-\eta+Z)/Z=3$, are all consistent with a system close to a magnetic instability – the Quantum Critical Point (QCP) of a 2D insulating magnet (Sachdev and Ye 1992, Chubukov et al. 1994, Millis 1993). The eventual saturation of κ at a finite value κ_0 in the zero T and ω limit implies an offset from the QCP in phase space, perhaps along the lines of the schematic representation in the upper left of the figure. The similarity of the wavevector of the dynamic incommensurate structure observed in $La_{2-x}Sr_xCuO_4$ to the static charge and spin ordering in compounds nearby in parameter space suggests stripe formation may be the driving mechanism. It has been proposed that this is an explanation for both the anomalous normal-state properties of the cuprate superconductors and the underlying origin of superconductivity (Castellani et al. 1998).

3.1.2. *Comparison of high-energy spin dynamics with La_2CuO_4*

The incommensurate fluctuations that typify the magnetic response of the metallic and superconducting compositions of $La_{2-x}Sr_xCuO_4$ are a low-energy feature, merging into a broad commensurate response above ~20 meV, similar to that seen in lightly doped insulating samples. Since the magnetic response of insulating $La_{2-x}Sr_xCuO_4$ extends over energies up to 320 meV one might expect a similar energy scale to be relevant in the superconducting compositions. This issue has been explored using the HET spectrometer at ISIS by Hayden et al. (1996a, 1998). Figure 16 shows a comparison of the energy and frequency dependence of the response in La_2CuO_4 and $La_{1.86}Sr_{0.14}CuO_4$ with the intensity

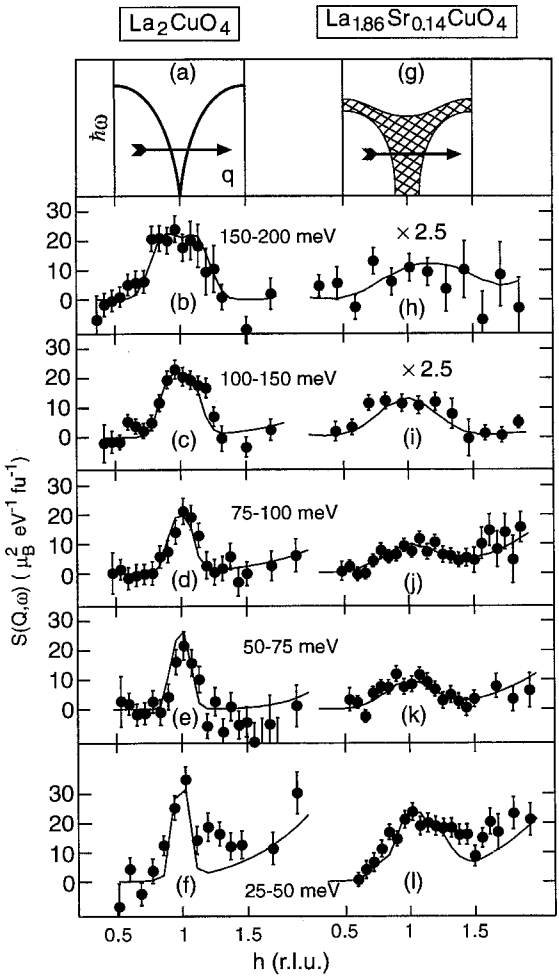

Fig. 16. Magnetic scattering from La_2CuO_4 (a–f) and from $La_{1.86}Sr_{0.14}CuO_4$ (g–l) between 25 and 200 meV. All scans are in the same absolute units. The overall energy scale in the two systems is comparable, but the magnetic peak is broader in the superconductor and the intensity is suppressed at higher frequencies. From Hayden et al. (1998).

units normalised to allow a detailed comparison. The schematic diagrams at the top of the figure give an impression of how the spectrum is modified by doping. The response emanating from the commensurate position is broader (reflecting shorter characteristic length scale) in momentum and falls off more rapidly with increasing frequency. The difference in the two spectra is most clear in the local susceptibility, obtained by integrating the response in momentum space. Figure 17 shows this comparison for the same two samples. The doped compound has spectral weight over the same large range of energies as the antiferromagnetic insulator, but there is a significant redistribution of spectral weight from high energy to a peak in the response at ~20–30 meV. In contrast, for the antiferromagnet the local susceptibility is peaked at the zone-boundary energy (not shown) due to the van Hove singularity in the spin-wave density of states. Interestingly,

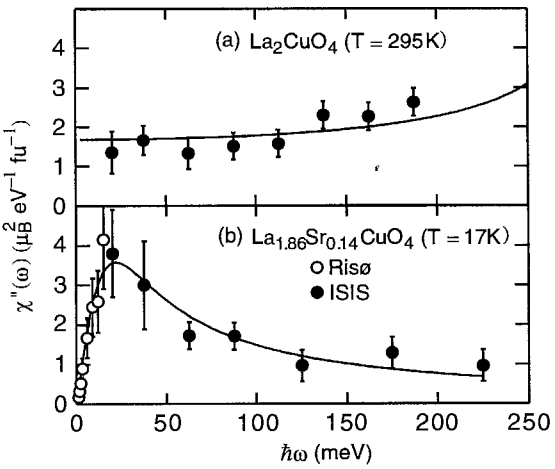

Fig. 17. Local ($\boldsymbol{Q}$-integrated) susceptibility for antiferromagnetic and superconducting $La_{2-x}Sr_xCuO_4$. The energies over which magnetic correlations exist are comparable for $x=0$ and $x=0.14$. However, the doped sample displays a low-energy peak in the spectrum at ~20–30 meV which is not present in the insulator (where the spectrum is maximum at the zone-boundary energy due to the van Hove singularity in the density of states). From Hayden et al. (1998).

the peak in the response in the $x=0.14$ sample occurs at the same energy that the incommensurate peaks merge into a broad commensurate feature.

3.2. *Superconductivity and the incommensurate spin fluctuations*

If the low-energy incommensurate peaks in $La_{2-x}Sr_xCuO_4$ can be thought of as arising from transitions across the Fermi surface in which a quasiparticle moves from an occupied to an unoccupied state, at the same time flipping its spin, then the superconducting transition should have a dramatic effect since such a particle–hole excitation will acquire a gap of 2Δ. In light of this it is perhaps not surprising that the low-energy spin fluctuations are suppressed by the onset of superconductivity. However, this simple physical picture ignores much of the complexity of the phenomena that were first observed by Mason et al. (1992). This effect has now been studied in detail for a number of superconducting samples. The effect of superconductivity on the incommensurate response is summarised in fig. 18, which shows both the low-energy suppression and the associated enhancement at somewhat higher frequencies. The cross-over between suppression and enhancement may be thought of as a measure of the superconducting gap (actually twice the gap) at the wavevectors connected by the Q probed in the simple picture. For the incommensurate wavevector this energy is 7 meV. Closer scrutiny of the data reveals more subtle behaviour than might be expected on the basis of the non-interacting Fermi surface particle–hole analogy. For a start, the suppression of the low-energy excitations is not complete for the 6.1 meV data shown in fig. 18, (the same is true down to 1.5 meV) – in a clean conventional superconductor there should be no particle–hole excitations below 2Δ. The size of the residual low-energy response is sample dependent, ranging from nearly 100% of the normal state response in samples with deliberately introduced Zn impurities (Matsuda et al. 1992) to nearly total suppression for higher-quality samples (Yamada et al. 1995), suggesting an impurity-induced low-energy response in the superconducting

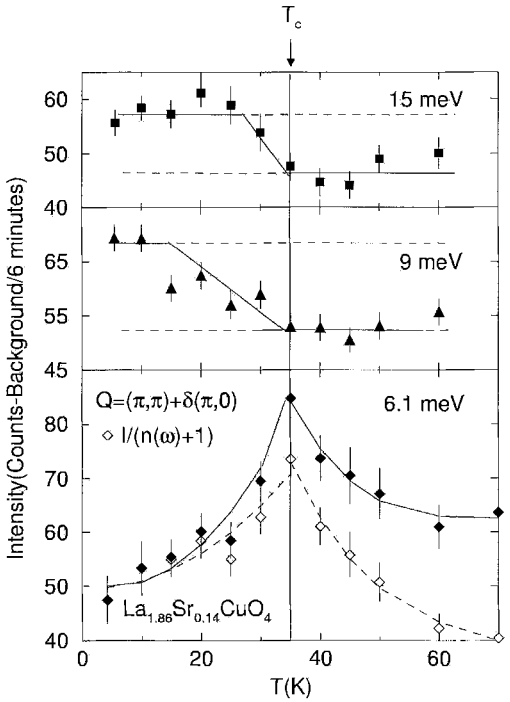

Fig. 18. Temperature dependence of the incommensurate magnetic response in $La_{1.86}Sr_{0.14}CuO_4$ for 6.1, 9, and 15 meV energy transfer. For energies below 7 meV, the spin fluctuations are suppressed, while above that energy, they are enhanced, in the superconducting state. From Mason et al. (1996).

state. Of course, a response at low energies does occur in a d-wave superconductor and therefore might well be expected in a high-T_c material. However, the calculations based on a d-wave order parameter predict a modification of the wavevector dependence of the low-energy response (Zha et al. 1993) which has not been observed (Mason et al. 1993). Another feature of the data which has not been accounted for theoretically is the fact that the enhancement below T_c for energies above 7 meV is restricted to a very narrow region of $\boldsymbol{Q}$ near the incommensurate peak, essentially limited by spectrometer resolution. This implies a very long coherence length, in excess of 50 Å, which is greater than any length scale present in the normal state.

4. Superconducting $YBa_2Cu_3O_{7-x}$

The initial measurements of the low-energy spin fluctuations in $YBa_2Cu_3O_{7-x}$ for samples with oxygen content beyond the $x\sim0.5$ required for superconductivity revealed a peak, centered on the commensurate (π,π) position, which is considerably broader in momentum than in insulating compositions (Tranquada et al. 1990, Chou et al. 1991, Rossat-Mignod et al. 1988, 1991). The evolution of the normal-state commensurate response as the doping is increased beyond $x=0.5$ is summarized in fig. 19: the general trend of a shift in the characteristic energy of the scattering and overall decrease in

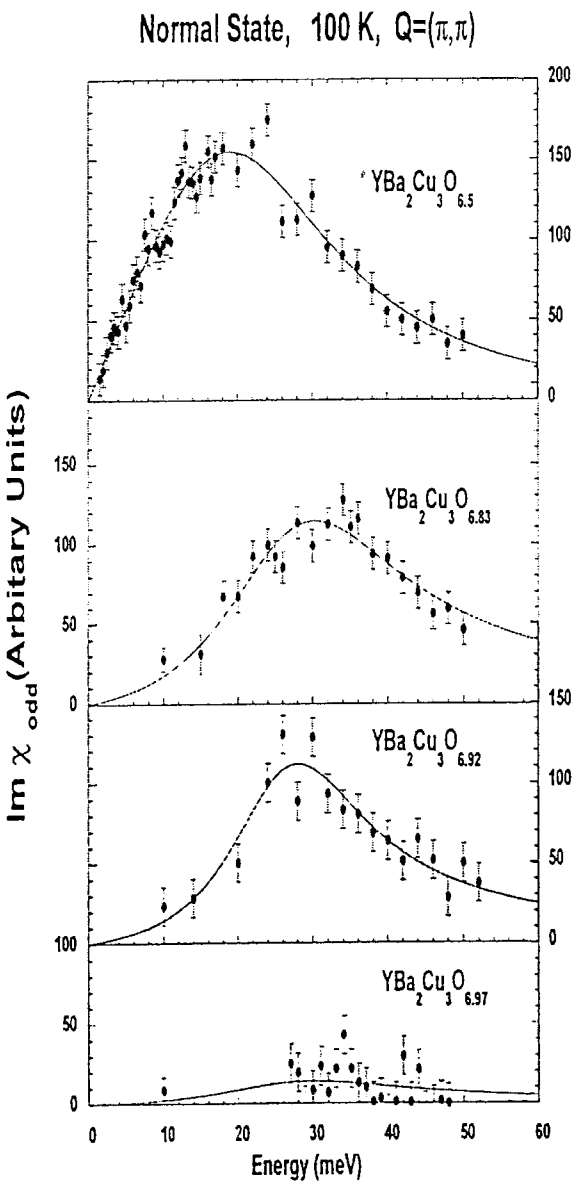

Fig. 19. Low-energy, commensurate [$\boldsymbol{Q}=(\pi,\pi)$, acoustic mode] response in the normal state of four different compositions of $YBa_2Cu_3O_{7-x}$ measured at 100 K. As the doping is increased the feature at (π,π) broadens and weakens, and there is very little normal state response at the commensurate position for the overdoped sample. From Bourges (1998).

intensity as the peak smears out in Q-space makes the measurements increasingly difficult – to the point that for overdoped samples the (π,π) response is barely observable.

The c-axis modulation due to the bilayer coupling which leads to an optic and acoustic mode in the spin-wave cross-section for antiferromagnetically ordered samples is also

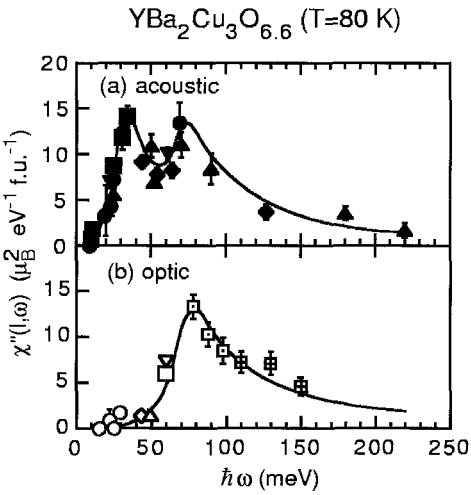

Fig. 20. Normal-state local (Q-integrated) response for $YBa_2Cu_3O_{6.6}$ as a function of energy transfer. The energy gap associated with the optical mode is comparable to that observed for the spin waves in antiferromagnetic, insulating $YBa_2Cu_3O_{6.15}$. From Hayden et al. (1998).

present for the fluctuations in metallic samples. As was the case for the spin waves discussed in sect. 2.3, the low-energy response is the acoustic mode, peaked at the c-axis wavevector that corresponds to a π phase shift within a bilayer. By selecting the c-axis momentum transfer, the acoustic and optic response can be probed separately, giving a determination of the optic gap, 43 meV, comparable to the spin-wave gap for the optic mode (Hayden et al. 1998, Reznik et al. 1996). Figure 20 summarizes this result for $x = 0.4$, showing the local (Q-integrated) susceptibility up to 200 meV (similar results have been obtained for $x = 0.5$ (Bourges 1998); including the unexplained second peak in the acoustic response at the same energy as the peak in the optic spectrum). The most striking feature of the data shown in fig. 20 is the significant difference in overall energy variation and the absolute intensity compared to that of fig. 11 for the spin waves in a sample with $x = 0.85$. There is a shift in spectral weight to lower frequencies in the metallic sample.

4.1. *Low-energy incommensurate response*

The fact that initial measurements of the inelastic magnetic response of superconducting compositions of $YBa_2Cu_3O_{7-x}$ found only a broad commensurate peak at low energies (in contrast to the incommensurate response found in $La_{2-x}Sr_xCuO_4$) was interpreted as arising from differences in the Fermi surface geometry of the two compounds (Si et al. 1993). There were indications that the Q-dependence of the cross-section for underdoped $YBa_2Cu_3O_{7-x}$ was better described in terms of unresolved incommensurate peaks, manifested as a flat-topped peak at (π,π) which was not well described by a single Gaussian (Sternlieb et al. 1994). More recently Dai et al. (1999) have shown for a sample with $x = 0.4$ (the same one as used for the data shown in fig. 20) a clear incommensurate response. Improvements to the HET spectrometer at ISIS, in the form of an array of position-sensitive detectors at low angles, have allowed a complete mapping of the incommensurate structure (see fig. 21). This feature is only visible at low temperatures ($T = 13$ K and 65 K for the data shown) and energies below ~30 meV, as was the case for

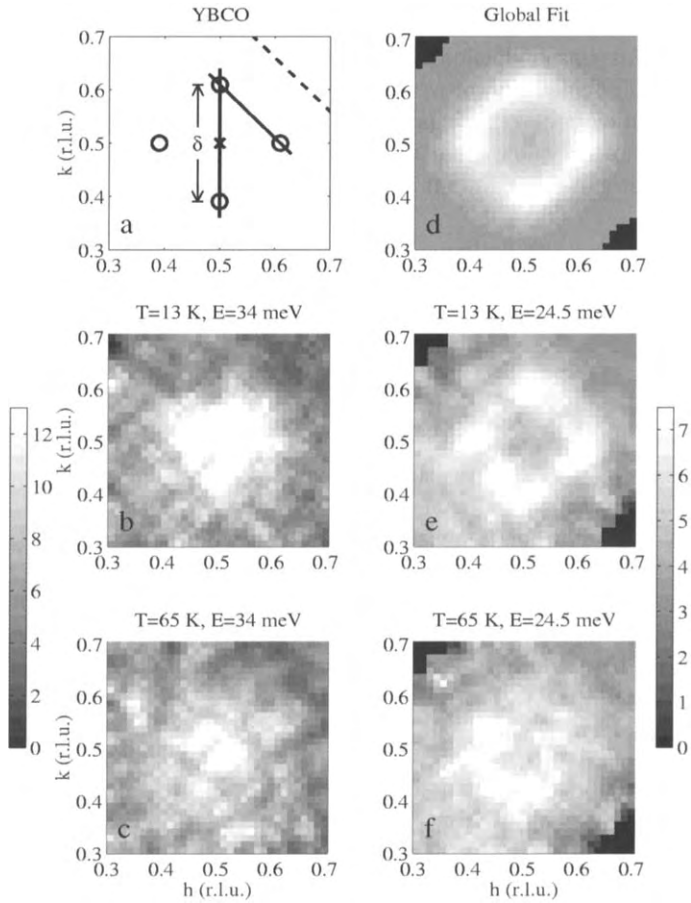

Fig. 21. Images of the magnetic scattering from $YBa_2Cu_3O_{6.6}$ above and below T_c at 34 and 24.5 meV in the two-dimensional reciprocal space of the CuO_2 planes. At the lower energy (e,f) an incommensurate response, described by the model shown in (d), appears at the positions noted in the schematic map (a). The resonance that appears at the (π,π) position (b,c) in the superconducting state is described in sect. 4.2. From Mook et al. (1998a).

$La_{2-x}Sr_xCuO_4$. Its emergence is not connected with the superconducting transition but is simply a sharpening as the temperature is lowered. The locations of the peaks are the same as for equivalently hole-doped $La_{1.9}Sr_{0.1}CuO_4$ (Mook et al. 1998a).

The discovery that the low-energy spin fluctuations in $YBa_2Cu_3O_{7-x}$, at least for underdoped samples, have the same incommensurate structure as $La_{2-x}Sr_xCuO_4$ suggests that this is a universal feature of high-T_c materials. It is also consistent with current understanding of the Fermi surface topology in both systems (see ch. 201). How the incommensuration evolves as the oxygen content is increased towards optimal-doped requires the type of detailed comparative study that has been carried out for $La_{2-x}Sr_xCuO_4$

(Yamada et al. 1998). The superconducting transition results in both a sharpening of the incommensurate peaks and an elimination of the lowest-energy fluctuations; identical behaviour is found in nearly optimally doped $La_{1.86}Sr_{0.14}CuO_4$(Mason et al. 1996).

4.2. *The (π,π) resonance*

Much of the interest in inelastic neutron scattering from high-temperature superconductors has been focussed on the dramatic effects below T_c often referred to as the resonance peak. Rossat-Mignod et al. (1991) first observed a sharp, intense peak at (π,π) that appeared below T_c in optimally doped 123. The detailed energy dependence was complicated by the presence of phonons, nearby in energy and momentum. The magnetic origin of the 41 meV resonance was confirmed for $x=0.07$ by Mook et al. (1993) using polarized neutrons (see fig. 22). This allowed the magnetic and lattice contributions to be separated and verified that the dominant feature in the magnetic

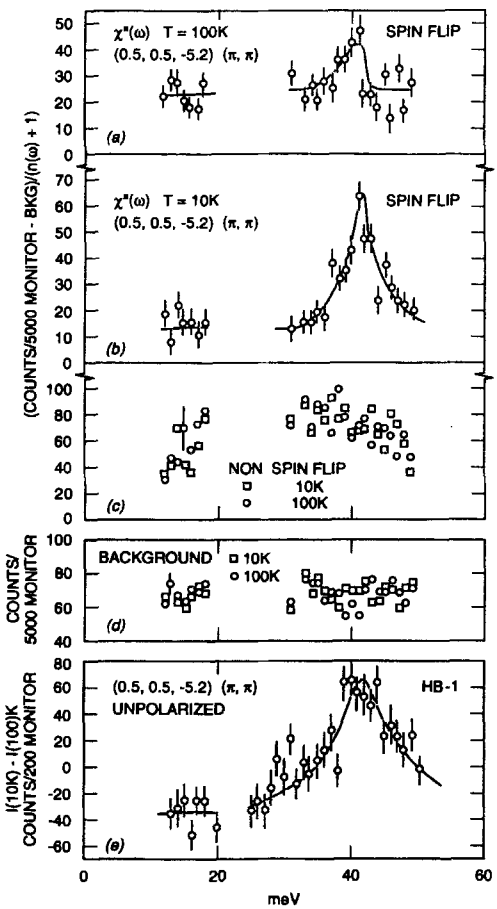

Fig. 22. Polarized-beam measurements of the magnetic excitations in $YBa_2Cu_3O_7$ confirming the magnetic origin of the resonance feature that appears at the (π,π) position at 41 meV below T_c. From Mook et al. (1993).

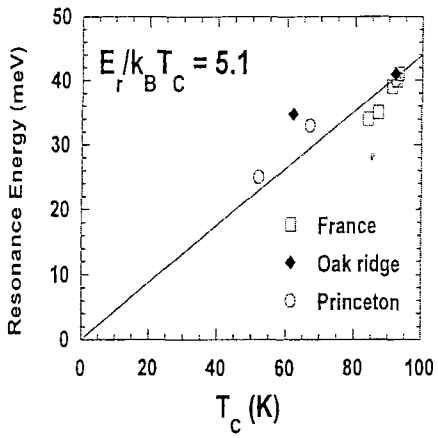

Fig. 23. Variation of the (π,π) resonance energy with superconducting transition temperature, T_c. From Bourges (1998).

response of the superconducting state was a sharp (in energy) peak at 41 meV, centered on the commensurate, (π,π), position. As the oxygen content is decreased the energy of the resonance peak decreases, following the same trend as the superconducting transition temperature. For $x = 0.4$ the resonance energy has been reduced to 34 meV; the overall variation with T_c is summarized in fig. 23.

There is a clear anomaly in the temperature dependence at the superconducting transition, with an abrupt jump in intensity above the level of a weaker normal-state response. The existence of a weak normal-state feature was disputed (see Fong et al. 1995); however, the different measurements were not performed on samples with the same oxygen content. The general trend of the normal-state response shown in fig. 19 indicates a gradual elimination of the intensity at (π,π) in the normal state as the oxygen content is increased beyond optimal doping (x 0.07).

For underdoped samples, where the normal-state intensity is quite significant, the presence of a peak at essentially the same energy as the resonance above T_c is clear (see fig. 24). The growth in the intensity at the resonance energy begins well above T_c although there is a rapid increase, and an associated reduction in energy width, which occurs just below T_c. The size of the peak in the normal state is reduced as the oxygen content is increased, and the temperature at which it becomes apparent is also reduced (this onset temperature appears to track the pseudo gap feature seen by NMR) (Dai et al. 1999).

There are a variety of theoretical descriptions of the origin of the (π,π) resonance, ranging from a superconducting coherence effect which occurs in the framework of an itinerant-electron picture (Ohashi and Shiba 1993, Monthoux and Scalapino 1994, Lu 1992, Bulut and Scalapino 1996, Lavagna and Stemmann 1994, Onufrieva and Rossat-Mignod 1995, Liu et al. 1995) to a collective mode associated with a multicomponent, SO(5), order parameter (Zhang 1997). In almost all descriptions of the resonance peak it is a direct consequence of the d-wave symmetry of the order parameter.

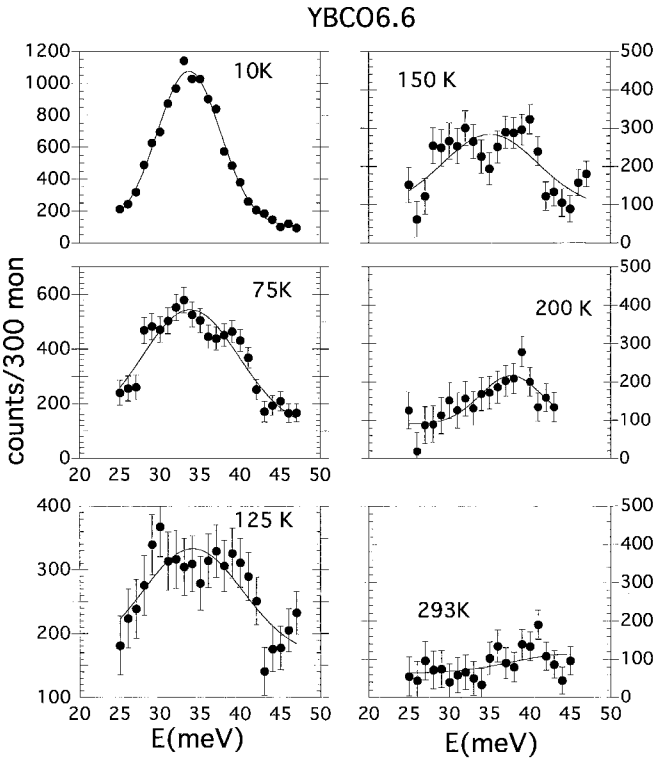

Fig. 24. Temperature dependence of the 35 meV resonance in $YBa_2Cu_3O_{6.6}$ with temperature. A broadened response at (π,π) persists in the normal state for underdoped compositions. From Mook et al. (1998b).

In many cases, however, the existence of a resonance above the superconducting transition poses a challenge.

5. Conclusions

The experimental difficulties posed by the large energy scale, weak spin-$\frac{1}{2}$ cross-section, and (for metallic samples) short characteristic length scale in high-temperature superconductors has necessitated advances in the state of the art in inelastic neutron scattering in order to develop an overall picture of the important features. The improved capabilities of neutron instrumentation, together with significant advances in crystal growth, particularly of large, high-quality crystals needed for this type of work, have led to a fairly consistent picture of spin fluctuations in the cuprates. Generally, when measurements on the same compounds (at the same doping level) exist, there is good agreement between different groups. The importance of these measurements to the field of high-temperature superconductivity as a whole relies on the special characteristics of

the neutron as a probe. It is the only technique which permits measurements of spin dynamics at finite momentum, with good energy and $\boldsymbol{Q}$ resolution.

The antiferromagnetically ordered insulators are well described by conventional spin-wave theory. The destruction of long-range antiferromagnetic order with doping leads to novel scaling behaviour, in a spectrum which is still reminiscent of the spin waves. Metallic cuprates have a low-energy response that is incommensurate and qualitatively quite different from the insulators. Furthermore, it is greatly affected by the superconducting transition. At higher energies the changes are much less dramatic as a function of doping and temperature. All of these features are shared by both families that have been extensively studied, $La_{2-x}Sr_xCuO_4$ and $YBa_2Cu_3O_{7-x}$. The one outstanding difference is the (π,π) resonance which has only been seen in $YBa_2Cu_3O_{7-x}$. A search for a commensurate resonance in $La_{2-x}Sr_xCuO_4$ is probably warranted given the otherwise similar picture which has emerged of the overall behaviour in comparison to $YBa_2Cu_3O_7$.

Acknowledgements

I would like to thank my colleagues for allowing me to reproduce figures, providing material prior to publication, and stimulating discussions. I would particularly like to thank my collaborators in experiments I have been involved in for their patience and guidance. The financial support received from the Natural Sciences and Engineering Research Council of Canada, the Canadian Institute for Advanced Research, and the Alfred P. Sloan Foundation is gratefully acknowledged. Work at Oak Ridge was supported by the US Department of Energy under Contract DE-AC05-00OR22725.

References

Aeppli, G., S.M. Hayden, H.A. Mook, Z. Fisk, S.-W. Cheong, D. Rytz, J.P. Remeika, G.P. Espinosa and A.S. Cooper, 1989, Phys. Rev. Lett. **62**, 2052.

Aeppli, G., S.M. Hayden and T.G. Perring, 1997a, Physics World **33**(December), 33.

Aeppli, G., T.E. Mason, S.M. Hayden, H.A. Mook and J. Kulda, 1997b, Science **278**, 1432.

Aharony, A., R.J. Birgeneau, A. Coniglio, M.A. Kastner and H.E. Stanley, 1988, Phys. Rev. Lett. **60**, 1330.

Anderson, O.K., A.I. Liechtenstein, O. Jepsen and F. Paulsen, 1995, J. Phys. Chem. Solids **56**, 1573.

Bénard, P., L. Chen and A.-M.S. Tremblay, 1993, Phys. Rev. B **47**, 15217.

Birgeneau, R.J., J. Als-Nielsen and G. Shirane, 1977, Phys. Rev. B **16**, 280.

Birgeneau, R.J., Y. Endoh, K. Kakurai, Y. Hidaka, T. Murakami, M.A. Kastner, T.R. Thurston, G. Shirane and K. Yamada, 1989, Phys. Rev. B **39**, 2868.

Birgeneau, R.J., A. Aharony, N.R. Belk, F.C. Chou, Y. Endoh, M. Greven, S. Hosoya, M.A. Kastner, C.H. Lee, Y.S. Lee, G. Shirane, S. Wakimoto, B.O. Wells and K. Yamada, 1995, J. Phys. Chem. Solids **56**, 1913.

Bourges, Ph., 1998, in: The Gap Symmetry and Fluctuations in High Temperature Superconductors, eds J. Bok, G. Deutscher and D. Pavuna (Plenum Press, Cambridge) pp. 349–371.

Bulut, N., and D.J. Scalapino, 1996, Phys. Rev. B **53**, 5149.

Bulut, N., D. Hone, D.J. Scalapino and N.E. Bickers, 1990, Phys. Rev. Lett. **64**, 2723.

Castellani, C., C. Di Castro and M. Grilli, 1998, J. Phys. Chem. Solids **59**, 1694.

Chakravarty, S., B.I. Halperin and D.R. Nelson, 1989, Phys. Rev. B **39**, 2344.

Cheong, S.-W., G. Aeppli, T.E. Mason, H.A. Mook, S.M. Hayden, P.C. Canfield, Z. Fisk, K.N. Clausen and J.L. Martinez, 1991, Phys. Rev. Lett. **67**, 1791.

Chou, H., J.M. Tranquada, G. Shirane, T.E. Mason, W.J.L. Buyers, S. Shamoto and M. Sato, 1991, Phys. Rev. B **43**, 8690.

Chubukov, A., S. Sachdev and J. Ye, 1994, Phys. Rev. B **49**, 11919.

Collins, M.F., 1989, Magnetic Critical Scattering (Oxford University Press, Oxford).

Dai, P., H.A. Mook, S.M. Hayden, G. Aeppli, T.G. Perring, R.D. Hunt and F. Dogan, 1999, Science **284**, 1344.

Emery, V.J., and S.A. Kivelson, 1993, Physica C **209**, 597.

Endoh, Y., K. Yamada, R.J. Birgeneau, D.R. Gabbe, H.P. Jenssen, M.A. Kastner, C.J. Peters, P.J. Picone, T.R. Thurston, J.M. Tranquada, G. Shirane, Y. Hidaka, M. Oda, Y. Enomoto, M. Suzuki and T. Murakami, 1988, Phys. Rev. B **37**, 7443.

Fong, H.F., B. Keimer, P.W. Anderson, D. Rezmik, F. Dogan and I.A. Aksay, 1995, Phys. Rev. Lett. **75**, 316.

Grempel, D.R., 1988, Phys. Rev. Lett. **61**, 1041.

Greven, M., R.J. Birgeneau, Y. Endoh, M.A. Kastner, B. Keimer, M. Matsuda, G. Shirane and T.R. Thurston, 1994, Phys. Rev. Lett. **72**, 1096.

Greven, M., R.J. Birgeneau, Y. Endoh, M.A. Kastner, M. Matsuda and G. Shirane, 1995, Z. Phys. B **96**, 465.

Harshman, D.R., G. Aeppli, G.P. Espinosa, A.S. Cooper, J.P. Remeika, E.J. Ansaldo, T.M. Riseman, D.Ll. Williams, D.R. Noakes, B. Ellman and T.F. Rosenbaum, 1988, Phys. Rev. B **38**, 852.

Hasenfratz, P., and F. Niedermayer, 1991, Phys. Lett. **268**, 231.

Hayden, S.M., G. Aeppli, H.A. Mook, S.-W. Cheong and Z. Fisk, 1990, Phys. Rev. B **42**, 10220.

Hayden, S.M., G. Aeppli, H.A. Mook, D. Rytz, M.F. Hundley and Z. Fisk, 1991a, Phys. Rev. Lett. **66**, 821.

Hayden, S.M., G. Aeppli, R. Osborn, A.D. Taylor, T.G. Perring, S.-W. Cheong and Z. Fisk, 1991b, Phys. Rev. Lett. **67**, 3622.

Hayden, S.M., G. Aeppli, H.A. Mook, T.G. Perring, T.E. Mason, S.-W. Cheong and Z. Fisk, 1996a, Phys. Rev. Lett. **76**, 1344.

Hayden, S.M., G. Aeppli, T.G. Perring, H.A. Mook and F. Dogan, 1996b, Phys. Rev. B **54**, R6905.

Hayden, S.M., G. Aeppli, P. Dai, H.A. Mook, T.G. Perring, S.-W. Cheong, Z. Fisk, F. Dogan and T.E. Mason, 1998, Physica B **241–243**, 765.

Igarashi, J., 1992a, Phys. Rev. B **46**, 10763.

Igarashi, J., 1992b, J. Phys.: Condens. Matter **4**, 10265.

Imai, T., C.P. Slichter, K. Yoshimara, M. Katoh and K. Kosuge, 1993, Phys. Rev. Lett. **71**, 1254.

Ivanov, A.S., Ph. Bourges, D. Petitgrand and J. Rossat-Mignod, 1995, Physica B **213–214**, 60.

Johnston, D.C., J.P. Stokes, D.P. Goshorn and J.T. Lewandowski, 1987, Phys. Rev. B **36**, 4007.

Kastner, M.A., R.J. Birgeneau, T.R. Thurston, P.J. Picone, H.P. Jenssen, D.R. Gabbe, M. Sato, K. Fukuda, S. Shamoto, Y. Endoh, K. Yamada and G. Shirane, 1988, Phys. Rev. B **38**, 6636.

Keimer, B., R.J. Birgeneau, A. Cassanho, Y. Endoh, R.W. Erwin, M.A. Kastner and G. Shirane, 1991, Phys. Rev. Lett. **67**, 1930.

Keimer, B., N.R. Belk, R.J. Birgeneau, A. Cassanho, C.Y. Chen, M. Greven, M.A. Kastner, A. Aharony, Y. Endoh, R.W. Erwin and G. Shirane, 1992, Phys. Rev. B **46**, 14034.

Lavagna, M., and G. Stemmann, 1994, Phys. Rev. B **49**, 4235.

Littlewood, P.B., J. Zaanen, G. Aeppli and H. Monien, 1993, Phys. Rev. B **48**, 487.

Liu, D.Z., Y. Zha and K. Levin, 1995, Phys. Rev. Lett. **75**, 4130.

Lovesey, S.W., 1984, Theory of Neutron Scattering from Condensed Matter (Clarendon Press, Oxford).

Lu, J.P., 1992, Phys. Rev. Lett. **68**, 125.

Mason, T.E., G. Aeppli and H.A. Mook, 1992, Phys. Rev. Lett. **68**, 1414.

Mason, T.E., G. Aeppli, S.M. Hayden, A.P. Ramirez and H.A. Mook, 1993, Phys. Rev. Lett. **71**, 919.

Mason, T.E., A. Schröder, G. Aeppli, H.A. Mook and S.M. Hayden, 1996, Phys. Rev. Lett. **77**, 1604.

Matsuda, M., Y. Endoh, K. Yamada, H. Kojima, I. Tanaka, R.J. Birgeneau, M.A. Kastner and G. Shirane, 1992, Phys. Rev. B **45**, 12548.

Matsuda, M., K. Kuroda, K. Yamada, Y. Endoh, H. Chou, G. Shirane, R.J. Birgeneau, M.A. Kastner, I. Tanaka and H. Kojima, 1993, J. Appl. Phys. **73**, 6333.

Millis, A.J., 1993, Phys. Rev. B **48**, 7183.

Millis, A.J., H. Monien and D. Pines, 1990, Phys. Rev. B **42**, 167.

Mitsuda, S., G. Shirane, S.K. Sinha, D.C. Johnston, M.S. Alvarez, D. Vaknin and D.E. Moncton, 1987, Phys. Rev. B **36**, 822.

Monthoux, P., and D.J. Scalapino, 1994, Phys. Rev. Lett. **72**, 2131.

Mook, H.A., M. Yethiraj, G. Aeppli, T.E. Mason and T. Armstrong, 1993, Phys. Rev. Lett. **70**, 3490.

Mook, H.A., P. Dai, S.M. Hayden, G. Aeppli, T.G. Perring and F. Dogan, 1998a, Nature **395**, 580.

Mook, H.A., P. Dai, R.D. Hunt and F. Dogan, 1998b, J. Phys. Chem. Solids **59**, 2140.

Noakes, D.R., T.M. Holden, E. Fawcett and P.C. Decamargo, 1990, Phys. Rev. Lett. **65**, 369.

Ohashi, Y., and H. Shiba, 1993, J. Phys. Soc. Jpn. **62**, 2783.

Onufrieva, F., and J. Rossat-Mignod, 1995, Phys. Rev. B **52**, 7572.

Petit, S., A.H. Moudden, B. Hennion, A. Vietkin and A. Revcolevschi, 1997, Physica B **234–236**, 800.

Reznik, D., Ph. Bourges, H.F. Fong, L.P. Regnault, J. Bossy, C. Vettier, D.L. Milius, I.A. Aksay and B. Keimer, 1996, Phys. Rev. B **53**, R14741.

Rossat-Mignod, J., P. Burlet, M.J. Jurgens, C. Vettier, L.P. Regnault, J.Y. Henry, C. Ayache, L. Forro, H. Noel, M. Potel, P. Gougeon and J.C. Levet, 1988, J. Phys. (Paris) Colloq. 49, C8–2119.

Rossat-Mignod, J., L.P. Regnault, D. Vettier, P. Burlet, J.Y. Henry and G. Lapertot, 1991, Physica B **169**, 58.

Sachdev, S., and J. Ye, 1992, Phys. Rev. Lett. **69**, 2411.

Sato, H., and K. Maki, 1974, Int. J. Magn. **6**, 183.

Shamoto, S., M. Sato, J.M. Tranquada, B.J. Sternlieb and G. Shirane, 1993, Phys. Rev. B **48**, 13817.

Shirane, G., Y. Endoh, R.J. Birgeneau, M.A. Kastner, Y. Hidaka, M. Oda, M. Suzuki and T. Murakami, 1987, Phys. Rev. Lett. **59**, 1613.

Shirane, G., R.J. Birgeneau, Y. Endoh, P.M. Gehring, M.A. Kastner, K. Kitazawa, H. Kojima, I. Tanaka, T.R. Thurston and K. Yamada, 1989, Phys. Rev. Lett. **63**, 330.

Shraiman, B.I., and E.I. Siggia, 1989, Phys. Rev. Lett. **62**, 1564.

Si, Q., Y. Zha, K. Levin, J.P. Lu and J.H. Kim, 1993, Phys. Rev. B **47**, 9055.

Singh, R.R.P., 1989, Phys. Rev. B **39**, 9760.

Singh, R.R.P., P.A. Fleury, K.B. Lyons and P.E. Sulewski, 1989, Phys. Rev. Lett. **62**, 2736.

Squires, G.L., 1978, Introduction to the Theory of Thermal Neutron Scattering (Cambridge University Press, Cambridge).

Statt, B.W., L.M. Song and C.E. Bird, 1997, Phys. Rev. B **55**, 11122.

Stern, R., M. Mali, J. Roos and D. Brinkmann, 1995, Phys. Rev. B **52**, 15734.

Sternlieb, B.J., G.M. Luke, Y.J. Uemura, T.M. Riseman, J.H. Brewer, P.M. Gehring, K. Yamada, Y. Hidaka, T. Murakami, T.R. Thurston and R.J. Birgeneau, 1990, Phys. Rev. B **41**, 8866.

Sternlieb, B.J., J.M. Tranquada, G. Shirane, S. Shamoto and M. Sato, 1994, Phys. Rev. B **50**, 12915.

Tanamoto, T., H. Kohno and H. Fukuyama, 1994, J. Phys. Soc. Jpn. **63**, 2739.

Thurston, T.R., R.J. Birgeneau, M.A. Kastner, N.W. Preyer, G. Shirane, Y. Fuji, K. Yamada, Y. Endoh, K. Kakurai, M. Matsuda, Y. Hidaka and T. Murakami, 1989, Phys. Rev. B **40**, 4585.

Tranquada, J.M., 1998, J. Phys. Chem. Solids **59**, 2150.

Tranquada, J.M., G. Shirane, B. Keimer, S. Shamoto and M. Sato, 1989, Phys. Rev. B **40**, 4503.

Tranquada, J.M., W.J.L. Buyers, H. Chou, T.E. Mason, M. Sato, S. Shamoto and G. Shirane, 1990, Phys. Rev. Lett. **64**, 800.

Tyc, S., B.I. Halperin and S. Chakravarty, 1989, **62**, 835.

Vaknin, D., S.K. Sinha, D.E. Moncton, D.C. Johnston, J.M. Newsam, C.R. Safinya and H.E. King, 1987, Phys. Rev. Lett. **58**, 2802.

Varma, C.M., P.B. Littlewood, S. Schmitt-Rink, E. Abrahams and A.E. Ruckenstein, 1989, Phys. Rev. Lett. **63**, 1996.

Yamada, K., K. Kakurai, Y. Endoh, T.R. Thurston, M.A. Kastner, R.J. Birgeneau, G. Shirane, Y. Hidaka and T. Murakami, 1989, Phys. Rev. B **40**, 4557.

Yamada, K., S. Wakimoto, G. Shirane, C.H. Lee, M.A. Kastner, S. Hosoya, M. Greven, Y. Endoh and R.J. Birgeneau, 1995, Phys. Rev. Lett. **75**, 1626.

Yamada, K., C.H. Lee, K. Kurahashi, J. Wada, S. Wakimoto, S. Ueki, H. Kimura, Y. Endoh, S. Hosoya, G. Shirane, R.J. Birgeneau, M. Greven, M.A. Kastner and Y.J. Kim, 1998, Phys. Rev. B **57**, 6165.

Zaanen, J., and O. Gunnarsson, 1989, Phys. Rev. B **40**, 7391.

Zha, Y., K. Levin and Q. Si, 1993, Phys. Rev. B **47**, 9124.

Zhang, S.-C., 1997, Science **275**, 1089.

Handbook on the Physics and Chemistry of Rare Earths
Vol. 31
edited by K.A. Gschneidner, Jr., L. Eyring and M.B. Maple

Chapter 199

NEUTRON SCATTERING STUDIES OF LANTHANIDE MAGNETIC ORDERING

J.W. LYNN
NIST Center for Neutron Research, National Institute of Standards and Technology, Gaithersburg, MD 20899, USA and Center for Superconductivity Research, Department of Physics, University of Maryland, College Park, MD 20742, USA

S. SKANTHAKUMAR
Chemistry Division, Argonne National Laboratory, Argonne, IL 60439, USA

Contents

List of symbols

1-2-3	$RBa_2Cu_3O_{6+x}$
2-4-8	$R_2Ba_4Cu_8O_{16}$
2-4-7	$R_2Ba_4Cu_7O_{15}$
2-1-4	$R_{2-x}Ce_xCuO_4$
2D	two-dimensional
3D	three-dimensional
A	average size of domain in the a–b layer
a, b, c	lattice parameters
C	instrumental constant for the calculation of neutron intensity
F_M	magnetic structure factor
$f(\tau)$	magnetic form factor
h, k, l	Miller indices of Bragg peaks
$I(\tau)$	neutron intensity at reciprocal lattice vector τ
$\boldsymbol{J}$	total angular momentum
J	exchange energy
J_{ab}	exchange interaction energy in the a–b plane
J_c	exchange interaction energy along the c-direction
k	Boltzmann constant
$\widehat{M}$	unit vector along the spin direction
$\boldsymbol{q}_m$	antiferromagnetic propagation vector
R	Lanthanide ion
RKKY	Ruderman–Kittel–Kasuya–Yosida

S	total spin momentum	λ	London penetration length
S_i	spin operator at site i	μ_B	Bohr magneton
T	temperature	$\langle \mu_z \rangle$	thermal average of the ordered magnetic moment
T_c	superconducting transition temperature		
T_N	antiferromagnetic ordering (Néel) temperature	ξ	superconducting coherence length
		$\boldsymbol{\tau}$	reciprocal lattice or scattering vector
t	reduced temperature $(1 - T/T_N)$	$\hat{\tau}$	unit vector along the reciprocal lattice vector $\boldsymbol{\tau}$
$\left(\frac{\gamma e^2}{2mc^2}\right)^2$	neutron–electron coupling constant, -0.27×10^{-12} cm		

1. Introduction

The effects of magnetic impurities and the possibility of magnetic ordering in superconductors have had a rich and interesting history (see the reviews by Maple 1976 and Fischer and Maple 1983). Magnetic impurities substituted into a superconductor were found to quickly suppress superconductivity due to the strong spin scattering that disrupts the Cooper pairs. Typically ~1% substitution was enough to completely extinguish the superconducting state, and such a low concentration of magnetic moments precludes the possibility of cooperative magnetic states forming and competing with the superconducting order parameter. The first exception to this behavior was realized for the $(Ce_{1-x}R_x)Ru_2$ system, where over 30% of non-magnetic Ce^{4+} could be replaced by the magnetic heavy lanthanides before superconductivity was suppressed. Strong ferromagnetic correlations were found to develop in the superconducting state, but no long-range order was present.

The first examples of true long-range magnetic order coexisting with superconductivity were provided by the ternary Chevrel-phase superconductors (RMo_6S_8) and related (RRh_4B_4) compounds (Fischer and Maple 1983). In these materials there is a separate, fully occupied lanthanide sublattice. The fact that these materials were superconducting at all implied that the magnetic ions and the superconducting electrons belonged to different, "isolated" sublattices, and thereby the conventional Abrikosov–Gorkov (1961) spin-depairing mechanism was suppressed. The magnetic ordering temperatures are all low, ~1 K, and thus it was argued that electromagnetic (dipolar) interactions should dominate the energetics of the magnetic system. For materials where these interactions favor antiferromagnetism the magnetization averages to zero on the length scale of a unit cell (a), which results in a weak influence on the superconducting state ($a \ll \xi, \lambda$). This is the most prevalent case found in nature, and apart from a few anomalies in properties such as the upper critical field, the antiferromagnetic order and superconductivity were found to readily accommodate one another. In the rare and more interesting situation where the magnetic interactions are ferromagnetic, there is strong coupling to the superconducting state that originates from the internally generated magnetic field. The competition with the superconducting order parameter gives rise to long wavelength oscillatory magnetic states and/or reentrant superconductivity; the neutron work has been

reviewed by Thomlinson et al. (1983), with some subsequent work (Lynn et al. 1984). The studies of these materials contributed greatly to our understanding of these two competing phenomena, but the possible role of exchange interactions in these systems, and the related question of how the dipolar interaction alone could be responsible for the antiferromagnetism in some materials while others (with the same crystal structure) are ferromagnets, remained unexplained.

The cuprate superconductors offer new and interesting perspectives into our understanding of "magnetic superconductors" for a number of reasons. In the materials typified by $RBa_2Cu_3O_{6+x}$ (1-2-3) and $R_2Ba_4Cu_8O_{16}$ (2-4-8), for example, the R ions appear to be electronically isolated from the Cu–O layers where the Cooper pairs form, similar to the ternary superconductors, and the low lanthanide ordering temperatures (~1 K) suggested that the cuprate superconductors were again prototypical "magnetic superconductors". They were also interesting because the layered crystal structure, with $c \approx 3a$, rendered them naturally two-dimensional (2D) in nature, and indeed some of the best 2D magnets known belong to this class of materials (see the review by Lynn 1992). However, there are also examples where the magnetic ordering temperature is much too high to be explained by dipolar interactions, and it has become clear that R–R exchange interactions actually must play a dominant role in the magnetism, as is also clearly the case for the new RNi_2B_2C class of superconductors (Lynn et al. 1997, Stassis and Goldman 1997). In contrast to the ternary superconductors, in the cuprates there is no clear separation of the lanthanide sublattice from the superconducting electrons. Moreover, one of the most interesting aspects of the cuprates concerns the magnetism associated with the Cu ions, which is the same sublattice where the superconducting pairing occurs. The undoped cuprates are antiferromagnetic insulators where the $S = \frac{1}{2}$ Cu spins order at high temperatures, typically near or above room temperature. The in-plane Cu exchange interactions are much stronger than along the c-axis, and thus again the magnetism is two-dimensional in nature. With doping, the materials lose the Cu long-range magnetic order and become high-T_c superconductors. However, the Cu moments and energetics are still present, and the essential role these quantum spin fluctuations play in the superconducting state is reviewed in ch. 198.

In the present chapter we review the neutron scattering investigations of the magnetic structures of the lanthanides in the cuprates. We start by discussing the tetragonal, single Cu–O layer electron-doped materials typified by $(Nd–Ce)_2CuO_4$. These are the simplest and best understood from a number of standpoints, but the lanthanide ions are clearly exchange coupled in these materials, and there is also an important coupling between the Cu and R moments. This is particularly evident when the Cu spins exhibit long-range order, and we will therefore briefly describe the nature of the Cu order as well, and its interaction with the lanthanide moments. We then discuss the 1-2-3- and 2-4-8-type layered materials, which often exhibit prototypical 2D behavior. Next we will turn to the behavior of the Pr ion in the cuprates, which is fundamentally different. In this case the 4f electrons hybridize with the conduction electrons, which results in Pr having the highest lanthanide ordering temperatures in this class of materials. This hybridization also typically extinguishes the superconductivity. Finally, we will summarize our overall

understanding of the lanthanide ordering in these materials, and briefly discuss future directions.

2. General trends

Before discussing the details of these materials, there are some general trends that should be noted. For the Cu spins, the central feature that controls many aspects of all the oxide materials is the strong copper–oxygen bonding, which results in a layered Cu–O crystal structure. In the undoped "parent" materials this strong bonding leads to an electrically insulating antiferromagnetic ground state. The exchange interactions within the layers are much stronger than between the layers, and typically an order-of-magnitude more energetic than the lattice dynamics. The associated spin dynamics and magnetic ordering of the Cu ions are thus driven by this two-dimensional nature. With electronic doping, long-range antiferromagnetic order for the Cu is suppressed as metallic behavior and then superconductivity appears, but strong antiferromagnetic spin correlations still persist in this regime. It is this large magnetic energy scale that is associated with the high superconducting transition temperature and exotic pairing, and these aspects are reviewed by Mason in ch. 198.

For the lanthanide magnetism, the overall behavior is quite different. In the single-layer R_2CuO_4 type materials the lanthanide exchange interactions are three-dimensional in nature, and typically the Cu and R systems exhibit relatively strong coupling. For the multi-layered materials, on the other hand, the distance along the stacking axis becomes quite large, and this physical separation renders the ordering two-dimensional in nature, but for very different reasons than for the Cu system. The R–Cu interactions also tend to be weaker and the lanthanide sublattice appears to be relatively isolated from the rest of the system, making them prototypical 2D magnets with low ordering temperatures.

In all of these systems, for both the Cu magnetic order as well as the lanthanide magnetic order, the spin structures are relatively simple commensurate antiferromagnetic configurations. In particular, no materials have been discovered yet that exhibit a net ferromagnetic component, with its associated macroscopic magnetization. By commensurate we mean that the antiferromagnetic unit cell is a simple integer multiple of the chemical unit cell. Within the Cu–O planes, for example, the nearest-neighbor spins have always been found to be antiparallel, and the spins always point along a common direction (i.e., they are collinear) within the a–b plane. However, there can be the complication that some of the structures are noncollinear, by which we mean that the direction of the spins between the layers is not necessarily along the same crystallographic direction. The added complication of having both Cu and R moments can then make the magnetism of these cuprates quite rich and interesting.

3. Single-layer systems

We start our discussion with the magnetic ordering in the electron-type R_2CuO_4 (2-1-4) materials. The basic crystal structure is tetragonal *I4/mmm* (T′ phase) in which the Cu

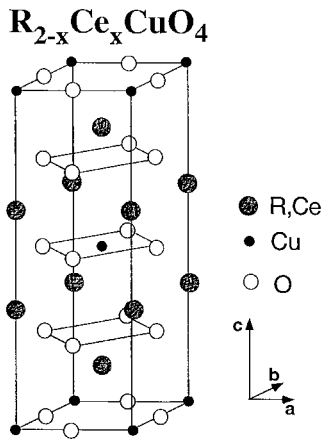

Fig. 1. T′ tetragonal crystal structure of the single Cu–O layer R_2CuO_4 system.

spins occupy a body-centered tetragonal (*bct*) lattice ($a \approx 3.91$ Å, $c \approx 11.9$ Å) as shown in fig. 1. The Cu–O bonding within the *a–b* plane results in strong exchange interactions within these layers, while the rare-earth ions form layers between these Cu–O planes. The Cu spins in the undoped ("parent") material are antiferromagnetically ordered and the material is insulating, while ~7.5% Ce or Th substituted onto the R site (R = Pr, Nd, Sm, Eu) gives the optimal doping for superconductivity, with $T_c \approx 25$ K. The phase diagrams as a function of doping for all of these cuprate materials are reviewed elsewhere in this Handbook (Maple 2000, Elschner and Loidl 2000). For the Cu spins the *c*-axis coupling is thus much weaker than the coupling in the *a–b* plane, giving rise to both two-dimensional magnetic properties and highly anisotropic superconducting behavior. Note, however, that the exchange interactions for both the Cu and R moments, as well as the superconducting order parameter, must be mediated through magnetically active layers.

When a material undergoes a transition from a paramagnet to a magnetically ordered state, new Bragg peaks develop that are associated with the long-range magnetic order. The positions of these new magnetic reciprocal lattice points $\boldsymbol{\tau}$ identify the magnetic configuration of the spins, while the size and spin direction of the moments can be determined from the intensities. For a simple collinear magnetic structure the neutron intensity is given by (Bacon 1975)

$$I(\boldsymbol{\tau}) = C\left(\frac{\gamma e^2}{2mc^2}\right)^2 \langle \mu_z \rangle^2 (f(\boldsymbol{\tau}))^2 |F_M|^2 \left\langle 1 - \left(\hat{\tau} \cdot \hat{M}\right)^2 \right\rangle, \tag{1}$$

where C is an instrumental constant, the quantity in large parentheses is the neutron–electron coupling constant (-0.27×10^{-12} cm), $\langle \mu_z \rangle$ is the thermal average of the ordered magnetic moment, $f(\boldsymbol{\tau})$ is the magnetic form factor (the Fourier transform of the atomic magnetization density), F_M is the magnetic structure factor, and $\hat{\tau}$ and $\hat{M}$ are unit vectors in the direction of the reciprocal lattice vector $\boldsymbol{\tau}$ and the spin direction, respectively. The orientation factor $\langle 1 - (\hat{\tau} \cdot \hat{M})^2 \rangle$ must be averaged over all possible

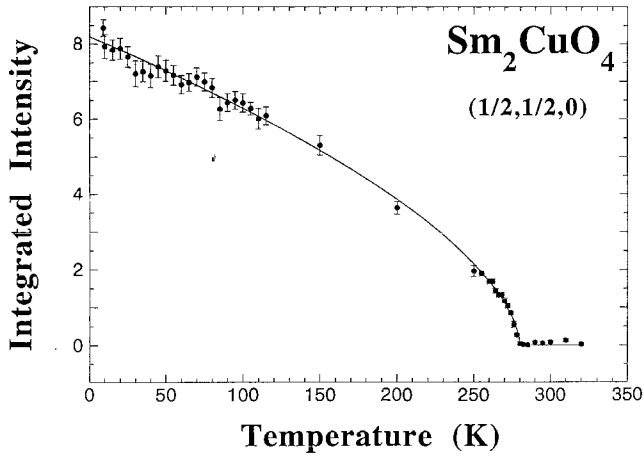

Fig. 2. Temperature dependence of the $(\frac{1}{2},\frac{1}{2},0)$ Cu magnetic Bragg peak in Sm_2CuO_4. The solid curve is a least-squares fit to a simple power law, $I = I_0(1 - T/T_N)^{2\beta}$, with $\beta = 0.30(1)$ and $T_N = 280(1)$ K (Skanthakumar et al. 1991).

domains. A similar, although more complicated, expression is obtained if the magnetic structure is noncollinear, but the general behavior in terms of magnetic moment, form factor, and determination of the spin directions is qualitatively the same.

Figure 2 shows the intensity of the $(\frac{1}{2},\frac{1}{2},0)$ magnetic Bragg peak associated with the Cu ordering in Sm_2CuO_4 (Skanthakumar et al. 1991). We see from eq. (1) that the intensity is proportional to the square of the ordered moment, which in this case is the sublattice magnetization. The smooth variation with temperature indicates that the ordered moment develops continuously below the Néel temperature of 280 K. However, we note that the intensity does not exhibit the usual saturation at low T typical of a conventional three-dimensional order parameter. The solid curve is a fit to a power law $t^{2\beta}$, where t is the reduced temperature and $\beta = 0.30 \pm 0.01$. This is the expected behavior near the ordering temperature, but it is unusual for a power law to fit the data over such a wide temperature range. This has been observed in other $S = \frac{1}{2}$ Cu–O systems, and is thought to originate from the two-dimensional quantum fluctuations present in these highly anisotropic antiferromagnets.

The magnetic Bragg peaks observed in the magnetically ordered state can be indexed as $(\frac{1}{2}h, \frac{1}{2}k, l)$ based on the chemical unit cell, where h and k are odd integers and l is any integer. Since the first two Miller indices are half integers, the Cu magnetic unit cell is double the chemical unit cell along the a and b directions while it is the same along c. This Cu magnetic unit cell is the same as that found for the other 2-1-4 systems. The interactions between spins within an a–b plane are antiferromagnetic as already discussed, so that nearest-neighbor spins within a layer are antiparallel, as is the case in all the cuprates. The nearest-neighbor exchange interaction $JS_i \cdot S_j$ between layers, on the other hand, is seen to cancel due to the body-centered tetragonal (bct) symmetry, further rendering the net Cu spin interactions 2D in nature. Hence the three-dimensional

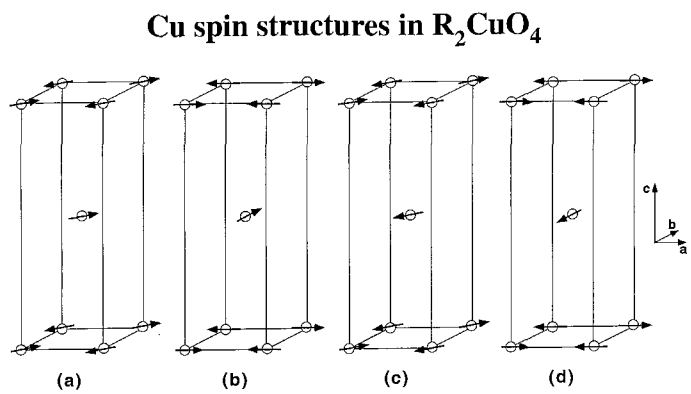

Fig. 3. The four possible Cu spin structures in tetragonal R_2CuO_4: (a) collinear with $\boldsymbol{q}_M \perp \widehat{M}$; (b) noncollinear-$Sm_2CuO_4$ type (c) collinear with $\boldsymbol{q}_M \parallel \widehat{M}$; (d) noncollinear-$Nd_2CuO_4$ type.

magnetic structure that is actually realized must be stabilized by higher-order interactions (Yildirim et al. 1996), as we will discuss shortly.

The detailed spin structure, which entails assigning a spin direction to each site, turns out to contain an ambiguity; there are two possible descriptions (figs. 3a,b) that may occur for the present case where the crystal structure has tetragonal symmetry, and it is not possible to distinguish between them with neutron diffraction data on a multidomain sample. One possibility is a collinear spin structure as shown in fig. 3a, which is the same structure as observed in orthorhombic La_2CuO_4 (Vaknin et al. 1987). The antiferromagnetic propagation vector $\boldsymbol{q}_M$ that describes this structure is along the $[1\bar{1}0]$ direction, while the spin direction $\widehat{M}$ is orthogonal, along [110]. The structure then consists of ferromagnetic sheets in the (110) plane, with the spins in adjacent sheets antiparallel ($\boldsymbol{q}_M \perp \widehat{M}$) and the magnetic symmetry is orthorhombic. A second, completely different possibility is the noncollinear spin assignments shown in fig. 3b. In this structure the spins within each Cu–O plane are again collinear and antiferromagnetically coupled as before, but the spins between adjacent planes are rotated by 90° and hence are noncollinear. The spin direction in this structure is either along the [100] axis or along the [010] axis, and the basic magnetic symmetry in this case is tetragonal rather than orthorhombic.

These two basic magnetic structures, collinear and noncollinear, are in fact closely related: the noncollinear structure can be obtained from the collinear structure by the *coherent* addition of two separate domains of the collinear structure. From a scattering point of view, the intensities of the magnetic Bragg peaks from a domain of the collinear structure would be quite different from those for the noncollinear structure. However, generally a material exhibiting the collinear structure would form equal populations of domains, and the intensities from the multiple-domain sample are identical to the intensities for the noncollinear structure. Thus in a zero-field experiment the two types of structures cannot be distinguished, and one must apply a symmetry-breaking magnetic field to identify the correct structure. If we apply the field along the [110] direction for

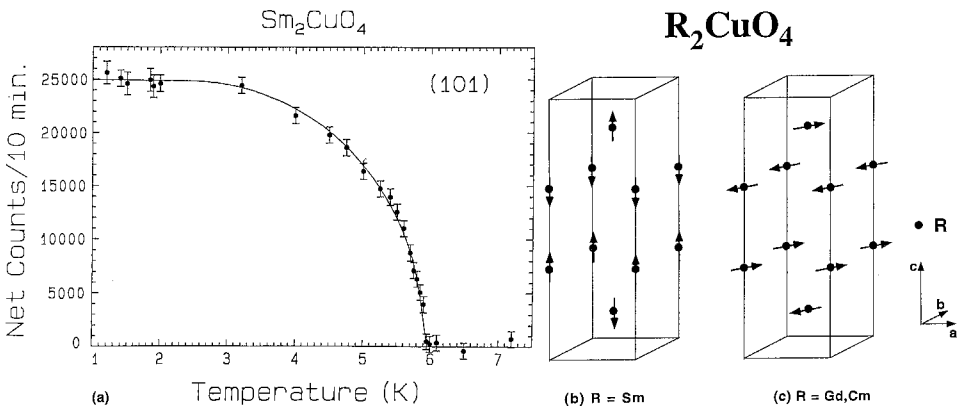

Fig. 4. (a) Temperature dependence of (1,0,1) Sm magnetic Bragg peak intensity (Sumarlin et al. 1992). (b) Sm magnetic structure. (c) Magnetic structure for Gd and Cm.

example, one can see from fig. 3 that the behavior of the spin system will be quite different depending on whether the structure is collinear, where spins are parallel or antiparallel to the field direction, or noncollinear, where the spins initially are at 45° to the field direction. The results for Nd_2CuO_4 (Skanthakumar et al. 1993a,b) demonstrate that the correct structure is the noncollinear one (Skanthakumar et al. 1989, Petitgrand et al. 1990), and the noncollinear structure appears also to be correct for Sm_2CuO_4 (Skanthakumar et al. 1993a), Pr_2CuO_4 (Sumarlin et al. 1995), and Eu_2CuO_4 (Chattopadhyay et al. 1994b).

For the lanthanide ordering, the simplest example is provided by Sm_2CuO_4, which also turns out to be an interesting example of the interaction between the lanthanide magnetism and superconductivity. All observed Sm magnetic peaks were found to coincide with nuclear peaks, and they can be indexed as (h,k,l) based on the chemical unit cell, where all h, k and l are integers and $h + k + l$ = even integer. The intensity of the [101] magnetic Bragg peak is shown in fig. 4a, where we find a Néel temperature of 5.95 K (Sumarlin et al. 1992). The magnetic transition is clearly very sharp, and indicates that the lanthanide and Cu magnetic structures do not interact significantly with each other. The fact that the Miller indices are integers signifies that the magnetic unit cell is identical to the chemical unit cell. The magnetic structure for the Sm moments is shown in fig. 4b, where we see that the moments form ferromagnetic sheets in the a–b plane, that are coupled antiferromagnetically along the c-axis, with the spin direction also along c. The Sm magnetic structure, which is in the I4/m′mm magnetic space group, then has a completely different symmetry than the Cu structure, and the spin directions are orthogonal as well, so that the two magnetic phases in this material are independent of each other to a very good approximation.

The ordered magnetic moment of the Sm ion is only $0.37(3)\mu_B$, which is quite small compared to the heavy lanthanides. With the high ordering temperature of ~6 K, it is quite clear that the energetics must be dominated by exchange interactions, with the dipolar interactions playing only a very minor role. In the doped superconducting

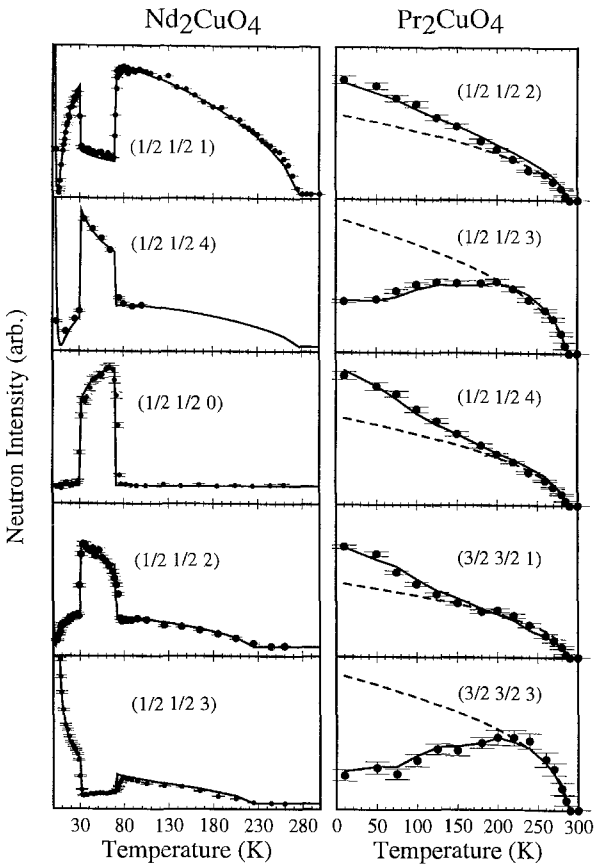

Fig. 5. (left) Temperature dependence of five Nd_2CuO_4 magnetic Bragg peaks (Skanthakumar et al. 1989, 1999). (right) Temperature dependence of five Pr_2CuO_4 magnetic Bragg peaks. The solid curves are fits to the theory (Sachidanandam et al. 1997); the dashed curves on the right show the contribution of the Cu spins to the intensities.

system, the dilution of the Sm sublattice smoothly decreases the Néel temperature to ~4.9 K, with little other effect on the magnetism. In the superconducting state ($T_c = 23$ K), but above the Sm antiferromagnetic ordering temperature, the Cu–O layers contain a mirror (m) symmetry, which the superconducting wave function must accommodate. When the Sm ions order magnetically, on the other hand, then the Cu–O layers contain an antimirror symmetry (m'), and the superconducting wave function must then accommodate this change in symmetry. Viewed along the c-axis, the system consists of alternating superconducting and ferromagnetic layers, which should require a change of sign of the superconducting order parameter in adjacent Cu–O layers. This "π-phase" model is predicted to substantially affect the superconducting state below the magnetic ordering temperature (Andreev et al. 1990), and this is an active area of interest both in this natural layered system and in artificially layered films.

The nature of the lanthanide moments and magnetic ordering can also have important consequences for the Cu magnetic structure, and vice versa, as we will now discuss. The column on the left of fig. 5 shows the temperature dependence of five magnetic

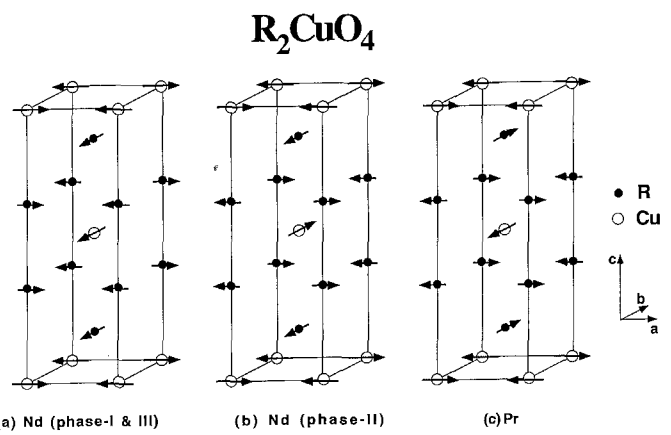

Fig. 6. Noncollinear spin structures for (a) Nd in phase I and III, (b) Nd in phase II, and (c) Pr.

Bragg peaks for Nd_2CuO_4. Five magnetic transitions have been identified (Skanthakumar et al. 1989, Endoh et al. 1989, Lynn et al. 1990, Matsuda et al. 1990). The initial ordering of the Cu spins occurs at a Néel temperature of 276 K for this sample, where all the $(\frac{1}{2},\frac{1}{2},l)$-type reflections increase in intensity with decreasing temperature in phase I ($75\,K \leqslant T \leqslant 276\,K$), and the noncollinear Cu spin structure is that shown in fig. 3d. We remark that the Cu ordering temperature is quite sensitive to small changes in the oxygen content, with T_N varying from 245 K to 276 K (Skanthakumar 1993). At 75 K the intensities of the odd-integral (odd-l) peaks suddenly drop, while the even-integral peaks increase abruptly in intensity. This indicates that a spin-reorientation transition for the Cu spins has occurred, and the new noncollinear Cu spin structure is shown in fig. 3b. At 30 K another abrupt spin reorientation takes place, where the spins rotate back to the original spin sense as indicated by the negligible intensity for $T < 30$ K of the $(\frac{1}{2},\frac{1}{2},0)$ peak, which has nonzero intensity only in Phase II ($30\,K \leqslant T \leqslant 75$ K). Note that this is the same peak that has the strongest intensity for Sm_2CuO_4, and it turns out that these transitions are the result of a spin reorientation from one noncollinear structure to the other, and then back again, as shown in fig. 6. Similar types of spin-reorientation transitions have been observed in some other related compounds (e.g. La_2CoO_4), but those transitions are accompanied by structural phase transitions (Yamada et al. 1989). In Nd_2CuO_4, there is no evidence for structural phase transitions accompanying the magnetic order, and hence the origin of these spin-reorientation transitions must be different. Finally, the Nd ions order antiferromagnetically in the vicinity of 1.5 K, also in a noncollinear spin arrangement, and the magnetic symmetry of the Nd spins is identical to that of Cu spins. In addition to all these transitions, there is a fifth transition of a continuous nature at 0.15 K, which is due to an induced ordering of the nuclear spins through the hyperfine interactions. Such a nuclear spin ordering was originally introduced to explain the low-temperature data of both Nd_2CuO_4 and Sm_2CuO_4, and has been recently investigated thoroughly in Nd_2CuO_4 (Chattopadhyay and Siemensmeyer 1995).

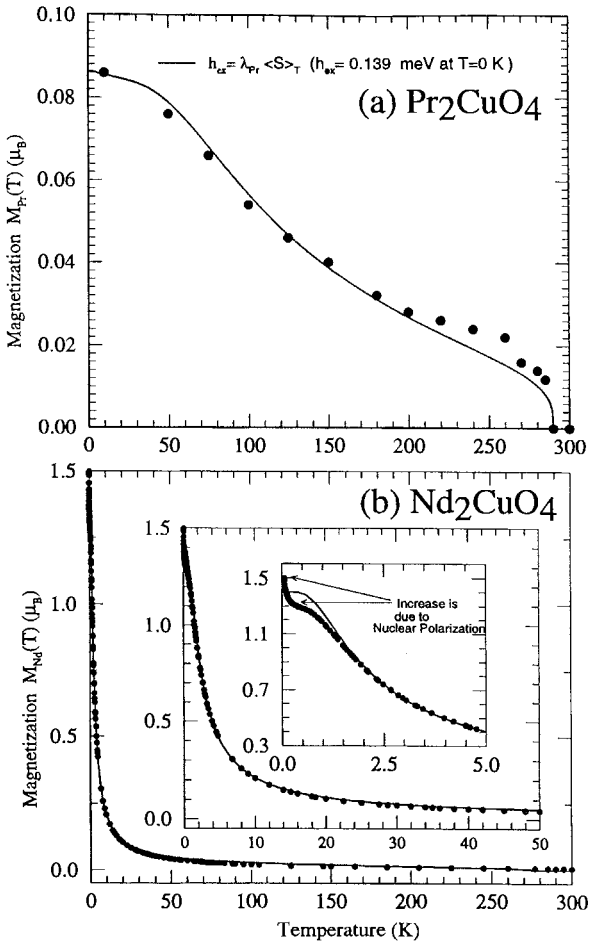

Fig. 7. Calculated polarization of the (a) Pr and (b) Nd moments in R_2CuO_4, via the interaction with the Cu ordered moments, as a function of temperature (Sachidanandam et al. 1997).

Below 30 K (phase III) the intensities evolve in a rather complicated way, and this turns out to be caused by the development of substantial (staggered) moments on the Nd sites as indicated in fig. 7b. Note in particular that the $(\frac{1}{2},\frac{1}{2},3)$ peak varies substantially in intensity at lower temperatures (fig. 5), and this is the strongest peak associated with the Nd ordering at low temperature (Lynn et al. 1990, Matsuda et al. 1990). The antiferromagnetically ordered Cu sublattice induces the Nd spins to order in a staggered arrangement. There are four Cu nearest-neighbor spins, one next-nearest-neighbor and four third-neighbors, for each Nd ion. The nearest-neighbor Cu–Nd interactions cancel exactly due to the tetragonal crystal symmetry. However, next-nearest-neighbor and third-neighbor interactions do not cancel, but instead produce a field that polarizes the Nd sublattice antiferromagnetically. This polarization field turns out to have the same symmetry as when the Nd ions order spontaneously, and thus the Nd ions are quite

susceptible even at elevated temperatures, and a net sublattice magnetization of the Nd ions is observed in all the ordered phases (fig. 7b). An induced Nd moment has also been observed in resonant X-ray scattering measurements (Hill et al. 1995). Magnetic structures for the Nd spins along with the Cu spins are shown in figs. 6a,b for all phases. Note that the induced moments at elevated temperatures (over 100 K), and the spontaneous order at low T, are noncollinear structures. Note also that the intensities of the $(\frac{1}{2},\frac{1}{2},1)$ and $(\frac{1}{2},\frac{1}{2},2)$ peaks increase with decreasing temperature in phase II, while the intensities of the $(\frac{1}{2},\frac{1}{2},0)$ and $(\frac{1}{2},\frac{1}{2},3)$ peaks decrease. This behavior is reversed in phase III, and these observations indicate that the Nd and Cu spins along the c-direction are coupled antiparallel in phase II, while they are parallel in phases I and III (figs. 6a,b). The temperature dependence of the other magnetic peaks as well as detailed refinements of the intensities (Skanthakumar 1993, Petitgrand et al. 1992) confirm this type of Nd–Cu coupling. The refined magnetic moment for Nd is 1.44, 0.04, and $0.014\mu_B$ at 0.4, 50 and 80 K, respectively. This shows in a direct way that the Nd and Cu spin systems are coupled, and because of the high temperatures involved this again must be exchange coupling rather than dipolar coupling. This has important implications for the superconductivity since the Nd moments and Nd ordering occur in the superconducting system; the conventional wisdom would say that the Abrikosov–Gorkov spin-depairing mechanism would surely destroy any chance for superconductivity in the material. Thus even if we were to discard the fact that there are Cu spin fluctuations in the superconducting phase of these materials, we still have to deal with the fact that the lanthanide moments are there, and are directly coupled through the superconducting planes.

The properties of both the Cu and lanthanide magnetic structures, ordered moments, and ordering temperatures are summarized in table 1, along with some related systems. For Pr_2CuO_4 the Cu spin structure (Cox et al. 1989, Allenspach et al. 1989, Matsuda et al. 1990, Sumarlin et al. 1995) is the same as that (fig. 3d) observed in Nd_2CuO_4 at high temperature. The temperature dependence of five typical magnetic peaks is shown in the right-hand column of fig. 5, where we see that the nonmonotonic behavior again indicates that R–Cu coupling is also present in Pr_2CuO_4. The spin structure is shown in fig. 6c, and the (small) induced Pr moment (obtained from theory discussed below) is shown in fig. 7a. We see that the Pr and Cu spins are coupled antiferromagnetically along the c-direction, in contrast to Nd_2CuO_4. Measurements under high pressure in Pr_2CuO_4 suggest spin-reorientation transitions (Katano et al. 1993) similar to Nd_2CuO_4, but the Nd system is the only one to exhibit these under ambient pressure. For Eu_2CuO_4, the Eu^{3+} ion has a non-magnetic ground state, and therefore only Cu magnetic ordering is observed in this system (Chattopadhyay et al. 1994b, Gukasov et al. 1992). In Gd_2CuO_4 (Chattopadhyay et al. 1991b, 1992) and Cm_2CuO_4 (Soderholm et al. 1999), the lanthanide and Cu spin structures are different. Gd and Cm order ferromagnetically in the a–b plane and are coupled antiferromagnetically along c like Sm_2CuO_4, with relatively high ordering temperatures. However, the spin direction is in the a–b plane, and the easy direction within this plane cannot be obtained by (zero-field) neutron data. Note that superconductivity does not occur in these two compounds for any Ce doping. Finally, we note that there

Table 1
Magnetic properties of R_2CuO_4[a]. The Cu ordering temperature, $T_N(Cu)$, and ordered moment, μ_{Cu}, change with oxygen concentration. Here we give the highest observed T_N and the corresponding μ_{Cu}

Material	$T_N(Cu)$ (K)	μ_{Cu} (μ_B)	Magnetic structure, Cu	$T_N(R)$ (K)	μ_R (μ_B)	Magnetic structure, R	Ref.
La_2CuO_4[b]	325	0.5	fig. 3a				1
Pr_2CuO_4	284	0.40(2)	fig. 3d	Induced	0.080(5)	fig. 6c	2–5
Nd_2CuO_4	276	0.46(5)	fig. 3d[c]	~1.5	1.44(5)	fig. 6a	4,6–14
Sm_2CuO_4	280	0.38(4)	fig. 3b	5.95(5)	0.37(3)	fig. 4b	8,15–17
Eu_2CuO_4	265	0.4(1)	fig. 3b		$J \equiv 0$		18,19
Gd_2CuO_4	285		fig. 3c or d	6.4	7	fig. 4c	20,21
Cm_2CuO_4			[d]	25	5.0(5)	fig. 4c	22
$Sr_2CuO_2Cl_2$	251	0.34(4)	fig. 3a or b				23,24
$Ca_2CuO_2Cl_2$	247	0.25(10)	[e]				25

[a] La, Eu, Sr and Ca ions do not a carry magnetic moment. The ground state of Pr is a nonmagnetic singlet and only a small induced moment is observed for Pr due to exchange mixing.
[b] Only La_2CuO_4 has an orthorhombic (Cmca) crystal structure; all others are tetragonal (I4/mmm). However, recently orthorhombic structural distortions have been reported in Eu_2CuO_4 and Gd_2CuO_4 (Vigoureux et al. 1997a,b).
[c] Spin reorientation occurs at 75 K and 30 K. Between these two temperatures the correct structure is represented by fig. 3b.
[d] Cu ordering in Cm_2CuO_4 has not been studied yet, but the Cu spin structure is not expected to be different from other R_2CuO_4 compounds.
[e] Cu spin structure is different from all other related materials. In this system, the magnetic unit cell is doubled along the c-direction.

References

[1] Vaknin et al. (1987); review: Lynn (1990)
[2] Cox et al. (1989)
[3] Allenspach et al. (1989)
[4] Matsuda et al. (1990)
[5] Sumarlin et al. (1995)
[6] Skanthakumar et al. (1989)
[7] Skanthakumar et al. (1993a)
[8] Skanthakumar et al. (1993b)
[9] Lynn et al. (1990)
[10] Endoh et al. (1989)
[11] Chattopadhyay et al. (1991a)
[12] Akimitsu et al. (1989)
[13] Rosseinsky et al. (1989)
[14] Petitgrand et al. (1990)
[15] Skanthakumar et al. (1991)
[16] Skanthakumar (1993)
[17] Sumarlin et al. (1992)
[18] Gukasov et al. (1992)
[19] Chattopadhyay et al. (1994b)
[20] Chattopadhyay et al. (1991b)
[21] Chattopadhyay et al. (1992)
[22] Soderholm et al. (1999)
[23] Vaknin et al. (1990)
[24] Yildirim et al. (1998)
[25] Vaknin et al. (1997)

is an indication for an induced Gd moment due to the polarization by the Cu sublattice in Gd_2CuO_4 (Chattopadhyay et al. 1994a), and in principle the Cu sublattice polarizes rare-earth spins in all these compounds. Superconductivity does not occur in any of the other R_2CuO_4 (R = Tb–Lu) systems, and no neutron diffraction experiments have been reported yet.

The effects of Ce doping on the magnetic ordering of R and Cu in $R_{2-x}Ce_xCuO_4$ have been studied for the Nd and Pr systems (Lynn et al. 1990, Skanthakumar et al. 1992, 1999, Skanthakumar 1993, Thurston et al. 1990, Rosseinsky et al. 1991, Zobkalo et al. 1991). Taking $Nd_{2-x}Ce_xCuO_4$ as an example, for small Ce concentrations ($x < 0.14$) the same non-collinear antiferromagnetic order (fig. 6) for both the Cu and Nd spins is observed. Both the average ordered Cu moment and T_N decrease with increasing Ce concentration x, and no long-range order is observed at optimal doping of $x = 0.15$ (7.5% substitution of Ce for Nd). The Cu spin-reorientation transitions also broaden rapidly with increasing x, while the fraction of Cu spins that participate in the spin reorientation also appears to decrease with increasing x.

On the other hand, the Nd ordering transition, which is smeared due to the strong Cu–Nd coupling in Nd_2CuO_4, becomes sharper with increasing x. The temperature dependence of the $(\frac{1}{2},\frac{1}{2},3)$ magnetic peak for crystals with various Ce concentrations is shown in fig. 8a. Since the ordered Cu moment decreases with increasing x, the strength of the Nd–Cu coupling and the associated induced moment also decrease with increasing x, allowing the transition to become sharper. To see this effect directly, the temperature dependence of the ratio between the ordered moments of Nd and Cu for various Ce concentrations is shown in fig. 8b. In the temperature regime where the dominant contribution to the Nd ordered moment is via the Nd–Cu interaction, these temperature-dependent moment ratios fall on a universal curve since the induced Nd moment is proportional to the ordered Cu moment. The proportionality constant depends on the magnetic susceptibility of the Nd ions, and we see that the Nd contribution to the magnetic susceptibility changes only marginally with cerium doping. At lower temperatures (< 1.5 K), the ordered Nd moment develops a contribution from the Nd–Nd interaction, and the ratios for different Ce concentrations depart from the universal curve. Nuclear spin ordering of Nd also contributes to the increase in intensity below ~0.4 K.

In the superconducting sample ($x = 0.15$), there is no indication for long-range Cu magnetic ordering. However, a transition to long-range antiferromagnetic order of Nd occurs at 1.2 K, with an ordered moment of $0.85\mu_B$, and this transition is relatively sharp as there is no ordered Cu moment to induce Nd ordering at higher temperatures. There is no indication for long-range ordering of either Cu or Nd in crystals with higher cerium concentrations ($x > 0.17$). However, at low temperatures, broad magnetic peaks with weak intensities due to short-range Nd order are observed. The intensities of these peaks are found to increase with decreasing temperature, analogous to an order parameter, while the widths are approximately temperature independent. This indicates that for higher cerium concentrations the domains are small (~150 Å).

Oxygen plays a crucial role in both the magnetic and transport properties of the high temperature superconductors. In the electron-doped $Nd_{2-x}Ce_xCuO_4$ system the superconducting properties were found to be very sensitive to both cerium and oxygen concentrations. In fact, even in optimally doped $Nd_{1.85}Ce_{0.15}CuO_4$, superconductivity can be achieved only by removing a small amount of oxygen from as-grown samples (Radaelli et al. 1994) and not by doping more Ce. The overall effects of oxygen reduction on the Cu magnetic ordering are similar to that of increasing the cerium concentration in

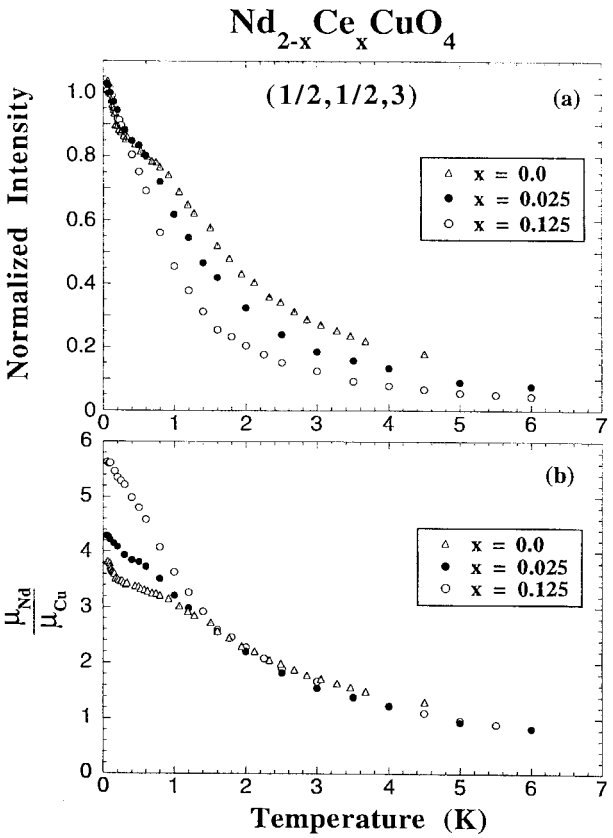

Fig. 8. (a) Temperature dependence of the $(\frac{1}{2},\frac{1}{2},3)$ magnetic Bragg peak for $Nd_{2-x}Ce_xCuO_4$ crystals with various Ce concentrations. (b) Temperature dependence of the ratio between the ordered moments of Nd and Cu. At higher temperatures, the ordered (induced) Nd moment is proportional to the Cu moment, and thus the curves for various crystals overlap. At lower temperatures (below 1.5 K), the Nd ions spontaneously order (Skanthakumar 1993, Skanthakumar et al. 1999).

$Nd_{2-x}Ce_xCuO_4$ (Skanthakumar 1993, Matsuda et al. 1992). In $Nd_{1.85}Ce_{0.15}CuO_4$, the observed magnetic intensities due to Nd ordering in as-grown samples were found to be larger than those of the deoxygenated (superconducting) samples. In addition, magnetic ordering of Cu and, therefore, the Nd–Cu coupling, are observed in as-grown samples, while they disappear when the excess oxygen is removed.

As mentioned earlier, the linear exchange interaction between Cu layers cancels due to the *bct* symmetry, and the actual spin structure is then a result of a delicate balance of superexchange, spin–orbit, and Coulomb exchange interactions (Yildirim et al. 1994, 1996). In the absence of the R ions, quantum fluctuations would be expected to yield the collinear magnetic structure (Yildirim 1999) and this may indeed be the case for the $Sr_2CuO_2Cl_2$ material (Yildirim et al. 1998). However, this leaves unexplained the

observation of the noncollinear structures in the R_2CuO_4, and quantum fluctuations certainly cannot explain the series of spin rotations that occur in Nd_2CuO_4. It is thus clear that the lanthanide exchange interactions and crystal-field anisotropies must play an essential role in determining the three-dimensional magnetic structures realized in these systems, and the correlation between lanthanide magnetism and superconductivity.

Considerable progress in properly taking into account the lanthanide exchange interactions and crystal field anisotropies has been achieved recently (Yildirim et al. 1994, Sachidanandam et al. 1997). The theory includes various novel anisotropic magnetic interactions in the cuprates that have a microscopic origin, along with R–R, R–Cu, and Cu–Cu exchange interactions. The calculations show that due to the exchange field acting on the lanthanide ion coupled with the crystalline electric field interactions, there is a strong single-ion anisotropy that orients both the Cu and R = Pr, Nd spins along the [100]-type directions, into the observed noncollinear spin arrangement. The model also successfully predicts the consecutive spin flop transitions observed in Nd_2CuO_4, and the calculations (solid curves) shown in fig. 5 are in excellent agreement with the data. The Cu spins order first, and then as the temperature decreases the Nd spins develop a significant polarization. As this polarization develops it disrupts the balance of energies along the c-axis, and this causes an abrupt (first-order) spin reorientation from one noncollinear structure to the other. As the Nd moment increases the energetics shift again and the spins rotate back to their original directions. The polarization of the Nd sublattice, as determined by fitting the model to the intensities of a series of magnetic Bragg peaks, is shown in fig. 7b. We see that there is a substantial induced moment on the Nd below ~100 K, while the Nd exchange orders the moments at ~1.5 K (in the absence of the Cu). This behavior contrasts with the situation for Pr_2CuO_4, where the Pr crystal-field ground state is a (non-magnetic) singlet (Sumarlin et al. 1995, Staub and Soderholm 2000). There is then a small moment that is present due to exchange mixing (Matsuda et al. 1990, Sumarlin et al. 1995), and the polarization of this moment as determined from the model is presented in fig. 7a; the excellent fits to the data are shown as solid curves in the right column of fig. 5. The model predicts that there is significant polarization all the way up to T_N(Cu), but this polarization is too small to cause spin reorientations in Pr_2CuO_4, in agreement with experiment. Finally, we note that this same type of calculation also predicts that the easy axis lies along [001] for Sm in Sm_2CuO_4, with no significant coupling of the lanthanide and Cu spin structures, again in agreement with observation. We conclude then that there is a good overall understanding of the microscopic magnetic interactions, and the consequent magnetic phases and associated spin dynamics, in the single-layer materials.

4. Multilayered systems

We have seen in the previous section that the single-layer materials exhibit substantial R–Cu exchange coupling, and they also have modest (for cuprates) superconducting transition temperatures. For the materials that contain multiple Cu–O layers the T_c values

are typically much higher because of the stronger coupling between the Cu–O layers. For the canonical $RBa_2Cu_3O_{6+x}$ (1-2-3) system, there are three copper–oxygen layers of ions in each chemical unit cell, which are stacked along the c-axis. Two of these layers have oxygen ions between the Cu ions in both the a and b crystallographic directions (the Cu-plane layers), and the oxygens cannot be removed. The third Cu layer only has O ions along one axis. This is the so-called "chain layer", and the oxygen concentration can be readily varied in this layer from full occupancy ($x=1$) to full depletion ($x=0$). Both the magnetic and superconducting properties are very sensitive functions of the oxygen concentration x; in the fully oxygenated case ($x=1$) the system is a 90^+ K superconductor for all the trivalent lanthanide elements R except Pr, while in the magnetic regime ($x \leqslant 0.4$) the Cu plane-spins order antiferromagnetically and the system is a Mott insulator.

The lanthanide ions are centered between the two Cu plane layers in the 1-2-3 system, but they turn out to be remarkably isolated electronically from the Cu–O layers. Indeed all the physical measurements on the $RBa_2Cu_3O_{6+x}$ (1-2-3), the $R_2Ba_4Cu_8O_{16}$ (2-4-8), and the $R_2Ba_4Cu_7O_{15}$ (2-4-7) systems show that the 4f electrons are effectively isolated from the Cu–O superconducting layers, as well as from each other. The single exception is for Pr, and we will discuss this unique case separately. The crystal-field splittings are also very important (except for Gd), and for the orthorhombic symmetry appropriate for these materials typically the lanthanide ground state is doubly degenerate for half-integral J (like Dy or Er) or singly degenerate (like Ho) for integral J (and hence non-magnetic). The crystal-field properties have been reviewed by Staub and Soderholm (2000). As far as the nature of the magnetic ordering is concerned for half-integral J, the higher crystal-field levels are at energies much larger than the ordering energy kT_N, and consequently do not play an important role in the ordered state. However, the first excited state for integral J is very close to the ground state (except for Tm), and therefore it is possible for the rare-earth ions to order magnetically in these materials as well. In Tm, the singlet ground state is well separated from higher states (~12 meV), and consequently lanthanide magnetic order is not observed in the Tm compounds. For the systems with a magnetic ground state the direct (exchange) overlap of the 4f wave functions is of course out of the question, and the indirect and superexchange interactions turn out to be relatively small. Thus the ordering temperatures are low (typically ~1 K), and dipolar interactions are important in these materials. Hence the lanthanide magnetism is similar in many regards to "conventional" magnetic-superconductor systems.

The sublattices for the lanthanide ions are shown in fig. 9 for the 1-2-3 (9a), 2-4-8 (9b), and 2-4-7 (9c) structures. Neglecting the small orthorhombic distortion in the a–b plane, the 1-2-3 lattice is simple tetragonal. The 2-4-8 system then consists of two 1-2-3 unit cells stacked on top of one another, but shifted by $b/2$. The 2-4-7 system, on the other hand, consists of two 1-2-3 cells stacked directly on top of one another, and then another two layers stacked on top, but shifted by $b/2$. Hence the 2-4-7 structure consists of 1-2-3 bilayers. The basic ingredient that lowers the effective dimensionality d of this class of magnetic materials to $d=2$ is that for all three structures the nearest-neighbor R distance along the c-axis is three times the nearest-neighbor distance in the a or b directions; typically $a \approx b \approx 3.9$ Å, and $c \approx 12$ Å. For a dipolar interaction

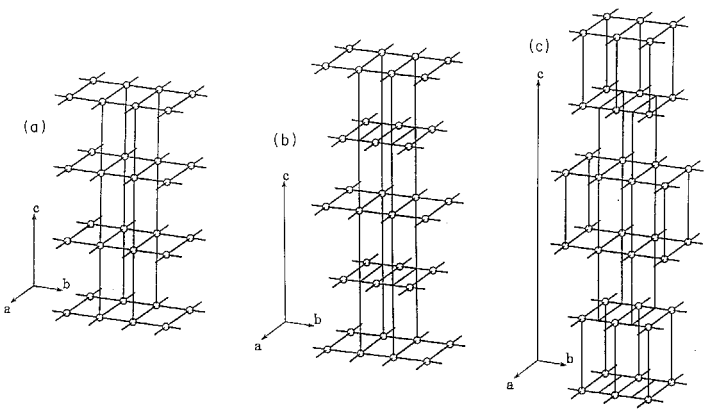

Fig. 9. Crystal structures for the rare-earth ions in the (a) 1-2-3, (b) 2-4-8, and (c) 2-4-7 systems. The two-dimensional behavior of the magnetism is due to the large inter-ion spacing along the c-axis compared to the a–b plane ($c \approx 3a$). In addition, in the 2-4-8 and 2-4-7 structures the net interactions along the c-axis cancel for some magnetic configurations.

($E \propto 1/r^3$) the strength of the coupling along c should be reduced by $\sim(a/c)^3 \approx 1/27$, while either direct or superexchange interactions would be expected to be reduced by even a larger factor. A significant indirect (RKKY) exchange might still be operative over this long distance, but the conduction electron density at the lanthanide site turns out to be small, and in fact the ordering temperatures in both the insulating and superconducting compounds (which in the 1-2-3 materials can be realized by simply varying the oxygen content) are comparable. The final conclusion is that the interaction along c is indeed considerably more than an order of magnitude smaller than the interactions operating within the a–b plane, and this generates the 2D-like magnetic behavior. This contrasts with the interactions in the 2-1-4 materials, where the nearest-neighbor R distances are all comparable, and there is no 2D-like behavior for the R magnetism.

4.1. *Cu spin ordering*

The high-temperature antiferromagnetic transition in the 1-2-3 system involves the ordering of the Cu spins in the Cu-plane layers. At $x = 0$ the Néel temperature T_N can exceed 500 K, and then T_N monotonically decreases to zero at $x \approx 0.4$. The spins within the a–b plane are antiferromagnetically aligned, as is always the case, with the spin direction also in the a–b plane. The Cu ions in adjacent layers are located immediately above and below each other along the c-axis, and the exchange interaction along the c-axis is also antiferromagnetic. In particular, the Cu lattice is not body-centered as in the single-layer materials, and hence there is no cancellation of the exchange interactions between layers. Nevertheless, the overall behavior is still quite 2D in nature because of the strong in-plane Cu-O bonding. It is also possible to dope the chain layers in the 1-2-3 material electronically, either from adjacent sites or directly on the Cu chains, and this can cause a moment to develop on the Cu chain sites, which can also order. This is not a problem for

the heavy lanthanides, but is an important difficulty encountered in the Pr system, and to a lesser extent in Nd 1-2-3. This coupling breaks the symmetry that the lanthanide site enjoys when only the Cu-plane layers are magnetic, and can consequently influence the lanthanide ordering and R–Cu coupling. We will return briefly to this problem when we review the Pr ordering.

For the 2-4-8 materials we note that it is not possible to vary the oxygen content significantly, while for the 2-4-7 systems it can be varied from 14 to 15. However, there is no long-range Cu order to consider in these superconducting systems.

4.2. *Lanthanide ordering in $RBa_2Cu_3O_7$*

The R–R interactions in these superconductors are all quite weak, and the antiferromagnetic ordering temperatures are typically ~1 K as already noted. The most thoroughly investigated system is probably $ErBa_2Cu_3O_7$, and this material turns out to be an ideal representation of a $S=\frac{1}{2}$ 2D Ising antiferromagnet. Early investigations were carried out on polycrystalline samples (Lynn et al. 1987), and were followed by detailed studies on single-crystal samples (Lynn et al. 1989, Paul et al. 1989, Chattopadhyay et al. 1988a, 1989). In the top portion of fig. 10 we present a diagram of reciprocal space, showing the positions of the nuclear (crystal structure) and magnetic (spin structure) Bragg peaks which occur at positions like $(\frac{1}{2}h,k,\frac{1}{2}l)$. If the system were purely 2D in character then we would expect to see rods of magnetic scattering as shown; above the ordering temperature this scattering originates from critical fluctuations, while below T_N it originates from low-energy spin waves. The lower portion of fig. 10 shows three scans through the rod, just above the ordering temperature. This strong rod of scattering develops for temperatures $\leqslant 1$ K, and at the temperature shown the width is solely instrumental in origin. Also shown in the figure is a scan along the rod, which demonstrates that the scattering intensity is essentially uniform. Hence there are no significant correlations between the spins in adjacent a–b layers, even though we are just above $T_N = 0.62$ K as indicated by the measured sublattice magnetization shown in fig. 11. The energetics are clearly 2D in nature, and we thus regard the phase transition at T_N as 2D in character.

The magnetic structure for Er 1-2-3 is shown in fig. 12a, and consists of chains of spins coupled ferromagnetically along the b-axis, and antiferromagnetic along a and c. The in-plane magnetic structure is found to be identical in the Er 2-4-8 and Er 2-4-7 systems. In the Dy (Goldman et al. 1987, Fischer et al. 1988, Clinton et al. 1991), Nd (Yang et al. 1989, Fischer et al. 1989), and Gd (Paul et al. 1988) 1-2-3 superconductors, on the other hand, nearest-neighbor spins are found to be antiparallel in all three directions, and they exhibit the magnetic structure shown in fig. 12c, with ordering temperatures of 0.9, 0.5, and 2.2 K, respectively. Tb does not form the 1-2-3 structure, but superconducting $TbSr_2Cu_{2.7}Mo_{0.3}O_7$ exhibits the same magnetic structure, with $T_N = 5.4$ K (Li et al. 1997). Tm 1-2-3, on the other hand, possesses a singlet crystal-field ground state, which must be non-magnetic. This illustrates an important point, that the crystal field plays an essential role in these systems (see ch. 194 of Vol. 30 of this Handbook, by Staub and Soderholm). The above four ions (Er, Dy, Gd, and Nd) are half-integral J lanthanide ions, and therefore

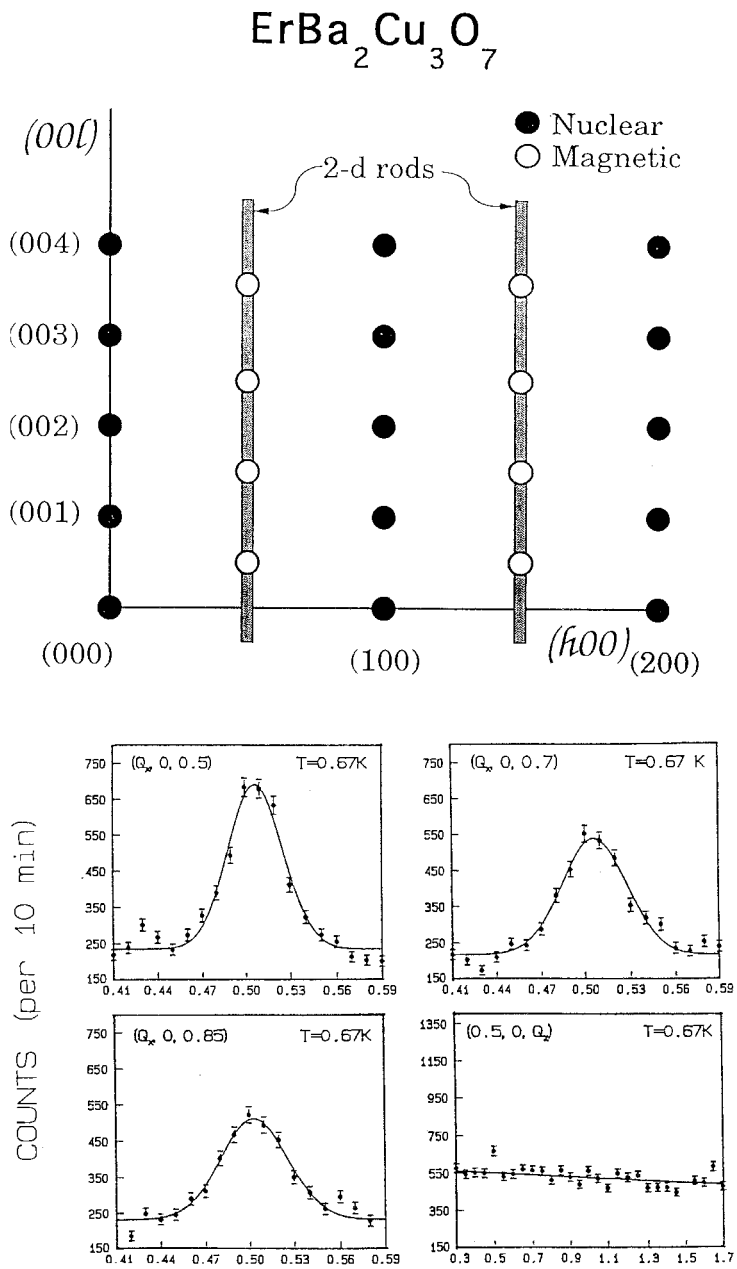

Fig. 10. (top) Reciprocal space for $ErBa_2Cu_3O_7$, showing the three-dimensional nuclear and magnetic Bragg peaks, and the two-dimensional rods of scattering. (bottom) Scans through the rod, and along the rod, just above the ordering temperature of 0.618 K, showing that there are strong spin correlations within the a–b planes, but no significant correlations between planes (Lynn et al. 1989).

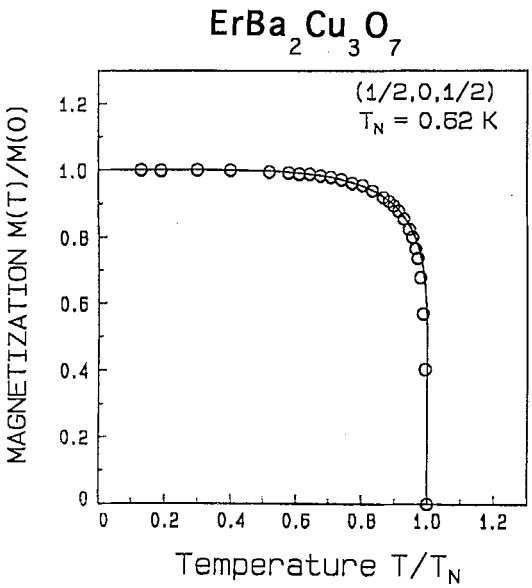

Fig. 11. Temperature dependence of the sublattice magnetization for $ErBa_2Cu_3O_7$. The solid curve is the fit to the data of Onsager's exact solution for the $S=\frac{1}{2}$, 2D Ising model (Lynn et al. 1989).

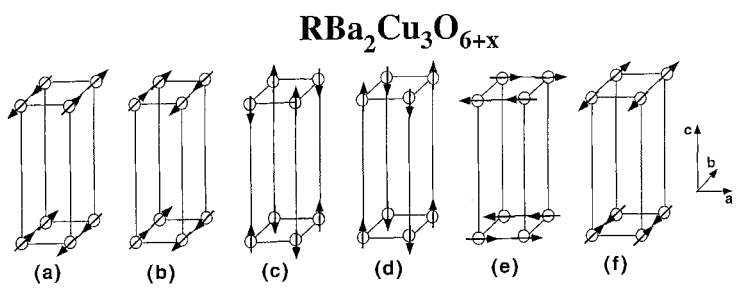

Fig. 12. Three-dimensional magnetic structures for the $RBa_2Cu_3O_{6+x}$ systems. (a) $ErBa_2Cu_3O_7$ (Lynn et al. 1987, 1989, Paul et al. 1989, Chattopadhyay et al. 1988a, Maletta et al. 1990, Clinton et al. 1995). (b) The Er spins in portions of some samples of $ErBa_2Cu_3O_{6+x}$ are coupled ferromagnetically along the c-axis (Chattopadhyay et al. 1988a, 1989, Paul et al. 1989, Clinton et al. 1995). (c) $DyBa_2Cu_3O_7$ (Goldman et al. 1987, Fischer et al. 1988, Clinton et al. 1991, 1995), $NdBa_2Cu_3O_{6+x}$ (Yang et al. 1989, Clinton et al. 1995), $PrBa_2Cu_3O_{6+x}$ (Li et al. 1989, Guillaume et al. 1993), $GdBa_2Cu_3O_{6.14}$ (Mook et al. 1988, Paul et al. 1988) and $TbSr_2Cu_{2.69}Mo_{0.3}O_7$ (Li et al. 1997). (d) $DyBa_2Cu_3O_6$ (Guillaume et al. 1994, Clinton et al. 1995), $GdBa_2Cu_3O_{6+x}$ (Chattopadhyay et al. 1988b, Guillaume et al. 1994). (e) Correlations in $HoBa_2Cu_3O_7$ (Roessli et al. 1993a). (f) $YbBa_2Cu_3O_7$ (Roessli et al. 1992).

in a (low-symmetry) crystal-field environment we expect the ground state to be (at least) doubly degenerate (so that $S=\frac{1}{2}$ is appropriate). Consequently the lanthanide ions will always carry a moment at low temperatures, and order magnetically. This is also the case for Yb 1-2-3, which orders antiferromagnetically at 0.4 K (Roessli et al. 1992). The situation for the case where J is whole-integral, on the other hand, results in a crystal-field ground state that is a (non-magnetic) singlet. Hence Tm 1-2-3 does not order

(Chattopadhyay et al. 1990). Ho also does not have a conventional magnetic transition, but the large nuclear moment and hyperfine field combine to drive a phase transition at 140 mK (Roessli et al. 1993a).

It is important to note that the dimensionality of the phase transition is also evident in other measurements such as specific heat and susceptibility, which measurements in fact often precede the neutron experiments and play an essential role in detecting the phase transition and revealing the nature of the magnetism. Specific heat as well as inelastic neutron scattering have also shown that the crystal-field ground state for the Er ion (as well as Dy and Nd) is a doublet, so that an $S=\frac{1}{2}$ (two-state) description is appropriate. Hence this system should be described by an $S=\frac{1}{2}$ 2D Ising antiferromagnet. Below the Néel temperature Bragg scattering is observed, and the temperature dependence of the sublattice magnetization (order parameter) is shown in fig. 11. The solid curve in the figure is the exact Onsager (1944) result for the $S=\frac{1}{2}$ 2D Ising model, and it is seen that experiment is in excellent accord with this exact theory. Analogous behavior has been observed in $DyBa_2Cu_3O_7$ (Clinton et al. 1991, 1995).

One of the interesting features of "2D" magnetic systems is that generally they will order three-dimensionally even if the interaction in the third direction is very weak (see Lynn 1992 for a review). To understand the origin of this behavior, we designate J_{ab} to be the basic interaction within the a–b plane, which will consist of possible exchange plus dipolar energies, and J_c as the energy (likely dominated by dipolar interactions) of interaction along the c-axis. The crystallography for the present systems dictates that $J_{ab} \gg J_c$, and hence the systems should display 2D-like behavior. By this we mean that for $kT \gg J_{ab}$ there will be no significant correlations in the system, and the magnetic (diffuse) scattering will be uniformly spread throughout the entire Brillouin zone. As kT becomes comparable to J_{ab}, strong correlations develop within the planes, while there will be no significant correlations between layers as has been found in the $ErBa_2Cu_3O_7$ and $DyBa_2Cu_3O_7$ systems just discussed. This will give rise to rods of critical scattering. For $J_{ab} > kT > J_c$ we will continue to see a rod of scattering; above the ordering temperature this will be critical scattering, while below the ordering temperature this will consist of low-energy spin waves.

For systems which are strictly two-dimensional, of course, only an Ising model (which we believe to be appropriate for the present materials) will exhibit true long-range order at finite temperature. However, even for the cases of xy or Heisenberg spins, 3D long-range order will be induced for $J_c \ll J_{ab}$. In the conventional two-dimensional systems such as K_2NiF_4 (Birgeneau et al. 1970) and K_2CoF_4 (Ikeda and Hirakawa 1974), and of course the Cu spins in the insulating cuprates, the 2D ordering and the 3D ordering in fact occur at (essentially) the same temperature. The reason for the induced 3D order can be understood by the following argument. Assume that a static moment has developed in the layers. There is then an energy $\pm J_c A$ between the layers, where A is the average size of a domain in the layer. The minus sign is for layers that are properly matched (e.g. antiferromagnet configuration if $J_c < 0$), where every spin is correctly paired with the adjacent layer. The + sign, on the other hand, is for layers that are mismatched,

in which every spin is incorrectly aligned. Thus even if the interlayer coupling is very weak, there is an energy difference $\sim 2J_cA$ between the "correct" and the "wrong" spin configurations, and this energy difference can be quite large since A is large. Hence as soon as 2D order is established, ordering is expected to be induced along the c-axis, producing 3D Bragg peaks. In the "conventional" 2D magnets studied to date, in fact, no difference has been discerned between $T_N(2D)$ and $T_N(3D)$. An interesting exception to this behavior will be discussed in the next section.

Another manifestation of the weak interactions along the c-axis is that the materials can get "confused" about what is the correct spin structure. The confusion may be caused by the influence of twin and grain boundaries, defects, intergrowths, variations in the oxygen content, etc., which can alter the delicate balance of the dipolar energies. The $ErBa_2Cu_3O_7$ structure, for example, corresponds to chains of moments that are aligned ferromagnetically along the b-axis, while adjacent chains are aligned antiparallel to form an overall antiferromagnetic configuration. In some samples, however, the spins along the c-axis are found to be parallel rather than antiparallel, forming ferromagnetic sheets of spins (Paul et al. 1989, Chattopadhyay et al. 1988a, 1989). The dipole energies for these two configurations are very similar, and the specific structure may depend on the metallurgical state of the sample. A similar dichotomy of structures has been observed for the Dy (Clinton et al. 1991, 1995, Goldman et al. 1987) and Gd (Mook et al. 1988, Chattopadhyay et al. 1988b) 1-2-3 compounds, and a multiplicity of magnetic structures may be a common feature of these systems. The magnetic structures for the 1-2-3 materials are summarized in fig. 12; additional details are reviewed elsewhere (Lynn 1990). Dipole–dipole interactions favor three different types of magnetic order in the a–b plane based on the direction of the magnetic moment, which is generally determined by the crystal-field anisotropy. If the moment is along the c-axis (Nd, Gd, Dy), nearest-neighbor spins order antiferromagnetically along both a and b directions (figs. 12c,d). If moments are along the b-axis (Er), they are coupled antiferromagnetically along a and ferromagnetically along b (figs. 12a,b), and this coupling is reversed for moments along the a-axis (fig. 12e) (Ho; Roessli et al. 1993a). All the a–b-plane spin configurations are the same for 2-4-7, 2-4-8, and for 1-2-3 compounds with different oxygen concentrations; the only known exception to this is Yb (Roessli et al. 1992), where the magnetic moment is along b like Er, but the coupling is ferromagnetic along a and antiferromagnetic along b (fig. 12f).

4.3. *$R_2Ba_4Cu_8O_{16}$ and $R_2Ba_4Cu_7O_{15}$ systems – ideal 2D magnetism*

The 2-4-8 and 2-4-7 systems are directly related to the 1-2-3 system, and the lanthanide sublattices are shown in fig. 9 (above). For the 2-4-8 system which we will discuss first, the basic difference with the 1-2-3 is that each layer along the c-axis is shifted by $b/2$, producing a face-centered type of lattice along the b-axis. The nearest-neighbor distance along the c-axis is still three times a or b, and hence the intrinsic magnetic interactions are highly anisotropic just like the 1-2-3 case. The low-temperature magnetic diffraction pattern for a powder sample of $Dy_2Ba_4Cu_8O_{16}$ (often called simply $RBa_2Cu_4O_8$) is

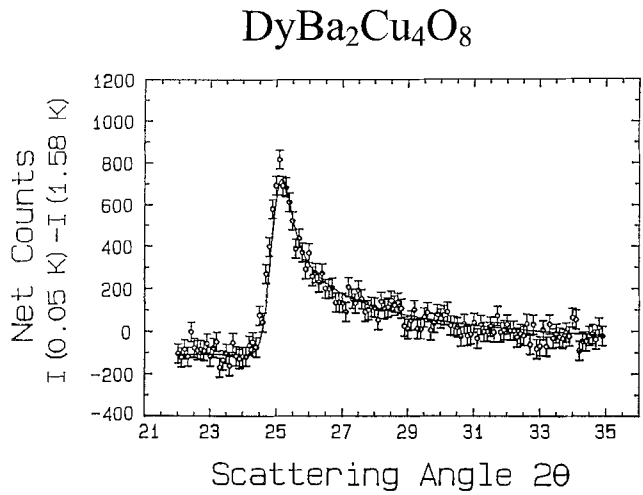

Fig. 13. Magnetic scattering for $DyBa_2Cu_4O_8$ at 0.05 K, well below the ordering temperature of 0.9 K. The data are obtained by subtracting the high temperature data from the data well below the ordering temperature, and the "negative" background is due to the absence of paramagnetic scattering in the ordered state. The magnetic scattering exhibits the classic shape for a two-dimensionally ordered material. No three-dimensional Bragg peaks are observed at any temperature (Zhang et al. 1990).

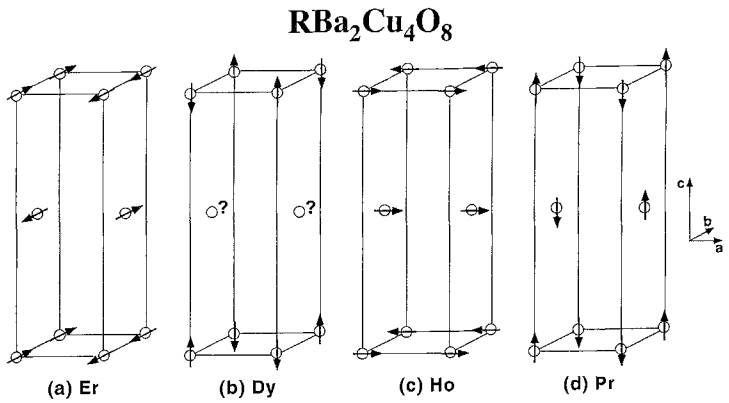

Fig. 14. Magnetic structures for the $RBa_2Cu_4O_8$ materials. (a) Er (Zhang et al. 1990). (b) Dy (Zhang et al. 1990, Roessli et al. 1993b). (c) Ho (Roessli et al. 1994). (d) Pr (Lin et al. 1998).

shown in fig. 13 (Zhang et al. 1990). Instead of 3D powder Bragg peaks, the scattering shows a 2D-like "sawtooth" profile even though we are well below the Néel temperature $T_N = 0.9$ K. The solid curve is in fact a fit to the 2D theory, assuming long-range order within the a–b plane and no correlations along the c-direction. The scattering corresponds to the $(\frac{1}{2},\frac{1}{2})$ 2D peak, which means that nearest neighbors within the a–b plane are antiparallel. The magnetic structure for Dy 2-4-8 (Zhang et al. 1990, Roessli et al. 1993b) is shown in fig. 14b, along with the other 2-4-8 systems investigated. In the first layer all

the spins are antiferromagnetically arranged. In the next layer up along the c-axis, all the spins are displaced by $b/2$. For the closest spins between layers, we will have two + spins and two − spins, and the net interaction is zero. Next-neighbor interactions also cancel, and in fact all the (point) interactions sum to zero by symmetry. Hence this is an example of a fully frustrated spin system for the interlayer coupling (indicated by the question mark in the figure), and the a–b layers are for practical purposes completely decoupled from one another. Similar behavior has been observed in the $Dy_2Ba_4Cu_7O_{15}$ system (Zhang et al. 1992). In this bilayer case the magnetic scattering appears as a modulated saw-tooth profile, with the modulation arising from the bilayer structure of the material. We expect a similar decoupling of adjacent layers or bilayers for any of the other lanthanide elements which have the same in-plane magnetic structure, which is in fact the most common occurrence. For $Er_2Ba_4Cu_8O_{16}$, on the other hand, the Er spins in the a–b plane form ferromagnetic chains (Zhang et al. 1990), as in the Er 1-2-3 case. This magnetic structure does not possess the frustration of the Dy material, and thus conventional three-dimensional Bragg peaks are observed below T_N. However, above T_N 2D correlations are still found, indicating that the basic interactions are 2D-like as expected.

Three-dimensional magnetic Bragg peaks are also observed in $Er_2Ba_4Cu_7O_{14.92}$ (Böttger et al. 1997), with a finite but large correlation length (~130 Å) along the c-axis. Specific-heat data on this compound can be described by an anisotropic 2D Ising antiferromagnet, and therefore the basic interactions are 2D in character like Er 1-2-3 and Er 2-4-8. The only other compound in this series that has been studied by neutron diffraction is Ho 2-4-8 (Roessli et al. 1994). The data are similar to Dy 2-4-8, and thus Ho 2-4-8 is fully frustrated for the interlayer coupling; the data show long-range 2D magnetic peaks with a short correlation length (~18 Å) along the c-axis.

4.4. *Oxygen dependence of the lanthanide ordering in $RBa_2Cu_3O_{6+x}$*

Significant variations of the magnetic ordering are observed as a function of oxygen concentration for various lanthanides, such as Er (Clinton et al. 1995, Maletta et al. 1990), Dy, and Nd (Clinton et al. 1993, 1995), while in $GdBa_2Cu_3O_{6+x}$ the oxygen concentration does not appear to affect the nature of the three-dimensional long-range magnetic order or the ordering temperature (~2.2 K) (Chattopadhyay et al. 1988b, Paul et al. 1988, Mook et al. 1988). In $ErBa_2Cu_3O_{6+x}$, for example, T_N is initially found to decrease with decreasing x, and for $x \gtrsim 0.5$ long-range 3D magnetic order occurs below T_N and 2D short-range correlations above T_N. For $x \lesssim 0.5$ 3D long-range magnetic order is lost, and only 2D correlations are observed. In $ErBa_2Cu_3O_6$, neither 2D nor 3D long-range order develops, and only 2D short-range correlations are observed. The superconducting phase of $DyBa_2Cu_3O_{6+x}$ exhibits the same behavior as Er, that is, no 3D correlations are observed above T_N (~0.9 K), while 3D long-range order is observed below T_N. In the insulating phase ($x < 0.4$), on the other hand, both 2D and 3D correlations develop at low temperatures, but 3D long-range order never occurs.

The concentration of oxygen appears to have the strongest effects in $NdBa_2Cu_3O_{6+x}$ (Yang et al. 1989, Clinton et al. 1993, 1995). For the fully oxygenated (and supercon-

ducting) materials 3D long-range order is observed, with $T_N = 0.53$ K. Modest reduction of the oxygen concentration to $x = 0.78$, however, completely destroys 3D order, and only short-range 2D correlations (~20 Å) are observed. At lower x where the insulating phase occurs (and the Cu spins are ordered) 3D order again develops with a T_N as high as 1.5 K. The transition is still sharp, as there is not much coupling to the Cu sublattice. The ordered moment for Nd is only about $1\mu_B$, so the high ordering temperature for Nd cannot be explained by dipole interactions alone.

All these observations indicate that there is some coupling between lanthanide moments and the Cu chain layer, since the magnetic ordering is strongly affected by the oxygen content. The detailed nature of these interactions, however, is not understood at this time.

4.5. $Pb_2Sr_2R_{1-x}Ca_xCu_3O_8$

Neutron studies (Wu et al. 1994, 1996, Hsieh et al. 1994b, Staub et al. 1995–1997) have been performed on the magnetic ordering in powder samples of $Pb_2Sr_2R_{1-x}Ca_xCu_3O_8$, which superconducts for $0.2 < x < 0.8$. In these materials all the lanthanides except Ce superconduct, with T_c as high as 80 K. The suppression of superconductivity in $Pb_2Sr_2Ce_{1-x}Ca_xCu_3O_8$ is not thought to be connected to the magnetism, but to the tetravalent nature of the Ce ion in this compound (Skanthakumar and Soderholm 1996).

The lanthanide ions in this system have a site environment that is similar to that in the 1-2-3 systems, and the 2D magnetic behavior that has been observed for R = Tb and Pr is not unexpected. The separation along the c-axis is about 15.8 Å, which is even larger than the 1-2-3 system. In $Pb_2Sr_2Tb_{1-x}Ca_xCu_3O_8$, the Tb spins are found to order with relatively high transition temperatures of 5.3 and 4 K for $x = 0.0$ and 0.5, respectively. These high ordering temperatures again demonstrate that exchange interactions dominate in these materials. In addition, magnetic susceptibility and inelastic neutron scattering experiments suggest that significant 2D Tb–Tb correlations persist even at temperatures above the superconducting transition temperature, which is more than an order of magnitude above T_N. Further work on this class of materials is warranted.

5. The special case of Pr

A singular exception to the low ordering temperatures of the lanthanides is found for the class of cuprates that contain Pr: these generally are not even metallic let alone superconducting. This unique behavior has inspired extensive studies of the physical properties of the Pr cuprates in order to determine why only Pr suppresses the superconducting state while the other lanthanides exhibit very little effect. The magnetic ordering of the Pr is also anomalous in that the ordering temperatures are an order of magnitude higher (~15 K) than for the other rare-earth systems, indicating much stronger exchange and hybridization effects for the 4f Pr electrons.

Investigations of the magnetic order of Pr in $PrBa_2Cu_3O_{6+x}$ have been complicated by a number of factors. One is that this material is a semiconductor for all x, and thus

the Cu spins always order at a much higher temperature than the Pr spins. A second complication is that with appropriate doping, either directly on the chain site or on the Ba site, the chain spins can also develop a moment and exhibit long-range magnetic order, either together with the plane spins or as a separate magnetic transition. Moreover, the development of chain moments turns out to be especially sensitive to even small levels of dopants in the Pr 1-2-3 system, which has been a particular problem with many flux-grown crystals. A further complication is that the ordered moments for Pr and Cu are comparable in magnitude, and this can lead to ambiguities in the interpretation of data. Finally, Pr has a tendency to occupy the Ba site in Pr 1-2-3, and this changes both the magnetic and electronic behavior.

These complications have led to possible ambiguities in interpretations and lively debates, but a consensus has now emerged about the nature of the Pr ordering in these materials. Nevertheless, the consensus is certainly not yet unanimous, and the debate will no doubt continue with the recent report by Zou et al. (1998) of superconductivity in a small fraction of a variant, not yet identified, phase of Pr 1-2-3. This contrasts with the semiconducting behavior found in the overwhelming majority of Pr 1-2-3 samples, as already noted. However, it has been shown that the susceptibility in the sample that exhibits superconductivity is a factor of two smaller than was reported initially (Narozhnyi and Drechsler 1999, Zou et al. 1999), suggesting that the Pr content is reduced by half, and thus it seems likely that the floating-zone technique produces small regions that are either Y-rich and/or Ba-rich with Ba occupying the Pr site. In particular, it is known that relatively modest substitution for Ca on the Pr site provides a 90 K superconductor (Xiong et al. 1998), and similar behavior would be expected for Ba. Thus it seems likely that the superconductivity does not originate from Pr 1-2-3, but rather from an alloy.

We start our discussion of the Pr magnetic ordering by considering $PrBa_2Cu_3O_{6+x}$, which was the first Pr material to be investigated with neutrons (Li et al. 1989). The system is a semiconductor for the full range of x, with the Cu ions retaining their high magnetic ordering temperature. The f-electron hybridization has been observed directly by inelastic neutron scattering experiments, which have found that there are substantial linewidths to the crystal-field excitations of the Pr (Staub and Soderholm 2000). The exchange interactions are thereby enhanced, increasing the ordering temperature and rendering the lanthanide ordering 3D in nature.

In this initial study a simple antiferromagnetic ordering was found to develop below $T_N = 17$ K, with antiferromagnetic coupling between nearest-neighbor Pr moments in all three directions in the crystal. The magnetic structure is the same as found in the Dy and Gd 1-2-3 systems, shown in fig. 12c. The observed ordering temperature was in good agreement with specific heat and susceptibility results, which studies have elucidated the systematics of this ordering by following it as a function of oxygen concentration and as a function of Y (and other lanthanides) substitution on the Pr site (for a review see Radousky 1992). Bulk measurements show that as oxygen is removed T_N(Pr) monotonically decreases to 12 K for $PrBa_2Cu_3O_6$, and this has been confirmed by neutron diffraction measurements on the depleted system (Guillaume et al. 1993).

Studies on single crystals of the "pure" $PrBa_2Cu_3O_{6+x}$ have been carried out subsequently, but the results have been complicated because of contamination of the samples from the crucible, and/or Pr substitution on the Ba site. In particular, it is now known that crystals grown in alumina or MgO crucibles by the flux technique become doped by Al or Mg (Casalta et al. 1994, Uma et al. 1998b). These (inadvertent) dopings can cause the Cu chain spins to order (Lynn et al. 1988, Li et al. 1988, 1990, Rosov et al. 1992a). This ordering varies with oxygen content x, and is strongly coupled to the Pr sublattice because the symmetry of the two magnetic structures is the same. The chain doping can also reduce the Néel temperature for the Pr ordering, and can change the nature of the Pr structure along the c-direction (Longmore et al. 1996, Boothroyd et al. 1997, Boothroyd 1998, 2000) so that the usual c-axis antiferromagnetic coupling is not found in these samples. During the course of these investigations there was also a suggestion from NMR measurements (Nehrke and Pieper 1996) that the Pr was actually non-magnetic in pure Pr 1-2-3, but a reinvestigation with neutrons (Skanthakumar et al. 1997b) on pure powders indicated that the Pr was indeed ordering, and this has also been confirmed on pure crystals by neutrons (Uma et al. 1998a) and by resonant X-ray scattering (Hill et al. 1998). It therefore appears likely that the NMR may have been detecting some Pr on the Ba site in that sample, which may well be in a nonmagnetic singlet crystal-field state, while the line due to the Pr on the R site is too broad to observe.

The relatively recent development of non-reactive $BaZrO_3$ crucibles has now permitted the growth and investigation of undoped single crystals. In a fully oxygenated single crystal the Cu spins order at 281 K, while the Pr moments order at 16.8 K as shown in fig. 15 (Uma et al. 1998a). The initial ordering is revealed by the intensity of the $(\frac{1}{2},\frac{1}{2},0)$ versus T shown in the center. This structure corresponds to antiferromagnetic alignment of spins in the a–b plane, while the spins along the c-direction are ferromagnetically aligned. The development of the ordered Pr moment is accompanied by a modest coupling to the Cu spins as indicated by the intensity of the $(\frac{1}{2},\frac{1}{2},2)$ Cu peak (top). At ~11 K (on cooling) a first-order "spin-flop" transition occurs to a Pr spin structure where the nearest-neighbor Pr moments along the c-axis flip to become antiparallel rather than parallel. This corresponds to the development of the $(\frac{1}{2},\frac{1}{2},\frac{1}{2})$-type peak as indicated in the bottom of the figure. The data clearly indicate that there is strong hysteresis in both types of Pr magnetic peaks, and the behavior is in good agreement with the specific heat and thermal expansion data taken on warming and cooling. The results on this pure single crystal are in general agreement with the data obtained on the polycrystalline sample, but the details with regard to the crossover from ferromagnetic to antiferromagnetic nearest-neighbor alignment along the c-axis are different. These differences are likely due to the delicate balance of interactions along the c-axis (Narozhnyi et al. 1999), and their subtle dependence on factors such as small concentrations of defects and impurities, oxygen content, strain, etc. There have also been indications of a small in-plane incommensurability of the magnetic peaks observed by X-ray resonant scattering (Hill et al. 1998).

Studies have also been carried out to observe the effects on both Cu and Pr order by chemical substitution on other sites in the Pr 1-2-3 system. Zn is found to substitute on

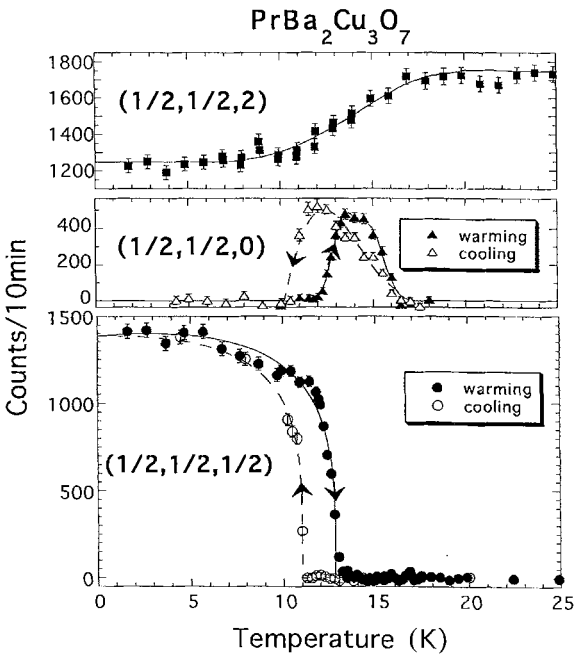

Fig. 15. Temperature dependence of the (top) $(\frac{1}{2},\frac{1}{2},2)$, (center) $(\frac{1}{2},\frac{1}{2},0)$, (bottom) $(\frac{1}{2},\frac{1}{2},\frac{1}{2})$ magnetic Bragg peaks in a pure single crystal of $PrBa_2Cu_3O_7$ (Uma et al. 1998a).

the Cu planes, and this has no effect on either the Pr ordering temperature or size of the ordered moment (Li et al. 1993), but it does change the coupling along the c-axis from antiferromagnetic to ferromagnetic. Ga, on the other hand, substitutes preferentially on the Cu chain sites. This again changes the magnetic structure along the c-axis from antiferromagnetic to ferromagnetic, but in addition T_N is reduced (Li et al. 1994) while the ordered moment remains unchanged. Neither of these substitutions has a significant effect on the Cu powder Bragg peaks in the temperature regime where the Pr orders. Another type of substitution can occur for "pure" $PrBa_2Cu_3O_{6+x}$, where the Pr can substitute on the Ba site forming $Pr_{1+x}Ba_{2-x}Cu_3O_{6+y}$. This has the effect of reducing the ordering temperature for the Pr (Malik et al. 1992), as does La substitution for Ba (Wang et al. 2000).

There has been considerable additional work investigating the magnetic ordering of the Pr in the cuprate class of materials, and the properties for Pr systems investigated with neutrons in this class of materials have been reviewed recently elsewhere (Lynn 1997). $PrBa_2Cu_4O_8$ also orders antiferromagnetically at $T_N \approx 17$ K like the 1-2-3 material, with an analogous magnetic structure (Lin et al. 1998, Li et al. 1999). For $PrBa_2Cu_2NbO_8$ (Rosov et al. 1993) the Cu chain layer is replaced with a (fully oxygenated) NbO_2 layer, which of course carries no moment. This eliminates the complication of the chain magnetism, and we still find a high ordering temperature for the Pr and no influence on the Cu plane ordering when the Pr subsystem orders. A similar situation occurs for $TlBa_2PrCu_2O_7$ (Hsieh et al. 1994a) where the CuO chains are replaced by TlO.

There is no observable interaction between the Cu and Pr order, as would be expected since the magnetic structures have different symmetries. Similar behavior is observed for the more complicated $Pr_{1.5}Ce_{0.5}Sr_2Cu_2(Nb,Ta)O_{10}$ system (Goodwin et al. 1997). Again there can be no Cu chain magnetism, and there is a high observed T_N for the Pr. The $Pb_2Sr_2PrCu_3O_8$ material (Hsieh et al. 1994b, Lin et al. 1997) is somewhat different in that it has no oxygen in the Cu chain layer, while the properties of the Pr are quite similar to the other systems. Finally, we note that the related $BaPrO_3$ material, which obviously has no complications of Cu ordering of any kind, exhibits a similar Pr ordering temperature and reduced moment (Rosov et al. 1992b) as for the cuprates. Thus in all the layered cuprates the Pr carries a moment and orders magnetically at much higher temperatures than the heavy lanthanides.

6. Lanthanide spin dynamics

Measurements of the spin dynamics of the lanthanide moments are considerably more difficult than determining the magnetic structures, but several investigations have been made which we briefly point out. If we introduce lanthanide exchange interactions, then this will give rise to magnetic excitons propagating in the lattice. This is revealed as dispersion of the crystal-field levels, and such dispersion has been observed for both Pr_2CuO_4 (Sumarlin et al. 1994, 1995) and Nd_2CuO_4 (Henggeler et al. 1996), and for the Ce-doped systems (Henggeler et al. 1997). The observed dispersion is as large as a few meV, which indicates that there are quite significant R–R exchange interactions in these materials. The spin dynamics of the exchange-split crystal-field ground state have also been investigated for Nd_2CuO_4 by Loewenhaupt et al. (1995), and more recently by Casalta et al. (1998) above the Nd magnetic ordering temperature. The latter authors find that there is a fluctuation component that persists up to room temperature, and is associated with the exchange field of the Cu spins acting on the Nd moments. This has decidedly 2D character and presumably originates from the 2D character of the Cu spin system. The other component originates from the usual paramagnetic spin fluctuations of the Nd moments above the ordering temperature. Below T_N the Nd and Cu modes are predicted to be mixed in the parent compound, and the theoretical predictions for the spin dynamics in the ordered state (Thalmeier 1996, Sachidanandam et al. 1997) are in reasonable agreement with experiment (Henggeler et al. 1997). There is predicted to be an additional mode that has yet to be observed, and additional work in this area is desirable. In the doped system the observed spin waves are simplified because the Cu spins are not ordered, and the model calculations are able to reproduce the data.

The spin dynamics of the lanthanide systems have also been investigated both above and below the ordering temperature in superconducting $ErBa_2Cu_3O_7$ (Skanthakumar et al. 1997a). In this case the Cu moments interact weakly with the Er and are not ordered, and the lanthanide system can thus be treated independently of the Cu. The ground-state dispersion relation along the [110] direction is shown in fig. 16. There is a large (compared to kT_N) gap of about 0.20 meV in the excitation spectrum, as would be

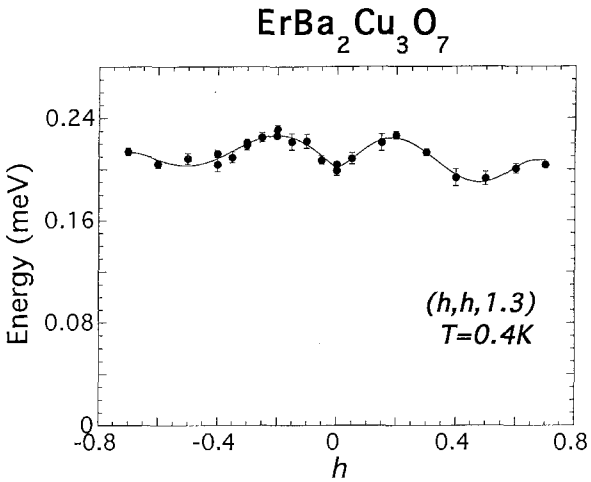

Fig. 16. Spin wave dispersion along [110] direction for $ErBa_2Cu_3O_7$. The solid curve is a guide to the eye (Skanthakumar et al. 1997a).

expected for an Ising system. However, for a pure Ising system S^z commutes with the Hamiltonian and thus the spin waves would be dispersionless, while there is clearly some observed dispersion in the a–b plane. Measurements along the c-axis indicate that these excitations have no measurable dispersion in that direction, and this behavior is expected because the magnetic interactions are weak along the c-direction. The Ising-type gap is still dominant, though, and the data of fig. 16 show that this material is still a good approximation to an Ising magnet.

Finally, we note that the spin dynamics for the Pr 1-2-3 system have been investigated in some detail, and not surprisingly, it is quite different than the other systems. A broad distribution of quasielastic scattering (and broad crystal field levels) was observed in powders (Skanthakumar et al. 1990). These energy widths could be due to exchange interactions, where the width is caused by the powder average of a dispersive excitation, or it could be intrinsically broad due to hybridization. Single-crystal measurements reveal a broad, dispersionless distribution of scattering (Lynn et al. 2000), indicating that hybridization is the cause. In addition, the distribution of magnetic scattering is temperature-independent, similar to what has been observed in non-Fermi liquid systems (Aronson et al. 1995). Lister et al. (2000) have also carried out inelastic measurements on single crystals recently and find a similar distribution of scattering, but with some structure in it. Further measurements will be needed to explore these details.

7. Overview and future directions

The magnetic ordering of the lanthanide ions in superconducting systems has been a topic of active interest for many years. In conventional "magnetic superconductors" such as the Chevrel phase and related materials the lanthanide moments are coupled very weakly both to the metallic electrons and to each other, resulting in very low

magnetic ordering temperatures and a delicate energetic balance with superconductivity. A similar situation occurs for the layered cuprates in that the development of long-range lanthanide magnetic order also occurs at very low temperatures. In contrast to the earlier systems, though, the superconductivity in the cuprates typically occurs at much higher temperatures, and the antiferromagnetic order that develops on the lanthanide sublattice coexists with the superconducting state. Neutron scattering has revealed the nature of the magnetic ordering of the lanthanide ions in the layered 1-2-3, 2-4-8, and 2-4-7 oxide superconductors, where the separation of the lanthanide ions is much larger along the c-axis than along the a–b directions. This renders these materials prototypical two-dimensional (2D) magnets, and with the spin–spin interactions being relatively weak compared to the anisotropies, this generally results in Ising-like magnetic behavior. Thus in the $ErBa_2Cu_3O_7$ material, for example, there is remarkable agreement between the observed order parameter and the exact solution for the $S=\frac{1}{2}$ 2D Ising model. Another textbook example is provided by the $DyBa_2Cu_4O_8$ system, where a geometric cancellation of the already weak interactions occurs along the c-axis, effectively decoupling the lanthanide a–b layers. The system thus exhibits no crossover to the 3D behavior usually found below the ordering temperature, making it the best example of a 2D magnet known to date. One of the interesting avenues of exploration will be to investigate the spin dynamics of these materials, as high-quality single crystals large enough for inelastic scattering become available.

The 2-1-4 class of materials, on the other hand, provides the first examples of superconductors where the exchange interactions unambiguously dominate the lanthanide energetics, such as Sm_2CuO_4 which has a dipole ordering temperature that is two orders of magnitude lower than the observed ordering temperature of 6 K. Thus the traditional picture of negligible exchange being necessary for a superconducting material to simultaneously exhibit long-range magnetic order has to be abandoned. Of course, the magnetic properties of the Cu ions are also of central interest, where the magnetic fluctuations may be directly involved in the formation of the superconducting state. The question of the origin of the superconductivity has by no means been settled yet, but even if magnetic fluctuations are not at the root of the superconductivity in these high-T_c materials, it is quite clear that the Cu–O layers are intimately involved in both the magnetism and superconductivity, and the striking magnetic behavior these materials display is of fundamental interest in its own right.

From the very early days of cuprate superconductors it was known that a dramatic exception to the overall behavior of these magnetic-superconductor systems occurs for Pr, and this singular exception has been the subject of extensive research. The magnetic ordering temperatures are an order of magnitude higher for Pr than for the other lanthanide materials, and consequently the magnetic coupling must be dominated by exchange. Moreover, with the exception of Pr_2CuO_4 where the crystal-field ground state is an isolated singlet, superconductivity is significantly affected in the Pr materials. The origins of this effect and the nature of the Pr magnetism are still under active investigation and debate, and this will certainly be an area that will receive attention from experimentalists and theorists alike.

Acknowledgments

We would like to thank all of our collaborators who have worked with us on various aspects of these problems. We thank Taner Yildirim for providing the calculations shown in figs. 5 and 7. We would also like to thank Taner, Frederic Bourdarot, and Dan Dender for a careful reading of the manuscript. Work at Argonne is supported by the DOE-BES, Chemical Sciences under contract W-31-109-ENG-38. Work at the University of Maryland supported in part by the NSF, DMR 97-01339.

References

Abrikosov, A.A., and L.P. Gorkov, 1961, Sov. Phys. JETP **12**, 1243.

Akimitsu, J., H. Sawa, T. Kobayashi, H. Fujiki and Y. Yamada, 1989, J. Phys. Soc. Jpn. **58**, 2646.

Allenspach, P., S.-W. Cheong, A. Dommann, P. Fischer, Z. Fisk, A. Furrer, H.R. Ott and B. Rupp, 1989, Z. Phys. B **77**, 185.

Andreev, A.V., A.I. Buzdin and R.M. Osgood, 1990, JETP Lett. **52**, 55.

Aronson, M.C., R. Osborn, R.A. Robinson, J.W. Lynn, R. Chau, C.L. Seaman and M.B. Maple, 1995, Phys. Rev. Lett. **75**, 725.

Bacon, G.E., 1975, Neutron Diffraction, 3rd Ed. (Oxford University Press, Oxford).

Birgeneau, R.J., H.J. Guggenheim and G. Shirane, 1970, Phys. Rev. B **1**, 2211.

Boothroyd, A.T., 1998, Physica B **241–243**, 792.

Boothroyd, A.T., 2000, J. Alloys & Compounds **303–304**, 489.

Boothroyd, A.T., A. Longmore, N.H. Andersen, E. Brecht and Th. Wolf, 1997, Phys. Rev. Lett. **78**, 130.

Böttger, G., P. Fisher, A. Dönni, P. Berastegui, Y. Aoki, H. Sato and F. Fauth, 1997, Phys. Rev. B **55**, 12005.

Casalta, H., P. Schleger, E. Brecht, W. Montfrooij, N.H. Andersen, B. Lebech, W.W. Schmahl, H. Fuess, R. Liang, W.N. Hardy and T. Wolf, 1994, Phys. Rev. B **50**, 9688.

Casalta, H., Ph. Bourges, M. D'Astuto, D. Petitgrand and A.S. Ivanov, 1998, Phys. Rev. B **57**, 471.

Chattopadhyay, T., and K. Siemensmeyer, 1995, Europhys. Lett. **29**, 579.

Chattopadhyay, T., P.J. Brown, D. Bonnenberg, S. Ewert and H. Maletta, 1988a, Europhys. Lett. **6**, 363.

Chattopadhyay, T., H. Maletta, W. Wirges, K. Fisher and P.J. Brown, 1988b, Phys. Rev. B **38**, 838.

Chattopadhyay, T., P.J. Brown, B.C. Sales, L.A. Boatner, H.A. Mook and H. Maletta, 1989, Phys. Rev. B **40**, 2624.

Chattopadhyay, T., O.B. Hyun and D.K. Finnemore, 1990, Solid State Commun. **73**, 721.

Chattopadhyay, T., P.J. Brown and U. Kobler, 1991a, Physica C **177**, 294.

Chattopadhyay, T., P.J. Brown, A.A. Stepanov, P. Wyder, J. Voiron, A.I. Zvyagin, S.N. Barilo, D.I. Zhigunov and I.A. Zobkalo, 1991b, Phys. Rev. B **44**, 9486.

Chattopadhyay, T., P.J. Brown, B. Roessli, A.A. Stepanov, S.N. Barilo and D.I. Zhigunov, 1992, Phys. Rev. B **46**, 5731.

Chattopadhyay, T., P.J. Brown and B. Roessli, 1994a, J. Appl. Phys. **75**, 6816.

Chattopadhyay, T., J.W. Lynn, N. Rosov, T.E. Grigereit, S.N. Barilo and D.I. Zhigunov, 1994b, Phys. Rev. B **49**, 9944.

Clinton, T.W., J.W. Lynn, J.Z. Liu, Y.X. Jia and R.N. Shelton, 1991, J. Appl. Phys. **70**, 5751.

Clinton, T.W., J.W. Lynn, B.W. Lee, M. Buchgeister and M.B. Maple, 1993, J. Appl. Phys. **73**, 6320.

Clinton, T.W., J.W. Lynn, J.Z. Liu, Y.X. Jia, T.J. Goodwin, R.N. Shelton, B.W. Lee, M. Buchgeister, M.B. Maple and J.L. Peng, 1995, Phys. Rev. B **51**, 15429.

Cox, D.E., A.I. Goldman, M.A. Subramanian, J. Gopalakrishnan and A.W. Sleight, 1989, Phys. Rev. B **40**, 6998.

Elschner, B., and A. Loidl, 2000, in: Handbook on the Physics and Chemistry of Rare Earths, Vol. 30, eds K.A. Gschneidner Jr, L. Eyring and M.B. Maple (Elsevier, Amsterdam) ch. 191.

Endoh, Y., M. Matsuda, K. Yamada, K. Kakurai, Y. Hidaka, G. Shirane and R.J. Birgeneau, 1989, Phys. Rev. B **40**, 7023.

Fischer, Ø., and M.B. Maple, eds, 1983, Superconductivity in Ternary Compounds, Vols. 32 and 34 of Topics in Current Physics (Springer, New York).

Fischer, P., K. Kakurai, M. Steiner, K.N. Clausen, B. Lebech, F. Hulliger, H.R. Ott, P. Brüesch and P. Unternährer, 1988, Physica C **152**, 145.

Fischer, P., B. Schmid, P. Brüesch, F. Stucki and P. Unternährer, 1989, Z. Phys. B **74**, 183.

Goldman, A.I., B.X. Yang, J.M. Tranquada, J.E. Crow and C.-S. Jee, 1987, Phys. Rev. B **36**, 7234.

Goodwin, T.J., R.N. Shelton, H.B. Radousky, N. Rosov and J.W. Lynn, 1997, Phys. Rev. B **55**, 3297.

Guillaume, M., P. Fischer, B. Roessli, A. Podlesnyak, J. Schefer and A. Furrer, 1993, Solid State Commun. **88**, 57.

Guillaume, M., P. Fischer, B. Roessli, P. Allenspach and V. Trounov, 1994, Physica C **235**, 1637.

Gukasov, A.G., S.Yu. Kokovin, V.P. Plakhty, I.A. Zobkalo, S.N. Barilo and D.I. Zhigunov, 1992, Physica B **180**, 455.

Henggeler, W., T. Chattopadhyay, B. Roessli, D.I. Zhigunov, S.N. Barilo and A. Furrer, 1996, Z. Phys. B **99**, 465.

Henggeler, W., T. Chattopadhyay, B. Roessli, P. Vorderwisch, P. Thalmeier, D.I. Zhigunov, S.N. Barilo and A. Furrer, 1997, Phys. Rev. B **55**, 1269.

Hill, J.P., A. Vigliante, D. Gibbs, J.L. Peng and R.L. Greene, 1995, Phys. Rev. B **52**, 6575.

Hill, J.P., A.T. Boothroyd, N.H. Andersen, E. Brecht and Th. Wolf, 1998, Phys. Rev. B **58**, 11211.

Hsieh, W.T., K.J. Chang, W.-H. Li, K.C. Lee, J.W. Lynn, C.C. Lai and H.C. Ku, 1994a, Phys. Rev. B **49**, 12200.

Hsieh, W.T., W.-H. Li, K.C. Lee, J.W. Lynn, J.H. Shieh and H.C. Ku, 1994b, J. Appl. Phys. **76**, 7124.

Ikeda, H., and K. Hirakawa, 1974, Solid State Commun. **14**, 529.

Katano, S., R.M. Nicklow, S. Funahashi, N. Mori, T. Kobayashi and J. Akimitsu, 1993, Physica C **215**, 92.

Li, W.-H., J.W. Lynn, H.A. Mook, B.C. Sales and Z. Fisk, 1988, Phys. Rev. B **37**, R9844.

Li, W.-H., J.W. Lynn, S. Skanthakumar, T.W. Clinton, A. Kebede, C.-S. Jee, J.E. Crow and T. Mihalisin, 1989, Phys. Rev. B **40**, R5300.

Li, W.-H., J.W. Lynn and Z. Fisk, 1990, Phys. Rev. B **41**, 4098.

Li, W.-H., K.J. Chang, W.T. Hsieh, K.C. Lee, J.W. Lynn and H.D. Yang, 1993, Phys. Rev. B **48**, 519.

Li, W.-H., C.J. Jou, S.T. Shyr, K.C. Lee, J.W. Lynn, H.L. Tsay and H.D. Yang, 1994, J. Appl. Phys. **76**, 7136.

Li, W.-H., W.Y. Chuang, S.Y. Wu, K.C. Lee, J.W. Lynn, H.L. Tsay and H.D. Yang, 1997, Phys. Rev. B **56**, 5631.

Li, W.-H., S.Y. Wu, Y.-C. Lin, K.C. Lee, J.W. Lynn, S.S. Weng, I.P. Hong, J.-Y. Lin and H.D. Yang, 1999, Phys. Rev. B **60**, 4212.

Lin, Y.-C., W.Y. Chuang, W.-H. Li, K.C. Lee, J.W. Lynn, C.L. Yang and H.C. Ku, 1997, J. Appl. Phys. **81**, 4940.

Lin, Y.-C., S.Y. Wu, W.-H. Li, K.C. Lee, J.W. Lynn, C.W. Lin, J.-Y. Lin and H.D. Yang, 1998, Physica B **241–243**, 702.

Lister, S.J.S., A.T. Boothroyd, N.H. Andersen, A.A. Zhokhov and A.N. Christensen, 2000, Physica B **276**, 799.

Loewenhaupt, M., P. Fabi, S. Horn, P. v. Aken and A. Severing, 1995, J. Magn. Magn. Mater. **140–144**, 1293.

Longmore, A., A.T. Boothroyd, C. Changkang, H. Yongle, M.P. Nutley, N.H. Andersen, H. Casalta, P. Schleger and A.N. Christensen, 1996, Phys. Rev. B **53**, 9382.

Lynn, J.W., ed., 1990, High Temperature Superconductivity (Springer, New York).

Lynn, J.W., 1992, J. Alloys & Compounds **181**, 419.

Lynn, J.W., 1997, J. Alloys & Compounds **250**, 552.

Lynn, J.W., J.A. Gotaas, R.W. Erwin, R.A. Ferrell, J.K. Bhattacharjee, R.N. Shelton and P. Klavins, 1984, Phys. Rev. Letters **52**, 133.

Lynn, J.W., W.-H. Li, Q. Li, H.C. Ku, H.D. Yang and R.N. Shelton, 1987, Phys. Rev. B **36**, R2374.

Lynn, J.W., W.-H. Li, H.A. Mook, B.C. Sales and Z. Fisk, 1988, Phys. Rev. Lett. **60**, 2781.

Lynn, J.W., T.W. Clinton, W.-H. Li, R.W. Erwin, J.Z. Liu, K. Vandervoort, R.N. Shelton and P. Klavins, 1989, Phys. Rev. Lett. **63**, 2606.

Lynn, J.W., I.W. Sumarlin, S. Skanthakumar, W.-H. Li, R.N. Shelton, J.L. Peng, Z. Fisk and S.-W. Cheong, 1990, Phys. Rev. B **41**, R2569.

Lynn, J.W., S. Skanthakumar, Q. Huang, S.K. Sinha, Z. Hossain, L.C. Gupta, R. Nagarajan and C. Godart, 1997, Phys. Rev. B **55**, 6584.

Lynn, J.W., N. Rosov, S.N. Barilo, L. Kurnevitch and A. Zhokhov, 2000, Chin. J. Phys. **38**, 286.

Maletta, H., E. Pörschke, T. Chattopadhyay and P.J. Brown, 1990, Physica C **166**, 9.

Malik, S.K., S.M. Pattalwar, C.V. Tomy, R. Prasad, N.C. Soni and K. Adhikary, 1992, Phys. Rev. B **46**, 524.

Maple, M.B., 1976, Appl. Phys. **9**, 179.

Maple, M.B., 2000, in: Handbook on the Physics and Chemistry of Rare Earths, Vol. 30, eds K.A. Gschneidner Jr, L. Eyring and M.B. Maple (Elsevier, Amsterdam) ch. 187.

Matsuda, M., K. Yamada, K. Kakurai, H. Kadowaki, T.R. Thurston, Y. Endoh, Y. Hidaka, R.J. Birgeneau, M.A. Kastner, P.M. Gehring, A.H. Moudden and G. Shirane, 1990, Phys. Rev. B **42** 10098.

Matsuda, M., Y. Endoh, K. Yamada, H. Kojima, I. Tanaka, R.J. Birgeneau, M.A. Kastner and G. Shirane, 1992, Phys. Rev. B **45**, 12548.

Mook, H.A., D.McK. Paul, B.C. Sales, L.A. Boatner and L. Cussen, 1988, Phys. Rev. B **38**, 12008.

Narozhnyi, V.N., and S.-L. Drechsler, 1999, Phys. Rev. Lett. **82**, 461.

Narozhnyi, V.N., D. Eckert, K.A. Nenkov, G. Fuchs, T.G. Uvarova and K.-H. Müller, 1999, Physica C **312**, 233.

Nehrke, K., and M.W. Pieper, 1996, Phys. Rev. Lett. **76**, 1936.

Onsager, L., 1944, Phys. Rev. **65**, 117.

Paul, D.McK., H.A. Mook, A.W. Hewit, B.C. Sales, L.A. Boatner, J.R. Thompson and M. Mostoller, 1988, Phys. Rev. B **37**, 2341.

Paul, D.McK., H.A. Mook, L.A. Boatner, B.C. Sales, J.O. Ramey and L. Cussen, 1989, Phys. Rev. B **39**, 4291.

Petitgrand, D., A.H. Moudden, P. Galez and P. Boutrouille, 1990, J. Less-Common Met. **164–165**, 768.

Petitgrand, D., L. Boudarène, Ph. Bourges and P. Galez, 1992, J. Magn. Magn. Mater. **104–107**, 585.

Radaelli, P.G., J.D. Jorgensen, A.J. Schultz, J.L. Peng and R.L. Greene, 1994, Phys. Rev. B **49**, 15322.

Radousky, H.B., 1992, J. Mater. Res. **7**, 1917.

Roessli, B., P. Allenspach, P. Fisher, J. Mesot, U. Staub, H. Maletta, P. Brüesch, C. Ritter and A.W. Hewat, 1992, Physica B **180&181**, 396.

Roessli, B., P. Fisher, U. Staub, M. Zolliker and A. Furrer, 1993a, Europhys. Lett. **23**, 511.

Roessli, B., P. Fisher, M. Zolliker, P. Allenspach, J. Mesot, U. Staub, A. Furrer, E. Kaldis, B. Bucher, J. Karpinski, E. Jilek and H. Mutka, 1993b, Z. Phys. B **91**, 149.

Roessli, B., P. Fisher, M. Guillaume, J. Mesot, U. Staub, M. Zolliker, A. Furrer, E. Kaldis, J. Karpinski and E. Jilek, 1994, J. Phys.: Condens. Matter **6**, 4147.

Rosov, N., J.W. Lynn, G. Cao, J.W. O'Reilly, P. Pernambuco-Wise and J.E. Crow, 1992a, Physica C **204**, 171.

Rosov, N., J.W. Lynn, Q. Lin, G. Cao, J.W. O'Reilly, P. Pernambuco-Wise and J.E. Crow, 1992b, Phys. Rev. B **45**, 982.

Rosov, N., J.W. Lynn, H.B. Radousky, M. Bennahmias, T.J. Goodwin, P. Klavins and R.N. Shelton, 1993, Phys. Rev. B **47**, 15256.

Rosseinsky, M.J., K. Prassides and P. Day, 1989, J. Chem. Soc., Chem. Commun. **22**, 1734.

Rosseinsky, M.J., K. Prassides and P. Day, 1991, Inorg. Chem. **30**, 2680.

Sachidanandam, R., T. Yildirim, A.B. Harris, A. Aharony and O. Entin-Wohlman, 1997, Phys. Rev. B **56**, 260.

Skanthakumar, S., 1993, Ph.D. Thesis (University of Maryland).

Skanthakumar, S., and L. Soderholm, 1996, Phys. Rev. B **53**, 920.

Skanthakumar, S., H. Zhang, T.W. Clinton, W.-H. Li, J.W. Lynn, Z. Fisk and S.-W. Cheong, 1989, Physica C **160**, 124.

Skanthakumar, S., W.-H. Li, J.W. Lynn, A. Kebede, J.E. Crow and T. Mihalisin, 1990, Physica B **163**, 239.

Skanthakumar, S., J.W. Lynn, J.L. Peng and Z.Y. Li, 1991, J. Appl. Phys. **69**, 4866.

Skanthakumar, S., J.W. Lynn, J.L. Peng and Z.Y. Li, 1992, J. Magn. Magn. Mater. **104–107**, 519.

Skanthakumar, S., J.W. Lynn, J.L. Peng and Z.Y. Li, 1993a, J. Appl. Phys. **73**, 6326.

Skanthakumar, S., J.W. Lynn, J.L. Peng and Z.Y. Li, 1993b, Phys. Rev. B **47**, R6173.

Skanthakumar, S., J.W. Lynn and F. Dogan, 1997a, J. Appl. Phys. **81**, 4934.

Skanthakumar, S., J.W. Lynn, N. Rosov, G. Cao and J.E. Crow, 1997b, Phys. Rev. B **55**, R3406.

Skanthakumar, S., J.W. Lynn, J.L. Peng and Z.Y. Li, 1999, private communication.

Soderholm, L., S. Skanthakumar and C.W. Williams, 1999, Phys. Rev. B **60**, 4302.

Stassis, C., and A.I. Goldman, 1997, J. Alloys & Compounds **250**, 603.

Staub, U., and L. Soderholm, 2000, in: Handbook on the Physics and Chemistry of Rare Earths, Vol. 30, eds K.A. Gschneidner Jr, L. Eyring and M.B. Maple (Elsevier, Amsterdam) ch. 194.

Staub, U., L. Soderholm, S. Skanthakumar and M.A. Antonio, 1995, Phys. Rev. B **52**, 9736.

Staub, U., L. Soderholm, S. Skanthakumar, S. Roskenkranz, C. Ritter and W. Kagunya, 1996, Europhys. Lett. **34**, 447.

Staub, U., L. Soderholm, S. Skanthakumar, S. Roskenkranz, C. Ritter and W. Kagunya, 1997, Z. Phys. B **104**, 37.

Sumarlin, I.W., S. Skanthakumar, J.W. Lynn, J.L. Peng, W. Jiang, Z.Y. Li and R.L. Greene, 1992, Phys. Rev. Lett. **68**, 2228.

Sumarlin, I.W., J.W. Lynn, T. Chattopadhyay, S.N. Barilo and D.I. Zhigunov, 1994, Physica C **219**, 195.

Sumarlin, I.W., J.W. Lynn, T. Chattopadhyay, S.N. Barilo, D.I. Zhigunov and J.L. Peng, 1995, Phys. Rev. B **51**, 5824.

Thalmeier, P., 1996, Physica C **266**, 89.

Thomlinson, W., G. Shirane, J.W. Lynn and D.E. Moncton, 1983, in: Superconductivity in Ternary Compounds, eds M.B. Maple and Ø. Fischer, Vol. 34 of Topics in Current Physics (Springer, New York) ch. 8.

Thurston, T.R., M. Matsuda, K. Kakurai, K. Yamada, Y. Endoh, R.J. Birgeneau, P.M. Gehring, Y. Hidaka, M.A. Kastner, T. Murakami and G. Shirane, 1990, Phys. Rev. Lett **65**, 263.

Uma, S., W. Schnelle, E. Gmelin, G. Rangarajan, S. Skanthakumar, J.W. Lynn, R. Walter, T. Lorenz, B. Bucher and A. Erb, 1998a, J. Phys. (Lett.) **10**, L33.

Uma, S., G. Rangarajan and E. Gmelin, 1998b, Physica C **301**, 141.

Vaknin, D., S.K. Sinha, D.E. Moncton, D.C. Johnston, J.M. Newsam, C.R. Safinya and H.E. King Jr, 1987, Phys. Rev. Lett. **58**, 2802.

Vaknin, D., S.K. Sinha, C. Stassis, L.L. Miller and D.C. Johnston, 1990, Phys. Rev. **41**, 1926.

Vaknin, D., L.L. Miller and J.L. Zarestky, 1997, Phys. Rev. B **56**, 8351.

Vigoureux, P., M. Braden, A.G. Gukasov, W. Paulus, Ph. Bourges, A. Cousson, D. Petitgrand, J.P. Lauriat, M. Meven, S.N. Barilo, D.I. Zhigunov, P. Adelmann and G. Heger, 1997a, Physica C **273**, 239.

Vigoureux, P., A.G. Gukasov, S.N. Barilo and D.I. Zhigunov, 1997b, Physica B **234–236**, 815.

Wang, H.Y., C.H.Chang, S.R. Hwang, W.-H. Li, K.C. Lee, J.W. Lynn, H.M. Luo and H.C. Ku, 2000, Phys. Rev. B **62**, 11549.

Wu, S.Y., W.T. Hsieh, W.-H. Li, K.C. Lee, J.W. Lynn and H.D. Yang, 1994, J. Appl. Phys. **75**, 6598.

Wu, S.Y., W.-H. Li, K.C. Lee, J.W. Lynn, T.H. Meen and H.D. Yang, 1996, Phys. Rev. B **54**, 10019.

Xiong, Y.F., Y.S. Yao, L.F. Xu, F. Wu, D. Jin and Z.X. Zhao, 1998, Solid State Commun. **107**, 509.

Yamada, K., M. Matsuda, Y. Endoh, B. Keimer, R.J. Birgeneau, S. Onodera, J. Mizusaki, T. Matsuura and G. Shirane, 1989, Phys. Rev. B **39**, 2336.

Yang, K.N., J.M. Ferreira, B.W. Lee, M.B. Maple, W.-H. Li, J.W. Lynn and R.W. Erwin, 1989, Phys. Rev. B **40**, 10963.

Yildirim, T., 1999, Turk. J. Phys. **23**, 47.

Yildirim, T., A.B. Harris, O.E. Wohlman and A. Aharony, 1994, Phys. Rev. Lett. **72**, 3710.

Yildirim, T., A.B. Harris and E.F. Shender, 1996, Phys. Rev. B **53**, 6455.

Yildirim, T., S. Skanthakumar and J.W. Lynn, 1998, private communication.

Zhang, H., J.W. Lynn, W.-H. Li, T.W. Clinton and D.E. Morris, 1990, Phys. Rev. B **41**, 11229.

Zhang, H., J.W. Lynn and D.E. Morris, 1992, Phys. Rev. B **45**, 10022.

Zobkalo, I.A., A.G. Gukasov, S.Yu. Kokovin, S.N. Barilo and D.I. Zhigunov, 1991, Solid State Commun. **80**, 921.

Zou, Z., J. Ye, K. Oka and Y. Nishihara, 1998, Phys. Rev. Lett. **80**, 1074.

Zou, Z., J. Ye, K. Oka and Y. Nishihara, 1999, Phys. Rev. Lett. **82**, 462.

Handbook on the Physics and Chemistry of Rare Earths
Vol. 31
edited by K.A. Gschneidner, Jr., L. Eyring and M.B. Maple

Chapter 200

HEAT CAPACITY

Peter M. ALLENSPACH
Laboratory for Neutron Scattering, ETH Zurich & PSI Villigen, 5232 Villigen PSI, Switzerland

M. Brian MAPLE
Department of Physics, University of California, San Diego, 9500 Gilman Drive, La Jolla, CA 92093-0319, USA

Contents

List of symbols and acronyms

2D	two-dimensional
3D	three-dimensional
CEF	crystalline electric field
J	total angular momentum
k_B	Boltzmann's constant
L	total orbital momentum
R	lanthanide
R1237	$RBa_2Cu_3O_7$
R123x	$RBa_2Cu_3O_x$
R124	$RBa_2Cu_4O_8$

R247	$R_2Ba_4Cu_7O_{14+x}$	β	cubic term of the specific heat
S	spin	μ	magnetic moment
γ	linear term of the specific heat	μ_B	Bohr magneton

1. Introduction

Low-temperature specific-heat measurements are especially useful in the investigation of magnetic ordering and crystalline electric field (CEF) effects in lanthanide (R) barium cuprate high-temperature superconductors for the following reasons: Anomalies in the magnetic susceptibility due to magnetic ordering of the R ions are masked by the large diamagnetic signal in the superconducting state (i.e. below 90 K). Neutron diffraction requires a great deal of effort in terms of measurement time, equipment (dilution refrigerator), and sample mass in order to investigate an entire series of samples with different oxygen contents at many different temperatures. In addition, short-range magnetic ordering as observed in R123x and R247 at certain oxygen contents yields only weak signals in neutron diffraction experiments. In this respect, an accurate knowledge of the magnetic specific heat as a function of stoichiometry and temperature provides an excellent basis for specific neutron investigations. On the other side, results from neutron diffraction and neutron spectroscopy (such as moment direction, size of the ordered moment, and CEF splitting) are indispensable in modeling the measured specific heat. Hence, we will often refer to ch. 194 of Vol. 30, and ch. 199 of the present volume of this Handbook series, or corresponding papers, especially to the review article by Fischer and Medarde (1998).

2. Contributions to the specific heat

2.1. *Electronic and lattice contribution to the specific heat*

The specific heat at low temperatures consists of electronic, lattice, magnetic, and hyperfine contributions (see for example, Junod 1996). The electronic contribution in a metal due to the conduction electrons is linear in temperature. In a BCS superconductor, the conduction electrons start to condense into Cooper pairs at T_c and the density of unpaired electrons decreases exponentially below this temperature. Hence, at the temperatures of interest in this chapter (i.e., below 4 K) the density of unpaired electrons is essentially zero as is expected for the electronic contribution. However, for $RBa_2Cu_3O_x$ (R123x) a linear term of the order of $\gamma = 3$–$6\,\mathrm{mJ\,mole^{-1}\,K^{-2}}$ was always observed (van der Meulen et al. 1988a,b, Junod 1996). This indicates that some conduction electrons do not pair at low temperatures, most likely due to an anisotropic or d-wave gap (i.e., with nodes). The lattice specific heat at temperatures not exceeding 10% of the Debye temperature can be approximated by $\beta \cdot T^3$. The Debye temperature for R123x lies between 350 and 450 K and $\beta = 0.3$–$0.5\,\mathrm{mJ\,mole^{-1}\,K^{-5}}$ (van der Meulen et al. 1988a,b, Junod 1996). In most of

the figures in this chapter the electronic and the lattice contributions ($\gamma \cdot T + \beta \cdot T^3$) have already been subtracted.

2.2. *Magnetic contribution*

On top of the electronic and lattice contributions, and in the temperature regime up to 4 K, much stronger possible magnetic contributions either from magnetic lanthanide ordering or thermal population of CEF states are found. If neither the total orbital momentum $\boldsymbol{L}$ nor the total angular momentum $\boldsymbol{J}$ of the ground-state J-multiplet of the lanthanide ion is zero, the degeneracy of this ground state $(2J + 1)$ is lifted by the CEF of the surrounding ions. The smallest final degeneracy for a lanthanide ion with an integer J is one (singlet), while for a half integer J (Kramers ion) the smallest degeneracy due to CEF is two (doublet). This lifting of degeneracy is called quenching of the total angular momentum and leads to a reduced moment compared to the free ion value of $g_J \sqrt{J(J+1)}\,\mu_B$ (Jensen and Mackintosh 1991). In the absence of magnetic ordering the thermal population of the CEF-split sequence of states leads to Schottky anomalies in the specific heat (per mole of lanthanide ions) given by

$$C_s = R \left[\sum_i \left(\frac{E_i}{k_B T} \right)^2 p_i - \left(\sum_i \frac{E_i}{k_B T} p_i \right)^2 \right], \tag{1}$$

where

$$p_i = \frac{1}{Z} \sum_i \exp\left(-\frac{E_i}{k_B T} \right) \quad \text{and} \quad Z = \sum_i \exp\left(-\frac{E_i}{k_B T} \right)$$

are the Boltzmann population and the partition function, respectively, k_B is the Boltzmann constant, R is the gas constant, and E_i is the energy of an individual CEF state. For well-separated CEF levels, the associated entropy change is

$$\Delta S = R \cdot \ln\left(\frac{t}{g} \right), \tag{2}$$

where t is the total number of levels involved (including degeneracy) and g is the degeneracy of the ground-state level. Hence, two doublets would yield an entropy of $R \ln 2$ which is the same as for two singlets. The entropy change can be obtained by integrating the magnetic contribution to the specific heat, C_m, over the temperature range $(T_a - T_b)$ of the anomaly:

$$\Delta S = \int_{T_a}^{T_b} \frac{C_m}{T} \, dT. \tag{3}$$

Equations (2) and (3) are still valid in the case of magnetic ordering, although for long-range magnetic order the broad Schottky peak is replaced by a sharp anomaly

whose form depends on the nature of the ordering. Plots of such anomalies, based on specific theoretical models (molecular field, Heisenberg, or Ising models) as well as dimensionality for spin-$\frac{1}{2}$ systems can be found in the review article by de Jongh and Miedema (1974). Except for the two-dimensional (2D) Ising model, the specific-heat anomaly associated with long-range ordering cannot be calculated analytically for any of the other models. Fortunately, as we will see, the character of the ordering for samples with high oxygen contents (R1237) turns out to be close to 2D Ising behavior.

As can be seen in the article by de Jongh and Miedema (1974) the specific-heat anomalies of low-dimensional systems are similar to Schottky peaks. The same is true for systems which have only short-range magnetic interactions.

2.3. *Hyperfine contribution*

The hyperfine contribution to the specific heat is observed as an upturn at very low temperatures (normally at temperatures well below 1 K) and is the high-temperature tail of a low-lying Schottky anomaly originating from a slightly split nuclear magnetic ground state. Except for oxygen, the isotopic mixture of the natural elements in the R123x compounds has an non-vanishing nuclear spin $\boldsymbol{I}$, and hence contributes to the hyperfine specific heat. Since the splitting of the nuclear magnetic states in a magnetic field is proportional to the nuclear magneton ($\mu_N = 3.1528 \times 10^{-5}$ meV/T), its magnetic field dependence is much weaker than that for electronic magnetism (whose splitting is proportional to the Bohr magneton $\mu_B = 5.7891 \times 10^{-2}$ meV/T). Therefore, low-temperature upturns in the specific heat can easily be identified as nuclear or electronic by applying a magnetic field and observing the corresponding shifts to higher temperatures.

Dunlap et al. (1987) pointed out that the nuclear magnetic hyperfine field in R1237 compounds is nearly proportional to the electronic magnetic moments of the lanthanide ions. By comparing the measured hyperfine field with the free-ion value they obtained an ordered moment for Dy and Er in R1237 which is close to the value obtained from neutron diffraction measurements ($6\mu_B$ instead of $7\mu_B$ for Dy and $4.5\mu_B$ instead of $4.9\mu_B$ for Er, respectively).

3. Experimental results for $RBa_2Cu_3O_7$

3.1. *R = Y, La, Ce, Pm, Eu, Gd, Tb, Lu*

$CeBa_2Cu_3O_x$ and $TbBa_2Cu_3O_x$ cannot be synthesized, while $PmBa_2Cu_3O_x$ has not been made due to the short lifetime of the radioactive Pm. We could not find any information in the literature about the specific heat of $LaBa_2Cu_3O_x$.

The specific heat of $YBa_2Cu_3O_x$ is extensively discussed in the review article by Junod (1996) and references therein. The specific heats of the nonmagnetic $EuBa_2Cu_3O_7$ and

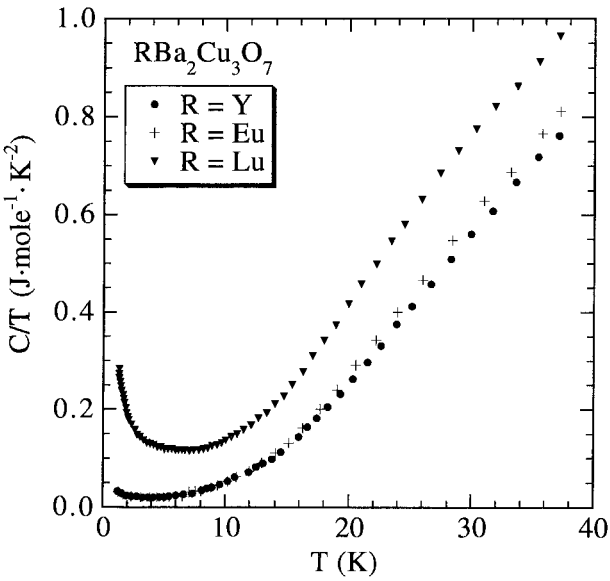

Fig. 1. Specific heat measured for the nonmagnetic compounds $YBa_2Cu_3O_{7-\delta}$, $EuBa_2Cu_3O_{7-\delta}$ and $LuBa_2Cu_3O_{7-\delta}$, after van der Meulen et al. (1988a). The up-turns at low temperatures are nuclear and magnetic impurity contributions.

$LuBa_2Cu_3O_7$ compounds are qualitatively similar to that of the Y-compound (fig. 1 shows typical results for R=Y, Eu, and Lu), but the specific-heat values are higher for $LuBa_2Cu_3O_7$. All three compounds show an upturn at low temperatures which is quite sensitive to applied magnetic fields and, hence, only a small part is due to nuclear magnetism (van der Meulen et al. 1988a,b, Kierspel et al. 1994). An obvious and very probable explanation for this upturn is the presence of magnetic impurities.

There are more than twenty reports in the literature (see table 1) of the low-temperature specific heat of $GdBa_2Cu_3O_7$ which essentially yield the same results. As can be seen in fig. 2, a sharp anomaly was observed around the ordering temperature $T_N = 2.2$–2.3 K, and a shoulder around 1 K (especially pronounced in a C/T plot). The magnetic ground state of Gd^{3+} in $GdBa_2Cu_3O_7$ is a pure S (=7/2) state and is therefore within first order unaffected by the CEF. The degeneracy of the ground state is $2S+1=8$. This degeneracy is totally lifted below the magnetic ordering temperature due to the molecular field, and according to eq. (2), the entropy of the anomaly in the magnetic specific heat at the ordering temperature is expected to be $R \ln 8$. The value for the entropy obtained from the measurements is close to this value. The decrease of the ordering temperature as a function of applied magnetic field (fig. 2) is a clear indication of antiferromagnetic ordering. Hydrostatic pressure measurements performed by Bloom et al. (1987) and Alekseevskii et al. (1988) (fig. 3) yield for dT_N/dp a value of $0.03\,\mathrm{K\,kbar^{-1}}$ and $0.007\,\mathrm{K\,kbar^{-1}}$, respectively.

Table 1
Sources of experimental data

Publication	Rare earths	Oxygen contents[a]	Temperature range (K)	Remarks[b]
Allenspach et al. (1993)	Nd	6–7	0.4–4	Ca doping, $Nd_{1+y}Ba_{2-y}Cu_3O_x$
Allenspach et al. (1994a)	Nd, Dy	6–7	0.4–6	Magnetic field
Allenspach et al. (1994b)	Nd, Dy	6–7	0.4–2.5	
Allenspach et al. (1995)	Nd, Dy	6–7	0.4–4	Magnetic field, pressure
Allenspach et al. (1996)	Sm	6–7	0.4–4	
Alekseevskii et al. (1988)	Gd	7	2–3.5	Pressure
Atake (1991)	Dy, Ho, Er, Tm	7	0.2–300	
Basu et al. (1989)	Ho	7	70–300	
Basu et al. (1991)	Ho	7	1.8–12	
Bloom et al. (1987)	Gd	7	1–5	Magnetic field
Brown et al. (1987)	Gd, Dy, Ho, Er	7	0.3–24	
Causa et al. (1987)	Gd, Dy	7	0.4–7	
Causa et al. (1988)	Gd	7	0.5–3	$(Eu_{1-y}Gd_y)Ba_2Cu_3O_7$
Chmist et al. (1988)	Eu	7	2.8–100	
Dirken and de Jongh (1987)	Dy	7	0.5–3	
Drössler et al. (1996)	Nd, Sm, Ho	6–7	0.1–6	Magnetic field
Dunlap et al. (1987)	Dy, Ho, Er	7	0.1–20	
Dunlap et al. (1988)	Gd	6+7	0.1–5	
Escribe-Filippini et al. (1988)	Sm	7	2–110	
Ferreira et al. (1988)	Eu, Ho, Tm, Yb	7	0.4–30	
Gering et al. (1988)	Pr, Nd, Gd, Tm	6+7	1–40	
Gurevich et al. (1990)	Tm	7	2–15	Sr doping
Heremans et al. (1988)	Eu, Gd, Dy, Er	7	220–500	
Hilscher et al. (1994)	Pr, Gd	6+7	1.6–70	Magnetic field, Sr doping
Ho et al. (1987)	Gd	7	1.8–10	
Jana and Bhuniya (1993)	Nd, Sm, Gd, Dy	7	100–300	
Kadowaki et al. (1987)	Gd	7	1–5	Magnetic field
Kierspel et al. (1994)	Nd, Eu, Gd, Dy, Ho, Er, Tm, Yb	7	0.1–8	Magnetic field
Kobayashi et al. (1987)	Gd, Dy, Ho, Er	7	0.1–22	
Kohara et al. (1987)	Gd	7	0.1–4	
Lazarev et al. (1988)	Gd, Ho	7	10–300	
Lee et al. (1988)	Nd, Sm, Gd, Dy, Er	7	0.4–30	
Lee et al. (1990)	Nd, Sm, Dy, Er	6–7	0.4–30	Magnetic field
Maple et al. (1989)	Pr, Nd, Sm, Gd, Dy, Ho, Er	6+7	0.4–24	$(Y_{1-y}Pr_y)Ba_2Cu_3O_7$
Meyer et al. (1987)	Gd	6+7	1.5–3	
Mori et al. (1988)	Gd	7	1.5–5	

continued on next page

Table 1, *continued*

Publication	Rare earths	Oxygen contents[a]	Temperature range (K)	Remarks[b]
Nakazawa et al. (1987)	Gd, Dy, Ho, Er, Tm	6+7	0.4–6	
Naumov et al. (1996)	Ho	7	10–300	
Niraimathi et al. (1994)	Nd	7	0.5–5	Ga doping
Niraimathi et al. (1995a)	Nd	6+7	0.5–4	Ga doping
Niraimathi et al. (1995b)	Nd	6.85-7	0.5–60	Ga doping
Oota and Kojima (1988)	Gd	6–7	1.8–30	Fe doping
Oota et al. (1989)	Gd	6–7	1.5–22	Fe doping
Plackowski and Wlosewicz (1996)	Er	7	10–300	$(Y_{1-y}Er_y)Ba_2Cu_3O_7$
Ramirez et al. (1987)	Pr, Nd, Sm, Gd, Dy	7	0.4–10	Magnetic field
Ravindran et al. (1995)	Nd	7	2–50	Zn doping
Reeves et al. (1987)	Gd	7	1.5–180	
Schaudy et al. (1992)	Pr, Gd	7	1.8–25	Magnetic field
Schaudy et al. (1993)	Pr	6+7	1.8–24	Magnetic field, $(Y_{1-y}Pr_y)Ba_2Cu_3O_7$
Simizu et al. (1987a)	Nd, Sm, Gd, Ho, Er	7	0.4–20	
Simizu et al. (1987b)	Gd, Ho, Er	7	0.4–100	
Simizu et al. (1989)	Er	6–7	0.1–7	
Slaski et al. (1988)	Gd, Dy, Ho, Er	6+7	0.1–20	
Thuy et al. (1992)	Er	7	2–40	
Uma et al. (1996)	Pr	7	1.8–25	Magnetic field, single crystal
van den Berg et al. (1987)	Gd	7	2–32	
van der Meulen et al. (1988a)	Pr, Sm, Eu, Gd, Dy, Ho, Er, Tm, Yb, Lu	7	1–40	Magnetic field
van der Meulen et al. (1988b)	Pr, Dy, Yb	7	1–25	Magnetic field
Wang et al. (1989)	Gd	7	80–90	
Willekers et al. (1990a)	Tm	7	0.05–0.8	
Willekers et al. (1990b)	Yb	7	0.1–1	
Willekers et al. (1991)	Ho, Er, Yb	7	0.05–1	
Willis et al. (1987)	Gd	7	1.5–25	
Yang et al. (1989)	Nd, Sm	6+7	0.4–4	
Zhu et al. (1988)	Gd	6+7	1.8–4.5	

[a] 7 means that a sample with an oxygen content close to 7 was investigated;
6+7, one close to 6 and one close to 7 was investigated;
6–7, a series of samples with different oxygen contents.
[b] Additional measurements and parameters.

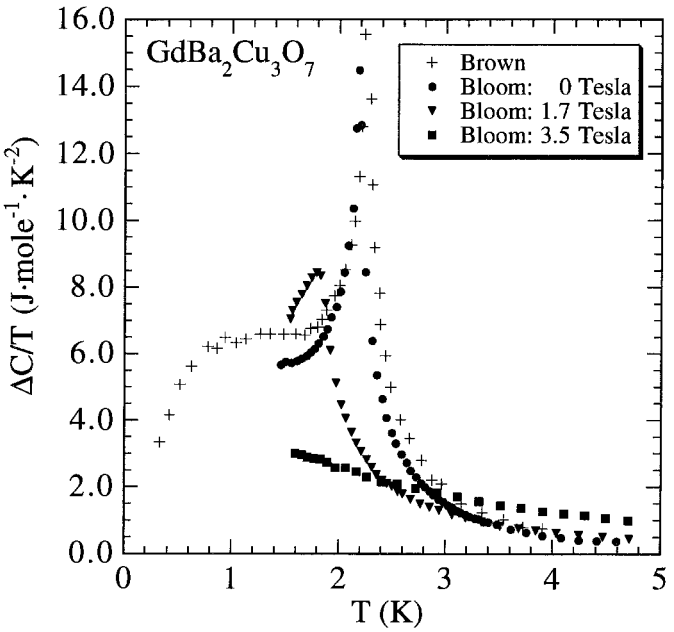

Fig. 2. Magnetic specific heat data for $GdBa_2Cu_3O_{7-\delta}$ with and without applied magnetic field according to Brown et al. (1987) and Bloom et al. (1987).

3.2. *Kramers ions (Nd, Sm, Dy, Er, Yb)*

$RBa_2Cu_3O_7$ compounds with a Kramers ion at the R site have been studied extensively in the past (table 1). The results are essentially all in agreement, with the following two exceptions: First, early specific-heat measurements on $NdBa_2Cu_3O_7$ do not show a sharp transition at the ordering temperature due to sample inhomogeneity (Ramirez et al. 1987, Simizu et al. 1987a). Second, magnetic features with entropies of the order of $1\,J\,mole^{-1}\,K^{-1}$ have been observed at 5.5 K for $SmBa_2Cu_3O_7$ (Escribe-Filippini et al. 1988), at 11 K for $DyBa_2Cu_3O_7$ (Lee et al. 1988, van der Meulen et al. 1988a,b), at 5 K for $ErBa_2Cu_3O_7$ (Brown et al. 1987, Dunlap et al. 1987, Simizu et al. 1987a,b, Slaski et al. 1988, van der Meulen et al. 1988a,b), and at 2 K for $YbBa_2Cu_3O_7$ (Ferreira et al. 1988, van der Meulen et al. 1988a,b), respectively. All of these features disappeared with better sample quality in subsequent studies. Figure 4 displays typical specific-heat anomalies of $RBa_2Cu_3O_7$ (R = Nd, Sm, Dy, Er, Yb) due to magnetic ordering. The ordering temperatures are 0.52, 0.61, 0.91, 0.60, and 0.26 K for Nd, Sm, Dy, Er, and Yb, respectively. Specific-heat measurements in an applied magnetic field (see, e.g., Kierspel et al. 1994) as well as neutron diffraction experiments (see ch. 199 of this volume) proved the ordering to be antiferromagnetic. For Dy, Er, and Yb, the anomalies are very sharp and almost symmetric, while for Nd and to a lesser extent for Sm there is a sharp cusp at T_N and a broad high-temperature tail. From neutron spectroscopy the

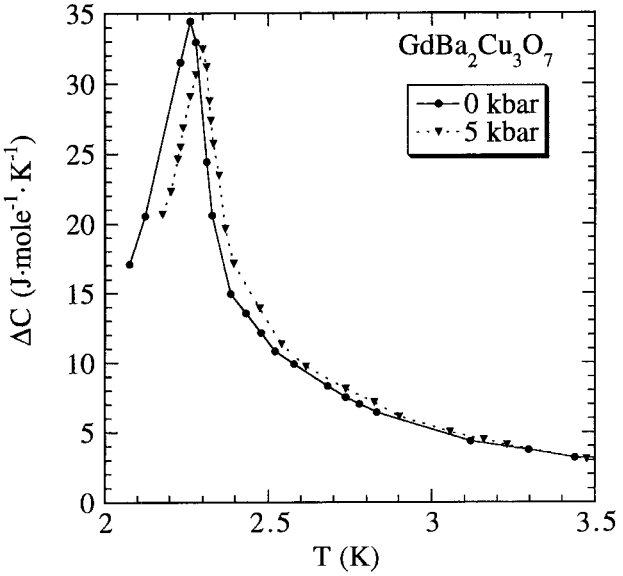

Fig. 3. Pressure dependence of the magnetic ordering of $GdBa_2Cu_3O_7$ (Alekseevskii et al. 1988). The lines are guides to the eye.

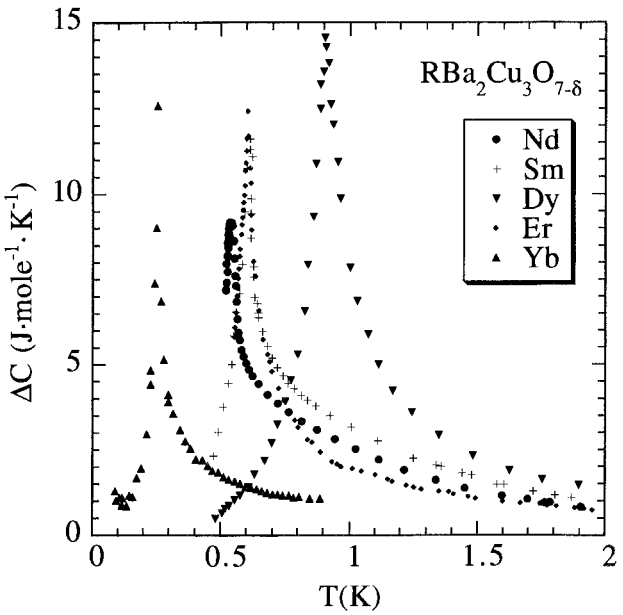

Fig. 4. Magnetic specific heat of $NdBa_2Cu_3O_{7-\delta}$ (Maple et al. 1989), $SmBa_2Cu_3O_{7-\delta}$, $DyBa_2Cu_3O_{7-\delta}$ and $ErBa_2Cu_3O_{7-\delta}$ (Lee et al. 1988), and $YbBa_2Cu_3O_{7-\delta}$ (Willekers et al. 1990b).

CEF level schemes for these four compounds are well known: The first excited states lie above 10 meV for Nd, Sm, Er, and Yb and hence do not contribute to the specific heat below 4 K (see Vol. 30, ch. 194 of this Handbook). For Er, the specific heat calculated from CEF parameters obtained by neutron spectroscopy were compared to measured data at 0 and 5 tesla by Mesot et al. (1993a). The first excited level for Dy lies at 3.3 meV and, as a result, the low-temperature tail of the corresponding Schottky anomaly is observed down to about 2 K (see, e.g., Dunlap et al. 1987) and has to be taken into account in the analysis of the ordering peak. Pressure measurements performed on $NdBa_2Cu_3O_{6.97}$ and $DyBa_2Cu_3O_{6.95}$ yield $dT_N/dp = 0.0049$ and $0.0035\,K\,kbar^{-1}$, respectively (Allenspach et al. 1995). Since the ordering temperatures for these two compounds (and $GdBa_2Cu_3O_7$, see previous paragraph) are not the same, a comparison of the values is only reasonable by taking the relative changes $(dT_N/T_N)/dp$. The results are: 0.0094 (Nd), 0.0054 (Dy), and $0.0031–0.0133\,K\,kbar^{-2}$ (Gd).

3.3. *Non-Kramers ions (Pr, Ho, Tm)*

In contrast to Kramers ions, non-Kramers ions do not automatically have a magnetic ground state. Here the low-temperature magnetic behavior is directly controlled by the CEF splitting. For $PrBa_2Cu_3O_7$ and $HoBa_2Cu_3O_7$, the ground state is formed by a quasi triplet and a quasi doublet, respectively. Induced magnetism results in magnetic ordering at 17 K for Pr and 0.17 K in the case of Ho. $TmBa_2Cu_3O_7$ has a well-isolated singlet ground state (see Vol. 30, ch. 194 of this Handbook) and does not order at all. The magnetic specific heats of the three compounds are displayed in fig. 5. Magnetic contributions at elevated temperatures have their origin in the population of higher CEF states. The Schottky specific heats calculated from the observed CEF level splitting measured with neutron spectroscopy are given by lines in fig. 5. The disagreement is mainly due to an inaccurate subtraction of the electronic and lattice part. $PrBa_2Cu_3O_7$ is an exception for many reasons: It is not superconducting[1], has an ordering temperature one order of magnitude higher than the rest of the lanthanides, and has no sharp CEF transitions. All this indicates strong hybridization with the surrounding oxygen and Cu orbitals.

4. Models for the magnetic ordering

The specific-heat observation of magnetic ordering (except for R = Eu, Tm, Lu) in $RBa_2Cu_3O_7$ was confirmed by neutron diffraction, and the ordering temperatures obtained by the two methods are in agreement. Very early in the specific-heat investigations in these compounds, the similarity of the measured anomalies at T_N with the analytical result of

[1] Superconductivity with $T_c \approx 85$ K has been reported in $PrBa_2Cu_3O_x$ samples prepared by the traveling-solvent floating zone method (Zou et al. 1998). These materials show large inhomogeneities in both lattice parameters and transport and magnetic properties. In parts of the sample that exhibit superconductivity, the *c*-axis lattice constant is reported to be larger than that of the nonsuperconducting ceramic polycrystalline or single-crystal samples prepared by standard methods.

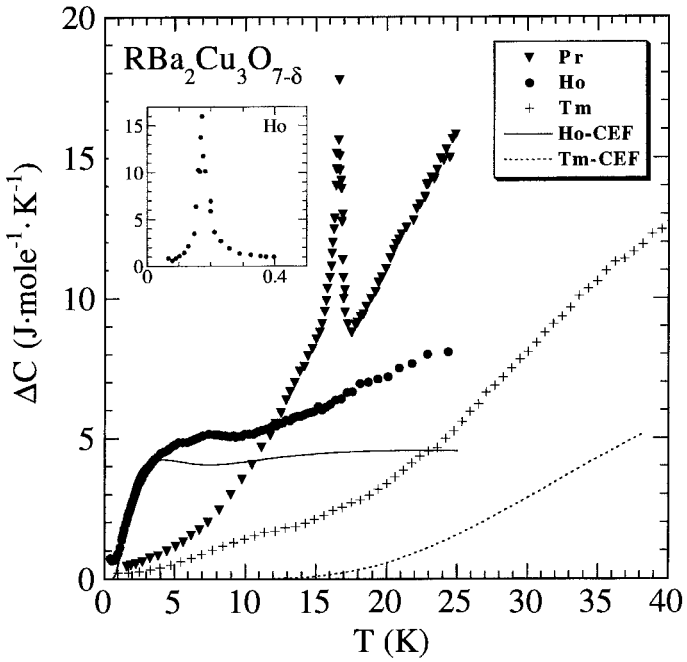

Fig. 5. Magnetic specific heat of $PrBa_2Cu_3O_{7-\delta}$ (Uma et al. 1996), $HoBa_2Cu_3O_{7-\delta}$ (Maple et al. 1989; inset: Willekers et al. 1991), and $TmBa_2Cu_3O_{7-\delta}$ (Gering et al. 1988). The CEF contributions were calculated from neutron spectroscopy data (see Vol. 30, ch. 194 of this Handbook).

Table 2
Magnetic exchange constants obtained by a pure 2D Ising fit

Rare earth	J_1 (μeV)	J_2 (μeV)	Reference
Nd	−59	−3.5	Allenspach et al. (1994a)
Sm	−60	−5.4	Lee et al. (1990)
Gd	−168	−45.7	Simizu et al. (1987a)
Dy	−63	−15.5	Lee et al. (1990)
Er	−47	−8.6	Lee et al. (1990)
Yb	−17.4	−4.3	Willekers et al. (1990b)

the 2D Ising model (Onsager 1944) was recognized by Simizu et al. (1987a,b). The in-plane coupling constants obtained by such a 2D Ising calculation are listed in table 2. Lee et al. (1990) pointed out that the anisotropy in the coupling constants in the plane necessary to explain the experimental data is lanthanide dependent: $J_1/J_2 = 50$, 11, 4, and 5 for Nd, Sm, Dy, and Er, respectively. These large anisotropies are surprising, in view of the fact that the orthorhombicity in these compounds, even at full oxidation, is not very large and that the orthorhombicity for the light lanthanide ions is the smallest. The

2D Ising model is based on nearest-neighbor interactions only, favoring superexchange and, to a lesser extent, the RKKY interaction over the long-range dipolar interaction. The usual way to distinguish exchange and dipolar interactions is to plot T_N as a function of the de Gennes factor $g_J - 1)^2 \cdot J(J+1)$ or as a function of the square of the ordered moment, respectively. These two types of plots are displayed in fig. 6. One problem with the de Gennes scaling is that at low temperatures where the ordering occurs, the whole ground-state J-multiplet is not thermally populated due to the CEF splitting. This leads to a quenching of the total angular momentum and hence the J in the de Gennes factor loses its meaning. We can artificially compensate for this effect by using $\mu = g_J \sqrt{J(J+1)}$ and inserting the ordered moment μ_{ord} for μ. The alternative de Gennes factor is equal to $(1 - 1/g_J)^2 \cdot \mu_{ord}^2$ (see fig. 6c). The ordering temperatures follow quite nicely the de Gennes scaling but, nevertheless, we cannot rule out the possibility that the dipolar interaction plays a role, since it is always present.

4.1. *Dipolar interaction*

We start with a calculation of the ordering temperature solely based on the dipolar interaction. According to calculations by Smit et al. (1987) the contributions to the dipolar fields due to adjacent R layers are insignificant; hence, a 2D calculation is sufficient to obtain an idea of the importance of the dipolar interaction. For our cluster calculations (following the method described by MacIsaac et al. 1992), we used the ordered magnetic moment obtained from neutron diffraction or – if no data were available – the value calculated from the CEF parameters. The size and direction of the moment together with the lattice constants used for our calculations are listed in table 3.

The Hamiltonian for dipolar interaction is given by

$$\hat{H}_{dip} = \sum_{i \neq j} \left[\frac{\vec{\mu}_i \cdot \vec{\mu}_j}{r_{ij}^3} - 3 \frac{(\vec{\mu}_i \cdot \vec{r}_{ij})(\vec{\mu}_j \cdot \vec{r}_{ij})}{r_{ij}^5} \right], \tag{4}$$

with $\vec{\mu}_i$ the magnetic moment at site i and $\vec{r}_{ij}$ the direction vector from site i to site j. For the magnetic ordering in $RBa_2Cu_3O_7$ we will, for simplicity, assume that the moments are parallel or antiparallel (Ising spins) to each other and the size of the moment is not site dependent. (We will see in a later section that for oxygen-deficient $PrBa_2Cu_3O_x$ and $NdBa_2Cu_3O_x$, the moments are tilted.) The Hamiltonian (4) then simplifies to

$$\hat{H}_{dip} = \sum_{i \neq j} \left[\pm \frac{\mu^2}{r_{ij}^3} (1 - 3\cos\theta_{ij}) \right], \tag{5}$$

where θ_{ij} is the angle between $\vec{r}_{ij}$ and the (fixed) moment direction. With the values listed in table 3 the unit of dipolar energy is $\mu_B^2/\text{Å}^3 = 5.368 \times 10^{-2}$ meV $= 0.623$ K. The ordering temperature was obtained by calculating the specific heat and determining the position of the maximum of the anomaly. The specific heat was the result of a Monte-Carlo evaluation

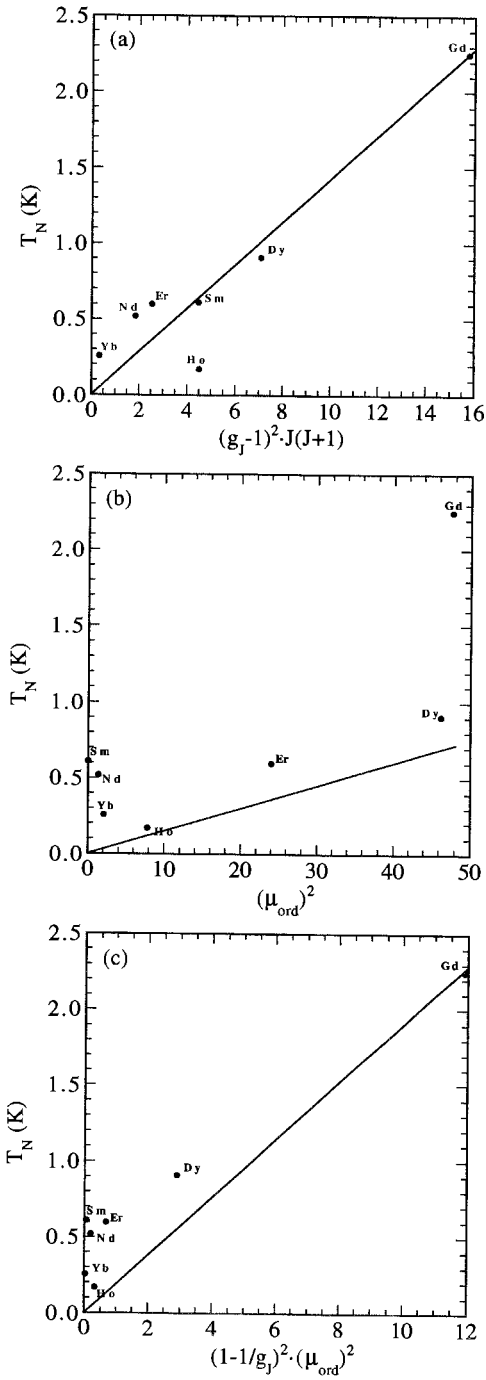

Fig. 6. Magnetic ordering temperatures as function of (a) the de Gennes factor, (b) the moment squared, and (c) the modified de Gennes factor.

Table 3
Measured in-plane lattice constants, size and direction of the magnetic moments, ordering temperatures used for the calculations[a], and calculated values for the ordering temperature (with dipolar interactions only) and the magnetic exchange constants (dipolar + exchange interaction calculations)

Rare earth	a (Å)	b (Å)	$\|\mu\|$ (μ_B)	μ-direction	T_N^{ex} (K)	T_N^{calc} (K)	J (μeV)	
							J_{calc}	J_{corr}[b]
Pr123	3.86	3.92	0.56	tilted	17	<0.02	−650	35 000
Nd123	3.86	3.91	1.14	c	0.52	<0.02	−59/−3.5	−323/−19.2
Sm123	3.84	3.90	0.34	a	0.61	<0.02	−60/−5.4	−83./−7.5
Gd123	3.83	3.89	6.9	c	2.25	0.62	−58/−58	−6.2/−6.2
Dy123	3.82	3.89	6.8	c	0.91	0.64	−8/−8	−2.8/−2.8
Ho123	3.82	3.88	2.8	a	0.17	0.23	–	–
Er123	3.81	3.88	4.9	b	0.60	0.61	−12/−12	−18.0/−18.0
Yb123	3.80	3.87	1.44	b	0.26	0.06	−17.4/−4.3	−537/−133
Dy124	3.84	3.87	5.9	c	1.00	0.47	−21/−21	−7.4/−7.4
Dy247	3.83	3.87	7	c	1.00	0.64	−12/−12	−4.2/−4.2
Er247	3.83	3.86	3.68	b	0.54	0.35	−27/−27	−41/−41

[a] Values hardly differ from author to author.
[b] Exchange constants corrected with the modified de Gennes factor (see text).

of $C = \frac{1}{k_B T^2}(\langle E_{dip}^2\rangle - \langle E_{dip}\rangle^2)$ (Yeomans 1992), where we started at low temperature with the moment arrangement found by neutron diffraction. The rare-earth cluster used for the calculation had a size of 10×10 ions. The eight adjacent clusters where included in the calculation in order to simulate the long-range character of the dipolar interaction. The spin arrangements of these patches were identical to the central one. Since this calculation should just provide an approximation, only 10^5 Monte-Carlo steps were calculated. The results of these calculations are listed in table 3. Obviously, dipolar interaction alone cannot account for the magnetic ordering temperatures, except for Ho and Er. For Dy the dipolar interaction is dominant, for Gd it is significant, and for Pr, Nd, Sm and Yb it is almost negligible. The form of a calculated specific-heat anomaly at the ordering temperature based solely on dipolar interaction (fig. 7) turns out to be similar to a 2D Ising curve (especially the high-temperature tail), hence the large anisotropy obtained for the coupling constants for the 2D Ising model might, for Dy or Er, have its origin in the presence of the dipolar interaction. However, this does not solve the problem of the even larger anisotropy for Nd or Sm where dipolar interactions are negligible.

4.2. *Superexchange and the RKKY interaction*

The good de Gennes scaling of the ordering temperatures was always regarded as a proof of the importance of the RKKY interaction despite the fact that all other experimental results did not support such an interpretation: With ^{155}Gd Mössbauer spectroscopy

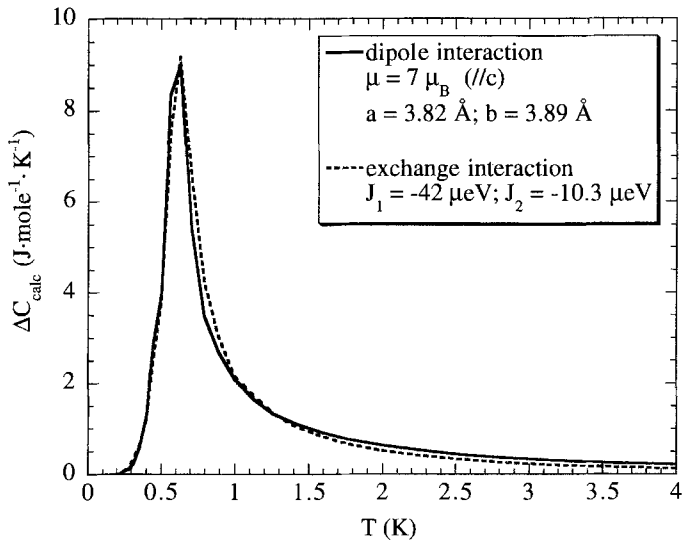

Fig. 7. Comparison of a specific heat anomaly calculated for Dy1237 with pure dipolar interaction and one calculated with a anisotropic exchange interaction (for both calculations a square of 10×10 magnetic ions was used). Since the dipolar interaction and the 2D Ising model belong to the same universality class it is not surprising to find exchange values which exactly reproduce the dipolar data.

(Smit et al. 1987), ESR (Causa et al. 1987) and NMR (Alloul et al. 1988), the density of charge carriers at the R site was found to be extremely small. By means of specific-heat measurements, the ordering temperatures in oxygen-reduced (insulating) samples (see sect. 5) were shown to be almost identical to those in the fully oxidized (metallic) samples (except for Pr, Nd). The transformation of an exchange Hamiltonian into the Heisenberg spin Hamiltonian (which results in the dependence of the ordering temperature on the de Gennes factor) is independent of the type of exchange interaction, be it RKKY or superexchange. For the reasons mentioned above, we believe that the superexchange interaction is – at least in the low-oxygen regime – more important than the RKKY interaction in these compounds. The superexchange interaction is mediated by the oxygen in the CuO_2 planes. Since the holes responsible for superconductivity are planar oxygen holes, some influence of the electronic properties within these planes on the magnetic ordering of the lanthanides is expected.

In order to include the spin-$\frac{1}{2}$ exchange interaction into our dipolar model, we extended the Hamiltonian (5) to

$$\widehat{H} = \sum_{i \neq j} \left[\pm \frac{\mu^2}{r_{ij}^3} \left(1 - 3\cos\theta_{ij}\right) \right] - 2 \sum_{\langle i,j \rangle} J_\alpha \left(S_i^z \cdot S_j^z \right), \tag{6}$$

where J_α is the exchange coupling in one of the two plane directions and $\langle i,j \rangle$ is the sum over neighboring pairs. The summation for the exchange part was only performed

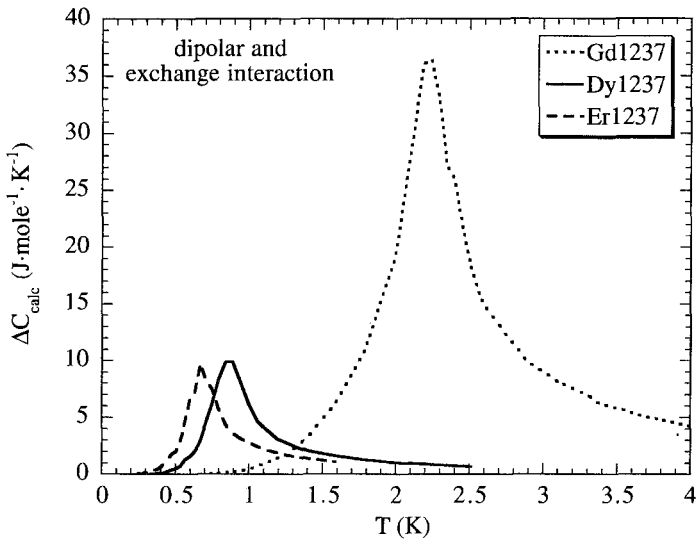

Fig. 8. Calculated specific heat anomaly (dipolar and exchange interaction; cluster size: 10×10) for $GdBa_2Cu_3O_{7-\delta}$, $DyBa_2Cu_3O_{7-\delta}$ and $ErBa_2Cu_3O_{7-\delta}$. The data for Dy and Er are very similar to the experimental data (see fig. 4), while for Gd the shoulder of unknown origin at 1 K is not reproduced (fig. 2).

in the central 10×10 spin cluster including the boarders (periodic boundary condition). The results of these calculations are shown in fig. 8 for the lanthanides with a strong dipolar contribution (the specific heat for the others can be modeled with the 2D Ising model alone). The coupling constants used for the calculation were chosen in order to reproduce the measured ordering temperature. In the exchange part of eq. (6), the modified de Gennes factor should actually appear, since we transformed the problem into spin space. We did not include this factor in order to obtain the raw coupling constants which can directly be related to the ordering temperatures during the calculation, but we listed the raw and corrected coupling constants in table 3. All the calculated anomalies are due to the limited size of the cluster, broader than the measured anomalies, but qualitatively they agree. For two compounds, namely Pr and Gd, the calculation based on a spin-$\frac{1}{2}$ model is obviously incorrect, since the ordering of Pr involves three levels (effective spin-1) and Gd is a spin-$\frac{7}{2}$ system. But it was mentioned by van den Berg et al. (1987) for Gd that the shape of the anomaly is very similar to that of the spin-$\frac{1}{2}$ model. But according to eq. (2), the size of the anomaly has to be scaled ($R \ln 8$, instead of $R \ln 2$, for the entropy; hence the calculated anomaly has to be multiplied by a factor of 3).

4.3. *Hyperfine interaction*

It was shown by Roessli et al. (1993a) that the induced magnetic ordering of Ho is driven by the hyperfine coupling which turned out to be 39 mK. The exchange constants obtained by Guillaume et al. (1994b) are $J_a = -J_b = 1.3(2)\,\mu eV$. A sizeable influence of

the hyperfine interaction on the magnetic ordering could not be found for any of the other compounds.

4.4. *Discussion*

In the preceding sections (4.1–4.3), we were able to show how the dipolar and exchange interaction together are responsible for the magnetic ordering in $RBa_2Cu_3O_7$. However, to achieve this result we had to make some simplifications: pure 2D ordering, Ising spins (spin-$\frac{1}{2}$), and very limited cluster sizes. Just from structural aspects and, in addition, from measurements of spin excitations in grain-aligned $HoBa_2Cu_3O_7$ (Staub et al. 1993), we know that the magnetic coupling along the c-direction is very weak. Nevertheless, in all $RBa_2Cu_3O_7$ compounds, three-dimensional (3D) ordering was found by neutron diffraction. Ising spins may be justified in the case where the single-ion anisotropy due to the CEF is large (Dy), but for lanthanides which are almost isotropic (Nd, Gd, Yb) or rare earths which possess an easy plane (Sm, Er) the question of why the agreement of the calculations with the measurements is nevertheless quite good remains unanswered. The limitation to small cluster sizes results in some quantitative, but not really qualitative, differences, i.e. the anomalies are broader and not as high as for larger clusters and the infinite 2D Ising model. An inclusion of 3D ordering and an increase of cluster size essentially depends only on the power of the computer used for the calculation, while a more general choice of the spins (e.g., Heisenberg spins) requires a much more elaborate quantum-mechanical Monte-Carlo routine (which is normally restricted to rather small clusters).

The choice of antiferromagnetic exchange constants is the result of observations of the magnetic ordering in systems with small influences from the dipolar interaction and the consideration of consistency (same sign for the exchange interaction for all of the lanthanides): For Nd and Gd where the dipolar interaction is weak (hence the magnetic ordering is controlled by the exchange interaction), antiferromagnetic ordering within the plane has been observed by neutron diffraction (Fischer et al. 1989, Chattopadhyay et al. 1988). The corrected exchange constants in table 3 should be equal for all of the lanthanides if their exchange coupling is the same. Obviously, the larger lanthanides are coupled more strongly than the smaller ones, which is due to a increased hybridization. The only exception is Yb, the smallest lanthanide ion in our investigation. Due to the limited amount of experimental data for Yb, a possible influence of the hyperfine interaction on the magnetic ordering cannot be ruled out.

5. Experimental results for oxygen-deficient $RBa_2Cu_3O_x$

5.1. *Introduction*

Oxygen reduction in R123x leads to a decrease in T_c which is dependent on the lanthanide (Buchgeister et al. 1990): For light lanthanide ions the decrease is rather rapid, while

for the heavier ions the superconducting regime extends down to low oxygen contents. This larger range of superconductivity is mainly due to the occurrence of the plateau structure of $T_c(x)$ observed for the heavier lanthanides. At a certain oxygen content (about 6.6 for Nd and 6.35 for Er), a transition from metallic to semiconducting behavior is observed. The reduction of the oxygen content causes a reduction of the mobile charge carriers (holes) in the CuO_2 planes, which is well documented by transport measurements. Such a variation of the carrier density is not expected to affect the dipolar interaction directly, but it may be influenced via an oxygen dependence of the lattice constants or the CEF. The former effect modifies the dipolar energy proportional to r^{-3}, while the latter may alter the size of the moment. (With neutron diffraction and CEF spectroscopy, it was shown that the moments in oxygen-reduced samples are slightly smaller than in fully oxidized samples.) These modifications in the dipolar interaction can be calculated directly and hence will not yield unexpected results. The RKKY interaction, which is an indirect exchange via the conduction electrons, will vitally depend on the density of charge carriers. Since the fully oxidized samples exhibit metallic behavior and the reduced samples display semiconducting behavior, the RKKY interaction is expected to weaken drastically as the oxygen content decreases from $x=7$ to $x=6$. A semiconducting or insulating matrix is ideal for the superexchange interaction; therefore, superexchange (if present) is expected to be strong in the reduced samples. Slight doping of such a magnetically ordered semiconductor might lead to a behavior described in a paper by Zener (1951) and in a comprehensive review article by de Gennes (1960). The main result of this so-called "double exchange" would be a simultaneous observation of ferromagnetic and antiferromagnetic neutron peaks and a canting of the magnetic moments. This theory was developed for 3d magnetic ions, and it is unclear if it could play a role in 4f systems. The expectation for higher carrier concentration is a superexchange influenced by a sea of free carriers and hence a possible competition between superexchange and RKKY interaction as described by Gonçalves da Silva and Falicov (1972). Carrier-density variations in the sample will then obviously have a strong influence on the magnetic ordering if both interactions become similar in strength.

5.2. $PrBa_2Cu_3O_x$

Measurements for Pr123 with $x=7$ and $x=6$ were made by Gering et al. (1988), Schaudy et al. (1993), and Hilscher et al. (1994). They all observed a decrease of the magnetic ordering temperature from 17 K to 11 K in going from the fully oxidized to the reduced sample (fig. 9). No samples with intermediate oxygen contents have been measured up to now.

In the whole range of oxygen content, Pr samples are insulators with a strong hybridization of the 4f bands with the 2p oxygen and the 3d copper bands. Boothroyd et al. (1997) have shown – based on neutron single-crystal diffraction – that the magnetic moments ($\mu=0.56\mu_B$ for $x=7$ and $1.15\mu_B$ for $x=6$) are canted.

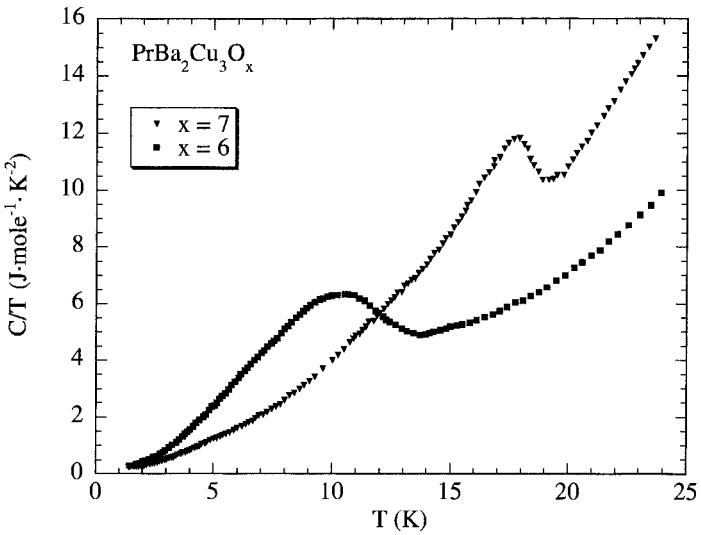

Fig. 9. Specific heat of $PrBa_2Cu_3O_x$ for two samples with oxygen contents close to 7 and 6, respectively (Schaudy et al. 1993).

5.3. *$NdBa_2Cu_3O_x$*

The low-temperature specific heat of reduced Nd123 was reported by Maple et al. (1989) and Yang et al. (1989). They observed a strong anomaly with a rounded maximum at 1.5 K in a non-superconducting sample. Investigations of seven samples with oxygen contents between 6.93 and 6.26 by the same group (Lee et al. 1990) yielded the observation of the most dramatic dependence of the magnetic ordering on the oxygen content (fig. 10): For very high oxygen contents (where long-range magnetic ordering still persists), the anisotropy J_1/J_2 obtained from the 2D Ising fits increases from 14 for $x = 6.97$ to 100 for $x = 6.90$ (Allenspach et al. 1996; fig. 11). Just below an oxygen content of 6.9, the long-range magnetic order collapses and only a broad peak in the magnetic specific heat can be observed. By further lowering the oxygen content to 6.6 this peak shifts to higher temperatures (for 6.64, the peak maximum is at 1.4 K). The shape, which is Schottky-like, remains almost unchanged, except for a small increase of the maximum value between 6.8 and 6.7. Then by entering the non-superconducting regime below 6.6, this feature starts to sharpen again and at 6.26 becomes an anomaly indicative for long-range 3D magnetic ordering at 1.65 K. This ordering could be shown to be antiferromagnetic by measurements of the magnetic-field dependence of the specific heat (Allenspach et al. 1995) and by neutron diffraction (Clinton et al. 1993). From the neutron diffraction measurements it could be concluded that the magnetic moment is canted by 45° relative to the *c*-direction and the moment is reduced compared to the moment in the fully oxidized sample.

Measurements of the magnetic specific heat in $Nd_{1+y}Ba_{2-y}Cu_3O_x$ (Allenspach et al. 1993; fig. 12) where the additional Nd occupies the Ba sites and acts as an electron donor

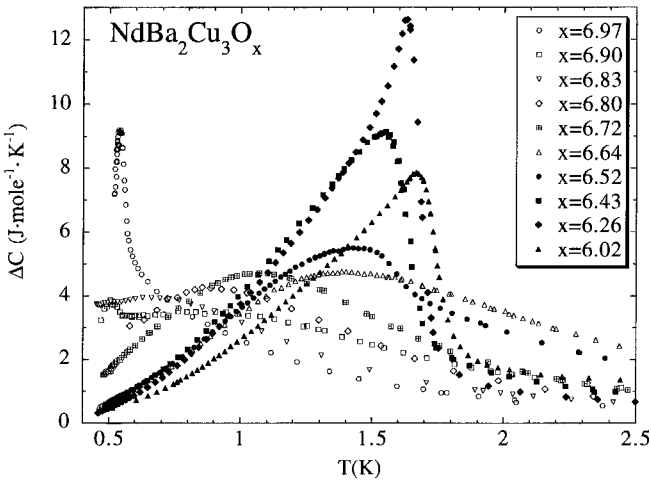

Fig. 10. Oxygen dependence of the magnetic specific heat of $NdBa_2Cu_3O_x$ (Allenspach et al. 1995). Superconducting samples are indicated by open symbols.

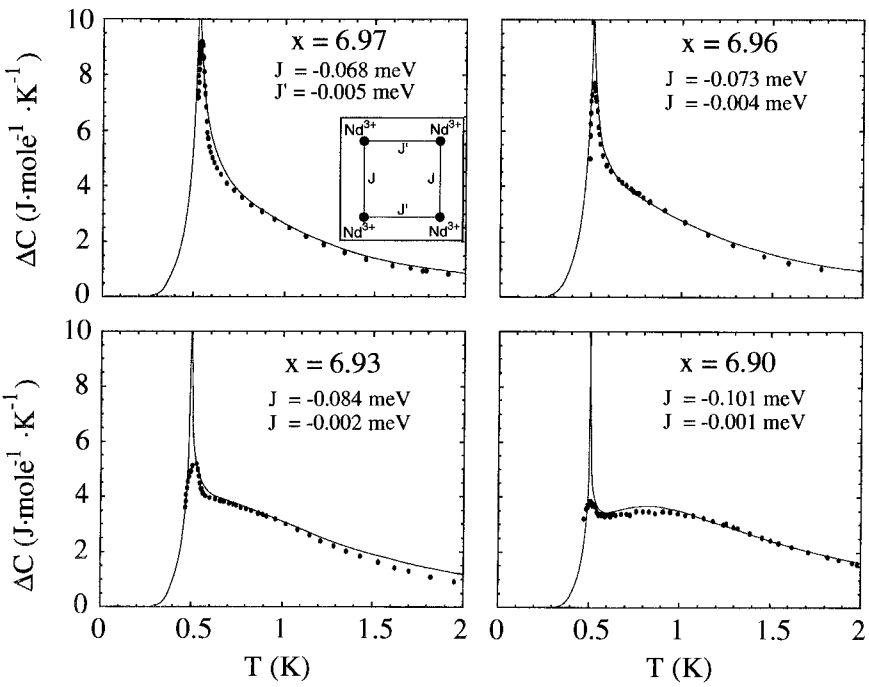

Fig. 11. Oxygen dependence of the magnetic specific heat of $NdBa_2Cu_3O_x$ for high oxygen contents (Allenspach et al. 1995). The lines are results of 2D Ising calculations with the coupling constants given in the individual figures.

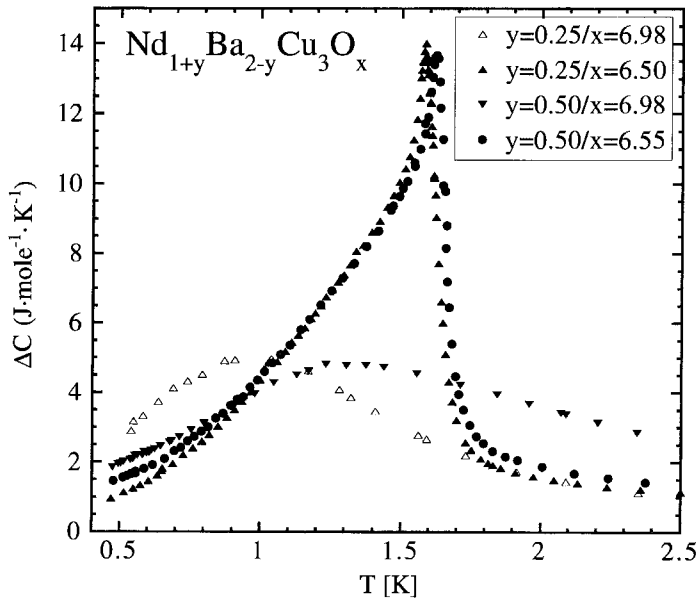

Fig. 12. Oxygen and Nd-doping dependence of the magnetic specific heat of $Nd_{1+y}Ba_{2-y}Cu_3O_x$ (Allenspach et al. 1993). The superconducting sample is indicated by open symbols.

(reducing the number of holes and destroying superconductivity) have proven the magnetic behavior of Nd123 to be solely controlled by the charge-carrier density within the CuO_2 planes. Low-temperature specific-heat measurements of $NdBaCu_{3-y}Ga_yO_x$ (where Ga similar to the oxygen reduction process reduces the hole concentration and depresses T_c) show a dependence of the magnetic ordering as a function of Ga content which is very similar to that of the undoped compound as a function of oxygen content (Niraimathi et al. 1994, 1995a,b).

5.4. *$SmBa_2Cu_3O_x$*

Magnetic specific-heat data for reduced $SmBa_2Cu_3O_x$ have been reported early by our group (Maple et al. 1989, Yang et al. 1989). Instead of the sharp anomaly observed for the fully oxidized compound, a broad feature peaking at around 1 K was obtained for the reduced sample. A more detailed investigation (Allenspach et al. 1996) revealed a behavior of the magnetic specific heat as a function of oxygen content similar to $NdBa_2Cu_3O_x$ (fig. 13): By going from $x=7$ to $x=6$, the in-plane anisotropy increases and long-range magnetic order is lost below $x=6.9$. Between $x=6.9$ and $x=6.4$ only broad (Schottky-like) features, as in the earlier papers, were observed. Below $x=6.4$, the magnetic signal sharpens again with the maximum at 0.7 K. To our knowledge, no neutron diffraction measurements of the magnetic ordering of Sm in $SmBa_2Cu_3O_x$ have been performed. Hence, the assumption of a re-appearance of long-range magnetic order

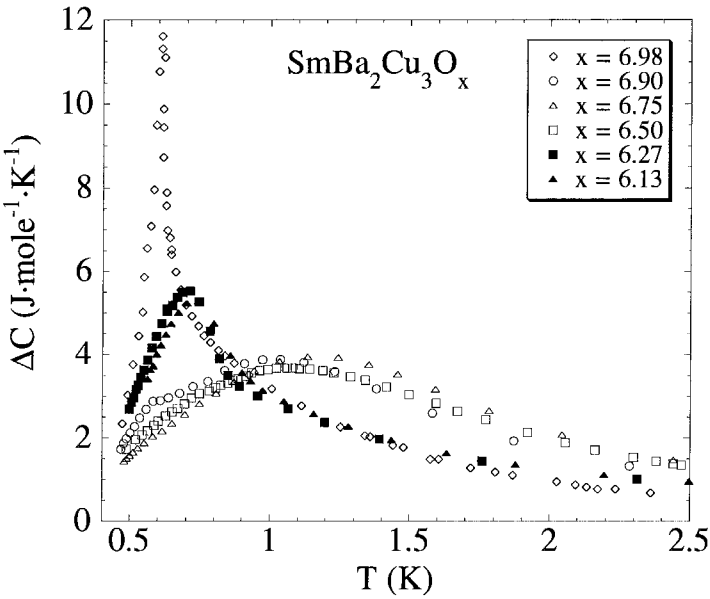

Fig. 13. Oxygen dependence of the magnetic specific heat of $SmBa_2Cu_3O_x$ (Allenspach et al. 1996). Superconducting samples are indicated by open symbols.

at low oxygen contents is only based on these specific-heat data and the similarity with other systems such as Nd, Dy, and Er. The disagreement of our data with those published by Drössler et al. (1996) seems to be due to the poor oxygen control of their sample preparation technique. (The same effect can be observed for Nd.)

5.5. *$GdBa_2Cu_3O_x$*

The absence of almost any oxygen dependence of the magnetic ordering of Gd in $GdBa_2Cu_3O_x$ observed with specific-heat measurements (Meyer et al. 1987, Nakazawa et al. 1987, Dunlap et al. 1988, Gering et al. 1988, Slaski et al. 1988, Zhu et al. 1988, Hilscher et al. 1994) was taken as one of the key arguments for a clear separation of the magnetic and the electronic sublattice and for the negligible influence of the RKKY interaction (since one sample is metallic and the other semiconducting). Nevertheless, neutron diffraction measurements revealed a dependence of the magnetic ordering on the oxygen content of the sample: Chattopadhyay et al. (1988) observed antiferromagnetic ordering along the c-axis in fully oxygenated $GdBa_2Cu_3O_x$, while this coupling was found to be ferromagnetic for a non-superconducting sample. Guillaume et al. (1994a) interpreted their data for a sample with $x = 6.1$ as a mixture of antiferromagnetic and ferromagnetic coupling (simultaneous appearance of the propagation vectors $[\frac{1}{2},\frac{1}{2},\frac{1}{2}]$ and $[\frac{1}{2},\frac{1}{2},0]$). The specific-heat data of Oota and Kojima (1988) and Oota et al. (1989) suggest an oxygen dependence of the specific-heat anomaly (fig. 14). Unfortunately, the number

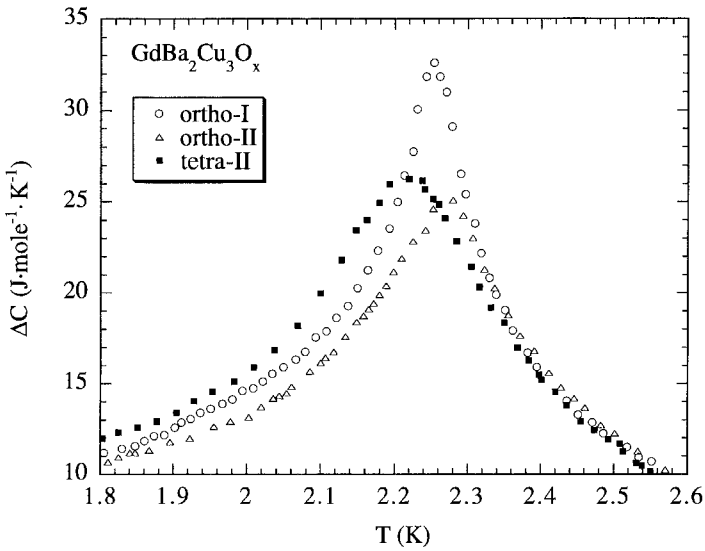

Fig. 14. Oxygen dependence of the magnetic specific heat of $GdBa_2Cu_3O_x$ (Oota and Kojima 1988). Superconducting samples are indicated by open symbols.

of measured samples (3) is too small to see any decay of the long-range order which is expected between the O-II and the T-II sample. Here further investigations on samples with different and well-controlled oxygen contents are needed.

5.6. *$DyBa_2Cu_3O_x$*

The first measurements of an oxygen-deficient sample of Dy123x by Nakazawa et al. (1987) resulted in an anomaly at about 0.8 K which is less intense and broader than that of the fully oxygenated sample (with $T_N = 0.9$ K). The authors could successfully fit these data with a spin-$\frac{1}{2}$ XY model and suggested that for the $x = 7$ sample, a uniaxial single-ion anisotropy in the plane (responsible for the Ising behavior) becomes more isotropic in the non-superconducting samples. Measurements by Lee et al. (1990) of a non-superconducting sample show a much broader (Schottky-like) feature with its maximum at about 1 K. Subsequent investigations by Allenspach et al. (1994a,b, 1995), displayed in fig. 15, revealed the consistency of the two earlier measurements under the assumption that the oxygen content of Nakazawa's sample was around 6.1 and that of Lee's sample was 6.3. The specific-heat behavior for Dy123x is similar to that observed for Nd123x in the sense that there exist sharp peaks for the samples with high and low oxygen contents, and there is an intermediate oxygen range with only short-range magnetic interactions (resulting in the broader peaks). In another sense the Dy123x results are quite different from those of Nd123x since there is almost no shift in the peak position and no high-temperature shoulders of the Dy123x samples.

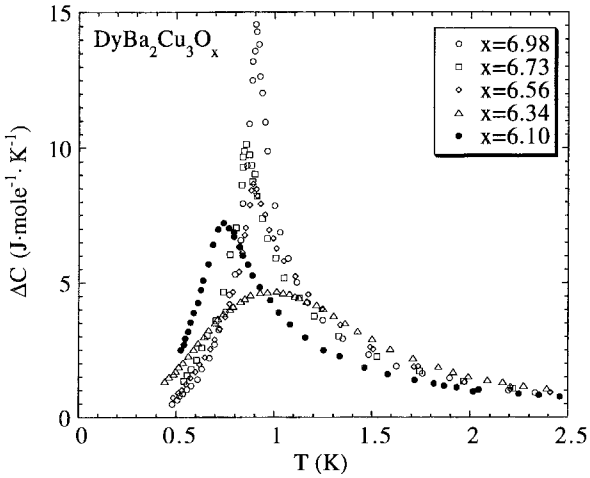

Fig. 15. Oxygen dependence of the magnetic specific heat of $DyBa_2Cu_3O_x$ (Allenspach et al. 1994a). Superconducting samples are indicated by open symbols.

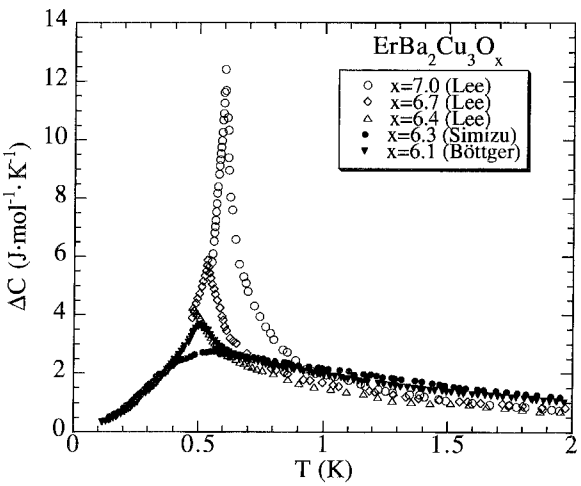

Fig. 16. Oxygen dependence of the magnetic specific heat of $ErBa_2Cu_3O_x$ (Lee et al. 1990, Simizu et al. 1989, Böttger et al. 1998a). Supposedly superconducting samples are indicated by open symbols (see text).

5.7. $ErBa_2Cu_3O_x$

No really consistent set of specific-heat measurements as a function of oxygen content exist for Er123x. Simizu et al. (1989) published a set of measurements on samples with different oxygen contents, but they obtained a discontinuous behavior below $x = 6.5$ which is most likely due to problems associated with the control of the effective oxygen concentration in the sample (which was the case for most of the samples made in the 1980s). Nevertheless, they found a broad peak in the magnetic specific heat for some of the samples, which they fitted with a 1D *XY* model. Lee et al. (1990) observed a gradual decrease of the size of the anomaly and a broadening by going from a 90 K to a 60 K superconductor and finally to an insulating sample, similar to the behavior

observed for Dy123x (see sect. 5.6). A recent measurement by Böttger et al. (1998a) for a sample with $x = 6.10(1)$ seems to confirm the similarity with Dy123x: fig. 16 displays a speculative sequence of magnetic specific-heat anomalies based on an assumed consistency with Dy123x and the observations made for $Er_2Ba_4Cu_7O_{14+x}$ (see sect. 8). Again we have sharp peaks for high and low oxygen contents, and broad peaks (short-range correlations) in between.

6. Discussion of the experimental results of $RBa_2Cu_3O_x$

For $RBa_2Cu_3O_x$ with R = Pr, Nd, Sm, Gd, Dy, Er, presented in the previous sections, the magnetic ordering for $x = 7$ is of antiferromagnetic and long-range character, while for oxygen concentrations close to $x = 6$, the specific-heat data show at least a clear tendency towards long-range magnetic ordering. For R = Nd, Sm, Dy, Er in an intermediate oxygen range (coinciding with the metal–insulator transition), only short-range magnetic interactions were observed by specific heat and, partially, by neutron diffraction measurements (see ch. 199 of this volume). For R = Pr and Gd, the number of samples investigated with different oxygen contents is too small to disprove the presence of such an oxygen regime with solely short-range magnetic ordering. Based on consistency with the other rare earths, we would expect such a regime. Due to this lack of information in the case of Pr and Gd, we will restrict our modelling of the magnetic specific heat to Nd, Sm, Dy, and Er.

As a first step we will concentrate on the oxygen regime where the samples are superconducting or just becoming semiconducting (i.e., for Nd: $x > 6.6$; Sm: $x > 6.4$; Dy: $x > 6.3$; Er: $x > 6.3$). We have been successful in the past in modelling the magnetic specific heat of $NdBa_2Cu_3O_x$ (Allenspach et al. 1994a,b, 1995). Since the Nd ions are almost exclusively coupled via the exchange interaction (see table 3), Nd123x is a good candidate for monitoring the variation of the exchange constants as a function of oxygen content. The magnetic specific-heat behavior over the whole range of oxygen concentration ($7 > x > 6.6$) could be explained assuming an increasing in-plane anisotropy of the exchange constants and a decay of the long-range magnetic ordering into magnetic clusters with antiferromagnetic coupling in one direction and ferromagnetic coupling in the other direction (fig. 17a). The exchange anisotropy was gradually changed from Ising to Heisenberg (fig. 17b) based on neutron spectroscopy investigations (Allenspach et al. 1994c). The only unrealistic result was the relatively large ferromagnetic coupling in the diagonal (via the Cu), originating from the very limited cluster size. The calculation of magnetically coupled Heisenberg clusters is very tedious and is limited to a relatively small cluster size. Hence, for the modelling of the specific heat of Sm, Dy, Er, the Ising model was used, keeping in mind its limitations and shortcomings. Nevertheless, the results seem to be quite reasonable. For the calculation, the Hamiltonian given in eq. (6) was used as explained in sect. 4.2. Since the ordered magnetic moment obtained for Sm in $SmBa_2Cu_3O_7$ (Guillaume et al. 1995) is very small, the dipolar interaction can be neglected for Sm123x (as well as for Nd123x) and the direction of the magnetic

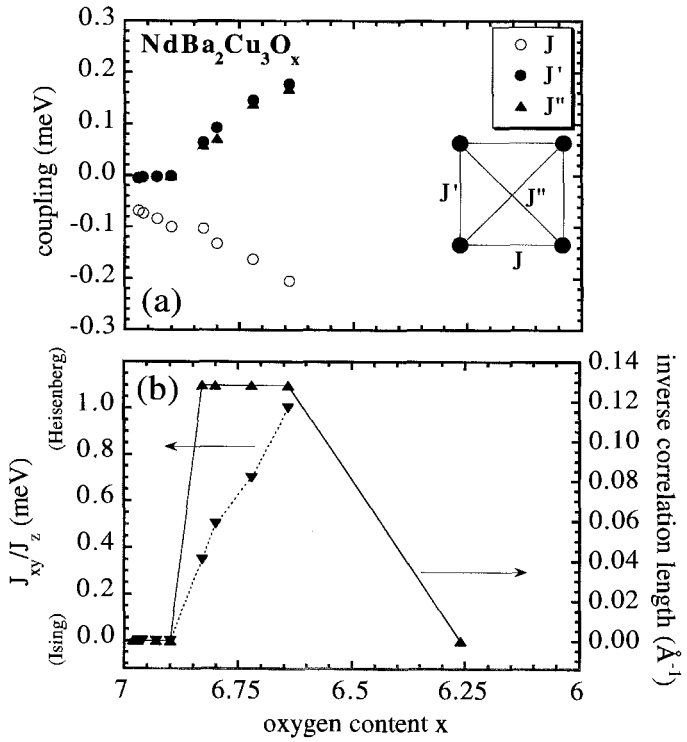

Fig. 17. (a) Magnetic exchange constants and (b) exchange anisotropy (▼ and dotted line) and inverse correlation length (▲ and solid line) obtained for $NdBa_2Cu_3O_x$ (Allenspach et al. 1995).

moment does not play a role in our calculation. For Dy and Er, a good part of the observed magnetic properties is due to the dipolar interaction and its competition with the exchange interaction. The magnetic phase diagram for an exchange-coupled and dipolar system has been published for moments parallel to the *c*-axis (MacIsaac et al. 1995) and perpendicular to the *c*-axis (MacIsaac et al. 1994). These two phase diagrams for Dy and Er, respectively, are displayed in fig. 18. Dy1237 lies clearly in the A/A regime (antiferromagnetic coupling in both plane directions). No variation in purely antiferromagnetic exchange constants will result in a phase transition into one of the other regimes or will result in a decay of the long-range into a short-range magnetically ordered system. Hence, from the observed magnetic specific-heat data and from analogy to Nd123x, we can conclude that for Dy123x at least one of the exchange constants has to become ferromagnetic upon reduction of the oxygen content. Er1237 is situated in the A/F regime (weakly coupled antiferromagnetic in the *a*-direction and strongly ferromagnetic in the *b*-direction due to the dipolar interaction). A variation of the exchange constant in either direction will finally result in a phase transition into the A/A or F/F regimes, respectively, (F/F: ferromagnetic in both directions). For both Dy and Er, an approach to a phase-transition line does not alter the character of the

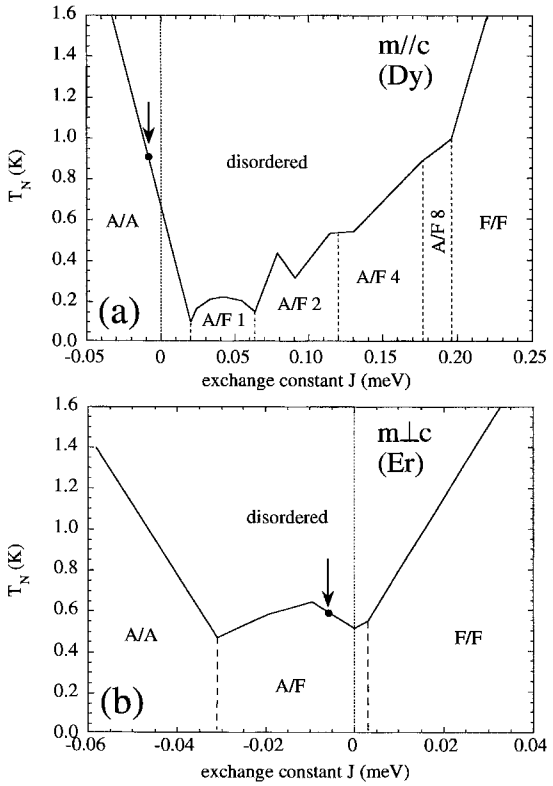

Fig. 18. Phase diagrams of (a) $DyBa_2Cu_3O_x$ and (b) $ErBa_2Cu_3O_x$ (MacIsaac et al. 1995 and 1994, respectively). The arrows indicate the position of the samples with $x=7$ obtained by our dipolar and exchange interaction calculation.

magnetic specific heat (except for the lowering of the ordering temperature) despite the fact that exactly at the transition line the effective coupling in one direction has to be zero. Such a 1D coupling would result in a broad peak in the specific heat, but the range where a variation of the character of the ordering is observed is much broader in oxygen content than expected from these theoretical considerations. Hence, the neighborhood of these phase-transition lines plays an important, but not an exclusive, role in the behavior of the magnetic ordering. A strong inhomogeneity in the electronic sublattice was observed in the oxygen range between $x=6.3$ and $x=6.9$ by neutron spectroscopy (Mesot et al. 1993b) and other local probes (see Vol. 30, ch. 194 of this Handbook). Such an inhomogeneous distribution of charge carriers is expected to result in a high inhomogeneity of the exchange constants. We took this effect into account by distributing the exchange constants for samples with $x<6.9$ randomly on the bonds in *a*- and *b*-directions.

The calculated magnetic specific-heat anomalies for Sm, Dy, and Er are displayed in fig. 19 and the exchange constants as a function of oxygen content in fig. 20. The anomalies reproduce the observed behavior quite well except that they are broader in the calculations due to the restriction to relatively small clusters (10×10). The exchange

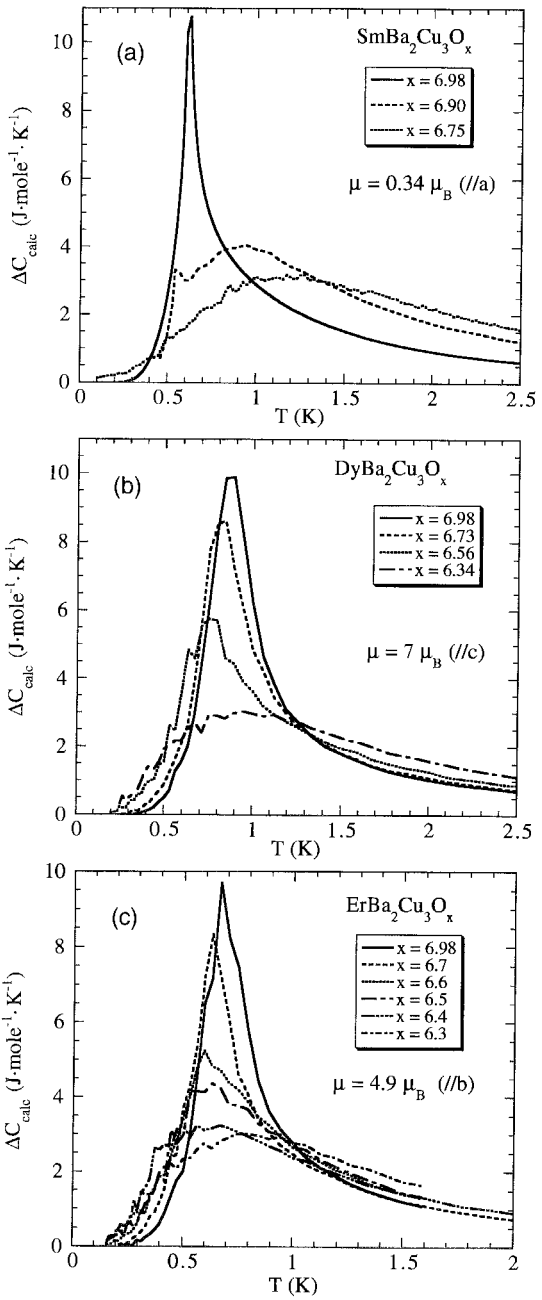

Fig. 19. Calculated oxygen dependence of the magnetic specific heat of (a) $SmBa_2Cu_3O_x$, (b) $DyBa_2Cu_3O_x$, and (c) $ErBa_2Cu_3O_x$ in the superconducting regime. These figures have to be compared with figs. 13, 15, and 16, respectively.

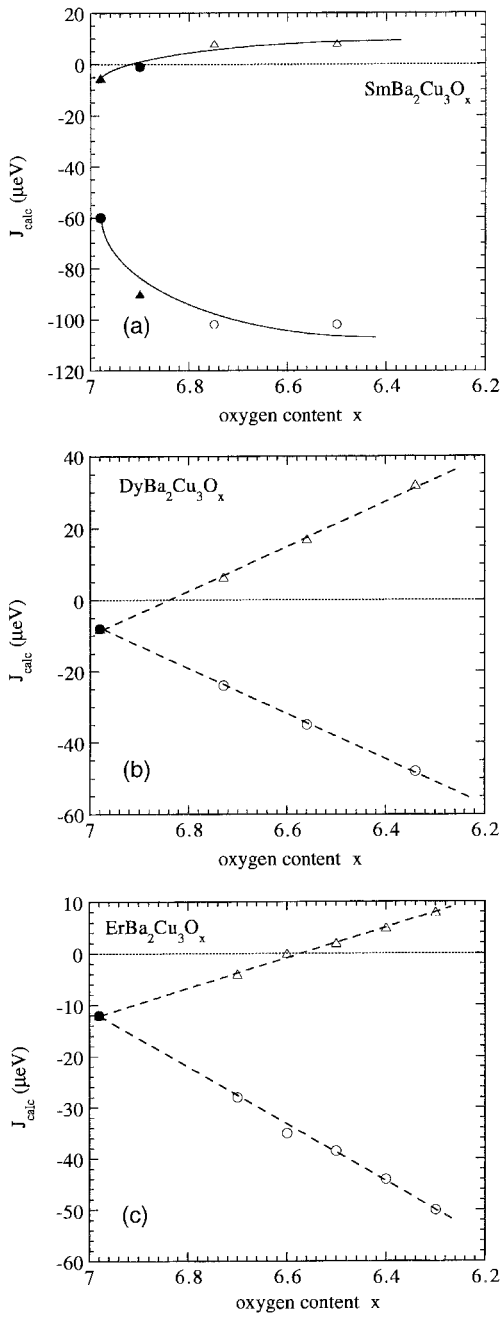

Fig. 20. Exchange constants obtained from the calculations shown in fig. 19 for (a) $SmBa_2Cu_3O_x$, (b) $DyBa_2Cu_3O_x$, and (c) $ErBa_2Cu_3O_x$. Closed symbols indicate well-defined values in *a*- and *b*-direction, while open symbols indicate a random distribution of the values in the two directions. The crosses for Sm stand for a superposition of both (see text). The lines are guides to the eye.

constants behave consistently and similar to that obtained earlier for Nd. The only difference is that for Nd the cluster size and the exchange anisotropy were varied, while for Sm, Dy, and Er the cluster size was kept fixed and only Ising spins were used. Since the magnetic correlation length is reduced by the random placement of the exchange constants, this has the same effect as the reduction of the cluster size. The microscopic mechanism responsible for the rather unusual behavior of the coupling constants is unknown, but it can be argued that the larger anisotropy at $x = 6.9$ compared to $x = 7$ is due to charge ordering (e.g., striped phase) which favors a distinctly different coupling in the two plane directions. The charge distribution in samples close to $x = 7$ is expected to be more metal-like, and the resulting coupling constants in the plane almost equal. For superconducting samples with oxygen contents below 6.9 – according to our results – the charge-carrier density allows charge ordering only on a local scale which is independent of the crystal directions.

As a second step, we will briefly compare the magnetic ordering at oxygen contents below the metal–insulator transition: As we discussed in sect. 5, the magnetic ordering temperature is almost the same for $x = 6$ as for $x = 7$ Sm, Gd, Dy, and Er compounds. According to neutron diffraction data, the magnetic ordering in samples with $x = 6$ tends to be more two-dimensional in character or at least a mixing of antiferromagnetic and ferromagnetic coupling along the c-direction was observed (see ch. 199 of this volume). This disruption or disorder in the magnetic interaction along c might be due to a double exchange interaction (Zener 1951, de Gennes 1960) present in these slightly doped systems. The moment direction is identical for $x = 7$ and $x = 6$ and the size of the moment is almost the same. The lowest oxygen content for reduced samples is of the order of $x = 6.1$, not 6. For $x = 6$, no double exchange would be expected and the magnetic ordering would be almost identical to the fully doped samples.

In the case of Pr and Nd, a large shift in the magnetic ordering temperature (by going from $x = 7$ to 6) was observed from 17 to 11 K in the case of Pr and 0.5 to 1.6 K for Nd, respectively. These two lanthanides are among the largest atoms in the lanthanide series, and hybridization cannot be neglected. (In the case of Pr this even destroys superconductivity.) Canting of the magnetic moments relative to the c-axis – which is a feature predicted by the theory of the double exchange – was observed for Pr with $x = 6$ and $x = 7$ (Boothroyd et al. 1997) and for Nd with $x = 6.3$ (Clinton et al. 1993). Such a canting lifts the high symmetry of the lanthanide site, and a coupling between the Cu spins (which order magnetically in the semiconducting regime) and the lanthanide spins can be realized. The hybridization might strengthen this coupling and explain why such a canting of the moments and variation of the ordering temperature was not observed for the other lanthanides.

An alternative approach to understand the appearance of ferromagnetic interactions and canting of the moments is provided by the theory of Gonçalves da Silva and Falicov (1972) who investigated the competition of superexchange and RKKY interaction as a function of free charge carriers. This competition resulted – in the simple model systems – in a series of different magnetic phases (antiferromagnetic, canted antiferromagnetic, helical,

and ferromagnetic). This alone would result in a series of different long-range magnetic phases by going from $x=6$ to 7, but would not explain the short-range order.

Hence both the large electronic disorder in the CuO_2 planes and the competition of superexchange and RKKY interaction are needed to account for the observed behavior of the magnetic lanthanide ordering in the R123x systems.

7. Experimental results for $RBa_2Cu_4O_8$

The $RBa_2Cu_4O_8$ (R124) compounds are close relatives of the R123 compounds. The R124 unit cell consists of two R123 units with double CuO chains which leads to a shift of the lanthanide ions in consecutive layers by half a unit cell in the *a*- and *b*-directions (see ch. 199 of this volume). This leads to frustration and almost pure 2D magnetic ordering. In contrast to the R123 compounds the oxygen content of the R124 compounds is fixed. While there are quite a few neutron diffraction papers about the magnetic ordering of the lanthanides in these compounds (see Fischer and Medarde 1998 and references therein), to our knowledge no specific-heat data have been published. This lack of data is mainly due to the fact that these compounds order magnetically in a long-range fashion only, and hence the information obtained from specific heat in addition to the neutron scattering data is very limited.

Our group performed specific-heat measurements to study the magnetic ordering of Dy in a $DyBa_2Cu_4O_8$ sample obtained from Professor E. Kaldis (ETH Zurich, Switzerland). The magnetic ordering is suppressed by an applied magnetic field as expected for antiferromagnets (fig. 21). Fitting the specific-heat curve with the 2D Ising model alone yields -60 and $-22\,\mu$eV for J_1 and J_2, respectively. Dipolar interactions would result in an ordering temperature of only 0.47 K ($\mu \| c$, $|\mu| = 5.9\mu_B$). The combination of dipolar and exchange interactions reproduces the observed ordering temperature of 1 K for $J_{calc} = -21\,\mu$eV (uncorrected) and $J_{corr} = 7.4\,\mu$eV (corrected with the modified de Gennes factor). J_{corr} for Dy124 is about 3 times larger than J_{corr} for Dy1237 (table 3), indicating a larger hybridization in the former compound. This result is supported by pressure measurements (fig. 22) where the relative change of the ordering temperature under pressure $(dT_N/T_N)/dp$ was found to be $0.0147\,\mathrm{K\,kbar^{-2}}$, which is about 3 times more than for Dy1237 (see end of sect. 3.2).

The CEF splitting for Dy124 (Roessli et al. 1993b), which is about the same as that for Dy1237 (Allenspach et al. 1989), consists of a doublet ground state isolated by more than 3 meV from the next-higher doublet. Hence, the entropy change expected for the magnetic ordering is at least $R \ln 2$, but only about 80% of this value is observed (fig. 23). Under pressure, the entropy increases to nearly the expected value. This implies that under ambient pressure not all the Dy ions participate in the magnetic ordering, and that applied pressure leads to a better magnetic coupling, resulting in a higher ratio of magnetically coupled Dy ions.

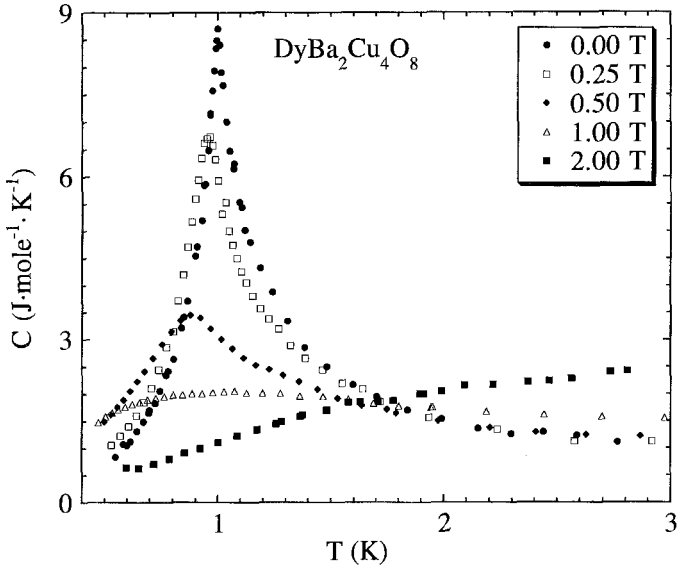

Fig. 21. Magnetic field dependence of the magnetic specific heat of $DyBa_2Cu_4O_8$.

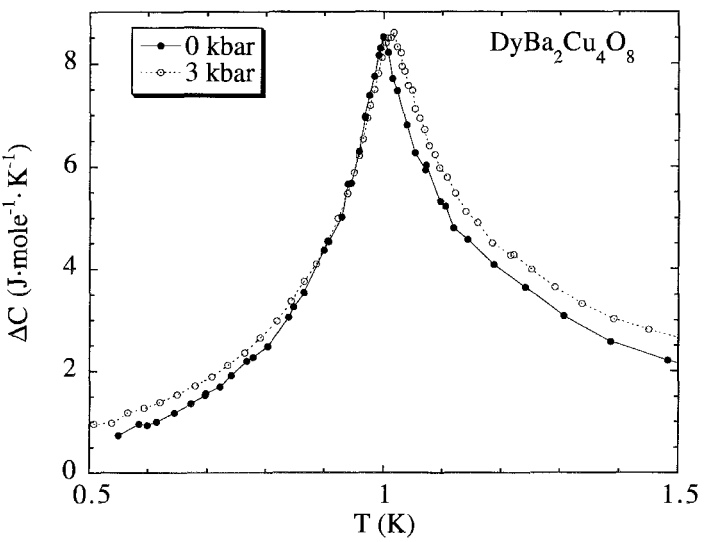

Fig. 22. Pressure dependence of the magnetic specific heat of $DyBa_2Cu_4O_8$.

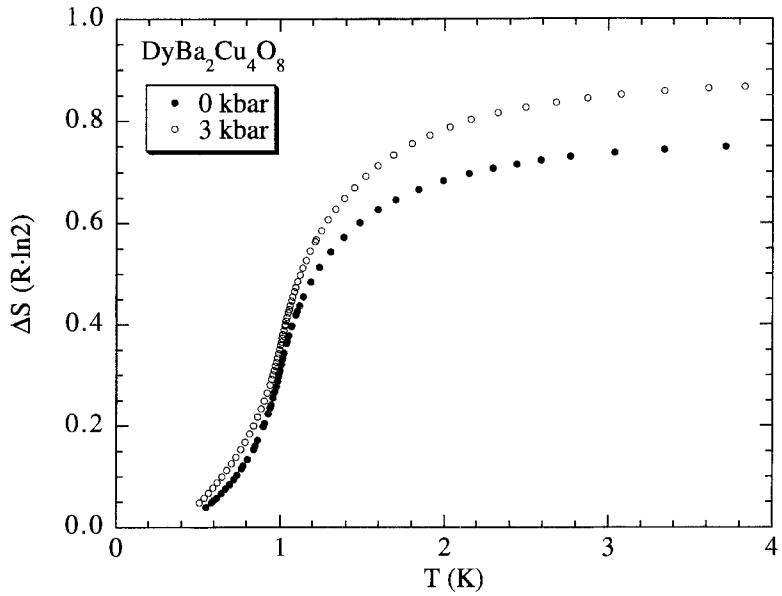

Fig. 23. Pressure dependence of the entropy of $DyBa_2Cu_4O_8$. Note the increase of the entropy towards the expected value of $R \ln 2$ under hydrostatic pressure.

8. Experimental results for $R_2Ba_4Cu_7O_{14+x}$

8.1. *Introduction*

Like the R123 and the R124 compounds, $R_2Ba_4Cu_7O_{14+x}$ (R247) contains superconducting, buckled CuO_2 planes and linear Cu–O chains. The structure of R247 consists of alternating 123 and 124 blocks in the c-direction. While the R^{3+} ions are surrounded by two equivalent CuO_2 planes in R123, they are surrounded by two inequivalent CuO_2 planes in R247. The single chains can be oxygen depleted as in the R123 phase, but the R247 compound remains superconducting due to the presence of stoichiometric R124 blocks. Removing oxygen from the single chains in the 123 blocks decreases T_c from 95 to 30 K (Genoud et al. 1992).

In the $R_2Ba_4Cu_{6+n}O_{14+n}$ ($n=0,1,2$) family, the R–R distance along the a- and b-directions is about 3.9 Å, while the distance along the c-direction is three times larger. Although the large separation between the R ions along the c-axis in R124 and R123 should favour 2D ordering, we know from neutron diffraction that 3D ordering is also realized. It is therefore not surprising that Er247 exhibits 3D ordering of the Er ions as well (Böttger et al. 1997a). Since a transition from 3D to 2D ordering of the Er ions can be achieved by oxygen removal in Er123 (Maletta et al. 1990), we expect a similar behaviour for Er247 upon oxygen depletion. An investigation of the dependence of the type of magnetic order upon x in $Er_2Ba_4Cu_7O_{14+x}$ is of special interest because Er247 is expected to be the only R247 compound that shows 3D ordering of the lanthanide ions (Zhang et al.

1992). Thus, the presumable transition from 3D to 2D order in R247 compounds should only be observable in Er247. Correspondingly, pure 2D ordering should be observed for, e.g., $Dy_2Ba_4Cu_7O_{15}$ as was confirmed by neutron diffraction studies (Zhang et al. 1992).

8.2. *Magnetic specific heat*

The oxygen dependence of the magnetic specific heat was reported for $Dy_2Ba_4Cu_7O_{14+x}$ (Böttger et al. 1998b) and $Er_2Ba_4Cu_7O_{14+x}$ (Böttger et al. 1997b); these data sets, together with recent measurements, are displayed in figs. 24 and 25, respectively.

As for Dy123x, the anomaly in the magnetic specific heat due to the magnetic ordering remains at almost the same temperature under oxygen depletion but becomes broader and smaller. We expect that for further depletion this trend would continue towards a behavior similar to that found for Dy123x with $x=6.34$ (i.e., a Schottky-like anomaly). A fit with only the anisotropic 2D Ising model (line in fig. 24) yields -71 and $-17\,\mu$eV for J_1 and J_2, respectively. Dipolar interaction would result in an ordering temperature of only 0.64 K ($\mu \| c$, $|\mu| = 7\mu_B$, according to Zhang et al. 1992). The combination of dipolar and exchange interactions reproduces the observed ordering temperature of 1.0 K for $J_{calc} = -12\,\mu$eV (uncorrected) and $J_{corr} = -4.2\,\mu$eV, which is 50% more than found for Dy1237 (see table 3).

The magnetic specific heat of $Er_2Ba_4Cu_7O_{14+x}$ differs from that of Er123x insofar as the anomaly for $x=0.3$ resembles more those observed for $NdBa_2Cu_3O_{6.90}$ and $SmBa_2Cu_3O_{6.90}$, but the tendency (long-range order for high and low oxygen contents and disorder in an intermediate range) is the same in both Er compounds. The exchange

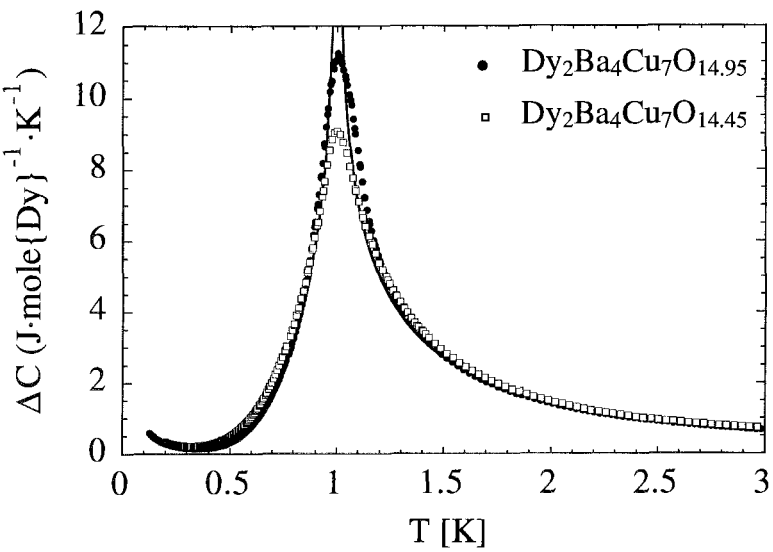

Fig. 24. Oxygen dependence of the magnetic specific heat of $Dy_2Ba_4Cu_7O_{14+x}$ (Böttger et al. 1998b). The line is a 2D Ising calculation with the exchange values given in table 3.

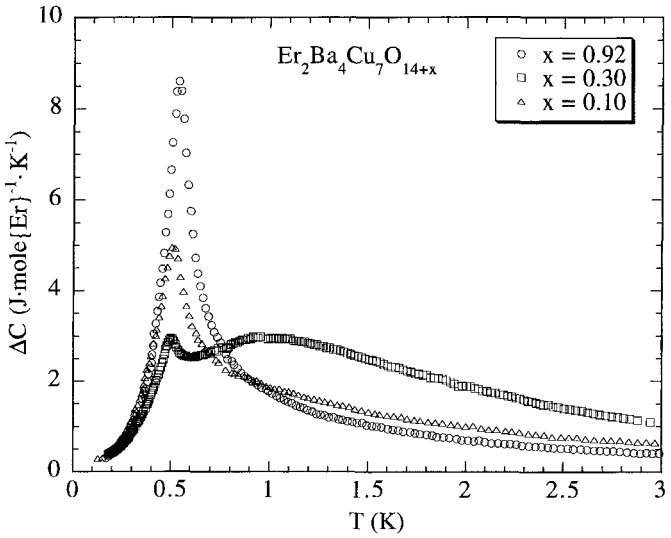

Fig. 25. Oxygen dependence of the magnetic specific heat of $Er_2Ba_4Cu_7O_{14+x}$ (Böttger et al. 1997b).

constants obtained using a pure anisotropic 2D Ising fit for $Er_2Ba_4Cu_7O_{14.92}$ are given by Böttger et al. (1997b) as $J_1 = \pm 39\,\mu eV$ and $J_2 = \mp 9\,\mu eV$ (taking into account the A/F ordering observed in neutron diffraction experiments by the same group, Böttger et al. 1997a). Dipolar interaction alone would yield an ordering temperature of 0.34 K ($\mu \parallel b$, $|\mu| = 3.7\mu_B$). The combination of dipolar and exchange interactions reproduces the observed ordering temperature of 0.54 K for $J_{calc} = -27\,\mu eV$ (uncorrected) and $J_{corr} = -41\,\mu eV$. This is more than twice the value of Er1237.

8.3. *Discussion*

A division of the values for T_N and J in the theoretical phase diagram of Er123 (fig. 18b) by a factor of 1.5 (due to different lattice constants and different magnetic moments) yields the phase diagram for Er247. The area of A/F ordering (which was observed in neutron diffraction) is restricted to $-20\,\mu eV \leqslant J \leqslant +1.8\,\mu eV$ and $0.31\,K \leqslant T_N \leqslant 0.42\,K$. The observed T_N of 0.54 K would be obtained for $J = -28\,\mu eV$ (A/A ordering) or $+8\,\mu eV$ (F/F ordering). This contradiction between experiment and theory can only be resolved by assuming an anisotropic exchange interaction in the plane. No unambiguous set of parameters (J_1, J_2) could be found, but typical sets are $(-9.3, 0.0\,\mu eV)$ and $(-15, -6\,\mu eV)$, which both fulfill the ordering-temperature condition. In contrast to all the other coupling constants mentioned so far, for Er247, J_1 can be identified with J_a and J_2 with J_b due to the moment direction and the necessity for anisotropic exchange values.

At lower oxygen contents ($x = 14.3$), the shape of the magnetic anomaly strikingly resembles the shape of a very anisotropic 2D Ising curve (as observed for Nd123 with $x = 6.90$). But in contrast to the Nd compound, the size of the anomaly does not

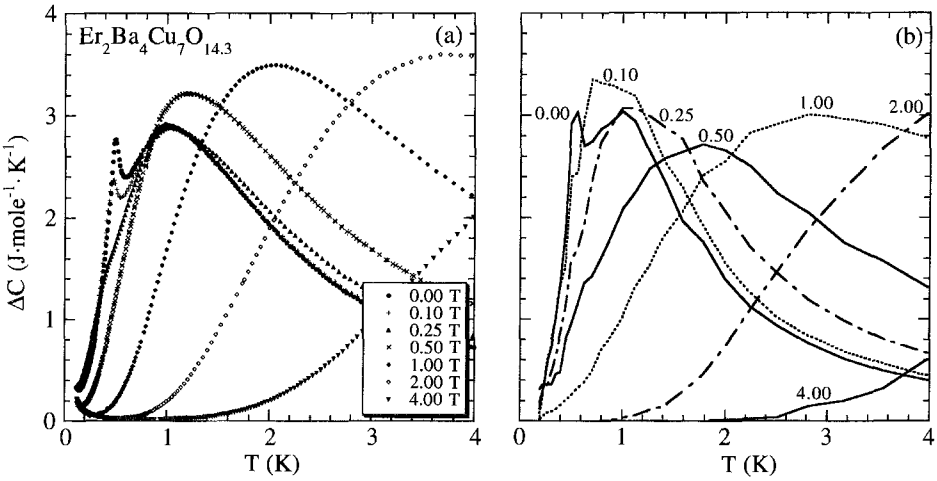

Fig. 26. (a) Magnetic field dependence of the magnetic specific heat of $Er_2Ba_4Cu_7O_{14.3}$ (Böttger et al. 1998a). (b) Calculation of the magnetic field dependence using a superposition of two different exchange contributions and the dipolar interaction (see text).

match the theoretical curve. This may be due to the fact that the order is not really long-range, leading to a kind of smeared-out peak. But neutron-spectroscopy data (with indications for electronic cluster formation) together with the structural peculiarity of the 247 compounds (alternating 123 and 124 blocks) point more in the direction of a superposition of two individual magnetic anomalies simultaneously present in the sample. Böttger et al. (1997b) have attributed these two contributions to areas in the samples with almost identical electronic and magnetic properties as found in the fully oxidized sample, and areas which are strongly disturbed electronically and magnetically. The inclusion of the dipolar interaction into the analysis results in an additional set of exchange constants (for the disturbed regions) which cannot be obtained unambiguously. (A set which reproduces the anomaly originating from disturbed regions is, e.g., −70/+30 μeV, where these two values are randomly distributed along *a* and *b*.) In order to reduce the parameter space for possible values for J_a and J_b in the undisturbed and disturbed regions, we performed specific heat measurements in applied magnetic fields for $Er_2Ba_4Cu_7O_{14.3}$ (fig. 26a). From this figure one can see that in fields above 0.5 tesla the magnetic specific heat manifests itself as a Schottky anomaly due to the splitting of the ground-state doublet [with a typical *g*-value of 6.8 which is close to the value 7.1 expected in a powder sample from $g_x = 5.7$, $g_y = 9.7$, and $g_z = 4.8$, calculated by Böttger (1998) from her neutron spectroscopy results]. Hence, magnetic interactions are effective only in a regime below 0.5 tesla. A reasonable (double) set of exchange parameters has to fulfill these criteria. Since Er247 is far from being an ideal Ising system (as can be seen from the *g*-values), more than qualitative agreement is not expected from such an analysis. The magnetic-field dependence of the magnetic specific heat of an Ising system [with $g = 9.7$; $J_a = -9.3$ μeV and $J_b = 0$ μeV (undisturbed regions) and $J_{a/b} = -70/+30$ μeV (disturbed

regions), respectively] is displayed in fig. 26b. As can be seen the qualitative behavior of the measured and the calculated curves is similar, with the increase of signal at a field of 0.1 tesla (in the calculation) being the largest discrepancy. This increase is due to an insufficient stiffness of the magnetic ordering in the undisturbed regions in the calculation. In addition, the calculation does not present a powder average. Such an average would diminish the 0.10-tesla increase and would restrict the shift of the Schottky anomaly to the observed value (i.e., a shift corresponding to $g \approx 7$).

9. Conclusions

We have presented above a phenomenological approach to the available magnetic heat-capacity data for the 123, 124 and 247 compounds. The model includes dipolar and exchange interactions. At high oxygen contents, all samples which order magnetically do so in a long-range fashion. Oxygen reduction leads in all these compounds to an increase of the anisotropy of the in-plane magnetic coupling due to the competition between the superexchange and the RKKY interactions and – for a restricted oxygen regime – to strong disorder in the electronic sublattice. Finally, at low oxygen contents, long-range magnetic ordering is recovered due to the reappearance of structural and electronic order in the totally reduced samples. Due to the crude theoretical tools at hand and the severe simplifications made (e.g., Ising model for all the rare earths), we did not actually fit theoretical results to the experimental data but just presented theoretical curves which demonstrate the qualitative agreement. The aim of this contribution should be to encourage more elaborate theoretical studies of the magnetic interactions and their dependence on doping in these fascinating compounds.

Besides the question concerning the origin of the observed magnetic ordering effects, there are still open questions and unexplored effects on the experimental side:

- No experimental data exist for Pr123 in the intermediate oxygen-content regime.
- In the intermediate oxygen regime of Sm123, the center of mass of the magnetic anomaly is higher than that of both the fully oxidized and the fully reduced samples. Is the transition towards the reduced sample sharp or gradual as towards the oxidized sample?
- Does an oxygen regime also exist for Gd123 where only short-range ordering is present? What is the origin of the 1 K shoulder?
- The specific-heat data of Er123 originate from different sources and the samples were not consistently characterized.
- The evolution of the magnetic ordering in Er247 is not yet studied sufficiently well and, hence, the origin of the formation of the two different magnetic regimes is still unclear.

Acknowledgment

Financial support by the US Department of Energy under Grant No. DE-FG03-86ER-45230 and the Swiss National Science Foundation is kindly acknowledged.

References

Alekseevskii, N.E., A.V. Gusev, G.G. Devyatykh, A.V. Kabanov, V.N. Narozhnyi, V.I. Nizhankovskii and E.P. Khlybov, 1988, JETP Lett. **48**(10), 585.

Allenspach, P., A. Furrer and F. Hulliger, 1989, Phys. Rev. B **39**(4), 2226.

Allenspach, P., B.W. Lee, D.A. Gajewski and M.B. Maple, 1993, J. Appl. Phys. **73**(10), 6317.

Allenspach, P., M.B. Maple and A. Furrer, 1994a, J. Alloys & Compounds **207–208**, 213.

Allenspach, P., B.W. Lee, D.A. Gajewski and M.B. Maple, 1994b, Physica C **235–240**, 1753.

Allenspach, P., J. Mesot, U. Staub, M. Guillaume, A. Furrer, S.-I. Yoo, M.J. Kramer, R.W. McCallum, H. Maletta, H. Blank, H. Mutka, R. Osborn, M. Arai, Z. Bowden and A.D. Taylor, 1994c, Z. Phys. B **95**, 301.

Allenspach, P., B.W. Lee, D.A. Gajewski, V.B. Barbeta, M.B. Maple, G. Nieva, S.-I. Yoo, M.J. Kramer, R.W. McCallum and L. Ben-Dor, 1995, Z. Phys. B **96**, 455.

Allenspach, P., M.C. de Andrade and M.B. Maple, 1996, Czech. J. Phys. **46**(Suppl. S4), 2103.

Alloul, H., P. Mendels, G. Collin and P. Monod, 1988, Phys. Rev. Lett. **61**, 746.

Atake, T., 1991, Thermochim. Acta **174**, 281.

Basu, B.K., S.M. Pattalwar, R.N. Dixit, S.Y. Shete, G. Chandra, A.K. Nigam and R.S. Sannabhadti, 1989, Physica C **159**, 379.

Basu, B.K., S.M. Pattalwar, R.N. Dixit and S.Y. Shete, 1991, Bull. Mater. Sci. **14**(3), 655.

Bloom, S.H., M.V. Kuric, R.P. Guertin, C.-S. Jee, D. Nichols, E. Kaczanowicz, J.E. Crow, G. Myer and R.E. Salomon, 1987, J. Magn. Magn. Mater. **68**, L135.

Boothroyd, A.T., L. Longmore, N.H. Andersen, E. Brecht and Th. Wolf, 1997, Phys. Rev. Lett. **78**(1), 130.

Böttger, G., 1998, Ph.D. Thesis (ETH Zurich).

Böttger, G., P. Fischer, A. Dönni, P. Berastegui, Y. Aoki, H. Sato and F. Fauth, 1997a, Phys. Rev. B **55**, R12005.

Böttger, G., P. Allenspach, A. Dönni, Y. Aoki and H. Sato, 1997b, Z. Phys. B **104**, 195.

Böttger, G., P. Allenspach, A. Dönni, Y. Aoki, T. Namiki and H. Sato, 1998a, unpublished.

Böttger, G., P. Allenspach, J. Mesot, A. Dönni, Y. Aoki and H. Sato, 1998b, J. Alloys & Compounds **275–277**, 560.

Brown, S.E., J.D. Thompson, J.O. Willis, R.M. Aikin, E. Zirngiebl, J.L. Smith, Z. Fisk and R.B. Schwarz, 1987, Phys. Rev. B **36**(4), 2298.

Buchgeister, M., W. Hiller, S.M. Hosseini, K. Kopitzki and D. Wagener, 1990, in: Proc. Int. Conf. on Transport Properties of Superconductors, Rio de Janeiro, Brazil (1990), ed. R. Niclosky (World Scientific, Singapore) p. 511.

Causa, M.T., S.M. Dutrus, C. Fainstein, G. Nieva, H.R. Salva, R. Sanchez, L.B. Steren, M. Tovar and R. Zysler, 1987, Int. J. Mod. Phys. B **1**(3&4), 989.

Causa, M.T., C. Fainstein, G. Nieva, R. Sanchez, L.B. Steren, M. Tovar and R. Zysler, 1988, Phys. Rev. B **38**(1), 257.

Chattopadhyay, T., H. Maletta, W. Wirges, K. Fischer and P.J. Brown, 1988, Phys. Rev. B **38**(1), 838.

Chmist, J., A. Lewicki, Z. Tarnawski, A. Kozlowski, J. Zukrowski, W.M. Woch, A. Kolodziejczyk and K. Krop, 1988, Acta Phys. Pol. A **74**, 757.

Clinton, T.W., J.W. Lynn, B.W. Lee, M. Buchgeister and M.B. Maple, 1993, J. Appl. Phys. **73**, 6320.

de Gennes, P.G., 1960, Phys. Rev. **118**(1), 141.

de Jongh, L.J., and A.R. Miedema, 1974, Adv. Phys. **23**(1), 1–260.

Dirken, M.W., and L.J. de Jongh, 1987, Solid State Commun. **64**(9), 1201.

Drössler, H., H.-D. Jostarndt, J. Harnischmacher, J. Kalenborn, U. Walter, A. Severing, W. Schlabitz and E. Holland-Moritz, 1996, Z. Phys B **100**, 1.

Dunlap, B.D., M. Slaski, D.G. Hinks, L. Soderholm, M.A. Beno, K. Zhang, C. Segre, G.W. Crabtree, W.K. Kwok, S.K. Malik, I.K. Schuller, J.D. Jorgensen and Z. Sungaila, 1987, J. Magn. Magn. Mater. **68**, L139.

Dunlap, B.D., M. Slaski, Z. Sungaila, D.G. Hinks, K. Zhang, C. Segre, S.K. Malik and E.E. Alp, 1988, Phys. Rev. B **37**(1), 592.

Escribe-Filippini, C., K. Konate, R. Buder, J. Marcus and C. Schlenker, 1988, Physica C **153–155**, 1030.

Ferreira, J.M., B.W. Lee, Y. Dalichaouch, M.S. Torikachvili, K.N. Yang and M.B. Maple, 1988, Phys. Rev. B **37**(4), 1580.

Fischer, P., and M. Medarde, 1998, in: Neutron Scattering in Layered Copper-Oxide Superconductors, ed. A. Furrer, Vol. 20 of Physics and Chemistry of Materials with Low-dimensional Structure (Kluwer Academic Publishers, Dordrecht) pp. 261–301.

Fischer, P., B. Schmid, P. Brüesch, F. Stucki and P. Unternährer, 1989, Z. Phys. B **74**, 183.

Genoud, J.-Y., T. Graf, G. Triscone, A. Junod and J. Muller, 1992, Physica C **192**, 137.

Gering, E., B. Renker, F. Gompf, D. Ewert, H. Schmidt, R. Arens, M. Bonnet and A. Dianoux, 1988, Physica C **153–155**, 184.

Gonçalves da Silva, C.E.T., and L.M. Falicov, 1972, J. Phys. C **5**, 63.

Guillaume, M., P. Fischer, B. Roessli, P. Allenspach and V. Trunov, 1994a, Physica C **235–240**, 1637.

Guillaume, M., U. Staub, F. Fauth, J. Mesot, A. Furrer and C. Carlile, 1994b, Physica C **223**, 333.

Guillaume, M., W. Henggeler, A. Furrer, R.S. Eccleston and V. Trounov, 1995, Phys. Rev. Lett. **74**(17), 3423.

Gurevich, A.M., V.I. Dotsenko, V.N. Eropkin, Y.V. Telezhenko and N.M. Chaikovskaya, 1990, Sov. J. Low Temp. Phys. **16**(1), 27.

Heremans, J., D.T. Morelli, G.W. Smith and S.C. Strite III, 1988, Phys. Rev. B **37**(4), 1604.

Hilscher, G., T. Holubar, G. Schaudy, J. Dumschat, M. Strecker, G. Wortmann, Z.X. Wang, B. Hellebrand and D. Bäuerle, 1994, Phys. Rev. B **49**, 535.

Ho, J.C., P.H. Hor, R.L. Meng, C.W. Chu and C.Y. Huang, 1987, Solid State Commun. **63**(8), 711.

Jana, P.C., and R.C. Bhuniya, 1993, Solid State Commun. **87**(8), 731.

Jensen, J., and A.R. Mackintosh, 1991, Rare Earth Magnetism (Clarendon Press, Oxford).

Junod, A., 1996, Specific heat of high temperature superconductors in high magnetic fields, in: Studies of High Temperature Superconductors, Vol. 19, ed A.V. Narlikar (Nova Science Publisher Inc., New York) p. 1.

Kadowaki, K., H.P. van der Meulen, J.C.P. Klaasse, M. van Sprang, J.Q.A. Koster, L.W. Roeland, F.R. de Boer, Y.K. Huang, A.A. Menovsky and J.J.M. Franse, 1987, Physica **145B**, 260.

Kierspel, H., F. Oster, H. Drössler, U. Callies, H. General, H. Geus, G. Jackel, H.-D. Jostarndt, J. Langen, A. Waldorfer, R. Müller, W. Schlabitz and D. Wohlleben, 1994, Low temperature specific heat and AC-susceptibility of $REBa_2Cu_3O_{7-\delta}$ (RE = Y, Nd, Eu, Gd, Dy, Ho, Er, Tm and Yb), in: High Temperature Superconductors: Physical and Material Properties, eds S.K. Malik and S.S. Jhah (Nova Science Publisher Inc., New York).

Kobayashi, T., K. Amaya, T. Kohara, K. Ueda, Y. Kohori, Y. Oda and K. Asayama, 1987, J. Phys. Soc. Jpn. **56**(11), 3805.

Kohara, T., Y. Oda, Y. Kohori, I. Nakada, Y. Yamada, K. Amaya, T. Kobayashi, E. Sakagami, T. Kaneko, H. Fujita, H. Toyoda and K. Asayama, 1987, Jpn. J. Appl. Phys. **26**(10), L1672.

Lazarev, V.B., I.S. Shaplygin, K.S. Gavrichev, I.A. Konovalova, V.E. Gorbunov and E.A. Tistchenko, 1988, Physica C **153–155**, 1024.

Lee, B.W., J.M. Ferreira, Y. Dalichaouch, M.S. Torikachvili, K.N. Yang and M.B. Maple, 1988, Phys. Rev. B **37**(4), 2368.

Lee, B.W., J.M. Ferreira, S. Ghamaty, K.N. Yang and M.B. Maple, 1990, in: Oxygen Disorder Effects in High-T_c Superconductors, eds J.L. Moran-Lopez and I.K. Schuller (Plenum, New York) p. 151.

MacIsaac, A.B., J.P. Whitehead, K. De'Bell and K. Sowmya Narayanan, 1992, Phys. Rev. B **46**(10), 6387.

MacIsaac, A.B., J.P. Whitehead, M.C. Robinson and K. De'Bell, 1994, Physica B **194–196**, 223.

MacIsaac, A.B., J.P. Whitehead, M.C. Robinson and K. De'Bell, 1995, Phys. Rev. B **51**(22), 16033.

Maletta, H., E. Pörschke, T. Chattopadhyay and P.J. Brown, 1990, Physica C **166**, 9.

Maple, M.B., J.M. Ferreira, R.R. Hake, B.W. Lee, J.J. Neumeier, C.L. Seaman, K.N. Yang and H. Zhou, 1989, J. Less-Common Met. **149**, 405.

Mesot, J., P. Allenspach, U. Staub, A. Furrer, H. Mutka, R. Osborn and A. Taylor, 1993a, Phys. Rev. B **47**(10), 6027.

Mesot, J., P. Allenspach, U. Staub, A. Furrer and H. Mutka, 1993b, Phys. Rev. Lett. **70**(6), 865.

Meyer, C., H.-J. Bornemann, H. Schmidt, R. Ahrens, D. Ewert, B. Renker and G. Czjzek, 1987, J. Phys. F **17**, L345.

Mori, K., K. Noto, M. Sasakawa, Y. Isikawa, K. Sato, N. Kobayashi and Y. Muto, 1988, Physica C **153–155**, 1515.

Nakazawa, Y., M. Ishikawa and T. Takabatake, 1987, Physica B **148**, 404.

Naumov, V.N., G.I. Frolova, E.B. Amitin, V.E. Fedorov and P.P. Samoilov, 1996, Physica C **262**, 143.

Niraimathi, A.M., E. Gmelin and G. Rangarajan, 1994, Physica C **235–240**, 857.

Niraimathi, A.M., G. Rangarajan, R.K. Kremer and E. Gmelin, 1995a, Ceramics Int. **21**, 367.

Niraimathi, A.M., E. Gmelin and G. Rangarajan, 1995b, Phys. Rev. B **51**(13), 8503.

Onsager, L., 1944, Phys. Rev. **65**, 117.

Oota, A., and T. Kojima, 1988, Jpn. J. Appl. Phys. **27**(3), L333.

Oota, A., T. Kojima and Y. Sasaki, 1989, Proc. MRS Int. Meetings on Adv. Mater. **6**, 341.

Plackowski, T., and D. Wlosewicz, 1996, Solid State Commun. **98**(1), 31.

Ramirez, A.P., L.F. Schneemeyer and J.V. Waszczak, 1987, Phys. Rev. B **36**(13), 7145.

Ravindran, N., T. Sarkar, S. Uma, G. Rangarajan and V. Sankaranarayanan, 1995, Phys. Rev. B **52**, 7656.

Reeves, M.E., D.S. Citrin, B.G. Pazol, T.A. Friedmann and D.M. Ginsberg, 1987, Phys. Rev. B **36**(13), 6915.

Roessli, B., P. Fischer, U. Staub, M. Zolliker and A. Furrer, 1993a, Europhys. Lett. **23**(7), 511.

Roessli, B., P. Fischer, M. Zolliker, P. Allenspach, J. Mesot, U. Staub, A. Furrer, E. Kaldis, B. Bucher, J. Karpinski, E. Jilek and H. Mutka, 1993b, Z. Phys. B **91**, 149.

Schaudy, G., T. Holubar, N. Pillmayr, G. Leitenbauer, G. Hilscher, P. Rogl and A. Hanninger, 1992, J. Magn. Magn. Mater. **104–107**, 477.

Schaudy, G., T. Holubar, M. Forsthuber, G. Hilscher, E. Holland-Moritz, V. Nekvasil and P. Rogl, 1993, in: Electronic Properties of High-T_c Superconductors, eds H. Kuzmany, M. Mehring and J. Fink, Vol. 113 of Springer Series in Solid-State Sciences (Springer, Berlin) p. 113.

Simizu, S., S.A. Friedberg, E.A. Hayri and M. Greenblatt, 1987a, Jpn. J. Appl. Phys. **26**(Suppl. 26-3), 2121.

Simizu, S., S.A. Friedberg, E.A. Hayri and M. Greenblatt, 1987b, Phys. Rev. B **36**, 7129.

Simizu, S., G.H. Bellesis, J. Lukin, S.A. Friedberg, H.S. Lessure, S.M. Fine and M. Greenblatt, 1989, Phys. Rev. B **39**(13), 9099.

Slaski, M., B.D. Dunlap, M.V. Nevitt and Z. Sungaila, 1988, in: High-T_c Superconductors, ed. H. Weber (Plenum, New York) p. 89.

Smit, H.H.A., M.W. Dirken, R.C. Thiel and L.J. de Jongh, 1987, Solid State Commun. **64**(5), 695.

Staub, U., F. Fauth, M. Guillaume, J. Mesot, A. Furrer, P. Dosanjh and H. Zhou, 1993, Europhys. Lett. **21**(8), 845.

Thuy, N.P., N.T. Hien, T.D. Hien and J.J.M. Franse, 1992, J. Magn. Magn. Mater. **104–107**, 489.

Uma, S., W. Schnelle, E. Gmelin, G. Rangarajan, A. Erb, E. Walker and R. Flükiger, 1996, Czech. J. Phys. **46**(Suppl. S5), 2677.

van den Berg, J., C.J. van der Beek, P.H. Kes, J.A. Mydosh, G.J. Nieuwenhuys and L.J. de Jongh, 1987, Solid State Commun. **64**(5), 699.

van der Meulen, H.P., J.J.M. Franse, Z. Tarnawski, K. Kadowaki, J.C.P. Klaasse and A.A. Menovsky, 1988a, Physica C **152**, 65.

van der Meulen, H.P., J.J.M. Franse, Z. Tarnawski, K. Kadowaki, J.C.P. Klaasse and A.A. Menovsky, 1988b, Physica C **153–155**, 1018.

Wang, K., Z. Chen, J. Xia, Z. Chen and Q. Zhang, 1989, Solid State Commun. **69**(12), 1145.

Willekers, R.W., H.C. Meijer, G. Rietfeld, F. Mathu and H. Postma, 1990a, Physica B **165–166**, 1333.

Willekers, R.W., H.C. Meijer, H. Postma and M.J.V. Menken, 1990b, Physica C **168**, 99.

Willekers, R.W., H.C. Meijer, F. Mathu and H. Postma, 1991, Cryogenics **31**, 168.

Willis, J.O., Z. Fisk, J.D. Thompson, S.-W. Cheong, R.M. Aikin, J.L. Smith and E. Zirngiebl, 1987, J. Magn. Magn. Mater. **67**, L139.

Yang, K.N., J.M. Ferreira, B.W. Lee, M.B. Maple, W.-H. Li, J.W. Lynn and R.W. Erwin, 1989, Phys. Rev. B **40**(16), 10963.

Yeomans, J.M., 1992, Statistical Mechanics of Phase Transformations (Clarendon Press, Oxford).

Zener, C., 1951, Phys. Rev. **82**(3), 403.

Zhang, H., J.W. Lynn and D.E. Morris, 1992, Phys. Rev. B **45**, 10022.

Zhu, C., Zhao Guo-meng and Q.-Z. Ran, 1988, Solid State Commun. **66**(7), 719.

Zou, Z., J. Ye, K. Oka and Y. Nishihara, 1998, Phys. Rev. Lett. **80**, 174.

Handbook on the Physics and Chemistry of Rare Earths
Vol. 31
edited by K.A. Gschneidner, Jr., L. Eyring and M.B. Maple

Chapter 201

ANGLE-RESOLVED PHOTOEMISSION STUDIES OF UNTWINNED YTTRIUM BARIUM COPPER OXIDE

Matthias SCHABEL
Remote Sensing Systems, 438 First St. Suite 200, Santa Rosa, CA 95401, USA

Z.-X. SHEN
Department of Applied Physics, Stanford University, Stanford, CA, USA

Contents

Abbreviations

ARPES	Angle-resolved photoelectron spectroscopy
BCS	Bardeen–Cooper–Schrieffer
Bi2212	$Bi_2Sr_2CaCu_2O_8$
BZ	Brillouin zone
CDW	Charge density wave
DOS	Density of states
EDC	Energy distribution curve
EELS	Electron energy loss spectroscopy
EVHS	Extended Van Hove singularity
FS	Fermi surface
HTS	High-temperature superconductor
LDA	Local density approximation
LHB	Lower Hubbard band
LMTO	Linearized muffin tin orbital
MIT	Metal–insulator transition
PES	Photoelectron spectroscopy
RESPES	Resonance photoelectron spectroscopy
SCF	Surface chain feature
STM	Scanning tunneling microscopy
TMO	Transition metal oxide
UHB	Upper hubbard band
UHV	Ultrahigh vacuum
UPS	Ultraviolet photoelectron spectroscopy
XAS	X-ray absorption spectroscopy
XPS	X-ray photoelectron spectroscopy
Y123	$YBa_2Cu_3O_7$
Y124	$YBa_2Cu_4O_8$

1. Introduction

In 1986 the world of condensed matter physics was set abuzz by Bednorz and Müller's discovery of superconductivity in $La_{2-x}Ba_xCuO_4$ (La214) at the unprecedented temperature of 38 K (Bednorz and Müller 1986). Perhaps even more dramatic than the extremely high superconducting transition temperature was its observation in a highly anisotropic, conductive ceramic oxide. This discovery immediately instigated an unparalleled effort in materials synthesis, leading to dramatic increases in transition temperatures in $YBa_2Cu_3O_{7-\delta}$ (Y123), $Bi_2Sr_2CaCu_2O_{8+\delta}$ (Bi2212), $Tl_2Ba_2Ca_2Cu_3O_{10+\delta}$ (Tl2223), and $HgBa_2Ca_2Cu_3O_{10+\delta}$ (Hg1223), with the three-plane Hg1223 material having the highest transition temperature known to date, reaching over 150 K under pressure (Chu et al. 1993, Maeda et al. 1988, Schilling et al. 1993, Sheng and Hermann 1988, Wu et al. 1987). Rapid strides in crystal growth techniques were paralleled by equally rapid developments in methods of experimental characterization.

Nevertheless, after more than a decade of intense study, the cuprate perovskites continue to challenge our understanding of electronic structure in general, and superconductivity in particular. Prior to the discovery of these novel materials, the Bardeen–Cooper–Schrieffer (BCS) theory provided a coherent and quantitative picture of the microscopic mechanism of superconductivity through electron–phonon coupling, although lacking in predictive power at the materials level (Bardeen et al. 1957). The astronomically high transition temperatures in oxide superconductors coupled with their other unconventional properties have necessitated a re-examination of the conventional theory, and have turned attention to other possible pairing mechanisms, particularly magnetic ones (Anderson 1987, Dagotto 1994, Dagotto et al. 1994, Fukuyama 1988, Kampf and Schrieffer 1990, Laughlin 1988, Markiewicz 1991, Millis et al. 1990, Monthoux et al. 1991, Nagaosa and Lee 1991, Scalapino et al. 1986, Schrieffer et al. 1988, Virosztek and Ruvalds 1990). Furthermore, the poorly understood aspects of electronic structure in correlated systems in general have been thrust to the forefront of theoretical efforts. Of the many experimental techniques used in the pursuit of insight into the cuprates, angle-resolved photoemission has taken a central role by virtue of its ability to directly probe both energy and momentum scales relevant to these strongly correlated materials.

While each family of cuprate superconductors differs in details, all share the same fundamental structure: one or more planar CuO_2 layers in which square plaquettes of Cu atoms fourfold coordinate to O atoms lying between them (fig. 1), with a comparatively inert interlayer separating the copper oxide planes. This interlayer serves as a charge reservoir for dopants, as well as stabilizing the CuO_2 structure. Their highly anisotropic two-dimensional character was implicated from the outset in their anomalous properties, but the exact role of reduced dimensionality remains unclear at this time (Anderson 1990, Varma et al. 1989). Within a family, monotonically increasing critical temperatures are observed with increasing number of CuO_2 units per elementary cell, from unilayers to trilayers, another behavior which remains poorly understood. Even the phenomenology of T_c dependence on the interlayer properties lacks systematics, although arguments have

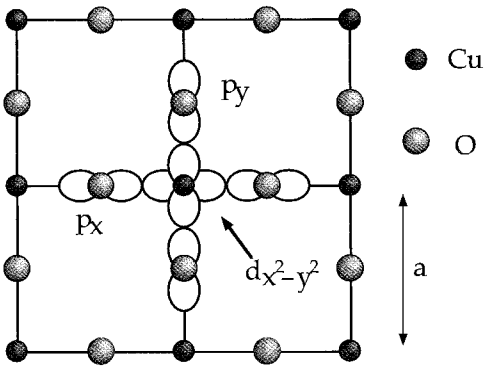

Fig. 1. The atomic structure of the ubiquitous CuO_2 planes, which are believed to play a pivotal role in the unusual properties of the cuprates. The in-plane lattice constant, a, is approximately 3.85 Å. A sketch of the Cu $3d_{x^2-y^2}$ and O $2p_{x,y}$ orbitals which hybridize to form the low energy states near the Fermi surface is superimposed.

been made for a correlation with in-plane lattice constant (Fisk and Sarrao 1995), or interlayer tunneling properties (Anderson 1990).

In the superconducting state, the cuprates also manifest a number of anomalous properties. Unlike conventional superconductors, which have superconducting coherence lengths, ξ, on the order of 10^3–10^4 Å, the Cooper pairs in high-temperature superconductors (HTS) are localized over a region 12–15 Å in the plane. Parallel to the c-axis, ξ is even smaller than the corresponding unit cell dimension (~2–5 Å). This tendency to strongly localize in real, rather than momentum space may be an indicator that the fundamental interactions responsible for pairing in the cuprates are strong, short-ranged forces rather than the weaker phonon-mediated mean-field forces causing pairing in conventional BCS materials (Scalapino 1995). Alternatively, localized polaron formation may lead to significant deviations from conventional behavior (Alexandrov and Mott 1995, Salje et al. 1995). Furthermore, it has been established with a high degree of certainty in the past few years that the symmetry of the superconducting order parameter has an anisotropic form, with a $\pi/2$ phase change associated with a 90° rotation along the Cu–O bonds, and lines of nodes (zero order parameter) along the plane diagonal (Ott and Brawner 1995, Tsuei et al. 1995, van Harlingen 1995, Wollman et al. 1995). This sort of behavior is consistent with a magnetic pairing force based on the strong tendency for antiferromagnetic alignment of unpaired spins in these materials (Bulut and Scalapino 1995, Scalapino 1995, 1996).

Stimulated by the unusual properties of the cuprate superconductors, interest in the electronic structure of highly correlated materials, particularly transition metal oxides (TMO), has experienced a renascence. These are systems for which conventional one-electron theory fails qualitatively, often predicting metallic behavior for compounds known to be large-gap insulators. In light of the great strides which have been made in understanding electronic structure from the perspective of band theory, this failure is particularly intriguing, and appears to have far-reaching ramifications for the theory of many-particle systems (Zaanen et al. 1985). In the HTS, the CuO_2 planes which are responsible for carrier transport, and are believed to be the critical element for high-T_c behavior, clearly fall into this class, and manifest many of the hallmarks of

strong correlations. Hybridization of the narrow band of localized Cu 3d states with an itinerant O 2p band leads to an antiferromagnetic parent compound which is a charge transfer insulator, and which rapidly evolves into a "strange metal" when doped with small concentrations of holes (Allen 1985, Fuggle and Inglesfield 1992, Zaanen et al. 1985, Zaanen and Sawatzky 1990). The curious and significant coexistence in the HTS of numerous phases with unusual magnetic order in a small doping regime parallels the empirical observation in normal superconductors that higher critical temperatures are typically associated with structural or electronic instabilities. The armaments of a vast number of experimental groups have been applied to studies of TMO in general, and HTS in particular, providing a wealth of often confusing, sometimes contradictory results (Cox 1992, Tokura and Fujimori 1995). The fact that their baffling properties are only slowly being unraveled is a testament to the complexity of these highly unconventional oxides. From the outset photoemission, particularly the angle-resolved technique (ARPES), has made critical contributions to these investigations. With improvements in materials quality and instrumentation, it has found itself at the forefront of debate centered on the electronic structure and nature of the pairing state. The lamellar nature of these materials allows, in the ideal case, unambiguous determination of the planar band structure due to the lack of dispersion between planes (Olson et al. 1989a,b). Issues of recent interest or current concern include the presence and relevance of an extended flat band van Hove singularity, existence, volume, and topology of the Fermi surface, the anisotropy of the superconducting gap and the symmetry of the order parameter, the doping dependence of the electronic structure, the appearance of a pseudogap above above the critical temperature, including the possibility of pairing without phase coherence, and the nature of the fundamental low-energy excitations (Levi 1993).

1.1. *Electronic structure*

An extremely simple way of visualizing the Mott metal–insulator transition is shown in fig. 2. If we consider a lattice of alkali metal atoms (each having a half-filled outer s orbital) in the metallic state (fig. 2a), it is clear that the valence electrons can decrease their kinetic energy by becoming highly delocalized, resulting in a nearly uniform probability amplitude throughout the crystal. Because the strongly screened Coulomb interaction with other electrons is weak and short-ranged, this delocalization is favored. However, as we adiabatically increase the interatomic distance, the orbital overlap, and consequently, the bandwidth, W, diminish rapidly. Ultimately we arrive at the situation depicted in fig. 2b, in which there is a lattice of isolated atoms, each independent of the others. In this limit of very large lattice parameter, conduction must proceed via hopping of a single electron between sites. Each atom is essentially unaffected by the presence of its neighbors due to the exponentially shrinking inter-site matrix element, and the formal imposition of Bloch's theorem is meaningless. Hopping of parallel spins is absolutely prohibited by Pauli exclusion in the case of a single orbital, while antiparallel spins may doubly occupy the orbital, in the process incurring an energy cost, U, due to the mutual Coulomb repulsion of two electrons on a single site.

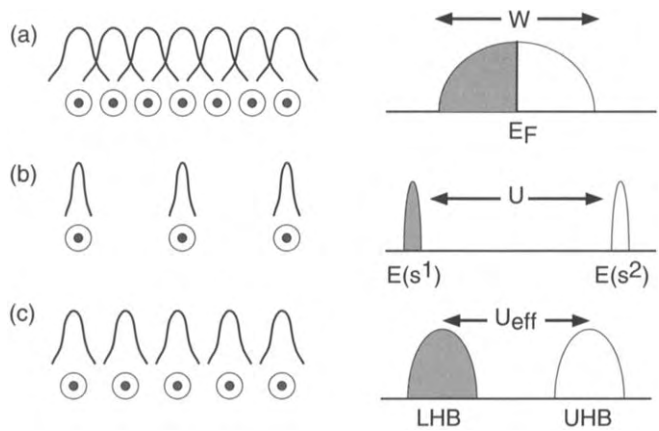

Fig. 2. Schematic illustration of the metal–insulator transition and formation of Hubbard bands in narrow-bandwidth materials. In the itinerant metal (a), strong overlap of the valence orbitals leads to formation of a broad hybridized energy band of width W. Electrons are essentially completely delocalized to minimize their kinetic energy. At the opposite extreme (b) is the atomic case, where the eigenstates are well defined and the Coulombic repulsion between two electrons in a single orbital costs an energy U. Transition-metal oxides and similar materials exist in the intermediate regime suggested in (c), with an effective Coulomb repulsion, larger than their bandwidth: $U_{eff} \gg W/2$, separating the upper (UHB) and lower (LHB) Hubbard bands.

The fascinating intermediate regime lying between itinerant electrons and isolated atomic states is illustrated in fig. 2c. Clearly, the extreme cases of metallic and atomic behavior must be separated by a phase transition demarcating the boundary between these qualitatively different situations, from a single strongly hybridized band of width W to two distinct energy levels separated by a finite $U = E(s^2) - E(s^1)$. It is precisely this phase boundary which defines the metal–insulator transition (MIT) in the Mott–Hubbard model, and is crucial for understanding the properties of TMO. The example constructed above is an artificial one, and neglects a host of other competing phenomena which can arise, including small polarons and Jahn–Teller distortions, charge density waves (CDW), local phase separation in the form of spin, charge, or orbital ordering, and structural phase transitions (such as the Peierls transition) in which changes in local or long-range order result in a lower ground-state energy. It is the fortuitous chemical conjunction of oxygen, which readily hybridizes to form delocalized ligand band states, and a 3d transition metal, having localized 3d and itinerant valence states, which gives the transition metal oxides their unique properties. By forming structurally stable crystals in which the O atoms act as spacers forcing the transition-metal atoms apart to reduce 3d orbital overlap, these systems exist in the parameter regime where the Mott–Hubbard transition occurs, and reveal a wealth of fascinating properties. Members run the gamut from conventional metals, semiconductors, and insulators to materials exhibiting metal–insulator transitions, a class which includes the cuprates. The effective Coulomb repulsion, U_{eff}, represents the energetic penalty incurred when the 3d orbital is doubly occupied, and is reduced from

that in the bare atom by screening effects. Nevertheless, it is clear that, when $U_{\text{eff}} \gg W/2$, we are in a regime qualitatively different from the picture described by band theory.

2. Photoelectron spectroscopy

The simplest *gedanken* photoemission experiment (fig. 3) consists of monochromatic ultraviolet (UPS) or X-ray (XPS) photons from a synchrotron, X-ray anode, or glow discharge lamp impinging on the surface of a solid sample, where a fraction are absorbed by electrons lying in bound states. Electrons bound by less than $h\nu - \Phi$, where Φ is the sample work function, escape the sample and propagate to a detector where their kinetic energy distribution is measured. Conservation of energy requires that the difference in energies between the initial state, with a photon in free space and an unperturbed solid, and the final state, with a photoelectron in free space and a single hole propagating in the solid, equal the energy of the photon. This does not, however, preclude the possibility of interactions between the photoelectron and photohole; much of the difficulty in interpreting photoemission data arises from such "final-state effects" (Cardona and Ley 1978a,b, Hüfner 1996). In addition, the extremely short mean free path for inelastic scattering of photoelectrons, typically on the order of 5 Å at the photon

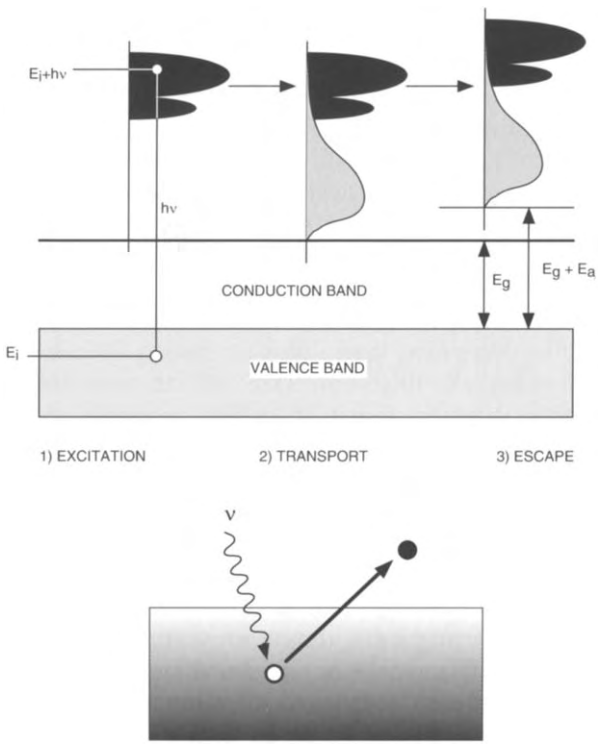

Fig. 3. A schematic depiction of the photoemission process within the context of the three-step model. An incident photon, with energy $h\nu$, is absorbed by a bound electron (e^-) in the solid, which is subsequently photoemitted with energy $h\nu - \Phi$, leaving behind a positively charged hole (h^+).

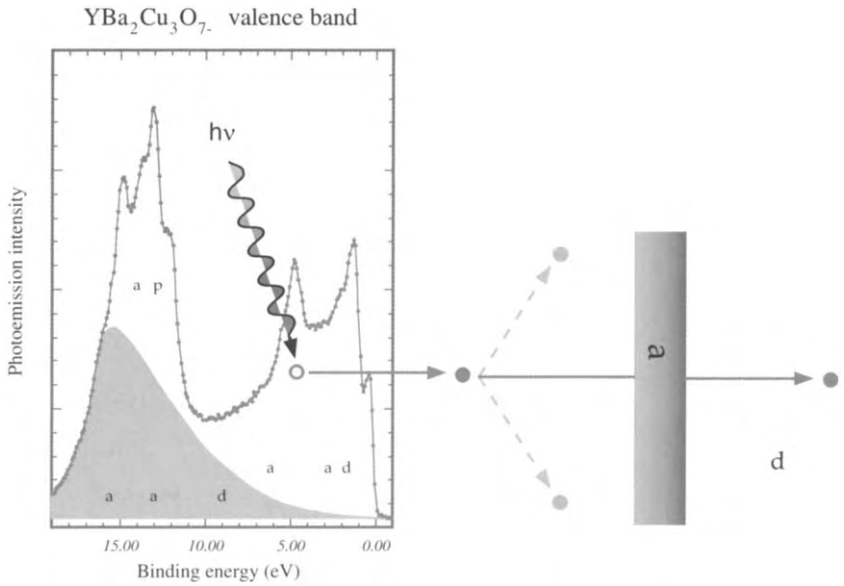

Fig. 4. The photoemission process, showing the valence band of Y123, along with the Ba 5p core level, and the background of inelastically scattered electrons. The incident photon is absorbed in the solid, producing a photoexcited electron and a positively charged hole. Energy losses during transport of the outgoing photoelectron give rise to the background, which should be proportional to the integrated weight of photoelectrons at higher kinetic energies. Both unscattered and scattered photoelectrons experience a step loss in energy passing through the surface work-function barrier (Φ) before propagating to the detector.

energies used in UPS (slightly longer in XPS), (Schabel et al. 1991, Seah and Dench 1979) makes the technique extremely sensitive to surface properties, necessitating the maintenance of ultrahigh vacuum (UHV) conditions ($\sim 10^{-11}$ torr), along with scrupulous care in sample preparation. This extreme surface sensitivity further complicates analysis of spectra, as the surface electronic structure may be quite dissimilar to the bulk, and may contribute significantly to the data. Both experimental and theoretical aspects of photoemission spectroscopy have been treated in a number of thorough reviews (Cardona and Ley 1978a,b, Hüfner 1996, Kevan 1992, Smith and Himpsel 1983), to which the interested reader is referred for more extensive discourse. Here our discussion will be limited to a brief overview of the aspects of PES methodology relevant to angle-resolved studies of the high-temperature superconductors.

A simple intuitive understanding of photoemission begins with the three-step model of Spicer and Berglund (Berglund and Spicer 1964) in which emission is broken up into distinct excitation, transport, and detection steps. A schematic illustration of this process is shown in fig. 4. Excitation involves occupation of an excited crystal state by the photoelectron within the bulk of the material via a crystal momentum ($\boldsymbol{k}$) conserving direct transition. This electron is then transported through the surface barrier and propagates to the detector. Within the framework of the independent-electron

approximation the excitation process can be viewed as the transfer of an electron from an occupied to an unoccupied single-particle state. In this picture, the energy distribution of electrons obtained in a photoemission experiment corresponds to the density of occupied states modulated by transition matrix elements from the photoabsorption cross-sections and superimposed on a smooth background arising from inelastic scattering processes. For materials which are well described by an independent-particle picture, and for photon energies sufficiently high that the photoelectron final states are plane-wave-like, this interpretation is sufficient to describe the essential features of the experimental spectra. Unfortunately, while heuristically useful, the three-step model lacks the sophistication to describe details quantitatively. In materials such as the cuprates, in which electron correlations play a crucial role in determining the electronic structure, localized interactions between the photoelectron and the photohole can significantly modify spectra, leading to satellite features which do not appear in band-theoretical calculations. Nevertheless, it is often fruitful to interpret photoemission results as far as possible within the framework of band theory, as unconventional behavior beyond that predicted by mean-field calculations provides crucial clues to the poorly understood aspects of a material's electronic structure.

2.1. *Angle-resolved photoelectron spectroscopy*

An extension of photoemission spectroscopy which has proven particularly powerful as a tool for experimental determination of band structure is angle-resolved photoelectron spectroscopy (ARPES). In an ARPES experiment, the distribution of photoelectrons from a crystalline sample is measured as a function of emission angle relative to the crystal axes (fig. 5). Conservation of crystal momentum, $\boldsymbol{k}$, parallel to the surface combined with energy conservation establishes a correspondence between the angles (θ_e, ϕ_e) and the components of $\boldsymbol{k}_{\|}$. Due to the non-conservation of $\boldsymbol{k}_{\perp}$, in general it is not possible to extract complete information on the $\boldsymbol{k}$-dependence of the bulk electronic structure. For this reason, extraction of band dispersions from three-dimensional materials is complicated, although judicious use of the ability to control photon energy can provide relative k_z information as well. Fortunately, in highly two-dimensional materials such as the cuprates there is very little c-axis (interlayer) dispersion, making the Brillouin zone nearly independent of k_z. In this case the perpendicular momentum component becomes irrelevant and the band structure is completely determined by the parallel components. The technique has been quite successful in measuring band dispersions in many materials including simple metals, semiconductors, transition-metal oxides and chalcogenides (Hüfner 1996, Shen and Dessau 1995, Smith and Himpsel 1983). It has been particularly powerful when used in conjunction with *ab initio* total energy calculations (Callaway and March 1984, Jones and Gunnarsson 1989), and is the only direct experimental means of probing the full band structure of solids.

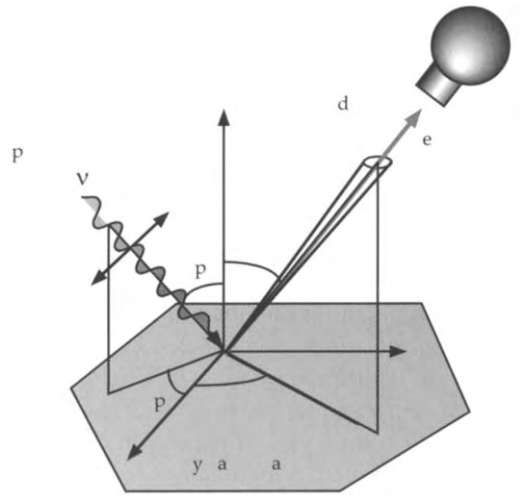

Fig. 5. A schematic illustration of an angle-resolved photoemission experiment. An incident photon, with wavevector $\boldsymbol{p}$ and polarization $\boldsymbol{E}$, strikes the sample with polar incidence angles (θ_p,ϕ_p) relative to the crystal axes. In practice the light source is generally fixed relative to either the crystal or the detector. However, the ability to vary the photon polarization from synchrotron sources provides a powerful tool for obtaining information on the symmetries of electronic states. By moving the analyzer or the sample (depending on the details of the experimental apparatus), photoelectrons leaving the surface at polar angles (θ_e,ϕ_e) are collected by the spectrometer; the component of their crystal momentum, $\boldsymbol{k}$, parallel to the sample surface is strictly conserved, allowing accurate determination of the two-dimensional band structure.

2.2. *Resonance photoemission*

Resonance photoemission (RESPES) is a powerful tool for extracting species specific spectral information in materials with localized orbitals. In the resonance process, two distinct quantum pathways exist for creation of a photoelectron: (i) the direct photoemission process in which a valence electron is directly emitted, and (ii) the Auger channel in which a photoemitted core electron occupies the partially filled valence orbital, followed by a Koster–Kronig Auger decay in which the core hole is occupied and the valence electron photoemitted. Quantum interference between these two channels near the resonance threshold leads to strong cross-section variations for the localized states, allowing their signal to be differentiated from the contributions of other atomic species. For the case of copper, the two processes are:

$$3p^6 3d^9 + h\nu \rightarrow 3p^6 3d^8 + e^-, \tag{i}$$

and

$$3p^6 3d^9 + h\nu \rightarrow 3p^5 3d^{10} \rightarrow 3p^6 3d^8 + e^-. \tag{ii}$$

Clearly, the latter channel is inaccessible until the photon energy is sufficient to create the core excitation, $h\nu \approx E_{3p}$, and will only have an appreciable effect near the absorption

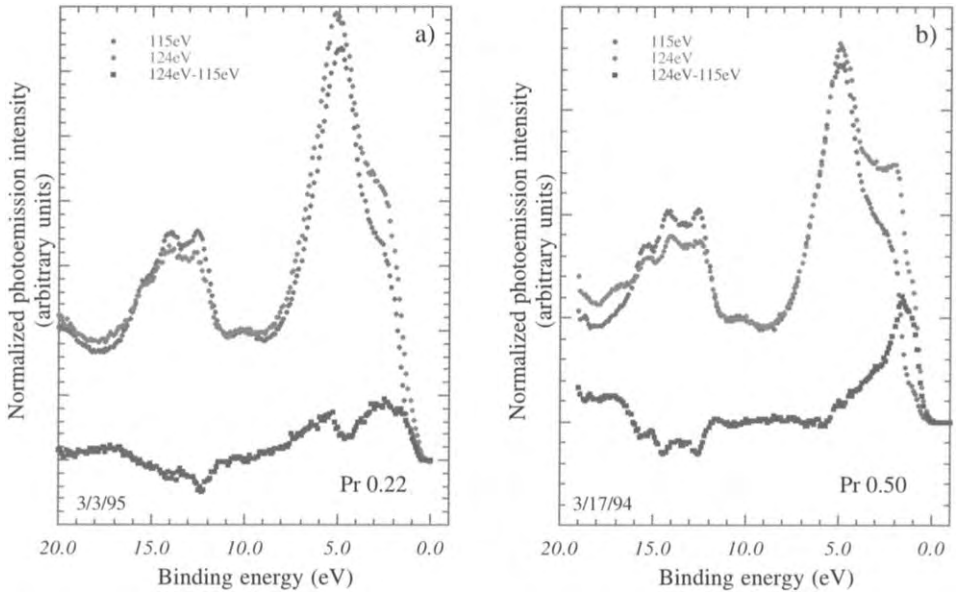

Fig. 6. Photoemission EDCs taken on twinned crystals of $Y_{1-x}Pr_xBa_2Cu_3O_{6.95}$, for $x=0.22$ and 0.50, below ($h\nu=115$ eV) and above ($h\nu=124$ eV) the Pr 4d resonance threshold. The Pr contribution to the density of states is clearly revealed in the near-E_F region of the difference curves, scaling with the doping level; slight antiresonance behavior is seen in the Ba 5p core levels.

resonance (Davis 1982). It is this fact which provides chemical specificity; a resonant enhancement of the emission will occur for photon energies which depend on the element-specific absorption threshold for core hole creation. The ability to separate the contributions of various species to the overall density of states in experimental spectra is of especially great value in studies of materials with many different constituent elements, such as the high-temperature superconductors. An excellent review of the RESPES technique as applied to studies of TMO, rare-earth oxides, and heavy-fermion materials has been given by Allen (1992). Figure 6 shows application of the the RESPES technique to samples of Y123 doped with varying amounts of Pr, which substitutes for Y in the inter-bilayer site and is known to cause dramatic suppression of T_c (Schabel et al. 1995). The clear presence of significant Pr 4f weight near E_F in this material is evidenced by a peak at low binding energy in the difference spectra which scales with Pr doping.

2.3. *Structure of Y123*

Stoichiometric $YBa_2Cu_3O_{7-\delta}$ ($\delta=0$) is a bilayer cuprate which is slightly above optimal hole doping, with a superconducting transition temperature a few degrees below the maximum value of 94 K found for $\delta=0.05$. Its crystal structure (fig. 7) has, in common with all other HTS, planar CuO_2 layers, with each bilayer separated by an atom of Y (or other rare-earth element). Unique to Y123, the interlayers are formed from quasi-one-

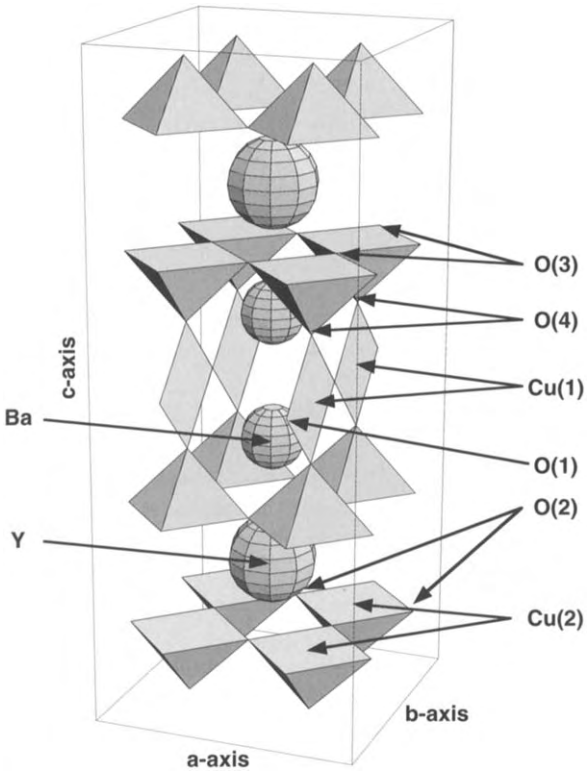

Fig. 7. The crystal structure of Y123, showing the pyramidal units formed by the planar Cu(2) atoms, each surrounded by four planar O(2) and O(3) atoms and one out-of-plane apical O(4). The large spheres represent the interbilayer Y atoms, and the smaller spheres the Ba atoms which fourfold coordinate with the apical oxygen. The chains running parallel to the *b*-axis, with each Cu(1) twofold coordinated to chain O(1) and twofold coordinated to apical O(4), are shown as vertically oriented plaquettes.

dimensional CuO_3 chains (stabilized by Ba) which run parallel to the *b*-axis, inducing significant orthorhombicity, as well as complicating interpretation of physical properties. Under normal growth conditions, crystals of Y123 have mixed domains with alternating orientation axes for the quasi-1D chains; such crystals are normally referred to as twinned. These twinned samples may be oriented to form untwinned crystals by an annealing procedure in which the crystals are simultaneously heated and subjected to uniaxial stress under a controlled oxygen atmosphere. This process can, in the best samples, produce almost perfectly oriented crystals with a single uniform domain. The close chemical and structural resemblance of the interlayers and planes also hinders spectroscopic studies. In the notation of the figure, there are two inequivalent copper atoms: chain Cu(1), and plane Cu(2). Of the four inequivalent oxygen sites, O(1) is referred to as the chain oxygen, O(2) and O(3) are plane oxygens, and O(4) is the apical oxygen. Structural studies of Y123 also reveal a clear buckling, or dimpling, of the CuO_2 bilayers, with the O(2) and O(3) atoms displaced out of the plane by Cu(2) toward the intercalated Y atom (Andersen et al. 1991, 1994, Pickett 1989), as well as static or extremely soft bending modes for the chain oxygens (Pickett 1995, Schleger et al. 1994, 1995, Sharma et al. 1996).

As mentioned above, Y123 in stoichiometric form is nearly optimally doped, with maximal T_c attained by slightly reducing the crystals to decrease their oxygen content. It is well known that the reduction process leads exclusively to loss of the chain O(1) atoms, leaving the structure of the CuO_2 planes unaltered while simultaneously introducing defects to the CuO_3 chains. For $\delta \approx 0.4$ there is structural evidence for an ordering transition to the Ortho-II phase, in which O(1) vacancies preferentially order in alternating chains, leaving neighboring chains intact. This transition, closely coinciding with the observed orthorhombic to tetragonal structural phase transition found near $O_{6.6}$, may also be responsible for the plateau found near this doping level in the T_c vs. δ curves. Further deoxygenation introduces defects in all chains, and the material ultimately becomes a tetragonal charge-transfer insulator, $YBa_2Cu_3O_6$, in which CuO_2 dumbbells replace the chains.

Y123 can also be doped with a wide variety of impurities, including Zn and Ni which substitute for Cu(2) and suppress T_c dramatically, Co which replaces Cu(1), and Ca or various rare earths for Y. The possibility to precisely manipulate the chemical composition and impurities in this material is unique among the cuprates, and is one of the principal reasons Y123 is an attractive system for scientific investigations. Substitution of the inter-bilayer Y in Y123 with various other rare-earth elements is found, in most cases, to have essentially no noticeable effect on the superconducting transition or properties. Crystals of the form $RBa_2Cu_3O_{7-\delta}$ (R123) are isostructural with Y123, having virtually identical lattice parameters, superconducting transition temperature, and physical properties. Among the fourteen rare earth elements, there are two notable exceptions to this rule: Ce and Pr.[1] Of these, the former does not crystallize in the Y123 structure, phase-separating into simpler constituent compounds instead. Surprisingly, Pr123 is isostructural but manifests completely different physical properties. Optimally doped Y123 is metallic, with a transition to the superconducting state at 94 K, and manifests antiferromagnetic alignment of Y moments at extremely low temperatures (~1 K), while the Pr material is an insulator which exhibits no tendency to superconduct, with Pr moments aligning at 17 K. Experimental results have been reviewed in a thorough article by Radousky (1992).

Doping of Y123 with various amounts of Pr to form $Y_{1-x}Pr_xBa_2Cu_3O_{7-\delta}$ (YPr123) results in a rapid suppression of T_c with x, reaching 0 K at $x = 0.55$. The absence of any significant tailing in magnetization measurements and the narrowness of the superconducting transition in resistivity measurements demonstrates that the Pr atoms are homogeneously distributed rather than phase segregated into regions of high and low Pr concentration. This observation supports a continuous microscopic mechanism of superconductivity suppression, which is of obvious importance as a clue to understanding the pairing mechanism in the cuprates, as it must depend on specific details of the electronic structure and chemistry of Pr. Early arguments centered on the simple possibility that Pr, substituting for Y^{3+}, takes on the Pr^{4+} oxidation state, thereby forcing

[1] The Tb compound is difficult to synthesize in crystalline form, but thin films have been grown successfully. Pm, which is unstable and radioactive, has not been studied.

the material into a highly underdoped insulating state (Liang et al. 1987, Okai et al. 1988, Soderholm et al. 1987). Numerous spectroscopic techniques, particularly X-ray absorption spectroscopy (XAS), electron energy loss spectroscopy (EELS), and PES, which are capable of directly comparing measured spectra with those from reference samples of known oxidation state, have ruled out this mechanism, clearly demonstrating that the Pr remains in the 3+ state (Soderholm and Goodman 1989). Other theoretical arguments include magnetic pair breaking (Guo and Temmerman 1990), changes in the relative chemical potential of the holes in the CuO_3 chains and CuO_2 planes (Khomskii 1993), and hybridization of the low-lying Pr 4f states with the O 2p orbitals on the cuprate planes, thereby localizing the normally mobile ligand holes (Fehrenbacher and Rice 1993, Liechtenstein and Mazin 1995). To date, none of these proposals have compellingly explained the behavior in this material, and the problem appears to remain an open one. Recent experimental work has also demonstrated superconductivity in these materials under growth conditions in which the *c*-axis lattice constant is reduced from its bulk value. It seems certain that a detailed understanding of this phenomenon will provide significant insight into the mechanism of superconductivity in cuprates.

2.4. *Surface termination of Y123*

The low-temperature STM studies of Edwards et al. (1992, 1994) clearly resolve regions of chains interspersed with indistinct stepped regions whose height is consistent with that expected for BaO planes. These results provide strong evidence for a mixed CuO_3/BaO surface termination in cleaved Y123 crystals. Photoemission corroborates this, revealing a strong Ba 5p surface-shifted component, shown in fig. 8, which is indicative of inequivalent bulk and surface Ba coordinations as would arise from a near-surface BaO layer (Halbritter et al. 1988). Resolving a similar shift in the chain Cu(1) levels is unfortunately complicated by the presence of two structurally inequivalent Cu atoms in the bulk unit cell, in addition to two possible inequivalent surface sites and the presence of satellite structures in the Cu core levels.

It is well known from studies of the electron attenuation length in photoemission experiments that the mean free path of unscattered photoelectrons at the photon energies used in ARPES experiments is extremely short, on the order of 5 Å (Seah and Dench 1979). This fact, and the relatively large *c*-axis lattice constant of Y123 (11.7 Å), combine to make the surface contribution in our spectra a substantial fraction of the total signal. A simple layer model allows us to quantitatively estimate the contribution of the surface and subsurface Ba atoms to the total photoemission intensity (Schabel et al. 1998b). We assume a mixed termination of BaO and CuO_3 with equal areas for both terminating surfaces, shown schematically in the inset of fig. 8, make the approximation that the various atomic planes are equally spaced, and regard all subsurface Ba atoms as equivalent to those in the bulk material. In this case, the Ba surface component comes entirely from the BaO surface, giving a surface to bulk ratio for the Ba core levels of 82%, in good qualitative agreement with the nearly equal contributions of the surface (high binding energy) and subsurface (low binding energy) features seen in fig. 8, as well as with the

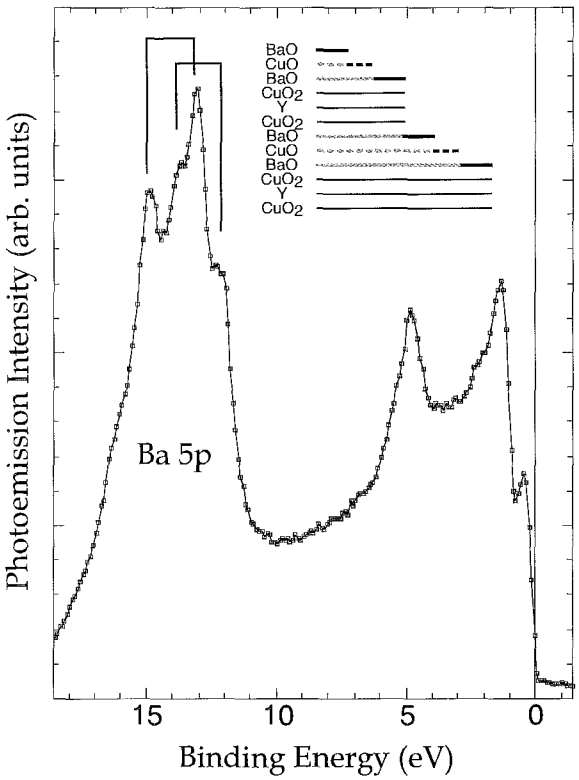

Fig. 8. The full valence band of YBCO, showing distinct bulk and surface shifted Ba 5p core levels. While there can be substantial sample to sample variation in the precise magnitude of the surface core-level shift, it can be clearly seen in nearly all spectra, indicating the presence of significant regions of BaO surface termination. The inset shows a schematic of the surface termination of cleaved Y123, with stepped terraces of BaO and CuO_3 chains, based on ARPES data and low-temperature STM results.

results of studies of the Ba 4d core levels reported by Veal and Gu (1994). A similar analysis may be performed for the Cu valence state intensities, allowing estimation of the contribution of "bulk" (subsurface) chain states relative to the surface chain states and bulk plane states. On the general grounds discussed above, we expect the surface contribution to the chain states to dominate the bulk chain emission. Assuming that the intrinsic emission from all states is equal (i.e., ignoring matrix element effects), and modifying the model used above for the Cu states leads to contributions of 59%, 32%, and 9% for the bulk planes, surface chains, and bulk chains, respectively. Even allowing for an escape depth twice as large (i.e. 10 Å) only changes the relative contributions of plane, surface, and chain to 64%, 18%, and 18%. Based on these estimates, it is likely that the bulk chain features of the electronic structure only make a small contribution to the measured photoemission spectra.

3. Photoemission studies of the cuprates

Progress in growth of high-quality single crystals of various high-T_c superconductors, particularly Y123 and Bi2212, was a development crucial to the success of ARPES

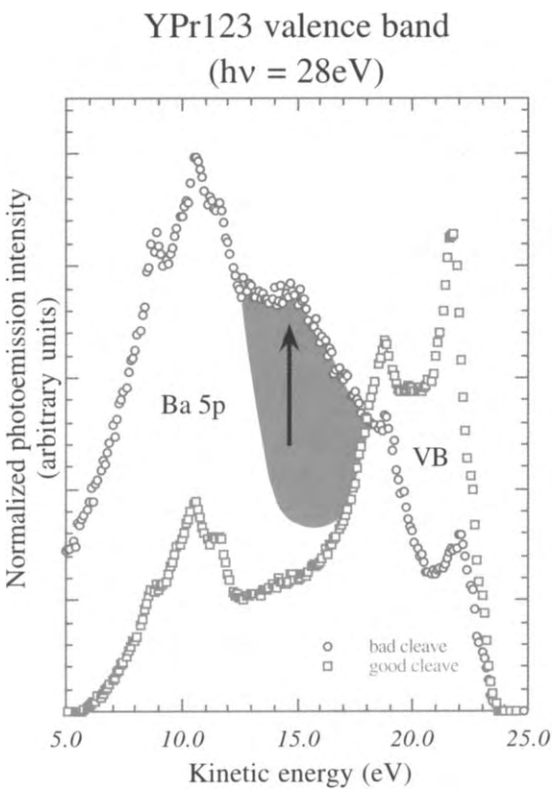

Fig. 9. Valence band spectra from two twinned $Y_{0.50}Pr_{0.50}Ba_2Cu_3O_{6.95}$ single crystals. The bad cleave has the characteristic contaminant peak at 9.5 eV binding energy filling in the region between the valence band and the Ba 5p core levels, while the good cleave shows little weight in that energy region, as well as marked enhancement of the valence-band intensity relative to the Ba cores.

studies of these materials (Lin et al. 1992, Mitzi et al. 1990). Early work on low-quality polycrystalline samples, which suffered from indeterminate surface structure, contamination, and high defect and impurity densities, routinely failed to manifest any Fermi edge structure at all, even when transport measurements indicated clear metallic character. The principal hallmark of low-quality or contaminated sample surfaces for the cuprates is the appearance of a large, indistinct feature near 9.5 eV binding energy in the photoemission data, an example of which is shown in fig. 9, while the presence of weight in a coherent dispersive peak near E_F is indicative of a good cleave. Another critical development was dramatic improvement in the spectrometer energy resolution, from typical values of 200 meV commonly considered adequate in semiconductor surface physics to values of 20 meV or less achievable today. Because superconductivity is a phenomenon whose energy scale is defined by some small constant times $k_B T_c$, resolution comparable to or smaller than this characteristic value is essential for direct observation of modifications in the near-E_F spectral weight associated with the onset of superconductivity.

Of the various cuprate materials, Bi2212 is by far the most extensively studied, owing to the availability of large, high-quality single crystal samples, the ease with which it

cleaves, and the existence of a reproducible unreconstructed surface uniformly terminated by comparatively inert BiO planes. Also, as the first high-temperature superconductor in which a superconducting gap was consistently observed by photoemission, an immense amount of work has been devoted to this aspect of the electronic structure. Details relevant to photoemission studies of optimally doped Bi2212 in both the normal and superconducting states have been discussed extensively in reviews by Shen and Dessau (1995) and Loeser et al. (1994). Significant efforts to investigate the electronic structure of Y123 have also been made, although the lack of a natural charge-neutral cleavage plane poses difficulties. Unlike Bi2212, all possible cleavage planes result in a mixed termination of two inequivalent surfaces. In addition, it appears that oxygen loss or disorder leads to formation of an insulating surface, even for optimally doped crystals, unless samples are cleaved and maintained at temperatures below 50 K (List et al. 1988). Unfortunately, this precludes cycling of temperature through the superconducting transition, making identification of superconductivity-related modifications of the spectral weight even more difficult.

Much of the experimental methodology and relevant results from photoemission studies of twinned Y123 have been discussed in a thorough review by Veal and Gu (1994). Here we focus primarily on untwinned crystals and the low binding energy region within 1 eV of E_F; details of the valence-band electronic structure, including the peak appearing at 1 eV binding energy, do not appear to have the same strong dependence on the *a*/*b*-axis asymmetry (Tobin et al. 1992). In the untwinned samples, orientation of the fourfold axis of samples is performed *ex situ* by Laue diffraction. Due to growth asymmetry, the chain axis may be determined visually as the long axis of the crystal; the accuracy of visual orientation is verified with X-ray diffraction. Typical studies are performed on crystals of extremely high quality (typical transition widths of 0.25 K), cleaved and maintained in UHV with a chamber base pressure less than 5×10^{-11} torr at a constant temperature of 20 K to avoid surface degradation (Edwards et al. 1992, List et al. 1988). Spectra are normally acquired at an energy resolution of 50 meV or better, with an angular acceptance of $\pm1°$.

3.1. *Normal-state electronic structure*

At the coarsest level, the poor state of overall understanding which applies to transition-metal oxides in general also plagues the high-temperature superconductors. In this sense, the crucial problem which faces scientists studying the cuprates is the normal-state electronic structure of these materials and how it relates to and deviates from conventional Fermi liquid theory. As a collective property which appears at low energy scales for relatively well-understood reasons, pairing superconductivity should emerge naturally as a low-temperature collective phenomenon once the ground-state properties have been clarified. Conversely, it may not be comprehensible without a thorough understanding of the anomalous normal state from which it arises. In addition to studies of the HTS in the temperature regime above their superconducting transition, there have been recent, fruitful efforts to study prototypical model compounds such as the insulating cuprate

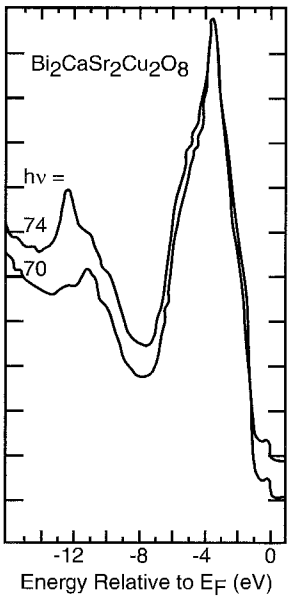

Fig. 10. Valence band spectra from Bi2212 single crystals above and below the Cu 2p resonance. An anomalous enhancement of spectral weight lying between 9 and 13 eV binding energy is a satellite feature due to many-body effects.

$Sr_2CuO_2Cl_2$ (Wells et al. 1995) and the quasi-1D cuprate Sr_2CuO_3 (Kim et al. 1996). These studies may help to elucidate the fundamental properties of the insulating ground state out of which cuprate superconductors are formed, and give further insight into the relevant low-energy degrees of freedom for theoretical models. Much current interest, both experimental and theoretical, is centered on the difficult topic of the transition from insulating parent compound to superconducting metal, as well as on the effects of reduced dimensionality in strongly correlated chain and ladder compounds (Dagotto and Rice 1996, Emery and Kivelson 1993, 1995, Rice et al. 1994a,b).

One indicator of strong electron correlations in solid-state systems is the presence of high-binding-energy satellite lines corresponding to localized excitations. The observation of such features in photoemission spectra of the cuprates provides strong evidence supporting the contention that Coulomb interactions play a critical role in determining the electronic structure of the CuO_2 planes which give rise to superconductivity. Satellites cannot be explained by conventional band theory because they arise from local excitations rather than itinerant electron states, but are evident in cluster calculations which explicitly include correlation effects (Tjeng et al. 1991, Zaanen et al. 1985). Photoemission experiments by Shen et al. (1989) find clear evidence of a high-energy satellite feature associated with the Cu 3d orbitals in Bi2212, with the spectral weight lying between 9 and 13 eV binding energy, as shown in fig. 10, anteceding similar measurements by Fujimori et al. and others on Y123 and La_2CuO_4 (Arko et al. 1989, Fujimori et al. 1987, List et al. 1989). Perhaps the most interesting characteristic of the metallic cuprates is the coexistence of these Cu satellites with low-energy quasiparticle states. This behavior correlates with their transitional nature, lying between conventional Fermi liquids and the

charge-transfer insulators from which they are derived, and lies at the heart of current debate over the appropriate theoretical framework for their description.

Current debate over the nature of the quasiparticle states in the cuprates and the pairing mechanism in the superconducting state has emphasized the uncertain applicability of conventional Fermi-liquid theory and focussed attention on unresolved questions in ARPES studies of materials considered to manifest normal Fermi-liquid properties. In particular, work by Claessen et al. (1992, 1996, 1997) has demonstrated that, in the layered chalcogenide $TiTe_2$, the ARPES lineshapes may be consistently and quantitatively fit with a model based on a Fermi-liquid-like self-energy. In marked contrast, very little progress has been made in the fitting of lineshapes in the high-T_c materials despite repeated attempts (Campuzano et al. 1991, Liu et al. 1991, Olson et al. 1990a). The universally observed presence of a significant fraction of the total spectral weight at low energies in apparently incoherent structure continues to be an enigmatic clue to the nature of their low-energy excitations.

The vast majority of recent photoemission experiments on the cuprates have focussed on the narrow, dispersive features found near the Fermi level, first observed by Arko et al. (1989). These states arise in a small foot in the lowest 1 eV below E_F, and grow more prominent as the doping level approaches the optimal value. Careful measurement of the amplitude and peak position of these quasiparticle features allows reconstruction of the band structure and the two-dimensional Fermi surface topology, and can reveal the presence and magnitude of a superconducting gap. Transport, optical, and electrical properties in the cuprate superconductors all manifest anomalous behavior; these also must be closely linked to the spectrum of low-energy excitations, since the relevant states lie within a few $k_B T$ of E_F.

In Y123 and Y124 an extended van Hove-like singularity (EVHS) is associated with an extremely narrow, resolution-limited peak ($\Delta \leqslant 10$ meV) along the $\Gamma X/\Gamma Y$ direction in twinned samples. This band appears approximately 250 meV below E_F at Γ, dispersing to within 10 meV (Y123) or 19 meV (Y124) of the Fermi level at approximately the midpoint between Γ and X/Y where it remains out to the Brillouin zone boundary. Along the zone boundary from X/Y to S a band is observed to disperse rapidly upward away from E_F which combines with the flat band to form the EVHS saddle point. A second singularity is also observed, but it lies significantly deeper in the valence band, with a binding energy of 115 meV, where it should not have any dramatic effects on the DOS. It should also be noted that the EVHS persists even in oxygen-deficient samples ($\delta = 0.5$) with substantially depressed T_c's and significantly different physical properties (Liu et al. 1992a,b).

The near-E_F singularity is one of the most intriguing features of the electronic structure of Y123. This peak appears to be essentially non-dispersive parallel to the $\Gamma X/\Gamma Y$ direction and strongly dispersive along XS/YS, forming the EVHS. It also manifests unusually strong photon energy dependence, being seen most strongly at $h\nu = 17$ and 28 eV, and also at 50 and 74 eV (Gu et al. 1993). In their early study of an untwinned single crystal of Y123, Tobin et al. (1992) observed this feature only near the Y point, and concluded that it was correlated with the CuO_3 chains. A similar conclusion was drawn for Y124 crystals by Campuzano et al. (1992), based on the relationship between

X/Y asymmetry and the uniformity of the cleaved sample surface, and for Y123 based on the results of oxygen doping dependence (Gu et al. 1993). However, observation of the peak along ΓY placed the non-dispersive direction parallel to the chain axis, rather than perpendicular as would be expected for quasi-1D states. This counterintuitive result is also inconsistent with both local density approximation (LDA) predictions of a chain-derived Fermi sheet parallel to the ΓX axis and the chain Fermi surface determined from positron-annihilation studies of untwinned crystals (Shukla et al. 1995). Subsequent photoemission work interpreted the EVHS as a CuO_2-plane-derived feature arising from the chain-induced orthorhombic distortion, and implicated the resulting singularity in the density of states as a possible origin for the high transition temperature (Abrikosov et al. 1993, Gofron et al. 1993, 1994). Much of this work was driven by the observation of an extended flat band near the Fermi energy in ARPES studies of Bi2212, even though that feature derives from a much broader band in the normal state and exhibits clear and dramatic modification in lineshape on passing into the superconducting state.

More recent results, obtained on untwinned Y123 crystals of exceptional quality, lead to a different picture of the electronic structure in Y123 and Y124, more consistent with earlier work on twinned crystals, and reveal numerous previously unobserved features (Schabel et al. 1997, 1998b). These data indicate that the near-E_F electronic structure along the *b*-axis is strongly masked by the presence of a narrow and intense surface resonance, or surface chain feature (SCF), arising primarily from the quasi-1D CuO_3 chains, making untwinned single crystals essential to have any hope of resolving a superconducting gap. In addition, varying the sample orientation with respect to the photon polarization is crucial for a complete understanding of the electronic structure of Y123.

3.2. *Surface chain feature*

The presence of a feature at the Y point, absent at X, does not of itself imply chain parentage (due to the orthorhombic distortion of the underlying lattice), but the extremity of the asymmetry and apparently one-dimensional behavior are difficult to reconcile with the 2D planar structure of the CuO_2 sheets. Also difficult to understand, assuming that the orthorhombic distortion is responsible for the asymmetry, is the nondispersive nature of the SCF with photon energy. A number of additional arguments, delineated below, provide strong support for the contention that the SCF is indeed derived from the CuO_3 chains.

Figure 11 shows ARPES EDCs taken at the X and Y points, with $h\nu = 28$ eV, for the three distinct polarization geometries; panel (a) corresponding to $\boldsymbol{E} \parallel b$, panel (b) to $\boldsymbol{E} \perp b$, and panel (c) to $\boldsymbol{E} \parallel \Gamma S$ (O_2, O_4, and O_1, respectively). It is important to recognize that, while the absolute value of the intensity axis is not significant, the relative amplitudes between spectra are, as they are scaled to the integrated valence-band emission, and may be compared quantitatively. To the extent that the chains are truly one-dimensional, photoemission spectra taken with photon polarization parallel to the *b*-axis should maximize their contribution to the signal, those with perpendicular polarization should be essentially free of chain signal, and those with intermediate polarization should

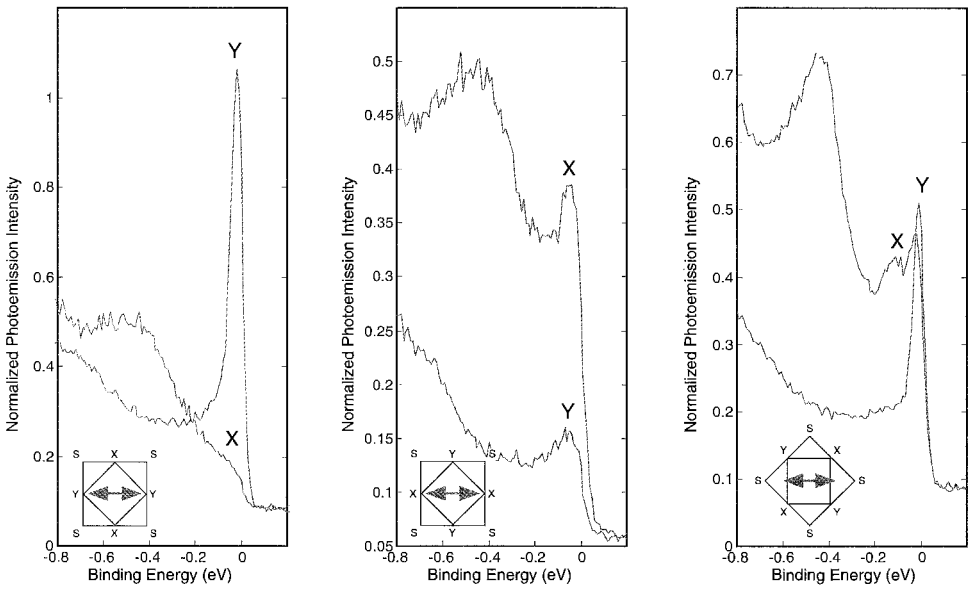

Fig. 11. Photoemission EDCs taken near the Fermi energy at the X and Y points of a single-crystal sample, for photon polarization (a) $\boldsymbol{E} \parallel b$, (b) $\boldsymbol{E} \perp b$, and (c) $\boldsymbol{E} \parallel \Gamma S$.

mix the two. Contrasting with this, the predominantly $d_{x^2-y^2}$ Cu 3d states hybridized with O 2p states to form the plane bands constituting the near-E_F structure should be comparatively unaffected by the 90° rotation, other than experiencing slight asymmetry due to the orthorhombic structure and the normal selection-rule effects for electron emission.

Examination of the spectra at Y dramatically demonstrates the dependence of the SCF on sample orientation; the spectrum with $\boldsymbol{E} \parallel \Gamma Y$ shows enormous enhancement, while the perpendicular geometry reveals nearly complete suppression, and the 45° spectrum shows almost exactly half the intensity of that in O_2, as expected from geometrical arguments. Furthermore, in addition to its factor-of-eight diminution in intensity, the small residual peak seen at Y in O_4 is qualitatively unlike the SCF, being much broader and lying at measurably higher binding energy, and presumably originates in the planes. This quasiparticle behaves in a manner qualitatively similar to that seen in Bi2212. A third feature of the electronic structure, which appears weakly as an extremely broad peak at a binding energy of 650 meV, is essentially unaffected by the polarization component parallel to the chains so it must also derive from the underlying CuO_2 plane states. Also important is the comparatively weak dependence of the overall intensity away from E_F on geometry, all three EDCs at Y lying between 0.25 and 0.45 at the high binding energy limit.

In fig. 12 we plot the difference between normalized spectra at the Y point in the geometry in which polarization is parallel to the chains and that in which it is

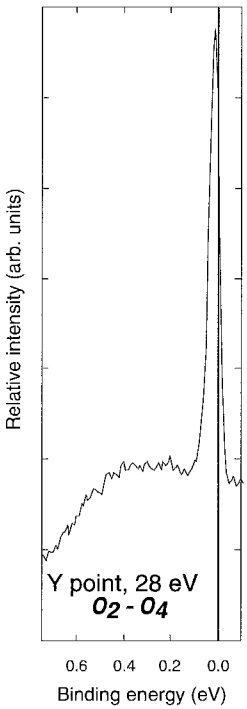

Fig. 12. Normalized difference between spectra taken near the Fermi energy at the Y point for photon polarization parallel to and perpendicular to the CuO_3 chains.

perpendicular to them. What is observed strikingly confirms the arguments above; the only significant difference between the two in the 0.5 eV below the Fermi energy is in the narrow peak lying at a binding energy of 13 meV, as reported in previous studies of the EVHS in Y123, and with a width which is almost entirely comprised of the instrument contribution. It is important to note that the two spectra were taken on the same sample, the only difference between them being the photon polarization relative to the chains. The extreme narrowness of this feature is in stark contrast with the other dispersive bands seen on the same sample, all of which are broader by a factor of 10 to 20. By this coexistence of both very narrow and very broad features in the photoemission spectra from one sample we are able to infer that the broad peaks are intrinsic in origin, and do not stem from poor sample quality or energy resolution.

Turning to the spectra at X, we immediately note the absence of any features in the near-E_F weight of comparable intensity to the SCF in any polarization orientation. As for the Y point, the high-binding-energy intensities are only weakly dependent on geometry, although the matrix elements at X appear to lead to overall enhancement for emission from this region of $\boldsymbol{k}$-space. Also as seen at Y, a broad higher-binding-energy feature (around 400 meV) with little dependence on the chain component of $\boldsymbol{E}$ is found. It is important to also consider the (likely) scenario of residual twinning of the crystals at the few percent level, as the detwinning procedure is never entirely perfect. In the case of a lightly twinned crystal, the intense feature near Y will be

mirrored at X, albeit with its intensity significantly reduced. Nevertheless, because this structure is so intense in the parallel polarization geometry, even a few percent can cause a significant and spurious addition of spectral weight in the energy region immediately below E_F.

The absence in Bi2212 of a feature comparable in width and anisotropy to the SCF provides an additional clue; the extended flat band in the Bi compound exhibits substantially greater dispersion, is observed symmetrically along both of the cubic axes, and is much broader than the SCF in Y123 (Dessau et al. 1993). Conversely, a similar SCF feature, with even greater intensity, is found in Y123's sister compound, Y124 (Gofron et al. 1993); the peculiarity of the SCF to compounds possessing CuO_3 chains is itself highly suggestive. Comparisons of the relative peak to background ratio, R_p (defined as the ratio of the peak height at Y to the incoherent spectral weight 0.2 eV below E_F), from various twinned and untwinned samples of Y123 and Y124 show that R_p in untwinned Y123 is roughly twice that of twinned samples, with untwinned Y124 twice again as large. This variation is easily explained by two facts. First, in a twinned sample the intensity from the Y point will be evenly distributed between X and Y. Second, as previously discussed, the principal structural distinction of the Y124 material is that it contains twice as many chains per unit cell and is naturally (partially) untwinned (Campuzano et al. 1992); it is expected that the cleaved surface should have a similarly disproportionate number of exposed chains, leading to an enhancement factor of two in samples with uniform cleavage planes. The specific ratio will, of course, depend on the sample and is expected to exhibit cleave-to-cleave variation due to differences in the BaO/CuO_3 distribution at the interface.

Finally, Pr doping, which substitutes Pr for the interplane Y atom, has the unique property among the substitutional rare earths of strongly suppressing the superconductivity of $Y_{1-x}Pr_x123$, inducing a metal–insulator transition at a Pr concentration of $x \approx 0.55$. Because the Pr atom lies between the CuO_2 planes and is quite isolated from the chains, it would be expected to have a comparatively large effect on plane-derived states and to only weakly affect chain features. In studies of twinned crystals of YPr123 (Schabel et al. 1995) it has been observed that the most dramatic changes in the electronic structure at low doping are indeed observed along the ΓS line, the main feature of which derives predominantly from plane states and is unaffected by the twinning. In contrast, the SCF is clearly present, even for $x = 0.22$, where T_c has been suppressed to 60 K. Our results strongly mimic changes observed in the near-E_F features of oxygen-deficient samples, indicating that Pr alters the relative charge balance between chains and planes, but does not affect the presence of the SCF at moderate doping levels.

Taken together, this evidence provides a consistent and compelling case for association of the SCF with a surface chain state which is uncharacteristic of the bulk electronic structure of Y123, and which, by virtue of its intensity and proximity to the Fermi energy, strongly masks the presence of any underlying states or gaps in the $\boldsymbol{k}$-space region near the Y point. Furthermore, except under the most favorable conditions and with almost perfectly detwinned samples, highly intense echoes of the SCF will appear near E_F at the X point as well, contaminating data from this region as well.

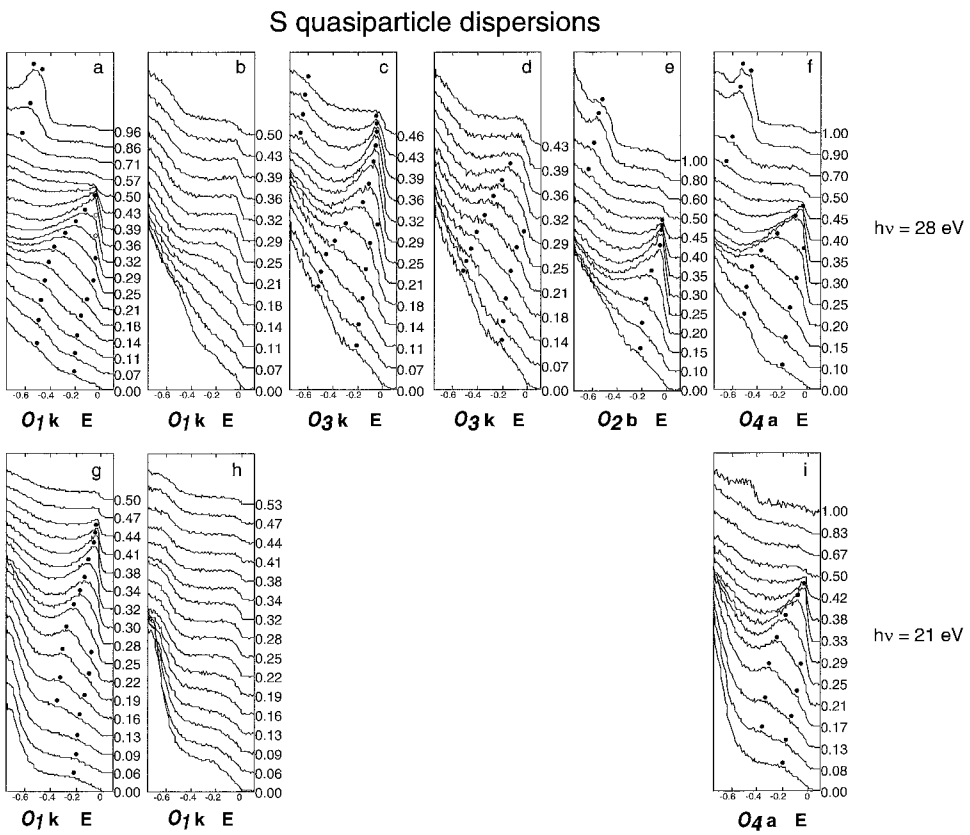

Fig. 13. Energy distribution curves along the ΓS symmetry line. Identifiable quasiparticle peaks are indicated by circles, with the k value of each EDC given as a fraction of the total distance between high symmetry points.

3.3. *Band structure*

Band dispersions along high-symmetry directions in the Brillouin zone have been presented in a number of studies of Y123, but these have been tainted by the mixing of inequivalent octants of the zone from twinning. Recent work on untwinned crystals has established a complete set of data for the high-symmetry directions ΓS, ΓX, ΓY, XS, and YS, in a number of polarization orientations with a photon energy of 28 eV, along with somewhat less complete data at 21 eV (Schabel et al. 1997, 1998b). Representative dispersion curves for ΓS, ΓX and ΓY are shown in figs. 13–15. In each set of energy distribution curves identifiable quasiparticle peaks are marked with a circle. Despite the intrinsic breadth of these features (comparable to the dispersive plane bands seen in photoemission data on Bi2212), statistics are sufficiently good to allow accurate identification of the centroid in most cases.

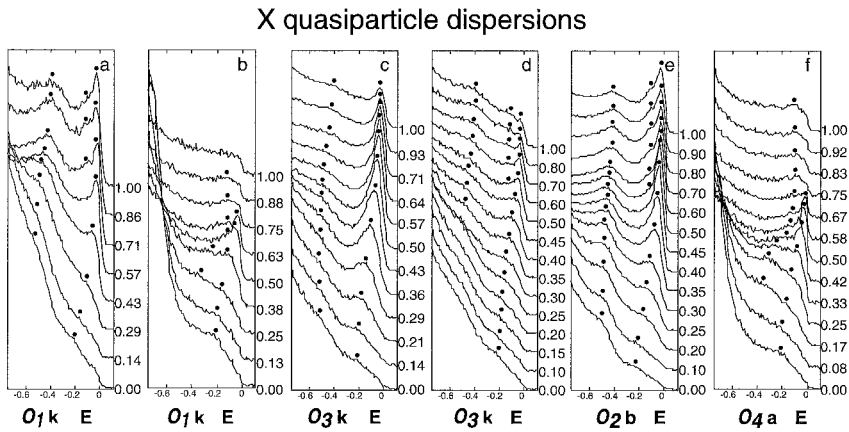

Fig. 14. Energy distribution curves along the ΓX symmetry line.

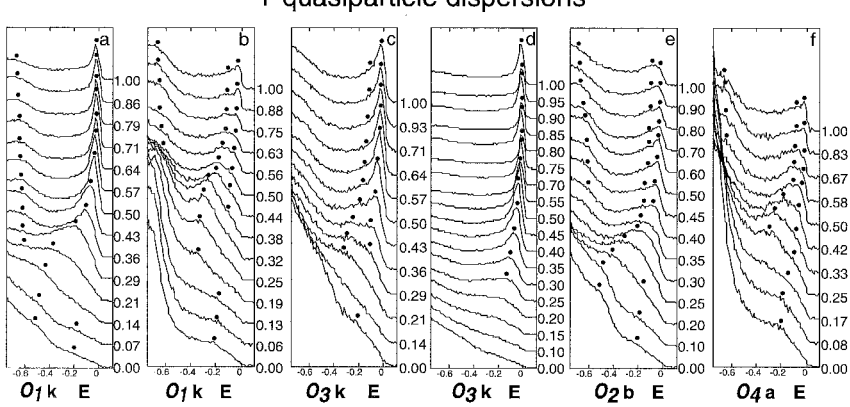

Fig. 15. Energy distribution curves along the ΓY symmetry line.

An overall picture of the quasiparticle dispersions along ΓS is shown in fig. 16, with the energies of features identified in the various panels of fig. 13 plotted against normalized fraction of the ΓS distance. There are several key observations to be made from fig. 16. First, the two clearly resolved quasiparticle features of plane origin are most sensibly attributed to the bonding and antibonding plane states of the CuO_2 bilayers. The lower-binding-energy feature (the antibonding σ^* state) dispersing from 0.22 eV at Γ to a crossing at near 25% of ΓS shows essentially no dispersion in k_z, with the data points from $h\nu = 21$ eV and 28 eV lying on the same curve. In contrast, the higher-energy feature (bonding σ state) found at 0.53 eV at Γ for $h\nu = 28$ eV and crossing the Fermi surface around 35% of ΓS, reveals significantly different dispersion at $h\nu = 21$ eV, with the maximum binding energy at Γ decreasing to approximately 0.42 eV, but with a nearly

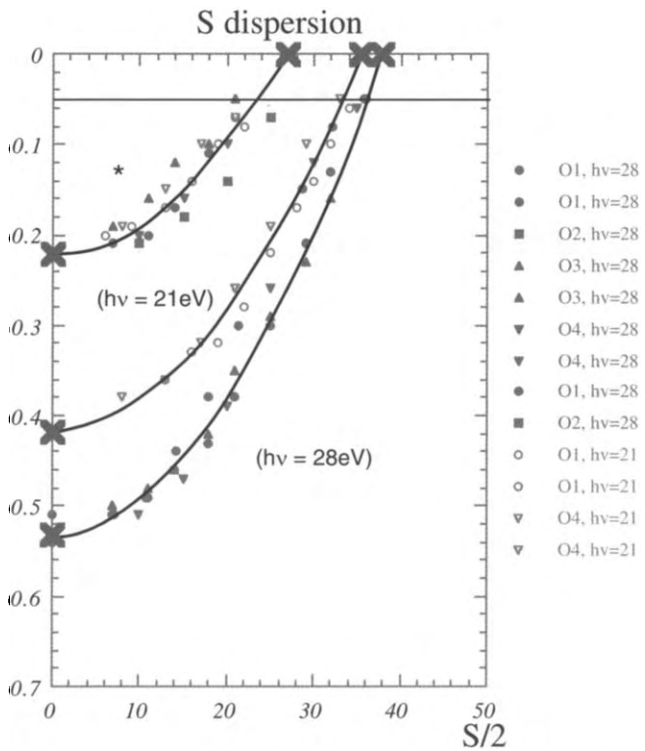

Fig. 16. Energy dispersion of quasiparticles along the ΓS symmetry line. Solid symbols indicate data points taken for $h\nu = 28$ eV, while open symbols correspond to $h\nu = 21$ eV. Band minima are indicated by crosses along the vertical axis, while the corresponding Fermi surface crossings are marked with crosses on the horizontal axis. The thick solid lines are smooth interpolations through the data as guides to the eye, while the thin horizontal line indicates the instrument resolution.

identical Fermi surface crossing position. By taking data along identical lines in (k_x, k_y) at different photon energies we sample different values of k_z. Thus, the observed energy dispersion of the plane bonding band with $h\nu$ is most simply interpreted as a hallmark of c-axis (k_z) dispersion of this state. Also significant is the degeneracy of the Fermi surface crossings for the two photon energies, implying that the c-axis dispersion which is large at high binding energies becomes vanishingly small at the Fermi energy. This result is consistent with LDA calculations which predict bilayer splitting of the bonding and antibonding plane states in Y123, although our observed magnitude of 0.2 to 0.3 eV (depending on k_z) is approximately one half the value expected from the *ab initio* results.

The E vs. $\boldsymbol{k}$ dispersion relations measured along the ΓX high-symmetry line are plotted in fig. 17. At high binding energy we see a weakly dispersive feature rising from 0.53 eV at Γ to 0.43 eV at X. While, based solely on its dispersion, it could be argued that this feature has chain-like behavior, it is clear from its polarization dependence that this

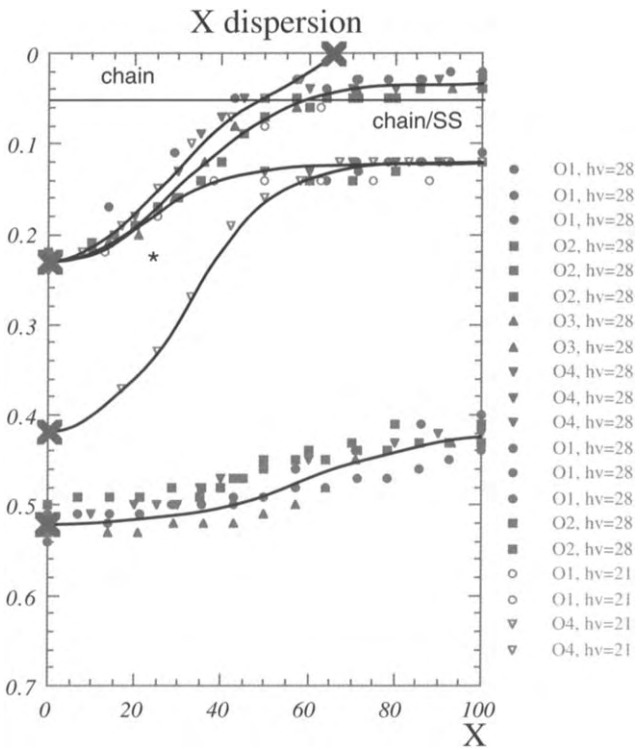

Fig. 17. Energy dispersion of quasiparticles along the ΓX symmetry line.

is not plausible, making the most sensible attribution that of the bonding σ state of the cuprate plane bilayer. These bonding (σ) plane bands are expected to be essentially non-dispersive parallel to both ΓX and ΓY based on LDA calculations of the band structure, further supporting attribution of this structure to the planes. The quasiparticle originating at lower binding energy at Γ disperses upward toward the Fermi energy, showing a tendency to flatten out just below E_F in the 28 eV data, but exhibiting a clear crossing in the vicinity of the 60% point for $h\nu = 21$ eV. From the discussion above, this behavior is consistent with a hybrid band arising from mixing of the antibonding plane and chain states. In the ***k***-space region near X, the weakly dispersing shoulder, at an energy of 0.13 eV, forms a van Hove singularity qualitatively similar to that seen in Bi2212. The data taken with 21 eV photons also show significant dispersion of the higher-binding-energy band, suggesting a band of mixed bonding and antibonding character.

Dispersion relations for ΓY are plotted in fig. 18. While the presence of the surface feature complicates the data somewhat, presented in this way there is actually quite a large degree of consistency with the data along ΓX. The bonding σ band appears at around 0.53 eV at Γ and disperses weakly downward to 0.67 eV at Y. A second band disperses upward to merge with the pure antibonding σ* state in a van Hove singularity with 0.12 eV

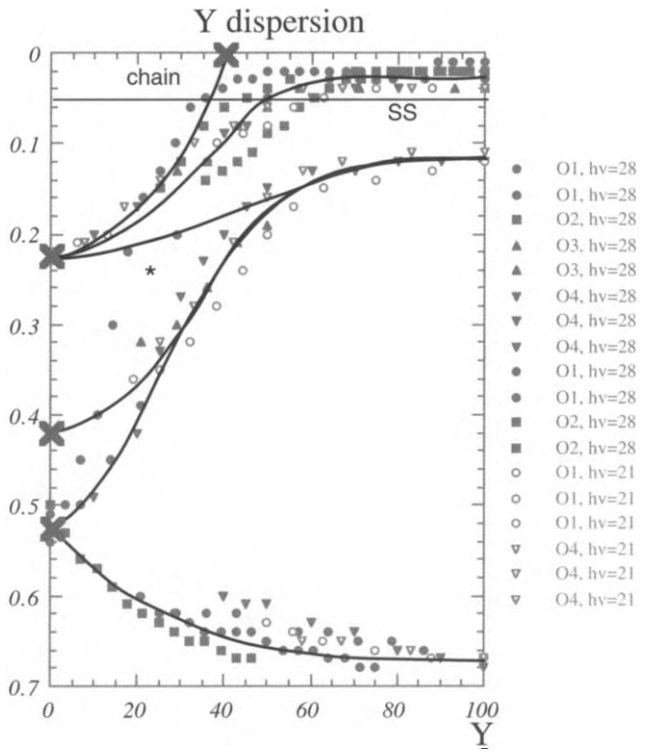

Fig. 18. Energy dispersion of quasiparticles along the ΓY symmetry line.

binding energy at Y. The expected chain Fermi surface crossing appears near 40% of ΓY, at which point a feature becomes prominent at very low binding energy. Corresponding band dispersions along XS and YS show both the bonding σ and antibonding σ* bands are clearly present, with two corresponding Fermi surface crossings at 31% and 18% of XS. The fact that the higher-binding-energy bonding band is not seen in studies of twinned crystals in O_2, as has been the convention in previous work, is significant, particularly as it is this state which reveals anisotropic shifts in the leading edge which mimic the gap behavior in Bi2212, as reported in previous work (Schabel et al. 1998a).

4. Fermi surface

Cuprates represent an ideal system for ARPES studies of the Fermi surface because of the direct correspondence between photoelectron emission angles and points in the Brillouin zone (BZ). This fact has been exploited in a number of experimental mappings for Bi2212, Bi2201, Y123, and NdCeCuO, revealing intriguing aspects of their electronic structure. In these experiments well-defined quasiparticle peaks are observed

near E_F and disperse with $\boldsymbol{k}$, with Fermi level crossings corresponding to spectra in which peaks suddenly lose intensity at one point in $\boldsymbol{k}$-space. These band-like features were initially hailed as strong confirmation of the applicability of an independent-particle model. However, the observation of substantial band-mass enhancements, satellite features, and extended saddle-point singularities casts doubt on the adequacy of band-theoretical treatments. Investigations incorporating many-body Hamiltonians such as the t–J model predict similar behavior and provide a more satisfactory explanation for the anomalous band dispersions while retaining conceptual continuity with the insulating parent compounds (Dagotto et al. 1994).

The observation of large, band-like Fermi surfaces in both electron- and hole-doped high-T_c superconductors with ARPES places strong constraints on many-body theories for these systems, and has led to extensive discussion of the Luttinger sum rule and the relevance of Fermi-liquid theory to the electronic structure of the cuprates in the metallic doping regime (Campuzano et al. 1990, Dessau et al. 1993, King et al. 1993, Liu et al. 1992a,b, Olson et al. 1989b). Two important questions can be addressed by Fermi surface (FS) measurements on two-layer cuprates: (i) do two FS pockets arising from coupling of the CuO_2 bilayers exist? and (ii) do "shadow bands" originating in antiferromagnetic correlations appear as echoes of the Fermi surface shifted by the antiferromagnetic wavevector, (π,π)? To adequately analyze these issues, it is essential to understand what is being measured in an ARPES experiment, how a FS is defined in a many-body correlated system which may be far from the Fermi-liquid ideal, and how that information is extracted from the experimental data. Here we briefly discuss various methods for extraction of Fermi surfaces from ARPES data (Aebi et al. 1994, Randeria et al. 1995, Santoni et al. 1991, Straub et al. 1997), along with their implementation and relative merits.

A high-resolution mapping of the Fermi surface of Y123 was presented by Liu et al. (1992b). Due to the presence of twinning in this material, the anisotropy between the X and Y points in reciprocal space is not observable. Matrix element effects are also exceptionally pronounced in Y123, leading to strong modulation of the peak intensities with photon energy and attendant difficulties in data interpretation. The Y123 Fermi surface appears to consist of a single nested sheet centered at (π,π) consistent with the other cuprates for which such measurements have been made, with the possibility of a second, nearly degenerate Fermi surface being less clearly resolved. The adequacy of this analysis has been questioned by some authors, and was discussed in the review by Shen and Dessau (1995). Here we emphasize the results of extensive polarization-dependent studies of the Fermi surface of untwinned Y123 (Schabel et al. 1997).

In $Bi_2Sr_2CaCu_2O_{8+\delta}$ (Bi2212), complications arising from superstructure have led to contradictory conclusions regarding the presence or absence of bilayer splitting, despite similar data (Dessau et al. 1993, Ding et al. 1996a), highlighting the subjectivity of conventional FS attribution. Because the predicted magnitude of the splitting in Bi2212 is much smaller than that for optimally doped Y123, the latter material is much more appropriate for such investigations. In addition, Y123 does not suffer from the Bi2212 superstructure distortion, although its FS is complicated by the presence of four distinct

segments and significant k_z dispersion, based on predictions of *ab initio* LDA calculations (Andersen et al. 1991, 1994, Pickett 1989). Also important is the fact that no complete FS mapping has been performed on an untwinned sample (Tobin et al. 1992), even though twinning renders interpretation of the data more difficult. Significant anisotropy is predicted in the band structure and FS of Y123 due to the CuO_3 chains breaking the fourfold tetragonal symmetry. This leads to smearing of the spectral functions and FS of twinned crystals by superimposition of the ΓXSΓ and ΓYSΓ octants of the Brillouin zone.

Interest in the possibility of directly observing strong antiferromagnetic correlation effects in the Fermi surface of the cuprates (Liu et al. 1992a) was brought to the forefront by Aebi's (1994) and Osterwalder's (1995) reports of antiferromagnetic "shadow bands" in data taken in photoelectron diffraction mode on optimally-doped Bi2212 in the normal state at room temperature. Such a dramatic manifestation of magnetic behavior in a doping and temperature regime where the antiferromagnetic correlation lengths are of the order of a planar lattice constant, at most, would have strong implications for the relevance of magnetically mediated pairing in the microscopic mechanism for superconductivity. Unfortunately, the possibility of a $c(2\times2)$ reconstruction in Bi2212 and other experimental difficulties hinder discrimination between such correlations and simple structural effects (Chakravarty 1995, Singh and Pickett 1995). The absence of these uncertainties in Y123, as well as a much better understanding of the details of the crystal structure, makes Y123 potentially better suited to address these questions as well.

4.1. *Methods for Fermi surface determination with ARPES*

Conventional ARPES FS determinations infer crossings from cuts through the BZ, subjectively identifying dispersive quasiparticles "by eye" in the EDCs. While it is impossible to attribute specific, quantitative criteria to human judgment, there are a number of guidelines which are useful in identification of crossing points. First, the centroid of the quasiparticle peak can be tracked in $\boldsymbol{k}$-space and extrapolated to its intersection with the Fermi energy, this point defining the Fermi surface boundary. Second, the total area beneath the quasiparticle peak can be monitored, with the crossing roughly corresponding to the point where this area has diminished by a factor of two. Finally, the energy position of the midpoint of the leading edge of the EDCs may be observed, with the crossing found at the point where this quantity reaches its maximum value. Depending on the particular preferences of the practitioner, one of these methods may be strictly adhered to or some synthesis of all three may be used. In either case, the subjective method is adequate for sketching out rough details of Fermi surface topology and for gaining a qualitative overview, but is neither quantitative nor unique, and cannot provide an unbiased, automatic means of extracting FS contours.

An alternative technique, based on photoelectron diffraction methods (Santoni et al. 1991), has been used by Aebi et al. (1994, 1996) and Osterwalder et al. (1995, 1996) to measure the Fermi surface of Bi2212, among other materials. In this approach, the total photoemission intensity in a narrow energy window centered on E_F is measured

as a function of $\boldsymbol{k}$ by scanning over the Brillouin zone. By acquiring a single data point rather than a complete EDC for each $\boldsymbol{k}$-vector, it is possible to densely sample the entire BZ much more rapidly and completely than is feasible in conventional EDC mode. However, there are four disadvantages to this method. First, it only provides information on the relative spectral weight near E_F, but does not allow the identification of dispersive quasiparticle features or determination of the band structure. Second, matrix element effects and cross-section fluctuations may lead to sizable variation of the total photoemission intensity in different parts of the BZ, over- or underemphasizing certain regions of $\boldsymbol{k}$-space. Third, while the technique has intuitive appeal, the precise physical meaning of the quantity being measured is not well defined. The essential assumption which is made is that the spectral weight at the Fermi level has a maximum at $\boldsymbol{k}_F$; this certainly holds in a simple Fermi-liquid model, but there is no particular reason to believe that this behavior is universal in strongly correlated systems. Fourth, in the instance of the high-T_c materials, or other systems where there is an extended region of $\boldsymbol{k}$-space having a high spectral density near but below the Fermi energy, the photoelectron diffraction method is unable to resolve true FS crossings from the near-E_F weight, and will actually include contributions from occupied states lying within the greater of the instrument resolution, σ, or kT, of E_F.

A third technique, which has been proposed by Randeria et al. (1995), relies on the approximate sum rule relating the spectral function to the momentum space density of states (DOS), $n(\boldsymbol{k})$. As noted in their letter, $n(\boldsymbol{k}) = \int_{-\infty}^{\infty} A(\boldsymbol{k}, \omega) f(\omega)\, d\omega$. To see how this relates to what is measured in an ARPES experiment, note that, within the sudden approximation, a valence-band ARPES spectrum may be *approximated* as a sum over bands of the product of a matrix element for each band with the corresponding single band spectral function: $I(\boldsymbol{k}, \omega) = \sum_n M_n(\boldsymbol{k}, h\nu) f(\omega) A_n(\boldsymbol{k}, \omega)$. It is further conjectured that ARPES spectra may be used to directly measure $n(\boldsymbol{k})$, through the aforementioned relationship between photoemission spectra and $A(\boldsymbol{k},\omega)$. This is true within a small region of $\boldsymbol{k}$-space, if we assume that $M_n(\boldsymbol{k},h\nu)$ is weakly varying and we further restrict ourselves to a single band, in which case we can integrate over ω to obtain $\int_{-\Delta_n}^{\infty} I(\boldsymbol{k}, \omega)\, d\omega = M_n(\boldsymbol{k}, h\nu)\, n(\boldsymbol{k})$, where Δ_n is the quasiparticle bandwidth. Then the energy-integrated ARPES spectrum is proportional to the momentum-space DOS, modulated by the photon energy and $\boldsymbol{k}$-dependence of the matrix element prefactor. Unfortunately, the situation in real, multiband materials is not nearly so simple. First, the photon energy dependence is non-trivial, and can lead to vastly different contributions from bands having different orbital character, especially in the UPS energy range. This is particularly true in structurally complex materials such as the cuprates, which have polyatomic bases with many atoms and, consequently, many overlapping bands. Second, for a global picture of the Fermi surface, the $\boldsymbol{k}$-dependence of the matrix element term is likely to be significant on the scale of the Brillouin zone. In these cases, it is difficult to justify, *a priori,* straightforward application of the $n(\boldsymbol{k})$ approach.

Despite these complications, it is possible to formulate a quantitative means of directly extracting Fermi surface information from a complete set of ARPES data spanning the Brillouin zone. It is well known that, within the Fermi-liquid framework, the momentum

distribution drops discontinuously at the Fermi surface, with the size of the step, Z_k, being directly related to the mass renormalization. Experimental broadening from the finite angular resolution will remove this discontinuity, leading to a sigmoid function of $\boldsymbol{k}$. In the case where multiple quasiparticles coexist, the momentum distribution will manifest several discrete drops, one for each band. If we consider the momentum space gradient of this function, $|\nabla_k n(\boldsymbol{k})|$, it is clear that a peak will occur at the position of each Fermi surface crossing, corresponding to the steps in the momentum density. Under the assumption that the matrix element term is slowly varying relative to the characteristic "width" of the Fermi surface (primarily defined by the angular resolution of the photoemission spectrometer), the derivative of the photoemission spectral weight will manifest essentially identical behavior, allowing the Fermi surface to be directly extracted from the data. In cases where the matrix element variation is non-negligible, a simple first-order correction may be made using the logarithmic derivative instead: $|\nabla_k \ln n(\boldsymbol{k})|$, thereby mapping out regions where the *relative* variation in $n(\boldsymbol{k})$ is large. This can be used to correct for variations in cross-section due to polarization effects when data is acquired with synchrotron radiation or other polarized photon sources.

By relying on conservation of spectral weight, the presence of weight near but below E_F will not affect the appearance of the Fermi surface determined in this way, unlike the photoelectron diffraction method, nor will the finite experimental energy resolution, since the Fermi statistics defining particle conservation are unaffected by the instrumental broadening. Similarly, conservation of spectral weight is a robust property of many-body systems, independent of the details of the interactions, making this approach equally valid for strongly correlated and non-Fermi liquid materials. An example is the Luttinger-liquid scenario, as discussed by Chakravarty et al. (1993) in which the delta-function singularity in the gradient is replaced by a power-law divergence; while the details of $n(\boldsymbol{k})$ are affected, the FS crossing appears in the expected region of $\boldsymbol{k}$-space. The main disadvantage of the gradient method is the fact that numerical differentiation, which magnifies the noise already present in the data, is necessary for extraction of the Fermi surface. This is particularly problematic for data taken in normal EDC acquisition mode, necessitating a degree of numerical smoothing for good results. The required smoothing results in slightly diminished effective $\boldsymbol{k}$-resolution relative to our actual instrumental contribution. The much denser $\boldsymbol{k}$-space sampling of the photoelectron diffraction measurements should allow significantly improved signal-to-noise ratio in applications of the derivative method.

4.2. *The Fermi surface of Y123*

The Fermi surface of optimally-doped Y123, calculated using the full-potential linear muffin-tin orbital (LMTO) method is shown in figs. 19c,d for $k_z = 0, \pi$ (Andersen et al. 1991, 1994). As studies on twinned Y123 and numerous other cuprates have made clear (Dessau et al. 1993, King et al. 1993, Liu et al. 1992a), band-theory predictions are at least qualitatively correct for these materials, provide the only *ab initio* theoretical predictions for comparison with the experimental data, and constitute a useful framework

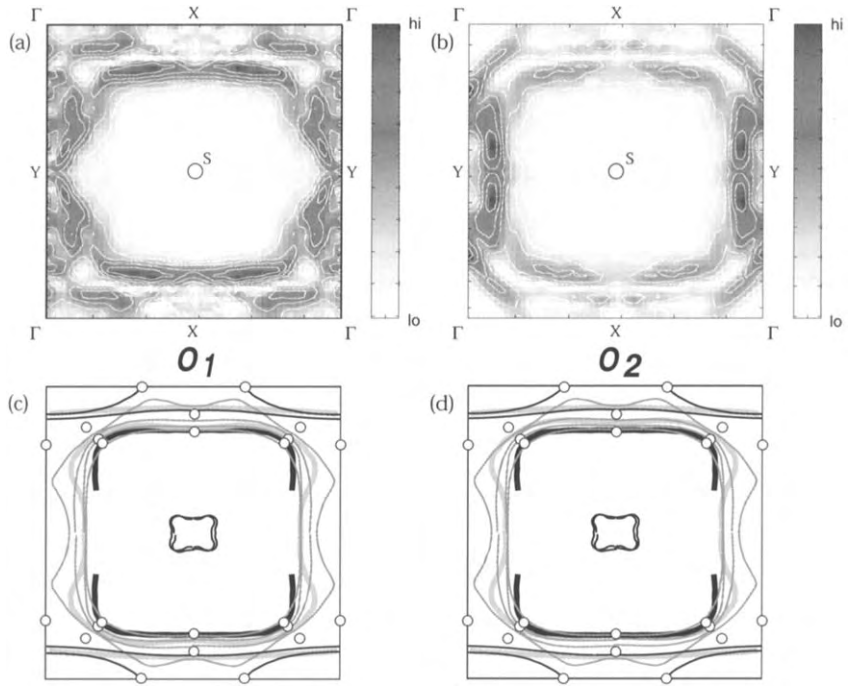

Fig. 19. Fermi surfaces determined from the logarithmic gradient of the photoemission intensity at the Fermi energy. The small segments near Γ are artifacts due to the small effective window of ω-integration. Panels (c) and (d) show the Fermi surfaces derived from the data (thick black and gray lines) along with Fermi surface crossings identified by conventional band dispersion measurements (open circles). Superimposed are the LMTO calculated Fermi surfaces for $k_z = 0, \pi$ (plane states are shown in gray, chains in black).

within which to discuss possible deviations from conventional behavior (Andersen et al. 1991, 1994, 1995, Pickett 1989). The principal features of the LMTO Fermi surface are two large CuO_2-plane-derived hole pockets centered on the S point, a chain-derived FS sheet running roughly parallel to ΓX, and a small pocket centered on S. Projection of the orbital character of the relevant bands reveals that the inner plane pocket is principally derived from the bonding pdσ plane states comprised of Cu(2) $3d_{x^2-y^2}$, O(2) $2p_x$, and O(3) $2p_y$ orbitals, while the more dispersive outer pocket derives from the corresponding antibonding pdσ* states. The small "stick" pocket at S arises primarily from bonding between the apical oxygen O(4) and Ba, while the remaining pdσ chain sheet weakly hybridizes with the bonding pdσ* band at $k_z = 0$ and strongly hybridizes with the antibonding pdσ band at $k_z = \pi$, resulting in substantial c-axis dispersion (Andersen et al. 1994).

Application of the gradient method to ARPES measurements on untwinned Y123 is presented in figs. 19a,b. Sample lifetime constraints and data acquisition time make it impossible to acquire an arbitrarily dense set of EDCs, necessitating interpolation of our data in $\boldsymbol{k}$-space to generate a uniform mesh which is then numerically smoothed

by convolution with a two-dimensional window function having a breadth 1.5 times the instrument width, and differentiated to form the quantity $|\nabla_{\boldsymbol{k}} \ln n(\boldsymbol{k})|$. Choice of the grids spanning the Brillouin zone was guided by previous investigations, allowing concentration of spectra in regions where there is appreciable spectral weight below E_F, and sampling the regions containing unoccupied states more sparsely. The logarithmic gradient was chosen to minimize the intensity variations seen over the BZ in the raw data; other than diminished contrast, the results of application of the bare gradient are essentially indistinguishable.

Examination of figs. 19a and 19b reveals the expected large hole pocket centered on S, with significantly narrower Fermi sections than observed in the photoemission intensity maps. In contrast with the photoemission intensity maps discussed above, the segments resolved with the gradient are comparable in width to the instrumental $\boldsymbol{k}$-resolution defined by our angular aperture (broadened by smoothing). It was verified from the band dispersions that the parallel segments near the Γ point result from the finite energy window, with a quasiparticle dispersing up from higher binding energy passing first through the lower edge of the energy window, then crossing the Fermi surface, as discussed above. The remaining portions are sections of the true Fermi surface, although segments in the vicinity of the surface peak at Y are aliased by the spurious spectral weight of this feature and are not representative of the bulk Fermi surface.

In both orientations we can clearly resolve the strongly nested inner (bonding) plane FS pocket, with weak indications of the outer (antibonding) pocket visible primarily near X and Y. While the derivative data are too noisy to unambiguously reveal both crossings along ΓS, detailed analysis of dispersion relations along this line clearly demonstrates their presence (Schabel et al. 1998a). The chain band is weakly apparent, though it presumably overlaps to a large degree with the antibonding plane segments around X. Figures 19c,d show subjective Fermi surfaces, determined from the plots in figs. 19a,b, as thick lines. Superimposed are LMTO Fermi surface contours for $k_z = 0, \pi$, with the plane bands in grey and chains in black. Experimental FS crossings determined from band dispersions using the conventional method are indicated by the open circles (Schabel et al. 1998a). The expected bifurcated saddle points in the antibonding Fermi surface may be resolved in segments paralleling ΓY, indicated by the thick gray lines. The ability to make quantitative statements about this region of the Brillouin zone is, however, compromised by the large contribution of the surface peak near Y. A complimentary bifurcation of the saddle point in the ΓX-direction, if present, is not well resolved, in contrast with LDA predictions. This is likely a consequence of strong c-axis dispersion distributing spectral weight over a larger region of $\boldsymbol{k}$-space for the dispersive pdσ* FS sheets in this part of the Brillouin zone. In O_2, where $\boldsymbol{E}$ is parallel to the CuO_3 chains, we note that even using the logarithmic gradient technique the emission from the feature near Y is by far the most prominent contribution, while the relative contributions are comparable in O_1.

To identify Fermi surface segments and crossing points more precisely, it is possible to examine $I(E_F)$ contours along lines paralleling both ΓY and ΓX for various values of k_x and k_y, respectively. In this approach, which is complementary to band-structure identification, with a peak being identified in $\boldsymbol{k}$ for fixed $\omega = E_F$, Fermi surface crossings

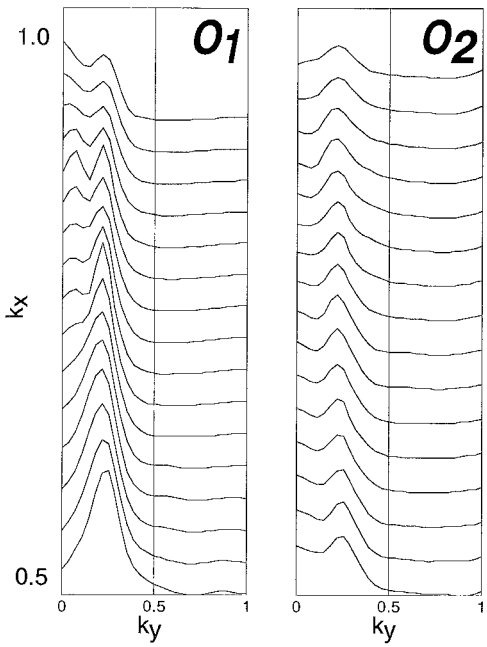

Fig. 20. Normalized cuts through the data used in fig. 19, parallel to ΓY for k_x ranging between 0.5 and 1.0. Two peaks corresponding to two separate Fermi surface crossings appear in the data in both sample geometries.

should appear as peaks in the intensity as a function of $\boldsymbol{k}$. Figure 20 shows normalized Fermi-level intensity curves for cuts parallel to ΓY for k_x between 0.5 and 1.0, corresponding to cross-sectional slices of the data. The data in both plots have a double peaked structure extending over a large fraction of the ΓX line, with a smaller feature near the $k_y = 0$ line and a more prominent one around $k_y = 0.2$, which merge into a single broader peak nearer to Γ in O_1, but remain distinct in O_2. An important technical detail which arises when performing such an analysis is the occurrence of spurious peaks when the line along which $I(E_F)$ is being interpolated lies parallel (or nearly so) to a segment of the Fermi surface. In this case, the actual Fermi "crossing" will be extremely broad, and noise in the data may give rise to features which do not correspond to the true Fermi surface. For this reason, data from these regions must be regarded as unreliable.

4.3. *Shadow bands in Y123*

The shadow bands observed in the Fermi surface of Bi2212 by Aebi et al. (Aebi et al. 1994, Osterwalder et al. 1995) seen in normal-state measurements of the photoemission intensity at room temperature, were attributed to echoes of the bonding FS shifted by (π,π) arising from strong antiferromagnetic correlations. This interpretation has been controversial; the appearance of these features in their experiment is particularly surprising because the data were taken on optimally doped, metallic Bi2212 at 300 K, which has an extremely short antiferromagnetic correlation length on the order of a planar lattice constant. A possible alternative explanation of this effect is a weak $c(2\times2)$

structural distortion which would mimic the effects of static antiferromagnetic order. The data on untwinned Y123, which were taken at low temperature (20 K), provide an independent test of this hypothesis on a material known to be free of such structural distortions. If static antiferromagnetic long-range order were present in Y123, we would expect the true LMTO FS to be mirrored by shifted echoes of the folding from the antiferromagnetic potential. One should be able to directly observe these echoes in the photoemission data experimentally, with the most prominent features of the unperturbed Fermi surface presumably having the strongest shadows as well. Examination of the experimental Fermi surfaces in fig. 19 does not reveal any indication of such a folding in any of the Y123 data. In addition, close inspection of EDCs along the ΓS line shows no evidence for the presence of a peak shifted by $(\frac{2}{3}\pi,\frac{2}{3}\pi)$ corresponding to the main Fermi surface crossing near $(\frac{1}{3}\pi,\frac{1}{3}\pi)$ (Schabel et al. 1997). These data suggest that the shadow bands seen in Bi2212 are structural in origin, and do not arise from the vestigial antiferromagnetic order in this material, and are consistent with earlier investigations searching for closed pockets along ΓS in twinned Y123 (Liu et al. 1992a).

4.4. *Evidence for bilayer splitting*

Bilayer splitting, which arises from bonding–antibonding pairing of interplane wavefunctions, is predicted to be approximately 0.75 eV at Γ in Y123, substantially larger than that expected in Bi2212. Some theoretical predictions, principally based on the short c-axis mean free paths in normal-state transport data, have argued that the conductivity data fundamentally contradict band-like behavior along this axis, thus precluding the possibility of this splitting (Anderson 1992). In particular, the interlayer tunneling mechanism of high-temperature superconductivity relies on incoherence of the inter-bilayer transport in the normal state. For this reason, it is important to critically evaluate the evidence for this splitting in Y123 and discuss its significance. The hallmark of bilayer splitting is the appearance of two nondegenerate bands arising from the CuO_2 planes, while a degeneracy of these bands might be, but is not necessarily, an indication of non-Fermi liquid behavior. While the data are normally taken in the superconducting state, the vastly different energy scales for the expected splitting and the superconductivity-induced modifications in the electronic structure make it unlikely that this is a relevant consideration.

As discussed above, the data clearly reveal two plane-derived quasiparticle features which have binding energies of 0.22 eV and 0.53 eV at Γ for $h\nu = 28$ eV, with the higher-energy peak showing at least 0.12 eV dispersion along the c-axis. In contrast, there is no apparent c-axis dispersion of the low-binding-energy feature in our data. These features disperse weakly upward toward X, appearing at 0.13 eV and 0.43 eV respectively, and exhibit Fermi surface crossing behavior agreeing well with qualitative aspects of LDA calculations. On the basis of this evidence, it appears that these features are in fact the expected bilayer split plane states, with the magnitude of the splitting diminished by roughly a factor of two from its calculated value, presumably due to correlation effects.

The apparent observation of bilayer splitting and c-axis dispersion in Y123 raises some intriguing questions regarding the qualitative disagreement between high-energy measurements such as photoemission and low-energy measurements such as transport. In most of the cuprates, the c-axis mean free path for electron transport is shorter than the lattice constant in that direction, making it plausible to argue that the transport in this direction is incoherent (Anderson 1992). However, this conclusion, based on the results of transport measurements at very small energy scales, does not necessarily imply that high-energy spectroscopies such as photoemission should not see fundamentally different effects (Laughlin 1997). In fact, the observation of bilayer splitting and c-axis dispersion in Y123 points to the need for a conceptual distinction between the two very different energy scales probed by these different techniques. Such a duality in which band-like dispersive quasiparticles are seen in photoemission measurements of materials which are clearly insulating in transport has been seen in a number of other systems, including NiO, $Sr_2CuO_2Cl_2$, and other Mott insulators.

5. Superconducting-state electronic structure

Observation of a superconducting gap for the first time in any material using photoemission was a remarkable accomplishment, and paved the way for the intense research which focussed on determination of the momentum-space dependence of the superconducting order parameter (Imer et al. 1989). Unfortunately, aside from isolated and largely irreproducible results on Y123 (Schroeder et al. 1993), Bi2212 was the only cuprate for which a gap could be reliably and reproducibly measured. Because of the absence of consistent data on other cuprates, a vast amount of work has focussed on Bi2212, leading to significant advances in our understanding of the superconducting state and sharpening the debate on the origin and character of the microscopic pairing mechanism.

Initial observations of the opening of a gap in the near-E_F states in Bi2212 were made in angle-integrated mode, demonstrating a shift in the leading edge of 20–30 meV and a pile-up of states similar to that expected from BCS theory (Chang et al. 1989, Imer et al. 1989). Early angle-resolved studies revealed an even more dramatic change in the DOS, finding an isotropic gap of 24±5 meV (Olson et al. 1990b). This evidence for a symmetric s-wave pairing mechanism contrasted strongly with numerous other experiments which clearly indicated the presence of an anisotropic gap; subsequent ARPES work by Wells et al. (1992) revealed for the first time a direct observation of $\boldsymbol{k}$-dependence of the gap. The sensitivity of gap measurements to scattering and disorder and the high energy resolution required to observe the appearance of a gap make these studies particularly demanding in terms of sample quality and surface preparation, with imperfections leading to homogenization of the angular dependence and an apparently isotropic gap.

Extensive studies by Shen et al. (1993), Shen (1994) and Ding et al. (1996a,b), have examined the question of gap anisotropy in Bi2212 in detail, finding strong evidence for $d_{x^2-y^2}$ symmetry in numerous samples. Due to their lack of phase sensitivity, ARPES measurements are incapable of rigorously determining the $\boldsymbol{k}$-dependence

of the superconducting order parameter; however, it is possible to set an upper bound on the magnitude of the gap along a hypothetical node line. Comparison of the momentum-space dependence observed with that expected for d-wave symmetry, ($\Delta(\boldsymbol{k}) = \Delta_0(\cos k_x a - \cos k_y a)$, demonstrates a strong linear correlation between the experimental data on a number of samples and the simple d-wave model. Alternate predictions for the order-parameter symmetry, such as the anisotropic s-wave, exist (Chakravarty et al. 1993), but a growing body of evidence from a number of techniques strongly favors the d-wave scenario. At present, the emerging consensus based on both ARPES and other phase-sensitive measurements (Ott and Brawner 1995, Tsuei et al. 1995, van Harlingen 1995, Wollman et al. 1995), appears to strongly favor pairing mechanisms which lead to d-wave symmetry.

Recently, several elegant experiments on Y123 have provided strong evidence for a phase change under 90° rotation, also with the d-wave hypothesis (Ott and Brawner 1995, Tsuei et al. 1995, Wollman et al. 1995). Angle-resolved photoemission, although only sensitive to the magnitude of the order parameter, is nevertheless able to place strong upper bounds on the maximum gap magnitude at the node line, and has the unique capability of directly measuring the $\boldsymbol{k}$-dependence of this quantity. Unfortunately, previous attempts to measure the gap in Y123 have failed. This absence is particularly puzzling in light of numerous results obtained with other experimental techniques, including Josephson tunneling (van Harlingen 1995), microwave absorption (Bonn and Hardy 1996), and scanning SQUID microscopy (Kirtley et al. 1995), which clearly reveal the appearance of a superconducting gap of comparable magnitude and anisotropy to that seen in Bi2212 (Shen and Dessau 1995). The absence of a gap is also inconsistent with scanning tunneling microscopy studies (Edwards et al. 1992), which are even more surface sensitive than ARPES.

In fig. 21 we present photoemission spectra from sample X III taken along six distinct cuts through the two-dimensional BZ, normalized to the weight above E_F arising from higher-order photons. Each panel clearly reveals a Fermi surface crossing, with a schematic representation of the points in the BZ corresponding to the spectra shown beneath. A crossing is identified by an abrupt loss of intensity in the quasiparticle feature as it moves above E_F. The importance of accurately determining the precise $\boldsymbol{k}$-space location of the crossing has been extensively discussed in the context of gap studies on Bi2212 (Shen et al. 1993). Crossings are identified using two criteria: (i) the point where the integrated intensity in the quasiparticle is reduced by half, and (ii) the point where the midpoint of the leading edge near E_F reaches the farthest forward (i.e. the lowest binding energy).

Figure 22 compares the leading edge regions of spectra taken at the FS crossing points; only four of the six crossings are shown for clarity. The Fermi edge spectrum from a Au reference sample is indicated by the thick line. A monotonic shift of the leading edge is seen as we move along the FS from ΓS toward XS, with the clear appearance of a gap in the spectra near X. While this behavior is similar to the gap phenomena seen in Bi2212, there are a number of important differences. In particular, we fail to observe the sharp peak which appears prominently near $\bar{M}$ (equivalent to X in Y123) in

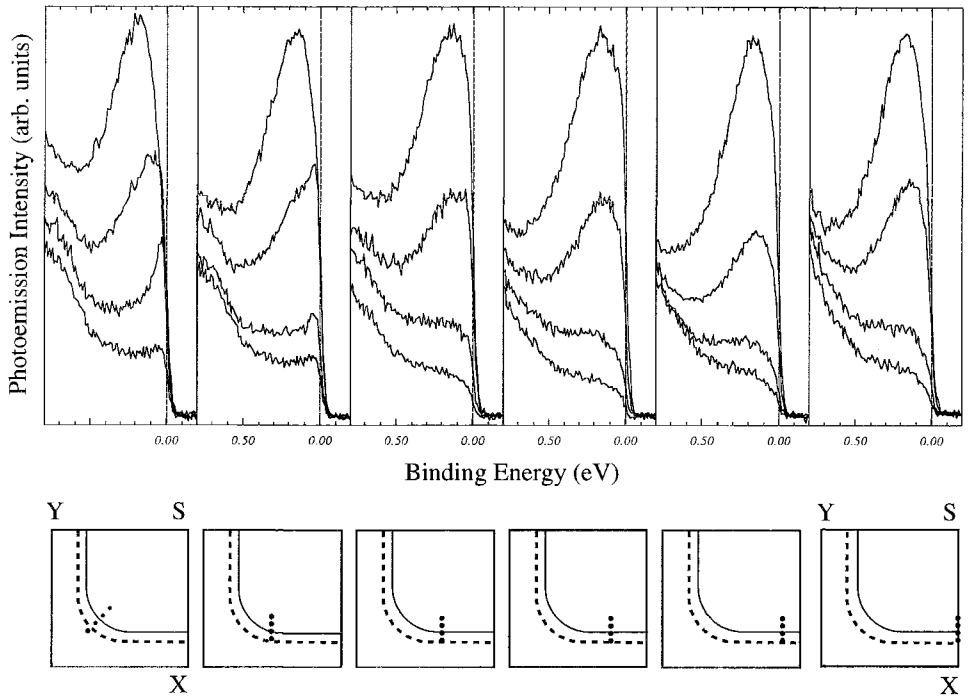

Fig. 21. Photoemission spectra along various cuts through the Brillouin zone, clearly revealing a Fermi surface crossing. The lower portion schematically illustrates the points in $\boldsymbol{k}$-space corresponding the each spectrum. A second Fermi surface sheet is indicated by the hatched line.

the superconducting state. Also, spectra along ΓS exhibit qualitatively different crossing behavior when compared with those along XS, with the former showing a pronounced sharpening while the latter diminish in intensity without significant changes in the lineshape. Finally the leading edges of the spectra nearest the ΓS line appear to lie significantly above the Fermi level as determined by our reference sample. This effect is also seen in Bi2212, but it is markedly more pronounced in our Y123 data. These observations are likely to be closely related, and may be understood by considering the interplay between the underlying spectral function and the finite instrument resolution.

The absence of a sharp peak at the XS crossing is a source of concern, particularly since it is such a prominent feature in the superconducting state of Bi2212. However, the presence of a gap of unknown origin in the excitation spectrum is clearly indicated by the data, and has been reproduced on four separate samples. Unlike Bi2212 in which the bands near $(\pi,0)$ are quite flat and remain near the Fermi level over an extended region of $\boldsymbol{k}$-space, we observe significant dispersion (~0.5 eV) near the Fermi surface crossing along XS, although an additional flatter band may also be seen near the X point. This large dispersion, in conjunction with decreased momentum resolution at the higher photon energies used on Y123, can lead to broadening of the spectra. We can make

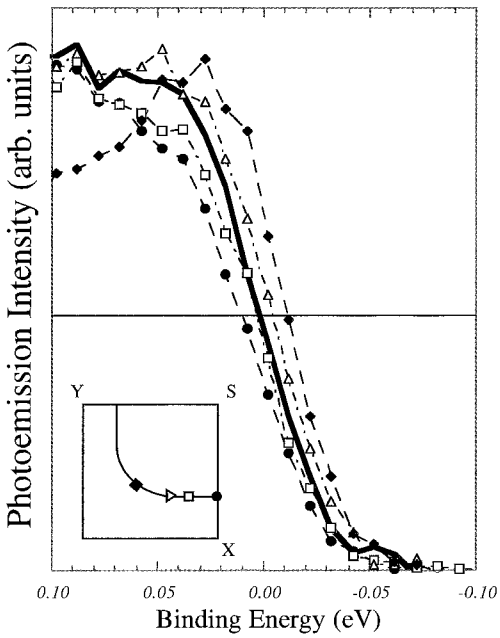

Fig. 22. The near-E_F region of spectra at the Fermi surface crossing are superimposed, revealing the presence of a monotonic shift of the leading edge to higher binding energies from the ΓS crossing to the XS crossing. A reference spectrum for a Au sample is shown by a thick line for comparison. Spectra are normalized for purposes of visualization.

a simple quantitative estimate of the momentum-related broadening by comparing the angular resolution of approximately 10% of the ΓX distance with the observed dispersion to find a total contribution of ~150 meV, significantly larger than the experimental energy resolution. In addition, there is some evidence to substantiate the LDA prediction of two distinct plane-derived Fermi surface sheets. The presence of such a bifurcation could lead to a strong overlap of two quasiparticle features in the photoemission spectra, obscuring any sharp features. With these caveats in mind, we believe that it is most reasonable to attribute the leading-edge shifts in the data to modifications due to the presence of a superconducting gap. This interpretation leads to a self-consistent picture which agrees with photoemission measurements of the superconducting gap on Bi2212 and with other experimental results on Y123. In this picture, the shifts of the leading edge along the Fermi surface will reflect, to first order, the relative variation in the magnitude of the superconducting gap at different points along the FS.

The measured leading edge shifts are presented in fig. 23. Due to the experimental uncertainty in determining the absolute magnitude of the gap along ΓS, all shifts are measured relative to the position of the leading edge at this crossing. The error bars in the figure represent the uncertainty in determination of the shift due to lineshape issues discussed above; errors due to uncertainty in the fitting parameters or in the reference E_F position are substantially smaller. Comparison of the relative shift with the characteristic $\boldsymbol{k}$-space dependence of a d-wave order parameter, $|\cos k_x - \cos k_y|/2$, reveals clear linear dependence for three of the four samples (X III, X VII, and X III 2), while the data from sample X V shows an extended node region, with the gap rapidly

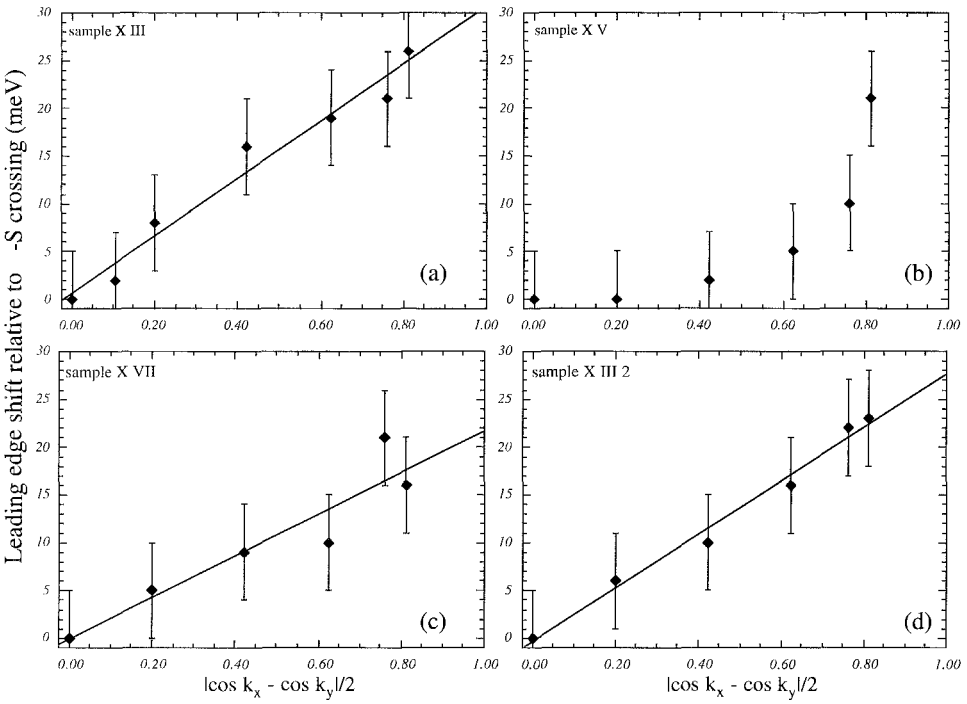

Fig. 23. Measured shifts (meV) in the leading edges of the photoemission spectra for four samples, taken at crossings along the Fermi surface, plotted relative to the quantity $|\cos k_x - \cos k_y|/2$. Samples X III, X VII, and X III 2 exhibit strong linear correlations, consistent with an order parameter having $d_{x^2-y^2}$ symmetry. The extended region of zero shift in sample X V may be indicative of "dirty" d-wave behavior.

growing only near the zone boundary. This behavior may be representative of a "dirty" d-wave material, and is consistent with our observations that the quasiparticle feature was substantially less distinct and the cleave visually inferior to those in other samples. Extrapolation of the linear region to the zone boundary provides values for $2\Delta_0/kT$ in the range of 5.4–7.6.

Our inability to compare spectra above and below T_c in Y123 makes careful analysis of lineshapes crucial. Simple numerical simulations of photoemission spectra can provide insight into the behavior seen in fig. 22, the details of which have been presented by Schabel et al. (1998b). Relying on the spectral function interpretation of the photoemission process, we can model a quasiparticle dispersing through E_F with a simple Lorentzian peak, cut by a Fermi function and convolved with a Gaussian corresponding to the experimental energy resolution. In order for a spectrum to exhibit a large shift of the leading edge above E_F, it is necessary for the underlying quasiparticle to be narrow and lie near the Fermi level, in which case the instrumental broadening will lead to a forward shift on the order of the Gaussian standard deviation. From the figure, we see a shift of approximately 15 meV, which is of the magnitude expected given the experimental

resolution. This implies that the peak at the ΓS crossing must have a small or zero gap. It is also important to note that the appearance of a gap in our photoemission spectra, as indicated by a shift of the leading edge below the Fermi level of the Au reference, cannot be explained without invoking a real gap.

The failure of previous studies to observe a superconducting gap in Y123 (see Veal and Gu 1994 for a review of earlier work), despite six years of effort, requires some explanation. Two critical elements of these experiments differ from the earlier attempts, enabling observation of the presence of leading edge shifts. First, *untwinned* samples, in which the CuO_3 chain axes are uniformly oriented, are used. Because twinning mixes the normally inequivalent X and Y points, significant mixing of the spectral function occurs throughout the Brillouin zone. Second, the photoemission spectra in three distinct sample orientations relative to the plane of photon polarization are examined, which enables identification of a previously unseen dispersive feature which is strongly enhanced in only one geometry. Also, the large dispersion of this band makes sample alignment critical, unlike the case of Bi2212. It is also important to note that, as in previous studies, we do not observe gap-like shifts in the leading edges of spectra taken near the X/Y points; our measurements correspond to the innermost Fermi surface sheet centered on the S point. This absence of a gap remains a puzzle, perhaps related to the strong hybridization of chain and antibonding plane states in conjunction with electronic structure effects from the chain-terminated surface.

6. Summary

In summary, extensive studies of the dispersive quasiparticle states in optimally doped untwinned single crystals of Y123 using polarization-dependent angle-resolved photoelectron spectroscopy have illuminated a number of points regarding the electronic structure of this material. Based on analysis of the Ba 5p core level and inference from other surface-sensitive probes, the observed surface-to-bulk intensity ratio can be reproduced with a simple model incorporating a mixed surface termination of BaO and CuO_3 regions. Furthermore, with an electron attenuation length in this material of approximately 5 Å, the bulk of the photoemission intensity arises from the surface and first subsurface CuO_2 planes, with significant attenuation of the signal from the bulk chains. Extensive arguments, based on photon polarization dependence, photon energy dependence, intensity variations between twinned, untwinned, and Y124 crystals, and oxygen, Co, and Pr doping results, favor attribution of the intense, narrow feature found near the Y point to a surface-related chain state. This feature, which appears at both X and Y in twinned crystals, is extrinsic to the bulk electronic states of Y123, and contaminates data in the crucial near-E_F region in crystals which are not exceptionally well detwinned.

The measured band dispersions clearly reveal two plane-derived quasiparticle states, one with a binding energy of 0.22 eV at Γ, and the other with 0.53 eV, which are associated with the antibonding and bonding bilayer bands. The former disperses upward to form a van Hove singularity with a binding energy of 0.13 eV at X, while the latter is weakly

dispersive along ΓX, and disperses rapidly upward along XS. While no measurable c-axis dispersion is seen in the antibonding band by changing the photon energy, the bonding band shifts upward by 0.11 eV when $h\nu$ is changed from 28 eV to 21 eV. Observation of two distinct plane states and c-axis dispersion provides clear evidence for bilayer splitting in Y123, consistent with the simplest band-theoretical arguments. Quantitative Fermi surface determination based on a momentum-space DOS analysis reveals a strongly nested inner Fermi surface pocket centered on S attributed to the CuO_2 bonding pdσ bands. The bilayer splitting of the plane bands, which is clearly resolved in polarization-dependent energy-distribution curves appears as a more weakly resolved outer sheet in the $\boldsymbol{k}$-space data. Vestiges of the principal chain sheet are also weakly apparent in some of the data, but are significantly suppressed, consistent with a strongly modified surface chain termination. The data show no sign of a "stick" Fermi surface centered at S, consistent with previous measurements but disagreeing with LMTO calculations. Evidence for antiferromagnetic shadow Fermi surfaces appears to be lacking in optimally doped Y123, supporting a structural origin for such features seen in Bi2212.

Finally, the presence of leading-edge shifts with a $\boldsymbol{k}$-dependence characteristic of pure d-wave order parameter untwinned Y123 has been observed. These shifts cannot be conclusively associated with the onset of the superconducting transition due to the surface instability of this material above T_c, but are consistent with a highly anisotropic superconducting gap of d-wave form. The lack of phase information makes it difficult to exclude the possibility of symmetries such as $d+id$ or highly anisotropic s-wave mimicking the d-wave form.

References

Abrikosov, A., J.C. Campuzano and K. Gofron, 1993, Physica C **214**, 73.

Aebi, P., J. Osterwalder, P. Schwaller, L. Schlapbach, M. Shimoda, T. Mochiku and K. Kadowaki, 1994, Phys. Rev. Lett. **72**, 2757.

Aebi, P., T. Kreutz, J. Osterwalder, R. Fasel, P. Schwaller and L. Schlapbach, 1996, Phys. Rev. Lett. **76**, 1150.

Alexandrov, A.S., and N.F. Mott, 1995, Polarons and Bipolarons (World Scientific, Singapore).

Allen, J., 1985, J. Magn. Magn. Mater. **47–48**, 168.

Allen, J., 1992, in: Synchrotron Radiation Research: Advances in Surface and Interface Science, Vol. 1: Techniques, ed. R. Bachrach (Plenum, New York) ch. 6.

Andersen, O.K., A.I. Liechtenstein, C.O. Rodriguez, I.I. Mazin, O. Jepsen, V.P. Antropov, O. Gunnarsson and S. Gopalan, 1991, Physica C **185**, 147.

Andersen, O.K., O. Jepsen, A.I. Liechtenstein and I.I. Mazin, 1994, Phys. Rev. B **49**, 4145.

Andersen, O.K., A.I. Liechtenstein, O. Jepsen and F. Paulsen, 1995, J. Phys. Chem. Solids **56**, 1573.

Anderson, P.W., 1987, Science **235**, 1196.

Anderson, P.W., 1990, Phys. Rev. Lett. **64**, 1839.

Anderson, P.W., 1992, Science **256**, 1526.

Arko, A.J., R. List, R. Bartlett, S.-W. Cheong, Z. Fisk, J.D. Thompson, C. Olson, A.-B. Yang, R. Liu, G. Gu, B.W. Veal, J. Liu, A. Paulikas and K. Vandervoort, 1989, Phys. Rev. B **40**, 2268.

Bardeen, J., L.N. Cooper and J.R. Schrieffer, 1957, Phys. Rev. **108**, 1175.

Bednorz, J.G., and K.A. Müller, 1986, Z. Phys. B **64**, 189.

Berglund, C., and W.E. Spicer, 1964, Phys. Rev. A **136**, 1030.

Bonn, D.A., and W.N. Hardy, 1996, in: Physical Properties of High-Temperature Superconductors, Vol. V, ed. D. Ginsberg (World Scientific, Singapore) ch. 9.

Bulut, N., and D.J. Scalapino, 1995, in: Proc. Conf. on

Spectroscopies in Novel Superconductors, Stanford 1995, J. Phys. Chem. Solids **56**, 1597.

Callaway, J., and N. March, 1984, in: Density Functional Methods: Theory and Applications, Vol. 38 of Solid State Physics, ed. H. Ehrenreich (Academic Press, New York) p. 135.

Campuzano, J.C., G. Jennings, M. Faiz, L. Beaulaigue, B. Veal, J. Liu, A. Paulikas, K. Vandervoort, H. Claus, R. List, A.J. Arko and R. Bartlett, 1990, Phys. Rev. Lett. **64**, 2308.

Campuzano, J.C., G. Jennings, A.J. Arko, R. List, B. Veal and R. Benedek, 1991, J. Phys. Chem. Solids **52**, 1411.

Campuzano, J.C., K. Gofron, R. Liu, H. Ding, B. Veal and B. Dabrowski, 1992, J. Phys. Chem. Solids **53**, 1577.

Cardona, M., and L. Ley, eds, 1978a, Photoemission in Solids, Vol. I (Springer, Berlin).

Cardona, M., and L. Ley, eds, 1978b, Photoemission in Solids, Vol. II (Springer, Berlin).

Chakravarty, S., 1995, Phys. Rev. Lett. **74**, 1885.

Chakravarty, S., A. Sudbø, P.W. Anderson and S.P. Strong, 1993, Science **261**, 337.

Chang, Y., M. Tang, R. Zanoni, M. Onellion, R. Joynt, D. Huber, G. Margaritondo, P. Morris, W. Bonner, J.M. Tarascon and N. Stoffel, 1989, Phys. Rev. B **39**, 4740.

Chu, C.W., L. Gao, F. Chen, Z.J. Huang, R.L. Meng and Y. Xue, 1993, Nature **365**, 323.

Claessen, R., R. Anderson, J. Allen, C. Olson, C. Janowitz, W. Ellis, S. Harm, M. Kalning, R. Manzke and M. Skibowski, 1992, Phys. Rev. Lett. **69**, 808.

Claessen, R., R. Anderson, G.-H. Gweon, J. Allen, W. Ellis, C. Janowitz, C. Olson, Z.-X. Shen, V. Eyert, M. Skibowski, K. Friemelt, E. Bucher and S. Hüfner, 1996, Phys. Rev. B **54**, 2453.

Claessen, R., T. Straub, P. Steiner, S. Hüfner, V. Eyert, R. Anderson, J. Allen, C. Janowitz and C. Olson, 1997, Physica B **230–232**, 294.

Cox, P., 1992, Transition Metal Oxides (Clarendon, Oxford).

Dagotto, E., 1994, Rev. Mod. Phys. **66**, 763.

Dagotto, E., and T.M. Rice, 1996, Science **271**, 618.

Dagotto, E., J. Riera, Y. Chen, A. Moreo, A. Nazarenko, F. Alcaraz and F. Ortolani, 1994, Phys. Rev. B **49**, 3548.

Davis, L., 1982, Phys. Rev. B **25**, 2911.

Dessau, D.S., Z.-X. Shen, D.M. King, D.S. Marshall, L.W. Lombardo, P. Dickinson, A.G. Loeser, J. DiCarlo, C.-H. Park, A. Kapitulnik and W.E. Spicer, 1993, Phys. Rev. Lett. **71**, 2781.

Ding, H., A. Bellman, J.C. Campuzano, M. Randeria, M.R. Norman, T. Yokoya, T. Takahashi, H. Katayama-Yoshida, T. Mochiku, K. Kadowaki, G. Jennings and G. Brivio, 1996a, Phys. Rev. Lett. **76**, 1533.

Ding, H., M.R. Norman, J.C. Campuzano, M. Randeria, A. Bellman, T. Yokoya, T. Takahashi, T. Mochiku and K. Kadowaki, 1996b, Phys. Rev. B **54**, 9678.

Edwards, H.L., J.T. Markert and A.L. de Lozanne, 1992, Phys. Rev. Lett. **69**, 2967.

Edwards, H.L., A.L. Barr, J.T. Markert and A.L. de Lozanne, 1994, Phys. Rev. Lett. **73**, 1154.

Emery, V.J., and S.A. Kivelson, 1993, Physica C **209**, 597.

Emery, V.J., and S.A. Kivelson, 1995, Nature **374**, 434.

Fehrenbacher, R., and T.M. Rice, 1993, Phys. Rev. Lett. **70**, 3471.

Fisk, Z., and J. Sarrao, 1995, J. Phys. Chem. Solids **56**, 1891.

Fuggle, J.C., and J.E. Inglesfield, eds, 1992, Unoccupied Electronic States: Fundamentals for XANES, EELS, IPS and BIS (Springer, Berlin).

Fujimori, A., E. Takayama-Muromachi, Y. Uchida and B. Okai, 1987, Phys. Rev. B **35**, 8814.

Fukuyama, H., 1988, Solid State Phys. **23**, 406.

Gofron, K., J.C. Campuzano, H. Ding, C. Gu, R. Liu, B. Dabrowski, B. Veal, W. Cramer and G. Jennings, 1993, J. Phys. Chem. Solids **54**, 1193.

Gofron, K., J.C. Campuzano, A. Abrikosov, M. Lindroos, A. Bansil, H. Ding, D. Koelling and B. Dabrowski, 1994, Phys. Rev. Lett. **73**, 3302.

Gu, C., B. Veal, R. Liu, H. Ding, A. Paulikas, J.C. Campuzano, P. Kostić, R. Wheeler, H. Zhang, C. Olson, X. Wu and D. Lynch, 1993, J. Phys. Chem. Solids **54**, 1177.

Guo, G., and W. Temmerman, 1990, Phys. Rev. B **41**, 6372.

Halbritter, J., P. Walk, H.-J. Mathes, W. Aarnink and I. Apfelstedt, 1988, Am. Inst. Phys. Conf. Proc. **182**, 208.

Hüfner, S., 1996, Photoelectron Spectroscopy: Principles and Applications, Vol. 82 of Springer Series in Solid-State Sciences (Springer, Berlin).

Imer, J.-M., F. Patthey, B. Dardel, W.-D. Scheider, Y. Baer, Y. Petroff and A. Zettl, 1989, Phys. Rev. Lett. **62**, 336.

Jones, R., and O. Gunnarsson, 1989, Rev. Mod. Phys. **61**, 689.

Kampf, A.P., and J.R. Schrieffer, 1990, Phys. Rev. B **42**, 7967.

Kevan, S., ed., 1992, Angle-resolved Photoemission: Theory and Current Applications (Elsevier, Amsterdam).

Khomskii, D., 1993, J. Superconductivity **6**, 69.

Kim, C., A. Matsuura, Z.-X. Shen, N. Motoyama, H. Eisaki, S. Uchida, T. Tohyama and S. Maekawa, 1996, Phys. Rev. Lett. **77**, 4054.

King, D.M., Z.-X. Shen, D.S. Dessau, B.O. Wells, W.E. Spicer, A.J. Arko, D.S. Marshall, J. DiCarlo, A.G. Loeser, C.-H. Park, E. Ratner, J. Peng, Z. Li and R.L. Greene, 1993, Phys. Rev. Lett. **70**, 3159.

Kirtley, J.R., C.C. Tsuei, J.Z. Sun, C.C. Chi, L.S. Yu-Jahnes, A. Gupta, M. Rupp and M.B. Ketchen, 1995, Nature **373**, 225.

Laughlin, R., 1988, Science **242**, 525.

Laughlin, R., 1997, private communication.

Levi, B., 1993, Phys. Today **46**, 17.

Liang, J., X. Xu, S. Xie, G. Rao, X. Shao and Z. Duan, 1987, Z. Phys. B **69**, 137.

Liechtenstein, A.I., and I.I. Mazin, 1995, Phys. Rev. Lett. **74**, 1000.

Lin, C., W. Zhou, W. Liang, E. Schönherr and H. Bender, 1992, Physica C **195**, 291.

List, R., A.J. Arko, Z. Fisk, S.-W. Cheong, S. Conradson, J.D. Thompson, C. Pierce, D. Peterson, R. Bartlett, N. Shinn, J. Schirber, B.W. Veal, A. Paulikas and J.C. Campuzano, 1988, Phys. Rev. B **38**, 11966.

List, R., A.J. Arko, R. Bartlett, C. Olson, A.-B. Yang, R. Liu, C. Gu, B. Veal, Y.C. Chang, P.-Z. Jiang, K. Vandervoort, A. Paulikas and J.C. Campuzano, 1989, Physica C **159**, 439.

Liu, L., R. Anderson and J. Allen, 1991, J. Phys. Chem. Solids **52**, 1473.

Liu, R., B. Veal, A. Paulikas, J. Downey, P. Kostić, S. Fleshler, U. Welp, C. Olson, X. Wu, A.J. Arko and J. Joyce, 1992a, Phys. Rev. B **46**, 11056.

Liu, R., B. Veal, A. Paulikas, J. Downey, H. Shi, C. Olson, C. Gu, A.J. Arko and J. Joyce, 1992b, Phys. Rev. B **45**, 5614.

Loeser, A.G., Z.-X. Shen, D.S. Dessau and W.E. Spicer, 1994, J. Electron Spectrosc. Relat. Phenom. **66**, 359.

Maeda, H., Y. Tanaka, M. Fukutomi and T. Asano, 1988, Jpn. J. Appl. Phys. **27**, 574.

Markiewicz, R., 1991, Int. J. Mod. Phys. B **5**, 2037.

Millis, A.J., H. Monien and D. Pines, 1990, Phys. Rev. B **42**, 167.

Mitzi, D.B., L.W. Lombardo, A. Kapitulnik, S. Laderman and R. Jacowitz, 1990, Phys. Rev. B **41**, 6564.

Monthoux, P., P. Balatsky and D. Pines, 1991, Phys. Rev. Lett. **67**, 3448.

Nagaosa, N., and P.A. Lee, 1991, Phys. Rev. B **43**, 1233.

Okai, B., M. Kosuge, H. Nozaki, K. Takahashi and M. Ohta, 1988, Jpn. J. Appl. Phys. **27**, L41.

Olson, C., R. Liu, D. Lynch, B. Veal, Y.C. Chang, P.-Z. Jiang, J. Liu, A. Paulikas, A.J. Arko and R. List, 1989a, Physica C **162**, 1697.

Olson, C., R. Liu, A.-B. Yang, D. Lynch, A.J. Arko, R. List, B. Veal, Y.C. Chang, P.-Z. Jiang and A. Paulikas, 1989b, Science **245**, 731.

Olson, C., R. Liu, D. Lynch, R. List, A.J. Arko, B. Veal, Y.C. Chang, P.-Z. Jiang and A. Paulikas, 1990a, Phys. Rev. B **42**, 381.

Olson, C., R. Liu, A.-B. Yang, D. Lynch, A.J. Arko, R. List, B. Veal, Y.C. Chang, P.-Z. Jiang and A. Paulikas, 1990b, Science **245**, 731.

Osterwalder, J., P. Aebi, P. Schwaller, L. Schlapbach, M. Shimoda, T. Mochiku and K. Kadowaki, 1995, Appl. Phys. A **60**, 247.

Osterwalder, J., T. Greber, P. Aebi, R. Fasel and L. Schlapbach, 1996, Phys. Rev. B **53**, 10209.

Ott, H.R., and D.A. Brawner, 1995, in: Proc. Conf. on Spectroscopies in Novel Superconductors, Stanford 1995. J. Phys. Chem. Solids **56**, 1783.

Pickett, W.E., 1989, Rev. Mod. Phys. **61**, 433.

Pickett, W.E., 1995, private communication.

Radousky, H., 1992, J. Mater. Res. **7**, 1917.

Randeria, M., H. Ding, J.C. Campuzano, A. Bellman, G. Jennings, T. Yokoya, T. Takahashi, H. Katayama-Yoshida, T. Mochiku and K. Kadowaki, 1995, Phys. Rev. Lett. **74**, 4951.

Rice, T.M., S. Gopalan and M. Sigrist, 1994a, Phys. Rev. B **199**, 378.

Rice, T.M., S. Gopalan, M. Sigrist and F.C. Zhang, 1994b, J. Low Temp. Phys. **95**, 299.

Salje, E.K.H., A.S. Alexandrov and W. Liang, eds, 1995, Polarons and Bipolarons (Cambridge University Press, Cambridge).

Santoni, A., L. Terminello, F. Himpsel and T. Takahashi, 1991, Appl. Phys. A **52**, 299.

Scalapino, D.J., 1995, Phys. Rep. **250**, 329.

Scalapino, D.J., 1996, Turk. J. Phys. **20**, 560.

Scalapino, D.J., E.Y. Loh and J.E. Hirsch, 1986, Phys. Rev. B **34**, 8190.

Schabel, M., I. Vitomirov, G. Waddill and J. Weaver, 1991, J. Electron Spectrosc. Relat. Phenom. **56**, 211.

Schabel, M., Z.-X. Shen, J. Peng and R.L. Greene, 1995, Unpublished.

Schabel, M., C.-H. Park, A. Matsuura, Z.-X. Shen, D.A. Bonn, R. Liang and W.N. Hardy, 1997, Phys. Rev. B **55**, 2796.

Schabel, M., C.-H. Park, A. Matsuura, Z.-X. Shen, D.A. Bonn, R. Liang and W.N. Hardy, 1998a, Phys. Rev. B **57**, 6090.

Schabel, M., C.-H. Park, A. Matsuura, Z.-X. Shen, D.A. Bonn, R. Liang and W.N. Hardy, 1998b, Phys. Rev. B **57**, 6107.

Schilling, A., M. Cantoni, J.D. Guo and H.R. Ott, 1993, Nature **363**, 56.

Schleger, P., W.N. Hardy and H. Casalta, 1994, Phys. Rev. B **49**, 514.

Schleger, P., R. Hadfield, H. Casalta, N.H. Andersen, H.F. Poulsen, M. von Zimmermann, J.R. Schneider, R. Liang, P. Dosanjh and W.N. Hardy, 1995, Phys. Rev. Lett. **74**, 1446.

Schrieffer, J.R., X.-G. Wen and S.-C. Zhang, 1988, Phys. Rev. Lett. **60**, 944.

Schroeder, N., R. Böttner, S. Ratz, E. Dietz, U. Gerhardt and T. Wolf, 1993, Phys. Rev. B **47**, 5287.

Seah, M., and W. Dench, 1979, Surf. Interface Anal. **1**, 1.

Sharma, R.P., T. Venkatesan, Z.H. Zhang, J.R. Liu, R. Chu and W.K. Chu, 1996, Phys. Rev. Lett. 77, 4624.

Shen, Z.-X., 1994, Physica B **197**, 632.

Shen, Z.-X., and D.S. Dessau, 1995, Phys. Rep. **253**, 2.

Shen, Z.-X., P. Lindberg, P. Soukiassian, C.B. Eom, I. Lindau, W.E. Spicer and T.H. Geballe, 1989, Phys. Rev. B **39**, 823.

Shen, Z.-X., D.S. Dessau, B.O. Wells, D.M. King, W.E. Spicer, A.J. Arko, D.S. Marshall, L.W. Lombardo, A. Kapitulnik, P. Dickinson, S. Doniach, J. DiCarlo, A.G. Loeser and C.H. Park, 1993, Phys. Rev. Lett. **70**, 1553.

Sheng, Z., and A. Hermann, 1988, Nature **332**, 138.

Shukla, A., L. Hoffmann, A. Manuel, E. Walker, B. Barbiellini and M. Peter, 1995, Phys. Rev. B **51**, 6028.

Singh, D.J., and W.E. Pickett, 1995, Phys. Rev. B **51**, 3128.

Smith, N., and F. Himpsel, 1983, in: Handbook on Synchrotron Radiation, Vol. 1, ed E. Koch (North-Holland, Amsterdam) ch. 9.

Soderholm, L., and G. Goodman, 1989, J. Solid State Chem. **81**, 121.

Soderholm, L., K. Zhang, D.G. Hinks, M.A. Beno, J.D. Jorgensen, C. Segre and I.K. Schuller, 1987, Nature **328**, 604.

Straub, T., R. Claessen, P. Steiner, S. Hüfner, V. Eyert, K. Friemelt and E. Bucher, 1997, Phys. Rev. B **55**, 13473.

Tjeng, L.H., C.T. Chen, J. Ghijsen, P. Rudolf and F. Sette, 1991, Phys. Rev. Lett. **67**, 501.

Tobin, J., C. Olson, C. Gu, J. Liu, F. Solal, M. Fluss, R. Howell, J. O'Brien, H. Radousky and P. Sterne, 1992, Phys. Rev. B **45**, 5563.

Tokura, Y., and A. Fujimori, 1995, in: Spectroscopy of Mott Insulators and Correlated Metals, Proc. 17th Taniguchi Symp., Kashikojima, Japan, October 24–28, 1994 (Springer, Berlin).

Tsuei, C.C., J.R. Kirtley, M. Rupp, J.Z. Sun, L.S. Yu-Jahnes, C.C. Chi, A. Gupta and M.B. Ketchen, 1995, in: Proc. Conf. on Spectroscopies in Novel Superconductors, Stanford 1995, J. Phys. Chem. Solids **56**, 1787.

van Harlingen, D.J., 1995, Rev. Mod. Phys. **67**, 515.

Varma, C.M., P.B. Littlewood, S. Schmitt-Rink, E. Abrahams and A.E. Ruckenstein, 1989, Phys. Rev. Lett. **63**, 1996.

Veal, B., and C. Gu, 1994, J. Electron Spectrosc. Relat. Phenom. **66**, 321.

Virosztek, A., and J. Ruvalds, 1990, Phys. Rev. B **42**, 4064.

Wells, B.O., Z.-X. Shen, D.S. Dessau, W.E. Spicer, D.B. Mitzi, L.W. Lombardo, A. Kapitulnik and A.J. Arko, 1992, Phys. Rev. B **46**, 11830.

Wells, B.O., Z.-X. Shen, A. Matsuura, D.M. King, M.A. Kastner, M. Greven and R.J. Birgeneau, 1995, Phys. Rev. Lett. **74**, 964.

Wollman, D.A., D.J. van Harlingen, J. Giapintzakis and D.M. Ginsberg, 1995, in: Proc. Conf. on Spectroscopies in Novel Superconductors, Stanford 1995, J. Phys. Chem. Solids **56**, 1797.

Wu, W.K., J.R. Ashburn, C.J. Torng, P.H. Hor, R.L. Meng, L. Gao, Z.J. Huang, Y.Q. Wang and C.W. Chu, 1987, Phys. Rev. Lett. **58**, 908.

Zaanen, J., and G.A. Sawatzky, 1990, Progr. Theor. Phys. Suppl. **101**, 231.

Zaanen, J., G.A. Sawatzky and J.W. Allen, 1985, Phys. Rev. Lett. **55**, 418.

Handbook on the Physics and Chemistry of Rare Earths
Vol. 31
edited by K.A. Gschneidner, Jr., L. Eyring and M.B. Maple

Chapter 202

INFRARED PROPERTIES OF HIGH-T_c SUPERCONDUCTORS: An Experimental Overview

D.N. BASOV[1] and T. TIMUSK[2]
[1] *Department of Physics, University of California San Diego, La Jolla, CA 92093-0319, USA;* [2] *Department of Physics and Astronomy, McMaster University, Hamilton, Ontario L8S 4M1, Canada*

Contents

List of symbols

$A(\Omega)$	Bosonic spectral function	e	Electronic charge
$\boldsymbol{E}$	Electric field	$\boldsymbol{F}_L$	Lorentz force
E_F	Fermi energy	H_c	Critical field
E_g	Charge transfer gap	$\boldsymbol{J}$	Current

J	Exchange energy
j_c	Josephson critical current
$G(k,\omega)$	Green's function of the electronic excitation
k	Pinning constant
n	Carrier density
N_{eff}	Effective spectral weight
N_{ab}	In-plane spectral weight
N_c	Interplane spectral weight
m^*	Effective mass
m_{ab}	*ab*-plane effective mass
m_c	*c*-axis effective mass
m_e	Free electron mass
m_v	Vortex mass
$\boldsymbol{Q}$	Wavevector
$R(\omega)$	Reflectivity
r	Complex reflectance
t	Hopping matrix element
t_{c0}	Interbilayer hopping
T	Temperature
T_c	Critical temperature
T_N	Néel temperature
T_{SDW}	Temperature of spin-density wave
T^*	Crossover temperature
U	Coulomb repulsion energy
v_s	Condensate velocity
v_v	Velocity
V	Volume
γ	Damping
Δ	Energy gap
Θ	Phase change
λ	Penetration depth
λ_a	*a*-axis penetration depth
λ_b	*b*-axis penetration depth
λ_c	*c*-axis penetration depth
λ_L	London penetration depth
ν	Damping
ξ	Coherence length
ξ_{ab}	*ab*-plane coherence length
ρ_{ab}	*ab*-plane resistivity
ρ_{dc}	dc resistivity
ρ_s	Superfluid density
$\Sigma(\omega)$	Electronic self-energy
$\Sigma_1(\omega)$	Real part of the electronic self-energy
$\Sigma_2(\omega)$	Imaginary part of the electronic self-energy
σ_{dc}	dc conductivity
$\sigma(\omega)$	Complex conductivity
$\sigma_1(\omega)$	Real part of the complex conductivity
$\sigma_2(\omega)$	Imaginary part of the complex conductivity
σ_1^I	Differential conductivity
τ	Relaxation time
τ_v	Vortex lifetime
ϕ_0	Magnetic flux
Ω	Frequency
Ω_0	Vortex core resonance
ω	Frequency
ω_0	Cut-off frequency
ω_c	Cyclotron frequency
ω_p	Plasma frequency
ω_{pa}	*a*-axis plasma frequency
ω_{pb}	*b*-axis plasma frequency
ω_{pc}	*c*-axis plasma frequency
ω_{pD}	Drude plasma frequency
ω_{pk}	Plasma frequency, Lorentzian oscillators
ω_{pn}	Plasma frequency, normal component
ω_{ps}	Superfluid plasma frequency

List of abbreviations

ARPES	Angular resolved photoemission spectroscopy
ASW	Anisotropic s-wave
BCS	Bardeen–Cooper–Schrieffer
BS	Bardeen–Stephen
CT	Charge transfer
DOS	Density of states
DW	d-wave
ESW	Extended s-wave
IR	Infrared
KK	Kramers–Kronig
NAFLM	Nearly antiferromagnetic Fermi liquid
NMR	Nuclear magnetic resonance

1. Introduction

High-temperature superconductivity in copper oxides (Bednorz and Müller 1986) has been at the focus of solid-state physics research for more than a decade. Despite an unprecedented attack by a force that comprised a large fraction of the condensed matter community, the central issue – the mechanism of high-T_c superconductivity – still remains to be unraveled.

Nevertheless, there have been several important advances in our understanding of the cuprate superconductors over the last several years. The search for the mechanism of high-T_c superconductivity in cuprates is in a phase dominated by experiments on well-characterized single crystals and thin films. This new generation of high-T_c materials reveals novel features which in the earlier work were obscured by defects. There is now excellent reproducibility between experiments performed on a given system by different research groups, and there is a clear tendency towards a convergence of results obtained with different experimental methods (transport, photoemission, nuclear magnetic resonance, etc).

As far as the electrodynamics of cuprates is concerned, perhaps one of the most significant accomplishments is a detailed survey of the interplane c-axis conductivity at least in the $YBa_2Cu_3O_x$ (Y123) and $La_{2-y}Sr_yCuO_4$ (La214) series. Prior to 1992, there were several reports of the c-axis properties but no systematic study of doping and temperature dependence had been reported. The reason behind this is that single crystals of appropriate thickness have become available only recently. The interplane properties showed novel features of cuprates such as the formation of the Josephson plasma resonance at $T < T_c$ (sect. 5.2) and of the normal-state pseudogap (sect. 5.4). The latter was found only in underdoped materials: those with T_c being reduced from the maximum value by diminishing the carrier density. While the role of the pseudogap in superconductivity remains controversial, its presence is not: there is mounting evidence coming from a variety of physical probes, all showing that the low-energy excitations in cuprates are suppressed at a temperature T^* significantly exceeding T_c (sect. 4.5). Experimental results on the interplane behavior provide us with information that is essential to test several theoretical approaches to the problem of understanding high-T_c superconductivity.

Single crystals of cuprates are now not only bigger in size but their quality has also improved in the recent past. A thorough study of the new generation of single crystals by a variety of transport and spectroscopic techniques has shown that the behavior of the earlier samples was often obscured by extrinsic effects. This holds true for infrared data as well. Although the ab-plane properties of $YBa_2Cu_3O_x$ ($x = 6$–7) materials were studied systematically in 1988–1991, recent samples revealed a number of novel features in the normal- and superconducting-state electrodynamics. Infrared measurements performed on Y123 crystals prepared in different laboratories now show excellent reproducibility. Other materials such as $Bi_2Sr_2CaCu_2O_8$ (Bi2212), $La_{2-y}Sr_yCuO_4$ and $Tl_2Ba_2CuO_{6+\delta}$ (Tl2201) also have been studied as a function of doping. The in-plane conductivity of cuprates along with the different approaches towards

the understanding of the charge dynamics in the CuO_2 planes is the subject of subsects. 4.2, 5.1 and 5.2.

Developments in crystal preparation techniques now make it possible to grow samples with a controlled amount of impurities. Both experimental and theoretical studies of the electromagnetic response in the presence of impurities have attracted a lot of attention. The primary motivation for these activities was to test the symmetry of the order parameter in cuprates. Such tests are possible since conventional superconductors (those with an isotropic s-wave gap) and exotic superconductors (those with a strongly anisotropic order parameter) are expected to behave differently in the presence of disorder (Sigrist and Ueda 1991). We will briefly review infrared results obtained in samples with non-magnetic and magnetic impurities in sect. 5.3.

It was realized quite early that the parent, undoped, compounds should be viewed as Mott insulators. More recent studies of the doping dependence have revealed the generic features between cuprates and other classes of Mott insulators. The principal trends in the evolution of the in-plane electronic conductivity with doping are in accord with the results of the calculations performed for Mott–Hubbard systems as will be described in sect. 3.

Finally, very interesting results were obtained through magneto-optical studies primarily of Y123 thin films. The challenge of these experiments is that the features of interest lie close to the low-frequency boundary of infrared methods. This demanded the development of novel spectroscopic techniques employing tunable far-infrared lasers and terahertz time-domain spectroscopy. Magneto-optical measurements were used to examine the structure of the vortices, and may become helpful in resolving the controversy regarding the relaxation mechanisms in these materials. Section 6 is dedicated to magneto-optics of cuprates.

There are several general review papers on the infrared properties of high-T_c superconductors (including those by Timusk and Tanner 1989, Tanner and Timusk 1992, and Thomas 1991), as well as a few covering more specific topics: phonons (Thomsen and Cardona 1989, Litvinchuk et al. 1994), polarons (Kastner and Birgeneau 1996), and the pseudogap state (Puchkov et al. 1996a). In this review, we will attempt to describe some recent developments in the studies of the electromagnetic response of cuprates that occurred primarily after 1992, although references to earlier work in some cases are necessary.

2. Energy scales and experimental techniques

A sketch showing several important energy scales in metals and superconductors (fig. 1) may be a good starting point for a discussion of the role that infrared and optical spectroscopy have played in the study of high-T_c materials. Infrared and optical spectroscopy probe the elementary excitations and collective modes in the energy region from about $10\,cm^{-1}$ up to $50\,000\,cm^{-1}$. Both boundaries are blurred, and the actual limits depend on many factors including sample size or surface irregularities. In any event,

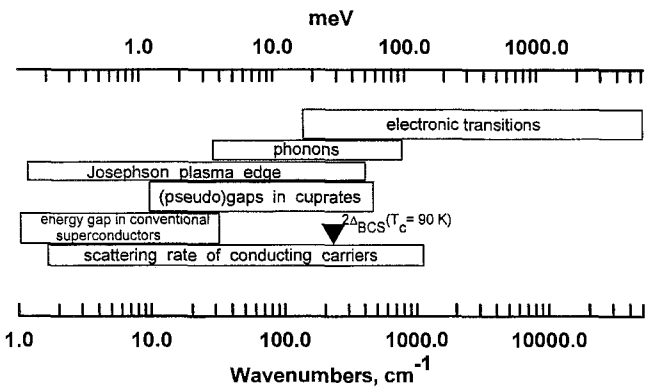

Fig. 1. Characteristic energy scales in high-T_c superconductors. Infrared and optical spectroscopies allow one to probe electronic excitations in the frequency range from ~20 cm^{-1} typically up to at least 50 000 cm^{-1}.

the accessible frequency range spans at least 3 decades in ω, establishing a link between zero- or low-frequency experiments (dc transport, microwaves, tunneling) and high-energy spectroscopies (photoemission, X-rays). Of special importance for superconductors is the far-infrared part of the spectrum ($\omega < 500\,cm^{-1}$), because this region includes the expected value for the superconducting energy gap 2Δ for materials with $T_c > 10\,K$ as well as the energy scale of the excitations (at least in some models of the phenomenon) responsible for pairing. An analysis of the spectral weight in infrared frequencies permits one to infer (through model-independent procedures) another fundamentally important parameter of a superconductor, the penetration depth λ.

An interesting trend of the last few years is a broadening of the range of experimental techniques used for infrared experiments. Traditionally, infrared properties of solids have been investigated by means of Michelson interferometers (or their modifications) using black-body sources and bolometric or photoconductive/photovoltaic detectors. In these experiments reflectance or transmission is measured over a broad energy range while the optical constants of the specimen under study are obtained through Kramers–Kronig (KK) analysis (see sect. 3.1). Michelson interferometers configured for reflectance measurements continue to be the primary workhorse in these experiments, with all system components being continuously refined (Homes et al. 1993a). An interesting novelty is the use of synchrotron light sources instead of globars or mercury lamps (Forro et al. 1990, Williams et al. 1990, Romero et al. 1992). Synchrotrons give an advantage in brightness compared to black-body sources. This brightness advantage is of special importance for studies where samples are small. This is often the case for new materials where the refinement of crystal growing techniques is not complete.

Another recent innovation is concerned with ellipsometric measurements in the far infrared (Kircher et al. 1997). The principal advantage of ellipsometry is that the optical constants of a system can be obtained without KK analysis and thus measurements do not have to be extended to $\omega \to 0$ and $\omega \to \infty$. Ellipsometry is an extremely successful technique in the near-IR–visible–near-ultraviolet regime where high-quality

optical components are available. There are several recent reports of ellipsometric measurements in the far infrared (Henn et al. 1996, Bernhard et al. 1998–2000). These original experiments demonstrate the general feasibility of the approach and indicate the great potential of ellipsometric studies in the far infrared. At the moment these experiments require samples of significantly larger size than conventional reflectance measurements.

An increasing number of experimentalists are using the technique of terahertz time-domain spectroscopy, originally proposed by Grishkovsky et al. (1990). Here infrared radiation is generated and detected using Hertz dipoles – metal stripes with a narrow gap prepared on the surface of an amorphous semiconducting substrate. A laser pulse creates photoconductive carriers in the semiconductor, thus activating the dipoles. The duration of the photocurrent is of the order of 1 ps and thus the dipole generates freely propagating radiation in the frequency region from 3 to 120 cm^{-1} (0.1–4 THz). By adjusting the time delay between the laser pulses which activate the source and the detector one is able to sample the time evolution of the terahertz electric field. By Fourier-transforming the detected pulse one is able to obtain both the real and the imaginary part of the conductivity of the medium through which the radiation propagates. At present this technique is used exclusively in transmission mode, and thus experiments rely on the availability of thin films. The crucial advantage of this technique is that it allows one to perform spectroscopy in the difficult frequency region below the traditional low-frequency boundary of infrared methods.

3. Doping antiferromagnetic insulators with charge carriers

3.1. *Complex conductivity and spectral weight*

A quantitative analysis of the electromagnetic response begins with the evaluation of the optical constants of a system (complex dielectric function, complex conductivity, etc.) from the experimentally accessible quantities such as reflectance, transmission or absorption. It is convenient to discuss the response of metals and superconductors in terms of the complex conductivity $\sigma(\omega) = \sigma_1(\omega) + i\sigma_2(\omega)$, defined from $\boldsymbol{J}(\omega) = \sigma(\omega)\boldsymbol{E}(\omega)$ where $\boldsymbol{J}$ is the current vector and $\boldsymbol{E}$ is the electric field vector. All optical constants are interrelated through simple analytical expressions and contain the same physical information. The advantage of the conductivity notation is that $\sigma(\omega)$ has no singularity at $\omega = 0$. Also, an extrapolation of $\sigma_1(\omega)$ to $\omega \to 0$ yields the dc conductivity of a metal.

An important characteristic of the optical constants is that they fall in a broad class of generalized susceptibilities with the fundamental property that their real and imaginary parts are connected by Kramers–Kronig (KK) integral relations (Landau and Lifshitz 1992). For the case of linear response, KK relations are model independent since they rely only on the causality principle and analytical properties of the complex susceptibilities. The physical reasoning behind the KK relations is that dissipation of energy of the

electromagnetic wave in a system and the phase change of the wave must be connected with each other. The KK integrals give a formal relation between the real and imaginary parts of the generalized susceptibilities.

Kramers–Kronig integrals can also be used to evaluate the optical constants from the experimentally measured reflectance or transmission. Let us consider the complex reflectance index $r = R^{1/2} \exp^{i\Theta}$, where $R(\omega)$ is the reflectivity of the solid and $\Theta(\omega)$ is the phase change between incident and reflected waves. KK integrals provide the connection between $\Theta(\omega)$ and $R(\omega)$:

$$\Theta(\omega) = \frac{2\omega}{\pi} \int_0^\infty \frac{\ln r(\Omega) - \ln r(\omega)}{\Omega^2 - \omega^2} \, d\omega. \tag{1}$$

A combination of R measured experimentally and Θ expressed in terms of R with eq. (1) allows one to obtain any set of optical constants (see Born and Wolf 1980). Analogously, the phase change can be inferred from transmission.

An important consequence of the KK relations is the possibility of formulating numerous sum rules for the optical constants (Smith 1985). In particular, the oscillator strength sum rule is essential for the quantitative analysis of the optical data:

$$\int_0^\infty \sigma_1(\omega) \, d\omega = \frac{\omega_p^2}{8} = \frac{4\pi n e^2}{m^*}, \tag{2}$$

where n is the carrier density and m is the carrier mass. If integration is performed up to to some cut-off frequency ω_0, eq. (2) yields the effective mass of carriers m^* [see also the discussion of eq. (4) in subsect. 3.3]. This sum rule is particularly important for superconductors because it can be used to evaluate the density of superconducting condensate as will be explained in sect. 5.

A sum rule for the imaginary part of the conductivity establishes a connection between the spectrum of $\sigma_2(\omega)$ and the dc conductivity of a solid which could be measured independently using a resistance probe:

$$\int_0^\infty \frac{\sigma_2(\omega)}{\omega} \, d\omega = \frac{\pi \sigma_{dc}}{2}. \tag{3}$$

The practical use of eq. (3) is to test the impact of extrapolations of the experimental reflectance to $\omega \to 0$ and $\omega \to \infty$. Such extrapolations are always required in accordance with eq. (1). However, if the energy region of the experimental data is sufficiently broad, extrapolations (in particular to $\omega \to \infty$) create only negligible error, and σ_{dc} obtained from eq. (3) should be close to the directly measured value.

3.2. *Parent insulating compounds*

It is well established that superconductivity in cuprates occurs when the CuO_2 planes, which are shared by all high-T_c compounds, are doped away from half filling either with

holes or with electrons. The parent undoped compounds are antiferromagnetic insulators with T_N ranging from 400 to 1000 K in different series. The dominant feature in the in-plane ($\boldsymbol{E} \parallel ab$) response of undoped cuprates is a sharp onset at $\omega = 1$–2 eV in $\sigma_1(\omega)$ which originates from a charge transfer (CT) gap (Fujimori et al. 1987, Tokura et al. 1990). Differences in the magnitude of the CT gap were ascribed primarily to different coordination of oxygen sites surrounding a Cu site. With increasing number of apical oxygen sites the magnitude of the gap is enhanced.

The absorption features at 1–2 eV are prominent for light polarized along the CuO_2 planes, while the c-axis response ($\boldsymbol{E} \parallel c$) shows no sharp structure in the CT region. This anisotropic character of the charge-transfer excitations suggests that they are mainly associated with transitions from O 2p to Cu $3d_{x^2-y^2}$ states (Fujimori et al. 1987, Tokura et al. 1990). In all compounds the absorption edge appears to be broadened. Detailed investigations of the temperature dependence of the 2 eV threshold in La_2CuO_4 by Falck et al. (1992), accompanied by photoconductivity experiments in the same energy range, suggest that the broadening could be attributed to coupling of the CT excitations to optical phonons.

The observation of the CT gap should be contrasted with the predictions of band theory. Local-density-approximation (LDA) calculations performed for a number of undoped materials predict these systems to be metals since the Cu 3d and O 2p orbitals form a conduction band which is half-filled (for a review see Pickett 1989). The spin-polarized version of this band theory is not sufficiently accurate to yield an antiferromagnetic state of the insulating compound (Pickett et al. 1992). Thus LDA calculations fail to account for the two principal features of undoped materials: the insulating gap and antiferromagnetic ordering. However, despite these serious problems these calculations do yield accurate values for the Fermi surface crossings as observed by angle-resolved photoemission (for a review see Pickett et al. 1992; see also ch. 201 of this Handbook).

The Hubbard model, on the other hand, successfully describes the antiferromagnetic insulator state. The Coulomb repulsion between Cu ions leads to a splitting of the 3d band into lower and upper Hubbard bands with an energy U separating the bands. This energy U is the cost of creating a doubly occupied Cu site in the upper Hubbard band. Another important control parameter of the Hubbard model is the inter-site hopping matrix element t. If the spins on neighboring sites are oppositely oriented, they can hop virtually from one site to another, lowering the energy of the system by a term proportional to $-t^2/U$ but only if (as required by the Pauli principle) their spins are antiparallel. This is equivalent to an exchange interaction with $J = 4t^2/U$, and gives rise to antiferromagnetism. In the cuprates the oxygen 2p band is located inside the Hubbard gap, which leads to a situation where the CT gap, E_g, is less than U. Adopting the classification proposed by Zaanen et al. (1985) this case is called a "charge-transfer" insulator. An appealing feature of the Mott–Hubbard scenario is that it is capable of yielding a variety of ground states including paramagnetic (metallic and insulating) states as well as antiferromagnetic (also metallic and insulating) ones (for a review see Georges et al. 1996). The evolution of the CT gap and the evolution of the spectral weight with

doping, which will be described in the next subsection, strongly support the soundness of the Mott–Hubbard approach with respect to the optical properties of cuprates.

3.3. *Evolution of the spectral weight with doping*

In the La_2CuO_4 system the substitution of La^{3+} with Sr^{2+} creates holes in the CuO_2 planes. Metallic or, more precisely, conducting behavior in the CuO_2 planes was observed in $La_{2-y}Sr_yCuO_4$ materials for dopings as low as $y=0.04$. In $Nd_{2-y}Ce_yCuO_4$, Nd^{3+} ions are substituted with Ce^{4+}, which leads to electron-like doping of the CuO_2 planes. A somewhat different type of doping is realized in the $YBa_2Cu_3O_x$ system where excess oxygen ions fill the one-dimensional Cu–O chains. In any event, in *all* of the cuprates the CuO_2 planes remain chemically unchanged in the process of doping: the dopants alter the composition of the so-called charge-reservoir layers [La–O, Nd–O, or Cu–O chains in Y123 and $YBa_2Cu_4O_8$ (Y124)]. The conducting properties of the cuprates are primarily associated with the CuO_2 planes (see sect. 3.2). Therefore, disorder in charge-reservoir layers, which is inevitable in metallic phases, does not necessarily introduce extra scattering in the *ab*-plane transport. The direct involvement of the charge reservoirs in transport and conductivity phenomena is not well studied. The Y123 and Y124 materials form an exception; there the contribution of the reservoir-layer Cu–O chains can be studied in detwinned crystals. The chain dc and ac conductivities in the normal state and the superfluid density at $T < T_c$ have been established by several different groups of experiments (Basov et al. 1995a, Tallon et al. 1995, Edwards et al. 1995, Sun et al. 1995).

A typical variation of the in-plane optical conductivity with doping is shown in fig. 2 for the $La_{2-y}Sr_yCuO_4$ system (Uchida et al. 1991). The principal result is that for $y > 0$ the

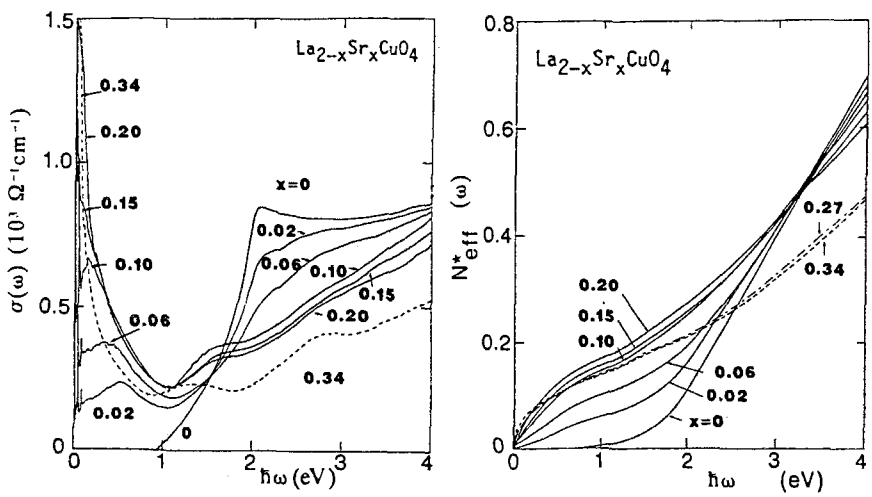

Fig. 2. The real part of the *ab*-plane conductivity (left panel) and the effective spectral weight determined from the conductivity using eq. (4) for La214 crystals, after Uchida et al. (1991).

energy region below the CT gap is filled with states at the expense of the spectral weight associated with the CT excitation in the undoped counterpart. Notably the conductivity at 1.5 eV is almost unchanged by doping. This isosbestic behavior at $\omega \approx 1.5$ eV is clearly observed in $Nd_{2-y}Ce_yCuO_4$ materials (Uchida et al. 1991, Tanner et al. 1996). Another characteristic of the doped samples is that a feature due to the CT gap persists in the spectra up to quite high levels of doping when the system is well in the metallic regime.

To quantify the changes in the optical conductivity induced by doping it is instructive to explore the behavior of the effective electron number $N_{\text{eff}}(\omega)$:

$$N_{\text{eff}}(\omega) = \frac{2m_e V}{\pi e^2} \int_0^{\omega} \sigma_1(\Omega)\, d\Omega, \tag{4}$$

where m_e is the free electron mass and V is the volume of the unit cell. N_{eff} is proportional to the number of electrons participating in the optical excitations with energies less than ω.

The right-hand panel of fig. 2 shows the frequency dependence of $N_{\text{eff}}(\omega)$ for the family of $La_{2-y}Sr_yCuO_4$ crystals. In undoped samples the major part of the spectral weight is accumulated from energies exceeding E_g, whereas in the region $\omega < 1.5$ eV, $N_{\text{eff}}(\omega)$ develops a plateau. With increasing y, the low-frequency spectral weight builds up rapidly. For $y < 0.1$, $N_{\text{eff}}(\omega < 1.5\text{ eV})$ varies nearly linearly with y. This growth of N_{eff} occurs at a faster rate than one would expect within the assumption that each Sr ion donates 1 hole per unit cell with an effective mass equal to the free-electron mass m_e. As shown by S.L. Cooper et al. (1990), a faster than expected growth of N_{eff} is also found for electron-doped $Pr_{2-y}Ce_yCuO_4$ materials. The slope of the N_{eff} versus y dependence is even steeper for electron-doped $Pr_{2-y}Ce_yCuO_4$ and $Nd_{2-y}Ce_yCuO_4$ (S.L. Cooper et al. 1990, Arima et al. 1993) than for hole-doped La214.

It follows from fig. 2 that doping affects electronic excitations located below 3 eV. Indeed, $N_{\text{eff}}(\omega)$ spectra converge at about 3 eV for all $y < 0.2$. An unexpected result of fig. 2 is that at $y > 0.2$, the total spectral weight *decreases* so that N_{eff} shows a non-monotonic dependence as a function of y, with the maximum located around $y = 0.2$ in the La214 series. Puchkov et al. (1996b) have analyzed the variation of the spectral weight with doping in a variety of high-T_c materials. Their conclusion is that N_{eff} either saturates or even decreases above optimal doping which was defined as the carrier density that corresponds to the maximum critical temperature.

Thus, the evolution of the in-plane spectral weight in cuprates with hole/electron doping reveals the following principal trends:

(i) the CT gap is filled with states which were located above E_g in undoped materials;
(ii) the total spectral weight ($\sigma(\omega)$ integrated up to 3 eV) is unchanged at small or moderate dopings and is suppressed in the overdoped regime ($y > 0.2$);
(iii) the low-frequency N_{eff} ($\sigma(\omega)$ integrated up to 1.5 eV) increases faster than y in underdoped samples and is suppressed in the overdoped regime.

Points (i)–(iii) should first be contrasted with the behaviour of a Fermi liquid with a large Fermi surface. Doping with holes reduces the size of the Fermi surface and one

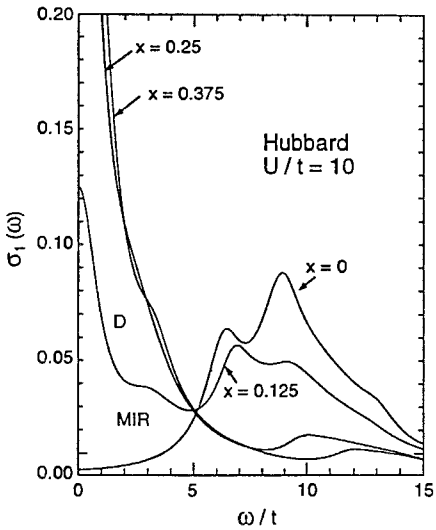

Fig. 3. The optical conductivity calculated within a one-band Hubbard model on a 4×4 cluster (Dagotto 1994). Parameter x stands for the hole-doping fraction. Calculations reproduce the principal trends of the experimental data on the evolution of the electromagnetic response with doping. In particular, theoretical spectra reveal: (i) the transfer of the spectral weight from the CT excitation to the low-frequency region; (ii) development of "mid-infrared" absorption at light doping (x = 0.125) and (iii) growth of the Drude-like feature at higher dopings ($x > 0.2$). Note that the isobestic point at $\omega/t = 5$ is also reproduced.

expects to see a *decrease* of spectral weight with doping x as $1 - x$ rather than the observed dependence that is proportional to x. On the other hand, these features seem to be generic for a broad variety of *Mott insulators,* including cuprates (S.L. Cooper et al. 1990, Orenstein et al. 1990, Arima et al. 1993), nickelates such as $La_{2-y}Sr_yNiO_4$ (Katsufuji et al. 1996), transition-metal oxides such as $(La,Pr,Nd,Sm,Y)_{2-x}Ca_xTiO_3$ (Katsufuji et al. 1995), spin-ladder compounds (Osafune et al. 1997) and vanadium oxides (Thomas et al. 1994, Rozenberg et al. 1995).

The Mott–Hubbard picture, which accounts for the AF insulator state of undoped compounds, also helps us in understanding the changes in the redistribution of the spectral weight with doping. The Hubbard model has two principal energy scales, U and t, and both can give rise to observable features of the optical conductivity. In the half-filled case, one expects to find an absorption band centered at U. Simple charge-counting arguments suggest that the spectral weight associated with this interband transition will decrease with hole doping while its energy remains unchanged (Stephan and Horsch 1990). This is clearly shown in fig. 3 where results of calculations for a one-band Hubbard model are presented (Dagotto 1994). Dagotto obtained spectra of $\sigma_1(\omega)$ that reproduce the principal trends of the experimental data for cuprates. The spectral weight removed from the CT transition is recovered at lower energies on the order of t. Note that the conductivity is identical for the hole doping fractions $x = 0.25$ and $x = 0.375$. This corresponds to a *non-monotonic evolution of the spectral weight* in the intragap region. This latter result is reproduced in several other calculations starting from a Mott–Hubbard Hamiltonian (Stephan and Horsch 1990, Jarell et al. 1995, Kajueter et al. 1996). Another noticeable feature of the theoretical spectra presented in fig. 3 is an isobestic point at $\omega/t = 5$. If t is taken to be equal to 0.3–0.4 eV as some calculations suggest (Hybertsen et al. 1990, Bacci et al. 1991), the calculated position of this point and of the CT gap $E_g \approx 6t$ would

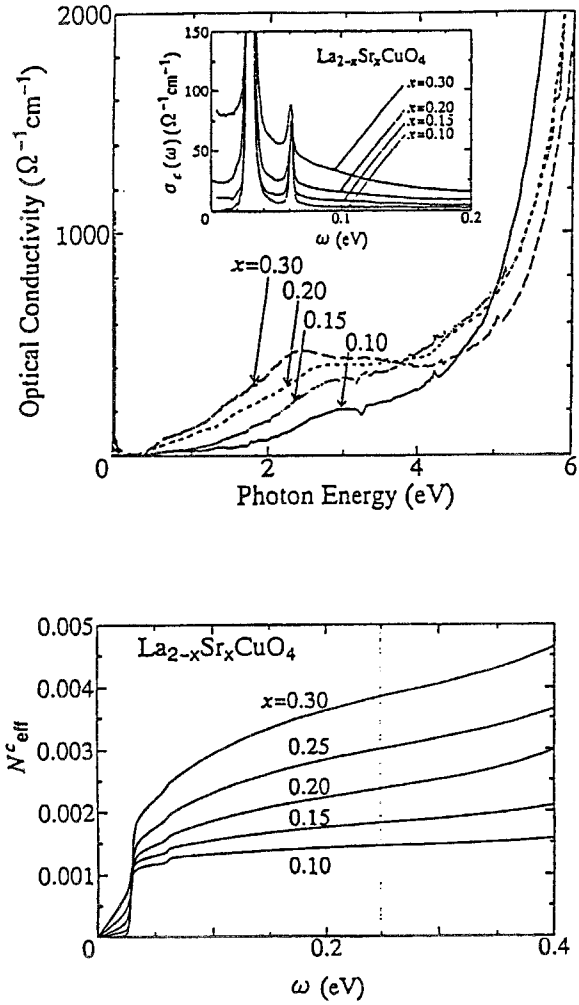

Fig. 4. The c-axis optical conductivity (top panel) and the effective spectral weight determined from eq. (4) for a series of $La_{2-x}Sr_xCuO_4$ single crystals (Uchida et al. 1996).

agree with experiment. Finally, by taking into account hybridization effects it was possible to reproduce the asymmetry between the doping dependence of the spectral weight for holes and for electrons (Eskes et al. 1991, Meinders et al. 1993, Tanner et al. 1996).

The doping dependence of the interplane c-axis conductivity has been studied so far only for La214 (Uchida et al. 1996) and $YBa_2Cu_3O_x$ (Homes et al. 1995a,b, Tajima et al. 1997). A brief examination of fig. 4 (the c-axis spectra for $La_{2-y}Sr_yCuO_4$) reveals an important difference between the in-plane and interplane properties. First, the CT gap at 1.5 eV is not seen in the interplane conductivity of La_2CuO_4. The electronic contribution to $\sigma_c(\omega)$ is strongly suppressed at $\omega < 5$ eV. The anisotropy of N_{eff} integrated up to 2 eV is as high as 10.

Upon doping, a certain part of the spectral weight in the 5–6 eV region is transferred to low frequencies. The c-axis spectral weight $N_c(y)$ integrated up to 2 eV increases linearly up to $y = 0.2$ and then saturates at higher dopings. This tendency resembles the behavior of $N_{ab}(y)$ (fig. 2). However a closer comparison of $N_{ab}(y)$ and $N_c(y)$ shows that the relative fraction of the spectral weight transferred to low frequencies is larger for the interplane conductivity. As a result, the anisotropy of N_{ab}/N_c decreases from 10 in undoped compounds down to 3 in overdoped materials. The anisotropy of the spectral weight should be distinguished from the anisotropy of the free-carrier (Drude) plasma frequencies $\omega_{pD}^2 = 4\pi ne^2/m^*$, where n is the concentration of free carriers and m^* is their effective mass. That is because the integral in the definition of $N_{eff}(\omega)$ includes the contributions of both free *and* bound carriers which both give rise to the conductivity at $\omega < E_g$. The analysis of the possible mechanisms behind the absorption in the intragap region is the subject of the next subsection.

We conclude this subsection by noting that Nd_2CuO_{4-z}, La_2CuO_{4+z} and some other materials could be doped not only by substitution of Nd or La with Ce or Sr but also by partial removal or addition of oxygen. Quijada et al. (1995) have studied the conductivity of oxygen-doped $La_2CuO_{4.12}$ – an Sr-free material with T_c as high as 40 K. Their results for the in-plane conductivity are in agreement with the data of Uchida et al. (1991) for the Sr-doped crystal near the optimal doping. This suggests that there is an equivalence between different approaches that introduce carriers in the CuO_2 planes.

3.4. *Excitations in mid-infrared frequencies*

The detailed analysis of the optical conductivity in the CT gap region reveals several distinct features which are particularly well resolved in samples with dilute concentration of charge carriers (figs. 2 and 5): (i) a broad resonance at 0.5 eV, which shows considerable softening as doping increases; (ii) a resonance at 0.25 eV; (iii) a Drude-like peak at $\omega = 0$. The existence of well-separated absorption features in the frequency dependence of $\sigma_{ab}(\omega)$ is the basis for multicomponent analysis of the conductivity. Within this approach (Tanner and Timusk 1992) the conductivity is assumed to have the form

$$\sigma(\omega) = \frac{\omega_{pD}^2 \tau}{4\pi(1 + i\omega\tau)} + \sum_k \frac{\omega_{pk}^2}{\omega(\omega_k - 1 - i\omega\gamma_k)}. \tag{5}$$

In eq. (5) the first term stands for the Drude free-carrier conductivity with plasma frequency ω_{pD} and scattering rate $1/\tau$. The second term accounts for the additional contributions to the conductivity that are modeled with Lorentzian oscillators centered at frequency ω_k with plasma frequency ω_{pk} and damping γ_{pk}. These additional contributions are assigned to two-magnon excitations, interband transitions, polarons and impurity states.

Thomas et al. (1992) have shown that peaks at 0.25 eV and 0.5 eV are found in a variety of cuprates including $YBa_2Cu_3O_{6+x}$, La_2CuO_{4+y} and Nd_2CuO_{4-y}. They analyzed the positions of these peaks and compared them with other related energy scales in these

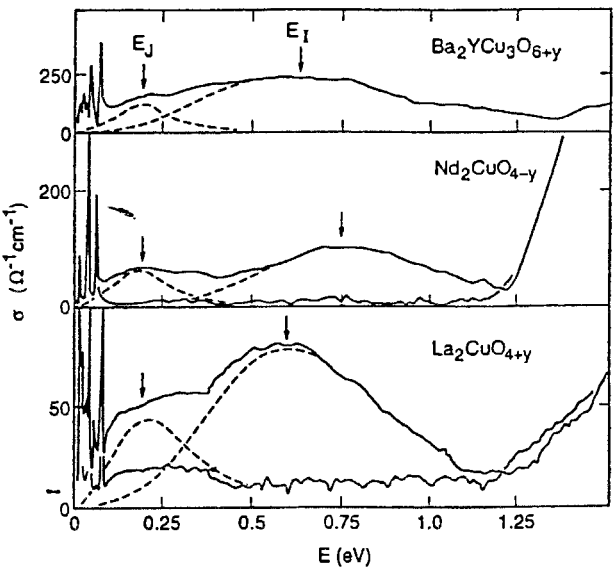

Fig. 5. Excitations in the mid-infrared range in lightly doped crystals of $Ba_2YCu_3O_{6+y}$, Nd_2CuO_{4-y} and La_2CuO_{4+y} (Thomas et al. 1992). In lightly doped crystals one can easily distinguish between several different absorption features in the mid-infrared.

materials. The frequency positions of the peaks do not scale in a simple way with the magnitude of the CT gap E_g. The location of the 0.25 eV feature is close to the Cu–Cu exchange energy J.

Interpretation of the structure in mid-infrared in terms of polarons has attracted a lot of attention. As pointed out by Falck et al. (1992), a polaron absorption model quantitatively describes the broadening of the charge-transfer excitation peak. Bi and Eklund (1993) applied the polaronic model to the analysis of the conductivity for $La_{2-y}Sr_yCuO_{4+\delta}$ and for $La_{2-y}Sr_yNiO_{4+\delta}$. Polaron-transport theory provides reasonably accurate fits to the measurements of the photo-induced infrared conductivity in $Tl_2Ba_2Ca_{0.98}Gd_{0.02}Cu_2O_8$, $YBa_2Cu_3O_{6.3}$ and La_2CuO_4 (Mihailovic et al. 1990).

The mid-infrared conductivity in undoped and lightly doped cuprates has also been discussed in terms of polarons by Dewing and Salje (1992), by Alexandrov et al. (1993) and by Yagil and Salje (1996). Calvani et al. (1996) have argued that the polaronic features persist in superconducting samples of $Nd_{2-y}Ce_yO_{4-\delta}$. Dolgov et al. (1997) have fitted the *ab*-plane conductivity data (Gao et al. 1993a) for superconducting La214 using a broad Lorentzian term that they associate with a polaron band. These and many other experiments suggest that electron–phonon interaction is an important factor in the electromagnetic response of cuprates. This interaction may be responsible for peculiar features in the conductivity spectra such as anomalous coupling of the in-plane charge carriers to the *c*-axis longitudinal modes first observed by Reedyk and Timusk (1992) or

a broad peak at 340 cm^{-1} seen in the c-axis spectra of underdoped Y123 crystals (Homes et al. 1993b, 1995b, Basov et al. 1994a, Hauff et al. 1996).

However, there is very little evidence to support the idea that interaction with the lattice modes in any form is the dominant mechanism of superconductivity at high critical temperatures. Allen (1992) and Emery and Kivelson (1995a) have pointed out a paradoxical situation with the electron–phonon interaction in cuprates and other doped insulators. In models based on the polaronic interpretation of the optical conductivity, or in models explaining the temperature dependence of the phonon frequencies (for a review see Litvinchuk et al. 1994), the electron–phonon interaction would be quite strong. However, there are no signatures of strong electron–phonon coupling in the transport properties. The in-plane resistivity of many cuprates varies linearly with T over the temperature region from T_c up to 1000 K with a zero intercept on the temperature axis, which is inconsistent with scattering of charge carriers by phonons where an intercept on the temperature axis of the order of θ_D is expected.

Perkins et al. (1993) have observed a feature at 0.35 eV in the absorption of the undoped materials La_2CuO_4, $Sr_2CuO_2Cl_2$, Nd_2CuO_4 and Pr_2CuO_4. Recently this weak absorption was also found in $YBa_2Cu_3O_6$ (Grüninger et al. 1996, Tanner et al. 1996). According to Lorenzana and Sawatzky (1995) this peak originates from the creation of a two-magnon quasibound state which is coupled to an optical phonon. Magnons are not expected to give rise to infrared absorption in materials with inversion symmetry such as La_2CuO_4 and other systems studied by Perkins et al. (1993). However, in a process involving a phonon and two magnons the symmetry of the lattice is effectively lower, and this absorption becomes allowed. Calculations reproduce the lineshape of the main band and indicate that the weak structure in the region of 0.6–1.2 eV may originate from higher-order processes. The magnitude of the superexchange energy $J = 0.121$ eV used in these calculations is close to estimates based on Raman scattering (Lyons et al. 1988). Also, the theory predicts a very different lineshape for structurally similar La_2NiO_4 in which Ni (spin 1) replaces copper (spin $\frac{1}{2}$). The experimental data obtained by Perkins et al. (1995) for Ni-based compounds indeed reveal different lineshape for the mid-infrared absorption.

4. Charge dynamics in the normal state

4.1. *One-component versus multicomponent description of the in-plane conductivity*

As the doping level increases, the sharp features in the mid-infrared energies acquire an increasing amount of oscillator strength (fig. 2). It is also more difficult to resolve these features in the superconducting phases as they blend into the broad Drude peak centered at zero frequency and a featureless background extending throughout the whole mid-infrared range. The La214 system is perhaps the only compound where well-structured mid-infrared absorption is observed in superconducting phases (Uchida et al. 1991, Startseva et al. 1999a,b). In most other cuprates, including Y123, Y124, Bi2212, Nd214, Tl2201 and others, the conductivity spectra obtained for metallic and superconducting phases

show smooth mid-infrared conductivity without any characteristic absorption bands. At frequencies below 500–800 cm^{-1} this behavior evolves into a Drude-like feature. It is important to emphasize that the qualifier "Drude-like" is used here only to indicate that the conductivity shows a peak centered at zero frequency which is typical for the response of a Drude metal. The detailed analysis of the lineshape of this feature shows that it *does not* have the Lorentzian shape suggested by a simple Drude formula (first term in eq. 5). Indeed, the fall-off of $\sigma_1(\omega)$ in Y123 and all other cuprates is significantly *slower* than is prescribed by eq. (5). As discussed in detail by Orenstein et al. (1990), it is impossible to fit the conductivity with a simple Drude formula. If the scattering rate in the Drude equation is set at a low value to reproduce the shape of the low-frequency peak in $\sigma_1(\omega)$, then the fit is completely wrong at higher frequencies. If the width of the Drude peak is chosen to be anomalously broad in accord with the behavior of the conductivity at $\omega > 600\,cm^{-1}$, then the model yields the wrong magnitude of the low-ω behavior and reveals strong disagreement with the dc conductivity.

The smooth mid-infrared continuum that follows the peak at $\omega = 0$ is found not only in doped cuprates, but also in ruthenates, cobaltates, and nickelates (Bozovic et al. 1994, Gervais et al. 1988), and thus may be regarded as another generic feature of the doped Mott insulator. Two principal approaches are commonly used to describe the deviations of the conductivity in mid-infrared frequencies from the Drude formula: a *multicomponent* and a *one-component* model. As pointed out in the previous subsection, the basic argument in favor of the multicomponent scenario (eq. 5) is that the spectra obtained for lightly doped materials reveal distinct and well-separated absorption resonances which evolve into a smooth background that blends in with the Drude band as one proceeds with doping. On the contrary, within the single-component approach it is assumed that the sole cause of the frequency dependence of $\sigma(\omega)$ is the response of itinerant carriers which acquire a frequency-dependent scattering rate $1/\tau(\omega)$ and a frequency-dependent mass $m^*(\omega)$ as the result of strong interactions in a system. This formalism is commonly referred to as the "extended Drude model":

$$\sigma(\omega, T) = \frac{1}{2\pi} \frac{\omega_{pD}^2}{1/\tau(\omega, T) - i\omega[m^*(\omega, T)/m]}. \tag{6}$$

Both single- and multicomponent approaches have their advantages and important shortcomings. The former picture offers a better treatment of the response at low frequencies. But its applicability at energies of the order of 1 eV is meaningless since at these high energies there are additional (interband) contributions to $\sigma(\omega)$. The effective mass $m^*(\omega)$ becomes negative at frequencies above $7000\,cm^{-1}$, clearly supporting the view that the high-energy part of the spectrum is influenced by additional excitations (Puchkov et al. 1996a). Band-structure calculation predict a rich variety of interband transitions in the frequency range starting from $1000\,cm^{-1}$ (Maksimov et al. 1989). However, it is not easy to separate contributions to the conductivity arising from "free" and "bound" carriers because there are no experimentally detectable signatures of the crossover from one behavior to another.

In an attempt to come up with a more rigorous procedure to separate the "free" carrier response from mid-infrared term, Romero et al. (1992) have analyzed the superconducting state response of $Bi_2Sr_2CaCu_2O_8$ single crystals. They assumed that at $T \ll T_c$, all free carriers condense and their spectrum consists simply of a delta function at $\omega = 0$. This is a reasonable picture since various experiments suggest that the in-plane response of high-T_c superconductors is in the clean limit (Bonn et al. 1992). The condition for the clean limit is that the residual *elastic* scattering rate due to impurities is much smaller than the magnitude of the superconducting gap. Thus, the remaining contribution to $\sigma(\omega)$ may be assigned to the mid-infrared term. Following this logic, the difference between the spectra in the normal state and in the superconducting state, $\sigma_1^I(\omega, T) = [\sigma_1(\omega, T > T_c) - \sigma_1(\omega, T \ll T_c)]$, yields the free-carrier contribution to the normal state conductivity.

Several qualitative arguments suggest that it is probably safe to employ the single-component picture to analyse the data at energies below 4000 cm^{-1}. First, as noted by Thomas et al. (1988), the number of carriers that one obtains using the sum-rule analysis for $\sigma_1(\omega)$ is consistent with estimates from chemical-valence arguments for the carrier density, provided the integration in eq. (2) is carried out up to a cut-off frequency ~8000 cm^{-1}. This is in accord with the notion that the response of conducting carriers is predominant at frequencies at least up to 4000 cm^{-1}. A somewhat similar estimate of the high-frequency limit of applicability of the one-component picture can be deduced indirectly from the fact that the temperature dependence of $\sigma_1(\omega)$ is also restricted to frequencies below 3000–4000 cm^{-1}. It is natural to assign the temperature-dependent part to "free" carriers while the temperature-independent contribution may be associated with mid-infrared terms due to bound carriers. Recently, Atkinson and Carbotte (1997) calculated the interband contribution from chain–plane transitions and found that in the case of Y123 the contribution to the *c*-axis response was substantial, but that for the *ab*-plane conductivity was a minor factor at $\omega < 2000$ cm^{-1}, suggesting that the main response comes from the intraband (Drude) processes.

4.2. *Models for the frequency-dependent scattering rate and effective mass*

In using the one-component model one should separate two steps of this analysis: (i) the extraction of the frequency-dependent scattering rate $1/\tau(\omega, T)$ and of the mass enhancement m^*/m_e from the experimental data; and (ii) the assignment of particular physical meaning to the spectra of $1/\tau(\omega, T)$ and m^*/m_e. The former step is a legitimate procedure since $1/\tau(\omega, T)$ and m^*/m_e can be viewed as the real and imaginary parts of another response function, the memory function $M(\omega)$ (Allen and Mikkelsen 1976, Mori 1965, Götze and Wölfle 1972). Expressing $\mathrm{Re}\,(M(\omega))$ and $\mathrm{Im}\,(M(\omega))$ through the complex conductivity one obtains the following relations:

$$\frac{1}{\tau(\omega)} = \frac{\omega_{pD}^2}{4\pi}\mathrm{Re}\left(\frac{1}{\sigma(\omega)}\right), \tag{7}$$

$$\frac{m^*}{m_e} = -\frac{\omega_{pD}^2}{4\pi}\frac{1}{\omega}\mathrm{Im}\left(\frac{1}{\sigma(\omega)}\right). \tag{8}$$

Since $\sigma(\omega)$ is causal, the scattering rate and the mass enhancement are not independent, and are connected through the Kramers–Kronig integral equation:

$$\frac{m^*}{m_e} = \frac{2}{\pi}\mathcal{P}\int_0^\infty \frac{1/\tau(\Omega)}{\Omega^2 - \omega^2}\,\mathrm{d}\Omega - 1. \tag{9}$$

From the discussion above it follows that $1/\tau(\omega)$ and m^*/m_e can be viewed as *optical constants*. For example, $1/\tau(\omega)$, if multiplied by the constant plasma frequency, can be viewed as a kind of optical resistivity (reducing to the dc resistivity at zero frequency). The spectra of $1/\tau(\omega)$ and m^*/m_e describe the response of a system to the electromagnetic field with the same success as any other pair of optical constants such as the conductivity or the dielectric function. Clearly, $1/\tau(\omega)$ and m^*/m_e do not contain new physical information as compared to the complex conductivity, but this description turns out to be much more enlightening in several cases as will be shown below.

However, the *interpretation* of $1/\tau(\omega)$ and m^*/m_e obtained from the one-component analysis is more difficult. Obviously, it is tempting to assign the frequency-dependent effective mass and the scattering rate to the real and imaginary parts of the electronic self-energy $\Sigma(\omega) = \Sigma_1(\omega) + i\Sigma_2(\omega)$ entering the equation for the spectral function of the electronic excitation $A(k, \omega)$:

$$A(\boldsymbol{k}, \omega) = -\frac{1}{\pi}\left|\mathrm{Im}\, G(\boldsymbol{k}, \omega)\right| = \frac{1}{\pi}\frac{\mathrm{Im}\,\Sigma(\omega)}{(\omega - \epsilon_k - \mathrm{Re}\,\Sigma(\omega))^2 + (\mathrm{Im}\,\Sigma(\omega))^2}. \tag{10}$$

Here, $G(k, \omega)$ is the Green's function of the electronic excitation. A connection between the effective mass and the scattering rate with the self-energy,

$$\Sigma(\omega) = 1 - \frac{m^*(\omega)}{m} - \frac{i}{\tau(\omega)}, \tag{11}$$

can be justified for a Fermi liquid in the limit of zero temperature. However, even in this simple case one should distinguish *transport* mass or relaxation rate, which are calculated theoretically, from the *optical* mass or relaxation rate which can be obtained from infrared experiments (Allen 1971, Shulga et al. 1991). A more complex situation arises in cuprate high-T_c superconductors where applicability of the Fermi liquid picture itself is questionable (Anderson 1987, Littlewood and Varma 1992, Emery and Kivelson 1995a).

Keeping in mind possible caveats with respect to the interpretation of the results inferred from the extended Drude model, we find that this approach to the data analysis is extremely fruitful and provides important insights into the charge dynamics in cuprates. It is instructive to examine the behavior of the frequency-dependent scattering rate and of the effective mass within simple models. Here we restrict ourselves to one model developed

by Allen (1971) for electron–boson scattering. For the case of finite temperatures, this model was generalized by Shulga et al. (1991):

$$\frac{1}{\tau}(\omega, T) = \frac{\pi}{\omega}\int_0^\infty d\Omega\, A(\Omega)\left[2\omega \coth\left(\frac{\Omega}{2T}\right) - (\omega+\Omega)\coth\left(\frac{\omega+\Omega}{2T}\right) + (\omega-\Omega)\coth\left(\frac{\omega-\Omega}{2T}\right)\right] + \frac{1}{\tau_{\text{imp}}}. \tag{12}$$

In this equation $A(\Omega)$ is a phonon (or more generally bosonic) density of states weighed by the amplitude for the large-angle scattering on the Fermi surface.

Figure 6 presents the results of calculations using eq. (12) (Puchkov et al. 1996a). The form of bosonic spectrum used for the calculations is a rectangle confined between $\omega_0/2$ and $2\omega_0/2$ (top panel). The lower panels show the real part of the conductivity, the relaxation rate and the mass enhancement. An obvious result of fig. 6 is that the effective mass at low temperatures is strongly enhanced by the electron–boson interaction. "Heavy" carriers dragging a bosonic cloud are more difficult to scatter, which may explain the suppression of $1/\tau(\omega)$ and of the width of the Drude-like feature in $\sigma_1(\omega)$ at low temperatures. This situation is known from studies of heavy-fermion materials where anomalously high effective masses lead to the formation of an extremely narrow mode in the spectra of $\sigma_1(\omega \to 0)$ (Bonn et al. 1988, Sulewski et al. 1988, Awasthi et al. 1993). Another way to understand the suppression of $1/\tau(\omega)$ is to turn to Allen's formula for the scattering rate in the limit of $T = 0$ when $1/\tau(\omega) \propto \int_0^\infty d\Omega\, A(\Omega)$. At low frequencies ($\omega < \omega_0/2$), the scattering rate $1/\tau(\omega)$ is small since there are no energetically accessible scattering excitations in this frequency range. As soon as the scattering channels become available ($\omega > \omega_0$), the scattering rate rapidly increases. However, by increasing the frequency above the high-energy cut-off ($3\omega_0/2$) one does not gain any additional scattering channels, which accounts for the saturation of $2/\tau(\omega)$ in the high-energy part of the spectra.

Recently, Carbotte et al. (1999) inverted eq. (12) in an attempt to extract the frequency dependence of the spectral function $A(\Omega)$. They found that $A(\Omega)$ peaks at approximately 40 meV in the optimally doped Y123 compounds. This energy coincides with the frequency or the resonant mode at (π, π) found in neutron scattering experiments. Further analysis revealed common trends in temperature and doping dependence of the neutron mode and the spectral function $A(\Omega)$. These results were interpreted in terms of strong coupling between the charge carriers and magnetic degrees of freedom.

It is important to mention one serious deficiency of the extended Drude analysis. This formalism is based on an isotropic version of Fermi-liquid theory which is highly questionable in cuprates where the electronic structure is in fact very anisotropic in the *ab*-plane. One approach that addresses this problem is to first calculate the conductivity, using a proper anisotropic theory with k-dependent Fermi velocity and scattering rate $1/\tau$, and then use the real and imaginary parts of the calculated conductivity to find the effective scattering rates $1/\tau(\omega)$ and m^*. Some steps in that direction have been made by Stojkovic and Pines (1996) and Branch and Carbotte (1998).

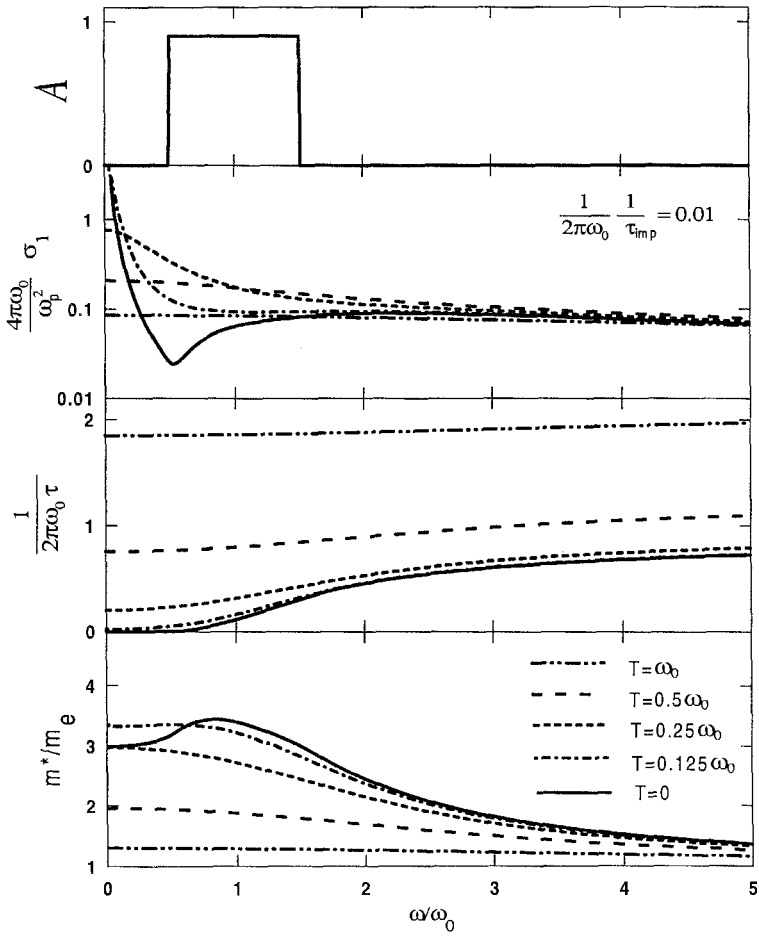

Fig. 6. Electron–boson model calculations (from Puchkov et al. 1996a). The top panel shows the bosonic spectral density, here a "square" spectrum; the next panel shows the optical conductivity; the third panel shows the scattering rate, and the bottom panel shows the mass renormalization. The coupling constant is equal to 1.

4.3. *Experimental results: in-plane conductivity*

The one-component analysis of the optical conductivity of $YBa_2Cu_3O_x$ was first applied by Thomas et al. (1988) and later employed by many groups to describe the response of a variety of high-T_c superconductors (Collins et al. 1989, Orenstein et al. 1990, Schlesinger et al. 1990, Rotter et al. 1991, Thomas et al. 1991, Bucher et al. 1992, S.L. Cooper et al. 1992, 1993a, Wachter et al. 1994, El Azrak et al. 1994, Basov et al. 1996, Puchkov et al. 1996c). The principal results of this analysis, which have attracted a great deal of attention can be formulated as follows: (i) the spectra of $1/\tau(\omega)$ taken at room temperature are nearly linear with ω over a broad range of frequencies and do not show any indications

of saturation at frequencies as high as 0.5 eV; (ii) the absolute value of $1/\tau(\omega)$ is on the order of the frequency. In particular (ii) challenges the applicability of the Fermi-liquid theory to high-T_c superconductors, since one of the basic assumptions of this theory is that the quasiparticle damping is much lower than the quasiparticle energy. Experimental results clearly suggest that this assumption is violated in (super)conducting phases of cuprates. From (i) and (ii) it appears that charge carriers in cuprates are heavily dressed due to strong interactions which are likely to be of electronic or magnetic origin.

A detailed discussion of the charge dynamics in cuprates from underdoped to overdoped regimes was reported by Puchkov et al. (1996a). Since it is difficult to access all doping regimes using one family of cuprates, they used Y123, Y124, Bi2212 and Tl2201 materials which in combination allow one to follow the general trends in the evolution of the electromagnetic response throughout the entire phase diagram. Below we review the main results of their studies.

Underdoped cuprates. The electromagnetic response of these materials has an additional temperature scale or crossover temperature T^* which can be as high as 300 K in strongly underdoped materials but which is diminished as doping increases toward optimal. The scattering rate is nearly linear with ω at $T > T^*$ (fig. 7), but at $T < T^*$, $1/\tau(\omega)$ is suppressed at low frequencies. This suppression corresponds to the rapid narrowing of the Drude-like feature in the conductivity spectra. A decrease of the scattering rate occurs only at low frequencies ($\omega < 700\,\mathrm{cm}^{-1}$) while at higher energies $1/\tau(\omega)$ is nearly temperature independent. The remarkable feature of underdoped samples is that electromagnetic response in the pseudogap state which is realized at $T_c < T < T^*$ is very similar to that in the superconducting state. The bottom panel of fig. 7 shows that interactions in underdoped materials lead to an enhancement of the effective mass of conducting carriers by as much as a factor of 5.

Optimally doped samples. Close to optimal doping, the threshold structure in the spectra of $1/\tau(\omega)$ at $T > T_c$ is either strongly suppressed (as in Bi2212 and Tl2201) or disappears completely (Y123) (fig. 8). The normal-state scattering rate in these crystals is a linear function of frequency and of temperature (Gurvitch and Fiory 1987). However, the behavior of $1/\tau(\omega)$ and m^* in the superconducting state is very similar to the behavior in the pseudogap state for underdoped crystals. The diminishing of $1/\tau(\omega \to 0)$ in the superconducting state is consistent with the observation of an abrupt drop of the scattering rate in the optimally doped samples at $T < T_c$ (Bonn et al. 1992, Romero et al. 1992). One difference from underdoped materials is that $1/\tau(\omega)$ acquires a weak temperature dependence at high frequencies. The effective mass of conducting carriers is somewhat reduced compared to the underdoped phases and does not exceed a factor of 3 in the normal state.

Overdoped crystals. In overdoped samples, a threshold structure in the $1/\tau(\omega)$ spectra is not observed (fig. 9). In sharp contrast to underdoped materials, the scattering rate shows a temperature dependence over a much broader frequency range, extending at least up to $2000\,\mathrm{cm}^{-1}$. There are indications that the frequency dependence of $1/\tau(\omega)$ becomes superlinear in the strongly overdoped cuprates. The overall magnitude of $1/\tau(\omega)$ is reduced compared to underdoped or even optimally doped materials. The effective

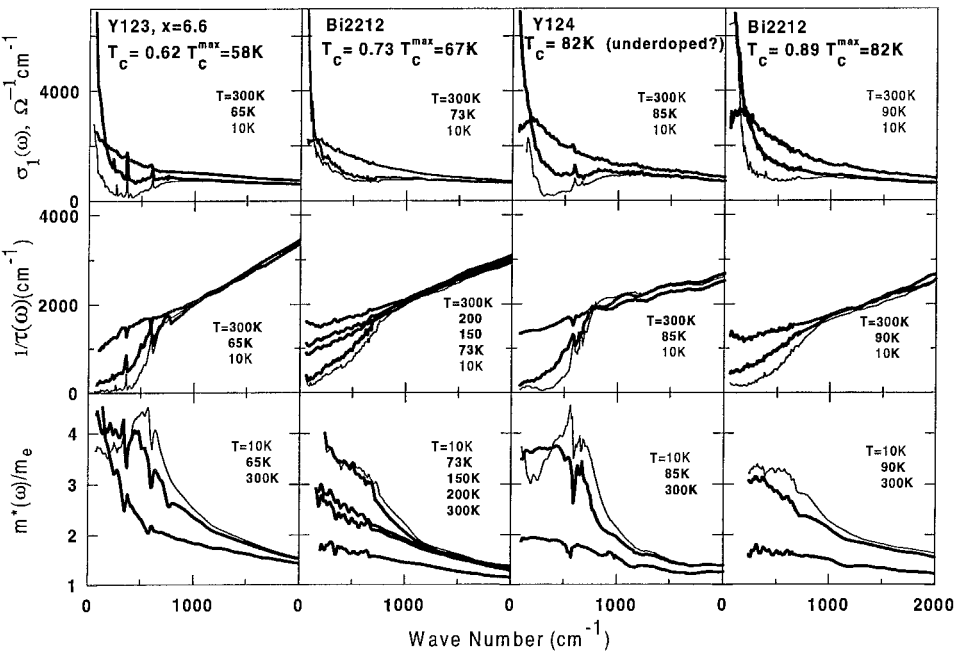

Fig. 7. Optical constants (in-plane) for a series of *underdoped* high-T_c superconductors. Top row: real part of the optical conductivity. Middle row: frequency dependent scattering rate. Bottom row: mass renormalization. Experimental data for Y123 and Y124 compounds from Basov et al. (1996); for Bi2212 compounds from Puchkov et al. (1996b). The scattering rate curves are essentially temperature independent above 1000 cm^{-1} but develop a depression at low temperature and at low frequency. The effective mass is enhanced at low temperature and at low frequency. Experimental results in the normal state at $T \approx T_c$ and in the superconducting state are remarkably similar.

mass is very close to m_e. These two results indicate that charge carriers in overdoped cuprates are no longer heavily dressed due to electron–electron and/or electron–boson interactions. Thus the sequence of figs. 7–9 reveals the evolution from a strongly correlated solid with interactions-enhanced effective mass to a weak-interaction material with $m^* \approx m_e$ as exemplified by overdoped Tl2201. Unfortunately, the experimental results for overdoped crystals are only fragmentary, and we are unaware of any systematic studies of charge dynamics in the overdoped regime besides those depicted in fig. 9. Therefore it remains to be seen if overdoping eventually leads to Fermi-liquid behavior. Based on the existing results for Tl2201 such a conclusion would be premature.

Figure 10 presents a simplified phase diagram based on the experimental results discussed above. The characteristic temperatures T^* and T_c are plotted as functions of the carrier density in the CuO_2 planes. We have chosen the superfluid density ω_{ps} for the horizontal axis in this particular plot because the magnitude of ω_{ps} can be determined unambiguously from infrared results (see sect. 5.1). Evaluation of the free-carrier density

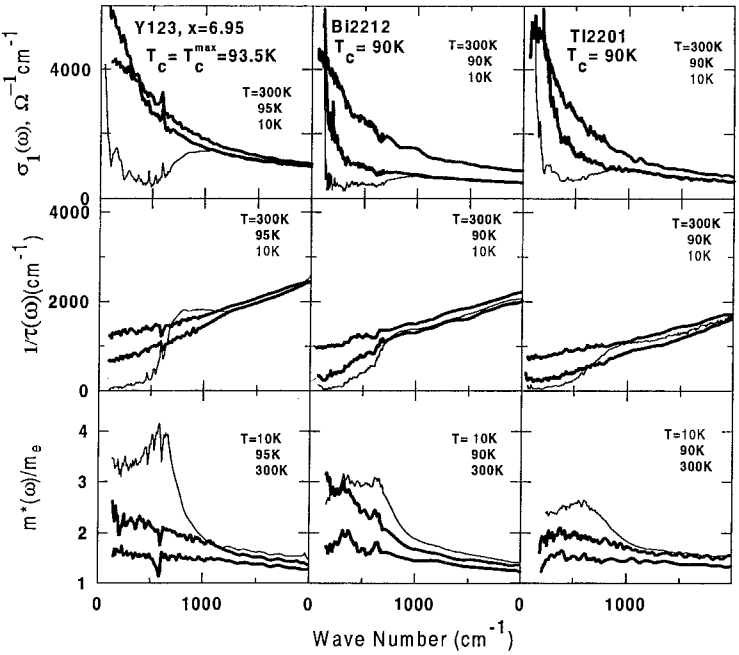

Fig. 8. Optical constants (in-plane) for a series of *optimally doped* high-T_c superconductors. Top row: real part of the optical conductivity. Middle row: frequency-dependent scattering rate. Bottom row: mass renormalization. Experimental data for Y123 compounds from Basov et al. (1996); for Bi2212 and Tl2201 compounds from Puchkov et al. (1996b). Depression of the scattering rate at low frequencies is now observed only in the superconducting state. Also, the spectra of $1/\tau(\omega)$ acquire some temperature dependence at high frequencies.

is difficult since the free-carrier contribution to $\sigma(\omega)$ is mixed up with the response of the bound carriers as discussed in sect 4.1.

In the underdoped samples there is considerable difference between T_c and T^*. The latter can be nearly as high as room temperature. There are indications that in the La214 series, T^* can exceed 300 K (Startseva et al. 1999a). A detailed examination of this issue will require infrared experiments to be conducted at elevated temperatures. As the doping is increased, T^* is suppressed while T_c increases. In the Y123–Y124 series, the two boundary lines merge close to optimal doping. But both in Bi2212 and in La214 (Puchkov et al. 1996c, Startseva et al. 1999a), the pseudogap can be seen in overdoped samples and $T^* > T_c$ at optimal doping. Combining the phase diagram of fig. 10 and the experimental data for under- and optimally doped cuprates (figs. 7, 8) it appears that the temperature T^* is associated with qualitative changes in the in-plane electrodynamics. Indeed, below this cross-over temperature the conductivity spectra show a significant narrowing of the Drude-like feature and a threshold structure around 500 cm^{-1}. In crystals for which $T^* \gg T_c$, a further decrease of temperature below T_c does not lead to significant changes in the conductivity, apart from the formation of the delta peak at $\omega = 0$ that will be discussed in sect. 5. So far, there is not enough experimental information to extend the

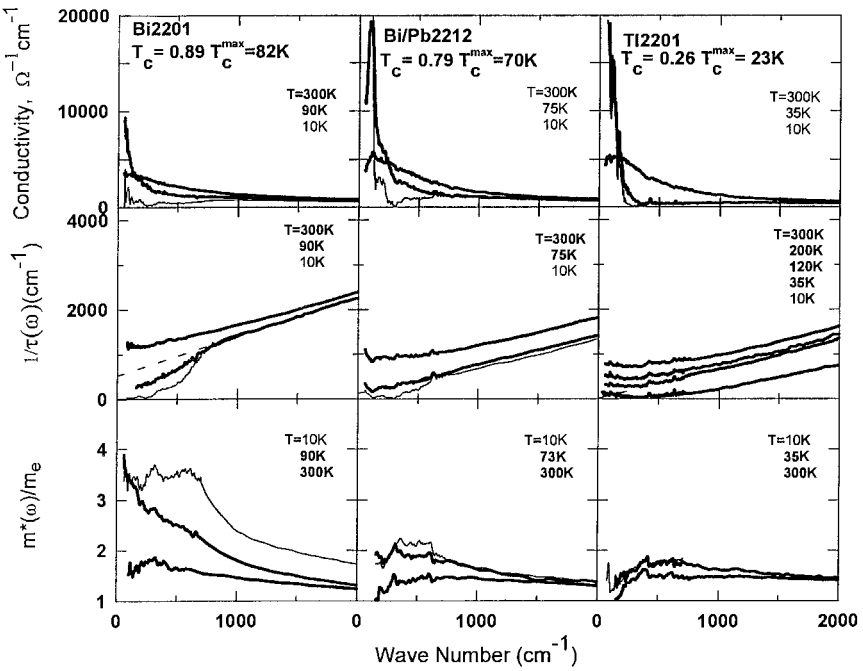

Fig. 9. Optical constants (in-plane) for a series of *overdoped* high-T_c superconductors. Top row: real part of the optical conductivity. Middle row: frequency dependent scattering rate. Bottom row: mass renormalization. Experimental data from Puchkov et al. (1996b). Note that the overall magnitude of $1/\tau(\omega)$ progressively decreases with doping.

phase diagram into the overdoped regime. The charge dynamics in strongly overdoped samples have been studied only for T2201 (Puchkov et al. 1996c), and it remains to be seen whether other systems will behave in a similar fashion in other materials.

4.4. *Experimental results: conductivity along the Cu–O chains*

From the structural point of view, a distinguishing feature of the $YBa_2Cu_3O_x$ and $YBa_2Cu_4O_8$ cuprates is the presence of one-dimensional Cu–O chains extending along the *b*-axis of the crystals. The principal role of the Cu–O chains is to provide carriers for the CuO_2 planes, and in this sense their function is similar to that of other charge-reservoir layers such as Bi–O or Tl–O layers in other compounds. Because the chains have a well-defined direction in the crystal it is feasible to study their response through spectroscopic experiments conducted with polarized light. Such experiments were performed as soon as the first untwinned samples became available. The main experimental result is that the reflectivity of Y123 crystals shows a remarkable anisotropy, the *b*-axis reflectance being enhanced (Bozovic et al. 1988, Petrov et al. 1988, Koch et al. 1989, Zibold et al. 1990, Schlesinger et al. 1990, Pham et al. 1991, Schützmann et al. 1992, S.L. Cooper et al. 1992, Tanner et al. 1992, Basov et al. 1995a). The position of the plasma minimum in

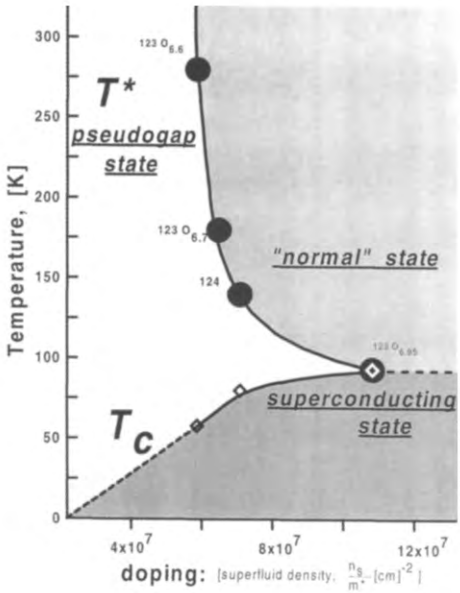

Fig. 10. Schematic phase diagram of Y123 and Y124 cuprate superconductors. In the underdoped regime, a *pseudogap state* forms below a temperature $T^* > T_c$. The curves for T^* and T_c cross at optimal doping where the pseudogap and the superconductivity develop at the same temperature. T^* is determined from the c-axis conductivity; the doping level is determined from the superfluid density $\omega_{ps}^2 = n_s/m^*$ in the CuO_2 planes. From Puchkov et al. (1996a).

reflectance is about 1.2 eV for $E \parallel a$ and about 2.0 eV for $E \parallel b$. The conductivity obtained through KK analysis shows significant enhancement of the b-axis spectral weight that can be interpreted in terms of an additional conductivity channel associated with the chains. The analysis of the superconducting-state conductivity shows that the superfluid density is also anisotropic (Basov et al. 1995a). In Y124 crystals which contain two Cu–O chains in each unit cell, the anisotropy of both the normal-state spectral weight (Bucher et al. 1990, Wachter et al. 1994, Kircher et al. 1993) and of the superfluid density (Basov et al. 1995a) is stronger than in the single-chain Y123.

The anisotropy is also observed in the dc conductivity, with σ_{dc} along b enhanced compared to the a-axis results (Friedmann et al. 1990, Welp et al. 1990, Rice et al. 1991). While there was considerable scatter in the data for the anisotropy in the samples studied in 1988–1992, more recent results seem to indicate that the ratio σ_b/σ_a is the same as $\omega_{pb}^2/\omega_{pa}^2$ (Zhang et al. 1994, Basov et al. 1995a). Applying a simple Drude formula to these results, $\sigma_{dc} = \omega_p^2/\tau$ suggests that the scattering rate is the same along the CuO_2 planes and along the chain direction.

The chains contribute to dc transport or to the superfluid density only if special care is taken to preserve them from structural disorder in the sample preparation process. Prior to 1991/92, Y123 single crystals were usually grown in Au or Al_2O_3 crucibles. Both Au and Al tend to substitute Cu sites in the Cu–O chains. Such contamination does not occur in more recent samples which are usually grown in yttria-stabilized zirconia crucibles. The in-plane response of the earlier crystals does not differ much from the properties found for the new generation of single crystals. However, the b-axis results are completely different. Rotter et al. (1991) and Schützmann et al. (1992) observed a peak at finite frequency in

the b-axis conductivity of the Cu–O chains which is characteristic for the response of a 1D metal with localized states. The penetration depth was found to be isotropic in these crystals. No localization peak was observed in more recent samples grown by two different groups (Basov et al. 1995a). The b-axis conductivity of these newer crystals was essentially identical to the a-axis results, except that the spectral weight was enhanced by a factor of 2.3. The same factor appears in the anisotropy of the resistivity and of the penetration depth.

4.5. *Experimental results: the interplane conductivity*

A common feature of all high-T_c superconductors is their layered structure which leads to a strong anisotropy of the electronic properties. While typical values of the in-plane conductivity in most cuprates are of the order of 3000–5000 Ω^{-1} cm^{-1} at room temperature, the interplane conductivity is much smaller, varying from a maximum of about 400 Ω^{-1} cm^{-1} in overdoped Y123 crystals down to 0.01 Ω^{-1} cm^{-1} in the most anisotropic $Bi_2Sr_2CaCu_2O_8$ compounds. The Y123- and Y124-series compounds are less anisotropic than other materials, which has been attributed to the presence of the Cu–O chains in the crystal structure. However, an estimate of the mean free path along the c-direction, l_c, carried out for even the most conductive overdoped samples shows that l_c is of the order of the interlayer spacing (Schützmann et al. 1994). This is clear evidence that the c-axis transport in cuprates is incoherent. A number of mechanisms have been proposed that would result in an incoherent conductivity spectrum (Kumar et al. 1990, Kumar and Jayannavar 1992, Rojo and Levin 1993, Ioffe et al. 1993, Nyhus et al. 1994, Clarke et al. 1995, Alexandrov et al. 1996).

With low electronic background, the c-axis conductivity spectra are dominated by sharp resonances due to infrared active phonons (fig. 4, fig. 11). There are strong indications for the interaction of phonon modes with the electronic background: (i) the frequency position and the width of phonon peaks is temperature dependent, with anomalies occurring at the onset of superconductivity (Thomsen and Cardona 1989, Litvinchuk et al. 1994); (ii) some of the phonon modes have an asymmetric (Fano) lineshape which is a signature of the coupling between a sharp line and a continuous background (Fano 1961). The line strengths, in contrast, are not anomalous; they are what one expects from lattice-dynamics models based on neutron scattering (Timusk et al. 1995a). The only exception is the mode at 560 cm^{-1} involving the apical oxygen atom, which appears to be anomalously strong. It is also the mode with the most asymmetric lineshape.

The first step in the analysis of the electronic contribution to the c-axis conductivity is to subtract the phonon part. Usually, the phonons are fitted with Lorentzian oscillators. The high-frequency modes have asymmetric shapes and are best fitted using Fano theory (Burlakov et al. 1989, Homes et al. 1993b). In general, this procedure of separating the conductivity into electronic and phonon channels is quite unambiguous since lattice modes are very narrow and can be easily distinguished from the flat electronic background. The underdoped Y123 and Y124 crystals are exceptions since an anomalously broad phonon-like feature develops at low temperatures (Homes et al. 1993b,

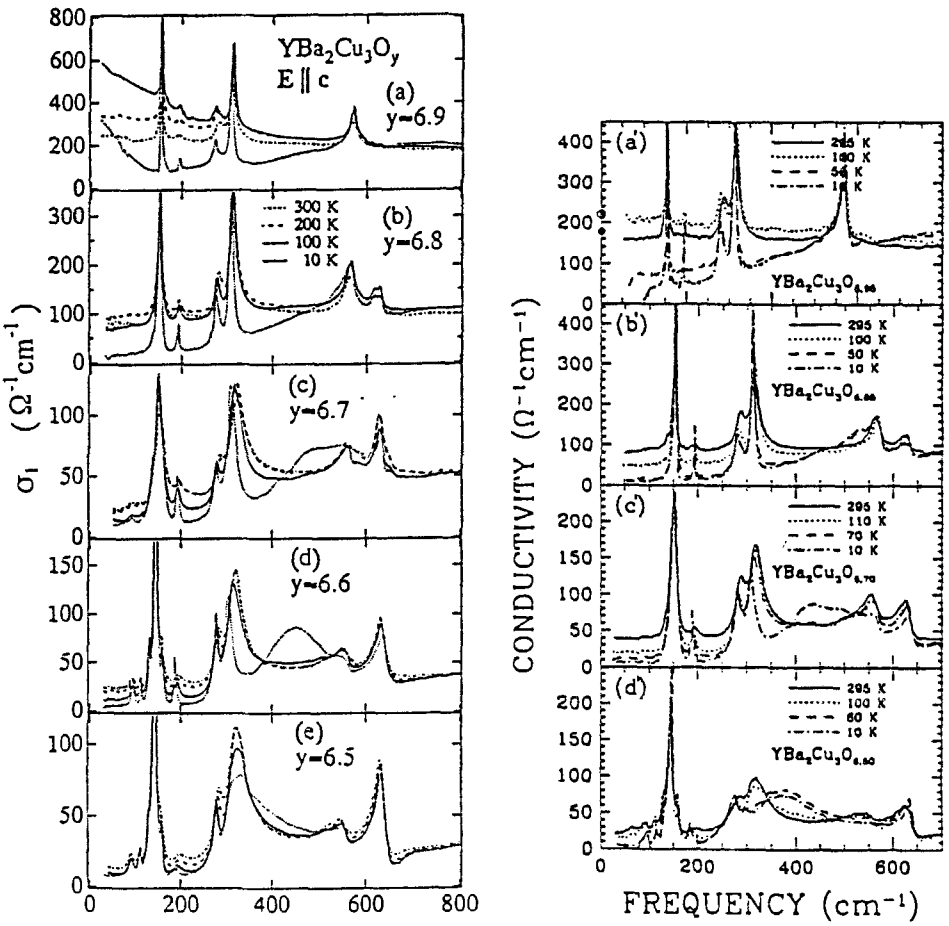

Fig. 11. Optical conductivity for $YBa_2Cu_3O_{6+x}$ for radiation polarized along the c-axis as a function of oxygen doping. Left panel: results by Tajima et al. (1998); right panel: results by Homes et al. (1995a). In the highly doped materials, a gap-like depression at $\omega < 500\,\mathrm{cm}^{-1}$ opens up below T_c, but at 10 K, the conductivity remains finite down to the lowest accessible frequencies. In the $x = 0.85$ material, the conductivity is clearly non-metallic, a trend which resolves itself into a pseudogap for $x < 0.70$.

Basov et al. 1994a, Hauff et al. 1996). Sum-rule arguments suggest that this mode is phonon-related: the spectral weight of this mode grows at low temperature at the expense of other phonon resonances. However, the halfwidth of this feature exceeds $50\,\mathrm{cm}^{-1}$, which is atypical for phonons in crystalline solids. An unexpected result is that this mode disappears when impurities are added in Y123 materials (Hauff et al. 1996). The frequency of this mode is proportional to T_c (Homes et al. 1993b) similar to the magnetic peak seen by neutron scattering (Rossat-Mignod et al. 1991, Mook et al. 1993, Fong et al. 1995), but the infrared line is at somewhat higher frequency. Possible caveats of coupling

between lattice modes and electronic conductivity were discussed by Grüninger et al. (2000), Munzar et al. (1999) and Bernhard et al. (2000).

The electronic background in the interplane conductivity shows a rich variety of behaviors as the system is doped with charge carriers. For a given series, higher conductivity correlates with higher doping levels. S.L. Cooper et al. (1993b) have suggested the following form for the c-axis response of Y123:

$$\sigma_c(\omega) \propto t_{c0}^2 \frac{\tau_c}{1 + \omega^2 \tau_c^2}, \tag{13}$$

where $1/\tau_c$ is the c-axis scattering rate and t_{c0} is the interbilayer hopping rate. For materials with an open Fermi surface in the c-direction, the interbilayer hopping is expected to scale linearly with the c-axis plasma frequency (Kwak 1982). Within this phenomenological model, the interbilayer hopping rate changes from 40–50 meV in the optimally doped Y123 samples down to 5 meV in the underdoped 60 K phase. However, it should be pointed out that this model assumes coherent interlayer transport, and since the Drude width (160 meV, Schützmann et al. 1994) exceeds the interlayer hopping there cannot be any coherent bands in the c-direction, and there is a complete breakdown of the Fermi-liquid picture these arguments rest on.

The slope of the dc resistivity $\rho_{dc} = 1/\sigma_{dc}$ changes from metallic ($d\rho/dT > 0$) in the optimally doped and overdoped samples to "semiconducting" ($d\rho/dT < 0$) in underdoped compounds (Ito et al. 1993, Nakamura and Uchida 1993). The cause of this peculiar behavior was unraveled by Homes et al. (1993a) who analyzed the conductivity spectra for $YBa_2Cu_3O_x$ crystals with $x = 6.95$ and $x = 6.7$. The room-temperature spectra measured for the optimally doped crystal showed a continuous background which was nearly independent of frequency in both compounds, in agreement with the earlier data (Koch et al. 1989, S.L. Cooper et al. 1993b). At lower temperature, the $x = 6.95$ crystal reveals weak metallic character: the low-frequency part of the conductivity shows weak Drude-like behavior and $\sigma_1(\omega \to 0)$ increases. This is in an agreement with the positive $d\rho/dT$ found in the resistivity measurements. But it should be noted that there is a very large residual resistance giving a mean free path for impurity scattering of the order of a lattice spacing.

A completely different temperature dependence was observed in the spectra of the underdoped $x = 6.7$ sample. In this crystal the spectra of $\sigma_1(\omega)$ at $T < 140$–160 K reveal a low-frequency *pseudogap*: the region in the frequency dependence located at $\omega < 200$–$300\,cm^{-1}$ where $\sigma_1(\omega)$ is suppressed but remains finite. Judging from the ω position of the step-like structure in the spectra of $\sigma_1(\omega)$, the magnitude of the pseudogap remains unchanged with temperature ($\sim 250\,cm^{-1}$). The opening of the pseudogap is associated with the transfer of the spectral weight from the low-energy part of the spectra to higher energies. This accounts for the increase of the dc resistivity, and in fact there is good agreement between the T-dependence of resistivity measured directly and that estimated estimated from $\sigma_1(\omega \to 0)$ (Homes et al. 1995a). An interesting result is that no qualitative changes are found in the conductivity spectra as underdoped

samples undergo the superconducting transition. That is in contrast with the behavior of conventional superconductors where the ac conductivity is zero below the gap frequency.

A pseudogap similar to that in fig. 11 was observed in stoichiometric $YBa_2Cu_4O_8$ crystals which are intrinsically underdoped (Basov et al. 1994a). Experiments by Homes et al. (1995a) and by Tajima et al. (1998) explored the evolution of a pseudogap with doping in the $YBa_2Cu_3O_x$ series. Their major finding is that the magnitude of the pseudogap is independent of doping but the temperature T^* at which the pseudogap structure appears in the spectra seems to increase as x is reduced. The dependence of T^* on carrier density in the CuO_2 planes is shown in fig. 10. In the samples with $x = 6.5$–6.6, the pseudogap is found already at 300 K.

It has been noted that the c-axis pseudogap is related to other anomalies observed in underdoped samples in the normal state. Homes et al. (1993a) have shown that the T-dependence of the conductivity in the pseudogap region agrees with the behavior of the Knight shift in $YBa_2Cu_3O_x$. A similar conclusion was drawn from the data for Y124 compounds (Basov et al. 1994a). Basov et al. (1996) have shown that the pseudogap in the interplane conductivity develops in the same temperature range and in the same doping regime as the suppression of the in-plane scattering rate. Previously, resistivity measurements conducted for currents along the *ab*-plane and along the c-axis demonstrated that suppression of the in-plane resistivity both in Y123 and in La214 crystals coincides with the cross-over to "semiconducting" behavior observed for the interplane currents (Nakamura and Uchida 1993, Takenaka and Uchida 1994). These results establish a link between the anomalies in the charge dynamics observed in the c-axis and in the *ab*-plane properties.

A different behavior was observed by Schützmann et al. (1994) in the c-axis response of lightly *overdoped* Y123 sample. The absolute value of the conductivity at $\omega \to 0$ increased, and the spectra clearly show a Drude-like peak at $\omega = 0$ which is characteristic for a metallic system. The authors analyzed their data within the extended Drude model (fig. 12). The results of this analysis reveal certain similarities with the in-plane properties of the Y123 series. Both the scattering rate $1/\tau(\omega)$ and the effective mass $m^*(\omega)$ show a pronounced frequency dependence. Comparing interplane spectra with the data for the in-plane response (fig. 8), one finds that the effective masses probed along the CuO_2 planes and along the c-direction do not differ by more than a factor of 2. This contradicts the predictions of the band-structure calculations where the anisotropy is found to be as high as 10 in $YBa_2Cu_3O_7$ (Pickett et al. 1990). Thus one is forced to conclude that the anisotropy of the dc resistivity, which is about 10 in $YBa_2Cu_3O_7$, cannot be completely accounted for by band-structure effects but can be connected with the peculiarities of the interplane tunneling or hopping. A naive interpretation of the interplane conductivity in terms of the Drude model suggests a strong enhancement of the scattering rate in the c-direction. Anisotropic damping is an interesting phenomenon that has been predicted as the result of spin–charge separation (Clarke et al. 1995, Chakravarty and Anderson 1994). However, one should strike a note of caution here about the applicability of the frequency-dependent scattering-rate formalism in a situation where the mean free path is clearly smaller than the lattice spacing and the conduction is incoherent.

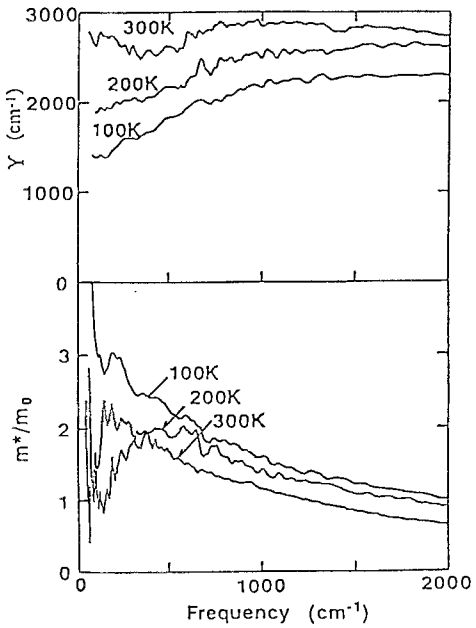

Fig. 12. The results of the extended-Drude analysis of the optical conductivity of a "fully oxygenated" Y123 single crystal measured with the polarization along the c-axis (Tajima et al. 1998). The crystal is likely to be overdoped as evidenced by the reduced $T_c = 89$ K and enhanced conductivity in the limit of $\omega \approx 0$. Note that the enhancement of the effective mass m^*/m_e does not exceed ~4 which is close to the in-plane values (figs. 8, 9).

The c-axis response of La214 crystals in a broad range of doping regimes has been investigated by Uchida et al. (1996). In the far infrared range the electronic background in the conductivity is nearly frequency independent. The main difference from the Y123 or Y124 series is that the conductivity background is much weaker, and even in overdoped samples $\sigma_c(\omega \rightarrow 0)$ does not exceed $40\,\Omega^{-1}\,\mathrm{cm}^{-1}$. Underdoped samples show a suppression of the conductivity in the low-frequency part. This is concomitant to the "semiconducting" behavior of the resistivity found in underdoped La214 (Nakamura and Uchida 1993). However, the energy scale that can be associated with the temperature dependence of the resistivity and especially the frequency dependence of $\sigma_1(\omega)$ is very different in the Y123 and La214 families. Basov et al. (1995b) have shown that the spectral weight removed from the low-frequency part is recovered at ω exceeding 0.4 eV. This suggests that a much broader energy scale is associated with the pseudogap in La214 materials. Batlogg et al. (1994) and Batlogg and Emery (1996) have presented arguments in favor of the existence of a temperature scale of the order of 1000 K which is relevant to the transport properties of high-T_c materials.

From an analysis of the anisotropy in the conductivity spectra of $La_{1.85}Sr_{0.15}CuO_4$, van der Marel and Kim (1995) concluded that m_c/m_{ab} does not exceed 5 in this compound. A larger anisotropy was inferred by Henn et al. (1996) from an analysis of ellipsometric data for $La_{1.87}Sr_{0.13}CuO_4$. This latter analysis is based on the extended Drude model. Again one must question the applicability of this model to the c-axis response of this compound since $\sigma_1(\omega)$ at $\omega \rightarrow 0$ is smaller than the minimum metallic conductivity.

4.6. *Comparison of the optical data with transport measurements and other spectroscopies*

In an attempt to understand the fundamental physics behind the electromagnetic response of cuprates it will be instructive to discuss connections to the results of other spectroscopic studies and, first of all, to transport measurements. It was realized early on that the linear *frequency* dependence of the scattering rate found in the response of the CuO_2 planes may be related to the linear *temperature* dependence of the *ab*-plane dc resistivity $\rho_{dc} = m/ne^2\tau$. These two effects occur when quasiparticles scatter from a hypothetical bosonic spectrum which is flat over a frequency scale $T < \omega < \omega_0$ (Littlewood and Varma 1992). Using this model, known as the Marginal Fermi Liquid (MFL) model, it was possible to rationalize the results obtained with photoemission, Raman or tunneling spectroscopies. Ruvalds (1996) discussed this behaviour as a consequence of Fermi surface nesting. However, the linear laws in $1/\tau(\omega)$ and in $d\rho/dT$ are *not universal,* and a more complicated response is observed in underdoped samples. Specifically, a broad range of physical probes show that below a characteristic temperature T^*, which can significantly exceed T_c, the response of the underdoped cuprates can be understood if one assumes there is a partial gap or a "pseudogap" in the spectrum of low-energy excitations.

Originally, the gap-like behavior in the normal-state properties was observed in the uniform spin susceptibility probed with nuclear magnetic resonance (NMR) measurements of the Knight shift (Warren et al. 1989, Yoshinari et al. 1990, Alloul et al. 1991). In ordinary metals and in the optimally doped cuprates, the Knight shift is temperature independent at $T > T_c$ but drops rapidly below the superconducting transition due to the formation of (singlet) Cooper pairs. However, in underdoped cuprates the Knight shift is suppressed already at temperatures well above T_c. This led Warren et al. to the conclusion that in underdoped samples *spin pairing* may take place well above the bulk superconducting transition at T_c, thus producing a normal-state energy gap, referred to as a "spin gap".

In the temperature range in the vicinity of T^*, the *ab*-plane resistivity in underdoped cuprates shows a deviation from the linear behavior (Bucher et al. 1993, Batlogg et al. 1994, Ito et al. 1993). Both in Y123 and in La214 materials the resistivity reveals a steeper than linear slope at $T < T^*$, with a cross-over to linear behavior at $T > T^*$. Bucher et al. (1993) and Batlogg et al. (1994) have shown that anomalies in resistivity and in NMR data occur in the same temperature range, and suggested that the two effects are interrelated. If the scattering mechanism responsible for the linear temperature dependence of $\rho_{ab}(T)$ involves spin fluctuations, then the spin gap seen in NMR below T^* would naturally account for the drop of $\rho_{ab}(T)$ below T^* as well. Suppression of the spin susceptibility is also seen in neutron scattering experiments (Rossat-Mignod et al. 1991, Tranquada et al. 1992) as well as by specific-heat measurements on underdoped Y123 (Loram et al. 1994). However, in the latter work it was shown that there is a large decrease in entropy below a temperature closely related to T^*, which cannot be accounted for by assuming a gap only in the spin degrees of freedom.

Recently, angle-resolved photoemission spectroscopy (ARPES) for Bi2212 showed that the electronic density of states of underdoped cuprates reveals a normal-state gap-

like depression (Marshall et al. 1996, Loeser et al. 1996, Ding et al. 1996, 1997). The momentum dependence of this normal state gap resembles that of the $d_{x^2-y^2}$ gap observed for $T < T_c$ (Loeser et al. 1996, Ding et al. 1997). This, and the fact that no significant changes are observed upon crossing into the superconducting regime, have led to the suggestion that the normal-state gap may be a precursor of the superconducting gap. As the doping level is increased to near- and above optimal, the normal-state gap-like feature seen in ARPES spectra disappears.

In the optical conductivity, the pseudogap state reveals itself in *two* distinct ways: (i) the in-plane scattering rate at $\omega < 700\,\mathrm{cm}^{-1}$ is reduced which inevitably leads to reduction of the in-plane resistivity (see discussion in sect. 4.3); (ii) the interplane conductivity is reduced at $\omega < 250\,\mathrm{cm}^{-1}$ which accounts for semiconducting behavior of the *c*-axis resistivity (see discussion in sect 4.5). Despite the difference in the energy scales seen in the in-plane and interplane transport, these two effect are clearly connected (Takenaka and Uchida 1994, Basov et al. 1996).

Recently, a gap in the normal state has also been seen by vacuum tunneling spectroscopy in underdoped cuprates (Tao et al. 1997, Renner et al. 1998, Krasnov et al. 2000). Renner et al. (1998) showed that in Bi2212, the pseudogap above T_c scales with the superconducting gap, and its width is temperature independent; i.e., *the gap does not close as the temperature is raised.* The maximum gap, assuming a d-wave gap, at optimal doping in Bi2212, $\Delta_0 = 41.5$ meV, is consistent with other spectroscopies. The gap starts with $\Delta_0 = 44$ meV for the underdoped sample with $T_c = 83$ K and decreases with doping to $\Delta_0 = 21$ meV in an overdoped sample with $T_c = 56$ K. Interestingly, Renner et al. (1998) find that even in an overdoped sample with $T_c = 74.3$ K there is a pseudogap in the normal state although it is very weak already at 89 K. These observations are consistent with the phase diagram shown in fig. 10 where the temperature T^* drops rapidly with doping, but in the case of Bi2212, at least, the temperature scales T^* and T_c do not cross at optimal doping but at a doping level that is substantially higher. This is also seen in the *ab*-plane scattering rate for Bi2212 (Puchkov et al. 1996a).

Raman spectroscopy is also capable of probing the pseudogap. In conventional superconductors, the Raman spectrum only shows a peak at the pair-breaking frequency 2Δ (Abrikosov and Fal'kovskii 1961). In the clean limit no other absorption is expected apart from a very low frequency band from free electrons, but in the cuprates, because of the strong incoherent scattering (Shastry and Shraiman 1990), a broad continuum appears that gives rise to a constant Raman background up to 2 eV (Varma et al. 1989).

A depression in this continuum at low frequency has widely been interpreted as evidence of the superconducting gap, but its presence in the normal state in underdoped samples originally cast doubt on this interpretation (Slakey et al. 1990). It is now becoming clear that this depression may well be associated with the pseudogap and that the Raman spectrum has parallels with the *ab*-plane scattering-rate spectrum (Blumberg et al. 1997).

At optimal doping, Raman spectra of B_{1g} and B_{2g} symmetry are quite different, with B_{1g} spectra emphasizing processes involving states in the $(\pi, 0)$ direction of the maximum gap, whereas the B_{2g} spectra involve states near (π, π) in the region of the nodes of

the $d_{x^2-y^2}$ function. Fits of a simple theory to the data for optimally doped Bi2212 in the superconducting state give a maximum gap value of $\Delta_0 = 280\,\mathrm{cm}^{-1}$ (34.7 meV) in reasonable agreement with the gap value estimated from other probes (Hackl et al. 1996).

Recent Raman studies of underdoped cuprates are being interpreted in terms of a pseudogap (Blumberg et al. 1997, Nemetschek et al. 1997). The opening of the pseudogap leads to a suppression of the electronic scattering at $\omega < 500\,\mathrm{cm}^{-1}$ with the simultaneous formation of a bound state at $\omega \approx 600\,\mathrm{cm}^{-1}$. These two effects are reminiscent of what is observed in Raman scattering in optimally doped cuprates as they undergo the superconducting transition. Blumberg et al. interpret the sharp bound state as being due to pair formation that takes place in underdoped crystals at a temperature significantly exceeding T_c.

There have been attempts to analyse the low-frequency Raman scattering in terms of the carrier lifetime $\Gamma(\Omega)$. In the simple Drude picture of the Raman continuum scattering in the normal state, the Raman cross-section is proportional to ω/Γ, where Γ is the scattering rate. In this model a depressed scattering rate in the pseudogap state would lead to an increased slope for the low-frequency scattering. Naeini et al. (1998) investigated overdoped $La_{2-x}Sr_xCuO_4$ using this analysis, finding no pseudogap for a sample with $x = 0.22$, in contrast to Startseva et al. (1999b) who found a pseudogap in the *ab*-plane conductivity scattering rate in the same material. Nemetschek et al. (1997) do find a depression in the Raman scattering of both Bi2212 and Y123 in the normal state below $700\,\mathrm{cm}^{-1}$ and 200 K in agreement with the *ab*-plane optical scattering rate data.

The anomalies observed in underdoped samples in the dc resistivity, the optical conductivity, neutron scattering, NMR and ARPES, Raman and tunneling spectroscopies are summarized in table 1. The similarities in the evolution of these anomalies with temperature and doping suggests they have a common physical origin. However, a closer look at experiments reveals several potential discrepancies. For example, the energy scale of the pseudogap varies substantially from one experimental probe to another. Also, there does not seem to be any simple relationship between the energy scale set by the magnitude of T^* and the frequency position of features seen in a variety of spectroscopies. The challenge for any theory is to give an account for all these distinctions and to reconcile (seemingly) conflicting results.

From table 1 it follows that the opening of the pseudogap in the electronic DOS as seen in ARPES and tunneling experiments is accompanied by an *enhancement* of the dc conductivity. It may seem that the higher dc conductivity contradicts the observation of a gap. Indeed, the opening of a gap at E_F reduces the spectral weight available for conduction. However, in a system where the scattering excitations themselves are gapped, $1/\tau$ collapses and this improves the dc conductivity. Chromium is a canonical example of a remarkably good metal where a gap corrupts most of the electronic states at E_F (for a comprehensive review, see Fawcett 1988). This partial gap is due to the spin-density-wave transition at $T_{SDW} = 312$ K. However, some fragments of the Fermi surface remain unaffected by the transition. The electrical resistivity shows a weak increase at $T \approx T_{SDW}$ which is followed by a fast drop of $\rho(T)$ with decreasing temperature. A similar mechanism of pseudogap formation in cuprates was discussed by Kampf and Schrieffer

Table 1
Transport and spectroscopic probes of the pseudogap state in cuprates

Experiment	Pseudogap at $T < T^*$	System	Characteristic T or ω	Reference
a-axis resistivity	faster than linear	La214	300–800 K	Batlogg et al. (1994)
	decrease of $\rho(T)$	Y123	120–300 K	Ito et al. (1993)
		Y124	140–180 K	Bucher et al. (1993)
		Bi2212	120–220 K	Watanabe et al. (1997)
$\sigma_a(\omega)$	suppression of the	La214	700 cm^{-1}	Startseva et al. (1999a,b)
	scattering rate	Y123	600 cm^{-1}	Basov et al. (1996)
		Y124	600 cm^{-1}	Basov et al. (1996)
		Bi2212	600 cm^{-1}	Puchkov et al. (1996b)
		Bi2201	600 cm^{-1}	Weber et al. (1997)
		Hg1223	1000 cm^{-1}	McGuire et al. (2000)
c-axis resistivity	"semiconducting" up-turn	La214	500–800 K	Nakamura and Uchida (1993)
		Y123	120–300 K	Takenaka and Uchida (1994)
		Bi2212	120–300 K	Watanabe et al. (1997)
$\sigma_c(\omega)$	suppressed in FIR	La214	2000 cm^{-1}	Basov et al. (1995b)
		Y123	<250 cm^{-1}	Homes et al. (1993b)
		Y124	<250 cm^{-1}	Basov et al. (1994a)
ARPES	incomplete gap at E_F,	Bi2212	<200 cm^{-1}	Loeser et al. (1996)
	d-wave symmetry	Bi2212	<160 cm^{-1}	Ding et al. (1997)
		Bi2201	<120 cm^{-1}	Harris et al. (1997)
Raman	suppressed electronic	Bi2212	<600 cm^{-1}	Blumberg et al. (1997)
	background	Y123	<700 cm^{-1}	Nemetschek et al. (1997)
Tunneling	gap with states at E_F	Bi2212	<700 cm^{-1}	Renner et al. (1998)
			<560 cm^{-1}	Krasnov et al. (2000)

(1990). According to the ARPES experiments, the pseudogap in cuprates is likely to have d-wave symmetry. Thus, the regions close to the nodes are capable of maintaining substantial conductivity. The dc conductivity will be determined by a competition between the reduction of the DOS and the collapse of the scattering rate. Experimental evidence suggests (figs. 7, 8) that the decline of $1/\tau$ prevails, thus leading to an increase of the dc conductivity in the pseudogap state. A striking example of this effect is the conductivity peak observed in microwave spectroscopy in the superconducting state of optimally doped cuprates (Bonn et al. 1992).

4.7. *Theoretical context*

A resonance in the scattering spectrum. In searching for possible connections between the anomalies observed in the pseudogap state (table 1), it may be instructive to perform one more step in the single-component analysis of the optical conductivity, that is, to extract the frequency dependence of $A(\Omega)$ from the experimental data. While it is difficult to

invert eq. (12), the gross features of the $A(\Omega)$ spectrum can be inferred from comparison of the data shown in figs. 7–9 with the model calculations described in sect. 4.2. The principal result of such a comparison is that eq. (12) can account for the experimental data *only* if the scattering spectrum $A(\Omega)$ is strongly dependent on temperature and doping. Indeed, the spectral weight in $A(\Omega)$ has to be suppressed at low frequencies in order to account for the development of a threshold feature in the $1/\tau(\omega)$ spectra for underdoped materials. Moreover, in optimally doped samples, and in particular in $YBa_2Cu_3O_{6.95}$, the threshold develops instantly at $T < T_c$, consistent with the observation of an abrupt drop of the scattering rate in the superconducting state by means of microwave measurements (Bonn et al. 1992). Finally, in overdoped materials, the absolute value of the scattering rate through the entire energy range is strongly diminished compared to compounds with lower doping. Within the electron–boson formalism this implies that the total spectral weight of $A(\Omega)$ is strongly reduced since $1/\tau \propto \int_0^\infty d\Omega\, A(\Omega)$.

A simple suppression of $A(\Omega)$ at low frequencies is not sufficient to model the weak T-dependence at $\omega > 700\,\mathrm{cm}^{-1}$ found in underdoped and optimally doped samples. To account for this effect the spectral weight of the scattering spectrum has to be recovered right above the threshold structure in $1/\tau(\omega)$. This was shown by Puchkov et al. (1996a) using the inversion formula proposed by Marsiglio and Carbotte (1997). The main difficulty with the inversion procedure is that differentiation greatly amplifies any noise in the experimental data. While it is not possible to find fine structure in $A(\Omega)$ with this analysis, it suggests that a resonance at $\omega \approx 500\,\mathrm{cm}^{-1}$ is formed in the pseudogap state. In the optimally doped samples, $1/\tau(\omega)$ becomes "gapped" only at $T < T_c$ and, therefore, the resonance is expected to occur only in the superconducting state. Thus, in principle, there exists an alternative explanation of many of the experiments listed in table 1 in terms of a gap in the scattering spectrum. This scenario does not necessarily have to be contrasted with the one in which the pseudogap is viewed as a suppression of the DOS. Indeed, if the scattering mechanism is of electronic nature, a distinction between the former and the latter approaches is difficult to make.

A resonance in the scattering spectrum defines the electronic self-energy $\Sigma(\omega)$, and thus would determine the behavior of the spectral function $A(k, \omega)$ according to eq. (10). It has been suggested that photoemission experiments can be interpreted in terms of the one-electron spectral function and, therefore, the photoemission lineshape can be calculated based on the knowledge of the self-energy (Mahan 1980, Kampf and Schrieffer 1990). This, in principle, allows one to check the consistency between infrared and photoemission results on a semi-quantitative level. Recently, Shen and Schrieffer (1997) and Norman et al. (1997) suggested that the photoemission spectra are consistent with quasiparticle coupling to a collective excitation centered near $\boldsymbol{Q} = (\pi, \pi)$. Norman et al. (1997) have argued that the "peak–dip" structure of the photoemission spectra seen in the superconducting state of the optimally doped samples can be accounted for if one assumes that this is a collective excitation that develops right below T_c. Extending their arguments to underdoped materials, one can suggest that the development of this collective mode in the underdoped regime is expected already in the normal state at $T < T^*$. Thus one can conclude that both the photoemission lineshape and the *ab*-plane optical conductivity

of cuprates can be described as the result of the interaction of quasiparticles with the collective mode which shows a remarkable temperature dependence. If this collective mode is related to the spin degree of freedom, this would reconcile numerous correlations between spin and charge responses observed in the cuprates. One of the likely candidates for such a collective mode is an anomalous magnetic peak at 41 meV that has been studied intensively over the last several years with neutron scattering (Rossat-Mignod et al. 1991, Mook et al. 1993, Fong et al. 1995, 1997). Evidence for coupling of charge carriers to a neutron mode was reported by Carbotte et al. (1999). Since many of the pseudogap-related features are sensitive to the presence of impurities (in particular, Zn) it will be interesting to explore if the 41 meV resonance is found in Zn-doped Y123 crystals.

Spin–charge separation. As discussed above, the suppression of the scattering rate at $T < T^*$ means that a gap or a pseudogap may open in the spectrum of excitations that scatter the conducting carriers. A close correspondence between charge properties probed with resistivity or in-plane optical conductivity and spin properties probed with NMR or with neutrons suggests that the primary source of scattering is related to the spin degree of freedom. This is what one expects within the model of spin–charge separation (Anderson 1987, Lee and Nagaosa 1992, Ioffe et al. 1994, Altshuller et al. 1996, Laughlin 1996, Millis and Monien 1996). The principal argument behind these ideas comes from NMR evidence for pairing of *neutral* fermions into singlets. This is to be distinguished from superconducting pairing since no precursors to superconductivity are observed in the pseudogap state: a Meissner effect is not observed in the pseudogap state and there is no paraconductivity due to superconducting fluctuations. This implies spin–charge separation where the in-plane carrier conductivity is due to holons but scattering is due to exchange of spinons. The phase diagram obtained by Lee and Nagaosa (1992) is very similar to that depicted in fig. 10. Thus, the spin–charge separation picture is consistent with the experimental situation on the pseudogap state, at least in materials where the maximum T_c coincides with the disappearance of the pseudogap.

Striped phases. An alternative suggestion is that cuprates are intrinsically inhomogeneous and form "charged stripes" (Emery et al. 1997 and references therein). An interaction between hole-rich stripes and hole-free antiferromagnetic regions is a form of magnetic proximity effect which is considered as a likely cause of high-T_c superconductivity. Within this picture, the mobile holes on an individual stripe acquire a spin gap by hopping between the stripe and its antiferromagnetic surrounding. This is a magnetic analog of the superconducting proximity effect. Recently Salkola et al. (1996) have been able to explain the lineshape observed in photoemission experiments using this model. The theory predicts two cross-over temperatures: the first is related to the formation of stripes, and the second is where the pairing (spin-gap) behavior emerges within a stripe. Then the pseudogap can be viewed as the result of superconducting pairs which are preformed already in the normal state (at $T < T^*$) (Uemura 1996). However, no bulk superconductivity is observed until these pairs gain global coherence, which occurs only below T_c. Emery and Kivelson (1995b) emphasized the role of phase fluctuations in the pseudogap state. A phase diagram with two cross-over temperatures has also been obtained recently by Zhang (1997), who suggests a unified approach towards

superconductivity and magnetism based on a 5-dimensional order parameter which contains both antiferromagnetic and superconducting components.

A different view of the experimental situation is formulated within the so-called nearly antiferromagnetic Fermi-liquid model (NAFLM) (Pines 1995, Chubukov et al. 1996). Within this approach, there is no spin–charge separation. One assumes Fermi-liquid behavior at all doping levels. The anomalous spin and charge behavior seen in the normal-state properties is believed to arise from a magnetic interaction between planar quasiparticles, which reflects the closeness to antiferromagnetism in the phase diagram. The evolution of the Fermi surface with doping is accompanied by the development of a precursor to a spin-density-wave state which gives rise to a pseudogap at low temperatures (Chubukov et al. 1996). Another related model is the spin-bag mechanism of Kampf and Schrieffer (1990) discussed above.

Finally, it should be pointed out that some of the intriguing features of the normal-state behavior of cuprates can be explained starting from the premise that the ground state is metallic but the layered structure is responsible for the complicated tunneling effects between the CuO_2 planes (Rojo and Levin 1993, Abrikosov 1995, 1996, Atkinson and Carbotte 1997, Zha et al. 1996). These models are very successful in explaining the behavior of the Y123 materials where many of the effects observed in the optical conductivity and in the penetration depth can be ascribed to the interband transitions involving CuO_2 planes and one-dimensional Cu–O chains (Atkinson and Carbotte 1995).

5. Electrodynamics in the superconducting state

5.1. *Searching for the superconducting energy gap*

Within the BCS model, the ground state of a superconductor is characterized by an energy gap 2Δ (Bardeen, Cooper and Schrieffer 1957). The first spectroscopic evidence for the existence of the energy gap in conventional superconductors as well as its correct magnitude was provided by Glover and Tinkham (1956) using far-infrared spectroscopy. These pioneering experiments preceded the appearance of the BCS theory but were soon found to be in excellent agreement with the BCS electrodynamics (Mattis and Bardeen 1958).

Spectroscopic measurements of the energy gap are based on the fundamental fact that absorption of radiation with frequency less than the magnitude of the gap is prohibited in a superconductor, and therefore the dissipative (real) part of the conductivity vanishes for $\omega < 2\Delta$. A clear threshold in the conductivity spectra at $\omega = 2\Delta$ is found only in dirty superconductors where $1/\tau > 2\Delta$. In clean materials where $1/\tau \ll 2\Delta$ the conductivity in the gap region is small even in the normal state, and unlike other spectroscopies where a sharp feature can be seen at the gap energy, there is little change in the overall optical properties at the gap frequency in a clean superconductor. A detailed discussion of this issue can be found in a review article by Timusk and Tanner (1989).

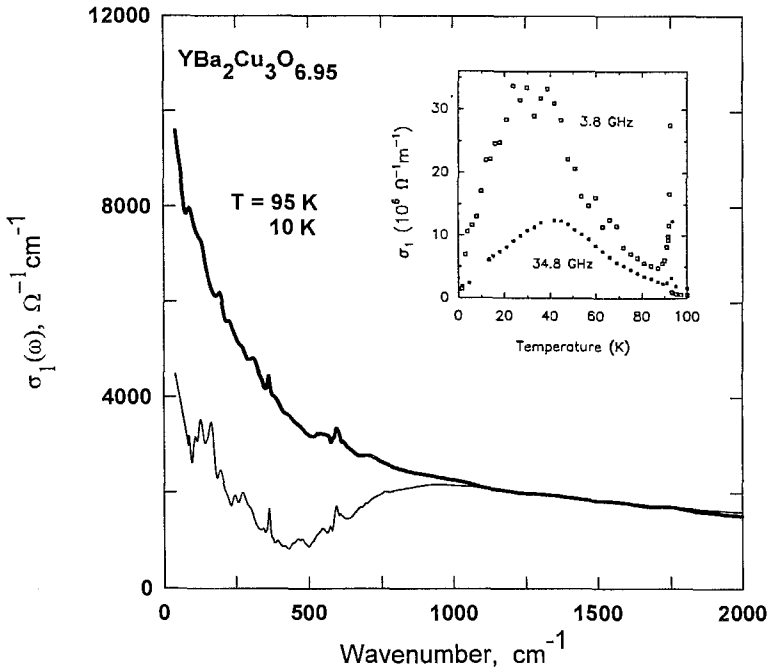

Fig. 13. Real part of the in-plane optical conductivity of a twinned single crystal of $YBa_2Cu_3O_{6.95}$ at $T \approx T_c$ and at $T = 10\,K$ (from Basov et al. 1994a). The inset shows the temperature dependence of the real part of the conductivity at $\omega = 34.8\,GHz = 0.99\,cm^{-1}$ and at $\omega = 3.8\,GHz = 0.11\,cm^{-1}$, obtained for the crystal from the same source with microwave methods (from Bonn et al. 1993).

Infrared spectroscopy is a powerful technique for the study of low-lying states in superconductors, and the number of papers devoted to this subject in the high-T_c materials is large. In order to isolate the essential features of the superconducting-state response it might be instructive to begin with the *ab*-plane conductivity of a twinned $YBa_2Cu_3O_{6.95}$ crystal, which is to date the best studied material. In the superconducting state, the conductivity is suppressed compared to the spectrum measured at $T \approx T_c$ over a broad energy range extending at least up to $1000\,cm^{-1}$ (fig. 13). The conductivity shows a broad minimum at $\omega \approx 500\,cm^{-1}$ which was often confused with the energy gap. However, there is no evidence whatsoever to assign this feature to the superconducting gap. This is because $\sigma_1(\omega)$ remains *finite* down to the lowest frequencies in the infrared *and* microwave frequency regions (Pham et al. 1990, 1991, Renk et al. 1991, Miller et al. 1993, 1995, Basov et al. 1994b). Also, as first pointed out by Reedyk et al. (1988), and subsequently by a number of authors (Tanner and Timusk 1992), in the underdoped samples the minimum of the conductivity is observed already in the normal state, and its frequency position does not scale with T_c (Orenstein et al. 1990). Finally, in the clean limit that applies to high-temperature superconductors (Bonn et al. 1992), no feature is expected in the conductivity at the gap frequency. Basov et al. (1996) have shown that the threshold of

absorption and the minimum in the conductivity originate from the suppression of the scattering rate at $T < T^*$. Its relation to the superconducting gap is still a matter of theoretical interpretation.

While it is difficult to extend infrared measurements below 30–40 cm^{-1}, microwave experiments (Bonn et al. 1993) performed on crystals from the same source clearly show the existence of a narrow quasiparticle mode with width $1/\tau \approx 1$–$3\,cm^{-1}$ at low temperatures. This is consistent with the vanishing of $1/\tau(\omega \to 0)$ obtained from the one-component analysis of the infrared conductivity (fig. 8). The width and the spectral weight of the narrow mode in $\sigma_1(\omega)$ are strongly temperature dependent. The competition between the suppression of the scattering rate in the superconducting state and the reduction of the spectral weight of the normal fluid (due to pair formation) produces a peak in the T-dependence of $\sigma_1(\omega)$ at $T \approx 30$–40 K (see inset of fig. 13).

The residual absorption in the superconducting state at $T \ll T_c$ is a well-established result. This absorption is found in *all* cuprates for which accurate data exist. The finite dissipation in the FIR region is remarkably well documented through direct absorption measurements using bolometric techniques (Pham et al. 1991, Miller et al. 1993). In particular, residual absorption was found in the measurements performed for untwinned Y123 and Y124 crystals for the polarization of the $\boldsymbol{E}$ vector along the a-axis (Pham et al. 1991, Schützmann et al. 1992, Basov et al. 1995a, Kircher et al. 1994, Holmes and Richards 1997). These latter experiments ruled out earlier suggestions that the residual losses are solely connected with the Cu–O chains. Indeed, in a-axis measurements, where the chains are normal to the polarization of the electromagnetic radiation, the chains do not contribute to the optical conductivity but $\sigma_1(\omega)$ was still found to be finite down to the lowest accessible frequencies. Moreover, Timusk et al. (1995b) have shown that the results obtained in three different groups for the a-axis conductivity are in good quantitative agreement with one another. Since there is almost no sample-to-sample variation in the a-axis response of Y123 it is difficult to assign residual absorption to sample imperfections. Chain-free $Pb_2Sr_2ReCu_3O_8$, Bi2212 and Tl2201 crystals also show finite FIR conductivity in the superconducting state (Reedyk 1992, Puchkov et al. 1995, 1996c, Barowski et al. 1996).

Somal et al. (1996) used a technique of reflectance spectroscopy at grazing angle of incidence to examine the FIR conductivity of $La_{1.85}Sr_{0.15}CuO_4$. The advantage of grazing-incidence measurements is that they significantly improve the experimental accuracy in determination of the optical constants for highly reflective substances. The results of these measurements, presented in fig. 14, convincingly show a residual conductivity in this material.

At the time of writing it still remains unclear whether or not the ab-plane response of the electron-doped superconductor $Nd_{2-y}Ce_yCuO_4$ is also characterized by residual losses. Microwave measurements seem to indicate conventional electrodynamic response consistent with an s-wave gap (Wu et al. 1993). But this assertion was not supported by a FIR transmission experiment which did not show any of the expected features of the s-wave BCS superconductor (Choi et al. 1996). The conclusion of an isotropic BCS gap with a magnitude between 4.1 and $4.9kT_c$ (Stadlober et al. 1995) was inferred from Raman

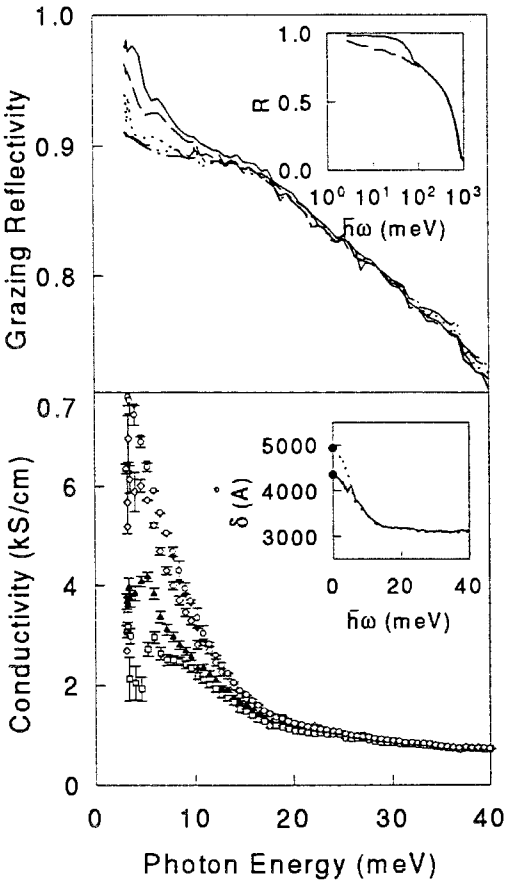

Fig. 14. Upper panel: *ab*-plane reflectivity of $La_{1.85}Sr_{0.15}CuO_4$ at 80° angle of incidence at 4 K (solid curve), 20 K (dashed), 27 K (dotted), 40 K (dash–double-dotted) and 50 K (chained). Inset: reflectivity at normal angle of incidence for 40 K (solid) and 300 K (dashed). Lower panel: optical conductivity at 50 K (inverted solid triangles), 40 K (circles), 27 K (lozenges), 20 K (solid triangles) and 4 K (squares) obtained from the reflectivities using Kramers–Kronig relations. Inset: skin depth for 4 K (solid) and 20 K (dashed). The solid dots are the penetration depth obtained from the conductivity sum rule.

measurements. In contrast, Choi et al. (1996) concluded that the electromagnetic response reveals certain similarities with the Y123 series which by no means can be classified as an s-wave system. J.R. Cooper (1996) suggested that $Nd_{2-y}Ce_yCuO_4$ can mimic the behavior of conventional superconductors because Nd acts as a magnetic impurity in this material. The controversy regarding an s-wave gap in electron-doped superconductors can be resolved by measurements of the optical constants in the superconducting state in the energy gap region ($2\Delta_{BCS} \approx 50\,cm^{-1}$). This is a demanding experiment, and the only available set of conductivity data does not extend below $50\,cm^{-1}$ (Homes et al. 1997).

The residual absorption found in the vast majority of cuprates is not consistent with s-wave symmetry of the superconducting order parameter. Since the DOS inside the gap region of an s-wave superconductor is exactly zero at $T = 0$, the dissipative part of the conductivity must vanish for $\omega < 2\Delta$, in clear contrast with the experimental data. There have been several attempts to explain the residual absorption in the superconducting state assuming d-wave symmetry. In a d-wave superconductor, the DOS is finite at all finite

frequencies, which is the necessary condition to account for non-vanishing absorption. However, detailed calculations for a d-wave superconductor show that the experimentally observed residual conductivity in the low-frequency region is still extremely large for any realistic choice of the scattering rate (Carbotte et al. 1995, Quinlan et al. 1996). Indeed, free-carrier absorption is prohibited in a clean metal by momentum conservation. Absorption is possible if impurities are introduced into the problem. But impurities are detrimental to the transition temperature of a d-wave superconductor (Rojo and Levin 1993, Radtke et al. 1993). Also, it is known that even minor concentrations of impurities lead to changes of the temperature dependences of the penetration depth $\lambda_{ab}(T)$ from linear in clean crystals to quadratic is disordered materials (Bonn et al. 1993). In this context, it is important to emphasize that the residual absorption is found in samples with the highest T_c for the Y123 series that exhibit a linear law for the penetration depth (Zhang et al. 1994, Basov et al. 1995a). In summary, the simple d-wave picture is capable of accounting for many important trends in the *ab*-plane response but not the residual conductivity in the low-frequency region. Recent calculations with resonant scattering from impurities, to be discussed below in the section on impurities, do offer a possible mechanism that accounts for the finite low-frequency conductivity (Lee 1993 and Branch and Carbotte 1998).

It is interesting to compare $\sigma_{dc}(T)$ and $\sigma_1(\omega)$ in the limit of zero temperature for superconducting crystals. The latter quantity can be determined relatively easily from the infrared measurements. But in order to obtain $\sigma_{dc}(T \rightarrow 0)$, superconductivity has to be suppressed. This has become possible due to recent progress in pulsed magnetic-field techniques which are now capable of achieving fields up to 60 T. Such fields are sufficient to suppress superconductivity in materials with T_c around 30 K (Boebinger et al. 1996) including $La_{1.85}Sr_{0.15}CuO_4$. Experiments by G. Boebinger and collaborators revealed a cross-over of $\rho(T)$ at $T < T_c$ to a non-metallic dependence: $\sigma_{dc}(T) = 1/\rho_{dc}(T)$ *decreases* with decreasing *temperature.* This suggests that the material has an unusual ground state at $T \rightarrow 0$. Measurements of the infrared conductivity for the same material (Somal et al. 1996) clearly show that $\sigma_1(\omega)$ increases with decreasing *frequency.* This latter behavior is consistent with a metallic ground state. We note that usual transport theories result in a similar T and ω dependence of the conductivity (Pines and Nozières 1966). As discussed in sect. 4.3 this T and ω behavior of the conductivity is similar in cuprates at $T > T_c$. A comparison of the results of Somal et al. (1996) with the data obtained by Boebinger shows that this correspondence is no longer observed at $T < T_c$ at least in La214. If this result is confirmed by measurements on the *same sample,* it will be indicative of completely novel transport phenomena in high-T_c cuprates.

We now turn to the discussion of superconducting-state properties for the case where the electric field and the induced currents are along the *c*-axis. The charge dynamics along the *c*-axis are incoherent, which in principle simplifies the search for the superconducting gap. At the time of writing, *c*-axis results in the superconducting state are available for Y123 (Bauer 1990, Homes et al. 1993b, Schützmann et al. 1994, Hauff et al. 1996, Lobo et al. 1996, Münzel et al. 1996, Homes et al. 1995a) for Y124 (Basov et al. 1994a, Tajima et al. 1998), $Bi_2Sr_2CaCu_2O_8$ (Tajima et al. 1993), for La214 (Tamasaku et al. 1992, Gerrits

et al. 1994), Uchida et al. 1996, Basov et al. 1995b, Henn et al. 1996, Schützmann et al. 1997, Birmingham et al. 1996), $Pb_2Sr_2ReCa_2Cu_3O_8$ (Reedyk et al. 1994), $Tl_2Ba_2CuO_{6+\delta}$ (Schützmann et al. 1997), and $La_2CuO_{4+\delta}$ (Quijada et al. 1995). In all these materials, the conductivity remains finite down to lowest frequencies and there is no evidence for the superconducting energy gap. Thus, the *c*-axis experiments (figs. 11, 12) reinforce the conclusion of the gapless response inferred from the in-plane studies.

There have been attempts to account for gapless *c*-axis conductivity with models where the order parameter is anisotropic. For the optimally doped compounds these attempts have had some success. Homes et al. (1993b) concluded that the superconducting-state conductivity of $YBa_2Cu_3O_{6.95}$ is consistent with the calculations performed for a p-wave superconductor (Hirschfeld et al. 1989). The principal feature of the data, which is in accord with a p-wave model, is that the conductivity varies linearly with frequency at $T \ll T_c$. Uchida (1997) also observed a linear variation of $\sigma_1(\omega)$ in the optimally doped $La_{1.85}Sr_{0.15}CuO_4$ crystal. They fitted the results with a model for a d-wave superconductor (Graf et al. 1995a,b). However neither d- nor p-wave models account for the conductivity in the underdoped Y123 samples. Indeed, in these materials the spectra of $\sigma_1(\omega)$ are dominated by the pseudogap which occurs in the normal state at $T < T^*$ (fig. 11). An interesting feature of the conductivity spectra obtained for underdoped crystals (both Y123 and La214) is the similarity of the normal-state results obtained at $T_c < T < T^*$ and the superconducting-state data. The same conclusion follows from the discussion of the in-plane conductivity of underdoped crystals shown in fig. 7.

It is often asserted that the similarity between superconducting- and normal-state data for underdoped cuprates is related to the fact that the pseudogap is a precursor of the superconducting gap. This "precursor hypothesis" is inconsistent with the *c*-axis conductivity of the Y123, Y124, and La214 series. At least in these materials, the formation of the pseudogap is arrested at $T \approx T_c$ (Basov et al. 1995b, Homes et al. 1995a). This conclusion follows from the analysis of the destination of the spectral weight at $T < T^*$ and T_c that can be determined from the imaginary part of the conductivity. When the spectral weight is transferred below the low-ω boundary of the measurements, the imaginary part of the conductivity is enhanced. The closest analogy of this process is the formation of the superconducting delta function at $\omega = 0$ which leads to the increase of $\sigma_2(\omega)$ depicted in fig. 15. On the contrary, when spectral weight is transferred to *higher* energies, $\sigma_2(\omega)$ is suppressed and can even become negative. The development of a pseudogap in the *c*-axis response is always associated with the latter process. On the other hand, suppression of $\sigma_1(\omega)$ in the superconducting state is associated with the formation of a superconducting condensate, and the spectral weight missing from $\sigma_1(\omega)$ at finite frequencies is recovered under the delta function at ω=0. Also, the two processes have markedly different energy scales. While the characteristic scale related to the pseudogap in the Y123 and Y124 series is about $300\,cm^{-1}$, the superconducting condensate is accumulated from energies extending up to at least $1000\,cm^{-1}$ (Basov et al. 1995b).

Perhaps the most intriguing feature of the *c*-axis response in the superconducting state is the development of a "plasma edge" (Bonn et al. 1987) in the far infrared. The effect is most clearly observed in the La214 system (fig. 16). In these strongly

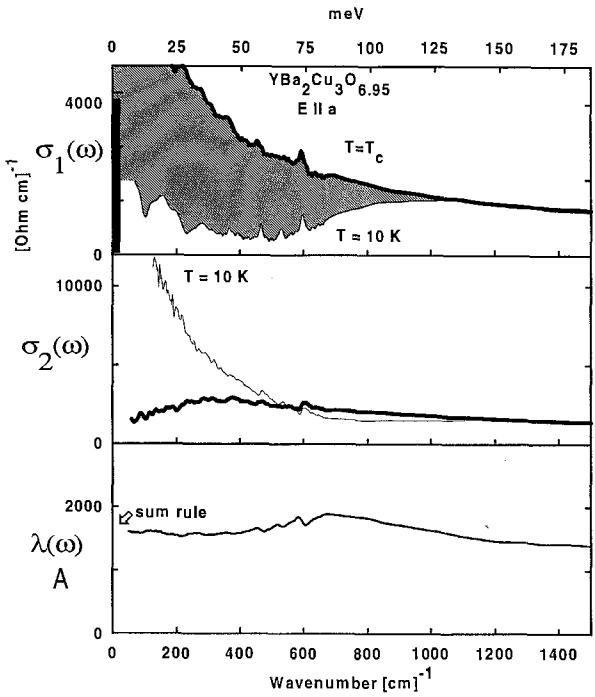

Fig. 15. Infrared probe of the penetration depth in superconductors. The top panel shows the frequency dependence of the real part of the conductivity obtained for the polarization of the incident radiation along the a-axis of a $YBa_2Cu_3O_{6.95}$ single crystal. Thick curve: $T \approx T_c$; thin curve: $T \ll T_c$. Upon transition to superconducting state, part of the spectral weight (shadowed area) is transferred to a delta function at $\omega = 0$. This is also indicated by a characteristic $1/\omega$ dependence of the imaginary part of the conductivity (middle panel). That the $1/\omega$ law for $\sigma(\omega)$ is indeed followed in the superconducting state is illustrated in the plot of $\lambda(\omega) = c/\sqrt{\omega \times \sigma_2(\omega)}$ (bottom panel). In the limit of zero frequency, $\lambda(\omega)$ extrapolates to the penetration depth which can alternatively be determined from the sum rule for the spectra of $\sigma_1(\omega)$ (eq. 14). Experimental results are from Basov et al. (1995a).

anisotropic materials, the reflectance spectra taken in the normal state are "insulator-like": one finds several strong phonon modes at $\omega > 200\,\mathrm{cm}^{-1}$ and a flat, frequency-independent background in the far infrared where $R \approx 0.5$ (Tamasaku et al. 1992, Basov et al. 1995b, van der Marel and Kim 1995, Gerrits et al. 1995, Birmingham et al. 1996, Uchida et al. 1996). There is very little temperature dependence in the spectra as T decreases from 300 K down to $T \approx T_c$. However, as soon as these samples undergo the superconducting transition the reflectance immediately changes its character: R nearly reaches unity at the lowest frequencies and then abruptly drops down to $R \approx 0.2$. At higher energies, the reflectance slowly recovers to the magnitude seen in the normal state. This behavior resembles the plasma resonance that occurs in ordinary metals at $\omega \approx \omega_p$.

Two different approaches have been used to explain the sudden appearance of this feature in the superconducting reflectance. As originally pointed out by Bonn et al. (1987) the sharp feature originates from a zero crossing of the real part of the dielectric function resulting from an interplay between the positive phonon contribution and the large negative contribution of the superconducting condensate. In the normal state the c-axis plasmon is strongly damped, but at $T < T_c$ the scattering rate suddenly drops and the plasma resonance becomes observable (van der Marel and Kim 1995). An alternative scenario is to interpret this feature as the result of Josephson coupling between the CuO_2 layers (Tamasaku et al. 1992, Basov et al. 1994a). Employing a theory developed in the early 1970s for the electrodynamics of an array of Josephson-

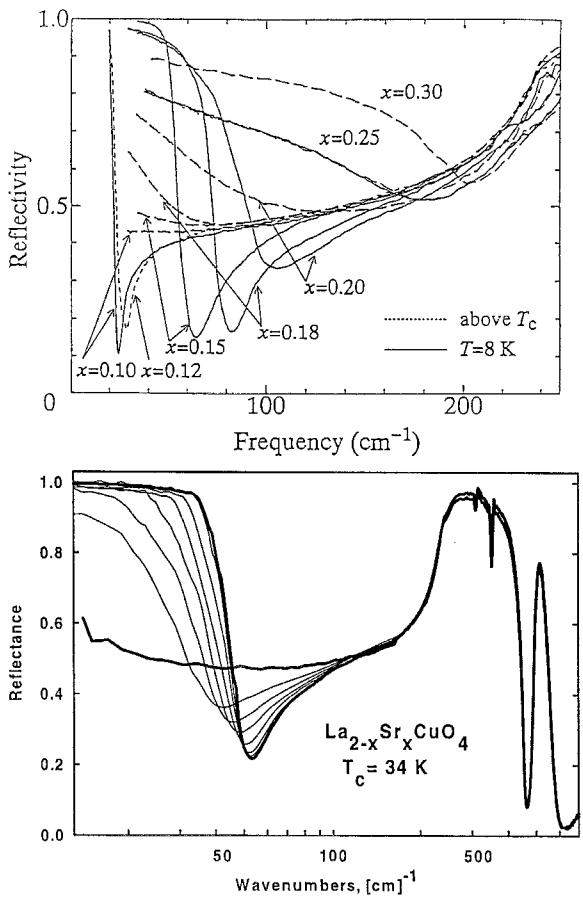

Fig. 16. Top panel: spectra of the c-axis reflectivity measured above ($T \approx 40$ K, dashed curves) and below T_c ($T = 8$ K, solid curves) for various compositions of $La_{2-x}Sr_xCuO_4$ single crystals between 0.10 and 0.30 (from Uchida et al. 1996). Bottom panel: spectra of the c-axis reflectivity for a single crystal of $La_{2-x}Sr_xCuO_4$ with T_c = 34 K measured at 8 K, 17 K, 20 K, 22 K, 25 K, 27 K, 32 K and 35 K (from Basov et al. 1995b).

coupled junctions (Lawrence and Doniach 1971, Bulaevskii 1973), it is possible to reproduce the frequency dependence of the observed reflectance. An obvious difference of cuprates from artificial Josephson contacts is that the "normal" barriers inside the unit cell of the crystal have thicknesses of the order of interatomic distances. This shifts the plasma edge from GHz frequencies, which are typical for artificial junctions of conventional superconductors, to the THz range (20–200 cm^{-1}) in cuprates. One also observes that the frequency position of the plasma resonances scales with doping in a series of $La_{2-x}Sr_xCuO_4$ crystals from 20 cm^{-1} in underdoped samples up to 120 cm^{-1} in overdoped materials. The consequences of Josephson currents for the c-axis penetration depth will be discussed in the next subsection.

Concluding this subsection, we stress that there is no experimental evidence for a clear superconducting energy gap in any of the cuprates. Residual absorption is universally found in high-T_c superconductors. This behavior is different from the response of other

novel superconductors such as K_3C_{60} and Rb_3C_{60} (Degiorgi et al. 1994, Koller et al. 1996) or borocarbides (Bommeli et al. 1997) which all show strong evidence in favor of a BCS gap in the infrared conductivity. Theoretically, the response of cuprates is better understood within a d-wave model, while, in our opinion, we still have a long way to go before the calculations yield a self-consistent explanation of infrared *and* microwave properties.

5.2. *Anisotropic penetration depth in cuprates*

Regardless of the microscopic details of the superconducting mechanism, the transition into the superconducting state is associated with the formation of a delta function in the real part of the conductivity at $\omega = 0$. From the point of view of the electrodynamic response, this implies that the spectra of $\sigma_1(\omega)$ must be suppressed at finite frequencies, with the spectral weight being transferred to the delta function. "The missing spectral weight" is identical to $1/\lambda^2$, according to the superconducting-state sum rule (Tinkham and Ferrell 1959). Alternatively, the magnitude of λ can be inferred from the imaginary part of the conductivity since a delta function $\sigma_1(0)$ with the spectral weight $1/\lambda^2$ implies by KK that $\sigma_2(\omega) \propto 1/(\lambda^2 \times \omega)$. Note that the penetration depth $1/\lambda^2 = n_s e^2/m$ is not equivalent to the London penetration depth defined as $1/\lambda_L^2 = ne^2/m$. The difference arises from the fact that the density of superconducting carriers n_s is usually smaller than the total carrier density n leading to $\lambda_L < \lambda$. The two quantities coincide only in the clean limit when the width of the Drude peak in $\sigma_1(\omega)$ is much smaller than the energy gap. In this case it is usually concluded that "all free carriers condense."

Figure 15 illustrates the two approaches towards the determination of the penetration depth from infrared where data for the *a*-axis conductivity of the $YBa_2Cu_3O_{6.95}$ compound (Basov et al. 1995b) are shown. The real part of the conductivity $\sigma_1(\omega)$ is suppressed at $T < T_c$. That the missing spectral weight (shadowed in the diagram) is transferred to a delta function at $\omega = 0$ is indicated by the frequency dependence of $\sigma_2(\omega)$ in the superconducting state. It acquires the characteristic $1/\omega$ dependence which signals that the spectral weight is recovered in the delta function. To show the presence of a $1/\omega$ term it is often instructive to plot the product of $1/\sqrt{\omega\sigma_2(\omega)}$, which in the zero-frequency limit yields the value of λ. Thus, the penetration depth or the superfluid density can be obtained from:

(i) the sum rule for the optical conductivity,

$$\frac{c}{\lambda^2} = \omega_{ps}^2 = \frac{120}{\pi} \int_0^\infty d\omega \, [\sigma_1(\omega, T \approx T_c) - \sigma_1(\omega, T \to 0)], \tag{14}$$

and/or

(ii) from examining the prefactor in front of the $1/\omega$ term in the imaginary conductivity:

$$\frac{c}{\lambda^2} = \omega_{ps}^2 = \omega \times \sigma_2(\omega, T \to 0). \tag{15}$$

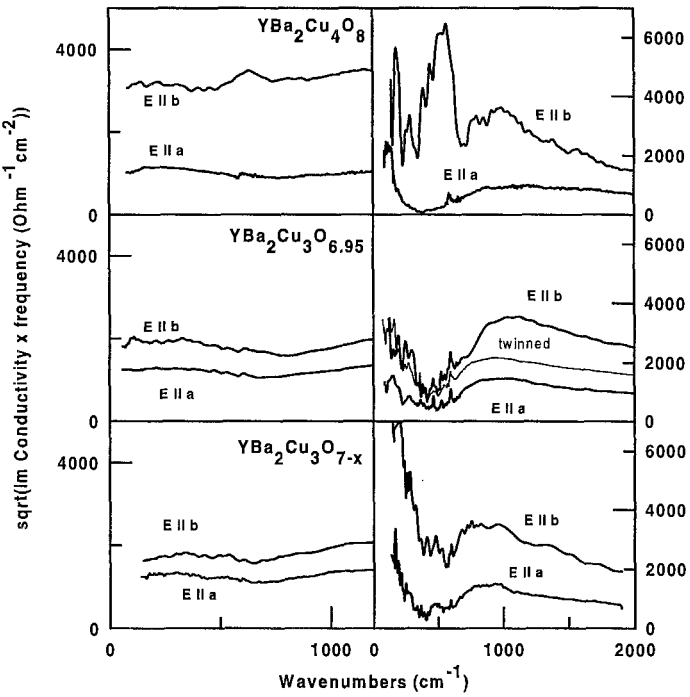

Fig. 17. Left-hand panels: Frequency-dependent penetration depth $\lambda = c/[\omega\sigma_2(\omega)]$ for a Y124 sample (upper panel), and two different Y123 samples (middle and bottom panels). Right-hand panels: the real part of the complex conductivity . All curves shown are at 10K. The left-hand panels reveal clear anisotropy of the penetration depth which is stronger for the double-chained Y124 material. From Basov et al. (1995a).

In our experience, in the case of the *ab*-plane response the sum-rule result for the penetration depth (eq. 14) often yields a larger value than the estimate from $\sigma_2(\omega)$. However, since the difference usually does not exceed 10% it may be premature to put too much trust in this result until the experimental accuracy is improved.

A unique advantage of infrared spectroscopy for studies of the penetration depth in cuprates is that *all diagonal components* of the penetration-depth tensor can be obtained from model-independent analysis of infrared data for single-crystal samples. The analysis using eqs. (14) and (15) can be applied to the conductivity probed with polarized light for the polarization of *E*-vectors both along the CuO_2 planes and along the *c*-axis. In the YBCO series, there is an additional anisotropy associated with the Cu–O chains. Infrared experiments carried out with incident radiation polarized along the chain direction (*b*-axis) and perpendicular to the chains (*a*-axis) made it possible to extract both λ_a and λ_b (Basov et al. 1995a).

The frequency dependence of $\lambda(\omega) = c/\sqrt{(\sigma_2(\omega) \times \omega)}$ for untwinned Y123 and Y124 crystals with polarizations of incident radiation along *a*- and *b*-axes is shown in fig. 17. In the limit of zero frequency, $\lambda(\omega)$ extrapolates to the penetration depth of a

superconductor. An interesting result is that the penetration depth is strongly suppressed when it is probed along the direction of the Cu–O chains ($E \parallel b$). In the double-chained Y124 crystal the anisotropy is larger. These observations are consistent with the notion that the chains are superconducting in YBCO compounds (Basov et al. 1995a). In high-quality $YBa_2Cu_3O_{6.95}$ crystals the anisotropy of the penetration depth is approximately the same as that of the dc resistivity or of the normal-state plasma frequency: $\lambda_a^2/\lambda_b^2 \approx rho_a/\rho_b \approx \omega_{p\,b}^2\omega_{p\,a}^2 \approx 2.3$. While the absolute values of λ_a and λ_b are different, the temperature dependence of these quantities is identical based on microwave measurements (Zhang et al. 1994). The frequency dependence of $\sigma_1(\omega)$ is also very similar for the two polarizations. This indicates that the electrodynamic response of $YBa_2Cu_3O_{6.95}$ is identical along the *a*- and *b*-directions, except for the additional spectral weight along the *a*-axis.

That the 1D Cu–O chains contribute to the superfluid density is a robust experimental observation first found with IR spectroscopy (Basov et al. 1995a) and later confirmed with muon-spin relaxation (μSR) spectroscopy (Tallon et al. 1995) and Josephson-tunneling measurements (Sun et al. 1995). With scanning tunneling spectroscopy, it was possible to detect a gap-like feature for the Cu–O chains similar in magnitude to that for the CuO_2 planes (Edwards et al. 1995). The interpretation of these results indicating superconductivity in the Cu–O chains is difficult. Most theoretical models start from the notion that the pairing mechanism is an exclusive property of the CuO_2 planes, whereas other elements of the unit cell are regarded as passive placeholders. Within this approach, one attributes the formation of the superconducting condensate in the chains to a proximity effect between "intrinsically superconducting" CuO_2 planes and "intrinsically normal" Cu–O chains (Kresin and Wolf 1992, Xiang and Wheatley 1995). The major problem with this interpretation is that proximity-based models cannot account for the identical temperature dependences of λ_a and λ_b found with microwave spectroscopy (Zhang et al. 1994). Indeed, one expects that proximity coupling induces a gap in the normal layer that has suppressed magnitude (Kresin and Wolf 1992, Atkinson and Carbotte 1995). This will inevitably lead to a difference in the T-dependence of the penetration depth (Atkinson and Carbotte 1995) and to a difference in the frequency dependence of $\sigma_1(\omega)$ (Atkinson and Carbotte 1997). Both of these expectations, based on the proximity-coupling model, are *inconsistent* with experiments. The failure of the proximity-based scenario to account for experimental observations may be suggestive that the Cu–O chains are also intrinsically superconducting.

In fig. 18, we summarize the experimental results for the in-plane penetration depth obtained with infrared spectroscopy for a variety of cuprates. There are two principal trends revealed by this plot:

(i) In many materials, T_c scales with the superfluid density. This was first discovered by Uemura et al. (1989, 1991) based on the analysis of the μSR data.

(ii) In YBCO materials containing Cu–O chains, only the *a*-axis superfluid density correlates with T_c. The anisotropy of the penetration depth may account for the "plateau regions" in the original Uemura plot observed for samples close to optimal doping. In disordered crystals, the linear dependence between the superfluid density

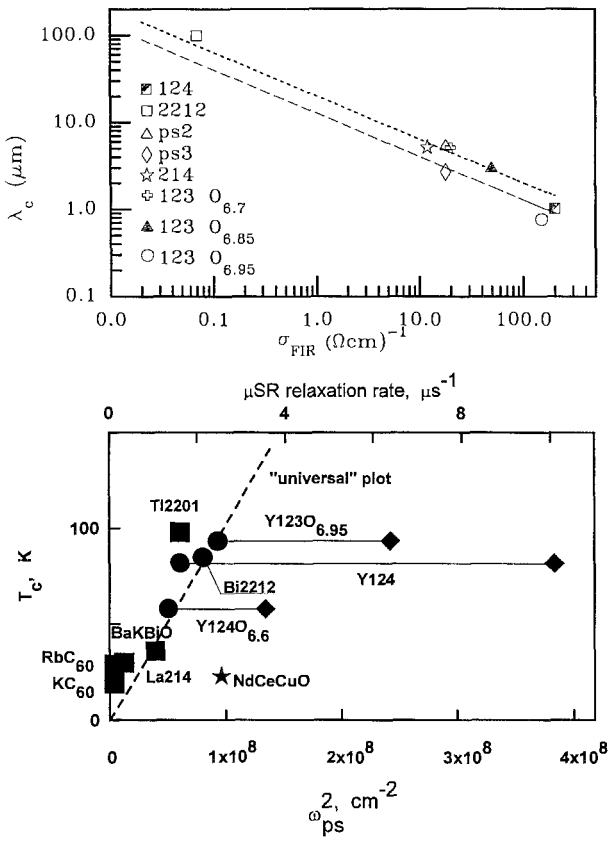

Fig. 18. Upper panel: Correlation between the values of the penetration depth λ_c and the c-axis conductivity of different high-T_c superconductors. Lines are calculations for the case of Josephson coupling between the CuO_2 planes assuming $2\Delta = 128\,cm^{-1}$ (short dashes) and $2\Delta = 320\,cm^{-1}$ (long dashes). From Basov et al. (1994a). Lower panel: in-plane superfluid density ω_{ps} in a variety of high-T_c superconductors. For the purpose of comparison with analogous plots based on the μSR data, units for the top axis are given in μSR relaxation rate. In many cuprates the critical temperature appears to be linearly dependent on n_s/m^* ("universal" Uemura plot). The b-axis superfluid density in the Y123 and Y124 series (diamonds) as well as the results for the electron-doped $Nd_{2-y}Ce_yCuO_4$ show remarkable deviation from this plot. Data: Y123, Y124, Basov et al. (1995a); Tl2201, Puchkov et al. (1995); Bi2212, Quijada et al. (1994); BaKBiO, Puchkov et al. (1996d); La214, Startseva et al. (1999a); RbC_{60}, KC_{60}, Degiorgi et al. (1994).

and T_c is violated (Nachumi et al. 1996, Bernhard et al. 1996) as will be discussed in subsection 5.3. Another notable deviation from the universal plot is found in electron-doped $Nd_{2-y}Ce_yCuO_4$ (Homes et al. 1997). The superfluid density in this material significantly exceeds that of other superconductors with $T_c \approx 20\,K$.

It should be noted that within the BCS theory one does not expect to observe any explicit correlation between T_c and the superfluid density in a clean-limit superconductor. The linear dependence between the transition temperature and n_s/m^* is expected if

superconductivity is viewed as Bose–Einstein condensation. The analysis of the absolute values of the penetration depth allows one to estimate the number of carriers per area of the coherence length squared, ξ_{ab}^2, on the conducting *ab*-plane (Uemura 1996). Both cuprates and organic superconductors have only several superconducting pairs per ξ^2, which puts these systems close to the limit of Bose–Einstein condensation (1 pair per $1/\xi^2$ rather than to the limit of BCS condensation where one finds more than 10 000 carriers per ξ^2). Emery and Kivelson (1995b) emphasized that in superconductors with low superfluid density (such as cuprates and organic materials), the role of phase fluctuations is dramatically enhanced. They argued that in the above materials the magnitude of the superfluid density controls the temperature of long-range phase order and thus determines T_c. This accounts for the striking deviations of the transition temperature from typical mean-field behavior.

The *c*-axis penetration depth is strongly enhanced in all high-T_c superconductors compared to λ_{ab} (fig. 18). Typical values of λ_c range from 100 μm in the most anisotropic Bi2212 crystals (Motohashi et al. 2000, J.R. Cooper et al. 1990) to about 1 μm in the most isotropic $YBa_2Cu_3O_{6.95}$ and Y124 crystals (Homes et al. 1993b, Basov et al. 1994a, Schützmann et al. 1994). The magnitude of λ_c shows a systematic correlation with the dc conductivity along the *c*-axis, σ_c (Basov et al. 1994a). It was emphasized that the proportionality $\lambda_c^{-2} \propto \Delta \times \sigma_c$ is expected for an array of Josephson junctions (Basov et al. 1994a). Thus, Josephson electrodynamics successfully describes the main features of the *c*-axis penetration depth in a broad variety of cuprates. Recently, Tajima et al. (2001) have used the *c*-axis Josephson plasma resonance in Nd-doped $La_{1.85-y}Nd_ySr_{0.15}CuO_4$ to show that stripe order in this material suppresses the interlayer phase coherence.

The anomalous *c*-axis properties of high-T_c superconductors and the strong evidence in favor of Josephson coupling between the CuO_2 layers give experimental support for the "confinement hypothesis" of high-T_c superconductivity (Chakravarty and Anderson 1994). Within this hypothesis, the hopping of single electrons between CuO_2 planes is inhibited in the normal state by spin–charge separation. However, tunneling of pairs is allowed at $T < T_c$, which leads to a gain of kinetic energy as Cooper pairs are formed and the superconductivity sets in. This energy is the Josephson coupling energy, and it is proportional to the square of the plasma frequency of condensate probed for the polarization where the *E*-vector is along the *c*-axis. Thus, if interlayer tunneling of Cooper pairs is the driving force for superconductivity, one expects to find a correlation between T_c and $1/\lambda_c$ (Anderson 1995). A brief examination of fig. 18 suggests that, in general, such a correlation is not followed in cuprates. For example, the T_c of the most anisotropic $Bi_2Sr_2CaCu_2O_8$ crystals is nearly the same as in the most isotropic Y123 and Y124 compounds. An accurate determination of the superfluid density in Bi2212 was done by Tsui et al. (1996) using microwave techniques; they found a plasma frequency of about 5 cm^{-1}. Within the interlayer-tunneling models these estimates are inconsistent with the T_c value of 90 K. However, it should be noted that the correlation between T_c and the superfluid density expected within the confinement hypothesis may be complicated in Y123 and Bi2212 systems where there are two CuO_2 layers per unit cell.

Careful examination of the spectral-weight balance at $T < T_c$ using eq. (14) and eq. (15) suggest that in underdoped cuprates the superfluid density (the area confined in the delta peak at $\omega = 0$) exceeds the weight missing from the real part of the conductivity Basov et al. (1999). This result can be interpreted in terms of kinetic energy change ΔK (Hirsch 1992, Anderson 1995, Chakravarty 1998). However the absolute values of ΔK are significantly smaller than the condensation energy, as first pointed out by van der Marel (1996) and later discussed in several other publications (Schützmann et al. 1997), Moler et al. 1998, Tsvetkov et al. 1998, Kirtley et al. 1998).

5.3. *Temperature dependence of the penetration depth*

Using infrared spectroscopy, it is virtually impossible to obtain optical constants of a material at more than a few different temperatures. This is an obvious disadvantage of infrared techniques compared to microwave methods which allow one to study the temperature dependence of the penetration depth and of the surface resistance in great detail (Bonn and Hardy 1996). However, it is usually difficult to determine the *absolute values* of the λ-tensor with microwaves. This drawback of microwave methods is easily overcome with infrared techniques which yield all the diagonal components of λ without the need to take into consideration any geometrical factors. A combination of infrared methods providing the absolute value of $\lambda_a(T \rightarrow 0)$, $\lambda_b(T \rightarrow 0)$, and $\lambda_c(T \rightarrow 0)$ with microwaves, giving a detailed and accurate temperature dependence $\Delta\lambda = \lambda(T) - \lambda(0)$, is becoming an indispensable tool in studying the penetration depth in high-T_c superconductors.

Figure 19 shows the temperature dependence of $\Delta\lambda$ for a-, b- and c-polarizations measured from the frequency change of a superconducting loop-gap resonator ($f_0 \approx 900$ MHz) (Hardy et al. 1996). IR-determined values of λ_0 are shown in table 2. The data set for overdoped $YBa_2Cu_3O_{6.99}$ is an exception where infrared measurements have not yet been done. At all doping regimes, both a and b components of the λ-tensor reveal linear behavior which was first observed in twinned $YBa_2Cu_3O_{6.95}$ samples (Hardy et al. 1993).

The linear variation of the penetration depth is different from what is expected for a BCS superconductor with an isotropic gap. An isotropic gap leads to an exponential dependence of $\lambda(T)$. While the thin-film specimens studied prior to 1992 tended to show a T^2 law for $\lambda(T)$, a series of more recent studies performed on high-quality single crystals show a T-linear law for $\lambda(T)$ (Ma 1995, Jacobs et al. 1995). A consensus is emerging in the field that the earlier observations of a T^2 dependence were dominated by impurity effects, whereas intrinsic behavior of the penetration depth can be found only in clean samples, and that variation is linear with T. This problem was studied in detail by the group at the University of British Columbia. Starting from a high-purity $YBa_2Cu_3O_{6.95}$ single crystal with $\Delta\lambda_{ab} \propto T$, Bonn et al. (1994) deliberately added Zn and Ni ions which are believed to substitute for Cu in the CuO_2 planes. They observed a cross-over to a $\Delta\lambda_{ab}(T) \propto T^2$ law in the crystal, containing as little as 0.31% Zn.

Recent thin-film samples also show a linear penetration depth at low temperatures. This behavior was first observed by Gao et al. (1993b) in their microwave experiments

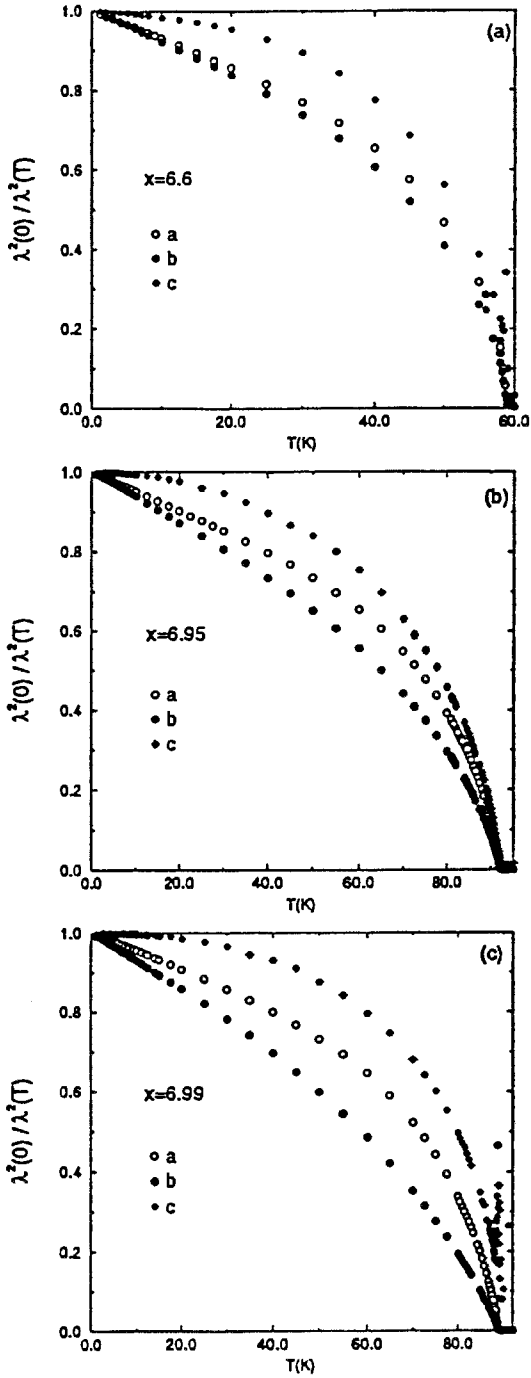

Fig. 19. $\lambda^2(0)/\lambda^2(T)$ versus T for a, b, and c directions in $YBa_2Cu_3O_x$ single crystals. The absolute values of $\lambda(0)$ are given in table 2. From Hardy et al. (1996).

Table 2
Values of $\lambda(0)$ obtained with IR spectroscopy (Basov et al. 1995a, 1996) used to generate $\lambda^2(0)/\lambda^2(T)$ in fig. 19 based on microwave measurements

x	T_c (K)	$\lambda_a(0)$ (Å)	$\lambda_b(0)$ (Å)	$\lambda_c(0)$ (Å)
6.60	59	2100	1600	65000
6.95	93.2	1600	1030	11000
6.99	89	1600[a]	800[a]	11000[b]

[a] Value estimated based on μSR results for λ_a/λ_b (Tallon et al. 1995).
[b] Value measured directly using microwave technique.

conducted at 10 GHz. Dahne et al. (1995) and de Vaulchier et al. (1996) used backward-wave oscillators operating at frequencies from 3 cm^{-1} up to 15 cm^{-1} to examine the temperature dependence of the penetration depth in thin-film samples of $YBa_2Cu_3O_{6.95}$. They also observed a linear behavior of $\lambda_{ab}(T)$. These recent observations are clearly consistent with the notion that the T^2 variation found in the earlier samples was of extrinsic origin and only high-purity crystals and films of YBCO show a linear penetration depth variation with temperature.

A penetration depth which varies linearly with temperature is expected for a superconductor with d-wave symmetry of the order parameter (Prohammer and Carbotte 1991, Hirschfeld et al. 1994). There are also a number of alternative explanations. For instance, a linear term in $\lambda(T)$ can be caused by the presence of normal 2D layers sandwiched between the CuO_2 planes (Klemm and Liu 1995). Another possibility is that a d-wave response can be mimicked by the complicated band structure of the YBCO system involving both plane and chain bands (Combescot and Leyronas 1995). It was also pointed out that Josephson coupling in a bilayer system can, in principle, lead to vanishing of the gap function at certain momenta and thus bilayered materials may imitate properties of d-wave superconductors without invoking a d-wave state (Gauzzi and Bok 1996). Finally, a number of theories suggest that the linear $\lambda(T)$ can originate from fluctuations of the phase of the order parameter (Radtke et al. 1993, Roddick and Stroud 1995, Coffey 1995, Emery and Kivelson 1995a). Further work is required to distinguish between the proposed models.

There has been one suggestion, based on microwave measurements, that the intrinsic behavior of the penetration depth in Y123 crystals can be different from linear. Srikanth et al. (1997) reported a *non-monotonic* behavior of $\lambda(T)$ in single crystals grown in BZO crucibles. Such crystals are claimed to have superior purity compared to the previous generation of Y123 samples grown in yttria-stabilized zirconia (YSZ) crucibles. So far, the experimental results are limited to twinned samples at optimal doping. However, a recent result on untwinned samples, also grown in BZO crucibles, fails to show this unusual behavior (Kamal et al. 1998).

Several groups have reported measurements of the temperature dependence of the c-axis penetration depth in YBCO (Basov et al. 1994a, Mao et al. 1995, Hardy et al. 1996, Lobo et al. 1996, Homes et al. 1997), $Bi_2Sr_2CaCu_2O_8$ (Jacobs et al. 1995) and La214

(Shibauchi et al. 1994, Basov et al. 1995b, Henn et al. 1996). The present experimental situation is controversial. In part, the variation in the data from different groups can be attributed to anomalous sensitivity of the *c*-axis properties of cuprates, even to minor variations of doping.

5.4. *Impurity effects*

A desire to establish the symmetry of the superconducting order parameter was the driving force of a large number of experimental programs. Among them were numerous attempts to distinguish between s- and d-pairing through studies of the effect of impurities on the transition temperature, the complex conductivity and the T-dependence of the penetration depth. Non-magnetic impurities have little effect on the superconductivity in elemental metals (Anderson 1958). On the contrary, anisotropic superconductors are expected to be anomalously sensitive to impurities or disorder, and impurities lead to a smearing of the gap anisotropy towards some average value. In particular, the average of the d-wave gap is equal to zero and, therefore, in a d-wave system, superconductivity is easily suppressed even with minute concentrations of impurities. In qualitative agreement with the picture of anisotropic superconductivity, the value of T_c in cuprates is diminished when thin films or single-crystalline samples are doped with non-magnetic Zn, or disordered by irradiation with low-energy ions (Valles et al. 1989, Sun et al. 1994, Tolpygo et al. 1996, Moffat 1997, Fukuzumi et al. 1996, Yoshizaki et al. 1996). Another theoretical prediction for d-wave superconductors is that impurities cause severe changes in the intragap density of states (Borkowski and Hirschfeld 1994, Fehrenbacher and Norman 1994, Preosti et al. 1994a,b, Palumbo and Graf 1996). Therefore, one expects to find dramatic effects of impurities on the temperature dependence of the penetration depth and on the frequency dependence of the complex conductivity, which both probe the low-energy excitations in a superconductor.

Early experimental studies of the infrared properties of deliberately disordered films of Y123 include the paper by Lippert et al. (1991) which was followed by the work of Sumner, Kim and Lemberger (1993) on Ni-doped Y123 films, and experiments on disordered Bi2212 thin films (Mandrus et al. 1993). Prior to 1992/93, when the above experiments were performed, it was widely believed that the high-T_c superconductors were s-wave. In the s-wave dirty limit an observation of the superconducting energy gap should be possible (Timusk and Tanner 1989, Kamarás et al. 1990, Tanner and Timusk 1992). Nevertheless, the structure at 2Δ that can be attributed to a conventional BCS gap did not appear in transmission or reflectance spectra even when impurity scattering was significantly enhanced by disorder. Instead, experiments showed that in disordered specimens, the distinction between the spectra in the normal and superconducting states became less pronounced (Ulm et al. 1995, Mandrus et al. 1993, Kim et al. 1994). The materials, in effect, acquired a strong "normal component" in the superconducting state.

Basov et al. (1994b) reported measurements of the *ab*-plane reflectance of a high-quality $YBa_2Cu_3O_{6.95}$ single crystal which they irradiated with low-energy He ions

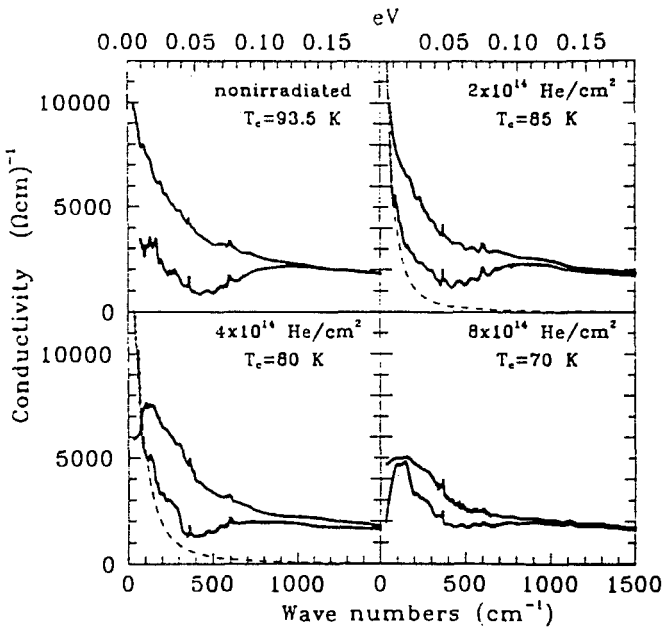

Fig. 20. Frequency dependence of the conductivity of He^+-irradiated single crystals of $YBa_2Cu_3O_{6.95}$. Upper curves in all panels were measured at temperatures slightly above T_c, while the lower curves were obtained at 10 K. The dashed curves show the fit of the narrow normal component in the superconducting conductivity to the Drude formula. After Basov et al. (1994b).

(fig. 20). Based on these measurements, they obtained the far-infrared conductivity which was analyzed within a phenomenological two-fluid model:

$$\sigma(\omega, T) = \frac{i(2\pi c)^2}{\omega\lambda^2(T)} + \frac{\omega_{pn}^2 \tau(\omega)/4\pi}{1 + i\omega\tau(\omega)}. \tag{16}$$

In eq. (16), the first term is imaginary and stands for the response of the superfluid with the spectral weight given by $1/\lambda^2$. The second term describes the residual absorption of the normal component with the simple Drude formula with the plasma frequency ω_{pn} and the scattering rate $1/\tau$. The sum rule fixes the total plasma frequency $\omega_{pD}^2 = \omega_{pn}^2 + 1/\lambda^2$. At frequencies below 150 cm^{-1}, the ω-dependence of $1/\tau$ can be neglected and, therefore, eq. (16) is adequate for the description of the low-energy results. It was found that ion damage reduced the amount of superfluid density and simultaneously enhanced the plasma frequency ω_{pn} associated with the normal component in the superconducting-state conductivity (fig. 20). The reduction of superfluid density in ion-damaged samples is consistent with the notion of pair breaking due to non-magnetic impurities. Basov et al. also concluded that irradiation has introduced sufficient impurity scattering so that an s-wave gap would be easily resolved in the spectra of $\sigma_1(\omega)$. However, there are no features in the spectra that could be attributed to such a gap. This is independent evidence

that Y123 is not an s-wave superconductor. Resonant scattering by impurities in a d-wave superconductor produces a finite density of states at the Fermi surface of magnitude $1/\tau$. This, in effect, cancels the τ factor in the Drude formula giving rise to a *universal conductivity* which is independent of impurity content (Lee 1993). Recent calculations of the optical conductivity in the presence of resonant scattering (Branch and Carbotte 1998) suggest that this mechanism may well account for the residual optical conductivity at low frequency in the high-temperature superconductors.

Carbotte et al. (1995) analyzed the complex conductivity in the presence of disorder in the weak Born-scattering limit assuming different symmetries of the order parameter. Their main result is that the data presented in fig. 20 are not consistent with an s-wave gap but can be qualitatively accounted for within a d-wave model. In particular, disordered d-wave superconductors are expected to reveal an enhancement of the spectral weight of the "normal component" in the superconducting state response. The frequency dependence of the conductivity at $T \ll T_c$ and its evolution with disorder are remarkably similar in the experimental data by Basov et al. (1994b) and in theoretical calculations by Jiang et al. (1996).

Palumbo and Graf (1996) considered an anisotropic layered superconductor which can be described as an array of superconductor–insulator (S–I–S) junctions. They calculated the superconducting conductivity in the presence of impurities for three different types of order parameters: anisotropic s-wave (ASW) $\Delta_{ASW}(\theta) = \Delta_0(1 + \cos(4\theta)/2)$, extended s-wave (ESW) $\Delta_{ESW}(\theta) = \Delta_0(1 + 3\cos(4\theta)/4)$, and d-wave (DW) $\Delta_{DW}(\theta) = \Delta_0 \cos(2\theta)$. All three order parameters have nodes on the Fermi surface, but only $\Delta_{ESW}(\theta)$ and $\Delta_{DW}(\theta)$ change sign. In order to be qualitatively consistent with the data at $T \ll T_c$, the change of sign of the order parameter is required. A similar conclusion was inferred from earlier theoretical work in the context of studies of the density of states in a disordered superconductor with anisotropic order parameter (Borkowski and Hirschfeld 1994, Fehrenbacher and Norman 1994, Preosti et al. 1994a,b). In the ASW case, disorder leads to the opening of a true gap in the superconducting DOS. On the contrary, in the DW system, the finite density of states develops in the limit $\omega \to 0$. Thus, the absorption of an ASW superconductor *decreases* in the presence of impurities contrary to the situation realized in ESW and DW superconductors. Comparison with experiment suggests that an ASW scenario can be ruled out, while both ESW and DW scenarios qualitatively agree with the data.

Disordered YBCO materials reveal additional effects connected with the presence of the one-dimensional Cu–O chains. As pointed out in sect. 5.4, in the first available *untwinned* single crystals, the chains were disordered due to contaminations with Au or Al coming from the crucibles used in the crystal growth. In this case, the response of the chains was similar to what one expects to find in disordered 1D conductors (Schützmann et al. 1992). Shibata et al. (1995) have studied the *a*- and *b*-axis conductivities of an untwinned Y123 crystal doped with Zn. Their results for the clean crystal are in accord with the data by Basov et al. (1995a): the only difference between $\sigma_{1a}(\omega)$ and $\sigma_{1b}(\omega)$ is in the magnitude of the conductivity, whereas the frequency dependence is the same. However, this similarity disappears in the crystal containing 3% Zn. The *b*-axis response

of the sample with Zn substitution shows a characteristic peak which was found in the conductivity of crystals with Ag or Au contaminations. Thus, it is conceivable that Zn occupies some of the Cu sites in the chains. Recently, Wang et al. (1998) reported a strong effect in the *b*-axis conductivity produced by Zn doping, corroborating the idea that some of the Zn impurities reside on the chains. Homes et al. (1999) reported on the conductivity of untwinned Y123 samples doped with up to 1% Ni. Their main result is that Ni induces dramatic changes in the conductivity along the chain *b*-direction, whereas the *a*-axis response is almost unchanged, even for the samples with 1% Ni. This is also in accord with the view that it is difficult to avoid distortions of the chains in the course of impurity doping.

Disorder also leads to a suppression of the *ab*-plane superfluid density in YBCO materials (Basov et al. 1994b, Ulm et al. 1995, Bernhard et al. 1996, Nachumi et al. 1996, Panagopoulos et al. 1996). The linear law between the magnitude of T_c and superfluid density in clean crystals is not observed in disordered crystals. In disordered compounds, ω_{ps} is suppressed much faster than the corresponding reduction of T_c. Ulm et al. (1995) analyzed the degradation of $\lambda_{ab}(0)$ in Ni- and Zn-doped Y123 and concluded that the increase of the in-plane penetration as a function of impurity concentration is much more rapid than the d-wave model predicts. Based on the μSR results for Zn-doped Y123, Bernhard et al. suggested that suppression of the superfluid density as the result of Zn doping is inconsistent with s-wave pairing but may be suggestive of a d-wave order parameter. Several authors discussed the possibility that the addition of impurities leads to a highly inhomogeneous state in the cuprates on a length scale comparable to the coherence length (Xiang and Wheatley 1996, Nachumi et al. 1996, Franz et al. 1997).

Even minor concentrations of impurities lead to a complete suppression of the anisotropy of the penetration depth in the *ab*-plane of the Y123 family. This effect has been observed for both Zn and Ni doping (Homes et al. 1999, Wang et al. 1998). Basov et al. (1998) have reported on the *a*-axis conductivity of $YBa_2Cu_4O_8$ crystals with Zn substitution for Cu. They show that Zn leads to the formation of a bound state in the response of the CuO_2 planes at $\omega \approx 10$ meV. The bound state corresponds to a peak in the real part of the complex conductivity which develops at the expense of the Drude-like excitation at $\omega = 0$. Peaks at finite frequency are often observed in strongly disordered conductors at the borderline of localization (Allen et al. 1975, Götze 1981, Gold et al. 1982, Ng et al. 1986, Jang et al. 1990). Many of the cuprates which are intrinsically or deliberately disordered also exhibit a peak at finite energy in the $\sigma_1(\omega)$ spectra. The former group includes twinned crystals and thin films of $YBa_2Cu_3O_{6.95}$ (Basov et al. 1994b, Kim et al. 1994). Among intrinsically disordered systems showing a peak in the conductivity, one finds $Pb_2Sr_2ReCa_2Cu_3O_8$ (Reedyk 1992), $Tl_2Ba_2CuO_6$ (Puchkov et al. 1995) or $Bi_2Sr_{2-x}La_xCuO_6$. (Weber et al. 1997). If the frequency position of these peaks in a variety of cuprates is chosen to characterize the energy scale related to localization, then this scale E_c does not exceed 120 cm^{-1}.

The results of Basov et al. (1998) for Zn-substituted $YBa_2Cu_4O_8$ demonstrate that the spectral weight from $\omega < E_c$ does not contribute to the superconducting condensate. This suggests a connection between the metal–insulator transition induced by impurities and

the degradation of T_c in disordered superconductors. Transport measurements by Valles et al. (1989), Sun et al. (1994), and Tolpygo et al. (1996) confirm the occurrence in cuprates of many of the universal trends of the superconductor–insulator transition previously seen in ultrathin films of elemental superconductors (for reviews see Liu and Goldman 1994, and Valles and Dynes 1990). So far, the studies of impurity effects (both transport and infrared) were primarily focused on underdoped and optimally doped cuprates.

Much less information is available on the effect of impurities on the c-axis conductivity. Hauff et al. (1996) analyzed the c-axis response of $YBa_2Cu_3O_{6.6}$ material with Zn substitution for Cu. The choice of this particular compound is determined by the fact that pure crystals of $YBa_2Cu_3O_{6.6}$ exhibit a well-defined pseudogap in the c-axis conductivity (see fig. 11). Another characteristic feature of the c-axis response of these crystals is a broad resonance located at $\omega \approx 400\,\mathrm{cm}^{-1}$. Homes et al. (1995b) and Hauff et al. (1996) suggested that this resonance is a product of strong coupling of oxygen modes to the electronic system. A similar mode is found in the response of $Pb_2Sr_2(Y/Ca)Cu_3O_8$ (Reedyk et al. 1994) and of $YBa_2Cu_4O_8$ (Basov et al. 1994a) but not in La214 (Basov et al. 1995b, Uchida et al. 1996). As first discussed by Hauff et al. (1996), Zn substitution reduces the strength of this resonance, while the low-frequency behavior of the conductivity in the pseudogap region ($\omega < 300\,\mathrm{cm}^{-1}$) is nearly unchanged. Zn-doped $YBa_2Cu_4O_8$ crystals also do not show this mode although, in the latter case, the authors observed considerable changes in the electronic conductivity as well (Basov et al. 1996, 1998).

6. Infrared properties of HTSC in a magnetic field

A static magnetic field enters a type-II superconductor in the form of an Abrikosov lattice of vortices, each vortex carrying a quantum of magnetic flux ϕ_0. For static fields normal to the ab-plane, the simple triangular lattice of conventional superconductors is slightly distorted due to the anisotropic penetration depth as seen in YBCO by Keimer et al. (1994) using small-angle neutron scattering. This distortion can be explained simply in terms of anisotropy of the penetration depth (Walker and Timusk 1995). In the case of YBCO, this anisotropy is large due to the superconductivity of the chains. At high temperature, near T_c, the flux lattice melts to form a fluid of vortices.

For magnetic fields normal to the c-axis, the currents that sustain the vortices must jump from plane to plane. As we have seen in the section on c-axis properties, single-particle transport in the c-direction is largely blocked in the normal state, but pair tunneling is possible through Josephson coupling of the planes in the superconducting state (Bulaevskii and Clem 1991).

Optical experiments have been done in both magnetic field geometries. With the field normal to the planes, thin-film transmission experiments probe the influence of the static magnetic field on the ab-plane transport. The conductivity can be obtained from the power transmission by Kramers–Kronig transformations or amplitude transmission by terahertz spectroscopy which yields the real and imaginary parts of the transmission

amplitude directly. To obtain the maximum information from the experiments, circularly polarized light is used to measure circular dichroism (Linh et al. 1996) or the measurements are carried out with the sample between crossed polarizers – a geometry that yields the off-diagonal component, σ_{xy}, of the Hall conductivity (Spielman et al. 1994). The complex transmission can be converted to the conductivity through $t^{\pm}(H) = [4n/(n+1)]/[Z_0 d\sigma^{\pm}(H) + n + 1]$, where $t^{\pm}$ is the complex transmission for right- and left-circularly polarized light, H is the magnetic field, d is the film thickness in cm, $Z_0 = 377$ is the impedance of free space in ohms, and n is the index of refraction of the substrate.

6.1. *The ab-plane conductivity in a magnetic field*

At microwave frequencies, the electrodynamics of HTSC have mostly been discussed in terms of phenomenological models of the response of the vortex system to an external ac field starting with Gittleman and Rosenblum (1966) and more recently by Coffey and Clem (1991). A more microscopic description, including effects of bound states in the vortex core, has been provided by Hsu (1993). For a recent review of the microwave work see Golosovsky et al. (1996).

The Lorentz force on a vortex at rest is $\boldsymbol{F}_L = \rho_s \Phi_0 [\boldsymbol{v}_s \times \boldsymbol{n}]$, where ρ_s is the charge density of the condensate and $\boldsymbol{v}_s$ is the condensate velocity. This force gives the vortex a velocity $\boldsymbol{v}_v$ normal to the current. In the rest frame of the vortex the superfluid now has an additional velocity $-\boldsymbol{v}_v$ giving rise to an additional Lorentz force (the Magnus force) of $\boldsymbol{F}_L = -\rho_s \Phi_0 [\mathbf{v}_v \times \boldsymbol{n}]$. The total force on the vortex is the sum of these: $\boldsymbol{F}_L = \rho_s \Phi_0 [(\boldsymbol{v}_s - \boldsymbol{v}_v) \times \boldsymbol{n}]$. To complete the equation of motion for the vortex, a pinning force $k\boldsymbol{r}$ and damping η are added, where $\boldsymbol{r}$ is the position of the vortex. At infrared frequencies the inertia of the vortex comes into play and a vortex mass m_v can be included in the equation of motion:

$$\rho_s \Phi_0 [(\boldsymbol{v}_s - \alpha \boldsymbol{v}_v) \times \boldsymbol{n}] - \eta \boldsymbol{v}_v - k\boldsymbol{r} = m_v \dot{\boldsymbol{v}}_v. \tag{17}$$

The parameter α has been included to parametrize the strength of the Magnus force.

With $\alpha = 0$, $m_v = 0$, we get the simple Gittleman and Rosenblum (GR) model with only two parameters, the viscous drag coefficient η and the force constant k associated with the vortex pinning. This simple model has been used extensively to fit microwave-loss data in magnetic fields (Golosovsky et al. 1996). There are several mechanisms that give rise to the η term. The Bardeen–Stephen mechanism (Bardeen and Stephen 1965) gives $\eta = \pi \hbar n \omega_c \tau$, where n and τ are the carrier concentration and relaxation rate in the vortex core and $\omega_c = eH_{c2}/mc$ is the cyclotron frequency in a field corresponding to H_{c2}. A model developed by Coffey and Clem (1991) allows one to calculate η and k from the measurements of the real and imaginary parts of the microwave surface impedance. Surprisingly, in a large number of experiments on a variety of samples this quantity is found to vary very little from the value of $\eta = 10^{-6}\,\mathrm{Ns/m^2}$, close to the Bardeen–Stephen prediction if a relaxation time of the order of the linearly extrapolated normal-state resistivity is used (Morgan et al. 1994). In contrast, the quasiparticle relaxation rate

in zero field, as determined from microwave-loss measurements, drops exponentially by several orders of magnitude just below T_c (Bonn et al. 1992). Similar results were obtained by Parks et al. (1995) using terahertz spectroscopy.

The vortex pinning constant k can roughly be estimated by the energy gained as the condensation energy $\mu_0 H_c^2/(8\pi) \times \pi\xi^2$ has to be supplied over the volume of the vortex if it is to be moved away from the pinning region. Setting this energy equal to the elastic energy $k\xi^2/2$ of pinning, one estimates $k \approx 0.25\mu_0 H_{c2}$ (Golosovsky et al. 1996). The measured value is $3 \times 10^{-6}\,\mathrm{N/m^2}$.

Solving the Gittelman–Rosenblum equations for the vortex conductivity, one finds a Lorentzian peak centered at zero frequency, with width $\omega_0 = k/\eta$, the so-called depinning frequency. From microwave data where η and k are measured separately, the depinning frequency is found to vary between 25 and 80 GHz. Far-infrared measurements of thin-film transmission yield a peak at $3.15\,\mathrm{cm^{-1}}$ [with a width of $10\,\mathrm{cm^{-1}}$ (300 GHz), considerably higher than the microwave estimate] (Linh et al. 1996). This is a result of a much smaller value of the vortex viscosity η, an order of magnitude smaller than the Bardeen–Stephen value of 1.5×10^6 (Parks et al. 1995). Parks et al. argue that the small value of η can be understood in a d-wave picture from a calculation of the d-wave density of states by Volovik (1993). They suggest that $\eta_{BS} = B_{c2}\phi_0\sigma_n$ be replaced by $\eta_{DW} = (BB_{c2})^{1/2}\phi_0\sigma_n$. They also suggest that the vortex stiffness k of the phenomenological model may not be the actual pinning parameter, but related to the changes in spectral weight of the large numbers of quasiparticles associated with each vortex in the d-wave scenario.

To be valid at higher frequencies, the simple RG vortex dynamics model has to be extended. One has to account for the vortex mass as well as excitations of the vortex core. A simple physical picture of these core excitations is a bound state of a quasiparticle confined to the vortex core of size of the coherence length ξ. This energy is approximately $\hbar\Omega = \hbar^2/(2m\xi^2) \approx \Delta^2/E_F$. The microscopic calculation of the dynamics of vortices has been done by Hsu (1993) and it gives a conductivity for circularly polarized fields,

$$\sigma_\pm = \frac{ine^2}{m\omega}\left[\frac{\omega(\omega \mp \bar{\Omega}_0) + (1-\Phi)(i\omega/\tau_v - \alpha^2)}{(\omega \mp \bar{\Omega}_0)(\omega \pm \omega_c) + i\omega/\tau_v - \alpha^2}\right], \tag{18}$$

with $\bar{\Omega} = (1-\Phi)\Omega$, a pinning constant $a\Phi = \omega_c/\Omega\,\alpha$, and the vortex lifetime τ_v. Choi et al. (1994) applied this formula to thin-film transmission experiments in circularly polarized light and found the following parameter values: $\tau_v = 40\pm5\,\mathrm{cm^{-1}}$, $\alpha = 50\pm2\,\mathrm{cm^{-1}}$. The cyclotron mass was taken to be $m = 3.1m_e$. They found a strong feature in the T^+/T^- transmission ratio at $25\,\mathrm{cm^{-1}}$ which they attribute to a hybridized pinning–cyclotron resonance frequency and a vortex-core resonance $\Omega_0 = 60\,\mathrm{cm^{-1}}$. Eldridge et al. (1995) studied the unpolarized reflectance of thicker films than those investigated by Choi et al. and, fitting Hsu's conductivity fixing $\Omega_0 = 15\,\mathrm{cm^{-1}}$, they find $\alpha = 133\,\mathrm{cm^{-1}}$ and $1/\tau = 197\,\mathrm{cm^{-1}}$.

6.2. *The c-axis conductivity in a magnetic field*

Here, measurements have focused on the low-lying plasma resonance, a hybrid mode involving the lattice oscillating antiphase to the electronic system first described by Bonn et al. (1987). The plasma edge has been interpreted in terms of the Josephson plasma resonance resulting from Josephson-pair tunneling between superconducting layers (Basov et al. 1994a). In this model, the relationship between the Josephson plasma frequency ω_p and the Josephson critical current is given by Bulaevskii (1973):

$$\omega_p = \frac{8\pi^2 csj_c}{\epsilon_0 \Phi_0}, \tag{19}$$

where d is the interlayer spacing and j_c is the Josephson critical current. It was shown by Bulaevskii et al. (1995) that a magnetic field of the order of $H_0 = \Phi_0/\gamma s^2$ can suppress the critical current and shift the plasma frequency according to

$$\omega_p(B) = \omega_p(0)\left[1 - \frac{\pi}{8}\frac{B}{H_0}\ln\left(\frac{H_0}{B}\right)\right]. \tag{20}$$

For $La_{1.85}Sr_{0.15}CuO_4$, this field is of the order of 50 T and the suppression of J_c is expected to be weak, whereas for $Bi_2Sr_2CaCu_2O_{8+\delta}$ where γ is of the order of 400, H_0 is only of the order of a few tesla.

In $La_{1.85}Sr_{0.15}CuO_4$, the c-axis conductivity has been measured in both $H \parallel c$ and $H \perp c$ by infrared reflectance spectroscopy on single crystals (Gerrits et al. 1995, van Bentum et al. 1997). In optimally doped $La_{1.85}Sr_{0.15}CuO_4$, Gerrits et al. found no shift of this plasma resonance with magnetic field ($H \perp c$), while in underdoped $La_{1.85}Sr_{0.15}CuO_4$, van Bentum et al. (1997) reported a large shift from 22 cm^{-1} at $B = 0$ to 12 cm^{-1} at $B = 22$ T. The shift was in approximate accord with the theory of Bulaevskii et al. (1995).

Similar large shifts have been reported for $Bi_2Sr_2CaCu_2O_{8+\delta}$ by Tsui et al. (1996) and Matsuda et al. (1995), and for $Tl_2Ba_2CaCu_2O_8$ by Dulic et al. (2001). It was found that the frequency of the plasma resonance, which was observed by sweeping the magnetic field at constant microwave frequency, varied as $\omega_p^2 \propto B^{-\nu}$, where $\nu \approx 0.7$–0.8, depending on the sample. The detailed angular dependence of the plasma resonance showed that as the direction of B came within 5° of alignment with the planes, the resonance field displayed a cusp, dropping by 6 T within a few degrees. These effects were predicted by Bulaevskii et al. (1996).

7. Conclusions and open questions

Experimental studies of a variety of high-T_c materials by means of infrared and optical spectroscopies have led to a reasonable consensus on several aspects of the properties of these fascinating materials.

Electronic structure. It is clear that the growth of the spectral weight with doping cannot be understood in terms of simple Fermi-liquid models with a large Fermi surface, and that an appropriate starting point for unraveling the exotic behavior of cuprates is the Mott–Hubbard scenario. Experimental results on the evolution of Drude weight with doping are in remarkable agreement with the calculations performed within the MH model. The charge carriers in conducting phases cannot be viewed as free electrons/holes, but should be regarded as correlated "objects" whose properties are strongly influenced by Coulomb effects and possibly by antiferromagnetic fluctuations.

An obvious challenge for any model is to explain the qualitative difference between in-plane and interplane properties of the cuprates. This difference goes beyond "strong anisotropy". For example, while the interplane transport is incoherent, at the same time in-plane properties are at least approximately described by a Drude model. Now that there is evidence that the in-plane and interplane charge dynamics are closely interrelated, any realistic description of a system must account for this relationship as well as the dramatic contrasts.

Progress in understanding the transport properties. While the principal trends in the growth of the electronic spectral weight with doping were established quite early on, systematic studies of the evolution of charge dynamics in high-T_c materials are still in progress. Nevertheless, several important trends have been revealed by recent experiments. Charge carriers in underdoped cuprates are characterized by a significant enhancement of the mass (up to $5m_e$) and pronounced frequency dependence of the scattering rate. It is likely that interactions giving rise to these properties are of electronic origin and are connected with the proximity of underdoped compounds to parent AF insulators. This latter conclusion is corroborated by the suppression of m^* and the frequency-dependent term in $1/\tau(\omega)$ spectra as one proceeds with doping.

In the optimally doped materials, the frequency-dependent scattering rate varies linearly with temperature and energy. In underdoped compounds, there is a stronger suppression of $1/\tau(\omega)$ at low frequencies and, at $T > T_c$, this correlates with the opening of a pseudogap as detected by other experimental techniques.

The symmetry of the superconducting order parameter. The evidence for strong Coulomb interaction creates formidable difficulties for a complete theory of cuprate superconductivity. One way for two electrons to avoid Coulomb repulsion is to spatially arrange themselves in a wave function of $d_{x^2-y^2}$ symmetry (for a review, see Scalapino 1995). This hypothesis ignited an extensive study of possibilities of pairing in $d_{x^2-y^2}$. Phase-sensitive tunneling probes support this picture (Van Harlingen 1995, Kirtley et al. 1995, Tsuei et al. 1997). Spectroscopic measurements of the penetration depth and of the complex conductivity provide valuable, albeit indirect support for an anisotropic (possibly d-wave) symmetry of the order parameter. The wealth of data on the electromagnetic response is not consistent with s-wave symmetry of the gap. Early experiments claiming s-wave gap are not reproduced with the new generation of high-purity samples which are well characterized by a variety of techniques.

As experiments with a number of probes show, the density of states in cuprates at $T \ll T_c$ is fundamentally different from conventional superconductors. Spectroscopic

evidence in favor of a finite density of states in the superconducting state is overwhelming, but it remains to be seen whether this complex experimental situation can be reconciled based solely on d-wave ideas. One of the last remaining "strongholds" for s-wave superconductivity is the response of the electron-doped material $Nd_{2-y}Ce_yCuO_4$. Further experimental work is required to understand if electron-doped systems are fundamentally different from other cuprates.

Some implications for the pairing mechanism. The analysis of the charge dynamics in the normal and the superconducting states which has been carried out for Y123 and Bi2212 compounds suggests that the scattering mechanisms are not due to phonons, but most likely, are related to the spin degree of freedom. Indirectly, this gives support for spin fluctuations being the mediator of superconducting pairing (Pines 1995). This particular pairing interaction gives rise to a d-wave order parameter which is consistent with many experiments (Scalapino 1995). A low-lying pseudogap in the spectrum of spin fluctuations has been shown to enhance the critical temperature of a superconductor (Schachinger et al. 1997). Such a pseudogap is a likely interpretation of the wealth of experimental data obtained for underdoped samples including infrared conductivity of oxygen-deficient Y123, Y124 and Bi2212 (Puchkov et al. 1996a, Timusk and Statt 1999).

Open questions. Despite the large existing literature, there are serious gaps in the available data: (i) The low-temperature properties of the single-layered materials are nearly unstudied. By doping, their T_c can be reduced to values comparable to low-T_c BCS materials, and some of the techniques used in low-temperature superconductivity can be applied, such as destruction of superconductivity in a high magnetic field. (ii) Another important issue is related to the properties of overdoped compounds. One of the dogmas in the field is that overdoping "restores Fermi-liquid behavior". There is little *experimental* data to support this claim. (iii) The large versus small Fermi surface problem. Why does the *ab*-plane conductivity vary linearly with doping x? The model of a large Fermi surface suggests that it should vary with $1-x$ as the doped holes reduce the size of the Fermi surface. It is hoped that in the near future k-sensitive experiments, such as ARPES and neutron scattering, will provide us with details on the nature of the electronic structure in the low-doping, pseudogap state.

Acknowledgements

The authors are indebted to the many individuals who have contributed to the research discussed in this article. In particular we would like to emphasize the impact of our long-term collaborators: D.A. Bonn, W.N. Hardy, A.V. Puchkov, C.C. Homes, J.P. Carbotte, D.B. Tanner, G.Blumberg, R. Liang, B. Dabrowski. We also benefitted from the discussions of many problems presented in this review with: A.A. Abrikosov, P.B. Allen, W. Atkinson, A. Balatskii, A.J. Berlinski, J.C. Cooper, O.V. Dolgov, R.C. Dynes, V.J. Emery, M. Franz, J. Hirsch, C. Kallin, S.A. Kivelson, P.A. Lee, A.G. Loeser, J.W. Loram, M.B. Maple, F. Marsiglio, A.J. Millis, M. Norman, J. Preston, M. Pham, D. Pines, Z.-X. Shen, M. Strongin, T. Startseva, T. Rõõm, M. Reedyk, S. Tajima, D. van

der Marel, and Y. Uemura. The work at UCSD is supported by NSF and DOE. The work at McMaster is supported by the Canadian Institute of Advanced Research (CIAR) and Natural Sciences and Engineering Research Council of Canada.

References

Abrikosov, A.A., 1995, Phys. Rev. B **52**, R7026.
Abrikosov, A.A., 1996, Phys. Rev. B **54**, 12003.
Abrikosov, A.A., and L.A. Fal'kovskii, 1961, Sov. Phys. JETP **13**, 179.
Alexandrov, A.S., A.M. Bratkovky, N.F. Mott and E.K.H. Salje, 1993, Physica C **215**, 359.
Alexandrov, A.S., V.V. Kabanov and N.F. Mott, 1996, Phys. Rev. Lett. **77**, 4799.
Allen, P., 1992, Comments Cond. Mat. Phys. **5–6**, 327.
Allen, P.B., 1971, Phys. Rev. B **3**, 305.
Allen, P.B., and J.C. Mikkelsen, 1976, Phys. Rev. B **15**, 2953.
Allen Jr, S.J., D.C. Tsui and F. DeRosa, 1975, Phys. Rev. Lett. **35**, 1359.
Alloul, H., P. Mendels, H. Casalta, J.F. Marucco and J. Arabski, 1991, Phys. Rev. Lett. **67**, 3140.
Altshuller, B.L., L.B. Ioffe and A.J. Millis, 1996, Phys. Rev. B **53**, 415.
Anderson, P.W., 1958, Phys. Rev. **109**, 1492.
Anderson, P.W., 1987, Science **235**, 1196.
Anderson, P.W., 1995, Science **268**, 1154.
Arima, T., Y. Tokura and S. Uchida, 1993, Phys. Rev. B **48**, 6597.
Atkinson, W.A., and J.P. Carbotte, 1995, Phys. Rev. B **52**, 10601.
Atkinson, W.A., and J.P. Carbotte, 1997, Phys. Rev. B **55**, 3230.
Awasthi, A.M., L. Degiorgi, G. Gruner, Y. Dalichaouch and M.B. Maple, 1993, Phys. Rev. B **48**, 10692.
Bacci, S.B., E.R. Gagliano, R.M. Martin and J.F. Annett, 1991, Phys. Rev. B **44**, 7504–7509.
Bardeen, J., and M.J. Stephen, 1965, Phys. Rev. **140**, A1197.
Bardeen, J., L.N. Cooper and J.R. Schrieffer, 1957, Phys. Rev. **108**, 1175.
Barowski, H.S., A. Arnold, R. Eder, M. Prenninger, A. Vogenauer, E.V. Pechen, K.F. Renk, W. Prusseit, H. Kinder, R.G. Buckley, D.M. Pooke and K. Kishio, 1996, SPIE **2696**, 66.
Basov, D.N., T. Timusk, B. Dabrowski and J.D. Jorgensen, 1994a, Phys. Rev. B **50**, 3511.
Basov, D.N., A.V. Puchkov, R.A. Hughes, T. Strach, J. Preston, T. Timusk, R. Liang, D.A. Bonn and W.N. Hardy, 1994b, Phys. Rev. B **49**, 12165.
Basov, D.N., R. Liang, D.A. Bonn, W.N. Hardy, B. Dabrowski, M.A. Quijada, D.B. Tanner, J.P. Rice, D.M. Ginsberg and T. Timusk, 1995a, Phys. Rev. Lett. **74**, 595.
Basov, D.N., H.A. Mook, B. Dabrowski and T. Timusk, 1995b, Phys. Rev. B **52**, R13141.
Basov, D.N., R. Liang, B. Dabrowski, D.A. Bonn, W.N. Hardy and T. Timusk, 1996, Phys. Rev. Lett. **77**, 4090.
Basov, D.N., B. Dabrowski and T. Timusk, 1998, Phys. Rev. Lett. **81**, 2132.
Basov, D.N., S.I. Woods, A.S. Katz, E.J. Singley, R.C. Dynes, M. Xu, D.G. Hinks, C.C. Homes and M. Strongin, 1999, Science **283**, 49.
Batlogg, B., and V.J. Emery, 1996, Nature **382**, 20.
Batlogg, B., H.Y. Hwang, H. Takagi, R.J. Cava, H.L. Kao and J. Kwo, 1994, Physica C **235–240**, 130.
Bauer, M., 1990, Ph.D. Thesis (University of Tübingen).
Bednorz, J.G., and K.A. Müller, 1986, Z. Phys. B **64**, 189.
Bernhard, C., J.L. Tallon, C. Bucci, R. de Renzi, G. Guidi, G.V.M. Williams and Ch. Niedermayer, 1996, Phys. Rev. Lett. **77**, 2304.
Bernhard, C., R. Henn, A. Wittlin, M. Kläser, T. Wolf, G. Müller-Vogt, C.T. Lin and M. Cardona, 1998, Phys. Rev. Lett. **80**, 1762.
Bernhard, C., D. Munzar, A. Wittlin, W. Konig, A. Golnik, C.T. Lin, M. Kläser, T. Wolf, G. Müller-Vogt and M. Cardona, 1999, Phys. Rev. B **59**, R6631.
Bernhard, C., D. Munzar, A. Golnik, C.T. Lin, A. Wittlin, J. Humlicek and M. Cardona, 2000, Phys. Rev. B **61**, 618.
Bi, X.-X., and P. Eklund, 1993, Phys. Rev. Lett. **70**, 2625.
Birmingham, J.T., S.M. Grannan, P.L. Richards, R. Henn, J. Kircher, M. Cardona, A. Wittlin, V.H.M. Duijn and A.A. Menovsky, 1996, SPIE **2696**, 56.
Blumberg, G., M. Kang, M.V. Klein, K. Kadowaki and C. Kendziora, 1997, Science **278**, 1427.

Boebinger, G., Y. Ando, A. Passner, T. Kimura, M. Okuya, J. Shimoyama, K. Kishio, K. Tamasaku, N. Ichikawa and S. Uchida, 1996, Phys. Rev. Lett. **77**, 5417.

Bommeli, F., L. Degiorgi, P. Wachter, B.K. Cho, P.C. Canfield, R. Chau and M.B. Maple, 1997, Phys. Rev. Lett. **78**, 547.

Bonn, D.A., and W.N. Hardy, 1996, Microwave surface impedance of high-T_c superconductors, in: Physical Properties of High Temperature Superconductors, Vol. I, ed. D.M. Ginsberg (World Scientific, Singapore).

Bonn, D.A., et al., 1987, Phys. Rev B **35**, 8843.

Bonn, D.A., J.D. Garret and T. Timusk, 1988, Phys. Rev. Lett. **61**, 1305.

Bonn, D.A., P. Dosanjh, R. Liang and W.N. Hardy, 1992, Phys. Rev. Lett. **68**, 2390.

Bonn, D.A., R. Liang, T.M. Reisman, D.J. Baar, D.C. Morgan, K. Zhang, P. Dosanjh, T.L. Duty, A. MacFarlane, G.D. Morris, J.H. Brewer, W.N. Hardy, C. Kallin and A.J. Berlinsky, 1993, Phys. Rev. B **47**, 11314.

Bonn, D.A., S. Kamal, K. Zhang, R. Liang, D.J. Baar, E. Klein and W.N. Hardy, 1994, Phys. Rev B **50**, 4051.

Borkowski, L.S., and P.J. Hirschfeld, 1994, Phys. Rev. B **49**, 15404.

Born, M., and E. Wolf, 1980, Principles of Optics (Pergamon Press, New York).

Bozovic, I., K. Char, S.J.B. Yoo, A. Kapitulnik, M.R. Beasley, T.H. Geballe, Z.Z. Wang, S. Hagen, N.P. Ong, D.E. Aspens and M.K. Kelly, 1988, Phys. Rev. B **38**, 5077.

Bozovic, I., J.H. Kim, J.S. Harris Jr, C.B. Eom, J.M. Phillips and J.T. Cheung, 1994, Phys. Rev. Lett. **73**, 1436.

Branch, D., and J.P. Carbotte, 1998, J. Phys. Chem. Solids **59**, 1965.

Bucher, B., J. Karpinski, E. Kaldis and P. Wachter, 1990, Physica C **167**, 324.

Bucher, B., J. Karpinski, E. Kaldis and P. Wachter, 1992, Phys. Rev. B **45**, 3026.

Bucher, B., P. Steiner, J. Karpinski, E. Kaldis and P. Wachter, 1993, Phys. Rev. Lett. **70**, 2012.

Bulaevskii, L.N., 1973, Sov. Phys. JETP **37**, 1133.

Bulaevskii, L.N., and J.R. Clem, 1991, Phys. Rev. B **44**, 10234.

Bulaevskii, L.N., M.P. Maley and M. Tachiki, 1995, Phys. Rev. Lett. **74**, 801.

Bulaevskii, L.N., M.P. Maley, H. Safar and D. Domínguez, 1996, Phys. Rev. B **53**, 6633.

Burlakov, V.M., K.V. Kraiskaya, A.G. Mitko and E.J. Firsov, 1989, Phys. Lett. A **142**, 514.

Calvani, P., M. Capizzi, S. Lupi, P. Maselli, A. Paolone and P. Roy, 1996, Phys. Rev. B **53**, 2756.

Carbotte, J.P., C. Jiang, D.N. Basov and T. Timusk, 1995, Phys. Rev. B **51** 11798.

Carbotte, J.P., E. Schachinger and D.N. Basov, 1999, Nature **401**, 354.

Chakravarty, S., 1998, Eur. Phys. J. B **5**, 337.

Chakravarty, S., and P.W. Anderson, 1994, Phys. Rev. Lett. **72**, 3218.

Choi, E.-J., H.-T. Linh, H.D. Drew and T.C. Hsu, 1994, Phys. Rev. B **49**, 13271.

Choi, E.-J., K.P. Stewart, S.K. Kaplan, H.D. Drew, S.N. Mao and T. Venkatesan, 1996, Phys. Rev. B **53**, 8859.

Chubukov, A.V., D. Pines and B.P. Stojkovic, 1996, J.Phys.:Condensed Matter **8**, 10017.

Clarke, D.G., S.P. Strong and P.W. Anderson, 1995, Phys. Rev. Lett. **74**, 4499.

Coffey, M.W., 1995, Phys. Lett. A **200**, 195.

Coffey, M.W., and J.R. Clem, 1991, Phys. Rev. Lett. **67**, 386.

Collins, R.T., Z. Schlesinger, F. Holtzberg, P. Chaudhari and C. Feild, 1989, Phys. Rev. Lett. **39**, 6571.

Combescot, R., and X. Leyronas, 1995, Phys. Rev. Lett. **75**, 3732.

Cooper, J.R., 1996, Phys. Rev. B **54**, R3753.

Cooper, J.R., L. Forro and B. Keszei, 1990, Nature **343**, 444.

Cooper, S.L., G.A. Thomas, J. Orensten, D.H. Rapkine, A.J. Millis, S.-W. Cheong, A.S. Cooper and Z. Fisk, 1990, Phys. Rev. B **41**, 11605.

Cooper, S.L., A.L. Kotz, M.A. Karlow, M.V. Klein, W.C. Lee, J. Giapintzakis and D.M. Ginsberg, 1992, Phys. Rev. B **45**, 2549.

Cooper, S.L., D. Reznik, A.L. Kotz, M.A. Karlow, R. Liu, M.V. Klein, W.C. Lee, J. Giapintzakis, D.M. Ginsberg, B.W. Veal and A.P. Paulikas, 1993a, Phys. Rev. B **47**, 8233.

Cooper, S.L., P. Nyhus, D. Reznik, M.V. Klein, W.C. Lee, D.M. Ginsberg, B.W. Veal, A.P. Paulikas and B. Dabrowski, 1993b, Phys. Rev. Lett. **70**, 1533.

Dagotto, E., 1994, Rev. Mod. Phys. **66**, 763.

Dahne, U., Y. Goncharov, N. Klein, N. Tellmann, G. Kozlov and K. Urban, 1995, J. Superconductivity **8**, 129.

de Vaulchier, L.A., J.P. Vieren, Y. Guldner, N. Bontemps, R. Combescot, Y. Lemaitre and J.C. Mage, 1996, Europhys. Lett. **33**, 153.

Degiorgi, L., E.J. Nicol, O. Klein, G. Grunner, P. Wachter, S.-M. Huang, J. Wiley and R.B. Kaner, 1994, Phys. Rev. B **49**, 7012.

Dewing, H.L., and E.K.H. Salje, 1992, Supercond. Sci. Technol. **5**, 50.

Ding, H., T. Yokoya, J.C. Campuzano, T. Takahashi, M. Randeria, M.R. Norman, T. Mochiku, K. Kadowaki and J. Giapintzakis, 1996, Nature **382**, 51.

Ding, H., M.R. Norman, T. Yokoya, T. Takeuchi, M. Randeria, J.C. Campuzano, T. Takahashi, T. Mochiku and K. Kadowaki, 1997, Phys. Rev. Lett. **78**, 2628.

Dolgov, O., H.J. Kaufmann, E.K.H. Salje and Y. Yagil, 1997, Physica C **279**, p113.

Dulic, D., S.J. Hak, D. van der Marel, W.N. Hardy, A.E. Koshelev, R. Liang, D.A. Bonn and B.A. Willemsen, 2001, Phys. Rev. Lett. **86**, 4660.

Edwards, H.L., D.J. Derro, A.L. Barr, J.T. Markert and A.L. de Lozanne, 1995, Phys. Rev. Lett. **75**, 1388.

El Azrak, A., R. Nahoum, N. Bontemps, M. Guilloux-Viry, C. Thivet, A. Perrin, S. Labdi, Z.Z. Li and H. Raffy, 1994, Phys. Rev. B **49**, 9846.

Eldridge, J.E., M. Dressel, D.J. Matz, B. Gross, Q.Y. Ma and W.N. Hardy, 1995, Phys. Rev B **52**, 4462.

Emery, V.J., and S.A. Kivelson, 1995a, Phys. Rev. Lett. **74**, 3253.

Emery, V.J., and S.A. Kivelson, 1995b, Nature **374**, 434.

Emery, V.J., S.A. Kivelson and O. Zachar, 1997, Phys. Rev. B **56**, 6120.

Eskes, H., M.B.J. Meinders and G.A. Sawatzky, 1991, Phys. Rev. Lett. **67**, 1035.

Falck, J.P., A. Levy, M.A. Kastner and R.J. Birgeneau, 1992, Phys. Rev. Lett. **69**, 1109.

Fano, U., 1961, Phys. Rev **121**, 1866.

Fawcett, E., 1988, Rev. Mod. Phys. **60**, 209–283.

Fehrenbacher, R., and M.R. Norman, 1994, Phys. Rev. B **50**, 3495.

Fong, H.F., B. Keimer, P.W. Anderson, D. Reznik, F. Dogan and I.A. Aksay, 1995, Phys. Rev. Lett. **75**, 316.

Fong, H.F., B. Keimer, D.L. Milius and I.A. Aksay, 1997, Phys. Rev. Lett. **78**, 713.

Forro, L., G.L. Carr, G.P. Williams, D. Mandrus and L. Mihaly, 1990, Phys. Rev. Lett. **65**, 1941.

Franz, M., C. Kallin, A.J. Berlinsky and M.I. Salkola, 1997, Phys. Rev. B **56** 7882.

Friedmann, T.A., M.W. Rabin, J. Giapintzakis, J.P. Rice and D.M. Ginsberg, 1990, Phys. Rev. B **42**, 6217.

Fujimori, A., E. Takayama-Muromachi, Y. Uchida and B. Okai, 1987, Phys. Rev. B **35**, 8814.

Fukuzumi, Y., K. Mizuhashi, K. Takenaka and S. Uchida, 1996, Phys. Rev. Lett. **76**, 684.

Gao, F., D.B. Romero, D.B. Tanner, J. Talvacchio and M.G. Forrester, 1993a, Phys. Rev. B **47**, 1036.

Gao, F., J.W. Kruse, C.E. Platt, M. Feng and M.V. Klein, 1993b, Appl. Phys. Lett. **63**, 2274.

Gauzzi, A., and J. Bok, 1996, J. Superconductivity **9**, 523.

Georges, A., G. Kotliar, W. Krauth and M.J. Rozenberg, 1996, Rev. Mod. Phys. **68**, 13.

Gerrits, A.M., et al., 1994, Physica C **235–240**, 1117.

Gerrits, A.M., M.E.J. Boonman, A. Wittlin, P.J.M. van Bentum, V.H.M. Duijn and A.A. Menovsky, 1995, Phys. Rev. B **51**, 12049.

Gervais, F., P. Echegut, J.M. Bassat and P. Odier, 1988, Phys. Rev. B **37**, 9364.

Gittleman, J.I., and B. Rosenblum, 1966, Phys. Rev. Lett. **16** 734.

Glover, R.E., and M. Tinkham, 1956, Phys. Rev. **104**, 844.

Gold, A., S.J. Allen, B.A. Wilson and D.C. Tsui, 1982, Phys. Rev. B **25**, 3519.

Golosovsky, M., M. Tsindlekht and D. Davidov, 1996, Supercond. Sci. Technol. **9**, 1.

Götze, W., 1981, Philos. Mag. B **43**, 219.

Götze, W., and P. Wölfle, 1972, Phys. Rev. B **6**, 1226.

Graf, M.J., D. Rainer and J.A. Sauls, 1995a, Phys. Rev. B **47**, 12089.

Graf, M.J., M. Palumbo and D. Rainer, 1995b, Phys. Rev. B **52**, 10588.

Grishkovsky, D., S. Keiding, M. van Exter and Ch. Fattinger, 1990, J. Opt. Soc. Am. **7**, 2006.

Grüninger, M., J. Münzel, A. Gaymann, A. Zibold and H.P. Geserich, 1996, Europhys. Lett. **35**, 55.

Grüninger, M., D. van der Marel, A.A. Tsvetkov and A. Erb, 2000, Phys. Rev. Lett. **84**, 1575.

Gurvitch, M., and A.T. Fiory, 1987, Phys. Rev. Lett. **59**, 1337.

Hackl, R., G. Krug, R. Nemetschek, M. Opel and B. Stadlober, 1996, in: Spectroscopic Studies of Superconductors, Vol. V, eds I. Bozovic and D. van der Marel, SPIE Proc. **2696**, 194.

Hardy, W.N., D.A. Bonn, D.C. Morgan, R. Liang and K. Zhang, 1993, Phys. Rev. Lett. **70**, 3999.

Hardy, W.N., S. Kamal, R. Liang, D.A. Bonn, C.C. Homes, D.N. Basov and T. Timusk, 1996, in: Proc. 10th Anniversary of High-T_c Workshop (World Scientific, Singapore) p. 223.

Harris, J.M., P.J. White, Z.-X. Shen, H. Ikeda, R. Yoshizaki, H. Eisaki, S. Uchida, W.D. Si,

J.W. Xiong, Z.-X. Zhao and D.S. Dessau, 1997, Phys. Rev. Lett. **79**, 143.

Hauff, R., S. Tajima, W.J. Jang and A.I. Rykov, 1996, Phys. Rev. Lett. **77** 4620.

Henn, R., J. Kircher, M. Cardona, A. Wittlin, V.H.M. Duijn and A.A. Menovsky, 1996, Phys. Rev. B **53**, 9353.

Hirsch, J.E., 1992, Physica C **199**, 305.

Hirschfeld, P.J., P. Wölfle, J.A. Sauls, D. Einzel and W.O. Putikka, 1989, Phys. Rev. B **40**, 6695.

Hirschfeld, P.J., W.O. Putikka and D.J. Scalapino, 1994, Phys. Rev. B **50**, 10250.

Holmes, W., and P.L. Richards, 1997, unpublished.

Homes, C.C., M. Reedyk, D.A. Crandles and T. Timusk, 1993a, Appl. Opt. **32**, 2976.

Homes, C.C., T. Timusk, R. Liang, D.A. Bonn and W.N. Hardy, 1993b, Phys. Rev. Lett. **71**, 1645.

Homes, C.C., T. Timusk, D.A. Bonn, R. Liang and W.N. Hardy, 1995a, Physica C **254**, 265.

Homes, C.C., T. Timusk, D.A. Bonn, R. Liang and W.N. Hardy, 1995b, Can. J. Phys. **73**, 663.

Homes, C.C., B.P. Clayman, J.L. Peng and R.L. Greene, 1997, Phys. Rev. B **56**, 5525.

Homes, C.C., D.A. Bonn, R. Liang, W.N. Hardy, D.N. Basov, T. Timusk and B.P. Clayman, 1999, Phys. Rev B **60**, 9782.

Hsu, T.C., 1993, Physica C **231**, 305; Phys. Rev. B **46**, 3680.

Hybertsen, M.S., E.B. Stechel, M. Schluter and D.R. Jennison, 1990, Phys. Rev. B **41**, 11068.

Ioffe, L.B., A.I. Larkin, A.A. Varlamov and L. Yu, 1993, Phys. Rev. B **47**, 8936.

Ioffe, L.B., A.I. Larkin, A.J. Millis and B.L. Altshuller, 1994, JETP Lett. **59**, 66.

Ito, T., K. Takenaka and S. Uchida, 1993, Phys. Rev. Lett. **70**, 3995.

Jacobs, T., S. Sridar, Q. Li, G.D. Gu and N. Koshizuka, 1995, Phys. Rev. Lett. **75**, 4516.

Jang, H.F., G. Cripps and T. Timusk, 1990, Phys. Rev. B **41**, 5152.

Jarell, M., J.K. Freericks and Th. Pruschke, 1995, Phys. Rev. B **51**, 11704.

Jiang, C., E. Schachinger, J.P. Carbotte, D.N. Basov and T. Timusk, 1996, Phys. Rev. B **54**, 1264.

Kajueter, H., G. Kotliar and G. Moeller, 1996, Phys. Rev. B **53** 16214.

Kamal, S., R. Liang, A. Hosseini, D.A. Bonn and W.N. Hardy, 1998, Phys. Rev. B **56**, R8933.

Kamarás, K., S.L. Herr, C.D. Porter, N. Tache, D.B. Tanner, S. Etemad, T. Venkatesan, E. Chase, A. Inam, X.D. Wu, M.S. Hegde and B. Dutta, 1990, Phys. Rev. Lett. **64**, 84.

Kampf, A.P., and J.R. Schrieffer, 1990, Phys. Rev. B **42**, 7967.

Kastner, M.A., and R.J. Birgeneau, 1996, SPIE **2696**, 45.

Katsufuji, T., Y. Okimoto and Y. Tokura, 1995, Phys. Rev. Lett. **75**, 3497.

Katsufuji, T., T. Tanabe, T. Ishikawa, Y. Fukuda, T. Arima and Y. Tokura, 1996, Phys. Rev. B **54**, R14230.

Keimer, B., W.Y. Shih, R.W. Erwin, J.W. Lynn, F. Dogan and I.A. Aksay, 1994, Phys. Rev. Lett. **73**, 3459.

Kim, J.-T., T.R. Lemberger, S.R. Foltyn and X. Wu, 1994, Phys. Rev. B **49**, 15970.

Kircher, J., M. Cardona, A. Zibold, H.P. Geserich, E. Kaldis, J. Karpinski and S. Rusiecki, 1993, Phys. Rev. B **48**, 3993.

Kircher, J., D. Miller, P.L. Richards, E. Kaldis and J. Karpinski, 1994, Physica C **235–240**, 1119.

Kircher, J., R. Henn, M. Cardona, P.L. Richards and G.R. Williams, 1997, J. Opt. Soc. Am. B **14**, 705.

Kirtley, J.R., C.C. Tsuei, J.Z. Sun, C.C. Chi, L.S. Yu-Jahnes, A. Gupta, M. Rupp and M.B. Ketchen, 1995, Nature **373**, 225.

Kirtley, J.R., K.A. Moler, G. Villard and A. Maignan, 1998, Phys. Rev. Lett. **81**, 2140.

Klemm, R.A., and S.H. Liu, 1995, Phys. Rev. Lett. **74**, 2343.

Koch, B., H.P. Geserich and Th. Wolf, 1989, Solid State Comm. **71**, 495.

Koller, D., et al., 1996, Phys. Rev. Lett. **77**, 4082.

Krasnov, V.M., A. Yurgens, D. Winkler, P. Delsing and T. Claeson, 2000, Phys. Rev. Lett. **84**, 5860.

Kresin, V.Z., and S.A. Wolf, 1992, Phys. Rev. B **46**, 6458.

Kumar, N., and A.M. Jayannavar, 1992, Phys. Rev. B **50**, 438.

Kumar, N., P.A. Lee and B. Shapiro, 1990, Physica A **168**, 447.

Kwak, J.F., 1982, Phys. Rev. B **26**, 4789.

Landau, L.D., and E.M. Lifshitz, 1992, Statistical Physics (Pergamon Press, Oxford).

Laughlin, R.B., 1996, Phys. Rev. Lett. **79**, 1726.

Lawrence, W.E., and S. Doniach, 1971, in: Proc. 12th Int. Conf. on Low Temperature Physics, ed. E. Kanda (Academic Press, New York) p. 361.

Lee, P.A., 1993, Phys. Rev. Lett. **71**, 1887.

Lee, P.A., and N. Nagaosa, 1992, Phys. Rev. B **46**, 5621.

Linh, H.-T., S. Wu, H.D. Drew, S.K. Kaplan, Q. Li and D.B. Fenner, 1996, Phys. Rev. Lett. **76**, 3810.

Lippert, M., J.P. Strobel, G. Saemann-Ishenko, S. Orbach, S. Hensen, G. Muller, H. Piel, J. Schützmann, K.F. Renk, B. Roas and W. Gieres, 1991, Physica C **185–189**, 1041.

Littlewood, P.B., and C.M. Varma, 1992, Phys. Rev. B **46**, 405.

Litvinchuk, A.P., C. Thomsen and M. Cardona, 1994, in: Physical Properties of High Temperature Superconductors, Vol. IV, ed. D.M. Ginsberg (World Scientific, Singapore).

Liu, Y., and A.M. Goldman, 1994, Mod. Phys. Lett. **8**, 277.

Lobo, R.P.S.M., F.J. Gotor, P. Odier and F. Gervais, 1996, Phys. Rev. B **53**, 410.

Loeser, A.G., Z.-X. Shen, D.S. Dessau, D.S. Marshall, C.-H. Park, P. Fournier and A. Kapitulnik, 1996, Science **273**, 325.

Loram, J.W., K.A. Mirza, J.R. Cooper and W.Y. Liang, 1994, J. Superconductivity **7**, 261.

Lorenzana, J., and G.A. Sawatzky, 1995, Phys. Rev. Lett. **74**, 1867.

Lyons, K.B., P.A. Fleury, J.P. Remeika, A.S. Cooper and T.J. Negran, 1988, Phys. Rev. B **37**, 2353.

Ma, Z., 1995, Ph.D. Thesis (Stanford University).

Mahan, G.D., 1980, Many-Particle Physics (Plenum Press, New York).

Maksimov, E.G., S.N. Rashkeev, S.Yu. Savrasov and Yu.A. Uspenski, 1989, Phys. Rev. Lett. **63**, 1880.

Mandrus, D., M.C. Martin, C. Kendziora, D. Koller, L. Forro and L. Mihaly, 1993, Phys. Rev. Lett. **70**, 2629.

Mao, J., D.H. Wu, J.L. Peng, R.L. Greene and S.M. Anlage, 1995, Phys. Rev. B **51**, 3316.

Marshall, D.S., D.S. Dessau, A.G. Loeser, C.-H. Park, Z.-X. Shen, A.Y. Matsuura, J.N. Eckstein, I. Bozovic, P. Fournier, A. Kapitulnik, W.E. Spicer and Z.-X. Shen, 1996, Phys. Rev. Lett. **76**, 4841.

Marsiglio, F., and J.P. Carbotte, 1997, Can. J. Phys. **75**, 509.

Matsuda, Y., M.B. Gaifullin, K. Kumagai, K. Kadowaki and T. Mochiku, 1995, Phys. Rev. Lett. **75**, 4512.

Mattis, D.C., and J. Bardeen, 1958, Phys. Rev. **111**, 412.

McGuire, J.J., M. Windt, T. Startseva, T. Timusk, D. Colson and V. Viallet-Guillen, 2000, Phys. Rev B **62**, 8711.

Meinders, M.B.J., H. Eskes and G.A. Sawatzky, 1993, Phys. Rev. B **48**, 3916.

Mihailovic, D., C.M. Foster, K. Voss and A.J. Heeger, 1990, Phys. Rev. B **42**, 7989.

Miller, D., P.L. Richards, S. Etemad, A. Inam, T. Venkatesan, B. Dutta, X.D. Wu, C.B. Eom, T.H. Geballe, N. Newman and B.F. Cole, 1993, Phys. Rev. B **47**, 8076.

Miller, D., P.L. Richards and P. Merchant, 1995, Phys. Rev. B **51**, 8385.

Millis, A.J., and H. Monien, 1996, Phys. Rev. B **54**, 16172.

Moffat, S., 1997, Ph.D. Thesis (McMaster University).

Moler, K.A., J.R. Kirtley, D.G. Hinks, T.W. Li and Ming Xu, 1998, Science **279**, 1193.

Mook, H.A., M. Yethiraj, G. Aeppli, T.E. Mason and T. Armstrong, 1993, Phys. Rev. Lett. **70**, 3490.

Morgan, D.C., et al., 1994, Physica C **235–240**, 2015.

Mori, H., 1965, Prog. Theor. Phys. **34**, 399.

Motohashi, T., J. Shimoyama, K. Kitazawa, K. Kishio, K.M. Kojima, S. Uchida and S. Tajima, 2000, Phys. Rev B **61**, R9269.

Munzar, D., C. Bernhard, A. Golnik, J. Humlicek and M. Cardona, 1999, Solid State Commun. **112**, 365.

Münzel, J., A. Zibold, H.P. Geserich and Th. Wolf, 1996, Europhys. Lett. **33**, 147.

Nachumi, B., A. Keren, K. Kojima, M. Larkin, G.M. Luke, J. Merrin, O. Tchernyshov, Y.J. Uemura, N. Ichikawa, M. Goto and S. Uchida, 1996, Phys. Rev. Lett. **77**, 5421.

Naeini, J.G., X.K. Chen, K.C. Hewitt, J.C. Irwin, T.P. Devereaux, M. Okuya, T. Kimura and K. Kishio, 1998, Phys. Rev. B **57**, R11077.

Nakamura, Y., and S. Uchida, 1993, Phys. Rev. B **47**, 8369.

Nemetschek, R., M. Opel, C. Hoffmann, P.F. Müller, R. Hackl, H. Berger, L. Forro, A. Erb and E. Walker, 1997, Phys. Rev. Lett. **78**, 4837.

Ng, H.K., M. Capizzi, G.A. Thomas, R.N. Bhatt and A.C. Gossard, 1986, Phys. Rev. Lett. **33**, 7329.

Norman, M.R., H. Ding, T. Yokoya, T. Takeuchi, M. Randeria, J.C. Campuzano, T. Takahashi, T. Mochiku and K. Kadowaki, 1997, Phys. Rev. Lett. **79**, 3506.

Nyhus, P., M.A. Karlow, S.L. Cooper, B. Veal and A.P. Paulikas, 1994, Phys. Rev. B **50**, 13898.

Orenstein, J., G.A. Thomas, A.J. Millis, S.L. Cooper, D.H. Rapkine, T. Timusk, L.F. Schneemeyer and J.V. Waszczak, 1990, Phys. Rev. B **42**, 6342.

Osafune, T., N. Motoyama, H. Eisaki and S. Uchida, 1997, Phys. Rev. Lett. **78**, 1980.

Palumbo, M., and M.J. Graf, 1996, Phys. Rev. B **53**, 2261.

Panagopoulos, C., J.R. Cooper, N. Athanassopoulou and J. Chrosch, 1996, Phys. Rev. B **54** 12721.

Parks, B., S. Spielman, J. Orenstein, D.T. Nemeth, F. Ludwig, J. Clarke, P. Merchant and D.J. Lew, 1995, Phys. Rev. Lett. **74**, 3265.

Perkins, J.D., J.M. Graybeal, M.A. Kastner, R.J. Birgeneau, J.P. Falck and M. Greven, 1993, Phys. Rev. Lett. **71**, 1621.

Perkins, J.D., D.S. Klenberg, M.A. Kastner, R.J. Birgeneau, Y. Endoh, K. Yamada and S. Hosoya, 1995, Phys. Rev. B **52**, R9863.

Petrov, M.P., A.I. Grachev, M.V. Krasnikova, A.A. Nechitailov, V.V. Prokofev, V.V. Poborchy, S.I. Shaigin and N.F. Kartenko, 1988, Solid State Comm. **67**, 1197.

Pham, T., H.D. Drew, S.H. Moseley and J.Z. Liu, 1990, Phys. Rev. B **41**, 11681.

Pham, T., M.W. Lee, H.D. Drew, U. Welp and Y. Fang, 1991, Phys. Rev. B **44**, 5377.

Pickett, W.E., 1989, Rev. Mod. Phys. **61**, 433.

Pickett, W.E., R.E. Cohen and H. Krakauer, 1990, Phys. Rev. B **42**, 8764.

Pickett, W.E., H. Krakauer, R.E. Cohen and D.J. Singh, 1992, Science **255**, 46.

Pines, D., 1995, in: High Temperature Superconductivity and the C_{60} Family, ed. H.C. Ren (Gordon and Breach, New York) p. 1.

Pines, D., and P. Nozières, 1966, The Theory of Quantum Liquids (Benjamin, New York).

Preosti, G., H. Kim and P. Muzikar, 1994a, Phys. Rev. B **50**, 1259.

Preosti, G., H. Kim and P. Muzikar, 1994b, Phys. Rev. B **50**, 13638.

Prohammer, M., and J.P. Carbotte, 1991, Phys. Rev. B **43**, 5370.

Puchkov, A.V., T. Timusk, S. Doyle and A.M. Herman, 1995, Phys. Rev. B **51**, 3312.

Puchkov, A.V., D.N. Basov and T. Timusk, 1996a, J.Phys.:Condensed Mat. **8**, 10049.

Puchkov, A.V., P. Fournier, T. Timusk and N.N. Kolesnikov, 1996b, Phys. Rev. Lett. **77**, 1853.

Puchkov, A.V., P. Fournier, D.N. Basov, T. Timusk, A. Kapitulnik and N.N. Kolesnikov, 1996c, Phys. Rev. Lett. **77**, 3212.

Puchkov, A.V., T. Timusk, M.A. Karlow, S.L. Cooper, P.D. Han and D.A. Payne, 1996d, Phys. Rev. B **54**, 6686.

Quijada, M.A., D.B. Tanner, R.J. Kelly and M. Onellion, 1994, Z. Phys. B **94**, 255.

Quijada, M.A., D.B. Tanner, F.C. Chou, D.C. Johnston and S.-W. Cheong, 1995, Phys. Rev. B **52**, 15485.

Quinlan, S.M., P.J. Hirschfeld and D.J. Scalapino, 1996, Phys. Rev. B **53**, 8575.

Radtke, R.J., K. Levin, H.-B. Shuttler and M.R. Norman, 1993, Phys. Rev. B **46**, 11975.

Reedyk, M., 1992, Ph.D. Thesis (McMaster University).

Reedyk, M., and T. Timusk, 1992, Phys. Rev. Lett. **69**, 2705.

Reedyk, M., D.A. Bonn, J.D. Garrett, J.E. Greedan, C.V. Stager, T. Timusk, K. Kamarás and D.B. Tanner, 1988, Phys. Rev. B **38**, 11981.

Reedyk, M., T. Timusk, J.S. Xue and J.E. Greedan, 1994, Phys. Rev. B **49**, 15984.

Renk, K.F., B. Gorshunov, J. Schützmann, A. Prükl, B. Brunner, J. Betz, S. Orbach, N. Klein, G. Müller and H. Piel, 1991, Europhys. Lett. **15**, 661.

Renner, Ch., B. Revaz, J.-Y. Genoud, K. Kadowaki and Ø. Fischer, 1998, Phys. Rev. Lett. **80**, 149.

Rice, J.P., J. Giapintzakis, D.M. Ginsberg and J.M. Mochel, 1991, Phys. Rev. B **44**, 10158.

Roddick, E., and D. Stroud, 1995, Phys. Rev. Lett. **74**, 1430.

Rojo, A.G., and K. Levin, 1993, Phys. Rev. B **48**, 16861.

Romero, D.B., C.D. Porter, D.B. Tanner, L. Forro, D. Mandrus, L. Mihaly, G.L. Carr and G.P. Williams, 1992, Phys. Rev. Lett. **68**, 1590.

Rossat-Mignod, J., L.P. Regnault, C. Vettier, Ph. Bourges, P. Burlet, J. Bossy, J.Y. Henry and G. Lapertot, 1991, Physica C **185–189**, 86.

Rotter, L.D., Z. Schlesinger, R.T. Collins, F. Holtzberg, C. Feild, U. Welp, G.W. Crabtree, J.Z. Liu, Y. Fang, K.G. Vandervoort and S. Fleshler, 1991, Phys. Rev. Lett. **67**, 2741.

Rozenberg, M.J., G. Kotliar, H. Kajueter, G.A. Thomas, D.H. Rapkine, J.M. Honig and P. Metcalf, 1995, Phys. Rev. Lett. **75**, 105.

Ruvalds, J., 1996, SPIE **2696**, 109.

Salkola, M.I., V.J. Emery and S.A. Kivelson, 1996, Phys. Rev. Lett. **77**, 155.

Scalapino, D.J., 1995, Phys. Rep. **250**, 329.

Schachinger, E., J.P. Carbotte and F. Marsiglio, 1997, Phys. Rev. B **56**, 2738.

Schlesinger, Z., R.T. Collins, F. Holtzberg, C. Feild, S.H. Blanton, U. Welp, G.W. Crabtree, Y. Fang and J.Z. Liu, 1990, Phys. Rev. Lett. **65**, 801.

Schützmann, J., B. Gorshunov, K.F. Renk, J. Münzel, A. Zibold, H.P. Geserich, A. Erb and G. Müller-Vogt, 1992, Phys. Rev. B **46**, 512.

Schützmann, J., S. Tajima, S. Miyamoto and S. Tanaka, 1994, Phys. Rev. Lett. **73**, 174.

Schützmann, J., H.S. Somal, A.A. Tsvetkov, D. van der Marel, G.E.J. Koops, N. Kolesnikov, Z.F. Ren, J.H. Wang, E. Bruk and A.A. Menovsky, 1997, Phys. Rev. B **55**, 11118.

Shastry, B.S., and B.I. Shraiman, 1990, Phys. Rev. Lett. **65** 1068.

Shen, Z.-X., and J.R. Schrieffer, 1997, Phys. Rev. Lett. **78**, 1771.

Shibata, H., K. Semba, A. Matsuda and T. Yamada, 1995, Phys. Rev. B **51**, 9294.

Shibauchi, T., H. Kitano, K. Uchinokura, A. Maeda, T. Kimura and K. Kishio, 1994, Phys. Rev. Lett. **72**, 2263.

Shulga, S.V., O.V. Dolgov and E.G. Maksimov, 1991, Physica C **178**, 266.

Sigrist, M., and K. Ueda, 1991, Rev. Mod. Phys. **63**, 239.

Slakey, F., M.V. Klein, J.P. Rice and D.M. Ginsberg, 1990, Phys. Rev. B **42** 2643.

Smith, D.Y., 1985, Dispersion theory, sum rules, and their application to the analysis of optical data, in: Handbook of Optical Constants of Solids, ed. E.D. Palik (Academic Press, Orlando, FL).

Somal, H.S., B.J. Feenstra, J. Schützmann, J.H. Kim, Z.H. Barber, V.H.M. Duijn, N.T. Hien, A.A. Menovsky, M. Palumbo and D. van der Marel, 1996, Phys. Rev. Lett. **76**, 1525.

Spielman, S., B. Parks, J. Orenstein, D.T. Nemeth, F. Ludwig, J. Clarke, P. Merchant and D.J. Lew, 1994, Phys. Rev. Lett. **73**, 1537.

Srikanth, H., B.A. Willemsen, T. Jacobs, S. Sridar, A. Erb, E. Walker and R. Flükiger, 1997, Phys. Rev. B **55**, R14733.

Stadlober, B., G. Krug, R. Nemetschek, R. Hackl, J.L. Cobb and J.T. Markert, 1995, Phys. Rev. Lett. **74** 4911.

Startseva, T., T. Timusk, A.V. Puchkov, D.N. Basov, H. Mook, M. Okuya, T. Kimura and K. Kishio, 1999a, Phys. Rev. B **59**, 7184.

Startseva, T., T. Timusk, M. Okuya, T. Kimura and K. Kishio, 1999b, Physica C, **321**, 135.

Stephan, W., and P. Horsch, 1990, Phys. Rev. B **42**, 8736.

Stojkovic, B.P., and D. Pines, 1996, Phys. Rev. Lett. **76**, 811.

Sulewski, P.E., A.J. Sievers, M.B. Maple, M.S. Torikachvili, J.L. Smith and Z. Fisk, 1988, Phys. Rev. B **38**, 5338.

Sumner, M.J., J.-T. Kim and T.R. Lemberger, 1993, Phys. Rev. B **47**, 12248.

Sun, A.G., L.M. Paulius, D.A. Gajewski, M.B. Maple and R.C. Dynes, 1994, Phys. Rev. B **50**, 3266.

Sun, A.G., S.H. Han, A.S. Katz, D.A. Gajewski, M.B. Maple and R.C. Dynes, 1995, Phys. Rev. B **52**, R15731.

Tajima, S., G.D. Gu, S. Miyamoto, A. Odagawa and N. Koshizuka, 1993, Phys. Rev. B **48**, 16164.

Tajima, S., J. Schützmann, S. Miyamoto, I. Terasaki, Y. Sato and R. Hauff, 1997, Phys. Rev. B **55**, 6051.

Tajima, S., N.L. Wang, R. Hauff, A.I. Rykov and T. Mimura, 1998, J. Phys. Chem. Solids **59**, 2015.

Tajima, S., T. Noda, H. Eisaki and S. Uchida, 2001, Phys. Rev. Lett. **86**, 500.

Takenaka, K., and S. Uchida, 1994, Phys. Rev. B **50**, 6534.

Tallon, J.L., C. Bernhard, U. Binninger, A. Hofer, G.V.M. Williams, E.J. Ansaldo, J.I. Budnick and Ch. Niedermayer, 1995, Phys. Rev. Lett. **74**, 1008.

Tamasaku, K., Y. Nakamura and S. Uchida, 1992, Phys. Rev. Lett. **69**, 1455.

Tanner, D.B., and T. Timusk, 1992, Infrared Properties of High T_c Superconductors, in: Physical Properties of High Temperature Superconductors, Vol. III, ed. D.M. Ginsberg (World Scientific, Singapore).

Tanner, D.B., F. Gao, M.A. Quijada, D.B. Romero, J.P. Rice, D.M. Ginsberg, J. Talivacchio, M.G. Forrester, L. Forro, D. Mandrus, L. Mihaly, G.L. Carr and G.P. Williams, 1992, J. Phys. Chem. Solids **53**, 1611.

Tanner, D.B., Y. Yoon, A. Zibold, H.L. Liu, M.A. Quijada, S.W. Moore, J.M. Graubeal, B.H. O, J.T. Market, R.J. Kelley, M. Onellion and J.-H. Cho, 1996, SPIE **2696**, 13.

Tao, H.J., Farun Lu and E.L. Wolf, 1997, Physica C **282–287**, 1507.

Thomas, G.A., 1991, in: Proc. 39th Scottish Universities Summer School in Physics of High-Temperature Superconductivity, eds D.P. Tunstall and W. Barford (Adam Hilger, Bristol) p. 169.

Thomas, G.A., J. Orenstein, D.H. Rapkine, M. Capizzi, A.J. Millis, R.N. Bhatt, L.F. Schneemeyer and J.V. Waszczak, 1988, Phys. Rev. Lett. **61**, 1313.

Thomas, G.A., D.H. Rapkine, S.L. Cooper, S.-W. Cheong and A.S. Cooper, 1991, Phys. Rev. Lett. **67**, 2906.

Thomas, G.A., D.H. Rapkine, S.L. Cooper, S.-W. Cheong, A.S. Cooper, L.F. Schneemeyer and J.V. Waszczak, 1992, Phys. Rev. B **45**, 2474.

Thomas, G.A., D.H. Rapkine, S.A. Carter, A.J. Millis, T.F. Rosenbaum, P. Metcalf and J.M. Honig, 1994, Phys. Rev. Lett. **73**, 1529.

Thomsen, C., and M. Cardona, 1989, in: Physical Properties of High Temperature Superconductors, Vol. I, ed. D.M. Ginsberg (World Scientific, Singapore).

Timusk, T., and B.W. Statt, 1999, Rep. Progr. Phys. **62**, 61.

Timusk, T., and D.B. Tanner, 1989, Infrared properties of high T_c superconductors, in: Physical Properties of High Temperature Superconductors, Vol. I, ed. D.M. Ginsberg (World Scientific, Singapore) p. 339.

Timusk, T., C.C. Homes and W. Reichardt, 1995a, in: Proc. Int. Workshop on Anharmonic Properties of High-T_c Cuprates, Bled, Slovenia, September 1994, eds D. Mihailovic, G. Ruani, E. Kaldis and K.A. Müller (World Scientific, Singapore) p. 171.

Timusk, T., D.N. Basov, C.C. Homes, A.V. Puchkov and M. Reedyk, 1995b, J. Superconductivity **8**, 437.

Tinkham, M., and R.A. Ferrell, 1959, Phys. Rev. Lett. **2**, 331.

Tokura, Y., S. Koshihara, T. Arima, H. Takagi, S. Ishibashi, T. Ido and S. Uchida, 1990, Phys. Rev. B **41**, 11657.

Tolpygo, S.K., J.-Y. Lin, M. Gurvitch, S.Y. Hou and J. Phillips, 1996, Phys. Rev. B **53**, 12454.

Tranquada, J.M., P.M. Gehring, G. Shirane, S. Shamoto and M. Sato, 1992, Phys. Rev. B **46**, 5561.

Tsuei, C.C., J.R. Kirtley, Z.F. Ren, J.H. Wang, H. Raffy and Z.Z. Li, 1997, Nature **238**, 481.

Tsui, O.K.C., N.P. Ong and J.B. Peterson, 1996, Phys. Rev. Lett. **76**, 819.

Tsvetkov, A.A., et al., 1998, Nature **395**, 360.

Uchida, S., 1997, Hyperfine Interactions **105**, 47.

Uchida, S., T. Ido, H. Takagi, T. Arima, Y. Tokura and S. Tajima, 1991, Phys. Rev. B **43**, 7942.

Uchida, S., K. Tamasaku and S. Tajima, 1996, Phys. Rev. B **53**, 1.

Uemura, Y.J., 1996, in: Proc. 10th Anniversary HTS Workshop (World Scientific, Singapore) p. 68.

Uemura, Y.J., G.M. Luke, B.J. Sternlieb, J.H. Brewer, J.F. Carolan, W.N. Hardy, R. Kadono, J.R. Kempton, R.F. Kiefl, S.R. Kreitzman, P. Mulhern, T.M. Riseman, D.Ll. Williams, B.X. Yang, S. Uchida, H. Takagi, J. Gopalakrishnan, A.W. Sleight, M.A. Subramanian, C.L. Chien, M.Z. Cieplak, G. Xiao, V.Y. Lee, B.W. Statt, C.E. Stronach, W.J. Kossler and X.H. Yu, 1989, Phys. Rev. Lett. **62**, 2317.

Uemura, Y.J., L.P. Le, G.M. Luke, B.J. Sternlieb, W.D. Wu, J.H. Brewer, T.M. Riseman, C.L. Seaman, M.B. Maple, M. Ishikawa, D.G. Hinks, J.D. Jorgensen, G. Saito and H. Yamochi, 1991, Phys. Rev. Lett. **66**, 2665.

Ulm, E., J.T. Kim, T. Lemberger, S.R. Foltyn and X. Wu, 1995, Phys. Rev. B **51**, 9193.

Valles Jr, J.M., and R.C. Dynes, 1990, Mater. Res. Soc. Proc. **195**, 375.

Valles Jr, J.M., A.E. White, K.T. Short, R.C. Dynes, J.P. Garno, A.F.J. Levi, M. Anzlowar and K. Balwin, 1989, Phys. Rev. B **39**, 11599.

van Bentum, P.J.M., A. Wittlin, M.E.J. Boonman, M. Gross, S. Uchida and J. Tamasaku, 1997, Physica C, **293**, 136.

van der Marel, D., 1996, in: Proc. 10th Anniversary HTS Workshop on Physics, Material and Applications (World Scientific, Singapore) p. 357.

van der Marel, D., and J.H. Kim, 1995, J. Phys. Chem. Solids, **56**, 1825.

van Harlingen, D.J., 1995, Rev. Mod. Phys. **67**, 515.

Varma, C.M., P.B. Littlewood, S. Schmitt-Rink, E. Abrahams and A.E. Ruckenstein, 1989, Phys. Rev. Lett. **63**, 1996.

Volovik, K.E., 1993, JETP Lett. **58**, 469.

Wachter, P., B. Bucher and R. Pittini, 1994, Phys. Rev. B **49**, 13164.

Walker, M.B., and T. Timusk, 1995, Phys. Rev. B **52**, 97.

Wang, N.L., S. Tajima, A.I. Rykov and K. Tomimoto, 1998, Phys. Rev. B **57**, R11081.

Warren, W.W., R.E. Walstedt, G.F. Brennert, R.J. Cava, R. Tycko, R.F. Bell and G. Dabbagh, 1989, Phys. Rev. Lett.**62**, 1193.

Watanabe, T., T. Fujici and A. Matsuda, 1997, Phys. Rev. Lett. **79**, 2113.

Weber, C., R. Yoshizaki and D.N. Basov, 1997, unpublished.

Welp, U., S. Fleshler, W.K. Kwok, J. Downey, Y. Fang and G.W. Crabtree, 1990, Phys. Rev. B **42**, 10188.

Williams, G.P., R.C. Budhani, C.J. Hirschmugl, G.L. Carr, S. Perkowitz, B. Lou and T.R. Yang, 1990, Phys. Rev. B **41**, 4752.

Wu, D.H., J. Mao, S.N. Mao, J.L. Peng, X.X. Xi, T. Venkatesan, R.L. Greene and S.M. Anlage, 1993, Phys. Rev. Lett. **70**, 85.

Xiang, T., and J.M. Wheatley, 1995, Phys. Rev. B **51**, 11721.

Xiang, T., and J.M. Wheatley, 1996, Phys. Rev. Lett. **76**, 134.

Yagil, Y., and E.K.H. Salje, 1996, Physica C **256**, 205.

Yoshinari, Y., H. Yasuoka, Y. Ueda, K. Koga and K. Kosuge, 1990, J. Phys. Soc. Jpn. **59**, 3698.

Yoshizaki, R., I. Tomitsuka, K. Ueno and H. Ikeda, 1996, J. Low Temp. Phys. **105**, 927.

Zaanen, J., G.A. Sawatzky and J.W. Allen, 1985, Phys. Rev. Let **55**, 418.

Zha, Y., S.L. Cooper and D. Pines, 1996, Phys. Rev. B **53**, 8253.

Zhang, K., D.A. Bonn, S. Kamal, R. Liang, D.J. Baar, W.N. Hardy, D.N. Basov and T. Timusk, 1994, Phys. Rev. Lett. **73**, 2484.

Zhang, S.-C., 1997, Science **275**, 1089.

Zibold, A., M. Durller, A. Gaymann, H.P. Geserich, A. Erb and G. Müller-Vogt, 1990, Physica C **171**, 151.

Handbook on the Physics and Chemistry of Rare Earths
Vol. 31
edited by K.A. Gschneidner, Jr., L. Eyring and M.B. Maple

Chapter 203

ELECTRONIC AND MAGNETIC RAMAN SCATTERING STUDIES OF THE HIGH-T_c CUPRATES

S.L. COOPER
Department of Physics, Frederick Seitz Materials Research Laboratory, and Science and Technology Center for Superconductivity, 1110 W. Green St., University of Illinois at Urbana-Champaign, Urbana, IL 61801-3080, USA

Contents

List of symbols and abbreviations

2D, 3D	Two-dimensional, three-dimensional
$\boldsymbol{A}(\boldsymbol{r})$	Vector potential
BCS	Bardeen–Cooper–Schrieffer
D	Diffusion constant
E_F	Fermi energy
$\boldsymbol{E}_I(\boldsymbol{r},t)$, $\boldsymbol{E}_S(\boldsymbol{r},t)$	Incident and scattered electric field vectors as a function of position and time
H	Magnetic field
H_{int}	Interaction Hamiltonian
$\mathrm{Im}\,\chi$	Imaginary part of the Raman response function
J	Superexchange coupling
$J_\perp$	Interlayer exchange coupling
$\boldsymbol{j}(\boldsymbol{r}),\boldsymbol{j}_q$	Particle current density and qth Fourier component of the particle current density
$\boldsymbol{k}_I, \boldsymbol{k}_S$	Incident and scattered wavevectors, respectively
MFL	Marginal Fermi liquid
$N(0)$	One-electron density of states at the Fermi level
n_I, n_S	Index of refraction of the incident and scattered media
$n(\omega)$	Bose thermal factor
P	Incident laser power
$\boldsymbol{P}(\boldsymbol{r},t)$	Polarization vector as a function of position and time
$\boldsymbol{p}$	Electron momentum
$\boldsymbol{q}$	Excitation wavevector
$\boldsymbol{r}$	Electron position
r_0	Thompson radius of the electron
$\boldsymbol{S}$	Total spin angular momentum
$S(\boldsymbol{q},\omega)$	Generalized dynamical structure factor
T_c	Superconducting critical temperature
T_N	Néel temperature
T^*	Cross-over temperature
T_I, T_S	Transmission coefficient of incident and scattered media
t	Hopping energy
U	On-site Coulomb interaction
V	Scattering volume
V_q	Coulomb interaction matrix element
v_F	Fermi velocity
$X(\boldsymbol{r},t)$	Generalized dynamical variable as a function of position and time
τ	Electron scattering time
Γ, Γ_L	Electron scattering rate, and electron scattering rate in Lth scattering channel
Γ_n	nth irreducible representation of the space group
γ	Electron–photon scattering vertex function
Δ	Superconducting gap
Δ_{CT}	Charge-transfer gap
$\varepsilon_I, \varepsilon_S$	Incident and scattered electric field polarization
$\varepsilon(\boldsymbol{q},\omega)$	Dielectric function
λ_k	Imaginary part of the Tsenuto function
μ	Effective mass tensor
ξ	Correlation length
$\rho(\boldsymbol{r}),\rho_q$	Particle number density and qth Fourier component of the particle number density
χ	Linear electric susceptibility tensor
χ_0	Static susceptibility tensor
$\chi(\boldsymbol{q},\omega)$	Raman response function
ω_I, ω_S	Incident and scattered light frequency, respectively
ω_p	Plasma frequency

1. Introduction

There is little question that the physics and chemistry of the high-T_c cuprates have been among the preeminent research topics in condensed-matter physics during the past decade. Much of the initial experimental and theoretical investigation of these materials was aimed at clarifying the mechanism responsible for high-T_c superconductivity. Yet, as the

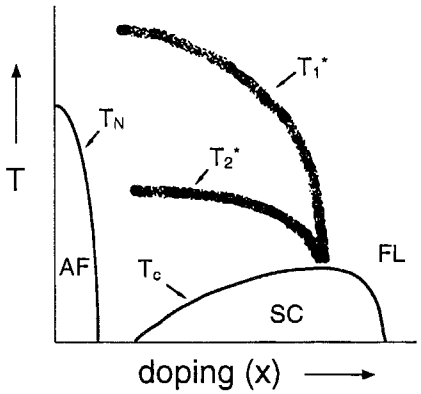

Fig. 1. Qualitative phase diagram for the high-T_c cuprates, illustrating the cross-over temperatures T_1^* and T_2^* described in the text, and the antiferromagnetic insulating (AF), superconducting (SC), and Fermi-liquid (FL) phases (adapted from Emery, Kivelson and Zachar 1997).

richness of the cuprate phase diagram has slowly emerged, a broader goal has evolved – to understand the nature of, and relationship among, the many diverse phases associated with these materials. Indeed, it is generally believed that the cuprates exhibit at least four distinct regimes as a function of doping (see fig. 1) (Batlogg and Emery 1996, Emery, Kivelson and Zachar 1997):

(i) *Antiferromagnetic insulator* – At zero doping, the cuprates are spin $S = \frac{1}{2}$ antiferromagnetic charge-transfer insulators ($T_N \approx 300$ K) with the spins localized primarily on the Cu^{2+} ions. From optical measurements, the in-plane Cu $d_{x^2-y^2}$ – O $p_{x,y}$ charge-transfer gap in these systems is known to be roughly $\Delta_{CT} \approx 1.75$ eV (Uchida et al. 1991, Cooper et al. 1993b), while neutron scattering (Aeppli et al. 1989) and two-magnon Raman scattering (Lyons et al. 1988a, 1988b) measurements indicate that the insulating cuprates have a Cu–Cu superexchange coupling constant of $J \approx 120$–140 meV. With increased hole doping in the plane, the 3D Néel temperature decreases rapidly due to a reduction of both the in-plane antiferromagnetic correlation length, ξ_{2D}, and the interlayer exchange coupling, $J_\perp$ (Aharony et al. 1988).

(ii) *Underdoped superconductors* – The underdoped cuprate superconductors have superconducting T_c's that are suppressed below their optimal values, and are "bad" metals in the sense that the carrier mean free path is less than the de Broglie wavelength (Emery and Kivelson 1995). Two cross-over temperatures have been identified with the underdoped superconductor phase (Batlogg and Emery 1996, Emery, Kivelson and Zachar 1997): (i) a temperature, T_1^*, below which charge inhomogeneities (i.e., "stripes") and short-range antiferromagnetic correlations appear to develop in the CuO_2 planes; and (ii) a temperature, T_2^* ($T_1^* > T_2^* > T_c$), characterized by the development of a "pseudogap". This pseudogap is manifested in a suppression of the spin susceptibility, as inferred from inelastic neutron scattering (Rossat-Mignod et al. 1991) and Cu spin relaxation nuclear magnetic resonance (NMR) measurements (Warren et al. 1989, Walstedt et al. 1990), as well as in a suppression of the electronic density of states, as observed in measurements of

specific heat (Ghiron et al. 1992, Loram et al. 1993), dc resistivity (Ito et al. 1993, Batlogg et al. 1994), in-plane and c-axis optical conductivity (Homes et al. 1993, Puchkov et al. 1996), and angle-resolved photoelectron spectroscopy (ARPES) (Loeser et al. 1996, Ding et al. 1996, Marshall et al. 1996). Unlike conventional superconductors, there is evidence that pair formation and phase coherence do not occur simulaneously at T_c in the underdoped cuprates (Micnas et al. 1988, 1990, Batlogg and Emery 1996). Rather, it has been suggested that superconductivity in this phase occurs in a manner akin to a Bose–Einstein condensation; i.e., involving the formation of normal state pairs above a cross-over temperature T^*, followed by the onset of phase coherence among the pairs below a lower, "superconducting" transition at T_c.

(iii) *Optimally doped superconductors* – At "optimal" doping, the transition temperatures of high-T_c superconductors attain their maximum values, and the two cross-over temperatures described above merge near the superconducting transition; consequently, there is an abrupt transition between the normal and superconducting states in the optimally doped regime. With some notable exceptions (Sun et al. 1994, Chaudhari and Lin 1994, Kouznetsov et al. 1997), measurements of the superconducting state in the hole-doped cuprates are largely consistent with a $d_{x^2-y^2}$ pairing state (Annett et al. 1996), including phase-sensitive SQUID experiments (Wollman et al. 1993, Brawner and Ott 1994, Van Harlingen 1995), phase-sensitive studies of the Josephson effect in oriented crystal composites (Tsuei et al. 1994), ARPES experiments (Shen et al. 1993, Ding et al. 1994), and Raman scattering measurements (Devereaux et al. 1994a, Devereaux and Einzel 1996a).

(iv) *Overdoped superconductors* – At still higher doping, T_c decreases below its optimal-doping value, and many of the transport and optical properties exhibit features suggestive of Fermi-liquid behavior (Uchida et al. 1991, Batlogg et al. 1994). For example, in this phase the resistivity exhibits a Fermi liquid-like temperature dependence, $\rho(T) \sim T^2$ (Batlogg et al. 1994).

In many respects, Raman scattering is a natural probe of the cuprates. As a technique that is sensitive to spin, electronic, and phonon degrees of freedom, Raman scattering can provide energy, symmetry, and lifetime information about many of the diverse excitations present throughout the complex phase diagram of the cuprates. Moreover, Raman scattering provides an ideal method with which to explore the evolution of charge, spin, and lattice excitations *between* different phases. Raman scattering lends itself particularly to the study of such important issues as the nature of the superconducting pairing mechanism, the manner in which antiferromagnetic correlations evolve into the metallic phase, and the relationship between "pseudogap" and superconducting phases in underdoped cuprates.

The purpose of this chapter is to review Raman scattering studies of the many diverse phases of high-T_c superconductors. As there are already comprehensive review articles dealing extensively with Raman-active phonons and phonon self-energy effects in high-T_c superconductors (Thomsen and Cardona 1989, Thomsen 1991, Cardona 1999), this review will primarily focus on the nature of electronic and magnetic excitations in the different

phase regimes of the high-T_c superconductors. The outline of this review is as follows: Section 2 discusses basic details regarding the Raman scattering process and technique. Section 3 examines the Raman scattering response in the insulating phase, focusing on scattering from two-magnon excitations, topological ("chiral") spin excitations, excitons, and crystal-field excitations. Section 4 describes the Raman scattering response of the unconventional metallic phase, including the anomalous *ab*-plane electronic scattering "continuum", interlayer electronic scattering, and electronic scattering in the underdoped phase. Section 5 discusses electronic Raman scattering studies of the superconducting state. Finally, sect. 6 concludes with remarks about possible future directions of Raman scattering in the high-T_c cuprates.

2. Fundamentals of Raman scattering

2.1. *Classical description*

Much of the essential physics of inelastic light scattering can be understood classically by considering the macroscopic polarization $\boldsymbol{P}(\boldsymbol{r},t)$ induced in the material by an incident electric field $\boldsymbol{E}_I(\boldsymbol{r},t)$,

$$\boldsymbol{P}(\boldsymbol{r},t) = \chi \boldsymbol{E}_I(\boldsymbol{r},t), \tag{1}$$

where χ is a second-rank tensor describing the linear electric susceptibility of the material. Elastic contributions to the light-scattering response arise from the induced polarization associated with the static susceptibility, χ_0. On the other hand, inelastic contributions to the light-scattering spectrum arise due to the presence of excited states that dynamically modulate the wavefunctions and energy levels in the material. In the semiclassical description, these excited states are represented by a dynamical variable, $X(\boldsymbol{r},t)$, which can be associated, for example, with deviations of atomic position, charge density, or spin density from equilibrium. The resulting induced polarization in the presence of excited states in the material is obtained by expanding the dynamical susceptibility χ in powers of X around the static susceptibility, χ_0:

$$\boldsymbol{P}(t) = \chi_0 \boldsymbol{E} + \frac{\mathrm{d}\chi_0}{\mathrm{d}X} X\boldsymbol{E} + \frac{1}{2}\frac{\mathrm{d}^2\chi_0}{\mathrm{d}X^2} X^2 \boldsymbol{E} + \cdots. \tag{2}$$

Thus, in addition to the elastic scattering contribution in eq. (2), inelastic contributions to the scattering response arise from the modulation of the polarization at the characteristic frequency of excitations in the material, $X = X_0 \mathrm{e}^{\mathrm{i}(\omega t + \varphi)}$. In particular, the contribution to the induced polarization that is linear in X is given by $\boldsymbol{P}^{(1)} = \boldsymbol{P}\mathrm{e}^{\mathrm{i}[(\omega_I \pm \omega)t + \varphi]}$, where ω_I is the frequency of the incident electric field. The resulting inelastic light-scattering cross-section includes two contributions: (a) the Stokes component, in which the incident light field $\boldsymbol{E}_I(\boldsymbol{r},t)$ creates an excitation of energy and wavevector, ω and $\boldsymbol{q}$, causing a

reduction in energy of the scattered field $\boldsymbol{E}_S(\boldsymbol{r},t)$, $\omega_S = \omega_I - \omega$; and (b) the anti-Stokes component, wherein the scattered field gains energy from thermally excited excitations in the sample, $\omega_S = \omega_I + \omega$. In scattering processes having time-reversal symmetry (i.e., non-magnetic excitations) and no resonant enhancement, the principle of detailed balance requires that the Stokes and anti-Stokes intensities be related by (Hayes and Loudon 1978) $I_{AS}(\omega) = I_S(\omega)(\omega_{AS}/\omega_S)^2 e^{-\hbar\omega/k_B T}$, where ω_S (ω_{As}) is the absolute frequency of Stokes (anti-Stokes) light, ω is the frequency of the excitation, and T is the temperature.

2.2. *Kinematical constraints*

In a pure crystal, i.e., one exhibiting translational invariance, kinematical constraints imposed by wavevector conservation dictate one of the most important constraints on the Stokes Raman scattering process, namely,

$$\boldsymbol{q} = \boldsymbol{k}_I - \boldsymbol{k}_S. \tag{3}$$

In typical experimental situations one has $\omega \ll \omega_I$ and $|\boldsymbol{k}_I| \approx |\boldsymbol{k}_S|$, and therefore the wavevector-conservation condition in eq. (3) can to a good approximation be written as

$$|\boldsymbol{q}| = 2\,|\boldsymbol{k}_I| \sin(\tfrac{1}{2}\theta). \tag{4}$$

As inelastic light scattering experiments are usually performed with incident frequencies in the visible frequency range, $\omega_I \approx 10^{14}$ Hz, the range of excitation wavevectors typically probed in light-scattering experiments is $0 < |\boldsymbol{q}| < 3\times10^{-3}$ Å^{-1} (Hayes and Loudon 1978), which is generally several orders of magnitude smaller than the size of the Brillouin zone boundary, $|\boldsymbol{k}_{ZB}| \approx 2\pi/a \approx 1$ Å^{-1}. Thus, Raman scattering generally probes only excitations very near the Brillouin zone center; i.e., $|\boldsymbol{q}| \approx 0$. This limitation is circumvented under certain circumstances, including when wavevector conservation is lost due to the presence of disorder, and when two-particle (e.g., two-phonon and two-magnon) excitations of equal and opposite momenta, $\boldsymbol{q}$ and $-\boldsymbol{q}$, are excited.

2.3. *The Raman scattering cross-section*

2.3.1. *Basic results*

In the quantum-mechanical derivation of the Raman scattering cross-section, one considers the two-photon process in which a photon changes its frequency ω, wavevector $\boldsymbol{k}$, and polarization ε via scattering from the values $(\omega_I, \boldsymbol{k}_I, \varepsilon_I)$ to the values $(\omega_S, \boldsymbol{k}_S, \varepsilon_S)$, while the scattering material experiences a transition from $|i\rangle$ to $|f\rangle$. The interaction Hamiltonian between light and matter is given by

$$H_{int} = -\frac{e}{c}\int d^3\boldsymbol{r}\,\boldsymbol{j}(r)\cdot\boldsymbol{A}(\boldsymbol{r}_j) + \frac{e^2}{2mc^2}\int d^3\boldsymbol{r}\,\rho(r)\boldsymbol{A}^2(\boldsymbol{r}_j), \tag{5}$$

where $\boldsymbol{A}(\boldsymbol{r})$ is the vector potential associated with the incident radiation field, $\boldsymbol{j}(r) = \frac{1}{2m}\sum_j (\boldsymbol{p}_j\delta(\boldsymbol{r}-\boldsymbol{r}_j) + \delta(\boldsymbol{r}-\boldsymbol{r}_j)\boldsymbol{p}_j)$ is the particle current density, $\boldsymbol{p}_j$ and $\boldsymbol{r}_j$ are the momentum and position of the jth particle, and $\rho(r) = \sum_j \delta(\boldsymbol{r}-\boldsymbol{r}_j)$ is the particle number density.

As Raman scattering is a two-photon process, the scattering cross-section is obtained by taking the A^2 term in eq. (5) to first order in perturbation theory, and the A term in eq. (5) to second order in perturbation theory.

The measured quantity in a typical Raman scattering measurement is related to the photon differential cross-section per unit scattered frequency range, $d^2\sigma/d\Omega\, d\omega_S$, which reflects the fraction of incident photons inelastically scattered in the energy interval, $d\omega_S$, per unit solid angle, $d\Omega$. The resulting quantum-mechanical photon scattering cross-section is given by

$$\frac{d^2\sigma}{d\Omega\, d\omega_S} = \frac{V^2\omega_I\omega_S^3}{c^4}\frac{n_S}{n_I}\sum_f \langle\langle |\langle f|\chi_{IS}|i\rangle|^2 \rangle\rangle\, \delta(\omega_I - \omega_S - \omega), \tag{6}$$

where $\langle\langle \cdots \rangle\rangle$ represents a thermodynamic average over the initial states of the scattering material. The transition susceptibility tensor χ in eq. (6) is the quantum-mechanical analogue of the classical susceptibility in eq. (1), and has matrix elements

$$\langle f|\chi_{IS}|i\rangle = \frac{e^2}{V\omega_S\omega_I}\sum_m \left[\frac{\langle f|\boldsymbol{\varepsilon}_S\cdot\boldsymbol{j}_{k_S}|m\rangle\langle m|\boldsymbol{\varepsilon}_I\cdot\boldsymbol{j}_{-k_I}|i\rangle}{[E_m - E_i - \hbar\omega_I]} + \frac{\langle f|\boldsymbol{\varepsilon}_I\cdot\boldsymbol{j}_{-k_I}|m\rangle\langle m|\boldsymbol{\varepsilon}_S\cdot\boldsymbol{j}_{k_S}|i\rangle}{[E_m - E_i + \hbar\omega_S]}\right] - \frac{e^2}{mV\omega_S\omega_I}\boldsymbol{\varepsilon}_I\cdot\boldsymbol{\varepsilon}_S\langle f|\rho_{-q}|i\rangle, \tag{7}$$

where $\boldsymbol{j}_q = \frac{1}{m}\sum_j e^{-i\boldsymbol{q}\cdot\boldsymbol{r}_j}(\boldsymbol{p}_j - \hbar\boldsymbol{q}/2)$ is the $\boldsymbol{q}$th Fourier component of the particle current density operator, and $\rho_q = \sum_j e^{-i\boldsymbol{q}\cdot\boldsymbol{r}_j}$ is the $\boldsymbol{q}$th Fourier component of the particle density operator. Thus, the Raman scattering cross-section for a particular excitation is given by the correlation function of the dynamical susceptibility at the wavevector $\boldsymbol{q}$ and frequency ω of the excitation.

2.3.2. *Phonon and magnon scattering*

In order to consider light scattering from phonons or spins, one typically treats the electron–phonon or electron–spin interaction as a perturbation and calculates the relevant scattering cross-sections using third- or higher-order perturbation theory (Hayes and Loudon 1978).

2.3.3. *Effects of the material's optical response*

The dependence of the scattering cross-section in eq. (6) on the optical constants of the incident and scattered media is deceptively benign ($\sim n_I/n_S$), and it should be noted that this factor is derived by considering only the radiated intensity *inside* the scattering medium. As the scattering intensity is measured outside the material, the differential scattering

cross-section is actually related to the measured scattering intensity, I, by several factors which depend upon the optical response of the material (Reznik et al. 1993),

$$\frac{\mathrm{d}\sigma}{\mathrm{d}\Omega\,\mathrm{d}\omega} = \frac{I}{P\,T_{\mathrm{I}}\,T_{\mathrm{S}}\,V\,\Omega_{\mathrm{in}}}, \tag{8}$$

where P is the incident laser power, T_{I} and T_{S} are the transmission coefficients at the air–sample interface for the incident and scattered photons, respectively; $V=(\alpha_{\mathrm{I}}+\alpha_{\mathrm{S}})^{-1}$ is the scattering volume, which depends upon the absorption coefficients at the incident (α_{I}) and scattered (α_{S}) photon frequencies; $\Omega_{\mathrm{in}}=\Omega_{\mathrm{out}}/n^2$ is the solid angle inside the material collected by the collection optics, where n is the index of refraction of the material, and Ω_{out} is the solid angle outside the material depending upon the f-number of the collecting lens. These optical corrections must be carefully accounted for, particularly when comparing Raman spectra as a function of doping.

2.3.4. *Resonance effects*

It is evident from eqs. (6) and (7) that second- and higher-order terms in the scattering cross-section involve transitions to virtual intermediate states that contribute energy denominators of the form $(E_m-E_i-\hbar\omega_{\mathrm{I}})$ and $(E_m-E_i+\hbar\omega_{\mathrm{S}})$. As a result, "resonant enhancements" of the scattering cross-section occur when the incident photon energy $\hbar\omega_{\mathrm{I}}$ approaches the energy difference between initial and intermediate states, causing the energy denominator to vanish. Various studies of the resonant Raman scattering intensity of phonon and bimagnon excitations as the incident photon frequency is tuned through real electronic transitions have been particularly useful for exploring the coupling between these excitations and the electronic bands in the cuprates; see, for example, Heyen et al. (1990, 1992), Wake et al. (1991), Yoshida et al. (1992), and Blumberg et al. (1996).

2.4. *Raman scattering selection rules*

The selection rules for the Raman scattering process are imposed by the susceptibility tensor in eqs. (1) and (6). Consider the matrix element $\langle f|\chi_{ab}|i\rangle$, where $|i\rangle$ and $|f\rangle$ are the initial and final states of the scattering medium, which transform like the irreducible representations of the material's point group, Γ_i and Γ_f, respectively, and where the susceptibility tensor χ associated with an excitation is decomposed into irreducible representations Γ_n of the point group of the crystal,

$$\chi_{ab}=\sum_n a_n\chi_{\Gamma_n}. \tag{9}$$

The transition susceptibility matrix element $\langle f|\chi_{ab}|i\rangle$ is nonzero only if the decomposition of the direct product $\Gamma_f^*\otimes\Gamma_n\otimes\Gamma_i$ contains the totally symmetric representation, Γ_1, or equivalently, if the decomposition of $\Gamma_f^*\otimes\Gamma_i$ contains Γ_n. Additionally, for an excitation to be "Raman-active", the relationship between the induced polarization $\boldsymbol{P}$, the susceptibility

Table 1
Irreducible representations of the allowed Raman tensors in both orthorhombic (D_{2h}) and tetragonal (D_{4h}) point groups

Point group	Orthorhombic (D_{2h})	Tetragonal (D_{4h})
A_{1g}	$\begin{pmatrix} xx & & \\ & yy & \\ & & zz \end{pmatrix}$	$\begin{pmatrix} xx & & \\ & yy & \\ & & zz \end{pmatrix}$
A_{2g}	–	$\begin{pmatrix} & xy & \\ -xy & & \\ & & \end{pmatrix}$
B_{1g}	$\begin{pmatrix} & xy & \\ yx & & \\ & & \end{pmatrix}$	$\begin{pmatrix} xx & & \\ & -xx & \\ & & \end{pmatrix}$
B_{2g}	$\begin{pmatrix} & & xz \\ & & \\ zx & & \end{pmatrix}$	$\begin{pmatrix} & xy & \\ xy & & \\ & & \end{pmatrix}$
B_{3g}	$\begin{pmatrix} & & xz \\ & & \\ & zy & \end{pmatrix}$	–
E_g	–	$\begin{pmatrix} & & xz \\ & & \\ zx & & \end{pmatrix}$ $\begin{pmatrix} & & \\ & & xz \\ & zx & \end{pmatrix}$

tensor χ, and the incident field $\boldsymbol{E}_I$ in eq. (1) must be covariant under all spatial transformations of the scattering medium. Since $\boldsymbol{P}_I$ and $\boldsymbol{E}_I$ are both polar vectors, this is equivalent to stating that an excitation is Raman-active only if it has a symmetry contained in the decomposition of $\Gamma^*_{PV} \otimes \Gamma_{PV}$. Table 1 lists the specific allowed Raman tensors for the orthorhombic D_{2h} and tetragonal D_{4h} point groups to which most high-T_c cuprates belong.

An extremely powerful feature of the Raman scattering technique, implicit in the susceptibility tensor coefficients in eq. (7), is that one can experimentally couple to different components of the susceptibility tensor – and thereby identify the symmetry of a given excitation – by varying the polarizations of the incident and scattered light relative to the sample's crystalline axes. The nomenclature typically used for describing the geometry of a Raman scattering experiment is $k_I(\varepsilon_I\, \varepsilon_S)k_S$, where k_I and k_S are the wavevector directions of the incident and scattered photons, respectively, and ε_I and ε_S are the polarization directions of the incident and scattered photons, respectively. For example, $z(x,y)\bar{z}$ indicates a depolarized, "true-backscattering" geometry in which the incident and

scattered wavevectors are directed along the z- and $-z$-axes of the crystal, respectively, and the incident and scattered photons are polarized along the x- and y-axes, respectively.

2.5. *Electronic Raman scattering*

2.5.1. *Fundamentals*

As this review is primarily concerned with low-energy electronic scattering in the "normal" and superconducting states of high-T_c superconductors, it is useful to consider in detail the cross-section for Raman scattering from intraband electronic excitations. Using eqs. (6) and (7), the electronic Raman scattering cross-section can be related to a correlation function associated with *an effective density* $\tilde{\rho}$,

$$\frac{d^2\sigma}{d\Omega\, d\omega_S} = r_0^2 \frac{\omega_S}{\omega_I}\frac{n_S}{n_I}\sum_f \langle\langle |\langle f|\tilde{\rho}_q|i\rangle|^2\rangle\rangle\, \delta(E_f - E_i - \hbar\omega), \tag{10}$$

where $\langle\langle \cdots \rangle\rangle$ represents a thermal average over the initial states i,

$$\tilde{\rho}_q = \sum_{n,k,\sigma} \gamma_{nk} c^\dagger_{nk+q,\sigma} c_{nk,\sigma}, \tag{11}$$

$c^\dagger$ and c are the electron creation and annihilation operators, respectively, $r_0 = e^2/mc^2$ is the Thomson radius of the electron, n is a band index, and γ_{nk} is the electron–photon Raman scattering "vertex". In the case of intraband electronic excitations, the initial and final band states in eq. (7) are taken to be the same, and γ_{nk} is given by (Abrikosov and Genkin 1974)

$$\gamma_{nk} = \boldsymbol{\varepsilon}_I \cdot \boldsymbol{\varepsilon}_S + \frac{1}{m}\sum_{n'}\left[\frac{\langle nk|\boldsymbol{\varepsilon}_S\cdot\boldsymbol{p}|n'k+k_I\rangle\langle n'k+k_I|\boldsymbol{\varepsilon}_I\cdot\boldsymbol{p}|nk\rangle}{E_{nk}-E_{n'k+k_I}+\hbar\omega_I} + \frac{\langle nk|\boldsymbol{\varepsilon}_I\cdot\boldsymbol{p}|n'k-k_S\rangle\langle n'k-k_S|\boldsymbol{\varepsilon}_S\cdot\boldsymbol{p}|nk\rangle}{E_{nk}-E_{n'k-k_S}-\hbar\omega_S}\right], \tag{12}$$

where the electronic states are represented by their band indices, n and n', and wavevectors, k, and it has been assumed that $|k_I| \approx |k_S|$ (see sect. 2.2).

The cross-section in eq. (10) can be equivalently written

$$\frac{d^2\sigma}{d\Omega\, d\omega_S} = r_0^2 \frac{\omega_S}{\omega_I}\frac{n_S}{n_I} S(q,\omega), \tag{13}$$

where $S(q,\omega)$ is a generalized dynamical structure factor, which can be related to the imaginary part of a Raman response function $\chi_{\tilde{\rho}\tilde{\rho}}$ via the fluctuation–dissipation theorem (Hayes and Loudon 1978),

$$S(q,\omega) = -\frac{1}{\pi}[1+n(\omega)]\,\mathrm{Im}\,\chi_{\tilde{\rho}\tilde{\rho}}(q,\omega), \tag{14}$$

where $n(\omega) = [\exp(\hbar\omega/k_B T) - 1]^{-1}$ is the Bose thermal factor. $\chi_{\tilde{\rho}\tilde{\rho}}$ is the Raman response function associated with fluctuations in the effective density $\tilde{\rho}$, and can be evaluated

to various levels of approximation using Green's function techniques. In particular, various self-energy "vertex" corrections are often included in $\chi_{\tilde{\rho}\tilde{\rho}}(\boldsymbol{q}, \omega)$ when considering electronic Raman scattering in metals and superconductors (see sect. 5.2.1), including those associated with electron–electron interactions (Virosztek and Ruvalds 1991, 1992), electron–impurity scattering (Zawadowski and Cardona 1990), electron–phonon scattering (Itai 1992), and Coulomb screening (Klein and Dierker 1984).

2.5.2. *The effective mass approximation*

Importantly, the Raman scattering vertex γ_{nk} in eq. (12) can be directly related to the inverse effective mass tensor $\boldsymbol{\mu}^{-1}$,

$$\gamma_{nk} = \boldsymbol{\varepsilon}_I \cdot \frac{m}{\boldsymbol{\mu}} \cdot \boldsymbol{\varepsilon}_S = m \sum_{i,j} \varepsilon_{Si} \frac{\partial^2 E_{nk}}{\hbar^2 \partial k_i \, \partial k_j} \varepsilon_{Ij}, \tag{15}$$

under certain circumstances, namely: (a) when the incident and scattered photon energies are far from a resonance condition, $\hbar\omega_I, \hbar\omega_S \ll |E_n - E_{n'}|$, so that the photon energies $\hbar\omega_I, \hbar\omega_S$ in the denominators of eq. (12) can be ignored; *and* (b) when virtual intraband transitions can be ignored, so that the sum in eq. (12) can be restricted to bands $n' \neq n$ (Strohm and Cardona 1997a). Within this "effective mass approximation", the electronic Raman scattering cross section in eq. (10) can be associated with effective mass fluctuations around the Fermi surface, the different symmetry components of which can be experimentally selected by varying the scattering geometry (i.e., $\boldsymbol{\varepsilon}_I$ and $\boldsymbol{\varepsilon}_S$) in the Raman scattering experiment (see eq. 15).

It is often useful to explicitly account for the crystalline symmetry of the material in the Raman scattering cross-section by expanding the Raman scattering vertex γ_{nk} in terms of Fermi surface harmonics Φ_L (Allen 1976, Klein and Dierker 1984, Devereaux and Einzel 1995),

$$\gamma_k = \sum_L \gamma_L^{\mu} \Phi_L^{\mu}(\boldsymbol{k}), \tag{16}$$

where L refers to the Lth-order contribution to the scattering vertex transforming like the μth irreducible representation of the crystal's point group. In the case of the tetragonal D_{4h} point group of the cuprates, the lowest-order terms for the vertices are given by (Devereaux and Einzel 1995),

$$\gamma_{\boldsymbol{k}}^{A_{1g}} = \gamma_0 + \gamma_{A_{1g}} \cos 4\varphi, \qquad \gamma_{\boldsymbol{k}}^{B_{1g}} = \gamma_{B_{1g}} \cos 2\varphi, \qquad \gamma_{\boldsymbol{k}}^{B_{2g}} = \gamma_{B_{2g}} \sin 2\varphi. \tag{17}$$

Equation (17) indicates that the B_{1g} and B_{2g} vertex contributions preferentially select Fermi surface regions $(\boldsymbol{k}_x, \boldsymbol{k}_y)$ near $\{(\pm\pi/a, 0), (0, \pm\pi/a)\}$ and $(\pm\pi/a, \pm\pi/a)$, respectively, while the A_{1g} vertex samples more uniformly around the Fermi surface (see fig. 2).

Note that the isotropic part ($L = 0$) of the Raman scattering vertex in eqs. (15) and (16), which comprises the entire electronic scattering response in the absence of interband

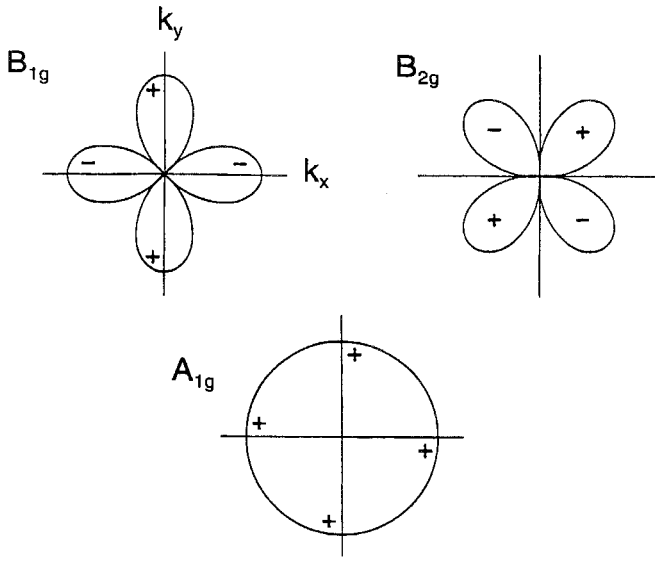

Fig. 2. The functional dependence of the Raman scattering vertices, γ_{nk}, associated with the tetragonal D_{4h} point group of the cuprates for: B_{1g} ($\gamma_k^{B_{1g}}$) symmetry; B_{2g} ($\gamma_k^{B_{2g}}$) symmetry; and A_{1g} ($\gamma_k^{A_{1g}}$) symmetry, for the case $\gamma_{A_{1g}} = 0$ (see eq. 17).

transitions or Fermi surface anisotropy, corresponds to scattering from ordinary density fluctuations, and has a Raman scattering cross-section given by

$$\frac{d^2\sigma}{d\Omega\, d\omega_S} = r_0^2 \left(\frac{\omega_S}{\omega_I}\right)^2 (\boldsymbol{\varepsilon}_I \cdot \boldsymbol{\varepsilon}_S)^2 [n(\omega) + 1] \frac{\hbar q^2 V}{4\pi e^2} \mathrm{Im}\left[\frac{-1}{\varepsilon(\boldsymbol{q}, \omega)}\right], \tag{18}$$

where $\mathrm{Im}[-1/\varepsilon(\boldsymbol{q},\omega)]$ is the dielectric loss function. The dynamical structure factor $S(\boldsymbol{q},\omega)$ associated with density fluctuations satisfies the f-sum rule (Pines 1963), $\int_0^\infty d\omega\, \omega S(\boldsymbol{q}, \omega) = Nq^2/2m$, where N is the number of particles of mass m. In the absence of strong screening by the long-range Coulomb interaction, most of this spectral response is associated with single-particle excitations, which are constrained by energy and crystal momentum conservation to fall in the energy range $0 < \hbar\omega < qv_F$. Such scattering has been observed, for example, in low-carrier-density systems such as n-type GaAs (Klein 1975). However, in high-carrier-density systems, Coulomb screening effects push most of the spectral weight associated with density fluctuations up to the plasma frequency. Consequently, one expects in this case a significant Raman response at ω_p due to plasmon scattering (Cerdeira et al. 1984), but a very weak intraband electronic Raman scattering response.

On the other hand, non-isotropic contributions ($L \neq 0$) to the Raman scattering vertex in eq. (16), which are nonzero in the presence of substantial Fermi surface anisotropy, a multi-sheeted Fermi surface, or interband scattering, are associated with mass fluctuations that do not involve a net change in the charge density. These scattering contributions

are not screened by the long-range Coulomb interaction, and do not satisfy a sum rule in general – consequently, the Raman scattering response associated with $L \neq 0$ mass fluctuations can have a large integrated intensity. In addition to anisotropic contributions to the Raman scattering vertex, Kosztin and Zawadowski (1991) have pointed out that intense intraband electronic Raman scattering in metals requires either impurity scattering, inelastic scattering, or strong electron–electron interactions to take up the momentum in the electronic scattering process between different regions of the Fermi surface. As a result, the $L \neq 0$ Raman scattering response is not limited by momentum considerations to frequencies less than qv_F.

2.5.3. *The collision-dominated scattering response*

Ipatova et al. (1981) first pointed out, in the context of "intervalley" electronic Raman scattering in doped semiconductors such as Ge and Si (Chandrasekhar et al. 1977, Contreras et al. 1985), that the electronic mean free path is often shorter than the optical penetration depth in the presence of strong electronic scattering; i.e., $l < \delta = q^{-1}$. In this case, the intraband electronic Raman scattering cross section is more appropriately described by a "collision-dominated" response (Ipatova et al. 1981, Zawadowski and Cardona 1990),

$$S_L \sim [n(\omega) + 1]\,|\gamma_L|^2 \frac{\omega \Gamma_L}{\omega^2 + \Gamma_L^2}, \tag{19}$$

where $S_L(\omega)$ is the electronic scattering response in channel L, Γ_L is the carrier scattering rate in channel L, and the amplitude factor $|\gamma_L|^2$ is the square of the Raman scattering vertex. Note that this Raman spectral response is quite similar to the Drude optical response, with the exception that the prefactor in the latter is a scalar quantity related to the squared plasma frequency, while the prefactor in eq. (19) is a symmetry-dependent factor related to the effective mass tensor. Therefore, by measuring the intraband Raman scattering response in different scattering geometries, one can isolate the carrier scattering rates associated with different scattering "channels", L (Zawadowski and Cardona 1990). On the other hand, unlike the optical conductivity, there is no sum rule on the intraband Raman scattering response. In addition to electronic scattering in doped semiconductors, the collision-dominated form has been used to describe electronic scattering in the presence of disorder (Zawadowski and Cardona 1990); strong electron–phonon scattering (Itai 1992); and electron–electron correlations in the cuprates (Klein et al. 1989, Cooper and Klein 1990), titanates (Katsufuji and Tokura 1994), manganites (Yoon et al. 1998), and hexaborides (Nyhus et al. 1997).

In the absence of strong electron–electron correlations or inelastic scattering, the carrier scattering rate in eq. (19) is generally taken to be frequency-independent, $\Gamma = 1/\tau + Dq^2$, where τ is the carrier scattering time and D is the diffusion constant (Ipatova et al. 1981, Chandrasekhar et al. 1977, Contreras et al. 1985). However, for strongly correlated systems, the scattering response in eq. (19) can be "extended" to account for correlation effects by using a frequency-dependent scattering rate, $\Gamma \equiv \Gamma(\omega, T)$ in eq. (19), in a

manner analogous to that done in the "extended Drude model" for the optical conductivity of strongly correlated systems (Uchida et al. 1991, Cooper et al. 1993b). For example, an "extended" collision-dominated scattering model has been used to describe the electronic Raman scattering responses of $Sr_xLa_{1-x}TiO_3$ (Katsufuji and Tokura 1994) and EuB_6 (Nyhus et al. 1997), employing eq. (19) and a "Fermi-liquid" scattering rate given by $\Gamma(\omega, T) = \Gamma_0(T) + \alpha\omega^2$, as well as the electronic Raman scattering response of the cuprates, which has been commonly described using eq. (19) with a scattering rate given by the Marginal Fermi Liquid (MFL) form, $\Gamma(\omega, T) = \alpha\sqrt{\omega^2 + \beta^2 T^2}$ (Klein et al. 1989, Cooper and Klein 1990).

3. Raman scattering in the antiferromagnetic insulator phase

It is now well known that in the insulating phase, high-T_c cuprates are spin $S = \frac{1}{2}$ antiferromagnetic charge-transfer insulators ($T_N \approx 300$ K) with the spins localized primarily on the Cu^{2+} ions, and with a superexchange interaction between spins of roughly $J \approx 120$ meV. A number of interesting excitations have been observed by Raman scattering in this phase, including two-spin excitations (Lyons et al. 1988a,b), "chiral" spin fluctuations (Shastry and Shraiman 1990, 1991, Khveshchenko and Wiegmann 1994, Sulewski et al. 1991), excitonic excitations (Liu et al. 1993a,b, Salamon et al. 1995), and crystal-field transitions associated with the lanthanide ions (Heyen et al. 1991, Ruf et al. 1992, Dufour et al. 1995, Sanjurjo et al. 1995, Jandl et al. 1995). These excitations are considered in greater detail in the following.

3.1. *Two-magnon scattering*

3.1.1. *Overview*

Raman scattering studies of the antiferromagnetic insulating cuprates have primarily focussed on two-magnon scattering, which arises when incident photons excite two magnons of opposing momenta, $\boldsymbol{q}$ and $-\boldsymbol{q}$. Much of the basic theory of two-magnon scattering evolved from attempts to understand Raman scattering measurements of "conventional" antiferromagnets such as K_2NiF_4 [$S = 1$] and MnF_2 [$S = \frac{5}{2}$] (Fleury and Loudon 1968, Fleury and Guggenheim 1970) (see fig. 3). The two-magnon scattering process occurs in three steps (see fig. 6), including electric dipole transitions in the initial and final steps and a double spin-flip in the intermediate step, and is described by the Hamiltonian (Parkinson 1969)

$$H_R = \sum_{ij} \left(\boldsymbol{E}_I \cdot \boldsymbol{\sigma}_{ij}\right)\left(\boldsymbol{E}_S \cdot \boldsymbol{\sigma}_{ij}\right) \boldsymbol{S}_i \cdot \boldsymbol{S}_j, \tag{20}$$

where $\boldsymbol{E}_I$ and $\boldsymbol{E}_S$ are the incident and scattered electric fields, respectively, $\boldsymbol{\sigma}_{ij}$ is a unit vector connecting sites i and j, and $\boldsymbol{S}$ is the spin operator. In the absence of anisotropy and magnon–magnon interaction effects, the zero-temperature magnon energy in a 2D Heisenberg antiferromagnet is given by

$$E_k^2 = (SJZ)^2 \left[1 - \tfrac{1}{4}\left(\cos(k_x a) + \cos(k_y a)\right)\right], \tag{21}$$

where $Z\,(=4)$ is the number of nearest neighbors, S is the spin, and J is the exchange interaction constant. As two-magnon Raman scattering is dominated by short-wavelength

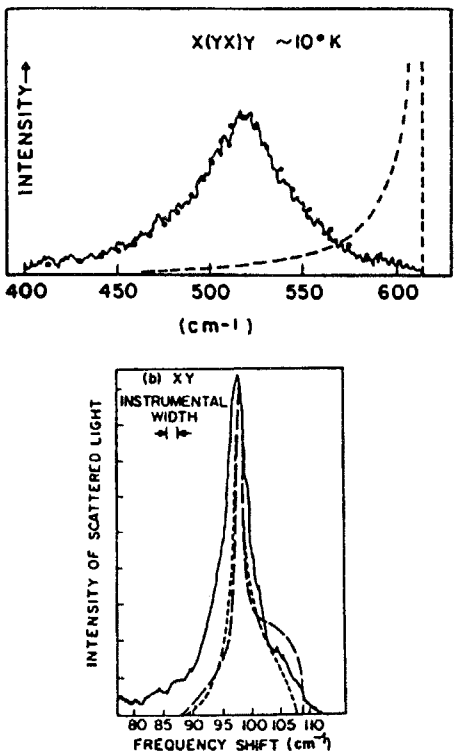

Fig. 3. (top) Two-magnon Raman scattering response of the spin-1 antiferromagnet K_2NiF_4 (after Fleury and Guggenheim 1970), and (bottom) two-magnon scattering from the spin-5/2 antiferromagnet MnF_2 (after Fleury and Loudon 1968).

spin excitations near the zone boundary where the density of states is large, the peak in the two-magnon scattering response of the spin-$\frac{1}{2}$ cuprates is predicted by eq. (21) to be $\hbar\omega_0 = 2SJZ = 4J$. However, magnon–magnon interaction effects are expected to reduce the energy of the two-magnon scattering peak by roughly $2JS$ (Parkinson 1969, Lyons et al. 1988b), resulting in a two-magnon energy of $\hbar\omega_0 = 3J$. A more precise accounting of the two-magnon scattering response using linear spin-wave theory gives a two-magnon peak energy at $\hbar\omega_0 = 2.7J$ for spin-$\frac{1}{2}$ antiferromagnets (Elliot et al. 1968, Elliot and Thorpe 1969, Parkinson 1969). Notably, for spin interactions involving only nearest-neighbor spins, spin-$\frac{1}{2}$ antiferromagnets with D_{4h} symmetry are predicted by eq. (20) to have two-magnon Raman scattering intensity only in the B_{1g} scattering geometry.

In the insulating cuprates, strong two-magnon scattering has indeed been observed in the B_{1g} geometries of La_2CuO_4 (Lyons et al. 1988a), $YBa_2Cu_3O_6$ (Lyons et al. 1988b), the T′-phase compounds such as Nd_2CuO_4 and Sm_2CuO_4 (Sulewski et al. 1990, Tokura et al. 1990, Cooper et al. 1990), and $Sr_2CuO_2Cl_2$ (Blumberg et al. 1996), from which exchange parameters of $J = 136$ meV, $J = 117$ meV, $J = 110$ meV, and $J = 130$ meV, respectively, were deduced. However, the observed two-magnon response in the cuprates differs in several important respects from the predictions of the standard approximations of eq. (20). First, in addition to strong B_{1g}-symmetry scattering, weak two-magnon scattering is also

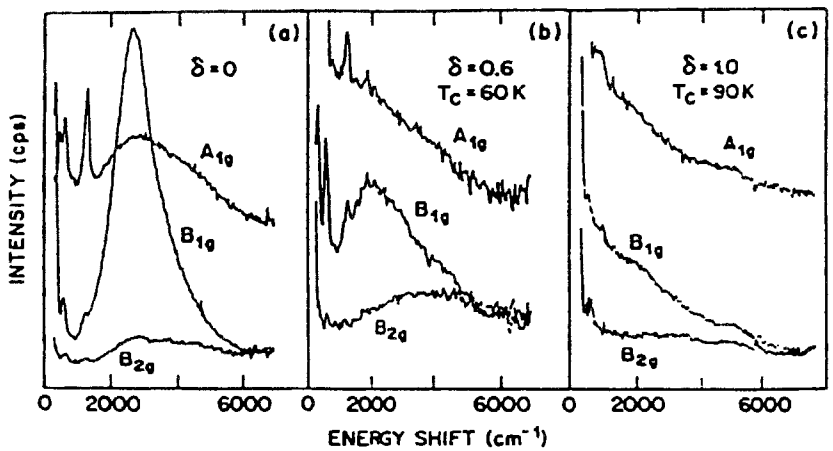

Fig. 4. A_{1g}-, B_{1g}-, and B_{2g}-symmetry room temperature Raman scattering spectra of $YBa_2Cu_3O_{6+\delta}$ in (a) the antiferromagnetic insulating phase ($\delta=0$), (b) the underdoped superconductor phase ($\delta=0$), and (c) the optimally doped superconductor phase ($\delta=1$) (after Lyons et al. 1991).

observed in the A_{1g} and B_{2g} geometries (Singh et al. 1989, Sulewski et al. 1990, Sugai et al. 1990a,b) (see fig. 4). This has been attributed in part to the importance of next-nearest-neighbor and longer-range spin interactions in eq. (20) (Singh et al. 1989). Second, the two-magnon lineshape observed in the insulating cuprates is significantly broader than that observed in spin-1 antiferromagnets such as K_2NiF_4, and is also extremely asymmetric, with a high-energy tail extending far beyond the classical cutoff energy of $4J$. Singh et al. (1989) attributed part of this broadening to quantum fluctuations associated with the small spin ($\frac{1}{2}$) of the cuprates. Multi-magnon processes are likely to be primarily responsible for the high-energy tail of the two-magnon response in the cuprates (Sugai et al. 1990a,b, Rübhausen et al. 1996), although calculations by Canali and Girvin (1992) suggest that the four-magnon intensity may be too weak to contribute a substantial peak near $4J$. Other contributions to the broad, asymmetric two-magnon scattering response of the cuprates have been suggested (Bacci and Gagliano 1991, Haas et al. 1994, Prelovsek and Jaklic 1996, Sandvik et al. 1998), including spin–phonon interactions (Weber and Ford 1989, Nori et al. 1992, 1995, Lee and Min 1996), and hopping disorder (Basu and Singh 1997). In particular, Freitas and Singh (2000) recently proposed that many of the discrepancies between the predictions of the Fleury–Loudon–Elliot theory of two-magnon scattering and the observed two-magnon spectra of the cuprates can be accounted for by considering spin–phonon interaction effects (Lorenzana and Sawatzky 1995a,b); these cause phonons to act as momentum sinks in the two-magnon scattering process, thereby allowing two-magnon states with arbitrary total momentum to contribute to the scattering response.

3.1.2. *Resonance effects*

Studies of the two-magnon spectrum as a function of incident photon energy in $YBa_2Cu_3O_6$ and $Sr_2CuO_2Cl_2$ (Lyons et al. 1988b, Sugai 1989, Yoshida et al. 1992,

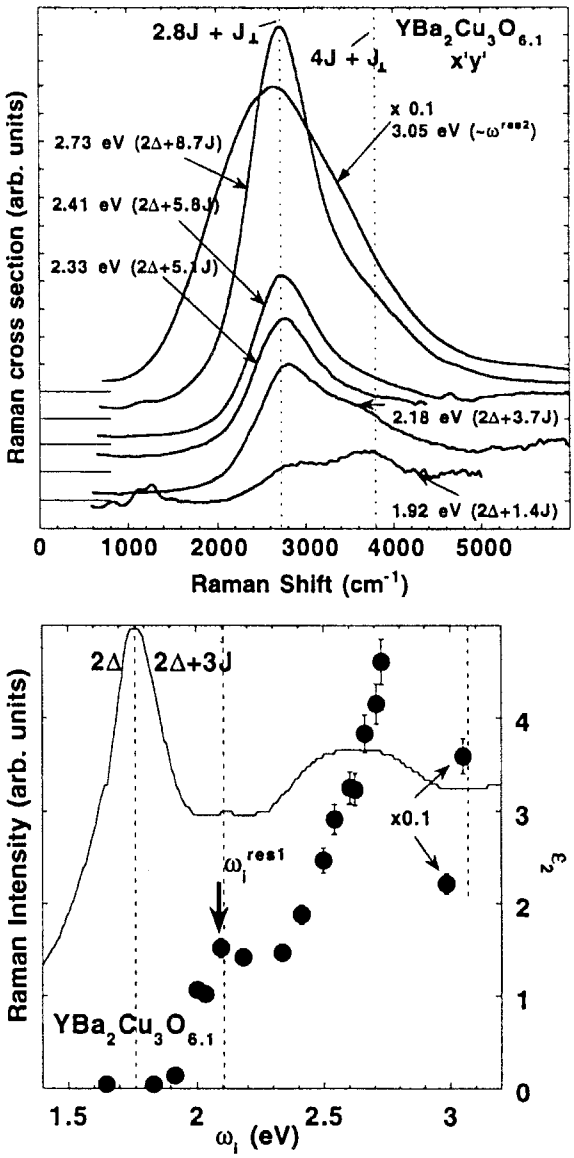

Fig. 5. (top) B_{1g}-symmetry two-magnon Raman scattering cross section in single crystals of $YBa_2Cu_3O_{6.1}$ for different excitations above the charge-transfer gap 2Δ [$=\Delta_{CT}$]. (bottom) Intensity of the B_{1g} two-magnon peak at 2.8 J as a function of excitation energy ω_i. Also shown for comparison is the imaginary part of the dielectric function, ε_2 (after Blumberg et al. 1996).

Cooper et al. 1993b, Liu et al. 1993b, Blumberg et al. 1996) demonstrate that two-magnon scattering is dramatically enhanced when incident photons are at least $2J$–$3J$ above the charge transfer gap energy, Δ_{CT} (see fig. 5). Qualitatively, this behavior is consistent with the specific three-step process responsible for two-magnon scattering in the cuprates (see fig. 6): (i) an incoming photon excites a spin-up $Cu(3d^9)$ hole to an

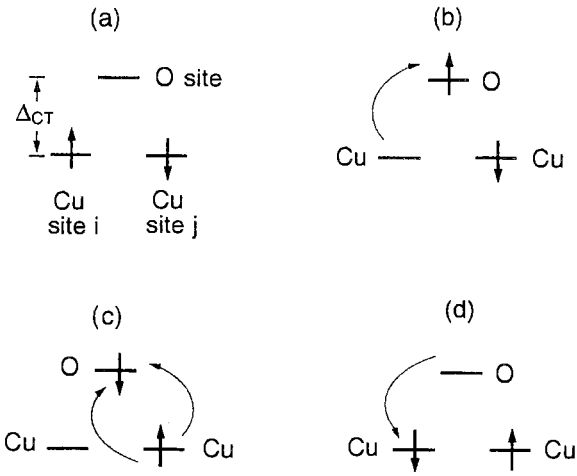

Fig. 6. Diagram of the two-magnon Raman scattering process in the cuprates: (a) initial antiferromagnetic spin configuration on the Cu sites; (b) incident photon excitation of a spin-up Cu($3d^9$) hole to an intermediate-state O(2p) orbital; (c) double spin flip due to direct spin exchange between the spin-up hole on the intermediate-state O(2p) site and a spin-down hole on a nearest-neighbor Cu site; (d) hopping of a spin-down hole from the O(2p) intermediate state to the original copper site, emitting the scattered photon.

intermediate-state O(2p) orbital (fig. 6b), a process which requires photon energies in excess of the charge-transfer gap, Δ_{CT}; (ii) a double spin-flip results from direct spin exchange between the spin-up hole on the intermediate-state O(2p) site and a spin-down hole on a nearest-neighbor Cu site (fig. 6c); (iii) the newly created spin-down hole on the O(2p) intermediate state returns to the original copper site (fig. 6d), emitting a photon. Several recent calculations using a spin-density wave formalism for the half-filled Hubbard model support this picture. In particular, these calculations suggest that the two-magnon resonance behavior in the cuprates is governed by a "triple resonance" condition, which arises from the vanishing of the three energy denominators in the two-magnon Raman scattering cross section associated with the three processes in fig. 6 [i.e., steps (i), (ii) and (iii) above] (Chubukov and Frenkel 1995, Morr and Chubukov 1997, Schönfeld et al. 1997). This "triple resonance" behavior accounts for several significant features observed in $YBa_2Cu_3O_{6.1}$, $Sr_2CuO_2Cl_2$ (Blumberg et al. 1996), and $PrBa_2Cu_3O_7$ (Rübhausen et al. 1996), including: (a) a linear dependence of the inverse scattering intensity on excitation frequency above the charge transfer gap; (b) the appearance of two peaks in the two-magnon response, one at the maximum two-magnon energy, $4J$, and another at roughly $2.8J$ due to magnon–magnon interactions; and (c) the presence of two-magnon scattering intensities in the A_{1g} and B_{1g} geometries.

3.1.3. *Influence of doping*

With increased hole doping, the two-magnon Raman intensity of the cuprates rapidly diminishes in intensity and shifts slightly to lower frequencies (see figs. 4 and 7), behavior generally attributed to spin disordering of the system by the doped carriers (Lyons et al. 1988a,b, 1991, Reznik et al. 1992, Tajima et al. 1993, Blumberg et al. 1994, Rübhausen et al. 1997, 1999). Because the two-magnon scattering process in the cuprates is resonant with the charge-transfer band, the diminution of scattering intensity

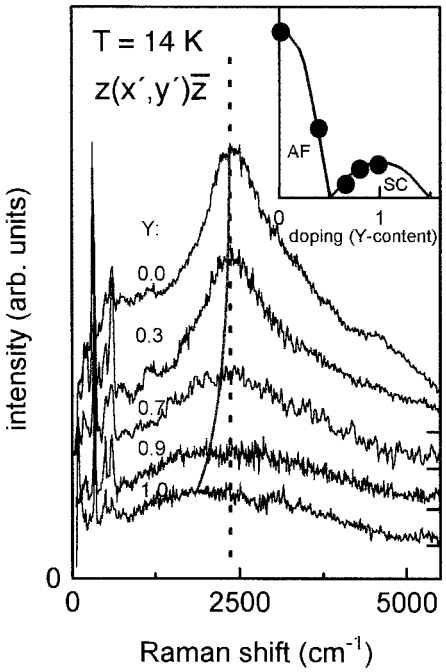

Fig. 7. Doping dependence of the B_{1g} Raman spectra of $Y_{1-x}Pr_xBa_2Cu_{3-y}Al_yO_7$ crystals at $T = 14$ K. The solid line represents the doping-dependent peak position of the two-magnon response (after Rübhausen et al. 1997).

with doping may also be affected by changes in the Raman scattering vertex due to the deleterious effects of doping on the charge-transfer band (Cooper et al. 1993b).

There is some controversy regarding the persistence of two-magnon scattering into the metallic/superconductor phase with increased doping. Early reports by Krol et al. (1989) and Reznik et al. (1992) found that two-magnon scattering disappears in the superconducting phases of $YBa_2Cu_3O_{6+x}$. However, Lyons et al. (1991), and more recently, Blumberg et al. (1994), and Rübhausen et al. (1997, 1999), reported that two-magnon scattering persists well into the metallic phases of $YBa_2Cu_4O_8$, $YBa_2Cu_3O_{6+x}$, $Y_{1-x}Pr_xBa_2Cu_3O_7$, and $Bi_2Sr_2CaCu_2O_8$, suggesting that antiferromagnetic fluctuations with a spatial extent of several lattice constants survive into the underdoped metallic phase (see figs. 4 and 7). A conclusive experimental resolution of this controversy is complicated by the fact that some of these materials are prone to a macroscopic mixing of phases away from optimal doping (Iliev et al. 1993). However, other measurements such as neutron scattering (Hayden et al. 1996) and nuclear magnetic resonance (NMR) (Pennington et al. 1989) have also found that overdamped spin excitations are present in the metallic phase of the cuprates; hence it is reasonable to expect that two-magnon scattering should also be present. Moreover, two-magnon excitations are dominated by short-wavelength spin excitations at the zone boundary that should be rather resilient to doping. Two-magnon scattering was also found to persist well into the metallic phase of the electron-doped system $Nd_{2-x}Ce_xCuO_4$ (Sugai and Hidaka 1991, Tomeno et al. 1991), offering further evidence for the robustness of short-range antiferromagnetic correlations against doping

in the cuprates. Importantly, two-magnon scattering seems to disappear upon doping into the overdoped phase of $Bi_2Sr_2CaCu_2O_8$ (Rübhausen et al. 1999), suggesting that the antiferromagnetic correlation length is less than twice the lattice parameter in the overdoped phase regime.

3.1.4. *Temperature dependence and spin–phonon coupling*

Knoll et al. (1990) studied the temperature dependence of the B_{1g} two-magnon response in $YBa_2Cu_3O_6$ (R = Y, Eu) (see fig. 8), finding a much more dramatic increase in the two-magnon linewidth than can be accounted for by damping due to magnon–magnon scattering or spin diffusion (Brenig and Monien 1992, Kampf and Brenig 1992). These authors consequently argued that spin–phonon scattering is the dominant relaxation mechanism for spin excitations in the insulating cuprates. Nori et al. (1995) further suggested, based on calculations using exact diagonalization and quantum Monte Carlo techniques, that the spin–phonon interaction is responsible not only for the broad, asymmetric lineshape of the two-magnon scattering response, but also for the presence of an A_{1g}-symmetry two-magnon response. The importance of the spin–phonon interaction to spin excitations in the insulating cuprates was also stressed in a slightly different context by Lorenzana and Sawatzky (1995a,b), who argued that sharp absorption peaks observed near 0.35 eV in the optical spectra of several insulating cuprates (Perkins et al. 1993) are actually two-magnon excitations that are infrared-allowed due to weak coupling with an optical phonon. Indeed, from fits to the infrared spectra with their model, Lorenzana and Sawatzky infer values for J comparable to those estimated from two-magnon Raman scattering measurements.

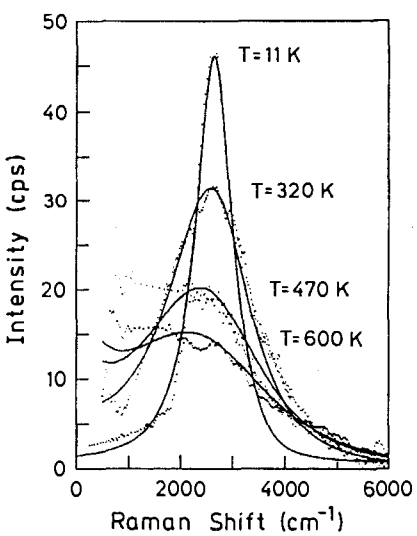

Fig. 8. Temperature dependence of the B_{1g} two-magnon response in $EuBa_2Cu_3O_7$ crystals for temperatures higher than T_N. The solid lines are fits using a model that accounts for spin–phonon interactions (after Knoll et al. 1990).

3.1.5. *Dependence on lattice parameter*

Two-magnon Raman scattering studies as a function of the rare-earth ion (Tokura et al. 1990, Cooper et al. 1990) and pressure (Aronson et al. 1991, Maksimov and Tartakovskii 1994) in the cuprates have shown that J has an anomalously weak dependence on the in-plane CuO spacing, r, $J \sim 1/r^n$ where $n \approx 3$–6, in comparison with the dependence of J on lattice parameter observed in conventional two-dimensional antiferromagnets such as K_2NiF_4 and K_2MnF_4, $J \sim 1/r^{12}$ (Jongh and Block 1975). The implications of this anomalous behavior in the cuprates can be explored by considering the relationship for the exchange interaction J in the two-band Hubbard model, which in the limit $t_{pd} \ll \Delta_{CT}$ is given by (Zhang and Rice 1988)

$$J = 4\frac{t_{pd}^4}{\Delta_{CT}^2}\left(\frac{1}{U_d} + \frac{1}{2\Delta_{CT} + U_p}\right), \tag{22}$$

where Δ_{CT} is the charge-transfer gap, J is the exchange constant, t_{pd} is the CuO hopping energy, and U_d and U_p are the d- and p-band on-site Coulomb interactions, respectively. Thus, the weak dependence of J on the CuO bond length suggests either an unusually small dependence of t_{pd} on r (Aronson et al. 1991), or an effective cancellation of the dependencies of t_{pd} and Δ_{CT} on r (see eq. 22) (Ohta et al. 1991).

3.2. *Chiral spin fluctuations*

In addition to the spin-pair scattering discussed above, it has been suggested that more exotic "topological" excitations such as chiral spin fluctuations should be observable by light scattering in two-dimensional spin-$\frac{1}{2}$ Heisenberg systems like the cuprates (Shastry and Shraiman 1990, 1991, Khveshchenko and Wiegmann 1994). Such *dynamical* fluctuations of spin chirality are expected, and directly observable via Raman scattering, in spite of the fact that the ground-state expectation value of the spin chirality is zero in the insulating Néel state of the cuprates. Raman scattering from chiral spin fluctuations occurs via the scattering Hamiltonian

$$H_R \propto \sum_{ijk} \boldsymbol{S}_i \cdot (\boldsymbol{S}_j \times \boldsymbol{S}_k), \tag{23}$$

which transforms like the completely antisymmetric representation of the crystal's space group; i.e., A_{2g} $[=xy(x^2-y^2)]$ in the D_{4h}-symmetry cuprates. Sulewski et al. (1991) first reported the observation of chiral spin fluctuations in the antiferromagnetic insulators, Gd_2CuO_4 and Pr_2CuO_4 (see fig. 9). In addition to exhibiting the proper A_{2g} symmetry, the scattering observed by Sulewski et al. has a peak energy near $5J$, which compares well with the chiral spin fluctuation energy estimated from spin-wave calculations.

Interestingly, it has also been proposed that chiral fluctuations are responsible for the anomalous normal-state properties of the metallic cuprates (Wen et al. 1989, Y. Chen et al. 1989, Nagaosa and Lee 1990, 1991); in particular, Nagaosa and Lee (1991) predicted the

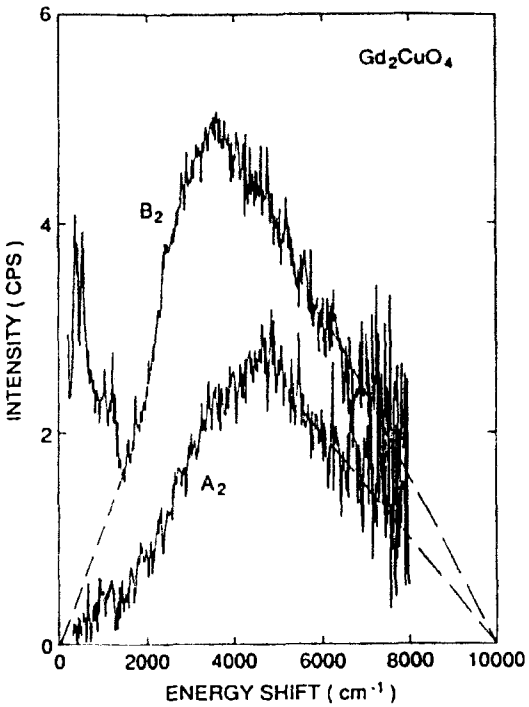

Fig. 9. Broad A_{2g} symmetry scattering in the antiferromagnetic insulator Gd_2CuO_4 attributed to chiral spin fluctuations (after Sulewski et al. 1991).

development of a quasielastic Raman response [$\mathrm{Im}\,\chi(\omega) = A\omega\Gamma/(\omega^2 + \Gamma^2)$], associated with closed-loop charge hopping in the Néel state, upon doping the antiferromagnetic insulating phase of the cuprates. Such a quasielastic response should also be distinguished by its appearance in the distinctive A_{2g} (in the D_{4h}-symmetry cuprates) scattering geometry. However, while evidence for such a quasielastic response has been observed in other doped antiferromagnetic oxides (Yoon et al. 2000), there is as yet no Raman scattering evidence for chiral spin fluctuations in the metallic phase of the cuprates.

3.3. *Excitonic scattering*

Large-energy-shift Raman scattering in the insulating phase of the cuprates also reveals sharp electric-dipole-forbidden electronic transitions with A_{2g}, B_{1g}, and A_{1g} symmetries roughly 0.2 eV below the 1.7 eV charge-transfer gap (Liu et al. 1993a, Salamon et al. 1995, 1996) (see fig. 10). These high-energy excitations have been variously attributed to excitations involving bound electron–hole pairs stabilized by topological "hedgehog"-type spin excitations (Khveshchenko and Wiegmann 1994), intrasite d^9–d^9 excitations (Liu et al. 1993a,b), and excitonic d^9–$d^{10}\underline{L}$ excitations involving a hole transition from the Cu $d_{x^2-y^2}$ state to a linear combination of Cu d_{xy} and nearest-neighbor O p_π orbitals (Salamon et al. 1995, Simon et al. 1996). The latter interpretation in particular appears to

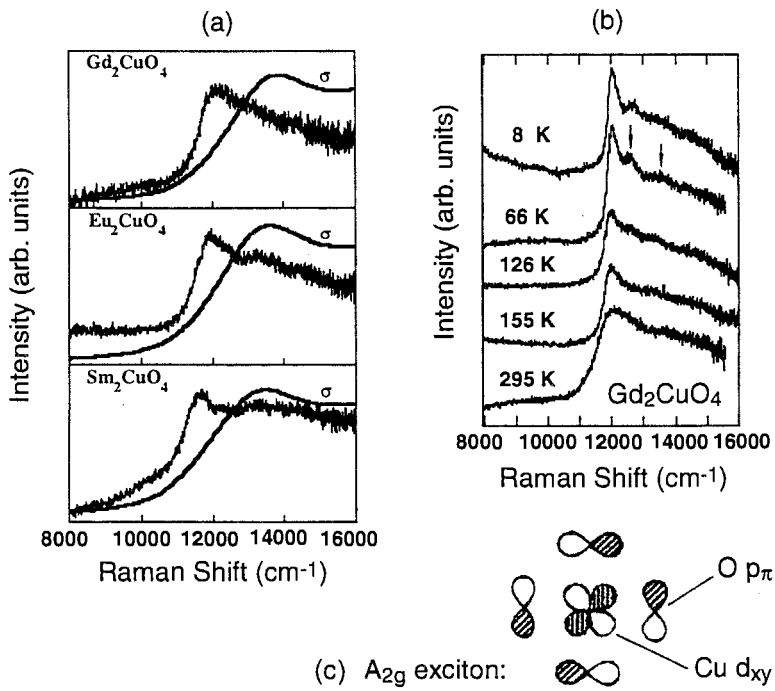

Fig. 10. Large-energy-shift Raman spectra in the antiferromagnetic insulators R_2CuO_4 (R = Gd, Eu, Sm): (a) A_{2g}-symmetry exciton peak roughly 0.2 eV below the charge-transfer absorption edge (σ) of several R_2CuO_4 insulators. (b) Temperature dependence of the A_{2g} exciton in Gd_2CuO_4, illustrating the sharpening of the main exciton peak, and the development of two side bands (see arrows). (c) Diagram of A_{2g} exciton involving hybridized Cu d_{xy}–O p_π states (after Salamon et al. 1995).

provide the best explanation for the A_{2g}-symmetry Raman excitation, as it is consistent with the observed scaling of the A_{2g} energy with Cu–O bond distance (Salamon et al. 1995), with estimates of d_{xy}–p_π exciton energies using an expanded Hubbard model involving six bands (Simon et al. 1996), and with the results of recent X-ray Raman scattering measurements of $Sr_2CuO_2Cl_2$ (Kuiper et al. 1998). The calculations of Simon et al. (1996) further suggest that the A_{1g}, E_{1g}-symmetry Raman excitations, as well as the E_u-symmetry absorption peak (Falck et al. 1992, Perkins et al. 1993), are attributable to the charge-transfer d–p excitations anticipated by the standard three-band Hubbard model.

At low temperatures, the A_{2g}-symmetry excitonic peak in many insulating cuprates sharpens dramatically, revealing two sidebands that are roughly 600 cm^{-1} (75 meV) and 1500 cm^{-1} (188 meV) higher in energy than the main 1.5 eV peak (see fig. 10). Based upon the proximity of these energy shifts to a 600 cm^{-1} in-plane O mode and the exchange energy, J, respectively, these sidebands were attributed to exciton + phonon and exciton + magnon scattering (Salamon et al. 1995). Similar sidebands on the high-energy side of two-magnon excitations in La_2CuO_4 were also observed in infrared

absorption measurements (Perkins et al. 1993), and similarly attributed to bimagnon+phonon emission (Lorenzana and Sawatzky 1995a,b).

3.4. *Crystal-field excitations*

Transitions between crystal-field-split f-electron multiplet levels of various trivalent lanthanide ions (R) have also been observed by Raman scattering in the insulating phase of high-T_c cuprates (Heyen et al. 1991, Ruf et al. 1992, Dufour et al. 1995, Sanjurjo et al. 1995, Jandl et al. 1995, Cardona 1999), particularly those containing Nd^{3+} ($^4I_{9/2}$), Pr^{3+} ($^3H_4$), and Sm^{3+} ($^6H_{5/2}$) ions. These studies have revealed both 'pure' crystal-field excitations in R_2CuO_4 systems, as well as crystal-field excitations in $RBa_2Cu_3O_6$ systems that derive their Raman intensities from a strong magneto-elastic coupling with phonons. For a more detailed discussion of these studies, the reader is referred to the recent review article by Cardona (1999).

4. Raman scattering in the "normal" metallic phase

4.1. *ab-plane electronic scattering in the optimally doped and overdoped regimes*

One of the most remarkable features of the Raman scattering spectra of high-T_c cuprates in the "normal" metallic phase is the presence of a broad, flat scattering "continuum" of electronic Raman scattering that extends from zero energy to energies as large as 1 eV (see fig. 11). This normal-state continuum was probably first observed in $YBa_2Cu_3O_7$ films (Bozovic et al. 1987) and polycrystals (Lyons et al. 1987, Bazhenov et al. 1987), then later in single crystals of $YBa_2Cu_3O_7$ (Cooper et al. 1988a, Thomsen et al. 1988, Sugai et al. 1988, X.K. Chen et al. 1993), $La_{2-x}Sr_xCuO_4$ (Katsufuji et al. 1993, X.K. Chen et al. 1994a), $Bi_2Sr_2CaCu_2O_8$ (Slakey et al. 1990a, Staufer et al. 1992, Kendziora and Rosenberg 1995), $Tl_2Ba_2Ca_2Cu_3O_{10}$ (Krantz et al. 1989, Hoffmann et al. 1994), and $Tl_2Ba_2CuO_6$ (Kang et al. 1996, Gasparov et al. 1997). Single-crystal studies of $YBa_2Cu_3O_7$ also revealed a strong coupling between the electronic Raman continuum and certain optical phonons, manifested as strong Fano phonon lineshapes (Cooper et al. 1988a, Thomsen et al. 1988). While the Raman continuum has generally been assumed to be of import to the unconventional normal-state properties of the cuprates (Varma et al. 1989, Cooper and Klein 1990, Virosztek and Ruvalds 1991, 1992), the origin of this scattering is still uncertain, and has been attributed variously to strong electron–electron scattering in the presence of Fermi surface nesting (Virosztek and Ruvalds 1991, 1992), strongly correlated, incoherent electronic scattering associated with a Mott–Hubbard system (Shastry and Shraiman 1990), electronic scattering from spin fluctuations (Branch and Carbotte 1995), the effects of inelastic and interband electronic scattering (Rashkeev and Wendin 1993), mass fluctuations between different parts of the cuprates' complex Fermi surface (Krantz and Cardona 1995), and chiral fluctuations in the normal state (Nagaosa and Lee 1990, 1991).

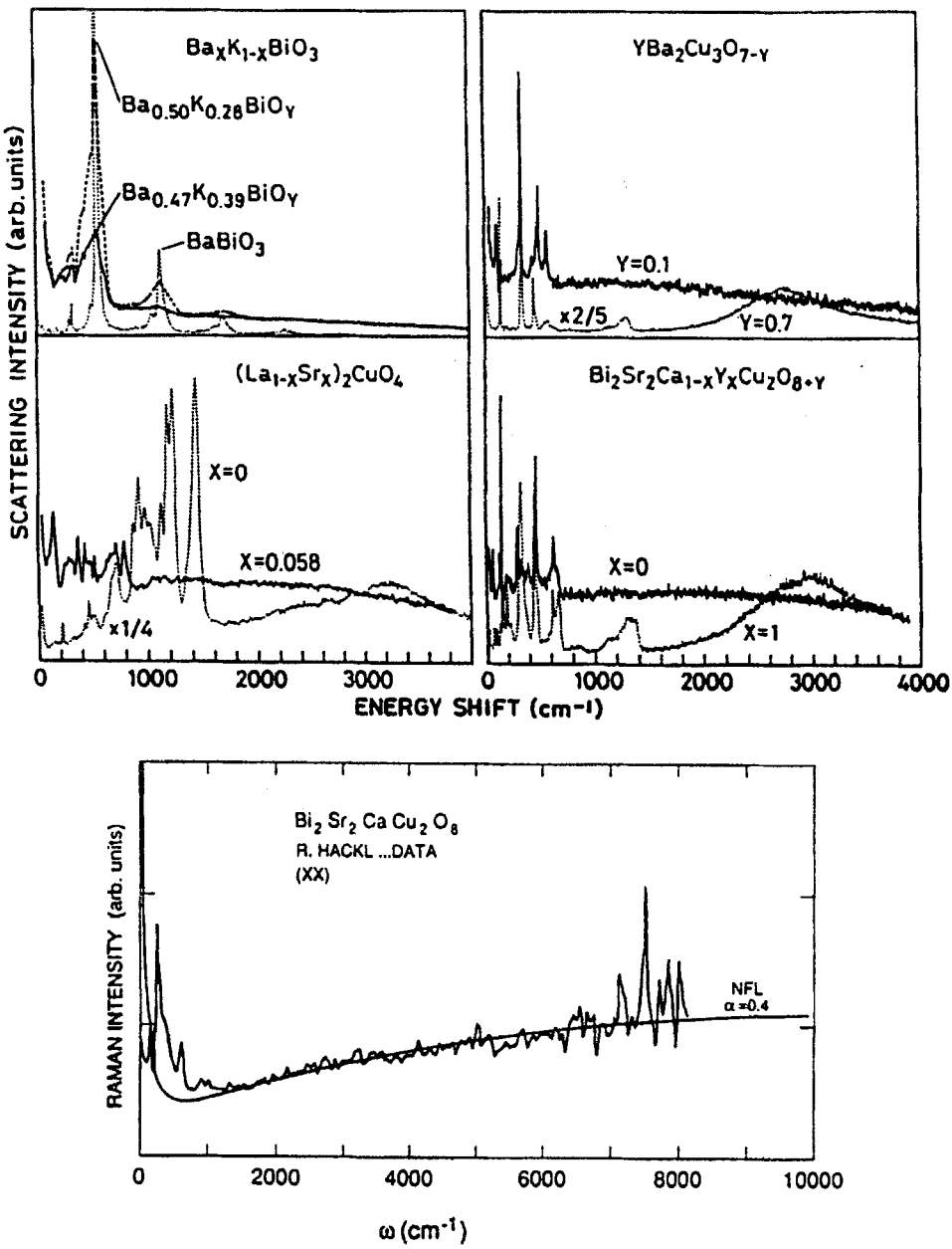

Fig. 11. (top) Broad, normal-state Raman continua in various oxide materials at room temperature (after Sugai et al. 1989). (bottom) Room-temperature Raman continuum in $Bi_2Sr_2CaCu_2O_8$ fit to a response involving the marginal and nested Fermi liquid scattering rate form (see eq. 26) (after Virosztek and Ruvalds 1992).

In the absence of a specific microscopic picture, the observed normal-state Raman continua of the cuprates have generally been modeled with a "collision-dominated" scattering response (see sect. 2.5.3), and associated with overdamped fluctuations in the strongly correlated normal-state fluid (Klein et al. 1989, Cooper and Klein 1990, Slakey et al. 1991),

$$\frac{\mathrm{d}^2\sigma}{\mathrm{d}\Omega\,\mathrm{d}\omega} \sim [n(\omega)+1]\,\frac{A\omega\Gamma}{\omega^2+\Gamma^2}, \tag{24}$$

where A is a scattering amplitude and $\Gamma = 1/\tau$ is the scattering rate. To adequately describe the flat scattering response of the "continuum" in the cuprates, the response function in eq. (24) suggests a scattering rate of the form (Klein et al. 1989, Cooper and Klein 1990, Virosztek and Ruvalds 1991, 1992)

$$\Gamma(\omega, T) = \alpha\sqrt{\omega^2+\beta^2T^2} \qquad [\hbar = k_B = 1]. \tag{25}$$

Note that eq. (25) is simply the phenomenological normal-state electronic scattering rate proposed by Varma et al. (1989) for "marginal" Fermi liquids (MFL), which has also been shown to arise from electron–electron scattering on a nested Fermi surface (Virosztek and Ruvalds 1991, 1992) and spin-fluctuation scattering (Moriya et al. 1990, Sokol and Pines 1993). As shown in the bottom panel of fig. 11, the phenomenological expression in eq. (24), combined with the MFL scattering rate in eq. (25), fits the normal-state continuum in $Bi_2Sr_2CaCu_2O_8$ over a wide frequency range. Furthermore, the A_{1g}-symmetry Raman continuum has been found to exhibit a MFL-like temperature dependence (Slakey et al. 1991, Reznik et al. 1993), suggesting that the "continuum" in this symmetry is associated with scattering from conduction electrons. On the other hand, the temperature dependence of the B_{1g}-symmetry continuum deviates from the MFL form (Reznik et al. 1993), possibly indicating that processes not associated with the conduction electrons contribute to the scattering response in this symmetry (see sect. 5.3.1 and X.K. Chen et al. 1993).

Additional evidence that the Raman continuum in the cuprates is associated with scattering from the conduction electrons, at least in the A_{1g} and B_{2g} symmetries, is suggested by the reasonably close connection between scattering rates extracted from the measured continuum response using eqs. (24) and (25), and transport scattering rates. For example, fits to the Raman scattering data of $YBa_2Cu_3O_{6+x}$ and $Bi_2Sr_2CaCu_2O_8$ using eq. (24) and a scattering rate form only slightly modified from eq. (25) (Hackl et al. 1996, Opel et al. 2000) show that the B_{2g}-continuum scattering rate compares well to the scattering rate estimated from transport measurements, both as a function of temperature and doping. By contrast, the scattering rates extracted from fits to the B_{1g}-symmetry continuum are in substantial excess of the transport scattering rate deduced from infrared (Tanner and Timusk 1992, Orenstein et al. 1990) and transport measurements. This suggests that transport lifetimes, at least in $Bi_2Sr_2CaCu_2O_8$, are dominated by scattering processes near the $(\boldsymbol{k}_x,\boldsymbol{k}_y)=(\pm\pi/a, \pm\pi/a)$ [i.e., B_{2g}] parts of the Fermi surface, while

scattering processes near the $(\boldsymbol{k}_x,\boldsymbol{k}_y)=\{(0,\pm\pi/a),(\pm\pi/a,0)\}$ points [i.e., B_{1g}] are short-lived and do not significantly influence transport lifetimes. Interestingly, however, Raman measurements of the B_{1g} scattering rate in overdoped $La_{2-x}Sr_xCuO_4$ by Naeini et al. (1998) not only imply that this contribution to the scattering rate is important to the transport properties, but also indicate that the temperature dependence of the B_{1g} scattering rate is more consistent with a nearly antiferromagnetic Fermi liquid (NAFL) model (Pines 1997) than the MFL picture. This is consistent with other measurements indicating a cross-over to more conventional Fermi-liquid behavior in the overdoped regime (see fig. 1) (Batlogg et al. 1994).

A fundamental question regarding the normal-state continuum in the cuprates concerns the nature of the Raman scattering vertex (i.e., γ in eqs. 15 and 19) associated with this process. Krantz et al. (1995) and Krantz and Cardona (1995) provided perhaps the best evidence that the normal-state continuum in the cuprates is attributable to mass fluctuations between different parts of the complex cuprate Fermi surface (see discussion in sect. 2.5.2). They calculated the electronic Raman scattering efficiency for $YBa_2Cu_3O_7$ in the "collision-dominated" regime, using a modification of the squared Raman scattering vertex in eq. (19) given by

$$|\gamma|^2 \sim \frac{r_0^2}{\pi} N(0) \left\langle \left| \boldsymbol{\varepsilon}_I \cdot \left(\boldsymbol{\mu}^{-1} - \langle \boldsymbol{\mu}^{-1} \rangle \right) \cdot \boldsymbol{\varepsilon}_S \right|^2 \right\rangle , \tag{26}$$

where $N(0)$ is the one-electron density of states at the Fermi level, and where one-electron band structure calculations (Andersen et al. 1991, 1994) were used as the basis for determining the effective mass tensor, $\boldsymbol{\mu}$. Significantly, these calculations appear to reproduce the relative intensities of the electronic continuum in different scattering geometries (see fig. 12), although the calculated absolute magnitudes are roughly an order of magnitude too large (Krantz et al. 1995, Krantz and Cardona 1995).

Perhaps the most important question related to the broad Raman continuum in the cuprates, however, concerns its relevance to the unusual normal- and superconducting-state properties of the cuprates. It is worth noting in this regard that broad, flat electronic scattering continua are not unique to the cuprates, and indeed have been observed in such diverse materials as $Ba_xK_{1-x}BiO_3$ (Sugai et al. 1989) (see fig. 11), $Sr_xLa_{1-x}TiO_3$ (Katsufuji and Tokura 1994), EuB_6 (Nyhus et al. 1997), $A_{1-x}A'_xMnO_3$ (Yoon et al. 1998), and $La_{0.5}Sr_{0.5}CoO_3$ and $Ca_{0.5}Sr_{0.5}RuO_3$ (Bozovic et al. 1994). The ubiquity of electronic Raman continua in strongly correlated materials supports the argument that such scattering should arise rather generally in materials with both a complex Fermi surface and strong electronic scattering (see discussion in sect. 2.5.2). Moreover, the prevalence of electronic Raman continua in strongly correlated materials raises obvious questions concerning the significance of this response to the distinctive normal-state properties of the high-T_c superconductors. However, Leggett (1998) recently suggested that it is not the mere presence of a strong mid-infrared dielectric response, but rather the unique *interplay* between this response and the low dimensionality of the cuprates that contributes to high-T_c superconductivity. Therefore, the importance of the broad normal-

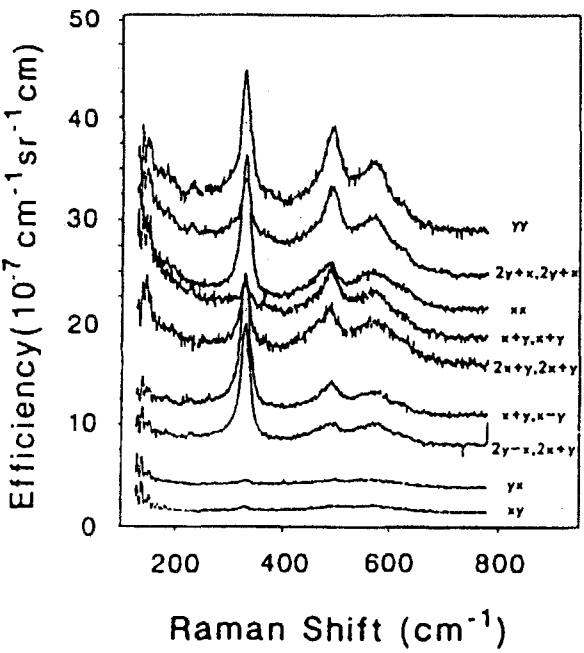

Fig. 12. 300 K Raman spectra of a $YBa_2Cu_3O_7$ single crystal in different polarizations. The spectra have consecutive offsets of $(0, 1, 2, \ldots, 8) \times 2.5$ (after Krantz et al. 1995).

state Raman continua in the cuprates to high-T_c superconductivity remains unresolved (see also sect. 5.3.5).

4.2. *c-axis electronic scattering*

In addition to their remarkable *ab*-plane properties, the high-T_c cuprates are among the most anisotropic material systems known, exhibiting resistivity ratios in the range $\rho_c/\rho_{ab} \approx 10^2$–$10^5$ (Cooper and Gray 1994). By comparison, the layered dichalcogenide superconductors $2H$-$NbSe_2$, $4Hb$-TaS_2, and $2H$-NbS_2 have resistivity anisotropies of $\rho_c/\rho_{ab} \approx 10^1$–$10^3$. The large anisotropy of the layered cuprates manifests itself in a number of normal- and superconducting-state properties, including the temperature-dependent resistivity (Ito et al. 1991), which is metallic in the *ab*-plane but often exhibits a "semiconducting-like" temperature dependence in the *c*-direction, and the optical conductivity (Uchida et al. 1991, Cooper et al. 1993a,b). These properties provide strong evidence that *c*-axis transport in the under- and optimally doped high-T_c cuprates is incoherent.

c-axis polarized $[(\boldsymbol{\varepsilon}_I, \boldsymbol{\varepsilon}_S) = (z,z)]$ electronic scattering has been reported in $YBa_2Cu_3O_{6+x}$ (Reznik et al., 1992, Cooper et al. 1993a,b, Nyhus et al. 1994), $TlBa_2CaCu_2O_7$ (Mihailovic et al. 1993), $Tl_2Ba_2CaCu_2O_8$ (Mihailovic et al. 1993), and $Bi_2Sr_2CaCu_2O_8$ (Liu et al. 1999). In $YBa_2Cu_3O_{6+x}$, for example, *c*-axis electronic scattering is characterized by a collision-dominated scattering response, $\mathrm{Im}\,\chi(\omega) = A\omega\Gamma/(\omega^2 + \Gamma^2)$, with a constant scattering rate $\Gamma = 1/\tau \approx 600\,\mathrm{cm}^{-1}$, and an intensity that increases roughly

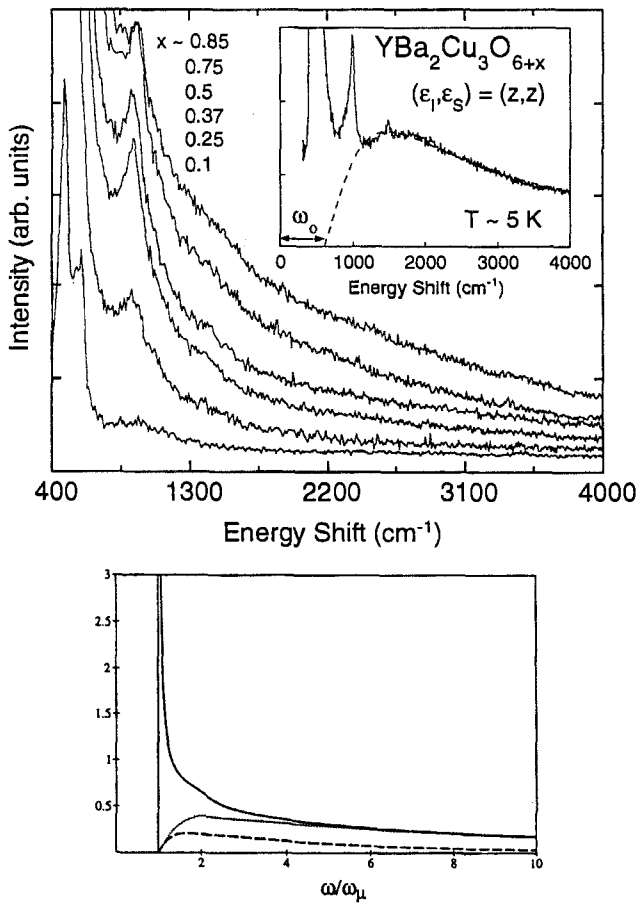

Fig. 13. (top) Room-temperature, c-axis polarized $[(\varepsilon_I, \varepsilon_S)=(z,z)]$ electronic scattering in $YBa_2Cu_3O_{6+x}$ as a function of doping (x); (inset) The $T=5$ K c-axis Raman spectrum of $YBa_2Cu_3O_{6.93}$, with a fit to a collision-dominated response function that has been shifted by the 500 cm^{-1} apical O(4) phonon energy (after Nyhus et al. 1994). (bottom) Calculated Raman spectrum of a single Einstein phonon coupled to a background continuum [dashed lines] (after Itai 1992).

linearly with carrier density (Cooper et al. 1993a,b, Nyhus et al. 1994) (see fig. 13). This incoherent c-axis scattering response reflects the fact that the carriers scatter many times in the plane before hopping between planes; i.e., $1/\tau_{ab} \gg 1/\tau_c$.

There is some evidence that phonons may participate in the c-axis continuum scattering response of $YBa_2Cu_3O_{6+x}$, via an "activated hopping" process (Nyhus et al. 1994). For example, the c-axis electronic scattering response in $YBa_2Cu_3O_{6+x}$ "turns on" for energies greater than the 500 cm^{-1} apical O(4) phonon frequency (see fig. 13), suggesting that this phonon is necessary for momentum conservation in the interlayer scattering process. Indeed, the process of Raman scattering from electron–hole pairs

with the emission of a phonon (bottom, fig. 13) has in fact been calculated by Itai (1992), and the results of these calculations describe the observed c-axis continuum response in $YBa_2Cu_3O_{6+x}$ well. Consequently, these results suggest the interesting possibility is that the strong c-axis electronic continuum in $YBa_2Cu_3O_{6+x}$ (and perhaps the Tl-based cuprates) betrays a transport mechanism in which c-axis phonons assist the hopping of carriers between the CuO layers. This would likely result from a dynamic modulation of the $O(4)p_z$–$Cu(1,2)d_{3z^2-1}$ overlap integral by the $500\,cm^{-1}$ apical O(4) optical phonon, which consequently modulates the interbilayer hopping rate in $YBa_2Cu_3O_{6+x}$. The sensitivity of interlayer coupling in both $La_{2-x}Sr_xCuO_4$ and $YBa_2Cu_3O_{6+x}$ to the hybridization between the apical O(4) p_z orbital and the in-plane Cu states is supported by X-ray absorption measurements of C.T. Chen et al. (1992) and resonance Raman scattering experiments of Heyen et al. (1990, 1992), and is a direct consequence of the weak interlayer hopping rates in the cuprates. Importantly, phonon-assisted c-axis hopping has been proposed as a possible contribution to the "semiconductor-like" c-axis resistivities observed in many of the cuprates (Kumar and Jayannavar 1992, Nyhus et al. 1994, Rojo and Levin 1993, Zha et al. 1996). However, a more recent Raman study and analysis of the c-axis electronic continuum in $YBa_2Cu_3O_8$ suggests that the c-axis Raman continua in Y-based cuprates are not strongly influenced by the presence of the CuO chains (and hence may not be directly related to c-axis transport) or by phonon scattering (Quilty et al. 2001). The exact origin of the c-axis continua in the cuprates, therefore, remains uncertain.

Interestingly, Wu and Carbotte (1997) have calculated the c-axis electronic Raman scattering response for a plane–chain bilayer coupled via single-particle tunneling, including both intraband and interband contributions. These results predict that interband scattering provides the dominant c-axis Raman scattering response in the limit of small plane–chain coupling, although intraband and interband scattering contributions are not well separated due to Coulomb screening. These calculations also suggest that "pseudogap" development, which in this model is associated with the splitting between plane and chain bands, should be observable in the c-axis Raman scattering spectrum as well as the c-axis optical conductivity (Homes et al. 1993). Interestingly, Quilty et al. (2001) recently observed a subtle depletion of spectral weight with decreasing temperature in the normal-state c-axis Raman continua of both $YBa_2Cu_3O_8$ and underdoped $YBa_2Cu_3O_{6+x}$ ($T_c \approx 80\,K$), which they attributed to pseudogap development. However, as the origin of the c-axis Raman continuum remains uncertain, the mechanism by which it is affected by pseudogap formation is not clear.

4.3. *Raman scattering in the underdoped cuprates*

The underdoped regime of the high-T_c cuprates is currently perhaps the most poorly understood and interesting phase regime. This phase is thought to be characterized by at least two cross-over temperatures (see fig. 1) (Batlogg and Emery 1996, Emery, Kivelson and Zachar 1997): (1) a temperature, T_1^*, below which charge inhomogeneities (stripes) and short-range antiferromagnetic correlations may be present in the CuO_2 planes; and

(2) a cross-over temperature, T_2^*, below which "pseudogap" behavior is observed (Rossat-Mignod et al. 1991, Warren et al. 1989, Walstedt et al. 1990, Loeser et al. 1996, Ding et al. 1996, Marshall et al. 1996) and pairing correlations may occur above T_c. Raman scattering studies of the underdoped phase of the cuprates have focused primarily on several related issues: (a) the possible persistence of antiferromagnetic correlations into the metallic phase; (b) evidence for pseudogap development in the Raman scattering spectra, and the relationship of this pseudogap to the superconducting and antiferromagnetic phases; and (c) evidence for normal-state pairing of quasiparticles above T_c.

4.3.1. *Presence of antiferromagnetic correlations*

As discussed in greater detail in sect. 3.1.3, there is some evidence (Lyons et al. 1991, Blumberg et al. 1994, Rübhausen et al. 1997, 1999) for the persistence of two-magnon Raman scattering in metallic $YBa_2Cu_3O_{6+x}$ (for $0.3 < x < 0.7$), $YBa_2Cu_4O_8$, $Y_{1-x}Pr_xBa_2Cu_3O_7$, and $Bi_2Sr_2CaCu_2O_8$, suggesting that antiferromagnetic fluctuations with a spatial extent of several lattice constants are present well into the underdoped phase of the cuprates. Moreover, Rübhausen et al. (1997, 1998) have reported that overdamped two-magnon excitations in the metallic phase of underdoped and optimally doped $Y_{1-x}Pr_xBa_2Cu_3O_7$ and $Bi_2Sr_2CaCu_2O_8$ are influenced by superconductivity, suggesting a coupling between the itinerant electronic states in the metallic phase and the remnant short-wavelength spin degrees of freedom. Note, however, that two-magnon scattering has been observed to disappear upon further doping into the overdoped phase of $Bi_2Sr_2CaCu_2O_8$ (Rübhausen et al. 1999), suggesting that antiferromagnetic correlations are less than twice the lattice parameter in this phase regime; the authors suggest that this behavior reflects a change in character from a doped antiferromagnetic phase (Dagotto 1994, Plakida et al. 1997) in the underdoped regime of the cuprates, to an antiferromagnetic Fermi liquid phase (Scalapino 1995, Anderson 1997, Pines 1997) in the overdoped regime.

A potentially interesting area of investigation for Raman scattering in the underdoped cuprates concerns the study of ordered charge and spin structures; i.e., "stripes", observed in neutron scattering and electron diffraction measurements of the cuprates (Tranquada et al. 1996) and nickelates (C.H. Chen et al. 1993, Tranquada et al. 1994). While Raman scattering from the charge and spin dynamics of such ordered structures has not yet been reported in the cuprates, Yamamoto et al. (1998) and Blumberg et al. (1998a) recently reported Raman scattering evidence for double-spin excitations associated with striped spin domains below the charge-ordering temperature of $La_{1.67}Sr_{0.33}NiO_4$. These results offer encouragement that studies of the inhomogeneous phases in underdoped cuprates might also be fruitful.

4.3.2. *Evidence for a pseudogap*

The first evidence for a "pseudogap" in the Raman scattering response of the cuprates was actually inferred from the anomalous temperature dependences of Raman- and infrared-active phonons (Litvinchuk et al. 1992). More recently, evidence for a pseudogap has

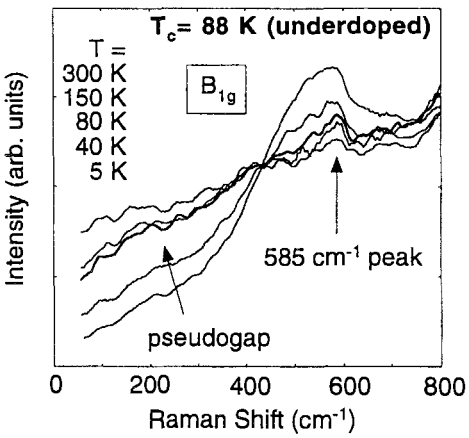

Fig. 14. The B_{1g} symmetry electronic Raman scattering response of underdoped $Bi_2Sr_2CaCu_2O_8$ as a function of temperature, illustrating evidence for pseudogap formation below ~450 cm^{-1}, and the development of a peak at 585 cm^{-1} that is associated with normal-state fermion pair formation (after Blumberg et al. 1998b).

been inferred from measurements of electronic Raman scattering in underdoped cuprates (X.K. Chen et al. 1997, 1998b, Nemetschek et al. 1997, Blumberg et al. 1997b, Quilty et al. 1998, Naeini et al. 1999, Hewitt et al. 1999, Opel et al. 2000), but the results and interpretations of different groups are not yet in agreement on all issues.

On one hand, there appears to be general agreement that underdoping in $YBa_2Cu_3O_{6+x}$ (X.K. Chen et al. 1998b), $La_{2-x}Sr_xCuO_4$ (Naeini et al. 1999), and $Bi_2Sr_2CaCu_2O_8$ (Hewitt et al. 1999) leads to a reduction of electronic scattering strength in the B_{1g} scattering geometry. As the B_{1g}-symmetry Raman vertex function preferentially samples Fermi surface regions $(\boldsymbol{k}_x,\boldsymbol{k}_y)$ near $\{(0,\pm\pi/a),(\pm\pi/a,0)\}$ (see eq. 17 and fig. 2), this reduction of B_{1g} electronic scattering intensity is consistent both with the development of a pseudogap near $(\boldsymbol{k}_x,\boldsymbol{k}_y)=\{(0,\pm\pi/a),(\pm\pi/a,0)\}$, and with angle-resolved photoemission spectroscopy (ARPES), which find that the pseudogap has a $d_{x^2-y^2}$ (B_{1g}) momentum dependence (Ding et al. 1996, Loeser et al. 1996).

There is less uniformity among different groups regarding the temperature dependence of the electronic Raman scattering intensity in the "pseudogap" phase. Nemetschek et al. (1997) inferred the presence of a pseudogap from the temperature-dependent reduction of B_{2g}-symmetry electronic scattering intensity in underdoped $Bi_2Sr_2(Ca_{0.62}Y_{0.38})Cu_2O_8$ and $YBa_2Cu_3O_{6+x}$. Significantly, however, this group did not observe a similar suppression of electronic scattering in the B_{1g} spectrum. This result appears to be at odds with the $d_{x^2-y^2}$-symmetry pseudogap inferred from ARPES measurements (Ding et al. 1996, Loeser et al. 1996), since the B_{2g}-symmetry Raman vertex function preferentially samples Fermi surface regions $(\boldsymbol{k}_x,\boldsymbol{k}_y)$ near $(\pm\pi/a,\pm\pi/a)$ (see eq. 17 and fig. 2) – by contrast, the large gap regions of a $d_{x^2-y^2}$-symmetry pseudogap should manifest themselves primarily in the B_{1g}-symmetry electronic Raman scattering response. X.K. Chen et al. (1997) also saw no evidence for a temperature-dependent reduction in B_{1g}-symmetry scattering that would be expected from the temperature development of a $d_{x^2-y^2}$ pseudogap. On the other hand, Blumberg et al. (1997b, 1998b), Quilty et al. (1998), and Hewitt et al. (1999) observed a temperature-dependent suppression of electronic scattering in the B_{1g}-

symmetry electronic spectrum of $Bi_2Sr_2CaCu_2O_8$ that is consistent with the development of a $d_{x^2-y^2}$ symmetry pseudogap (see fig. 14) below $T^* > T_c$. The disparity among various Raman results in the underdoped phase is puzzling and requires further investigation.

4.3.3. *Evidence for normal-state pairing*

Among the principal explanations for the development of a normal-state "pseudogap" in the underdoped cuprates are (i) the pairing of spinons above T_c (Wen and Lee 1996, Anderson 1987), and (ii) the formation of normal-state fermion pairs (Emery and Kivelson 1995, Ranninger and Robin 1996). The former interpretation appears to be favored by several Raman scattering studies (X.K. Chen et al. 1997, Naeini et al. 1999, Hewitt et al. 1999, Opel et al. 2000) which find the magnitude of the pseudogap to be given by $E_g \approx J \approx 100$ meV, where J is the antiferromagnetic superexchange coupling constant, but which find no evidence for a connection between the pseudogap and superconducting gap.

On the other hand, the latter interpretation does appear to be supported by ARPES measurements (Ding et al. 1996, Loeser et al. 1996), which indicate that the pseudogap (a) has $d_{x^2-y^2}$ symmetry, (b) has a magnitude on the order of the superconducting gap, $E_g \approx \Delta$, and (c) evolves continuously into the superconducting state. Significantly, there are several Raman scattering studies of the underdoped cuprates that have also been cited as evidence for some form of normal-state pairing. For example, Slakey et al. (1990b) observed that a 500 cm^{-1} B_{1g}-symmetry peak normally associated with pair breaking in the optimally doped superconducting phase (see sect. 5.1) persists well above T_c in underdoped $YBa_2Cu_3O_{6+x}$. However, two recent measurements of underdoped $YBa_2Cu_3O_{6+x}$ found no evidence for a B_{1g}-symmetry Raman peak above T_c (Nemetschek et al. 1997, X.K. Chen et al. 1997).

Several groups (Blumberg et al. 1997b, Quilty et al. 1998, Hewitt et al. 1999) have reported that the suppression of low-frequency electronic scattering with decreasing temperature in underdoped $Bi_2Sr_2CaCu_2O_8$, ostensibly due to pseudogap formation, is accompanied by the development of a 585 cm^{-1} (73 meV), B_{1g} ($d_{x^2-y^2}$) symmetry peak above T_c (see fig. 14). Blumberg et al. (1997b) attributed the development of this peak to precursor pairing of doped holes into B_{1g}-symmetry states above T_c. This interpretation is consistent with the model of Emery, Kivelson and Zachar (1997), which predicts that bound fermion pairs in the pseudogap phase of the cuprates should have a Raman-active, charge-0, spin-0 collective excitation with B_{1g} symmetry and an energy, $\sqrt{3}\Delta_s \approx 70$ meV, based upon neutron scattering measurements of the spin gap, Δ_s (= 40 meV, Fong et al. 1995, 1996). However, more recent Raman measurements question this interpretation of the 585 cm^{-1} peak: measurements of the ~585 cm^{-1} B_{1g}-symmetry peak in oxygen-deficient $Bi_2Sr_2CaCu_2O_8$ by Hewitt et al. (1999) demonstrated that it softens by 3.8% upon isotopic substitution of ^{16}O by ^{18}O. Furthermore, these researchers found that this peak is not observed in samples underdoped by Y-substitution, rather than by oxygen-deficiency. Based upon these observations, Hewitt et al. (1999) concluded that

the 585 cm^{-1} B_{1g}-symmetry peak in $Bi_2Sr_2CaCu_2O_8$ is vibrational in origin, probably arising from phonons activated by oxygen defects.

5. Electronic scattering in the superconducting state

5.1. *Overview*

It was first pointed out by Abrikosov and Fal'kovskii (1961) that the superconducting gap should manifest itself in the electronic Raman scattering response as an abrupt onset of scattering intensity at the pair-breaking energy, $\hbar\omega = 2\Delta$. Extensions of this initial calculation of the Raman scattering cross section of a superconductor later included the effects of Coulomb interactions (Abrikosov and Genkin 1974, Cuden 1976), and considered the influence of Fermi surface anisotropy (Abrikosov and Genkin 1974).

Most early theoretical treatments of Raman scattering in superconductors assumed that the optical skin depth δ was less than the coherence length ξ_0 of the superconductor. However, the first experimental observations of Raman scattering from superconducting gap excitations were actually made in conventional s-wave superconductors for which $\xi_0 \ll \delta$, including the layered dichalcogenide compound $2H$-$NbSe_2$ (Sooryakumar and Klein 1980, 1981), and the A15 compounds Nb_3Sn and V_3Si (Dierker et al. 1983, Hackl, Kaiser and Schicktanz 1983, Hackl and Kaiser 1988, Hackl, Kaiser and Gläser 1989) (see fig. 15). In many of these studies, it was reported that Raman intensity at 2Δ in certain symmetries was gained at the expense of intensity in a Raman-active phonon (Sooryakumar and Klein 1980, 1981, Hackl and Kaiser 1988, Hackl, Kaiser and Gläser 1989), suggesting that the "gap modes" in these symmetries derive their Raman activities from a coupling between phonons and electronic excitations (Balseiro and Falicov 1980, Littlewood and Varma 1981, 1982, Browne and Levin 1983, Lei et al. 1985, Zeyher and Zwicknagel 1990).

In Nb_3Sn and V_3Si, however, an onset of electronic scattering at 2Δ is also observed in scattering geometries for which there are no Raman-active phonons, and therefore can only arise from direct Raman scattering from quasiparticle pairs. A BCS-based calculation of Raman scattering from quasiparticle pairs for the case $\xi_0 \ll \delta$ ($q v_F \ll 2\Delta$) was first presented by Klein and Dierker (1984) for the limit $q \to 0$; this calculation incorporated the effects of both Coulomb screening and the attractive pairing interaction, and examined the polarization dependence arising from gap anisotropy. Abrikosov and Fal'kovskii (1988) later extended this calculation to include the first correction to the scattering cross section that is nonzero in the parameter $q v_F/\Delta$. More recent calculations of the electronic Raman scattering cross-section in the superconducting state examined the effects of a $\boldsymbol{k}$-dependent energy gap with line nodes (Fal'kovskii and Klama 1990), impurity scattering (Devereaux 1992, 1993), strong electron–phonon coupling in the presence of anisotropy (Kostur 1992), and final-state interactions governing the formation of excitonic and electron-pair bound states (Monien and Zawadowski 1990, Zawadowski 1990).

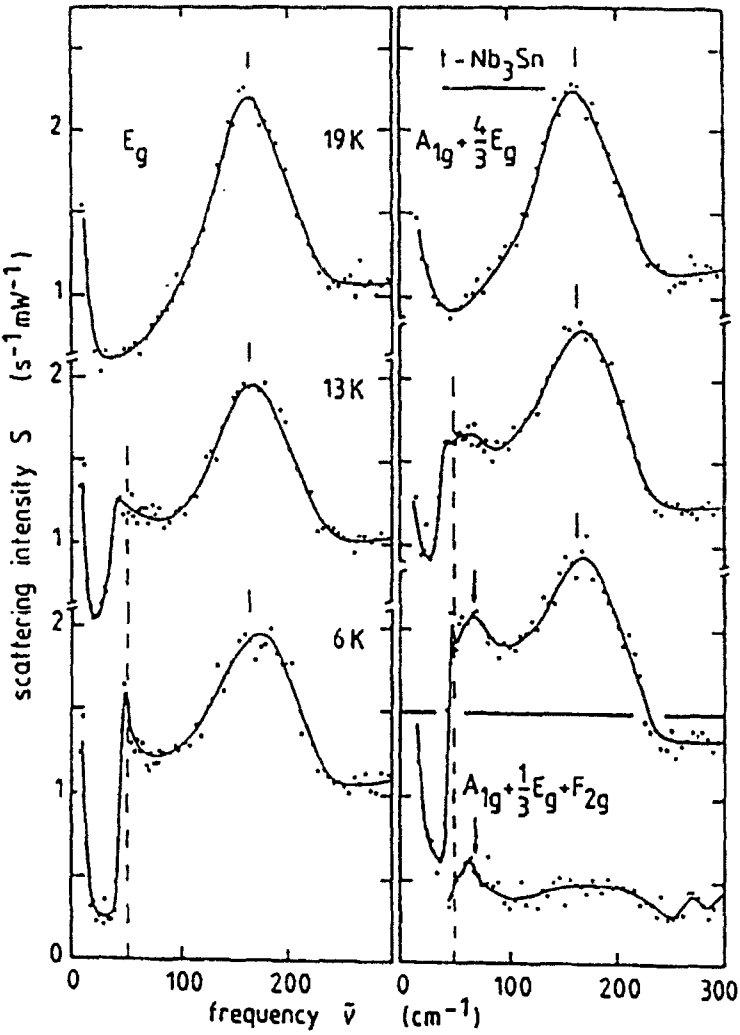

Fig. 15. Raman scattering from superconducting gap excitations in Nb_3Sn as a function of symmetry and temperature, showing the abrupt onset of scattering for $\hbar\omega \geqslant 2\Delta$ ($\approx 50\,cm^{-1}$) below T_c, and the presence of gap modes (after Hackl et al. 1989).

In the high-T_c cuprates, Raman scattering from quasiparticle pair excitations was first observed in polycrystalline samples as a broad scattering peak near $400\,cm^{-1}$ (Lyons et al. 1987, Bazhenov et al. 1987). The development of this "pair-breaking" peak in the electronic Raman scattering spectrum below T_c was later corroborated in measurements of single-crystal $YBa_2Cu_3O_7$ (Cooper et al. 1988a, Thomsen et al. 1988), $Bi_2Sr_2CaCu_2O_8$ (Kirillov et al. 1988, Yamanaka et al. 1988, Slakey et al. 1990a), $Tl_2Ba_2Ca_2Cu_3O_{10}$ (Krantz et al. 1989, Hoffmann et al. 1994), $La_{2-x}Sr_xCuO_4$ (X.K. Chen et al. 1994a),

$YBa_2Cu_4O_8$ (Donovan et al. 1995), $Tl_2Ba_2CuO_6$ (Nemetschek et al. 1993, Kang et al. 1996, Gasparov et al. 1997), and $HgBa_2CaCu_2O_6$ (Sacuto et al. 1997, Zhou et al. 1997) (see fig. 16). Significantly, several key features of the superconducting-state Raman response of high-T_c cuprates betray an unconventional gap in these materials. First, while there is a substantial suppression of low-frequency electronic scattering in the superconducting state of the high-T_c cuprates, there is no well-defined gap in the scattering spectrum down to the lowest measured temperature and energy (Cooper et al. 1988a), a feature which distinguishes the high-T_c cuprates from the complete suppression of scattering observed below 2Δ in conventional superconductors such as Nb_3Sn (Dierker et al. 1983) and V_3Si (Hackl, Kaiser and Schicktanz 1983). Second, the putative "pair-breaking" or "coherence" peak observed in the electronic Raman scattering response of optimally doped high-T_c superconductors has several distinctive properties: (i) it has a substantially larger energy, $\sim 8k_BT_c$, than that expected in a BCS superconductor, $2\Delta_{BCS} \approx 3.5k_BT_c$; (ii) it is essentially temperature independent below T_c, a feature also not expected in a BCS superconductor; and (iii) it has a roughly 30% higher value in the B_{1g} ($d_{x^2-y^2}$) scattering geometry than in the A_{1g} and B_{2g} (d_{xy}) scattering geometries in most cuprates, e.g., $YBa_2Cu_3O_7$ (Hackl et al. 1988, Cooper et al. 1988b), $Bi_2Sr_2CaCu_2O_8$ (Staufer et al. 1992, Devereaux et al. 1994a, Kendziora and Rosenberg 1995), $La_{2-x}Sr_xCuO_4$ (X.K. Chen et al. 1994a), and $Tl_2Ba_2CuO_6$ (Kang et al. 1996, Gasparov et al. 1997). Finally, the superconducting state Raman responses of most cuprates, including $Bi_2Sr_2CaCu_2O_8$ (Devereaux et al. 1994a), $La_{2-x}Sr_xCuO_4$ (X.K. Chen et al. 1994a), $Tl_2Ba_2CuO_6$ (Gasparov et al. 1997), and $HgBa_2Ca_2Cu_3O_8$ (Sacuto et al. 2000), exhibit a ω^3 frequency dependence in the B_{1g} ($d_{x^2-y^2}$) scattering geometry, but a linear-in-ω dependence in the A_{1g} and B_{2g} scattering geometries.

Devereaux and coworkers (Devereaux et al. 1994a,b, Devereaux and Einzel 1996a) offered the first theoretical evidence that many of these unconventional properties could be identified as the electronic Raman scattering response of a superconductor with a $d_{x^2-y^2}$ pairing state. To understand the basis for this interpretation, it is first useful to consider in more detail the general theory of electronic Raman scattering in a superconductor.

5.2. *Theory of Raman scattering in superconductors*

5.2.1. *The Raman scattering cross-section*

The electronic Raman scattering cross-section in the superconducting state of a superconductor is derived by considering the relationship (Klein and Dierker 1984)

$$\begin{aligned}\frac{d^2\sigma}{d\Omega\, d\omega_S} &= r_0^2 \frac{\omega_S}{\omega_I}\frac{n_S}{n_I}\sum_f \langle\langle |\langle f\,|\,\rho_{\boldsymbol{q}}\,|\,i\rangle|^2\rangle\rangle\, \delta(E_f - E_i - \hbar\omega), \\ &\propto r_0^2 \frac{\omega_S}{\omega_I}\frac{n_S}{n_I}\,[n(\omega)+1]\,\mathrm{Im}\,\chi_{\tilde{\rho}\tilde{\rho}}(\boldsymbol{q},\omega),\end{aligned} \tag{27}$$

where the Raman response function $\chi_{\tilde{\rho}\tilde{\rho}}(\boldsymbol{q},\omega)$ is evaluated using the Bardeen–Cooper–Schrieffer (BCS) ground state. Klein and Dierker (1984) performed this calculation

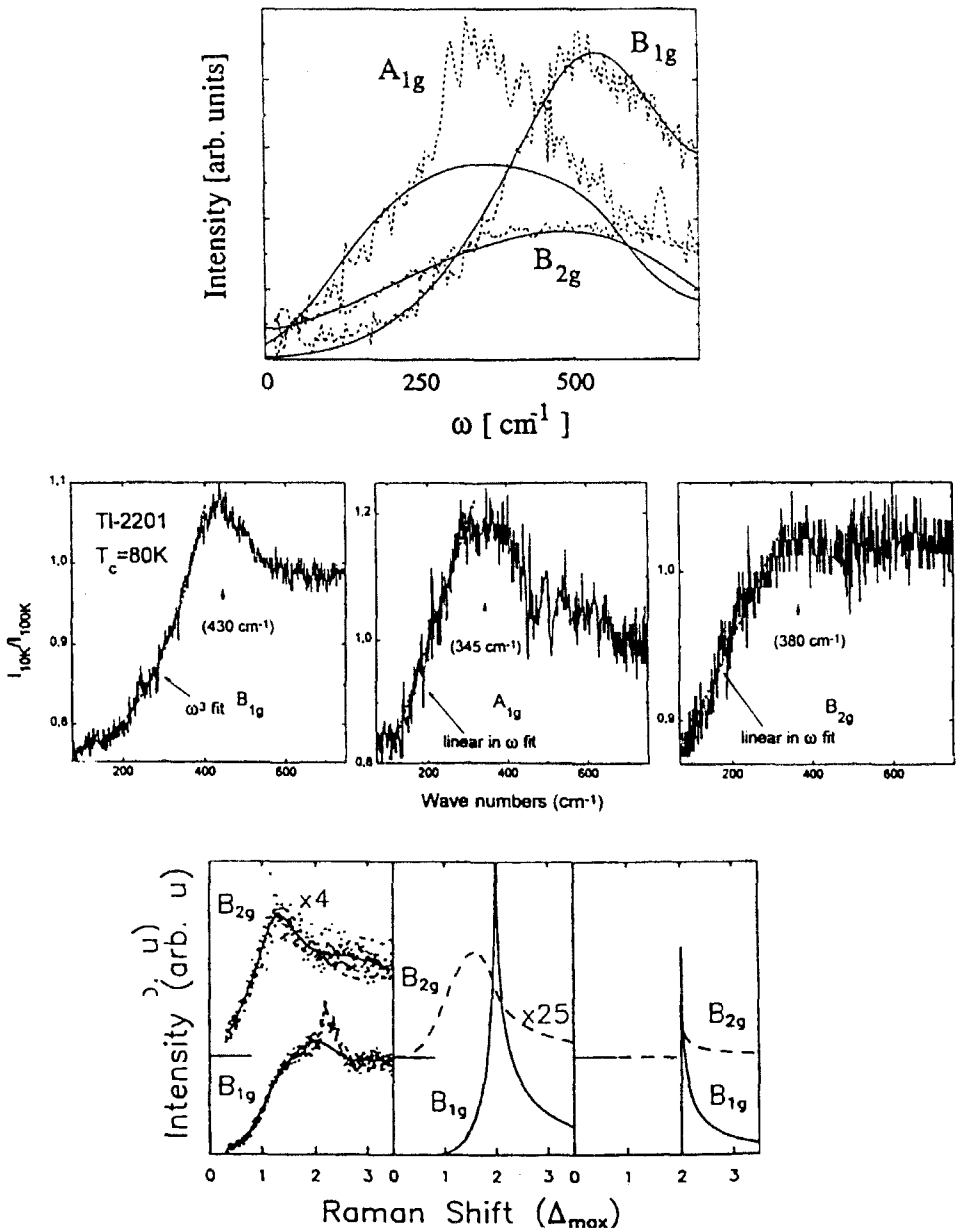

Fig. 16. Symmetry dependence of electronic Raman scattering from superconducting gap excitations in various high-T_c cuprates, including optimally doped (top) $Bi_2Sr_2CaCu_2O_8$ (after Devereaux and Einzel 1996a), (middle) single-layer $Tl_2Ba_2CuO_6$ (after Gasparov et al. 1997), and (bottom) $La_{2-x}Sr_xCuO_4$ (X.K. Chen et al. 1994a). Note the ω^3 low-frequency dependence of the B_{1g} scattering response in these materials, but the linear-in-ω dependence in A_{1g} and B_{1g} scattering responses.

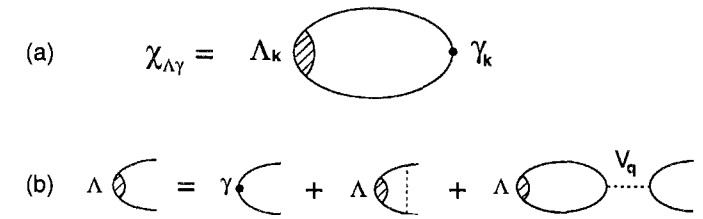

Fig. 17. (a) Polarization bubble diagrams for computing the gauge-invariant Raman scattering response of superconductors, $\chi_{\tilde{\rho}\tilde{\rho}}(\boldsymbol{q}, \omega) = \chi_{\Lambda\gamma}(\boldsymbol{q}, \omega)$, where Λ and γ are the renormalized and bare Raman scattering vertices, and the two solid lines represent the excitation of quasiparticle pairs. (b) Self-energy corrections to the Raman scattering vertex, including corrections due to pairing correlations (middle diagram on right-hand side) and Coulomb screening within the RPA approximation (final diagram on right-hand side).

including the effects of pair breaking and Coulomb screening within the Random Phase Approximation (RPA) (Pines 1963): the Raman scattering response function is associated with a susceptibility, $\chi_{\tilde{\rho}\tilde{\rho}}(\boldsymbol{q}, \omega) = \chi_{\Lambda\gamma}(\boldsymbol{q}, \omega)$, consisting of renormalized and bare Raman scattering vertices, Λ and γ, respectively, and a pair of Green's function lines associated with the excitation of quasiparticle pairs (see fig. 17). The resulting expression for the Raman scattering response function is

$$\chi_{\tilde{\rho}\tilde{\rho}}(\boldsymbol{q}, \omega) = \chi_{\Lambda\gamma}(\boldsymbol{q}, \omega) = \chi_{\gamma\gamma}(\boldsymbol{q}, \omega) - \frac{\chi_{\gamma 1}^2(\boldsymbol{q}, \omega)}{\chi_{11}(\boldsymbol{q}, \omega)} + \frac{\chi_{\gamma 1}^2(\boldsymbol{q}, \omega)}{\chi_{11}(\boldsymbol{q}, \omega)} \left(\frac{1}{\varepsilon(\boldsymbol{q}, \omega)} \right), \tag{28}$$

where the first term on the right-hand side is the "bare" Raman scattering response, the second term reflects transverse screening, and the final term is associated with longitudinal screening, where $\varepsilon(\boldsymbol{q}, \omega) = 1 - V_q \chi_{11}(\boldsymbol{q}, \omega)$ is the dielectric function and $V_q = 4\pi e^2/q^2$ is the Coulomb interaction matrix element. The longitudinal screening term is of order $O(q^2/\varepsilon)$ (Devereaux and Einzel 1995), and therefore can be ignored when considering the $q \to 0$ Raman scattering process. Consequently, under the conditions that (a) the superconducting gap Δ is much smaller than the Fermi energy, $\Delta \ll E_F$, and (b) the momentum transfer of light $\boldsymbol{q}$ is small compared to the Fermi momentum, the imaginary part of the ($T = 0$) electronic Raman scattering response function for a superconductor, including Coulomb screening effects, can be written (Klein and Dierker 1984, Devereaux et al. 1994b, Devereaux and Einzel 1995) as

$$\operatorname{Im} \chi_{\tilde{\rho}\tilde{\rho}}(\boldsymbol{q}, \omega) = \operatorname{Im}\left[\chi_{\gamma\gamma} - \frac{\chi_{\gamma 1}^2}{\chi_{11}} \right] = \operatorname{Im}\left[\left\langle |\gamma_{nk}|^2 \lambda_k \right\rangle - \frac{\langle \gamma_{nk} \lambda_k \rangle^2}{\langle \lambda_k \rangle} \right], \tag{29}$$

where $\langle \cdots \rangle$ represents an average over the Fermi surface, γ_{nk} is the bare Raman scattering vertex for band n in the non-resonant limit given in eq. (15), and λ_k is the imaginary part of the Tsuneto function for $T = 0$ (Tsuneto 1960):

$$\lambda_k = \frac{4 |\Delta_k|^2}{\omega \sqrt{\omega^2 - 4 |\Delta_k|^2}} \qquad [\hbar = 1]. \tag{30}$$

Note, from eq. (30), that in an s-wave superconductor, the unscreened superconducting-state Raman scattering response, $\propto \operatorname{Im} \chi_{\gamma\gamma}$, is zero for $\omega < 2\Delta$, but has a scattering

peak at $\omega = 2\Delta$ due to quasiparticle scattering above the energy gap. In the infrared conductivity, by contrast, spectral weight suppressed below 2Δ in the superconducting state appears as a delta function at $\omega = 0$, reflecting absorption by the superfluid (Tanner and Timusk 1992). The different frequency dependences of the Raman and infrared responses in the superconducting state derive from the different BCS coherence factors (Tinkham 1975) associated with the respective Raman scattering (Type-I) and infrared (Type-II) Hamiltonians, $H_R \sim \boldsymbol{A} \cdot \boldsymbol{\mu}^{-1} \cdot \boldsymbol{A}$ and $H_{IR} \sim \boldsymbol{A} \cdot \boldsymbol{p}$.

5.2.2. *Coulomb screening effects*

Coulomb screening has several important consequences for the Raman scattering response in superconductors. First, it minimizes the effects of pairing correlations (middle diagram in fig. 17b) on the low-frequency Raman scattering spectrum by pushing the zero-frequency Goldstone mode, associated with phase fluctuations of the order parameter, up to the plasma frequency ω_p (Klein and Dierker 1984, Devereaux and Einzel 1995, Strohm and Cardona 1997a). Second, screening has a strong influence on the scattering response in certain symmetries. Devereaux et al. (1994a,b) [see also Kostur (1992)] pointed out that in tetragonal (D_{4h}) crystals, the second, Coulomb screening, term in the brackets of eq. (29) vanishes due to symmetry in $L = 2$ scattering symmetries such as B_{1g} and B_{2g}. This is because the Tsuneto function λ_k ($\propto \Delta^2$) has the full symmetry of the space group, A_{1g}, and therefore the factor $\langle \gamma_{nk} \lambda_k \rangle$ in the second term of eq. (29) vanishes in a tetragonal superconductor unless the Raman vertex γ_{nk} also has A_{1g} symmetry. Thus, the gauge-invariant, $T = 0$ Raman scattering response in the B_{1g} and B_{2g} scattering geometries of a tetragonal superconductor can be described by the Raman response function with *bare* Raman scattering vertices ($\hbar = 1$):

$$\operatorname{Im} \chi_{\gamma\gamma}(\boldsymbol{q} \to 0, \omega) = 4N(0) \operatorname{Re} \left\langle \frac{|\gamma_{nk}|^2 |\Delta_k|^2}{\omega \sqrt{\omega^2 - 4|\Delta_k|^2}} \right\rangle . \tag{31}$$

where $N(0)$ is the density of states at the Fermi level for one spin orientation.

On the other hand, screening effects are expected to strongly suppress scattering strength in the A_{1g} ($L = 0$) geometry, based upon the symmetry arguments delineated above. However, as discussed in more detail below, the *observed* A_{1g} superconducting-state Raman response in the cuprates is *not* in general strongly suppressed, a fact which has motivated consideration of several other effects on the A_{1g}-symmetry Raman scattering response, including resonance enhancements and multilayer effects (Krantz and Cardona 1994, 1995).

5.2.3. *The influence of gap anisotropy*

It is important to note that the Tsuneto function in eq. (30) depends upon the square of the gap function, $|\Delta_k|^2$, and hence the Raman scattering response in eq. (31) is sensitive only to the *amplitude* of the superconducting gap function, and not to its *phase*. Consequently, Raman scattering cannot distinguish, for example, between a

d-wave pairing state, $\Delta_k = \Delta_0(k_x^2 - k_y^2)$, and an anisotropic s-wave pairing state, such as $\Delta_k = \Delta_0|k_x^2 - k_y^2|$, although Devereaux (1995) and Wu and Carbotte (1998) have suggested that electronic Raman scattering in the presence of impurities can be used to distinguish such pairing states. On the other hand, it is clear from eq. (31) that the Raman scattering response in the superconducting state can provide substantial information concerning the k-dependence of Δ_k, since eq. (31) involves an average of the $T=0$ Tsuneto function ($\hbar=1$), $\lambda_k = 4|\Delta_k|^2/\omega\sqrt{\omega^2 - 4|\Delta_k|^2}$, over the Fermi surface, weighted by the square of the Raman vertex, $|\gamma_{nk}|^2$. Thus, in a superconductor with an isotropic gap, $\Delta_k =$ constant, the Raman scattering response $\mathrm{Im}\,\chi_{\gamma\gamma}$ will have a polarization-independent "pair-breaking" peak at $\omega=2\Delta$. On the other hand, in a superconductor with an anisotropic gap, $\Delta_k = f(k)$, the peak position and frequency dependence of the electronic scattering response depends upon the scattering geometry due to the weighting function $|\gamma_{nk}|^2$.

5.3. *Analysis of the superconducting response in high-T_c superconductors*

5.3.1. *The $d_{x^2-y^2}$ pairing state*

Devereaux et al. (1994a) and Devereaux and Einzel (1996a) first pointed out that in a tetragonal superconductor with a $d_{x^2-y^2}$ pairing state, $\Delta_k = \Delta_0(k_x^2 - k_y^2)$, the asymptotic low-frequency behavior of $\mathrm{Im}\,\chi_{\gamma\gamma}$ should exhibit an ω^3 low-frequency dependence in the B_{1g} electronic scattering response, but a linear-in-ω dependence in the A_{1g} and B_{2g} symmetries (see table 2). This difference results rather generally from the fact that the $T=0$ low-frequency density of states of a $d_{x^2-y^2}$ superconductor is governed by the nodes, and hence varies linearly with energy. Consequently, one expects the low-frequency B_{2g} Raman response to vary linearly with frequency in a $d_{x^2-y^2}$ superconductor, since the B_{2g} vertex function is finite around the nodes, while the B_{1g}-symmetry response varies as ω^3 because the $d_{x^2-y^2}$ pairing and B_{1g} vertex functions vanish at the same points in k-space (see fig. 2). It has been pointed out that the presence of strong inelastic carrier scattering should significantly broaden and increase the energy of the peak in the B_{1g} response of a $d_{x^2-y^2}$ superconductor, but should not strongly influence the ω^3 low-frequency dependence (Jiang and Carbotte 1995). As shown in fig. 16 (top), the calculated Raman cross-section for a $d_{x^2-y^2}$ pairing state describes the observed superconducting-state electronic Raman scattering response of $Bi_2Sr_2CaCu_2O_8$

Table 2
The asymptotic low-frequency behavior of the electronic Raman scattering response function, $\mathrm{Im}\,\chi_{\gamma\gamma}(\omega \to 0)$, for a $d_{x^2-y^2}$ superconductor in different symmetries[a]

Symmetry	$\mathrm{Im}\,\chi_{\gamma\gamma}(\omega \to 0)$
B_{1g}	$\sim(\hbar\omega/2\Delta_0)^3$
A_{1g}	$\sim\hbar\omega/2\Delta_0$
B_{2g}	$\sim\hbar\omega/2\Delta_0$

[a] After Devereaux et al. (1994a). Logarithmic factors have not been included.

reasonably well (Devereaux et al. 1994a, Devereaux and Einzel 1996a). Subsequent measurements and analysis of the symmetry-dependent Raman scattering responses of other cuprates, including $La_{2-x}Sr_xCuO_4$ (X.K. Chen et al. 1994a), $Tl_2Ba_2CuO_6$ (Gasparov et al. 1997), and $HgBa_2Ca_2Cu_3O_8$ (Sacuto et al. 2000) are also consistent with the scattering response of a $d_{x^2-y^2}$ superconductor (see fig. 16).

Notably, in the initial calculations of Devereaux et al. (1994a,b), the observed large anisotropy between the B_{2g} and A_{1g} pair-breaking energies was associated with Coulomb screening of the A_{1g} component, which shifted this contribution down in energy from 2Δ to nearly Δ in the calculations. However, this effect is now known to be an artifact (Devereaux and Einzel 1996a,b) caused by ignoring higher-order Fermi-surface harmonics in the expansion of the A_{1g}-symmetry Raman scattering vertex (eq. 16). More recent calculations of the Raman scattering cross-section in eq. (31) for a $d_{x^2-y^2}$ superconductor, using more realistic approximations of the Raman vertex γ_{nk} (X.K. Chen et al. 1994b, X.K. Chen and Irwin 1994, Branch and Carbotte 1995, Krantz et al. 1995, Krantz and Cardona 1995, Devereaux et al. 1996, Wenger and Käll 1997, Strohm and Cardona 1997a), including approximations involving 2D tight-binding model calculations and 2D and 3D local-density approximation (LDA) band-structure calculations, do not reproduce the large measured differences in the peak positions of the A_{1g} and B_{1g} responses. Nevertheless, these calculations generally appear to support a $d_{x^2-y^2}$ pairing state for the high-T_c superconductors, as they reproduce the data reasonably accurately in most other respects (Devereaux et al. 1996, Strohm and Cardona 1997a). It is clear from these calculations, however, that the *frequency dependence* of the low-frequency superconducting Raman response in different scattering geometries is a better probe of the pairing state than the anisotropy of the pair-breaking energy. Importantly, the large anisotropy in the measured A_{1g} and B_{1g} peak energies remains unexplained – while calculations by Manske et al. (1997) suggest that screening of the B_{1g} Raman response is responsible for this difference, these calculations have been questioned [see Comment by Strohm, Munzar and Cardona (1998) and Reply by Manske et al. (1998)]. Indeed, the differences between the measured A_{1g} and B_{1g} superconducting-state Raman responses may indicate that the B_{1g} response has a different origin than the A_{1g} response: X.K. Chen et al. (1993) have suggested that the B_{1g}-symmetry peak in $YBa_2Cu_3O_7$ in fact arises from spin fluctuations, based in part on the sensitivity of this response to doping. This issue clearly remains one of the outstanding questions facing future Raman scattering studies of high-T_c superconductors.

5.3.2. *Effects of orthorhombic distortions*

While the initial calculations of Devereaux et al. (1994a,b) assumed a tetragonal superconductor with a $d_{x^2-y^2}$ gap, orthorhombic distortions have consequences in a $d_{x^2-y^2}$ superconductor that are expected to manifest themselves differently in the orthorhombic compounds $YBa_2Cu_3O_7$ and $Bi_2Sr_2CaCu_2O_8$ (Annett et al. 1996, Strohm and Cardona 1997a,b). In particular, in a tetragonal $d_{x^2-y^2}$ cuprate superconductor, the B_{1g}-symmetry Raman vertex and the $d_{x^2-y^2}$ gap function both have nodes in

the $[\pm 1, \pm 1, 0]$ directions, resulting in the characteristic ω^3 low-frequency B_{1g} Raman response discussed above. In $YBa_2Cu_3O_7$, the orthorhombic distortion removes the mirror plane symmetry through (110), causing a shift of the B_{1g} Raman vertex nodes away from the [110] direction, and a consequent admixing of ω and ω^3 low-energy scattering contributions in the B_{1g} geometry. By contrast, the orthorhombic unit cell in $Bi_2Sr_2CaCu_2O_8$ is rotated by 45° relative to that of $YBa_2Cu_3O_7$. Consequently, the orthorhombic distortion preserves the mirror plane symmetry along (110), and the superconducting-state Raman response in the B_{1g} scattering geometry is expected to maintain its pure ω^3 dependence. This difference may in part account for discrepancies observed between the B_{1g} spectra of $YBa_2Cu_3O_7$ and $Bi_2Sr_2CaCu_2O_8$ (Devereaux and Einzel 1995), although Devereaux and Einzel have also pointed out that different Fano interaction effects between the optical phonons and low-frequency continua of $YBa_2Cu_3O_7$ and $Bi_2Sr_2CaCu_2O_8$ may contribute to the slightly different low-frequency spectral responses observed in these materials.

5.3.3. *Multilayer effects*

One of the remaining puzzles related to the superconducting-state Raman response in the high-T_c cuprates is the observation of a substantial scattering response in the A_{1g} geometry, which, as noted above, is in defiance of theoretical predictions that the A_{1g} response should be strongly suppressed by Coulomb screening. Krantz and Cardona (1995) and Strohm and Cardona (1997a) have argued, by analogy with strong A_{1g} scattering seen in multicomponent plasma systems, that effective mass fluctuations between different Fermi surface sheets in *multilayer* cuprate materials lead to the unscreened A_{1g} scattering. A natural test of this supposition is to examine the superconducting Raman response of single-layer cuprates. Such measurements were made in single-layer $Tl_2Ba_2CuO_6$ by Gasparov et al. (1997) and Kang et al. (1997), and it was found that the A_{1g} scattering response is still strong in single-layer materials, although perhaps somewhat weaker than in multilayer materials (see middle plot, fig. 16). Recent studies of single-layer $La_{2-x}Sr_xCuO_4$ at optimal doping by X.K. Chen et al. (1998a) also show no differences between the spectral response of single- and double-layer cuprates, further suggesting that multilayer effects on the normal- and superconducting-state Raman response of the cuprates are probably weak. Thus, the origin of the strong A_{1g} Raman response remains an open question. Further study is needed to elucidate the role that strong Fermi-surface anisotropy, particularly that associated with the extreme in-plane/c-axis anisotropy, plays in the strong A_{1g} scattering in the cuprates.

5.3.4. *Other reported pairing states*

While the calculations of Devereaux et al. and others appear to show that many of the anomalous features observed in the superconducting-state electronic Raman scattering response of high-T_c cuprates can be explained assuming a $d_{x^2-y^2}$ pairing state, there are several noteworthy exceptions to this interpretation.

Stadlober et al. (1995) observed that the electron-doped system $Nd_{2-x}Ce_xCuO_4$ exhibits a redistribution of electronic scattering below T_c (≈ 20 K), but neither the pair-breaking energy nor the low-frequency ω dependence of electronic scattering below T_c in $Nd_{2-x}Ce_xCuO_4$ was found to be symmetry dependent. Moreover, the maximum pair-breaking energy inferred from these Raman scattering measurements, $2\Delta_{max} \approx 4.9 k_B T_c$, was much smaller than that estimated from studies of the hole-doped cuprates, $2\Delta_{max} \approx 8 k_B T_c$. Stadlober et al. (1995) concluded from these results that $Nd_{2-x}Ce_xCuO_4$ is a nearly isotropic s-wave superconductor, corroborating the interpretation of temperature-dependent penetration depth measurements of this material (Wu et al. 1993).

Kendziora et al. (1996) also reported that overdoped $Tl_2Ba_2CuO_6$ and $Bi_2Sr_2CaCu_2O_8$ are isotropic s-wave superconductors, based upon their observation of a small pair-breaking energy, $2\Delta \approx 3.9 k_B T_c$, and a small difference (~10%) between the B_{1g}- and B_{2g}-symmetry "pair-breaking" peak energies in these materials. However, as mentioned above, the symmetry dependence of the "pair-breaking" energy is not a good measure of the pairing state in Raman scattering [concerning this point, see also Devereaux and Einzel (1995), as well as the Comment by Hewitt et al. (1997) and Reply by Kendziora and Onellion (1997)]. Instead, a better measure is the frequency dependence of low-energy electronic scattering in different scattering geometries, and recent measurements of the superconducting state Raman scattering response in overdoped $Tl_2Ba_2CuO_6$ (Gasparov et al. 1998a,b) and $Bi_2Sr_2CaCu_2O_8$ (Blumberg et al. 1997b) reveal a ω^3 dependence in the B_{1g} geometry and a linear ω dependence in the B_{2g} geometry, characteristic of a $d_{x^2-y^2}$ pairing state (see fig. 18). These results suggest strongly that the $d_{x^2-y^2}$ pairing state persists even into the overdoped phases of the Bi- and Tl-based cuprates.

Finally, more complicated pairing states have also been inferred from superconducting-state Raman scattering data. For example, Krantz (1996) has considered the effects of interlayer pairing on the pairing state of $YBa_2Cu_3O_7$, arguing that Raman scattering and tunneling data of this compound are consistent with the presence of B_{1g}- and A_{1g}-symmetry gaps associated with the even and odd Fermi surfaces, respectively (i.e., $d_{x^2-y^2} + i\alpha s$, $\alpha < 1$). On the other hand, Annett et al. (1996) have argued against such even- and odd-parity pairing in bilayer materials based upon the fundamental similarity between the superconducting-state properties of one- and two-layer cuprates, and in particular upon the absence of evidence for a second transition in bilayer materials. Also, in Raman scattering measurements of optimally doped $HgBa_2CaCu_2O_6$, Sacuto et al. (1997, 1998) [see also Correction to Sacuto et al. (1998) in Sacuto et al. (1999)] first reported a linear-in-ω contribution to the low-frequency scattering response in both the B_{1g} and B_{2g} geometries. As this material is tetragonal, and consequently immune to any mixing of ω and ω^3 contributions due to orthorhombicity (see sect. 5.3.2), the authors concluded from this that the nodes in the gap function are shifted slightly away from the $[\pm 1, \pm 1, 0]$ directions in $HgBa_2CaCu_2O_6$, and that the pairing function in this compound is consequently described by either a "g-wave" state [i.e., A_{2g} symmetry = $xy(x^2 - y^2)$] (Sacuto et al. 1997, 1998) or a d + s state (Beal-Monod et al. 1997). However, in more recent measurements of underdoped $HgBa_2Ca_2Cu_3O_8$, in which sample surface

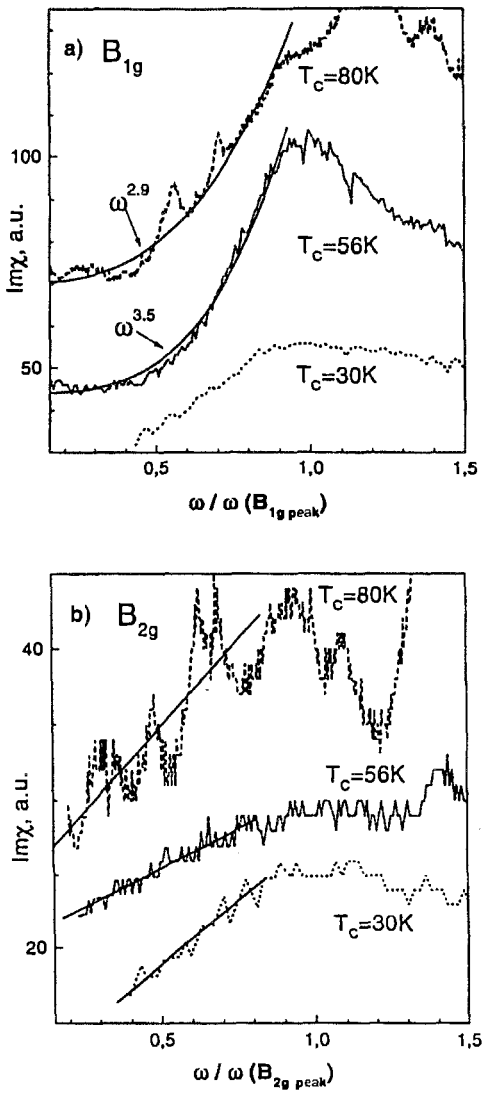

Fig. 18. Symmetry dependence of electronic Raman scattering in the superconducting state of overdoped $Tl_2Ba_2CuO_6$ (after Gasparov et al. 1998a,b), showing the ω^3 low-frequency dependence of the B_{1g} scattering response and the linear-in-ω dependence in A_{1g} and B_{1g}.

problems were believed to be under better control, Sacuto et al. (2000) found frequency dependences of the B_{1g}, B_{2g}, and A_{1g} electronic Raman scattering intensities that were largely consistent with a $d_{x^2-y^2}$ pairing state. It is also perhaps appropriate to point out in this regard that the efficacy of Raman scattering for deducing subtle details related to the pairing state is limited by several factors, including the phase insensitivity of the technique (see sect. 5.2.3), the model dependence implicit in the analysis of the Raman response, and the inherent difficulties involved in extracting the intrinsic low-frequency scattering

response due to material quality and extraneous scattering contributions. Therefore, subtle details associated with the pairing function, for example related to multilayer effects and precise nodal position, must ultimately be adjudicated by more sensitive (e.g., phase-sensitive) techniques.

5.3.5. *Relationship to the "normal"-state response*

Significantly, models of electronic Raman scattering in the superconducting state of high-T_c superconductors neither explain the anomalous normal-state electronic Raman continuum, nor rely upon this scattering to explain the development of a pair-breaking peak below T_c. Rather, peaks in the superconducting-state Raman scattering response are expected to develop near 2Δ in these models, even in the absence of normal-state scattering, due to the development of unscreened (i.e., $L \neq 0$) collective bound state and quasiparticle pair-breaking excitations below T_c (see, for example, Anderson 1958a,b, Bogoliubov 1958, Tsuneto 1960, Bardasis and Schrieffer 1961, Monien and Zawadowski 1990). However, Kang et al. (1996) reported experimental evidence for at least an indirect connection between the normal-state continuum and the superconducting-state "pair breaking" peak in $Tl_2Ba_2CuO_6$, finding that both features exhibit a resonant enhancement associated with the 3.4 eV absorption band. They attribute this absorption band in $Tl_2Ba_2CuO_6$ to a transition from the Fermi level to the upper Hubbard band (UHB), and associate the resonance profile of these features to the enhancement of the electronic and quasiparticle Raman scattering intensities by real interband transitions to the UHB. However, the nature of this connection between the normal- and superconducting-state Raman responses in $Tl_2Ba_2CuO_6$ is not understood, nor has a similar connection been observed in other cuprates.

5.4. *Electronic Raman scattering in high magnetic fields*

Until recently, Raman scattering studies of the high-T_c cuprates in high magnetic fields were primarily limited to studies of Raman-active phonons (Ruf et al. 1988, Podobedov et al. 1997, Loa et al. 1997) and crystal-field–phonon coupling (Ruf et al. 1992). Blumberg et al. (1997a) observed, however, that the Raman scattering "pair-breaking" peak in overdoped $Tl_2Ba_2CuO_6$ is substantially suppressed by a magnetic field (see fig. 19). From the field and temperature dependencies of their Raman spectra, Blumberg et al. deduced that the upper critical field $H^*_{c2}(T)$ in overdoped $Tl_2Ba_2CuO_6$ has a conventional temperature dependence, in contrast to the anomalous temperature dependence of $H^*_{c2}(T)$ inferred from magnetoresistance measurements (Dalichaouch et al. 1990, Almasan et al. 1992, Mackenzie et al. 1993, 1996, Osofsky et al. 1993). They further observed a non-linear field dependence of the "pair-breaking" peak intensity, which they attributed to a renormalization of the quasiparticle density near the vortex cores. Interestingly, recent calculations of the Raman scattering intensity by Vekhter et al. (1999), which account for the Doppler energy shift of the extended quasiparticle states in the mixed phase of a d-wave superconductor, reveal several features that are qualitatively consistent with these measurements: (a) the Raman intensity below the average Doppler shift energy develops

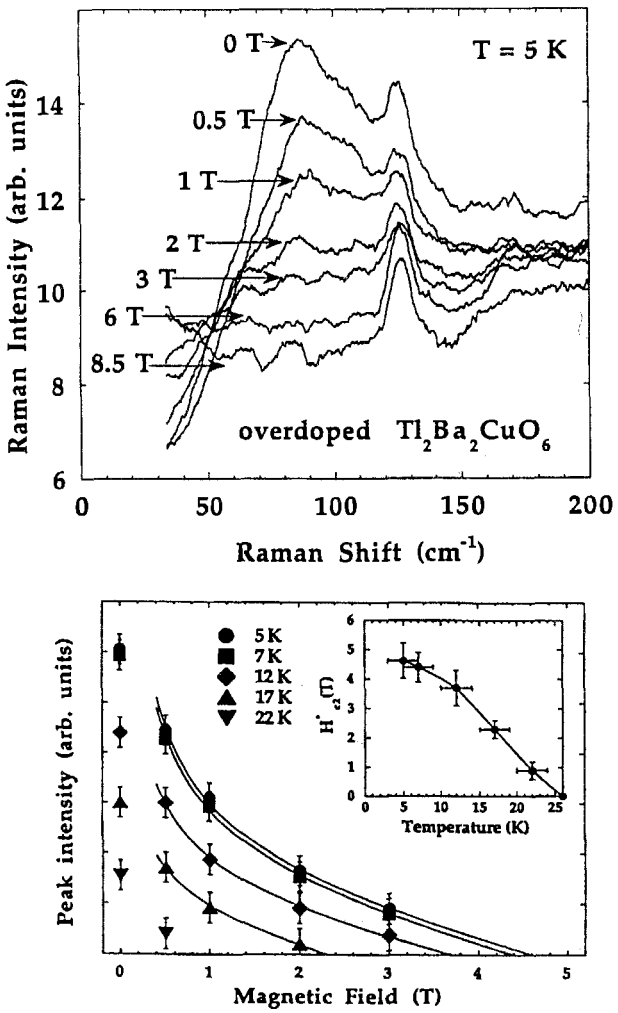

Fig. 19. (top) Magnetic field dependence of the superconducting-state electronic Raman scattering response in overdoped $Tl_2Ba_2CuO_6$, showing a suppression of the "pair-breaking" peak with increasing magnetic field. (bottom) Field and temperature dependence of the "pair-breaking" peak intensity. (inset) Temperature dependence of the upper critical field, $H^*_{c2}(T)$, obtained from fits to these data (after Blumberg et al. 1997a).

quartic and quadratic frequency dependences in the B_{1g} and B_{2g} spectra, respectively; (b) the 2Δ peak intensity decreases linearly with magnetic field; and (c) the normalized integrated Raman intensity scales with $\sqrt{H}$.

An interesting possible area of future Raman scattering investigation in high magnetic fields involves studies of the discrete quasiparticle spectrum inside the vortex cores of high-T_c superconductors. The energy spacing of these discrete states is governed by the

confinement energy associated with the vortex (Caroli, de Gennes and Matricon 1964), and thus should fall in an accessible frequency range for infrared and Raman spectroscopies in small-coherence-length superconductors such as the high-T_c superconductors ($\xi_0 \approx 10$–20 Å). However, while quasiparticle pair excitations were reported by Karrai et al. (1992) using infrared measurements, there have as yet been no reports of vortex excitations observed with Raman scattering.

6. Conclusions

There have been an enormous number of Raman scattering studies of the high-T_c superconductors in the past decade or so, but such is the richness of these remarkable materials that many veins of interesting physics have yet to be fully explored with this technique. First, Raman scattering in high magnetic fields is potentially interesting as a means of studying transitions between bound states in the vortex core. Second, Raman scattering in the underdoped cuprates is relatively untapped, and shows promise both as a means of investigating possible differences in the "pairing" and "phasing" temperatures in underdoped cuprates, and as a method for studying charge and spin domain structures that may exist in this phase regime. Raman scattering also lends itself to a number of techniques which may be particularly useful in the study of underdoped and other phases, including time-resolved, high-pressure, magnetic-field, and micro- and near-field-Raman scattering techniques. For example, recent high-pressure Raman scattering studies of two-magnon spectra in lamellar cuprates have revealed interesting magnon–phonon interaction effects not accessible using other techniques (Struzhkin et al. 2000). Using Raman scattering to study high-T_c cuprate microstructures is also potentially interesting, not only as a means of spectroscopically investigating superconductivity in mesoscopic systems, but also as a versatile diagnostic tool for evaluating high-T_c devices (Bock et al. 1993). Finally, resonant X-ray Raman spectroscopy has recently evolved as a promising new probe of excitations in the cuprates, particularly in the insulating phase (Kuiper et al. 1998, Abbamonte et al. 1999). Indeed, given the remarkable, and often unexpected, past successes achieved in Raman scattering studies of high-T_c cuprates and other complex oxides, ultimately one can only speculate about the exciting directions that future Raman scattering studies of these materials will take.

Acknowledgements

I would like to acknowledge the fruitful interactions I have had at Illinois with a number of people whose work in the area of Raman scattering from high-T_c superconductors or related topics contributed to this review: Pete Abbamonte, Girsh Blumberg, Don Ginsberg, Laura Greene, Moonsoo Kang, Marvin Karlow, Miles Klein, Art Kotz, Tony Leggett, Ran Liu, Paul Nyhus, Dmitri Reznik, Michael Rübhausen, David Salamon, Myron Salamon, Francis Slakey, Charlie Slichter, Dale Van Harlingen, Doug Wake, and Ali Yazdani.

I would like to particularly thank Miles Klein for his critical reading of this manuscript prior to publication. Finally, I would like to thank my wife, Laura Clower, and children, Duncan, Sarah, and Patrick, for their patience and support while I was writing this chapter. I also gratefully acknowledge support from the Department of Energy under grant DEFG02-96ER4539, and from the Science and Technology Center for Superconductivity under grant NSF DMR91-20000.

References

Abbamonte, P., C.A. Burns, E.D. Isaacs, P.M. Platzman, L.L. Miller, S.-W. Cheong and M.V. Klein, 1999, Phys. Rev. Lett. **83**, 860.

Abrikosov, A.A., and L.A. Fal'kovskii, 1961, Sov. Phys. JETP **13**, 179.

Abrikosov, A.A., and L.A. Fal'kovskii, 1988, Physica C **156**, 1.

Abrikosov, A.A., and V.M. Genkin, 1974, Sov. Phys. JETP **38**, 417.

Aeppli, G., S.M. Hayden, H.A. Mook, Z. Fisk, S.-W. Cheong, D. Rytz, J.P. Remeika, G.P. Espinosa and A.S. Cooper, 1989, Phys. Rev. Lett. **62**, 2052.

Aharony, A., R.J. Birgeneau, A. Coniglio, M.A. Kastner and H.E. Stanley, 1988, Phys. Rev. Lett. **60**, 1330.

Allen, P.B., 1976, Phys. Rev. B **13**, 1416.

Almasan, C.C., M.C. de Andrade, Y. Dalichaouch, J.J. Neumeier, C.L. Seaman, M.B. Maple, R.P. Guertin, M.V. Kuric and J.C. Garland, 1992, Phys. Rev. Lett. **69**, 3812.

Andersen, O.K., A.I. Liechtenstein, C.O. Rodriguez, I.I. Mazin, O. Jepsen, V.P. Antropov, O. Gunnarsson and S. Gopalan, 1991, Physica C **185–189**, 147.

Andersen, O.K., O. Jepsen, A.I. Liechtenstein and I.I. Mazin, 1994, Phys. Rev. B **49**, 4145.

Anderson, P.W., 1958a, Phys. Rev. **110**, 827.

Anderson, P.W., 1958b, Phys. Rev. **112**, 1900.

Anderson, P.W., 1987, Science **235**, 1196.

Anderson, P.W., 1997, The Theory of Superconductivity in High T_c Cuprates (Princeton University Press, Princeton, NJ).

Annett, J.F., N.D. Goldenfeld and A.J. Leggett, 1996, in: Physical Properties of High Temperature Superconductors, Vol. V, ed. D.M. Ginsberg (World Scientific, Singapore) p. 375.

Aronson, M.C., S.B. Dierker, B.W. Dennis, S.-W. Cheong and Z. Fisk, 1991, Phys. Rev. B **44**, 4657.

Bacci, S.B., and E.R. Gagliano, 1991, Phys. Rev. B **43**, 6224.

Balseiro, C.A., and L.M. Falicov, 1980, Phys. Rev. Lett. **45**, 662.

Bardasis, A., and J.R. Schrieffer, 1961, Phys. Rev. **121**, 1050.

Basu, S., and A. Singh, 1997, Phys. Rev. B **55**, 12338.

Batlogg, B., and V.J. Emery, 1996, Nature **382**, 20.

Batlogg, B., H.Y. Hwang, H. Takagi, R.J. Cava, H.L. Kao and J. Kwo, 1994, Physica C **235–240**, 130.

Bazhenov, A.V., A.V. Gorbunov, N.V. Klassen, S.F. Kodakov, I.V. Kukushkin, V.D. Kalakovskii, O.V. Misochko, V.B. Timofeev, L.I. Chernyshova and B.N. Shepel, 1987, Pis'ma Zh. Eksp. Teor. Fiz. **46**, 35 [JETP Lett. **46**, 32].

Beal-Monod, M.T., J.B. Bieri and K. Maki, 1997, Europhys. Lett. **40**, 201.

Blumberg, G., R. Liu, M.V. Klein, W.C. Lee, D.M. Ginsberg, C. Gu, B.W. Veal and B. Dabrowski, 1994, Phys. Rev. B **49**, 13295.

Blumberg, G., P. Abbamonte, M.V. Klein, W.C. Lee, D.M. Ginsberg, L.L. Miller and A. Zibold, 1996, Phys. Rev. B **53**, R11930.

Blumberg, G., M. Kang and M.V. Klein, 1997a, Phys. Rev. Lett. **78**, 2461.

Blumberg, G., M. Kang, M.V. Klein, K. Kadowaki and C. Kendziora, 1997b, Science **278**, 1427.

Blumberg, G., M.V. Klein and S.-W. Cheong, 1998a, Phys. Rev. Lett. **80**, 564.

Blumberg, G., M.V. Klein, K. Kadowaki, C. Kendziora, P. Guptasarma and D. Hinks, 1998b, J. Phys. Chem. Solids **59**, 1932.

Bock, A., J.C. Fretwurst and U. Merkt, 1993, J. Phys. Chem. Solids **54**, 1343.

Bogoliubov, N.N., 1958, Nuovo Cim. **7**, 6.

Bozovic, I., D. Kirillov, A. Kapitulnik, K. Char, M.R. Hahn, M.R. Beasley, T.H. Geballe, Y.H. Kim and A.J. Heeger, 1987, Phys. Rev. Lett. **59**, 2219.

Bozovic, I., J.H. Kim, J.S. Harris, C.B. Eom, J.M. Phillips and J.T. Cheung, 1994, Phys. Rev. Lett. **73**, 1436.

Branch, D., and J.P. Carbotte, 1995, Phys. Rev. B **52**, 603.

Brawner, D.A., and H.R. Ott, 1994, Phys. Rev. B **50**, 6530.

Brenig, W., and H. Monien, 1992, Solid State Commun. **83**, 1009.

Browne, D.A., and K. Levin, 1983, Phys. Rev. B **28**, 4029.

Canali, C.M., and S.M. Girvin, 1992, Phys. Rev. B **45**, 7127.

Cardona, M., 1999, Physica C **318**, 30.

Caroli, C., P.G. de Gennes and J. Matricon, 1964, Phys. Lett. **9**, 307.

Cerdeira, F., N. Mestres and M. Cardona, 1984, Phys. Rev. B **29**, 3737.

Chandrasekhar, M., M. Cardona and E.O. Kane, 1977, Phys. Rev. B **16**, 3579.

Chaudhari, P., and S.-Y. Lin, 1994, Phys. Rev. Lett. **72**, 1084.

Chen, C.H., S.-W. Cheong and A.S. Cooper, 1993, Phys. Rev. Lett. **71**, 2461.

Chen, C.T., L.H. Tjeng, J. Kwo, H.L. Kao, P. Rudolf, F. Sette and R.M. Flemming, 1992, Phys. Rev. Lett. **68**, 2543.

Chen, X.K., and J.C. Irwin, 1994, Physica **235–240**, 1087.

Chen, X.K., E. Altendorf, J.C. Irwin, R. Liang and W.N. Hardy, 1993, Phys. Rev. B **48**, 10530.

Chen, X.K., J.C. Irwin, H.J. Trodahl, T. Kimura and K. Kishio, 1994a, Phys. Rev. Lett. **73**, 3290.

Chen, X.K., J.C. Irwin, R. Liang and W.N. Hardy, 1994b, Physica C **227**, 113.

Chen, X.K., J.G. Naeini, K.C. Hewitt, J.C. Irwin, R. Liang and W.N. Hardy, 1997, Phys. Rev. B **56**, R513.

Chen, X.K., J.C. Irwin, H.J. Trodahl, M. Okuya, T. Kimura and K. Kishio, 1998a, Physica C **295**, 80.

Chen, X.K., J.G. Naeini, J.C. Irwin, R. Liang and W.N. Hardy, 1998b, J. Phys. Chem. Solids **59**, 1968.

Chen, Y., F. Wilczek, E. Witten and B. Halperin, 1989, Int. J. Mod. Phys. B **3**, 1001.

Chubukov, A.V., and D.M. Frenkel, 1995, Phys. Rev. Lett. **74**, 3057.

Contreras, G., A.K. Sood and M. Cardona, 1985, Phys. Rev. B **32**, 930.

Cooper, S.L., and K.E. Gray, 1994, in: Physical Properties of High Temperature Superconductors, Vol. IV, ed. D.M. Ginsberg (World Scientific, Singapore) p. 61.

Cooper, S.L., and M.V. Klein, 1990, Comm. Condens. Matter Phys. **15**, 19.

Cooper, S.L., M.V. Klein, B.G. Pazol, J.P. Rice and D.M. Ginsberg, 1988a, Phys. Rev. B **37**, 5920.

Cooper, S.L., F. Slakey, M.V. Klein, J.P. Rice, E.D. Bukowski and D.M. Ginsberg, 1988b, Phys. Rev. B **38**, 11934.

Cooper, S.L., G.A. Thomas, A.J. Millis, P.E. Sulewski, J. Orenstein, D.H. Rapkine, S.-W. Cheong and P.L. Trevor, 1990, Phys. Rev. B **42**, 10785.

Cooper, S.L., P. Nyhus, D. Reznik, M.V. Klein, W.C. Lee, D.M. Ginsberg, B.W. Veal, A.P. Paulikas and B. Dabrowski, 1993a, Phys. Rev. Lett. **70**, 1533.

Cooper, S.L., D. Reznik, A.L. Kotz, M.A. Karlow, R. Liu, M.V. Klein, W.C. Lee, J. Giapintzakis, D.M. Ginsberg, B.W. Veal and A.P. Paulikas, 1993b, Phys. Rev. B **47**, 8233.

Cuden, C.B., 1976, Phys. Rev. B **13**, 1993.

Dagotto, E., 1994, Rev. Mod. Phys. **66**, 763.

Dalichaouch, Y., B.W. Lee, C.L. Seaman, J.T. Markert and M.B. Maple, 1990, Phys. Rev. Lett. **64**, 599.

Devereaux, T.P., 1992, Phys. Rev. B **45**, 12965.

Devereaux, T.P., 1993, Phys. Rev. B **47**, 5230.

Devereaux, T.P., 1995, Phys. Rev. Lett. **74**, 4313.

Devereaux, T.P., and D. Einzel, 1995, Phys. Rev. B **51**, 16336.

Devereaux, T.P., and D. Einzel, 1996a, Phys. Rev. B **54**, 15547(E).

Devereaux, T.P., and D. Einzel, 1996b, Phys. Rev. B **54**, 15548(E).

Devereaux, T.P., D. Einzel, B. Stadlober, R. Hackl, D.H. Leach and J.J. Neumeier, 1994a, Phys. Rev. Lett. **72**, 396.

Devereaux, T.P., D. Einzel, B. Stadlober and R. Hackl, 1994b, Phys. Rev. Lett. **72**, 3291.

Devereaux, T.P., A. Virosztek and A. Zawadowski, 1996, Phys. Rev. B **54**, 12523.

Dierker, S.B., M.V. Klein, G.W. Webb and Z. Fisk, 1983, Phys. Rev. Lett. **50**, 853.

Ding, H., J.C. Campuzano, K. Gofron, G. Gu, R. Liu, B.W. Veal and G. Jennings, 1994, Phys. Rev. B **50**, 1333.

Ding, H., T. Yokoya, J.C. Campuzano, T. Takahashi, M. Randeria, M.R. Norman, T. Mochiku, K. Kadowaki and J. Giapintzakis, 1996, Nature **382**, 51.

Donovan, S., J. Kircher, J. Karpinski, E. Kaldis and M. Cardona, 1995, J. Supercond. **8**, 417.

Dufour, P., S. Jandl, C. Thomsen, M. Cardona, B.M. Wanklyn and C. Changkang, 1995, Phys. Rev. B **51**, 1053.

Elliot, R.J., and M.F. Thorpe, 1969, J. Phys. C **2**, 1630.

Elliot, R.J., M.F. Thorpe, G.F. Inbusch, R. Loudon and J.B. Parkinson, 1968, Phys. Rev. Lett. **21**, 147.

Emery, V.J., and S.A. Kivelson, 1995, Phys. Rev. Lett. **74**, 3253.

Emery, V.J., S.A. Kivelson and O. Zachar, 1997, Phys. Rev. B **56**, 6120.

Falck, J.P., A. Levy, M.A. Kastner and R.J. Birgeneau, 1992, Phys. Rev. Lett. **69**, 1109.

Fal'kovskii, L.A., and S. Klama, 1990, Physica C **172**, 242.

Fleury, P.A., and H.J. Guggenheim, 1970, Phys. Rev. Lett. **24**, 1346.

Fleury, P.A., and R. Loudon, 1968, Phys. Rev. **166**, 514.

Fong, H.F., B. Keimer, D. Reznik, D.L. Milius and I.A. Aksay, 1995, Phys. Rev. Lett. **75**, 316.

Fong, H.F., B. Keimer, P.W. Anderson, D. Reznik, F. Dogan and I.A. Aksay, 1996, Phys. Rev. B **54**, 6708.

Freitas, P.J., and R.R.P. Singh, 2000, Phys. Rev. B **62**, 5525.

Gasparov, L.V., P. Lemmens, M. Brinkmann, N.N. Kolesnikov and G. Güntherodt, 1997, Phys. Rev. B **55**, 1223.

Gasparov, L.V., P. Lemmens, N.N. Kolesnikov and G. Güntherodt, 1998a, Physica B **244**, 54.

Gasparov, L.V., P. Lemmens, N.N. Kolesnikov and G. Güntherodt, 1998b, Phys. Rev. B **58**, 11753.

Ghiron, K., M.B. Salamon, B.W. Veal, A.P. Paulikas and J.W. Downey, 1992, Phys. Rev. B **46**, 5837.

Haas, S., E. Dagotto, J. Riera, R. Merlin and F. Nori, 1994, J. Appl. Phys. **75**, 6340.

Hackl, R., and R. Kaiser, 1988, J. Phys. C **21**, L453.

Hackl, R., R. Kaiser and S. Schicktanz, 1983, J. Phys. C **16**, 1729.

Hackl, R., W. Gläser, P. Müller, D. Einzel and K. Andres, 1988, Phys. Rev. B **38** 7133.

Hackl, R., R. Kaiser and W. Gläser, 1989, Physica C **162–164**, 431.

Hackl, R., M. Opel, P. Müller, G. Krug, B. Stadlober, R. Nemetschek, H. Berger and L. Forro, 1996, J. Low Temp. Phys. **105**, 733.

Hayden, S.M., G. Aeppli, H.A. Mook, T.G. Perring, T.E. Mason, S.-W. Cheong and Z. Fisk, 1996, Phys. Rev. Lett. **76**, 1344.

Hayes, W., and R. Loudon, 1978, Scattering of Light by Crystals (Wiley, New York).

Hewitt, K.C., T.P. Devereaux, X.K. Chen, X.-Z. Wang, J.G. Naeini, A.E. Curzon and J.C. Irwin, 1997, Phys. Rev. Lett. **78**, 4891.

Hewitt, K.C., N.L. Wang, J.C. Irwin, D.M. Pooke, A.E. Pantoja and H.J. Trodahl, 1999, Phys. Rev. B **60**, R9943.

Heyen, E.T., S.N. Rashkeev, I.I. Mazin, O.K. Andersen, R. Liu, M. Cardona and O. Jepsen, 1990, Phys. Rev. Lett. **65**, 3048.

Heyen, E.T., R. Wegerer, E. Schönherr and M. Cardona, 1991, Phys. Rev. B **44**, 10195.

Heyen, E.T., J. Kircher and M. Cardona, 1992, Phys. Rev. B **45**, 3037.

Hoffmann, A., P. Lemmens, G. Güntherodt, V. Thomas and K. Winzer, 1994, Physica C **235–240**, 1897.

Homes, C.C., T. Timusk, R. Liang, D.A. Bonn and W.N. Hardy, 1993, Phys. Rev. Lett. **71**, 1645.

Iliev, M., C. Thomsen, V. Hadjiev and M. Cardona, 1993, Phys. Rev. B **47**, 12341.

Ipatova, I.P., A.V. Subashiev and V.A. Voitenko, 1981, Solid State Commun. **37**, 893.

Itai, K., 1992, Phys. Rev. B **45**, 707.

Ito, T., Y. Nakamura, H. Takagi and S. Uchida, 1991, Physica C **185–189**, 1267.

Ito, T., K. Takenaka and S. Uchida, 1993, Phys. Rev. Lett. **70**, 3995.

Jandl, S., P. Dufour, T. Ruf, M. Cardona, V. Nekvasil, C. Chen and B.M. Wanklyn, 1995, Phys. Rev. B **52**, 15558.

Jiang, C., and J.P. Carbotte, 1995, Solid State Commun. **95**, 643.

Jongh, L.J., and R. Block, 1975, Physica B+C **79**, 568.

Kampf, A.P., and W. Brenig, 1992, Z. Phys. B **89**, 313.

Kang, M., G. Blumberg, M.V. Klein and N.N. Kolesnikov, 1996, Phys. Rev. Lett. **77**, 4434.

Kang, M., G. Blumberg, M.V. Klein and N.N. Kolesnikov, 1997, Phys. Rev. B **56**, R11427.

Karrai, K., E.-J. Choi, F. Dunmore, S. Liu, H.D. Drew, Q. Li, D.B. Fenner, Y.D. Zhu and F.-C. Zhang, 1992, Phys. Rev. Lett. **69**, 152.

Katsufuji, T., and Y. Tokura, 1994, Phys. Rev. B **49**, 4372.

Katsufuji, T., Y. Tokura, T. Ido and S. Uchida, 1993, Phys. Rev. B **48**, 16131.

Kendziora, C., and M. Onellion, 1997, Phys. Rev. Lett. **78**, 4892.

Kendziora, C., and A. Rosenberg, 1995, Phys. Rev. B **52**, R9867.
Kendziora, C., R. Kelley and M. Onellion, 1996, Phys. Rev. Lett. **77**, 727.
Khveshchenko, D.V., and P.B. Wiegmann, 1994, Phys. Rev. Lett. **73**, 500.
Kirillov, D., I. Bozovic, T.H. Geballe, A. Kapitulnik and D.B. Mitzi, 1988, Phys. Rev. B **38**, 11955.
Klein, M.V., 1975, in: Light Scattering in Solids, Vol. I, ed. M. Cardona, Vol. 8 of Topics in Applied Physics (Springer, Berlin) p. 147.
Klein, M.V., and S.B. Dierker, 1984, Phys. Rev. B **29**, 4976.
Klein, M.V., S.L. Cooper, F. Slakey, J.P. Rice, E.D. Bukowski and D.M. Ginsberg, 1989, in: Strong Correlations and Superconductivity, eds H. Fukuyama, S. Maekawa and A.P. Malozemoff (Springer, Berlin) p. 226.
Knoll, P., C. Thomsen, M. Cardona and P. Murugaraj, 1990, Phys. Rev. B **42**, 4842.
Kostur, V.N., 1992, Z. Phys. B **89**, 149.
Kosztin, J., and A. Zawadowski, 1991, Solid State Commun. **78**, 1029.
Kouznetsov, K.A., A.G. Sun, B. Chen, A.S. Katz, S.R. Bahcall, J. Clarke, R.C. Dynes, D.A. Gajewski, S.H. Han, M.B. Maple, J. Giapintzakis, J.-T. Kim and D.M. Ginsberg, 1997, Phys. Rev. Lett. **79**, 3050.
Krantz, M.C., 1996, Phys. Rev. B **54**, 1334.
Krantz, M.C., and M. Cardona, 1994, Phys. Rev. Lett. **72**, 3290.
Krantz, M.C., and M. Cardona, 1995, J. Low Temp. Phys. **99**, 205.
Krantz, M.C., H.J. Rosen, J.Y.T. Wei and D.E. Morris, 1989, Phys. Rev. B **40**, 2635.
Krantz, M.C., I.I. Mazin, D.H. Leach, W.Y. Lee and M. Cardona, 1995, Phys. Rev. B **51**, 5949.
Krol, D.M., M. Stavola, L.F. Schneemeyer, J.V. Waszczak and S.A. Sunshine, 1989, J. Opt. Soc. Am. B **6**, 448.
Kuiper, P., J.-H. Guo, C. Såthe, L.-C. Duda, J. Nordgren, J.J.M. Pothuizen, F.M.F. de Groot and G.A. Sawatzky, 1998, Phys. Rev. Lett. **80**, 5204.
Kumar, N., and A.M. Jayannavar, 1992, Phys. Rev. B **45**, 5001.
Lee, J.D., and B.I. Min, 1996, Solid State Commun. **99**, 627.
Leggett, A.J., 1998, J. Phys. Chem. Solids **59**, 1729.
Lei, X.L., J.L. Birman and C.S. Ting, 1985, Physica B **135**, 486.
Littlewood, P.B., and C.M. Varma, 1981, Phys. Rev. Lett. **47**, 811.
Littlewood, P.B., and C.M. Varma, 1982, Phys. Rev. B **26**, 4883.
Litvinchuk, A.P., C. Thomsen and M. Cardona, 1992, Solid State Commun. **83**, 343.
Liu, H.L., G. Blumberg, M.V. Klein, P. Guptasarma and D.G. Hinks, 1999, Phys. Rev. Lett. **82**, 3524.
Liu, R., D. Salamon, M.V. Klein, S.L. Cooper, W.C. Lee, S.-W. Cheong and D.M. Ginsberg, 1993a, Phys. Rev. Lett. **71**, 3709.
Liu, R., M.V. Klein, D. Salamon, S.L. Cooper, W.C. Lee, S.-W. Cheong and D.M. Ginsberg, 1993b, J. Phys. Chem. Solids **54**, 1347.
Loa, I., J. Hofmann and C. Thomsen, 1997, Phys. Status Solidi b **201**, R3.
Loeser, A.G., Z.-X. Shen, D.S. Dessau, D.S. Marshall, C.-H. Park, P. Fournier and A. Kapitulnik, 1996, Science **273**, 325.
Loram, J.W., K.A. Mirza, J.R. Cooper and W.Y. Liang, 1993, Phys. Rev. Lett. **71**, 1740.
Lorenzana, J., and G.A. Sawatzky, 1995a, Phys. Rev. Lett. **74**, 1867.
Lorenzana, J., and G.A. Sawatzky, 1995b, Phys. Rev. B **52**, 9576.
Lyons, K.B., S.H. Liou, M. Hong, H.S. Chen, J. Kwo and T.J. Negran, 1987, Phys. Rev. B **36**, 5592.
Lyons, K.B., P.A. Fleury, J.P. Remeika, A.S. Cooper and T.J. Negran, 1988a, Phys. Rev. B **37**, 2353.
Lyons, K.B., P.A. Fleury, L.F. Schneemeyer and J.V. Waszczak, 1988b, Phys. Rev. Lett. **60**, 732.
Lyons, K.B., P.A. Fleury, R.R.P. Singh and P.E. Sulewski, 1991, in: Dynamics of Magnetic Fluctuations in High Temperature Superconductors, eds G. Reiter, P. Horsch and G.C. Psaltakis (Plenum, New York) p. 159.
Mackenzie, A.P., S.R. Julian, G.G. Lonzarich, A. Carrington, S.D. Hughes, R.S. Liu and D.C. Sinclair, 1993, Phys. Rev. Lett. **71**, 1238.
Mackenzie, A.P., S.R. Julian, D.C. Sinclair and C.T. Lin, 1996, Phys. Rev. B **53**, 5848.
Maksimov, A.A., and I.I. Tartakovskii, 1994, J. Supercond. **7**, 439.
Manske, D., C.T. Rieck, R. Das Sharma, A. Bock and D. Fay, 1997, Phys. Rev. B **56**, R2940.
Manske, D., A. Bock, C.T. Rieck and D. Fay, 1998, Phys. Rev. B **58**, 8841.
Marshall, D.S., D.S. Dessau, A.G. Loeser, C.-H. Park, A.Y. Matsuvra, J.N. Eckstein, I. Bozovic, P. Fournier, A. Kapitulnik, W.E. Spicer and Z.-X. Shen, 1996, Phys. Rev. Lett. **76**, 4841.
Micnas, R., J. Ranninger, S. Robaszkiewicz and S. Tabor, 1988, Phys. Rev. B **37**, 9410.

Micnas, R., J. Ranninger and S. Robaszkiewicz, 1990, Rev. Mod. Phys. **62**, 113.

Mihailovic, D., K.F. McCarty and D.S. Ginley, 1993, Phys. Rev. B **47**, 8910.

Monien, H., and A. Zawadowski, 1990, Phys. Rev. B **41**, 8798.

Moriya, T., Y. Takahashi and K. Ueda, 1990, J. Phys. Soc. Japan **52**, 2905.

Morr, D.K., and A.V. Chubukov, 1997, Phys. Rev. B **56**, 9134.

Naeini, J.G., X.K. Chen, K.C. Hewitt, J.C. Irwin, T.P. Devereaux, M. Okuya, T. Kimura and K. Kishio, 1998, Phys. Rev. B **57**, R11077.

Naeini, J.G., X.K. Chen, J.C. Irwin, M. Okuya, T. Kimura and K. Kishio, 1999, Phys. Rev. B **59**, 9642.

Nagaosa, N., and P.A. Lee, 1990, Phys. Rev. Lett. **64**, 2450.

Nagaosa, N., and P.A. Lee, 1991, Phys. Rev. B **43**, 1233.

Nemetschek, R., O.V. Misochko, B. Stadlober and R. Hackl, 1993, Phys. Rev. B **47**, 3450.

Nemetschek, R., M. Opel, C. Hoffmann, P.F. Müller, R. Hackl, H. Berger, L. Forro, A. Erb and E. Walker, 1997, Phys. Rev. Lett. **78**, 4837.

Nori, F., E.R. Gagliano and S.B. Bacci, 1992, Phys. Rev. Lett. **68**, 240.

Nori, F., R. Merlin, S. Haas, A.W. Sandvik and E. Dagotto, 1995, Phys. Rev. Lett. **75**, 553.

Nyhus, P., M.A. Karlow, S.L. Cooper, B.W. Veal and A.P. Paulikas, 1994, Phys. Rev. B **50**, 13898.

Nyhus, P., S. Yoon, M. Kauffman, S.L. Cooper, Z. Fisk and J. Sarrao, 1997, Phys. Rev. B **56**, 2717.

Ohta, Y., T. Tohyama and S. Maekawa, 1991, Phys. Rev. Lett. **66**, 1228.

Opel, M., R. Nemetschek, C. Hoffmann, R. Philipp, P.F. Müller, R. Hackl, I. Tutto, A. Erb, B. Revaz, E. Walker, H. Berger and L. Forro, 2000, Phys. Rev. B **61**, 9752.

Orenstein, J., G.A. Thomas, A.J. Millis, S.L. Cooper, D.H. Rapkine, T. Timusk, L.F. Schneemeyer and J.V. Waszczak, 1990, Phys. Rev. B **42**, 6342.

Osofsky, M.S., R.J. Soulen, S.A. Wolf, J.M. Broto, H. Rakoto, J.C. Ousset, G. Coffe, S. Askenazy, P. Pari, I. Bozovic, J.N. Eckstein and G.F. Virshup, 1993, Phys. Rev. Lett. **71**, 2315.

Parkinson, J.B., 1969, J. Phys. C **2**, 2012.

Pennington, C.H., D.J. Durand, C.P. Slichter, J.P. Rice, E.D. Bukowski and D.M. Ginsberg, 1989, Phys. Rev. B **39**, 274.

Perkins, J.D., J.M. Graybeal, M.A. Kastner, R.J. Birgeneau, J.P. Falck and M. Greven, 1993, Phys. Rev. Lett. **71**, 1621.

Pines, D., 1963, Elementary Excitations in Solids (Addison-Wesley, Reading, MA).

Pines, D., 1997, Physica C **282–287**, 273.

Plakida, N.M., V.S. Oudovenko, P. Horsch and A.I. Liechtenstein, 1997, Phys. Rev. B **55**, R11997.

Podobedov, V.B., J.P. Rice, A. Weber and H.D. Drew, 1997, J. Supercond. **10**, 205.

Prelovsek, P., and J. Jaklic, 1996, Phys. Rev. B **53**, 15095.

Puchkov, A.V., D.N. Basov and T. Timusk, 1996, J. Phys.: Condens. Matter **8**, 10049.

Quilty, J.W., H.J. Trodahl and D.M. Pooke, 1998, Phys. Rev. B **57**, R11097.

Quilty, J.W., S. Tajima, S. Adachi and A. Yamanaka, 2001, Phys. Rev. B **63**, 100508(R).

Ranninger, J., and J.M. Robin, 1996, Phys. Rev. B **53**, R11961.

Rashkeev, S.N., and G. Wendin, 1993, Phys. Rev. B **47**, 11603.

Reznik, D., M.V. Klein, W.C. Lee, D.M. Ginsberg and S.-W. Cheong, 1992, Phys. Rev. B **46**, 11725.

Reznik, D., S.L. Cooper, M.V. Klein, W.C. Lee, D.M. Ginsberg, A.A. Maksimov, A.V. Puchkov, I.I. Tartakovskii and S.-W. Cheong, 1993, Phys. Rev. B **48**, 7624.

Rojo, A.G., and K. Levin, 1993, Phys. Rev. B **48**, 16861.

Rossat-Mignod, J., L.P. Regnault, C. Vettier, P. Burlet, J.Y. Henry and G. Lapertot, 1991, Physica B **169**, 58.

Rübhausen, M., N. Dieckmann, A. Bock, U. Merkt, W. Widder and H.F. Braun, 1996, Phys. Rev. B **53**, 8619.

Rübhausen, M., C.T. Rieck, N. Dieckmann, K.-O. Subke, A. Bock and U. Merkt, 1997, Phys. Rev. B **56**, 14797.

Rübhausen, M., P. Guptasarma, D.G. Hinks and M.V. Klein, 1998, Phys. Rev. B **58**, 3462.

Rübhausen, M., O.A. Hammerstein, A. Bock, U. Merkt, C.T. Rieck, P. Guptasarma, D.G. Hinks and M.V. Klein, 1999, Phys. Rev. Lett. **82**, 5349.

Ruf, T., C. Thomsen, R. Liu and M. Cardona, 1988, Phys. Rev. B **38**, 11985.

Ruf, T., E.T. Heyen, M. Cardona, J. Mesot and A. Furrer, 1992, Phys. Rev. B **46**, 11792.

Sacuto, A., R. Combescot, N. Bontemps, P. Monod, V. Viallet and D. Colson, 1997, Europhys. Lett. **39**, 207.

Sacuto, A., R. Combescot, N. Bontemps, C.A. Müller, V. Viallet and D. Colson, 1998, Phys. Rev. B **58**, 11721.

Sacuto, A., R. Combescot, N. Bontemps, C.A. Müller, V. Viallet and D. Colson, 1999, Phys. Rev. B **59**, 11605.

Sacuto, A., J. Cayssol, P. Monod and D. Colson, 2000, Phys. Rev. B **61**, 7122.

Salamon, D., R. Liu, M.V. Klein, M.A. Karlow, S.L. Cooper, S.-W. Cheong, W.C. Lee and D.M. Ginsberg, 1995, Phys. Rev. B **51**, 6617.

Salamon, D., P. Abbamonte, R. Liu, M.V. Klein, W.C. Lee, D.M. Ginsberg, I.I. Tartakovskii and B.W. Veal, 1996, Phys. Rev. B **53**, 886.

Sandvik, A.W., S. Capponi, D. Poilblanc and E. Dagotto, 1998, Phys. Rev. B **57**, 8478.

Sanjurjo, J.A., G.B. Martins, P.G. Pagliuso, E. Granado, I. Torriani, C. Rettori, S. Oseroff and Z. Fisk, 1995, Phys. Rev. B **51**, 1185.

Scalapino, D.J., 1995, Phys. Rep. **250**, 330.

Schönfeld, F., A.P. Kampf and E. Müller-Hartmann, 1997, Z. Phys. B **102**, 25.

Shastry, B.S., and B.I. Shraiman, 1990, Phys. Rev. Lett. **65**, 1068.

Shastry, B.S., and B.I. Shraiman, 1991, Int. J. Mod. Phys. B **5**, 365.

Shen, Z.-X., D.S. Dessau, B.O. Wells, D.M. King, W.E. Spicer, A.J. Arko, D.S. Marshall, L.W. Lombardo, A. Kapitulnik, P. Dickinson, S. Doniach, J. DiCarlo, A.G. Loeser and C.-H. Park, 1993, Phys. Rev. Lett. **70**, 1553.

Simon, M.E., A.A. Aligia, C.D. Batista, E.R. Gagliano and F. Lema, 1996, Phys. Rev. B **54**, R3780.

Singh, R.R.P., P.A. Fleury, K.B. Lyons and P.E. Sulewski, 1989, Phys. Rev. Lett. **62**, 2736.

Slakey, F., M.V. Klein, E.D. Bukowski and D.M. Ginsberg, 1990a, Phys. Rev. B **41**, 2109.

Slakey, F., M.V. Klein, J.P. Rice and D.M. Ginsberg, 1990b, Phys. Rev. B **42**, 2643.

Slakey, F., M.V. Klein, J.P. Rice and D.M. Ginsberg, 1991, Phys. Rev. B **43**, 3764.

Sokol, A., and D. Pines, 1993, Phys. Rev. Lett. **71**, 2813.

Sooryakumar, R., and M.V. Klein, 1980, Phys. Rev. Lett. **45**, 660.

Sooryakumar, R., and M.V. Klein, 1981, Phys. Rev. B **23**, 3213.

Stadlober, B., G. Krug, R. Nemetschek and R. Hackl, 1995, Phys. Rev. Lett. **74**, 4911.

Staufer, T., R. Nemetschek, R. Hackl, P. Müller and H. Veith, 1992, Phys. Rev. Lett. **68**, 1069.

Strohm, T., and M. Cardona, 1997a, Phys. Rev. B **55**, 12725.

Strohm, T., and M. Cardona, 1997b, Solid State Commun. **104**, 233.

Strohm, T., D. Munzar and M. Cardona, 1998, Phys. Rev. B **58**, 8839.

Struzhkin, V.V., A.F. Goncharov, H.K. Mao, R.J. Hemley, S.W. Moore, J.M. Graybeal, J. Sarrao and Z. Fisk, 2000, Phys. Rev. B **62**, 3895.

Sugai, S., 1989, Phys. Rev. B **39**, 4306.

Sugai, S., and Y. Hidaka, 1991, Phys. Rev. B **44**, 809.

Sugai, S., H. Takagi, S. Uchida and S. Tanaka, 1988, Jpn. J. Appl. Phys. **27**, L1290.

Sugai, S., Y. Enomoto and T. Murakami, 1989, Solid State Commun. **72**, 1193.

Sugai, S., M. Sato, T. Kobayashi, J. Akimitsu, T. Ho, H. Takagi, S. Uchida, S. Hosoya, T. Kajitani and T. Fukuda, 1990a, Phys. Rev. B **42**, 1045.

Sugai, S., M. Sato, T. Ito, T. Ido, H. Takagi, S. Uchida, T. Kobayashi, J. Akimitsu, Y. Hidaka, T. Murakami, S. Hosoya, T. Kajitani and T. Fukuda, 1990b, Physica B **165–166**, 1263.

Sulewski, P.E., P.A. Fleury, K.B. Lyons, S.-W. Cheong and Z. Fisk, 1990, Phys. Rev. B **41**, 225.

Sulewski, P.E., P.A. Fleury, K.B. Lyons and S.-W. Cheong, 1991, Phys. Rev. Lett. **67**, 3864.

Sun, A.G., D.A. Gajewski, M.B. Maple and R.C. Dynes, 1994, Phys. Rev. Lett. **72**, 2267.

Tajima, S., Y. Mizuo, M. Yoshida, T. Wada, Y. Yaegashi, T. Takata, M. Kagiya, N. Koshizuka, H. Uamauchi, K. Tamasaku and S. Uchida, 1993, Phys. Rev. B **47**, 12126.

Tanner, D.B., and T. Timusk, 1992, in: Physical Properties of High Temperature Superconductors, Vol. III, ed. D.M. Ginsberg (World Scientific, Singapore) p. 61.

Thomsen, C., 1991, in: Light Scattering in Solids. Vol. VI, eds M. Cardona and G. Güntherodt, Vol. 68 of Topics in Applied Physics (Springer, Berlin) p. 285.

Thomsen, C., and M. Cardona, 1989, in: Physical Properties of High Temperature Superconductors, Vol. I, ed. D.M. Ginsberg (World Scientific, Singapore) p. 409.

Thomsen, C., M. Cardona, B. Gegenheimer, R. Liu and A. Simon, 1988, Phys. Rev. B **37**, 9860.

Tinkham, M., 1975, Introduction to Superconductivity (McGraw-Hill, New York).

Tokura, Y., S. Koshihara, T. Arima, H. Takagi, S. Ishibashi, T. Ido and S. Uchida, 1990, Phys. Rev. B **41**, 11657.

Tomeno, I., M. Yoshida, K. Ikeda, K. Tai, K. Takamuku, N. Koshizuka, S. Tanaka, K. Oka and H. Unoki, 1991, Phys. Rev. B **43**, 3009.

Tranquada, J.M., D.J. Buttrey, V. Sachan and J.E. Lorenzo, 1994, Phys. Rev. Lett. **73**, 1003.

Tranquada, J.M., J.D. Axe, N. Ichikawa, Y. Nakamura, S. Uchida and B. Nachumi, 1996, Phys. Rev. B **54**, 7489.

Tsuei, C.C., J.R. Kirtley, C.C. Chi, L.S. Yu-Jahnes, A. Gupta, T. Shaw, J.Z. Sun and M.B. Ketchen, 1994, Phys. Rev. Lett. **73**, 593.

Tsuneto, T., 1960, Phys. Rev. **118**, 1029.

Uchida, S., T. Ido, H. Takagi, T. Arima, Y. Tokura and S. Tajima, 1991, Phys. Rev. B **43**, 7942.

van Harlingen, D.J., 1995, Rev. Mod. Phys. **67**, 515.

Varma, C.M., P.B. Littlewood, S. Schmitt-Rink, E. Abrahams and A.E. Ruckenstein, 1989, Phys. Rev. Lett. **63**, 1996.

Vekhter, I., J.P. Carbotte and E.J. Nicol, 1999, Phys. Rev. B **59**, 1417.

Virosztek, A., and J. Ruvalds, 1991, Phys. Rev. Lett. **67**, 1657.

Virosztek, A., and J. Ruvalds, 1992, Phys. Rev. B **45**, 347.

Wake, D.R., F. Slakey, M.V. Klein, J.P. Rice and D.M. Ginsberg, 1991, Phys. Rev. Lett. **67**, 3728.

Walstedt, R.E., W.W. Warren, R.F. Bell, R.J. Cava, G.P. Espinosa, L.F. Schneemeyer and J.V. Waszczak, 1990, Phys. Rev. B **41**, 9574.

Warren, W.W., R.E. Walstedt, G.F. Brennert, R.J. Cava, R. Tycko, R.F. Bell and G. Dabbagh, 1989, Phys. Rev. Lett. **62**, 1193.

Weber, W.H., and G.W. Ford, 1989, Phys. Rev. B **40**, 6890.

Wen, X.G., and P.A. Lee, 1996, Phys. Rev. Lett. **76**, 503.

Wen, X.G., F. Wilczek and A. Zee, 1989, Phys. Rev. B **39**, 11413.

Wenger, F., and M. Käll, 1997, Phys. Rev. B **55**, 97.

Wollman, D.A., D.J. van Harlingen, W.C. Lee, D.M. Ginsberg and A.J. Leggett, 1993, Phys. Rev. Lett. **71**, 2134.

Wu, D.H., J. Mao, S.N. Mao, J.L. Peng, X.X. Xi, T. Venkatesan, R.L. Greene and S.M. Anlage, 1993, Phys. Rev. Lett. **70**, 85.

Wu, W.C., and J.P. Carbotte, 1997, Phys. Rev. B **56**, 6327.

Wu, W.C., and J.P. Carbotte, 1998, Phys. Rev. B **57**, R5614.

Yamamoto, K., T. Katsufuji, T. Tanabe and Y. Tokura, 1998, Phys. Rev. Lett. **80**, 1493.

Yamanaka, A., T. Kimura, F. Minami, K. Inoue and S. Takekawa, 1988, Jpn. J. Appl. Phys. **27**, L1902.

Yoon, S., H.L. Liu, G. Schollerer, S.L. Cooper, P.D. Han, D.A. Payne, S.-W. Cheong and Z. Fisk, 1998, Phys. Rev. B **58**, 2795.

Yoon, S., M. Rübhausen, S.L. Cooper, K.H. Kim and S.-W. Cheong, 2000, Phys. Rev. Lett. **85**, 3297.

Yoshida, M., S. Tajima, N. Koshizuka, S. Tanaka, S. Uchida and T. Itoh, 1992, Phys. Rev. B **46**, 6505.

Zawadowski, A., 1990, in: Electronic Properties of High T_c Superconductors and Related Compounds, eds H. Kuzmany, M. Mehring and J. Fink (Springer, Berlin) p. 306.

Zawadowski, A., and M. Cardona, 1990, Phys. Rev. B **42**, 10732.

Zeyher, R., and G. Zwicknagel, 1990, Z. Phys. B **78**, 175.

Zha, Y., S.L. Cooper and D. Pines, 1996, Phys. Rev. B **53**, 8253.

Zhang, F.C., and T.M. Rice, 1988, Phys. Rev. B **37**, 3759.

Zhou, X., M. Cardona, D. Colson and V. Viallet, 1997, Physica C **282–287**, 1007.

Handbook on the Physics and Chemistry of Rare Earths
Vol. 31
edited by K.A. Gschneidner, Jr., L. Eyring and M.B. Maple

Chapter 204

CHARACTERIZATION OF CUPRATE SUPERCONDUCTORS USING TUNNELING SPECTRA AND SCANNING TUNNELING MICROSCOPY

Hiroharu SUGAWARA[a,c*], Tetsuya HASEGAWA[b,c] and Koichi KITAZAWA[a,c]
[a] *Department of Applied Chemistry and Department of Superconductivity, University of Tokyo, 7-3-1 Hongo, Bunkyo-ku, Tokyo 113-8656, Japan;* [b] *Materials and Structures Laboratory, Tokyo Institute of Technology, 4259 Nagatsutacho, Yokohama 226-8503, Japan;* [c] *Core Research for Exploratory Science and Technology (CREST), Japan Science and Technology Corporation (JST)*

Contents

* Present address: Department of Electronic Systems Engineering, Tokyo Metropolitan Institute of Technology, 6-6 Asahigaoka, Hino, Tokyo 191-0065, Japan.

Symbols

E_F	Fermi energy
$f(E)$	distribution function
e	electronic charge
$G(V)$	differential conductance at the bias voltage V [$= (dI/dV)_V$]
I_c	critical current
I_t	tunneling current
J	spin exchange energy
j	current density
j_c	critical current density
$\vec{k}$	wavevector of electron
k_B	Boltzmann's constant
$N(0)$	density of states at the Fermi energy
$N(E)$	density of states at the energy E above the Fermi energy
n	carrier density
p	hole concentration per CuO_2 unit
p_F	momentum at Fermi energy
R_N	electrical resistivity in normal state
R_t	tunneling resistance
T	temperature
T_B	temperature below which the charge carriers pair up
T_c	superconducting transition temperature
T_{RVB}	temperature below which RVB state is obtained to result in anomalous metallic state
T^*	temperature below which a gap is thought to be open up in the spin excitation spectrum
T_0, T_m	temperature below which various properties show anomaly in view of the Fermi liquid
t	reduced temperature ($= T/T_c$)
t	transfer energy in t–J model
V_B	bias voltage
V_{sample}	sample voltage
V_{tip}	tip voltage
Γ	lifetime of quasiparticle
Δ	superconducting gap
$\Delta(\vec{k})$	superconducting gap along the direction of $\vec{k}$
Δ_{pp}	superconducting gap value defined peak-to-peak
$\Delta(T)$	superconducting gap at temperature T
Φ	magnetic flux density of phonon states
Φ_0	magnetic flux quanta
$\sigma(E)$	tunneling conductance of quasiparticles at the energy E above the Fermi energy
ξ	coherence length
χ	magnetic susceptibility

Acronyms

AF	antiferromagnetic (phase or region)
AM	anomalous metal (region)
ARPES	angle resolved photoemission spectroscopy
BCS	Bardeen–Cooper–Schrieffer
Bi2212	$Bi_2Sr_2CaCu_2O_{8+\delta}$
BTK	Blonder–Tinkham–Klapwijk (formula)
DOS	density of states
FL	Fermi liquid
HTSC	high temperature superconductor(s)
ITJ	intrinsic Josephson (tunneling) junctions
La214	$La_{2-x}Sr_xCuO_4$
NIN	normal metal–insulator–normal metal (junction)
NMR	nuclear magnetic resonance
PES	photoemission spectroscopy
RVB	resonating valence band
SC	superconducting (region/phase)
SG	spin gap (region)
SIN	superconductor–insulator–normal metal (junction)
SIS	superconductor–insulator–superconductor (junction)
SQUID	superconducting quantum interference device

STM	scanning tunneling microscope (microscopy)	UHV	ultrahigh vacuum
		Y123	$YBa_2Cu_3O_y$
STS	scanning tunneling spectroscopy	ZBCP	zero-bias conductance peak
Tl2223	$Tl_2Ba_2Ca_2Cu_3O_{10+\delta}$	ZES	zero-energy states

1. Introduction

Tunneling spectroscopy is a powerful tool for exploring density of states near the Fermi level from measurements of the tunneling current versus the voltage between the sample and the counter metal electrode. Its energy resolution ($\lesssim$1 meV) is higher than any other techniques, which is crucial for the experimental determination of the gap structures of superconductors. It has been quite successful for conventional superconductors: it proved the BCS mechanism for these materials and described the fine structures outside the gap edges on the basis of the electron–phonon interaction.

This technique was expected to be useful also for the oxide high-critical-temperature superconductors (HTSC). A number of results have been reported so far, though their usefulness was rather limited compared to conventional superconductors because of the difficulty in obtaining an ideal tunneling junction on HTSC, which exhibit extremely short coherence lengths and inhomogeneous electronic structures. Tunneling results published in the early years after the discovery of HTSC were poorly reproducible, and there was little agreement as to which features were real in the superconducting gap spectra. Through efforts towards achieving better-characterized specimen and junctions, tunneling results have been converging, except for the details, in the last several years. This situation has been reviewed in several articles, e.g. Hasegawa et al. (1992a).

At that time, the most important agreement was about the size of the superconducting gap. The superconducting gap values Δ are in the extremely strong coupling regime with reduced gap parameters $2\Delta/k_B T_c \approx 6$–$9$ (optimal carrier density), compared to the BCS weak coupling value of 3.52. The BCS theory and its modified version were adopted to fit the spectra, though they failed to elucidate this large coupling strength.

The observed tunneling spectra exhibited strange features. The differential conductance (dI/dV) inside the gap is finite, and sometimes even a peak appears (zero-bias anomaly). Various energy dependences, including linear and parabolic functions, were often observed for the background spectra outside the gap region. The origins of these features have been argued to be characteristic properties of these materials, though no clear answer was given.

With the advent of cryogenic scanning tunneling microscopy (STM) it became possible to achieve vacuum tunneling gap conditions between sample and counter electrode, and to achieve atomic resolution on the surfaces of these materials. Vacuum tunneling is considered to be the best experimental situation, because it can avoid chemical reactions on the interface between the specimen and the insulating layer. In parallel to the above advancement, various physical properties of these materials have been intensively investigated, and many unique features of HTSC have been revealed.

Above all, an order parameter other than s-wave symmetry has been argued for intensively in order to explain the experimental results from, e.g., NMR, penetration depth, specific heat, neutron scattering, and phase-sensitive SQUID measurements. Up to now, it seems that the argument has been converging to consider that the symmetry of the order parameter in these materials essentially has d-wave symmetry.

Also, tunneling data have been discussed in the framework of unconventional pairing, and theoretical models have also been rewritten. It is claimed that several features such as the zero-bias anomaly observed in transverse geometry are indications of $d_{x^2-y^2}$-wave symmetry of the order parameter (see sec. 6), while some of the latest investigations on $YBa_2Cu_3O_y$ show the admixture of s- and d-waves.

It is also noted that an anomalous energy gap, now called the "pseudogap", opens up in HTSC above T_c. Tunneling spectroscopy has been one of the major tools for characterizing the pseudogap, which has added another mystery to the HTSC (see sec. 5.2).

In this chapter, tunneling results published in the past several years are discussed with emphasis on STM results on $Bi_2Sr_2CaCu_2O_y$ (Bi2212) and $YBa_2Cu_3O_y$ (Y123), the most intensively investigated HTSC compounds. The theoretical description and predictions closely related to the anisotropic superconductors are also examined. Following the comparison of various junction fabrication methods in sect. 2, characterizations of tunneling junctions by STM images are given. Superconducting spectra are then discussed from various viewpoints, and finally recent results on vortex imaging and phase-sensitive experiments are reviewed.

2. Various junction structures

Tunneling spectroscopy is quite sensitive to the local electronic states formed at the surface. Therefore, the surface condition should be carefully examined. Unfortunately, the surface of oxide superconductors can readily be deteriorated in ambient atmosphere. It is pointed out that some of the Cu-based high-T_c superconductors lose oxygen easily, and an O-deficient surface region can be formed when the surface is exposed to an ambient low O_2 partial pressure. It then loses its superconducting properties. The extent of the problem depends on the HTSC material itself. The problem is very severe in Y123, because of the large mobility of oxygen. On the other hand, Bi2212 compounds do not easily lose oxygen on the cleaved surface, although they are sensitive to electron-beam irradiation of the surface for incident-electron energies between 1 and 2 keV (Balzarotti et al. 1991).

The surface nonstoichiometry has made it very difficult to use inherently surface-sensitive analytical techniques like tunneling measurements, thus one should be always reminded that the surface electronic properties may be different from those of the bulk.

2.1. *Artificial junctions for tunneling measurements*

The fabrication of the tunneling junction is an important experimental step in obtaining reliable measurements. The following four methods have been attempted for oxide superconductors:

(1) Planar-type junction. An artificial insulating layer and a conducting layer (as a counter electrode) are deposited successively on the sample surface.
(2) Point contact. A metal tip is pushed onto the sample surface. The native insulating layer either on the tip or the sample is used. The Schottky barrier formed at the interface can be used as well when a heavily doped semiconductor is used as the tip material.
(3) Break junction. The sample is mechanically broken into two pieces, which are then brought close to each other so that a tunneling current is observed. In this geometry, both electrodes are the same superconductors, and hence Josephson tunneling is expected.
(4) Scanning Tunneling Microscope. This is similar to the case of the point contact if the tip is in contact with the sample surface. However, the best performance is expected in the "vacuum" tunneling mode where the tunneling tip does not touch the sample surface. When the tip apex is composed of several atoms, tunneling takes place in a limited area on the surface, and a topographic image can be obtained by rastering the tip position on the sample surface.

The planar-type junction and point-contact methods were first attempted on the HTSC. The reproducibility, however, was poor, and hence the results obtained by these methods need justification by the other methods.

If a planar-type junction is ideally fabricated, it should be suited especially for performing measuring with high energy resolution and for measuring temperature dependence, because of the stability of the insulating layer.

While the native oxide layer on conventional metal superconductors passivates the surface, this is not the case for HTSC. A short-circuit in a native or artificial insulating layer has been considered to be responsible for the appearance of zero-bias peaks accompanied by the proximity effect. Mechanical damage at the interface may also create small particles, causing a charging effect, which then gives rise to various spurious features in the spectrum such as multi-peak conductance. Another difficulty in point-contact methods is the arbitrariness of the results due to the dependence on the contact pressure.

Nevertheless, macrojunctions, e.g. between Pb and Y123, have been claimed to be successful, and are extensively used for some phase-sensitive measurements. It is also reported that good-quality planar junctions can be formed by atomic-layer epitaxial growth (Matsumoto et al. 1995).

The break junction technique is also useful to acquire a clean interface, when the breakage is performed *in situ* in vacuum. Nevertheless, the resulting interface may be fractured into many pieces or into stepped structures, so one should be careful to check whether the momentum conservation is preserved or not.

Contrary to the above techniques, a better junction quality seems to have been obtained with relative easiness by STM, because virtually no additional surface treatment is required. However, the application of this method is, in general, limited to easy-cleavage planes, or to natural as-grown surfaces.

2.2. *Intrinsic Josephson junctions*

The cuprate superconductors have layered structures in which, it has been pointed out, Josephson junctions are built within the layered structure itself. In Bi2212, each of the CuO_2 bilayers stacking with a period of 1.5 nm acts as a pair of superconductor electrodes separated by an insulating layer.

The formation of built-in Josephson junctions or *intrinsic Josephson junctions* (ITJ) along the *c*-axis in Bi2212 was claimed by Kleiner et al. (1992) and Kleiner and Müller (1994), who performed microwave emission experiments in small single crystals.

Measurements of tunneling currents parallel to ITJ were then attempted for Bi2212 and $Tl_2Ba_2Ca_2Cu_3O_{10+\delta}$ (Tl2223). In earlier measurements using large and many (typically 1000) junctions, no gap structure was observed, possibly due to heating effects, in the current–voltage characteristics. A clear gap structure has been observed only with small and thin junctions in which a large tunneling current density can be achieved and heating effects can be eliminated (Kleiner et al. 1992, Kleiner and Müller 1994).

The I–V characteristics of small stacked junctions of underdoped Bi2212 single crystals were investigated by Tanabe et al. (1996). The I–V characteristic of an intrinsic junction stack exhibits a superconducting branch and a large number of branches in the resistive state. This structure can be explained by assuming that the I–V characteristic of every individual junction exhibits a superconducting and a resistive branch, similar to the I–V characteristics of standard Josephson junctions.

As shown in fig. 1, for a small bias current just above the critical current I_c, the junction exhibits a periodic voltage jump. For a large bias current, larger hysteresis and negative resistance were observed.

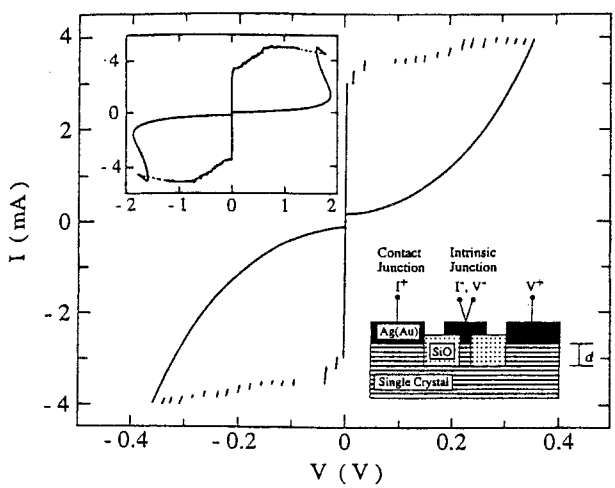

Fig. 1. I–V characteristics of a 300 nm thick junction stack at 11 K. The inset shows the curve for a larger bias current. The critical current density j_c is 750–1250 A/m^2. The schematic cross-sectional view of the junction stacks is also shown. After Tanabe et al. (1996, fig. 1).

The voltage jump V_j was found to be independent of the junction thickness and was 15–20 mV. A quite similar value was reported by Kleiner et al. (1992) and Kleiner and Müller (1994), and Schlenga et al. (1996, 1998) observed voltage jumps of about 22 mV in Bi2212 and about 23 mV in $Tl_2Ba_2Ca_2Cu_3O_{10+\delta}$. The interval V_j of the step voltage was about 50% of the gap width (2Δ) of Bi2212 observed by photoemission and other tunneling methods. Tanabe et al. (1996) attributed the effect of gap suppression primarily to nonequilibrium superconductivity.

The value I_cR_N is a measure of the superconducting gap Δ because the relation $I_cR_N = \pi\Delta/2e$ holds for a conventional energy gap. The I_cR_N product turns out to be about 5 mV, which is less than 20% of the maximum energy gap Δ_0/e.

It is pointed out that the current–voltage characteristics below the gap are consistent with tunneling into d-wave superconductors. The tunneling quasiparticle current $I(V)$ is calculated using the expression

$$I(V) = \frac{1}{R_N}\int_{-\infty}^{\infty} N(E)N(E-eV)(f(E-eV)-f(E)), \tag{1}$$

where the normalized quasiparticle density of states $N(E)$ for tunneling along the c-axis is given by

$$N(E) = \mathrm{Re}\int_0^{2\pi}\left[\frac{E}{\sqrt{E^2-\Delta^2(\theta)}}\right]. \tag{2}$$

The I–V characteristic calculated based on a d-wave order parameter,

$$\Delta(\theta) = \Delta_0\cos(2\theta), \tag{3}$$

was in good agreement with the experimental results well below the gap, except for a deviation seen near the gap voltage. Inside the gap, dI/dV is proportional to V^2, which was claimed to be consistent with d-wave symmetry.

Schlenga et al. (1996, 1998) reported the observation of subgap structures in I–V characteristics in step-edge junctions of $Tl_2Ba_2Ca_2Cu_2O_{10+\delta}$ and Bi2212. Well below the gap value $\simeq$50 mV, the quasiparticle branch exhibits pronounced subgap structures, which were reported also by Yurgens et al. (1996). These structures were investigated as a function of several parameters such as temperature, direction and magnitude of applied magnetic field, and thickness of the junctions. Schlenga et al. claimed that the subgap structure was best explained by a resonant coupling mechanism between infrared-active optical c-axis phonons and an oscillating Josephson current proposed by Helm et al. (1997).

3. Electronic phase diagram and tunneling process

3.1. *Electronic phase diagram*

3.1.1. *Electronic phase diagram and pseudogap*

It has become increasingly important to understand the anomalous metallic state in order to understand the HTSC mechanism. Above all, the understanding of the pseudogap behavior in the hole-concentration vs. temperature phase diagram seems to be a key issue.

The parent compounds of cuprate superconductors, which do not possess any holes, are antiferromagnetic insulators with a localized spin on each Cu site. Upon hole doping, which introduces holes mainly into the O 2p orbitals, the electronic system as a whole becomes mobile and metallic. The hole density p needs to be about 0.02 per CuO_2 unit to destroy the long-range order of antiferromagnetism, and about 0.05 to induce the insulator-to-metal transition. Superconductivity also appears, starting at this composition, and T_c reaches a maximum at $p = 0.15$, decreases again, and finally disappears at $p = 0.28$, as shown in fig. 2. The same p–T_c dependence has been observed among all the cuprate superconductors.

Many anomalous features deviating from Fermi-liquid behavior have been found in the region $p < 0.28$; these are called the "abnormal normal properties". The superconducting region in the p–T phase diagram is located in the low-temperature region of the "abnormal normal region", suggesting that high-temperature superconductivity manifests itself on this background.

It has been experimentally revealed that the p–T phase diagram includes two additional pseudo-boundary lines, T^* and T_0, as shown in fig. 2. The former was introduced initially as the line below which an energy gap seems to open up in the spin excitation, while the T_0 line was defined as the temperature at which the static magnetic susceptibility χ exhibits a broad maximum, χ_{max}. The χ–T curve was reported to be scaled well by χ_{max}

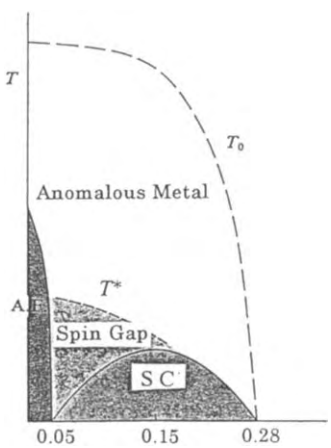

Fig. 2. Commonly observed electronic phase diagram of the high-temperature superconductors. The superconducting (SC) region spreads over the hole concentration p per CuO_2 unit from 0.05 to 0.28, showing the maximum T_c at 0.15. Below $p = 0.02$, the antiferromagnetic (AF) phase is obtained. T_0 is the temperature below which various properties show anomalies with respect to the Fermi liquid, while below T^* a gap is thought to open up in the spin excitation spectrum.

and T_0 by Johnston (1989) and Nakano et al. (1994). Up to now the precise locations of the two lines are controversial, and besides it is not clear whether the two lines are independent or they just indicate a broad cross-over zone between them. In this context, the abnormal properties start being observed below T_0 and more clearly below T^*.

3.1.2. *Spin gap and pseudogap*

The concept of the resonating valence bond (RVB) proposed by Anderson (1987) has stirred a great interest in the HTSC electronic structure. Anderson proposed that in the nearly half-filled band of strongly correlated electronic systems the electrons form spin-singlet pairs, leaving two types of quasiparticles; holons (charge) and spinons (spin). Suzumura et al. (1988) presented an electronic phase diagram, as shown in fig. 3, based on the t–J model, predicting T^* as the spin gap line prior to the experimental findings. It was described that below T_c holons also pair up, creating Cooper pairs.

Nagaosa and Lee (1990) introduced a gauge theory to relate the dynamics of holons and spinons and explained many of the "abnormal normal properties" observed experimentally by then, hence providing support to the RVB approach.

It was Yasuoka et al. (1989) who suggested for the first time the presence of the "spin gap" based on experiment. They observed a sharp increase in the nuclear spin relaxation lifetime below T^* ($T^* > T_c$) in the underdoped region. This was attributed to the opening of a "spin gap". They presumed that the spin freedom of electrons dies down below T^*. Alloul et al. (1989) soon also assumed the spin gap from NMR Knight shift measurements.

The existence of the spin gap was then more directly observed in neutron inelastic scattering spectra by Rossat-Mignod et al. (1991).

As early as 1988, Ikuta et al. (1988) observed, with a point-contact junction, an energy-gap-like feature similar to the superconducting gap even up to room temperature in the tunneling spectra.

It was Takagi et al. (1992) and then Nakamura and Uchida (1993) who noticed that the resistivity–temperature curve deviates from linearity and starts decreasing sharper towards lower temperatures below T^*. More recent results were summarized by Nakano et al. (1994).

On the other hand, Nishikawa et al. (1994) and Hwang et al. (1994) pointed out that the Hall coefficient starts deviating from typically metallic at T_0, as they tagged it, which was

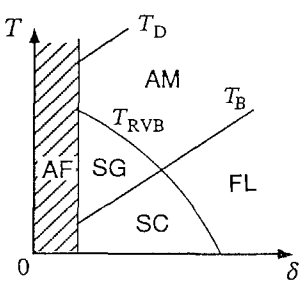

Fig. 3. An electronic phase diagram predicted by the t–J model based on a mean-field slave boson approximation (Fukuyama diagram). AF: antiferromagnetic region, AM: anomalous metal region, SG: spin gap region, SC: superconducting region, and FL: Fermi-liquid region. Below T_{RVB} the spin gap appears, while below T_B the charge carriers, i.e. holons, pair up. T_B is the temperature below which a uniform RVB state is obtained, resulting in an anomalous metallic state.

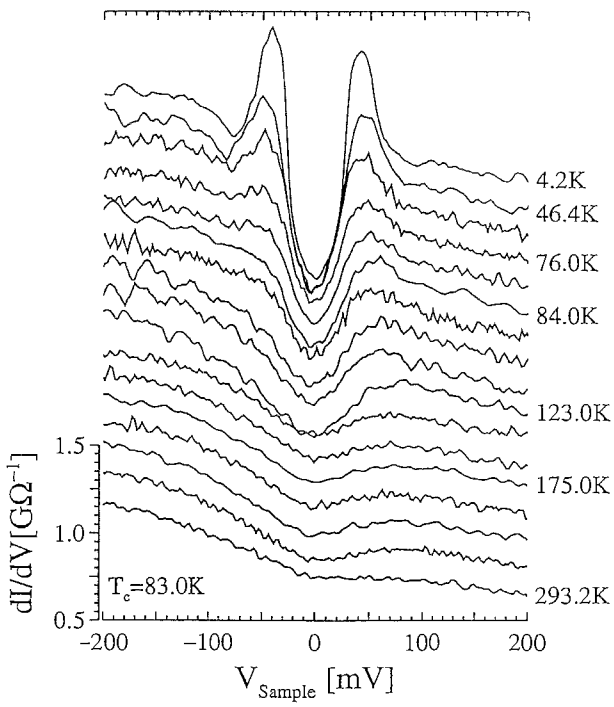

Fig. 4. Tunneling spectra of the basal plane of under-doped Bi2212 with $T_c = 83$ K at various temperatures. After Renner et al. (1998a, fig. 2).

much higher than T^*, in correspondence with the temperature where the static magnetic susceptibility had been reported to show a broad maximum. Tallon et al. (1995) reported that thermoelectric power also showed the anomaly below T_0.

From specific-heat measurements, Loram et al. (1993, 1994) observed an anomalous decrease in the electronic entropy at a much higher temperature than T^* as well. According to them, however, the magnitude of entropy loss with decreasing T was larger than that expected from the formation of a spin gap, and hence some of the charge freedom had to be lost.

Optical measurements are thought to sense charge excitation, but to be insensitive to the spin excitation. The presence of a charge gap was supported by Slakey et al. (1990), Homes et al. (1993) and Schlesinger (1994), while these observations have been disputed by Tajima et al. (1996) and by Basov et al. (1996) from their experimental studies.

Recent STM tunneling results by Renner and Fischer (1995) and Renner et al. (1998a) have shown that the gap structure persists above T_c and even near room temperature. Besides, the gap-like structure did not exhibit a large change across T_c, but just grew continuously, as shown in fig. 4. Surprisingly, they also observed a nearly T-independent size, not only for the pseudogap in the normal region, but for the superconducting gap as well. They also succeeded in observing the vortex core for the first time by STM in the high-

temperature superconductors (see sect. 5.4). In the case of Bi2212, they observed a gap-like structure in the vortex core which was similar to that of the pseudogap. Hence, they attributed the observed gap to the persistence of the pseudogap in the vortex-core region.

As described above, there have been abundant results indicating the presence of some kind of energy gap which may be called either the pseudogap or the spin gap. Although the temperatures T_0 and T^* below which the anomalies are noticed are not well defined, they both exhibit a similar dependence upon the carrier density, i.e., going up as the carrier density decreases into the underdoped regime, as summarized by Nakano et al. (1994).

The observation of the pseudogap has been mostly limited to the underdoped region, although some studies, especially performed by tunneling spectroscopy and specific heat on Bi2212, did report the extension of the pseudogap into the overdoped region. On the other hand, the T_0 curve has been reported to be extending deep into the overdoped region not only in Bi2212 but also in Y123.

3.1.3. *Energy and temperature scales of the pseudogap*

As results accumulated, it was a matter of concern how the characteristic temperatures T^*, T_0 and T_c, as well as the gap energy Δ, relate to each other, and how they depend on the carrier density. Although controversies still remain, it is interesting to note that T_c does not scale either with T^* or T_0. On the other hand, the latter two temperatures seem to rise in the underdoped region, while T_c falls. Another important indication is that the gap energy Δ remains rather constant as the temperature changes. Besides, Δ does not scale with T_c, which it does for a BCS superconductor as $2\Delta/k_B T_c = 3.52$.

Oda et al. (1997a), who examined the details of the tunneling spectra and other transport and magnetic susceptibility results on Bi2212 (fig. 5), have pointed out that Δ rather closely scales with T^* and T_0. They claimed that $2\Delta/k_B T^*$ is 4 to 5, which is close to the predicted value for BCS d-wave pairing. According to them, T^* and T_0 are also related as T_0/T^* being nearly equal to 2 for Bi2212. It is rather surprising that the gap energy in the superconducting state scales with T^* or T_0, which are characteristic quantities in the normal state, but not with T_c.

However, experimental results are still contradicting each other in a quantitative sense, and hence reliability of the results must be examined critically. To start with, it is not experimentally clear whether T^* and T_0 are independent. Some interpret T_0 as the initiation of short-range antiferromagnetic correlation, while others claim it to be the temperature where superconducting Cooper pairs are pre-formed. On the other hand, T^* has been interpreted as the spin-gap temperature by some, while it is also claimed to be the temperature where long-range antiferromagnetic correlation grows but fluctuates.

The region with pre-formed pairs is the "superconducting" region, but without phase coherence. Only after the development of phase coherence is the "zero-resistivity" superconducting state brought about. Hence, the abnormal metallic region is thought to be the phase-fluctuation region of superconductivity. The extremely large fluctuation is attributed to the low-dimensional structure.

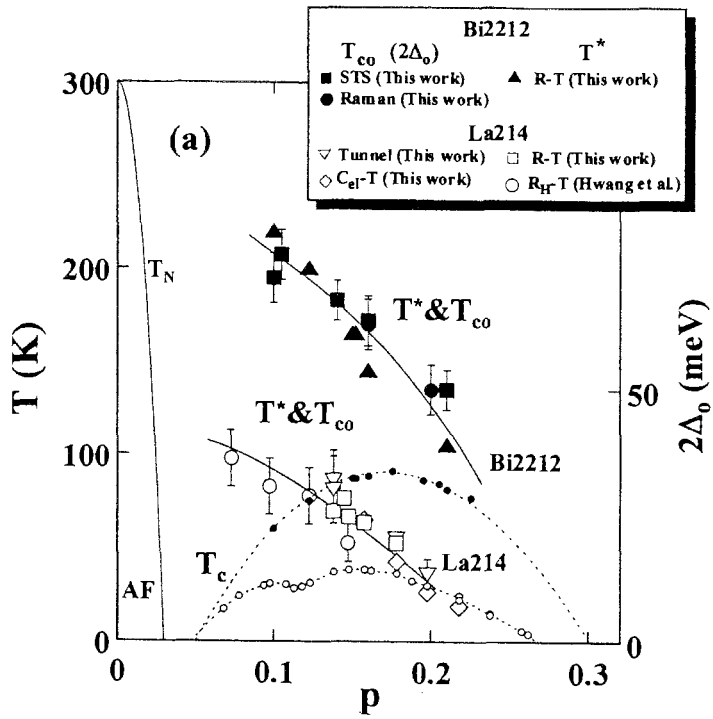

Fig. 5. Dependence of T_c, T_0 (or T_m) and T^* for La214 and for Bi2212, respectively. Data from Hwang et al. (1994) and Momono et al. (1999). After Momono et al. (1999, fig. 2a).

Another idea is that the antiferromagnetic correlation sets in at T_0 and the system becomes abnormal. At a further, lower temperature T^*, especially in the underdoped region, the long-range order develops. This may compete with or assist in the manifestation of superconductivity. Some even think that the antiferromagnetically ordered regions form stripes alternated with non-ordered conducting regions.

The tunneling spectrum in any case is expected to exhibit a gap anomaly below T_0 and more clearly below T^*. It is hence highly important to further understand the nature of the pseudogap region in order to elucidate the superconducting mechanism. Tunneling measurements should be able to give the most precise information about the change in the gap feature with temperature and carrier density.

3.1.4. *Anisotropy of the pseudogap*

Differing from the conventional s-wave superconductors, the symmetry of the Cooper pair in the HTSC has been established by now to be of d-wave symmetry. Its angular dependence was determined by ARPES (angle-resolved photoemission spectroscopy) to be $d_{x^2-y^2}$ by Loeser et al. (1996) and (Ding et al. 1996). Furthermore, they have observed that the pseudogap above T_c also possesses $d_{x^2-y^2}$ symmetry. These results

make it tempting to assume that the mechanisms of creating the pseudogap and creating superconductivity are similar in origin.

According to recent ARPES measurements, the pseudogap opens on the Fermi surface near $\vec{k} = (\pi, 0)$ or $(0, \pi)$, called the "hot spots", while the surface near $(\frac{1}{2}\pi, \frac{1}{2}\pi)$ remains unchanged, "cold spots", in accordance with $d_{x^2-y^2}$ symmetry.

3.2. *Tunneling process*

Let us consider electron tunneling through a metal (sample M1)–insulator (I)–metal (sample M2) interface, where the x and y-axes are defined parallel to the interface plane and the z-axis perpendicular to it. For simplicity, M2 is assumed to be an ideal metal with a spherical Fermi surface.

If the interface planes are ideally flat, the wavenumbers of the tunneling electrons parallel to the plane, k_x, k_y, are conserved. In this case, referred to as "specular tunneling", the M1–I–M2 tunneling mainly senses the excitation spectrum $N(\sim E_F, k_z)$ of the sample with k_z, because the tunneling decay length is proportional to $\sqrt{k_z}$. Thus, by fabricating tunnel junctions on different crystallographic specimens, the momentum dependence of $N(E, \vec{k})$ can be probed.

If the interface has roughness of the order of the mean free path, the tunneling electrons are scattered at the interface (diffusive tunneling), and the resultant tunneling spectrum is momentum-averaged, approximately equivalent to the density of states $N(E)$. It seems that most of the tunneling processes through planar-type junctions on HTSC are close to the diffusive limit, so that anisotropy in the excitation spectrum can hardly be detected.

In scanning tunneling spectroscopy (STS), on the other hand, the lateral (x, y) locations of tunneling electrons are established with an inaccuracy of the same order as the spatial resolution of STM, $\Delta x, \Delta y < 1$ nm. Thus, the obtained tunneling spectrum, in principle, suffers from averaging in the momentum space $\Sigma w(\vec{k}) N(E, \vec{k})$, with an appropriate weight $w(\vec{k})$, which is determined by the shape of the tip apex.

Once the specimen turns to a superconducting state, the obtained superconductor–insulator–normal metal (SIN) spectrum probes the quasiparticle excitation in the superconductor, which directly reflects the symmetry of the order parameter $\Delta(\vec{k})$. If $\Delta(\vec{k})$ has simple s-wave symmetry, as is realized in conventional low-temperature superconductors, one expects a finite gap of Δ with overshooting peaks just outside the gap in $N(E)$, as illustrated in fig. 6. Even if $\Delta(\vec{k})$ possesses anisotropic s-wave symmetry, a finite gap, corresponding to the minimum gap, appears. In $d_{x^2-y^2}$ superconductors with $\Delta(\vec{k}) = \cos 2k_x - \cos 2k_y$, in contrast, $N(E)$ is gapless with linear $N(E)$ for $E \ll \Delta$. It is noted that the extended-s wave $\Delta(\vec{k}) = \cos 2k_x + \cos 2k_y$ is also characterized to possess a gapless feature with two singularities at $E = \Delta_1$ and Δ_2.

As has been pointed out by several groups, the tunneling matrix element M, which is the prefactor in the expression for the tunneling current, is also an important factor to determine the shape of gap structures in the STS tunneling spectrum of HTSC. Since HTSC possess highly directional covalent bonds, the tunneling probability is substantially dependent on the shape of the atomic orbital, to or from which the conduction electrons

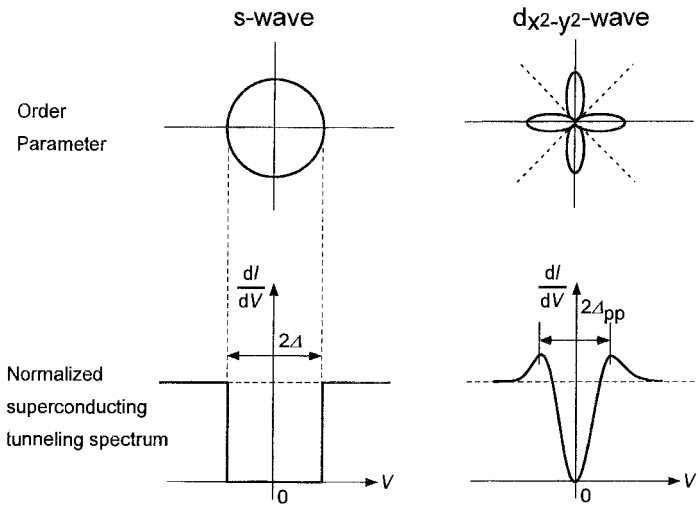

Fig. 6. Differential conductance spectra expected for the tunneling from normal metal to superconductor with s-wave symmetry and d-wave symmetry.

tunnel. Accordingly, if the tunneling current dominantly flows along a specific direction, the tunneling spectrum is mainly contributed from $N(E,\vec{k})$ for that direction (directional tunneling). Therefore, it is possible that STS tunneling spectroscopy sees a finite gap even in a $d_{x^2-y^2}$-wave superconductor, if the tunneling electrons flow along the Cu–O direction, in which $\Delta_{x^2-y^2}(\vec{k})$ is maximized.

4. Characterization of surface by STM

Little consensus about features of tunneling spectra has emerged until recently, in spite of the fact that many tunneling spectra have been reported for Bi2212 (J.-X. Liu et al. 1991, Hasegawa et al. 1991b, Chang et al. 1992, Ichimura and Nomura 1993, J. Liu et al. 1994, Wolf et al. 1994, Renner and Fischer 1995, Murakami and Aoki 1995, Oda et al. 1996, Mallet et al. 1996) and Y123 (Valles et al. 1991, Edwards et al. 1992, Miller et al. 1993, Nantoh et al. 1994, Maggio-Aprile et al. 1995). Various types of superconducting gap structures, as well as background (outside the gap) shapes, have been reported. Although the situation is quite complicated, it is reasonable to assume that the wide variety of results reported is due to the wide variety of physical and chemical conditions of the surfaces, insulating layer, and counter metal electrode, as well as bulk properties of specimen. In order to examine these results, one should carefully take the experimental conditions into account.

On the other hand, STM is a powerful tool to investigate the tunneling spectra from this viewpoint, because a surface topographic image can be obtained during the measurement of the tunneling spectra.

In this section, STM images and tunneling spectra obtained by STM on Bi2212 and Y123 are reviewed.

4.1. *Bi2212 (001) surface*

It has been pointed out that the surface of Bi2212 is easily deteriorated in ambient atmosphere. In order to detect the intrinsic tunneling spectrum, the basal plane of Bi2212, which is easily mechanically cleaved and relatively stable, has been investigated by numerous groups.

The cleavage takes place between adjacent BiO bilayers, resulting in exposure of the BiO plane on top, as demonstrated by room-temperature STM images reported so far (Kirk et al. 1988, Shih et al. 1988, Wang et al. 1990, Wu et al. 1990, 1991).

In low-temperature STM images of cleaved surfaces taken under a relatively large bias voltage $|V_B| \gtrsim 0.1$ V, one can clearly see the modulation structure along the b-direction with a period of ~2.6 nm, as shown in fig. 7). The orthorhombic lattice with $a_0 \approx b_0 = 0.54$ nm is also observed, which indicates the topmost layer to be the Bi–O layer. These images have also been reported by other researchers (Hasegawa et al. 1991a,b, Manabe et al. 1994, Oda et al. 1996, Kaneko et al. 1998)

Oda et al. (1996) reported STM images taken at lower temperatures under a much lower bias voltage $V_B = 20$ mV. As shown in fig. 8, a square atomic lattice with an interval of ~0.4 nm and a weak modulation structure with a ~2.5 nm period along the diagonal direction were observed. They claimed that the Sr–O and Ca planes are insulating and the tunneling current under low bias comes mainly from the metallic Cu–O plane, hence, the atomic corrugations observed in their STM image indicate a Cu–O–Cu network.

Renner and Fischer's group reported a detailed low-temperature STM investigation (Barbiellini et al. 1994, Renner et al. 1994). On the surface cleaved under ultrahigh vacuum (UHV) conditions (~3×10^{-8} torr) at room temperature, STM measurements were made under helium gas atmosphere without exposure to air.

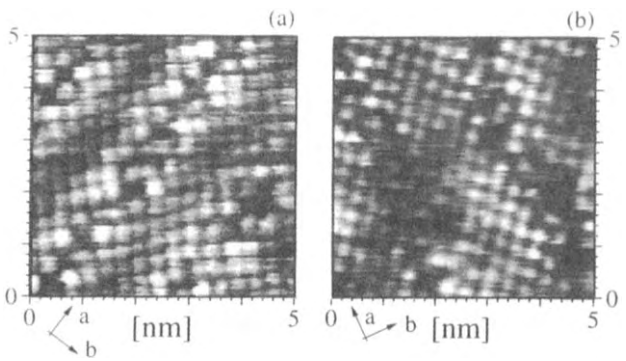

Fig. 7. Constant-current STM topographic images of *in situ* cleaved Bi2212 single crystals at 4.8 K (raw data). (a) Surface which shows a semiconducting gap (imaging parameter: $I_t = 275$ pA, $V_{sample} = 0.5$ V, $R_t = 1.8$ GΩ). (b) Surface which shows a semiconducting gap ($I_t = 300$ pA, $V_{sample} = 0.5$ V, $R_t = 1.7$ GΩ). After Renner and Fischer (1995, fig. 1).

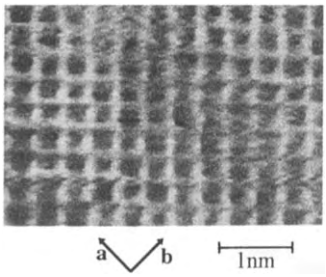

Fig. 8. Low-bias STM image of Bi2212 cleaved surface taken under constant height mode for $V = 20\,\mathrm{mV}$ and initial current $I_t = 1\,\mathrm{nA}$ at 6 K. After Oda et al. (1996, fig. 2a).

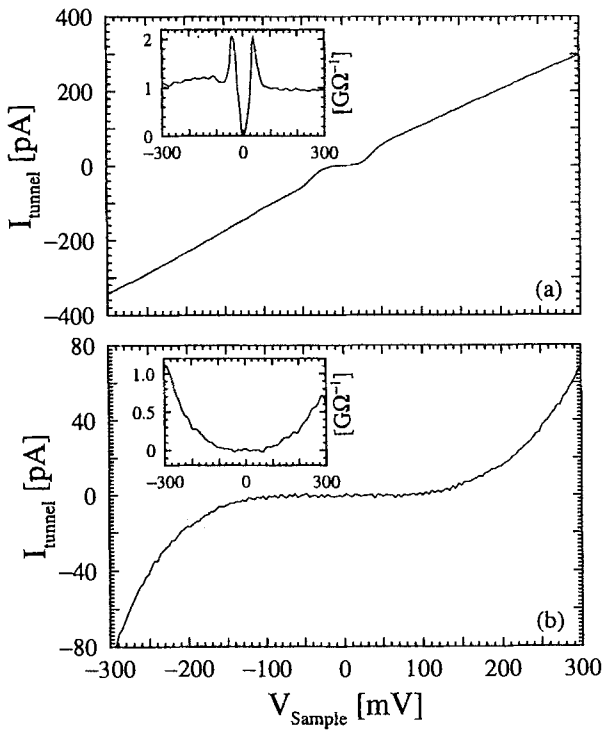

Fig. 9. I–V characteristics of Bi2212 at 4.8 K by Au tip, and differential conductance curves (inset) acquired by numerical differentiation. The numerical derivative of each I–V curve is shown in the inset. (a) Superconducting spectrum acquired in the region of fig. 7a with $R_t = 2.0\,\mathrm{G\Omega}$. (b) Semiconducting spectrum observed in the region of fig. 7b with $R_t = 1.0\,\mathrm{G\Omega}$. After Renner et al. (1994, fig. 2).

Topographic images with atomic resolution (fig. 7) were obtained at relatively higher tunneling resistance ($V_{tip} = 0.5\,\mathrm{V}$, $I \approx 300\,\mathrm{pA}$, $R_t \approx 1.8\,\mathrm{G\Omega}$). By successive cleaving of the same sample, they could obtain either a superconducting or a semiconducting spectrum (figs. 9a,b), while an atomic-resolution image was taken. On the other hand, a superconducting gap was obtained even when atomic resolution was lost. Hence, they claimed that atomic resolution is neither necessary nor sufficient to guarantee high-quality tunneling spectroscopy.

Surfaces cleaved under vacuum conditions were also examined by Kaneko et al. (1998). According to them, the tunneling spectra can be grouped into three types, as shown in

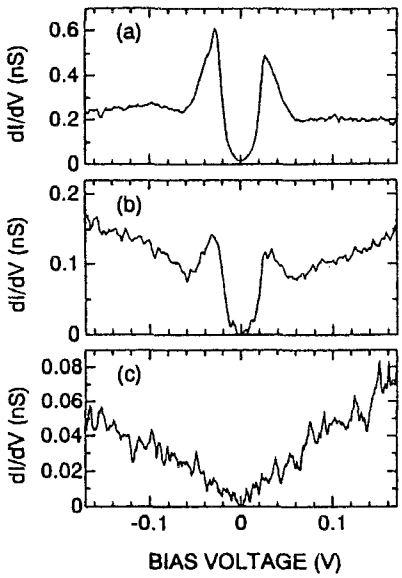

Fig. 10. Three types of differential conductance spectra typically observed on the cleaved Bi2212 surface. $V_B = 0.5$ V and $I_t = 0.1$ nA at 4.2 K. After Kaneko et al. (1998, fig. 6).

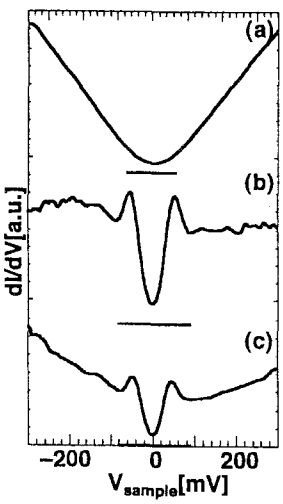

Fig. 11. Typical tunneling spectra observed on the as-cleaved surfaces of Bi2212 at 4.2 K. Spectra are characterized by (a) a semiconducting gap, (b) a superconducting gap with flat background, (c) a superconducting gap with V-shaped background. The sample bias voltage and the set-point currents are: (a) 45 mV and 2.51 nA, (b) 49 mV and 2.23 nA, (c) 56 mV and 1.64 nA, respectively. After Matsuura et al. (1998, fig. 2).

fig. 10: spectra exhibiting a clear gap structure with a flat background outside the gap; a gap with a V-shaped background; and a semiconducting or insulating gap structure. These three types of spectra were observed irrespective of whether or not atomic images were observable.

Matsuura et al. (1998) have recently found that the cleaved surface could be further removed or "etched" by the STM tip to create two types of tunneling spectra, as shown in fig. 11, which is similar to those shown in fig. 10. Most of the spectra revealed a semi-

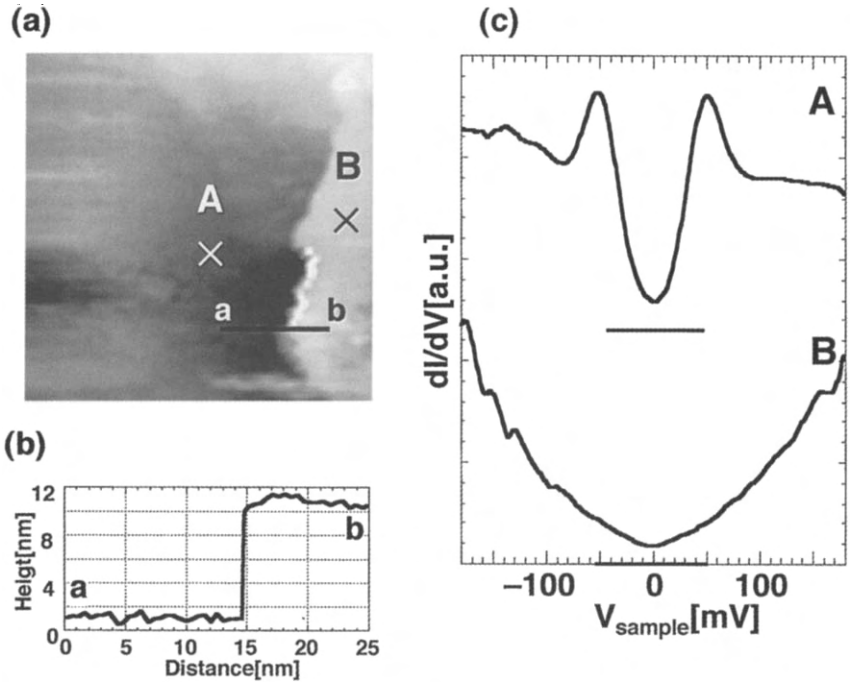

Fig. 12. (a) STM image including an "etched" surface of Bi2212; (b) a cross-sectional profile of the *a–b* plane in (a). (c) Tunneling spectra observed on (A) the as-cleaved and (B) the etched surfaces. The sample bias voltage (V_{sample}) and the set-point current for (a) are 990 mV and 0.71 nA, respectively. The spectroscopic measurement positions are marked as crosses in (a). After Matsuura et al. (1998, fig. 3).

conducting character with V-shaped or parabolic conductance. A clear superconducting gap was only occasionally observed, while the background outside the gap was found to be either V-shaped or flat with respect to the bias voltage, as shown in figs. 11b and 11c, respectively. Consecutive rastering on the sample leads to a removal or "etching" of such an insulating layer, as shown in fig. 12a, when the tip-to-sample distance is very small, e.g. in this case, the bias voltage is low, ~50 mV, and the set-point current is high, $\gtrsim$2 nA, corresponding to a tunneling resistance $\lesssim$25 MΩ. In the etched region, a clear superconducting gap structure with overshooting peaks appears, as shown in fig. 12b.

Removal or "etching" of the surface was also reported in Bi2212 by Mallet et al. (1996), who observed at room temperature in a helium gas atmosphere that small clusters of 100–300 Å in size were cleaned by consecutive scanning on the sample. They speculate that these small clusters of different oxygen content were formed by chemical reaction on the surface. A similar observation was reported by Harmer et al. (1991).

Surface-dependent tunneling spectra have been observed by Murakami and Aoki (1995). They performed low-temperature STM/STS measurements on a cleaved surface of Bi2212, and found three terraces eventually exposed by *in situ* cleavage. Here, as shown in fig. 13, the lowest and highest terraces had a one-step difference in height, and a square

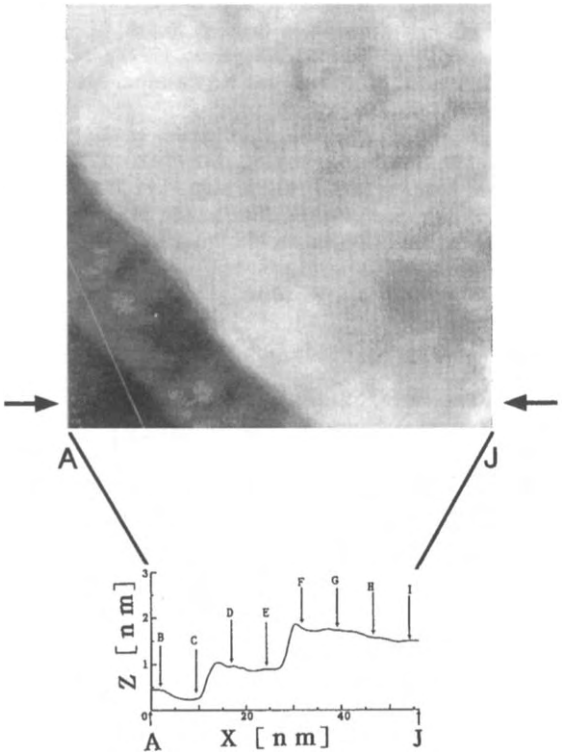

Fig. 13. (a) STM image (image size: 56 nm×56 nm) of a Bi2212 cleaved surface; (b) a cross-sectional profile along the line A and J in the topograph (a). After Murakami and Aoki (1995, figs. 1a,c).

lattice arrangement was observed in the STM image, indicating the exposure of BiO layers. The intermediate terrace, which did not give an atomic image, hence, was unlikely to be a BiO layer. They observed quite different tunneling behavior on the top/bottom planes and intermediate terrace, as shown in fig. 14. On the highest and lowest terraces, although a clear superconducting gap was observed, the spectra taken under higher bias were semiconducting. On the other hand, in the intermediate-terrace region, the superconducting spectra showed a gap with rather a flat bottom. They speculated that in the intermediate terrace, a Ca-layer site between the two CuO_2 layers was likely to be exposed.

The results described above suggest that tunneling spectra from cleaved surfaces still differ from one to another. Nevertheless, several researchers (Renner and Fischer 1995, Kaneko et al. 1998) have claimed that reproducible spectra are obtained when the cleavage and the measurements are performed under very inert conditions. They agree on some important features: vanishing differential conductance at zero bias, and flat background. Such reproducible spectra do not change their shape regardless of the measurement position and the tip-to-sample distances.

It has been questioned whether tunneling spectra are dependent on the tip-to-sample distance, a quantity experimentally determined by bias voltage and set-point current.

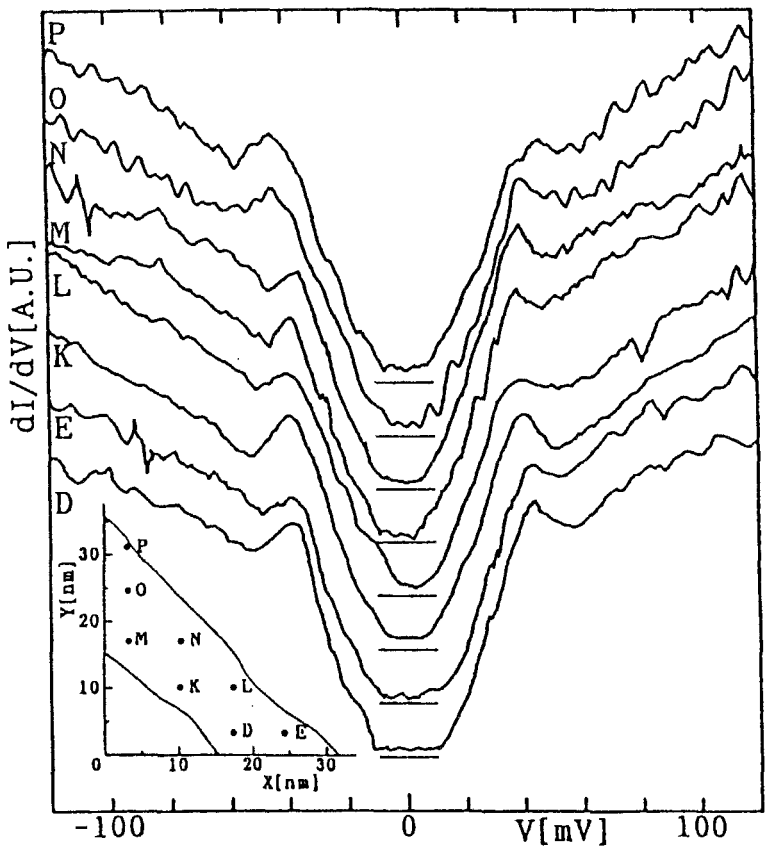

Fig. 14. STS spectrum characteristics at different points in the mid-terrace region of the cleaved surface of the same Bi2212 sample used in fig. 13. After Murakami and Aoki (1995, fig. 6).

Hasegawa et al. (1991a), Ichimura and Nomura (1993), and Murakami and Aoki (1995) reported a strong dependence on the tip-to-sample distance, while the others did not.

V-shaped background spectra have been reported by many research groups (Renner and Fischer 1995, Honcotte et al. 1995, Mallet et al. 1996, Kaneko et al. 1998), and their results have been discussed in terms of an anomalous normal-state property of the material (Anderson and Zou 1988, Flensberg et al. 1988, Varma et al. 1989, Kirtley and Scalapino 1990).

4.2. *Y123*

Observation of an atomic image in Y123 was less frequently reported than in Bi2212. This seems to be due to the fact that there is no stable cleavage surface in a bulk single crystal. In addition, the fractured surface is chemically unstable in air, and oxygen is released under low-pressure oxygen conditions. According to Edwards et al. (1994b), oxygen release is suppressed when the cleaving is performed below 60 K. Nevertheless,

the atomic arrangement and the superconducting gap structure has been observed on the surface of single crystals or thin films.

4.2.1. *(001)-oriented plane*

On the surface of epitaxial Y123 thin films, several topographic features of crystal growth have been observed, such as spiral (Hawley et al. 1991, Lang et al. 1991), ledge (Moreland et al. 1991), and needle (Muenchausen et al. 1992) types, which indicates that the surface during the growth of thin films is much more chemically stable (Lang et al. 1991) than the fractured surface (Narlikar et al. 1992, 1996).

Hasegawa et al. (1993) and Nantoh et al. (1994) have observed Y123 (001)-oriented thin epitaxial films grown by laser ablation. As shown in fig. 15, the STM image taken at 4.2 K clearly shows atomic arrangement with an average spacing of 0.35 nm.

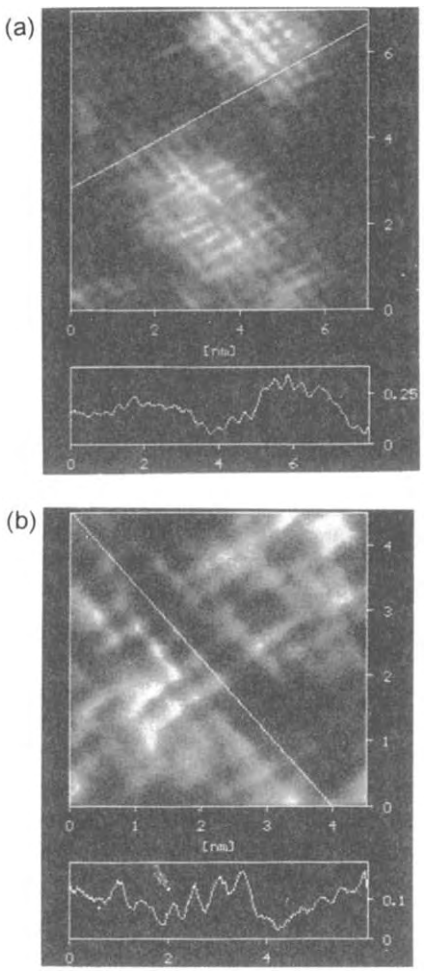

Fig. 15. STM image of a (001)-oriented Y123 thin film taken at 4.2 K. (a) $V_{bias} = 500$ mV, $I_t = 50$ pA, imaging size: 7×7 nm^2. (b) $V_{bias} = 500$ mV, $I_t = 15$ pA, imaging size: 4.5×4.5 nm^2. A square surface lattice with average spacing of 0.4 nm corresponds to the *a*- or *b*-spacing of the unit cell. After Nantoh et al. (1994, figs. 1d,e).

According to Edwards et al. (1992, 1994a,b, 1995), a clear atomic image could be obtained for Y123 single crystals grown by the flux method only when the cleavage and the measurement were performed below 60 K. Their images show one-dimensional structures, which they claimed to correspond to the CuO chain. The one-dimensional structure had a limited length up to about 13 Å, and appeared to form dimers. The electronic character of the surface was semiconducting, and hence they claimed that a finite gap appeared in the tunneling spectrum due to the formation of a charge-density wave.

Maggio-Aprile et al. (1995) observed no atomic image on single crystals, while a superconducting spectrum could be detected on the surface. They succeeded in observing variation of the tunneling spectrum in the vortex-core regions (see sect. 5.4).

4.2.2. *(110)-oriented plane*

It is believed that a large anisotropy should exist along direction of the Cu–O chain, but Nantoh et al. (1995) reported a controversial result. Figure 16 presents STM images of (110) surfaces of Y123 epitaxial films, in which an orthorhombic lattice of surface atoms is clearly observed. The image of the CuO chain is brighter than that of the CuO_2 layer, and the contrast is enhanced for lower bias voltage. This implies that the density of states at the Fermi level is higher in the CuO chain than in the CuO_2 layer. The semiconductive nature of the CuO chain is claimed to have smaller anisotropy as compared to other HTSC materials.

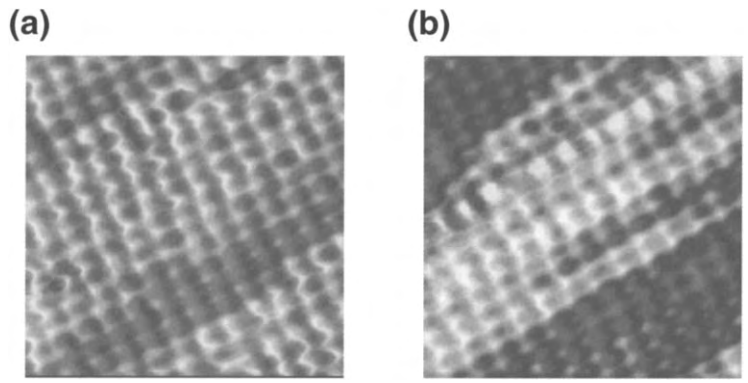

Fig. 16. STM images of a (110)-oriented Y123 epitaxial film taken at 4.2 K. (a) $V_{tip} = -1.9$ V, $I_t = 0.13$ nA. (b) $V_{tip} = -0.75$ V, $I_t = 0.09$ nA. Imaging size: 6.5×6.5 nm^2. After Kawasaki and Nantoh (1994).

5. Tunneling spectroscopy

5.1. *Superconducting gap structure*

The details of the superconducting gap structure form a rich source of information about the pairing mechanism. If the pairing is of typical s-wave symmetry, a finite gap is

opened and hence the in-gap conductance is very low. If it is of p- or d-wave type, the gap is not completely opened and hence the conductance is finite, decreasing with a certain slope towards zero bias. In conventional superconductors, finite gaps have been observed in support of the s-wave. In the case that the electron–phonon interaction is sufficiently strong, a fine structure is observed in the tunneling spectrum outside the gap. Detailed analysis of the fine structure has provided the spectrum of the electron–phonon interaction which gives the most decisive proof for the phonon-mediated superconducting mechanism by comparing it with the independent phonon spectrum determined by neutron scattering.

In the HTSC, although some fine structure has frequently been observed, there has been little understanding of the fine structure, and experimental consistency has not been fully examined. So far the greatest attention has been paid to the main gap structure: gap size and in-gap conductance.

In the initial period of studies on HTSC, tunneling spectrum measurements were quite inconsistent from one to another, as summarized by Hasegawa et al. (1992a). Multiple-peak and multiple-gap structures were frequently reported feeding speculations about the exotic nature of the HTSC mechanism. However, especially owing to the development of the STM tunneling method, the results gradually converged to the rather simple single-gap structure. This was because the junction under the STM tip was thought to be undamaged compared to the other techniques. Therefore, experiments with other methods started utilizing the STM results as a standard to judge the quality of their junctions.

STM techniques in the early days were, however, immature with respect to the limitations of atmosphere, temperature and stability against noise. The preparation of the surface was another problem. By now, several groups have achieved *in situ* cleavage of the sample, or at least cleavage in high vacuum. Also, it has been found that *in situ* etching under certain bias conditions provides a surface on which reproducible measurements can be performed. These results have been reviewed by Kitazawa et al. (1996) and by Sugawara et al. (1996). The controversial issue then was whether the gap feature was s-like or d-like.

Comparing the available tunneling spectra on Bi2212 and Y123, Kitazawa et al. (1996) noted that there were essentially two kinds of results: one exhibiting a clear gap, as in a BCS metallic superconductor with a rather flat bottom, the other exhibiting a gap with a large zero-bias conductance and/or a sharp V-shaped conductance close to zero bias, as shown in figs. 17 and 18.

The former type was reported by Hasegawa et al. (1991b), Hasegawa et al. (1992b) and by Murakami and Aoki (1995); they observed this type of gap only on a non-BiO surface produced accidentally on a part of the sample. On the other hand, the latter type was reported as well by these authors, and by many other groups: Renner et al. (1994), Manabe et al. (1994), Honcotte et al. (1995), Maggio-Aprile et al. (1995), Ueda et al. (1995), Mandrus et al. (1993) and Matsuura et al. (1998). Hence, the latter type was the typical commonly observed spectrum for the HTSC, although some experimental ambiguities remain as to why the spectra appeared differently on different surfaces.

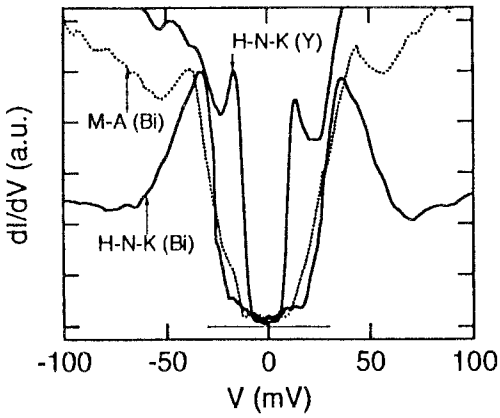

Fig. 17. Tunneling spectra on the basal plane of Bi2212 and Y123 with the terminating layer claimed to be a CuO_2 plane, or a SrO (Bi2212) or BaO (Y123) plane covering the CuO_2 layer. Curves H–N–K (Bi) Hasegawa et al. (1991b), H–N–K (Y) Hasegawa et al. (1991b, 1993), Nantoh et al. (1991, 1994, 1995), M–A (Bi) Murakami and Aoki (1995) are for Bi2212, Y123, and Bi2212, respectively. After Kitazawa et al. (1996, fig. 1).

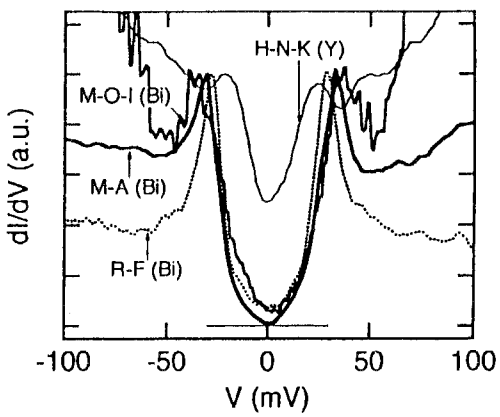

Fig. 18. Tunneling spectra on the basal plane of Bi2212 and Y123 with the terminating layer claimed to be a BiO and CuO chain plane, respectively. The references for the curves are: H–N–K, Hasegawa et al. (1991b, 1993), Nantoh et al. (1991, 1994, 1995); R–F, Renner and Fischer (1995); M–O–I, Manabe et al. (1994, 1997); and M–A (Bi), Murakami and Aoki (1995). After Kitazawa et al. (1996, fig. 2).

It was difficult to interpret the latter type of spectrum in an s-wave framework, unless a rare case such as extended s-wave was assumed. In the meantime, many other observations made by different methods such as NMR, specific heat, phase-sensitive SQUID method, ARPES, etc., supported d-wave symmetry, and as a result, tunneling spectra of this kind were analyzed according to d-wave symmetry and are now regarded more positively as one category of evidence to support it.

SIS-junction spectra observed on the naturally occurring built-in layer structure of Bi2212 single crystals have been reported by several groups. These spectra also give rather high and linearly increasing in-gap conductance, again in accord with the d-wave pairing mechanism (Tanabe et al. 1996, Schlenga et al. 1996, 1998).

Kashiwaya and Tanaka (Kashiwaya et al. 1994b, 1995b, 1996, Y. Tanaka and Kashiwaya 1995) have examined both theoretically and experimentally the interface effect of anisotropic superconductors, predicting the occurrence of the zero-bias conductance peak and its splitting in some cases due to the formation of Andreev bound states

at interfaces (or surfaces). Their systematic results were again consistent with $d_{x^2-y^2}$ symmetry (see sect. 6).

Therefore, as far as the symmetry of the Cooper pair is concerned, it is thought that d-wave symmetry has been well established. The differences between experimental results then seem to be attributable to surface- and/or angle-dependent phenomena.

The second interesting issue is the size of the gap, especially the gap dependence on temperature and on composition. Ikuta et al. (1988) was the first to report that a superconducting-gap-like feature persists in the HTSC well above the critical temperature. Detailed results by Renner et al. (1998a) and Matsuda et al. (1999) have indicated that the change in the gap size in the superconducting temperature range is small. In addition, they note that the gap survives continuously in the tunneling spectrum above T_c. Interestingly, the gap gradually vanishes in that the gap is gradually filled up rather than closed, even above T_c.

This temperature dependence is quite surprising, considering that in a BCS superconductor the gap decreases sharply as the temperature approaches T_c, and closes there. This is in accord with the idea that the bonding strength of the Cooper pair is also lost at T_c. In the HTSC, however, the observed temperature dependence rather suggests that the Cooper pair keeps the same binding strength even at T_c while the total number of pairs decreases gradually. However the pairs do not totally disappear at T_c, surviving to much higher temperature.

It is quite important to know whether pairs above T_c can ever be Cooper pairs. At the present moment, we do not have a clear answer to this important question. However, it should be quite difficult to assume completely different nature for bound pairs below and above T_c. If the pairs below and above T_c are both Cooper pairs, then T_c should not be determined by the binding force, as is the case for conventional superconductors. Emery and Kivelson (1995) have proposed the idea of "pre-formed pairs", with their hypothesis that T_c is the temperature where complete coherence is established among the Cooper pairs. T_c decreases towards underdoping, because the density of Cooper pairs decreases and establishment of coherence is more difficult.

The model described above is challenged mainly by two other ideas. One is to assume that the pair above T_c is a "spin singlet" in the framework of spin–charge separation of an electron. T_c then is the temperature where the charge part of the freedom of an electron also pairs up, i.e. holon pairing. Another model assumes the pair formation to be electron pairing on the Fermi surface, but taking place in different ways on the surface: near $\vec{k} = (\pi, 0)$ at much higher temperatures, but near $(\frac{1}{2}\pi, \frac{1}{2}\pi)$ at much lower temperature. Only when sufficient numbers of electrons form pairs does superconductivity set in according to the latter model.

At any rate, it is then clear that the scaling rule $2\Delta/T_c \approx 3.52$ should not be observed in HTSC. Indeed it has been reported that T_c decreases towards underdoping, while the gap size remains nearly the same (Renner et al. 1998a) or even increases (Miyakawa et al. 1998). This will be discussed further in section 5.2.

As for Y123 crystals, no consensus has emerged about the intrinsic tunneling spectra. Maggio-Aprile et al. (1995) investigated tunneling spectra on a fully oxygenated Y123

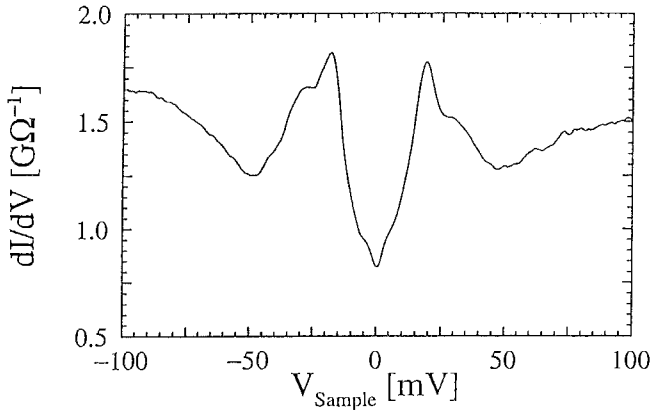

Fig. 19. Differential conductance spectrum of an Y123 single crystal at 4.2 K. After Maggio-Aprile et al. (1995, fig. 1).

twinned as-grown single crystal from growth in a $BaZrO_3$ crucible, which did not react with the reactive melts used as solvents for Y123. As shown in fig. 19, the tunneling spectrum taken at 4.2 K showed gap-like features, with main conductance peaks at 20±2 mV. The background conductance outside the gap increased linearly with increasing bias. Note that the zero-bias conductance amounted to about 60–70% of the normal conductance, which was reproducible for various tip-to-sample distances and various vertical measuring positions. Similar features were also observed with a planar junction by Valles et al. (1991).

The tunneling spectra depicted in fig. 19 are quite different from those in Bi2212 single crystals. The gap structure is not consistent with an isotropic BCS s-wave state, and is different from the simple d-wave picture. The multi-peak structure resembles the spectrum expected for extended s-wave, except for the large zero-bias conductivity.

5.2. *Temperature and doping dependence*

5.2.1. *Carrier concentration dependence of superconducting gap*

In BCS weak-coupling superconductors, the magnitude of the superconducting gap Δ is proportional to T_c, following $2\Delta = 3.52 k_B T_c$. The correlation between Δ and T_c in HTSC was first investigated by Tsai et al. (1989). They performed point-contact tunneling spectroscopy on Y123 thin films with various T_c, which were prepared by controlling the film growth conditions. As a result, they confirmed a linear relationship $\Delta \propto T_c$. Recently, however, several groups have attempted systematic tunneling measurements on a series of Bi2212 specimens with different carrier concentrations, n, reporting the possibility that Δ does not scale with T_c at all, but rather is governed by other temperature scales, such as T^* and T_0.

Momono et al. (1999) performed STS tunneling spectroscopy on La214 and Bi2212 with different doping levels. As shown in fig. 5, they found that for both systems

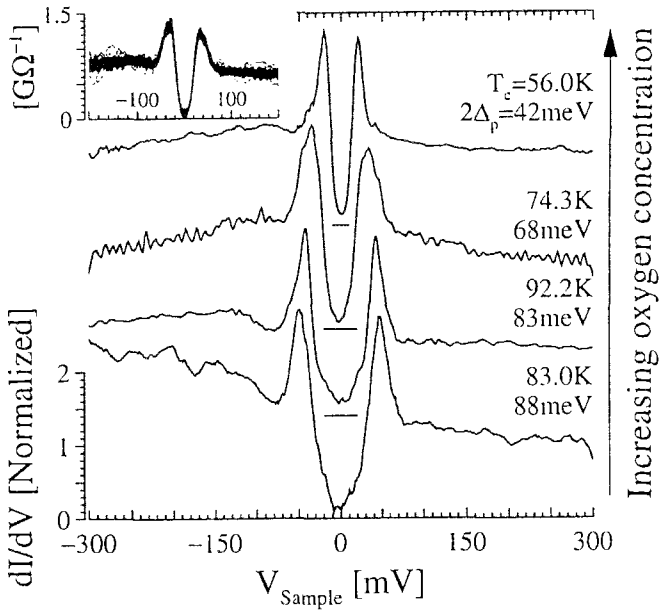

Fig. 20. Tunneling spectra of Bi2212 at 4.2 K for different oxygen doping levels. After Renner et al. (1998a, fig. 1).

the Δ values increased monotonously with decreasing carrier concentration n, through underdoped to overdoped regions, which is consistent with the results of Raman measurements by Kendziora and Rosenberg (1994). That is, Δ in the underdoped specimen is larger than that of the optimally doped one with the highest T_c. Interestingly, the obtained Δ value scales as T_0, as determined from magnetic measurements, although the scaling factor, $r = k_B T_0/\Delta$, differs for the two HTSC systems: $r \approx 5$ for Bi2212 and $r \approx 1$ for La214. They also found that the reduced gap $2\Delta/k_B T^*$ for different doping levels fell in a narrow range of 4–5, which is comparable to the mean-field value for the d-wave pairing state, ~4.3, leading to the conclusion that the temperature T^* gives the mean-field values of T_c. This situation favors the pre-formed pair model that the origin of the anomalous behavior around T_c is essentially identical to that of superconductivity.

Experimentally, the correlation between Δ and n is controversial at the present stage. Renner et al. (1998a) reported STS tunneling spectroscopy on Bi2212, where the specimens were cleaved in UHV. Figure 20 qualitatively illustrates the relationship between n (the oxygen content) and Δ at 4.2 K. It is notable that Δ increases as n is lowered, similar to the STS results by Oda et al. (1997b). Also see the comparison of tunneling, photoemission, and penetration depth data given by Panagopoulos and Xiang (1998). Based on quite stable STS measurements on Bi2212, however, Matsuda et al. (1999) advocated a different Δ–n correlation. They reported Δ as a function of oxygen content x, which is considered to be a measure of n. As shown in fig. 21, Δ is maximized around optimal $x \approx 8.25$, where T_c is also maximized, although Δ does not show a strong

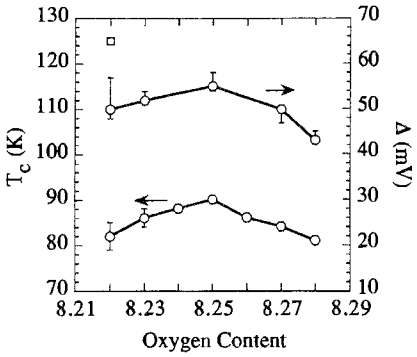

Fig. 21. Oxygen content dependence of the critical temperature (T_c) and the superconducting gap value Δ. After Matsuda et al. (1999, fig. 1).

x-dependence in the underdoped region. In these observations, anyway, there exists no correlation between Δ and T_c.

Miyakawa et al. (1998) reported tunneling measurements using a break junction on Bi2212 with various oxygen contents. They found a trend that Δ decreases monotonously with increasing n over a narrow doping region where T_c exhibited a maximum.

The experimental inconsistencies described above may be due to the inhomogeneity of n, especially for underdoped samples. Further detailed studies are desired.

5.2.2. *Temperature dependence of superconducting and pseudogaps*

In the mean-field theory of superconductivity, the order parameter Δ is almost constant up to the reduced temperature $t = T/T_c \approx 0.5$, and then goes to zero as T approaches T_c. For HTSC, the temperature dependence of Δ reported so far can be classified into two groups. In the first category, the peak-to-peak separation energy $2\Delta_{pp}$ follows the BCS prediction, while in the second category $2\Delta_{pp}$ increases as the temperature is raised. Here, it should be emphasized that Δ_{pp} does not correspond to Δ at higher temperatures, because the thermal smearing effect tends to shift Δ_{pp} to the higher-energy side. In the superconducting states, the energy gap $\Delta(T)$ opens up at the Fermi energy, so that the quasi-particle density of states, $N(E)$, for $E > \Delta(T)$ is higher than that for $E > \Delta(T)$. Thus, a smearing phenomenon, in general, including lifetime broadening as well as thermal broadening, causes the upper deviation of $\Delta_{pp}(T)$ in the $\Delta(T)$–T curve. The extent of deviation depends on the magnitude of Δ and the shape of the $N(E)$ function inside Δ. In conventional weak-coupling BCS superconductors, indeed, $\Delta_{pp}(T)$ increases monotonously with T. The experimental disagreement for $\Delta(T)$, described above, may be explained by differences in the apparent tunneling conductance $\sigma(E)$ inside the gap. For example, if Andreev reflection takes place, $\sigma(E)$ for $E < \Delta$ is apparently enhanced, compared with $N(E)$, and thus, Δ_{pp} is less influenced by the smearing effects.

Recently, STS measurements on clean surfaces of Bi2212 prepared *in situ* have shown a slight increase of Δ at higher temperature, as plotted in figs. 4 and 22. Matsuda et al. (1999) analyzed the observed tunneling conductance curve, assuming a d-wave gap function and lifetime and thermal broadening effects, and demonstrated that Δ increased

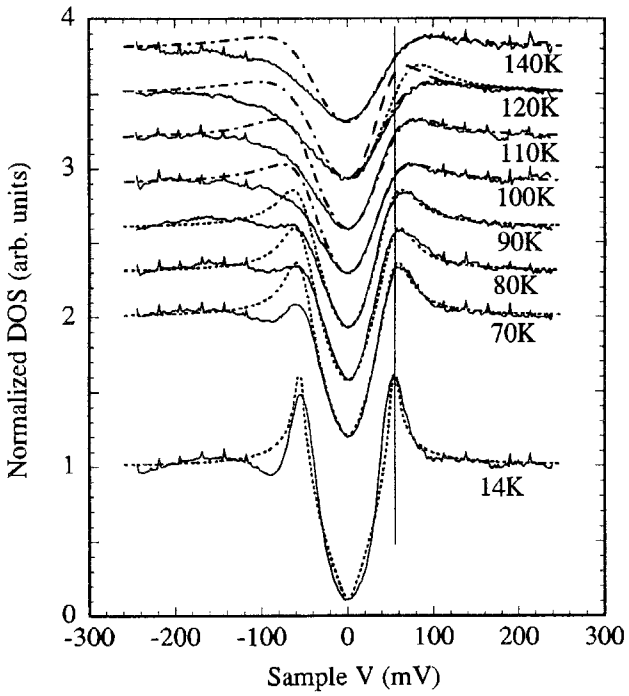

Fig. 22. Temperature dependence of tunneling DOS for the optimum doped Bi2212 sample ($T_c \approx 90$ K). Data are normalized to 2.5 at –250 meV. After Matsuda et al. (1999, fig. 4).

with temperature, as shown in fig. 23. They also claim that the damping parameter Γ is rapidly enhanced near T_c, which is qualitatively consistent with the results of microwave response and optical measurements.

In conventional superconductors, as mentioned above, Δ closes at $T = T_c$, and the sign of Δ appears only as the superconducting fluctuation for $T > T_c$. On the contrary, it is a quite distinctive and unique feature for HTSC that the gap structure still remains up to temperatures significantly above T_c. In underdoped Bi2212, Renner et al. (1998a) observed a temperature dependence of tunneling spectrum over a wide temperature range between 4.2 K and room temperature. They found that a pseudogap, equivalent to Δ at 4.2 K, still remains even above $T_c \approx 83$ K, and does not change much with temperature up to room temperature. This observation is in striking contrast to the PES results, which indicate the reduction of the pseudogap around $T^* = 170$ K for the underdoped sample. Notably, Renner et al. (1998a) have reported a similar pseudogap structure even for the overdoped sample at least up to 80 K above $T_c = 74.3$ K. This also disagrees with the conclusion obtained from PES that the pseudogap for $T > T_c$ can be seen only in the underdoped region.

Recently, Matsuda et al. (1999) have performed a more detailed study on the pseudogap of Bi2212 as a function of temperature and carrier concentration. All specimens

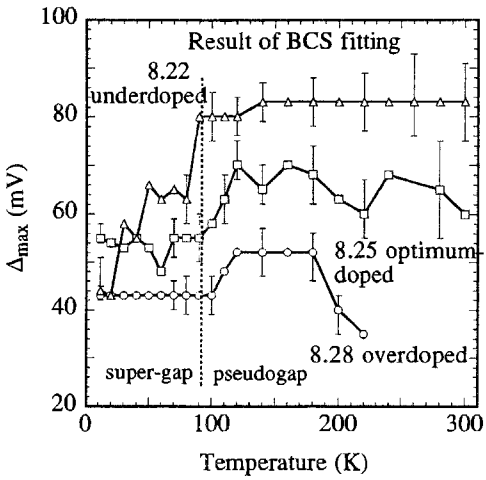

Fig. 23. The fitted results for Δ for several doping levels. After Matsuda et al. (1999, fig. 5a).

investigated showed a pseudogap structure even at room temperature, although it tends to be smeared out more rapidly with temperature in the overdoped samples.

The inconsistency between STS and PES can be interpreted in the following ways. Firstly, both probes, which possess different probing energies and are based on different excitation mechanisms, may sense different aspects of the excitation spectrum of HTSC. Secondly, PES has poorer energy resolution $\Delta E \approx 20$ mV in comparison with STS. Thus, PES may be less sensitive to the change of pseudogap structure, particularly in the case that $N(0)$ is continuously increased without closing the gap at higher temperatures. Thirdly, the origin of the inconsistency may be the slight loss of oxygen atoms from surfaces, resulting in decreased n in the surface layer. STS, being a more surface-sensitive technique, is expected to be more affected by the local reduction of n.

It should be stressed here that at a first sight the gap structure shows no discontinuous change at T_c. It seems to vary continuously as a function of temperature. On careful inspection of figs. 4 and 22, one may recognize a slight discontinuity across T_c. Figure 24 is a 3D plot of fig. 4, in which the energy value E_p giving maximum tunneling conductance is traced as function of temperature. As can be seen, E_p jumps abruptly at T_c. The result of curve-fitting analysis by Matsuda et al. (1999) more directly indicates that the Δ value is discontinuously enhanced at T_c with rising temperature (fig. 23). Consequently, they claimed that the pseudogap above T_c and the superconducting gap below T_c come from different origins, and compete with each other. In this scenario, then, the latter overcomes the former at T_c. However, the discontinuity in E_p or Δ at T_c may result from a substantial increase of quasiparticle damping just below T_c, which smears the tunneling spectrum. As mentioned earlier, the smearing effect tends to shift E_p to the higher-energy side, and could cause a larger uncertainty in Δ estimated from the curve-fitting procedure.

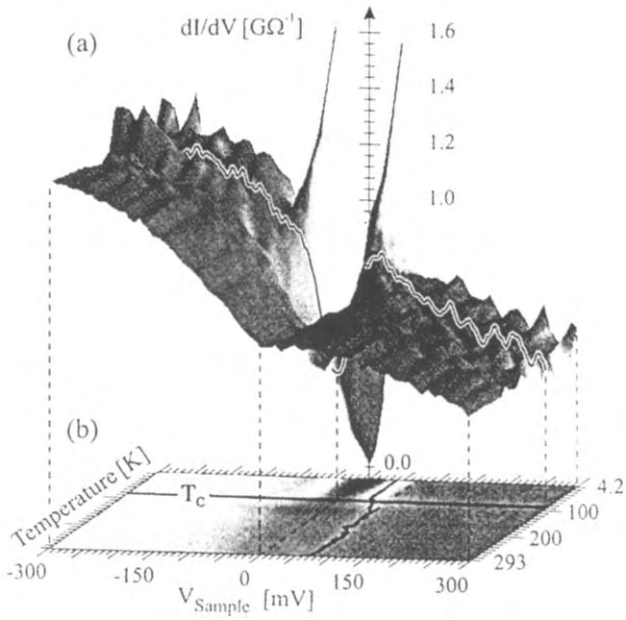

Fig. 24. (a) Three-dimensional view of the conductance data shown in fig. 4. (b) Projection onto the energy–temperature plane. The line at positive bias indicates the position of the positive-bias conductance peak which clearly shifts to higher energies above T_c. After Renner et al. (1998a, fig. 3).

5.3. *Impurity effects*

The variation of the superconducting gap with respect to T_c is an issue to be investigated in view of the understanding of the mechanism of high-T_c superconductivity. It was found in earlier experiments that the influence of impurity atoms on T_c in HTSC is different from that of conventional superconductors. For example, the substitution of Zn, a nonmagnetic ion, in $La_{2-x}Sr_xCuO_4$ (La214) compounds leads to the decrease of T_c to nearly the same extent as that of magnetic Ni. Nonmagnetic impurities induce little suppression of superconductivity in conventional superconductivity (Anderson's theorem of disorder). On the other hand, magnetic impurities like Ni and Fe in Y123 compounds yield a smaller T_c suppression compared to Zn. Numerous experiments indicate that effective substitution at the Cu site in the CuO_2 plane leads to significant changes and to a reduction of T_c. However, only a few studies on tunneling spectroscopy are available.

Broekholt et al. (1992) reported tunneling measurements by the point-contact method for Bi2212 with the substitution of Co for Cu. With increasing Co content, the transition temperature T_c decreased monotonically, while the superconducting gap Δ decreased more rapidly than T_c; the reduction at higher Co content was much stronger than the relation $2\Delta/k_B T_c \approx 5.7$ which they found for oxygen-deficient pure Bi2212 single crystals.

Hancotte et al. (1997) investigated Zn- and Ni-substituted Bi2212 single crystals by STM and break-junction methods. While their pure sample showed $T_c = 85$ K,

Ni-substituted (content 1.3–1.5%) sample showed $T_c = 75$ K. The superconducting gap value varied more significantly than for the pure sample, and the prominent gap value was $2\Delta_{pp} \approx 77$ meV, which was larger than the pure-sample value $2\Delta_{pp} \approx 52$ meV, indicating increased coupling strength. The temperature-variant measurement by means of the break-junction method revealed that the $2\Delta_{pp}$ value did not decrease monotonically with respect to the measuring temperature T but slightly increased in the reduced temperature range $T/T_c = 0.3$–0.5.

On the other hand, the substitution of Zn (content ~1%) showed $T_c \approx 79$ K, and the gap value $2\Delta_{pp} \approx 50$ meV was almost the same value as that of the pure sample. However, the conductance at zero bias was increased. This increase, estimated to a residual DOS of ~0.4, was in good agreement with the results of NMR experiments (Ishida et al. 1993). Their results were compared with theoretical results of impurity effects in d-wave superconductors in the unitary limit (Balatsky and Salkola 1996, Salkola et al. 1996), though they did not claim that the zero-bias anomaly observed in Zn-substituted Bi2212 is explained by their prediction. These variations in the substituent atoms seem to indicate that Co, Zn and Ni affect the electronic states in different ways.

Note that Kane et al. (1998) recently investigated Pb-doped Bi2212 single crystals, and indicated that the in-plane energy gap was little influence by lead doping up to 4%, in spite of decreasing T_c.

5.4. *Inner vortex excitation*

Another issue to be investigated is the excitation spectrum inside the vortex core, where the penetration of the magnetic field leads to local breakage of the time-reversal symmetry, resulting in local reduction of the order parameter. STM is a suitable tool to detect the spatial variation of the excitation spectrum inside the core.

In the past, this technique was applied to the investigation of vortex lines in $2H$-$NbSe_2$ by Hess et al. (1989) and $2H$-$Nb_{1-x}Ta_xSe_2$ by Renner et al. (1991). At the vortex core, the differential conductance (dI/dV) at zero bias voltage showed a peak, which gradually disappeared when the measurement position moved away from the core center, while small peak structures appear at finite bias voltages. Finally, far from the vortex-core center, the excitation spectrum becomes coincident with the bulk spectrum. It was found that the peak structures correspond to bound states of quasiparticles confined in the vortex core, and they were reproduced by a calculation based on the quasiclassical Eilenberger theory of the BCS s-wave order parameter (Caroli et al. 1964). Furthermore, mapping of the ratio of the conductance values at different bias voltages revealed a vortex lattice structure. In $NbSe_2$, the vortex-core structure had 6-fold symmetry, which was explained by the effect of the crystal field.

It was pointed out that the symmetry of the order parameter, either s-wave or d-wave, should be clarified from tunneling conductance in the vicinity of zero bias. The excitation spectrum of an s-wave superconductor forms discrete bound states, which are equally spaced to Δ/E_F. On the other hand, several authors (Won and Maki 1996, Maki et al. 1996, Schopohl and Maki 1995, Ichioka et al. 1996) predict, by solving the Eilenberger

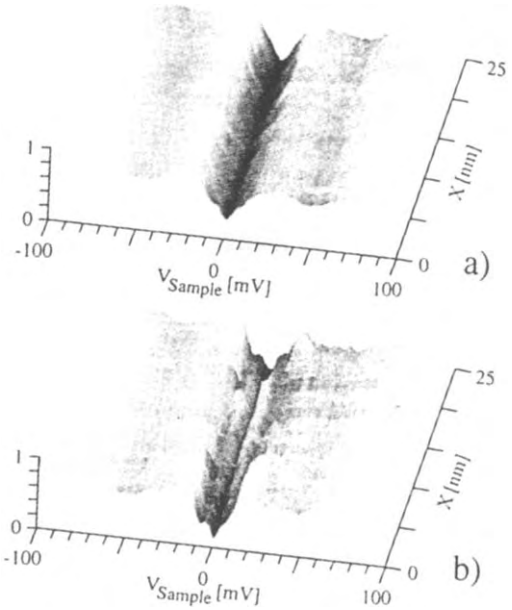

Fig. 25. Differential conductance spectra measured as a function of position on an Y123 single-crystal sample at 4.2 K with applied field of 6 T: (a) between the vortex cores, (b) across a vortex core. The paths are 25 mm long. After Maggio-Aprile et al. (1995, fig. 3).

equation, that in d-wave superconductors quasiparticles within the vortex are in an extended state due to vanishing order parameter at $\vec{k} = (\pm\frac{1}{2}\pi, \pm\frac{1}{2}\pi)$ directions, and instead a differential conductance (dI/dV) peak evolves at zero bias.

In cuprate superconductors, Maggio-Aprile et al. (1995) have successfully observed the vortex lattice in Y123 for the first time. A fully oxygenated Y123 twinned single crystal grown in a novel crucible material, $BaZrO_3$, was used in order to reduce contamination from the crucible during crystal growth.

The low-temperature tunneling spectrum, shown in fig. 19 without magnetic field, changed as shown in fig. 25 under a field of 6 T. The spectra varied while approaching the vortex core. The main ± 20 meV conductance peaks decreased in magnitude and totally disappeared at the center of the core. At the same time, two new peaks grew at ± 5.5 meV. The 27 meV peak did not vanish completely, and a broad bump remained. However, no zero-bias peak was found at the center of the vortex, in contrast to what is found in s-wave $NbSe_2$.

Maggio-Aprile et al. (1995) tentatively interpreted the new peaks at 5.5 mV as the lowest bound state for a vortex in s-wave superconductors. Here, the lowest bound energy is given approximately by $E = \Delta/(\pi p_F \xi)$, where p_F and ξ are the Fermi momentum and the coherence length, respectively, implying $p_F \xi \simeq 1$, the extreme quantum limit. It is also advocated that higher bound states are missing on the core spectrum, because their excitation energies exceed the superconducting gap Δ.

Theoretical models beyond the simple BCS mechanism are discussed to elucidate the inconsistency between the tunneling results inside the vortex core and other data

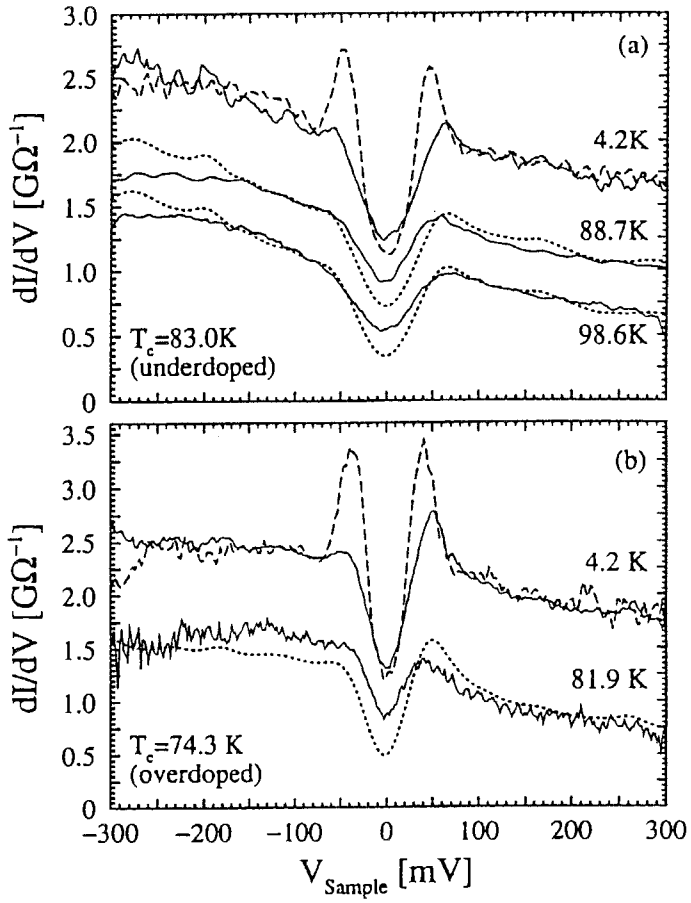

Fig. 26. Tunneling spectra of Bi2212 in the (a) underdoped and (b) overdoped regions. The spectra at 4.2 K were measured under a 6 T magnetic field at the center of the vortex core (solid line) and between vortices (dashed line). The spectra above T_c displayed as solid lines were measured in zero field, and reflect the normal-state pseudogap structure. The dotted curves were obtained by numerically smearing the spectra measured at the center of the cores at 4.2 K and 6 T to the temperature(s) indicated for each doping level. They illustrate the striking resemblance of the vortex-core pseudogap and the normal-state pseudogap. For clarity, the 4.2 K curves are offset by 1.0 GΩ^{-1} and the 88.7 K curves by 0.4 GΩ^{-1}. After Renner et al. (1998b, fig. 3).

supporting d-wave. Moriya et al. (1997) claimed that the analysis from the Eilenberger equation is invalid in the case of Y123 with its large value of $p_F\xi$, and that a calculation based on a more strict model (Bogoliubov–de Gennes equation) of d-wave superconductivity demonstrated that inner vortex excitation without a clear zero-bias peak. On the other hand, Ogata and his group (Himeda et al. 1997) theoretically showed from a calculation based on the t–J model that an s-wave component of the order parameter induced within a vortex leads to the splitting of the zero-bias peak;

hence, the splitting of the peak structures indicates the admixure of d-wave and s-wave symmetries.

Renner and coworkers (Renner et al. 1998b) have succeeded in observing vortex cores in under- and overdoped Bi2212 by STM. At the vortex core, they found a pseudogap-like feature without quasiparticle bound state. The inner-core gap structure at low temperature, as shown in fig. 26, is similar to the pseudogap above T_c, suggesting that both gap structures reflect the same normal state containing incoherent Cooper pairs. The missing bound states in Bi2212, in contrast to the Y123 case, suggest that the relatively larger gap in Bi2212 pushes up the first bound states $E_{\pm 1/2}$ beyond the superconducting gap.

6. Phase-sensitive measurement

While the quasiparticle tunneling process into superconductors is considered to be insensitive to the phase of the quasiparticle, several theoretical investigations have revealed that it is sensitive when the order parameter is anisotropic. In this section, two kinds of approaches to determine the symmetry order parameter of HTSC are reviewed.

The first kind of approaches is to investigate the differential conductance (dI/dV) spectrum with various geometries in SIN or SIS junctions. The other type is to measure the dependence of the Josephson critical current J_c as a function of applied magnetic field.

6.1. *Dependence on surface orientations*

6.1.1. *In-plane anisotropy*

The group of Kane and Ng (Kane et al. 1994, Kane and Ng 1996) have adopted an unconventional junction geometry to observe the in-plane gap energy of Bi2212. Here, an edge of a single crystal faced in close proximity a normal-metal counter-electrode or a matching edge of the same crystal. The angular dependence of the energy gap was completely mapped by assuming fourfold symmetry with an experimental uncertainty of about 8 mV. The in-plane gap anisotropy was clearly observed with a minimum value of 20 mV along the CuO_2 bond. The maximum gap direction was 45° away, with a value of about 40 mV. The gap variation was larger than the experimental uncertainty of about 8 meV. It is not clear why there was a 45° difference between tunneling and photoemission results. No direct evidence of a nodal line was observed in the angular dependence.

6.1.2. *Surface orientations and zero-bias anomaly*

The tunneling process across a SIN (superconductor–insulator–normal metal) junction is more complicated than across a NIN (normal metal–insulator–normal metal) junction described in sec. 3.2. An electron reaching an insulator (I) from a normal metal (N) takes either one of four elementary processes, i.e., (1) reflection as an electron

(normal reflection), (2) reflection as a hole after the interaction with an electron-like quasiparticle (Andreev reflection), (3) transmission as an electron-like quasiparticle, and (4) transmission as a hole-like quasiparticle. The tunneling current should include these processes, and the differential conductance is given by the Blonder–Tinkham–Klapwijk (BTK) formula (Blonder et al. 1982).

The tunneling conductance for anisotropic superconductors in general was calculated by Tanaka and Kashiwaya (Y. Tanaka and Kashiwaya 1995, Kashiwaya et al. 1995b, 1996). Their formula reproduces the Blonder–Tinkham–Klapwijk (BTK) formula for s-wave superconductors when the barrier height is sufficiently high, i.e., tunneling conductance approximates the quasiparticle density of states. On the other hand, the tunneling conductance for d-wave superconductors is sensitive to the phase of the quasiparticles. In the case of tunneling in an oblique direction, the phase difference of pair potentials induces zero-energy states (ZES's) at zero energy of quasiparticles (Hu 1994), which create a conductance peak at zero bias (ZBCP). The ZBCP is not expected for s-wave superconductors of any orientation, nor for the basal (*ab*-) plane of d-wave superconductors. Hence, the appearance of ZBCP for tunneling in transverse direction is considered to be support for an anisotropic superconductor, in particular, $d_{x^2-y^2}$-wave.

Tunneling experiments have been performed for several surface orientations; some results were in agreement with the theoretical predictions above, others were in contradiction. Observations of the ZBCP are reported on (110) surfaces of Y123 (Alff et al. 1997, Wei et al. 1998), and also on (100) surfaces of Y123 (Kashiwaya et al. 1995a,b, Suzuki et al. 1999, Covington et al. 1996b, Wei et al. 1998) and (100) surfaces of La214 (S. Tanaka et al. 1995a,b). However, the ZBCP was not observed on (110) surfaces of Y123 by Nantoh et al. (1995), Kane et al. (1994) and Suzuki et al. (1999), and not observed on (110) surfaces of La214 by S. Tanaka et al. (1995a,b).

Tanuma et al. (1998) calculated the tunneling density of states on the uneven surface of d-wave superconductors and showed that their calculation reproduced various types of anomalous features observed in the actual tunneling experiments, such as ZBCP, double-peak and multiple-dip structures, and a suppressed superconducting gap. They claimed that the wide variety of experimental data showing these features are natural for anisotropic superconductors, and hence, should not be rejected as unidentified spectra observed on degraded surface or in "bad junctions" (Kashiwaya et al. 1994a).

6.2. *Josephson tunneling under magnetic field*

6.2.1. *Josephson tunneling across Y123/Pb junction in the ab-plane*

Several measurements have been performed to study the dependence of Josephson critical current flowing within the CuO_2 planes on applied magnetic field (i.e. Fraunhofer pattern) for a junction made of Y123 and Pb. These measurements have been proposed to determine whether the order parameter of Y123 has d-wave symmetry or not; the diffraction pattern should be dependent on the configuration of the junction, as shown in fig. 27. For a junction between two s-wave superconductors, or for an "edge" junction between d-wave and s-wave superconductors (fig. 27a), the diffraction pattern is normal

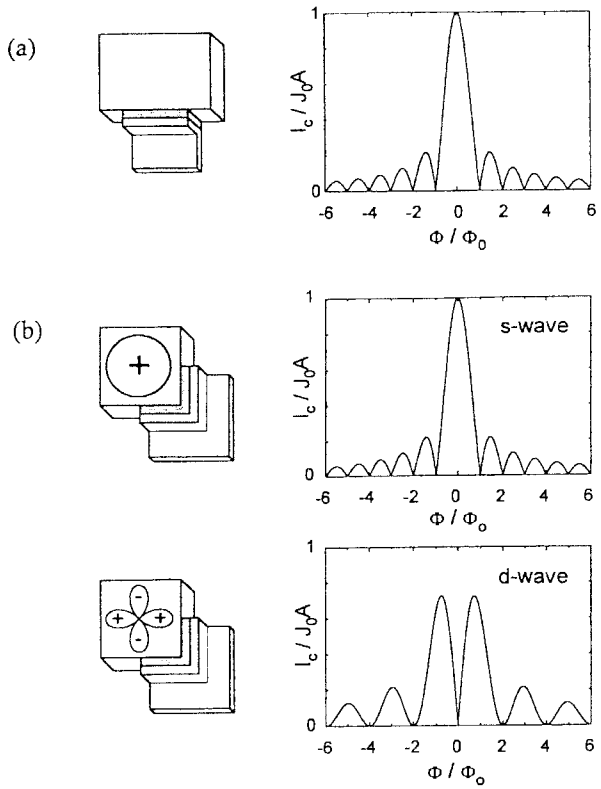

Fig. 27. (a) Fraunhofer diffraction pattern for the critical current vs magnetic flux threading the junction barrier that is characteristic of a single Josephson tunnel junction. (b) Diffraction patterns expected for a single corner junction with s-wave (isotropic or anisotropic) and $d_{x^2-y^2}$ pairing symmetry. After Wollman et al. (1995, fig. 1).

Fraunhofer-like. The Josephson critical current oscillates according to the following equation:

$$I_c(\Phi) = I_c \left| \frac{\sin(\pi\Phi/\Phi_0)}{\pi\Phi/\Phi_0} \right|, \tag{4}$$

where Φ_0 is the magnetic flux quantum. On the other hand, the corresponding expression for a "corner" junction (fig. 27b) between the s-wave and d-wave superconductors is

$$I_c(\Phi) = I_c \left| \frac{\sin^2(\pi\Phi/2\Phi_0)}{\pi\Phi/2\Phi_0} \right|. \tag{5}$$

Wollman et al. (1993, 1995) reported detailed measurements of the magnetic field dependence of the Josephson critical current for Y123/Au/Pb junctions formed on Y123 crystals. The observed results of the dependences for the edge junction and the corner junction are as shown in fig. 28. Double peak structures were seen for the corner junction, as expected from equation (5), indicating that Y123 is a d-wave superconductor.

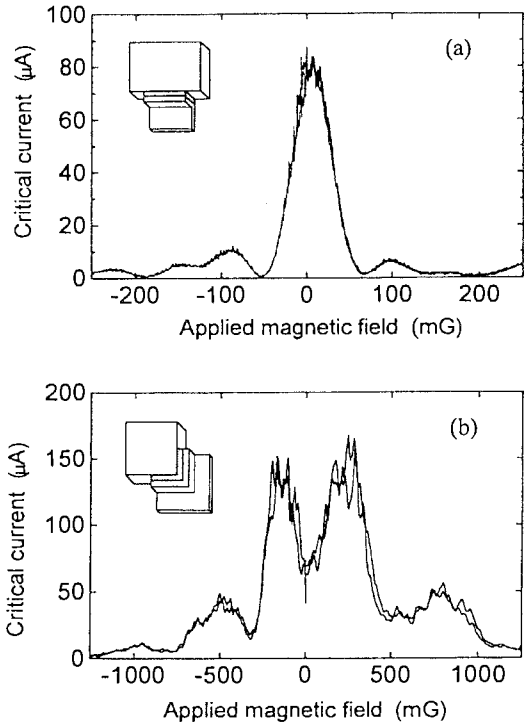

Fig. 28. Measured critical current vs. applied magnetic field for (a) an "edge" Y123/Pb junction and (b) a "corner" junction including *ab* faces. After Wollman et al. (1995, fig. 3).

When a trapped flux was present, the double peak structures were found to be deformed asymmetrically, which was attributed to a nonuniform magnetic field across the junction barrier.

Corner-junction experiments by other groups (Brawner and Ott 1994, Mathai et al. 1995, Miller et al. 1995) and tricrystal ring experiments (Tsuei et al. 1994, Kirtley et al. 1995) also provide evidence for d-wave pairing symmetry.

6.2.2. *Josephson tunneling across Y123/Pb junction along the c-axis*

Contrary to the results of phase-sensitive measurements involving current flowing within the CuO_2 planes, measurements of Josephson tunneling currents perpendicular to the CuO_2 planes between heavily twinned Y123 and a conventional s-wave superconductor (Sun et al. 1994, 1996, Katz et al. 1995, Lesueur et al. 1997, Kleiner et al. 1996) resulted in the observation of finite supercurrents, suggesting a significant s-wave component.

In order to elucidate this contradiction, Dynes and his group (Kouznetsov et al. 1997) measured the Josephson-pair tunneling current along the *c*-axis from conventional Pb superconductors across thin insulating layers into crystals or thin films of Y123. Pb is deposited across a single twin boundary of Y123 crystal, as shown in fig. 29.

A *c*-axis Josephson current is sensitive to the net phase difference with any d-wave component. The current flowing into the Pb electrode is the sum of the tunneling currents

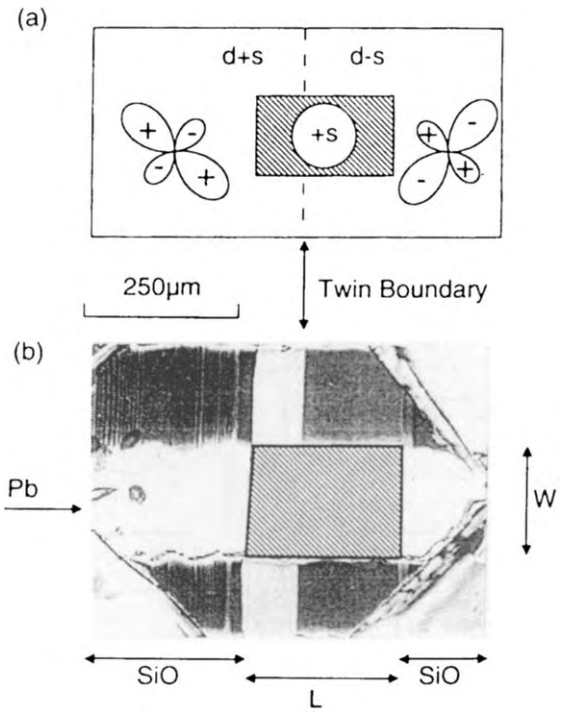

Fig. 29. (a) Schematic diagram of a Pb/Y123 junction (hatched region) grown across a twin boundary (dashed line). For the Y123 order parameter shown, the s-wave component changes sign across the boundary. (b) Nemarsky microscope photograph of junction. The twin boundary runs vertically through the center of the photograph; the Pb strip is the horizontal white region. After Kouznetsov et al. (1997, fig 1).

from each of the twin domains. If Y123 were predominantly d-wave, the phase of the $d_{x^2-y^2}$-wave order parameter should be maintained across the twin boundary, and the resulting wavefunction can be written as sums of a $d_{x^2-y^2}$-wave state and an s-wave state, specifically as d+s and d−s. Under the same assumption, the Josephson critical current is expected to be strongly dependent on the direction of the magnetic field applied within the plane because the s-component would change sign across the twin boundary.

Figure 30 shows the Josephson critical current measured under external fields along different directions. With the field perpendicular to the twin boundary ($\phi \approx \pm 90°$ in the figure), the plot of the critical current exhibited the same Fraunhofer pattern as observed in an ordinary junction, except for a lower peak current. With the field parallel to the boundary ($\phi = 0$), a dip rather than a peak appeared at zero field ($B = 0$), and the maximum current occurred at a field value corresponding to half-integer quantum flux, $\frac{1}{2}\phi_0$. These observations indicate that the flux cancels the phase difference between the two domains and causes a current flow in the same direction. These observations indicate that Y123 favors d-wave symmetry with some s-wave admixture.

6.2.3. *Splitting of zero-bias conductance peak in zero magnetic field*

The conductance peak near zero bias voltage (ZBCP) has been observed when tunneling takes place into *ab*-oriented Y123 thin films (Geerk et al. 1988, Lesueur et al. 1992,

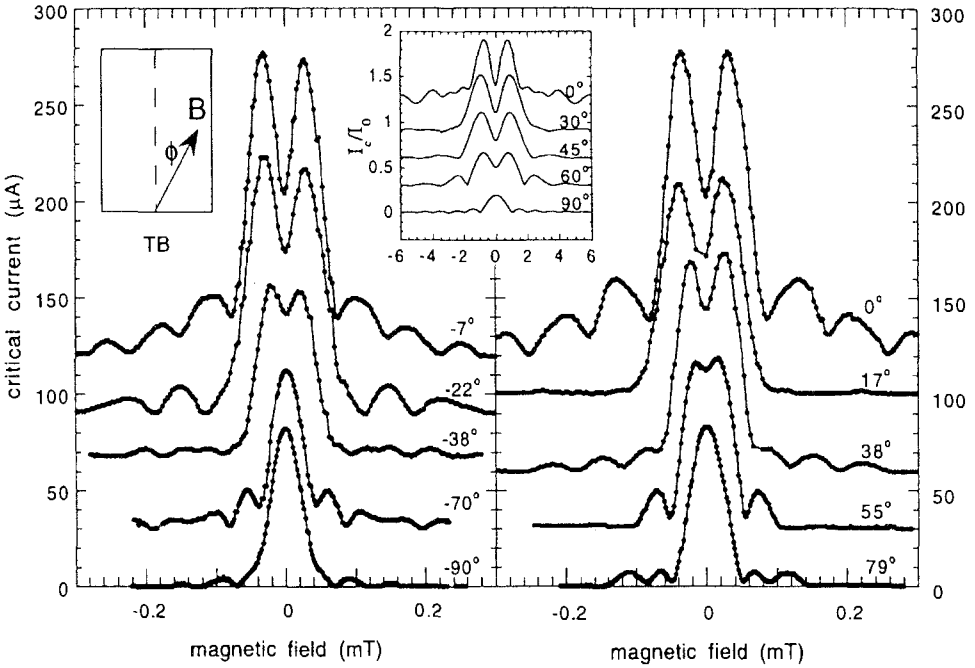

Fig. 30. The critical current $I_c(B)$ measured for ten values of angle ϕ relative to the twin boundary (TB) in Pb/Y123 junction. Successive plots are offset vertically by 30 μA. Center inset: Computed values of I_c/I_0 vs Φ/Φ_0 for a junction with sign reversal of the s-wave component. Successive plots are offset vertically by 0.3. After Kouznetsov et al. (1997, fig. 3).

Covington et al. 1996a). It was reported that the zero-bias conductance peak split when a magnetic field is applied (Lesueur et al. 1992); however, Covington et al. (1997) observed that the conductance peak split even when no magnetic field was applied, once the temperature was lowered below about 7 K, as shown in fig. 31.

In the experiment of Covington et al. (1997), Y123/insulator/Cu planar tunneling junctions were fabricated on Y123 *ab*-oriented thin films. It was found that the zero-bias conductance $G(0)=(\mathrm{d}I/\mathrm{d}V)|_{V=0}$ increased with decreasing temperature around 10 K, below which it decreased. The applied magnetic field induced further splitting that grew nonlinearly with increasing field. The field dependence of $G(0)$ showed significant discrepancy with the calculation based on spin-flip scattering due to the magnetic impurities proposed by Lesueur et al. (1992), as shown in the inset of fig. 31.

On the other hand, Covington et al. (1997) have claimed that the splitting of the ZBCP indicates a broken time-reversal symmetry state at the surface of Y123, where the Andreev bound state shifts to finite energy, resulting in a split of ZBCP (Fogelström et al. 1997, Matsumoto and Shiba 1996). The phase diagram for the broken time-reversal symmetry state calculated by Fogelström et al. (1997) was in good agreement with their results. The gap-like feature and ZBCP were observed at equal strength in the

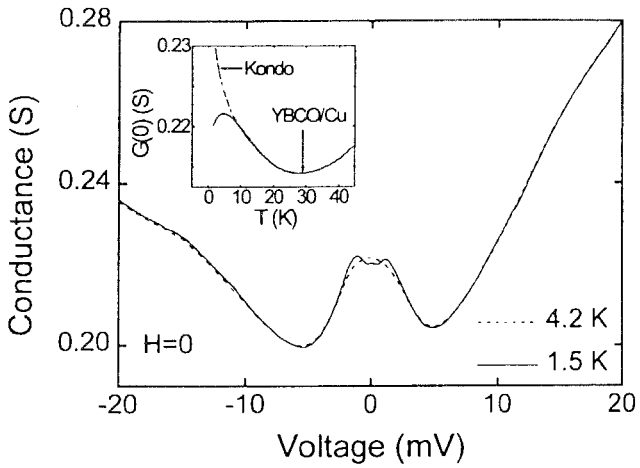

Fig. 31. Temperature-dependent conductance data from a Y123/Cu tunnel junction. Voltage is defined to be the voltage of Cu with respect to Y123. The ZBCP is observed to split in zero magnetic field at 1.5 K. Inset: zero-bias conductance, $G(0)$, versus temperature for the same junction, also in zero field. The downturn in $G(0)$ below 10 K is in contrast to the $G(0) \sim \ln(T)$ behavior expected from spin-flip scattering proposed by Lesueur et al. (1992), which is indicated by the dotted line. After Covington et al. (1997, fig. 1).

tunneling conductance for (100)- and (110)-oriented films, which indicates comparable pair breaking for both orientations; this suggests that s-wave is the most plausible subdominant gap symmetry.

7. Summary

Recent achievements in the tunneling study for cuprate superconductors are summarized as follows:

(1) In the high-temperature oxide superconductors, in particular Bi2212 and Tl2223, alternating stacking of superconducting and blocking layers is recognized as intrinsic Josephson junctions. Tunneling currents flowing through small junctions have been extensively investigated, indicating Josephson plasma excitation, characteristic for cuprate superconductors.

(2) Vacuum tunneling has been performed utilizing scanning tunneling microscope at low temperature. Removing the topmost surface by cleavage in vacuum or an inert gas atmosphere prior to tunneling measurements has been demonstrated to be indispensable to observe intrinsic superconducting gap structure in Bi2212.

The reported superconducting gap spectra have been analyzed in the framework of d-wave superconductivity. It has been found that results can be, in principle, described in terms of the d-wave order parameter.

(3) Hole doping and temperature dependence have been further investigated. Gap-like structures have been reported for underdoped Bi2212 samples above T_c. These

gap-like structures should be understood in accordance with the "pseudogap" observed in other types of measurements.

(4) Using STM, inner vortex structures of the differential conductance were successfully visualized for Bi2212 and Y123 crystals. The inner vortex excitation spectra are found to be quite different from those expected from a simple d-wave mechanism.

(5) Phase-sensitive measurements have been carried out for Y123 crystals with different orientations. Josephson tunneling at the interface between conventional and high-temperature superconductors has also been investigated. The observed tunneling spectra are highly dependent on geometry; some results agree with theoretical predictions from d-wave symmetry, while others do not. Better theoretical models, including the admixture of d-wave and s-wave order parameters, have been proposed.

Acknowledgement

We acknowledge the Japan Science and Technology (JST) corporation for supporting this work.

References

Alff, L., H. Takashima, S. Kashiwaya, N. Terada, H. Ihara, Y. Tanaka, M. Koyanagi and K. Kajimura, 1997, Phys. Rev. B **55**, 14757.

Alloul, P., T. Ohno and P. Mendels, 1989, Phys. Rev. Lett. **63**, 1700.

Anderson, P.W., 1987, Science **235**, 1196.

Anderson, P.W., and Z. Zou, 1988, Phys. Rev. Lett. **60**, 132.

Balatsky, A.V., and M.I. Salkola, 1996, Phys. Rev. Lett. **76**, 2386.

Balzarotti, A., M. de Crescenzi, F. Patella, A. Sgarlata, P. Paroli, G. Balestrino and M. Marinelli, 1991, Phys. Rev. B **43**, 11500.

Barbiellini, B., Ø. Fischer, M. Peter, Ch. Renner and M. Wegner, 1994, Physica C **220**, 55.

Basov, D.N., R. Liang, B. Dabrowski, D.A. Bonn, W.N. Hardy and T. Timusk, 1996, Phys. Rev. Lett. **77**, 4090.

Blonder, G., M. Tinkham and T. Klapwijk, 1982, Phys. Rev. B **25**, 4515.

Brawner, D.A., and H.R. Ott, 1994, Phys. Rev. B **50**, 6530.

Broekholt, M., T. Bollmeier, L. Buschmann, M. Fleuster and G. Güntherodt, 1992, Physica C **198**, 33.

Caroli, C., P.G. de Gennes and J. Matricon, 1964, Phys. Lett. **9**, 307.

Chang, A., Z.Y. Rong, Yu.M. Ivanchenko, F. Lu and E.L. Wolf, 1992, Phys. Rev. B **46**, 5692.

Covington, M., R. Scheuerer, K. Bloom and L. Greene, 1996a, Appl. Phys. Lett. **68**, 1717.

Covington, M., F. Xu, C. Feldmann and L. Greene, 1996b, Czech. J. Phys. **46**, 1341.

Covington, M., M. Aprile, E. Paraoanu and L. Greene, 1997, Phys. Rev. Lett. **79**, 277.

Ding, H., M.R. Norman, J.C. Campuzano, M. Randeria, A. Bellman, T. Yokoya, T. Takahashi, T. Mochiku and K. Kadowaki, 1996, Phys. Rev. B **54**, 9678.

Edwards, H.L., J.T. Markert and A.L. de Lozanne, 1992, Phys. Rev. Lett. **69**, 2967.

Edwards, H.L., A.L. Barr, J.T. Markert and A.L. de Lozanne, 1994a, Phys. Rev. Lett. **73**, 1154.

Edwards, H.L., J.T. Markert and A.L. de Lozanne, 1994b, J. Vac. Sci. Technol. B **12**, 1886.

Edwards, H.L., D.J. Derro, A.L. Barr, J.T. Markert and A.L. de Lozanne, 1995, Phys. Rev. Lett. **75**, 1387.

Emery, V.J., and S.A. Kivelson, 1995, Phys. Rev. Lett. **74**, 3253.

Flensberg, K., P. Hedegård and M. Pedersen, 1988, Phys. Rev. B **38**, 841.

Fogelström, M., D. Rainer and J.A. Sauls, 1997, Phys. Rev. Lett. **79**, 281.

Geerk, J., X. Xi and G. Linker, 1988, Z. Phys. B **73**, 329.

Hancotte, H., R. Deltour, D. Davydov, A. Jansen and P. Wyder, 1997, Phys. Rev. B **55**, 3410.

Harmer, M., C. Fincher and B. Parkinson, 1991, J. Appl. Phys. **70**, 2760.

Hasegawa, T., M. Nantoh, H. Ikuta and K. Kitazawa, 1991a, Physica C **185–189**, 1743.

Hasegawa, T., M. Nantoh and K. Kitazawa, 1991b, Jpn. J. Appl. Phys. **30**, L276.

Hasegawa, T., H. Ikuta and K. Kitazawa, 1992a, in: Physical Properties of High Temperature Superconductors. Vol. III, ed. D. Ginsberg (World Scientific, Singapore) p. 525.

Hasegawa, T., A. Takagi, H. Ikuta, M. Kawasaki, H. Koinuma and K. Kitazawa, 1992b, J. Phys. Chem. Solids **53**, 1643.

Hasegawa, T., M. Nantoh, S. Heike, A. Takagi, M. Ogino, M. Kawasaki, H. Koinuma and K. Kitazawa, 1993, J. Phys. Chem. Solids **54**, 1351.

Hawley, M., I.D. Raistrick, J.G. Beery and R.J. Houlton, 1991, Science **251**, 1587.

Helm, C., C. Preis, F. Forsthofer, J. Keller, K. Schlenga, R. Kleiner and P. Müller, 1997, Phys. Rev. Lett. **79**, 737.

Hess, H.F., R.B. Robinson, R.C. Dynes, J.M. Valles Jr and J.V. Waszczak, 1989, Phys. Rev. Lett. **62**, 214.

Himeda, A., M. Ogata, Y. Tanuma and S. Kashiwaya, 1997, J. Phys. Soc. Jpn. **66**, 3367.

Homes, C.C., T. Timusk, R. Liang, D.A. Bonn and W.N. Hardy, 1993, Phys. Rev. Lett. **71**, 1645.

Honcotte, H., D. Davydov, M. Ye and R. Deltour, 1995, Physica B **204**, 206.

Hu, C., 1994, Phys. Rev. Lett. **72**, 1526.

Hwang, H.Y., B. Batlogg, H. Takagi, H.L. Kao, J. Kwo, R.J. Cava, J.J. Krajewski and W.F. Peck Jr, 1994, Phys. Rev. Lett. **72**, 2636.

Ichimura, K., and K. Nomura, 1993, J. Phys. Soc. Jpn. **62**, 3661.

Ichioka, M., N. Hayashi, N. Enomoto and K. Machida, 1996, Phys. Rev. B **53**, 15316.

Ikuta, H., A. Maeda and K. Uchinokura, 1988, Jpn. J. Appl. Phys. **27**, L1039.

Ishida, K., Y. Kitaoka, N. Ogata, T. Kamino, K. Asayama, J.R. Cooper and N. Athanassopoulou, 1993, J. Phys. Soc. Japan **62**, 2803.

Johnston, D., 1989, Phys. Rev. Lett. **62**, 957.

Kane, J., and K.-W. Ng, 1996, Phys. Rev. B **53**, 2819.

Kane, J., Q. Chen, K.-W. Ng and H.-J. Tao, 1994, Phys. Rev. Lett. **72**, 128.

Kane, J., K.-W. Ng and D. Moecher, 1998, Physica C **294**, 176.

Kaneko, S., N. Nishida, T. Mochiku and K. Kadowaki, 1998, Physica C **298**, 105.

Kashiwaya, S., M. Koyanagi, H. Takashima, M. Matsuda and K. Kajimura, 1994a, in: Advances in Superconductivity. Vol. VI, eds T. Fujita and Y. Shiohara (Springer, Tokyo) p. 73.

Kashiwaya, S., M. Koyanagu, M. Matsuda and K. Kajimura, 1994b, Physica B **194–196**, 2119.

Kashiwaya, S., Y. Tanaka, M. Koyanagi, H. Takashima and K. Kajimura, 1995a, J. Phys. Chem. Solids **56**, 1721.

Kashiwaya, S., Y. Tanaka, M. Koyanagi, H. Takashima and K. Kajimura, 1995b, Phys. Rev. B **51**, 1350.

Kashiwaya, S., Y. Tanaka, M. Koyanagi and K. Kajimura, 1996, Phys. Rev. B **53**, 2667.

Katz, A.S., A.G. Sun, R.C. Dynes and K. Char, 1995, Appl. Phys. Lett. **66**, 105.

Kawasaki, M., and M. Nantoh, 1994, MRS Bulletin **XIX**, 33.

Kendziora, C., and A. Rosenberg, 1994, Physica C **235–240**, 1121.

Kirk, M., J. Nogami, A. Baski, D.B. Mitzi, A. Kapitulnik, T.H. Geballe and C. Quate, 1988, Science **242**, 1673.

Kirtley, J.R., and D.J. Scalapino, 1990, Phys. Rev. Lett. **65**, 798.

Kirtley, J.R., C.C. Tsuei, J.Z. Sun, C.C. Chi, L.S. Yu-Jahnes, A. Gupta, M. Rupp and M.B. Ketchen, 1995, Nature **373**, 225.

Kitazawa, K., H. Sugawara and T. Hasegawa, 1996, Physica C **263**, 214.

Kleiner, R., and P. Müller, 1994, Phys. Rev. B **49**, 1327.

Kleiner, R., F. Steinmeyer, G. Kunkel and P. Müller, 1992, Phys. Rev. Lett. **68**, 2394.

Kleiner, R., A.S. Katz, A.G. Sun, R. Summer, D.A. Gajewski, S.H. Han, S.I. Woods, E. Dantsker, B. Chen, K. Char, M.B. Maple, R.C. Dynes and J. Clarke, 1996, Phys. Rev. Lett. **76**, 2161.

Kouznetsov, K.A., A.G. Sun, B. Chen, A.S. Katz, S.R. Bahcall, J. Clarke, R.C. Dynes, D.A. Gajewski, S.H. Han, M.B. Maple, J. Giapintzakis, J.-T. Kim and D.M. Ginsberg, 1997, Phys. Rev. Lett. **79**, 3050.

Lang, H., T. Frey and H.-J. Güntherodt, 1991, Europhys. Lett. **15**, 667.

Lesueur, J., L. Greene, W. Feldmann and I. Inam, 1992, Physica C **191**, 325.

Lesueur, J., M. Aprili, A. Goulan, T. Horton and L. Dumoulin, 1997, Phys. Rev. B **55**, 3398.

Liu, J., Y. Li and C. Lieber, 1994, Phys. Rev. B **49**, 6234.

Liu, J.-X., J.-C. Wan, A. Goldman, Y.C. Chang and P.-Z. Jiang, 1991, Phys. Rev. Lett. **67**, 2195.

Loeser, A.G., Z.-X. Shen, D.S. Dessau, C.-H. Park, P. Fournier and A. Kapitulnik, 1996, Science **273**, 325.

Loram, J.W., K.A. Mirza, J.R. Cooper and W.Y. Liang, 1993, Phys. Rev. Lett. **71**, 1740.

Loram, J.W., K.A. Mirza, J.R. Cooper, W.Y. Liang and J.M. Wade, 1994, J. Supercond. **7**, 243.

Maggio-Aprile, I., Ch. Renner, A. Erb, E. Walker and Ø. Fischer, 1995, Phys. Rev. Lett. **75**, 2754.

Maki, K., Y. Sun and H. Won, 1996, Czech. J. Phys. **46**(Suppl. 6), 3151.

Mallet, P., D. Roditchev, W. Sacks, D. Défourneau and J. Klein, 1996, Phys. Rev. B **54**, 13324.

Manabe, C., M. Oda and M. Ido, 1994, Physica C **235–240**, 797.

Manabe, C., M. Oda and M. Ido, 1997, J. Phys. Soc. Jpn. **66**, 1776.

Mandrus, D., J. Hartge, C. Kendziora, L. Mihaly and L. Forro, 1993, Europhys. Lett. **22**, 199.

Mathai, A., Y. Gim, R. Black, A. Amar and F. Wellstood, 1995, Phys. Rev. Lett. **74**, 4523.

Matsuda, A., S. Sugita and T. Watanabe, 1999, Phys. Rev. B **60**, 1377.

Matsumoto, M., and H. Shiba, 1996, J. Phys. Soc. Jpn. **65**, 2194.

Matsumoto, T., S. Choopun and T. Kawai, 1995, Phys. Rev. B **52**, 591.

Matsuura, S., T. Taneda, W. Yamaguchi, H. Sugawara, T. Hasegawa and K. Kitazawa, 1998, Physica C **300**, 26.

Miller, J., Q. Ying, Z. Zou, N. Fan, J. Xu, M. Davis and J. Wolfe, 1995, Phys. Rev. Lett. **74**, 2347.

Miller, T., M. McElfresh and R. Reifenberger, 1993, Phys. Rev. B **48**, 7499.

Miyakawa, N., P. Guptasarma, J. Zasadzinski, D. Hinks and K. Gray, 1998, Phys. Rev. Lett. **80**, 157.

Momono, N., R. Dipasupil, H. Ishiguro, S. Saigo, T. Nakano, M. Oda and M. Ido, 1999, Physica C **317–318**, 603.

Moreland, J., P. Rice, S. Russek, B. Jeanneret, A. Roshko, R. Ono and D. Rudman, 1991, Appl. Phys. Lett. **59**, 3039.

Moriya, Y., M. Kohmoto and K. Maki, 1997, Phys. Rev. Lett. **78**, 4841.

Muenchausen, R., M. Hawley, S.R. Foltyn, X. Wu, R. Dye and F. Garzon, 1992, Physica C **199**, 445.

Murakami, H., and R. Aoki, 1995, J. Phys. Soc. Jpn. **64**, 1287.

Nagaosa, N., and P.A. Lee, 1990, Phys. Rev. Lett. **64**, 2450.

Nakamura, T., and S. Uchida, 1993, Phys. Rev.B **47**, 8369.

Nakano, T., M. Oda, C. Manabe, N. Momono, Y. Miura and M. Ido, 1994, Phys. Rev. B **49**, 16000.

Nantoh, M., S. Heike, H. Ikuta, T. Hasegawa and K. Kitazawa, 1991, Physica C **185–189**, 861.

Nantoh, M., T. Hasegawa, W. Yamaguchi, A. Takagi, M. Ogino, M. Kawasaki, J. Gong, H. Koinuma and K. Kitazawa, 1994, J. Appl. Phys. **75**, 5227.

Nantoh, M., M. Kawasaki, T. Hasegawa, K. Fujito, W. Yamaguchi, H. Koinuma and K. Kitazawa, 1995, Physica C **242**, 277.

Narlikar, A., P. Dutta, S. Samanta, O. Srivastava, P. Ramasamy, S. Sabharwal, M. Gupta and B. Padalia, 1992, J. Cryst. Growth **116**, 37.

Narlikar, A., S. Samanta, C. Changkang, H. Yongle, J. Hodby and B. Wanklyn, 1996, J. Cryst. Growth **158**, 248.

Nishikawa, T., J. Takeda and M. Sato, 1994, J. Phys. Soc. Jpn. **63**, 1441.

Oda, M., C. Manabe and M. Ido, 1996, Phys. Rev. B **53**, 2253.

Oda, M., K. Hoya, R. Kubota, C. Manabe, N. Momono, T. Nakano and M. Ido, 1997a, Physica C **281**, 135.

Oda, M., K. Hoya, R. Kubota, C. Manabe, N. Momono, T. Nakano and M. Ido, 1997b, Physica C **282–287**, 1499.

Panagopoulos, C., and T. Xiang, 1998, Phys. Rev. Lett. **81**, 2336.

Renner, Ch., and Ø. Fischer, 1995, Phys. Rev. B **51**, 9208.

Renner, Ch., A. Kent, P. Niedermann, Ø. Fischer and F. Lévy, 1991, Phys. Rev. Lett. **67**, 1650.

Renner, Ch., Ø. Fischer, A. Kent, D.B. Mitzi and A. Kapitulnik, 1994, Physica B **194**, 1689.

Renner, Ch., B. Revaz, J.-Y. Genoud, K. Kadowaki and Ø. Fischer, 1998a, Phys. Rev. Lett. **80**, 149.

Renner, Ch., B. Revaz, K. Kadowaki, I. Maggio-Aprile and Ø. Fischer, 1998b, Phys. Rev. Lett. **80**, 3606.

Rossat-Mignod, J., L.P. Regnault, C. Vettier, P. Burlet, J.Y. Henry and G. Lapertot, 1991, Physica B **169**, 58.

Salkola, M.I., A.V. Balatsky and D.J. Scalapino, 1996, Phys. Rev. Lett. **77**, 1841.

Schlenga, K., G. Hechtfischer, R. Kleiner, W. Walkenhorst, P. Müller, H. Johnson and E. Steinbeiß, 1996, Phys. Rev. Lett. **76**, 4943.

Schlenga, K., R. Kleiner, G. Hechtfischer, M. Mößle, S. Schmitt, P. Müller, C. Helm, C. Preis,

F. Forsthofer, J. Keller, H. Johnson, M. Veith and E. Steinbeiß, 1998, Phys. Rev. B **57**, 14518.
Schlesinger, Z., 1994, Physica C **235–240**, 49.
Schopohl, N., and K. Maki, 1995, Phys. Rev. B **52**, 490.
Shih, C., R. Feenstra, J. Kirtley and G. Chandrashekhar, 1988, Phys. Rev. B **40**, 2682.
Slakey, F., M.V. Klein, J.P. Rice and D.M. Ginsberg, 1990, Phys. Rev. B **42**, 2643.
Sugawara, H., M. Nantoh, T. Hasegawa and K. Kitazawa, 1996, in: Studies on High Temperature Superconductors, Vol. 20 (Nova Science Publishers, New York) pp. 1–39.
Sun, A.G., D.A. Gajewski, M.B. Maple and R.C. Dynes, 1994, Phys. Rev. Lett. **72**, 2267.
Sun, A.G., A. Truscott, A.S. Katz, R.C. Dynes, B. Veal and C. Gu, 1996, Phys. Rev. B **54**, 6734.
Suzuki, K., K. Ichimura, K. Nomura and S. Takekawa, 1999, J. Phys.: Condens. Matter **11**, 3133.
Suzumura, Y., Y. Hasegawa and H. Fukuyama, 1988, J. Phys. Soc. Jpn. **57**, 1278.
Tajima, S., J. Schutzmann, S. Miyamoto, I. Terasaki, Y. Sato and R. Hauff, 1996, Phys. Rev. B **55**, 6051.
Takagi, H., B. Batlogg, H.L. Kao, J. Kwo, R.J. Cava, J.J. Krajewski and W.F. Peck Jr, 1992, Phys. Rev. Lett. **69**, 2975.
Tallon, J.L., J.R. Cooper, P. de Silva, G. Williams and J.W. Loram, 1995, Phys. Rev. Lett. **75**, 4114.
Tanabe, K., Y. Hidaka, S. Karimoto and M. Suzuki, 1996, Phys. Rev. B **53**, 9348.
Tanaka, S., E. Ueda, M. Sato, K. Tamasaku and S. Uchida, 1995a, J. Phys. Soc. Jpn. **64**, 1476.
Tanaka, S., E. Ueda, M. Sato, K. Tamasaku and S. Uchida, 1995b, J. Phys. Soc. Jpn. **65**, 2212.
Tanaka, Y., and S. Kashiwaya, 1995, Phys. Rev. Lett. **74**, 3451.
Tanuma, Y., Y. Tanaka, M. Yamashiro and S. Kashiwaya, 1998, Phys. Rev. B **57**, 7977.
Tsai, J., I. Takeuchi, J. Fujita, S. Miura, T. Terashima and Y. Bando, 1989, Physica C **157**, 537.
Tsuei, C.C., J.R. Kirtley, C.C. Chi, L.S. Yu-Jahnes, A. Gupta, T. Shaw, J.Z. Sun and M.B. Ketchen, 1994, Phys. Rev. Lett. **73**, 593.
Ueda, E., S. Tanaka, M. Sato, K. Tamasaku and S. Uchida, 1995, Physica C **249**, 181.
Valles Jr, J.M., R.C. Dynes, A.M. Cucolo, M. Gurvitch, L.F. Schneemeyer, J.P. Garno and J.V. Waszczak, 1991, Phys. Rev. B **44**, 11986.
Varma, C.M., P.B. Littlewood, S. Schmitt-Rink, E. Abrahams and A.E. Ruckenstein, 1989, Phys. Rev. Lett. **63**, 1996.
Wang, C., B. Giambattista, C. Slough, R. Coleman and M. Subramanian, 1990, Phys. Rev. B **42**, 8890.
Wei, J., N.-C. Yeh, D. Garrigus and M. Strasik, 1998, Phys. Rev. Lett. **81**, 2542.
Wolf, E.L., A. Chang, Z.Y. Rong, Yu.M. Ivanchenko and F. Lu, 1994, J. Supercond. **7**, 355.
Wollman, D.A., D.J. van Harlingen, W.C. Lee, D.M. Ginsberg and A.J. Leggett, 1993, Phys. Rev. Lett. **71**, 2134.
Wollman, D.A., D.J. van Harlingen, J. Giapintzakis and D.M. Ginsberg, 1995, Phys. Rev. Lett. **74**, 797.
Won, H., and K. Maki, 1996, J. Phys. I **6**, 2317.
Wu, X., Z. Zhang, Y. Wang and C. Lieber, 1990, Science **248**, 1211.
Wu, X., Y. Wang, Z. Zhang and C. Lieber, 1991, Phys. Rev. B **43**, 8729.
Yasuoka, H., T. Imai and T. Shimizu, 1989, in: Strong Correlations and Superconductivity, eds H. Fukuyama, S. Maekawa and A.P. Malozemoff (Springer, Berlin) p. 254.
Yurgens, A., D. Winkler, N. Zavaritsky and T. Claeson, 1996, Phys. Rev. B **53**, 8887.

SUBJECT INDEX